
Sādhana

(Academy Proceedings in Engineering Sciences)

Volume 20

1995

Published by the Indian Academy of Sciences
Bangalore 560 080

Sādhana

Academy Proceedings in Engineering Sciences

(Volumes 1–6 published as Proceedings of the Indian Academy of Sciences,
Engineering Sciences)

Editor

N Viswanadham

Indian Institute of Science, Bangalore

Associate Editor

G Prathap

National Aerospace Laboratories, Bangalore

Editorial Board

D Banerjee, *Defence Metallurgical Research Laboratory, Hyderabad*

I Chopra, *University of Maryland, College Park, MD*

B L Deekshatulu, *National Remote Sensing Agency, Hyderabad*

S C Dutta Roy, *Indian Institute of Technology, New Delhi*

Y Jaluria, *Rutgers University, New Brunswick, NJ*

K Kasturirangan, *Department of Space, Bangalore*

B D Kulkarni, *National Chemical Laboratory, Pune*

R Narayana Iyengar, *Central Building Research Institute, Roorkee*

M A Pai, *University of Illinois, Urbana-Champaign, IL*

P Ramachandra Rao, *National Metallurgical Laboratory, Jamshedpur*

V U Reddy, *Indian Institute of Science, Bangalore*

R K Shyamasundar, *Tata Institute of Fundamental Research, Bombay*

J Srinivasan, *Indian Institute of Science, Bangalore*

S P Sukhatme, *Indian Institute of Technology, Bombay*

C E Veni Madhavan, *Indian Institute of Science, Bangalore*

M Vidyasagar, *Centre for Artificial Intelligence and Robotics, Bangalore*

Editor of Publications of the Academy

V K Gaur

CSIR Centre for Mathematical Modelling and Computer Simulation, Bangalore

Subscription Rates (Effective from 1996)

All countries except India

(Price includes AIR MAIL charges)

Institutional

US\$100

Individuals

US\$40

India

Rs. 150

Rs. 75

All correspondence regarding subscription should be addressed to **The Circulation Department** of the Academy.

Editorial Office

Indian Academy of Sciences, C V Raman Avenue

P.B. No. 8005, Sadashivanagar

Bangalore 560 080, India

Telephone: (080) 3342546

Telex: 0845-2178 ACAD IN

Telefax: 91-80-3346094

© 1995 by the Indian Academy of Sciences. All rights reserved.

“Notes on the preparation of papers” are printed in the last issue of every volume.

Sādhana

Academy Proceedings in Engineering Sciences

Volume 20, 1995

CONTENTS

Estimation of the order of an auto-regressive model <i>N Sudarshan Rao and P S Moharir</i>	749-758
Surface characterization and parameter estimation for industrial vision system <i>S Jagdish, Prabir K Biswas, Jayanta Mukherjee and B N Chatterji</i>	759-780
High temperature effects in hypersonic flows <i>Dinesh K Prabhu</i>	781-814
Trends in radar absorbing materials (RAM) technology <i>K J Vinoy and R M Jha</i>	815-850
Growth and development of <i>Thiobacillus ferrooxidans</i> for engineering applications <i>Sanghamitra Mukhopadhyay and K A Natarajan</i>	851-869
Three-dimensional vortex flow field around a circular cylinder in a quasi-equilibrium scour hole <i>Subhasish Dey</i>	871-885
Studies in multigrid acceleration of some equations of interest in fluid dynamics <i>J P Singh</i>	887-914
Numerical simulation of a 2-D jet-crossflow interaction related to film cooling applications: Effects of blowing rate, injection angle and free-stream turbulence <i>S Sarkar and T K Bose</i>	915-935
Development of picosecond time resolution optical and X-ray streak cameras <i>V N Rai, M Shukla, H C Pant and D D Bhawalkar</i>	937-954
Steady flow simulation in irrigation canals <i>Rajeev Misra</i>	955-969
Errata	971
Special Issue on Integrity of Engineering Components	
Foreword <i>P Ramachandra Rao</i>	1-3
Non-destructive testing and evaluation for structural integrity <i>Baldev Raj, T Jayakumar and B P C Rao</i>	5-38
Residual stresses of types II and III and their estimation <i>P Kesavan Nair and R Vasudevan</i>	39-52
Creep crack growth in power plant materials <i>Parmeet S Grover and Ashok Saxena</i>	53-85
Remaining life assessment of high temperature components using threshold stress concept <i>Raghubir Singh</i>	87-101

Multiaxial fatigue – An overview	<i>V M Radhakrishnan</i>	103–122
High temperature low cycle fatigue	<i>P Rodriguez and S L Mannan</i>	123–164
Stress corrosion cracking and component failure: Causes and prevention	<i>U K Chatterjee</i>	165–184
Mathematical modelling of creep/environment interactions	<i>B F Dyson and S Osgerby</i>	185–198
The effect of hydrogen induced cracking on the integrity of steel components	<i>Indranil Chatteraj</i>	199–211
Weldability and weld joint failures	<i>M N Chandrasekharaiah</i>	213–232
Application of fracture mechanics for weld integrity assessment	<i>V R Ranganath and S Tarafder</i>	233–246
Studies on fatigue crack growth for airframe structural integrity applications	<i>R Sunder</i>	247–285
Mechanisms and modelling of creep in superalloys	<i>M McLean, L M Pan and R N Ghosh</i>	287–300
Life assessment technology for fossil power plants	<i>R Viswanathan</i>	301–329
Creep life extension of high temperature components under wall thinning conditions	<i>R N Ghosh, S Chaudhuri, N Roy and L Chattopadhyay</i>	331–339
Special Issue on Advances in Nonlinear Problems in Structural Dynamics		
Foreword	<i>R N Iyengar</i>	341–343
Methods of nonlinear random vibration analysis	<i>C S Manohar</i>	345–371
Higher order averaging method of coefficients in Fokker–Planck equation	<i>Nguyen Dong Anh</i>	373–387
Transient and stationary response statistics of Van der Pol oscillators subjected to broad band random excitation	<i>A Naess and B K Hegstad</i>	389–402
Random excitation of nonlinear elastic structures with internal resonances	<i>R A Ibrahim and B H Lee</i>	403–426
Nonlinear deterministic and random response of shallow shells	<i>R Heuer, H Irschik and F Ziegler</i>	427–439
Homology design of vibration mode shape under uncertain boundary conditions	<i>Shigeru Nakagiri and Nobuhiro Yoshikawa</i>	441–450
Effects of distributed delays on the stability of structures under seismic excitation and multiplicative noise	<i>Karmeshu and Henri Schurz</i>	451–474
Stochastic control of hysteretic structural systems	<i>Yoshiyuki Suzuki</i>	475–488
Active control of non-stationary response of a two-degree of freedom vehicle model with nonlinear suspension	<i>G V Raju and S Narayanan</i>	489–499

Nonlinear dynamics of offshore structures under sea-wave and earthquake forces	<i>K Venkataramana and Kenji Kawano</i>	501–512
Stochastic response of guyed tower under second-order wave force	<i>T K Datta, R S Bisht and A K Jain</i>	513–527
Chaos in mechanical systems: A review	<i>P Sekar and S Narayanan</i>	529–582
Some aspects of chaotic and stochastic dynamics for structural systems	<i>N Sri Namachchivaya, M M Doyle and N Malhotra</i>	583–613
Analysis of nonlinear structural dynamics by the concept of stability measure	<i>W Schiehlen and B Hu</i>	615–626
Dynamical behaviour of a friction oscillator with simultaneous self and external excitation	<i>K Popp, N Hinrichs and M Oestreich</i>	627–654
Computation of the Kolmogorov entropy for MDOF systems	<i>F Bontempi and F Casciati</i>	655–669
Non-periodic flutter of a buckled composite panel	<i>Naresh K Chandiramani, Raymond H Plaut and Liviu I Librescu</i>	671–689
Coupled in-line and transverse flow-induced structural vibration: Higher order harmonic solutions	<i>R Ghanem, P Spanos and S Swerdon</i>	691–707
Analysis of the equations of motion of linearized controlled structures	<i>Fai Ma</i>	709–719
On refined nonlinear theories of laminated composite structures with piezoelectric laminae	<i>J N Reddy and J A Mitchell</i>	721–747
Subject Index		973–978
Author Index		979–981

Integrity of Engineering Components

Foreword

Engineering components are subjected to varieties of stress as well as environmental conditions while in service. This introduces, with passage of time, a process of degeneration of the components and therefore may not permit their further use. Such components may be part of a power plant, off-shore structure, refinery, aircraft or automobile, rolling mill or even of a large machine with weldings, and so on. The designer, by anticipating some of the service conditions, may be able to prescribe the component for a stipulated period of service. In real-life, however, a number of imponderables offset the calculations thereby shortening the expected design-life. Furthermore, a design, by convention, uses a factor-of-safety term that indeed may be making a component less competitive techno-economically and be providing a "life expectation" that is too conservative.

Both retiring a component 'too early' or 'too late' force a penalty which may be quite high. For example, retiring a costly power plant component too early would be uneconomical while not replacing it at the appropriate time might result in sudden failures and outages which would eventually be not only uneconomical but also lead to casualties and litigation in some cases. Therefore, an evaluation of integrity of components is considered very useful and pragmatic in the present highly competitive industrial scenario with emphasis on quality and safety. The case for integrity evaluation is further strengthened when consideration is also given to an extension of 'useful life' leading to cost effectiveness. The latter is only possible when the health and integrity of critical components are accurately established.

The above issues assume great importance in view of the fact that a large proportion of power, petroleum and chemical plants, the world over, have been in operation for very long. Critical components in many of them have indeed outlived their design lives and decisions regarding their continuance are overdue. This is particularly true in India, where prohibitive costs of replacement, unwillingness on the part of owners to venture into substitution or retrofitting, and a lethargy of attitude, have all contributed to delays. An enhanced level of information and knowledge on the integrity evaluation techniques, if properly disseminated, will bring about a change in the prevailing climate.

Significantly, the theme of integrity evaluation combines both a high level of theoretical analysis and field application. There are, for example, several techniques of NDT (viz. magneto-acoustic emission, ultrasonics using attenuation and resonance, special eddy current testings etc.) that are strongly based on high science/technology and have been very useful to the shop floor operator as well, in recent times.

Simultaneously, physics-based understanding of behaviour of materials under specific service conditions (i.e. creep, fatigue, their interaction and so on) has helped analyse the behaviour of plant materials and components. This has extended the horizon of candidate materials while contributing to improved plant performance.

Taking all these into account it was felt by the editors of '*Sadhana*' that a special issue on the integrity aspects of industrial components would be very timely. A number of experts, drawn from various specialised disciplines from India and abroad, have contributed articles to this issue. It will perhaps be appreciated that the area of component integrity is so wide in its scope that it could easily fill-in several thick volumes. What has, however, been attempted within the confines of one issue of '*Sadhana*', is to provide an insight into the various broad generic areas and address important issues relating to component integrity.

At the very root of integrity-evaluation of any component, lies an estimate of the nature and quantum of damage accumulated either in service or during manufacture/assembly. More often than not, one is not allowed to perform "destructive" tests in many of these situations. Therefore, the first article deals with various non-destructive methods used in component integrity evaluation particularly emphasizing the newer but established techniques.

Any industrial component would normally experience some 'applied stress' in operation – the nature could be monotonic or cyclic. However, presence of any residual stress in the component, along with the applied one, would very much affect its real-life behaviour and performance. Hence, the second and third articles discuss the varieties of residual stresses – their origin, nature and evaluation techniques. The environment under which a component works, primarily affects its performance, health and thus the integrity. A number of articles, covering different aspects of stress corrosion and hydrogen embrittlement, as well as the modelling of various environment conditions have also been included.

Any modern industrial operation would involve joining of parts through welding. This is a very broad area and in its own right has the potential to cover a full issue of any standard journal. However, the two articles on welding primarily deal with weld joint failures and application of fracture toughness concepts to life prediction.

A large number of power plant components, in particular, operate at high (400°C) temperatures and simultaneously under pressure. This would place them under 'creep' conditions and without a knowledge-base of the creep behaviour of metallic materials it would not be possible even to design, let alone establish the integrity of these components (e.g. boiler tubes, headers, economisers, super heaters and so on). A set of papers on creep deal with various general aspects of creep life prediction as well as with the emerging concepts of creep crack growth.

Components in a variety of machines, automobiles and aircraft experience fluctuating stress conditions during operation, and therefore demand consideration of fatigue for design and for damage estimation in service. Again, superimposed with temperature, the connotations of fatigue will change. Hence, the articles on fatigue address both high- and low-temperature situations; further they also dwell on low-cycle fatigue, which is experienced by line-pipes and components in a power plant apart from other industrial components.

Finally, the section on applications deals with several specific situations and components. The basic and generic concepts and their utility in engineering components are discussed here through a number of articles.

The guest editors of this issue would like to express their appreciation to the Editorial Board of '*Sadhana*' for the opportunity given for this compilation, for undertaking the publication of this issue and, above all, for all the guidance and cooperation at all stages of preparing the manuscript. The spontaneous and generous coöperation received from all the authors is gratefully acknowledged.

February 1995

P RAMACHANDRA RAO
O N MOHANTY
Guest Editors



Non-destructive testing and evaluation for structural integrity

BALDEV RAJ, T JAYAKUMAR and B P C RAO

Division for PIE & NDT Development, Indira Gandhi Centre for Atomic Research, Kalpakkam 603 102, India

Abstract. Reliable performance of a component or structure depends on pre-service quality of the component and in-service degradation of the component under operating conditions. The role of non-destructive evaluation (NDE) in ensuring pre-service quality and also monitoring in-service degradation to avoid premature failure of the components/structures is ever increasing. There are many NDE techniques based on various physical principles. The end objective of NDE is detection and characterisation of anomalies such as defects, stresses and microstructural degradations in materials. This is accomplished by establishing correlation between a non-destructively measured physical/derived parameter and quantitative information on defects/stresses/microstructures. The NDE information together with design parameters are taken into consideration for evaluation of integrity and life assessment of the components/structures. In this paper, a brief description of the physical concepts of NDE methods and the physical/derived parameters that are used for assessing defects, stresses and microstructures are given. A few case studies highlighting the importance of non-destructive testing and evaluation for structural integrity assessment are also discussed based on the investigations carried out at the authors' laboratory. Emerging concepts like intelligent processing of materials, expert systems, neural networks, use of multisensors with fusion of data and exploitation of signal analysis and imaging approaches are also addressed in this paper.

Keywords. Non-destructive evaluation; structural integrity; life assessment; defects; stresses; microstructures.

1. Introduction

Assessment of integrity of engineering components and structures is becoming increasingly important for both economic and safety reasons. It is now widely accepted that all components and structures possess "defects" from the start of their service life (this forms an important and initial assumption in fracture mechanics) and that defect assessment is the way to control structural integrity reliably. Defects are those anomalies which when not removed or repaired might lead to ultimate loss of structural integrity of the material or component. Such defects include surface and

sub-surface cracks, inclusions, pores, incompletely joined regions in welds or other joints and residual stresses, macro- or microstructural degradations etc. in metallic materials and delaminated or debonded regions, fibre fracture, matrix crazing etc. in composites. While surface defects are of immediate concern, due consideration is also to be given to sub-surface defects and other anomalies. In either case, it is important to understand the factors that govern the likely growth of defects/anomalies or cracks originating from them. In particular the size of the defect, its nature, its location, the stress to which it is subjected and the local properties of the material in which it is embedded, all play a major role in determining its rate of growth (Silk & Whaphan 1989). According to fracture mechanics, defects present in materials lead to failure by growing to a critical, self-propagating size. The fracture mechanics concepts allow one to calculate the critical sizes of defects as a function of their depth, length, active stress system and stress intensity and such properties of the material as its elastic modulus, yield strength and fracture toughness (David 1981). On the other hand, by knowing the dimensions of defects present in a component, it is possible to estimate both remaining life of the component and extent of degradation.

In the pre-service scenario, defects may be present at the raw material stage or might have been introduced during machining, fabrication, heat treatment and assembling. Similarly, defects may be generated due to deterioration of the material/component/structure as a result of one or a combination of operating conditions like temperature, stress, chemical environment and irradiation leading to mechanisms such as creep, fatigue, stress corrosion, embrittlement etc. These mechanisms result in deterioration of mechanical properties, crack initiation and propagation, leaks in pressurised components and catastrophic failures. Hence, reliable performance of a component/structure depends on the pre-service quality and in-service degradation of the component under operating conditions. The pre-service quality can be achieved by good engineering practices i.e. by way of selecting suitable quality raw materials and ensuring that harmful defects are not produced during the subsequent stages of fabrication and assembly. In-service degradation of the component can be assessed by quantitative characterisation of anomalies such as defects, stresses and micro-structural degradations. Their early detection and assessment is essential to avoid damage and loss of structural integrity of components. In this regard, non-destructive evaluation (NDE) plays an important role for the reliable assessment of the anomalies by performing inspections at various stages. To give an example, the acoustic emission technique is used for detection of initiation or propagation of any microcracks, and also any fluid leakage at inaccessible locations, by picking up signals from accessible locations. Using this technique, on-line monitoring of critical components and structures can give advance warning before occurrence of an accident or catastrophe due to material degradation under service conditions.

There are many non-destructive test (NDT) techniques based on various physical principles. The interaction of a medium (like electromagnetic radiation, sound waves) with various types of anomalies present in a material under study are used to quantitatively assess structural integrity. NDE procedures involve establishing correlations between non-destructively measured physical/derived parameters and quantitative information about anomalies. To give an example, eddy-current NDT involves measurement of change impedance and determination of its correlation with anomalies such as change in electrical conductivity or microstructure, or the presence of a crack. These correlations, together with design parameters and inputs from fracture mechanics,

are taken into consideration for integrity and life assessment of the component. It should be emphasised that anomaly assessment information by NDE techniques is more meaningful when applied together with expertise from other related disciplines such as metallurgy, corrosion, fracture mechanics, stress analysis, design and operation. This approach enables evaluation of the degradation vis-a-vis performance and life prediction of components. Application of computers and robotics during inspection further enhances the sensitivity for defect detection. Though engineering structures are fabricated from metallic substances, as well as ceramics and composites, the discussions in this paper essentially pertain to integrity monitoring of structures of metallic origin.

There has been a continuous and ever-increasing demand from the industry for the NDE professionals in developing new techniques and procedures to achieve the "minimum defect component with maximum confidence and reliability" goal. There has been a tremendous effort put in worldwide to meet this challenge and encouraging results have been obtained. For example, due to fracture mechanics considerations, it is required to detect defects smaller than 100 microns in structures, made of engineering ceramics. This requirement calls for development, implementation and application of high resolution and high sensitivity techniques. High frequency ultrasonics and microtomography are the two recently evolved techniques to meet the above demands. At the same time, industry is more conscious of utilising the benefits of NDE towards better performance and extension of life of various components/structures.

The knowledge of microstructural variations in a component is also very important to ensure the desired performance. Traditionally, microstructures are investigated by microscopic methods which are destructive in nature. At the authors' laboratory pioneering work has been done to adopt NDE techniques for the investigation of microstructural degradations. These techniques are useful for damage assessment, life estimation and extension applications of ageing plants and components, in particular, for continued service of components subjected to unacceptable service conditions during system malfunction or under accidental conditions.

In addition to the information about defects and microstructures, knowledge of residual stresses in a component is also essential for reliable assessment of structural integrity. Residual stresses are the system of stresses which exist in a material or component when it is free from external loads. The maximum value to which the residual stress can reach in a material is its elastic limit. Manufacturing processes are the most common causes of residual stress. In some instances, residual stress may also be induced later in the life of the structure during installation, or assembly or operation. Another common cause of residual stress is in-service repair or modification. Among the three types of residual stresses viz. macroscopic, microscopic and sub-microscopic, macroscopic residual stresses are important. They are generally caused by inhomogeneous plastic strains in a structure. During welding, plastic deformation is introduced mainly by thermal stresses due to large temperature gradients present at various stages of the welding process. Most of the engineering applications and fracture mechanics calculations require the knowledge of residual stresses of this type only. Again in this type, tensile residual stresses are generally detrimental, increasing the susceptibility of a component to failures due to such causes as fatigue and stress corrosion. Compressive residual stresses are usually beneficial, tending to reduce the above susceptibilities. Thus residual compressive stresses are often deliberately created on the surface. The role of NDE in detecting and assessing residual stresses is ever increasing and today well established techniques/procedures exist in this regard.

In this paper, a brief description of the physical concepts of various NDT methods and the physical/derived parameters which are used for assessing the above mentioned anomalies, namely defects/stresses/microstructure, are given. A few case studies highlighting the importance of non-destructive testing and evaluation for structural integrity assessment are discussed. In many cases, the investigations carried out at the authors' laboratory are given as examples. This paper also gives an account of the emerging concepts like expert systems, imaging, robotics, intelligent processing of materials, fusion of NDT data and signal analysis approaches that are responsible for enhanced reliability in NDE. Finally, the paper also brings out various research and development activities carried out at the authors' laboratory leading to new techniques and procedures.

2. NDE techniques for structural integrity monitoring

The main aim of NDE is to detect and characterise anomalies that can adversely affect the performance of the component under test without impairing its intended service. NDE implies complete responsibility to assess the seriousness of a situation realistically in order to enable the management to make the right decisions. Thus, NDE is *testing, evaluation and responsibility*. This almost always implies something more than the mere detection of defects. It is now widely accepted that locations where residual stresses and microstructural degradations exist are potential sites for the origin of defects. Hence, NDE involves detection and characterisation of defects, stresses and microstructural degradations. Their early detection is essential to avoid damage and loss of structural integrity of components. In this regard, the role of NDE is ever increasing to ensure reliability of performance in both pre-service and in-service stages.

Usually, to properly assess defect severity, one needs to know the type of defect, its location, approximate size, shape and orientation. NDT techniques available for the assessment of integrity of structures/components prior to, during and after their installation, are many. Some of the widely used techniques include visual examination, liquid penetrant testing, leak testing, vibration monitoring, magnetic particle inspection, ultrasonic testing, eddy current testing, gamma and X-radiography, acoustic emission, tomography, magnetic flux leakage method, laser holography and interferometry, infrared thermography etc. Broadly, these techniques can be classified into two categories, depending on the nature of inspection capability, viz. static and dynamic techniques. While static techniques can be used to detect cracks in materials off-line, dynamic techniques are used for on-line monitoring. Two widely used dynamic NDT techniques are acoustic emission and infrared thermography. All other techniques mentioned above come under the category of static techniques.

Since the interrogating field and the interactions are different, the minimum detectable defect sizes are different in different NDT techniques and mainly depend on the instrumentation. Consistency and repeatability of measured parameters have to be ensured. While selecting an NDT technique for a specific application, not only the minimum detectable defect size, but also the probability and the confidence level of detection are to be considered. Most NDT techniques have a wide range of applications and capabilities and comparison of data is valid only for a particular application, a specific type of defect and a particular material. For example, for detection of fatigue cracks in light-alloy panels, it is not surprising that eddy current and penetrant testing

are superior to ultrasonic testing and radiography. Hence, choice of the NDT technique depends on factors such as applicability, accessibility and suitability based on analysis and past experience. It may sometimes be necessary to use a combination of two or more techniques, in the best complementary way, to carry out complete and reliable inspection. Information about material composition, properties, micro-structure, fabrication procedure and environment is essential to identify the potential sites for origin of defects, their nature, probable size and orientation. All the above mentioned details would aid in selecting a suitable combination of techniques. In this regard, detailed mock-up studies are essential prior to actual inspection, to optimise equipment parameters, design and selection of sensors, selection of standard defects, operating conditions and procedure for recording and evaluation of NDT data to arrive at the desired sensitivity and reliability. Reliability is also ensured by following procedures as per codes and standards. A more recent concept in this direction is fusion of NDT data, which attempts to create a global picture of the fitness for purpose of the inspected zones. It involves combining data from more than one NDT method and displaying of a 3-D visual of the anomaly. In other words, if the "shadow" information from a radiograph is combined with depth information from an ultrasonic shear wave probe and surface breaking information from magnetic particle inspection, then the NDE personnel can provide a comprehensive description of the defect. This information can be presented and manipulated in a 3-D graphical format, making it much easier for a non-specialist to interpret the results of inspection in a reliable manner (Edwards *et al* 1993).

It is now well established from fracture mechanics considerations that planar defects (cracks, lack of fusion etc.) are more serious than volumetric defects (porosity, gas holes, round inclusions etc.) from the loss of strength point view. It is now clear that the depth or height of defect is more detrimental than its length and also surface breaking defects are more harmful than totally internal defects. A consequence of these findings is the changes in the acceptance levels for different types of defects.

For pre-service inspection, a definite requirement exists for more accurate NDT techniques which could be applied with the aim of producing a structure with no flaws greater than a predetermined size which can be as small as the defect detectable by NDT methods. Advancements in the fields of electronics and computer sciences, development of new methodologies, better understanding of interaction between the interrogating media and materials and new challenging requirements are pushing the NDE technology to achieve significant progress. A major spin-off in the recent past in this direction is "intelligent processing of materials". This concept ensures 100% acceptability of raw materials and fabricated components by providing feedback to the manufacturing/fabrication processes about the presence/occurrence of defects on-line thus allowing for immediate corrective action (Baldev Raj 1994b).

Imaging techniques show a promise towards enhanced detection and characterisation of defects in components. It has often been said that an NDE image is worth a thousand NDE signals. NDE personnel feel more comfortable in interpreting images than analysing signals. Imaging can be done with many different media, including optical, infrared, X-ray, gamma-ray, ultrasound, eddy current, thermal wave, magnetic resonance etc. Thus, there is a broad spectrum of techniques from which selection can be made. Infrared imaging, ultrasonic C-scan imaging, scanning acoustic microscopy, scanning laser acoustic microscopy, computer aided tomography and eddy current imaging are some of the techniques currently being used worldwide for wide-ranging

applications. The imaging format provides a global perspective of the inspected region and allows a balanced interpretation. Also, imaging techniques have the potential of automating the measurement process, providing estimates of defect size from the image data, producing accurate characterisation of cracks and improving the probability of detection (Baldev Raj 1993a).

The latest state of the art in NDE is the development of expert systems. Expert systems are interactive computer programs which attempt to simulate the expert's thought processes and provide a wide range of advice. An unusual feature of these systems in comparison with more traditional algorithmic programs is the ability to handle heuristics, or rules-of-thumb. This feature makes the expert system an attractive tool for evaluation of NDT data and failure analysis. The use of robotic devices for reliable NDE of components is assuming great importance in many applications like the nuclear, space and chemical industries especially when there is a need for high probability of defect detection, reduction in radiation exposure to NDE personnel and limiting the operator dependency. Manipulators based on robotic principles have come into existence and the demand for manipulators with computerised data acquisition, processing and evaluation is growing faster for pre-service and in-service inspections (Baldev Raj 1992).

In the following sections, the principles, capabilities and applications of some of the widely used NDE techniques for the assessment of structural integrity are discussed. Special emphasis has been laid on discussing the physical principles of NDT techniques and the interaction of the interrogating medium/field with the anomalies that affect structural integrity. Besides an attempt has been made to briefly discuss the recent trends in various techniques.

2.1 Visual inspection

Visual inspection (VI) constitutes an important and widely used NDE method for structural integrity evaluation. VI is a very valuable method for the evaluation of discontinuities open to the surface. However, it is not suitable for detecting subsurface and interior discontinuities. VI is a relatively simple and effective technique that is complete without detailed analysis of data/signals/patterns like other NDT techniques. In VI, an NDE inspector arrives at an immediate decision solely on what he observes during inspection. Capabilities of VI can be enhanced considerably by using simple aids such as magnifying glass, microscopes etc. for viewing, dimensional measurements etc. The advances in the area of optics have had far-reaching consequences in the field of visual inspection. Industrial telescopes, usually known as borescopes or introsopes enable inspection of inaccessible surfaces. They are best known for *in-situ* examination of inner surfaces of tubes/piping and also for the inspection of surfaces of turbine blades in aero-engines for the detection of cracks and corrosion without needing dismantling (Halmshaw 1989). The advent of fibrosopes with rotating head has increased the versatility of visual inspection. With significant advances in display, storage and handling of images, it is now possible to record the information permanently and to carry out detailed investigations referring to the records of prior inspections to determine whether there has been crack growth, formation of additional cracks, or other progressive changes. The use of image processing techniques greatly enhances the sensitivity of defect detection and helps in obtaining reliable information about their dimensional measurements.

2.2 Liquid penetrant inspection

Liquid penetrant inspection (LPI) is another widely used NDE method for the detection of discontinuities open to the surface in any material/component which has a non-absorbant surface, irrespective of the component geometry and its material properties. LPI utilises the natural accumulation of a fluid, called penetrant, around a discontinuity to create a recognisable indication of a crack or other surface opening. A typical example to understand the principle involved in LPI is the ready visibility of cracks in concrete structures after a rain. LPI is directly concerned with the behaviour of fluids on surface (Halmshaw 1989). Surface tension and capillary are the two areas of fluid mechanics relevant to LPI. Surface tension is the property that affects the flow of the fluid on the surface to be inspected. Capillary forces drive the penetrant along the material surface into the surface openings and, finally out of them and into the developer. In brief, in LPI a liquid is applied to the surface of the component for a certain predetermined time (dwell time) during which the penetrant seeps through the surface discontinuity. After this, the excess penetrant is removed from the surface. The surface is then dried and a developer is applied to it. The penetrant that remains in the discontinuity is absorbed by the developer indicating the presence as well as the location, size and nature of the discontinuity. Optical recognition exploiting the full range of light spectrum from visible to ultraviolet light, is used for the defect detection in LPI.

The LPI processes are typically classified by the indicating method i.e. visible or fluorescent dye and the method used to remove the excess penetrant from the component surface. The three widely adopted LPI systems are water-washable, post-emulsifiable and solvent removable. Fluorescent dye penetrants have high sensitivity and are particularly useful for detecting cracks of small widths (down to 0.5 microns). The increased sensitivity is due to the absence of any visible background (either white or coloured) layer covering the area under inspection which would otherwise absorb a part of the incident light. LPI technique is very useful for detection of fatigue cracks, stress corrosion cracks and other service-induced defects open to the surface. The absence of a volumetric interrogating medium in LPI restricts the technique to detect variations/abnormalities open to the surface. Microstructure and stresses in the components cannot be assessed by LPI.

2.3 Magnetic methods

Magnetic methods of NDE are among the oldest and most pervasive because of the dominant production and use of steel and related ferromagnetic materials in the industry. When a ferromagnetic component is magnetised, the magnetic lines of force (the magnetic flux) are predominantly inside the material. However when there is a surface breaking or a sub-surface discontinuity, the field is distorted, causing local magnetic flux leakage fields. Effectively, the discontinuity causes a sudden localised change in magnetic permeability. These leakage fields are monitored/detected/recorded either by sprinkling finely divided ferromagnetic powders or by using sensors and the information on the location, shape and extent of the discontinuity producing the leakage field is obtained (Mix 1987). On the basis of recording and evaluation of the leakage fields, the magnetic methods can be classified into magnetic particle inspection

(MPI) and magnetic leakage flux (MLF) and magnetic Barkhausen Noise (MBN) techniques. Because of the added advantage of these techniques over LPI in detecting subsurface defects, it is logical to specify magnetic methods for the structural integrity evaluation of all ferromagnetic materials. After the inspection by magnetic methods, it is necessary to subject the component to demagnetisation, an act of reducing the flux density level in the component to a level at which its external field does not cause problems in service such as (a) wear due to pick-up of ferromagnetic parts in the case of rotating components, (b) arc deflection during welding and (c) interference effect on nearby instruments etc.

MPI consists of magnetisation of the component, application of magnetic powder and examination of powder patterns. The indications of defects are preserved by photography or video recording or by the use of peel-off transparent adhesive films. To obtain higher sensitivity for defect detection, fluorescent magnetic particles suspended in oil or kerosene are employed rather than the dry powders. Magnetic silicone rubber containing magnetic particles in suspension are widely used for the inspection of relatively inaccessible regions e.g. bolt holes and internal threads. These areas are of great concern in military aircraft and detection of cracks in these regions is challenging. In this method, a highly viscous rubber solution is applied on the component surface before magnetisation. After magnetisation, sufficient time is allowed for the particles to migrate to the leakage fields before the solution is cured. This method is also known as magnetic rubber inspection (Zheng & Zhu 1993).

One major limitation of MPI is the necessity for application of magnetic field in different directions. This is because of the fact that the leakage field, and in turn the sensitivity in MPI, is maximum only when a defect is perpendicular to the direction of the magnetic field. Hence, in order to detect defects in different orientations, the magnetic field has to be applied in more than one direction. There are a wide variety of methods to magnetise a component such as prod, head shot, central conductor, yoke, cable etc. These methods essentially aim at producing circular and/or longitudinal magnetisation in the component. The method selected depends on such factors as the geometry of the component, desired direction of magnetic field, the expected orientation of defects and whether or not the defects are subsurface. Both AC and DC methods can be used. Because of the skin depth effect, AC methods are restricted to the detection of near-surface defects and therefore are not very effective for detection of subsurface cracks.

Procedures based on wet fluorescent MPI techniques have been successfully developed at the authors' laboratory for the structural integrity evaluation of 235MW low pressure turbine rotors of PHWRs (Baldev Raj 1993b). This effort consisted of performing MPI on turbine blades of all five stages and fir-tree root regions of all stages adopting cable and yoke methods of magnetisation respectively. Current ratings and sensitivity were optimised with the help of field indicators and gauss meters. These procedures have also been successfully used to perform MPI *in-situ* without lifting the rotor from the turbine bed. Defects detected by these procedures were characterised using direct current potential drop technique (refer §2.8 below). Detailed *in-situ* metallography and residual stress measurements (X-ray diffraction technique) were carried out to supplement the MPI observations and to assess the damage at those regions. *In-situ* metallography involves polishing, etching, examination of the suspected regions with a portable microscope and recording of indications by the replication method.

In MLF method, the presence and extent of defects is detected by monitoring the surface for localised fluctuations in the magnetic field with sensors like inductive coils, Hall probes, magnetometers and magnetoresistive, magnetic resonance and magnetographic type probes (Forster 1977). As in MPI, in this technique also, two forms of magnetisation i.e. DC and AC are commonly used. The AC method has higher detection sensitivity than the DC method and defect signals are proportional to the depth of the defect. Since magnetisation is local, demagnetisation is not required. However, DC method is capable of detecting sub-surface defects and is relatively insensitive to interference from the material surface noise caused by roughness, scale etc. (Junger & Brock 1990).

The higher sensitivity of the flux leakage methods (close to that of magnetic particle inspection) and the additional advantage of automatic evaluation without a human inspector makes the technique amenable to on-line inspection at the shop floor. AC MFL technique is used to characterise stresses in high strength steels and their welds. One of the primary application areas for practical MLF systems is that of axisymmetric components i.e. tubes, pipes, rods, bars, rounds, billets etc. Components of these geometries are particularly amenable to fully automated and relatively high speed scanning in a production line during their manufacture. MLF method is also widely accepted for in-service inspection of underground pipes in petrochemical industries (Collins *et al* 1984). This method has been successfully applied for the detection and assessment of defects in highly irregular component such as helicopter rotor blade D-spars, gear teeth, artillery projectiles etc. Another successful application is the inspection of rolling element anti-friction bearings which form critical components in gas turbine engines, high performance aircraft, helicopters, rocket engines, satellites etc. (Beissner *et al* 1980). Advances in sensor technology and data acquisition and analysis have resulted in realisation of fully automated MLF inspection method. More recently, Finite Element (FE) computer programs are being used to simulate this method for both simple and complex crack/component configurations. For defects such as fatigue cracks where there is evidence of a variable permeability effects, FE modelling provides an opportunity of realistic method of analysis (University Communique 1987).

Magnetic methods are potential methods for evaluation of microstructural degradations. Magnetic flux perturbation and acoustic emissions are generated when an induced magnetic field in ferromagnetic materials is swept in a hysteresis loop. The former is referred to as Magnetic Barkhausen Noise (MBN) and the latter is called Acoustic Barkhausen Noise (ABN). MBN signals are produced as a result of discrete changes in magnetisation caused mainly by the motion of the 180° domain walls as the magnetic field is varied. The signals are detected by a search coil. Similarly ABN signals are generated during the hysteresis sweep due to the rotation of the 90° domain walls and the associated magnetostriction. Since MBN is related to the nucleation and movement of magnetic domain walls and their interactions with various microstructural features such as grain boundaries, precipitates, stresses etc. this technique is found to be useful for several applications including microstructural characterisation, characterisation of post-weld heat treatment in the weld joints and the measurement of residual stresses. Significant work has been done at the authors' laboratory in this direction (Bhattacharya 1994). In the case of 17-4 PH steel, MBN technique has been employed to identify the stages i.e. (i) build up of coherency strains, (ii) loss of coherency and (iii) interlath austenitic formation which otherwise need transmission electron microscopy and field ion microscopy investigations (Bhattacharya *et al* 1992b). In the

case of 2-25Cr-1Mo steel, precipitation of Mo_2C could be identified using the MBN technique. Recrystallisation from martensite structure leading to ferrite formation in addition to coarse carbide precipitation could also be characterised. In 9Cr-1Mo steel, the incipient occurrence of delta ferrite could be detected by magnetic techniques. Even by transmission electron microscopy, it is difficult to identify the incipient occurrence. MBN technique has been successfully used for the characterisation of post-weld heat treatment in the weld joints of steam generator modules of the proposed Prototype Fast Breeder Reactor. These studies efficiently brought out the adaptability of MBN analysis for quality assurance of welds. ABN technique has been used for assessment of residual stresses in weld joints of structural steels (Bhattacharya *et al* 1992a). The rms voltage of the ABN signal has been used as a parameter for studying the influence of stress relief annealing on the stress distribution. Increase in the rms voltage of the ABN signal corresponding to the decrease in the residual stresses could be observed. In the as-welded condition, stresses are higher at the centre of the weld region and decrease gradually at the regions away from it. Reduction in stresses due to annealing could be identified in the form of increase in ABN signal. The utilisation of magnetic parameters derived from hysteresis loop measurement and MBN and ABN signals for assessment of microstructures is emerging as a very promising technique for structural integrity monitoring.

2.4 Radiographic techniques

Radiographic techniques (RT) are effective industrial methods for the NDE of components/structures. Radiographic techniques use a beam of penetrating radiation such as X-rays or gamma rays or atomic particles such as neutrons, protons and electrons (Baldev Raj & Venkatraman 1989). When the beam passes through a component, some of the radiation energy is absorbed and the intensity of the beam is reduced. Variations in beam intensity are recorded on a film or fluoroscopic screen with digital system coupled with video monitors, and are seen as difference in shading typical of the type and size of any defect present. When the defect is an absence of material such as void or porosity, the image will appear darker than the surroundings. On the other hand, when the material in the defect is more absorptive than the surrounding material, the image will be lighter in appearance. In other words, the density of defect indications on the film or other recording media mentioned above, is inversely related to the total linear density of the material in the beam path. Decreased densities in the appearances of the indications on the radiographs will therefore indicate more dense material along the total beam path. Hence, porosity i.e., gas hole in the material, would appear on the radiograph as a spot or a field of spots darker than the surrounding material and foreign inclusions would appear as either darker or lighter spots depending on the density of the foreign material relative to the component (Bray & Stanley 1989b). Corrosion is readily detected using radiography, since material loss affects the exposure of the film. The detectability of discontinuities by radiography is highly dependent on the shape and orientation of the anomaly as well as on the density. Microstructural degradations are difficult to detect by X or gamma radiography. However, neutron radiography can be used for metallurgical examination of irradiated materials with limited success.

While X-ray tubes, van de Graaff generators, betatrons, linear electron accelerators (LINACS) and microtrons form sources for X-rays, radioisotopes like cobalt-60,

iridium-192, caesium-137, thulium-170 and ytterbium-169 are used as typical gamma ray sources. Recent advances in X-ray tube technology have resulted in focal spots which are an order of magnitude smaller, thus giving rise to a whole new classification of microfocus radiography techniques (Peugeot 1982). It is thus possible to detect minute defects in thin components, thin welds of steel, aluminium or titanium alloys which was not possible earlier using conventional radiography. The most impressive feature of the microfocus X-ray source is its ability to produce extremely sharp radiographs at exceedingly short film-to-focus distances (Halmshaw 1989). In X-ray tubes, a small focal spot size of about 10 microns could be realised by electromagnetic and electrostatic focusing techniques of the electron beam. An outstanding example that brings out this capability is the work carried out at the authors' laboratory on the radiography of tube-to-tube sheet welds in 2.25 Cr-1 Mo steel tubes of steam generators of Prototype Fast Breeder Test Reactor (PFBR). Using rod anodes with true radial panoramic emission, full circumferential radiographs can be obtained at around 80 kV in less than one minute on a Agfa D2 film with a sensitivity better than 1%. This sensitivity is much better than that can be obtained with the best radio-isotope based technique (Venkatraman *et al* 1993c). The advent of X-ray image intensifiers has resulted in replacing the conventional fluoroscopy system to a real time radiography system. X-ray radiography is an important post-irradiation examination technique for the evaluation of nuclear fuel elements. This application is, however, beset with a problem called gamma fogging (exposing of film to gamma rays coming from fuel) which makes the interpretation of the radiographs difficult if not impossible. Successful procedures utilising post radiography image processing methods have been developed at the authors' laboratory to minimise gamma fogging.

Radiography with thermal neutrons (energies between 0.01 and 0.3 eV) has emerged as a powerful NDT technique, called Neutron Radiography (NR), for examination of nuclear materials and many other non-nuclear applications as well. Thermal neutrons have some properties which make them especially interesting for radiography. While the attenuation of X-rays in materials increases with atomic number in an orderly manner, the mass absorption co-efficients of elements for thermal neutrons appear almost random since neutron absorption does not depend on the electronic structure of the atom, but on the interaction with the atomic nucleus. Hence, X-rays are stopped by dense materials and passed by light materials and in many instances neutrons have the reverse quality. For example, neutrons will penetrate the body of a large metal valve to give a good image of an internal rubber seal while X-rays will give the defects present in the metallic portion. It is now widely accepted that X-radiography and neutron radiography are complimentary to each other (Baldev Raj 1994a). NR is used in the metallurgical examination of irradiated fuel sub-assemblies, fuel pins and control rods. Also it can reveal information about movement of fuel pellets in fuel pin, dimensional changes of pins and pellets, pin to pin spacing, and plutonium distribution in the pellets. In aerospace industries NR has been used for inspecting the presence of solidified oil and grease in lubrication holes and passages. NR has been used to detect earlier stages of corrosion in aircraft structures that cannot be found with X-radiography. Other applications of NR include, inspection of rubber seals, plastics insulations, capacitors, potting of transformers, explosives and turbine blades made by investment casting and archaeological structures etc. At the authors' laboratory, a 30 kW uranium 233 fuelled swimming pool type reactor called Kalpakkam Mini (KAMINI) is nearing completion. The flux at the core is expected to be around 10^{13} n/cm²/s and the flux at the

radiographic site would be 3×10^6 to 10^7 n/cm²/s. Two beam tubes are available for radiographic purposes, one for active sample radiography and the other for non-active sample radiography. Special gadgetry has been designed indigenously for precise positioning/rotation of components in front of neutron beam, remote controlled cassette drive mechanism and for carrying out real time imaging. A resolution of the order of 30 to 40 microns is expected (Kasiviswanathan *et al* 1989).

The major constraints of conventional radiography include (a) inability to accurately reveal the depth and height of defects so important for the structural integrity assessment by means of fracture mechanics, (b) poor discrimination of changes in density of an object being detected, and (c) confusion caused due to two-dimensional image of three-dimensional component. These limitations are overcome by Computer-aided Tomography (CT) which is a useful concept for NDE. In CT, the transmission of radiation beams (X-ray, gamma-ray or neutron) through an object in a single plane is measured under various object angles and positions. From the transmitted intensities for many beam orientations, a CT image representing a map of absorption coefficients in the measured cross-sections is calculated and presented in visual form on a video display using a graphic system and colour-coded scales that represent various densities as different colours (Vontz *et al* 1988). Cracks, pores and density fluctuations in the material can be displayed by a change of colour. CT can be obtained in a digital form and can be further mathematically processed to extract the required information (Halmshaw 1989). A typical interesting application of CT is the assessment of engineering ceramics. Engineering ceramics have a number of excellent properties, in particular, high strength at elevated temperatures and oxidation resistance, which make them attractive materials for a variety of applications. On the other hand, the monolithic ceramics are very brittle (i.e. they possess very low fracture toughness), and the permitted defect is as small as 20 microns in certain applications. CT has been applied to the examination of advanced ceramics and has proven to be a very efficient method within the required detection limits (Arnold 1990). While gamma and X-ray are used for general applications the former is preferred for the inspection of thicker components. Neutrons are also being used for CT especially for the evaluation of nuclear fuel sub-assemblies and fuel pellets.

The latest state-of-the-art is development of expert systems using artificial intelligence for radiography. Efforts are underway at the authors' laboratory to develop an expert system for optimisation of procedure for radiography (Venkatraman *et al* 1993b).

2.5 Ultrasonic testing

Ultrasonic testing (UT) uses sound waves having frequencies usually in the mega cycle range. A sound wave travelling through a material will lose energy when it encounters an anomaly. This is manifested by a loss in pulse amplitude as well as a change in its appearance. There are three basic processes that account for loss of pulse energy, namely beam spreading, absorption and scattering. Beam spreading is primarily a geometric function where the intensity decreases with the square of the distance travelled. Absorption accounts for the mechanical energy converted to heat energy as the wave propagates. Scattering results from reflection at grain boundaries, small cracks and other anomalies. This phenomenon is utilised to non-destructively measure grain size in materials (Bray & Stanley 1989a).

Two basic methods in UT are pulse-echo and through transmission. While the former method makes use of a single transducer, the latter makes use of two. In the pulse-echo method, a transducer made of piezoelectric material (also called probe) transmits a pulse of mechanical energy into the component. The energy passes into the material, reflects from the back surface, and is detected by the same transducer, yielding a signal on an oscilloscope with a time-base. The oscilloscope would normally show the original pulse of the ultrasonic transducer (front surface echo), the back reflection and any extra blip indicating a reflection from a defect in the material. From the oscilloscope timing, the depth of the defect below the surface can be determined. Alternatively, in the transmission method, transducers are placed on opposite sides of the component and any reduced intensity sensed by the receiving transducer indicates the defect shadowing part of the ultrasonic radiation. The location of the defect cannot be obtained. Both pulse-echo reflection and transmission methods are in use and their selection depends on the accessible surface of the component. UT can detect defects oriented both in the plane of and normal to the surface of components using normal beam or angle beam transducers. By suitable design of ultrasonic transducer, ultrasonic beams can be introduced into a material at almost any angle. There are several forms of ultrasonic waves, the most widely used in NDT being compressional (longitudinal) and transverse (shear) waves. In a specific application of tube testing for detecting defects normal to the wall, the beam is converted to a shear wave which is propagated around the circumference or along the axis. In order to detect defects efficiently by UT, it is necessary to make the wavelength comparable to the expected defect size. Hence, for detection and assessment of smaller defects, it is necessary to use high frequency. The UT data can be displayed in three modes viz. A-scan, B-scan and C-scan (Szilard 1982; Baldev Raj *et al* 1994a).

Ultrasonic attenuation can be used to monitor material properties. Empirical correlations have been obtained between ultrasonic attenuation and the impact strength, fracture toughness, grain size and tensile strength of steels. Similarly, ultrasonic velocity measurements can be used to measure residual stresses in materials. This methodology uses shear waves polarised in two mutually perpendicular directions. These waves have slightly different velocities and so interfere, so that as the transducer is rotated, the interference vanishes when the polarising planes are parallel and perpendicular to the stress axis. Once this axis is known, the actual stress can be computed from the velocities (Halmshaw 1989). Stress measurements using ultrasonic technique are also dependent on the acousto-elastic effect i.e. strain-induced ultrasonic wave velocity variations in materials. By precise measurement of ultrasonic velocity, information about stress can be obtained. Using pulse-echo overlap method, accuracy of transit time measurements of the order of ± 1 nano second have been achieved by us (Palanichamy *et al* 1992a).

Ultrasonic methods are also widely used for detection and characterisation of defects in structural welds (Pelseneer & Louis 1974). We have developed procedures for reliable and automated detection of defects down to 5% wall thickness in the end cap weld joints of thin-walled fuel elements of PHWRs (Subramanian *et al* 1991). In view of the difficulties encountered during conventional UT due to upsets produced during welding process, easily implementable signal analysis approaches have been used (Baldev Raj *et al* 1992). High sensitivity defect detection and characterisation in weldments of maraging steels used for rocket motor casings in the aerospace industry is of great importance. Tight cracks (3 mm \times 1 mm) produced in these welds by fatigue

loadings were detected by us using cluster and pattern analysis of UT data. Detection of such small defects enhances the payload capacity of the rocket (Kalyanasundaram *et al* 1991a).

Austenitic stainless steel (AUSS) components and structures find extensive applications in various industries and they enjoy a dominant position (75% approximately) among other stainless steels. This is chiefly because of high level of fabricability and corrosion resistance. UT is the most widely used NDE technique for the assessment of AUSS and their welds. UT of AUSS welds and castings is much more difficult than that of other stainless steels because of the following: (a) severe attenuation at high frequencies, (b) presence of anisotropic grain structure (dendrites) which cause the ultrasonic beam to bend (beam skewing), and (c) noisy behaviour of the material masking the pulses from defects (Juva & Haarvisto 1977). A whole range of new UT methodologies have been investigated in order to improve the UT inspection of AUSS welds and castings. Some of them include ultrasonic spectroscopy, acoustic holography and SAFT etc. Automated systems are now available for the inspection of pipe welds in critical components in nuclear, oil and other industries with limited access. An integrated prototype rule based expert system (ES) which helps in taking quick and reliable decisions in the UT procedures to be adopted for efficient NDE of AUSS welds has been developed at the authors' laboratory (Rajagopalan *et al* 1992). This ES considers the following details before making a decision: dendritic microstructure of the weld, weld dimensions, geometry, joint type, welding procedure, metallurgical history, reflective characteristics of various types of defects, equipment parameters etc. Inspection of inaccessible regions and complex geometries would become simpler if the ultrasonic beam path is known. Visualisation of software for simulating the path taken by an acoustic/ultrasonic wave inside the weld is currently under development at the authors' laboratory.

A wide variety of conventional UT methods are available to measure crack depth like (i) defect echo height method, (ii) decibel drop method, (iii) edge echo method, (iv) scattering method and (v) composite aperture method. However, characterisation and sizing of defects requires sophisticated instrumentation, methodologies and computer-based automation. A few techniques/concepts that have proven capabilities for defect and material characterisation include; ultrasonic phased array (ALOK), time of flight diffraction (TOFD) and synthetic aperture focusing technique (SAFT). Electromagnetic acoustic transducers (EMAT), being of the non-contact type offer the potential advantage of performing inspection of high temperature components without the need for any physical coupling. Similarly, laser generated ultrasonic sound generation and interferometric detection techniques show a great promise in this regard for characterisation of materials at high temperatures or in hazardous environments. This technique has been used to detect laminar defects in red-hot steel billets. Space limitations preclude full-fledged discussion of these advanced techniques. However, the reader may refer to the literature available on these topics (Silk 1984; Muller *et al* 1986; Bohn *et al* 1987).

Ultrasonic phased arrays hold out considerable promise. By using a number of elements excited with different time delays, it is possible to both steer and focus the beam in transmission and to image on reception of the beam. The ability to electronically control the beam characteristics of the phased array probe has an attraction in automated systems where a large number of different probe angles may be utilised for reliable inspection (Cochran *et al* 1991).

ALOK (Amplituden und Laufzeit Orts Kurven) meaning "amplitude and time of flight locus curves" is a recent development with its origin in Germany. This method incorporates all the features required for automated inspection of pressurised components in any industry viz. high sensitivity and resolution, reliability and reproducibility, quick information on the condition of the component and ability to analyse a crack without re-examination. These inspection systems have the capability to detect cracks even in complex geometries. In contrast to conventional assessment of amplitude information, the ALOK method uses the time-of-flight of the echo signals to get complete information about the cracks like its position, size, shape and orientation. The time-of-flight locus curves are obtained from the time-of-flight (e.g. echo from a reflector) vs. probe position during its transit. To get the time-of-flight (and the corresponding amplitude) information, only the peak amplitudes from an A-scan and their times-of-flight (selected out of the rf signal) are recorded. This results in significant reduction in data without any loss of information. The data are also displayed in the form of B- and C-scans. Flow reconstruction is made by geometric planar triangulation or by iterative methods.

SAFT is another promising technique in ultrasonic NDE. The basic idea of SAFT is to measure the complete sound field scattered by a crack on an orbit around the crack. During reconstruction, this sound field is calculated back into that region where the scattering occurred making use of well-known wave propagation formulae. The result is the three-dimensional amplitude distribution of the sound field inside the scanned orbit. In an ideal case, sound field will be non-zero only on the surface of the scatterer, thus obtaining an image of the crack by describing its surface. Because a 360° scanning around a defect may be possible only in a few cases like rods or shafts, one is forced to reduce the scanned aperture to only the part corresponding to the accessible surface. Therefore, only that part of the crack which could be interrogated by the ultrasonic beam would be imaged. To maximize the interrogated area of the crack, probes with large beam opening angles have to be used i.e. small probes or the defocused part of the far field probes. In addition, it is possible to synthesize scanning around the defect using different beam angles and different inspection techniques like pitch-catch or tandem.

Another innovation in the recent past is the time-of-flight diffraction (TOFD) technique. TOFD is widely used for accurate location and sizing of cracks. Interaction of an acoustic wave with a crack results in the generation of diffracted waves. It is important to note that the diffracted energy can produce a significantly large pulse. While this pulse will be smaller than the largest that can be obtained with reflection techniques, it will usually be comparable with pulse echoes obtained in practice. As a result of diffraction, a cylindrical wave front effectively originates at the crack tip. By suitable measurements of this diffracted wave, it is possible to locate the origin of the cylindrical wave, or in other words, to locate the tip of the crack. This leads to the concept of the use of diffracted ultrasound to size cracks. In order to achieve this, the most obvious measurements to make on the diffracted pulses are their arrival times. This, in turn, couples 'diffraction' and 'time of flight' together. The technique was originally pioneered on surface-breaking cracks. But, with improvements in data processing techniques, it has been possible to evaluate subsurface and internal defects. The technique produces a significant improvement in accuracy of defect sizing as compared to conventional pulse echo data (Temple 1987).

The technique that has established itself as a powerful tool for defect and material characterisation during PSI and ISI is acoustic microscopy. Acoustic microscopy

produces very high resolution and high magnification images of internal features in a component through the use of short wavelength (very high and ultrahigh frequencies) ultrasound. There are three types of acoustic microscopy systems. They are scanning acoustic microscopy (SAM), scanning laser acoustic microscopy (SLAM) and C-SAM. In SAM, a point source of ultrasound is produced in a fluid such as water by a highly focused transducer. The transducer is pulsed and alternately acts as a transmitter and receiver. The transducer scans in a rectilinear raster pattern to obtain the image. In SLAM, a focused laser beam is employed as an ultrasonic wave detector by virtue of the fact that displacement at an interrogated surface modulates light reflected from the material. The displacement is localised within acoustic dimensions. The image of the sample is produced by using plane waves of ultrasound and scanning by laser over the field of view at the rate of 30 images per second which is about 300 times faster than SAM. SLAM is generally used in transmission mode whereas SAM is used in reflection mode. C-SAM is somewhat analogous to the C-scan ultrasonic technique. The acoustic microscopy techniques have been used for detection and characterisation of cracks in a variety of materials such as ceramics, metals, polymers and composites and they have the capability to be utilised from initial characterisation of the base materials to the final quality check of the precision fabricated assemblies. They have been found useful in crack detection in thin, flat or smoothly curved surfaces. With the use of phased array and a solid coupling system, acoustic microscopy could become an effective method for inspecting components/structures both during pre-service and in-service. This method has been used to detect and characterise surface and sub-surface cracks down to 100 microns in ceramics (Baldev Raj *et al* 1994b).

Fibre-reinforced composite materials are being increasingly used in defence, space and commercial applications due to their low weight, high strength and stiffness properties. This necessitates the development and standardisation of NDE techniques for meeting fitness-for-purpose requirements. UT enjoys the status of being a reliable method for evaluation of composite structures in spite of the difficulties posed by composite structures, for example high attenuating behaviour, heterogeneous nature and anisotropic properties. Different kinds of defects that can occur in fibre-reinforced plates during fabrication and in-service are contaminants, voids, unpolymerised resin, resin-rich and resin-starved areas, ply gaps, foreign inclusions, delaminations, crazing, surface scratches etc. Detection and characterisation of some of these defects has been carried out by us using an automatic ultrasonic scanning system. Two different experimental methods (ultrasonic immersion and dry coupling) have been used. For effective detection and characterisation of defects, procedures have been developed using advanced signal processing and analytical approaches such as auto-power spectrum, total spectral energy content and demodulated auto-correlation pattern etc. (Kalyanasundaram *et al* 1991b).

In the area of microstructural characterisation, we have successfully adopted ultrasonic velocity and attenuation measurements in the following applications; (i) characterisation of precipitation behaviour and estimation of volume fraction of r' in Nimonic alloy PE 16 (ii) assessment of microstructural degradation (dissolution of tempered martensite structure to ferrite and carbides) in 9Cr-1 Mo steel, (iii) characterisation of precipitation hardening behaviour in 17-4 PH steel (iv) characterisation of various microstructures in A533B pressure vessel steel, (v) estimation of porosity in aluminium alloy weldments, (vi) determination of texture coefficients in cold worked AISI type 304 stainless steel, and (vii) assessment of creep damage in low alloy ferritic

steels (Jayakumar *et al* 1992a). Many of these results would be useful in developing procedures for micro-structural degradation and damage assessment applications utilising ultrasonic techniques (Bhattacharya *et al* 1993; Jayakumar *et al* 1993, 1994).

Ultrasonic velocity measurements are useful for determining several important material parameters like moduli, Poisson's ratio, residual stresses, texture, porosity and characterisation of secondary phases in microstructure etc. Some of these parameters influence the velocity only by an order of 0.1%. In order to study these variations, high resolution techniques for ultrasonic velocity measurements are necessary. We have devised a methodology for precise ultrasonic velocity measurements using cross-correlation technique. The accuracy in the velocity measurements is enhanced by adopting cubic spline fitting of the cross-correlation function. The resolution in time delay measurements required for computing the velocity was of the order of 0.5 ns. This methodology has been applied for finding the influence of microstructure on ultrasonic velocity in 9 Cr-1 Mo ferritic steel and 17-4 PH stainless steel (Rao *et al* 1993b). In the next sub-section, the possibility for use of ultrasonic velocity measurements in aiding quality control during fabrication and damage assessment during service are discussed.

2.5a Ultrasonic velocity measurements for microstructural evaluation in 9 Cr-1 Mo steel - A case study: 9Cr-1 Mo steel is a candidate material for boiler/super heater steam circuitry of power plants. Ultrasonic velocity measurements were carried out on various heat-treated 9 Cr-1 Mo ferritic steel specimens with a view to study the influence of microstructure on ultrasonic velocity. Heat treatment consists of aging treatment at 823, 923 and 1023 K for durations of 2, 10, 50, 200, 500 and 1000 h. Ultrasonic velocity measurements were carried out on these specimens using a 15 MHz longitudinal transducer. The microstructure after standard treatment (normalising at 1323 K for 30 min followed by tempering at 1023 K for 1 h) is martensite with M_2X carbides at lath boundaries and small amounts of ferrite due to partial dissolution of martensite (reference specimen). The reference specimen has the lowest velocity compared to all the aged specimens. At all the temperatures, it is observed that as the aging time increases, velocity first increases and then decreases or remains almost constant after attaining a peak depending on the temperature. The increase in velocity is lower at 1023 K as compared to that at 823 and 923 K. This is attributed to the formation of smaller volume fraction of M_2X at 1023 K due to simultaneous formation of ferrite and $M_{23}C_6$ by dissolution of some of the martensite. It can also be observed that the maximum in velocity has occurred at lower durations of aging with increase in aging temperatures due to faster precipitation of carbides at higher temperatures. The time periods for maximum in velocity at 823, 923 and 1023 K are 200, 100 and 10 h respectively. At 1023 K beyond 10 h of aging, the velocity is found to decrease steadily whereas at 823 and 923 K the velocity remains almost constant or decreases slightly after attaining the peak. The steady decrease in velocity at 1023 K after 10 h of aging is attributed to the continuous dissolution of martensite forming ferrite and $M_{23}C_6$. Since very little or no ferrite formation takes place even upto 1000 h at 823 and 923 K, the velocity remains constant after attaining the peak.

These measurements clearly indicate that formation of M_2X precipitates and ferrite influence the ultrasonic velocity. Any increase in velocity with time at a given location on a component indicates formation of precipitates of M_2X . Similarly, a decrease in velocity with time clearly indicates formation of ferrite which reduces the strength properties. Similarly, for a given material, the influence of an unwanted phase in other

materials on the velocity can be established and in-service degradation can be assessed periodically by performing velocity measurements.

2.6 *Acoustic methods*

Acoustic methods (AM), also known as sonic testing; vibration testing and mechanical impedance testing, depend on exciting vibrations in a specimen by local impact and then measuring some properties of the vibrations such as resonance frequency, decay time etc. A simple example of an acoustic method is the inspection of a railway wheel by tapping it with a hammer and detecting the vibrations with a transducer. There are several other important applications of acoustic methods, the most important being testing of cast iron specimens where it has been shown that the nature and size of carbon content can be related directly to the resonance frequency of the casting. This method is extensively used for quality control of malleable iron castings. Bonded joints, defects in composites and plastic components have been located and assessed using this technique. Testing of adhesive bonding in laminates and honeycomb structures for aerospace applications is nowadays carried out by these methods. Using much lower frequencies of the order of a few kilohertz, masonry structures have been tested by these methods. The structure is excited by a blow with a steel-tipped hammer and the frequency of the propagated signal is analysed through a transient recorder in conjunction with a computer. When the method was applied to masonry bridge structures, the signal was found to be sensitive to significant defects such as large voids and cracks (Halmshaw 1989).

Vibration monitoring of operating plant and machinery to give early warning of impending failure or potential fault conditions forms a popular NDE method. Even the most simple machinery has a number of sources of vibration and these vibrations are transmitted through the machine structure. The vibration spectrum depends on the machine speed, loading, lubrication etc. The vibration is characterised by amplitude, frequency and phase and is usually measured by a small electromechanical transducer that senses displacement, velocity, and acceleration. Periodic measurements carried out on a machine provide information on any significant changes that are indicative of deterioration in the machinery. These measurements may be continuous, on-line or periodic.

2.7 *Eddy current testing*

Eddy current testing (ECT) methodology uses the principles of electromagnetic induction to inspect electrically conducting components for detection, characterisation and classification of abnormalities. In ECT, an alternating current (frequency range kHz–MHz) is made to flow in a coil (also called probe) which, in turn, produces an alternating magnetic field around it. This coil when brought close to the electrically conducting surface of the material to be inspected, induces an eddy current flow in it due to electromagnetic induction. These eddy currents are generally parallel to the direction of coil winding. The presence of any defect or discontinuity in the material disturbs the eddy current flow. These eddy currents, in turn, generate an alternating magnetic field (in the opposite direction) which may be detected either as a voltage across a second coil or by the perturbation of the impedance of the original coil (Libby

1971). The impedance change in the probe coil is mainly affected by electrical conductivity, magnetic permeability and geometry of the material test frequency, spacing between the coil and the material (also called lift-off or fill factor), and also by the presence of any defect or discontinuity in the material. The impedance change can be measured and can be correlated with changes in the above parameters. When an eddy current probe is scanned over a component consisting of a defect, the amplitude of the eddy current signal (impedance change trajectories) provides information about the severity of the defect, and the phase angle provides information about its depth. Natural cracks or sets of artificial defects made by electric-discharge machining (EDM) or specially produced fatigue cracks are used to calibrate the ECT instruments and to characterise cracks/defects in a reliable manner.

A change in microstructure is generally associated with a change in either electrical conductivity or magnetic permeability. Hence, ECT can be used to assess microstructural degradation of components. While dislocation structures and residual stresses created in the materials affect the electrical conductivity, the formation of magnetic phases affect the magnetic permeability. Studies were carried out by us on the solution annealed AISI 304 stainless steel plates subjected to different degrees of cold work. A good correlation was observed between degree of cold work and the ECT output. Formation of magnetic phases beyond 25% cold work was also observed and confirmed qualitatively by ferritoscope and microscopy (Kasiviswanathan *et al* 1986). These studies clearly indicate the possible use of ECT for detection and quantification of microstructural degradation. Other important applications of ECT include metal sorting, thickness measurement, corrosion monitoring, fatigue crack detection, liquid sodium level monitoring, conductivity measurements etc.

During the last two decades, significant progress has been made in the theoretical and practical aspects of ECT (Shyamsunder & Rao 1992). Axi-symmetric finite difference and finite element models (FEM) have enabled understanding the physics of electromagnetic field/defect interactions. At our laboratory, the work has shown significant promise. A 2D FEM code capable of operating on a personal computer has been developed. This model has been used to predict the impedance changes, the magnetic flux line and eddy current density contours to typify the interactions in ECT. The model was used to optimise probe design for garter spring location in the coolant channels of Pressurised Heavy Water Reactors, the details of which would be given in the case study described at the end of this section. Signal trajectories were predicted for various coil designs (of same cross-sectional area) and optimum design parameters viz. width of coil, depth of coil and spacing between two differential coils of the probe were arrived at, considering the maximum amplitude signal with differential nature. Very good agreement between the predicted and experimental trajectories was observed for ECT probes with varying design parameters due to the presence of a garter spring (Rao *et al* 1990).

Stress corrosion cracking is the major failure mode observed in the case of heat exchanger tubes, since they are subjected to continuous flow of high temperature fluids, steam, and other aggressive environments. The deterioration of the tube material leads to the possibility of leaks. ECT is the most popular technique for periodic monitoring of these tubes because of its ease of operation, versatility and reliability. Conventional single frequency ECT is inadequate when interferences arise from such sources as support plates and other interferences/structures. Many a times, it is under the support plates that corrosion damage often takes place. Multifrequency techniques which

eliminate signals from unwanted parameters like support plate, probe wobble etc. are widely used. This technique involves simultaneous excitation of more than one frequency in ECT probe and processing of the corresponding analog signals to eliminate signals due to unwanted parameters. We have standardised procedures for condition monitoring of steam generators and condensers using two frequency ECT and successfully carried out inspection of such components in power and petrochemical industries. Procedures have also been developed by us to eliminate three parameters (support plates, probe wobble and sodium deposits) that would be present during ECT of heat exchangers of fast breeder reactors (Rao *et al* 1989).

ECT of ferromagnetic heat exchanger tubes is difficult due to their high and continuously varying magnetic permeability. These variations produce high amplitude ECT signals that mask the signals from defects. The use of magnetic saturation can overcome these difficulties to a large extent. Ferromagnetic tubes can be satisfactorily inspected by ECT if they are magnetically saturated. Magnetic saturation essentially indicates a condition where all magnetic dipoles are aligned in the same direction parallel to each other and the material starts behaving non-ferromagnetically. Magnetic saturation is easily achieved during tube manufacture using an external DC saturation coil and eddy current testing is carried out using an encircling eddy current probe. However, the same cannot be implemented during in-service inspection (ISI) of heat exchangers or steam generators due to limited space from the boreside of the tube. In-service inspection of ferromagnetic tubes by eddy current testing (ECT) is a major challenge. In this area, we have successfully designed high strength SmCo_5 permanent magnet-based eddy current probe and results were evaluated using a calibration tube with artificial defects (Shyamsunder *et al* 1993).

For pre-service and in-service inspection of ferromagnetic tubes, a new technique that is showing great promise and potential is remote field eddy current testing (RFECT). The primary advantage of this technique is the ability to inspect tubular products with equal sensitivity to both internal and external metal loss or other anomalies, linear relationship between wall thickness and the measured phase lag and absence of lift-off problems. The technique features the ability to inspect both ferro and non-ferromagnetic materials with equal sensitivity to internal or external anomalies (Kilmore & Ramachandran 1989). Pioneering work has been carried out by us with respect to the development of an RFECT instrument and the computer simulation of the technique. Wall loss down to 15% was detected using an indigenously developed RFECT instrument. The presence of transition and remote field zone and the affect of tube diameter and wall thickness on them have been studied using a 2D-FEM code (Rao *et al* 1993a). Efforts are underway to optimise the frequency and other parameters to obtain better detection sensitivity.

At our laboratory, procedures employing ECT for integrity evaluation of small diameter thin wall fuel cladding tubes of fast reactors (Fast Breeder Test Reactor, 5.1 mm outer dia and 0.38 mm thick; Prototype Fast Breeder Reactor, 8.2 mm outer dia and 0.5 mm thick) have also been standardised. Seven percent wall thickness deep longitudinal and transverse notches and natural defects produced during manufacturing stage have been successfully characterised (Barat *et al* 1982). Complementary capabilities of ECT and ultrasonic testing techniques have been established. These procedures are applicable for carrying out NDE during manufacturing stages, prior to and after irradiation stages. The special probes and gadgetries required for carrying out inspection of irradiated fuel cladding tubes, because of radioactivity and other associated problems have been developed in-house.

One recent technique that has shown tremendous potential in detecting defects in expansion transition zones and rolled joints of heat exchangers with equal sensitivity to both longitudinal and transverse defects in Phased Array ECT (PAECT). This system uses a substantially different bridge circuit and probes that produce a constant magnitude rotating magnetic field which is insensitive to expansion transition zone, tube sheet or support plate. We have designed and developed a tandem PAECT probe that minimises the insensitive zones, in turn, leading to enhanced sensitivity for inspection of tubes (Shyamsunder *et al* 1994).

ECT has benefited with the availability of relatively low cost Personal Computers (PCs) and the accompanying revolution in digital technology (Rao *et al* 1992). A recent outcome of these advances in the area of ECT is eddy current imaging (ECI). We have developed computer-based ECI system to scan the object surface and create impedance images in the form of gray levels or pseudo colours. This consists of a PC-controlled X-Y scanner which scans the component point-by-point in a raster fashion with an ECT probe, acquires data using a 12-bit analogue to digital converter card, and finally processes and displays data in the form of images. Using ECI, it is possible to obtain images of defects in two dimensions enhancing the defect detection capability. Fatigue cracks, corrosion pits, EDM notches and other types of defects have been imaged and characterised (Rao *et al* 1993c). In the case of fatigue cracks, ECI is found to be capable of revealing the orientation of the crack which is an important feature for fatigue crack growth and fracture mechanics studies. ECI has also been used to detect the weld centre line in stainless steel welds with an accuracy of 0.1 mm. This could enable scanning of the welds during angle beam UT and obtaining accurate information on defect location. Other developmental works carried out include: optimisation of probe design for ECI and implementation of filtering and image processing methodologies to improve the quality of images. The above discussions clearly indicate the potential of ECI in detecting and characterising defects in metallic materials effectively.

NDE plays a major role in ensuring safe and reliable operation of Indian nuclear reactors. One of the important condition monitoring technique used in these reactors is ECT. In the following section, such application of ECT i.e. structural integrity evaluation of pressure tube (PT)/Calandria tube (CT) assemblies of Pressurised Heavy Water Reactors (PHWRs) is discussed.

2.7a ECT for structural integrity of PT/CT assemblies – a case study: Pressurised Heavy Water Reactors are the backbone of India's nuclear power programme. These reactors use natural UO_2 as fuel and heavy water as moderator (that slows down the neutrons for their effective participation in the heat generating fission reaction). These reactors are located at Kota, Rajasthan (RAPS) Kalpakkam, Tamilnadu (MAPS), Narora, Uttar Pradesh (NAPS) and Kakrapar, Gujarat (KAPP). A typical 235 MW PHWR consists of 306 channels. Each of these channels consists of a pressure tube (9220 mm long, 82.6 mm dia and 4 mm thick) made of Zircaloy-2 which is positioned horizontally between two tube sheets. Each PT contains 12 fuel bundles and heavy water coolant passes through it. The outlet from all 306 PTs forms the primary heat transport system. Each PT is surrounded by a Calandria tube (107.8 mm diameter and 1 mm thick) again made of Zircaloy-2 leaving a nominal gap of 8.5 mm. Outer regions of the CT form the moderator system. Garter springs (two in earlier reactors and 4 in more recent reactors) are positioned in each of the annular channels so that gaps between the PTs and CTs are maintained (i.e. they do not touch each other during

reactor operation) to prevent heat transfer from primary heat transport system to moderator system. The garter springs are made of an alloy of zirconium, niobium and copper. The material of construction of PTs and CTs is changed to zirconium-2.5% niobium alloy from Kakrapar Atomic Power Project (KAPP) onwards because of its better creep and corrosion properties.

Subsequent to the failure of a PT in the Pickering-2 reactor, similar to PHWR, in Canada in 1983, it was realised that the garter springs could get displaced during hot conditioning and/or during the operating of the reactor (Field *et al* 1984). This displacement increases the unsupported length of the PTs. This increase, coupled with the in-reactor creep of the PTs may make the outer surface of the PTs (at a max. temp. of 548 K) touch the cold inner surface of the CTs (at a temperature of 333 K) leading to the formation of a cold spot and, further, to the generation of massive hydrides through intense hydrogen diffusion to the cold spot region. This, in turn, results in formation of blisters and cracks leading to ultimate failure of the PT. In view of this, the structural integrity of PTs needs to be considered not only with respect to their own properties, but together with the CTs and the garter springs as well. This can be accomplished by performing NDE at various stages viz. during pre-hot conditioning, post-hot conditioning and in-service to monitor the following:

- (a) location of garter springs between PT and CT;
- (b) profiling of gap between PT and CT;
- (c) defect detection in PT.

ECT has been proven to be one of the best technique to fulfill the above mentioned requirements. Development of procedures, design of required ECT probes and training of personnel for carrying out the above mentioned assignments have been undertaken by the authors' laboratory. FEM model has been developed and used to optimise probe design for garter spring locations. Such probes have been successfully used for carrying out PT inspections at various PHWRs. The accuracy of garter spring locations has been ± 5 mm and that of gap profile ± 0.5 mm. Significant work has also been done at the authors' laboratory for the development of a PC-based data acquisition system for acquiring data from an ECT equipment and a database software package for documentation, evaluation and analysis of garter spring data from different reactors during various inspection campaigns (Rao *et al* 1991). The defect detection in the PTs is mainly concerned with the detection of localised hydride blisters, if any. However, other types of defects may also be present. In a full-scale mock-up assembly consisting of various artificial notches, 5% wall thickness deep longitudinal notch and 8% wall thickness deep transverse notch were detected unambiguously.

2.8 Potential drop techniques

Potential drop technique is widely used for crack depth measurements in metallic materials. A crack detected by other NDT techniques can be reliably assessed for its length and orientation by this technique. Also this technique is used to monitor the growth of a crack during the service life of a component. The instruments required for this technique are simple, and portable. Basically, there are two types of techniques, namely Direct Current Potential Drop (DCPD) technique and Alternating Current Potential Drop (ACPD) technique. While the former is useful for detecting and assessing surface and subsurface defects, the latter is useful for detecting and assessing

only surface defects since current is confined to the surface layers only due to classical skin effect phenomenon (Baldev Raj *et al* 1994b).

In these techniques, current is sent into the component perpendicular to the crack through two current electrodes, and the voltage drop across the crack is measured using two voltage electrodes (or the current electrodes themselves and also called probe) and evaluated for parameters of the crack such as depth and inclination to the surface. When the two electrodes of the probe separated by a distance of D units, straddle a crack of depth h , the path length between the electrodes becomes $D + h$, producing a potential difference of V_2 as against V_1 for crack-free regions. The potential differences V_1 and V_2 are measured and the crack depth is computed. The instrument, therefore, consists essentially of a power supply unit to set up the field and a sensitive voltmeter and a suitable probe with two current points spaced by a known distance. The DCPD technique is not affected by the magnetic permeability, but only affected by the electrical resistivity and the geometry of the specimen. In order to evaluate the crack parameters from the measured voltages, calibration charts are needed. We have used this technique to size the fatigue cracks detected by magnetic particle inspection technique in a turbine rotor.

Numerical modelling offers the possibility of obtaining calibration charts for specimens and cracks with complicated geometries and with variations in material properties. Because of need for good electrical contact, the ACPD technique requires extensive cleaning of the component surface. This makes it difficult to deploy in the field. Also the ACPD technique is really suited only for the sizing of cracks already found by other techniques. These drawbacks can be overcome by adopting new technique called alternating current field measurement (ACFM). ACFM involves the measurement of magnetic field disturbances rather than electrical fields. The electrical field is introduced by induction (and therefore requires no electrical contact) and the probe is designed to introduce a uniform input field approximately perpendicular to the expected orientation of the crack. With two orthogonal field sensors, it is possible to both detect and size surface breaking defects without calibration. This technique has been successfully used for reliable and cost-effective inspection of wide range of metallic components including offshore platforms/structures, pressure vessels, pipe supports, threads, sub-sea structures etc. (Topp 1994).

2.9 Acoustic emission technique

Acoustic Emission Technique (AET) has established its rightful place among the available NDE techniques. Acoustic emissions (AE) are the spontaneously generated elastic waves created by discrete movements within the volume of a material being stressed. AE can be detected from the movements as small as those created by phase transformations within a crystalline structure or from movements as large as the propagation of a fatigue crack under low cycle fatigue conditions. Thus, an AE source is the site of a dynamic change in the material which responds to stimuli by releasing part of the energy in the form of elastic stress waves (McIntire & Miller 1987). This dynamic nature of AET makes it a highly potential technique for monitoring the structural integrity of components/structures in various industries with respect to identifying growing cracks in them. AET enables detection and location of defects even in complex geometries. The detection of AE is usually accomplished with a piezoelectric crystal sensor coupled to the part under test. The sensor output is amplified through a high

gain-low noise preamplifier, filtered in order to remove any extraneous low frequency hardware noises, conditioned and displayed. Conventional displays of AE data depict rate of AE, total cumulative counts and amplitude of AE, r.m.s. voltage versus other environmental parameters such as load, temperature, time etc. Various AE signal parameters helpful in evaluating cracks include ringdown counts, events, peak amplitude and their distributions, r.m.s. value, rise time and event duration. Signal analysis, pattern recognition and neural network approaches offer promising possibilities for enhancing the usefulness of this technique.

AET is particularly useful for monitoring structural integrity as it can detect growing cracks down to size of 25 microns, even in the presence of noisy environments. Also, the cracks originating from the inner surface are as easily detectable and distinguishable as those from the outer surface. AET assesses the behaviour of defects under test conditions, an information of major significance for performance evaluation. Further, AET is very useful in predicting fatigue failures in advance (Moore & Tsang 1977). AET has been successfully applied to the detection and monitoring of corrosion fatigue, hydrogen embrittlement and stress corrosion cracking. The inherent advantages of AET are that it is non-localised, it is not necessary to examine specific regions of a structure – a large volume can be tested at one time etc. Many components in high performance aircraft structures are fabricated from structural alloys which, while having high strength levels, have relatively poor crack arresting capability. Small cracks, which have a greater potential to remain undetected, can approach critical size with very little extension. For these types of structures, only AET offers reliable capability to detect any increment of crack growth during structural loading. AET is best suited for on-line monitoring of welds, as it can detect and locate weld defects as they occur. This possibility enables control of quality and any repairs required can be carried out expeditiously and economically. Event rate and r.m.s. voltage of AE signals could be used to detect, locate and differentiate weld cracking, inclusions and process equipment malfunctions like short circuit, current variations and arc drifting etc. (Holroyd 1986).

In our laboratory, we have emphasized the use of AET for both structural integrity monitoring and materials research applications (fracture, deformation, phase transformations, oxidation etc.) (Khanna *et al* 1987; Baldev Raj *et al* 1989, 1990). AET has been used to assess the integrity of pressurised components in operating plants by way of detecting leaks. Pressurized pipes, such as gap pipe lines and heat transport piping in power stations, are generally designed to satisfy the leak-before-break concept (i.e. a crack in a tube grows to cause a small leak long before reaching the critical crack size for catastrophic pipe rupture). However, this concept requires that a leak is detected at an early stage. Thus, AE monitoring is a potential technique for continuous surveillance for detection of cracks (Jayakumar *et al* 1992b).

AET has been applied at the authors' laboratory for understanding deformation and fracture process in austenitic alloys (AISI type 316 stainless steel and Nimonic alloy PE-16), oxidation behaviour in ferritic steels, glass-crystalline transition temperature determination and structural relaxation studies in metallic glasses and martensite transformation in unstable austenite (AISI type 304 stainless steel). In the case of Nimonic PE-16 alloy, various AE parameters have been used to correlate the AE behaviour with particle shearing and Orwan looping processes taking place in the presence of gamma prime and decohesion and fracture of MC occurring during tensile deformation (Jayakumar *et al* 1991). AET has been used by us to study martensite formation in cold worked AISI type 316 stainless steel during cooling after aging and to

determine the temperature range for its formation during cooling (Mukhopadhyay *et al* 1994).

As the AE signals generated in austenitic stainless steel are weak, an innovative technique has been developed by us to amplify the AE signals (Baldev Raj *et al* 1990). The technique is based on the understanding that external injection of ultrasonic waves simultaneously is expected to interact with subcritical AE sources and give rise to enhanced AE signals which otherwise would not have been released at those stress levels. Amplification factors of 2 to 20 could be obtained for peak-to-peak voltage of 0.2 to 0.7 V of the injected signals (Baldev Raj 1990). AET has also been applied for finding possible growth of a repaired crack during service of a pipeline carrying steam at high pressure and temperature. Comparison of AE data near the crack region and at a region away from it indicated events with higher mean peak amplitude near the crack region indicating growth of crack. Subsequent radiographic examination indicated missing of root-pass weld which might have acted as the source for stress concentration/crack initiation. In the following section, a case study highlighting the successful application of AET for detection and location of leak paths in the end shield and pressure tubes of PHWRs is discussed.

2.9a AET for leak detection in PHWR components: AET has been successfully applied for detection and location of leak paths present on an inaccessible side of an end shield of unit 1 of Rajasthan Atomic Power Station (RAPS) (Kalyanasundaram *et al* 1989). This methodology was based on the fact that air and water-leak AE signals have different characteristic features. Baseline data was generated from a sound end shield of a PHWR for characterising the background noise. A mock up end shield system with saw-cut leak paths was used to verify the validity of the methodology. AET was carried out to detect light-water leakage from one of the end shields. Time-domain analysis of AE signals obtained by air pressurisation of the end shield to 0.124 MPa was used for detection and location of leak paths. However, time-domain analysis could not be applied for detection of subsequent leaks, found after repair and operation of the system, as there was limit on maximum air pressurisation of the end shield to 0.035 MPa. Since, the time-domain analysis did not provide any meaningful results, frequency spectral analysis approach was used. Autopower spectra showed presence of characteristic frequency associated with the air leaks. It was also observed that the characteristic frequency of the signal was different for the two leak paths and was attributed to the size, shape and morphology of the leak paths. In another instance, for findings a leaking pressure tube of MAPS, another PHWR type of reactor, advanced frequency analysis approaches have been adopted (Kalyanasundaram *et al* 1992). In this case, simple frequency spectrum could not be used for detection of the leaking pressure tube. Only by using the spectral energy ratio at two different frequency bands and its change with pressure, it was possible to identify the leaking pressure tube. The above studies indicate the advantage of frequency domain analysis over time-domain analysis for detection and location of leaks occurring relatively at low pressures and under noisy environments.

2.10 Infrared thermography

Infrared thermography (IRT) refers to the mapping of the temperature face of an object. This technique utilises the infrared spectral band

radiation. With the aid of a suitable detector, infrared radiation can be converted into an image and visualized for interpretations. The method uses a special television camera with an IR sensitive detector and a lens which transmits IR radiation. Such cameras can operate at conventional video rates. The temperature variations in the object under investigation are displayed as shades of gray or can be converted into a pseudo-colour image. Temperature variations as small as 0.2 degrees can be detected. At ambient temperatures and above, all objects emit electromagnetic radiations predominantly in the infrared region which is invisible to the eye. Variations in the temperature of the surface of the object can be converted into a thermal image and visualised. This helps detection of deviations from normal temperature distribution, from a distance. It is this advantage that the technique exploits. The basic idea behind thermographic NDE is that if a pulse of heat is applied to one side of a specimen, the spatial distribution of the heat flux on the opposite surface will depend on the homogeneity of the specimen (i.e. the presence of internal defects), the diffusivity (which is related to thermal conductivity and volume capacity) and time. The difference between thermographic methods and other methods using electromagnetic radiations is that in the IRT method the heat is propagated by a diffusion process and not instantaneously. The difference in temperature on the surface facing the detector can be measured and related to the size of the internal defect. Infrared thermography can be classified basically into two categories viz. passive and active. In passive technique, the natural heat distribution is measured over the surface of a hot structure. This is generally used for temperature monitoring of structures for assessing their integrity. In an active technique, heating or cooling is induced or applied to the part or complete surface and the redistribution of heat or temperature across of test surface is measured. This is generally used in NDE (Baldev Raj *et al* 1990a).

IRT has several important features which make it attractive for inspection of materials, components and plants. The method is non-contact, dry, safe, fast and displays results of inspection in a convenient visual format. IRT has established a unique position for testing and evaluation of circuit boards, transmission lines, furnaces, air-conditioned enclosures, gas and fluid transfer lines etc. This technique is ideally suited for wear determination of refractories in blast furnaces, hot blast stoves and steel stoves and in the inspection of rotary kiln lining. It has been proved to be a very important tool for predictive maintenance in electrical systems. It can locate any impending failures or locate points which are likely to cause trouble. The technique, being noncontact, is very promising for remote applications.

In the field of materials evaluation, IRT has been applied for monitoring fatigue damage and for mapping of stress fields during cyclic mechanical testing. The technique has also found applications in the control of hot rolling and welding process, detection of surface cracks and surface defects in induction-heated hot-rolled plates (Kubiak 1968). Recent applications of thermography include on-line detection of hot spots, fatigue damage and weld defects in components. Detection of initiation and growth of cracks is also possible using this technique (Cielo *et al* 1987).

Thermography is used extensively to monitor the structural integrity of electrical plants and substations (Venkatraman *et al* 1992). In this direction, various condition monitoring campaigns have been successfully performed by the authors' laboratory, some of them include; 230 kV main transformer of PHWRs, 33 kV switchyard at Indira Gandhi Centre for Atomic Research (IGCAR) and concrete wall of turbine building of Fast Breeder Test Reactor (FBTR). Similarly, IRT has proved to be indispensable for

predictive maintenance in petrochemical industry. In a campaign at a petrochemical industry, hot oil heaters, charge heaters and stack duct-to-air preheaters were inspected by us. Hot spots were observed in certain zones on the hot oil heaters. They were attributed to thinning down of the refractory lining inside the oil heaters and recommended for maintenance during subsequent shutdown. The above-mentioned campaigns have clearly established the capability of IRT technique for condition monitoring.

Apart from this, thermography is being used as a valuable tool for the investigation of weld pools. At our laboratory, studies are being carried out on the adaptability of thermography for on-line monitoring of welds (Venkatraman *et al* 1993a). Thermographic methods are widely used in aerospace and transport industries for the testing of non-metallic materials such as composites and laminates where conventional NDE techniques like RT and UT produce results which are difficult to interpret. IRT has proven to be a valuable tool for detection of impact damage, debonds etc. in composites (McLaughlin *et al* 1980).

2.11 Laser holography

Holography is becoming more and more popular in NDE as its capabilities are understood better. When light is incident on an object, the envelop of the scattered light (called object wave front) contains the visual information of the object. Holography is a technique for recording and reconstructing this object wavefront. Holographic interferometry (HI) technique essentially involves the interference of the object and reference beams (laser) emanating from the component under investigation and recording of the interference pattern on a high resolution photographic plate (hologram). The information in the hologram is extracted by reconstruction of the image by passing a wave similar to the reference beam. The HI technique, being non-contact, is finding place as a complementary or sometimes unique NDE technique in many specialised applications. It is being routinely used in the aircraft industry for inspection of aircraft tyres, microwave antenna etc. This method has shown promising results in the NDE of composite panels, honeycomb structures and bond assessment in adhesively bonded structures (Babu Rao & Baldev Raj 1990). HI technique can be used to investigate the deformation states on the surfaces of pressure vessels. The defects in such components can be differentiated on the basis of their severity. Fringe pattern density is used to find the nature of defects (symmetric or asymmetric etc.). We have used such methodology for the inspection of pressure vessels (Baldev Raj *et al* 1986). Using this method, the effect of stimuli (like load, temperature etc.) can also be assessed. Fabrication and welding processes alter the mechanical properties of the material and introduce residual stresses leading to manifestation of non-uniform deformations. HI technique is well suited to measure these deformations, establish fitness-for-purpose and suggest changes in the manufacturing process and design. HI has been used to establish accept/reject criterion based on measurement of residual stress introduced during pressure testing in a high energy rate formed stainless steel pressure vessel. Good quality vessels are characterised by small and reasonably uniform deformation fields. On the other hand, poor quality vessels exhibit large local yielding and much greater overall residual strains (Halmshaw 1989). Holographic NDT is particularly useful on complex shapes where other NDE methods such as UT, RT are difficult or time consuming to apply.

We have developed new methodology employing project interferometry for profiling of stainless steel fuel cladding tubes of fast reactors. Diameter variations of the order of few microns have been reliably measured (Babu Rao *et al* 1992). This work established the adaptability of this methodology for quality control of tubes towards enhanced structural integrity.

2.12 X-ray diffraction technique

X-ray diffraction (XRD) technique is widely used for measuring residual stresses (RS) in components. RS are generally caused by inhomogeneous plastic strains in a structure. Tensile residual stresses are generally detrimental, increasing the susceptibility of a component to failures due to such causes as fatigue and stress corrosion. On the contrary, compressive residual stresses are usually beneficial, tending to reduce the above susceptibilities (Palanichamy *et al* 1992b). Thus residual compressive stresses are often deliberately created on the surface. The role of NDE in detecting and assessing residual stresses is ever increasing. NDE techniques that have shown capability include UT, MBN and X-ray diffraction (Palanichamy *et al* 1992b).

XRD technique measures the interplanar spacing of the lattice to arrive at elastic strains on the surface layers (generally up to 20–30 microns depending on the density) of the material and converts these data into stresses. To find stress, it is not necessary to obtain the separations of the crystallographic lattice planes in the unstressed condition. The X-ray technique can rapidly measure applied and residual stresses on a small area on the surface of polycrystalline materials. This technique is based on the fact that the shift of location of the diffraction profile (also called the peak position) is proportional to the stress value. Thus peak position determination is of fundamental importance in X-ray stress analysis. PC-based systems are now available for reliable and rapid measurement of stresses (Kurita 1987).

We have successfully used this technique to assess residual stress and post weld heat treatment (PWHT) in autogenous butt weld joints of 2.25 Cr–1 Mo steel tubes which will be used in the steam generator assemblies of the prototype fast breeder reactor. The XRD data has shown the nature of stress at the weld centre. XRD technique studies have confirmed that the proposed PWHT at 988 K for 30 min is sufficient to remove the residuals stresses (Bhattacharya *et al* 1992c). This has been further validated by microhardness measurements in weld and parent metal regions. Residual stresses in explosively welded aluminium and stainless steel joints have also been analysed (Rai *et al* 1993). Residual stress measurements have been carried out on AISI type 304L stainless steel dished ends which failed due to transgranular stress corrosion cracking (Rai *et al* 1994). Residual stress measurements have also been carried out in another important structural material i.e. carbon steel, using XRD, UT and ABN techniques (Palanichamy *et al* 1993). The above studies clearly reveal the capability and potential of XRD technique for the assessment of residual stresses in components, an essential information for structural integrity evaluation.

3. Concluding remarks

An overview on the capabilities and limitations of various NDT techniques that can be used for the structural integrity of components is discussed. A few case studies related to

Table 1. Summary of applicability and capability of various NDT techniques used for assessment of anomalies[®] in materials.

Method	Materials type	Detection capability			Inspection of in accessible regions	On-line monitoring through automated inspection	Capability to size and characterise		
		Surface	Sub surface	Internal			Defects	Stresses	Microstructures
VI	A	Y	N	N	Y	Y	Y	N	N
LPI	A	Y	N	N	*	N	Y	N	N
MPI	M	Y	Y	N	Y	*	Y	N	N
PD	E	Y	Y	N	N	*	Y	N	N
UT	A	Y	Y	Y	Y	Y	Y	Y	Y
ECT	E	Y	Y	Y1	*	Y	Y	*	Y
RT	A	Y	Y	Y	N	Y	Y	N	N
AET [#]	A	Y	Y	Y	Y	Y	Y	N	N
IRT [#]	A	Y	Y	*	*2	Y	Y	N	N
MLFT	M	Y	Y	*	*	Y	Y	Y	*
XRD	A	Y	*	N	N	*	N	Y	*
HIT	A	Y	*	*	*	*	Y	Y	N
AM/VM	A	Y	Y	Y	Y	Y	Y	*	*
MBN/ABN	M	Y	*	N	*	*	N	Y	Y

[®]Defects, stresses and microstructures; [#]dynamic techniques; *—feasibility exists 1—max. 6 mm depth; 2—visual access required; Y—possible; N—not possible; A—all materials; E—electrically conducting materials; M—magnetic materials.

Abbreviations: VI—visual inspection; LPI—liquid penetrant inspection; MPI—magnetic particle inspection; PD—potential drop technique; UT—ultrasonic test; ECT—eddy current test; RT—radiography test; AET—acoustic emission test; IRT—thermography; MLFT—magnetic leakage flux test; XRD—X-ray diffraction technique; HIT—holographic interferometry; AM—acoustic method; VM—vibration monitoring; MBN—magnetic Barkhausen noise; ABN—acoustic Barkhausen noise.

structural integrity based on the investigations carried out by us have been described. The conventional NDT techniques called the big five, viz. magnetic particle, radiography, ultrasonic, eddy current and liquid penetrant techniques can be adapted for many situations. Newer techniques like acoustic emission and thermography are found to be extremely useful and effective for assessment of integrity of components because of their dynamic nature. Table 1 provides information about the capability and applicability of various NDE techniques for the assessment of defects, stresses and microstructural degradations in materials. Improvements in the existing techniques/methodologies and development of new techniques have paved the way for obtaining quantitative information about the anomalies such as defects, stresses and microstructural degradations for easy, sensitive and reliable structural integrity evaluation. A few examples are acoustic microscopy, SAFT, TOFD, eddy current imaging, microtomography, Barkhausen noise analysis (magnetic and acoustic) methods, X-ray stress analysis etc. In recent years, NDT has benefited much with the advent of digital computers, compatible cards and interfacing boards. It is now possible to perform computer modelling to simulate real-life situations to study the interactions between interrogating fields and anomalies. This enables optimised equipment parameters and NDT sensor design for enhancing the sensitivity for anomaly detection. Expert systems, neural network analysis and signal processing and analysis procedures along with the newer NDT procedures provide added impetus to meet the challenges of quality assurance, in-service inspection and failure analysis. However, it is necessary to fully appreciate the capabilities and limitations and the complementary nature of various NDE techniques to enable accurate, reliable and cost-effective inspection.

We wish to thank Dr Placid Rodriguez for his keen interest and constant encouragement during the course of this work.

References

- Arnold W 1990 Tomography of advanced ceramics. *Proc. of Indo-German Conf. on Material Characterisation by Non-Destr. Test Techniques* (Bombay: BARC)
- Babu Rao C, Baldev Raj 1990 Laser techniques in metrology and materials evaluation. *Met. Mater. Processes* 2: 93-116
- Babu Rao C, Vanmathi R, Baldev Raj 1992 Profiling of FBTR clad tubes using projected interferometry. *Proc. of laser symposium Madras*, pp. 338-339
- Baldev Raj 1990 *Acoustic emission for characterising deformation and fracture during tensile testing in austenitic stainless steels*. PhD dissertation, Indian Institute of Science, Bangalore
- Baldev Raj 1992 Looking into future: New techniques in NDT and their potentials. *Proc. of National Seminar NDE-92* (eds) C R L Murthy, Baldev Raj, O Prabhakar, A Sreenivasulu (Bangalore: Interline) 1: 23-38
- Baldev Raj 1993a Status of NDE research and applications in India. *Proc. of the 7th Asia-Pacific Conf. on Non-Destr. Test*. Shanghai, China, pp. 18-37
- Baldev Raj 1993b Inspection of MAPS II turbine LP rotor. Internal report No. IGC/DPEND/93/2
- Baldev Raj 1994a Neutron radiography and gaging - an overview. *Proc. of First Nat. Workshop on Neutron Radiography and Gauging*, Shar, Sriharikota
- Baldev Raj 1994b Intelligent processing of materials. *Proc. of Conf. on Adv. Non-Destr. Test. Techniques* (Hyderabad: Nuclear Fuel Complex)

- Baldev Raj, Ananthakrishna G, Kalyanasundaram P, Barat P, Jayakumar T 1990a Stimulated amplification of acoustic emission signals during deformation. *Scr. Metall.* 24: 69–74
- Baldev Raj, Babu Rao C, Shyamsunder M T, Venkatraman B, Bhattacharya D K 1986 NDE of pressurised vessel by laser holography. *Proc. of National Seminar on Non-Destr. Eval. in Eng. Industry*, Coimbatore, D1: 1–5
- Baldev Raj, Jayakumar T, Thavasimuthu M 1994a *Practical non-destructive testing* (to be published)
- Baldev Raj, Jayakumar T, Rao B P C 1994b Non-destructive test techniques for assessment of cracks. *J. Aeronaut. Soc. India* 46: 101–105
- Baldev Raj, Kalyanasundaram P, Jayakumar T, Barat P 1989 Influence of grain size on frequency spectra of AE signal generated during tensile deformation in an AISI type 316 stainless steel. *J. Acoustic Emission* 8: S140–S144
- Baldev Raj, Thavasimuthu M, Subramanian C V, Kalyanasundaram P, Rajagopalan C 1992 Ultrasonic evaluation of end cap weld joints of PHWR fuel element using signal analysis. *Proc. 13th World Conf. on Non-Destr. Test* (eds) C Hallai, H Kulscar (Amsterdam: Elsevier) 1: 1065–1070
- Baldev Raj, Venkatraman B 1989 *Ionising radiations for non-destructive evaluation*. Indian Institute of Radiation Physics, Kalpakkam, Monograph, Chapter ISRP (K)-TD-1
- Baldev Raj, Venkatraman B, Babu Rao C 1990b An overview of non-destructive applications of thermography. *J. Non-Destr. Eval.* 10: 1–13
- Barat P, Baldev Raj, Bhattacharya D K 1982 A standard procedure for eddy current testing of stainless steel, thin walled nuclear fuel element cladding tubes. *Non-Destr. Test Int.* 15: 251–255
- Beissner R E, Matzkanin G A, Teller C M 1980 New applications of magnetic leakage field methods. NDT Information Analysis Centre, Southwest Research Institute, Texas, Report No. NTIAC-80-1: 1–45
- Bhattacharya D K 1994 *Microstructural characterisation of 2.25 Cr–1 Mo steel, 9 Cr–1 Mo steel and 17–4 PH steel by magnetic Barkhausen noise analysis technique*. PhD dissertation, Indian Institute of Science, Bangalore (submitted)
- Bhattacharya D K, Jayakumar T, Baldev Raj 1992a Magnetic methods for characterisation of microstructure, creep, fatigue damage and residual stresses. *Proc. of National Seminar NDE-92* (eds) C R L Murthy, Baldev Raj, O Prabhakar, A Sreenivasulu (Bangalore: Interline) 1: 110–127
- Bhattacharya D K, Jayakumar T, Palanichamy P, Baldev Raj 1993 Microstructural characterisation using ultrasonic velocity and attenuation measurements. *Proc. 7th Asia-Pacific Conf. on Non-Destr. Test*. Shanghai, China, pp. 110–126
- Bhattacharya D K, Jayakumar T, Vaidyanathan S, Baldev Raj 1992b Magnetic Barkhausen noise analysis for the assessment of microstructures in heat treated 2.25Cr–1Mo and 17–4–PH steel. *Proc. 13th Word Conf. on Non-Destr. Test* (eds) C Hallai, H Kulscar (Amsterdam: Elsevier) 1: 424–428
- Bhattacharya D K, Rai S, Babu Rao C, Vaidyanathan S, Baldev Raj 1992c Assessment of residual stresses and post weld heat treatment in butt weld joints of 2.25Cr–1 Mo steel tubes by X-ray diffraction technique and Barkhausen noise analysis. *Proc. of National Welding Seminar*, Calcutta
- Bohn H, Kroning M *et al* 1987 Proving the capabilities of the phase array probe/ALOK inspection technique. *Nucl. Eng. Des.* 102: 361–367
- Bray D E, Stanley R K 1989a *Non-destructive evaluation—A tool for design, manufacturing and service* (New York: McGraw-Hill) pp. 45–301
- Bray D E, Stanley R K 1989b *Non-destructive evaluation—A tool for design, manufacturing and service* (New York: McGraw-Hill) pp. 365–515
- Cielo P, Maldauge X, Deom A A, Lewak R 1987 Thermographic non-destructive evaluation of industrial materials and structures. *Mater. Eval.* 45: 452–460
- Cochran A McNab A, Hayward G 1991 Flaw monitoring using ultrasonic arrays in-situ. *Br. J. Non-Destr. Test.* 33: 495–505
- Collins R, Mirshekar S D, Micheal D H 1984 Surface current distributions around surface flaws in metals. *Proc. R. Soc. A* 393: 159–170
- David W L 1981 Some implications of fracture mechanics for non-destructive testing. *Proc. of Int. Adv. Non-Destr. Test* (New York: Gordon and Breach) 7: 1–11

- Edwards I, Gros X E, Lowden D W, Strachan P 1993 Fusion of non-destructive testing data. *Br. J. Non-Destr. Test.* 35: 710-713
- Field G J, Dunn J T, Cheadle B A 1984 Analysis of the pressure tube failure at pickering ANG unit 2. AECL-8335, Atomic Energy Canada Limited.
- Forster F 1977 Non-destructive inspection of tubing and round billets by means of leakage flux probes. *Br. J. Non-Destr. Test* 19: 26-32
- Halmshaw R 1989 *Non-destructive testing* 2nd edn (London: Edward Arnold)
- Holroyd T J 1986 Practical applications of acoustic emission. *Br. J. Non-Destr. Test* 28: 224-227
- Jayakumar T, Baldev Raj, Willems H 1991 Acoustic methods for characterisation of microstructures and deformation processes in nimonic alloy PE16. *Trans. Indian Inst. Met.* 44: 327-338
- Jayakumar T, Bhattacharya D K, Baldev Raj 1992a Ultrasonic characterisation of metals and alloys. *Proc. of National Seminar NDE-92* (eds) C R L Murthy, Baldev Raj, O Prabhakar, A Sreenivasulu (Bangalore: Interline) 1: 128-140
- Jayakumar T, Bhattacharya D K, Baldev Raj 1994 Microstructural characterisation by ultrasonic and magnetic methods towards assessment of ageing induced damage in-service. *Proc. of Ageing Management of Nucl. Facilities AMNF-94*, (Bombay: BARC) S7-S33
- Jayakumar T, Bhattacharya D K, Palanichamy P 1993a Ultrasonic attenuation measurements for microstructural characterisation in 17-4 PH steel. *J. Non-Destr. Eval.* (in press)
- Jayakumar T, Bhattacharya D K, Thavasimuthu M, Palanichamy P, Baldev Raj 1993b Ultrasonic measurements for microstructural characterisation in 9Cr-1 Mo steel. *Proc. 7th Asia-Pacific Conf. on Non-Destr. Test.*, Shanghai, China, pp. 216-222
- Jayakumar T, Moorthy V, Bhattacharya D K, Baldev Raj 1992b Acoustic emission studies for leak detection. *Proc. of 13th World Conf. on Non-Destr. Test.* (eds) C Hallai, H Kulscar (Amsterdam: Elsevier) 1: 50-54
- Junger M, Brook C 1990 Beginners guide to principles, sensor selection and evaluation techniques for magnetic flux leakage technique. *Br. J. Non-Destr. Test.* 32: 513-515
- Juva A, Haarvisto M 1977 On the effects of microstructure on the attenuation of ultrasonic waves in austenitic stainless steels. *Br. J. Non-Destr. Test.* 19: 293-297
- Kalyanasundaram P, Baldev Raj, Barat P, Jayakumar T 1989 Reliability of detection of small defects in noisy weldments by advanced signals processing and pattern recognition techniques. *Int. J. Pressure Vessels Piping* 36: 103-109
- Kalyanasundaram P, Baldev Raj, Kasiviswanathan K V, Jayakumar T, Murthy C R L 1992 Leak detection in pressure tubes of pressurised heavy water reactors by AE technique. *Br. J. Non-Destr. Test.* 34: 539-543
- Kalyanasundaram P, Rajagopalan C, Baldev Raj, Prabhakar O, Sarma D G R 1991a High sensitivity detection and classification of defects in austenitic weldments using cluster analysis and pattern recognition. *Br. J. Non-Destr. Test.* 33: 290-297
- Kalyanasundaram P, Rajagopalan C, Subramanian C V, Thavasimuthu M, Baldev Raj 1991b Ultrasonic signal analysis for defect characterisation in composite materials *Br. J. Non-Destr. Test.* 33: 221-226
- Kasiviswanathan K V, Venkatraman B, Baldev Raj 1989 Neutron radiography facilities at IGCAR. *Proc. of Post Irradiation Examination in Nuclear Programme*, (Bombay: BARC) 2: 52-58
- Kasiviswanathan K V, Venugopal V, Baldev Raj 1986 Eddy current studies on stainless steel after mechanical working and thermal annealing. *Proc. National Symposium on Metallography and Non-Destr. Test* (Bombay: BARC) 1: 9/g/1-9/g/10
- Khanna A S, Jha B B, Baldev Raj 1987 The application of acoustic emission techniques in high temperature oxidation studies. *J. Acoustic Emission* 4: 209-213
- Kilmore R J, Ramachandran S 1989 Remote field eddy current testing of small diameter carbon steel tubes. *Mater. Eval.* 47: 32-36
- Kubiak E J 1968 Infrared detection of fatigue cracks and other near surface defects. *Appl. Opt.* 7: 1743-1751
- Kurita M 1987 A new X-ray method for measuring residual stress and diffraction line broadness and its automation. *Non-Destr. Test Int.* 20: 277-283
- Libby H L 1971 *Introduction to electromagnetic non-destructive test methods* (New York: Wiley-Interscience)

- McIntire P, Miller R K 1987 *Non-destructive testing handbook*. Vol. 5, *Acoustic Emission* 2nd edn (Am. Soc. Non-Destr. Test.)
- McLaughlin P V, McAssey V, Deitrich R 1980 Non-destructive examination of fibre composite structure by thermal field technique. *Non-Destr. Test Int.* 13: 56–64
- Mix P E 1987 *Introduction to non-destructive testing – A training guide* (New York: John Wiley & Sons)
- Moore J F, Tsang S 1977 Non-destructive test methods for the early prediction of fatigue cracks. *Proc. Int. Adv. in Non-Destr. Test.* (Gordon and Breach Science) 5: 161–173
- Mukhopadhyay C K, Kasiviswanathan K V, Jayakumar T, Baldev Raj 1994 Acoustic emission from aging-induced martensite formation in cold worked AISI type 304 stainless steel. *Scr. Metall.* 30: 303–307
- Muller W, Schmitz V, Schafer G 1986 Reconstruction by the synthetic aperture focusing technique. *Nucl. Eng. Des.* 94: 393–397
- Palanichamy P, Joseph A, Bhattacharya D K, Baldev Raj 1992a Non-destructive evaluation of residual stresses in austenitic stainless steel butt weld joints by ultrasonic technique. *Proc. of National Welding Seminar*
- Palanichamy P, Joseph A, Jayakumar T, Bhattacharya D K, Baldev Raj 1992b Residual stresses and their evaluation in welds. *Welding engineering handbook* (Trichy: Welding Research Institute) 1: 269–296
- Palanichamy P, Joseph A, Rai S, Bhattacharya D K, Kasiviswanathan K V, Jayakumar T 1993 Non-destructive measurement of residual stresses in carbon steel weld joints. *Proc. of National Welding Seminar* 39(a)–39(d)
- Pelseneer J P, Louis G 1974 Ultrasonic testing of austenitic steel castings and welds. *Br. J. Non-Destr. Test.* 16: 107–113
- Peugeot R S 1982 Theoretical and practical considerations of microfocus radiography. *Mater. Eval.* 40: 150–152
- Rai S, Babu Rao C, Bhattacharya D K, Baldev Raj 1993 Residual stress measurement of explosively welded Al-SS plates using X-ray diffraction technique *Proc. of National seminar NDE-93*, Madras.
- Rai S, Babu Rao C, Bhattacharya D K, Baldev Raj 1994 Evaluation of residual stresses in AISI 304L stainless steel dished ends. *J. Non-Destr. Eval.* (in press)
- Rajagopalan C, Kalyanasundaram P, Baldev Raj 1992 An expert system for ultrasonic testing of austenitic stainless steel welds *Proc. of National Seminar NDE-92* (eds) C R L Murthy, Baldev Raj, O Prabhakar, A Sreenivasulu (Bangalore: Interline) 1: 155–168
- Rao B P C, Babu Rao C, Baldev Raj 1993a Modelling of remote field eddy current test phenomenon. *J. Non-Destr. Eval.* (in press)
- Rao B P C, Jayakumar T, Bhattacharya D K, Baldev Raj 1993b New methodology for precise ultrasonic velocity measurements and its applications. *J. Pure Appl. Ultrasonics* 15: 13–19
- Rao B P C, Shyamsunder M T, Babu Rao C, Baldev Raj 1993c Eddy current impedance imaging of surface defects. *Proc. 7th Asia-Pacific Conf. on Non-Destr. Test.* Shanghai, China pp. 687–693
- Rao B P C, Shyamsunder M T, Babu Rao, Bhattacharya D K, Baldev Raj 1992 Computers in eddy current testing. *J. Non-Destr. Eval.* 12: 13–18
- Rao B P C, Shyamsunder M T, Bhattacharya D K, Baldev Raj 1989 Multifrequency eddy current inspection of heat exchanger assemblies. *Proc. of Seminar on Research in Materials & Management of Corrosion in Industries*, Baroda
- Rao B P C, Shyamsunder M T, Bhattacharya D K, Baldev Raj 1990 Optimisation of eddy current probe for detection of garter springs in PHWRs. *Nucl. Technol.* 90: 389–393
- Rao B P C, Shyamsunder M T, Kalyanasundaram P, Bhattacharya D K, Baldev Raj 1991 Development of eddy current test techniques for condition monitoring of pressure tube/calandria tube assemblies of Indian Pressurised Heavy Water Reactors. *Br. J. Non-Destr. Test.* 33: 437–440
- Shyamsunder M T, Rao B P C 1992 Recent advances in eddy current testing *Proc. of National Seminar NDE-92* (eds) C R L Murthy, Baldev Raj, O Prabhakar, A Sreenivasulu (Bangalore: Interline) 1: 141–154
- Shyamsunder M T, Rao B P C, Babu Rao C, Bhattacharya D K, Baldev Raj 1993 Partial saturation eddy current inspection of ferromagnetic steam generator tubes *Proc. of National Seminar NDE-93* Madras

- Shyamsunder M T, Rao B P C, Babu Rao C, Bhattacharya D K, Baldev Raj, 1994 A new tandem probe design for phased-array eddy current testing. *Insight* 36: 434-436
- Silk M G 1984 The use of diffraction-based time of flight measurements to locate and size defects. *Br. J. Non-Destr. Test.* 26: 208-215
- Silk M G, Whapham A G 1989 Living with defects. *Br. J. Non-Destr. Test.* 31: 307-313
- Subramanian C V, Thavasimuthu, Rajagopalan C, Kalyanasundaram P, Bhattacharya D K, Baldev Raj 1991 Development of ultrasonic evaluation methodology for Zircaloy end cap weld joints in thin walled fuel elements for pressurised heavy water reactor. *Proc. of National Welding Seminar, Madras* 1: 304-311
- Szilard J 1982 *Ultrasonic testing* (New York: Wiley-Interscience)
- Temple J A G 1987 Time of flight diffraction technique. *Int. J. Pressure Vessels Piping* 27: 191-208
- Topp D A 1994 Reliable inspection of offshore structures by ACFM technique. *Insight* 36: 422-425
- University Communique 1987 *Br. J. Non-Destr. Test.* 29: 28-36
- Venkatraman B, Kanmani S, Babu Rao C, Bhattacharya D K, Baldev Raj 1992 In-service inspection of electrical components in atomic power stations by infrared thermographic imaging. *Proc. of National Seminar NDE-92* (eds) C R L Murthy, Baldev Raj, O Prabhakar, A Sreenivasulu (Bangalore: Interline) 1: 102-109
- Venkatraman B, Kanmani S, Babu Rao C, Bhattacharya D K, Baldev Raj 1993a On-line monitoring of welds by infrared imaging. *Proc. 7th Asia-Pacific Conf. on Non-Destr. Test Shanghai, China*, pp. 909-916
- Venkatraman B, Rajagopal C, Baldev Raj 1993b An expert system to aid radiographic testing. *J. Non-Destr. Eval.* (in press)
- Venkatraman B, Sethi V K, Bhattacharya D K 1993c High definition radiography of evaporator welds of steam generator of prototype fast breeder reactor. *Proc. of National Welding Seminar* 1: 26(a)-26(c)/231-237
- Vontz T, Geobbels K, Maisl M, Reiter H, Hireskorn S 1988 Computer aided tomography. *Rev. of Progress in Qualitative Non-Destr. Test.* (eds) D O Thompson, D E Chimenti (New York: Plenum) 7A: 389-397
- Zheng W, Zhu M 1993 A new NDT technique for location of small flaws in small holes. *Proc. 7th Asia-Pacific Conf. on Non-Destr. Test. Shanghai, China*, pp. 708-713

Residual stresses of types II and III and their estimation

P KESAVAN NAIR and R VASUDEVAN

Department of Metallurgical Engineering, Indian Institute of Technology,
Madras 600 036, India

Abstract. Residual stresses (RS) are induced in metallic materials by a variety of working and fabrication processes. They are generally classified into three categories (types I, II and III) depending upon their range of influence. Separation of type I and II stresses often requires stress measurements on thin specimens. Type III stresses are related closely to grain fragmentation and micro-strains associated with plastic deformation. Perhaps the oldest and the most rigorous method of estimating these stresses is still the Warren–Averbach analysis developed during the late forties/early fifties. Other techniques involving integral breadths and variance of the profiles have also been developed. In all these methods developed during the early stages, prior to seventies, a major requirement was well-separated non-overlapping profiles. The late sixties and early seventies saw a dramatic increase in computational capabilities with the advent of powerful electronic computers. This led to the introduction of curve-fitting procedures into the field of X-ray diffraction. The most remarkable achievement of this period is the development of the Rietveld Method. Although this method was initially developed to tackle the neutron diffraction profiles, which are as a rule nearly symmetric and Gaussian in nature, the method saw rapid developments during the eighties. At present, techniques based on concepts developed by Rietveld could be applied to essentially asymmetric and non-Gaussian multiple spectral components of X-ray diffraction profiles. Pattern decomposition techniques which separate composite powder diffraction profiles into individual profiles are now available. In combination with single line profile analysis techniques, this provides a powerful tool in the hands of researchers. A typical example of such a single line profile analysis is given.

Keywords. Residual stresses; microstresses; microstrain; line profile analysis; profile fitting.

1. Introduction

Residual stresses present in a material can be broadly classified into two major categories: macro- and micro-residual stresses. The macro residual stresses are some times referred to as stresses of type I. Following the latter scheme, the micro-residual

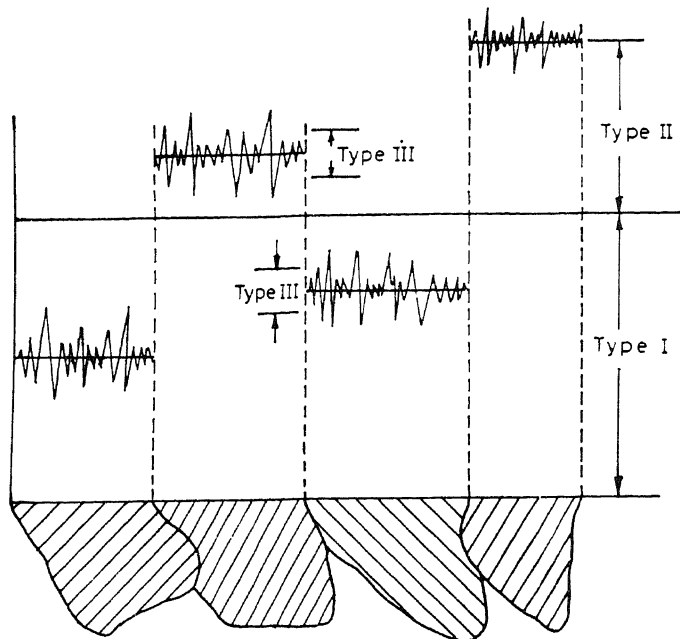


Figure 1. Schematic representation of residual stresses of types I, II and III.

stresses are further classified into two: stresses of types II and III. The basis of this classification is shown in figure 1. The evaluation of type I or macro residual stresses are by now well established (Macherauch *et al* 1973; Hauk & Macherauch 1984). This paper gives an introduction to the more widely used methods for the evaluation of stresses of types II and III. Although both these stresses are commonly referred to as micro-residual stresses, the estimation of these two types of stresses follows different principles. While the evaluation of type III stresses has achieved a relatively high degree of sophistication, that of type II stresses is still relatively difficult; accurate and reliable methods comparable to those available for the evaluation of the other two types are still to be evolved. The principle of X-ray evaluation of type I stresses is based on an accurate measurement of interplanar spacings of a particular set of crystallographic planes. Since both types I and II stresses affect this spacings in a similar manner, any attempt to evaluate the former without taking into account the effect of the latter is bound to be inaccurate. The estimation of type II stresses is discussed in this specific context.

2. Evaluation of type II stresses

In general, all the three types of stresses are likely to be present in a polycrystalline bulk sample. Stresses of types II & III will directly affect the lattice strains. A possible definition of type II stresses could be that it is those stresses existing in the crystals even after complete removal of type I stresses. Indeed, strictly speaking, type II stresses will vary greatly from grain to grain. In a fine-grained polycrystalline material it becomes

rather difficult to evaluate such stresses on a grain-to-grain basis. This necessarily means that only an average value can be obtained. The method of measurement is the usual multiple exposure X-ray diffraction (XRD) technique. Since both type I and type II stresses affect the diffraction profile in a similar fashion, the results obtained through a routine residual stress measurement through the multiple exposure technique are, in general, a sum of these two stresses. The proportion in which they contribute to the total can vary greatly.

Type II stresses can be defined in a more precise way as

$$\sigma_{II} = [\sigma da/da]_{\text{one crystallite}} - \sigma_I \quad (1)$$

where

$$\sigma = \sigma_I + \sigma_{II} + \sigma_{III} \quad (2)$$

and the subscripts I, II, and III means the stresses of types I, II, and III.

The separation of type I and type II stresses is possible only if the distribution is of a specific type, in specimens conforming to definite geometrical requirements (Hauk & Nkolin 1988): for example, in strips and sheets, if the distribution is symmetrical, it is possible to estimate the distribution across the depth. This stipulation arises from the fact that individual estimation of type I or type II stresses can be done only through deflection methods. As is well known, the principle behind the estimation of residual stresses through deflection methods depends upon relating the dimensional or shape changes of a specimen caused by removal of material to the relieved stresses. This in turn requires that the geometry of the specimen be simple (Treuting & Read 1951).

Taking the case of thick strips with a symmetrical stress distribution of type I and type II stresses, a procedure having the following steps can be adopted: (1) Successive layers are removed from both top and bottom surfaces of the specimen in a symmetrical fashion, which ensures that the removal as such will not have any significant effect on the subsequent measurements. Consequently, a routine measurement employing a multiple exposure technique on the surface layers after symmetrical etching can provide type I + type II stress distributions as functions of depth in this type of specimen. (2) A straightforward stress estimation employing the deflection methods can provide the distribution of type I stresses alone. In this case the removal of material is only from one side. The deflection produced can be related to the stresses of type I present in the material. (3) Thin specimens are carefully removed from various positions of the sample in such a way that the removed thin slice is essentially free of type I stresses (Hauk 1983). A routine residual stress measurement employing multiple exposure technique can provide the distribution of type II stresses. The essential features of the above three steps are illustrated in figure 2. If step 3 could be successfully completed, a direct evaluation of type II stresses is obtained, which can be cross checked employing the additive nature of type I and type II stresses obtained in steps 1 and 2. However, it is to be remembered that steps such as the one just detailed are rather specific in application. A general method to evaluate the type II stress distribution is not yet available.

It is clear from the above discussions that the estimation of type II stresses involves residual stress measurement employing multiple exposure X-ray diffraction techniques. All the limitations applicable to the evaluation of residual stresses employing this technique such as linearity of the D vs $\sin^2\Psi$ plots, existence of sharp stress gradients normal to the surface, coarse grain size etc can cause problems in these cases as well (Hauk 1986).

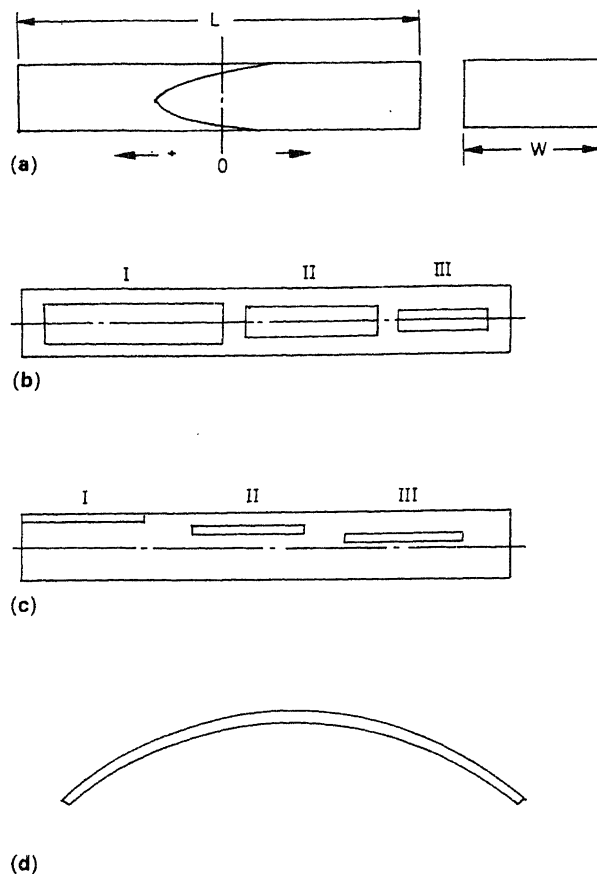


Figure 2. Evaluation of various types of stresses on samples with symmetrical distribution of residual stresses across the thickness, (a) Geometry of specimen with residual stress distribution. (b) Location of specimen for evaluation of $\sigma_I + \sigma_{II}$ after symmetrical etching. (c) location of specimen for evaluation of II. (d) Deflection of specimen on etching on one side for estimation of σ_I .

3. Type III stresses and their evaluation

Type III stresses, as illustrated in figure 1, have a range of action relatively small when compared to the other two. As a consequence, they are estimated as average values. Their effect on the diffraction profile is also different. If present, they tend to change the shape of the profile, rather than the position. Unfortunately, there are quite a number of factors which can affect the shape of the diffraction profile: the dimensions and morphology of the coherently diffracting domains, nonstoichiometry, faults dislocations, instrument geometry etc., apart from internal stresses. This list is only illustrative and not exhaustive. Although a number of parameters are required to characterize the shapes of diffraction profiles, the one most widely used is the breadth of the line profile.

It is generally accepted that the observed diffraction profile (the $h(2\theta)$ profile) is a convolution of the instrument aberration ($g(2\theta)$ profile) and the pure diffraction profile which is due to the specific micro features of the sample ($f(2\theta)$ profile) (Wilson 1963; Warren 1969). The can be written as

$$h(2\theta) = g(2\theta) \times f(2\theta) = g(2\theta')f(2\theta - 2\theta')d(2\theta). \quad (3)$$

Since each point in the observed profile is assumed to be the result of a summation of the product of g and f over all possible values of $f(2\theta)$, the computations involved are quite time consuming. One option would be to do this computation in Fourier space; alternately it can be done analytically, rather than numerically, through a proper choice of functions to present the individual profiles. Chronologically, the Fourier methods found wide acceptance, much before the second option was implemented.

The components contributing to the diffraction profile as mentioned above are discussed individually below.

3.1 The pure diffraction profile f

The principal contributors to this profile are the 'particle size' or the coherently diffracting domain size. This size D is related to the breadth of the size profile through the relation named after Scherrer:

$$\beta(D) = k\lambda/D \cos\theta, \quad (4)$$

where θ is the Bragg angle, and k a constant close to 1.

The second contributing factor to the f profile is the microstrain or the residual stresses of type III. This also broadens the residual stress profile according to the relation:

$$\beta(e) = 4\epsilon \tan\theta. \quad (5)$$

It is generally believed that both these profiles are symmetrical in shape. The former due to particle size is assumed to be having a Cauchy (Lorentzian) and the latter a Gaussian profile (Halder & Wagner 1966; Nandi & Sengupta 1978; de Keijser *et al* 1982).

It is to be remembered that other factors such as compositional inhomogeneities might also affect the breadths of this profile. But generally such effects are assumed to be negligible.

Although the term particle size is used to refer to the coherently diffracting domain size, the terminology is valid perhaps only in the case of inorganic materials where strain effects are negligible. The apparent domain size derived from the breadth of the diffraction profile is a mean length normal to the diffracting planes, averaged over the entire irradiated diffracting volume of the sample. It is to be remembered that size broadening depends strongly on the shape or form of the domain. Consequently the breadth of the profile is likely to be anisotropic in the sense that there might be considerable variations depending upon the reflections considered.

The breadth usually could be the full width at half maximum (FWHM) or the integral breadth (IB). While the former is not amenable to any direct physical interpretation, the latter, in reciprocal space, can be thought of as the volume weighted average crystalline size i.e.

$$D = \beta^* = \beta \cos\theta / \lambda, \quad (6)$$

where β is the integral breadth on a 2θ scale and β^* is the integral breadth on a d^* (i.e. $\sin\theta/\lambda$) scale.

3.2 The strain broadening

As mentioned before, the broadening due to the lattice strain is considered to be nearer to Gaussian in shape. However due to anisotropy of elastic properties, the breadths

need not vary smoothly with Bragg angle (Delhez *et al* 1980). The breadth will thus very much depend upon the particular reflection considered.

3.3 The instrumental profile g

The instrumental profiles vary smoothly with angle (Cox *et al* 1988). The profile shape may also vary between pure Gaussian and pure Cauchy. At low angles, geometric aberrations are predominant and at high angles, effects due to wavelength distributions predominate. Usually the g profile is experimentally obtained as the profile from a well-annealed defect-free standard sample.

3.4 Separation of size and strain effects

3.4a Methods based on integral breadths: Classical or conventional ways of separation require at least two orders of the same reflection in order to separate the size and strain effects. However, before attempting such a separation it is essential that the instrumental effects are eliminated from the observed profile. For this purpose the experimentally obtained g profile from an appropriate standard material is used. As a first step the effect due to the doublets is eliminated through analytical procedures such as the Rachinger's method (Pease 1948; Rachinger 1948) and the pure diffraction profile f is obtained through any of the following relationships (Jagodzinski 1949; Anantharaman & Christian 1956; Taylor 1961),

$$\beta = B - b$$

$$\beta = B - b^2/B$$

$$\beta^2 = B^2 - b^2$$

where β is the corrected breadth, B and b are the breadths of observed and instrumental profiles after eliminating the wavelength dispersion effects. Equation (7) assumes that both the observed profiles are Lorentzian and (9) assumes that both are Gaussian in shape. Equation (8) yields a value in between. This corrected breadth β includes the effects due to both size and strain effects.

The procedure for obtaining the strain or particle size from this corrected breadth involves the assumption that the breadth of the size profile β_D and that of the strain profile β_e are related through (Anantharaman 1959; Rama Rao & Anantharaman 1963)

$$\beta^2 = \beta_D^2 + \beta_e^2. \quad (10)$$

This when combined with (4) and (5) above yields a linear relationship between $(\beta \cos \theta / \lambda)^2$ and $(\sin \theta / \lambda)^2$ with a slope of $16\epsilon^2$ and an intercept of the reciprocal of the square of the apparent crystallite size. It is the necessity of plotting (10) to obtain the slope and intercept, which dictates that at least two orders of reflections be available. Alternately, if the sample is reasonably isotropic, one can use the breadths of other reflections as well for the above plot. The size obtained in this manner includes effects due to stacking faults, dislocations etc.

Yet another method of obtaining the pure diffraction profile in a more direct fashion is the well-known Stoke's correction (Stokes 1948; Warren 1969). Here the removal of effects due to the instrumental profile is carried out in Fourier space by expressing the

observed and the experimentally obtained g profile as a Fourier series. The Fourier coefficient of f profile can be shown to be given by

$$F(n) = H(n)/G(n), \quad (11)$$

where n is the harmonic number and $F(n)$, $G(n)$ and $H(n)$ are the respective Fourier coefficients of f , g and h profiles. This method is completely rigorous and makes no special assumptions regarding the profile shape. Once the coefficients of the pure diffraction profile are obtained, the latter can be synthesized and treated in a similar fashion as above. However, a more elegant way of separating the strain and size effects is the Warren-Averbach Method, discussed below (Warren & Averbach 1950, 1952).

3.4b The Warren-Averbach method: The Fourier real coefficients of the pure diffraction profile can be related to the coefficients of the size and strain profiles through

$$A(L) = A^D(L)A^\epsilon(L), \quad (12)$$

where L refers to a distance normal to the diffracting planes and the superscripts D and ϵ to particle size and strain respectively. For small values of L , the coefficients of the size and strain profiles can be approximated by

$$A^D(L) = 1 - L/D_{hkl}, \quad (13)$$

$$A^\epsilon(L) = 1 - 2\pi^2 L^2 [\langle \epsilon^2 \rangle - \langle \epsilon \rangle^2] S_0^2, \quad (14)$$

where D_{hkl} is the domain size normal to the reflecting planes hkl and ϵ is the microstrain or type III strain. S_0^2 is given by

$$S_0^2 = (2\sin\theta/\lambda)^2 = (h^2 + k^2 + l^2)/a^2. \quad (15)$$

Combining (12)–(14) for small values of L , one obtains

$$\ln A(L) = \ln A^D(L) - 2\pi^2 L^2 [\langle \epsilon^2 \rangle - \langle \epsilon \rangle^2] S_0^2. \quad (16)$$

Thus a plot of $\ln A(L)$ against S_0^2 will be a linear one with the intercept giving $\ln A^D(L)$, the particle size coefficient. The slope of this plot is a measure of the microstrain, given by $[\langle \epsilon^2 \rangle - \langle \epsilon \rangle^2]$:

$$\begin{aligned} \langle \epsilon_L^2 \rangle^{1/2} &= [\langle \epsilon^2 \rangle - \langle \epsilon \rangle^2]^{1/2} \\ &= [\ln A^D(L) - \ln A(L)]^{1/2} / (2\pi) L S_0, \end{aligned} \quad (17)$$

where ϵ_L is the component of the strain normal to the reflection plane, averaged over the distance L . This strain is a function of the averaging distance and usually decreases with L , reaching an asymptotic value for large L . An accurate and acceptable interpretation of this plot is still not available.

3.5 Limitations on the application of integral breadth and Fourier methods

Both integral methods and Fourier methods presume the existence of well separated and independent reflections from the sample. All too often situations arise where the peaks are extensively overlapped by neighbouring reflections. Very often even moderately well-resolved reflections might be absent. Such complex patterns are very common in modern materials such as composites, ceramics, polymers etc. The reflections may rise

not only from well crystallized grains, but also from quasicrystalline, nanocrystalline or amorphous materials. Analysis of such patterns are becoming a necessity in the present day context. Fortunately, pattern decomposition methods are available now which enable one to handle such situations with a reasonable degree of confidence.

3.6 Methods based on profile refinement

As mentioned above, most of the classical methods require well-resolved powder diffraction profiles and input data of high quality. These two requirements often lead to a dead end. The entire process of profile analysis got new life and interest in it was renewed with the introduction of least squares structure refinement based on concepts originally proposed by Rietveld (1967, 1969). The basic idea was to least square refine the parameters until the best fit is obtained between the entire observed diffraction pattern as a whole and a calculated pattern based on simultaneously refined parameters which affect the diffractogram one way or the other. Factors Such as crystal structure, instrumental effects, specimen imperfections or any other effect could be included so long as they can be modelled. An important feature of this method is the feedback during the refinement process itself between the improving goodness of fit and the relevant structural parameters. What is refined are the parameters themselves and not the profile. Although the method was originally proposed for the analysis of neutron diffraction profiles, it was quickly realized that its domain of application is really vast. In the present context the method has high potential to provide data on the structural imperfections of the material to be analysed.

An essential requirement for this purpose is to ascribe a suitable analytical function to the line profile. Early workers, as already mentioned, assumed a wholly Gaussian or a Lorentzian profile. However, later it was shown that deficiencies do exist in both these cases (Suortti *et al* 1979; Young 1980). At present it is recognized that a pseudo-Voigt or a Pearson VII profile shape function can be considered to be most suitable for the purpose (Hall *et al* 1977; Young *et al* 1982; Thompson *et al* 1987). The Voigt function is the result of an analytical convolution of a Gaussian and a Lorentzian,

$$V(x) = I_0 [\beta/\beta_c \beta_g] \int C^V(z) G^V(x-z) dz \quad (18)$$

with

$$C^V(x) = [1 + (\pi^2 x^2 / \beta_c^2)^{-1} = (1 + 4x^2)/(2w_c)^2]^{-1}$$

and

$$G^V(x) = \exp(-\pi x^2 / \beta_g^2) = \exp[(-4 \ln 2) x^2 / (2w_g)^2]$$

where C^V and G^V indicate the Cauchy and Gaussian components having integral breadths of β_c and β_g respectively with $2w_c$ and $2w_g$ as the corresponding full widths at half maximum. I_0 is the peak maximum intensity (at $x = 0$) and β the integral breadth of the Voigt profile, $V(x)$. As can be seen, the range of profiles that can be handled varies from pure Gaussian to pure Cauchy, depending on the ratio of the component widths. The pseudo-Voigt function on the other hand provides for a mixing parameter in the form of fractions of superposed Lorentzian and Gaussian components needed to fit an observed profile (Hindeleh & Johnson 1972),

$$pV(x) = I_0 [C^{pV}(x) + G^{pV}(x)], \quad (19)$$

where

$$C^{pV}(x) = \eta [1 + \Pi^2 x^2 / (\beta_{C'})^2]^{-1},$$

$$G^{pV}(x) = (1 - \eta) \exp[-\Pi^2 x^2 / (\beta_{G'})^2],$$

with

$$0 \leq \eta \leq 1.$$

The subscripts C' and G' denote that the respective integral breadths refer to Cauchy and Gaussian profiles respectively. η is the fraction of the Cauchy component required to obtain the best fit during the least squares process. In most of the modern computer programs this fraction itself is one of the parameters to be refined during execution. Since the Gaussian is a relatively broad profile and the Lorentzian a narrow one, the mixing of the two can represent a symmetric profile. The Pearson VII is also a symmetric profile function which can equally well represent a symmetric diffraction profile:

$$pVII(x) = I_0 (1 + x^2 / ma^2)^{-m}, \quad 1 \leq m \leq \infty, \quad (20)$$

with

$$a = \beta \Gamma(m) / [m\pi]^{1/2} \Gamma(m - 1/2),$$

where $m = 1$ implies a pure Cauchy profile and $m = \infty$, a pure Gaussian one. The Gamma Function is denoted by the symbol Γ . Both Voigt and Pearson VII functions can represent asymmetrical profiles by employing the respective split-type functions. In this case, the diffraction profile is split into a low angle side and a high angle side at the peak maximum. Two different Pearson VII or Voigt functions, as the case may be, are then fitted on either side. In other words the profile is represented by two functions having a common peak maximum position and intensity (Snyder 1993). However, they may have different values of full width at half maximum, decay rates, and other profile parameters. Further, the functions denoted by $P(x)_{low}$ and $P(x)_{high}$, representing the low and high angle sides of the profile should satisfy the following condition:

$$\int_{-\infty}^T P(x)_{low} dx + \int_T^{+\infty} P(x)_{high} dx = 1. \quad (21)$$

In most of these refinement procedures a number of profile parameters like FWHM, the integrated intensity, the peak position etc. are simultaneously refined and final optimized values obtained. Once an optimized profile fit is obtained, the Gaussian and the Cauchy components of the profile can be separated, and the size and strain calculated based on (4) and (5) assuming the Cauchy breadth for size and the Gaussian breadth for strain (de Keijser *et al* 1982).

Another approach is to obtain the Cauchy and Gaussian integral breadths from the experimental values of the integral breadth (β) and the ratio (ϕ) of the fullwidth at half maximum to the integral breadth of the g and h profiles. This can be done graphically (Langford *et al* 1988) or using empirical equations such as (de Keijser *et al* 1982),

$$\beta_C = \beta(2.0207 - 0.4803 \phi - 1.7756 \phi^2), \quad (22)$$

$$\beta_G = \beta[0.6442 + 1.4187(\phi - 2/\pi)^{1/2} - 2.2043 \phi + 1.8706 \phi^2]. \quad (23)$$

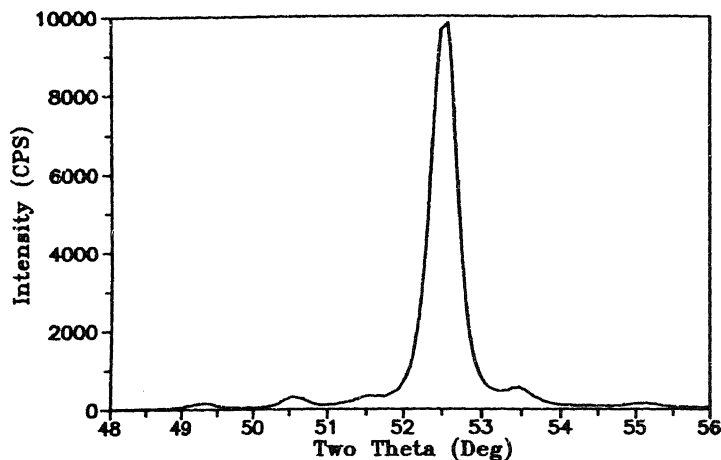


Figure 3. The experimental profile from electroless Ni-P deposit with 4.4 wt. % phosphorus after annealing at 400°C for 2 h.

Once the Cauchy and Gaussian breadths of the experimental g and h profiles are known those of the f profile can be calculated employing equations similar to (7) and (9). Further, the crystalline size and strain could be estimated using the Cauchy and Gaussian breadths of the f profile in (6) and (5) respectively.

Alternately, if two orders of the reflection are available, the integral breadths of the total profile can be straightaway made use of to obtain the size and strain components.

A cross-comparison between the results of a multiple line analysis and single line analysis might not produce identical values for profile parameters. This is mainly

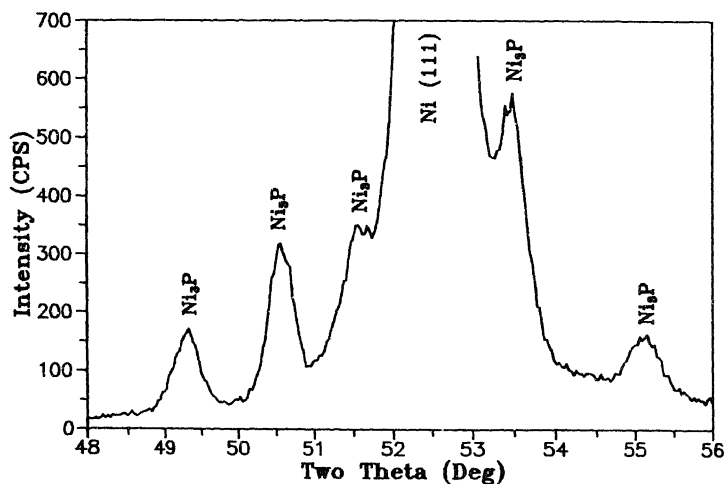


Figure 4. The experimental profile from electroless Ni-P deposit with 4.4 wt. % phosphorus after annealing at 400°C for 2 h (enlarged intensity scale).

because the weightage of the Gaussian and Cauchy contents for different orders of reflection will not, in general, be the same (de Keijser *et al* 1983).

A typical example of a single line size-strain analysis is given below in order to demonstrate the capabilities of the approach.

3.7 Profile separation and single line profile analysis: An example

In figure 3 an experimental profile obtained from a Ni-P electroless deposit on mild steel substrate is presented. The diffractogram was obtained after annealing the sample for 2 h at 400°C. The P content of the deposit was 4.4%. As is evident there is extensive overlap between the main high intensity Ni (111) profile and the emerging Ni₃P peaks. The same pattern is shown on an enlarged scale to have a better appreciation of the extensive overlap between the profiles in figure 4. The profile was deconvoluted with a least square fitting procedure employing the pseudo Voigt function (Toraya 1986). The separated profiles are presented in figure 5. As mentioned earlier, a number of parameters are simultaneously refined. The final refined parameters are presented in table 1.

For the purpose of single line analysis, annealed pure Ni powder was used as a standard. The refined parameters obtained from this profile (not shown) were used for correcting the observed profile breadths and the size and strain calculated employing (4) and (5).

4. Concluding remarks

Procedures for separating type I and type II stresses are discussed. The separation procedure is a combination of X-ray diffraction and mechanical dissection type of techniques. Consequently a complete distribution of type II stresses can be obtained

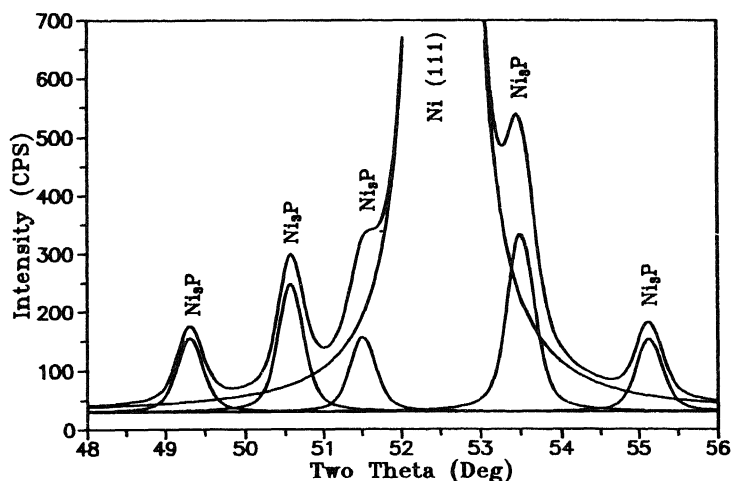


Figure 5. The deconvoluted individual diffraction profiles and total profile corresponding to figure 4.

Table 1. Parameters from profile fitting and results of single line analysis.

Parameters from profile fitting		
<i>Parameters are in degrees (Two theta scale)</i>		
Profile shape : pseudo-Voigt		
Radiation used : cobalt		
$L1 = 1.788965, L2 = 1.792850, K = 0.4970$		
Theta range : 48.00–56.00 Step : 0.03		
$B1 = 30.03, B2 = 0.00, B3 = 0.00$		
<i>Profile identification : Ni(111)</i>		
Integrated Intensity	:	5179.866000
Peak intensity ($A1 + A2$)	:	10018.730000
Peak intensity position	:	52.529820
Integral breadth ($A1 + A2$)	:	0.517018
Alpha 1 and alpha 2 separation	:	0.122791
	<i>Alpha 1</i>	<i>Alpha 2</i>
Integrated intensity	:	3453.244000 1726.622000
Peak intensity	:	7273.720000 3612.031000
Peak maximum position	:	52.504000 52.626790
Integral breadth	:	0.474756 0.478020
FWHM	:	0.357625 0.357625
Cauchy content	:	0.519539 0.537562
Gaussian content	:	0.480461 0.462438
Cauchy breadth	:	0.309947 0.320140
Gaussian breadth	:	0.249624 0.244629
Results of single line analysis		
<i>Profile identification : Ni(111)</i>		
Integral breadth of diffraction profile	=	0.3875569
FWHM of diffraction profile	=	0.3038880
Cauchy breadth of diffraction profile	=	0.1888990
Gaussian breadth of diffraction profile	=	0.2057786
Cauchy content of diffraction profile	=	0.5129336
Gaussian content of diffraction profile	=	0.4870664
<i>Particle size = 605 Å</i>		
<i>Micro strain = 1.821 E – 03</i>		

only under limited conditions. The estimation of type III stresses has made remarkable advance in recent years. Induction of the Rietveld concepts into profile analysis has given greater flexibility in their estimation.

References

- Anantharaman T R 1959 *Indian Institute of Science Golden Jubilee Research Volume*, p. 280
 Anantharaman T R, Christian J W 1956 The measurement of growth and deformation faulting in hexagonal cobalt. *Acta Crystallogr.* 9: 479

- Cox D E, Toby B H, Eddy M M 1988 Acquisition of powder diffraction data with synchrotron radiation. *Aust. J. Phys.* 41: 117-131
- De Keijser Th H, Langford J I, Mittemeijer E J, Vogels A B P 1982 Use of Voigt function in a single line method for analysis of X-ray diffraction line broadening. *J. Appl. Crystallogr.* 15: 308-314
- De Keijser Th H, Mittemeijer E J, Rozendaal H C F 1983 The determination of crystallite size and lattice strain parameters in conjunction with the profile refinement method for the determination of crystal structures. *J. Appl. Crystallogr.* 16: 309-316
- Delhez R, De Keijser Th H, Mittemeijer E J 1980 *Accuracy on powder diffraction: Natl. Bur. Stand. Special Publication 567* (eds) S Block, C R Hubbard (Washington, DC: NBS) pp. 212-253
- Halder N C, Wagner C N J 1966 Analysis of broadening of powder pattern peaks using variance, integral breadth and fourier coefficient of line profile. *Adv. X-ray Anal.* 9: 91-102
- Hall Jr, Veeraraghavan M M, Rubinh V G, Winchell P G 1977 Approximation of symmetric X-ray peaks by Pearson Type-VII distribution. *J. Appl. Crystallogr.* 10: 66-68
- Hauk V 1983 *Residual stresses, their importance in science and technology* (eds) E Macherauch, V Hauk (Oberursel: Deutsche Gesellschaft fuer Materialkunde (DGM)) pp. 1-9
- Hauk V 1986 *Residual stresses in science and technology* (eds) E Macherauch, V Hauk (Oberursel: Deutsche Gesellschaft fuer Materialkunde (DGM)) 1: 353-361
- Hauk V, Macherauch E 1984 A useful guide for X-ray stress evaluation. *Adv. X-ray Anal.* 27: 81-99
- Hauk V, Nkolin H J 1988 *Texture Microstruct.* 8 & 9: 693-716
- Hindeleh A M, Johnson D J 1972 Crystallinity and crystallite size measurement in cellulose fibres: 1 Ramie and Fortisan. *Polymer* 11: 423-430
- Jagodzinski H 1949 Ein Dimensionale Fehlordnung in Kristallen und ihr Einfluss auf die Roentgeninterferenzen. *Acta Crystallogr.* 2: 201
- Langford J I, 1978 A rapid method for analysing the breadths of diffraction and spectral lines using the voigt function. *J. Appl. Crystallogr.* 11: 10-14
- Langford J I, Delhez R, De Keijser Th H, Mittemeijer E J 1988 Profile analysis for micro crystalline properties by the fourier and other methods. *Aust. J. Phys.* 41: 173-81
- Macherauch E, Wohlfahrt H, Wolfsteig U 1973 Zur Zweckmassigen Definition von Eigenspannungen. *Haertere-Tech. Mitt.* 28: 201-211
- Nandi R K, Sengupta S P 1978 Analysis of X-ray diffraction profiles from imperfect solids by an application of convolution relations. *J. Appl. Crystallogr.* 11: 6-9
- Pease R S 1948 The resolution of X-ray double diffraction lines into α_1, α_2 components. *J. Sci. Instrum.* 5: 353
- Rachinger W A 1948 A correction for α_1, α_2 doublet in the measurement of widths of X-ray diffraction lines. *J. Sci. Instrum.* 25: 254
- Ramarao P, Anantharaman T R 1963 X-ray line breadth analysis of deformed metals. *Z. Metallkd.* 54: 658-663
- Rietveld H M 1967 Line profiles of neutron powder diffraction peaks for structure refinement. *Acta Crystallogr.* 22: 151-152
- Rietveld H M 1969 A profile refinement method for nuclear and magnetic structures. *J. Appl. Crystallogr.* 2: 65-71
- Snyder R L 1993 *The Rietveld method* (ed.) R A Young (London: Oxford University Press) pp. 111-131
- Stokes A R 1948 A numerical Fourier analysis method for the correction of widths and shapes of lines on X-ray powder photographs. *Proc. Phys. Soc. London* 61: 382-391
- Suortti P, Ahtee M, Unonius Z 1979 Voigt function fit of X-ray and neutron powder diffraction profiles. *J. Appl. Crystallogr.* 12: 365-369
- Taylor A 1961 *X-ray metallography* (New York: John Wiley & Sons) p. 686
- Thompson P, Cox D E, Hastings J B 1987 Rietveld refinement of Debye-Scherrer synchrotron X-ray data from Al_2O_3 . *J. Appl. Crystallogr.* 20: 79-83
- Toraya H 1986 Whole powder pattern fitting without reference to a structure model: Application to X-ray powder diffractometer data. *J. Appl. Crystallogr.* 19: 440-447
- Treuting R G, Read W F Jr 1951 A mechanical determination of biaxial residual stress in sheet materials. *J. Appl. Phys.* 22: 130-134

- Warren B E 1969 *X-ray diffraction* (Reading, MA: Addison-Wesley)
- Warren B E, Averbach B L 1950 The effect of cold work distortion on X-ray patterns. *J. Appl. Phys.* 21: 595-599
- Warren B E, Averbach B L 1952 The separation of cold work distortion and particle size broadening in X-ray patterns. *J. Appl. Phys.* 23: 497-498
- Wilson A J C 1963 *Mathematical theory of X-ray diffractometry* (Eindhoven: Centrex)
- Young R A 1980 *Accuracy on powder diffraction*. *Natl. Bur. Stand. Special Publication 567* (eds) S Block, C R Hubbard (Washington, DC: NBS) pp 143-163
- Young R A, Prince E, Sparks R A 1982 Suggested guidelines for the publication of Rietveld analyses and pattern decomposition studies. *J. Appl. Crystallogr.* 15: 357-358

Creep crack growth in power plant materials

PARMEET S GROVER and ASHOK SAXENA

School of Materials Science & Engineering, Georgia Institute of Technology,
Atlanta, GA 30332-0245, USA

Abstract. Economic considerations have made it desirable to extend the 30 to 40 year operating life of power plants by another 10 to 20 years. Crack growth at elevated temperatures is an important consideration in estimating the remaining life, determining operating conditions and deciding inspection criteria and intervals for power plant materials. This paper presents an overview of high-temperature crack growth phenomenon in such materials. The focus is on various techniques used for characterizing creep crack growth (CCG) and creep-fatigue crack growth (CFCG) in high-temperature materials. The collection of data, their analysis and the interpretation of results is discussed in detail, especially for CFCG laboratory testing. The discussion is primarily focussed on creep-ductile materials such as those used in power plant applications. Special considerations for elevated temperature crack growth in weldments are also presented. Finally, the application of these concepts to the life prediction of power plant components is also discussed.

Keywords. Creep crack growth; power plant applications; creep-fatigue crack growth; high temperature crack growth; life of power plants.

1. Introduction

A significant number of power plants all over the world have been in operation for durations close to their design lives of 30 to 40 years. Due to economic considerations it is desirable to extend their operating life by another 10 to 20 years. According to economic studies, the cost of life extension of a typical power plant is only 20% to 30% of the cost of building a new plant whereas the benefits are much higher (Dooley & Viswanathan 1987). In order to ensure that power plant components are retired for cause rather than on the basis of their 'design life', *remaining-life-assessment* must be made. Crack growth at elevated temperatures becomes an important consideration in the estimation of remaining life, in the determination of operating conditions and in deciding inspection criterion and intervals. Fracture mechanics approaches that have been developed over the past few decades have proven useful in providing a rigorous framework for accomplishing these goals.

In the next few sections, an overview of the materials commonly used in fossil power plant components, the service conditions they are exposed to and the types of failures

that are commonly encountered during service is provided. This information is used as the basis to provide motivation for the use of remaining crack growth life assessment technology for life prediction and deciding safe inspection intervals for components in these power plants. The relevance of high temperature crack growth and fracture mechanics approaches in this context has been highlighted.

1.1 *Materials used in power plant components*

Power plant components are made of a variety of materials which are capable of withstanding a wide range of operating conditions in the plant, depending upon the local conditions of pressure, temperature and chemical environment (Viswanathan 1989). Low-alloy ferritic steels containing carbon, molybdenum and/or vanadium constitute the bulk of the material used in steam power plants (Viswanathan 1989). High-alloyed tempered martensitic steels containing ~ 12% Cr along with Ni and Co based superalloys are the other widely used materials. Table 1.1 in Altekian (1980) gives the properties required for various components in steam power plants and the materials used for their construction.

The materials mentioned above are subjected to demanding pressure and temperature conditions which are summarized by Jaffee (1979) for a steam power plant. These demanding conditions lead to the degradation of these materials and consequently to the partial or complete failure of the component.

1.2 *Definitions of failure of components*

While catastrophic fracture or rupture is the most evident form of failure, table 1 (Viswanathan & Dooley 1986) shows the various failure criteria and definitions used by the industry to retire a component before such failures occur. Failure of a component

Table 1. Failure criteria and definitions of component life.

History-based criteria

30 to 40 years have elapsed

Statistics of prior failures indicate impending failure

Frequency of repair renders continued operation uneconomical

Calculations indicate life exhaustion

Performance-based criteria

Severe loss of efficiency indicating component degradation

Large crack manifested by leakage, severe vibration, or other malfunction

Catastrophic burst

Inspection-based criteria

Dimensional changes have occurred, leading to distortions and changes in clearances

Inspection shows microscopic damage

Inspection shows crack initiation

Inspection shows large crack approaching critical size

Criteria based on destructive evaluation

Metallographic or mechanical testing indicates life exhaustion

From Viswanathan & Dooley (1986)

may generally be defined as the inability to perform its intended function reliably, economically and/or safely (Viswanathan 1989).

1.2a Crack growth at elevated temperatures: A number of crack growth mechanisms operate at the elevated temperatures to which power plant components are subjected. These include creep, creep-fatigue, oxidation, stress corrosion cracking, corrosion-fatigue and thermal-fatigue. Often more than one of these operate simultaneously and probably have synergistic effects on the rate of crack growth and, consequently, on the material degradation. Hence, the study of elevated temperature crack growth is vital for understanding failure of power plant components.

1.2b Retirement of components from service: Economics rather than technical need has often formed the basis for decisions to retire components from service in the past because an investigation into the cost to benefit ratio of keeping the component in service may prove expensive. This is due to the high cost of carrying out remaining-life calculations based on the operating history, regular inspections and material testing. Further, if the decision arrived at after expensive analysis is not favorable, the economic penalties can be severe. This requires that life prediction methods be accurate and must also be inexpensive to perform.

1.3 Motivation for life prediction

Due to the high expenses associated with a forced plant outage, the conservative practice has been to replace certain components, or those which have a history of failure, after a fixed interval of time regardless of their actual condition. However, with the recent developments in areas such as fracture mechanics, materials testing and NDE techniques, confidence has increased in the application of these concepts for life prediction and consequently extending component life beyond their 'design life' and up to their 'actual life'. Some other factors which have contributed to the desire of extending plant life and consequently encouraging the use of remaining-life-assessment technology are (Viswanathan 1989):

- (a) the escalating cost of new construction and diminishing capital resources;
- (b) extended lead times in plant construction;
- (c) uncertainties in projected demand growth rates;
- (d) limited availability of suitable sites for new construction;
- (e) increasingly stringent environmental, safety and other regulations.

A very important use of life-prediction procedures, besides extending plant life, is the determination of safe intervals for inspection, repair and maintenance. Thus, in order to carry out these steps of remaining-life-assessment technology, study of high-temperature crack growth in power plant materials becomes very important.

1.4 Objectives of this paper

In keeping with the current needs of the power generation industry to extend the operating life of existing power plants, a study of high-temperature crack growth phenomenon in power plant materials is presented. Various techniques developed for

characterizing elevated temperature crack growth have been discussed with emphasis on data collection, analysis and interpretation of results. Essentially, fracture mechanics approaches have been presented. Creep crack growth (CCG) and creep-fatigue crack growth (CFCG) have been discussed in detail with emphasis on the latter. The discussion is primarily focussed on creep-ductile materials¹. Special considerations for high-temperature crack growth in weldments have also been discussed. Finally, all these concepts have been applied to life prediction of power plant components like steam-turbine casings. This presentation is aimed to be application oriented. Some recommendations for future research in this area are also provided.

2. Review of time-dependent crack-tip parameters

Fracture mechanics approaches are extrapolative i.e. the results obtained using small laboratory specimens can be "extrapolated" to make predictions in actual components. Various crack-tip parameters have been proposed which characterize the state of stress at the crack tip. The underlying idea behind these crack-tip parameters is that they act as a 'transfer function' from a specimen in the laboratory to actual structural behaviour. Identical conditions of stress and deformation at the crack tip result in the same value of these crack-tip parameters regardless of the shape and size of the specimens or the structures.

When a cracked body is subjected to constant load at elevated temperatures, the initial stress-strain response due to sudden loading is similar to that under subcreep temperatures. A $1/r^{1/2}$ -type and HRR-type (Hutchinson-Rice-Rosengren type) singular stress field is formed in elastic and elastic-plastic materials, respectively. However, with the passage of time, creep strains (inelastic in nature) begin to accumulate. Their magnitude near the crack tip is relatively large because of the high level of initial stresses. This causes the crack-tip stresses to relax, and, the initial strong singularity at the crack-tip is relaxed to a weaker one governed by material creep behaviour.

Under the aforementioned conditions, the stress-intensity parameter, K , and the J -integral cannot be used to uniquely characterize the crack growth. This has led to the extensive development of time-dependent fracture mechanics (TDFM) concepts using analogy to the elastic-plastic fracture mechanics (EPFM) concepts (Riedel 1987; Saxena 1989). Three regimes of crack growth – small scale, transient and steady-state – are observed in creeping materials, depending on the size of the crack-tip creep zone relative to the specimen dimensions. Figure 1 (Saxena 1986) schematically defines these regimes. The reader is referred to Saxena (1986, 1991) for definitions and details. The best example of an analogy between TDFM and EPFM concepts is the relation between the creep strain rate and the stress for the steady-state creep regime in a creeping material. This relation is analogous to the relation between instantaneous plastic strain and stress in an elastic-plastic (EL-PL) material under fully plastic conditions. The first crack tip parameter defined in TDFM is C^* , which specifically addresses the steady-state (large-scale) creep crack growth regime. Crack tip parameters used in TDFM are discussed in the following sections.

¹ Creep-ductile materials are defined as those in which the crack growth is negligible compared to the creep zone expansion rate, i.e. these materials are highly susceptible to creep deformation.

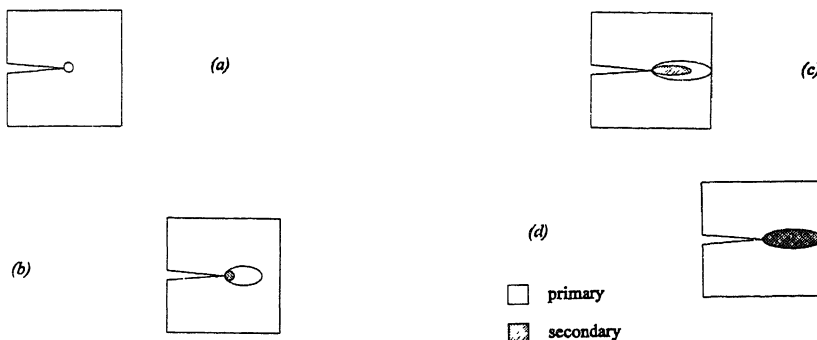


Figure 1. Stages of creep deformation in cracked bodies subjected to primary and secondary creep deformation. (a) Small-scale primary creep conditions. (b) Secondary creep zone growing within the primary creep zone which is now comparable in size to the uncracked ligament. (c) Extensive primary creep conditions with a substantial secondary creep zone. (d) Extensive secondary creep conditions (from Saxena 1986).

2.1 The C^* parameter

C^* was defined (Landes & Begley 1976; Nikbin *et al* 1976) as a path independent integral with direct analogy to the J -integral (Rice 1968) in EPFM.

$$C^* = \int_{\Gamma} W^* dy - T_i (\partial \dot{u}_i / \partial x) ds, \quad (1)$$

where W^* is the strain-rate-energy density given by

$$W^* = \int_0^{\epsilon_{ij}} \sigma_{ij} d\epsilon_{ij} \quad (2)$$

In (1), T_i is the traction vector defined by the outward unit normal vector n_j along the path Γ , which is taken from any point along the lower crack surface, counter-clockwise around the crack tip to end at the top surface. σ_{ij} and ϵ_{ij} are the stress and strain-rate tensors, \dot{u}_j is the deflection-rate vector along the direction of the traction and ds is the length along Γ . The physical significance of C^* lies in that it represents the power difference between two identically loaded bodies having incrementally different crack lengths, i.e.

$$C^* = -(1/B)(dU^*/da), \quad (3)$$

where \dot{U}^* is the power (energy rate) input to the cracked body to grow the crack by an increment da . Equation (3) is also analogous to the physical significance of J . This makes C^* measurable as a physical entity at the loading pins where the external load is applied. Further, its path-independence definition ensures that a unique σ - $\dot{\epsilon}$ relationship holds in the near field of the crack tip as well as in the far field where the external load is applied. The stress and strain-rate fields at the crack tip are characterized by C^* as follows:

$$\sigma_{ij} = (C^*/AI_n r)^{1/(n+1)} \bar{\sigma}_{ij}(\theta), \quad (4)$$

$$\dot{\epsilon}_{ij} = A(C^*/AI_n r)^{n/(n+1)} \bar{\epsilon}_{ij}(\theta). \quad (5)$$

in (4) above, C^* represents the intensity of the stress singularity at the crack tip (Goldman & Hutchinson 1975). r is the radial distance from the crack tip and θ is the angle from the plane of the crack. I_n is a nondimensional constant and $\tilde{\sigma}_{ij}(\theta)$ and $\tilde{\epsilon}_{ij}(\theta)$ are angular functions listed in Shih (1983). A and n are the steady-state creep constant and exponent, respectively, in the following constitutive law used to describe the unique relationship that exists between stress (σ) and strain-rate ($\dot{\epsilon}$) for a material undergoing secondary creep,

$$\dot{\epsilon} = A\sigma^n. \quad (6)$$

In brief, C^* satisfies the following characteristics which make it an attractive choice for a crack-tip parameter under large-scale (steady-state) creep conditions.

- (a) It is associated with a path-independent integral, (1);
- (b) it has a physical interpretation, (3), and can be measured at the loading pins;
- (c) it characterizes the crack-tip stress and strain-rate fields, (4), (5).

However, due to its definition being analogous to the J -integral used under fully-plastic conditions, the usefulness of C^* for characterization of CCG is limited because it is not applicable under small-scale-creep conditions (SSC conditions) and transition creep conditions. Since most components in service are made from materials designed to resist large-scale creep, C^* cannot be used to characterize creep crack growth in these components because SSC conditions dominate.

2.2 $C(t)$ - integral

Equation (6) can be modified to represent the creep behaviour of elastic-creeping materials as follows:

$$\dot{\epsilon} = (\dot{\sigma}/E) + A\sigma^n, \quad (7)$$

where, E is the elastic modulus of the material. The dots represent the derivatives w.r.t. time. In accordance with (7), under transient creep conditions (non-steady state conditions) in elastic-creeping materials, strain-rate is a function of both time and stress at every point inside or outside the creep zone boundary because stress also varies with time. Hence, the integral defined in (1) is no longer path independent i.e. it varies for each contour, and even for the same contour the value of the integral varies with time resulting in a non-unique σ - $\dot{\epsilon}$ relationship. Further, it no longer has the energy rate interpretation. Since crack-tip stresses also vary with time, C^* does not uniquely characterize them under these conditions. Thus, it loses its utility as a crack-tip parameter.

The $C(t)$ - integral was defined to extend C^* to the small-scale creep regime via its path-integral definition, (1). This involves selecting an integration path in the small creep strain dominated region, just ahead of the crack tip, contained within the elastic strain dominated fields. Thus, the integral defining C^* , (1), is path-independent and also characterizes the crack tip stress and strain rate singularities at any given time. This integral is the $C(t)$ -integral. Under extensive creep conditions $C(t) = C^*$. These attributes make $C(t)$ a candidate parameter for characterizing CCG and CFCG. Details regarding the definition and evaluation of the $C(t)$ -integral can be found in the literature (Ohje *et al* 1979; Riedel & Rice 1980; Ehlers & Riedel 1981). Recent numerical studies (Leung *et al* 1988; McDowell & Leung 1988; Bassani *et al* 1989) have confirmed

the validity of the expression proposed by Ehlers & Riedel (1981) for evaluating $C(t)$ in the transition creep regime. However, the $C(t)$ -integral cannot be related to the stress-power dissipation rate and cannot be measured at the loading-pins. This limits the practical use of $C(t)$ as a crack-tip parameter.

2.3 C_t -parameter

In order to overcome the aforementioned limitations of C^* and $C(t)$ parameters, C^* was extended into the transient creep regime via its stress-power dissipation rate definition, (3), by Saxena (1986). C_t represents the instantaneous stress-power dissipation rate during the transient while C^* represents the steady state rate. C_t is defined as follows:

$$C_t = \lim_{\Delta a \rightarrow 0} \left(-\frac{1}{B} \frac{\Delta U_t^*}{\Delta a} \right) = -\frac{1}{B} \frac{\partial U_t^*}{\partial a} \quad (8)$$

where U_t^* is instantaneous stress-power (energy-rate). The subscript 't' denotes that the value of U is at a fixed time t . Thus, C_t is defined in terms of the difference in the energy-rates (or power) supplied to two cracked bodies with identical creep deformation histories, but having cracks differing in length by Δa , as they are loaded to different deflection-rate levels. In other words, C_t is the power supplied to a cracked body, undergoing creep deformation, at any instant of time to grow the crack infinitesimally. Further details are presented by Saxena (1986). Under transient creep conditions, the C_t -parameter does not characterize the singular crack tip stress fields but is uniquely related to the creep zone expansion rate (Saxena 1986).

Methods for evaluation of C_t under small-scale and steady-state creep conditions are discussed in subsequent sections.

2.4 Crack tip parameters for CFCG

Under creep-fatigue type of loading, using trapezoidal or other waveshapes (figure 2) (Saxena 1993), elastic, plastic and creep deformation can occur at the crack tip. The extent of creep is governed by the rate of loading. The extent of creep deformation depends on the length of the hold period, while the extent of creep deformation during the loading part of the cycle is affected by the rate of loading. Stress redistribution occurs due to creep during the hold time and causes change in the elastic strains (Saxena 1993). If the hold time is sufficiently long, extensive creep conditions may occur whence the stress for a stationary crack becomes constant and further deformation occurs only by creep (Riedel & Rice 1980; Saxena 1980; Bassani & McClintok 1981). For the case of a trapezoidal waveform involving fast loading followed by a significant period of sustained loading, the normalized crack tip stress as a function of normalized time at a fixed distance ahead of the crack tip is given as in figure 3, taken from the work of Riedel (1993). Formulating analytical approaches for crack-tip stress analysis under CFCG conditions is not an easy task because the combinations of loading and material behaviour involved are complex, including effects due to cyclic plasticity mixed with primary and secondary creep deformation. Consequently, numerical approaches are frequently employed (Saxena 1993). Also, the CFCG experimental studies carried out for explaining CFCG behaviour outnumber the analytical studies. These experimental

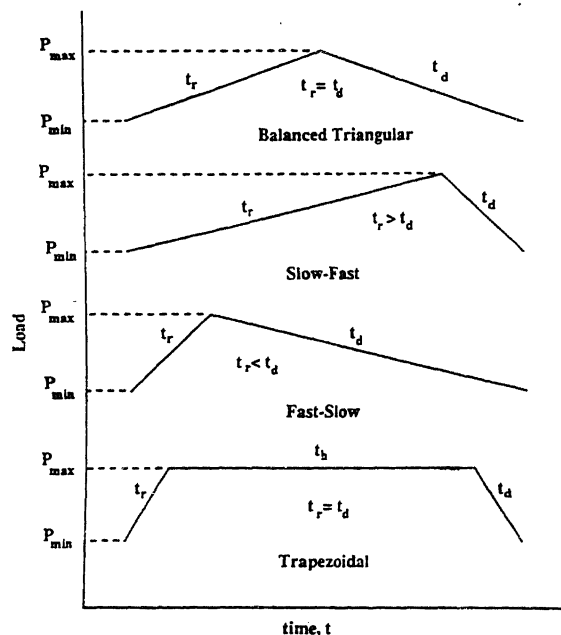


Figure 2. Typical loading waveforms used during creep-fatigue crack growth testing in the laboratory.

studies have resulted in the identification of relevant crack tip parameters. The discussion here will focus on the ΔJ_c (Ohtani *et al* 1981, 1989; Ohji 1986; Kuwabara *et al* 1988) and the $(C_t)_{avg}$ (Saxena & Gieseke 1990) parameters.

For trapezoidal waveform with rapid loading/unloading as compared to the hold time, ΔJ_c is given by (Ohtani *et al* 1981, 1989; Ohji 1986; Kuwabara *et al* 1988)

$$\Delta J_c = \int_0^{t_h} J^* dt, \quad (9)$$

where J^* is identical to C^* described in § 2.1, t_h is the hold time.

$(C_t)_{avg}$ is defined as (Saxena & Gieseke 1990; Yoon *et al* 1992, 1993)

$$(C_t)_{avg} = \frac{1}{t_h} \int_0^{t_h} C_t dt, \quad (10)$$

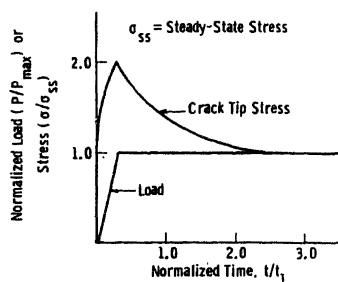


Figure 3. Normalized crack tip stress as a function of normalized time at a fixed distance ahead of the crack tip for fast loading followed by sustained load (from Riedel 1983).

for materials showing 'creep reversal' i.e. the creep deformation is significantly reversed during every cycle because these materials have low resistance to cyclic plasticity. For materials that do not exhibit creep reversal effects, C_t is not reinstated after each cycle. The following expression is used to calculate $(C_t)_{\text{avg}}$ for such materials (Adefris 1993),

$$(C_t)_{\text{avg}} = \frac{1}{t_h} \int_{N-1}^N C_t dt. \quad (11)$$

As mentioned in the previous section, under extensive creep conditions, C_t and C^* (or J^*) are the same by definition. Hence, (9) and (10) imply that ΔJ_c and $(C_t)_{\text{avg}}$ are uniquely related in the extensive creep regime as:

$$\Delta J_c = t_h (C_t)_{\text{avg}}. \quad (12)$$

Under conditions of small scale creep C_t and C^* (or J^*) are not the same. However, in the case of correlations based on experimental measurements of these parameters, differences in the numerical values of the two are not significant (Saxena 1986; Bassani *et al* 1989). On the other hand, if the parameters are calculated, significant differences could result if the influence of small-scale-creep conditions is not included in the calculations of C_t . Thus, $(C_t)_{\text{avg}}$ and ΔJ_c differ significantly, and, in general, are not related by (12).

In summary, $(C_t)_{\text{avg}}$ and ΔJ_c parameters are equivalent under extensive creep conditions but not under small-scale-creep conditions where ΔJ_c can only be operationally defined (Saxena 1993). The operational definition of ΔJ_c is based on experimental load-line deflection measurements (Saxena 1993). Thus, $(C_t)_{\text{avg}}$ is the more widely applicable parameter.

3. Test methods and crack growth data

Test methods for conducting CCG and CFCG tests are discussed in the following sections along with the data collection and data reduction steps. Insights into the analysis of these data is also provided. An accelerated test procedure (Grover & Saxena 1994) recently proposed for CFCG testing is discussed in some detail.

3.1 Creep crack growth testing and data analysis

The objective of creep crack growth testing, according to the ASTM (1992) standard on creep crack growth testing, is to determine the relationship between the time rate of crack growth, da/dt , and the applied value of the $C^*(t)$ -integral, where $C^*(t)$ is the time-dependent value of C^* defined in (1) and has been defined to extend the validity of C^* into the extensive primary creep regime (Saxena 1989a, 1991). The creep crack growth rates expressed as a function of $C^*(t)$ characterize the resistance of a material to crack growth under extensive creep conditions. However, it has been shown (Riedel & Detampel 1987; Saxena 1989a), as discussed later, that C_t correlates the da/dt data better than $C^*(t)$ and it characterizes the creep crack growth resistance of a material under a wide range of creep conditions, including small-scale creep and transition creep conditions. Hence, C_t is the crack-tip parameter of choice in this study.

A variety of specimen geometries are used in fracture mechanics studies to simulate the service loading conditions in the laboratory. Some of these are illustrated in figure 4.

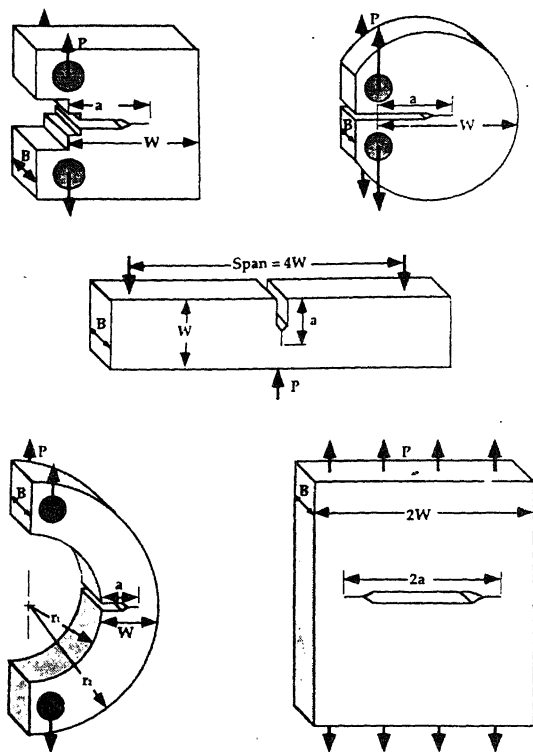


Figure 4. Typical specimens used in fracture mechanics for testing, after Anderson. (1991) (a) Compact specimen. (b) Disk shaped compact specimen. (c) Single edge notched bend (SENB) specimen. (d) Arc shaped specimen. (e) Middle tension (MT) specimen.

Compact type (CT) and the centre cracked tension (CCT) specimens are commonly used. However CT specimens are the preferred geometry for CCG and CFCG studies, to be discussed later. They require lower load levels and the transition time for steady-state conditions to develop from SSC conditions is longer for CT specimens than for CCT specimens having comparable widths. Thus, CT specimens are better suited for longer elevated temperature tests. Further, a displacement gauge can be conveniently placed at the load-line of a CT specimen for measuring the load-line deflection. The schematic in figure 5 (ASTM 1992) shows a deflection gauge placed at the load-line in a CT specimen.

Specimens are pre-cracked using fatigue loading. They are subjected to dead-weight loading at test temperature in suitable furnaces. The crack length and the load-line displacements are continuously recorded as a function of time. Electric potential drop method (DC or AC) is usually used to measure crack lengths. These data can be collected digitally using a suitable data-acquisition system, or it can be recorded on a strip-chart recorder. The latter is usually used as a backup even when a data-acquisition system is used. Monitoring of the temperature is required to ensure that it remains constant within allowable limits during the test. A record of load versus time must be maintained if servo-mechanical loading systems are used to achieve constant load conditions (ASTM 1992).

The load, load-line displacement and the crack length data are subsequently processed to obtain the correlations between the creep crack growth rates and a crack

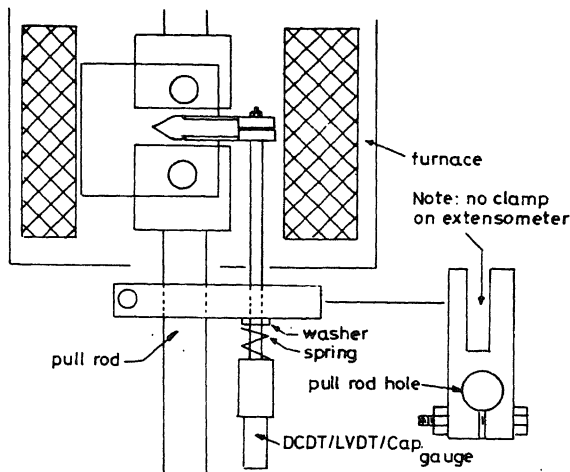


Figure 5. Schematic of the overall test set-up showing the clip gauge as attached to the specimen (from ASTM 1992).

tip parameter, C_t in this study. Expressing da/dt as a function of C_t generally provides results that are independent of the specimen size and planar geometry for the same crack-tip stress state. This is useful in comparing data from a variety of specimen configurations and loading conditions. Assuming similitude, i.e. that cracks of different length subjected to the same nominal value of C_t advance by equal increments of crack extension per unit time, the data obtained from these tests can be utilized in the design and evaluation of engineering structures operated at elevated temperatures. Material selection criteria and inspection requirements for damage tolerant applications can also be established using this data. However, results from these tests should not be applied to cracks in structures with wide-spread creep damage around the crack tip.

The crack growth rates are calculated from the crack length versus time (a vs t) data. C_t is calculated for a wide range of creep conditions from the load-line deflection rates in the specimen using the following expression,

$$C_t = \frac{P \dot{V}_c F'}{BW F} + C^*(t), \quad (13)$$

where, P is the load applied to the specimen having width W and thickness B . F is the K -calibration factor $= (K/P)BW^{1/2}$ and $F' = dF/d(a/W)$. V_c is the contribution to the measured load-line deflection rate due to creep. It is obtained using (14) (Saxena 1986, 1991; ASTM 1992).

$$\dot{V}_c = \dot{V} - (\dot{a}B/P)[(2K^2/E) + (m+1)J_p] - \dot{P}C, \quad (14)$$

where \dot{a} is the crack growth rate, J_p is the plastic part of J calculated from expressions provided in Riedel & Detampel (1987), m is the plasticity constant of the material, C is the machine compliance. For constant load tests, the load rate, $\dot{P} = 0$ and the last term on the right hand side of (14) drops out.

$C^*(t)$ in (13) can also be measured in test specimens (Lee 1987),

$$C^*(t) = (P \dot{V}_c / BW) \eta(a/W, n, n_1), \quad (15)$$

where η is a function of the crack size to width ratio, a/W , the secondary and primary creep constants, n and n_1 respectively. For practical purposes, for CT specimens it is defined as (Saxena 1991)

$$\eta = [n/(n+1)] \{ [2/(1-a/W)] + 0.522 \}. \quad (16)$$

However, the term $n/(n+1)$ on the right hand side is strictly valid for secondary creep only and it has to be replaced by $n_1/(n_1+1)$ when most of the time is spent under primary creep conditions (Saxena 1991). Further details on this issue are provided in Saxena (1991).

3.2 Experimental correlations of creep crack growth data

In this section, experimental evidence is provided in support of the suitability of the C_i parameter over other crack tip parameters, $C(t)$ and C^* , for characterizing CCG. The creep crack growth trends of austenitic and ferritic steels used at elevated temperatures are also discussed.

Figures 6 to 8 (Saxena 1989a) show plots of the creep crack growth rate, da/dt , as a function of C^* , $C(t)$ and C_i respectively. The data shown include that from tests where transient conditions prevailed for significant lengths of time before the steady state

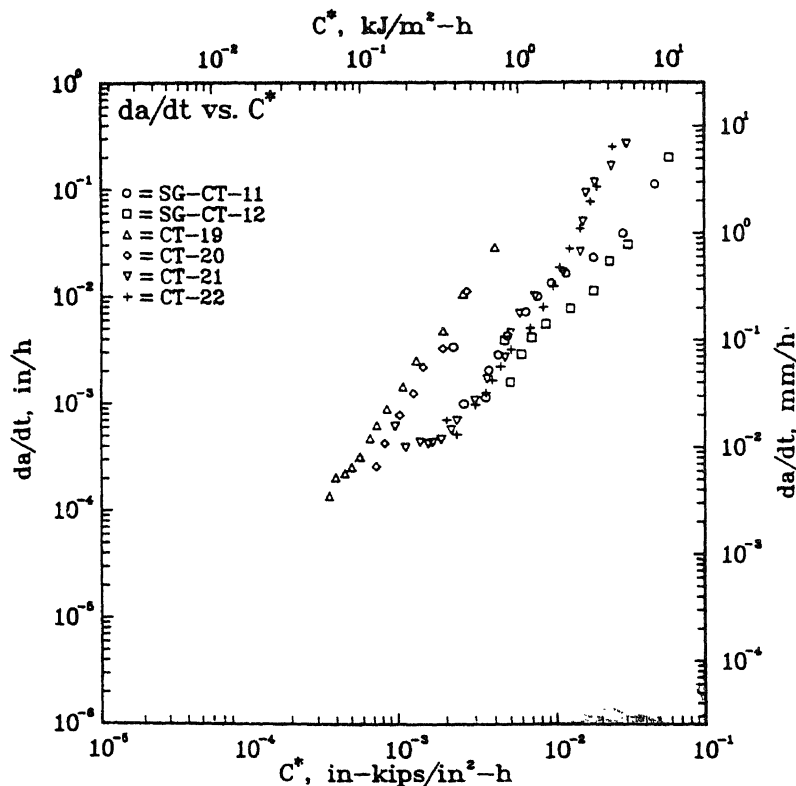


Figure 6. Creep crack growth rate as a function of C^* (from Saxena 1989a).

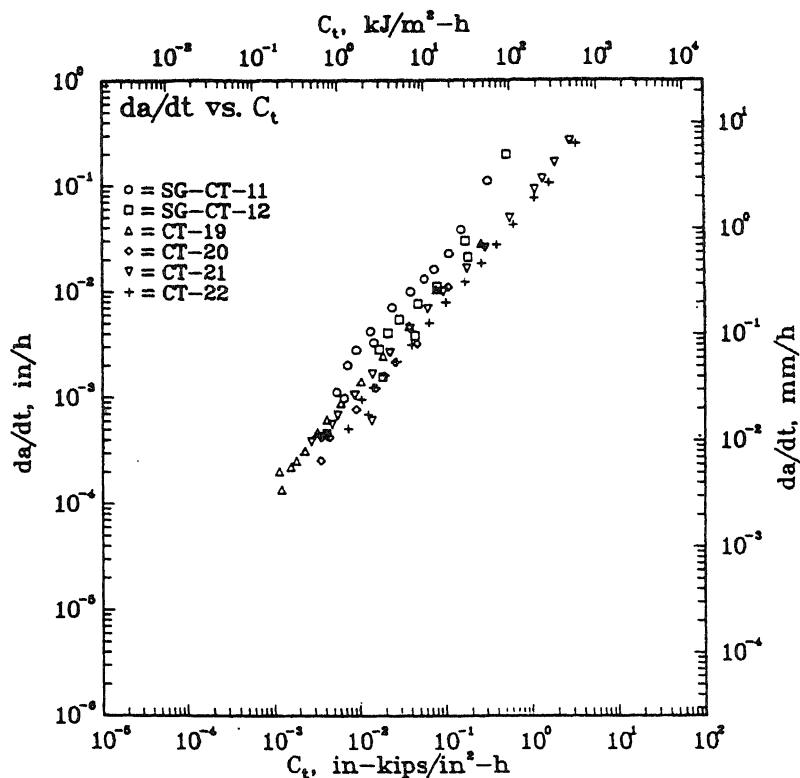


Figure 7. Creep crack growth rate as a function of the $C(t)$ parameter, in a Cr-Mo-V steel (from Saxena 1989a).

conditions were reached. It can be clearly seen that the data do not correlate well with either C^* or $C(t)$ while it does with C_t . Riedel & Detampel (1987) have also shown C_t to be the parameter of choice for correlating creep crack growth rate (CCGR) data. For further discussion, readers are referred to Saxena (1989a).

Creep cracks in most high temperature steels grow by grain boundary cavitation and the effect of the environment is minimal. Figure 9 (Saxena 1989a) shows the CCG behaviour of ex-service and new Cr-Mo and Cr-Mo-V steels commonly used in power plants. Despite the varying material compositions and thermal histories of these materials, their CCG behaviours show similarity and almost all the data lie within a 95% confidence scatter band. Correlating CCG rates with C_t (or C^* , for only steady state conditions) provides a first-order normalization with respect to changes in temperature, provided there is no substantial change in the rupture ductilities due to changes in temperature, composition, or thermal history (Saxena 1989a). Thus, CCGR data at different temperatures show the same trend when correlated with C_t , even though the creep deformation rates at those temperatures for the material are very different. This is illustrated in figure 10, while figure 11 shows the creep deformation behaviour of the material (Saxena 1989a). This lack of temperature dependence of the da/dt vs C_t plots is useful because the life predictions made for a component operating at one temperature would be valid for its operation at a different temperature. Further,

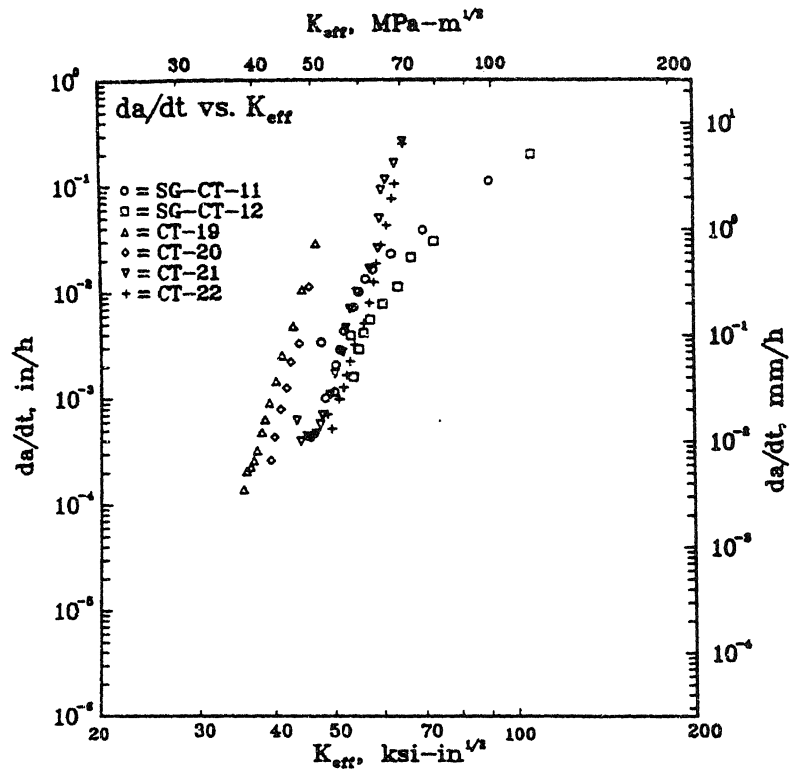


Figure 8. Creep crack growth rate as a function of C_t (from Saxena 1989a).

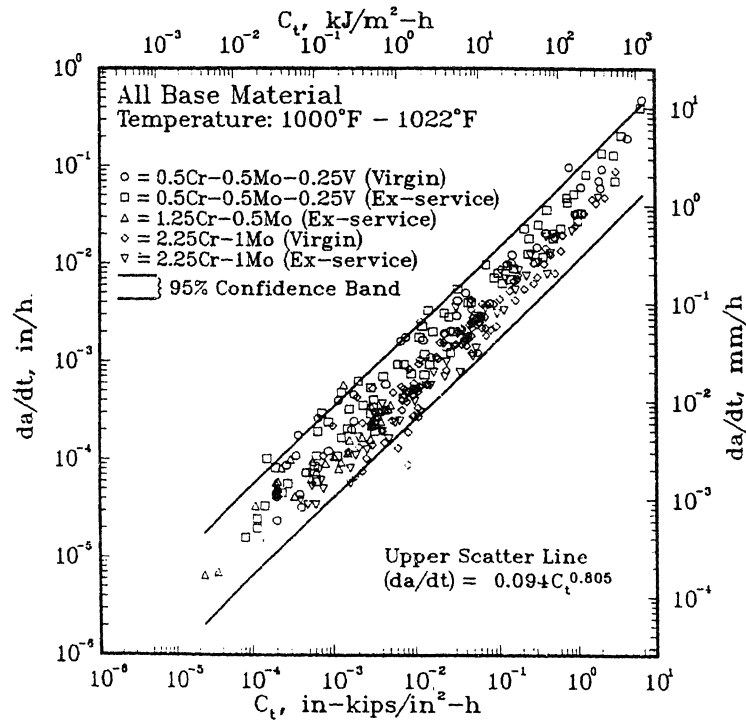


Figure 9. Creep crack growth behaviour of Cr-Mo and Cr-Mo-V base material. The data include all ex-service and new material data (from Saxena 1989a).

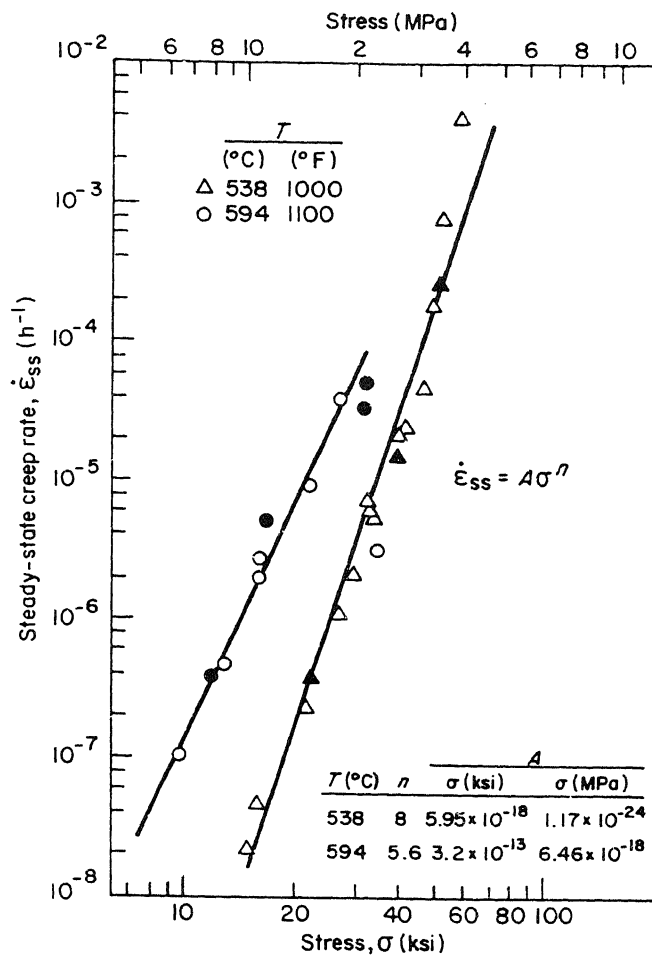
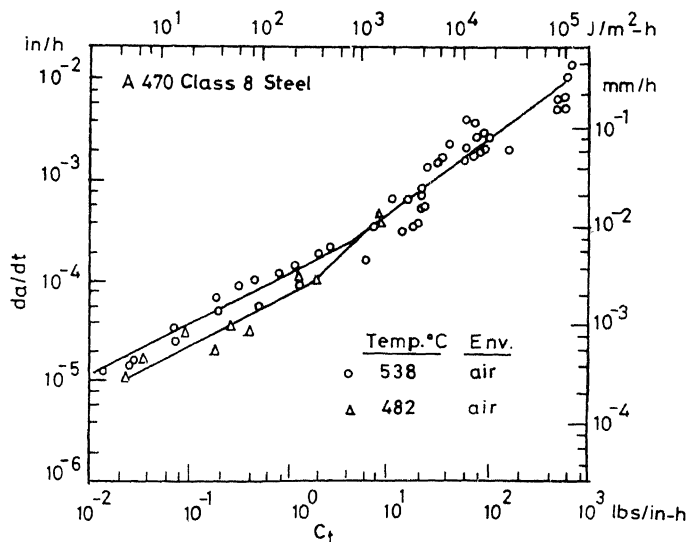


Figure 10. Creep crack growth behaviour of 1Cr-1Mo-0.25V steel as a function of temperature (from Saxena 1989a).



if the CCGR data for a certain temperature are not available, design parameters can be decided and life predictions for the component can be made on the basis of the CCGR data for a different temperature. However, service conditions may result in a significant change in the creep ductilities causing the da/dt vs C_r relationship to change with temperature and it may be different for two parts of the same component subjected to different temperatures. This is generally due to the microstructural changes in the material resulting from exposure to varying service temperatures. An example of this is the higher CCGR that results in the "hot end" of a steam header as compared to its "cold end", due to the coarsening of grain boundary carbides under the higher operating temperatures of the hot end.

3.3 Creep fatigue crack growth testing and data analysis

Under creep fatigue crack growth conditions, crack growth occurs due to both creep and fatigue processes. A trapezoidal waveform simulates creep fatigue loading conditions. Creep deformation occurs mainly during the sustained loading period, the hold time (t_h), while fatigue processes contribute to the crack growth during the loading part (rise time - t_r) and unloading part (decay time - t_d) of the trapezoidal wave, provided the rise and decay times are small in comparison to the hold time. However, if the loading rate at high temperatures is slow, creep can occur during the loading part of the cycle as well.

Unlike the ASTM (1992) standard for CCG testing, a standard test method has not been adopted for CFCG testing as yet. However, CFCG test methods and data analysis techniques have been discussed in detail by Grover & Saxena (1994).

Accelerated CFCG tests lasting a few days to a few weeks are conducted to obtain data that are used to predict service behaviours up to 30–40 years.

CT specimens are the preferred geometry for CFCG testing due to reasons discussed earlier. Their size is determined on the basis of the amount of material available, the desired orientation of the crack, the size/shape of the available furnaces and the load-line deflection gauge to be used. The specimens are mounted on clevises placed in high temperature chambers/furnaces to heat them to the desired temperature. This is generally the same as the service temperature although higher temperatures may be used to decrease the test time, provided the creep deformation processes remain the same. Servohydraulic machines are used for loading the specimens under the desired waveform.

The trapezoidal waveform, mentioned earlier, is most commonly used because it simulates actual service conditions, especially in power plant materials. Figure 12 (Lee 1987) shows the stress as a function of time for various locations in a steam header. Having selected the waveform, the K -level/load levels are decided on the basis of the crack growth rates required during the test. These crack growth rates should be approximately those encountered by the material during service (Grover & Saxena 1994). However, often the time constraints on the duration of a test dictate the choice of the crack growth rates to be achieved during the test. Thus K -levels, have to be chosen in conjunction with the hold times of the loading waveform (Grover & Saxena 1994). Other than the K -levels to be used, the sensitivity of the load-line deflection measurement gauge/amplifier system also affects the choice of the hold times. The reader is referred to Grover & Saxena (1994) for further details.

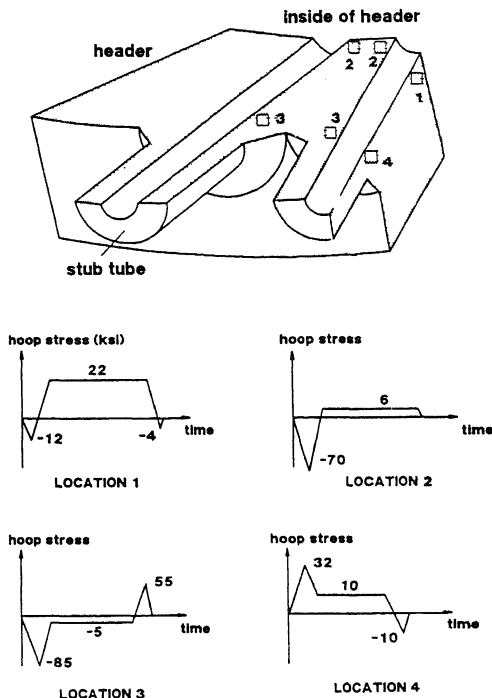


Figure 12. Stress versus time histories at different locations in a steam header.

The measurements made during the test are the deflection change during hold time, the total load-line deflection and the crack length at different stages in the test. It is advisable to monitor the load during hold time to ensure that the deflection changes are not due to random variations in the load (Grover & Saxena 1994). Strip chart recorders or computerized data acquisition systems can be used to record the aforementioned data. Strip charts are useful because the deflection change traces can be visually inspected for the quality of the data. As in the case of CCG tests, crack length is measured using electric potential drop. Details on the DC potential drop method are given in ASTM (1991).

In order to obtain the influence of creep, the crack length data is reduced to time dependent crack growth rates, da/dt . The average values of these, $(da/dt)_{avg}$, are plotted against $(C_t)_{avg}$, which is the average value of C_t . The average of C_t is used to correlate CFCG data because of the experimental limitations involved in measuring C_t during hold times.

$(C_t)_{avg}$ is evaluated using the measured load-line deflection change rate during the hold time as follows:

$$(C_t)_{avg} = \frac{\Delta P \Delta V_c F'}{BW t_h F} - \left(\frac{F'}{F \eta} - 1 \right) C^*(t), \quad (17)$$

where ΔP is the applied load range and ΔV_c is the load-line deflection change due to creep during hold time t_h . Rest of the terms are as defined earlier.

ΔV_c is obtained from the total measured deflection change, ΔV , using the following expression,

$$\Delta V_c = \Delta V - \frac{B t_h}{P} \left(\frac{da}{dt} \right)_{avg} \left[\frac{2 K_{eff}^2}{E} + (m+1) J_p \right], \quad (18)$$

where m is the plasticity exponent in the Ramberg–Osgood equation and P is the applied load level. K_{eff} is the value of K corresponding to the 'effective' crack length corrected for plasticity.

It is noted that the ΔV_c value which is obtained using (18), from the total load-line deflection change, ΔV , by deflection partitioning approach (Saxena *et al* 1983) includes both primary and secondary creep contributions to the load-line deflection change. J_p is the fully plastic part of J and is obtained from expressions listed in Kumar *et al* (1981). $C^*(t)$ can be determined using procedures outlined in Kumar *et al* (1981) and must include the contributions of secondary and primary creep. The $(da/dt)_{\text{avg}}$ is calculated using

$$\left(\frac{da}{dt}\right)_{\text{avg}} = \frac{1}{t_h} \left[\left(\frac{da}{dN}\right) - \left(\frac{da}{dN}\right)_{\text{cycle}} \right], \quad (19)$$

where $(da/dN)_{\text{cycle}}$ is the cyclic crack growth rate and has to be obtained from a FCGR test carried out for which the rise and decay times are same as the trapezoidal waveform used in the CFCG tests.

The effects of fatigue on the crack growth are studied by obtaining correlations between the cycle dependent crack growth rate, $(da/dN)_{\text{cycle}}$, and ΔK , which is expressed as

$$\Delta K = (\Delta P/BW^{1/2})F(a/W). \quad (20)$$

All terms in the expression have been defined earlier.

The overall crack growth rate during a fatigue cycle, da/dN , is defined as

$$\frac{da}{dN} = \left(\frac{da}{dN}\right)_0 + \int_0^{t_h} \left(\frac{da}{dt}\right) dt, \quad (21)$$

and is measured during a CFCG test.

3.4 Experimental correlations and modelling of CFCG data

This section includes a discussion on the experimental correlations of CFCG data and the development of life prediction models for components using this data.

Figure 13 (Grover 1993) shows plots of da/dN vs ΔK for a 2.25Cr–1.0Mo steel at 594°C (1100°C). The regression line through the FCGR ($t_h = 0$) is used to get the cycle-dependent part in modelling the CFCG data. The lack of correlation between da/dN and ΔK for the CFCG tests is evident from the scatter in the data in this figure. Such lack of correlation has also been shown in Cr–Mo–V steel, figure 14 (Harrison & Sandor 1971). A discussion on the limitations of using ΔK for correlating high temperature crack growth is presented in (Saxena 1988, 1993; Grover 1993). An increase in the da/dN with increasing hold time for fixed ΔK is observed in figures 13 and 15 (Saxena & Bassani 1984). This is due to the increasing contribution of time-dependent crack growth (Grover & Saxena 1994). Creep damage at the crack tip, influence of the environment, or microstructural changes such as formation of cavities which occur during loading at elevated temperatures could be responsible for this behaviour (Saxena 1993).

The average time dependent crack growth rates, $(da/dt)_{\text{avg}}$, are correlated with $(C_t)_{\text{avg}}$. Figures 16 (Grover 1993) and 17 (Yoon *et al* 1993) show plots of $(da/dt)_{\text{avg}}$ vs

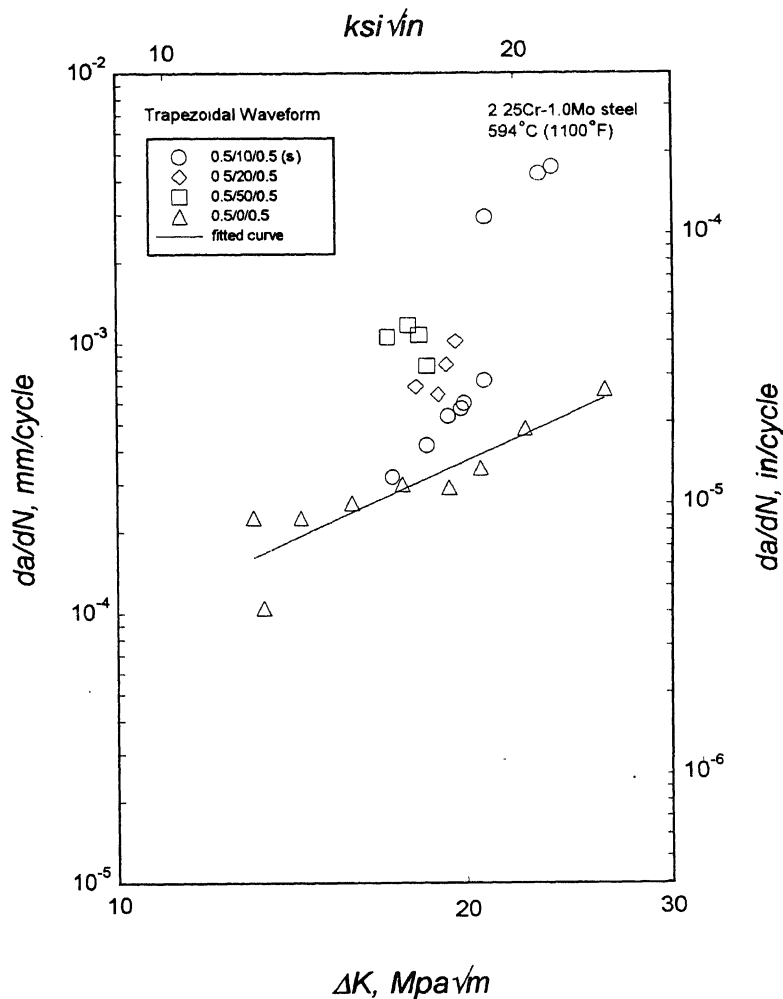


Figure 13. Fatigue crack growth data with various hold times and without hold time (from Grover 1993).

$(C_t)_{avg}$ for 2.25Cr-1.0Mo and 1.25Cr-0.5Mo steels, respectively, for various hold times at elevated temperatures. All data show a clear trend and fall into a narrow scatter band despite the range of hold times used. This strongly indicates the usefulness of $(C_t)_{avg}$ in characterizing CFCG rates. Further, the CCG data for each of these materials have also been plotted on these graphs. However, da/dt has been correlated with C_t for the CCG data. All the CCG and CFCG data show the same trend. This has the important implication that life prediction procedures for these materials would be considerably simplified because CCG data could be used to predict the life of components under CFCG conditions and vice-versa. In comparing a $(da/dt)_{avg}$ vs $(C_t)_{avg}$ relation of CFCG with a da/dt vs C_t relation of CCG, it must be kept in mind that although C_t and $(C_t)_{avg}$ are equivalent parameters with the same physical interpretation, their exact values may differ slightly in the SSC regime by a constant factor for a given material (Yoon *et al*

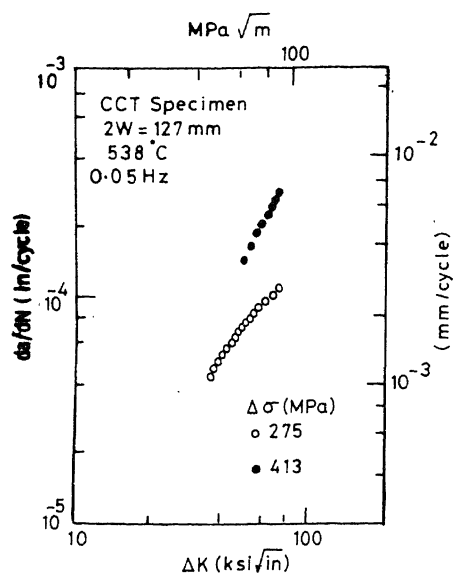


Figure 14. Elevated temperature fatigue crack growth behaviour of Cr-Mo-V steel plotted as a function of ΔK (from Harrison & Sandor 1971).

1993). The value of this constant ranges from 1 to 1.3 for different materials, and further details are also presented (Yoon *et al* 1993).

The time dependence of the life-prediction model is obtained by generating a regression line through all the data. The total fatigue crack growth rate per cycle is

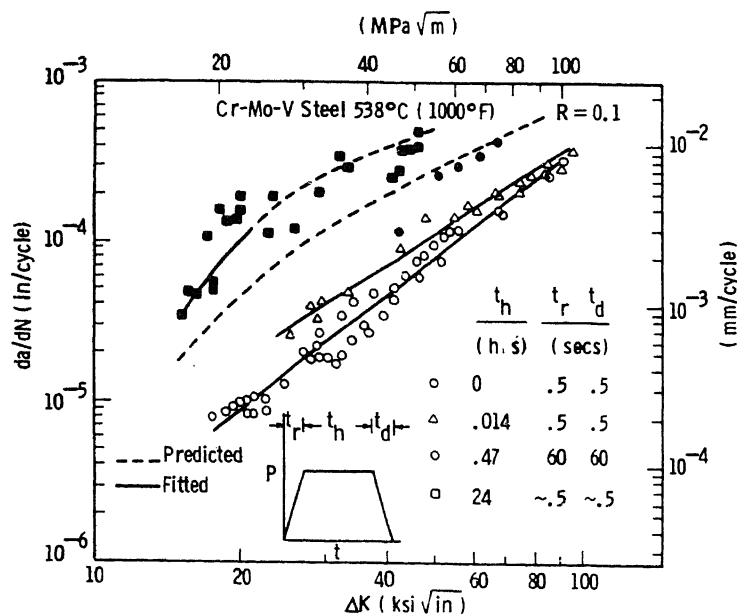


Figure 15. Effect of hold time of the fatigue crack growth behaviour of a Cr-Mo-V steel (from Saxena *et al* 1984).

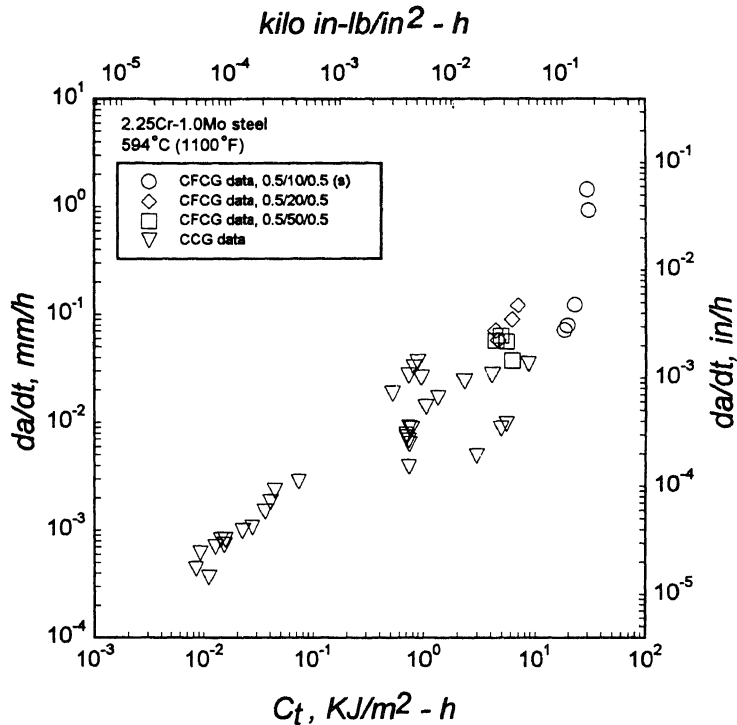


Figure 16. Correlation of crack growth rates with the measured values of C_t . (The average values of da/dt and C_t are plotted for CFCG data, from Grover 1993).

a linear summation of the cycle and time-dependent crack growth rates. Such an expression obtained for 2.25Cr-1.0Mo steel at 594°C (1100°F) under trapezoidal loading waveshapes is given in (22), (23) (Grover & Saxena 1994) which are expressed in SI and British units, respectively.

$$da/dN = 1.08 \times 10^{-6} \Delta K^{1.94} + 1.46 \times 10^{-2} [(C_t)_{avg}]^{0.722} t_h \quad (22)$$

$$da/dN = 5.11 \times 10^{-8} \Delta K^{1.94} + 2.40 \times 10^{-2} [(C_t)_{avg}]^{0.722} t_h \quad (23)$$

The first term in the equations above represents the cycle-dependent crack growth rate and the other term represents the time-dependent crack growth rate. These equations can be effectively used to predict the service life of high temperature components made of 2.25Cr-1.0Mo steel under, both, CCG and CFCG conditions at 594°C (1100°F). An upper and lower scatter band can also be generated for the data in figure 16 for design purposes. This model has been established under the assumption that the crack growth during hold time is only due to creep deformation. Any other time-dependent effects like oxidation at the crack tip have not been incorporated (Grover & Saxena 1994). Neither have any synergistic effects due to any complicated interactions of the creep and fatigue mechanisms of crack growth during unloading/reloading been incorporated. However, their exclusion in the light of the assumption that the unloading/reloading times are much smaller compared to the hold times seems justified (Grover & Saxena 1994). If such effects were to be considered, depending

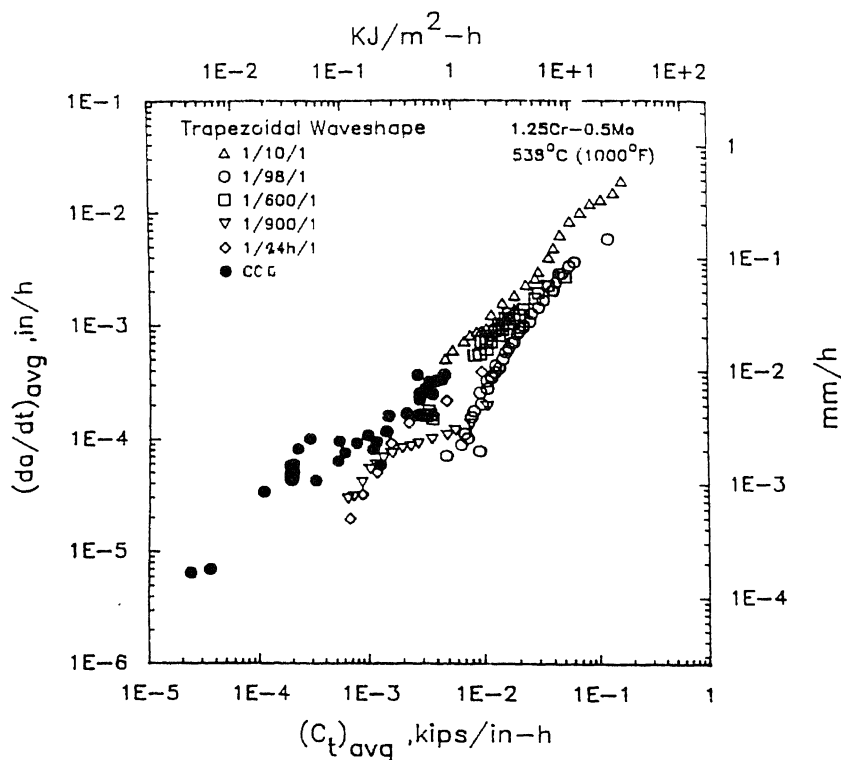


Figure 17. Correlation of crack growth rates for creep and creep-fatigue crack growth data in 1.25Cr-0.5Mo steel (from Yoon *et al* 1993).

on the material, an equation of the type presented above would be too simplistic in its description of the CFCG behaviour of a material.

3.5 Calculating CCG and CFCG crack tip parameters in components

In §§ 3-1-3-4 the discussion concentrated on obtaining and correlating experimental data with crack tip parameters, C_t and $(C_t)_{avg}$, calculated from experimental quantities measured in the laboratory. Use of directly measured deflection changes to obtain these parameters has advantages discussed by Grover (1993). However, often there is a need to calculate these crack-tip parameters for components in service due to limitations or constraints that might exist in carrying out laboratory tests on the component material. In such an event, the expressions outlined in this section may be used to calculate C_t and $(C_t)_{avg}$ for components, making use of material properties.

C_t is related to the rate of expansion of the creep zone for small-scale creep conditions and is expressed as

$$(C_t)_{SSC} = 2(1 - \nu^2)(K^2/EW)(F'/F)\beta\dot{r}_c \quad (24)$$

where $\beta = 1/3$ is a factor obtained from finite element analysis, ν is the Poisson's ratio and \dot{r}_c is the rate of creep zone expansion which is given by (25) and (27) for

materials deforming by elastic-secondary creep (EL-SC) and elastic-primary creep (EL-PC) respectively. Other terms have been defined earlier,

$$\dot{\epsilon}_c = 2\alpha/(n-1)K^2 t^{-(n-3)/(n-1)}(EA)^{2/(n-1)}\tilde{r}_c(\theta, n), \quad (25)$$

where t is time and $\tilde{r}_c(\theta, n)$ is a nondimensional constant which varies with the secondary creep constant n . α is a scaling factor also dependent on n and is defined below.

$$\alpha = (1/2\pi)[(n+1)^2/(2n\alpha_n^{n+1})]^{2/(n-1)} \quad (26)$$

where $\alpha_n^{n+1} \simeq 0.69$ for $3 \leq n \leq 13$ (Riedel & Rice 1980).

For EL-PC materials

$$\begin{aligned} \dot{\epsilon}_c = \frac{K^2}{2\pi} \left[\frac{I_{n_1} E}{2\pi(1-\nu^2)} \right]^{2/(n_1-1)} [(1+n_1)(1+p)A_1]^{2/(1+p)(n_1-1)} \\ \times \left[\frac{\tilde{r}_c(\theta, n_1)}{1+p} \right] \left[\frac{2}{n_1-1} \right] (t)^{[2/(1+p)(n_1-1)]-1} \end{aligned} \quad (27)$$

where I_{n_1} is a nondimensional constant dependent on the primary creep constant n_1 . A_1 and p are also primary creep constants².

For a wide range of creep conditions C_t is expressed as

$$C_t = (C_t)_{\text{SSC}} + C^*(t). \quad (28)$$

Expressions for $(C_t)_{\text{avg}}$ can be obtained using (10) and (11) for materials exhibiting complete creep reversal and those that do not, respectively. Corrections can be made for the effects of crack-tip cyclic plasticity (Yoon *et al* 1992; Grover & Saxena 1994).

For elastic-cyclic plastic-secondary creep (EL-CPL-SC) materials showing complete creep reversal,

$$\begin{aligned} [(C_t)_{\text{avg}}]_{\text{SC}} = \frac{2\alpha\beta\tilde{r}_c(\theta, n)}{E}(1-\nu^2)\frac{\Delta K^4 F'}{W F}(EA)^{2/(n-1)} \\ \times \left[\frac{(t_h + t_{pl})^{2/(n-1)} + (t_{pl})^{2/(n-1)}}{t_h} \right] + C_s^*, \end{aligned} \quad (29)$$

where C_s^* is the steady-state part of C^* . t_{pl} is the time for the crack-tip creep zone to grow out of the cyclic plastic zone (Yoon *et al* 1992); thus, it accounts for retardation in the creep zone expansion rate due to the presence of cyclic plasticity. It can be calculated analytically using (30) or (31) (Yoon *et al* 1992; Grover & Saxena 1994) for elastic-cyclic plastic-secondary creep (EL-CPL-SC) and elastic-cyclic plastic-primary-secondary creep (EL-CPL-PC-SC) materials. It can also be obtained experimentally (Yoon *et al* 1992; Grover & Saxena 1994).

$$t_{pl} = \frac{1}{EA} \left[\xi \left(\frac{m-1}{m+1} \right) \left(\frac{1}{2\sigma_{ys}^c} \right)^2 \frac{1}{\alpha\tilde{r}_c(90^\circ, n)} \right]^{(n-1)/2}, \quad (30)$$

² n_1, A_1, p are regression constants in the following constitutive equation used to describe the creep behaviour of a material.

$$\dot{\epsilon} = (\dot{\sigma}/E) + A_1 e^{-p} \sigma^{n_1(1+p)} + A\sigma^n.$$

for EL-CPL-SC materials.

$$t_{pl} = \frac{1}{(1+p)(1+n_1)A_1} \left(\frac{2\pi(1-\nu^2)}{I_{n_1}E} \left[\xi \frac{2\pi}{\tilde{r}_c(\theta, n_1)} \left(\frac{m-1}{m+1} \right) \left(\frac{1}{2\sigma_y^c} \right)^2 \right]^{(n_1-1)/2} \right)^{(1+p)}, \quad (31)$$

where m is the plasticity exponent and σ_y^c is the cyclic yield strength of the material. This equation accounts for primary creep effects and is thus suitable for EL-CPL-PC-SC materials.

When primary creep dominates the small-scale creep conditions and then the secondary creep zone grows out from within the primary creep zone, to dominate the steady-state creep condition, $(C_t)_{avg}$ for EL-CPL-PC-SC materials is expressed as

$$\begin{aligned} [(C_t)_{avg}]_{PC-SC} = & \frac{\beta \tilde{r}_c(\theta)}{\pi E} (1-\nu^2) \frac{(\Delta K)^4 F'}{W F} \left[\frac{I_{n_1} E}{2\pi(1-\nu^2)} \right]^{2/(n_1-1)} \\ & \times [(1+n_1)(1+p)A_1]^{2/[l(n_1-1)(1+p)]} \\ & \times \left[\frac{(t_h + t_{pl})^{2/[l(n_1-1)(1+p)]} - (t_{pl})^{2/[l(n_1-1)(1+p)]}}{t_h} \right] \\ & + C_s^* \left[1 + (1+p)(t_2)^{p/(1+p)} \left(\frac{(t_h + t_{pl})^{1/(1+p)} - (t_{pl})^{1/(1+p)}}{t_h} \right) \right] \end{aligned} \quad (32)$$

where t_2 is the transition time for extensive secondary creep conditions to develop from small-scale secondary creep zone contained within the primary creep field (Yoon 1990; Saxena 1991).

The crack-growth rate vs crack-tip parameter correlations are then used for life assessment of components as discussed in the next section.

4. Applications to life prediction

The primary objective of this section is to briefly describe life prediction procedures, for power plant components, based on the crack-growth concepts discussed earlier. Life assessment of a steam-turbine casing has been discussed as a specific illustration.

4.1 Remaining life assessment using crack growth models

The remaining crack growth life assessment methodology includes time-independent fatigue crack growth, time-dependent creep crack growth and creep-fatigue interactions affecting crack growth. These crack growth vs crack tip parameter ($\Delta K, C_t$) correlations, obtained as discussed in §3, are used in the life prediction steps as illustrated in figure 18 (Chell *et al* 1993) which is a schematic of the steps involved in using time-dependent fracture mechanics concepts for remaining crack-growth life prediction. Material data, including tensile properties, elastic and creep deformation constants, fracture toughness of the material and the CCG and CFCG constants of the material are required. Stress analysis is conducted on the component based on the operating conditions and the geometry of the cracked component, and the appropriate crack growth model (fatigue/creep/creep-fatigue) is selected for the material. Estimation

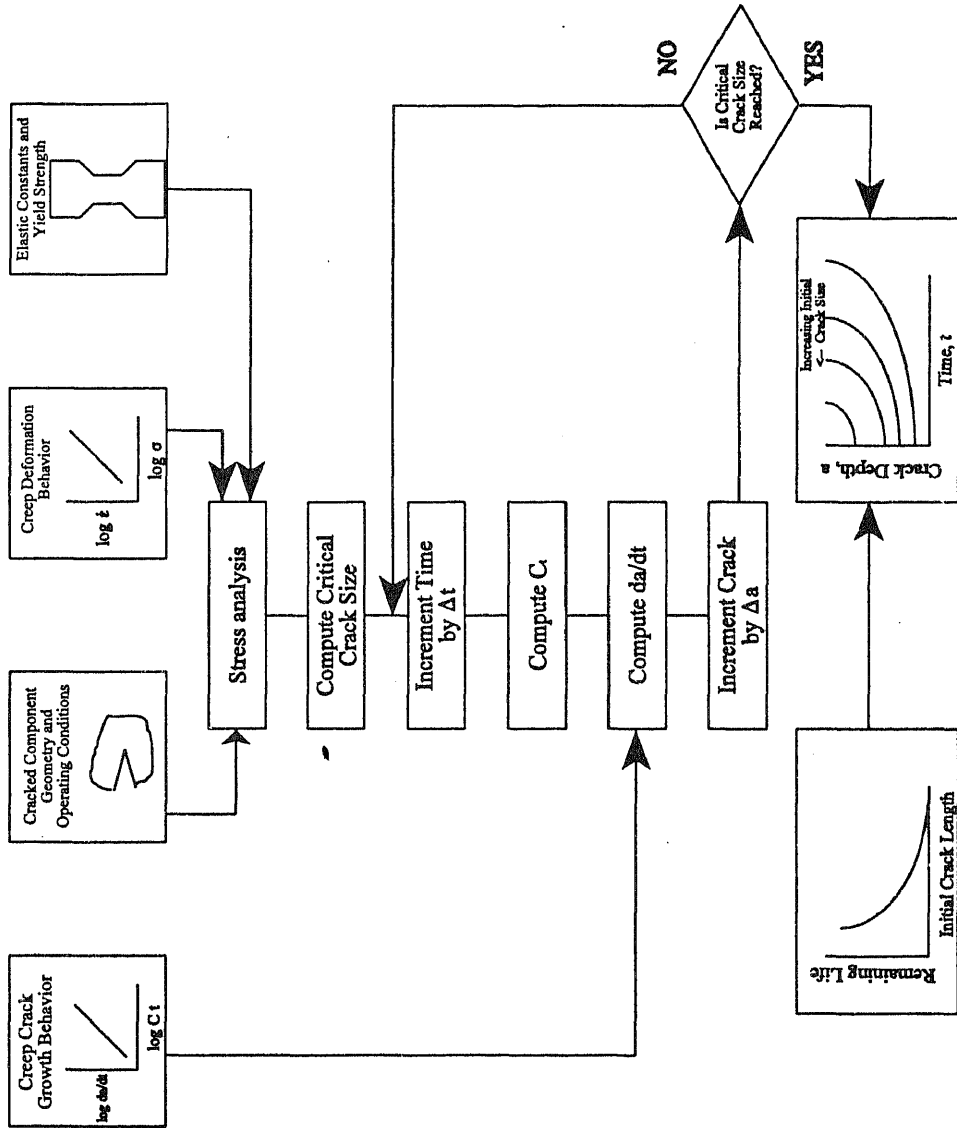


Figure 18. Schematic illustration of the time-dependent fracture mechanics analysis for remaining life assessment (from Chell *et al* 1993).

of parameters like K and C^* in order to obtain C_t is done using expressions available in handbooks (Kumar *et al* 1981; Tada *et al* 1986; Zahoor 1991).

Either static or cyclic analysis can be performed for calculating the remaining life. In a static analysis, a component such as a steam pipe or a header is assumed to operate continuously, uninterrupted by start-up and shut-down (Saxena 1993). The life is then estimated as the time for the defect/crack to grow from its initial size, a_o , to its final size, a_f . a_o is the crack size at inspection and a_f is the critical size at which fracture can occur and is determined from fracture conditions. In a cyclic analysis, explicit account is taken of the start-ups and shut-downs and the life is expressed as the number of such cycles required to grow the crack from a_o to a_f (Saxena 1993).

Under static conditions, the remaining life, t_R , is obtained by integrating the CCG rate law (Saxena 1993).

$$t_R = \int_{a_o}^{a_f} \frac{da}{C_1 [C_t(a, t)]^q} \quad (33)$$

The creep crack growth rate law (Saxena 1986; Saxena *et al* 1988) is of the form

$$da/dt = C_1 [C_t(a, t)]^q, \quad (34)$$

where, C_1 and q are regression parameters.

Under cyclic loading, the cyclic crack growth rate is first obtained for a given crack size using empirical equations that are in the form of (22) and then a numerical integration is carried out to obtain t_R using (Saxena 1993),

$$t_R = \int_{a_o}^{a_f} \frac{da}{(da/dN)} \quad (35)$$

4.2 Life assessment of turbine casings

Steam-turbine casings are large castings that encase the stationary and rotating components of the turbine. Their main function is to contain the steam pressure and maintain the alignment of internal components (Viswanathan 1989). These are made from 1.25Cr-0.5Mo, 2.25Cr-1Mo and 1Cr-1Mo-0.25V steels. Many steam turbines have been used beyond their design lives and, due to economic considerations, the trend has been to use them for cyclic operation. Such factors have made cracking a major concern with regards to the safe operation and operating life of these components. This section aims at briefly providing an insight into the nature of cracking in turbine casings and illustrating the use of remaining crack growth life assessment methodology discussed above.

4.2a Damage mechanisms and failure sites: Cracks in casings are typically located at the steam inlets of HP and IP turbine sections because the local thermal stresses are higher. Figure 19 (Logsdon 1986) shows a schematic of a casing showing inlet steam passages. Cracking in the HP and IP sections is typically found on the interior surfaces of steam chests, valve bodies, bolt holes, seal casings and nozzle chambers (Viswanathan 1989). Figure 20 is a schematic of the crack locations in the nozzle area of a steam-turbine casing (Rasmussen 1986). The primary cause of crack initiation and propagation in turbine casings is fatigue, creep-fatigue and brittle fracture (Logsdon 1986). Thermal stresses are responsible for fatigue and creep-fatigue cracking

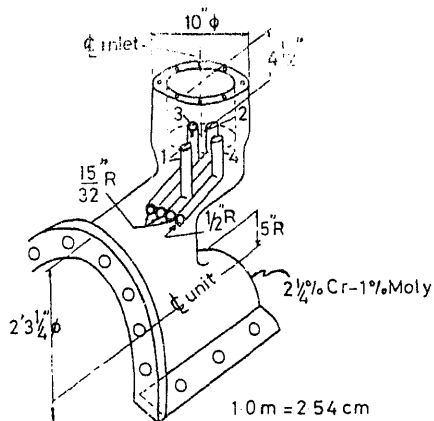


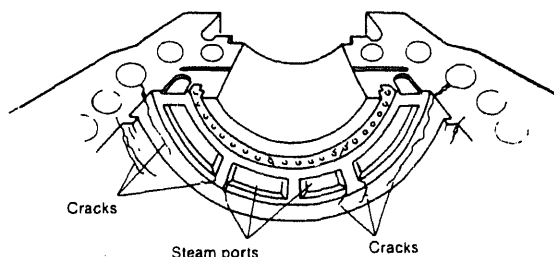
Figure 19. Schematic of steam turbine casing showing inlet steam passages (from Logsdon *et al* 1986).

while creep contributes to crack growth in regions where temperature exceeds 427°C (800°F) (Saxena 1993). The reader is referred to (Viswanathan 1989; Saxena 1993) for further details on the damage mechanisms and failure sites in turbine casings.

4.2b Remaining life estimation: Casings are made of relatively ductile materials and have large section areas which are not highly stressed. Thus, remaining-life assessments are generally based on crack-growth considerations rather than crack-initiation considerations, which are more useful at the design stage (Viswanathan 1989). The basic information needed for remaining life estimation of turbine casings is given below (Saxena 1993).

- * Operating history, including the number and type of starts (cold/warm/hot) per year. The thermal ramp rates during heating and cooling, the amount of prewarming and metal temperature at each stage in order to determine thermal stresses.
- * Material properties like monotonic and cyclic stress-strain behaviour, creep stress relaxation rates, fracture toughness, and, the fatigue and creep-fatigue crack initiation behaviour as a function of temperature. Further, this information is also needed for weldments, if they are involved.

Determination of various material properties is described by Saxena *et al* (1986). Using the above information, remaining life estimation can be performed following the steps listed below.



Cracks at various locations are indicated by wiggly lines.

Figure 20. Crack locations in first-stage nozzle area of a steam-turbine casing (from Rasmussen 1986).

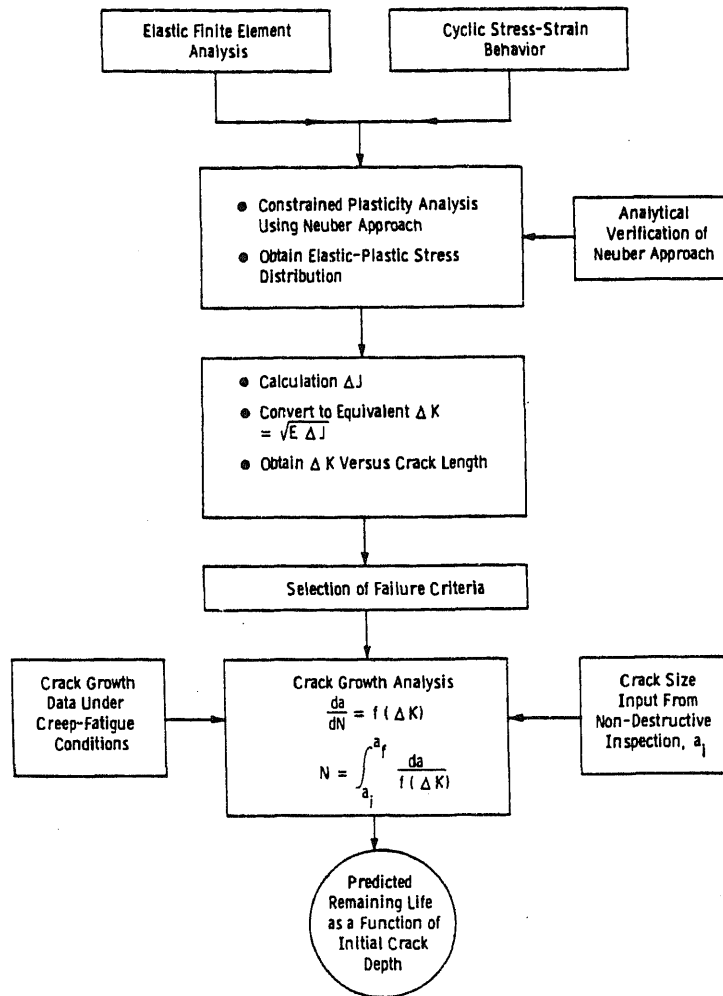


Figure 21. Schematic of the methodology for remaining life prediction (from Saxena *et al* 1986).

- (1) Determine the transient cyclic stresses for the turbine casing for the various operating histories by conducting a finite element analysis for the specific casing design. The first step in this analysis is the generation of transient temperature distribution using heat transfer analysis. The temperatures thus obtained are input into the stress analysis portion of the program along with the pressure and external loads.
- (2) The stress-strain and time histories at critical locations are then used to predict the fatigue and creep-fatigue crack initiation and propagation behaviour using the models described earlier. The total remaining life is the sum of the crack initiation and the crack propagation lives. However, if cracks have already initiated, only crack propagation life must be determined.

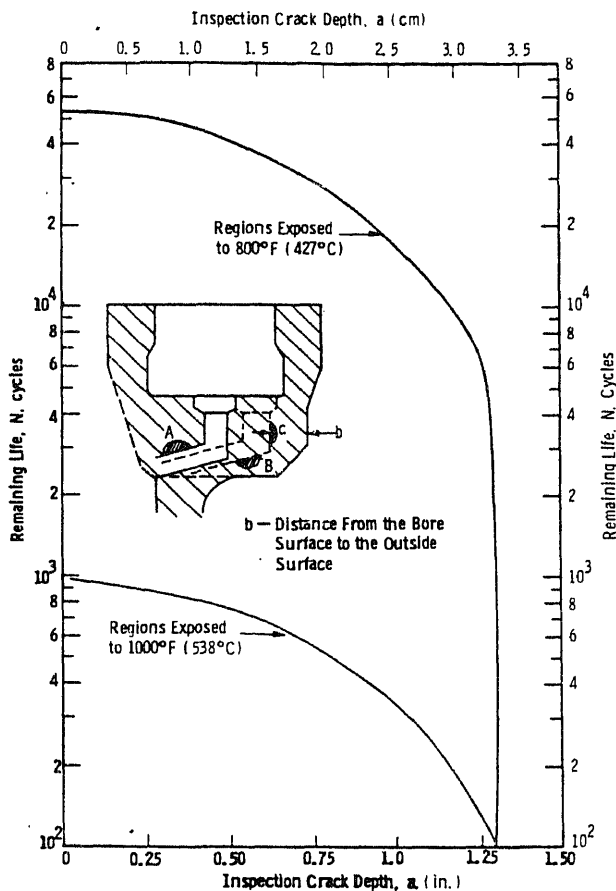


Figure 22. Remaining life as a function of crack depth for cracks in a steam turbine casing (from Saxena *et al* 1986).

Figure 21 (Saxena *et al* 1986) is a schematic of the various steps involved in conducting fracture mechanics analysis for remaining life prediction of a cracked turbine casing. Further, figure 22 (Saxena *et al* 1966) shows the results of calculation of remaining life as a function of initial crack size for a ship's service turbine generator casing (SSTG casing).

5. Special considerations for high-temperature crack growth in weldments

Most of the problems encountered in heavy-section piping occur at welded joints. Thus, it is desirable to focus damage-assessment techniques on these areas rather than on the base metal. However, many problems that are unique to weldments make both stress analysis and material characterization extremely challenging (Viswanathan 1989). Some of these problems are discussed below.

- (1) The weldment can be considered a composite material consisting of the base metal, three or more heat-affected zones (HAZ) and the weld metal. Thus, there is an unpredictability in the modeling of its mechanical behaviour.

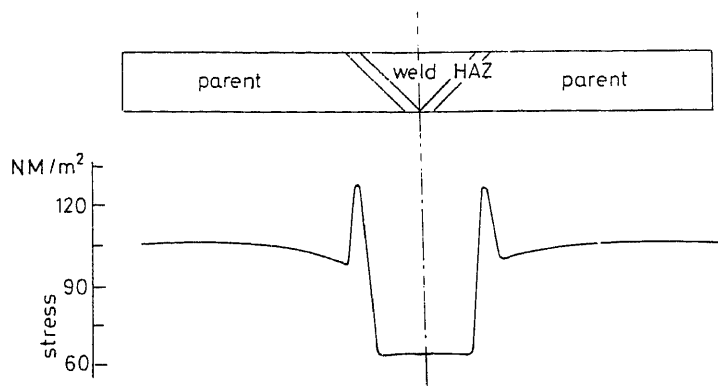


Figure 23. Distribution of steady-state hoop stress across a girth weld in a steam pipe. The initially uniform elastic stress distribution redistributes such that weak metal off-loads stress to the stronger parent metal (from Viswanathan *et al* 1982).

- (2) Collection of impurities and inclusions occurs at the fusion line between the weld and the HAZ because it is the last region to solidify. This creates complications in stress analysis.
- (3) Uniaxial creep rupture data for a material cannot be used to predict the rupture properties of the weld because multiaxial stress state exists at a weld. This is due to the complex geometry and influence of complex loading. Consequently, the creep resistances of the base metal, the weld metal and the HAZ are quite different and cause the redistribution of initial elastic stresses in complex ways. These distributions can be different for girth welds and for seam welds. In girth welds the pressure stresses in the axial and hoop directions peak at the most creep-resistant (strongest) location, i.e. the HAZ, and are lowest at the weld metal, which is the least creep-resistant location (Cane 1982). This is shown in figure 23 (Viswanathan *et al* 1982). However, in seam welds, the peak stresses after stress redistribution occur in the weld metal (weakest location) and the lowest stresses are encountered in the HAZ (Wells 1987).
- (4) A good material-property database does not exist for weldments. The limited amount of available data pertains only to pure base metal, weld metal, or just to the HAZ material. Thus, prediction of crack growth in weldments is not a trivial task. Generation of such data in the laboratory is not easy either. Thus, in the absence of a reliable database, the convenient practice has been to assume the weld to be always weaker than the base metal and then using base metal properties to model the weld behaviour by applying arbitrary safety factors.
- (5) Welds also serve as sites for fabrication defects which can act as stress raisers and preferred sites for cavity growth and crack initiation. The presence of impurities like sulphur further worsens the situation.

As mentioned above, both the crack growth database and the analytical procedures are inadequate. Significant developments are thus needed in addressing cracking problems in elevated temperature weldments.

References

- Anderson T L 1991 *Fracture mechanics – Fundamentals and applications* (Boca Raton, FL: CRC Press)
- Adefris N 1993 *Creep-fatigue crack growth behaviour of 1%G-1.1Mo-1/4%V rotor steel*. Doctoral thesis, School of Materials Science and Engineering, Georgia Institute of Technology, Atlanta, GA
- Altekar V A 1980 Power crisis and the metallurgical engineers, N P Gandhi Memorial Lecture, Indian Institute of Metals, Baroda
- ASTM 1991 Standard test method for measurements of fatigue crack growth rates: ASTM Standard E 647-91. *ASTM Book of Standards*, Vol. 03.01; pp. 654–681
- ASTM 1992 Standard test method for measurement of creep crack growth rates in metals: ASTM Standard E 1457-92. *ASTM Book of Standards*, vol. 03.01, pp. 1031–1043
- Bassani J L, Hawk D E, Saxena A 1989 Evaluation of the C_r -parameter for characterizing creep crack growth rate in the transient regime. In *Nonlinear fracture mechanics: Volume I – Time dependent fracture* (eds) A Saxena et al ASTM STP 995, pp. 7–26
- Bassani J L, McClintok F A 1981 Creep relaxation of stress around a crack tip. In *Int. J. Solids Struct.* 7: 479–492
- Cane B J 1982 In *Proceedings of International Conference on Welding Technology for Energy Applications* ORNL Conference 820554, Gatlinburg, TN, pp. 623–639
- Cheil G G, Hudak S J, Swaminathan V P, Leung C P, Saxena A 1993 A high-temperature fitness-for service assessment methodology for petrochemical processing vessels. (ASME) (in press)
- Dooley R B, Viswanathan R (eds) 1987 *Life extension and assessment of fossil power plants*. (Palo Alto, CA: Electric Power Research Institute) EPRI CS 5208
- Ehlers R, Riedel H 1981 A finite element analysis of creep deformation in a specimen containing a macroscopic crack. In *Advances in fracture research: Proceedings of the Fifth International Conference on Fracture* (New York: Pergamon) ICF-5: 691–698
- Goldman N L, Hutchinson J W 1975 Fully plastic crack problems: The center-cracked strip under plane strain. *Int. J. Solids Struct.* 11: 575–591
- Grover P S 1993 An accelerated test methodology for creep-fatigue crack growth testing. *M S thesis*, School of Materials Science and Engineering, Georgia Institute of Technology, Atlanta, GA
- Grover P S, Saxena A 1994a Developments in creep-fatigue crack growth testing and data analysis. Paper to be presented at the *Tenth European Conference on Fracture*, Berlin, Germany
- Grover P S, Saxena A 1994b Characterization of creep-fatigue crack growth behavior in 2.25Cr-1.0Mo steel using $(C_r)_{avg}$. *Int. J. Fract.* (submitted)
- Harrison C B, Sandor G N 1971 *Eng. Fract. Mech.* 3: 403–420
- Jaffee R I 1979 Metallurgical problems and opportunities in coal fired steam power plants. *Metall. Trans.* A10: 139–165
- Kumar V, German M D, Shih C F 1981 An engineering approach to elastic-plastic analysis. Technical Report EPRI NP-1931, Electric Power Research Institute
- Kuwabara K, Nitta K, Kitamura T, Ogata T 1988 Effect of small-scale creep on crack initiation and propagation under cyclic loading. In *Basic questions in fatigue* (eds) R P Wei, R P Gangloff. ASTM STP 924, vol. 2, p. 41
- Landes J D, Begley J A 1976 A fracture mechanics approach to creep crack growth. In *Mechanics of crack growth* ASTM STP 590, pp. 128–148
- Lee D R 1987 personal communication
- Leung C P, McDowell D L, Saxena A 1988 Consideration of primary creep at stationary crack tips: Implications for the C_r -parameter. *Int. J. Fracture* 36: 275–289
- Logsdon W A, Liaw P K, Saxena A, Hulina V E 1986 Residual life prediction and retirement for cause criteria for SSTG upper casings I – Mechanical and fracture mechanics materials properties development. *Eng. Fract. Mech.* 25: 259–288
- McDowell D L, Leung C P 1988 Estimation of the C_r -parameter for primary creep. Technical Report E-18-621, GA Technologies, Palo Alto, CA

- Nikbin K M, Webster G A, Turner C E 1976 Relevance of nonlinear fracture mechanics to creep cracking. In *Cracks and fracture* ASTM STP 601, pp. 47-62
- Ohji K 1986 Fracture mechanics approach to creep-fatigue crack growth. In *Role of fracture mechanics in modern technology* (Fukuoka, Japan) (eds) G C Sih, H Nisitani, T Ishihara (Elsevier Science)
- Ohji K, Ogura K, Kubo S 1979 Stress-strain field and modified J -integral in the vicinity of a crack tip under transient creep conditions. *Jpn. Soc. Mech. Eng.* 790 (13): 18-20 (in Japanese)
- Ohtani R, Kitamura T, Nitta A, Kuwabara K 1989 *High-temperature low-cycle fatigue crack propagation and life laws of smooth specimens derived from the crack propagation laws* (eds) H Solomon, G Halford, L Kaisand, B Leis; ASTM STP 942, pp. 1163-1180
- Ohtani R, Kitamura T, Yamada K 1981 A nonlinear fracture mechanics approach to crack propagation in the creep-fatigue interaction range. In *Fracture mechanics of tough and ductile materials and its application to energy related structures* (eds) H Liu, T Kumio, V Weiss (Martinus Nijhoff) pp. 263-270
- Rasmussen D M 1986 Steam turbine case repairs to extend operating life. In *Workshop Proceedings: Life assessment and repair of steam turbine casings* (ed.) R Viswanathan (Palo Alto, CA: Electric Power Research Institute) CS 4676 SR, pp. 6.1-7.1
- Rice J R 1968 A path independent integral and the approximate analysis of strain concentration by notches and cracks. *J. Appl. Mech.* 35: 379-386
- Riedel H 1983 Crack tip stress fields and crack growth under creep-fatigue conditions. In *Elastic-Plastic Fracture: Second Symposium, Volume I - Inelastic Crack Analysis* ASTM STP 803, pp 505-520
- Riedel H 1987 *Fracture at high temperature* (Berlin: Springer-Verlag)
- Riedel H, Detampel V 1987 Creep crack growth in ductile, creep resistant steels. *Int. J. Fracture* 33: 239-262
- Riedel H, Rice J R 1980 Tensile cracks in creeping solids. In *Fracture mechanics: Twelfth Conference* ASTM STP 700, pp. 112-130
- Saxena A 1980 Evaluation of C^* for the characterization of creep crack growth behaviour in 304 SS. In *Fracture mechanics: Twelfth Conference* ASTM STP 700, pp. 131-151
- Saxena A 1986 Creep crack growth under non-steady-state conditions. In *Fracture mechanics* (eds) J H Underwood *et al* ASTM STP 905, 17: 185-201
- Saxena A 1988 Limits of linear elastic fracture mechanics in characterization of high-temperature fatigue crack growth. In *Basic questions in fatigue* (eds) R P Wei, R P Gangloff, ASTM STP 924, 2: 27-40
- Saxena A 1989a Mechanics and mechanisms of creep crack growth. In *Fracture mechanics: Microstructure and micromechanisms* (eds) S Nair *et al* (Metals Park, OH: ASM International) Chap. 10, pp. 283-334
- Saxena A 1989b Recent advances in elevated temperature crack growth and models for life prediction. In *Advances in Fracture Research: Proceedings of the Seventh International Conference on fracture* (eds) K Salama *et al* (New York: Pergamon) ICF-7: 1675-1687
- Saxena A 1991 Creep crack growth in high temperature ductile materials, *Engineering fracture mechanics* 40: 721-736
- Saxena A 1993 Fracture mechanics approach for characterizing creep-fatigue crack growth (Review Paper). *Jpn Soc. Mech. Eng. Int. J.* A36: 1-20
- Saxena A 1993 *Life assessment methods and codes* (Palo Alto, CA: Electric Power Research Institute)
- Saxena A, Bassani J L 1984 Time dependent fatigue crack growth behavior at elevated temperature. In *Fracture: Interactions of microstructure, mechanics and mechanics* ASTM STP 743, (Warrendale, PA: The Metallurgical Society of AIME)
- Saxena A, Ernst H A, Landes J D 1983 Creep crack growth behavior in 316 stainless steel at 594°C. *Int. J. Fracture* 23: 245-257
- Saxena A, Gieseke B 1990 Transients in elevated-temperature crack growth. In *International Seminar on High Temperature Fracture Mechanics and Mechanics, EGF-6* (Dourdan, France: Elsevier) 3: 19-36
- Saxena A, Han J, Banerji K 1988 Creep crack growth behavior in power plant boiler and steam pipe steels. *J. Pressure Vessel Technol.* 110: 137-146

- Saxena A, Liaw P K, Logsdon W A, Hulina V E 1986 Residual life prediction and retirement for cause criteria for SSTG upper casting II – fracture mechanics analysis. *Eng. Fract. Mech.* 25: 289–303
- Shih C F 1983 Tables of Hutchinson–Rice–Rosengren singular field quantities. Technical Report MRL E-147, Brown University, Providence, RI
- Tada H, Paris P, Irwin G R 1986 *Stress analysis of cracks handbook* (St. Louis, MO: Del Research Co)
- Viswanathan R 1989 *Damage mechanisms and life assessment of high-temperature components* (Metals Park, OH: ASM International)
- Viswanathan R, Dooley R B 1986 Creep life assessment techniques for fossil plant boiler pressure parts. *Proceedings of International Conference on Creep*, JSME–IME–ASTM–ASME, Tokyo, pp. 349–359
- Viswanathan R, Messing A, Narayanan T V 1982 Improved life assessment techniques for boiler superheater/reheater pressure parts. EPRI Project Report RP 2253–13, Electric Power Research Institute, Palo Alto, CA
- Wells C H 1987 On the life prediction of longitudinal seam welds. In *Life extension and assessment of fossil power plants* (eds) R B Dooley, R Viswanathan (Palo Alto, CA: Electric Power Research Institute) CS 5208
- Yoon K B 1990 *Characterization of creep-fatigue crack growth behaviour using the G-parameter* Doctoral thesis. School of Mechanical Engineering, Georgia Institute of Technology, Atlanta, GA
- Yoon K B, Saxena A, Liaw P K 1993 Characterization of creep fatigue crack growth behavior under trapezoidal waveshape using C_f -parameter. In *Int. J. Fracture* 59: 95–114
- Yoon K B, Saxena A, McDowell D L 1992 Influence of crack tip cyclic plasticity on creep-fatigue crack growth. In *Fracture Mechanics: Twenty Second Symposium* (eds) H A Ernst, A Saxena, D L McDowell ASTM STP 1131, pp. 367–392
- Zahoor A 1991 *Ductile fracture handbook* (Palo Alto, CA: Electric Power Research Institute) EPRI 1757-69



Remaining life assessment of high temperature components using threshold stress concept

RAGHUBIR SINGH

Materials Evaluation Division, National Metallurgical Laboratory, Jamshedpur 831 007, India

Abstract. The paper first presents global experience, including that of our laboratory, mainly with power plant components to show that it is possible to extend the life of some critical components 2–3 fold over the design life. Different approaches for remaining life assessment are also briefly discussed.

It appears that the main creep damage in so far as Cr–Mo and Cr–Mo–V steels are concerned, is an accumulation of creep strain. Hence, this paper suggests a new approach for creep life prediction based on threshold stress concept and stress-strain rate relationship. The approach is based on the analysis of creep and hot tensile data generated on a popular 1 Cr–0.3 Mo–0.25 V steel in the service exposed and the virgin states and also on samples with a wide range of microstructures prepared from the virgin states. A summary of the main finding leading to development of a new approach has been given.

Keywords. Creep resistant steels; creep strain damage; threshold stress; remaining life.

1. Introduction

Low alloy ferritic steels, 1 Cr–0.5 Mo, 2.25 Cr–1 Mo–0.5 Cr–Mo–V, are extensively used for high temperature applications in the power, chemical and oil industries. This is because they have very good elevated temperature creep strength together with good resistance to oxidation and hydrogen embrittlement. These steels have been used in power industries for components such as turbine rotors, cylinders, steam chests, steam pipes, headers etc. The typical service temperature and stress in the power industry are about 550°C and 50 MPa respectively. Thus the components operate in the temperature range where the creep is the main life limiting factor. Prolonged service exposure of boiler and turbine components could lead to degradation of their mechanical properties and hence these are designed for a certain definite life (10–20 years). In many cases component replacement after design life expiry is not necessary due to ‘conservatism’ at the design stage and hence, calls for methods for full life exploitation. In other cases, however, operating conditions can be more burdensome than envisaged by the designer and hence plant integrity assessment may be required before the design life is

reached to ensure safety. Thus, the need for remaining life assessment both for economic and safety cannot be obviated.

The available approaches for creep life prediction can be broadly classified into the following (Cane & Townsend 1983; Viswanath 1989):

- operational parameter approach;
- post-service examination approach.

The first approach depends on the evaluation of the service temperature/stress history for a given component. Once the history is known then combining it with the lower bound value of the standard material data and the life fraction rule an estimate of remaining life can be obtained as illustrated in figure 1. However, this approach has not been fully successful because of several limitations:

- The operational data with requisite precision are not always available;
- standard material data have a wide scatter and often cannot be reliably extrapolated to the rather low operating stresses;
- Life fraction rule used in this approach is not always applicable.

Thus the approach at best can serve the purpose of obtaining a very rough estimate of creep life.

The second approach based on direct evaluation of the component after prolonged service exposure is undoubtedly more accurate and also does not require detailed knowledge of the service history. Hence it is widely used. Among the numerous techniques available for post-service evaluation listed in table 1 the accelerated stress rupture testing is the most common. In order to obtain results within a reasonable period of time, these tests have to be accelerated by testing: either at higher stresses or at high temperatures or both. The short-term rupture data so obtained, are extrapolated to ascertain long-term life at lower stresses/temperature as illustrated in figure 2(a,b). This approach has the following limitations.

- being empirical its validity is limited to the domain of available database, i.e. the short-term data have only limited extrapolation capacity;
- The procedure is time consuming and expensive.

On the whole, the method gives a first estimate of the life.

It is important to recall here that the critical components are allowed to undergo only a limited creep strain (1–2%) and there are evidences (Wufee 1983; Weber 1993)

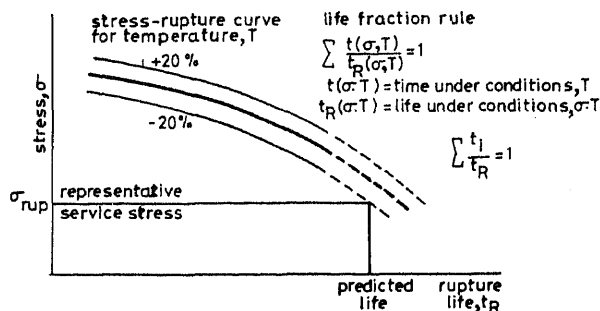


Figure 1. Schematic representation of operational parameter approach (Cane & Townsend 1983).

Table 1. Techniques available for post-service evaluation.

Technique	Comments
<i>Physical:</i>	
Density, resistivity, magnetic permeability, small-angle neutron scatter	May be suitable for cavity assessment
<i>Mechanical:</i>	
Tensile (Room temperature), tensile (hot), hardness, charpy	May be useful for rough assessment
Low-cycle fatigue	limited applicability
Metallographic examination using acetate replica; micro-sample removal	Useful provided coupled with creep strength.
NDE method: Oxide scale thickness measurement	Useful if damage mechanism is oxidation
Accelerated stress-rupture testing	Useful provided extrapolation is done judiciously

to suggest that the Cr–Mo and Cr–Mo–V types of steel can sustain this strain without entering into the tertiary stage.

In view of this it appears to be more appropriate to develop life prediction methodology based essentially on the creep deformation data such as creep rate vs stress relationship particularly when the service stress is lower than the threshold stress as has been proposed by the author (Singh & Banerjee 1992).

In what follows is a brief presentation of global experience and that of NML about the vital issue of “in-service degradation” mainly to bring into focus the need for creep deformation data base in the low-stress region to:

- determine the threshold stress;
- develop a reliable relationship between creep strain rate-stress for life prediction.

2. Global experience

The assessment of accumulated damage and the estimation of remaining life of components particularly of boiler pressure parts has been the subject of intense study for the past several years. A large volume of information has been generated as can be seen in the proceedings of recent conferences (Wufee 1983; Dooley 1987). This information must be critically analysed to evolve a reliable method for predicting remaining life of components. Indeed, this will vary from component to component depending on the operating condition.

In steam power plants, the following components have received special attention for life extension:

- superheater (SH) and reheater (RH);
- headers;
- main steam pipes;
- superheater and reheater.

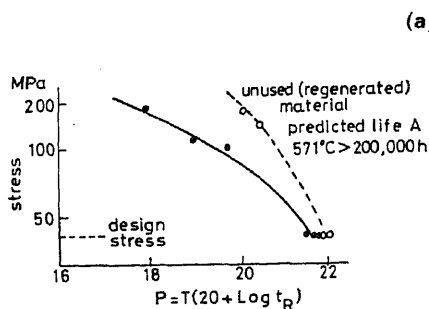
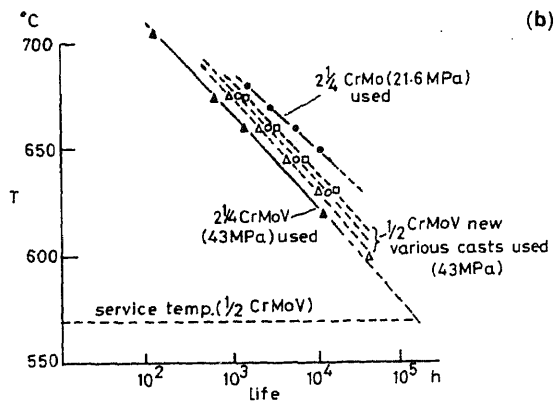


Figure 2. Post service examination approach (Cane and Townsend 1983): (a) stress vs Larson-Miller parameter plots; (b) temperature vs rupture life plots.

SH and RH fail due to one or a combination of the following causes:

- overheating;
- short-term overheat;
- long-term overheat;
- corrosion;
- fire-side corrosion;
- steam-side corrosion;
- stress-corrosion cracking;
- fly-ash erosion;
- exfoliation.

This clearly reveals that life assessment of SH and RH shall require a comprehensive approach which takes into account all the factors responsible for the failure. This is outside the scope of this paper. However, some approaches have been discussed in another article of this issue (Ghosh *et al* 1995).

3. Header and main steam pipe

Unlike SH and RH, the headers and steam piping operate fairly under steady state stress and temperature. These are very expensive components and the failure besides causing long-term outages can be catastrophic. Hence, they deserve special attention.

Header and main steam pipe essentially undergo two processes during service exposure:

- creep deformation under long-term influence temperature/stress;
- change(s) in microstructure and properties under the long-term influence of temperature/stress.

Information on these two aspects is of crucial importance for the life assessment and extension.

4. Creep deformation in service

In the coded design, the limit on creep strain rate is 10^{-7} /h and the accumulated creep strain should be less than 1%. That the actual creep rate is much lower than that envisaged at the design stage is borne out by the table 2 (Wufee 1983) and table 3 (Auerkan 1983). It is significant that hardly 0.2% creep had occurred after the service life of 100,000 h. Though the data given in table 3 do not report the value of accumulated creep strain, the operational time as high as 2,50,000 h indirectly reflects that the creep rate was much less than 10^{-7} /h. Similar service experience has been widely reported recently (Dooley 1987).

In some of the plants diametrical expansion of the steam pipe is also measured at regular intervals. The expansions are measured at certain pre-fixed locations; the measurements are made along both horizontal and vertical axes. Some such data are shown in figures 3, 4 (Weber 1983). These data besides showing that the actual creep rate is generally less than 10^{-7} /h, bring out another important fact: The mode of creep deformation remained essentially the steady state and the tertiary creep had not set in even when the creep strain had nearly touched the prescribed limit of 1%. This is a very useful information from the view-point of life prediction based on the knowledge of the creep rate at the operating stress and temperature. This aspect has been dealt with subsequently. Another interesting point that transpires from figures 3 & 4 is that the expansion along horizontal axis is often larger than that along vertical axis.

Table 2. Practical examples of life prediction by the comprehensive analysis method and assessment of results (Wufee 1993)

Name of pipe work*	Material	Total operation duration of sampling (h)	Life prediction – Stress evaluation			Creep strain (%)	Conclusion (continue operation hours)	Operation duration up to now ($\times 10^5$ h)
			σ_{10^5} (MPa)	σ_{zs} (MPa)	K			
MSP	12CrMo	107675	133.3	46.4	2.9	<0.2	10^5	~ 1.9
MSHS	15CrMo	~ 137000	109.8	46.6	2.4		10^5	~ 2.1
MSP	12Cr1MoV	90000	107.8	57.2	1.9	0.15	10^5	~ 1.7
MSP	12Cr1MoV	110660	107.8	57.2	1.9	0.15	10^5	~ 1.9
MSP	12Cr1MoV	101794	110.8	61.8	1.8	0.13	10^5	~ 1.7

* MSP – main steam pipe; MSHS – main steam header system; σ_{10^5} : stress for rupture in 10^5 h; σ_{zs} : service hoop stress; K : $\sigma_{10^5}/\sigma_{zs}$

Table 3. Inspected steam pipings (Auerkan 1983).

Plant	Nominal steam values (°C/MPa)	Type of material	Operational time, h (design life 100,000 h)
A	510°/6	1Cr-0.5 Mo	238,000
B	480°/6	1 Cr-0.5 Mo	250,000
C	530°/11.5	1 Cr-0.5 Mo	148,000
		2.25 Cr-1 Mo	
D	520°/6	1 Cr-0.5 Mo	156,000
E	525°/11.5	1 Cr-0.5 Mo	135,000

Some reasons suggested for the gap between anticipated and actual creep rate are:

- the mean diameter formula used for calculating hoop stress yields 15% higher values (Cane 1983).
- the steels used for such critical components have the creep properties better than the 'minimum' property data used for design.
- stress exponent of ~ 4 generally used by designers could be higher.

For steam pipes which work under the stipulated design condition life extension to a period as high as 40 years for straight portions of the pipes has been suggested (Neubauer & Wadel 1983).

5. Microstructure and property changes

Microstructural changes developed after prolonged service at high temperature has attracted the attention of material scientists world wide for their study and

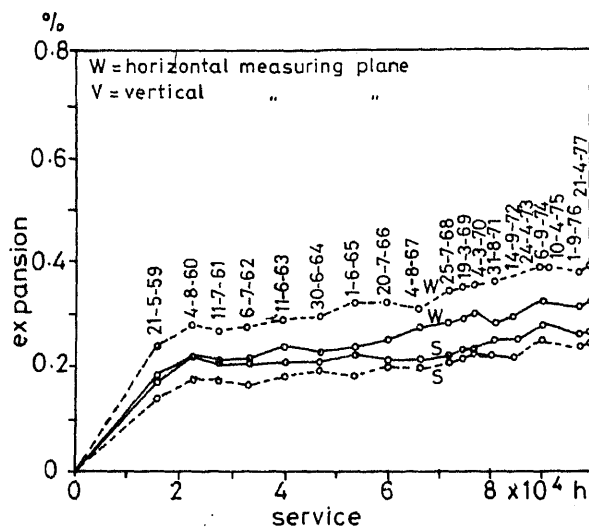


Figure 3. Expansion of intermediate superheater line of 1Cr-0.5 Mo, 398 (OD) \times 18 mm wall, temperature = 530°C (Weber 1993).

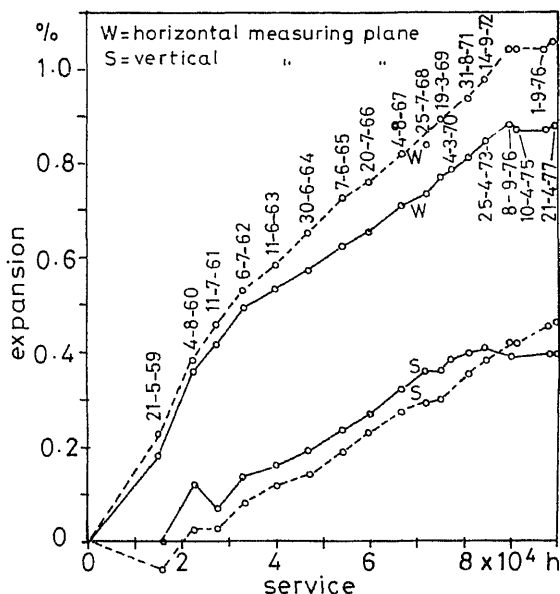


Figure 4. Expansion of life steam line of 1Cr-0.5Mo, 318 OD x 40 mm wall, temperature = 530°C (Weber 1983).

characterization can be a very attractive tool for remaining life assessment. Though information available (Foldina *et al* 1973; William & Wilshire 1981; Senior 1988; Singh & Banerjee 1991) is sizeable, the goal has so far been elusive.

The changes in microstructure mainly consist of coarsening of carbides, compositional and morphological changes in the carbides, increase in the inter-particle spacing formation of new carbides, grain coarsening etc. Here, it is noteworthy that creep damage after prolonged service exposure in the form of grain boundary cavities has rarely been reported in so far as Cr-Mo and Cr-Mo-V steels are concerned. It appears there exists a critical strain limit for initiation of grain boundary cavities. According to one report (Weber & Wellnitz 1993), the limits are: 3% for 2-25Cr-1 Mo, 2% for 1-25Cr-0.5 Mo and 1% for 0.5Cr-0.5 Mo-0.25 V as well as 12Cr-Mo-V steels.

Post-exposure samples have been tested by a number of workers (Cane & Townsend 1983; Weber 1983; Nakashiro *et al* 1990; Singh & Banerjee 1991) and some typical results are reported in figures 5 & 6. One interesting fact transpires: indeed there is degradation in the rupture strengths of the service-exposed sample but this occurs up to a certain stress level. At low stresses (long-term rupture strengths) virgin and service exposed materials are hardly distinguishable. Even milder degradation has recently been reported (Cheruvu 1989) in case of turbine rotors where service temperatures are quite lower.

NML experience is also by and large in conformity with the above observation as will be seen later.

6. NML's experience with boiler and steam pipe

The author, jointly with other team members, has investigated over the last two decades a large number of tube failures received from various steam power plants in the country. Also, a sizeable number of samples have been investigated for health assessment and life extension.

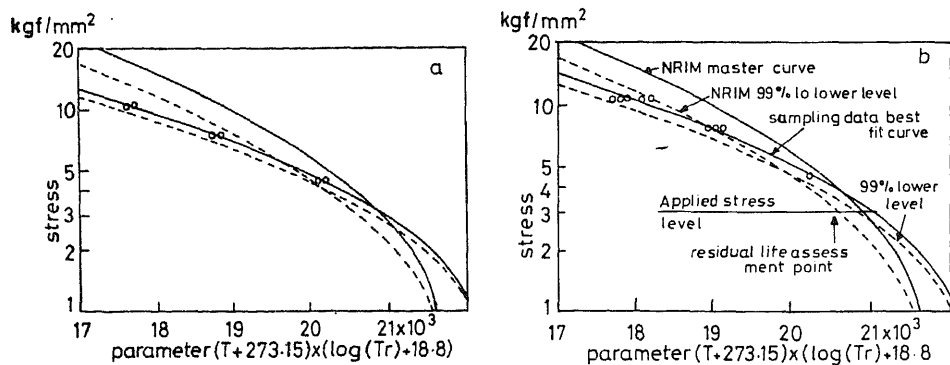


Figure 5. Stress vs Larson-Miller parameter curve of superheater tube (2.25 Cr-1 Mo steel) after 111,940 and 175,562 hour service at plant (Nakashiro 1990).

Premature failure of tubes in the different zones of boilers such as that of steam generators, superheaters and reheaters were found to have occurred due to a variety of reasons; a summary has been reported (Singh 1993). Overheating is indeed an important factor leading to premature failures which could be grouped under two categories:

- short-term excursion of runaway nature, and
- long-term excursion of temperature.

The majority of failures belonged to be first category and only a few to the second. This indirectly suggests that in the design creep has been adequately taken care of and also that the situation calls for the full exploitation of 'safe life'.

Samples for remaining life assessment and life extension recently received at NML are summarised in table 4. Accelerated stress-rupture tests, metallographic examination and also other tests did not show any major sign of degradation after ten years of service.

Notwithstanding that a lot of information on life assessment and extension studies is available in the literature, often they are too fragmented to get a complete picture. That

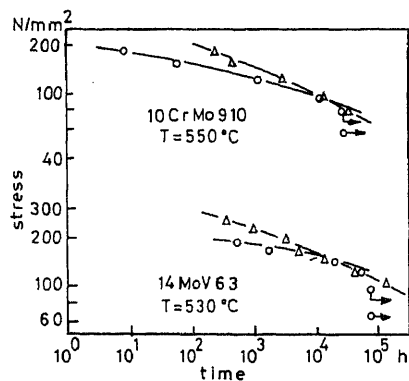


Figure 6. Creep isotherms with (O) and without (Δ) service exposure, main steam pipe of 1 Cr-0.3 Mo-0.25 V steel (Weber 1983).

Table 4. Samples for life extension recently investigated at NML.

Sample	Source	Steam value/ exposure (°C/atm/years)	Recommended remaining life
Main steam pipe 1 Cr-0.3 Mo-0.25 V: 8 Nos. 273(OD) × 22 mm thick	NLC	540/90/10	10 ⁵
Reheater 2.25 Cr-1 Mo	Korba	550/35/10	10 ⁵
Superheater 1 Cr-0.3 Mo-0.25 V	SAIL	450/40/10	10 ⁵
Heater tube 1.25 Cr-0.5 Mo	IPCL	600/7/11	10 ⁵
CCU reactor C-Mn (ASTM 201) 300(OD) × 23 mm thick	BPCL	480/2.1/35	10 ⁵
Catalytic reforming tube 5 Cr-0.5 Mo 219(OD) × 16 mm thick	IOC	500/5/20	10 ⁵

Abbreviations: NLC – Neyveli Lignite Corporation; SAIL – Steel Authority of India Ltd; IPCL – Indian Petrochemicals Corporation Ltd; BPCL – Bharat Petrochemicals Corporation Ltd; IOC – Indian Oil Corporation.

is comprehensive information like microstructure, mechanical properties, creep-rupture properties etc., for a specific type of steel in both virgin and service-exposed states is hardly available. Hence, a strong need was felt by the author to carry out a systematic study covering all these aspects: Post-exposure analyses of microstructural changes as well as that of degradation in creep strengths and ductilities over wide ranging stresses/temperatures, changes in hardness, room and elevated temperatures and tensile properties. A brief account of the work which led to the proposal of a new life prediction methodology based on threshold stress concept is presented.

7. Experimental

The new method for creep life prediction being proposed in this paper is based on a systematic study carried out on a sample of the main steam pipe of 1 Cr-0.3 Mo-0.25 V steel. Experimental details and findings have been reported in other papers (Singh & Banerjee 1991, 1992). However, a brief summary may be in order here.

Microstructural changes encountered during long-term creep exposure and their adverse impact on creep properties have been central to the most of the R & D work in the field. But useful conclusions can be derived only when both the creep and the microstructural aspects are simultaneously and extensively studied using a proper mix of samples. The study is a unique attempt to meet this objective since it is extensively devoted to:

- detailed study of the morphological and compositional changes of the carbides in both virgin and service-exposed samples (Singh & Banerjee 1990, 1991);

Table 5. Details of the 1 Cr-0.3 Mo-0.25 V steel samples investigated.

Sample	State/dimension	Heat treatment*	Microstructure/ hardness
VN	Virgin pipe 273 mm OD ×	Commercially N at 980 + T at 700	90% ferrite 10% bainite 156
SE	22 mm thick	Same as VN	90% ferrite 152
RHV1	15 mm dia	austenitized	100% bainite 210
RHV2	15 mm dia	N at 980°C(1 h) + T at 700°C(2 h)	80% ferrite 190 20% bainite
RHV3	15 mm dia	N at 980°C(1 h) + T at 700°C(72 h)	80% ferrite 160 20% tempered bainite

*N – normalized; T – tempered

- extensive creep-rupture and hot tensile properties of samples having widely varying microstructures including the one produced in the service exposed material.

The details of the five samples that have been studied are given in table 5. The chemical composition is reported in table 6.

The SE samples are removed from the region close to the boiler end which had seen the highest service temperature. It is remarkable that the VN and the SE samples belonged to the same manufacturing batch.

Our findings of microstructural study (Singh & Banerjee 1990, 1991) have brought out a significant point that morphological and compositional changes of the carbides impair the creep only at high stresses where the Orowan Bowing is a dominant creep deformation mechanism. On the other hand, creep strength at low stresses customarily experienced by engineering components is not affected appreciably.

The main findings concerning the creep and hot tensile studies which have provided the basis for the new approach are discussed subsequently.

8. The threshold stress

The threshold stresses for the five different microstructures were obtained using the Lagneborg–Bergman (1976) approach. This is schematically shown in figure 7 wherein the creep data are plotted in the form of the fourth roots of the minimum creep rates ($\dot{\epsilon}$)^{0.25} vs the applied stresses, σ . Line 1 corresponds to the low stress sensitivity ($n = 4$) obtained at lower stresses and line 2 corresponds to the high stress sensitivity ($n \gg 4$) obtained at higher stresses. The extension of line 2 to a strain rate equal to zero gives

Table 6. Chemical composition (wt%) of the pipe investigated.

C	Mn	P	S	Si	Cr	Mo	V	N
0.11	0.30	0.01	0.007	0.35	1.01	0.28	0.23	0.023

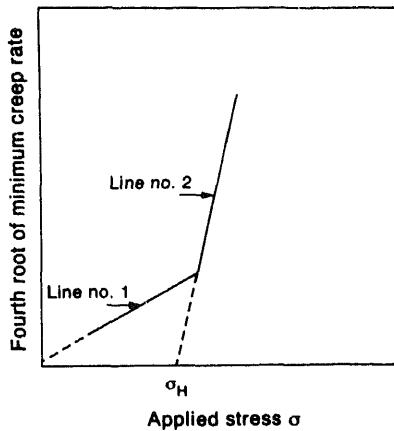


Figure 7. Schematic representation: Determination of threshold stress from creep data for a given microstructure.

the value of the threshold stress σ_H . The threshold stress obviously implies that it is the highest value of the applied stress which if exceeded produces runaway creep (high value of n).

Figure 8 shows $(\dot{\epsilon})^{0.25}$ vs σ plot in the high and in the low stress sensitivity regions for each of the five microstructural states. The intercepts of the lines A, B, C, D and E with the abscissa give the values of σ_H . The transition stress, σ_T , represents the stress level above which change in creep deformation mechanism is believed to occur (Lagneborg & Bergman 1976; Blum & Reppich 1985).

The figure shows the following important points:

- The values of σ_H for the VN and the SE samples differ only by 12 MPa, which means that a service exposure of 10^5 h produces only a mild degradation. This observation was also in keeping with the insignificant micro structural changes observed after an exposure of 10^5 in service (Singh & Banerjee 1991).

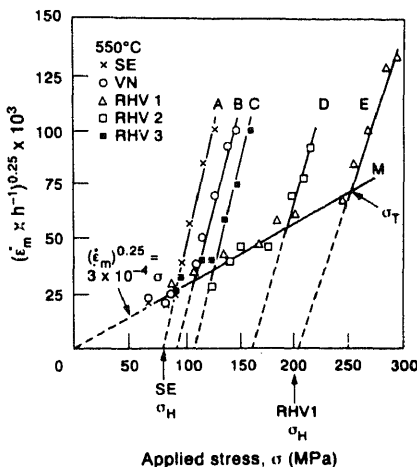


Figure 8. Threshold stress for different microstructures in 1Cr-0.3Mo-0.25V steel. (Singh & Banerjee 1992).

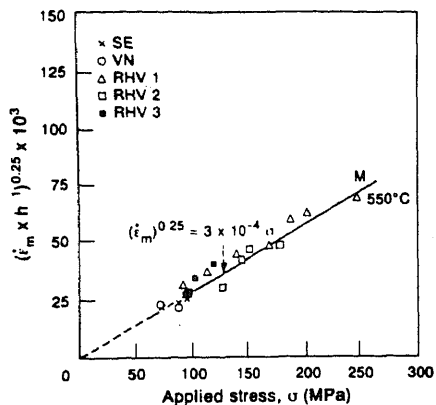


Figure 9. Minimum creep rate in the low stress sensitivity region (Singh & Banerjee 1992).

- The creep strength varies significantly with change in original microstructures but only at higher stresses. When $\sigma < \sigma_T$ the data points for all microstructures fall on the same line OM.
- The best fit line OM (see figure 9) passes through the origin. The equation of the line OM is:

$$(\dot{\epsilon})^{0.25} = M\sigma, \quad (1)$$

where

$$M = 3 \times 10^{-4}, (h)^{0.25} / \text{MPa}.$$

It may be noted that the line OM is microstructure-independent and hence can be used for any given microstructure for life prediction. It is also noteworthy that the 2.25Cr-1Mo steel (Wolf 1990) exhibited a similar trend (figure 10). However, the difference in respect of lower values of σ_H and M , may be noted. This is understandable in view of the lower creep strength of 2.25Cr-1Mo.

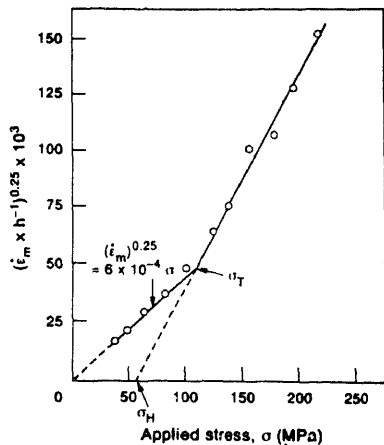


Figure 10. Threshold stress of 2.25Cr-1Mo steel based on published data (Wolf 1990).

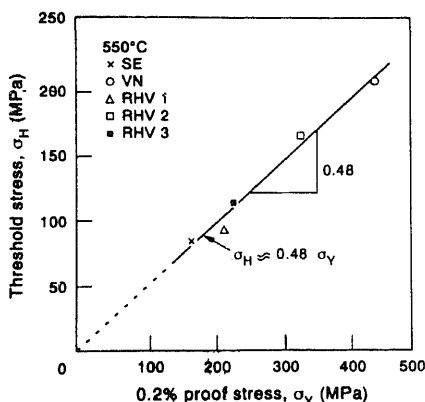


Figure 11. Threshold stress vs hot yield stress at 550°C (Singh & Banerjee 1992).

9. Correlation of σ_H with hot yield strength

σ_H can indicate the extent of microstructural change during creep exposure. It has also been contended that σ_H "can be used as a design-limiting strength property" (Russel *et al* 1985). Notwithstanding this contention, it should be noted that to achieve significantly long life, the stress level in a power plant component used in high temperature service, must be considerably lower than σ_H . On the other hand, σ_H represents an upper-bound value of the permissible stress. Indeed, the service stress at any point of time must always be less than σ_H to avoid runaway creep deformation. Therefore, a simple experimental method to determine σ_H should be useful. The metallographic methods to determine σ_H are difficult to carry out and liable to yield uncertain results (Cane & Townsend 1983).

Hence, the correlation of σ_H with the hot tensile yield strength, σ_Y as observed by us is significant. This is plotted in figure 11, which indicates that

$$\sigma_H = 0.48 \sigma_Y. \quad (2)$$

Similar observation has been made on Ni-base superalloys (Russel *et al* 1985) where $\sigma_H = 0.7 \sigma_Y$; Purushothaman & Tien (1978) have also theoretically predicted the tensile flow stress and found that it is nearly equal to σ_H . This indicates that the threshold stress is nearly equal to the Orowan stress and is proportional to the hot yield strength. Also, it can decrease to a lower limit of about one-half of hot yield strength, as temperature increases and/or strain rate decreases (Purushothaman & Tien 1978).

10. Conclusions

Procedure for creep life prediction

Based on the main findings as represented by (1) and (2) the following steps can be suggested for a rapid assessment of the remaining creep life of a component made of 1Cr-0.3Mo-0.25V steel and subjected to the usual service temperatures of 550°C (barrings accidental short-term excursion to a higher temperature).

- (1) Determine the hot yield strength, σ_Y , at the service temperature and estimate σ_H from the relationship $\sigma_H = 0.48 \sigma_Y$.

- (2) Determine $\dot{\epsilon}_m$ at six stress levels, three of them between 0.4 and 0.5 times and the other three at 0.6, 0.7 and 0.8 times hot yield stress. The maximum duration of one such test is 1500 hours only.
- (3) Plot $(\dot{\epsilon}_m)^{0.25}$ vs σ curve in a manner similar to that in figure 5 and determine σ_H .
- (4) If σ_H is greater than the service stress, σ , calculate the residual life in terms of the time required to produce the balance amount of strain to make up the maximum permissible strain of 1%. The calculation uses the simple relationship:

$$(\dot{\epsilon}_m)^{0.25} = M\sigma.$$
- (5) If σ_H is less than the service stress, σ , retire the component and replace it at the earliest.

At present, the total duration of creep testing using the stress-rupture approach for creep-life prediction is about 15,000 h. This can reduce five-fold if the new approach is used. Furthermore, if (1) and (2) are fully established, creep testing can be completely dispensed with.

Further study

There is need to generate a strong database at stresses approaching the service stress of 30–60 MPa and at several temperatures between 500 and 650°C. This should be done for various grades of both virgin and service-exposed steels so that (1) and (2) can be fully established.

It would also be interesting to assess the lowest possible value of the threshold stress after say 20–30 years of exposure. This will reveal if σ_H will ever go as low as the service stress.

Generation of data at low stresses is rather tedious and would require very close control of the temperature ($\pm 1^\circ\text{C}$) and LVDTs with improved stability and sensitivity.

References

- Auerkan 1983 Remanent creep life estimation of old power plant steam piping systems *Int. Conf. on Adv. in Life Prediction Methods* (eds) D A Woodford, J R Whitehead (New York: ASME) pp. 353–356
- Blum W, Reppich B 1985 Creep behaviour of crystalline solids. *Progress in creep and fracture* (eds) B Wilshire, R W Evans (Swansea: Univ. College) vol. 3
- Cane B J, Townsend R D 1983 Production of remaining life in low-alloy steels *Flow and fracture at elevated temperatures* (ed) R Raj (Metals Park, OH: ASME) pp. 279–316
- Cheruvu N S 1989 Degradation of mechanical properties of Cr–Mo–V and 2.25 Cr–1 Mo steel components after long-term service at elevated temperatures. *Metall. Trans. A20*: 87–97
- Dooley B (ed.) 1987 *Conf. Proceeding: Life extension and assessment of fossil power plants* (Palo Alto, CA: EPRI)
- Foldina V, Jakobove A, Prinka T, Sabotk J, 1973 Influence of microstructure on creep properties of low-alloy ferritic Cr–Mo–V steels. *Proc. Conf. on creep strength in steels and alloys*, (London: The Met. Soc.) pp. 230–236
- Ghosh R N, Chaudhury S, Roy N, Chattopadhyay L 1995 *Sadhana* 20: 331–339
- Lagneborg R, Bergman B 1976 The stress/creep rate behaviour of precipitation hardened alloys *Metall. Sci.* 10: 20–28
- Nakashiro M, Kihara S, Kishimoto F, Fujimori T 1990 Evaluation of long-term creep strength of 2.25 Cr–1 Mo heat transfer tube in actual service stress level range. *Iron Steel Inst. Jpn. Int.* 30: 823–828
- Neubauer B, Wadel U 1983 Rest life estimation of creeping components by means of replicas. *Int. Conf. Adv. in Life Prediction Methods* (eds) D A Woodford, J R Whitehead (New York: ASME) pp. 307–313

- Purushothaman S, Tien J K 1978 Role of back stress in the creep behaviour of particle strengthened alloys. *Acta Metall.* 26: 519–528
- Russel R, Jeneson R R, Tien J K 1985 Temperature and strain dependence of stress-strain behaviour in a Ni-base superalloys. *Metall. Trans.* A16: 1049–1068
- Senior B A 1988 A critical review of precipitation behaviour in 1 Cr–Mo–V rotor steels. *Mater. Sci. Eng.* A103: 263–271
- Singh R 1993 Assessment of fracture and failure. *Familiarisation programme on power plant metallurgy*. NTPC, Vindhyachal Super Power Project organised by NML, Jamshedpur (ed) R Singh, pp. R1–R12
- Singh R, Banerjee S 1990 Morphological and compositional changes of the carbides in a ferritic steel after long-term service exposure. *Scr. Metall. Mater.* 24: 1093–1098
- Singh R, Banerjee S 1991 Morphological and compositional changes of the carbides in Cr–Mo–V ferritic steel. *Mater. Sci. Eng.* 132: 203–211
- Singh R, Banerjee S 1992 Resisting stress of a low alloy steel after creep exposure in service. *Acta Metall. Mater.* 40: 2607–2616
- Viswanathan R 1989 Damage mechanism and life assessment of high temperature components. (Metals Park, OH: ASME)
- Weber H 1983 Report No. 35-V, Mannesman, Germany
- Weber H, Wellnitz G 1993 Assessment of creep affected materials to determine remaining service life. *Proc. Int. Workshop on Power Plant Remaining Life Evaluation, Prediction, Extension and Optionization* (Calcutta: ASME - Indian Chapter)
- William K R, Wilshire B 1981 Microstructural instability of 0.5 Cr–0.5 Mo–0.25 V creep-resistant steel during service at elevated temperatures. *Mater. Sci. Eng.* 47: 151–160
- Wolf H 1990 *Kriechender Legierungen NiCr22Co12Mo und 10CrMo910 BEI Konstanter und zyklischer Beanspruchung*, PhD thesis, Univ. of Erlangen, Nurnberg, Germany.
- Woodford D A, Whitehead J R (eds) 1983 *Int. Conf. Adv. in Life Prediction Methods* (New York: ASME)
- Wufee V 1983 A study of life prediction techniques for main steam pipes made of pearlitic steels in power plants in China. *Int. Conf. Adv. in Life Prediction Methods* (eds) D A Woodford, J R Whitehead (New York: ASME) pp. 347–351



1



2

3

4

5

6

7

8

9

10

11

12

13

14

15

16

17

18

19

20

21

22

23

24

25

26

27

28

29

30

31

32

33

34

35

36

37

38

39

40

41

42

43

44

45

46

47

48

49

50

51

52

53

54

55

56

57

58

59

60

61

62

63

64

65

66

67

68

69

70

71

72

73

74

75

76

77

78

79

80

81

82

83

84

85

86

87

88

89

90

91

92

93

94

95

96

97

98

99

100

Multiaxial fatigue – An overview

V M RADHAKRISHNAN

Metallurgical Engineering Department, Indian Institute of Technology,
Madras 600 036, India

Abstract. Many engineering components are subjected to multiaxial type of fatigue loading and the fatigue life relation based on uniaxial testing needs modifications before it could be used for multiaxial condition. In this paper a brief review of the different approaches based on stress and strain is presented for the correlation of bulk parameters with the fatigue life and the merits and limitations are discussed.

Keywords. Multiaxial fatigue; stress-strain parameters; in-phase out-of-phase fatigue; high temperature fatigue; life assessment.

1. Introduction

Multiaxial fatigue is the major consideration in the design of many of the structural components such as automobile parts, gas turbine components, power reactors etc. The parts will be subjected to varying loads of different amplitudes and frequencies in two or three directions depending on the thickness. This will give rise to biaxial or multiaxial fatigue and the assessment of fatigue life is an important design requirement for reliable operation and safety.

Most of the fatigue data are obtained based on tests performed under uniaxial loading condition. However, engineering components in general, are subjected to complex loading involving bending, torsion and axial forces. The design of these components is carried out based on fatigue properties under uniaxial loading conditions. It will be in the form of endurance limit or the low cycle strain range fatigue life relation. However, these data can serve only as an input information for the life prediction of components subjected to biaxial or multiaxial fatigue. The safe life assessment has to be carried out through suitable methods based on the deformation mechanisms that will be operative during the fatigue process. An excellent review of the state-of-the-art up to 1980 has been presented by Garud (1981). Many symposium proceedings have also been brought out in the last decade highlighting the developments made in the area of multiaxial fatigue (Miller & Brown 1985; Brown & Miller 1989; Kussmaul *et al* 1991).

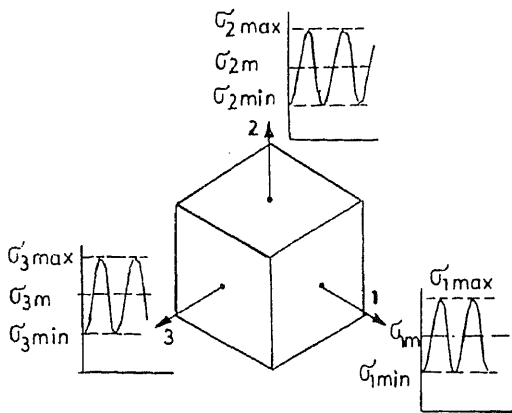


Figure 1. An element subjected to triaxial fatigue stressing.

2. Life prediction models

2.1 State of stress and strain

Normally components are designed based on high cycle fatigue data where the stress levels are below the yield strength of the material and general yielding of the material is not present. The design approach is based on the state of stress acting on the component. A typical element subjected to triaxial fatigue loading is shown in figure 1 and Mohr's circle for state of stress is shown in figure 2. Three principal stresses in general, σ_1 , σ_2 , and σ_3 , are considered for evaluating the equivalent stress that is taken for life calculations. The stress that governs the deformation could be the maximum principal stress, σ_1 , or the maximum shear stress, τ_{\max} , given by the relation

$$\tau_{\max} = (\sigma_1 - \sigma_3)/2. \quad (1)$$

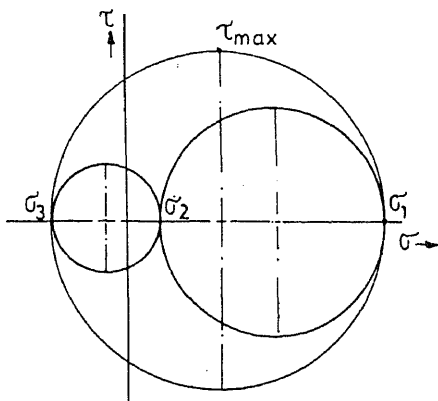


Figure 2. Mohr's circle for triaxial state of stress.

Octahedral shear stress, τ_{oct} , is also considered as a controlling parameter for deformation and is given by

$$\tau_{\text{oct}} = (1/3)[(\sigma_1 - \sigma_2)^2 + (\sigma_2 - \sigma_3)^2 + (\sigma_3 - \sigma_1)^2]^{1/2}. \quad (2)$$

The corresponding strains, i.e., maximum shear strain and the octahedral shear strain are given by

$$\gamma_{\text{max}} = \varepsilon_1 - \varepsilon_2, \quad (3)$$

and

$$\gamma_{\text{oct}} = (2/3)[(\varepsilon_1 - \varepsilon_2)^2 + (\varepsilon_2 - \varepsilon_3)^2 + (\varepsilon_3 - \varepsilon_1)^2]^{1/2}. \quad (4)$$

In terms of equivalent normal stress and strain we have

$$\tau_{\text{oct}} = 2^{1/2}/3 \bar{\sigma}, \quad (5)$$

and

$$\gamma_{\text{oct}} = 2^{1/2} \bar{\varepsilon}. \quad (6)$$

In the following, stress- and strain-based approaches for multiaxial fatigue are considered for the calculation of the equivalent parameters.

2.2 Stress based approach

Consider a machine member subjected to a triaxial pulsating load along the three principal axes. The stresses vary from a minimum to a maximum with a mean value. For simplicity it is assumed that the stresses are in-phase and the principal axes are fixed. Under such a condition, Sines (1955) proposed a relation in the form

$$[(\sigma_{a1} - \sigma_{a2})^2 + (\sigma_{a2} - \sigma_{a3})^2 + (\sigma_{a3} - \sigma_{a1})^2]^{1/2} + [A(\sigma_{m1} + \sigma_{m2} + \sigma_{m3})] = 2^{1/2} \sigma_n, \quad (7)$$

where σ_{ai} is the alternating principal stress, σ_{mi} the mean stress, A a constant, σ_n the uniaxial fully reversed fatigue stress that is expected to give the same life on smooth specimens as the multiaxial state.

The above relation for biaxial loading will be reduced to

$$(\sigma_{a1}^2 - \sigma_{a1}\sigma_{a2} + \sigma_{a2}^2)^{1/2} + A(\sigma_{m1} + \sigma_{m2})/2^{1/2} = \sigma_n. \quad (8)$$

This relation gives a family of ellipses with their centres decided by the mean stresses σ_{m1} and σ_{m2} , as shown in figure 3. Thus, lines of constant octahedral shear stress are ellipses in such a plane. The different ellipses give the areas of safe alternating stresses on a stress plane for biaxial stresses. For any biaxial in-phase alternating stress that corresponds to the fatigue criterion, successive instantaneous states of stress are represented by points on a diameter of such an ellipse. The centre of the ellipse is the mean stress. Ellipses that are located on a line of constant octahedral normal mean stress 45° downward to the right, are of equal size. Increasing the mean stress decreases the size of the ellipse. The approach assumes that (i) there is no gross yielding, and (ii) the alternating stresses can be represented by principal alternating stresses along fixed principal axes.

Sines (1955) showed a good correlation with experimental results in fatigue. Static torsion has been found to have less effect than static alternating fatigue strength when gross yielding is avoided.

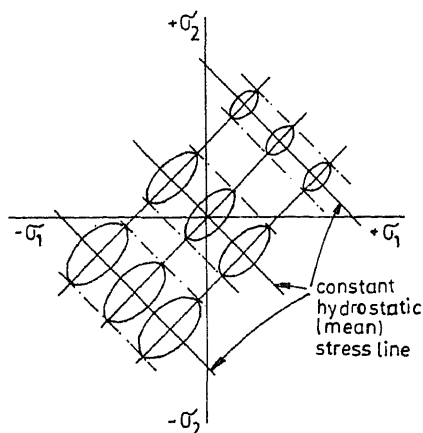


Figure 3. Areas of safe alternating stresses on a biaxial stress-plane.

Findley (1957, 1959) introduced the influence of normal stress acting on the maximum shear stress plane and has given the fatigue life relation as

$$\tau_a + k\sigma_{n \max} = f(N_f) \quad (9)$$

where k is a constant. Thus the allowable alternating shear stress, τ_a , for a given fatigue life decreases with an increase in the maximum normal stress $\sigma_{n \max}$ on the plane of the critical alternating shear stress.

Combining the approaches due to Sines and Findley, an equation for the fatigue equivalent stress has been proposed in the form,

$$[(\sigma_{a1} - \sigma_{a2})^2 + (\sigma_{a2} - \sigma_{a3})^2 + (\sigma_{a3} - \sigma_{a1})^2]^{0.5} + A[\sigma_{m1} + \sigma_{m2} + \sigma_{m3}] + B[\sigma_{a1} + \sigma_{a2} + \sigma_{a3}] = C, \quad (10)$$

where σ_{ai} are the principal alternating stress ranges, and σ_{mi} the principal static stresses.

Kakuno & Kawada (1979) were able to show good correlation with experimental results obtained from bending and torsion fatigue testing. The above criterion implies that there will be fatigue failure under hydrostatic alternating stresses i.e., $\sigma_{a1} = \sigma_{a2} = \sigma_{a3}$. The constant B which determines the contribution of the hydrostatic alternating component could be positive or negative indicating the detrimental or beneficial effects. However, for cases where there is phase lag, the effect is not clearly brought out in the equation.

McDiarmid (1985, 1987, 1991, 1993) introduced a modification in the stress approach and gave the modified equation in the form

$$\tau_a(1 + (\sigma_{n \max}/2\sigma_{ult})) = F(N_f), \quad (11)$$

where σ_{ult} is the tensile strength. The function F depends on whether the cracking grows along the surface (mode III) or grows into the surface (mode II). The first case occurs in torsion loading and the second one under biaxial tension loading. The theory has been extended for the cases of out-of-phase biaxial stresses and has been shown that the out-of-phase stresses produce shorter fatigue lives than equal in-phase stresses. Typical

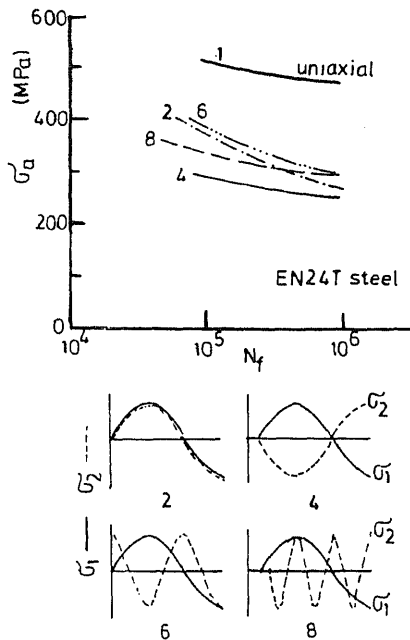


Figure 4. Effect of phase lag and different frequency on $S-N$ curve of EN 24 steel.

experimental results for both out-of-phase and different frequencies are shown in figure 4 for the material EN 24 steel. $S-N$ curve (case 1) gives for uniaxial condition. In biaxial condition, when σ_1 and σ_2 are both in-phase (case 2), the fatigue strength is reduced as compared to uniaxial loading. When both of them are completely out-of-phase (case 4), the strength is still lower. Similarly, it can be seen that different frequencies for σ_1 and σ_2 also (cases 6 and 8) reduce the fatigue strength as compared to the uniaxial condition.

A relation of the type

$$\tau_{\max} + k\sigma_{n\max} = CN_f^{-\alpha} \quad (12)$$

has been used to compute the life.

For out-of-phase angle of 90°

$$\tau + k\delta_n = \tau \cos wt + k\sigma \sin wt \quad (13)$$

For maximum value of $(\tau + k\sigma_n)$ we have

$$\tan wt = k\sigma/\tau = k/\lambda_\sigma, \quad (14)$$

where $\lambda_\sigma = \tau_a/\sigma_a$.

Thus the maximum value of $(\tau + k\sigma_n)$ can be found for different values of $\lambda_\sigma (= \tau_a/\sigma_a)$.

The analysis can also be extended to cases of different frequencies. The experimental results on 1045 steel and the applicability of the model are shown in figure 5. In the out-of-phase loading the damage is likely to be more severe. Though, in the out-of-phase cases, the maximum normal stresses do not occur simultaneously with maximum shear stresses in any plane, the analysis used here maximises the $(\tau + k\sigma_n)$ critical parameter for each particular loading condition.

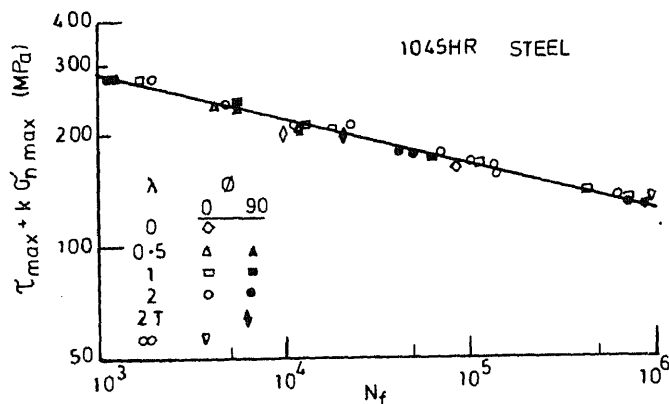


Figure 5. Relation between the equivalent stress due to McDiarmid and fatigue life of 1045 steel.

In the stress based approach two criteria are normally used – one based on maximum shear stress amplitude (Tresca) to correlate the life and incorporated in the ASME Boiler and Pressure Vessel Code Section III – and the other based on octahedral shear stress amplitude (von Mises) incorporated in Code Case N-47-12 of Section III.

Both these methods compute an equivalent fully reversed uniaxial stress amplitude from an applied multiaxial state of stress. Life estimation is made by using the relation

$$\sigma_{eq} = \sigma'_f (N_f)^{-\alpha} \quad (15)$$

Notches are quite common in components subjected to multiaxial fatigue, such as crank shafts, connecting rods, transmission shafts etc., and hence stress concentration factors should also be taken into consideration.

In cases of shafts or machine members subjected to both bending and torsion the amplitude of the maximum shearing stress used as equivalent stress amplitude in the above equation, is calculated using the Tresca criterion as

$$\tau_{max} = \sigma/2 [1 + K^2 + (1 + 2K^2 \cos(2\phi) + K^4)^{0.5}]^{1/2}, \quad (16)$$

where σ is the notch bend stress amplitude including the stress concentration factor Kb in bending, τ is the notch torsional shearing stress amplitude including the stress concentration factor Kt in torsion, $K = 2\tau/\sigma$ and ϕ is the phase angle between applied bending and torsional loading.

In the second approach, based on octahedral shear stress amplitude, the equivalent stress amplitude, τ_{eq} , is given by

$$\tau_{eq} = (\sigma/2) [1 + 3/4 K^2 + (1 + (3/2) K^2 \cos(2\phi) + (9/16) K^4)^{0.5}]^{0.5}. \quad (17)$$

The effects of stress concentration in bending and torsion are to be included in both the approaches. In some cases the fatigue notch factor K_f could be assumed to be unity. However, this assumption is likely to lead to over estimation of fatigue life, specially in high strength materials. In high cycle fatigue, out-of-phase loading appears to be more damaging than in-phase loading for the same applied load levels.

2.3 Strain based approach

Fatigue lives under multiaxial loading may differ significantly from those observed under equivalent uniaxial loading conditions due to additional damage and deformation mechanisms that are activated under first condition. Many investigations have been conducted over the last two decades on thin-walled tubular specimens to characterize the fatigue behaviour of several engineering alloys under combined axial and torsional loading conditions. These investigations involved both in-phase and out-of-phase strain-controlled axial–torsional fatigue tests. The materials investigated included aluminium alloys, low alloy steels, stainless steels, and nickel base super alloys (Socie & Shield 1984; Fatemi & Stephens 1989; Jayaraman & Ditmars 1989; Nitta *et al* 1989; Sreeramesh & Bonacuse 1993).

Many life prediction models have been proposed to estimate fatigue life under combined cyclic axial–torsional loading conditions (Haverd & Topper 1971; Miller & Brown 1984; Fatemi & Kurath 1988; Fatemi & Socie 1988; Socie 1989). Some of these models include parameters based on the von Mises equivalent strain range, the principal stresses or strains and on a combination of maximum shear strain and the normal stress and/or normal strain acting on the maximum shear plane. Most of these life prediction models have been verified with room temperature axial–torsional data.

The local strain based approach has become an important tool for prediction of fatigue life. Many attempts have been made to identify the damage parameters capable of predicting multiaxial fatigue. The important among them are

- (a) maximum principal strain amplitude;
- (b) maximum shear strain amplitude;
- (c) von Mises effective strain amplitude;
- (d) Brown–Miller approach;
- (e) Lohr–Ellison approach;
- (f) other strain-based approaches;
- (g) energy-based approach.

2.3a Maximum principal strain approach: In the maximum principal strain approach the principal strain $\varepsilon_1, \varepsilon_2, \varepsilon_3$ are determined by an appropriate transformation of the measured or applied strains ε_{ij} . For correlating multiaxial fatigue tests, the range of maximum principal strain on the plane that experiences the maximum principal strain range is considered the dominant parameter to describe damage. The strain life equation is written in the form

$$\Delta\varepsilon_1 = A(N_f)^{-\alpha} + B(N_f)^{-\beta}, \quad (18)$$

where, $A = \sigma'_f/E$ and $B = \varepsilon'_f$.

2.3b Maximum shear strain approach: In the case of maximum shear strain range approach the shear strain range $\Delta\gamma_{\max}$ is given by

$$\Delta\gamma_{\max} = (\varepsilon_1 - \varepsilon_3)_{\max}. \quad (19)$$

This can be related to the fatigue life N_f as

$$\Delta\gamma_{\max} = A(N_f)^{-\alpha} + B(N_f)^{-\beta}. \quad (20)$$

In the case of a shaft with a notch subjected to bending and torsion the relation for shear strain range, $\Delta\gamma$ can be written as

$$\Delta\gamma_{\max} = [\Delta\epsilon_x^2(1 + \nu)^2 + \Delta\gamma_{xy}^2]^{0.5}, \quad \text{for in-phase loading,} \quad (21)$$

and

$$\Delta\gamma_{\max} = \text{greater of} \left[\frac{\Delta\gamma_{xy}}{\Delta\epsilon_x(1 + \nu)} \right], \quad \text{for } 90^\circ \text{ out-of-phase loading,} \quad (22)$$

$\Delta\gamma_{\max}$ is the range of notch maximum shear strain, $\Delta\epsilon_x$ is stabilized notch bending strain range, and $\Delta\gamma_{xy}$ is stabilized notch torsional shear strain range.

The equivalent strain range is found from

$$\Delta\bar{\epsilon} = \Delta\gamma_{\max}/(1 + \nu).$$

The elastic and plastic values of Poisson's ratio have been taken as 0.29 and 0.5.

2.3c The von Mises equivalent strain range model: The von Mises effective strain may be thought of as the root mean square of the maximum principal shear strain normalised to axial loading. It is also called the octahedral shear strain.

This model gives the multiaxial equivalent strain range in the form

$$\Delta\bar{\epsilon} = [1/(2^{1/2}(1 + \nu))]/[(\Delta\epsilon_1 - \Delta\epsilon_2)^2 + (\Delta\epsilon_2 - \Delta\epsilon_3)^2 + (\Delta\epsilon_3 - \Delta\epsilon_1)^2]^{1/2}, \quad (23)$$

where

$$\Delta\bar{\epsilon} = \text{von Mises effective strain amplitude.}$$

In the case of combined bending and torsion the relation can be written as

$$\Delta\epsilon_1 \text{ or } \Delta\epsilon_2 = (1/2)(\Delta\epsilon_x + \Delta\epsilon_y) \pm [(\Delta\epsilon_x - \Delta\epsilon_y)^2 + \Delta\gamma_{xy}^2]^{0.5} \quad (24)$$

$$\Delta\epsilon_3 = [-\nu/(1 - \nu)](\Delta\epsilon_1 + \Delta\epsilon_2), \quad (25)$$

where $\Delta\epsilon_y$ is the circumferential strain range.

The effective strain is used as an equivalent uniaxial strain amplitude to predict fatigue life. The variable Poisson's ratio, ν , is defined as

$$\nu = (\nu_e \epsilon_e + \nu_p \epsilon_p)/\epsilon_t \quad (26)$$

where ϵ_e , ϵ_p , ϵ_t are elastic, plastic and total strains respectively and are used in cases of proportional loading.

2.3d The Brown-Miller approach: Figure 6 shows the Mohr's circle based on maximum principal strain in triaxial loading situation. In fatigue fracture two strain parameters are important, that is, (i) the size of the largest circle created in a cycle ($\epsilon_1 - \epsilon_3$), and (ii) the location of this circle in strain space, i.e., $(\epsilon_1 + \epsilon_3)/2$. Thus it can be seen that equivalent stress or strain calculation on the basis of Tresca or von Mises criterion may not be sufficient to calculate the fatigue life.

Brown & Miller (1973) (B-M) postulated that failure under multiaxial fatigue is governed by a functional relation between the maximum range of shear strain and the range of normal strain acting on the plane where the former occurs. Thus

$$(\epsilon_1 - \epsilon_3)/2 = f[\epsilon_1 + \epsilon_3]/2 \quad (27)$$

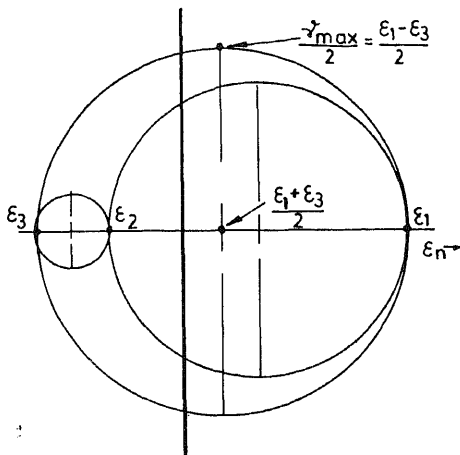


Figure 6. Mohr's circle based on maximum principal strains.

The approach proposed is for fixed principal strain axes and in-phase straining. The function f is not defined and varies with life.

The B-M approach considers that, in addition to the amplitude of the maximum shear strain γ_{\max} , the amplitude of the normal strain ε_n acting perpendicular to the plane of maximum shear strain amplitude. Thus we have

$$(\gamma_{\max}/g)^i + (\varepsilon_n/h)^i = 1. \quad (28)$$

Contours of constant life on γ_{\max} versus ε_n called Lamda planes are obtained. The constants g , h , and i were found to vary with life. However, it was suggested that a safe and simple design criterion could be established with $i = 2$, so that

$$(\gamma_{\max}/g)^2 + (\varepsilon_n/h)^2 = 1 \quad (29)$$

A typical Lamda plane and the constant life contours on the γ_{\max} and $(\varepsilon_1 + \varepsilon_3)/2$ axes are shown in figure 7. The figure also shows how stage I and stage II cracks grow in relation to the surface. There are two cases (A) and (B). Stage I growth plane is inclined at 45° to the principal direction while stage II is perpendicular. In case (A) type, cracks are contained in the surface layers. This state occurs in torsion testing and the growth of these cracks is by mode II along the surface and mode III in depth. In case (B) type, the crack growth situation is more dangerous. The cracks grow from the surface to inside the material. The stage I crack is driven inside by a mode II mechanism, but the mode I plays an increasing role as crack enters stage II. As can be seen in figure 7, the same life time of 500 cycles occurs when the plastic shear strain is 0.325 in a plane strain test and 0.6 in a pure torsion test. ε_n is zero in both cases. This is because in the former case a dangerous case (B) type crack is generated while in the latter case of torsion test, a case (A) type crack propagates along the surface.

Extending this approach Kandil *et al* (1982) showed that the life, N_f , can be related to the strain criterion in the form

$$\Delta\gamma_{\max} + S\varepsilon_n = A_1(\sigma'_f/E)(N_f)^{-\alpha} + A_2\varepsilon'_f(N_f)^{-\beta}, \quad (30)$$

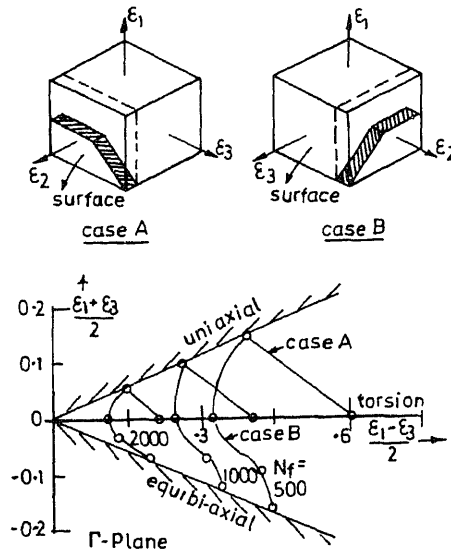


Figure 7. Representation of constant life contours on the Lambda plane. Two types of crack growth (A) along the surface and (B) inside the material are also shown.

where S = material parameter = unity,

$$A_1 = 2(1 + v_e) + S(1 - v_e) = 3.3,$$

$$A_2 = 2(1 + v_p) + S(1 - v_p) = 3.5.$$

2.3e The Lohr-Ellison approach: Taking into consideration the shear strain range that makes the crack propagate from the surface to inside the material, Lohr & Ellison (1980) proposed a critical plane theory, leading to the formulation of the relation

$$\Delta\gamma^* + k\epsilon_n^* = C. \quad (31)$$

$\Delta\gamma^*$ is the maximum shear strain acting on a plane which intersects the surface at 45° and will control fatigue life in the low cycle regime. $\Delta\epsilon_n^*$ is the direct strain normal to this plane and may have a modifying influence.

When the minimum principal strain is primarily normal to the surface the $\Delta\gamma^*$ is given by

$$\Delta\gamma^*/2 = \Delta(\epsilon_1 - \epsilon_2)_{\max}/2 \quad (32)$$

If the second principal strain is most nearly normal to the surface, the value is given by

$$\Delta\gamma^*/2 = \Delta(\epsilon_1 - \epsilon_2). \quad (33)$$

The normal strain to the plane of shear is given by

$$\Delta\epsilon_n/2 = [\epsilon_1 + \epsilon_3 \text{ (or } \epsilon_2)]/4. \quad (34)$$

The third (or the second) principal strain is normal to the surface.

A life relationship based on the parameter can be developed as

$$\Delta\gamma^* + k\epsilon_n^* = 2.88(\sigma'_f/E)(2N_f)^{-\alpha} + 3.2\epsilon'_f(2N_f)^{-\beta}, \quad (35)$$

where $k = 0.4$. The constants depend on the value of k as in the previous example.

The above relation proposed by Lohr & Ellison (1980) is similar to the theory proposed by Kandil *et al* (1982) which yields the relation

$$\Delta\gamma_p + S\varepsilon_p = F(N_f). \quad (36)$$

Thus both the theories with suitable values for the constants k and S should fit the data equally well.

2.3f Other strain based approaches: Walker (1970) proposed an effective strain, ε_{eff} parameter for biaxial fatigue loading as

$$\varepsilon_{\text{eff}} = (\Delta\gamma_0)^m (\varepsilon_T)^{1-m}, \quad (37)$$

where

$$\Delta\gamma_0 = 2/3 [\Delta\gamma_x^2 + (\Delta\gamma_x - \Delta\gamma_y)^2 + \Delta\gamma_y^2]^{1/2}, \quad (38)$$

$$\varepsilon_T = \langle \varepsilon_x \rangle + \langle \varepsilon_y \rangle + \langle \varepsilon_z \rangle. \quad (39)$$

$\Delta\gamma_i$ is the principal shearing strain ranges, ε_i is the principal normal strains that give the maximum value of ε_T , $\langle \varepsilon \rangle = \varepsilon$, if $\varepsilon > 0$, are zero otherwise.

The $\Delta\gamma_0$ parameter, referred to as the octahedral shearing strain range, is considered the main parameter coupled with the total strain ε_T .

A total strain criterion in the form

$$\varepsilon_T = (2/3)^{1/2} [\varepsilon_1^2 + \varepsilon_2^2 + \varepsilon_3^2]_{\text{max}}^{1/2} \quad (40)$$

was proposed by Zamrik (1972).

ε_i are the three instantaneous principal strains. ε_T is the maximum value of the right hand side. This approach is similar to von Mises criterion. The total strain ε_T was related to N_f in the form,

$$\varepsilon_T = A(N_f)^{-\alpha}, \quad (41)$$

and was found to give good correlation for both in-phase and out-of-phase combined torsion and push-pull straining of tubular specimens.

2.3g Energy based approach: Plastic work approach uses uniaxial stress-strain data to compute the hysteresis energy per cycle, resulting from bending and torsional straining, in-phase and out-of-phase. The plastic work per cycle is defined for this loading as

$$W_p = \int \sigma_x d\varepsilon_x^p + \tau_{xy} d\gamma_{xy}^p, \quad (42)$$

where σ_x and τ_{xy} are the axial and torsional components of the stress tensor. $d\varepsilon_x^p$ and $d\gamma_{xy}^p$ are the corresponding infinitesimal load increment. It is assumed that

$$W_p = AN_f^{-\alpha} \quad (43)$$

where the constants A and α are fitted from uniaxial strain life data.

3. Data analysis and discussion

Figure 8(a-e) show the correlation of experimental data with prediction based on (a) principal strain theory, (b) von Mises criterion, (c) maximum shear strain theory, (d)

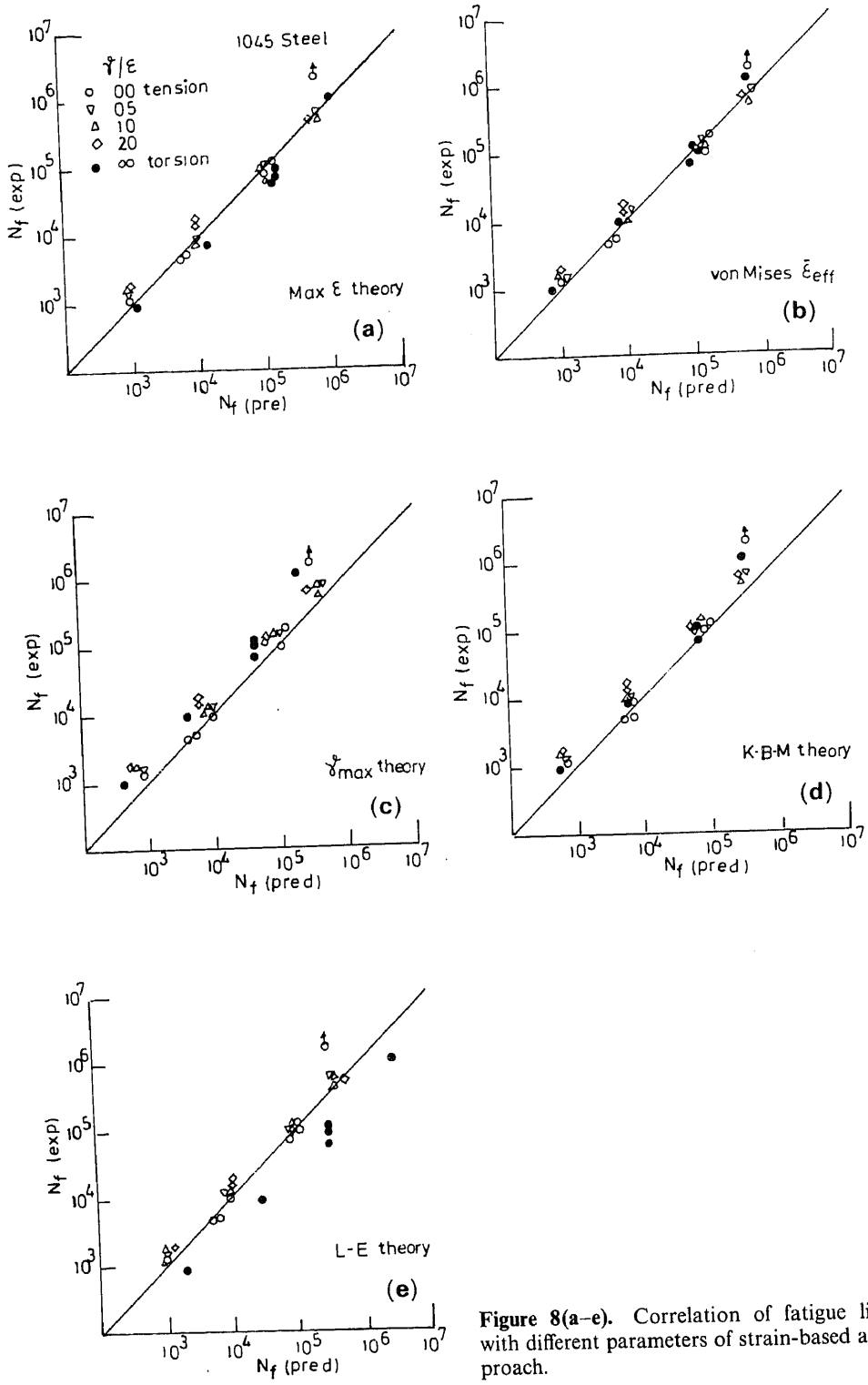


Figure 8(a-e). Correlation of fatigue life with different parameters of strain-based approach.

Kandil, Brown and Miller theory and (e) Lohr and Ellison approach. The material tested was 1045 steel and results are for smooth thin walled tubular specimen (Fash *et al* 1985). It can be seen that the maximum strain theory and von Mises criterion give good correlation with evenly distributed scatter. In the case of maximum shear strain approach, the prediction is conservative at low as well as high cycles regions. So is the case with the Kandil–Brown–Miller approach also. In the case of the Lohr–Ellison approach the scatter is wide and the torsion results consistently fall out with the prediction which is always non-conservative. Fash *et al* (1985) also found that the aforementioned approaches offer considerably less correlation for notched shaft specimens.

A comparison of the degree of correlation found using a number of failure criterion as applied to automobile steel is shown in figure 9 (McDiarmid 1993). The octahedral shear strain approach as also the approaches due to Brown & Miller (1973) and McDiarmid (1993) modified shear stress approach appear to give fairly good correlation within a factor of ± 2 . Other approaches give large scatter. The octahedral shear strain criterion has the disadvantage of not being able to account for the effect of mean stress or strain. The other two criteria can account for mean stress/strain within their normal stress/strain terms. Thus the modified shear stress based on the critical plane criterion of failure, i.e.,

$$\tau_{\max}^* + k\sigma_{n\max}^* = \text{constant} \quad (44)$$

could reasonably be accurate in correlating both the in-phase and 90° out-of-phase tension–torsion SAE experimental data.

SAE experimental programme (Tipton 1989) has shown that von Mises criterion provided reasonably good estimates of finite life under in-phase loading. In the case of out-of-phase loading non-conservative estimates are obtained. It was also observed by Tipton that all the methods gave somewhat more conservative predictions for pure torsion or loadings with higher ratios of torsion to bending. Further, all prediction methods were conservative at long life and somewhat non-conservative at lower cycles, particularly for bending or loadings with larger ratios of bending to torsion.

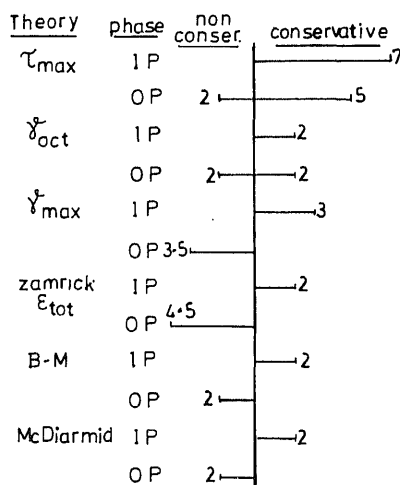


Figure 9. Degree of correlation (scatter width) based on different parametric approaches.

Multiaxial fatigue behaviour of notched specimens will depend on stress concentration and stress gradient, as in uniaxial fatigue, and also on the specific type of notch geometry and its influence on cracking behaviour.

Correlations made by conventional strain based methods (Tresca and von Mises) for in-phase tests are fairly sensitive to the Poisson's ratio assumed (i.e., the degree of plasticity). The use of a variable Poisson's ratio with the von Mises approach eliminates this sensitivity. However, the use of a variable Poisson's ratio is invalid for out-of-phase loading.

The ASME Boiler and Pressure Vessel Elevated Temperature Code Sec III uses the von Mises correlation for non-proportional loading with Poisson's ratio as 0.5 (the fully plastic value). However, predictions made by this approach are generally worse (more non-conservative) than predictions made by the same procedure with Poisson's ratio = 0.29 (the fully elastic value). All out-of-phase predictions using this approach are non-conservative, regardless of Poisson's ratio.

The Lohr-Ellison method makes life predictions similar to those of the Brown and Miller approach for bending dominated loading. However, for tests where torsional loading dominates, predictions are nonconservative. The application of this approach to out-of-phase loading is not clearly possible since cracks which are deemed harmless by this approach, could grow detrimentally due to rotating principal stresses.

In the case of out-of-phase biaxial fatigue, constant amplitude stresses of different frequencies produce non-constant amplitude shear stress variations (Miller *et al* 1967). For these conditions the normal stress acting on the maximum shear stress plane is also of non-constant amplitude. The analysis of McDiarmid (1985) concludes that the maximum shear stress criterion using damaging shear stress amplitude appears to be a reasonable basis for fatigue life evaluation under out-of-phase biaxial stresses of different frequencies.

In general out-of-phase stresses could be more damaging than in-phase stresses of the same magnitude, though opposite trends are also observed in certain materials. The total strain approach due to Zamrik (1972) can be applied to out-of-phase loading by maximizing the function ε_T . However, the total strain expression reduces to von Mises criterion when the Poisson's ratio is 0.5. Kanazawa *et al* (1977, 1979) showed that out-of-phase loading in 1% Cr-Mo-V steel is more damaging than in-phase loading in the low cycle regime. Further, they observed that both the Tresca and von Mises type criteria are not conservative for out-of-phase multiaxial loading. They proposed that the shear strain range and the normal strain amplitude on the maximum shear plane should govern out-of-phase multiaxial fatigue, but offered no functional relationship.

When ε_1 , ε_2 , and ε_3 rotate during every cycle in out-of-phase loading, a number of cracking systems will start operating and endurance will be reduced because of the large value of ε_n that can be obtained. However, in some cases, the life time may be extended due to crack growth on one plane being obstructed by other cracks on other planes. Taking a simple bi-axial loading, $\sigma_1 = \sigma_2$ and $\sigma_3 = \text{zero}$, three distinct cracking systems can operate in the material. Depending on the phase angle ϕ one or more cracks will grow thereby either increasing or decreasing the endurance life. Figure 10 shows the effect of phase angle ϕ on the endurance cycles in such a simple system of loading (Miller & Brown 1984).

The plastic work life predictions are comparable to those made by the von Mises and the Brown and Miller approaches for in-phase and are reasonably good for

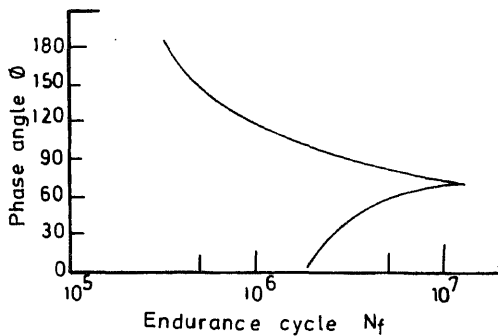


Figure 10. Effect of phase angle on the endurance life.

out-of-phase loadings. However, the main difficulty with this approach is that when plastic strains are small, slight variations in their computation can lead to large differences in predicted life. Further, numerical difficulties may be encountered in incremental plasticity routines specially in 90° out-of-phase loading.

Several new equivalent strain criteria have been proposed in recent times, as other criteria like Tresca, octahedral shear strain etc., do not give good predictions, even for in-phase loading. The inadequacy of the octahedral shear strain approach is clearly shown in the case of EN 15 R steel for in-phase tension torsion test results as shown in figure 11a. If $R(\varepsilon)$ is the ratio of γ_{oct} to $\gamma_{\text{oct torsion}}$, i.e.,

$$R(\varepsilon) = \gamma_{\text{oct}} / \gamma_{\text{oct torsion}} \quad (45)$$

it should be equal to unity if octahedral shear strain criterion is valid. However, the values of $R(\varepsilon_{pp})$ (push-pull loading) deviate significantly from unity indicating the inadequacy of the γ_{oct} criterion.

Realising the above inadequacy of von Mises criterion, Troshchenko *et al* (1993) proposed a modified octahedral shear strain approach. The octahedral shear stress component γ_{oct^*} is taken in the form,

$$\gamma_{\text{oct}^*} = 0.816 \left[(4/3)(1 + \nu^*)^2 \varepsilon_x^2 + \gamma_{z\theta}^2 \right]^{1/2}, \quad (46)$$

for a material subjected to axial and torsional loading.

ν^* is the Poisson's ratio corresponding to the achieved level of strains. The modified $\delta_{\text{oct(modified)}}$ is a function of state of strain and N_f . Thus

$$\gamma_{\text{oct(modified)}} = 4\psi(\varepsilon, N_f) \gamma_{\text{oct}^*} \quad (47)$$

The function $\psi(\varepsilon, N_f)$ can be evaluated for different phase angles. The correlation between the modified octahedral shear strain and the fatigue life is shown in figure 11b for En 15 R steel. The agreement appears to be good for both in-phase and out-of-phase loading, though separate endurance curves for reversed tension-compression and for torsion are required for the computation. The approach which takes into account the non-proportionality of the deformation process and the dependence of the equivalent strain parameter on life time, is somewhat complicated and involves detailed calculation.

Sreeramesh & Bonacuse (1993) have analysed the behaviour of Haynes 188 alloy in in-phase and out-of-phase axial-torsional fatigue at 760°C . The correlation based on the von

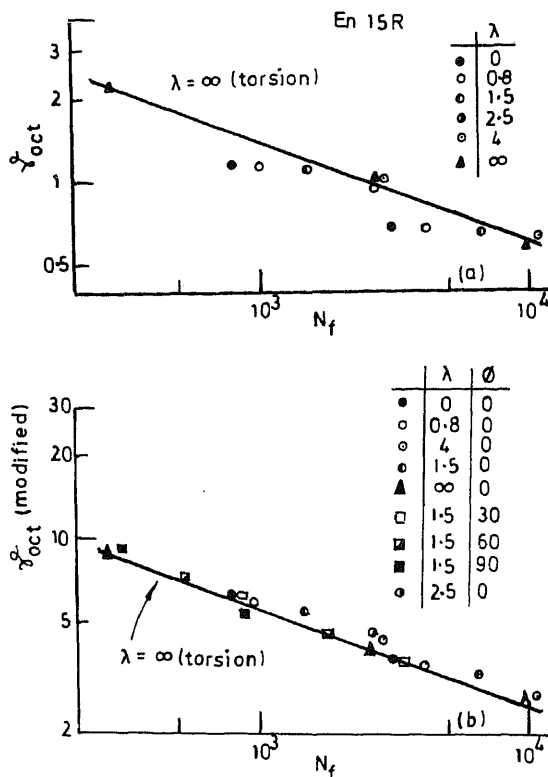


Figure 11. (a) Relation between octahedral shear strain and fatigue life for different phase angles. (b) Correlation of fatigue life with the modified octahedral shear.

Mises criterion, Fatemi-Socie-Kurath (F-S-K) (1988) and Smith-Watson-Topper (S-W-T) (1970) approaches are shown in figures 12a, b and c respectively.

The von Mises equivalent strain range $\Delta \varepsilon_{eq}$ is given by

$$\Delta \varepsilon_{eq} = \{ [\Delta \varepsilon_x - \Delta \varepsilon_y]^2 + (\Delta \varepsilon_y - \Delta \varepsilon_z)^2 + (\Delta \varepsilon_z - \Delta \varepsilon_x)^2 \}^{1/2} + (3/2) [\Delta \gamma_{xy}^2 + \Delta \gamma_{yz}^2 + \Delta \gamma_{zx}^2]^{1/2} / [2^{1/2} (1 + v_{eff})],$$

with

$$v_{eff} = [(\Delta \varepsilon_e v_e + \Delta \varepsilon_p v_p) / \Delta \varepsilon_t]. \quad (48)$$

The von Mises equivalent strain range for in-phase tests has been computed with the maximum axial strain as the reference because in an in-phase test the axial and engineering shear strains reach their respective maxima simultaneously. However, in an out-of-phase test the axial and the engineering shear strains reach their respective maxima at separate points in a cycle. Therefore for each out-of-phase axial torsion test the equivalent strain range is computed twice: once with the maximum axial strain as the reference and a second time with the maximum shear strain as the reference. The larger of the two values is used for fatigue life prediction.

The F-S-K parameter is given as

$$\gamma_{max} [1 + k(\sigma_n^{max} / \sigma_{yield})] = F(N_f) \quad (49)$$

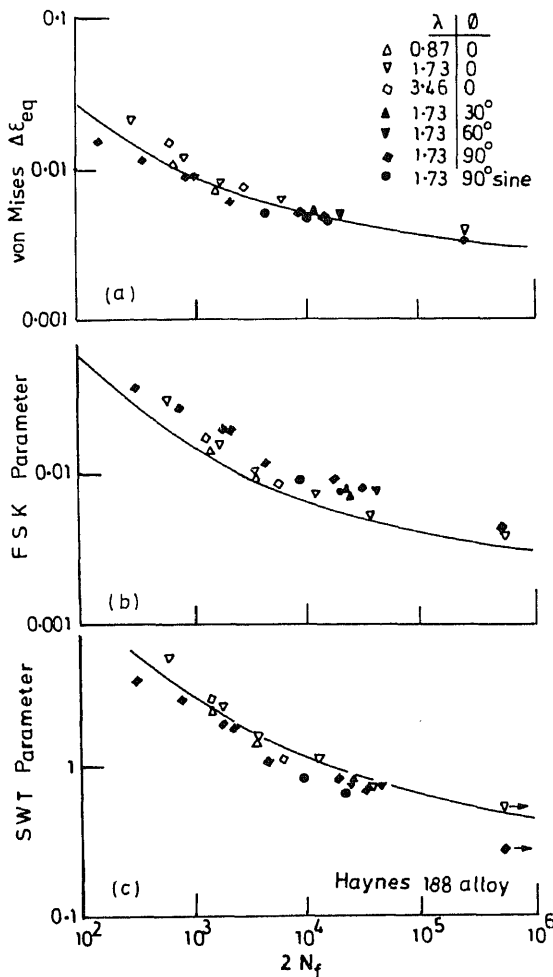


Figure 12(a-c). Correlation of elevated temperature fatigue life of Haynes 188 alloy with different parameters.

The F-S-K model has been successfully used to predict room temperature in- and out-of-phase axial torsional fatigue lives for materials that exhibit a shear mode of failure.

The S-W-T parameter is given by

$$\Delta\epsilon_1 \sigma_{1\max} = \sigma'_f \epsilon'_f (2N_f)^{-\beta} + (\sigma'_f/E)(2N_f)^{-\alpha}. \quad (50)$$

In the S-W-T model the magnitude and the plane of the maximum principal strain amplitude $\Delta\epsilon_1$ are determined first for a given cyclic of axial torsional loading. Then $\Delta\epsilon_1$ is multiplied by the maximum normal stress σ_1 that occurs on that plane. The constants in (50) are obtained from uniaxial fatigue properties. The S-W-T parameter is successful in predicting the room temperature fatigue life under in- and out-of-phase axial torsional loading specially in materials where cracks initiate and propagate perpendicular to the maximum principal strain direction.

The description of the results by von Mises criterion appears to be the best among the three approaches considered. The F-S-K parameter is very conservative and

under-predicts, whereas the scatter in the S-W-T approach is large and the prediction is somewhat non-conservative upto a factor of 4.

In high temperature multiaxial fatigue, damage accumulation is accelerated by the presence of mean component of stress and strain. The effect of time-dependent creep should also be taken into account in such cases. Further, ratchetting phenomenon will take place which will increase the strain accumulation. Hence the analysis becomes more complicated compared to ambient temperature multiaxial fatigue.

4. Concluding remarks

Important criteria and parameters for multiaxial fatigue are reviewed in this presentation. The Tresca and von Mises criteria appear to be inadequate and hence approaches which take into account both shear stress/strain and normal stress/strain acting on critical planes as the controlling parameters have been developed. However, they are also not able to predict the fatigue life under different conditions of loading. Many times the predictions are either conservative or non-conservative and the scatter is more than by a ± 2 factor.

The stress-based approaches can be applied to high cycle fatigue where gross yielding is not encountered. In low cycle fatigue, strain-based criteria will be better suited. Energy-based approach shows promise in predicting the life. However, energy is a scalar quantity and fatigue crack growth is controlled by stress/strain on certain critical planes which is a vector quantity. Further accurate computing of the plastic work where the plastic strain range is small will be difficult and will lead to erroneous results.

The stress-strain path in multiaxial loading condition is more important in the fatigue failure process (Wu & Yang 1987) and hence the deformation mode under multiaxial loading must also be considered for crack nucleation and its subsequent growth.

Thus the prediction methodology of life in multiaxial fatigue is rather very much involved and as their development stands to-day the approaches made are not complete in all respects.

List of symbols

A, B, C	constants;
E	Young's modulus;
F	function;
K	ratio shear stress/normal stress;
N	number of cycles to failure;
ν	Poisson's ratio;
α, β	exponents;
γ	shear strain;
Δ	range;
$\Delta\sigma$	stress range = $2\sigma_a$;
$\varepsilon_1, \varepsilon_2, \varepsilon_3$	principal strains;
λ	biaxial strain ratio, γ/ε ;
τ	stress;

$\rho_1, \sigma_2, \sigma_3$	principal stresses;
σ_n	normal stress;
σ_{eq}	equivalent stress;
σ_f	fatigue strength coefficient;
σ_m	mean stress;
σ_a	alternating component of the stress;
τ	shear stress;
ϕ	phase angle.

Suffixes

1, 2, 3	principal directions.
---------	-----------------------

References

- Brown M W, Miller K J 1973 A theory for fatigue failure under multiaxial stress strain condition. *Proc. Inst. Eng. London* 187: 745–755
- Brown M W, Miller K J (eds) 1989 *Biaxial and multiaxial fatigue*, EFG-3 (London: Mechanical Engineering Publications)
- Fash J W, Socie D F, McDowell 1985 Fatigue life estimates for a simple notched component under biaxial loading. *ASTM STP 853*: 497–513
- Fatemi A, Kurath P 1988 Multiaxial fatigue life predictions under the influence of mean stresses. *J. Eng. Mater. Technol.* 110: 380–388
- Fatemi A, Socie D F 1988 A critical plane approach to multiaxial fatigue damage including out-of-phase loading. *Fatigue Fracture Eng. Mater. Struct.* 11: 149–165
- Fatemi A, Stephens R I 1989 Biaxial fatigue of 1045 steel under in-phase and 90° out-of-phase loading conditions. *Multiaxial fatigue: Analysis and experiments*. AE-14 (eds) G E Leese, D Socie (Warrendale, PA: Soc. Automotive Eng.) pp. 77–92
- Findley W N 1957 Fatigue of metals under combined stresses. *Trans. Am. Soc. Mech. Eng.* 79: 1337–1348
- Findley W N 1959 A theory for the effect of mean stress on fatigue of metals under combined torsion and axial load or bending. *J. Eng. Ind.*: 301–306
- Garud Y S 1981 Multiaxial fatigue – A survey of the state of the art. *J. Test Eval.* 9: 165–178
- Haverd D G, Topper T H 1971 A criterion for biaxial fatigue of mild steel at low endurance. *Proc. First International Conference on Structural Mechanics in Reactor Technology*, pp. 413–432
- Jayaraman N, Ditmars M M 1989 Torsional and biaxial (tension–torsion) fatigue damage mechanisms in waspalloy at room temperature. *Int. J. Fatigue*, 11: 309–318
- Kakuno H, Kawada Y 1979 A new criterion of fatigue strength of a round bar subjected to combined static and repeated bending and torsion. *Fatigue Eng. Mater. Struct.* 2: 229–236
- Kanazawa K, Miller K, Brown M W 1977 Low cycle fatigue under out-of-phase loading conditions. *J. Eng. Mater. Technol.* 99: 222–228
- Kanazawa K, Miller K J, Brown M W 1979 Cyclic deformation of 1% Cr–Mo–V steel under out-of-phase loads. *Fatigue Eng. Mater. Struct.* 2: 217–229
- Kandil F A, Brown M W, Miller K J 1982 *Biaxial low cycle fatigue of 316 stainless steel at elevated temperature*. Book 280 (London: The Metal Society) pp. 203–210
- Kussmaul K, McDiarmid D L, Socie D F (eds) *Fatigue under biaxial and multiaxial loading*. ESIS-10 (London: Mechanical Engineering Publications)
- Lohr R D, Ellison E G 1980 A simple theory for low cycle multiaxial fatigue. *Fatigue Eng. Mater. Struct.* 3: 1–17
- McDiarmid D L 1985 Fatigue under out-of-phase biaxial stresses of different frequencies. *ASTM STP 853*: 606–621
- McDiarmid D L 1987 Fatigue under out-of-phase bending and torsion, *Fatigue Fracture Eng. Mater. Struct.* 9(6): 457–475

- McDiarmid D L 1991 A general criterion for high cycle multiaxial fatigue failure. *Fatigue Fracture Eng. Mater. Struct.* 14: 429–453
- McDiarmid D L 1993 Multiaxial fatigue life prediction using a shear stress based critical plane failure criterion in fatigue design. ESIS-16 (London: Mechanical Engineering Publications) pp. 213–220
- Miller W R, Ohji K, Martin J 1967 Rotating principal stress axes in high cycle fatigue. *ASME J. Basic Eng.* 89: 76–80
- Miller K J, Brown M W 1984 Multiaxial fatigue – A brief review. *Fracture 84, Proc. of the 6th International Conference on Fracture*, New Delhi (New York: Pergamon) pp. 31–56
- Miller K J, Brown M W (eds) 1985 *Multiaxial fatigue*. ASTM STP 853
- Nitta A, Ogata T, Kuwabara K 1989 Fracture mechanisms and life assessment under high strain bi-axial loading of type 304 stainless steel. *Fatigue Fracture Eng. Mater. Struct.* 12: 77–92
- Sines G 1955 Failure of materials under combined repeated stresses with superimposed static stresses. NACA TN 3495 (Washington DC, USA)
- Smith K N, Watson P, Topper T H 1970 A stress-strain function for the fatigue of metals. *J. Mater.* 5: 767–778
- Socie D F 1989 Multiaxial fatigue damage models. *J. Eng. Mater. Technol.* 109: 293–298
- Socie D F, Shield T W 1984 Mean stress effects in biaxial fatigue of inconel 718. *J. Eng. Mater. Technol.* 106: 227–232
- Sreeramesh K, Bonacuse P J 1993 In-phase and out-of-phase axial-torsional fatigue behaviour of Haynes 188 superalloy at 760°C. In *Advances in multiaxial fatigue*. (eds) D L McDowell, R Ellis, ASTM STP 1191, pp. 133–150
- Tipton S M 1989 Multiaxial fatigue life prediction of the SAE specimen using strain based approaches. *Multiaxial fatigue – Analysis and experiments*, AE-14 (Warrendale, PA: Soc. Automotive Eng.) pp. 67–80
- Troshchenko A V, Miller K J, Fernando U S 1993 A simple criterion for multiaxial fatigue life prediction under in-phase and out-of-phase tension and torsion. In *Fatigue design* (eds) J Solin *et al*, ESIS-16 (London: Mechanical Engineering Publications) pp. 231–240
- Walker K 1970 An effective strain concept for crack propagation and fatigue life with specific application to biaxial stress fatigue. AFFDL-TR-70-144, Ario Force Dynamics Lab. Wright-Patterson Airforce Base, Ohio, pp. 225–233
- Wu H C, Yang C C 1987 On the influence of strain path in multiaxial fatigue failure. *J. Eng. Mater. Technol.* 109: 107–113
- Zamrik S Y 1972 An investigation of strain cycling behaviour of 7075 T6 aluminium under combined state of strain. NASA CR-72843 Washington, DC

High temperature low cycle fatigue

P RODRIGUEZ and S L MANNAN

Indira Gandhi Centre for Atomic Research, Kalpakkam 603 102, India

Abstract. Fatigue at high temperature is a complex phenomenon as it is influenced by a number of time-dependent processes which become important at elevated temperatures. These processes include creep, oxidation, phase instabilities and dynamic strain ageing (DSA), acting either independently or synergistically influence fatigue behaviour, often lowering the fatigue life. Current design approaches employ linear summation of fatigue and creep damage with suitable factors on permissible damage to take care of uncertainties in interaction between cyclic and time-dependent processes. It is, therefore, important to develop a deeper understanding of the processes that occur during high temperature fatigue so that realistic life predictions could be made.

Results on the high temperature fatigue behaviour of austenitic stainless steels, ferritic steels and nickel base alloys are presented here. The important mechanisms of interaction of high temperature time-dependent processes with fatigue under various conditions are discussed in detail. Emphasis is placed on cyclic stress response, fatigue life, deformation substructure and fracture behaviour. This is followed by a review of important life prediction techniques under combined creep-fatigue loading conditions. Life prediction techniques considered here include linear damage summation, strain range partitioning, ductility exhaustion approach, frequency modified and frequency separation methods, techniques based on hysteresis energy and damage rate models, and methods based on crack-cavitation interaction models.

Keywords. Low cycle fatigue; creep-fatigue interaction; environmental effects; dynamic strain ageing; life prediction techniques.

1. Introduction

Low cycle fatigue (LCF) is an important design consideration in structural integrity analysis of components operating at high temperatures. Repeated thermal stresses are generated as a result of temperature gradients which occur on heating and cooling during start-up, shut-down and thermal transient conditions. LCF resulting from start-ups and shut-downs occurs under essentially strain-controlled conditions, since the surface region is constrained by the bulk of the component. Figure 1 shows schematically the stress and strain cycles to which a boiler or a steam turbine component may be

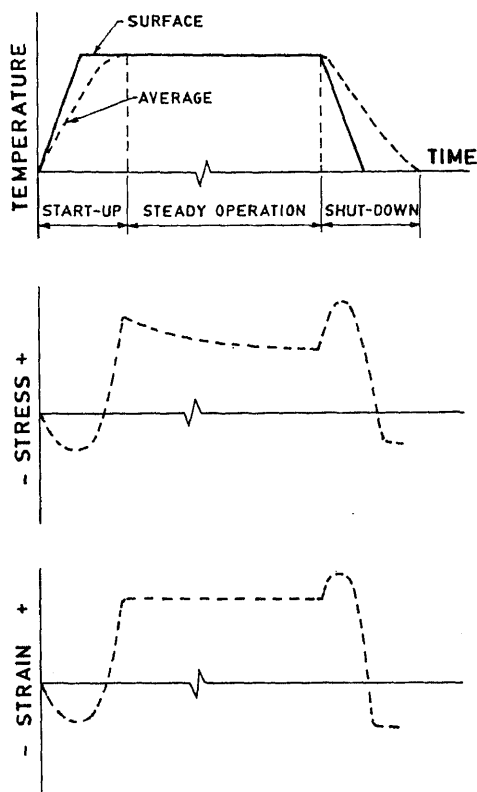


Figure 1. Schematic diagram illustrating thermal stresses/strains to which boiler or steam turbine component may be subjected.

subjected to as a result of rapid start, steady-state operation or a sudden shut-down. Typical temperature-time transients experienced by the surface of thick components in a fast reactor as a result of reactor trip (down shock) or secondary circuit failure (up shock) and the resulting stress-strain cycles are shown in figure 2.

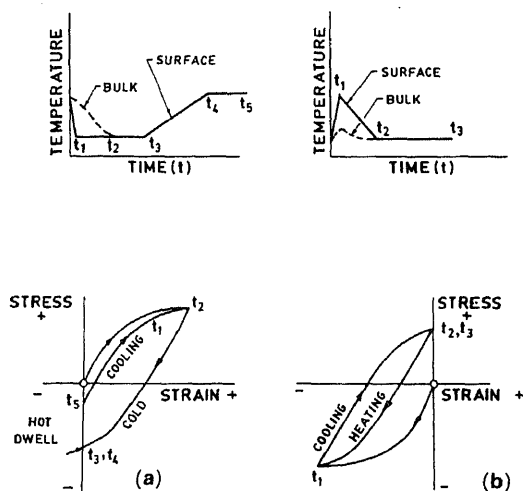


Figure 2. Surface hysteresis loops following reactor trip transient (a), heating transient (b), after secondary circuit failure in a fast breeder reactor.

To represent the component behaviour in a laboratory test, the thermal strains are replaced by mechanical strains, introduced and controlled under isothermal conditions, figure 3. The slow start-up/shut-down cycle is replaced by a symmetrical and continuous fatigue cycle of equal strain rates in tension and compression with a hold period at a constant peak strain to simulate the on-load period i.e. creep-fatigue interaction (figures 3b-d). Slow-fast and fast-slow strain-time wave forms represent another category used to evaluate creep-fatigue interaction effects (figures 3e-f). In slow-fast cycle, tension-going strain rate is less than that in compression cycle, while in fast-slow cycle, compression-going strain rate is less than that in tension. Tension hold alone, compression hold alone, slow-fast and fast-slow wave forms are considered unbalanced cycles.

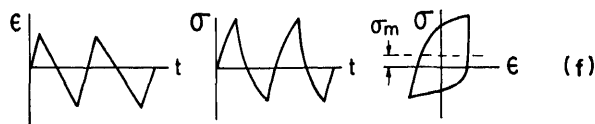
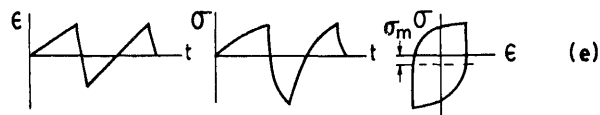
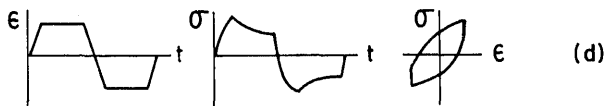
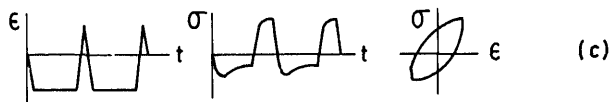
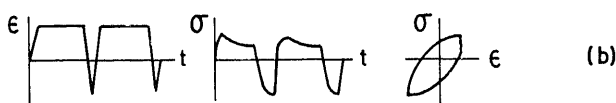
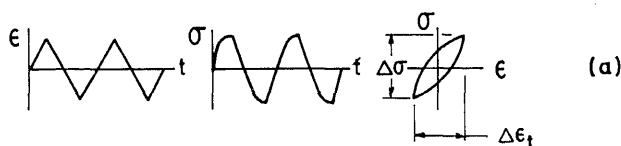


Figure 3. Typical waveforms employed in LCF testing. $\Delta\sigma$ = total stress range, $\Delta\epsilon_t$ = total strain range and σ_m = mean stress. (a) Continuous strain cycling; (b) tension strain hold; (c) compression strain hold; (d) tension and compression strain hold; (e) slow-fast cycling; (f) fast-slow cycling.

LCF behaviour of materials at high temperatures and low test frequencies is influenced by the interaction of time-dependent processes like creep, oxidation, dynamic strain ageing (DSA) and metallurgical instabilities with cyclic deformation. In general, fatigue life decreases with increasing temperature and decreasing frequency. A few exceptions, however, have been reported as in the case of type 304 Stainless Steel (SS) (Bhanu Sankara Rao 1989), type 316 SS (Kanazawa & Yoshida 1975) and 12% Cr ferritic steel (Kanazawa 1978). In the case of type 304 SS (Bhanu Sankara Rao 1989), the observed increase in fatigue life with temperature correlated with the precipitation of $M_{23}C_6$ carbides during testing. Carbide precipitation along grain boundaries inhibits grain boundary sliding, thereby preventing grain boundary crack formation. Since LCF life at elevated temperature is governed by intergranular crack initiation and propagation, reduced tendency for grain boundary cracking due to precipitation leads to enhanced life with increasing temperature (Bhanu Sankara Rao 1989).

Elevated temperature fatigue tests conducted in air generally yield lower life than those carried out in vacuum, suggesting the deleterious effects of oxidation on fatigue properties (Coffin 1972a; Solomon & Coffin 1973; Cook & Skelton 1979). High temperature low cycle fatigue studies in ferritic steels such as 2.25 Cr–1 Mo (Sandhya *et al* 1989) and 9 Cr–1 Mo steels (Choudhary *et al* 1991a) indicate that oxidation enhances intergranular damage and consequently causes reduction in life. The effect of oxidation was more dominant in tests conducted at low strain amplitudes. Fatigue-oxidation interaction has also been observed to degrade the life in austenitic stainless steels (Bhanu Sankara Rao *et al* 1986a). Creep-fatigue interaction behaviour of type 304 SS has been studied employing hold time tests (Bhanu Sankara Rao 1989). The results of this study indicate that tensile hold caused more damage to life than either compression hold or symmetrical (tension + compression) hold. Under tensile hold conditions, the accumulation of intergranular creep damage in the form of cavities enhanced the tendency for intergranular mode of fatigue crack propagation leading to shorter fatigue life. Degradation in life has been observed (Hirakawa *et al* 1978; Yamaguchi *et al* 1978) also under test conditions where creep and oxidation effects are expected to be minimal. It has been shown that another time-dependent process, namely, dynamic strain ageing interacts with fatigue and leads to life reduction.

In this paper, the role of environment, DSA and creep in determining the LCF behaviour will be first discussed. This is followed by a discussion on important techniques for life prediction under conditions of time-dependent fatigue. Empirical techniques as well as those with a mechanistic basis would be discussed.

2. Environmental effects on fatigue behaviour

One of the major factors responsible for the degradation of fatigue properties at elevated temperatures is the interaction of environment (oxygen or air) with fatigue process. In general, it is observed that materials exhibit superior fatigue properties in vacuum or in an inert medium compared to those observed in air (Coffin 1963, 1972, 1973, 1979; Asada & Mitsuhashi 1980; Bressers & Roth 1983; Marshall 1983; Jianting *et al* 1984). The influence of environment becomes more pronounced with lowering of frequency (strain rate), decreasing strain amplitude, and imposition of hold during fatigue testing. Depending on test frequency, three regimes of interaction of fatigue with environment could be identified (figure 4): (a) frequency independent regime (where

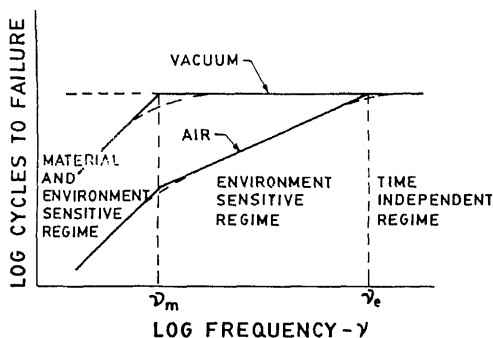


Figure 4. Effect of frequency on fatigue life at elevated temperatures (Coffin 1977).

time-dependent deformation mechanisms are not significant), (b) environment sensitive regime, and (c) deformation mode and environment interaction regime (Coffin 1977). At very high frequencies ($\nu > \nu_e$), fatigue crack is open only for a short while, and therefore enough time is not available for environmental interaction. Crack growth in this regime is not dependent on environment. At lower frequencies ($\nu_e > \nu > \nu_m$), environment influences the crack growth process and a change in the mode of crack growth from transgranular to intergranular takes place. At still lower frequencies ($\nu < \nu_m$), the fracture mode is entirely intergranular and for a specific plastic strain range, time to failure remains constant (independent of frequency) (Coffin 1977).

A few experimental results would be considered to illustrate the role of environment in determining fatigue life. The effect of frequency and strain range on LCF behaviour of type 304 SS has been extensively investigated at elevated temperatures in air using balanced cycles (Bhanu Sankara Rao 1989). Decreasing frequency was found to degrade fatigue resistance of type 304 SS (figure 5) (Bhanu Sankara Rao 1989; Bhanu Sankara Rao *et al* 1991). No creep damage in the form of grain boundary cavities and cracks was noticed. It was also observed that as the frequency was lowered, crack initiation changed from slip band induced transgranular to oxidation induced intergranular mode (figure 6). The role of oxidation in determining fatigue life has been clearly brought out in comparative tests in air and vacuum environments on A286, figure 7 (Coffin 1972b). Fatigue life has been found to decrease with decrease in frequency in air environment while life is independent of frequency in vacuum.

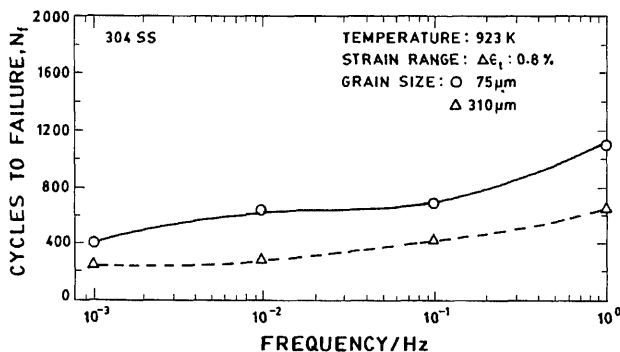


Figure 5. Influence of frequency on fatigue life as a function of grain size in 304 SS.

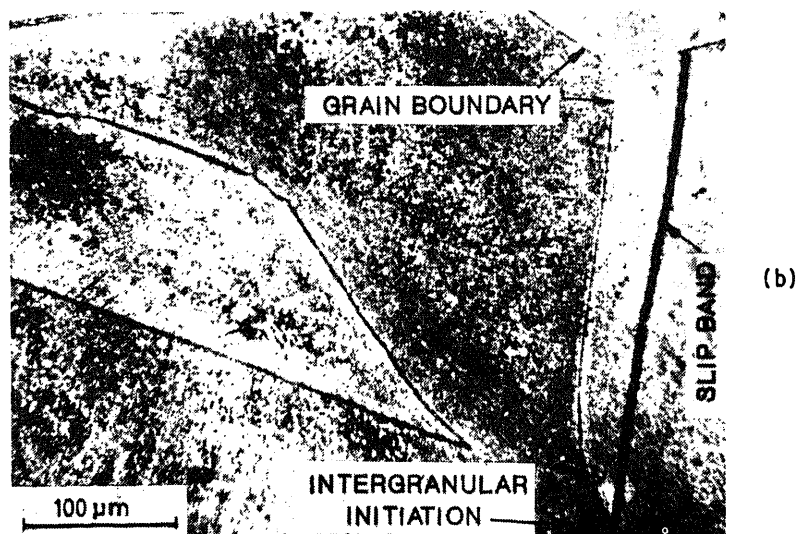
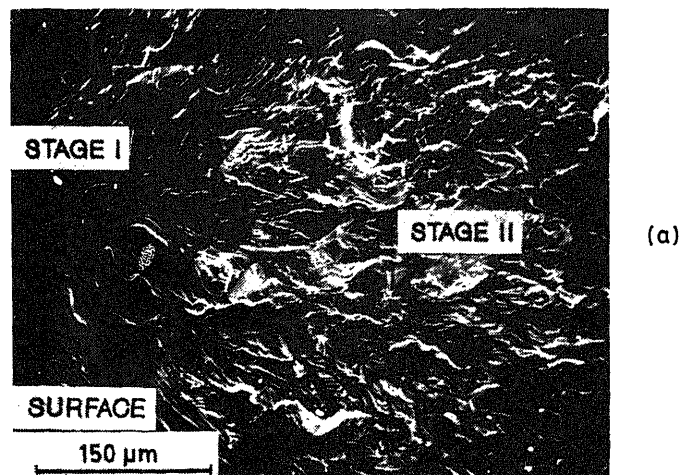


Figure 6. Crack initiation modes in type 304 SS LCF tested at 923 K. (a) Transgranular crack initiation ($\Delta\epsilon_f = 0.66\%$, $\nu = 1.0$ Hz) and (b) oxidation assisted transgranular crack initiation at $\nu = 0.001$ Hz.

Strain amplitude also has significant influence in determining environmental effects. During low strain amplitude fatigue tests, material is exposed for longer durations to air environment at high temperatures. This provides sufficient time for oxidation to affect the failure process. A two-slope behaviour observed in a 2.25Cr–1 Mo steel has been attributed to the enhanced oxidation effects at low strain amplitudes, figure 8 (Sandhya *et al* 1989).

Enhanced environmental interaction has also been reported in hold time tests. For 2.25Cr–1 Mo steel, compressive holds have been found to be more damaging than tensile holds (Teranishi & McEvily 1980; Challenger *et al* 1981). This has been

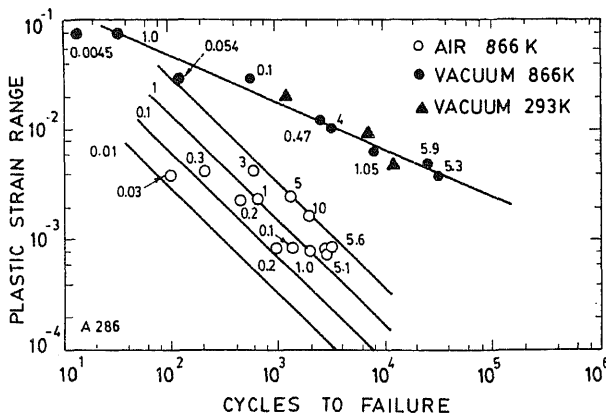


Figure 7. Plastic strain range vs fatigue life of A286 in air at 866 K and in vacuum at 293 K and 866 K. Numbers adjacent to test points indicate frequency in cycles per minute (Coffin 1972b).

attributed to the behaviour of the oxide formed during hold period (Teranishi & McEvily 1980). The oxide spalls from the specimen surface after a tension hold, leaving behind a relatively smooth surface. On the other hand, after a hold in compression, the oxide cracks, facilitating early crack nucleation in the underlying metal. This behaviour was later related to the tensile strain in the oxide by Challenger *et al* (1981). According to these authors, the loading waveform determines the tensile strain experienced by the oxide. Since the oxide formed during compression hold is subjected to a tensile strain equal to the total strain range of the test on a strain reversal, it is more likely to crack in a direction perpendicular to the applied stress. The vulnerability of superalloys to compressive dwell periods has also been interpreted in terms of environmental interaction on similar lines (Manson *et al* 1984). On the other hand, Sandhya *et al* (1989) have found tensile holds to be more damaging in normalized and tempered 2.25 Cr-1 Mo steel and have interpreted the results in terms of faster crack growth rates under tensile holds. Accelerated crack growth rates due to oxidation has been reported by various investigators (Smith *et al* 1969; Solomon & Coffin 1973;

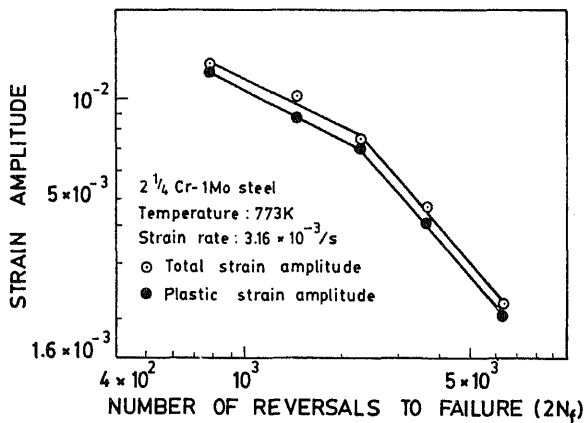


Figure 8. Coffin-Manson plots for 2.25 Cr-1 Mo steel at 773 K.

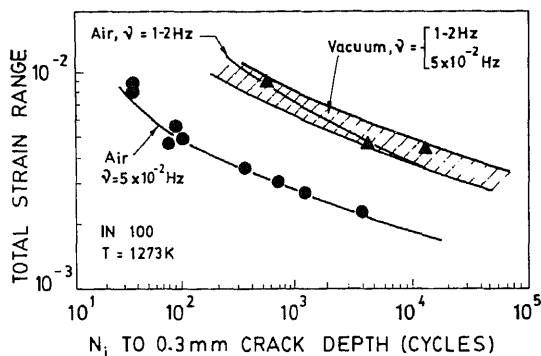


Figure 9. Oxidation induced frequency effect on the number of cycles spent in initiating a crack of 0.3 mm in IN 100 at 1273 K (Reger & Remy 1986).

Fransson *et al* 1974; James & Knecht 1975; Skelton 1978). Oxidation accelerates fatigue crack initiation, and generally leads to increased number density of micro-cracks, figure 9 (Bressers *et al* 1983; Reger & Remy 1986). The large reduction in number of cycles for crack initiation is often associated with a change in the mode of cracking from transgranular to intergranular. The transition in the mode of fatigue crack initiation in a gamma-prime strengthened PM Astroloy and in a carbide and solid solution strengthened alloy 800H are compared in figure 10 (Bressers 1985). PM Astroloy when tested in vacuum shows a transition from transgranular to intergranular mode of crack initiation at a temperature much higher compared to that in air, whereas for alloy 800H, the change in transition temperature was very small. The trans- to intergranular transition in the PM Astroloy has been attributed to environmental effects while in Alloy 800H, it has been shown to be creep controlled.

The effect of frequency on fatigue crack propagation rate has been studied by Solomon & Coffin (1973) for A286, at 866 K, and Scarlin (1977) on Nimonic 105 at 1023 K and IN738 LC at 1123 K. In the investigation on A286 (Solomon & Coffin 1973), it is found that, in air at very high frequencies crack propagation is due to frequency independent fatigue, with transgranular fracture (figure 11). However, as frequency decreases the environmental effects interact with the fatigue process thereby increasing crack growth rate. At still lower frequencies, the influence of other time-dependent processes such as creep becomes dominant resulting in intergranular

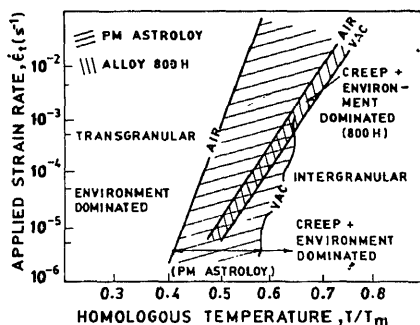


Figure 10. Transition in the mode of crack initiation of PM Astroloy and of Alloy 800H as a function of the applied strain rate and temperature in air and in vacuum (Bressers 1985).

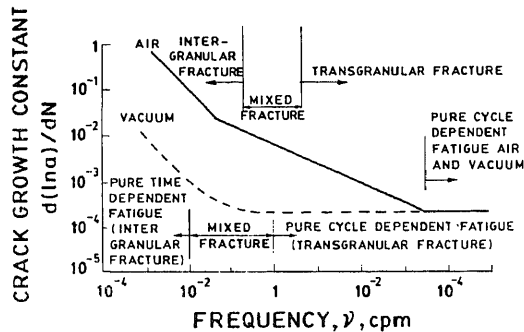


Figure 11. Effect of frequency and environment on low cycle fatigue crack propagation of A286 at 866 K (Solomon & Coffin 1973).

fracture. The dependence of crack growth on frequency sets in at a lower frequency in vacuum compared to air.

It must be pointed out that oxidation is not always detrimental to fatigue (Gell & Leverant 1973). Oxidation strengthening has been reported in Mar-M200 alloy and attributed to increased crack tip radius and blunting of the crack by oxidation. Further, corrosion products at the crack tip can cause closure during unloading which decreases the effective stress intensity range and thus retard cracking (Floreen & Raj 1985).

Damage from oxidation is viewed as a synergistic phenomenon when plastic deformation or fracture occurs at a free surface or at an exposed crack tip. Brittle protective oxide films formed are ruptured exposing fresh nascent material and chemical attack of the material then proceeds until newly formed protective films intervene. With fatigue, this process of straining, film rupture and attack occurs repeatedly, leading to localization of the cyclic strain and an abundance of reaction products (McMahon & Coffin 1970; Sidey & Coffin 1979). Various mechanisms have been suggested to account for the effect of environment on fatigue life (Cook & Skelton 1979; Duquette 1979; Ericsson 1979). At temperatures below and test frequencies above the range of intergranular cracking, the effect of oxidation on stage I cracking in planar slip alloys has been explained on the basis of slip step passivation mechanism reducing the degree of slip reversibility and thus enhancing crack nucleation at slip steps (Fujita 1958). Alternatively, cyclically generated slip bands may concentrate oxygen through strain-induced vacancy generation, thus accelerating transition from slip band to microcrack by preventing the rewelding of nascent cracks (Thompson *et al* 1955). It has also been suggested that crack nucleation is speeded up as a result of dislocation accumulation against surface oxide films, leading to cavity formation on the slip band (Shen *et al* 1966). The preferential oxidation of second phases which intersect the surface, such as carbides in nickel base alloys has also been invoked to rationalise fast crack initiation (Coffin 1973b; Reuchet & Remy 1983). In the intergranular failure regime, faster crack initiation is related to the existence of an easier path for chemical reaction. Inward diffusion of oxygen and its interaction with segregated elements or carbides present on the grain boundary can produce gaseous species, which may facilitate nucleation of cavities (Bricknell & Woodford 1981; Nich & Nix 1981; Dyson 1982; Taplin *et al* 1983). Oxygen could promote cavitation by lowering the surface energy and thereby decreasing the threshold stress for cavity nucleation (Yoo & Trinkaus 1983) or by enabling the reduction in the critical radius of cavity for growth (Taplin *et al* 1984).

3. Dynamic strain ageing

DSA arises due to the interactions between solute atoms and mobile dislocations during plastic deformation. Its characteristics in tensile deformation have been reviewed in detail by several investigators (Mannan 1981; Rodriguez 1984; Abdel-Azim Metwally 1986; Venkadesan 1991). Important manifestations of DSA in tensile deformation include serrations on stress-strain curves, peak/plateau in flow stress variation with temperature, negative strain rate sensitivity of flow stress, and increased work hardening rate and decrease in tensile ductility with increasing temperature or decreasing strain rate. Serrations occur on the stress-strain curve after the material has been deformed to a critical strain ϵ_c . The value of ϵ_c depends on test temperature, strain rate and material condition. The characteristics of different types of serrations and the experimental conditions that produce them have been discussed in detail by Rodriguez (1984). Various models have been proposed to explain the phenomenon of DSA and observed characteristics in tensile deformation (Cottrell 1953; Sleeswyk 1958; McCormick 1972; Mulford & Kocks 1979; Van den Beukel & Kocks 1982; Hayes & Hayes 1984; Kubin & Estrin 1990).

3.1 Effect of DSA on LCF

Even though DSA has been investigated in detail in tensile deformation, its role in influencing LCF has been examined to a limited extent (Conway 1968; Bressers & Verheghe 1981; Bhanu Sankara Rao 1989; Bhanu Sankara Rao *et al* 1990, 1991; Srinivasan *et al* 1991; Valsan *et al* 1994) and recently Mannan (1993) has reviewed this subject. The important manifestations of DSA in LCF include serrated flow in plastic portion of the stress-strain hysteresis loop (figure 12), a rapid strain hardening (figure 13), an increase in stress response with decreasing strain rate (negative strain rate sensitivity) or increasing temperature, and a minimum in the plastic strain component of the cycle at half life (Bhanu Sankara Rao *et al* 1990, 1991; Srinivasan *et al*

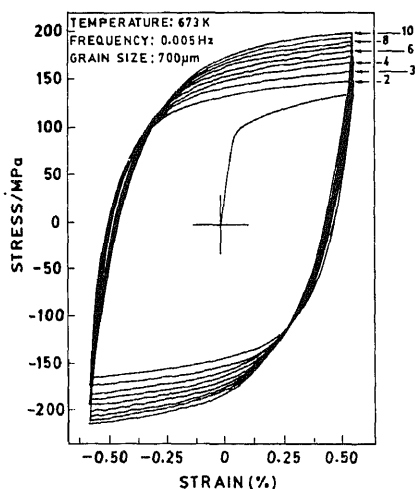


Figure 12. Stress-strain hysteresis loops exhibiting serrated flow in LCF test conducted at 673 K (304 SS; grain size: 700 μm ; strain range: 1-2%).

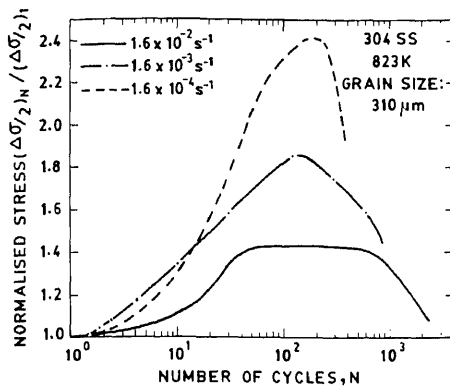


Figure 13. Normalized cyclic hardening curves illustrating the influence of strain rate at 823 K for type 304 SS (GS: 310 μm ; strain amplitude: $\pm 0.4\%$).

1991; Valsan *et al* 1994). Figure 13 shows the influence of strain rate on the normalized peak stress $((\Delta\sigma/2)/(\Delta\sigma/2)_1)$ for a type 304 SS at 823 K. When strain rate is decreased from 1.6×10^{-2} to $1.6 \times 10^{-4} \text{ s}^{-1}$ there is an increase in the cyclic stress response. Another example of the influence of DSA on cyclic stress response is shown in figure 14, which shows the results on Nimonic PE-16 alloy at 823 K over strain rates varying from $3 \times 10^{-5} \text{ s}^{-1}$ to $3 \times 10^{-2} \text{ s}^{-1}$ (Valsan *et al* 1994). The negative strain rate sensitivity of cyclic stress response is clearly seen in this figure.

A comparison of LCF and tensile deformation (Bhanu Sankara Rao *et al* 1990) indicates that serrated flow occurs over a wider temperature range in LCF than in tensile deformation. Onset of serrations in LCF occurs at a lower temperature compared to that in monotonic deformation. This is attributed to the enhanced diffusion of solute atoms with the aid of non-equilibrium vacancies generated during fatigue cycling. Reverse straining generates vacancies at a rate greater than unidirectional deformation (Johnson & Johnson 1965; Essman & Mughrabi 1979; Quesnel & Tsou 1983; Bhanu Sankara Rao *et al* 1986b).

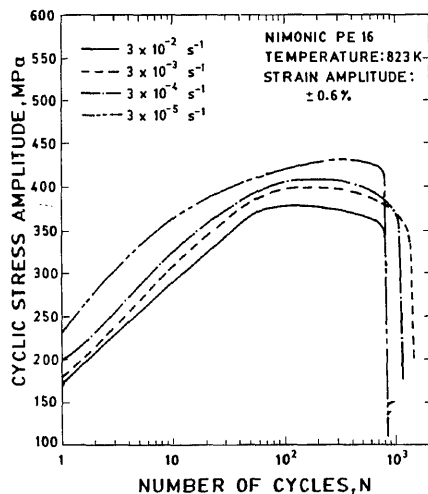
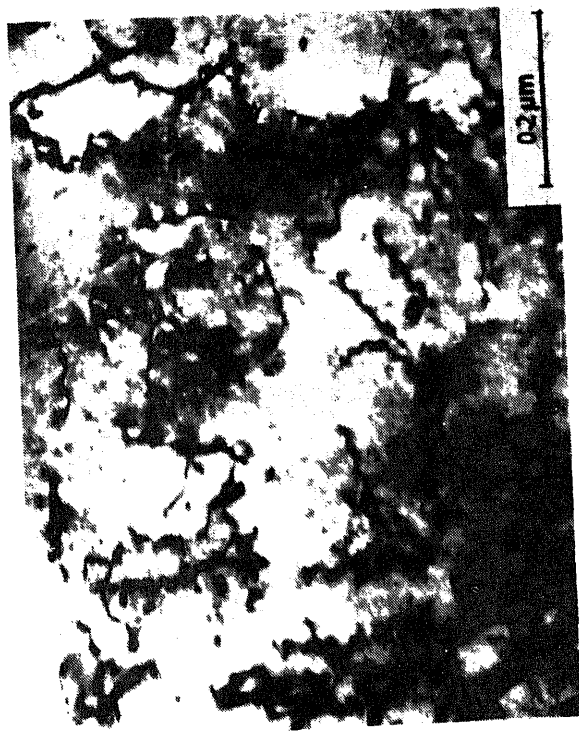


Figure 14. Cyclic stress response of Nimonic PE16 as a function of strain rate at 823 K.

The occurrence of DSA during cyclic deformation influences dislocation substructure. In type 310SS (Kanazawa *et al* 1988) the substructure changes from cells at temperatures below 473 K to a planar arrangement at temperatures between 473–823 K (DSA range) and back to cell/subgrains structure beyond 823 K. In the DSA regime, the formation of cells/subgrains is retarded by locking of dislocations by solute atoms thereby restricting cross slip and climb processes. Detailed studies carried out in the authors' laboratory on 316LN SS over a temperature range 298–873 K have clearly confirmed the transition from cells to planar slip bands in the temperature range 573–873 K, where DSA effects are predominant (Srinivasan *et al* 1991), figure 15. Further, studies conducted on 304SS at 823 K over the strain rate range 1.6×10^{-2} to $1.6 \times 10^{-4} \text{ s}^{-1}$ (Bhanu Sankara Rao *et al* 1991) showed an increase in the slip planarity with decrease in strain rate. Typical intense planar slip bands developed in the alloy at $1.6 \times 10^{-4} \text{ s}^{-1}$ are shown in figure 16. It may be noticed that there is a uniform distribution of dislocations in the interband region. It has been suggested that DSA enhances the degree of inhomogeneity of deformation during LCF by solute locking of slow moving dislocations between slip bands. Presumably, dislocation velocities inside the slip bands are too high for dynamic ageing of mobile dislocations to take place and consequently DSA enhances the partitioning of cyclic strains into separate regions marked by high and low amplitudes of dislocation movement (Wilson & Tromans 1970; Abdel-Raouf *et al* 1973; Bhanu Sankara Rao *et al* 1989; Valsan *et al* 1994).

DSA during LCF has been found to localize deformation. Figure 17 shows the variation of slip band spacing '*i*' with strain rate in PE-16 alloy (Valsan *et al* 1994). The increase in '*i*' at lower strain rates and higher temperatures is attributed to enhanced DSA effects. Intergranular cracking due to impingement of slip bands has been observed in many alloys (Tsuzaki *et al* 1983; Bhanu Sankara Rao *et al* 1988; Bhanu Sankara Rao 1989; Valsan *et al* 1994) under conditions of dynamic strain ageing.

It must be pointed out that planar slip generally enhances slip reversibility and hence resistance to both transgranular crack initiation and propagation (Valsan 1991; Valsan *et al* 1992). However, if stress concentrations associated with dislocation pile-ups cause intergranular cracks, or localized deformation in widely spaced slip bands causes transgranular cleavage cracks, then development of slip planarity will reduce fatigue life. Fracture mode has been found to be influenced under DSA conditions in LCF. SEM studies on type 304SS (Bhanu Sankara Rao *et al* 1990) revealed that at the two higher strain rates ($1.6 \times 10^{-3} \text{ s}^{-1}$ and $1.6 \times 10^{-2} \text{ s}^{-1}$) fatigue crack propagated transgranularly by ductile striation mechanism, and by a mixed transgranular and intergranular mode at the lowest strain rate ($1.6 \times 10^{-4} \text{ s}^{-1}$), figure 18. It should be noted that the occurrence of serrated flow coincided with the development of intergranular cracking. Also, where negative strain rate sensitivity existed but no serrated flow occurred, crack propagation remained transgranular. Intergranular decohesion at $\dot{\epsilon} = 1.6 \times 10^{-4} \text{ s}^{-1}$ (figure 18c), was caused by the impingement of slip bands on grain boundaries. Further, the higher stress response developed during strain controlled LCF in the DSA range (figures 13 and 14) would lead to a large stress concentration at the crack tip and increased crack growth rates (Bhanu Sankara Rao 1989; Valsan *et al* 1994). Moreover, higher response stresses would act to reduce the critical crack size for final fracture thus reducing cyclic life (Bressers & Verheghee 1981).



(a)



(b)



(c)



(d)

Figure 15. Dislocation sub-structures in LCF tested 316LN SS as a function of temperature (a) Crude cells with random arrangement of dislocations in cell walls at 298 K (b) well developed cell structure at 573 K, (c) planar dislocations and dislocation loops at 773 K, and (d) well developed planar slip bands at 873 K.

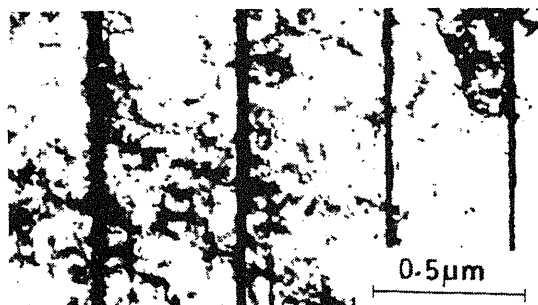


Figure 16. Slip bands and uniform distribution of dislocations in the interband regions (304 SS, grain size: $310\text{ }\mu\text{m}$, $\dot{\epsilon} = 1.6 \times 10^{-4}\text{ s}^{-1}$).

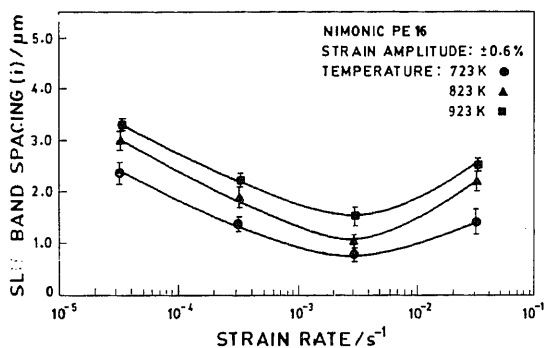
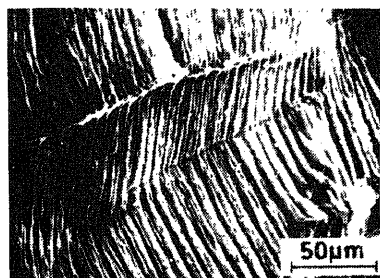
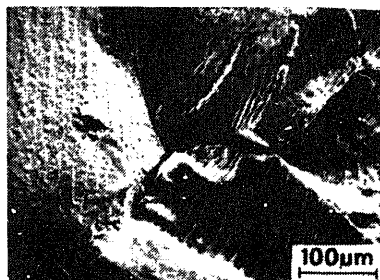


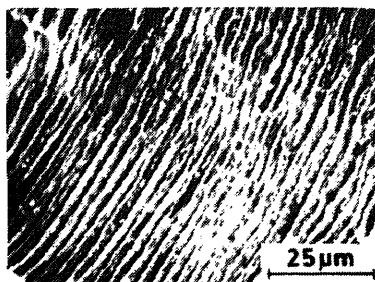
Figure 17. Variation of average slip band spacing ' i ' with strain rate in Nimonic PE16.



(a)



(c)



(b)

Figure 18. Crack propagation modes as a function of strain rate at 823 K in type 304 SS. (a) Transgranular stage II propagation ($\dot{\epsilon} = 1.6 \times 10^{-2}\text{ s}^{-1}$) (b) transgranular stage II propagation ($\dot{\epsilon} = 1.6 \times 10^{-3}\text{ s}^{-1}$) and (c) mixed mode propagation ($\dot{\epsilon} = 1.6 \times 10^{-4}\text{ s}^{-1}$).

4. Creep-fatigue interaction

Creep-fatigue interaction refers to the situation in which the rate of damage accumulation under complex loading differs from linear summation of damage rates produced by creep component and cyclic component. This subject has recently been reviewed by Rodriguez & Bhanu Sankara Rao (1993). Creep-fatigue interaction studies are generally carried out by introducing a component of creep into normal fatigue cycle (figure 3). This can be done by means of constant strain tensile (or compressive) dwell (figures 3b–d) or by reducing the tensile (or compressive) strain rate in the cycle (figures 3e and f). As the creep component of the cycle is increased by increasing the tensile dwell period or by reducing the tensile strain rate, failure mode also changes. The failure modes observed can be categorized into three distinct regimes:

- (1) fatigue dominated,
- (2) fatigue-creep interaction, and
- (3) creep dominated.

These three types of failure modes are shown in figure 19. Fatigue dominated failure arises due to growth of surface fatigue cracks through the specimen, with no evidence of interaction with creep damage (figure 19a). During fatigue-creep interaction, creep cavitation damage is found within the material in addition to surface fatigue damage. Fatigue and creep damages initially develop independently and the likelihood of true interaction depends on the balance between them. In tensile hold time tests on 316 SS at elevated temperatures, it is found that initial fatigue crack growth rates are similar to those occurring under continuous cycling conditions as demonstrated by fatigue striation measurements (Wareing 1977). However, eventually the fatigue crack interacts with creep damage, resulting in accelerated crack growth, a reduction in endurance and creep-fatigue interaction failure (figure 19b). When such interaction occurs, the failure path would become mixed (trans-plus intergranular). Finally, under certain testing conditions, the creep component of the cycle dominates and intergranular fracture due to the accumulation of grain boundary cavitation results (figure 19c); under these conditions there is no interaction with fatigue damage.

To understand creep-fatigue interaction let us first consider microstructural characteristics of creep failure and fatigue failure. Creep failure is caused by cavitation damage

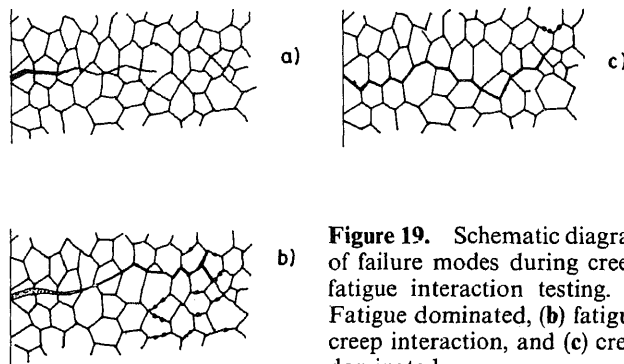


Figure 19. Schematic diagram of failure modes during creep-fatigue interaction testing. (a) Fatigue dominated, (b) fatigue-creep interaction, and (c) creep dominated.

while fatigue failure occurs by crack damage. The creep-fatigue failure can then be viewed from two points:

- (1) influence of cyclic loading on cavitation damage,
- (2) influence of cavitation on crack initiation and propagation.

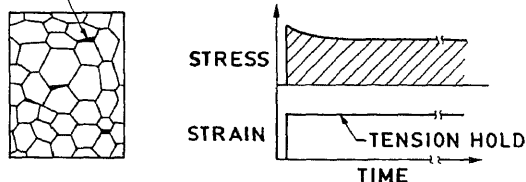
Creep-fatigue failure can be dominated by either cavitation-damage or by crack-damage. Conceptual mechanisms for each of these have been proposed by Raj (1985). These are illustrated in figures 20 and 21. In the case of cavitation damage, the imposition of cyclic loading enhances the rate of damage formation (figure 20). It can be seen that the integrated stress-time area is smaller for cyclic loading than it is for monotonic loading, yet cavitation damage is greater. Influence of cavitation damage on fatigue crack initiation and propagation is illustrated in figure 21. Here cavitation may enhance either crack initiation or propagation. Experimental evidence indicates that in pure fatigue, only one or two cracks are initiated, whereas, in creep-fatigue many grain boundaries at the surface develop cracks, and the largest among them propagates as the major crack. In the case of cavitation enhanced crack propagation, cracks can grow by lengths much greater than crack tip opening displacement due to the linkage of cavities ahead of the crack tip. Tomkins & Wareing (1977), Wareing *et al* (1980) and Rie *et al* (1988) have analysed the problem of fatigue crack growth in the presence of grain boundary cavitation and have suggested that fast crack growth rates occur when the following condition is satisfied.

$$\delta/2 = \lambda - p, \quad (1)$$

where, δ is the crack tip opening displacement, and p and λ are average cavity size and spacing respectively.

Extensive creep-fatigue interaction tests conducted on several high temperature alloys have shown that addition of tensile dwell periods dramatically reduces life compared to continuous cycling (Berling & Conway 1970; Brinkman *et al* 1972; Conway *et al* 1975; Wareing 1975, 1977, 1981; Maiya & Majumdar 1977; Schmitt *et al*

(a) W-CAVITATION DAMAGE



(b)

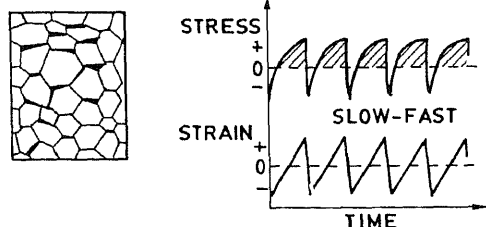


Figure 20. In a cavitation dominated failure, cyclic loading enhances the rate of damage accumulation. For example the integrated stress time area is smaller for cyclic loading (b), than it is for monotonic loading (a), yet the damage is greater for cyclic loading (Raj 1985).

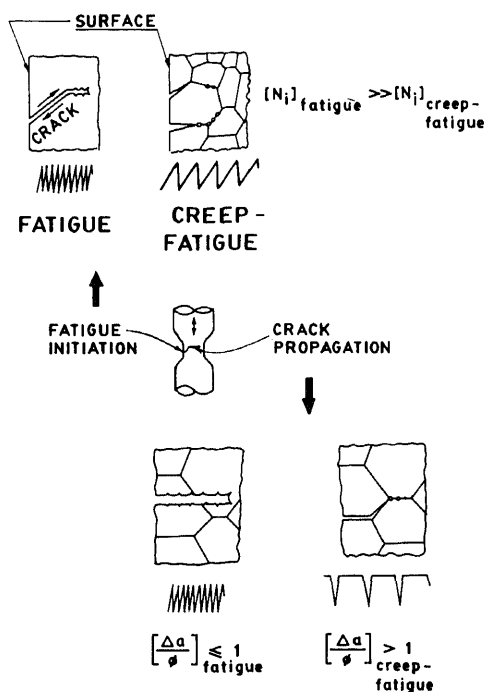


Figure 21. In crack dominated failure, cavitation can accelerate either crack initiation or crack propagation. (N_i = cycles for crack initiation $\Delta a/\phi$ = (crack advance per cycle)/(crack tip opening displacement) (Raj 1985).

1979; Brinkman 1985; Meurer *et al* 1984; Bhanu Sankara Rao *et al* 1986a, 1993). Balancing tensile dwell with compressive dwell has been shown to enhance the life time compared to dwell in tension alone (figure 22) (Ellison & Patterson 1976). This has been attributed to reduced intergranular creep damage due to introduction of compression dwell. On the other hand, endurance of 9Cr-1Mo steel has not been found to be influenced by the introduction of tensile dwell (Wood *et al* 1979; Choudhary *et al* 1991a). This material is characterized by a high creep ductility and no evidence of intergranular cracking is found in the tensile dwell period tests. These results suggest that creep ductility is a very important parameter in influencing endurance in hold time tests. Figure 23 shows data for several ferritic steels (Miller *et al* 1984). It is evident that, lower the ductility, the lower is the fatigue-creep endurance. In addition, it is clear that long dwell periods, small strain ranges and low ductility favour creep dominated failures, whereas, intermediate strain ranges, short dwell periods and high creep ductility favour fatigue-creep interaction failures.

Extensive tests on austenitic alloys have revealed that influence of hold time on fatigue lives depends not only on ramp rate, position and length of the hold, but also on microstructure (Maiya & Majumdar 1977; Wareing 1981; Bhanu Sankara Rao 1989; Bhanu Sankara Rao *et al* 1993). Figure 24 illustrates the combined influence of tensile strain holds, ramp strain rate and temperature on the endurance of 304 SS (Schmitt *et al* 1979). There is a reduction in life as dwell period is increased at elevated temperature; however at temperatures below 823 K, hold period does not seem to have any significant influence. Apart from the accumulation of damage during the hold period, a substantial part of the damage is generated during loading and unloading periods as well (figure 24).

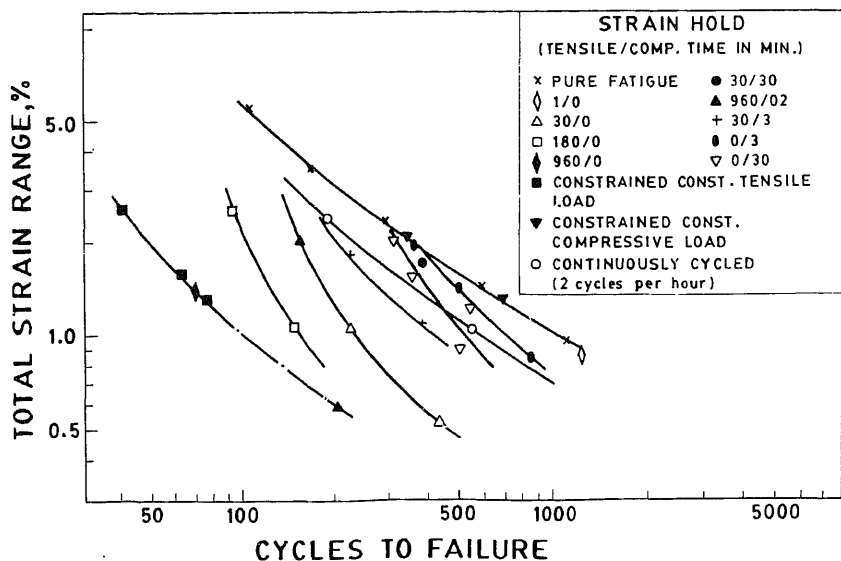


Figure 22. Plot of total strain range vs. cycles to failure for 1 CrMoV steel at 838 K (Ellison & Patterson 1976).

Creep-fatigue interaction behaviour of 304 SS base metal and 308 weld metal have been recently investigated by Bhanu Sankara Rao *et al* (1993). These tests were conducted at 923 K employing a total strain range of 1.0% and hold period of 1 minute in tension, compression and in both tension and compression. Fatigue life of weld metal

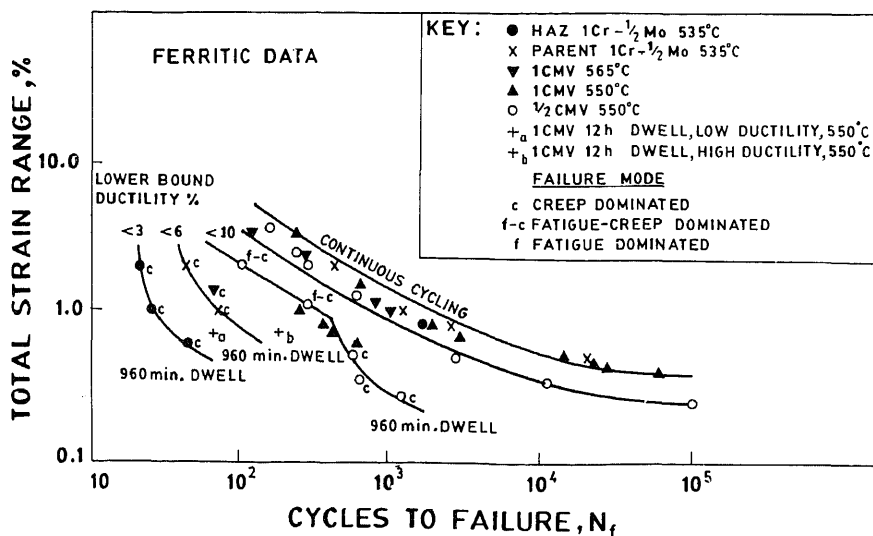


Figure 23. Effect of ductility on endurance and fracture mode in low alloy ferritic steels (Miller *et al* 1984).

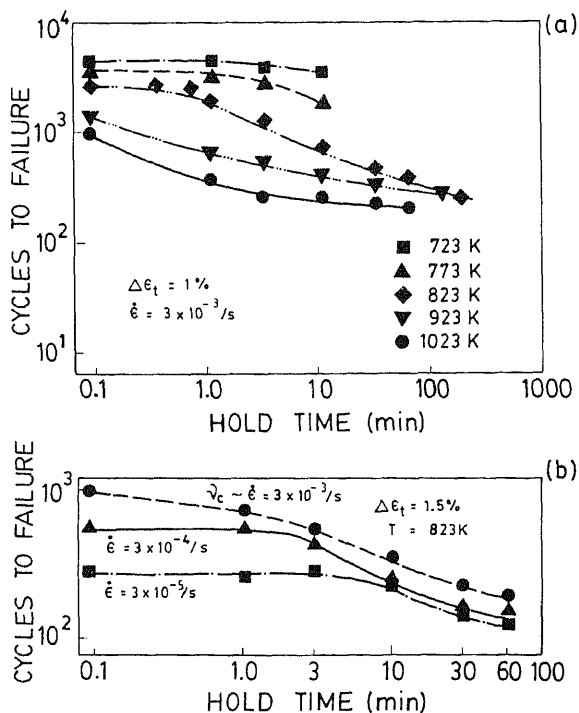
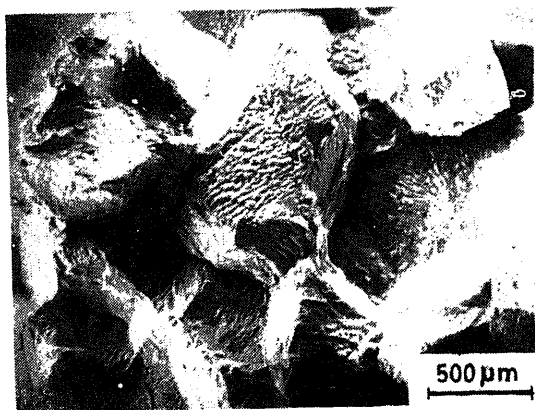


Figure 24. The influence of tensile hold duration on fatigue life of type 304 SS (a) for different temperatures, (b) for different strain rates (Schmitt *et al* 1979).

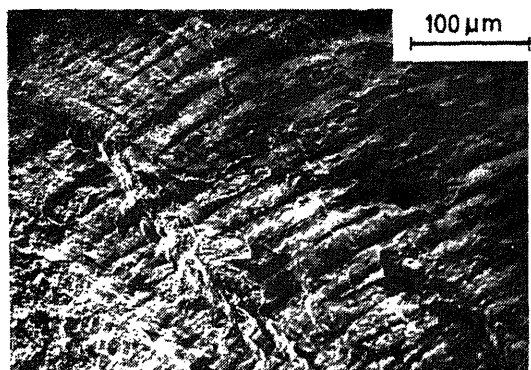
was inferior to base metal (Brinkman *et al* 1974; Bhanu Sankara Rao *et al* 1993). Effect of hold period on life was dependent not only on the material condition and duration of hold, but also on the position of the hold in the cycle. 304 SS reveals a severe degradation in life with a tension hold compared with continuous cycling. Compression hold lowered life marginally while for hold both in tension and compression, life values in between those for hold in tension alone and compression alone were observed. Mean stress was not found to be the reason for the observed differences in the behaviour. Fractographic investigations revealed bulk creep damage in tests with tension hold periods (figure 25a) while fracture modes associated with compression holds and continuous cycling were characterized by ductile striations (figures 25b and c).

In nickel base alloys, compressive strain holds have been found to be more detrimental than tensile hold (Wells & Sullivan 1969; Lord & Coffin 1973; Ostergren 1976a; Antunes & Hancock 1978). Development of tensile mean stress (Plumbridge & Ellison 1987), differences in the shapes of cavities formed during tension and compression (Wells & Sullivan 1969) and load shedding effects due to multiplicity of cracks in tensile dwell (Nazmy 1983a, 1983b) have been suggested as possible reasons for observed damaging effects of compression hold.

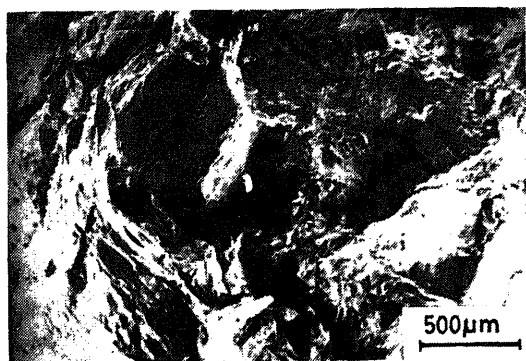
Creep-fatigue interaction has also been investigated employing slow-fast and fast-slow types of waveforms (figures 3e and f). Generally maximum fatigue endurance has been observed in fast-fast cycling and minimum in slow-fast (Majumdar & Maiya 1979; Bhanu Sankara Rao *et al* 1986c, 1988; Kempf *et al* 1987). Factors which contribute to the observed differences in the failure modes and fatigue lives in these tests have been recently discussed by Rodriguez & Bhanu Sankara Rao (1993). Development



(a)



(b)



(c) **Figure 25.** Crack propagation in 1 min hold time tests on 304 SS at 923 K. (a) Tension hold: intergranular propagation; (b) compression hold: transgranular propagation; and (c) tension plus compression hold: mixed mode propagation.

of cavitation damage due to slow strain rates is considered to be responsible for reduced fatigue lives.

Actual components in high temperature plants are subjected to complex cyclic loading situations where creep-fatigue interaction plays a dominant role. An in-depth knowledge of high temperature fatigue behaviour is necessary for design as well as life assessment and remnant life estimation of structural components. Various life predic-

tion methods applicable to high temperature fatigue condition have been proposed and these are reviewed in the following section.

5. Life prediction methods for high temperature low cycle fatigue

Several life prediction methods have been developed to assess fatigue life of the components under time-dependent fatigue conditions, and these include:

- (1) prediction based on monotonic tensile properties;
- (2) damage summation method;
- (3) frequency modified and frequency separation methods;
- (4) strain range and strain energy partitioning methods;
- (5) hysteresis energy method;
- (6) ductility exhaustion approach;
- (7) damage rate model;
- (8) Tomkins and Wareing's model; and
- (9) Cavitation model by Rie *et al* (1988).

Detailed reviews of most of the models mentioned above are available in the literature (Lloyd & Wareing 1981; Miller *et al* 1984; Rodriguez *et al* 1989; Viswanathan 1989; Rodriguez 1993; Rodriguez & Bhanu Sankara Rao 1993). Marriott (1992) has recently reviewed the current trends in high temperature design rules covering creep and fatigue conditions. In the following section, the salient features of various life prediction methods are discussed.

5.1 Method of universal slopes and 10% rule

This method has been formulated to predict fatigue life from strength and ductility parameters derived from short time tension tests. The fatigue life is given as the summation of the elastic strain amplitude, $\Delta\epsilon_e/2$ (Basquin 1910), and the plastic strain amplitude, $\Delta\epsilon_p/2$ (Coffin 1954; Manson 1954) given by:

$$\Delta\epsilon_e/2 = (\sigma'_f/E)(2N_f)^{-\gamma}, \quad (2)$$

$$\Delta\epsilon_p/2 = (\epsilon'_f)(2N_f)^{-\beta}, \quad (3)$$

where, σ'_f = fatigue strength coefficient, E = elastic modulus, γ = fatigue strength exponent, ϵ'_f = fatigue ductility coefficient, β = fatigue ductility exponent and N_f = number of cycles to failure. Based on the results on a variety of materials, Manson (1965) has suggested that the exponents and coefficients of these relationships can be universalised and proposed a generalized form for the strain-life relationship (universal slopes equation),

$$\Delta\epsilon_t = 3.5(\sigma_u/E)N_f^{-0.12} + D^{0.6}N_f^{-0.6} \quad (4)$$

where, σ_u = ultimate tensile strength, D = ductility = $\ln(100/(100 - \%RA))$, RA = reduction in area and N_f = number of cycles to failure.

The deterioration in fatigue life at high temperatures aided by intergranular crack initiation and propagation has been empirically accounted for, in 10% rule (Manson & Halford 1968) by factoring the fatigue life obtained from universal slopes equation by 10.

Further, a creep modified 10% rule has been proposed (Manson & Halford 1967) to evaluate fatigue life under those situations where the creep effects decrease fatigue life by more than a factor of 10.

Universal slopes method and its modifications are useful in the early stages of design when fatigue properties of a material of interest may not have been measured yet. However, these methods cannot adequately account for the deterioration in fatigue life by creep and other time-dependent processes at high temperatures.

5.2 Linear damage summation – time and cycle fraction rule

This approach involves the linear summation of time and cycle fractions, wherein time fractions are used as a measure of creep damage (Robinson 1952) and cycle fractions are used as a measure of fatigue damage (Miner 1945). Failure in a creep-fatigue situation is expressed as,

$$n/N_f + t/t_r = 1 \quad (5)$$

where, n = number of cycles at a strain range, N_f = pure fatigue endurance at the same strain range, t = time at a given stress and t_r = time to rupture at the stress under pure monotonic loading.

The ASME design criterion (1992) based on this summation rule proposes a limit for allowable damage D . Further, N_f and t_r are replaced by N_d and T_d respectively

$$\sum_{j=1}^p (n/N_d)_j + \sum_{k=1}^q (t/T_d)_k \leq D, \quad (6)$$

where D = total allowable creep-fatigue damage value, n = number of cycles of loading condition j , N_d = number of design-allowable cycles of loading condition j , t = time duration of load condition k and T_d = allowable time at a given stress intensity. The values for D are different for different materials. D is unity for Alloy 800 H but is in the range 0.6 to 1.0 for types 304 and 316 stainless steels (ASME Code Case N47 1992).

A creep-fatigue interaction diagram based on linear damage summation approach developed in our laboratory for 9 Cr–1 Mo steel thick section forging (Choudhary *et al* 1991b) is provided in figure 26a. This figure also incorporates thin section data from Wood *et al* (1979). Figure 26b gives creep-fatigue interaction diagram for 2.25 Cr–1 Mo (Valsan *et al* 1988) based on the data available in literature (Booker & Majumdar 1982; Swindeman & Strizak 1982). It may be seen that for 9 Cr–1 Mo steel the data points lie above the $D = 1$ line, while for 2.25 Cr–1 Mo steel damage values less than unity are needed for encompassing the test data.

The damage summation method is extensively employed in design codes in view of its simplicity as it requires only S–N curves and stress rupture curves for life prediction. However, this approach has the following limitation:

- (1) The value of damage D is specific for each material.
- (2) Tensile and compressive hold periods are considered equally damaging. In practice, compression holds are found to have a healing effect in austenitic steel (Bhanu Sankara Rao *et al* 1993, 1994) but in nickel-base superalloys they are more detrimental than tension holds (Wells & Sullivan 1969; Antunes & Hancock 1978).
- (3) The strain rate dependence of creep damage accumulation is not incorporated in this model.

(b)

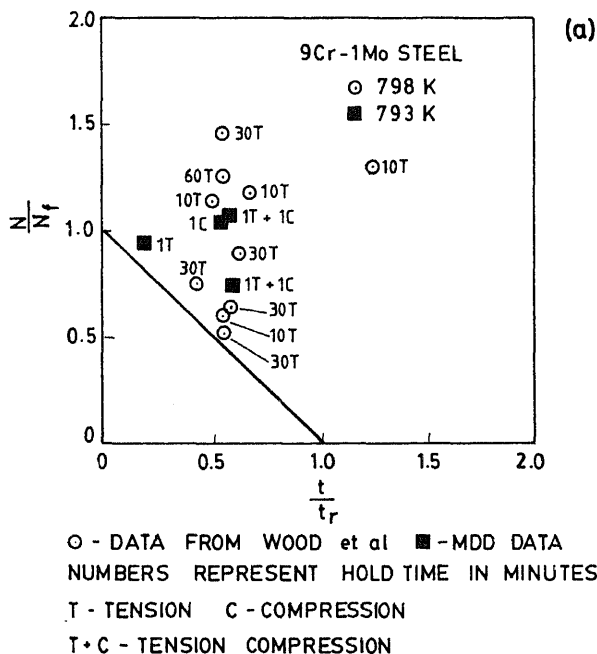
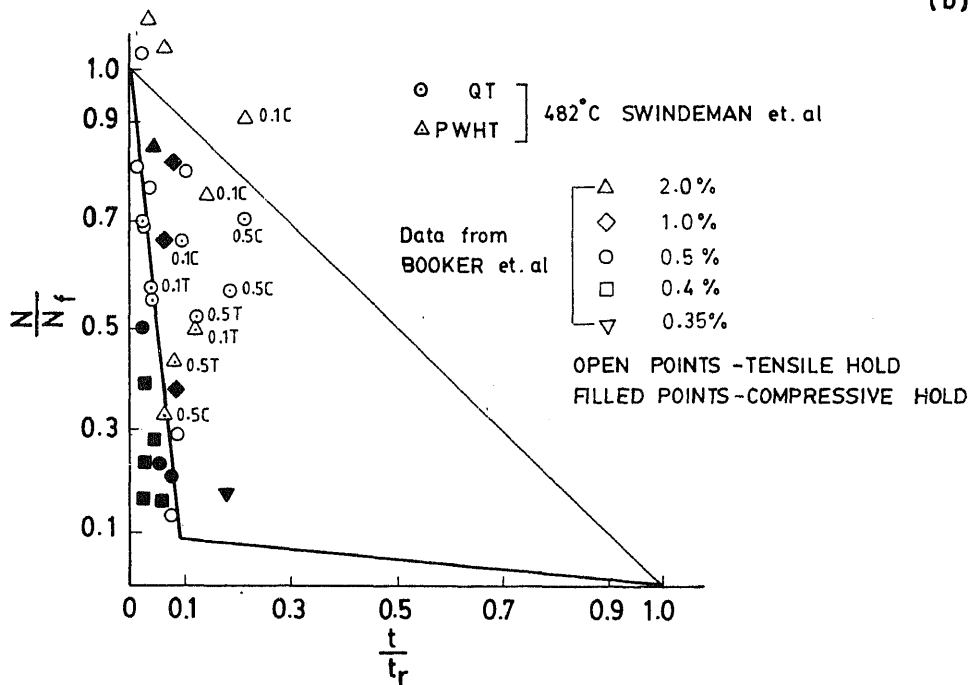


Figure 26. Linear damage summation diagram for (a) 9 Cr-1 Mo steel and (b) 2.25 Cr-1 Mo steel.

- (4) Stress rupture properties are determined from virgin material, whereas materials cyclically harden/soften depending on the alloy composition, metallurgical and testing conditions.

(5) This method assumes a load path independence for fatigue and creep damages.

5.3 Frequency modified and frequency separation methods

This approach is essentially a modification of the Coffin–Manson relationship for pure fatigue (Coffin 1969, 1971, 1976, 1977). The time parameter is introduced to account for the environmental and other time-dependent factors, by incorporating a frequency term as follows:

$$\Delta \varepsilon_p = A_1 (N_f v^{k-1})^{-\beta}, \quad (7)$$

where A_1 , k and β are temperature-dependent constants. k is a material parameter derived from the Eckel relationship (1951)

$$v^k t_f = \text{constant} = f(\Delta \varepsilon_p), \quad (8)$$

and $N_f v^{k-1}$ is the frequency modified life. Similarly, Basquin relationship is modified and summed to provide a relationship of total strain range.

$$\Delta \varepsilon_t = A_1 (N_f v^{k-1})^{-\beta} + A_2 N_f^{-\beta'} v^{k_1}, \quad (9)$$

where A_2 , β' and k_1 are material and temperature-dependent constants. For treating hold time effects, the frequency is calculated from $v = 1/(t + t_h)$, where t is the time for strain reversal and t_h is the hold time in each cycle.

The concept of total cycle time does not adequately predict the fatigue behaviour for complex wave shapes. The effects of wave shape on damage are associated with tension going time and hysteresis loop imbalance. Frequency separation equation can be written as:

$$N_f = (A_1 / \Delta \varepsilon_p')^{1/\beta} (v_t/2)^{1-k}, \quad (10)$$

where $\Delta \varepsilon_p'$ represents the loop imbalance (Coffin 1977) and the term $(v_t/2)^{1-k}$, accounts for the time spent in the tension part of the cycle. $\Delta \varepsilon_p'$ is the equivalent plastic strain defined as:

$$\Delta \varepsilon_p' = \Delta \varepsilon_p [((v_c/v_t)^{k_1} + 1)/2]^{1/\beta} \quad (11)$$

$$k_1 = k' + \beta'(k - 1) \quad (12)$$

where v_t = tension-going frequency, v_c = compression-going frequency, and β' and k_1 are the appropriate constants derived from the Basquin law. The frequency separation method has been found to give a good correlation between the experimental and the predicted lives for a variety of wave shapes and dwell times, figure 27 (Coffin 1977).

Advantages of frequency based approaches:

- (1) Total strain is a major correlating parameter and hence is of direct use to designers.
- (2) Subdivision of inelastic strains into various components is not made as in strain range partitioning method. Here the inelastic strain arising from a host of deformation processes is considered to be inseparable.
- (3) Implicit in the method is an assumption that significant damage for a cycle occurs near the peak tensile strain and is affected by strain rate in reaching this maximum.

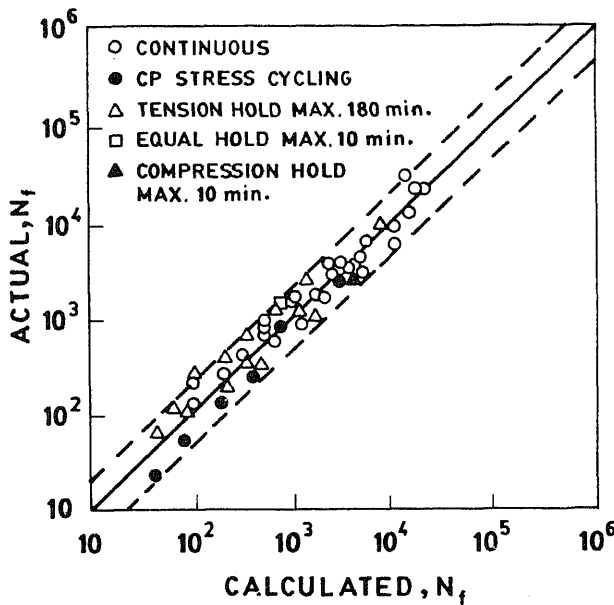


Figure 27. Fatigue life prediction for various heats of type 304 SS at 867 K by frequency separation method (Coffin 1977).

Disadvantages:

- (1) It is implied that the fatigue life decreases continuously with decrease in frequency. However, in certain materials homogenization of deformation (Valsan *et al* 1994) and thermal ageing cause improvement in fatigue life (Bhanu Sankara Rao 1989).
- (2) No distinction is made between tension and compression dwell periods and to their damaging effects which are material dependent.
- (3) Variable temperature effects are not accounted for.
- (4) Analysis assumes that hysteresis loop is closed. Hence it cannot take care of strain ratchetting.
- (5) Evaluation of the equation needs determination of several parameters.
- (6) For complex loops, determination of frequency is difficult.

5.4 Strain range partitioning approach

In strain range partitioning (SRP) method (Manson *et al* 1971), the total inelastic strain range is partitioned into four possible components depending on the directions of straining (tension or compression) and the type of inelastic strain (creep or time-independent plasticity), figure 28 (Hirschberg & Halford 1976):

- $\Delta\epsilon_{PP}$: tensile plastic strain reversed by compressive plastic strain;
- $\Delta\epsilon_{CP}$: tensile creep strain reversed by compressive plastic strain;
- $\Delta\epsilon_{PC}$: tensile plastic strain reversed by compressive creep strain;
- $\Delta\epsilon_{CC}$: tensile creep strain reversed by compressive creep strain.

Partitioning of a generalized hysteresis loop is illustrated in figure 29 (Hirschberg & Halford 1976). Only three of these four generic strain ranges can exist in a given

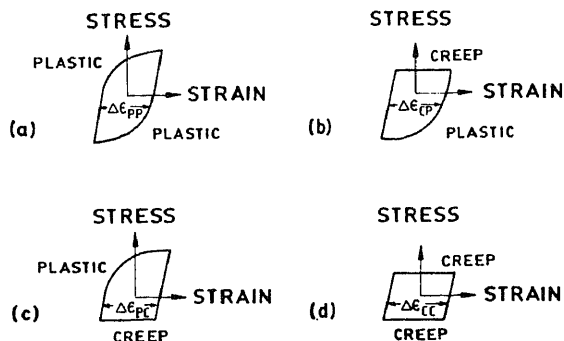


Figure 28. Idealised hysteresis loops for defining individual partitioned strain range-life relationships (a) PP , (b) CP , (c) PC and (d) CC type of cycles (Hirschberg & Halford 1976).

hysteresis loop. $\Delta\epsilon_{PC}$ and $\Delta\epsilon_{CP}$ cannot co-exist. By choosing suitable experiments, relations between inelastic strains and life, can be determined for a material of interest for each of these strain ranges:

$$N_{jk} = A_{jk} \Delta\epsilon_{jk}^{\beta_{jk}},$$

where j and k represent plasticity or creep (Manson *et al* 1971; Hirschberg & Halford 1976). The damage fractions resulting from each of the partitioned strain range components are summed up by an interaction damage rule (figure 30),

$$F_{PP}/N_{PP} + F_{PC}/N_{PC} (\text{or } F_{CP}/N_{CP}) + F_{CC}/N_{CC} = 1/N_{pred} \quad (13)$$

Here N_{PP} , N_{PC} , N_{CP} and N_{CC} are obtained from the four generic life relationships as shown in figure 30 and $F_{PP} = \Delta\epsilon_{PP}/\Delta\epsilon_{in}$; $F_{PC} = \Delta\epsilon_{PC}/\Delta\epsilon_{in}$; $F_{CP} = \Delta\epsilon_{CP}/\Delta\epsilon_{in}$ and $F_{CC} = \Delta\epsilon_{CC}/\Delta\epsilon_{in}$, where $\Delta\epsilon_{in}$ is the total inelastic strain range.

In several high temperature alloys SRP has been found to satisfactorily predict life within a factor of 2 (Halford *et al* 1972; Hirschberg & Halford 1976; Hoffelner *et al* 1983). Several modifications have been proposed to the SRP approach subsequently. A ductility normalized SRP has been suggested to take into account the effect

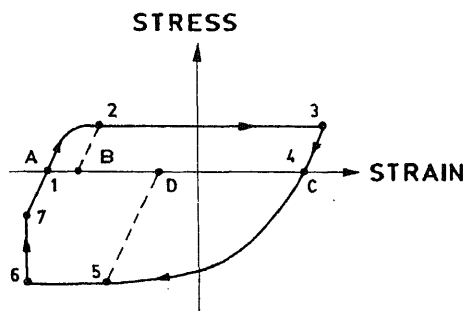


Figure 29. Defining partitioned strain range components of complex hysteresis loop (Hirschberg & Halford 1976).

$$\begin{aligned} \Delta\epsilon_{PP} &= AB & \Delta\epsilon_{CC} &= DA \\ \Delta\epsilon_{PC} &= 0 & \Delta\epsilon_{CP} &= (BC - DA) \\ \Delta\epsilon_{IN} &= \Delta\epsilon_{PP} + \Delta\epsilon_{CC} + \Delta\epsilon_{CP} = AC \end{aligned}$$

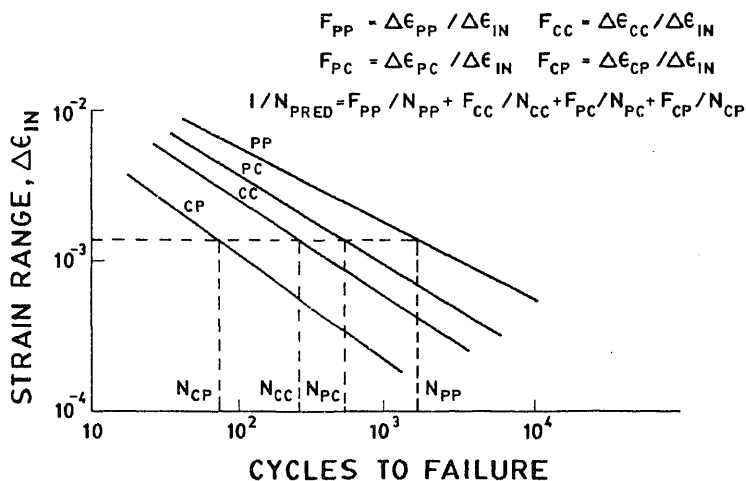


Figure 30. Definition of terms for an interaction damage rule (Hirschberg & Halford 1976).

of variables like environment, heat to heat variations, degree of cold work, heat treatment, radiation damage and thermal exposure (Halford *et al* 1977). A total strain range version of the original SRP has been put forth to evaluate creep-fatigue interaction under low strain conditions (Halford & Saltsman 1983; Saltsman & Halford 1985), where inelastic strains cannot be determined with sufficient accuracy to make reliable life predictions. Recently, SRP has been modified by Duan *et al* (1988) to enable life prediction in high strength low ductility alloys. This approach synthesises the energy concept of Ostergren (1976b) and the inelastic strain partitioning of the SRP.

Detailed investigation on the time dependency of strain range partitioning approach for CP cycles has been examined by Kalluri & Manson (1984). For CP cycle, the time taken for introducing a given amount of creep strain depends on the position and the type (stress or strain) of hold. For example, the creep strain accumulated during stress relaxation in a tensile strain hold test can be obtained within a much shorter time in a corresponding stress hold test. Hence, the time required to complete the hysteresis loop differs, and therefore, suitable modifications to the CP life relationships incorporating the time parameter has been proposed to take into account various time-dependent damaging processes (Kalluri & Manson 1984).

Some of the advantages of SRP include the following:

- SRP can be used to establish upper and lower bounds on life from the most conservative and least conservative of partitioned strain range versus life relationships;
- Wave shape effects are treated directly;
- Fatigue relationships are relatively temperature insensitive. The effect of temperature is to alter creep and plasticity in a cycle;
- Environmental effects are introduced through basic ductility normalized relationship.

This approach suffers from the following disadvantages.

- (a) Accurate knowledge of the cyclic history of service components is required, complex loops become naturally difficult to partition;
- (b) Hysteresis loops need to be closed;
- (c) Life predictions may be inaccurate in situations where the dominant degrading mechanism is environmental;
- (d) If the failure relationships lie close to each other or when there is a cross over between them, choice of a strain range component that causes maximum damage becomes difficult.

5.5 Hysteresis energy approach

Ostergren (1976b) has proposed a damage function based on net tensile hysteresis energy for predicting fatigue life under different frequencies and hold time conditions. Further, the mean stress concept is introduced to take into account the detrimental effects of compression holds in some nickel base superalloys (Leven 1973; Lord & Coffin 1973; Ostergren 1976b). The tensile hysteresis energy is approximated as $\Delta W_T = \sigma_T \Delta \epsilon_p$ where σ_T is the tensile stress range and $\Delta \epsilon_p$ is the plastic strain range. It is then assumed that universality of Coffin-Manson law applies to the hysteresis energy and hence

$$\sigma_T \Delta \epsilon_p N_f^\beta = \text{constant.} \quad (14)$$

Here $\sigma_T = \sigma_m + \Delta \sigma / 2$, where σ_m = mean stress and $\Delta \sigma$ is the stress range corresponding to a given $\Delta \epsilon_p$. The above equation has been modified for frequency and hold time conditions during which, time-dependent damages become significant as,

$$\sigma_T \Delta \epsilon_p N_f^\beta v^{\beta(k-1)} = \text{constant.} \quad (15)$$

Frequency is suitably defined depending upon the damaging effects of compression and tension holds. In this way, the beneficial and harmful effects of compression holds could be accounted for.

5.6 Ductility exhaustion approach

In the ductility exhaustion approach (Edmunds & White 1966) it is assumed that the specimen failure occurs when the accumulated creep relaxation strain in a hold time test becomes equal to the monotonic creep ductility of the material. Life predicted using this approach, however, is found to be highly conservative. It was proposed (Priest & Ellison 1980, 1981) that only a fraction of the relaxed strain should be compared with creep ductility. This fraction was defined by a transition strain rate above which matrix deformation dominates and contributes to fatigue damage and below which grain boundary damage accumulates and creep becomes important (figure 31). Here $\Delta \epsilon_c$ corresponds to the creep strain accumulated in a hold cycle and $\Delta \epsilon_p$ = "effective" plastic strain component (i.e. part of the inelastic strain range not associated with the grain boundary damage) and $\Delta \epsilon_{pp}$ = plastic strain corresponding to pure fatigue. Transition strain rates corresponding to the damage processes are obtained from deformation mechanism maps typically as shown in figure 32 for 1 Cr-1 Mo-V steel, 565°C, grain size 23 μm (Priest & Ellison 1981).

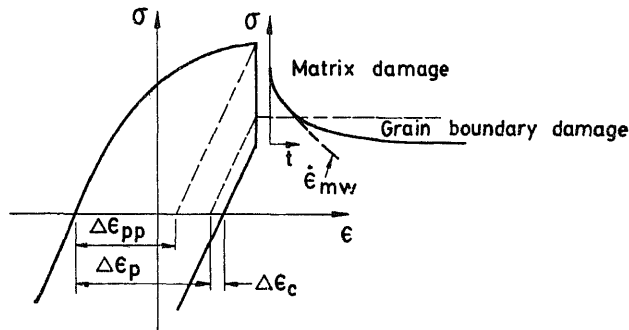


Figure 31. Partitioning of a typical cyclic-hold hysteresis loop (Priest & Ellison 1981).

In this method, creep and fatigue are considered to be independent damaging processes which compete to cause failure. The one that reaches its critical ductility exhaustion in the least number of cycles dominates the mode of failure. A creep-fatigue loading situation is creep dominated when $N_c \Delta \epsilon_c = D_c$, where D_c is the tensile creep ductility, and N_c is the life. Rupture ductility of a material is not a constant but depends on temperature, strain rate, metallurgical variables and state of deformation (i.e., constrained or unconstrained). Fatigue damage dominated life times are similarly expressed by an equation $N_p \Delta \epsilon_p = D_p$, where N_p = fatigue dominated life time and D_p = fatigue ductility defined by the strain intercept at one reversal from Coffin-Manson plot. For creep-fatigue interaction, the two mechanisms are summed linearly as

$$1/N_c + 1/N_p = 1/N_{pred}. \quad (16)$$

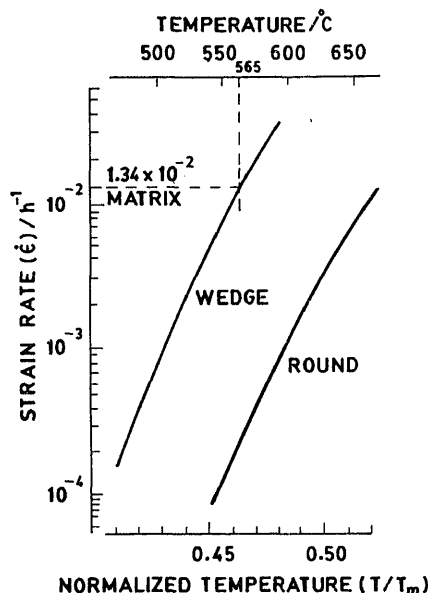


Figure 32. Variation in dominant damage mechanisms with temperature and strain rate (1Cr-Mo-V steel; $d \approx 23 \mu\text{m}$) (Priest & Ellison 1981).

Good predictions have been reported by the application of this technique to 1 Cr-Mo-V steel data, figure 33 (Priest & Ellison 1981). This method has been used successfully for predicting creep-fatigue life by a number of investigators for both ferritic and austenitic steels (Miller *et al* 1982; Priest *et al* 1983; Tomkins 1983; Wood *et al* 1988) and also for 17 Cr-8 Ni-2 Mo weld metal (Wood *et al* 1988). Damage healing effects can be accommodated by the ductility exhaustion technique (Priest *et al* 1983). This method can also be employed for slow-fast cycling conditions (Tomkins 1983).

Ductility exhaustion method has the following limitations.

- Severe damaging effects of compressive dwells seen in nickel base alloys are difficult to predict by this method.
- Ductility is not a unique material property. Coffin-Manson plots exhibit two-slope behaviour under certain circumstances; determination of fatigue ductility in those situations is uncertain. Variability in creep ductility from heat to heat makes it difficult to select appropriate ductility values for creep damage. Further, tensile creep ductility may not be the appropriate one to use in compression hold conditions.
- Determination of transition strain rate in hold tests needs elaborate metallographic investigations.
- Deformation mechanism maps used for establishing the damage regime boundaries are only as good as the equations from which they are derived. Semi-empirical nature of the maps casts doubts with respect to their applicability to different sets of data.

5.7 Damage rate model

A strain-based approach which takes into account the rate of damage development has been suggested by Majumdar & Maiya (1976a, 1976b, 1979) and Maiya & Majumdar

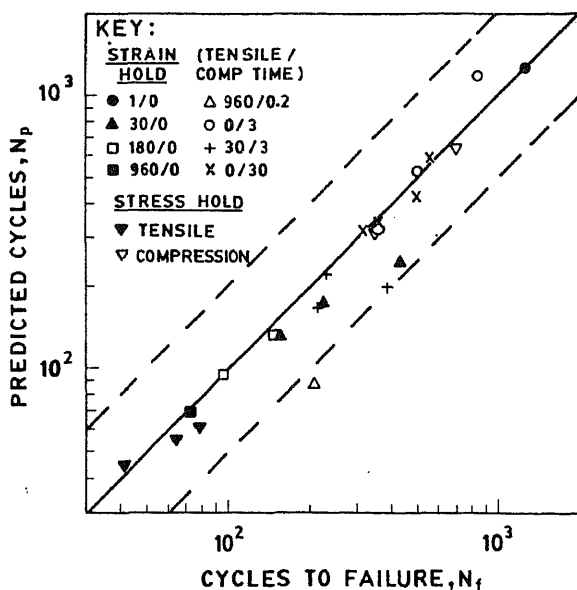


Figure 33. Comparison of observed and predicted lives by ductility exhaustion approach for various cycle shapes (data from Priest & Ellison 1981).

(1977). It is assumed that there are two types of damage namely cracks (fatigue) and cavities (creep) in creep-fatigue situation. If the two damage mechanisms are additive, the damage rate is given by the sum of equations:

$$\frac{1}{a} \frac{da}{dt} = \begin{cases} T |\epsilon_p|^m |\dot{\epsilon}_p|^{k_a} & \text{(for tension),} \\ C |\epsilon_p|^m |\dot{\epsilon}_p|^{k_a} & \text{(for compression),} \end{cases} \quad (17)$$

and

$$\frac{1}{c} \frac{dc}{dt} = \begin{cases} G |\epsilon_p|^m |\dot{\epsilon}_p|^{k_c} & \text{(for tension),} \\ -G |\epsilon_p|^m |\dot{\epsilon}_p|^{k_c} & \text{(for compression).} \end{cases} \quad (18)$$

Equation (17) describes the crack damage due to fatigue and (18) describes the cavitation damage due to creep. T , C , G , k_a , k_c and m are material parameters which are functions of temperature, environment and metallurgical state of the material; ϵ_p and $\dot{\epsilon}_p$ are current absolute values of plastic strain and strain rate respectively, and a and c are the crack size and cavity size respectively at time, t . T and C are included to account for differences in growth rates occurring in tension and compression. G or $-G$ is used to denote tension or compression. Final failure is calculated as the reciprocal of the sum of crack and cavity damage.

For the cases where the fatigue and creep damages are interactive, crack damage (17) has been modified as,

$$(1/a) da/dt = \{T \text{ or } C\} (1 + \alpha \ln c/c_0) |\epsilon_p|^m |\dot{\epsilon}_p|^{k_a}, \quad (19)$$

and the expression for cavitation damage remains the same.

In the cavity growth formulation, (18), it is assumed that the cavities are widely separated and hence growth occurs independently. Further, the presence of cracks do not influence the growth of cavities. However, cavities of size greater than c_0 interact with crack and increase the crack growth rate. This is considered in the interactive damage rule by introducing a term $(1 + \alpha \ln c/c_0)$ into (19).

In the interactive damage rule, failure is assumed to occur when the crack length a reaches the size for failure a_f . If $\alpha = 0$, the fatigue crack growth is unaffected by cavities and (19) reverts to continuous cycling, (17).

The interactive damage rate model has been found to satisfactorily predict fatigue lives for several high temperature alloys (Majumdar & Maiya 1976a). The main advantage of this model is that it takes into account microstructural damage parameters and their evolution with time. Secondly, it incorporates interaction between fatigue and creep damage modes. Strain history of components can be calculated more reliably than their stress history, making this method more useful to designers. Moreover, the model can also be applied to situations when the stress-strain hysteresis loops are not closed. However, determination of a large number of parameters involved in these equations needs elaborate experimentation. Further, definition of initial crack and cavity sizes needs careful consideration.

5.8 Tomkins and Wareing's model

Tomkins & Wareing (1977) and Wareing *et al* (1980) have extended the model proposed by Tomkins (1968) for fatigue crack growth to include the influence of cavitation. In Tomkins' model (1968) it is assumed that crack initiation is a negligible

phase and the entire life is spent for crack propagation. During crack growth, a new crack surface is generated by shear decohesion mechanism at the crack tip. The extent of decohesion is related to the extent of intense crack tip deformation (D) and the applied plastic strain range. In other words, the factors determining the crack growth rate per cycle are the magnitude of the applied stress-strain field, the current crack length and a material strength parameter. Fatigue endurance is determined by the initial crack size, rate of crack growth and the critical crack size.

In this model, the crack propagation rate is expressed as,

$$da/dN = \Delta\epsilon_p D/2^{1/2}, \quad (20)$$

where

$$D = 2^{1/2} [\sec(\pi\sigma_T/2\bar{T}) - 1]a$$

$$\sigma_T = K' \Delta\epsilon_p^{n'};$$

K' = cyclic strain hardening co-efficient;

n' = cyclic strain hardening exponent;

\bar{T} = approximately equal to cyclic UTS;

a = instantaneous crack length;

D = extent of deformation at the crack tip;

$\Delta\epsilon_p$ = applied plastic strain range.

For $\sigma_T/\bar{T} < 0.6$ and a power law for σ_T , integration of (20) gives Coffin-Manson law.

$$\Delta\epsilon_p N_f^\alpha = [(8/\pi^2)(\bar{T}/K')^2 \ln(a_f/a_0)]^\alpha, \quad (21)$$

where

$$\alpha = 1/(2n' + 1)$$

a_f = final crack length; 2/3 of the specimen section,

a_0 = initial crack length (10 μm for ductile materials).

From (21) it follows that the slope of the fatigue life curve is related only to the slope of cyclic stress strain curve. The position of fatigue curve is dependent on the ratios (\bar{T}/K') and (a_f/a_0) . As \bar{T} and K' are both strength parameters, variations in strength levels alone will not affect endurance for cycling at a given strain range. As the ratio a_f/a_0 is in the logarithmic form in (21), this must change drastically to effect a significant positional change. The slope of the cyclic stress-strain curve is then the most significant factor affecting endurance.

Applicability of Tomkins' model has been examined for austenitic stainless steels (Wareing 1988), ferritic steels (Wareing 1988; Choudhary *et al* 1991b) and a magnesium alloy (Wareing 1988). In the case of austenitic stainless steels, a good agreement between predicted and experimental lives has been obtained for various testing and microstructural conditions. However, major differences between the predicted and experimental lives were noticed at low strain ranges (figure 34), where number of cycles required for crack initiation becomes significant. The ability of the crack propagation model, based primarily on stress parameter, to predict fatigue endurance at ambient and elevated temperatures is a consequence of the

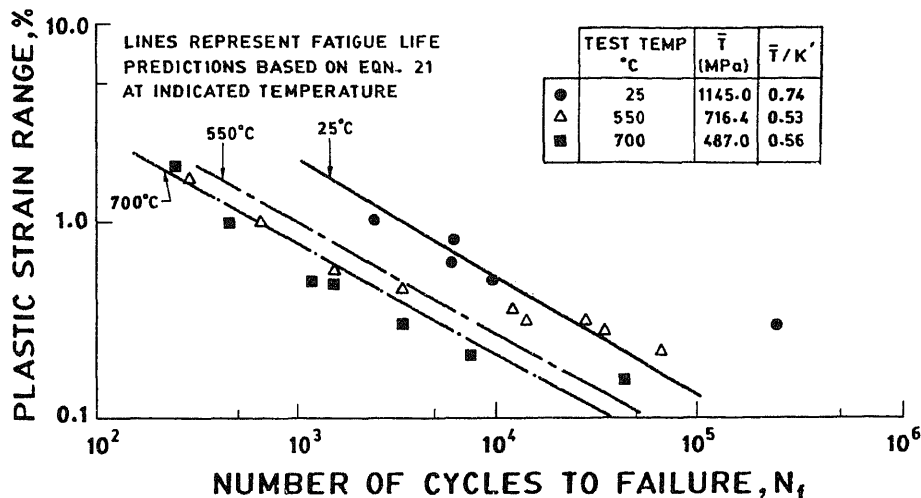


Figure 34. Coffin-Manson plots for type 316 SS at various temperatures (Waring 1988).

balanced nature of cycle which precludes the formation of creep damage at elevated temperatures.

Crack propagation during creep-fatigue situation occurs in three distinct phases: Phase I is characterised by ductile striations and the growth rate in a tensile hold test is identical to that observed for the same applied strain amplitude without dwell period in the cycle. Phase II which occupies a major portion of the fracture surface occurs very rapidly compared to phase I and follows intergranular path. The reason for the large increase in growth rate is the attainment of cavity linkage at the crack tip. This triggers the unzipping of the cavitated material by the crack tip displacement field. Finally phase III, unstable fracture, occurs in a single cycle. The criterion for the onset of phase II is given by (1). An approximate solution for δ in a fully plastic field is given by (Tomkins 1975):

$$\delta/2 = \ln(\sec(\pi\sigma_T/2\bar{T}))[(2\bar{T}/E) + (2\Delta\epsilon_p/(1+n'))]a. \quad (22)$$

Because phase II is so rapid, the life of a specimen failing by this mechanism is the cycle for initiation and phase I growth, i.e., the number of cycles to attain the critical crack size a'_f , commensurate with the prevailing cavity spacing. For rapid crack initiation, this is obtained by substituting a_0 (10 μm) and a'_f in Tomkins' model.

Predictions of this model are compared with experimental data for 316 SS at 843 K for various tensile hold time tests in figure 35. Continuous cycling data are in good agreement with the prediction of (21). For the hold time tests, the data at the highest strains are in line with the prediction (1 and 22) for a cavity spacing of 1 μm . With decreasing strain range, the data are more in line with prediction based on spacings of 0.2 and 0.1 μm . However, at the lowest strain range (0.15%), prediction overestimates life data. For strain ranges greater than 0.15%, fracture surfaces were predominantly intergranular with fatigue striations close to the specimen surface, thus confirming the model proposed for crack-cavity interaction during creep-fatigue failure.

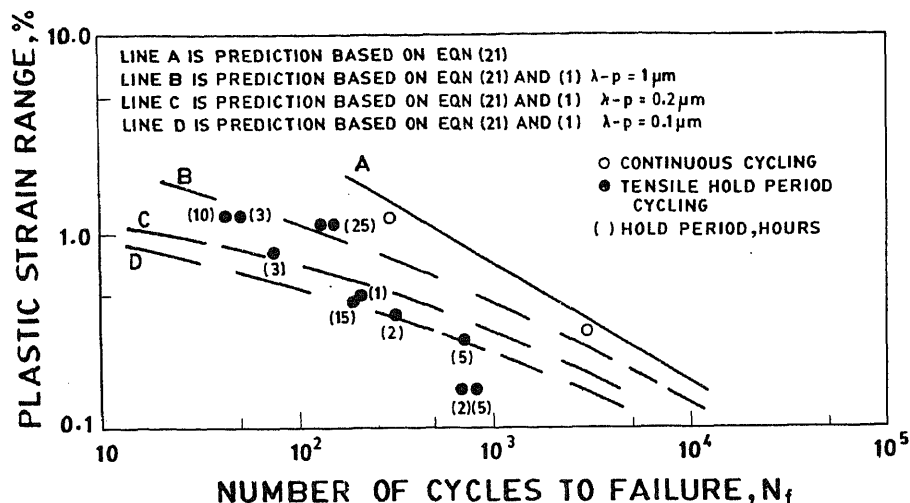


Figure 35. Comparison of predicted and experimental data of fatigue life in type 316 SS tested at 843 K with various tensile hold periods (Wareing 1988).

5.9 Cavitation model of Rie *et al*

A model has been proposed by Rie *et al* (1988) which takes into account the nucleation and growth of r -type cavities on the grain boundaries under creep-fatigue conditions. Fatigue life is defined by unstable crack advance; this happens if the crack tip opening displacement becomes equal to the spacing of the nucleated intergranular cavities, (1), which leads to unzipping of cavitated material by crack tip displacement field.

Suitable expressions for λ , p and δ have been derived based on physical models of cavity nucleation, their growth and crack-tip opening displacement due to creep-fatigue. A cycle-dependent cavity nucleation under cyclic creep and low cycle fatigue conditions with superimposed hold time is considered for evaluating the number of cavities at the grain boundaries perpendicular to load axis. Cavity spacing, λ is then determined from cavity density. While the nucleation of cavities is governed by deformation of the matrix, cavity growth is controlled by diffusion (Miller *et al* 1979). The crack-tip opening displacement includes an elastic term plus a contribution due to plastic deformation and thermally activated time-dependent processes (Ilschner 1982). The fatigue life is then estimated using criterion of the critical cavity configuration. The predicted and experimental fatigue lives are compared in figure 36. The method is capable of predicting lives even for conditions of long hold periods. This model is physically more reasonable compared to Tomkins & Wareing's (1977), model even though the failure criterion for unstable crack growth is same for both (1). In Tomkins and Wareing's model, arbitrary empirical values are assumed for $(\lambda - p)$ term to get the best fit for the experimental fatigue life, whereas, in the model of Rie *et al* (1988) suitable mathematical expressions for λ and p are derived based on theoretical consideration including contribution to δ due to creep.

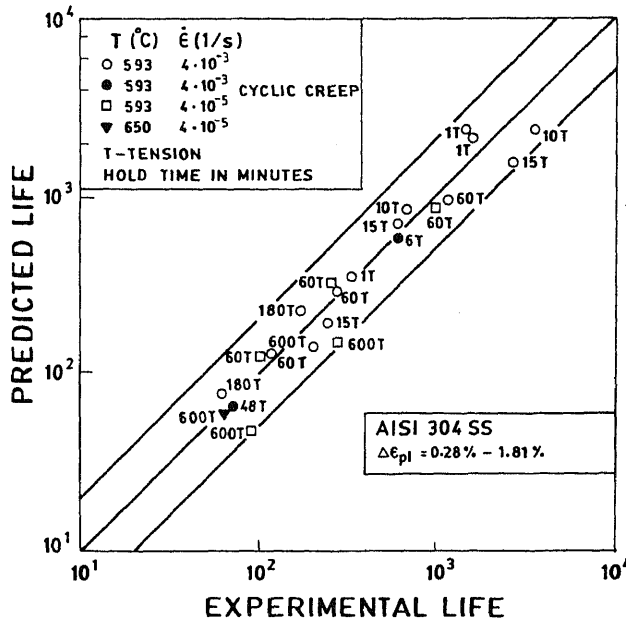


Figure 36. Comparison of experimental life and predicted life following the cavitation model proposed by Rie *et al* (1988) in AISI type 304 SS.

6. Concluding remarks

In this review, the complex nature of high temperature low cycle fatigue phenomenon has been highlighted. It is shown that various time-dependent phenomena like oxidation, dynamic strain ageing and creep interact with cyclic loading to determine life of high temperature components. The importance of a particular time-dependent process depends on the material, its microstructural condition and test parameters like strain range, frequency, position and duration of hold and temperature. Important life prediction techniques for components subjected to high temperature fatigue have been briefly reviewed. The applicability of these approaches is dependent on material and service parameters. A complete understanding of the different processes that occur during time-dependent low cycle fatigue is required before a unified approach applicable to different conditions could be developed.

Oxidation can cause severe degradation in fatigue life influencing both crack initiation and propagation processes. The influence of environment becomes more pronounced with lowering of frequency, decreasing strain amplitude and imposition of hold during fatigue testing. In tests on 304 SS, it was observed that as the frequency was lowered, crack initiation changed from transgranular (induced by slip band) to intergranular mode (induced by oxidation). From comparative tests in air and vacuum environments, it is seen that while life decreases with decrease in frequency in air environment, frequency has little effect in vacuum. Oxidation effects become more important at low strain amplitudes. Depending on the material under consideration, either tensile or compressive holds could be more damaging. This has been attributed to the behaviour of oxide formed during the hold period on subsequent loading. A variety of mechanisms have been identified for oxidation-fatigue interaction that contribute to deterioration in life.

Dynamic strain ageing (DSA) has been found to exert a significant influence on LCF behaviour at high temperatures. Occurrence of DSA manifests during total strain-controlled fatigue tests in the form of serrations in stress-strain hysteresis loops, increased cyclic work hardening, reduced plastic strain range and increase in response stress with decrease in strain rate or increase in temperature. Further, DSA causes localisation of plastic flow leading to enhanced planarity of slip and widely-spaced slip bands. Impingement of slip bands on grain boundaries causes increased grain boundary decohesion, leading to reduced fatigue life.

Unbalanced slow-fast cycling and tensile hold conditions introduce cavitation damage in addition to fatigue cracking. In creep-fatigue interaction, cyclic loading increases creep cavitation damage and cavitation has been found to enhance fatigue crack initiation and propagation. Rapid crack growth occurs under conditions where fatigue crack can link-up with grain boundary cavities. The susceptibility of a material to creep-fatigue damage is sensitively dependent on the creep ductility of the material. Creep brittle materials are particularly sensitive to interaction damage. While generally tensile holds are more detrimental to life in most of the materials, compressive holds have been found to be deleterious for nickel base alloys.

Several life prediction techniques have been proposed for components under creep-fatigue interaction. These range from purely empirical to mechanistic models based on microstructural observations. Best known among these techniques are linear damage summation rule, strain range partitioning, frequency modification approaches and models based on micromechanistic considerations like ductility exhaustion, damage rate and fatigue crack-cavity interaction. To be reliable, the techniques must take into account the physical damage processes occurring during creep-fatigue interaction. The understanding of creep-fatigue interaction behaviour would aid in extrapolation of short term laboratory data to long term service conditions, involving complex loading situations under operating conditions for a wide range of materials. While linear damage rule does not have a mechanistic basis, it is still the best available tool to design engineers, because of its simplicity. Refinements to the linear damage approach could be achieved by replacing creep damage term t/T_d by $\varepsilon/\varepsilon_r$, where ε is the accumulated creep strain and ε_r is the appropriate rupture ductility, thereby introducing deformation and fracture into failure criterion. Creep damage term $(\Delta\varepsilon_c/D_c)$ of the ductility exhaustion method could also be incorporated in the linear damage rule to predict realistic damage fraction due to creep rather than the term t/T_d . Fatigue crack-cavitation interaction models appear quite promising as they are based on sound mechanistic considerations. These would be particularly applicable to situations where extensive creep cavitation is encountered.

The authors gratefully acknowledge the collaboration of Dr M Valsan, A Veeramani and G Sasikala in the preparation of this paper.

References

- Abdel-Azim Metwally 1986 *Mechanical properties of some high temperature alloys (Alloy 800 H and Alloy 617)*. Ph D thesis, Cairo University
- Abdel-Raouf H, Plumtree A, Topper T H 1973 Effects of temperature and deformation rate on cyclic strength and fracture of low carbon steel. In *Cyclic stress-strain behaviour: analysis, experimentation and failure prediction*. ASTM STP 519, pp. 28-57

- Antunes V T A, Hancock P 1978 AGARD Conf. Proc. 243
- Asada Y, Mitsuhashi S 1980 Creep-fatigue interaction of type 304 stainless steel in air and vacuum. In *Int. Conf. Eng. Aspects of Creep* (Sheffield: Inst. Mech. Eng.) 1: 199–202
- ASME 1992 Boiler and Pressure Vessel Code, Section III, Case N47-14, *Class I components in elevated temperature service* (New York: ASME)
- Basquin O H 1910 The exponential law of endurance tests. *Proc. Am. Soc. Test. Mater.* 10: 625–630
- Berling J T, Conway J B 1970 Effect of hold time on the low cycle fatigue resistance of 304 stainless steel at 1200°F. *Proc. 1st Int. Conf. Pressure Vessel Tech. Part II* (New York: ASME) pp. 1233–1246
- Bhanu Sankara Rao K 1989 *Influence of metallurgical variables on low cycle fatigue behaviour of type 304 stainless steel*. Ph D thesis, University of Madras
- Bhanu Sankara Rao K, Mannan S L, Rodriguez P, Schuster H, Schiffrers H, Meurer H P, Nickel H 1988 Proc. Indo-German Seminar on Trends and Techniques in Modern Materials Research, IGCAR-Kalpakkam, Report No. 99c, pp. 81–92
- Bhanu Sankara Rao K, Meurer H P, Schuster H 1988 Creep-fatigue interaction of Inconel 617 at 950°C in simulated nuclear reactor helium. *Mater. Sci. Eng.* A104: 37–51
- Bhanu Sankara Rao K, Sandhya R, Mannan S L 1993 Creep-fatigue interaction behaviour of type 308 stainless steel weld metal and type 304 stainless steel base metal. *Int. J. Fatigue* 15: 221–229
- Bhanu Sankara Rao K, Schiffrers H, Schuster H 1986c (Unpublished) Research Work (KFA-Julich, Germany)
- Bhanu Sankara Rao K, Valsan M, Sandhya R, Mannan S L 1994 (Unpublished) Research Work, Kalpakkam
- Bhanu Sankara Rao K, Valsan M, Sandhya R, Mannan S L, Rodriguez P 1986a Grain size dependence of creep-fatigue-environment interaction in AISI 304 stainless steel. *Int. Conf. on Creep* (Tokyo: JSME, Inst. Mech. Eng. ASME, ASTM) pp. 77–83
- Bhanu Sankara Rao K, Valsan M, Sandhya R, Mannan S L, Rodriguez P 1986b Dynamic strain ageing effects in low cycle fatigue. *High Temp. Mater. Proc.* 7: 171–177
- Bhanu Sankara Rao K, Valsan M, Sandhya R, Mannan S L, Rodriguez P 1989 Grain size dependence of dynamic strain ageing during low cycle fatigue in type 304 stainless steel, *7th Int. Conf. Fracture, Adv. in Fracture Research*, (eds) K Salama, K Ravi Chandar, D M R Taplin, P Rama Rao (London: Pergamon) 2: 1037–1044
- Bhanu Sankara Rao K, Valsan M, Sandhya R, Mannan S L, Rodriguez P 1990 Manifestations of dynamic strain ageing during low cycle fatigue of type 304 stainless steel. *Metall. Mater. Proc.* 2: 17–36
- Bhanu Sankara Rao K, Valsan M, Sandhya R, Mannan S L, Rodriguez P 1991 Synergistic interactions during high temperature fatigue of type 304 stainless steel – grain size dependence. *Trans. Indian Inst. Met.* 44: 255–270
- Booker M K, Majumdar S 1982 Specialists Meeting on “Structural material data” held at the Power Reactor and Nuclear Fuel Development Corporation, Tokyo, Japan
- Bressers J 1985 Fatigue and microstructure. *Proc. Int. Conf. on High Temperature Alloys and their Exploitable Potential* (eds) J B Marriott, M Merz, J Nihoul, J Ward (London: Elsevier) pp. 385–410
- Bressers J, De Cat R, Fenske E 1983 Crack initiation and growth in high temperature low cycle fatigue. Cost 501, III Final Report EVR 8808 EN
- Bressers J, Roth M 1983 The effect of time-dependent processes in high temperature low cycle fatigue endurance of PM Astroloy. *Proc. of ASME Int. Conf. on Advances in Life Prediction Methods* (eds) D A Woodford, J R Whitehead (New York: ASME) pp. 85–92
- Bressers J, Verheghe B 1981 *Res. Mech. Lett.* 1: 55
- Bricknell R H, Woodford D A 1981 The embrittlement of nickel following high temperature air exposure. *Metall. Trans.* A12: 425–433
- Brinkman C R 1985 High temperature time-dependent fatigue behaviour of several engineering structural alloys. *Int. Metall. Rev.* 30: 235–258
- Brinkman C R, Korth G E, Beeston J M 1974 Comparison of the strain-controlled low cycle fatigue behaviour of stainless type 304/308 weld and base metal. *Int. Conf. on Creep and Fatigue in Elevated Temperature Applications* (Sheffield: Inst. Mech. Eng.) paper C218-73, pp. 218-1–218-11
- Brinkman C R, Korth G E, Hobbings R R 1972 Estimates of creep-fatigue interaction in irradiated and unirradiated austenitic stainless steels. *Nucl. Technol.* 16: 297–307

- Challenger K D, Miller A K, Brinkman C R 1981 An explanation for the effects of hold periods on the elevated temperature fatigue behaviour of 2.25 Cr-1 Mo steel. *Trans. ASME, J. Eng. Mater. Technol.* 103: 7-14
- Choudhary B K, Bhanu Sankara Rao K, Mannan S L 1991a High temperature low cycle fatigue properties of a thick-section 9 wt.% Cr-1 wt.% Mo ferritic steel forging. *Mater. Sci. Eng.* A148: 267-278
- Choudhary B K, Bhanu Sankara Rao K, Mannan S L 1991b Application of 9 Cr-1 Mo steel low cycle fatigue data in the design of fast reactor steam generator thick components. *Proc. Int. Symp. on Fatigue and Fracture in Steel and Concrete Struct.* (eds) A G Madhava Rao, T V S R Appa Rao (New Delhi: Oxford & IBH) 2: 883-894
- Coffin L F 1954 A study of the effects of cyclic thermal stresses on a ductile metal. *Trans. Am. Soc. Mech. Eng.* 76: 931-950
- Coffin L F 1963 *Trans. Am. Soc. Mech. Eng.* 56: 339
- Coffin L F 1969 Predictive parameters and their application to high temperature, low cycle fatigue fracture. *Proc. of 2nd Int. Conf. on Fracture.* (ed.) P L Pratt (London: Chapman and Hall) pp. 643-654
- Coffin L F 1971 The effect of frequency on the cyclic strain and low cycle fatigue behaviour of cast Udimet 500 at elevated temperatures. *Metall. Trans.* 2: 3105-3113
- Coffin L F 1972a The effect of high vacuum on the low cycle fatigue law. *Metall. Trans.* 3: 1777-1788
- Coffin L F Jr. 1972b Corrosion fatigue. *Proc. Int. Conf. on Fatigue Chemistry, Mechanics and Microstructure*, NACE-2, Houston, Texas (National Association of Corrosion Engineers) pp. 590-600
- Coffin L F 1973a Fatigue at high temperature. *Fatigue at elevated temperature* (eds) A E Carden, A J McEvily, C H Wells ASTM STP 520, pp. 5-34
- Coffin L F 1973b *Proc. Int. Conf. Fatigue 3* (Munich) p. 441
- Coffin L F 1976 The concept of frequency separation in life prediction for time-dependent fatigue. *Symp. on Creep-Fatigue Interaction*. ASME-MPC-3, pp. 349-363
- Coffin L F 1977 The concept of frequency separation in life prediction for time-dependent fatigue. General Electric, Report No. 76 CRD269
- Coffin L F 1979 *Proc. DVC Symp. of Low Cycle Fatigue Strength and Elasto-plastic behaviour of materials* Stuttgart (eds) K T Rie, E Hamback (Deutscher Verband for material prufung) pp. 73-82
- Conway J B 1968 General electric nuclear material and propulsion operation. Report No. 1004, Cincinnati, Ohio
- Conway J B, Stenz R H, Berling J T 1975 Fatigue, tensile and relaxation behaviour of stainless steels. TID-26135, US Atomic Energy Commission Report
- Cook R H, Skelton R P 1979 *Int. Metall. Rev.* 19: 199
- Cottrell A H 1953 *Philos. Mag.* 44: 829
- Duan Z, He J, Ning Y, Dong Z 1988 Strain energy partitioning approach and its application to low cycle fatigue life prediction for some heat resistant alloys. In *Low cycle fatigue* (eds) H D Solomon, G R Halford, L R Kaisand, B N Leis ASTM STP 942, pp. 1133-1143
- Duquette D J 1979 A mechanistic understanding of the effects of environment on fatigue crack initiation and propagation. *Proc. Int. Conf. on Environment Sensitive Fracture of Engineering Materials* (ed.) Z A Forouli (AIME) pp. 521-537
- Dyson B F 1982 An analysis of carbon/oxygen gas bubble formation in some nickel alloys. *Acta Metall.* 30: 1639-1646
- Eckel J F 1951 The influence of frequency on the repeated bending life of acid lead. *Proc. Am. Soc. Test. Mater.* 51: 745-760
- Edmunds H G, White D J 1966 Observations of the effect of creep relaxation on high strain fatigue. *J. Mech. Eng. Sci.* 8: 310-321
- Ellison E G, Patterson A T F 1976 Creep-fatigue interaction in a 1 Cr-Mo-V steel. *Proc. Inst. Mech. Eng.* 190: 321-350
- Ericsson T 1979 *Can. Metall. Q.* 18: 177
- Essman U, Mughrabi H 1979 Annihilation of dislocations during tensile and cyclic deformation and limits of dislocation densities. *Philos. Mag.* A40: 731-756
- Floreen S, Raj R 1985 Environmental effects in nickel base alloys. In *Flow and fracture at elevated temperatures* (ed.) R Rishi (Metals Park, OH: ASM) chap. 12 pp. 383-405

- Frandsen J O, Paton N E, Marcus H L 1974 The influence of gaseous environment on fatigue crack growth in a nickel-copper alloy. *Metall. Trans.* A5: 1665-1661
- Fujita F E 1958 Dislocation theory of fracture of crystals. *Acta Metall.* 6: 543-551
- Gell M, Leverant G R 1973 Mechanisms of high temperature fatigue. In *Fatigue at elevated temperatures* (eds) A E Carden, A J McEvily, C H Wells ASTM STP 520, pp. 37-67
- Halford G R, Hirschberg M H, Manson S S 1972 Temperature effects on the strainrange partitioning approach for creep-fatigue analysis. NASA TM X-68023
- Halford G R, Saltsman J F 1983 Strainrange partitioning - a total strain range version. NASA TM-83023
- Halford G R, Saltsman J F, Hirschberg M H 1977 Ductility normalized strainrange partitioning life relations for creep-fatigue life predictions. NASA TM-73737
- Hayes R W, Hayes W C 1984 A proposed model for the disappearance of serrated flow in two Fe-alloys. *Acta Metall.* 32: 259-267
- Hirakawa K, Tokiwasa K, Toyama K 1978 *J. Soc. Mater. Sci. Jpn.* 27: 948
- Hirschberg M H, Halford G R 1976, Use of strainrange partitioning to predict high temperature, low cycle fatigue life NASA TN D-8072
- Hoffelner W, Melton K N, Wutbrich C 1983 On life-time prediction with the strainrange partitioning method. *Fatigue Eng. Mater. Struct.* 6: 77-87
- Ilshner B 1982 *Mechanical and thermal behaviour of metallic materials* (Bologna: Soc. Ital. Fis.) p. 188
- James L A, Knecht R L 1975 *Metall. Trans.* A6: 109
- Jianting G, Ranuci D, Picco E, Strocchi P M 1984 Effect of environment on the low cycle fatigue behaviour of cast nickel base superalloy IN738LC. *Int. J. Fatigue* 6: 95-99
- Johnson E W, Johnson H H 1965 *Trans. Metall. Soc. AIME* 233: 1332
- Kalluri S, Manson S S 1984 Time dependency of strainrange partitioning life relationships. NASA Contractor Report-174946
- Kanazawa K 1978 *Trans. Nat. Res. Inst. Met.* 20: 321
- Kanazawa K, Yamaguchi K, Nishijima S 1988 Mapping of low cycle fatigue mechanisms at elevated temperatures for an austenitic stainless steel. *Low Cycle Fatigue* (eds) H D Solomon, G R Halford, L R Kaisand, B N Leis ASTM STP 942, pp. 519-530
- Kanazawa K, Yoshida S 1975 Effect of temperature and strain rate on the high temperature low cycle fatigue behaviour of austenitic stainless steels. In *Creep and fatigue in elevated temperature applications* (London: Inst. Mech. Eng.) 1: pp. 226-1-226-10
- Kempf B, Bothe K, Gerold V 1987 Damage mechanisms under creep-fatigue conditions in Alloy 800H. In *Proc. 2nd Int. Conf. on Elasto-Plastic Behaviour of Materials*, (ed.) K T Rie (New York: Elsevier) pp. 271-276
- Kubin L P, Estrin Y 1990 Evolution of dislocation densities and the critical conditions for the Portevin-Le Chatelier effect. *Acta Metall.* 38: 697-708
- Leven M M 1973 Interaction of creep and fatigue for a rotor steel. *Exp. Mech.* 13: 353-372
- Lloyd G J, Wareing J 1981 Life-prediction methods for combined creep-fatigue endurance. *Metall. Technol.* 8: 297-304
- Lord D C, Coffin L F 1973 Low cycle fatigue hold time behaviour of cast Rene80. *Metall. Trans.* 4: 1647-1654
- Maiya P S, Majumdar S 1977 Elevated temperature low cycle fatigue behaviour of different heats of type 304 stainless steel. *Metall. Trans.* A8: 1651-1660
- Majumdar S, Maiya P S 1976a A damage equation for creep-fatigue interaction. In *ASME-MPC Symp. on Creep-Fatigue Interaction, MPC-3* (New York: ASME) pp. 323-335
- Majumdar S, Maiya P S 1976b *Proc. 2nd Int. Conf. on Mechanical Behaviour of Materials* (Metals Park, OH: ASM) p. 924
- Majumdar S, Maiya P S 1979 Creep-fatigue interaction in an austenitic stainless steel. *Can. Metall. Q.* 18: 57-64
- Mannan S L 1981 *Influence of grain size on flow and fracture in AISI type 316 stainless steel*. Ph D thesis, Indian Institute of Science, Bangalore
- Mannan S L 1993 Role of dynamic strain ageing in low cycle fatigue. *Bull. Mater. Sci.* 16: 561-582
- Manson S S 1954 Behaviour of materials under conditions of thermal stresses. Nat. Adv. Comm. Aero, Technical Note 2933
- Manson S S 1965 Fatigue: A complex subject - some simple approximations. *Exp. Mech.* 5: 157-190

- Manson S S, Halford G R 1967 *Proc. of Int. Conf. on Thermal and High Strain Fatigue* (London: Met. Metall. Trust) p. 15^d
- Manson S S, Halford G R 1968 *Trans. Am. Soc. Metall.* 61: 94
- Manson S S, Halford G R, Hirschberg M H 1971 Creep-fatigue analysis by strain-range partitioning. NASA TM X-67838
- Manson S S, Halford G R, Oldrieve R E 1984 Report NASA, TM-83473, Lewis Research Center, Cleveland, OH
- Marriott D L 1992 Current trends in high temperature design. *Int. J. Pressure Vessels Piping* 50: 13-35
- Marshall P 1983 *Fatigue at high temperature* (ed.) R P Skelton (London: Elsevier) p. 259
- McCormick P G 1972 A model for the Portevin-Le Chatelier effect in substitutional alloys. *Acta Metall.* 20: 351-354
- McMahon C J, Coffin L F 1970 Mechanisms of damage and fracture in high temperature low cycle fatigue of a cast nickel base superalloy. *Metall. Trans.* 1: 3443-3450
- Meurer H P, Breitling H, Grosser E D 1984 Creep-fatigue evaluation of austenitic stainless steel for SNR 300 - present status and future efforts. *Nucl. Eng. Design* 83: 355-366
- Miller D A, Hamm C D, Philips J L 1982 A mechanistic approach to the prediction of creep-dominated failure during simultaneous creep-fatigue. *Mater. Sci. Eng.* 53: 233-244
- Miller D A, Mohamed F A, Langdon T G 1979 An analysis of cavitation failure incorporating cavity nucleation with strain. *Mater. Sci. Eng.* 40: 159-166
- Miller D A, Priest R H, Ellison E G 1984 A review of material response and life prediction techniques under fatigue-creep loading conditions. *High Temp. Mater. Proc.* 6: 155-194
- Miner M A 1945 *J. Appl. Mech.* A12: 159
- Mulford R A, Kocks U F 1979 New observation on the mechanisms of dynamic strain ageing and jerky flow. *Acta Metall.* 27: 1125-1134
- Nazmy M Y 1983a High temperature low cycle fatigue of IN738 and application of strain range partitioning. *Metall. Trans.* A14: 449-461
- Nazmy M Y 1983b Effect of multiple crack propagation on the high temperature low cycle fatigue of a cast nickel base alloy. *Scr. Metall.* 17: 491-494
- Nich T G, Nix W D 1981 Embrittlement of Cu due to segregation of oxygen to grain boundaries. *Metall. Trans.* A12: 893-901
- Ostergren W J 1976a Correlation of hold time effects in elevated temperature LCF using a frequency modified damage function. *Symp. on 'Creep-Fatigue Interaction* (ed.) R M Curran (New York: ASME-MPC) pp. 179-202
- Ostergren W J 1976b A damage function and associated failure equations for predicting hold time and frequency effects in elevated temperature low cycle fatigue. *J. Test. Eval.* 4: 327-339
- Plumbridge W J, Ellison E G 1987 Low cycle fatigue behaviour of superalloy blade materials at elevated temperature. *Mater. Sci. Technol.* 3: 706-715
- Priest R H, Beauchamp D J, Ellison E G 1983 Damage during creep-fatigue. In *Proc. Conf. Advances in Life Prediction Methods* (Schenectady, NY: Am. Soc. Metall.) pp. 115-121
- Priest R H, Ellison E G 1980 Estimation of cyclic creep damage by strain and strain rate considerations. In *Proc. Int. Conf. on Eng. aspects of creep* (Sheffield: Inst. Mech. Eng.) pp. 185-192
- Priest R H, Ellison E G 1981 A combined deformation map - ductility exhaustion approach to creep-fatigue analysis. *Mater. Sci. Eng.* 49: 7-17
- Quesnel D J, Tsou J C 1983 A quantitative approach to cell shuttling model. *Mater. Sci. Eng.* 59: 91-98
- Raj R (ed.) 1985 Mechanisms of creep-fatigue interaction. In *Flow and fracture at elevated temperatures* (Metals Park, OH: ASM) pp. 215-249
- Reger M, Remy L 1986 *High temperature fatigue*. Journees, Internationales de Printemps, Commission de Fatigue, SFM, Paris
- Reuchet J, Remy L 1983 High temperature LCF of MAR-M 509 superalloy - I: The influence of temperature on the LCF behaviour from 20 to 1100°C. *Mater. Sci. Eng.* 58: 19-32
- Rie K T, Schmidt R M, Ilschner B, Nam S W 1988 A model for predicting low cycle fatigue life under creep-fatigue interaction. *Low cycle fatigue* (eds) H D Solomon, G R Halford, L R Kaisand, B N Leis ASTM STP 942, pp. 313-328
- Robinson E L 1952 *Trans. Am. Soc. Mech. Eng.* 74: 777

- Rodriguez P 1984 Serrated plastic flow. *Bull. Mater. Sci.* 6: 653–663
- Rodriguez P 1993 Mechanistic approach to low cycle fatigue life prediction. Prof. T Ramachandran Lecture Series 1993 KREC, Suratkal
- Rodriguez P, Bhanu Sankara Rao K 1993 Nucleation and growth of cracks and cavities under creep-fatigue interaction. *Prog. Mater. Sci.* 37: 403–480
- Rodriguez P, Mannan S L, Bhanu Sankara Rao K 1989 Life prediction methods for creep-fatigue conditions. *Trans. Indian Inst. Met.* 42: S25–S43
- Saltsman J F, Halford G R 1985 An update of the total-strain version of SRP, NASA TP-2499
- Sandhya R, Bhanu Sankara Rao K, Mannan S L 1989 Low cycle fatigue and creep-fatigue interaction of Bainitic 2.25 Cr–1 Mo steel. *Trans. Indian Inst. Met.* 42: S217–S227
- Scarlin R B 1977 Effects of loading frequency and environment on high temperature fatigue crack growth in nickel base alloys, ICF-4 (ed.) D M R Taplin (New York: Pergamon) 1: 849–857
- Schmitt R, Scheibe W, Anderko K 1979 Creep-fatigue interaction on 1-4948 austenitic stainless steel, including irradiation effects. *Proc. SMIRT-5 Berlin*, Paper No. L 12/7
- Shen H, Podlasek S E, Kramer K I 1966 Effect of vacuum on the fatigue life of aluminium. *Acta Metall.* 14: 341–346
- Sidey D, Coffin L F Jr 1979 Low cycle fatigue damage mechanisms at high temperature. In *Proc. Symp. Fatigue mechanisms* (ed.) J T Fong ASTM STP 675, pp. 528–568
- Skelton R P 1978 Environmental crack growth in 0.5 Cr–Mo–V steel during isothermal high strain fatigue and temperature cycling. *Mater. Sci. Eng.* 35: 287–298
- Sleeswyk A W 1958 Slow strain hardening of ingot iron. *Acta Metall.* 6: 598–603
- Smith H H, Shahinian P, Achter M R 1969 *Trans. Metall. Soc. AIME* 245: 947
- Solomon H D, Coffin L F 1973 Effects of frequency and environment on fatigue crack growth in A286 at 1100°F. In *Fatigue at elevated temperatures* ASTM STP 520, pp. 112–122
- Srinivasan V S, Sandhya R, Bhanu Sankara Rao K, Mannan S L, Raghavan K S 1991 Effects of temperature on the low cycle fatigue behaviour of nitrogen alloyed type 316L stainless steel. *Int. J. Fatigue* 13: 471
- Swindeman R W, Strizak J P 1982 ORNL TN-8392, Oak Ridge, TN
- Taplin D M R, Tang N Y, Liepholz H H E 1984 On fatigue-creep-environment interaction and the feasibility of fatigue maps. *Proc. 6th Int. Conf. on Fracture. Advances in Fracture Research* (eds) S R Valluri, D M R Taplin, P Rama Rao, J F Knott, R Dubey, vol 1: pp. 127–142
- Taplin D M R, Topper T H, Tang N Y 1983 *Proc. ICF Int. Symp. on Fracture Mechanics*, Beijing
- Teranishi H, McEvily A J 1980 On fatigue crack initiation and propagation at elevated temperature. *Proc. of 5th Int. Conf. on Fracture, ICF5, Adv. Fracture Research* (ed.) O Francois (Cannes, France: Pergamon) 5: 2439–2447
- Thompson N, Wadsworth M J, Louat N 1955 The origin of fatigue fracture in copper. *Philos. Mag.* 1: 113–126
- Tomkins B 1968 Fatigue crack propagation – An analysis. *Philos. Mag.* 18: 1041–1066
- Tomkins B 1975 The development of fatigue crack propagation models for engineering applications at elevated temperatures. *Trans ASME, J. Eng. Mater. Technol.* 97: 289–297
- Tomkins B 1983 Life prediction at elevated temperatures. *Trans ASME, J. Pressure Vessel Technol.* 105: 269–272
- Tomkins B, Wareing J 1977 Elevated temperature fatigue interaction in engineering materials. *Metall. Sci.* 11: 414–424
- Tsuzaki K, Hori T, Maki T, Tanura I 1983 Dynamic strain ageing during fatigue deformation in type 304 austenitic stainless steel. *Mater. Sci. Eng.* 61: 247–260
- Valsan M 1991 *Some aspects of deformation and fracture in low cycle fatigue of a Nimonic PE-16 Superalloy*. Ph D thesis, Indian Institute of Science, Bangalore
- Valsan M, Choudhary B K, Bhanu Sankara Rao K, Mannan S L, Rodriguez P 1988 Internal Report MDD/71-4/88/01, Kalpakkam
- Valsan M, Parameswaran P, Bhanu Sankara Rao K, Vijayalakshmi M, Mannan S L, Shastry D H 1992 High temperature low cycle fatigue behaviour of a NIMONIC PE-16 superalloy – Correlation with deformation and fracture. *Metall. Trans.* A23: 1751–1761
- Valsan M, Sastry D H, Bhanu Sankara Rao K, Mannan S L 1994 Effect of strain rate on the high temperature low cycle fatigue properties of a Nimonic PE-16 Superalloy. *Metall. Mater. Trans.* A25: 159–171

- Van den Beukel A, Kocks U F 1982 The strain dependence of static and dynamic strain ageing. *Acta Metall.* 30: 1027-1041
- Venkadesan S 1991 *Development and characterisation of the tensile deformation behaviour of a titanium modified austenitic stainless steel*. Ph D thesis, Indian Institute of Technology, Madras
- Viswanathan R 1989 *Damage mechanisms and life assessment of high temperature components* (Metals Park, OH: ASM) chap. 4, pp. 111-182
- Wareing J 1975 Fatigue crack growth in a type 316 stainless steel and a 20 pct Cr/25 pct Ni/Nb stainless steel at elevated temperatures. *Metall. Trans.* A6: 1367-1377
- Wareing J 1977 Creep-fatigue interaction in austenitic stainless steels. *Metall. Trans.* A8: 711-721
- Wareing J 1981 Creep-fatigue behaviour of four casts of type 316 stainless steel. *Fatigue Eng. Mater. Struct.* 4: 131-145
- Wareing J 1988 Influence of material microstructure on low cycle fatigue failure, with particular reference to austenitic steel. In *Low cycle fatigue* (eds) H D Solomon, G R Halford, L R Kaisand and B N Leis ASTM STP 942, pp. 711-727
- Wareing J, Vaughan H G, Tomkins B 1980 Mechanisms of elevated temperature fatigue and failure in type 316 stainless steel. In *Creep-Fatigue-Environment Interaction Proc. TMS-AIME Symp. Fall Meeting* (eds) R M Pefloux, N S Stoloff pp. 129-150
- Wells C H, Sullivan C P 1969 Interactions between creep and low cycle fatigue in Udimet 700 at 1400°F. In *Fatigue at high temperature*, ASTM STP 459, pp. 59-74
- Wilson D V, Tromans J K 1970 Effects of strain ageing on fatigue damage in low carbon steel. *Acta Metall.* 18: 1197-1208
- Wood D S, Baldwin A B, Williamson K 1979 The creep/fatigue behaviour of 9 Cr steel at 525°C. Proc. IAEA Meet on 'Time and Load Dependent Degradation of Pressure Boundary Materials', Report IWG-RRPC-79/2 (Innsbruck), pp. 88-101
- Wood D S, Wynn J, Austin C, Green J G 1988 A ductility exhaustion evaluation of some long term creep/fatigue tests on austenitic steel. *Fatigue Fracture Eng. Mater. Struct.* 11: 371-381
- Yamaguchi K, Kanazawa K, Yoshida S 1978 Crack propagation in low cycle fatigue of type 316 stainless steel at temperatures below 600°C observed by scanning electron microscopy. *Mater. Sci. Eng.* 33: 175-181
- Yoo M H, Trinkaus H 1983 Crack and cavity nucleation at interfaces during creep. *Metall. Trans.* A14: 547-593

Stress corrosion cracking and component failure: Causes and prevention

U K CHATTERJEE

Department of Metallurgical & Materials Engineering, Indian Institute of Technology, Kharagpur 721 302, India

Abstract. The century-old problem of stress corrosion cracking (SCC) in metals and alloys has been reviewed highlighting the metallurgical factors like grain boundary precipitation and grain boundary segregation contributing to the process, the electrochemical aspects of the phenomenon and the current knowledge of the mechanisms which can be broadly classified as dissolution-based and cleavage-based models. The introduction covers some field examples of SCC. SCC test methods and preventive measures for SCC have also been discussed.

Keywords. Stress corrosion cracking; SCC tests; grain boundary precipitation, grain boundary segregation; repassivation; dissolution mechanisms; cleavage mechanisms; preventive measures.

1. Introduction

Stress corrosion cracking (SCC) may be defined as the delayed failure of alloys by cracking when exposed to certain environments in the presence of a static tensile stress. The importance of a conjoint action of corrosion and stress as well as the nature of stress is reflected in the definition. The stress level at which the failure occurs is well below the stress required for a mechanical failure in the absence of corrosion. Again, corrosion alone in the absence of stress does not produce cracking. The stress can be applied or residual. A compressive stress does not cause stress corrosion cracking, rather it is used to prevent this phenomenon. Environmentally induced crack propagation due to cyclic loading is not stress corrosion cracking, but is defined as corrosion fatigue. Environmentally induced cracking in the presence of stress is also encountered in non-metallic materials, e.g. glass and alumina in water or organic polymers in polar solvents. The discussion in the present paper will, however, be confined to SCC in metallic materials.

The earliest report on SCC is probably the occurrence of 'season cracking' in brass cartridge cases in ammonia-bearing environments in the beginning of the present century. Caustic embrittlement of riveted steel boiler plates is another classical example of SCC encountered in the early steam-driven locomotives. The causes of SCC in this case were the residual stress developed due to riveting operations and sodium

hydroxide present in these areas. Many alloy-environment combinations leading to SCC were discovered with the passage of time. It was recognized with concern that almost all alloys of engineering interest were susceptible to this type of catastrophic degradation in some environment or other, the only silver lining being that all alloys were not susceptible to SCC in all the environments. It was also noticed that pure metals were immune to SCC in the environments in which their alloys showed ready and rapid cracking. A list of alloy-environment systems exhibiting SCC is presented in table 1.

It should be remembered that the table is not exhaustive; newer combinations and newer environments causing SCC in a particular alloy are being regularly discovered and added to this list. The so-called 'specificity' of the environment with respect to an alloy is no longer true. The immunity of pure metals to SCC is also no longer valid. Nevertheless, still only a small number of corrodents cause SCC in a particular alloy and SCC of a pure metal is still confined to laboratory tests.

Practical examples of SCC in engineering alloys, on the other hand, are abundant and varied. Intensive SCC was observed in a high-pressure autoclave made of 18–8 stainless steel (Fontana & Greene 1967). The failure in service took place in a matter of hours and was traced to the build up of chloride concentration on the outside surface because of evaporation of the water used for cooling which originally contained only a negligible amount of chloride. Yet another interesting example of SCC was the development of longitudinal cracks in a cold-drawn brass tube which had its origin in the bird droppings that provided the ammonia necessary for corrosion (Barer & Peters 1970). The occurrence of SCC arising from chloride-contaminated moisture has been reported in high-strength aluminium alloy components in low-flying British military aircraft which led to the ban on the use of the material till a solution was found through cladding of the material with pure aluminium. Carbonate–bicarbonate environments have been identified as the probable cause of cracking in natural gas transmission steel pipe lines (Parkins 1980).

Numerous cases of SCC in chemical process plants and power-generation plants have been reported in the literature. Oxygenated pure or impure high temperature water has caused failures in steam generator shells made of carbon or low-alloy steels (Congleton *et al* 1985). Extensive failures have taken place in austenitic 18 Mn–4 Cr steel rotor end-retaining rings in contamination with oxygenated high temperature water (Viswanathan 1982). SCC of austenitic stainless steel pipes caused by the same environment in boiling water reactors (BWR) has cost the world's nuclear power industries as much as 10 billion dollars (Stachle 1990). SCC of nickel based alloy 600 in reducing high temperature water and supercritical steam in pressurized water reactors (PWR) has been reported (Coriou *et al* 1969). Room temperature cracking of sensitized austenitic stainless steels produced by polythionic acid was first experienced in catalytic reformers used in the petroleum industry (Dravnicks & Samans 1957). Titanium alloys, so reputed for their excellent corrosion resistance in some of the most aggressive media, are known to fail by SCC in many environments including red fuming nitric acid (RFNA), hot molten salts, methanol, liquid dinitrogen tetroxide (N_2O_4) and salt water (Blackburn *et al* 1972). Hot salt SCC of titanium alloys was first discovered at fingerprints on creep test specimens (Jackson & Boyd 1966). Dinitrogen tetroxide is used as an oxidant in rocket engines. Interestingly, SCC in this environment is inhibited by the traces of NO.

Stress corrosion cracking thus affects the performance of metallic components, whether mundane or exotic, in environments of diverse chemical nature, some of which

Table 1. Alloy-environment combinations exhibiting stress corrosion cracking.

Alloy	Environment	Alloy	Environment
Aluminium alloys	Air with water vapour Potable water Seawater NaCl solutions NaCl-H ₂ O ₂ solutions	Stainless steels Austenitic	Hot acid chloride solutions NaCl-H ₂ O ₂ solutions
			NaOH-H ₂ S solutions Seawater Concentrated caustic solutions Neutral halides-Br ⁻ , I ⁻ , F ⁻
Carbon steels	Caustic NaOH solutions Calcium, ammonium and sodium nitrate solutions	Austenitic (sensitized)	Polythionic acids (H ₂ S _n O ₆) Sulphurous acid Pressurized hot water containing 2 ppm dissolved oxygen
	HCN solutions Acidified H ₂ S solutions Anhydrous liquid ammonia Carbonate/bicarbonate CO/CO ₂ solutions Seawater	Ferritic	H ₂ S, NH ₄ Cl, NH ₄ NO ₃ , hypochlorite solutions
		Martensitic	Caustic NaOH solutions
Copper alloys	Ammoniacal solutions Amines Nitrites	Titanium alloys	Red fuming nitric acid Hot salts, molten salts
Nickel alloys	Caustic alkaline solutions High-temperature chloride solutions High purity steam Acidic fluoride solutions		N ₂ O ₄ Metanol halide

are apparently innocent. No wonder then that the last four decades witnessed a spurt of research activities in this area for an understanding of the phenomenon as well as for its prevention. A commendable review of activities in the period 1965–1990 has been made by Newman & Proctor (1990).

2. General features of SCC

The following features are generally common to SCC:

- (1) Pure metals are almost immune to cracking in environments where their alloys crack readily.
- (2) The existence of a tensile stress, either applied or present as a residual stress, is essential for the cracking process.
- (3) SCC for a given alloy usually occurs more readily in a rather specific environment.
- (4) The microscopic appearance of stress corrosion cracks, which are either intergranular or transgranular (figures 1 & 2), is that of a brittle fracture although the metal itself may still be quite ductile in mechanical test. The brittle nature of fracture is quite evident in SEM fractography (figure 3).
- (5) In order for SCC to occur a threshold stress or stress intensity must be exceeded.

- (6) SCC, in general, can be accelerated by the application of anodic currents and can be stopped by the application of cathodic currents showing that the process is, at least partly, electrochemical.

Stress corrosion cracking is a complicated subject. It is an outcome of material–environment–stress interaction. Metallurgical and electrochemical factors and also the manner in which a specimen is stressed greatly influence the process. Some of them will be discussed in the subsequent sections. Before that, it will be useful to introduce the various SCC testing methods and the parameters used for ascertaining the susceptibility to SCC.

3. Testing methods

The SCC testing methods can be categorized as below.

- (1) Constant-strain or constant-deformation tests;
- (2) tests on statically loaded smooth samples;
- (3) tests on statically loaded precracked samples;
- (4) slow strain-rate testing (SSRT).

Constant-strain tests make use of U-bend, C-ring, bent-beam specimens or tensile specimens in a small loading frame with nuts on the threaded ends of the specimen. Although the stress distribution within the specimen cannot be precisely known and the stress conditions are difficult to duplicate from specimen to specimen, U-bend specimens have found wide use in evaluating qualitatively the resistance of various alloys to various solution conditions. Time to failure, t_f , is the parameter used to measure the resistance to SCC.

Tests on statically loaded smooth samples are usually conducted at various fixed stress levels, and the time to failure is measured. A dead-weight load is hung from one end of the specimen, directly or by means of a lever system. Most of the constant deformation specimens can be adapted to constant load by adding a spring in the device. Figure 4 illustrates the typical results obtained from this type of test. A threshold stress below which the time of failure approaches infinity is encountered in some systems, whereas in other systems it is not observed. Time to failure, t_f , essentially is made up of two components: the time for crack initiation (t_i), and the time for crack propagation, t_p , so that,

$$t_i + t_p = t_f.$$

Different metallurgical and electrochemical variables do affect t_f , but it is difficult, if not impossible, to ascertain these effects separately on t_i and t_p . In smooth specimens usually $t_i \gg t_p$, whereas in practical situations a pit or a surface roughness feature acts as an already initiated crack and the question of its propagation under different variables assumes more importance. The use of pre-cracked specimens, notched or fatigue-precracked, and the application of linear elastic fracture mechanics (LEFM) technique is stress corrosion crack propagation have evolved as a consequence.

Tests on statically loaded precracked samples are usually conducted with a constant applied load and the velocity of crack propagation, da/dt , as a function of stress-intensity factor, k , is measured. The value of k is calculated from $k = \sigma C^{1/2}$ where σ is the applied

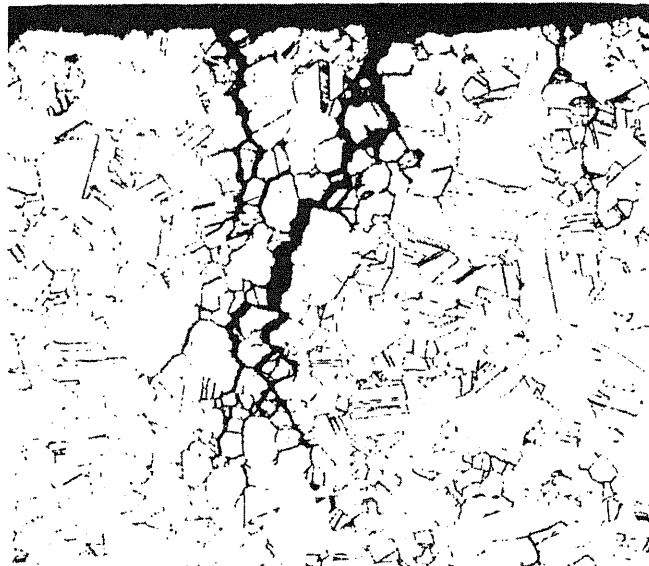


Figure 1. Intergranular stress corrosion cracks in 70-30 brass exposed to ammoniacal solution.

stress and C is the crack length. Figure 5 gives the schematic representation of a typical da/dt versus k plot. Three regions in the plot are identified as stages I, II and III. No crack propagation is observed below some threshold stress-intensity level, k_{ISCC} . In stage I, the crack-propagation rate increases rapidly with the stress-intensity factor. In



Figure 2. Transgranular stress corrosion cracking in type 304 austenitic stainless steel in boiling $MgCl_2$ solution.

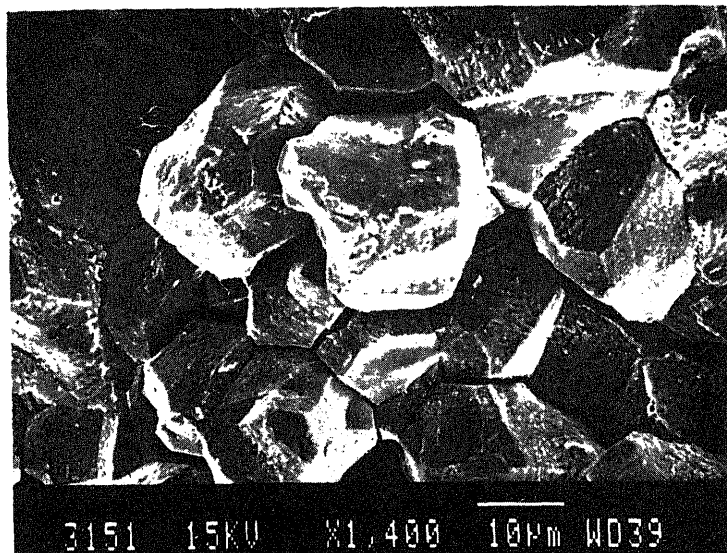


Figure 3. SEM fractograph of intergranular SCC of type 316 stainless steel in polythionic acid showing brittle features.

stage II, the crack-propagation rate approaches some constant velocity, referred to as the plateau velocity, which is characteristic of the alloy/environment combination and is a result of rate-limiting diffusion of the reactant species to the crack tip. The effect of variations in composition, changes in heat treatment, electrochemical variables and changes to the environment get reflected in the plateau velocity and such data become helpful in alloy selection. Alloys which have a low plateau velocity can be chosen in preference to the alloys with a high plateau velocity under the similar conditions of the environment.

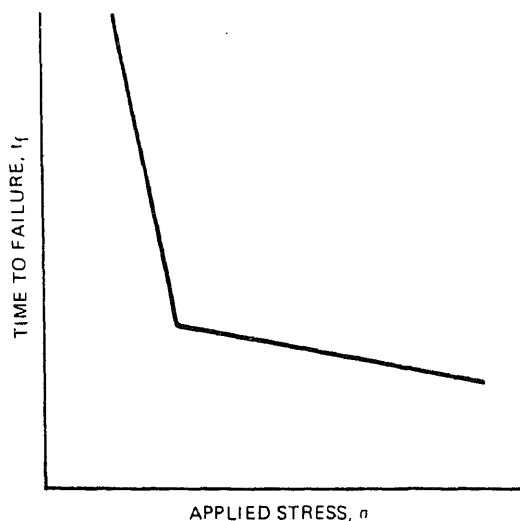


Figure 4. Time-to-failure and applied stress relationship obtained in a constant-load type SCC test.

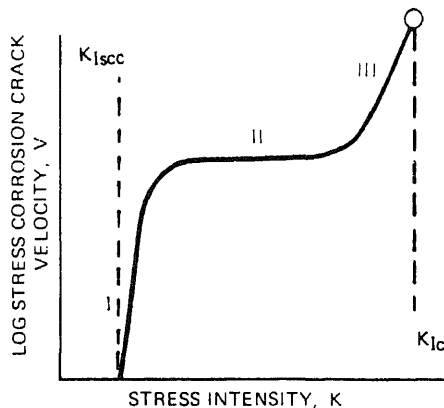


Figure 5. General relationship between stress corrosion crack velocity and stress intensity factor.

The earliest studies involving precracked specimens and LEFM were carried out by Brown & Beachem [1965] at the US Naval Research Laboratory. They showed that high strength titanium alloys, which were thought to be immune to SCC in dilute aqueous chloride environments on the basis of conventional, smooth specimen stress corrosion tests, were in fact highly susceptible when evaluated using fatigue precracked specimens. Actually, these alloys are resistant to pitting in these environments and stress corrosion crack initiation through pitting does not take place. However, pre-existing flaws and defects make these alloys susceptible to SCC.

Slow strain rate testing is a procedure in which a smooth or a pre-cracked specimen exposed to the corrosive environment is strained at a low crosshead speed (10^{-5} to 10^{-9} m/s) to failure. The strain to failure in the corrosive environment and the strain to failure in an inert environment can then be plotted against strain rate, or rather a ratio of these measurements as shown in figure 6. The ratio of other tensile measurements, such as reduction in area and ultimate tensile strength, may be plotted. The plot in figure 6 shows the similar behaviour of the two alloys at high strain rates, the ductility ratio approaching unity, indicating that the failure is through mechanical fracture as SCC crack initiation has not been possible at these high strain rates. Alloy B shows SCC susceptibility in a narrow range of strain rate, higher rate of repassivation of the alloy in the environment resists SCC at slower strain rates. Alloy A shows the behaviour of an alloy which does not repassivate in the environment concerned. The importance of repassivation in SCC will be discussed later.

The slow strain rate technique has the advantage over the constant-strain or constant-load test methods in that the experiment can be completed in a short period of time to ascertain the susceptibility to SCC of an alloy in a given environment. The test conditions, however, are more aggressive than the other methods. So it can be said that an alloy showing resistance in this test should be resistant in service with similar corrosive conditions, but an alloy showing SCC in a slow strain-rate test would not necessarily fail in service, where a forced, continuous strain is absent.

4. Metallurgical aspects of SCC

Virtually all alloys are susceptible to SCC in the appropriate environments. The

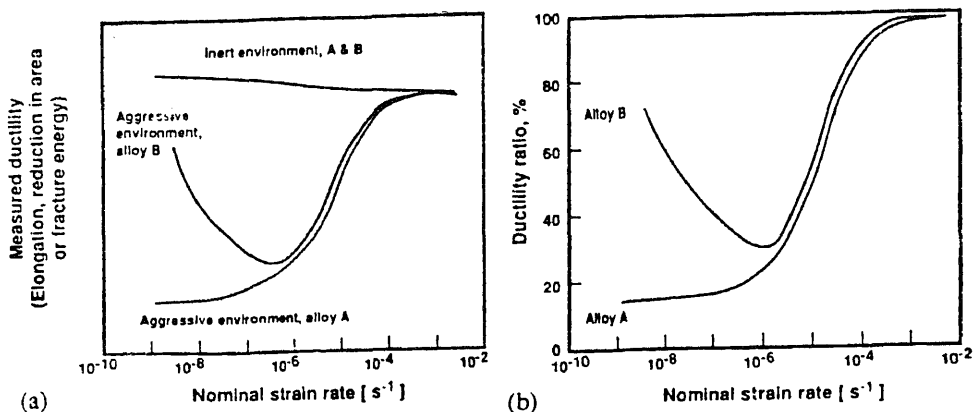


Figure 6. Strain-to-failure plots resulting from slow strain rate testing (a) Schematic of typical ductility versus strain rate behaviour of two different types of alloys tested by the slow-strain-rate technique, (b) schematic of the ductility ratio versus strain-rate behaviour of two different types of alloys. The ductility ratio is the ratio of a ductility measurement such as elongation, reduction in area, or fracture energy measured in the aggressive environment to that obtained in the inert reference environment.

susceptibility to SCC is affected by the chemical composition of the alloy, grain size and preferential orientation of grains, composition and distribution of precipitates, dislocation interactions and the progress of phase transformation. Bulk alloy composition can affect passive-film stability and phase distribution (for example, chromium in stainless steel), minor alloying elements can cause local changes in passive-film forming elements (for example, carbon in stainless steel causing sensitization), impurity elements can segregate to grain boundaries and cause local difference in the corrosion rate (for example, phosphorus in nickel or nickel-base alloys), and inclusions can cause changes in the local crack-tip chemistry as the cracks intersect them (for example, manganese sulphide in steel).

The effect of bulk alloy composition on SCC susceptibility is best exemplified in stainless steels and copper alloys. Figure 7 shows the effect of nickel content on SCC in stainless steels exposed to boiling 42% magnesium chloride solution, a common SCC medium used in the laboratory to simulate the cracking in hot chloride environments (Copson 1959). The beneficial effect of high nickel content is clearly visible. However, a ferritic stainless steel devoid of nickel, which is generally resistant to SCC in most common service environments that attack austenitic stainless steels, becomes susceptible with the addition of 1.5 to 2% nickel. Duplex stainless steels with high chromium and low nickel content are more resistant to SCC than austenitic stainless steels. Pure copper which is almost immune to SCC in ammoniacal environments becomes readily susceptible with the alloying of 1% silicon or 0.2% phosphorus (Thompson & Tracy 1949). Brasses with a zinc content below 15% are resistant to SCC. Addition of a third element like Si, Al, to 70 Cu–30 Zn brass changes the mode of cracking from intergranular to transgranular (Baumann 1962).

Grain-boundary precipitation and grain-boundary segregation play a major role in intergranular stress corrosion cracking. Austenitic stainless steels heated in the temperature range of 500 to 850°C, develop a chromium-depleted zone along the grain boundary through the precipitation of chromium carbide, a phenomenon known as

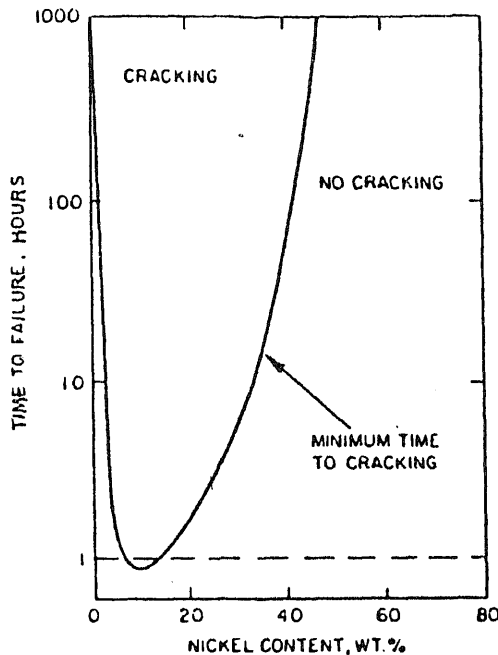


Figure 7. Effect of nickel content on the susceptibility to SCC of stainless steel wires containing 18–20% chromium in boiling MgCl_2 solution.

sensitization. Susceptibility to intergranular SCC and the crack growth rate are related to the degree of sensitization. Intergranular SCC of sensitized austenitic stainless steels is a recurring problem in cooling-water piping of boiling-water nuclear power plants (Gordon 1987). The Ni–Cr–Fe alloy 600 also gets sensitized through chromium depletion at the grain boundary and has been reported to fail by intergranular SCC in high temperature pressurized water (Pessal *et al* 1979). Grain-boundary precipitation has been identified as a contributing factor in the intergranular SCC of aluminium alloys (Hollingsworth & Hunsicker 1987). 7000 Series alloys (Al–Zn–Mg–Cu) are most susceptible in the peak-aged condition, the susceptibility is reduced with overaging.

Grain boundary segregation of alloying elements or impurities has been identified as the causative factor of intergranular SCC in many alloys. Grain-boundary enrichment of magnesium in Al–Mg alloys accounts for the increased anodic activity or possible formation of magnesium hydride along the grain boundaries (Pow *et al* 1981; Holroyd & Scamans 1985). Grain boundary enrichment of impurities such as phosphorus, sulphur, carbon and silicon contributes to the intergranular SCC of iron-base alloys, austenitic stainless steels and nickel-base alloys. The enrichment of impurities in the grain boundaries can be as high as 50% within a region 1 to 2 nm thick, facilitating the propagation of a stress corrosion crack along the grain boundary (Jones & Ricker 1992).

The effect of variation of carbon on the SCC of very low carbon steels were studied (Long & Uhlig 1965). Carbon segregation at the grain boundary was considered to provide suitable imperfection sites for adsorption of nitrates to promote SCC, and at a very low level of bulk carbon content such segregation was not attainable. Parkins (1969) discussed the role of carbon and/or nitrogen segregation to grain boundaries in SCC of carbon steels and found experimentally that about 0.01% C was required to cause SCC in nitrate or caustic environments, which is above the room temperature

solubility limit. Phosphorus segregation has been shown by several authors to promote intergranular SCC of low alloy steels (Cr–Mo or Ni–Cr–Mo–V) in caustic or water environments at relatively oxidizing potentials (Harrison *et al* 1977; Burnstein & Woodward 1983; Bandyopadhyay & Briant 1983). Phosphorus segregation has also been identified as a contributory factor in the intergranular SCC of austenitic stainless steels containing less than 0.002% carbon (Jones 1985) and also in nickel alloy 600 (Guttman *et al* 1981). Grain-boundary segregation of impurities is deemed responsible for the intergranular SCC of pure iron (Parkins 1990).

In transgranular SCC, alloying effect on slip planarity is a major factor. A number of crack growth models have been proposed based on the planar slip-localized corrosion processes. Planar slip occurs in alloys with low stacking-fault energy, alloys containing ordered phases, or alloys exhibiting short or long range ordering. Addition of nickel to stainless steels (Pickering & Swann 1963) and manganese to copper (Chatterjee *et al* 1970) have been reported to develop planar array of dislocations due to the lowering of stacking fault energy and consequently a susceptibility to transgranular SCC. Alloys, on the other hand, are prone to dealloying. It has been suggested that the dealloyed layer acts as a cleavage crack initiator in brass, copper, gold and stainless steels (Sieradzki & Newman 1987).

5. Electrochemical aspects of SCC

A number of environmental parameters influence stress corrosion cracking susceptibility, both in terms of crack initiation and crack growth, as well as the cracking mode in an alloy. Important among these parameters are temperature, nature of solute species and its concentration, pH and the electrochemical potential. Although the 'specificity' of an environment is no longer valid, still only a few environments can induce SCC in any particular alloy system and the susceptibility varies significantly with potential and pH.

In this pioneering work, Mattsson (1961) showed the dependence of the cracking time of alpha brass on the solution pH. The results were discussed in the background of the potential–pH diagram for Cu–H₂O–NH₃ system. The formation of an oxide film (Cu₂O) and its rupture providing an active dissolution front were thought to be essential requirements for the SCC in this system. The SCC of brass has been shown to be potential dependent (figure 8) with cracking mode changing over from intergranular to transgranular beyond a certain value of applied anodic potential (Sircar *et al* 1972). For SCC of mild steel in various environments, potential–pH conditions for severe cracking susceptibility have been identified (Congleton *et al* 1985) which also coincide with the regions of thermodynamically stable protective films (figure 9).

For an inherently reactive metal like mild steel most of the exposed surface will remain inactive if the surface is passivated. Nitrates, hydroxides and carbonates, which are anodic inhibitors of corrosion of carbon steels in appropriate circumstances, have the characteristics of passivating the surface. Along with this inactivity of most of the surface, the environment must also permit the formation of soluble species at the crack tip, so that the dissolution and hence crack propagation can occur. Both these conditions call for a border-line passivity. The ranges of potential within which cracking occurs are therefore expected to coincide with those ranges within which soluble species form. Such ranges are just above the active–passive potential zone in the

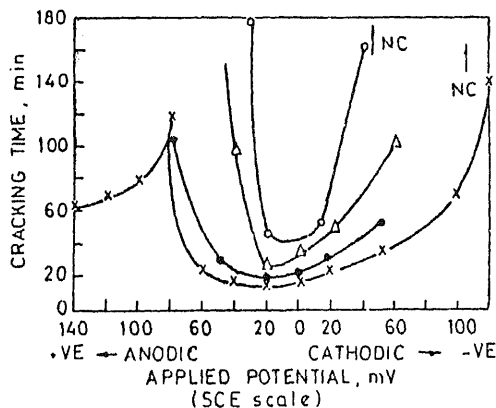


Figure 8. Effect of applied potential on the time-to-fracture of α -brass in Mattson's solutions of pH 7 containing 1 g/mol/l NH_4^+ and different compositions of dissolved copper.

anodic polarisation curves. For austenitic stainless steels in chloride media the transgranular SCC takes place at potentials around the breakdown potential and the crack initiation is usually associated with pit formation. These ranges are shown schematically in figure 10.

The effects of additions in causing the free corrosion potential to move in relation to the potential range for cracking have considerable practical significance. The addition of small amounts of nitrates to concentrated NaOH causes the free corrosion potential to become significantly more positive than the cracking potential in alkali, and failure is no longer observed. The free corrosion potential of some mild steels is likely to be at the boundary of cracking range in hydroxide so that the stress corrosion does not occur. The addition of a small amount of lead oxide causes the free corrosion potential to move into the cracking range and the failure then occurs readily at these potentials. The potential and pH conditions inside the crack are not the same as those in the bulk of the

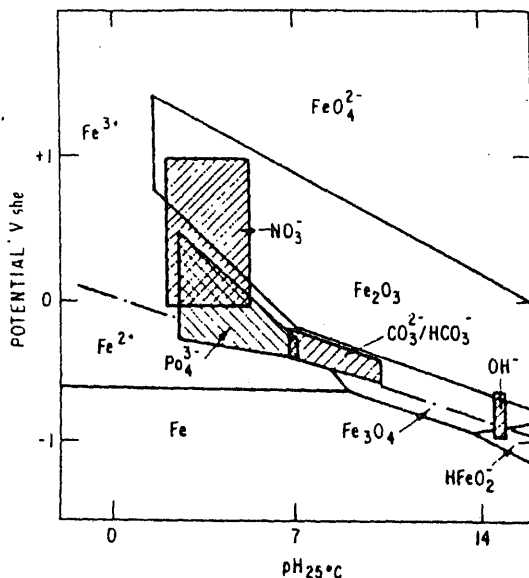


Figure 9. Relationship between pH/potential conditions for severe cracking susceptibility of mild steel in various environments and the stability regions for solid and dissolved species on the potential-pH diagram. Note that severe susceptibility is encountered where a protective film (phosphate, mixed carbonate, magnetite etc.) is thermodynamically stable, but if ruptured, a soluble species (Fe^{2+} , HFeO_2) is metastable.

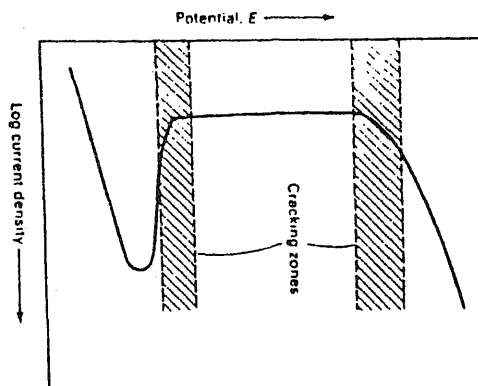


Figure 10. Schematic anodic polarization curve showing zones of susceptibility to stress corrosion cracking.

solution or at the surface of the alloy and so a correlation may not always be possible with the potential-pH diagram. However, it is reasonable to believe that the conditions prevailing inside the crack essentially meet electrochemical requirements as presented above for the SCC to occur.

If the mechanism whereby stress corrosion crack propagation involves dissolution at the crack tip, then crack velocities may be expected to be related through Faraday's law to the current density at the crack tip according to the equation,

$$v = i_a M / zF\rho$$

where, i_a is the current density, M is the molecular mass of the material, z is the valency of the solvated ions, F is Faraday's constant and ρ is the density of the metal. Taking the effective current density as the largest difference between fast and slow sweep rate polarisation curves, or the maximum current densities observed in scarping or straining electrode experiments at appropriate potentials, a plot of these current densities against calculated crack velocities for a variety of stress corrosion systems yields a straight line (Parkins 1979). There is good correlation in some cases whereby the mechanism postulating initiation and propagation of cracks through dissolution is collaborated. The deviation can be accounted for by attributing the role of dissolution in the crack initiation only, triggering a mechanical fracture propagation step.

'Specificity' of environment also can be explained from the electrochemical standpoint. In very general terms, it is clear that potent solutions will need to promote a critical balance between activity and passivity, since a highly active condition will result in general corrosion or pitting, while a completely passive condition cannot, by definition, lead to stress corrosion. Whilst the relative inactivity of all exposed surfaces except the crack tip may be derived from a noble metal film in the case of alloys containing sufficiently noble elements, for the great majority of engineering alloys inactivity at exposed surfaces is the result of the presence of oxide films overlaying metal surfaces. It is not surprising therefore to find that the alloys of high inherent corrosion resistance (such as those based upon aluminium or titanium, or the austenitic stainless steels, that readily develop protective films) require an aggressive ion, such as a halide to promote stress corrosion cracking. On the other hand, to crack the metals of low inherent corrosion resistance, such as carbon steels or magnesium base alloys, we require the presence of an environment that is itself partially passivating. Thus, carbon steels can be made to fail in solutions of anodic inhibitors, such as hydroxides or

carbonates, and the cracking of magnesium-base alloys is achieved with an appropriate mixture of CrO_4^{2-} and Cl^- ions, but not with either of these species alone.

6. Mechanisms of SCC

Any mechanism of stress corrosion cracking should explain the characteristic features of the process, viz. the susceptibility of an alloy in a limited number of environments, the role of stress and the nature of cracking apart from the influence of various metallurgical and environmental factors in the cracking process. Since stress corrosion cracking essentially involves a corrosive environment, mechanisms based on localized dissolution of metal have been postulated. On the other hand, the essential brittle fracture feature of stress corrosion cracking has led to the postulation of mechanism based on cleavage. There are several variations of these two basic mechanisms. According to some models, the so-called continuous electrochemical mechanisms, the initiation and propagation of cracks are both dissolution-controlled. According to the periodic electrochemical-mechanical mechanism, the initiation of cracks or the embrittlement of the region ahead of the crack tip has been dissolution controlled while the propagation is a mechanical brittle fracture step. There is a third group, where the role of dissolution is de-emphasized in the embrittlement process.

6.1 Dissolution mechanisms

According to this mechanism a crack advances by preferential dissolution at its tip. The restriction of the dissolution process at the crack tip has been attributed to either a pre-existing active path or to strain-generated active path.

The pre-existing active path mechanism: This is the oldest mechanism proposed (Dix 1940). Grain-boundary segregation or precipitation, as discussed in the previous section, brings about substantial change in the microchemistry of the grain boundary with respect to the bulk alloy. These segregated solutes or precipitated phases may act as anode in the local cell or, by acting as an efficient cathode, may cause the dissolution to be localized upon the immediately adjacent matrix. The role of stress here is to keep the crack open for the accessibility of the corrosive medium to the crack tip. The stress concentration at the crack tip producing yielding has also been considered to accelerate dissolution due to the so-called 'mechanochemical effect' (Hoar & West 1962). Intergranular stress corrosion cracking (IGSCC) of sensitized stainless steel in various environments, including high purity water, of carbon steels exposed to nitrate, hydroxide or carbonate-bicarbonate solutions and of aluminium alloys exposed to chloride solutions have been explained in these terms. However, a propensity for intergranular corrosion is no guarantee for IGSCC. It has been shown that though the nickel-base superalloy IN718 and Ticolloy show intergranular corrosion in NaCl solution, in deaerated solutions they may crack transgranularly (Wang *et al* 1992).

Strain-generated active path mechanism: The SCC in alloys which do not have a pre-existing path has been explained by dissolution of strain-generated active path and there are two distinct models: the *film-rupture model* (Logan 1952) and the *slip-step dissolution model* (Vermilyea 1969). According to the film-rupture model, the stress

opens up the crack and the localized plastic deformation at the crack tip ruptures the passivating film, exposing the bare metal which dissolves rapidly, resulting in crack extension. The crack tip remains bare if the rate of film rupture at the crack tip exceeds the rate of repassivation. If the situation is reverse, the crack tip repassivates completely and is periodically ruptured by the emergence of slip steps and the bare slip-step sustains dissolution till the next repassivation.

Since many of the stress corroding systems are associated with film formation and the SCC occurs under some sort of borderline passivity condition (discussed earlier), most investigators now agree that film rupture is essential to initiate cracking. The emerging slip-steps at the surface as a result of deformation also provide an explanation for transgranular crack initiation. However, controversy persists in regard of a crack propagation by continued dissolution. For example, transgranular cracking would be expected to grow on the active slip plane, where deformation would cause continual film rupture, contrary to the experimental fact that cracks grow on planes of the type $\{100\}$ or $\{110\}$ (Liu *et al* 1980). Also, a crack growing by electrochemical dissolution at unfilmed crack tip should leave a relatively smooth, featureless surface, but crystallographic cleavage, often with arrest marks (for transgranular SCC), and well-defined grain boundary (for intergranular SCC) features are often present on fracture surfaces. Although the slip-step dissolution model accounts for the presence of arrest marks, it fails to account for the matching opposite fracture surfaces.

A corrosion tunnel model (Swann & Pickering 1963) has emerged where dissolution and mechanical fracture have been combined. It assumes that a fine array of small corrosion tunnels form at the emerging slip steps. These tunnels grow in diameter and length until the stress in the remaining ligaments causes ductile deformation and fracture. However, such a model should produce grooved fracture surface with evidence of microvoid coalescence at the broken ligaments, which have not been observed experimentally. So this model has been modified subsequently (Silcock & Swann 1979) by suggesting that the application of a tensile stress results in a change in the morphology of corrosion damage from tunnels to thin, flat slots. The width of the corrosion slots approach atomic dimensions and a close correspondence of matching surfaces is expected.

6.2 Cleavage mechanisms

Several mechanisms have been postulated to explain the cleavage type cracking encountered in SCC. These are: hydrogen-assisted cracking, tarnish-rupture, film induced cleavage, adsorption induced cleavage and atomic surface mobility mechanisms.

Hydrogen assisted cracking is very often described by the decohesion model in which atomically dissolved hydrogen acts to weaken the interatomic bonds in the plain-strain region of the crack tip by lowering the surface energy γ_s in the Griffith equation,

$$\sigma_c = (2E\gamma_s/\pi c)^{1/2},$$

where σ_c is the fracture stress necessary to cause the propagation of an elliptical crack of length $2c$ and E is the Young's modulus. Blocked glide planes have been considered to provide the initial Griffith cracks (Petch & Stables 1952). It has also been suggested (Jani *et al* 1990) that hydrogen decreases the stacking fault energy to induce coplanar deformation at the tip. Embrittlement would then result from Lomer-Cottrell supersessile

dislocations on the intersecting slip planes. A somewhat similar model has been presented to explain the hydrogen assisted cracking in Fe-3Si single crystals and the observed crack arrest marks (Chen & Gerberich 1991). The embrittlement of Nb, Ta, Ti, V and Zr is due to the stress-assisted formation of brittle hydride phase ahead of the crack tip which facilitates crack growth by cleavage, with cracks arresting at the boundary where the relatively tough matrix is encountered. Another particle of hydride then forms in the region of crack tip and the process is repeated, resulting in discontinuous crack growth.

Hydrogen assisted crack growth in the manner described has been suggested as the SCC mechanism for ferritic steels, nickel base alloys, austenitic stainless steels, aluminium alloys and intermetallic compounds. The most probable source for atomic hydrogen to enter into the metal is the cathodic reduction of hydrogen ions accompanying the anodic dissolution in the aqueous environments. Materials with impurities like sulphur, phosphorus, antimony and tin segregated at grain boundaries have been found to be more susceptible to hydrogen-induced cracking, because these impurities act as hydrogen-evolution poisons (Latanision & Opperhauser 1974). On the other hand, the growing stress corrosion cracks have been stopped effectively in low-strength ductile alloys by cathodic polarisation, refuting the validity of hydrogen-assisted SCC in these alloys. Again, all the environments and conditions under which SCC is encountered do not produce hydrogen and some of them produce surface films which constitute an effective barrier to hydrogen entry (Hardie 1990). These restrict the universal applicability of hydrogen-induced cracking as SCC mechanism.

The adsorption-induced cleavage mechanism or the stress-sorption cracking mechanism (Uhlig 1959) is based on the hypothesis that adsorption of environmental species lowers the interatomic bond strength and the stress required for cleavage fracture, an idea similar to the decohesion model of hydrogen-induced cracking. Adsorption is assumed to be potential dependent which accounts for the stoppage of SCC by cathodic polarisation below a critical potential. The specificity of the species for inducing SCC in a particular alloy can also be conveniently explained in terms of preferential adsorption. However, this model does not explain how the crack maintains an atomically sharp tip in a normally ductile material and it also fails to explain the discontinuous nature of crack propagation (Parkins 1990).

The tarnish-rupture mechanism was originally proposed to explain discontinuous transgranular crack growth of α -brass single crystals in ammoniacal solutions (Edeleanu & Forty 1960; Forty & Humble 1963). According to this model, a brittle surface film or tarnish forms on the metal which fractures under the applied stress. The exposed bare metal reacts rapidly with the environment, the film grows again and the cycle of growth and fracture of the tarnish is repeated. The model was modified subsequently (McEvily & Bond 1965; Beavers *et al* 1972) for intergranular SCC proposing that the tarnish penetrates along the grain boundary ahead of the crack tip. At present, experimental results are insufficient to confirm or refute this mechanism, though some workers (Pinchback *et al* 1976) have questioned the validity of grain-boundary penetration in all systems.

The film-induced cleavage mechanism developed as a consequence of the tarnish-rupture model (Pugh 1985; Sieradzki & Newman 1985). In this model it is assumed that

dissolution leads to the formation of a surface film and a crack growing in the film propagates further into the underlying metal. From an initial arrest position, the crack advances by cleavage for a limited distance, after which the crack becomes progressively blunted by plastic deformation until the propagation stage is repeated. The film may be a dealloyed layer or oxide, in which nanoporosity is considered to be the key feature leading to the injection of a sharp crack into the substrate. Experimental results showing the correlation of SCC with dealloying have been given for Cu-Zn and Cu-Al alloys (Sieradzki *et al* 1987), and also for stainless steel (Newman *et al* 1989). Certain objections have been put forward against this mechanism. The crack advance distance as measured from arrest marks is typically of the order of a few micrometers and doubts have been raised (Gerberich & Chen 1990) as to whether a cleavage crack could penetrate that far from an initiating film that is only of the order of 30 nm thick. Dealloyed layers are also unlikely to have sufficient adhesion to the substrate or inherent brittleness to sustain cracking.

The atomic surface mobility mechanism (Galvele 1987) suggests that many forms of environmentally induced cracking, including hydrogen embrittlement, SCC and liquid-metal embrittlement, grow by the capture of surface vacancies at the crack tip and counter-current surface diffusion of atoms away from the crack tip. The coefficient of surface self-diffusion will dominate the crack growth rate and the role of the environment is to change that diffusivity which is directly related with the presence of low melting surface compounds. However, it has been pointed out (Parkins 1990) that although carbon steel cracks in nitrates which form low-melting compounds with iron, it also cracks in the presence of high melting point Fe_3O_4 . Oriani (1990) puts an opposite viewpoint by suggesting that the flux of atoms in the region of a stressed crack tip should be the reverse of what the mechanism requires, by analogy with diffusional creep. It has been criticized (Newman & Procter 1990) that many of the correlations postulated in this mechanism would work equally well if the criterion was surface energy reduction, rather than increase in diffusivity, and thus it becomes indistinguishable from earlier surface energy models.

The proposed mechanisms of SCC thus differ immensely from one another; some suggesting an exclusive role of dissolution while some others giving dissolution a marginal or no role at all in the cracking process. While the proponents of a particular mechanism have produced enough evidence in support of the mechanism, observations not conforming to the mechanism have also been cited in plenty. Though there have been attempts from time to time to find a unified theory explaining all features of SCC in all the alloy-environment systems, it appears more reasonable to believe that the mechanism varies from system to system. It is also probable that no particular mechanism operates exclusively in one system but that more than one mechanism is at play. Decades ago, Parkins (1976) proposed that the different mechanisms of stress corrosion should be considered as occurring within a continuous spectrum, with a gradual transition from one to the other as the dominance of corrosive processes is replaced by stress or strain leading to a brittle fracture (table 2). The picture appears to have remained unchanged.

7. Preventive measures

Control of stress: Lowering of applied stress below threshold stress or stress intensity by suitable changes in design and lowering or removal of residual stress by annealing

treatment are effective means to reduce the incidence of SCC in service. The seasonal cracking of brass cartridge cases was prevented by proper stress relief annealing treatment. It is recommended practice to give such a treatment to brass tubes after drawing or to steel tubes after welding for use in sour oil wells. However, annealing may be impractical for some stainless steels which sensitize and become susceptible to intergranular attack.

Since a tensile component of stress is required in SCC, it can be prevented by putting the surface of a component into compression, e.g. by shot-peening. The treatment needs to be applied uniformly. It will not be effective if pitting occurs on the compressive layer.

Control of corrosion: The elimination or reduction of the damaging species is desirable, but often difficult to achieve in practice. The initial non-damaging concentration of the species may become high in the crevices or under high temperature conditions bringing about failures. However, the prevention of intergranular SCC of sensitized stainless steel, a recurring and expensive problem in cooling-water piping of boiling water nuclear power plants, has been achieved by minimizing both dissolved oxygen and chloride (Williams 1959).

Use of inhibitors reduces or even eliminates SCC, possibly by moving the corrosion potential outside the range of cracking. The addition of small amounts of nitrates to concentrated NaOH prevents SCC of steel, as discussed in section 4. Substances like H_3PO_2 , Na_2O_4 and $\text{CO}(\text{NH}_2)_2$, which may be expected to form insoluble products with iron, retard or prevent cracking in nitrates. Addition of traces of NO to N_2O_4 or 1–2% H_2O to RFNA or $\text{CH}_3\text{OH}/\text{HCl}$ mixtures prevent SCC of titanium alloys in these media (Blackburn *et al* 1972). The addition of water causes anodic inhibition by shifting the potential to the safe passive potential range. However, there are some practical limitations for the use of inhibitors. Many failures occur in steam or under condensation conditions, and in both these cases the transport of inhibitors to sites of crack initiation is not feasible.

Increasing the corrosion rate to reduce SCC might appear to be a ridiculous proposition. But since SCC is a form of highly localized corrosion, extending corrosion over the whole of the surface will usually lessen the probability of such failures. This approach is unlikely ever to be a permanent remedy. It is employed in making up mixtures containing HCl to clean austenitic stainless steel parts in chemical plants, the corrosion rate is maintained > 10 mpy (Laque & Copson 1965).

Electrochemical protection: Cathodic protection will control SCC in alloys which crack by anodic dissolution mechanism, but is likely to accelerate hydrogen-induced cracking, particularly in high strength alloys. SCC failure of Kraft continuous digesters in pulp and paper industry in NaOH– Na_2S environment at 140°C has been reported (Singbell & Garner 1987) to have been mitigated by the application of anodic protection.

Material selection: Choosing a different alloy resistant to the particular environment is a popular option to prevent SCC. An alloy having the lowest plateau velocity, as discussed in section 3, can be chosen from among a number of susceptible alloys. Mitigation of SCC by alloy development has been a rare endeavour. However, it is reported (Newman & Procter 1990) that a relatively inexpensive stainless steel has been

developed by Japanese workers which resists SCC up to 140°C in crevice tests with 20% NaCl in which 304 stainless steel will fail at 60°C. The addition of copper raises the lower critical potential for SCC. Minimisation of phosphorus content in austenitic stainless steels is also a key approach to make them resistant to chloride induced SCC.

The cladding of high strength aluminium alloys with pure aluminium to mitigate SCC in aircraft components has been mentioned in § 1. The relatively low susceptibility of pure metals to SCC has been utilized in this preventive measure.

Liberal help has been taken from the review articles of Scully (1979), Newman & Procter (1990), Parkins (1992), Jones & Ricker (1992) and the text book by Jones (1992) in the preparation of this article.

References*

- Bandyopadhyay N, Briant C L 1983 *Metall. Trans.* A14: 2005
Barer R D, Peters B F 1970 *Why metals fail* (New York: Gordon and Beach) 6: 177
Baumann G 1962 *The Brown Boveri Review* 49: 323
Beavers J A, Rosenberg J C, Pugh E N 1972 In *Proc. 1972 Tri-Science Conf. Corrosion, MCIC* 73-19 (Metals and Ceramic Information Center) p. 57
Blackburn M J, Smyth W H, Feeney J A 1972 In *Stress corrosion cracking in high strength steels and titanium and aluminium alloys* (ed.) B F Brown (Washington DC: Naval Research Lab.)
Brown B F, Beachem C D 1965 *Corros. Sci.* 5: 745
Burnstein G T, Woodward J 1983 *Metall. Sci.* 17: 111
Chatterjee U K, Sircar S C, Banerjee T 1970 *Corrosion* 26: 141
Chen X, Gerberich W W 1991 *Metall. Trans.* A22: 59
Congleton J, Shoji T, Parkins R N 1985 *Corros. Sci.* 25: 633
Copson H R 1959 In *Physical metallurgy of stress corrosion fracture* (ed.) T N Rhodin (New York: Interscience) p. 247
Coriou H, Grall L, Olivier P, Willermoz H 1969 In *Fundamental aspects of stress corrosion cracking* (eds) R W Staehle, A J Forty, D Van Rooyen (Houston, TX: NACE) p. 352
Dix E H 1940 *Trans. Am. Inst. Min. Metall. Eng.* 137: 11
Dravnick A, Samans C H 1957 *Proc. Am. Petroleum Inst.* 37: 100
Edeleanu C, Forty A J 1960 *Philos. Mag.* 5: 1029-1040
Fontana M G, Greene N D 1967 *Corrosion engineering* (New York: McGraw Hill) 3: 102
Forty A J, Humble P 1963 *Philos. Mag.* 8: 247
Galvele R 1987 *Corros. Sci.* 27: 1
Gerberich W W, Chen S 1990 In *Environment-induced fracture of metals* (eds) R P Gangloff, M B Ives (Houston, TX: NACE) p. 167
Gordon B M 1987 In *Metals handbook* 9th edn (Metals Park, OH: ASM Int.) 13: 590
Guttman M, Dumonlin P, Tan Tai N, Fontaie P 1981 *Corrosion* 37: 416
Hardie D 1990 In *Environment-induced fracture of metals* (eds) R P Gangloff, M B Ives (Houston, TX: NACE) p. 347
Harrison R P, Jones D De G, Newman F G 1977 In *Stress corrosion cracking and hydrogen embrittlement of iron-base alloys* (eds) R W Staehle, J Hochman, R D McCright, J E Slater (Houston, TX: NACE) p. 659
Hoar T P, West J M 1962 *Proc. R. Soc.* A268: 304
Hollingsworth E H, Hunsicker H Y 1987 In *Metals handbook* 9th edn (Metals Park, OH: ASM Int.) 13: 590

*These references are not in our usual format. Readers may please bear with us

- Holroyd N J H, Scamans G M 1985 *Scr. Metall.* 19: 915
- Jackson J D, Boyd W K 1966 *DMIC technical note* (Columbus: Battelle Memorial Institute)
- Jani S C, Marek M, Hochman R E, Meletis C I 1990 In *Environment-induced fracture of metals* (eds) R P Gangloff, M B Ives (Houston, TX: NACE) p. 541
- Jones D A 1992 *Principles and prevention of corrosion* (New York: Macmillan)
- Jones R H 1985 In *Proc. Int. Symp. Environmental Degradation of Materials in Nuclear Power System - Water Reactors* (Am. Nucl. Soc.) p. 173
- Jones R H, Ricker R E 1992 In *Stress corrosion cracking: Materials performance and evaluation* (ed.) R H Jones (Metals Park, OH: ASM Int.) 1: 20
- Laque F L, Cospon H R 1963 In *The corrosion resistance of metals and alloys* (New York: Reinhold) p. 392
- Latanision R M, Oppenheimer H 1974 *Metall. Trans.* 5: 483
- Liu R, Narita N, Alstetter C, Birnbaum H, Pugh E N 1980 *Metall. Trans.* A11: 1563
- Logan H L 1952 *J. Res. Natl. Bur. Stand.* 48: 99
- Long L M, Uhlig H H 1965 *J. Electrochem. Soc.* 112: 964
- Mattson E 1961 *Electrochim. Acta* 3: 279
- McEvily A J, Bond P A 1965 *J. Electrochem. Soc.* 112: 141
- Newman R C, Corderman R R, Sieradzki K 1989 *Br. Corros. J.* 24: 143
- Newman R C, Procter R P M 1990 *Br. Corros. J.* 25: 259
- Oriani R A 1990 In *Environment-induced fracture of metals* (eds) R P Gangloff, M B Ives (Houston, TX: NACE) p. 263
- Parkins R N 1969 In *Fundamental aspects of stress corrosion cracking* (eds) R W Staehle, A J Forty, D Van Rooyen (Houston, TX: NACE) p. 361
- Parkins R N 1976 In *Corrosion* (ed.) L L Shreir (London: Newnes-Butterworths) vol. 1, chap. 8, p. 24
- Parkins R N 1979 *Br. Corros. J.* 14: 5
- Parkins R N 1980 *Br. Corros. Sci.* 20: 147
- Parkins R N 1990 In *Environment-induced fracture of metals* (eds) R P Gangloff, M B Ives (Houston, TX: NACE) p. 1
- Parkins R N 1992 *J. Metall.* 44: 12
- Pessal N, Airey G P, Lingenfelter B P 1979 *Corrosion* 35: 100
- Petch N J, Stables P 1952 *Nature (London)* 169: 842
- Pickering H W, Swann P R 1963 *Corrosion* 26: 45
- Pinchback T R, Clough S P, Heldt L A 1976 *Metall. Trans.* A7: 1241
- Pow E C, Gerberich W W, Toth L E 1981 *Scr. Metall.* 15: 55
- Pugh E N 1985 *Corrosion* 41: 517
- Scully J C 1979 In *Corrosion chemistry* (American Chemical Society) p. 321
- Sieradzki K, Newman R C 1985 *Philos. Mag.* 51: 95
- Sieradzki K, Kim J S, Cole A T, Newman R C 1987 *J. Phys. Chem. Solids* 48: 1101
- Sieradzki K, Newman R C 1987 *J. Phys. Chem. Solids* 48: 1101
- Silcock J M, Swann P R 1979 In *Environment-sensitive fracture of engineering materials* (ed.) Z A Foroulis (The Metallurgical Society) p. 33
- Singbell D, Garner A 1987 *Mater. Perform.* 26: 31
- Sircar S C, Chatterjee U K, Zamin M, Vijayendra H G 1972 *Corros. Sci.* 12: 217
- Staehle R W 1990 In *Environment-induced fracture of metals* (eds) R P Gangloff, M B Ives (Houston, TX: NACE) p. 561
- Swann P R, Pickering H W 1963 *Corrosion* 19: 102t
- Thompson D H, Tracy A W 1949 *Trans. Am. Inst. Mech. Eng.* 185: 100
- Uhlig H H 1959 In *Physical metallurgy of stress corrosion fracture* (ed.) T N Rhodin (New York: Interscience) p. 1
- Vermilyea D A 1969 *Fundamental aspects of stress corrosion cracking* (eds) R W Staehle, A J Forty, D Van Rooyen (Houston, TX: NACE) p. 15
- Viswanathan R 1982 In *Retaining Ring Failures: EPRI Workshop on Retaining Rings* p. 24
- Wang P C et al 1992 In *Parkins symposium on fundamental aspects of stress corrosion cracking* (eds) S M Bruemmer et al (Warrendale: TMS) 399
- Williams W L 1959 *Corrosion* 13: 539t

Mathematical modelling of creep/environment interactions

B F DYSON* and S OSGERBY

Division of Materials Metrology, National Physical Laboratory, Teddington, TW11 0LW, UK

*Present address: Department of Materials, Imperial College of Science, Technology and Medicine, London SW7 2BP, UK

Abstract. Physically-based creep Continuum Damage Mechanics (CDM) is briefly reviewed to introduce the formalism necessary for mathematical modelling of creep and fracture in the presence of a chemically-interacting fluid environment. A recently developed theory of creep in precipitation-hardened alloys is presented in the form of a constitutive equation and two important creep/environment interactions are discussed in detail. Spallation of oxide scales during creep of a low-alloy ferritic steel is one and is modelled using the new creep constitutive equation which incorporates particle-ageing as the principal intrinsic damage mechanism. Lack of experimental data has meant that only qualitative support for the model predictions could be given. Carbon dioxide gas bubble formation along grain boundaries in nickel alloys is the other form of environmental attack considered; a new kinetic model based upon oxygen diffusion-control is described and shown to be in quantitative agreement with a large experimental dataset.

Keywords. Continuum damage mechanics; creep modelling; reaction-front kinetics; diffusion; degradation; damage; gas bubble formation.

1. Introduction

Mechanical test data for creep design are mainly procured in a laboratory air environment, whereas materials entering service in component form are often exposed to oxidising, sulphidising or carburising atmospheres. The potential for material degradation (or 'damage') in these environments is an unwelcome irritant to those concerned with predicting long-term component performance in service using data from short-term laboratory tests. However, environmentally-induced degradation of a material is only one of many mechanisms that can adversely affect a component's creep lifetime and its quantification cannot therefore be considered in isolation: the

state of stress experienced by a component or its fabrication route are two well-researched areas that can also reduce lifetimes to well below those predicted simply on the basis of uniaxial data. For example, material in bent pipework can be made much less ductile (with a consequent reduction in lifetime relative to virgin material) because of plastic strain-induced grain boundary cavitation; similarly, low ductility fractures are induced by a combination of local changes of microstructure and triaxial stresses created during welding. Predictive modelling of creep/environment interactions must therefore be within an overall life prediction framework.

The present paper first presents a brief state-of-the-art review of physically-based creep Continuum Damage Mechanics (CDM). This mechanics has evolved over the past decade to deal quantitatively with design and remanent life prediction in situations where a variety of material damage mechanisms can control failure. The damage equations have been incorporated individually into a new constitutive description of creep that is relevant to nickel-base superalloys, ferritic steels and aluminium alloys. A multi-damage version is then used to advance further the quantification of two important creep/environment interactions.

2. Mechanics framework for creep lifetime prediction

In an effort to 'build bridges' between engineers engaged in lifetime prediction and metal scientists endeavouring to understand the underlying micromechanisms of material degradation, Ashby & Dyson (1984) proposed what has become known as physically-based creep Continuum Damage Mechanics (CDM). Four broad categories of material-damage were identified, each containing more than one micromechanism: (i) loss of external load-bearing section due to deformation at constant volume; (ii) loss of effective internal load-bearing section due to voiding or cracking; (iii) a progressive softening caused by degradation of the dislocation and/or particulate microstructure; (iv) a surface weakening due to chemical interaction with the environment. A non-dimensional 'damage parameter', S , was defined for each micromechanism and its rate of evolution and interaction with strain rate $\dot{\epsilon}$, quantified. When each micro-mechanism acted alone, the strain rate was found to be represented generally by

$$\dot{\epsilon} = \dot{\epsilon}(\sigma TS), \quad (1)$$

while the damage rate had one of four forms:

$$\dot{S} = \dot{S}(\sigma TS), \quad (2)$$

$$\dot{S} = \dot{S}(TS), \quad (3)$$

$$\dot{S} = \dot{S}(\sigma TSR), \quad (4)$$

$$\dot{S} = \dot{S}(TSR). \quad (5)$$

In (1)–(5), σ is the applied uniaxial stress; T is temperature and R is the radius of a cylindrical testpiece.

Only (3) – describing damage due to coarsening of particles – and (5) – describing damage due to internal oxidation – are independent of deformation rate. Equations (4) and (5) describe damage due to chemical interactions with the environment and thus depend on radius R – the larger the testpiece, the smaller the interaction.

Table 1. Creep damage categories, mechanisms, parameters, rates and effects on uniaxial strain rates using a hyperbolic sine law material model.

Creep damage category	Damage mechanism	Damage parameter (S, ω)	Damage rate ($\dot{S}, \dot{\omega}$)	Strain rate ($\dot{\epsilon}$)
Strain-induced $\dot{\omega} = \dot{\omega}(\sigma, T, \omega)$ or $\dot{S} = \dot{S}(\sigma, T, S)$	Uniform straining under constant load	$S_1 = 1 - (\sigma_i/\sigma)$	$\dot{S}_1 = (1 - S_1)\dot{\epsilon}$	$\dot{\epsilon}_0 \sinh [\sigma_i/\sigma_0(1 - S_1)]$
	Creep-constrained cavity growth	$\omega_1 = (\pi d^2 N/4)$	$\dot{\omega}_1 = 0$	$\dot{\epsilon}_0 \sinh [\sigma/\sigma_0(1 - \omega_1)]$
	Continuous cavity nucleation with creep constraint	$\omega_2 = (r/l)^2$ $\omega_3 = (\pi d^2 N/4)$	$\dot{\omega}_2 = (d/2l\omega_2^{1/2})\dot{\epsilon}$ $\dot{\omega}_3 = (1/3\epsilon_0)\dot{\epsilon}$	$\dot{\epsilon}_0 \sinh [\sigma/\sigma_0(1 - \omega_3)]$
Thermally-induced $\dot{S} = \dot{S}(T, S)$ Environmentally-induced $\dot{S} = \dot{S}(\sigma, T, S, R)$ or $\dot{S} = \dot{S}(T, S, R)$	Multiplication of the dislocation substructure	$S_2 = 1 - (\rho_i/\rho)$	$\dot{S}_2 = C(1 - S_2)^2\dot{\epsilon}$	$\dot{\epsilon}_0(1 - S_2)^{-1} \sinh(\sigma/\sigma_0)$
	Particle-coarsening	$S_3 = 1 - (P_i/P)$	$\dot{S}_3 = (K'/3)(1 - S_3)^4$	$\dot{\epsilon}_0 \sinh [\sigma/\sigma_0(1 - S_3)]$
	Fracture of corrosion product	$S_4 = (2x/R)$	$\dot{S}_4 = (1/R)(2K_p\dot{\epsilon}/\epsilon^*)^{1/2}$	$\dot{\epsilon}_0 \sinh(\sigma/\sigma_0(1 - S_4))$
	Internal oxidation	$S_5 = (2x/R)$	$\dot{S}_5 = (2K/R^2 S_5)$	$\dot{\epsilon}_0 \sinh [\sigma/\sigma_0(1 - f S_5)]$

Ashby & Dyson (1984) used a material model with a power law stress function to formulate explicit pairs of equations consisting of (1) combined with various appropriate forms of the damage equations (2)–(5). Over the past decade, several developments have taken place: a recognition of the importance of a two-damage formulation for particle-strengthened engineering alloys, even under constant applied stress (Dyson & Gibbons 1987); a multiaxial formulation for use in finite element analyses of components (Othman *et al* 1993); a methodology (CRISPEN) for extracting model parameters to fit certain equation-sets (Ion *et al* 1986; Barbosa *et al* 1988); and development of a new material model for precipitation-hardened materials that is based on a hyperbolic sine stress function (Dyson 1994).

A hyperbolic sine stress-function rationalises the stress dependent ' n ' values widely reported in the literature on precipitation-hardened engineering alloys. In addition, the new theory has suggested a totally different interaction between particle-coarsening and strain rate which has been validated using creep data obtained on virgin and aged 1Cr1/2Mo steel (Dyson & Osgerby 1993). Table 1 summarises the state-of-the-art for single damage CDM models using the hyperbolic sine formulation.

In the light of the above brief review of the status of CDM, the next section presents some new information on creep modelling in the presence of damage due to interaction with oxygen in the surrounding environment.

3. Modelling of creep/oxygen-environment attack

Exposure of pure metals or solid solution alloys to air during creep often results in lower creep rates and longer lives compared to data obtained in vacuum. The reason is simply due to the higher creep strength and greater volume of the surface oxide and is facilitated by a combination of a weak alloy with a fast-growing oxide. In contrast, ferritic steels and nickel base superalloys often display creep lifetimes in air that are often much shorter than in vacuum or inert atmosphere. Two quite different micromechanisms have been identified as being responsible: (i) in low-alloy ferritic steels, oxides have been observed to spall, reducing the load-bearing section and accelerating creep (Cane & Manning 1981); (ii) in nickel-base superalloys, oxygen penetrates into the material during heat treatment and creates a surface zone of grain boundary cavitation which manifests itself in much reduced ductilities and lifetimes during subsequent creep at lower temperatures (Pandey *et al* 1984).

3.1 Modelling damage due to oxygen penetration

The mechanism of degradation when oxygen penetrates into a nickel-base material at high temperatures is believed to be carbon dioxide bubble formation along grain boundaries. The experiments of Bricknell & Woodford (1982) demonstrated conclusively that carbon dioxide gas bubbles were formed along grain boundaries of dilute nickel-carbon alloys when exposed to air at temperatures of the order of 1000°C. Their presence seriously reduced ductilities in subsequent creep at lower temperatures. Much evidence has been accumulated by Bricknell & Woodford (1982), Pandey *et al* (1984) and Osgerby & Dyson (1990a) that points to a similar effect occurring in nickel-base superalloys: creep ductilities are reduced even more dramatically than in nickel-carbon alloys, but the evidence for a carbon dioxide gas reaction, although strong,

remains largely circumstantial since bubbles have never been found after heat treatment alone. Carbon monoxide formation has been detected by mass spectroscopy in one system after pre-exposure and creep (Pandey *et al* 1992).

One of the major findings of Pandey *et al* (1984) that under certain conditions (higher temperatures), oxygen is able to penetrate into the material more easily under reduced oxygen potentials, has now been substantiated by other investigations (Pandey *et al* 1986; Osgerby & Dyson 1990b). This finding has focussed attention on the need for a better understanding of the kinetics of carbon dioxide formation in addition to the kinetics of formation of barrier oxides such as alumina and chromia. CDM also requires a quantitative damage evolution rate which necessitates better knowledge of the kinetics of formation of both CO₂ gas bubbles and oxide scales under reduced pressure. Kinetic data on carbon dioxide gas bubble formation are sparse but Iacocca & Woodford (1988) report an activation energy for the rate of advance of the bubble interface that is close to the volume self diffusion coefficient in nickel, D_v . Oxygen diffuses interstitially in nickel with an activation energy approximately 0.6 that of D_v (Park & Alstetter 1988); the implication must be therefore that more than one activation process is important in determining the rate of advance of the reaction-front. The next section proposes a kinetic model for CO₂ gas bubble formation and exemplifies its potential using data from a nickel-carbon alloy.

3.1a New kinetic model for CO₂ gas bubble formation: Consider figure 1 which illustrates the planar concentration profile of dissolved oxygen in nickel containing a surface film of NiO that maintains a concentration $C'_{[O]}$ for all time, t . The reaction-front occurs at a distance d below the surface at an oxygen concentration of $C'_{[O],R}$. If the diffusivity of oxygen in nickel, $D_{[O]}$, is reasonably assumed to be independent of distance x , then the oxygen profile as a function of x and t is given in standard treatments (Crank 1956) as

$$C_{[O]} = C'_{[O]} \operatorname{erfc}(x/2(D_{[O]}t)^{1/2}) \quad (6)$$

and therefore

$$C_{[O],R} = C'_{[O]} \operatorname{erfc}[d/2(D_{[O]}t)^{1/2}]. \quad (7)$$

When the ratio $C_{[O],R}/C'_{[O]}$ is independent of temperature, then $D_{[O]} \propto d^2/t$ and

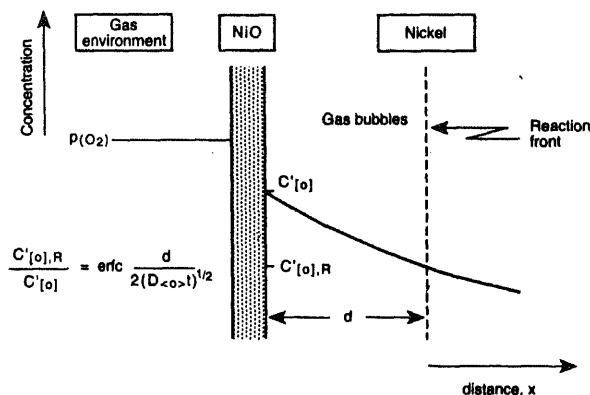


Figure 1. Schematic of the oxygen profile in nickel ahead of the reaction front.

the activation energy of the reaction-front kinetics becomes equal to that for diffusion. This will not be true in general since $C_{[O],R}$ and $C'_{[O]}$ are both functions of temperature.

$C'_{[O]}$ is maintained at a level proportional to the square root of the dissociation pressure $P_{(O_2)}$ of NiO and is given by

$$C'_{[O]} = K(T) \exp[\Delta\mu_{(NiO)}^0/RT], \quad (8)$$

where $K(T)$ is the equilibrium constant for solution of oxygen in nickel and $\Delta\mu_{(NiO)}^0$ is the standard free energy of formation of NiO.

The nucleation condition for CO_2 bubble formation is reached when $P_{(CO_2h)} = 2\gamma/r_c = P^*$, where γ is the surface tension and r_c the critical bubble radius. Consideration of the CO_2 reaction kinetics at the bubble/matrix interface, gives:

$$C_{[O],R} = K(T)[P^*/a_{[C]}]^{1/2} \exp[\Delta\mu_{(CO_2)}^0/2RT] \quad (9)$$

where $a_{[C]}$ is activity of carbon in nickel and $\Delta\mu_{(CO_2)}^0$ is the standard free energy of formation of CO_2 .

The ratio $C_{[O],R}/C'_{[O]}$ can now be calculated using (7)–(9)

$$\frac{C_{[O],R}}{C'_{[O]}} = \left[\frac{P^*}{a_{[C]}} \right]^{1/4} \exp \left[\frac{\Delta\mu_{(CO_2)}^0 - 2\Delta\mu_{(NiO)}^0}{2RT} \right] = \operatorname{erfc} \left[\frac{d}{2(D_{[O]}t)^{1/2}} \right]. \quad (10)$$

3.1b *Application to a nickel–carbon alloy:* Kubaschewski & Alcock (1979) have tabulated equations for $\Delta\mu_{(CO_2)}^0$ and $\Delta\mu_{(NiO)}^0$:

$$\Delta\mu_{(CO_2h)}^0 = -[3.96 \times 10^5 + 0.84T] \text{ J mol}^{-1},$$

$$\Delta\mu_{(NiO)}^0 = -[2.35 \times 10^5 - 85.6T] \text{ J mol}^{-1}.$$

Substituting into (10) gives

$$\operatorname{erfc}[d/2(D_{[O]}t)^{1/2}] = 3.55 \times 10^{-5} [P^*/a_{[C]}]^{1/2} \exp(4450/T). \quad (11)$$

The activity coefficient for carbon in nickel, γ_c , has been derived previously (Dyson 1982):

$$\gamma_c = 2 \exp[4763/T]. \quad (12)$$

Substituting (12) into (11) gives

$$\operatorname{erfc}[d/2(D_{[O]}t)^{1/2}] = 2.5 \times 10^{-5} [P^*/C_{[C]}]^{1/2} \exp(2069/T). \quad (13)$$

where $C_{[C]}$ is the atom fraction of carbon in nickel.

Homogeneous nucleation of carbon dioxide gas bubbles in nickel requires pressures of the order of 10^5 atmospheres and is an unlikely event (Dyson 1982). We will assume P^* to be one tenth of this value, implying heterogeneous nucleation at sites having defects a few nanometres in radius. This is consistent with gas bubbles lying only along grain boundaries. Substituting for P^* in (13) gives

$$\operatorname{erfc}[d/2(D_{[O]}t)^{1/2}] = 2.5 \times 10^{-3} [C_{[C]}]^{-1/2} \exp(2069/T). \quad (14)$$

The experiments of Iacocca & Woodford (1988) used an alloy containing 135 ppm of carbon by weight, i.e. $C_{[C]} = 6.6 \times 10^{-4}$. Thus, from (14),

$$\operatorname{erfc}[d/2(D_{[O]}t)^{1/2}] = 9.8 \times 10^{-2} \exp(2069/T). \quad (15)$$

In order to derive an apparent activation energy, values of the parameter d^2/t were calculated as a function of temperature using tables of the Error Function Complement and the equation for D_{IOI} given by Park & Alstetter (1988)

$$D_{\text{IOI}} = 4.9 \times 10^{-6} \exp(-19700/T). \quad (16)$$

Values of d^2/t are plotted against $1/T$ in the conventional manner in figure 2, from which an activation energy of 211 kJ mol^{-1} can be derived. This activation energy is substantially greater than the diffusion activation energy of $163.8 \text{ kJ mol}^{-1}$ input through (11). Figure 2 demonstrates that the frequently used practice of deducing activation energies for oxygen diffusion from measurements on reaction-front kinetics can be very misleading.

It has often been assumed (Bricknell & Woodford 1982; Iacocca & Woodford 1988) that oxygen diffuses faster down grain boundaries and so gives rise to the CO_2 gas bubbles found preferentially along grain boundaries. However, even a cursory inspection of the rates of transport of substitutional solutes through grains relative to those along grain boundaries indicates that at these high temperatures (greater than $0.7 T_m$), most of the flux will be transported through the grains. Dyson & Hondros (1985) demonstrated this quantitatively and also pointed out that even when grain boundary transport is dominant, reaction-front kinetics will obey a $t^{1/4}$ law with a low activation energy and not the $t^{1/2}$ law with a high activation energy observed experimentally for CO_2 bubble formation. A further piece of evidence favouring mass transport of oxygen through the grain interiors is shown in figure 3, which compares the tracer volume diffusion data of nickel in a Ni-20% Cr alloy (Frost & Ashby 1982) with the relatively recent data of oxygen in nickel by Park & Alstetter (1988). The less complete and older data of Kerr (1972) are also included in figure 3. It is clear that oxygen diffusivities are considerably greater than tracer nickel diffusivities and that oxygen diffuses with a lower activation energy. Thus oxygen almost certainly diffuses interstitially in nickel

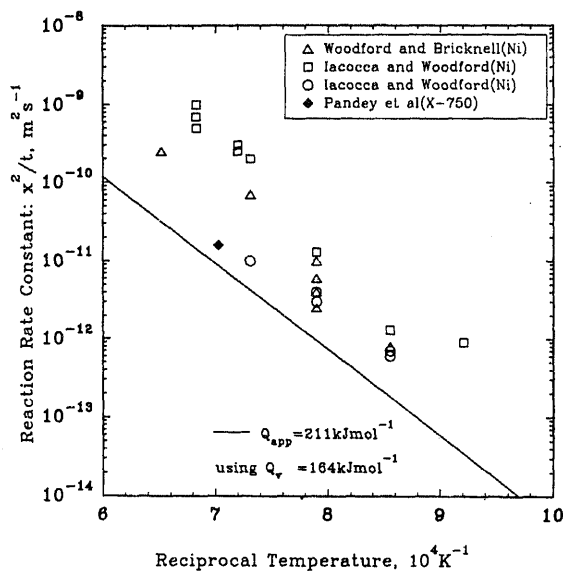


Figure 2. Comparison of predicted reaction-rate constant for CO_2 bubble formation (solid line giving an activation energy of 211 kJ mol^{-1}) with experimental data.

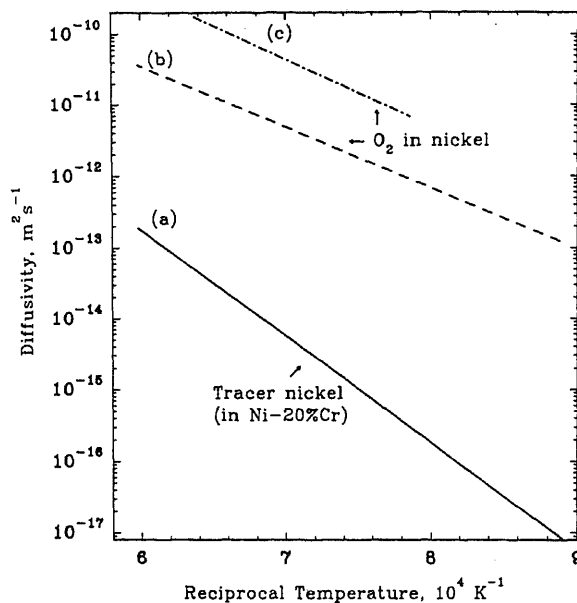


Figure 3. Comparison of experimental diffusivities of tracer Ni in a nickel-chromium alloy with two sets of measurements of oxygen diffusion in nickel. (a) Frost & Ashby (1982), (b) Park & Alstetter (1988), (c) Kerr (1972).

and will have little or no tendency to diffuse faster along grain boundaries. The reason for the appearance of CO_2 bubbles only along grain boundaries cannot therefore be due to rapid transport down the boundaries, as Woodford and co-workers have consistently suggested, but must be a consequence of preferential nucleation. This is consistent with the assumption of a constant CO_2 pressure term, P^* , in § 3.1a.

The model predictions of d^2/t can be compared in figure 2 with the CO_2 penetration rate data of Woodford and co-workers on nickel and the single datum point of Pandey *et al* (1986) on the nickel superalloy X-750. The model predictions fall slightly below the lower limit of the experimental dataset but the agreement must be considered satisfactory considering the independent data input to the model and the large experimental scatter (due in part to the use of cylindrical section thicknesses which, according to Iacocca & Woodford (1988), were too small relative to the diffusion distance and so overestimated d^2/t because of an assumed infinite plane slab of material in their analysis). Better agreement with the dataset could have been achieved using the (poorer pedigree) oxygen diffusivity data of Kerr (1972).

3.1c Incorporation into the CDM framework: During creep, the presence of a sub-surface layer containing cavity nuclei implies pre-existing damage in the material. The damage parameter and its effect on creep rate are identical to those given in table 1 under the internal oxidation mechanism; in this particular case of pre-exposure to the environment, the damage accumulation rate is zero. Pandey *et al* (1986) and Osgerby & Dyson (1990a) showed that for the wrought Ni-base superalloy, Inconel X-750, the measured creep rate in testpieces exposed to air at 1000°C for various times showed good agreement with model predictions of penetration depth when f was assigned a value $= 1/3$, a value that corresponds to cavitation on every transverse grain boundary in the environmentally damaged region.

3.2 Modelling damage due to periodic oxide-spallation

The equation-set developed to describe uniaxial creep behaviour of low-alloy ferritic steels in the *absence* of environmental attack (Dyson & Osgerby 1993) is

$$\left. \begin{aligned} \dot{\epsilon} &= \dot{\epsilon}_0 \sinh[\sigma(1-H)/\{\sigma_0(1-S)(1-\omega)\}], \\ \dot{H} &= (h'/\sigma)[1 - (H/H^*)]\dot{\epsilon}, \\ \dot{S} &= (K'/3)(1-S)^4, \\ \dot{\omega} &= (1/3\epsilon_u)\dot{\epsilon}. \end{aligned} \right\} \quad (17)$$

Under the usual laboratory conditions of constant load, there is a further constraint on the change of stress with time given by $\dot{\sigma} = \sigma\dot{\epsilon}$.

The model material parameters $\dot{\epsilon}_0$, σ_0 , h' , H^* , K' and the uniaxial ductility ϵ_u are generally functions of temperature, but Dyson & Osgerby (1993) found that the primary creep parameters h' and H^* could be regarded as constants without significant change in predicted lifetimes. Two of the model parameters, $\dot{\epsilon}_0$ and K' , are exponentially related to temperature with activation energies dictated by physics to lie within well-defined narrow bands. The parameter σ_0 is related to the volume fraction and initial dispersion of the particles. The coarsening of the dispersion with time is given by the Greenwood (1956), Wagner (1961) or Lifshitz-Slyozov (1961) expression for particle coarsening, \dot{S} , and the variation of particle volume-fraction with temperature is currently accounted for in an empirical way.

Table 2 gives values for the intrinsic (i.e. in the absence of environmental-attack) model material parameters determined for a normalised and tempered 1% Cr 1/2% Mo ferritic steel over the temperature range 530–625°C (Dyson & Osgerby 1993).

Equation-set (17) can be integrated numerically to give lifetimes under a variety of imposed external constraints. Figure 4 is an example under constant load and temperature: two temperature, 550°C and 625°C, are given and at each temperature, lifetimes are predicted both with and (artificially) without the ageing term \dot{S} operating. The importance of particle ageing during the test in curtailing lifetimes, particularly under service conditions, is amply demonstrated in figure 4: at a typical service stress of 40 MPa at 550°C, ageing will reduce lifetimes by more than two orders of magnitude.

Environmental-attack by oxygen to create an oxide which then spalls periodically was identified as a problem for remanent lifetime prediction by Cane & Manning (1981). They pointed out that data obtained in a laboratory on testpieces (approximate diameter 10 mm) may give a pessimistic estimate of remanent lifetime of components that are often in excess of 100 mm in section: testpiece data would fail prematurely due

Table 2. Intrinsic model material parameters for a 1 Cr 1/2 Mo ferritic steel.

$\dot{\epsilon}$ (h^{-1})	σ_0 (MPa)	h' (MPa)	H^*	K' (h^{-1})
$\frac{1.4 \times 10^9}{\sigma_0} \exp - \left[\frac{31000}{T} \right]$	$8 \times 10^{-3} \exp \left[\frac{6000}{T} \right]$	10^5	0.4	$1.4 \times 10^{12} \sigma_0^3 \exp - \left[\frac{36000}{T} \right]$

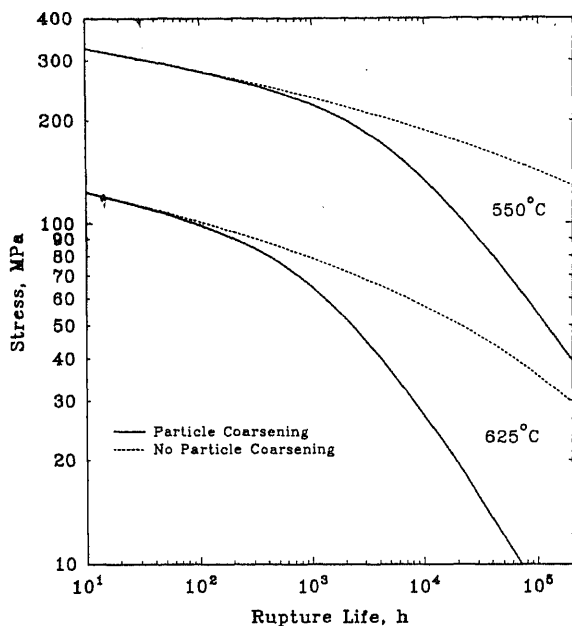


Figure 4. Model predictions of creep lifetime as a function of stress at two temperatures. The solid lines refer to material undergoing particle-ageing and the dashed lines to a hypothetical "non-ageing" material. Model parameters for 1Cr 1/2Mo steel (Dyson & Osgerby 1993).

to the greater rate of loss of load-bearing area in 10 mm section size compared to 100 mm.

Various models have been proposed for the damage rate, \dot{S}_c , due to this mechanism (Manning 1981; Ashby & Dyson 1984; Dyson & Osgerby 1989). It was shown by Dyson & Osgerby (1989) that these could all be written in the following way:

$$\dot{S}_c = (2/R)\kappa\dot{\epsilon}^\alpha, \quad (18)$$

where α is either 0.4 or 0.5 and κ is a term containing the parabolic rate constant for oxidation, K_p ; κ is proportional to either $K_p^{0.5}$ or $K_p^{0.6}$. Table 1 gives the formalism due to Ashby & Dyson (1984).

Equation (18) was incorporated into equation-set (17) to assess the effect of spallation on predicted creep lifetimes. The creep strain rate equation becomes

$$\dot{\epsilon} = \dot{\epsilon}_0 \sinh[\sigma(1-H)/\{\sigma_0(1-S)(1-S_c)(1-\omega)\}]. \quad (19)$$

The spalling criterion proposed by Manning (1981) has been used here to give an equation for \dot{S}_c :

$$\dot{S}_c = \frac{2}{R} \left(\frac{4E}{15\gamma_i} \right)^{0.2} K_p^{0.6} \dot{\epsilon}^{0.4} \quad (20)$$

where the oxide modulus $E = 200$ GPa; and the oxide/metal interfacial energy $\gamma_i = 2$ Nm⁻¹. γ_i could be considerably lower than this and thus represents a lower bound on \dot{S}_c . However even a ten-fold decrease in γ_i would result in only a 60% increase in \dot{S}_c . A much more sensitive parameter is K_p . Data for K_p as a function of temperature have been reported for a number of low-alloy ferritic steels (Pinder 1977). A mean line

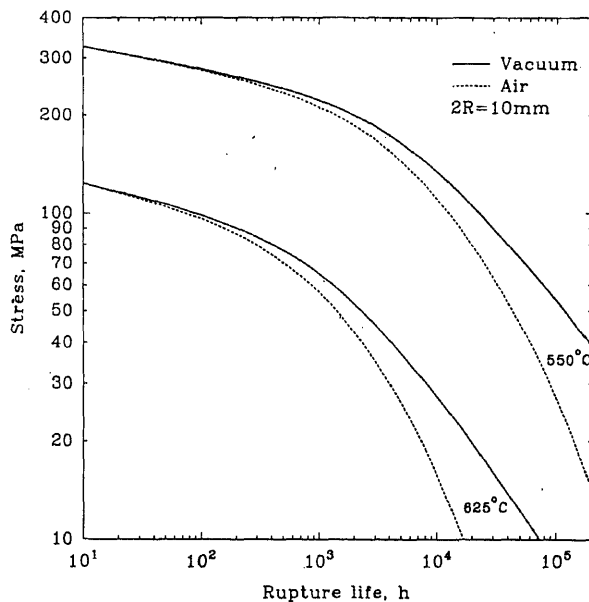


Figure 5. Model predictions of creep lifetime in air and in vacuum as a function of stress at two temperatures. Model parameters for 1Cr1/2Mo steel (Dyson & Osgerby 1993).

through these data has been calculated for the present work:

$$K_p = 7.7 \times 10^{-6} \exp - [13000/T] \text{m}^2 \text{h}^{-1}. \quad (21)$$

Equation (21) applies only to the temperature range 500–625°C.

Lifetimes were calculated at 550°C and 625°C using (19)–(21), along with the intrinsic model parameters given in table 2 and assuming a testpiece diameter, $2R$,

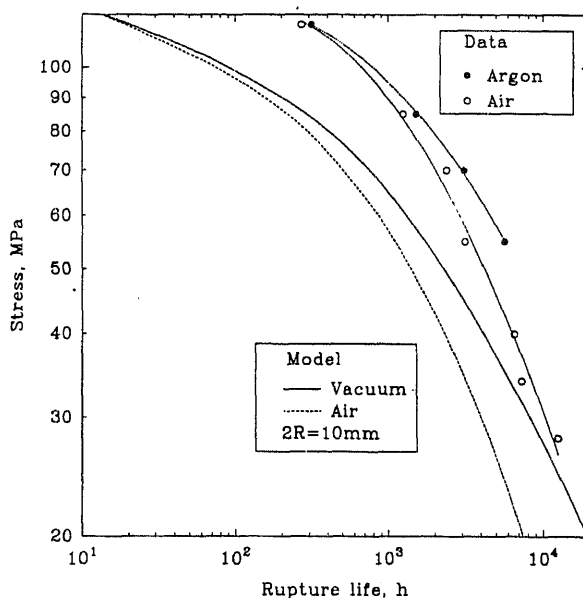


Figure 6. Illustrating that the predicted effect of air exposure on a 1Cr1/2Mo steel at 625°C is qualitatively similar to the measured effect on a 1/2Cr1/2Mo 1/4V steel.

equal to 10 mm (figure 5). The predictions cannot yet be verified for this alloy since there do not appear to be experimental data in the literature. However, qualitative support for the model is shown in figure 6 which reproduces experimental data in air and argon using a 1%Cr 1/2%Mo 1/4%V steel (Cane & Townsend 1985). The important point to note is the similarity in the relative lifetimes between argon and air, since the longer absolute lifetimes of the CrMoV steel simply reflect its greater intrinsic creep resistance.

4. Concluding remarks

Physics-based creep continuum damage mechanics is emerging as a powerful quantitative tool in design and remanent lifetime prediction. Its computer-friendly format makes it ideal for finite element work which will increasingly become less specialised as the ratio of price to computational power continues to fall. This paper has focused on two mechanisms of creep/environmental interaction; there are almost certainly others to identify but the strength of a physics-based approach is that these can be accommodated without prejudicing the conclusions of existing models.

Attack of nickel-base alloys by oxygen diffusing into the metal from the environment and forming CO₂ bubbles is now a well-studied phenomenon, but work still needs to be done to validate predictions of the CDM model, particularly in extending the temperature/time range of applicability of the damage-rate kinetics. The paper has made some progress particularly with regard to defusing the idea prevalent in the literature that the process is controlled by oxygen diffusion along grain boundaries. A kinetic model utilising oxygen diffusion within the matrix has been proposed which can account satisfactorily for the large experimental dataset on this subject.

The authors would like to thank Dr M C Pandey (Defence Metallurgical Research Lab, Hyderabad) for general discussions and for bringing to their attention the papers by Iacocca & Woodford (1988) and Park & Alstetter (1988).

List of symbols

A dot over any symbol signifies the derivative with respect to time

$a_{[c]}$	activity of carbon in nickel;
$C_{[C]}$	atom fraction of carbon dissolved in nickel;
$C_{[O]}$	oxygen concentration;
$C_{[O],R}$	oxygen concentration at reaction-front;
$C_{[O]}'$	oxygen concentration at scale interface;
$D_{[O]}$	diffusivity of oxygen in nickel;
D_v	volume self diffusion coefficient;
d	distance of reaction-front from surface;
E	Young's modulus;
H	internal variable describing material hardening during primary creep;
H^*	saturation value of H ;

h'	coefficient for material hardening during primary creep;
K'	coefficient for material softening due to precipitate coarsening;
K_p	parabolic rate constant for oxidation;
$K(T)$	equilibrium constant for solution of oxygen in nickel;
n	stress exponent for power law creep;
$P_{(\text{CO}_2)}$	pressure of carbon dioxide in bubble;
$P_{(\text{O}_2)}$	dissociation pressure of nickel oxide;
P^*	critical pressure for nucleation of carbon dioxide gas bubbles;
R	radius of cylindrical testpiece;
r_c	critical radius for gas bubble;
S	internal variable describing material softening;
S_c	internal variable describing material softening due to corrosion;
T	temperature;
t	time;
α	exponent for damage due to oxide scale spallation;
γ	surface tension;
γ_i	oxide/metal interfacial energy;
ε	creep strain rate;
ε_0	material parameter in sinh law;
ε_u	uniaxial creep ductility;
κ	coefficient for damage due to oxide scale spallation;
$\Delta\mu_{(\text{NiO})}^0$	standard free energy of formation for nickel oxide;
$\Delta\mu_{(\text{CO}_2)}^0$	standard free energy of formation for carbon dioxide;
σ	applied uniaxial stress;
σ_0	material strength parameter in sinh law;
ω	internal variable describing material softening and fracture due to creep cavitation.

References

- Ashby M F, Dyson B F 1984 Creep damage mechanics and micromechanisms. In *Advances in fracture research* (eds) S R Valluri *et al* (Oxford: Pergamon) pp. 3–30
- Barbosa A, Taylor N G, Ashby M F, Dyson B F, McLean M 1988 A model-based computer analysis of creep data (CRISPEN)-applications to nickel-base superalloys. In *Superalloys 88* (eds) D N Dahl *et al* (Warrendale, PA: The Metallurgical Society) pp. 683–692
- Bricknell R H, Woodford D A 1982 The mechanism of cavity formation during high temperature oxidation of nickel. *Acta Metall.* 30: 257–264
- Cane B J, Manning M I 1981 Effect of testpiece oxidation on rupture data. CERL Note LM/MATS/407
- Cane B J, Townsend R D 1985 Prediction of remaining life in low-alloy steels. *Flow and fracture at elevated temperatures* (Ohio: ASM) pp. 279–316
- Dyson B F 1982 Analysis of carbon/oxygen gas bubble formation in some nickel alloys. *Acta Metall.* 30: 1639–1646
- Dyson B F, Gibbons T B 1987 Tertiary creep in nickel-base superalloys: analysis of experimental data and theoretical synthesis. *Acta Metall.* 35: 2355–2369
- Dyson B F, Hondros E D 1985 Chemical environment effects on creep fracture. *Advances in fracture research* (eds) S R Valluri *et al* (Oxford: Pergamon) pp. 3753–3772
- Dyson B F, Osgerby S 1989 Modelling synergy between creep and corrosion for engineering design. In *Materials for engineering design: The next decade* (eds) B F Dyson, D R Hayhurst (London: Institute of Metals) pp. 373–379

- Frost H J, Ashby M F 1982 *Deformation mechanism maps: the plasticity and creep of metals and ceramics* (Oxford: Pergamon)
- Greenwood G W 1956 The growth of dispersed precipitates in solution *Acta Metall.* 4: 243–248
- Iacocca R G, Woodford D A 1988 The growth of dispersed precipitates in nickel and its relevance to weldment cracking. *Metall. Trans. A* A19: 2305–2313
- Ion J, Barbosa A, Ashby M F, Dyson B F, McLean M 1986 The modelling of creep for engineering design – I. NPL Report, DMA (A) 115
- Kerr R A 1972 M S Thesis, Ohio State University, Columbus, Ohio
- Kubaschewski O, Alcock C B 1979 *Metallurgical thermochemistry* 5th edn (Oxford: Pergamon)
- Lifshitz J M, Slyozov V V 1961 The kinetics of precipitation from supersaturated solid solutions. *J. Phys. Chem. Solids* 19: 35–50
- Manning M I 1981 *Corrosion and mechanical stress at high temperature* (eds) V Guttman, W Merz (London: Applied Science) pp. 323–338
- Osgerby S, Dyson B F 1990a Effects of oxygen on creep performance: Mechanisms and predictive modelling. *Mater. Sci. Technol.* 6: 2–8
- Osgerby S, Dyson B F 1990b Environmental embrittlement of superalloys during coating processes. In *Surface engineering practice; Processes, fundamentals and applications* (eds) K N Strafford, P K Datta, J S Gray (Chichester: Ellis Horwood) pp. 466–474
- Othman A M, Hayhurst D R, Dyson B F 1993 Skeletal point stresses in circumferentially notched tension bars undergoing tertiary creep modelled with physically-based constitutive equations. *Proc. R. Soc. London A*441: 343–358
- Pandey M C, Dyson B F, Taplin D M R 1984 Environmental, stress-state and section size synergisms during creep. *Proc. R. Soc. London A*393: 117–131
- Pandey M C, Taplin D M R, Ashby M F, Dyson B F 1986 The effect of prior exposure time on air-environment/creep interactions. *Acta Metall.* 34: 2225–2233
- Pandey M C, Satyanarayana D V V, Rama Rao P 1992 An analysis of the creep-environment interaction of Inconel alloy X-750. *Mater High Temp.* 9: 167–173
- Park J W, Alstetter C J 1988 The diffusion and solubility of oxygen in solid nickel. *Metall. Trans.* A18: 43–50
- Pinder L W 1977 Oxidation kinetics and scale morphology of mild steel and low chromium alloy steels in $N_2/20\%O_2$ between 500 and 850°C. CEGB Report, SSD/MID/R58/77
- Wagner C 1961 Theory of the ageing of precipitates by redissolution (Ostwald maturing). *Elektrochem.* 65: 581–591
- Woodford D A, Bricknell R H 1986 Embrittlement of high temperature alloys. Treatise on materials science and technology. *Embrittlement of engineering alloys* (London: Academic Press) vol. 25, pp. 157–199

The effect of hydrogen induced cracking on the integrity of steel components

INDRANIL CHATTORAJ

National Metallurgical Laboratory, Jamshedpur 831 007, India

Abstract. The occurrence of hydrogen embrittlement is a much researched phenomenon, known to cause mechanical property degradation and catastrophic failures. The ductility loss brought about by hydrogen ingress is encountered even in unstressed bodies where such cracking is termed hydrogen induced cracking (HIC) and is in phenomenological contrast to catastrophic failures encountered by stressed bodies subjected to hydrogen producing environments. This article will discuss HIC in some detail. This form of cracking is especially detrimental and often observed in oil country tubular goods (OCTG) which are subjected to sour gas. Consequently, the significance of HIC is most appreciated by oil companies at various stages of oil extraction, transportation and storage. In this article the chemical and metallurgical genesis of HIC, its harmful impact on material and component integrity are discussed. It has been noted that MnS inclusions are extremely harmful to this form of cracking. Similarly, centreline segregation in the ingot stage and deoxidation practices during steelmaking were found to affect HIC. Some case studies of HIC obtained from literature are presented. The variables affecting the propensity to HIC are provided in brief. Suitable measures to reduce or eliminate HIC in steels are also discussed.

Keywords. Hydrogen-induced cracking; embrittlement, decohesion theory; hydrogen absorption.

1. Introduction

Hydrogen-induced cracking (HIC) is a phenomenon widely encountered by components exposed to environments capable of introducing hydrogen into the component material, especially sour environments to which oil and gas installations and transmission systems are exposed. The presence of H_2S in such environments catalyse hydrogen entry into steels. HIC can be thought of as one form of hydrogen embrittlement, and is differentiated from the other forms of hydrogen embrittlement phenomena by the appearance, morphology and sites of cracking and by the mode of crack propagation. Hydrogen induced cracking occurs at ambient or near-ambient conditions and in stressed as well as unstressed components. These cracks have a planar appearance, with

different cracks linked in a stepwise fashion. HIC is often accompanied by surface blisters.

This article deals with the general occurrence of hydrogen entry and hydrogen trapping and with the theories of hydrogen embrittlement, to provide a background of the various kinetic processes causing material degradation by hydrogen ingress. Subsequently hydrogen induced cracking is dealt with by providing a brief introduction of the phenomenon, discussing the variables affecting HIC and providing case studies including our recent experiences with this failure mode. The various preventive measures to counter HIC are also discussed.

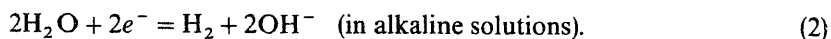
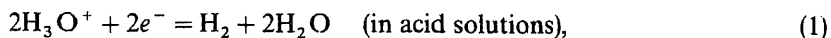
2. Hydrogen entry

The hydrogen evolution reaction was characterized by McBreen & Genshaw (1967). The evolution of hydrogen occurs frequently due to cathodic reduction of H^+ ions in aqueous corroding solutions, or hydrogen may be absorbed due to the use of high pressure hydrogen gas in the environment. In addition, the material itself may have hydrogen retained from the process of ore reduction (steelmaking for example). Hydrogen either absorbed from the environment or present in the material can lead to unpredictable catastrophic failure. This is evident in the various failures in the oil and gas industry, aircraft and automotive industries.

The problem of hydrogen embrittlement of any material involves various mechanisms which finally lead to embrittlement. The steps can be broadly classified as follows.

- (1) Hydrogen adsorption at the metal/alloy surface.
- (2) Hydrogen evolution at the metal/alloy surface.
- (3) Absorption of some of the adsorbed hydrogen into the bulk of the metal.
- (4) Transport of absorbed hydrogen to normal lattice sites as well as potential sites for cracking, under the influence of a naturally existing or externally applied chemical potential gradient.
- (5) Accumulation of hydrogen at the crack sites leading to catastrophic failure.

Various schematics have been proposed for the reaction sequence mentioned above. McBreen & Genshaw (1967) proposed a simple scheme for the evolution and entry reaction and over the years it has served as a satisfactory basis for iron and steels and is included here in figure 1. The overall reaction of hydrogen evolution in solutions are as follows,



The overall reaction can proceed by two mechanisms namely:

(a) *The recombination mechanism* which involves chemical recombination of adsorbed hydrogen atoms as follows



(b) *The electrochemical desorption mechanism* which involves the following

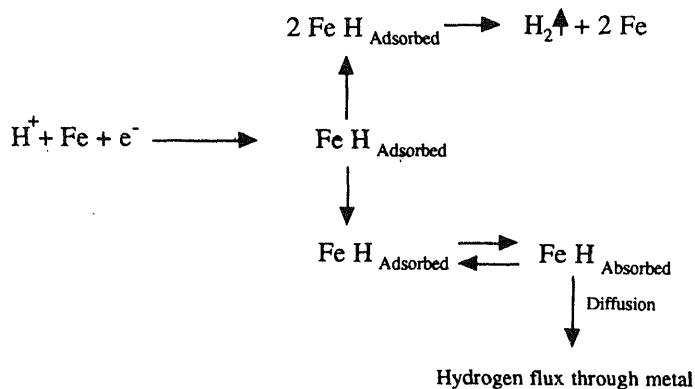
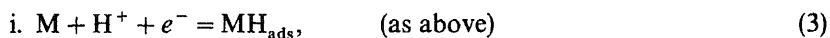


Figure 1. Hydrogen evolution and entry scheme (according to McBreen & Genshaw 1967).

electrochemical steps,



As a result of the need for multiple steps, it is obvious that one of the reaction steps can become rate controlling in the overall reaction path.

3. Hydrogen trapping

Darken & Smith (1949) were the first to observe that hydrogen diffusion in steels was affected by imperfections in the lattice. The first formalism for trapping in steels was developed by McNabb & Foster (1972). They suggested a trapping and a detrapping parameter and they came up with a mathematical formulation based on the assumption of local equilibrium between trapped and normal lattice sites. Their formalism considered only the reversible traps; irreversible traps were considered not to influence the diffusion as they represented sinks with hydrogen essentially removed from the permeation system. The works of McNabb & Foster (1972), and Oriani & Josephic (1974) considered a single population of reversible traps. Pressouyre & Bernstein (1978) characterized the trapping behaviour of different kinds of traps, both reversible and irreversible, by controlling the type and number of traps and by observing their effect on permeation transient. Johnson *et al* (1979) analysed saturable and non-saturable traps by considering relationships between the trapped hydrogen concentration and the lattice hydrogen content and redefining effective hydrogen diffusivity in terms of these relationships. According to their theoretical development, one can predict an increase in apparent hydrogen diffusivity with lattice hydrogen content when saturable traps are present, while the reverse is true for non-saturable traps. To summarize, we can consider traps as either reversible or irreversible depending on the depth of the potential well they present to hydrogen diffusion. Trapping manifests itself by changing apparent diffusivity values. The amount and direction of such a change from perfect lattice diffusion depends on the amount and type of traps present in the lattice. Simultaneous creation of traps and their

influence on hydrogen ingress, also known as dynamic trapping, occurs during straining of hydrogen charged specimen.

This brief introduction to hydrogen trapping was necessary, since the trapping of hydrogen at MnS inclusions is the factor most responsible for HIC. The trapped hydrogen causes decohesion of the matrix-inclusion interface, either by pressurization or by reducing the interatomic bond strength. The net effect is the generation of delaminations and cracks near inclusions.

4. Hydrogen embrittlement theories

Although many theories have been proposed to explain the hydrogen embrittlement phenomenon, two have gained substantial popularity.

4.1 Decohesion theory

This theory was developed by Troiano and others (Troiano 1960; Mortlet *et al* 1958; Johnson & Troiano 1957) to explain the synergistic effects of hydrogen on material degradation. Troiano refuted the pressure theory and various surface adsorption theories for embrittlement, as these would predict an initial loss in ductility, in variance with experimental observations. Troiano and co-workers (Troiano 1960; Mortlet *et al* 1958; Johnson & Troiano 1957) proposed that the degree of embrittlement would vary as the hydrogen concentration in the region of maximum triaxiality in the lattice. Whereas the other theories were concerned with hydrogen content in cracks and voids, this theory renders hydrogen in voids harmless entities, and only hydrogen in special lattice positions as significant in embrittlement. The role of voids and cracks is to act as stress raisers, so that the region of maximum triaxiality is generally near such imperfections. The disappearance of hydrogen embrittlement at low temperatures can be explained by the decrease of hydrogen diffusivity and at high temperatures by the conflicting effects of stress induced diffusion and increased homogenization. Troiano (1960), made the observation that crack initiation and propagation in HE occurs in three distinct stages: (a) incubation, (b) slow crack growth and (c) catastrophic failure. From fractographic observations, Troiano concluded that the third stage of catastrophic failure was essentially overload failure and there was no effect of hydrogen in this stage. The incubation period according to Troiano was the time required for hydrogen to reach a critical concentration in the region of maximum triaxiality. The slow crack growth in the second stage is essentially the rate of hydrogen diffusion to regions in front of the crack tip, thus implying discontinuous cracking. Troiano suggested a decrease in cohesive strength of the lattice due to presence of hydrogen; this coupled with the observation that hydrogen accumulates at regions of high triaxial stresses near imperfections, explained the embrittlement phenomenon. Troiano's original speculation was that hydrogen atoms in solution in transition metals donate their electrons to the *d* band of the metallic core, thus increasing the repulsion of metallic cores. This theory predicted that addition of copper to nickel would increase embrittlement initially and then decrease it as the *3d* band in nickel is progressively filled; this prediction was substantiated by experimental findings.

Tetelman & Robertson (1963) observed that crack growth due to hydrogen charging occurred discontinuously. Oriani & Josephic (1974) demonstrated the existence of

a threshold stress at a given hydrogen fugacity and conversely a threshold fugacity at a given stress intensity, below which crack growth did not occur in steels. They observed that the threshold values for deuterium were consistently higher than those for hydrogen. This observation can only be reconciled with the decohesion theory; deuterium has a lower molal volume than hydrogen in α -iron, thus it is less effective in concentrating at triaxiality sites due to stress induced diffusion. According to Oriani, decohesion due to hydrogen is manifested in high strength steels by an increase in cleavage fracture and in low strength steels by an enhancement of microvoid nucleation. Stress relaxation studies (Oriani & Josephic 1979) on AISI 1045 steels were explained by suggesting that since hydrogen causes decohesion, it favours microvoid generation over relaxation by dislocation activity. Oriani & Josephic (1980) also proposed that the reduction of Peierl's stress and the reduction of screw dislocation cross slip in *bcc* iron are due to reduced cohesive strength in the presence of hydrogen.

Birnbaum's objection to this concept of lowering of cohesive strength is that such a reduction should also manifest itself in the reduction of atomic force constants and elastic constants. In the case of *fcc* metals a decrease in these constants is indeed observed in the presence of hydrogen. However in group Vb metals like niobium, even at very high hydrogen charging, there is significant increase in C_{11} and bulk modulus values (Birnbaum & Mazzolai 1985). The other criticism of this theory is in the appearance of fractures. Decohesion theory predicts that intergranular fracture surface should show the morphology of grain interface whereas actual observations with high resolution microscopes reveal fracture along slip planes near grain boundaries, often crossing over into adjacent grains along slip planes (Robertson *et al* 1984). In spite of these criticisms, decohesion theory is one of the more popular theories of HE. Calculations based on the embedded atom model and the cluster variation method (Briant & Messmer 1980) do suggest that hydrogen would indeed cause decohesion, thus vindicating this theory.

4.2 Internal pressure theory

A theory of hydrogen embrittlement based on hydrogen accumulation at voids was proposed by Zapffe & Sims (1941). According to these authors hydrogen atoms accumulate at voids until an equilibrium pressure is attained. When this pressure attains a value close to the elastic strength of the metal, the metal embrittles, de Kazinczy (1954) elaborated on this concept by suggesting that crack growth is facilitated by the energy released by expanding hydrogen gas in cracks. de Kazinczy utilized Griffith's theory of brittle fracture, which states that for a stable crack to grow, the system must undergo a total decrease in the energy content. He suggested that part of the total energy of the material charged with hydrogen is due to the energy content of hydrogen gas in the cracks and voids. On crack propagation, the gas expands releasing energy and thus the energy due to strain required to meet Griffith's criterion is reduced, that is, the strain at which crack propagates is lower. This model however requires that the material have preexisting cracks in it. However Bilby & Hewitt (1962) and Garofalo *et al* (1960) proposed that crack initiation could be due to dislocation pile-up under the influence of external stress. Bastien & Azou (1951) suggested that hydrogen is concentrated in Cottrell atmospheres of dislocations and is transported along with dislocations to the cavities. This dislocation enhanced diffusion of hydrogen would account for the incubation time and temperature effects of embrittlement.

Bockris & Subramanyan (1971) developed relationships for the hydrogen fugacity in microcracks and voids as a function of overpotential, in electrochemical charging of hydrogen. Based on theoretical calculations, they predicted which rate controlling mechanisms for hydrogen evolution would cause embrittlement when pressure theory was valid. Beck *et al* (1965) suggested that blister formation due to high internal pressure of hydrogen in cavities would lead to plastic deformation in the vicinity of blisters. This was supposed to increase the dislocation density near blisters, which would act as crack initiation sites.

There are two criticisms to this theory. Johnson & Hirth (1976) showed that hydrogen supersaturations obtainable at dislocations were greatly overestimated in literature, and dislocation transport, even if it was effective, could not account for large internal pressure required by this theory. The findings of Hancock & Johnson (1965), that crack propagation occurs even at very low hydrogen pressure environments, also contradicts the internal pressure mechanism of embrittlement. Such a mechanism might be effective in high fugacity environments but cannot be accepted as a general theory.

5. Hydrogen-induced cracking (HIC)

In the previous sections an introduction to the broad area of hydrogen embrittlement was provided. This was done to impress upon the readers that the general effect of hydrogen entry into alloys, especially steels, is a deterioration of their mechanical properties. However the external manifestation of such deterioration can take up various forms depending on the presence or absence of other variables in the system. The aim of this paper is to concentrate on HIC which is a specific type of hydrogen embrittlement, and is often encountered by components exposed to sour environments. The rest of this article will deal with the various parameters enhancing HIC, a few case studies of HIC observed in service, and measures adopted to counter HIC.

Whereas the problem of stress cracking in a wet sour environment was identified as early as the 1950s, it was only a couple of decades later that hydrogen induced cracking as a mode of pipeline failure was appreciated (Moore & Warg 1976). This is different from sulphide stress cracking (SSC) in that it can occur in stressed as well as unstressed bodies. Burns (1976) pointed out the difference in the appearance of these two types of sour environment cracks. HIC was identified as cracking due to a mechanism involving the formation, growth and linkage of internal blisters which often gave it the appearance of a series of steps and hence its alternate name – “stepwise cracking (SWC)”. In this article I have used the terms HIC and SWC interchangeably, signifying the same phenomenon. Ikeda *et al* (1977) provided a schematic of the SWC process, which has been included here as figure 2.

6. Variables affecting HIC

6.1 Environmental variables

The important environmental variables are pH, chloride content, temperature, H_2S concentration, presence of dissolved oxygen and the exposure time. The findings of

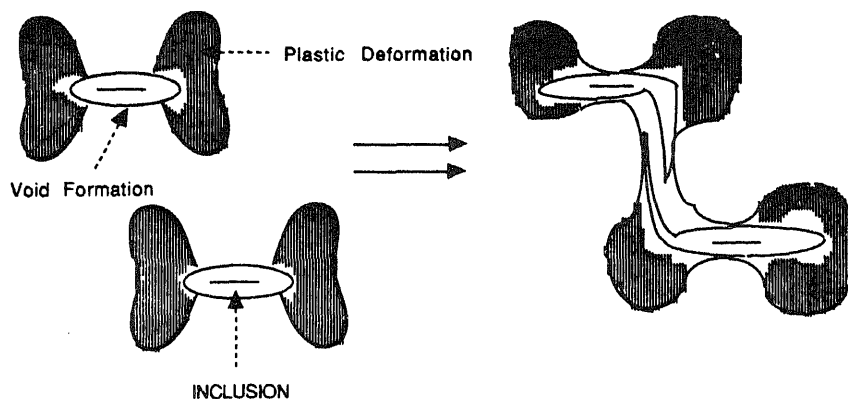


Figure 2. Direct linkage of two closely spaced cracks producing steps. After Ikeda *et al* (1977).

Ikeda *et al* (1980) indicated that lower pH environment accelerated corrosion as well as stepwise cracking (SWC). They also demonstrated that higher concentration of dissolved chlorides increased the severity of the environment. The extent of hydrogen damage was found (Kowaka *et al* 1975) to be maximum in the temperature range of 15 to 35°C. Sharp reduction in SWC at temperatures above 35°C is attributed to the decreased concentration of H_2S in the saturated solutions. A threshold concentration of H_2S is often reported (Nakasugi *et al* 1979) below which HIC does not occur.

6.2 Metallurgical variables

One of the most important considerations is the casting practice with particular reference to the segregation of impurities and alloying elements occurring during casting. Moore & Warga (1976) recommended the study of specimens from the pipe section of ingots (segregation zone), as these are most sensitive to SWC. They also found that the deoxidation practice during casting leads to increased SWC sensitivity so that fully killed steels are almost always more susceptible to HIC as compared to semi-killed steels of a similar composition. Moore & Warga pointed out that increased deoxidation increases sulphur solubility as well as promotes the formation of detrimental type II (stringers) MnS inclusions in comparison to the type I inclusions. Similarly, the practice of controlled rolling is conducive to the formation of MnS stringers. Coldren & Tither (1976) concluded that SWC arises because of voids at non-metallic inclusion/steel interfaces. Wilde *et al* (1980) confirmed that SWC initiated at elongated type II MnS inclusions. Herbsleb *et al* (1980) also concluded that inclusions with sharp edges and large surfaces are preferred sites for initiation of SWC. After the realization that MnS inclusion shape and type are of vital importance in HIC, various modifications in steelmaking practices have been tried out to control these inclusions. Decreasing the sulphur content was found beneficial by Herbsleb *et al* (1980) and by Brown & Jones (1984). The inclusion shape control by calcium or rare earth metal addition have been found to improve HIC resistance.

Miyoshi *et al* (1976) found that SWC propagated along anomalous microstructures composed of low temperature transformation products. Microstructural banding

(pearlite or martensite) has also been found to increase crack propagation. The formation of banded microstructures in pipeline steels is due to dendritic segregation of manganese and phosphorus. According to Taira *et al* (1984) restricting the segregation zone hardness to below 300 HV is needed to eliminate HIC, since hard "banded" structures of bainite or martensite are susceptible to hydrogen embrittlement as well as HIC. Thus homogenization of microstructures by quenching and tempering would also reduce SSC.

6.3 Stress variables

A correlation has not yet been established between steel strength and SWC susceptibility. HIC has been reported for a wide range of tensile strengths (300 to 800 MPa). It seems that nonmetallic inclusions and anomalous microstructures are more important factors in determining HIC susceptibility as compared to the strength of the steel. The SWC mechanism involves segregation of hydrogen atoms to internal interfaces followed by decohesion at these interfaces possibly by hydrogen pressurization. The plastic regions generated at the blister crack tips are embrittled by hydrogen, and transverse cracks propagate through the embrittled regions to join parallel cracks thus giving the appearance of steps. SWC occurs not only in unstressed components, but also in steels under elastic tensile stresses. Very few studies have been conducted to investigate the effect of welding residual stresses on the occurrence of SWC. The study of Taira *et al* (1979) seems to suggest that there is no effect of residual stresses.

6.4 Chemical variables

The addition of copper has often been found (Inagaki *et al* 1978) beneficial to SWC resistance of linepipe steels. This was attributed to the formation of a black protective film of Mackinawite, FeS_{1-x} , enriched with Cu. This reduces the corrosion rate as well as the amount of absorbed hydrogen. Thus Cu-alloying is beneficial only in environments where a protective film can form. Similarly Cr additions were also found to improve SWC resistance. Nishimura *et al* (1977), and Parrini & Devito (1978) had observed the beneficial effects of Cr. Ni was also found to greatly reduce hydrogen absorption from sour environments (Nishimura *et al* 1977). Researchers have found that Co, Bi and Rh additions cause decrease in hydrogen absorption by steels from H_2S containing environments (Iino *et al* 1979).

7. Case studies

7.1 First reported failures

Parades & Mize (1954) were the first to report service failure due to stepwise cracking (SWC). This occurred in 1951–52 on a API-5LX grade 359 transmission linepipe, after several months of service. It was found that the imperfections necessary for blistering were abundant in the material. Delaminations and blistering were evident with some blisters observed to have initiated at the delaminations. The analysis of the gas in the blister was found to contain 94% hydrogen, 2% methane, with traces of carbon dioxide

and carbon monoxide. Class (1963) reported the failure of a pipeline in sour service. These were made from killed steels, were longitudinally welded by resistance welding and were used in sour service. Analysis revealed manganese sulphide and silicate inclusions in the material. It was also observed that seamless pipes performed significantly better in service.

7.2 Hydrogen damage in a failed pressure vessel

McHenry *et al* (1982) reported their investigation on a pressure vessel rupture at an oil refinery resulted in the death of 17 people and extensive property damage. The vessel was a 18.8 m high steel cylinder used to strip hydrogen sulphide from a process stream of propane and butane. The vessel was observed to fracture circumferentially adjacent to a repair weld made to replace a section damaged earlier by hydrogen blisters and delaminations. McHenry *et al* (1982) observed five types of hydrogen damage.

Hydrogen blisters and delaminations were observed in the bottom part of the cylinder. Blisters and delaminations were often close enough to the surface to cause visible bulging. The material was found to be quite susceptible to hydrogen induced cracking. These delaminations were indirectly responsible for failure as they led to the replacement of a section of the vessel. The steel matrix between the interfacial cracks was found to fail by cleavage because the hydrostatic stresses generated by absorbed hydrogen at blisters, inhibit plastic deformation. In addition, hydrogen induced cold cracking was observed in the heat affected zone of the repair weld. However McHenry *et al* (1982) did not believe that these modes were primarily responsible for failure. According to them, hydrogen stress cracks developed during operation of the vessel at the inside surface adjacent to the repair welds and hydrogen pressure cracking caused these surface cracks to propagate in a zigzag fashion through the vessel wall. These were facilitated by hydrogen embrittlement of the material which reduced the fracture toughness of the material by more than half.

7.3 Stepwise cracking in a spirally welded pipeline

Moore & Warga (1976) reported that in 1974, three service ruptures occurred in a spirally welded, API 5LX-Grade 42 sour gas transmission pipeline between four to seven weeks after commissioning. It was found that extensive blistering and cracking had occurred over 10 km of this 90 km pipeline. The failures could be attributed to stepwise cracking near elongated MnS inclusions. Although the failures occurred near the spiral weld, they could not be associated with any kind of weld defects. Moore & Warga used a test proposed by Cotton to study the HIC susceptibility of the material. They found that the most important factor affecting the hydrogen cracking sensitivity of steels was the MnS inclusion morphology. Elongated type II, MnS stringers were observed to render the steel very crack sensitive. Moreover, since all fully killed steels except those treated with rare earth elements contain type II MnS inclusions, they would be more susceptible to HIC than semi-killed steels. Moore & Warga were of the opinion that although steels can be made insensitive to HIC, a completely immune steel was not feasible.

7.4 Ongoing research at the National Metallurgical Laboratory, Jamshedpur

Under the aegis of The Component Integrity Evaluation Programme (CIEP), which is a concerted effort on life estimation of various components, one of the projects is focusing on the studies of HIC in API 5LX Grade 52 pipeline steel exposed to simulated sour environment. This investigation is an attempt at an 'in toto' observation of the mechanical property degradation brought about by sour environment exposure, and is one of the few attempts at correlating the extent of HIC with the loss in ductility of the material. One of the observations of this study was that the extent of HIC was a monotonically increasing function of the time of exposure to the sour environment. It was found that even after twenty-eight days of exposure to the NACE prescribed sour environment, no saturation of the HIC damage occurred. This observation indicated the great potential of lattice imperfections to trap hydrogen. In this investigation the mechanical property deterioration caused by HIC was studied in some detail through slow straining after exposure to the sour environments. The investigators found that, surprisingly, hydrogen induced cracks, *per se*, did not cause a deterioration of ductility. Such deterioration was the result of the presence of mobile lattice hydrogen which are distinct from hydrogen trapped at interfaces of matrix/ inclusions, the latter being responsible for HIC. This investigation has so far revealed the clearly distinct roles of mobile lattice hydrogen and trapped hydrogen, each causing different types of damage to the matrix, the former causing lattice embrittlement most observable on dynamic straining and the latter causing cracking under static conditions.

8. Preventive measures

The preventive measure which can be adopted during service include the injection of inhibitors, desulphurization and dehydration of the gas passing through the line. National Association of Corrosion Engineers (NACE) recommended a hardness limit of HRC 22 for steels in use in sour environments. Various metallurgical parameters can also be controlled to reduce HIC.

There are three well-known measures to improve the HIC resistance.

- (1) reduction of hydrogen entering into steels by the formation of protective films.
- (2) reduction of MnS and inclusion shape control.
- (3) control of microstructures, especially segregation zones.

The first of these methods is often insufficient as the film formation is pH dependent and in aggressive media (low pH) protective films are often not formed. It was argued earlier that the beneficial effect of Cu alloying was due to the enrichment of the protective surface film of mackinawite. The more effective preventive measures are the modification of inclusion shape and amount, and the control of the microstructure.

Taira *et al* (1984) found that complete elimination of inclusion improves SSC resistance as well as HIC resistance. It was mentioned earlier that fully killed steels were more prone to HIC, however, due to their better mechanical properties, it is often desirable to use them in spite of the HIC limitation. This calls for modifications in the steelmaking practice. Sulphide shape control by rare earth additions is often used. However since the amount of rare earth addition has to be very precise, steelmakers are often tentative about following this practice. Moreover, rare earth sulphides tend to

produce ionization effects which interfere with arc stability in automatic welding processes. Calcium treated steels were also found to have improved resistance to HIC (Brown & Jones 1984; Taira *et al* 1984). According to Taira *et al* (1984) calcium content must be delicately controlled so that neither manganese sulphide, nor calcium sulphide clusters are present. They believed that the HIC resistance of a calcium-treated steel depended on the ratio of the Ca content to the S content. Brown & Jones (1984) found that HIC resistance increased with Ca:S ratio. They observed that rare earth metal treated steels were less resistant than Ca-treated steels.

HIC is often found to propagate along microstructural bands (pearlitic). The formation of the latter is a result of dendritic segregation of Mn and P. The hardness of the centre segregation in steel plates is one of the most important factors affecting HIC susceptibility of high strength line pipe steels. Matsumoto *et al* (1986) found that lowering the carbon content to below 0.05% decreased the hardness of the segregation zones. They also found that homogenization treatments were effective in decreasing the same. However such treatments are time consuming due to the slow diffusion of Mn and may not be practical, causing reduced industrial productivity. Brown & Jones (1984) advocated the use of quenched and tempered steels and reduction of manganese to reduce banding. They also suggest the use of modern casting techniques like superheat temperature control and electromagnetic stirring to reduce the centreline segregation in continuously cast steels.

References

- Bastien P, Azou P 1951 Influence de l'amplitude vitesse des deformations plastiques sur la segregation de la hydrogene dans le fer et les aciers. *Compte. Rendus* 232: 69-71
- Beck W, Bockris J O'M, McBreen J, Nanis L 1965 Hydrogen permeation in metals as a function of stress temperature and dissolved hydrogen concentration. *Proc. R. Soc. A* 290: 220-235
- Bilby B A, Hewitt J W 1962 Hydrogen in steels - the stability of microcracks. *Acta Metall.* 10: 587-600
- Birnbaum H K, Mazzolai F M 1985 Elastic constants and ultrasonic attenuation of the alpha-alpha prime phase of the Nb-H(D) system. *J. Phys.* F15: 507-542
- Bockris J O'M, Subramanyan P K 1971 The equivalent pressure of molecular hydrogen in cavities within metals in terms of the overpotential developed during the evolution of hydrogen. *Electrochim. Acta* 16: 2169-2179
- Briant C L, Messmer R P 1980 Electronic effects of sulphur in nickel - A model for grain boundary embrittlement. *Philos. Mag.* 42: 569-576
- Brown A, Jones C L 1984 Hydrogen induced cracking in pipeline steels. *Corrosion* 40: 330-336
- Burns D S 1986 Laboratory tests for evaluating alloys for hydrogen sulphide service. *Mat. Perf.* 15: 21-28
- Class I 1963 Report on investigation of sulphide stress corrosion cracking of steels, particularly of steels of comparatively low tensile strength. *2nd Int. Conf. Met. Corr.*, New York
- Coldren A P, Tither G J 1976 Metallographic study of hydrogen induced cracking in line pipe steel. *J. Metall.* 28(5): 5-10
- Darken L S, Smith R P 1949 Behaviour of hydrogen in steel during and after immersion in acid. *Corrosion* 5: 1-16
- de Kazinczy F 1954 A theory of hydrogen embrittlement. *J. Iron. Steel Inst.* 177: 85-92
- Garofalo F, Chotu Y T, Ambegaokar V 1960 Effect of hydrogen on stability of microcracks in iron and steels. *Acta Metall.* 8: 504-512
- Hancock G G, Johnson H H 1965 Hydrogen oxygen and subcritical crack growth in a high strength steel. *Trans. Metall. Soc. AIME* 236: 513-516

- Herbsleb G, Popperling R K, Schwenk W 1980 Occurrence and prevention of hydrogen induced stepwise cracking and stress corrosion cracking of low alloy pipeline steels. *NACE Natl. Conf.*, Chicago, NACE
- Iino M, Nomura N, Takezawa H, Gondoh H 1979 Aciers pour pipe-lines resistant au cloquage et au criquage dus a l'hydrogene. *Rev. Metall.* 76: 591
- Ikeda A, Morita Y, Terasaki F, Takeyama M 1977 On the hydrogen induced cracking of line-pipe steel under wet hydrogen sulphide environment. *2nd Int. Cong. on hydrogen in metals*, Paris Paper no. 4A7
- Ikeda A, Terasaki F, Kaneko T 1980 Influence of environment conditions and metallurgical factors on hydrogen induced cracking of line pipe steel. *NACE Natl. Conf.* Chicago
- Inagaki H, Tanimura M, Matsushima L, Nishimura T 1978 Effect of Cu on the hydrogen induced cracking of pipeline steel. *Trans. Iron Steel Inst. Jpn.* 18: 149-156
- Johnson H H, Troiano A R 1957 Crack initiation in hydrogenated steels. *Nature (London)* 179: 777
- Johnson H H, Hirth J P 1976 Internal hydrogen supersaturation produced by dislocation transport. *Metall. Trans.* A7: 1543-1548
- Johnson H H, Quick N, Kumnick A J 1979 Hydrogen trapping mechanisms by permeation techniques. *Scr. Met.* 13: 67-72
- Kowaka M, Terasaki F, Nagata S, Ikeda A 1975 The test method of hydrogen induced cracking of rolled steels under wet hydrogen sulfide environment. *The Sumitomo Search* 14(11): 36
- Matsumoto K, Kobayashi Y, Ume K, Murakami K, Taira K, Arikata K 1986 Hydrogen induced cracking susceptibility of high strength linepipe steels. *Corrosion* 42: 337-345
- McBreen J, Genshaw M A 1967 *Proc. Intl. Symp. on SSC*, NACE Houston
- McHenry H I, Purtscher P T, Shives T R 1982 Observations of hydrogen damage in a failed pressure vessel. *Corrosion Sci.* 27: 1041-1057
- McNabb A, Foster P K 1972 A new analysis of the diffusion of hydrogen in iron and ferritic steels. *Trans Metall. Soc. AIME* 227: 618-627
- Miyoshi E, Tanaka T, Terasaki F, Ikeda A 1976 A hydrogen induced cracking of steels under wet hydrogen sulphide environment. *Trans. ASME, J. Eng. Ind.* B98: 1221
- Moore E M, Wargha J J 1976 Factors influencing the hydrogen cracking sensitivity of pipeline steels. *Mater. Perform.* 15(6): 17-23
- Mortlet J G, Johnson H H, Troiano A R 1958 A new concept of hydrogen embrittlement in steels. *J. Iron. Steel Inst.* 189: 37-44
- Nakasugi H, Sugimura S, Matsuda H, Murata T 1979 Development of new linepipe steels for sour gas service. *Nippon Steel Tech. Report* 14(12): 66
- Nishimura T, Inagaki H, Tanimura M 1977 Hydrogen cracking in sour gas pipeline steel. *2nd Intl. Cong. on hydrogen in metals*, Paris, Paper No. 3E9
- Oriani R A, Josephic P H 1974 Equilibrium aspects of hydrogen induced cracking of steels. *Acta Metall.* 22: 1065-1074
- Oriani R A, Josephic P H 1979 Hydrogen enhanced load relaxation in a deformed medium carbon steel. *Acta Metall.* 27: 997-1005
- Oriani R A, Josephic P H 1980 Effect of hydrogen on the plastic properties of medium carbon steels. *Metall. Trans.* A11: 1809-1820
- Parades F, Mize W W 1954 *Oil Gas J.* 53: 99
- Parrini C, Devito A 1978 High strength microalloyed pipe steels resistant to hydrogen induced failures. *Proc. MICON'78*, Houston, (Ohio: ASM)
- Pressouyre G M, Bernstein I M 1978 A quantitative analysis of hydrogen trapping. *Metall. Trans.* A9: 1571-1580
- Robertson I M, Tabata T, Wei W, Heubaum F, Birnbaum H K 1984 Hydrogen embrittlement and grain boundary fracture. *Scr. Metall.* 18: 841-846
- Smialowski M 1962 *Hydrogen in steels* (London: Pergamon)
- Taira T, Kobayashi Y, Inagaki H, Watanabe T 1979 Sulphide corrosion cracking of line-pipe for sour service. *NACE Natl. Conf. Atlanta* 1979
- Taira T, Kobayashi Y, Matsumoto K, Tsukada K 1984 Resistance of line pipe steels to wet sour gas. *Corrosion* 40: 478-486
- Tetelman A S, Robertson W D 1963 Direct observations and analysis of crack propagation in iron - 3% silicon single crystals. *Acta Metall.* 11: 415-426

- Troiano A R 1960 The role of hydrogen and other interstitials in the mechanical behaviour of metals. *Trans. Am. Soc. Metall.* 52: 54-80
- Wilde B E, Kim C D, Phelps E H 1980 Some observations on the role of inclusions in hydrogen induced blister cracking of linepipe steels in sulphide environments. *NACE Natl. Conf.*, Chicago
- Zapffe C A, Sims C E 1941 Hydrogen embrittlement internal stress and defects in steels. *Trans. Am. Inst. Min. Metall. Eng.* 145: 225-259

Weldability and weld joint failures

M N CHANDRASEKHARAI AH

Welding Research Institute, Bharat Heavy Electricals Ltd,
Tiruchirappalli 620 014, India

Abstract. Welding plays a prominent role in the fabrication and erection of structures and components in the industry. Weld failures when they do occur, either during fabrication or service, involve considerable rework, apart from production, time and material losses. Hence, it is essential to adopt appropriate welding procedures depending on the material, weld configuration and the service requirement. In addition, the weldability of the material should be established with adequate laboratory tests in order to minimise the tendency towards hot and cold cracking susceptibilities. The mechanisms of such cracking and the tests to be undertaken to evaluate the cracking susceptibility are enumerated in this paper along with a brief report on weld failures and criteria to be adopted for their repair.

Keywords. Weld failures; weld repair; weldability; cold cracking; hot cracking.

1. Introduction

Welding plays a significant role in the fabrication, erection and commissioning of plants and machinery for power, petroleum, chemical, steel and other industrial sectors. With the improvement in steel-making technology and the availability of better and cleaner steel grades with higher strength-to-weight ratios, the capacity, efficiency and availability of plants and machinery are continuously increasing. The advent of better design capabilities, using complex structural analysis with finite element and other methods, has enabled optimisation of section thickness with reduced factor of safety and considerable savings in material and fabrication costs. Manual metal arc welding is being replaced by better, automated and sophisticated welding technologies which reduce the fabrication and erection time considerably and also give better and consistent quality of welds.

The effect of these technological advances is that the pressure parts and other components are now exposed to severe temperature, pressure and environmental conditions for prolonged periods of time which may, sometimes, lead to unforeseen and catastrophic failures. The weldments and heat affected zones (HAZ), which are structurally non-integral with the base metal, are more prone to such failures. Apart from the cost and time required for the weld repair of such components, the plant outage leads to considerable financial losses. Hence, it is important to understand the factors responsible for such

Table 1. Welding defects and their effects.

Defect	Possible effects	Action
Incomplete penetration	Reduces strength and notch toughness	Complete removal necessary
Lack of fusion	Reduced fatigue strength and static and impact strength	Remove and reweld
Undercut	Reduces fatigue strength, increases incidence of hot tears	Addition of weld metal
Overlap	Reduces fatigue strength	Removal by grinding
Slag entrapment	Irregular and large lenticular inclusions may reduce strength and act as sites for initiation of brittle fracture.	Chipping, cleaning and rewelding
Porosity	Dense porosity reduces load carrying area and acts as stress raiser	Excessive amount necessitates removal & rewelding.
Incorrect weld size and profile	Static and fatigue strength may get affected, may often indicate presence of other defects e.g. lack of penetration	Many require rewelding
Poor surface appearance	Acts as stress raiser and may affect fatigue strength	Grinding and chipping followed by welding may be necessary where it is particularly bad
Weld or HAZ cracking	May propagate and lead to brittle failure	Grinding and rewelding

weld failures and try to eliminate or at least minimise them to the extent possible. The present paper aims at discussing the various metallurgical and other welding related factors that can cause weld failures and methods of preventing them. Creep, fatigue and fracture mechanics are excluded from the scope of the present paper since they are covered elsewhere in the book. Similarly, corrosion aspects are also outside the purview of this paper.

2. General considerations for welding

A wide variety of metals and alloys are used to fabricate the structurals and pressure parts in the industry and a number of welding technologies are available for the same. The welding processes commonly used can be broadly divided into three categories based on the heat input.

- (a) Low heat input
(manual metal arc) 1.0 to 1.8 kJ/mm
- (b) Intermediate heat input
(submerged arc, metal inert gas, cored wire etc.) 1.8 to 4.0 kJ/mm

- (c) High heat input 10 to 40 kJ/mm.
(electroslag, electrogas etc.)

While it is desirable to achieve the fastest possible deposition rate consistent with the properties required as per design, the welding process is generally dictated by several factors such as section thickness, type of joint, welding position, equipment and manpower availability and shop/site environments. Well established welding procedures are adopted in each case with welders trained for that material, joint configuration and welding position.

Despite these precautions, weld failures do occur occasionally, either during the manufacturing stage itself or during service. These failures could be in the form of porosities, lack of fusion, crack etc. which will have a direct bearing on the performance of the component. Table 1 lists some of these defects, their possible effects and remedial actions to be taken on them.

3. Welding of structural and pressure vessel steels

A large number of steel grades are extensively used in welding fabrication. They can be classified into three broad categories (Doty 1970) for their usage in structural and pressure vessel welding fabrication (table 2). Apart from carbon and low alloy steels, several grades of high alloyed and microalloyed steels are also used for specialised fabrication.

Generally all steel grades, either in the plate or pipe form, are amenable for all welding processes. The plate material composition, however, can affect the following mechanical and metallurgical properties of the welded joints.

Table 2. Classification of structural and pressure vessel steels (Doty 1970).

Composition	Thermal history	Minimum yield strength (N/mm ²)
Carbon steels*	Non heat treated	207-345
	Normalised	207-345
	Quenched & tempered	345-689
Low alloy steels**	Non heat treated	276-482
	Normalised	345-413
	Quenched & tempered	413-689
Alloy steels***	Normalised	241-345
	Normalised & tempered	345-552
	Quenched & tempered	345-1241
*	0.33% max. C, C-Mn-Si and with certain alloying elements.	
**	0.26% max. C, C with upto about one percent total of Cu, Ni, Cr, V & Nb.	
***	0.25% max. C, C with 0.5% or more of Ni, Cr or Mo.	

- Mechanical strength of the joint;
- Fracture toughness of the base metal, HAZ and weld metal;
- HAZ cracking sensitivity;
- Weld metal cracking sensitivity;
- Stress corrosion susceptibility.

Adequate precautions are to be taken to eliminate the above mentioned problems. The relationship between heat input, chemical composition and thickness must be reasonably defined in a practical manner and the effects of general and local restraint taken care in establishing adequate welding procedures.

4. Welding of stainless steels

Among the stainless steels, austenitic stainless steels are used for more than 90% of the fabrication because of their excellent weldability (Castner 1993). They have lower melting points, higher electrical resistance, lower coefficients of thermal conductivity and higher coefficients of thermal expansion than carbon steels. Austenitic stainless steels are amenable to all welding processes if a few of the factors are taken into account.

- Solidification cracking is the most frequently encountered problem;
- autogenous welds may be subjected to variable penetration;
- the welding procedure may affect corrosion resistance;
- several factors must be considered if post weld heat treatment (PWHT) is required;
- welding of austenitic stainless steels can result in greater distortion than carbon steels;
- welding fumes present potential hazard to workers;
- dissimilar metal weld joints require proper selection of filler metals and procedures.

Solidification cracking is a problem when the welds solidify primarily as austenite. Instead, if the weld metal is solidified primarily with delta ferrite, the hot cracking propensity is the least. The delta ferrite content can be estimated by Schaeffler and Delong diagrams. Presently, the Welding Research Council (WRC) has published modified diagrams in 1992 (figure 1) that allow accurate prediction of delta ferrite number (FN) in austenitic stainless steels.

A number of sources recommend a minimum of 4 FN to prevent hot cracking in arc welds of austenitic stainless steels. However, in certain situations involving higher welding speeds and deep and narrow weld beads, this may not be adequate to prevent hot cracking and hence a higher range of 5–20 FN is recommended. Care must be taken not to go for higher FN where the possibility of sigma phase formation increases.

Minor variation in the chemical composition of austenitic stainless steels can sometimes cause problems of variable penetration for autogenous full penetration welds. These problems referred to as 'cast-to-cast' or 'heat-to-heat' variation are particularly evident in heats containing less than 0.003% sulphur. They are always associated with the surface active elements on the fluid flow of the metal. Recommendations to avoid variable penetration include; avoiding calcium and rare earth treated steels, avoiding steels with less than 0.005% sulphur and with aluminium content of higher than 0.02%. When such steels have to be used, careful control of process parameters have to be worked out.

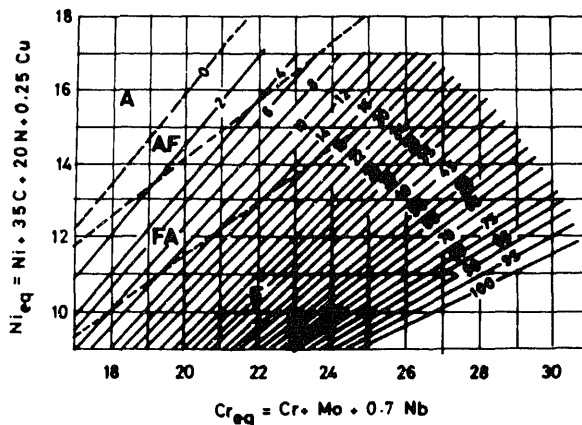


Figure 1. Welding Research Council (1992) constitutional diagram for stainless steel welds.

Welding can reduce corrosion resistance of HAZ regions that are exposed to temperatures between 425 and 900°C for long enough time to precipitate chromium carbide at grain boundaries. The most widely used method to prevent sensitisation of HAZ is to use low carbon stainless steel. Another approach is to use stabilized grades that contain titanium or columbium. Low carbon stainless steels have lower strengths than stabilized grades. Stabilized grades, on the other hand, may be more hot crack sensitive and may require careful ferrite control. They may also be susceptible to the localised precipitation of carbides in narrow regions of HAZ that can lead to intergranular corrosion known as knifeline attack.

Austenitic stainless steel weldments are normally used in service in the as-welded condition. However, to minimise residual stresses, prevent distortion and also in environments that can cause stress corrosion cracking, PWHT may be required.

The PWHT must be done in such a way as to avoid the following problems.

- Heating in the range 425–900°C can result in sensitisation.
- Heating weld between 540 and 925°C can transform ferrite to a hard brittle sigma phase.

For these reasons, PWHT usually involves solution annealing at temperatures of 1065–1120°C followed by rapid cooling or water quenching. Sigma phase can be minimised if the weld metal FN is limited to 10–12 FN.

5. Weldability

As mentioned earlier, depending on the heat input, the consumables used, the restraint on the weld and the cooling rate, a weld failure which manifests as porosity, lack of fusion or cracking may occur. To understand these behaviours, it is essential to study the weldability of the material. Weldability has been defined by the International Institute of Welding (IIW, document no. IIW/IIS-22-59) as: 'A metallic material is considered to be weldable to a certain degree by a given process and for a given purpose when a continuous metallic connection can be obtained by welding using

a suitable procedure so that the joints comply with the requirements specified both in regard to their local properties and their influence on the construction of which they form a part'.

This definition properly refers to both metallurgical and structural standpoint. Thus, any test to evaluate the weldability of a material should take into account all aspects of welding, the heating cycle, the cooling cycle, the stresses induced during solidification and fusion, and also the structural variations. All these factors, individually or collectively, can cause cracking in the weldments. The weldment cracking is broadly classified into two categories: cracks which develop above the solidus of the metal are called 'supersolidus cracks' and those that develop below the solidus temperature are called 'subsolidus cracks'. They are also commonly referred to as 'hot cracks' and 'cold cracks' depending on the temperature at which they develop.

6. Cold cracking in weldments

Cold cracking essentially depends on the underbead hardness, the hardness of the HAZ and the restraint imposed on the structure during cooling. The maximum possible hardness of the steel depends primarily on its carbon content. It is also influenced by the other chemical elements present in the steel and the weld thermal cycle. The methods of predicting the hardness have, by and large, focussed on defining and determining the carbon equivalent of the steel which takes into account the effect of various alloying elements. The effect of restraint history is evaluated separately by weldability tests such as implant and controlled thermal severity tests. The effect of thermal history is evaluated by determining/predicting the microstructure in weld simulation during cooling between 800 and 500°C.

Cold cracking is also sometimes referred to as hydrogen-induced cracking (HIC) since hydrogen is known to play a major role in this method of cracking. In ferritic steels, the phase changes which accompany welding may lead to hardened structures (like martensite formation) in either the weld metal or HAZ or both. These structures have low ductility which is further reduced by the presence of hydrogen, unavoidably introduced into the weld. This is because the solubility of hydrogen decreases as the temperature decreases. When the austenite contains hydrogen, the transformation during cooling results in the liberation of molecular hydrogen. In such cases, cracking or brittle fracture may occur following welding under the influence of residual stress and applied stress from the system (Baker *et al* 1966). The critical hardness levels of the weld will alter with type of joint, hydrogen potential of the welding process and the strength and composition of the parent metal. A typical cold crack is shown in figure 2.

6.1 Carbon equivalent

While assessing a plate material for its cold cracking susceptibility due to welding, the important aspect of carbon equivalent (CE) should be taken into account. The limiting value of CE is, in essence, an index of the HAZ hardening that may be allowed without cracking and this affects the rate of cooling which can occur during welding. Also for a given value of carbon equivalent, there is a thermal conductivity balance which necessitates higher preheat temperatures to avoid HAZ cold cracks in thicker plates.

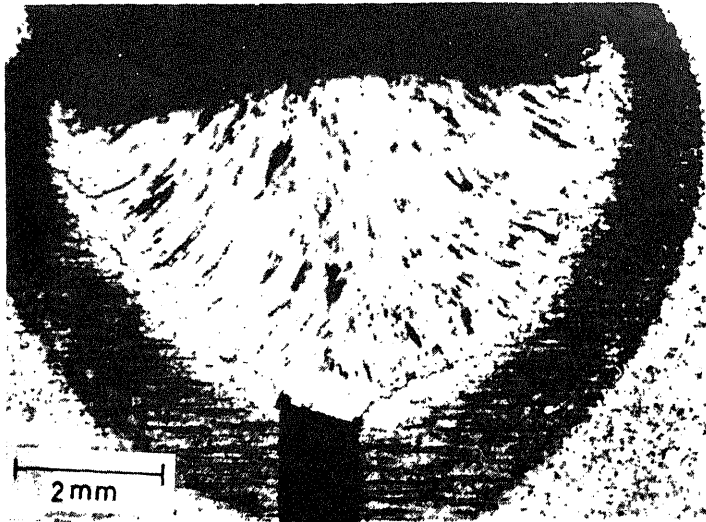


Figure 2. Cold cracking in the root run of butt weld.

A large number of carbon equivalent formulae have been proposed by different workers (de Meester 1991) which essentially predict the hardenability of the steel. Among these, the most widely used is the IIW carbon equivalent formula proposed by Dearden & O'Neil in 1940 and incorporated in the national standards of various countries.

$$CE_{IIW} = \frac{C + Mn}{6} + \frac{Ni + Cu}{15} + \frac{Cr + Mo + V}{5}.$$

This formula can be conveniently used for steels with carbon content of more than 0.18 or for steels with $t_{800/500}$ cooling time of longer than about 12 s.

The preheat temperatures suggested for several ranges of equivalent carbon content are:

<i>CE</i>	<i>Suggested preheat temperature °C</i>
Upto 0.45%	Optional
0.45 to 0.60%	95 to 200
above 0.60%	200 to 370

The above suggested preheat temperatures are for arc welding processes. They may be affected by the thickness of the workpiece. For gas welding processes, however, preheating is usually not required owing to the slow cooling rates associated with such processes.

6.2 *Effect of hydrogen*

More than 50% of the in-service failures, to date, have been attributed to the hydrogen induced cracking. The accident at the off-shore oil drill platform of North Sea in Ireland (Alexander 1981), the failure of the first stage rocket motor casing during

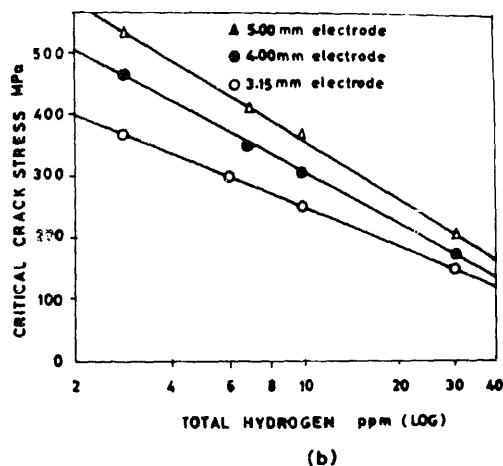
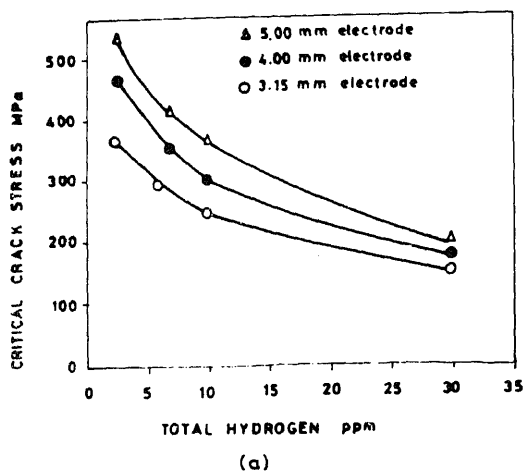


Figure 3. Critical crack stress determined by implant tests on carbon steel vs total hydrogen (ppm) plotted on (a) linear and (b) logarithmic scale (Evans & Christensen 1971).

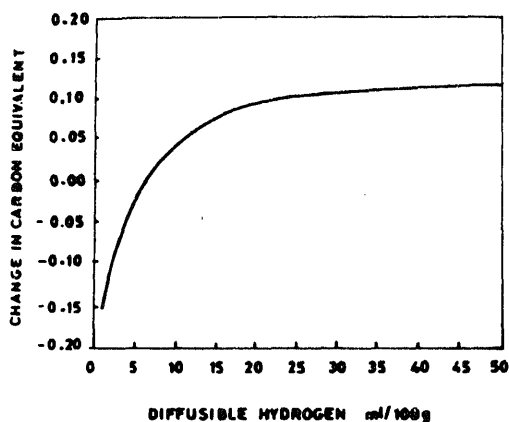
hydrotest at NASA (Kula & Anetil 1977) and the brittle fracture of an ammonia pressure vessel (Rosenfield & Reid 1977) are some of the major weld failures that have been reported and attributed to HIC.

Hydrogen is inadvertently introduced during welding in the weld metal. During cooling, this gas diffuses rapidly towards HAZ while the solidification and phase transformation progress in the opposite direction. This explains the formation of 'underbead cracking' in the HAZ close to the fusion boundary in which hydrogen is known to play a major role.

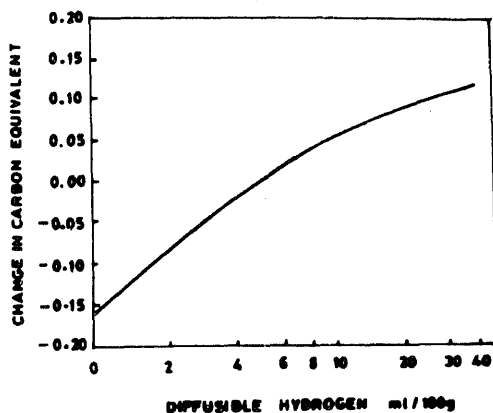
Among the techniques for diffusible hydrogen measurement, the glycerine method, mercury method and gas chromatography method are popular. The glycerine method, which was almost exclusively used in 50's and 60's is now considered not very accurate because some of the hydrogen dissolves in glycerine. The IIW and the American Welding Society (AWS) committees are trying to standardise the test conditions for mercury and gas chromatography methods and a detailed status report can be found in the literature (Kotecki 1992).

There has also been considerable work on the effect of diffusible hydrogen on cracking. Many researchers (Evans & Christensen 1971) have examined the critical cracking stress by the implant test of a variety of steels as a function of hydrogen content in the weld metal. Figures 3a and 3b show the data for a 0.17% C and 1.36% Mn steel and it is apparent that the critical cracking stress (implant rupture stress) is a linear function of the logarithm of the hydrogen content. Another method of representing the data is via the critical preheat temperature needed to avoid cracking as a function of diffusible hydrogen and hardenability; the latter expressed as carbon equivalent. The results are shown in figures 4a and 4b (Christensen & Simonsen 1981) and again the critical CE at a given preheat temperature is an approximate linear function of the logarithm of the weld metal diffusible hydrogen. Similar analysis has been conducted by other workers also (McParlan & Graville 1976).

Attempts are being made to develop and introduce low and very low hydrogen electrodes in order to combat the above problem. The AWS specifications (A5.1 and 5.5) define a 'low hydrogen coated electrode' as having no more than 0.6% moisture



(a)



(b)

Figure 4. Carbon equivalent adjustment plotted against diffusible hydrogen on (a) linear and (b) logarithmic scale (Christensen & Simonsen 1981).

content. The IIW definition of 'hydrogen controlled electrodes' are those producing 15 ml/100 g of hydrogen with 10 ml and 5 ml/100 g defining progressively better consumables. The 15 ml/100 g compares well with 0.6 percent coating moisture of AWS specification, while 16 ml/100 g plotted on a logarithmic scale fits in exactly with 0.6% moisture. Hence, the AWS committee, (Kotecki 1992) has decided to introduce three designations 'H16', 'H8' and 'H4' corresponding to hydrogen levels of 16, 8 and 4 ml/100 g respectively. This system would be introduced for covered mild steel electrodes (ANSI/AWS A5.1), covered low alloy steel electrodes (A5.5), submerged arc mild steel wires and fluxes (A5.17), submerged arc low alloy steel wires and fluxes (A5.23), gas shielded mild steel wires (A5.18), gas shielded low alloy steel wires (A5.28), flux cored mild steel wires (A5.20) and flux cored low alloy steel wires (A5.29). Some of these eight specifications have since been introduced and others are in the process of being revised. For all critical applications these low hydrogen consumables can be used to minimise the problem of HIC.

6.3 Weldability tests for cold cracking

The susceptibility of a steel for cold cracking depends on a multitude of events that any single test employing a set of standard parameters cannot adequately and with a degree of certainty quantitatively predict the cracking susceptibility (Veeraraghavan *et al* 1988). Controlled thermal severity and implant tests have been used for long to evaluate the cold cracking susceptibility.

Controlled thermal severity (CTS) test (Granjon 1960) consists of two plates with varying thicknesses fastened to one another by a central bolt and two lateral weld beads, called anchor runs- C_1 , are run (figure 5). The test beads C_2 and C_3 are run in a sequential order with the assembly being preheated to a select temperature. Since the assembly is not symmetrical, the bead C_3 cools more rapidly than the bead C_2 which has a lower thermal severity. The cooling rate in the critical zone can be modified by varying the plate thickness and the preheating temperature. Combined thickness of the plates, expressed in quarters of an inch is denoted as the thermal severity number (TSN). Fillet welding is done with increasing thickness until cold cracking occurs at a particular TSN. The demerit of this test is that the plate thickness determines both the HAZ hardening tendency as well as restraint values which cannot be varied independently.

The implant test, also proposed by Granjon (1969), is also being widely used to evaluate the cold cracking susceptibility. The standard procedure has been specified by the IIW and incorporated in the national standards of several countries. It is essentially a constant load rupture test of real HAZ of a steel immediately after welding. Taking fracture of specimen as a criterion, the critical stress applied for fracture at specific conditions of welding can be evaluated which can serve as an index to describe the hydrogen induced cracking susceptibility of the steel. One can also evolve the welding conditions under which the critical stress (σ_{cr}) cracking will be brought equal to or a specified percentage of the yield strength in order to select a welding procedure for the steel.

Many times cracks have been found to develop despite the above mentioned tests indicating positive results. This is because in most of the cases, the rigidity of the structure or the restraint which is not exactly quantified, is the contributory factor for

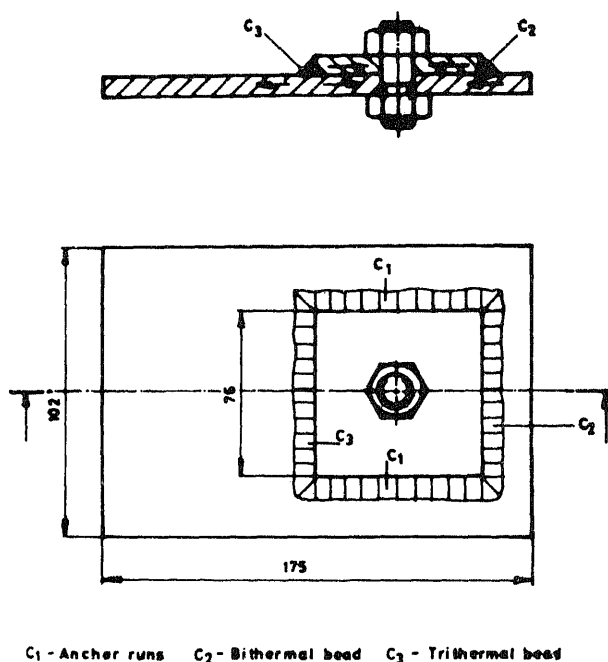


Figure 5. Controlled thermal severity test.

the cold cracking in welds. To overcome this problem, Rigid Restraint Cracking (RRC) tests (Sato & Matsui 1968) were developed. In RRC tests, specimens prepared for butt weld are perfectly rigidly clamped during welding and cooling down period, and the restraint intensity is measured. It is varied by varying the specimen length. The test enables one to assess the critical reactive stress (σ_{cr}) and the critical restraint intensity (K_{cr}) for a given material, under a set of welding conditions.

The disadvantages of the above test are that it requires sophisticated equipment for perfect clamping and maintaining constant gauge length during testing. Also long lengths of specimens are needed for obtaining low restraint intensity which increases the material requirement and cost.

To obviate these disadvantages, alternate methods known as Elastic Restraint Cracking (ERC) tests were developed at CSSR and elsewhere. Of these, the test method developed by Povezan (1978) of Bratislava Welding Research Institute has been adopted by us in WRI, Tiruchirapalli and is shown in figure 6. Window type elastic frames are used and the test plates are clamped by means of high strength bolts. The side arms of the clamping elements are provided with resistant strain gauges enabling recording of the reactive force during the tests. The effective restraint of the weld joint will depend upon the restraint intensity of the frame, restraint intensity of specimen and the length of the weld bead deposited. The development of weld reactive force is monitored with a time chart recorder. After allowing a day for development of cold crack, the weldment is evaluated by NDT and metallography for the presence of crack which can easily be correlated with the weld reactive force data. The test method is economical and easy to conduct and can serve as a standard test for the evaluation of cold cracking susceptibility of structural steels.

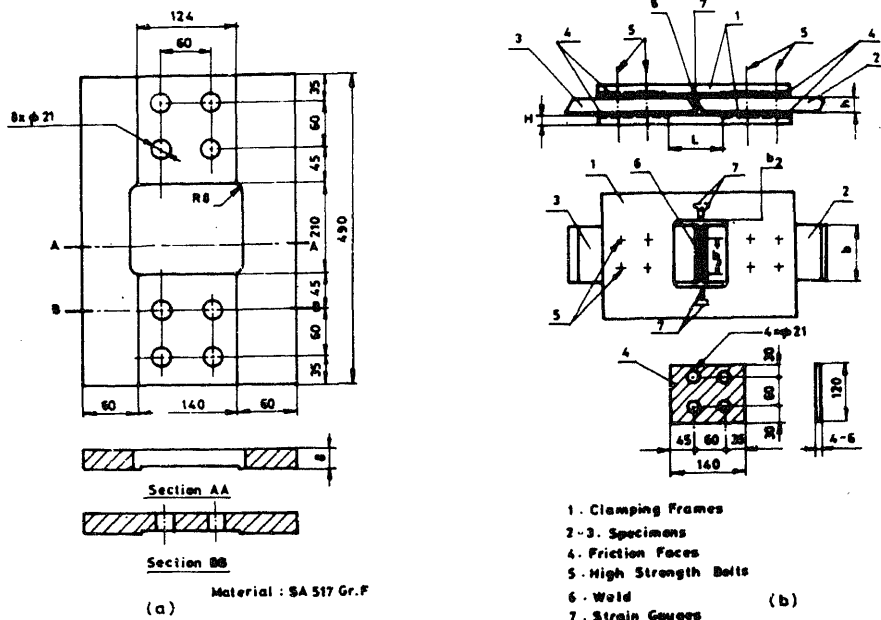


Figure 6. (a) Restraining frames for ERC test; (b) ERC test assembly (Veeraraghavan *et al* 1988).

7. Hot cracking in weldments

Hot cracking in weldments develop during or after solidification and are generally associated with the phase transformation and shrinkage strains. Depending on the conditions of cracking, they are classified as solidification cracking, liquation cracking, lamellar tearing and reheat cracking.

Many types of hot cracking tests have been proposed to evaluate the weldability of materials (Wilken & Schoenherr 1975). They are divided into two categories: self restraint type and external restraint type. Typical examples of self-restraint tests are the Houldcraft test and the Lehigh restraint tests. However, these tests give rise to considerable scatter in the results due to their inability to reproduce strain fields. These strain fields depend on the thermal pattern which is largely uncontrollable. Typical methods which use external restraint forces are the Varestreint test and the tensile restraint cracking test with bending and/or tensile restraint respectively.

7.1 Solidification cracking

During solidification of the weld metal, grains grow from the fusion boundary to the central region of the weld pool, impurities and alloying elements are rejected ahead of the growing crystals and become more and more concentrated in the liquid that solidifies later. Their presence lowers the melting point of this liquid. As solidification proceeds, contraction strains will develop across the weld as a result of the cooling of

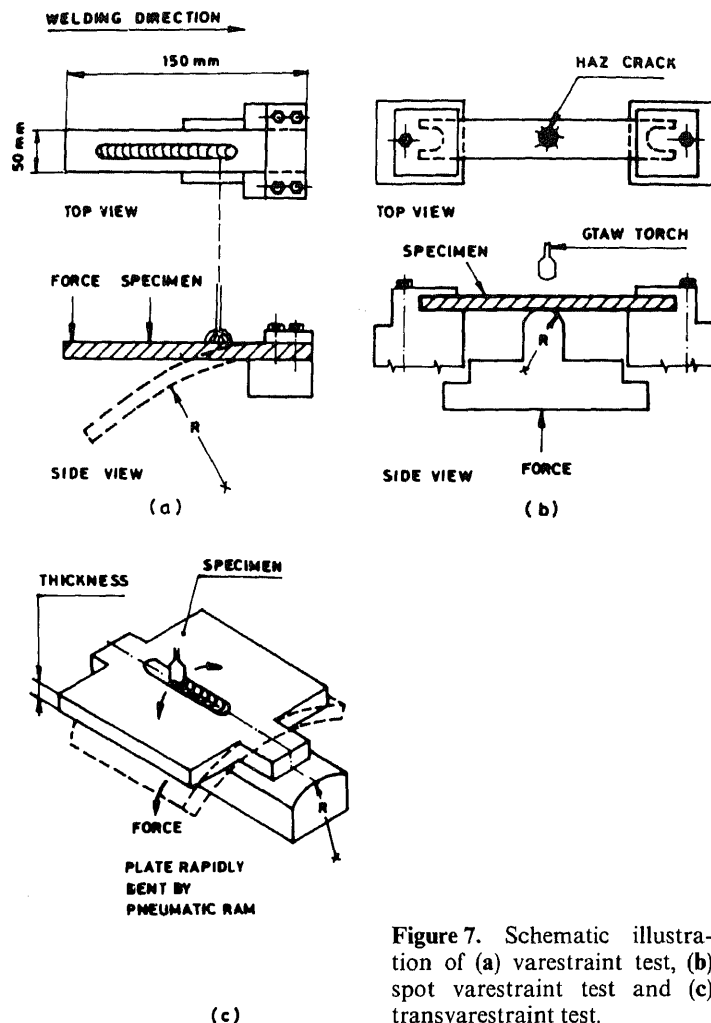


Figure 7. Schematic illustration of (a) vareststraint test, (b) spot vareststraint test and (c) transvareststraint test.

the weld and the surrounding material. If the ductility is lowered sufficiently by the persistence of the liquid films, cracking may result longitudinal to the weld bead.

The incidence of this problem is most likely in high dilution processes such as the welding of the root run and submerged arc welding of plates. Another form of crack transverse to the weld is also possible. Thus, a satisfactory assessment procedure should fulfil:

- application of controlled strain both longitudinally and transversely about the test weld;
- determination of critical strain parameter as a function of dilution;
- assessment of welding techniques like TIG, SMAW and SAW;
- correlation must be established between test results and practical joints

Such tests for assessing solidification cracking could be carried out using both Vareststraint (Savage & Lundin 1965) and the Transvareststraint tests (McKeown 1970)

Both these tests satisfy the requirements 'a' to 'c' but further work is required to establish 'd'. A third variant of the test called Spot-Varestraint test (Tigama-Jig test) has also been developed (Savage *et al* 1977). All these tests are schematically illustrated in figure 7 (a to c).

All these tests are similar in principle and differ only in the direction of application of strain with respect to weld direction. The test piece is a flat plate fixed at one end (figure 7a) or at both ends (figure 7b) or in the middle (figure 7c) on a rigid block the surface of which comprises a cylinder of radius R . After the weld is run to a certain length (figures 7a & c) or at a spot (figure 7b) the plate is rapidly bent against the cylindrical part of the block. The test severity is expressed in terms of the strain which varies with the plate thickness and with the radius R . It is relatively easy to evaluate the susceptibility to cracking by the strain above which the cracks appear or by the total length of the crack for a given strain. Several investigators have used different criteria for interpretation of result of varestraint tests (figure 8) (Dixon 1983). The degree of cracking can be quantified by the average crack length, or the total number of cracks, or the maximum crack length or the cracked HAZ length – all as a function of strain. Thus, considerable subjectivity exists in the interpretation of results.

In addition to the varestraint tests, hot ductility tests can also be used to quantify the HAZ cracking susceptibility. The hot-ductility test characterises the ductility of the material at elevated temperatures and relates this data to the cracking susceptibility. Basically, small tensile specimens are fractured rapidly at some specific temperatures during either heating or cooling cycles of a thermal cycle in a thermomechanical simulator. The transverse reduction in area of the fractured sample is subsequently determined providing a measure of ductility. Both the on-heating and on-cooling curves in the vicinity of the solidus temperature can be obtained as shown in figure 9 and the nil ductility temperature (NDT), nil strength temperature (NST) and the ductility recovery temperatures (DRT) determined. In addition to the hot ductility, the hot strength of the material can also be evaluated.

In order to obviate the subjectivity in the interpretation of data in the above tests, Lin *et al* (1993) have evolved a new methodology for quantifying HAZ liquation cracking susceptibility by defining the thermal crack susceptibility of the region of the material, which is a material specific parameter. This region can be determined using Gleeble hot

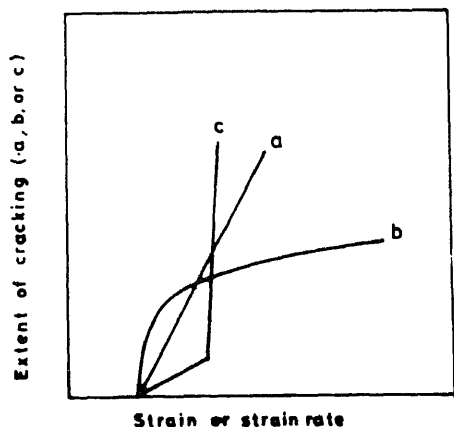


Figure 8. Shape of graphs obtained by the different testing procedures: (a) Average crack length vs. strain (Farrar & Garland 1973), crack area vs strain rate (Konishchev *et al* 1977), number of cracks vs strain (Nakagawa *et al* 1974). (b) Maximum crack length vs strain (Savage & Lundin 1965). (c) Modification to (a) by Bailey (1978).

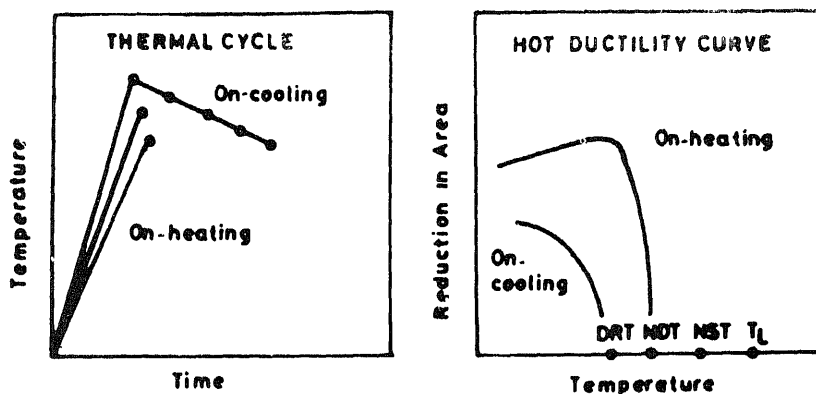


Figure 9. Representation of results obtained from hot ductility test. DRT – ductility recovery temperature, NDT – nil ductility temperature, NST – nil strength temperature, T_L – liquation temperature.

ductility, spot or longitudinal vareststraint tests. However, the authors also acknowledge that these data alone cannot easily accommodate the variations in weld restraint that often dictate the occurrence and severity of cracking.

A similar comparative study of hot ductility rate test and modified vareststraint tests were attempted in Germany over a wide range of materials obtained from different steel manufacturers (Rawlings & Wilken 1992). In the hot ductility test, the maximum transverse deformation rate which can be endured without causing hot cracking on the surface of the weld deposit was used as the criteria. In the vareststraint test, the total length of all the hot cracks found under the stereomicroscope at a magnification of 25X was used as the criteria. Remarkably good correlations were obtained between the two methods on all the materials tested by SMAW, TIG and MIG techniques. The results are under discussion for standardisation by the German Welding Society.

7.2 Burning or liquation cracking

At the high temperatures reached during welding in the HAZ adjacent to the fusion boundary, local melting may occur as a result of the presence of non-metallic impurities giving rise to the phenomenon known as 'burning' (Boniszewski & Watkinson 1964). These cracks are intergranular with respect to prior austenite grains and occur in the HAZ normal to the fusion line of the weld (figure 10a). Hemsworth *et al* (1969) classified such cracks, also sometimes known as 'hot tears', depending on whether they occurred because of the segregation leading to grain boundary liquation or precipitation of brittle constituents or a loss in ductility dip and consequent tearing.

In ferritic steels the problem is principally caused by carbon, sulphur, phosphorus and manganese. An increase in the concentration of the first three elements and a decrease in the concentration of the fourth one leads to an increase in the incidence of cracking. Control of this problem lies in the ability to avoid susceptible compositions with due care to the welding process, trace elements and other deleterious factors. Carbide formers are helpful in that they remove the carbon from the solution. Increase

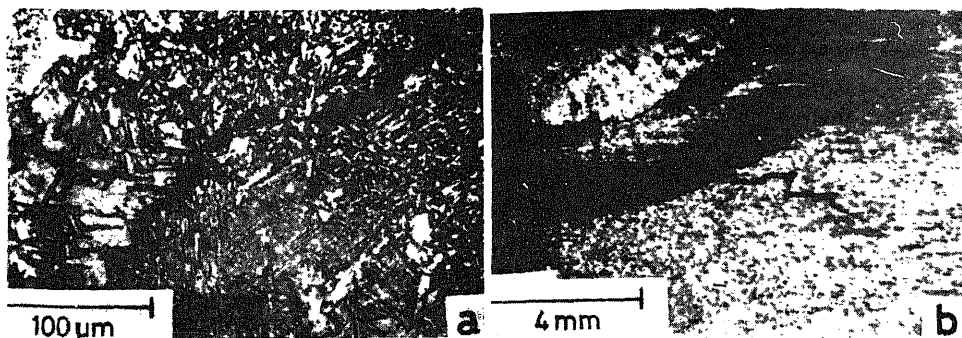


Figure 10. (a) Hot tear across HAZ and weld metal and (b) lamellar tearing in T-butt weld.

in manganese content and, in general, a higher Mn/S ratio is considered helpful (Meitzner & Stout 1966).

A possible test for detecting liquation cracking is by mechanical testing of specimens at elevated temperatures during a simulated HAZ thermal cycle. A cylindrical test specimen is heated by resistance or induction heating and the strength and ductility are measured either at the peak temperature or immediately after, and these properties are correlated with the occurrence of burning and liquation cracking in the HAZ of the welds made with specific levels of heat input (Widgery 1971).

7.3 Lamellar tearing

The problem of weld failures has become more common with increased use of higher strength and thicker steels, particularly where the plate material is welded normal to its surface with high restraint being imposed, as in the case of full penetration T-butt welds. The problem may arise where high strain rates may develop in the short transverse direction of a plate. Cracking may result which is primarily due to the presence of inclusions lying on planes parallel to the plate surface which reduces the short transverse ductility. Substantial parts of the fracture path lie in planes parallel to the surface of the plate. In contrast to HIC, lamellar tearing may propagate both within and outside the visible HAZ (figure 10b). A tensile test is the simplest of the destructive tests for examining the short transverse properties. Measurement of reduction in area has been shown to correlate well with fabrication susceptibility to lamellar tearing (Farrar *et al* 1969). Some anomalies can be expected where plates of low inclusion content show low values of reduction in area, and this can arise when individual inclusions are large compared with the specimen cross-section area.

7.4 Reheat cracking

When a weld joint is reheated after welding, whether for stress relief or during service, the residual stress remaining after welding will be relaxed by high temperature deformation. This relaxation is accompanied by plastic deformation in the weld metal and HAZ and, at points of stress concentration such as the toes of fillet welds, the degree

Table 3. Weld cracks and methods of testing.

Potential problem	Specification tests	Batch quality control tests
Hydrogen induced cracking	Continuous cooling transformation assessment Fracture mechanics susceptibility tests Granjon implant test	Chemical analysis Taper hardness test
Solidification cracking	Varestraint and transvarestraint test Hot deformation rate test	—
Burning or liquation cracking	High temperature test on thermally simulated specimen	Side or face bend tests
Lamellar tearing	Short transverse tensile test Crack notched bend test Automated inclusion counting	Ultrasonics S T tensiles Automated inclusion counting
Reheat cracking	Fracture mechanics stress relaxation and constant load tests at elevated temperatures	—

of local strain may be considerable. In certain steels with poor high temperature ductility, the deformation may be too great to be accommodated and cracking may result. Such cracks, known as reheat cracks or stress relief cracks, are intergranular in nature and appear in the HAZ and occasionally in the weld metal.

Historically, reheat cracks were observed in austenitic stainless steels SS 347, 321 and then in other grades of low alloy steels used in superheaters, turbine rotors, forgings etc. (Dhooze & Vinckier 1992). After extensive investigations, Lundin & Khan (1990) concluded that chemical composition is the most significant factor in PWHT cracking. The elements found to be deleterious are either those that promote formation of carbides of M_2C or M_4C_3 types or those which are known to have grain boundary embrittling effects.

Multitude of tests have been employed by different researchers to evaluate reheat cracking and the test results are difficult to compare and sometimes confusing (Lundin & Khan 1990). The remedy against reheat cracking is careful dressing of the surface of the weld. Temper beading, if correctly performed, combined with weld dressing, should provide a microstructure and surface favourable for avoiding initiation and propagation of cracks.

The various forms of cracking discussed above and the possible tests for evaluating the cracking susceptibility are tabulated in table 3.

8. Weld failures and their repair

Weld failures can be broadly divided into two categories: first, failures that occur during fabrication when a weldment fails to satisfy appropriate inspection criteria, e.g.

undercut or porosity which may exceed the permitted limits or more seriously, flaws such as hydrogen cracking. These are normally repair welded with adequate precautions and using well-established repair procedures. The second category covers weldments that experience cracking or are damaged during service. These include fatigue cracking, stress corrosion cracking and fracture. Their repair may be difficult and time consuming and in some cases, the failure may be in inaccessible locations without adequate data on the previous history of the components involved which makes weld repair very difficult. All the factors to be considered during the weld repair are enumerated in the IIW Commission XV in their document No. IIS/IIW-956-87.

In this context, the 'fitness-for-purpose' approach using fracture mechanics concepts and a thorough knowledge of the stress, imperfection size and material properties, help in taking crucial decisions on whether to repair a weld crack which may not propagate under the given service conditions. In fact, there is considerable evidence that the repair of innocuous imperfection may be positively harmful when working to arbitrary acceptance criteria. Three case studies from literature will be briefly described to illustrate the three conditions enumerated above.

What is considered as the most successful and difficult weld repair, was carried out on a steam turbine casing which had developed 21 cracks totalling approximately 508 cm in length (Yosh & Captoon 1992). The failure was due to a combination of low cycle fatigue and creep. After excessive trials on weldability establishment, carbon equivalent consideration, possible distortion and necessary heat treatments, the repair was carried out on a 1 Cr-1 Mo-1/4 V material with a preheat of $343 \pm 27^\circ\text{C}$ using AWS 8018 B2L iron powder, low hydrogen electrodes with sufficient clampings to prevent distortion and sufficient padding to maintain adequate preheat. The job is reported to be functioning satisfactorily since 1987.

Perhaps the most striking example of the effect of inappropriate weld repair procedures was the explosion at the Union Oil Refinery near Chicago in 1984 which caused the deaths of 17 people (McHenry *et al* 1986). The failure was associated with a circumferential weld used to join a replacement section in a manoethanalomine contactor vessel to the original shell. The replacement was necessary due to the extensive damage to the original casing caused by HIC. All materials were A516 Gr.70. The vessel was originally fabricated using submerged arc welding with very high heat input, which led to low HAZ hardness values. The repair weld done in the field in the 2G position had to be made using SMAW electrodes at a much lower heat input. This inevitably led to much higher hardness levels in the repair weld HAZ such that, during service, hydrogen from the process entered the steel and initiated cracking in the hardened HAZ. This crack propagated in a mechanism similar to hydrogen induced cracking until full penetration of the vessel wall was reached and then a catastrophic fast fracture ensued.

Another example is a decision made not to repair a crack in view of the possible differences in toughness in the case of North Caramount Jacket failure (Harrison 1981). The original welds were made by SAW process and had excellent toughness. At a late stage of the fabrication of the jacket, cracks were discovered in the longitudinal seams of the tubular members forming the legs of the structure. Repairs were considered but trials carried out prior to repair indicated that manual welding repair will have much lower toughness than the original welds. This factor led to the decision not to repair the pre-existing discontinuities in the seam welds.

Weld joints are particularly tolerant to some types of discontinuity and fracture mechanics techniques are now available which allow rational decisions on the significance of weld discontinuities to be made. If these techniques are more widely applied, the number of weld repairs carried out could be reduced significantly.

9. Conclusion

Weld failures and their repairs affect the productivity and safety of any industrial organisation. While weld failures that occur during fabrication can be repaired rather easily, those that occur during service pose serious problems during repair. Inaccessibility of the area, inability to use the shop practices with appropriate preheat and post-weld heat treatments and lack of adequate data on the previous history of the components are some of the problems. Hence, during welding of carbon steels, low alloy high strength or stainless steels, adequate data on the weldability of the material including carbon equivalent, hydrogen induced cracking, solidification cracking, lamellar tearing etc. should be established. Several testing methods are available to evaluate the cracking susceptibility. In addition, fracture mechanics and fitness-for-purpose criteria should be adopted and an appropriate weld repair technique can be judiciously selected.

The author wishes to thank the management of the Bharat Heavy Electricals Limited for all their encouragement.

References

- Alexander L K 1981 *Norges Offentlige Utredning* (Oslo: University Press) p. 11
- Bailey N 1978 Effect of wire composition and flux type on solidification cracking when submerged arc welding C-Mn steels. *Weld. Res. Int.* 8: 215-239
- Baker R G, Watkinson F, Newmann R P 1966 *Proc. of 2nd Commonwealth Welding Conf.* (London: The Welding Inst.) pp 125-131
- Boniszewski T, Watkinson F 1964 Examination of hot tearing in the weld heat affected-zone of ferritic steels. *Br. Weld. J.* 11: 610-619
- Castner H R 1993 What you should know about austenitic stainless steels. *Weld. J. (Miami)* 72: 53-60
- Christensen N, Simonsen T 1981 Assessment of weldability by the implant method. *Scand. J. Metal.* 10:120-126
- Dearden J, O'Neil H 1940 A guide to the selection and welding of low alloy structural steels. *Trans. Inst. Weld.* 3: 203-214
- de Meester B 1991 Selection of steels according to their charpy-V properties in order to avoid brittle fracture. *Indian Weld. J.* 23: 26-30
- Dhooge A, Vinckier A 1992 Reheat cracking - Review of recent studies. *Weld. World* 30: 44-71
- Dixon B 1983 Tests for weldmetal solidification cracking-A Review. *Aust. Weld. J.* 28: 16-22
- Doty W D 1970 in *Weldability of structural and pressure vessel steels. Conf. Proc.* (London: The Welding Inst.) 1: 163-176
- Evans G M, Christensen N 1971 Correlation of weld metal hydrogen content with HAZ embrittlement. *Metal Constr. Br. Weld. J.* 3: 188-189
- Farrar J C M, Dolby R E, Baker R G 1969 Lamellar tearing in welded structural steels. *Weld. J. Res.* 48 (Suppl.): 274s-282s

- Farrar J C M, Garland J G 1973 The Welding Inst. Res. Rep. M/77/73
- Granjon H 1960 *Rev. Met.* 57: 319
- Granjon H 1969 The implant method for studying the weldability of high strength steels. *Metal Constr. Br. Weld. J.* 1: 509–515
- Harrison J D 1981 The economics of a fitness-for-purpose approach to weld defect acceptance. In *Fitness-for-purpose validation of welded construction* (London: The Welding Inst.)
- Hemsworth B, Boniszewski T, Eaton N F 1969 Classification and definition of high temperature welding cracks in alloys. *Metal Constr. Br. Weld. J.* 1: 5–16
- Konishchev B P, Yakuskin B F, Polymin G E 1977 *Svar. Proizvod* 24: 12–13
- Kotecki D J 1992 Hydrogen reconsidered. *Weld. J. (Miami)* 71: 35–43
- Kula E B, Anetil A A 1977 In *Case studies in fracture mechanics*, AMMRC report
- Lin W, Lippold J C, Baeslack W A III An evaluation of heat-affected zone liquation cracking susceptibility Part 1, Development of a method for quantification. *Weld. J. Res.* 72 (Suppl.): 135s–153s
- Lundin C D, Khan K K 1990 WRC Progress Report
- McHenry H I, Shives T R, Read D T, McColskey J D, Brady C H, Purtscher P T 1986 Examination of a pressure vessel that ruptured at the Chicago refinery of the Union Oil Company on July 23, 1984, NBS Report, NBSIR 86–3049
- McKeown D 1970 Versatile weld metal cracking tests *Metal Constr. Br. Weld. J.* 2: 351–352
- McParlan M, Graville B A 1976 Hydrogen cracking in weld metals. *Weld. J. Res.* 55 (Suppl.): 94s–102s
- Meitzner C F, Stout R D 1966 Microcracking and delayed cracking in welded, quenched and tempered steels. *Weld. J. Res.* 55 (Suppl.): 393s–400s
- Nakagawa H, Hamanaka T, Matsuda F, Senda T 1975 Weld solidification crack susceptibility of high tensile low nickel alloy steel (Report 6). *Trans. Jpn. Weld. Soc.* 6: 10–16
- Povezan J 1978 Restraint intensity – a significant factor for evaluation of cold cracking of the welds. *Weld. News.* 2: 31–45
- Rawlings G N, Wilken K 1992 Comparing the effectiveness of new hot cracking test methods. *Schweissen Schneiden* 44: E75–E78
- Rosenfeld A R, Reid C N 1977 In 'Case Studies in Fracture Mechanics', AMMRC report
- Satoh K, Matsui M 1968 Reaction stress and weld cracking under hindered constructions, IIW/IIS doc. No. IX-574/68
- Savage W F, Lundin C D 1965 The vareststraint test. *Weld. J. Res.* 44 (Suppl.): 433s–442s
- Savage W F, Nippes E F, Goodman G M 1977 Effect of minor elements on hot-cracking tendencies of Inconel 600, *Weld. J. Res.* 56 (Suppl.): 243s–245s
- Veeraraghavan R, Raghupathy V P, Chandrasekharaiah M N 1988 *Weldability evaluation of structural steels—A new perspective* (Vishakhapatnam: Indian Inst. Weld.)
- Widgery D J 1971 Welding Institute Report
- Wilken K, Schoenherr W 1975 Description of four hot cracking tests without self-restraint. *Weld. World* 13: 238–249
- Yosh D, Captoon A 1992 Successful welding repair of turbine casing cracks. *Weld. J.* 71: 29–32

Application of fracture mechanics for weld integrity assessment

V R RANGANATH and S TARAFDER

Fracture & Fatigue Group, Materials Evaluation Division, National Metallurgical Laboratory, Jamshedpur 831 007, India

Abstract. The structural integrity assessment of a weld joint by conventional techniques is inadequate, because of unavoidable defects in the weld composite. The stress situation in a component having a defect is quite different from that of a homogeneous material. The significance of fracture mechanics to deal with such integrity assessments is brought out. A brief review on the basic formulations in the application of fracture mechanics is followed by established guidelines for evaluating the integrity of engineering components containing crack-like defects.

Keywords. Fracture mechanics; integrity assessment; welding; crack tip opening displacement; J -integral; fracture toughness; stress intensity factor.

1. Introduction

The advent of high toughness structural materials necessitated a corresponding research in the area of welding – the process which is extensively used in fabrication. The specific properties that characterize a good weld are the homogeneity of the weldment and matching strength of the weld joint to that of the base metal. While these properties are not difficult to achieve in the weld metal zone, in the zone lying between the weld zone and the base metal, termed as the heat affected zone (HAZ), control of property is often difficult to achieve. The successive heating and cooling of the HAZ during multipass welding could result in a microstructure which is prone to brittle fracture (Lancaster 1980). In fact, a number of catastrophic failures, resulting in huge losses in terms of personnel and financial, have been reported to have originated from the HAZ of weld joints (Williams & Ellinger 1953; Bennett & Mindlin 1973; Ghosh *et al* 1990).

In order to evaluate the health of a weld joint, a number of test procedures have been evolved (ASW 1990). Depending on the convenience and mutual agreement between the manufacturer and the consumer, conventional tests, like the 'U' bend test for assessing the ductility, and controlled thermal severity test (CTS) for assessing tendency towards cold cracking are generally carried out. These tests, however, serve to qualitatively assess the weld joint as a whole. For a more objective and scientific assessment of the weld joint, the composite comprising three zones that constitute the weld joint, viz., the base metal, the HAZ and the weld metal, have to be individually

assessed with regard to their tendency to cracking (Ranganath *et al* 1991). It is now widely recognized that any weld joint will invariably contain defects. Defects could arise due to improper welding e.g., voids, slag entrapments, or under-cutting. An incipiently embrittled HAZ microstructure may also be considered as a defect (Barsom & Rolfe 1987a). During service, all the defects in a weld composite are candidate sites for cracks to initiate. Once initiated, the cracks grow through a component, following a path of least resistance, leading to failure. A recent tool in analysing and characterizing the behaviour of cracks is fracture mechanics. The theoretical and functional basis of fracture mechanics has been sufficiently well developed in order for it to be applied to the prediction and prevention of service failures in engineering components. The present paper explores the use of fracture mechanics in failure analysis, life estimation and integrity assessments, with particular reference to weldments.

2. Origin of fracture mechanics

Many engineering components fail much below their design stress level, even though they are designed and inspected as per the relevant codes. This is because cracks or crack-like defects are always present in the material/component and failure is a result of such cracks extending to their critical length. The incipient flaws, which act as cracks or crack initiators, severely affect the local stress field and the severity of the stress near and around these flaws could be significantly higher than the design stress (Kanninen & Popelar 1985). Usually, general design practices do not take such stress intensities into account while calculating the design stresses. Fracture mechanics originates from this lacunae and provides the basis by which the effects of intensified stresses on the integrity of components can be accounted for.

2.1 Modes of failure in a cracked body

The modes of failures are schematically shown in figure 1. The three modes are represented as I for opening mode (tensile stress in y direction), II for edge sliding mode (shear stress in z direction) and III for screw-sliding mode (shear stress in x direction). In metals, most of the crack-related failures occur in mode I. Hence, mode I fracture is widely discussed (Knott 1973).

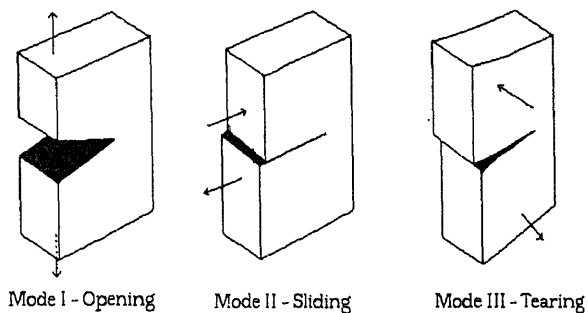


Figure 1. Various modes of loading.

2.2 Stress intensity factor

The *stress intensity factor* (SIF) is a term coined to characterize the *stress magnitude around the crack tip*, in a cracked body, and is denoted as K . Although in-service components encounter a mixture of modes I, II and III stresses, the contribution of stresses of modes II and III to the fracture process is negligible. Due to this reason, the SIF is indicated as K_I , implying opening type of loading (mode I, tensile) on the crack faces. When the stress intensity approaches a critical value beyond which the stressed component fails in a catastrophic manner, the applied stress intensity, K_I , is termed as K_{Ic} . This K_{Ic} is called as *critical stress intensity factor*. Analogous to yield stress, σ_y , K_{Ic} is a material property. Customarily, it is known as plane-strain fracture toughness and indicates the material's resistance to crack propagation. Mathematically, the SIF is represented as (Broek 1986):

$$K_I = \sigma a^{0.5} f(g), \quad (1)$$

where σ is the applied stress, a is the crack depth and $f(g)$ is a factor depending on the geometry of the stressed component.

As can be seen from (1), K_I is a function of load, geometry of the component and size of the crack. A number of relationships between the SIF and various body configurations, for varying crack sizes, orientations, shapes and loading conditions are available from hand books (Tada *et al* 1973; Rooke & Cartwright 1976).

2.3 Determination of SIF

Stress intensity factors can be calculated by using numerical methods such as weight function, boundary collocation and finite element methods (Kanninen & Popelar 1985). Whereas in these techniques most of the conditions are idealized, the experimental techniques narrow the gap between a service component stress field history and the laboratory calibration.

A variety of test specimen geometries can be used to determine the fracture toughness, K_{Ic} , of metallic materials as described in ASTM (1992a). Two of the most popular specimen geometries are the compact tension and the three-point bend specimen. Figure 2 shows a schematic of these specimens.

2.3a Test procedure: In order to produce a sharp crack, so that the situation in a service component may be simulated, the test specimen is first subjected to fatigue pre-cracking under predominantly linear elastic loading conditions. The crack length, a , thus generated should be about half of the specimen width, W . The specimen is then loaded monotonically till it fractures completely. An autographic load vs. displacement plot obtained during loading is then analyzed for K_{Ic} . A typical plot of such a test is shown in figure 3.

The load point identified as P_q in the plot is considered as critical load at which crack extension starts. From P_q onwards, up to the maximum load, the crack extends in a stable manner, beyond which it becomes unstable. A tentative fracture toughness K_q is calculated as:

$$K_q = [P/B(W - a)] a^{0.5} F(a, W). \quad (2)$$

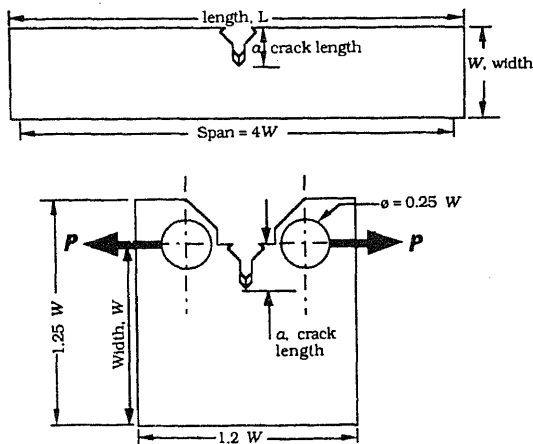


Figure 2. Popular fracture mechanics test specimen geometries. (a) Three point bend specimen; (b) compact tension specimen.

If the specimen thickness, B , and the crack length, a , are greater than $2.5(K_q/\sigma_y)^2$, the K_q is validated as K_{Ic} which has units of $\text{MPa m}^{0.5}$ ($\text{MNm}^{-1.5}$). K_{Ic} is a material property and is independent of size and geometry of the specimen.

Having known K_{Ic} of a material, it can be readily applied to evaluate the criticality of a crack detected in a service component during routine inspection by employing the equation:

$$a_{cr} = [K_{Ic}/(\sigma F(a/W))]^2, \quad (3)$$

where a_{cr} is the critical crack length, K_{Ic} is the plane-strain fracture toughness, σ is the net section stress and $F(a/W)$ is the specimen geometry factor, based on crack length to width ratio. Depending on the difference between the detected crack length and the calculated critical crack length, as per (3), decisions can be taken on immediate replacement or time interval for next inspection.

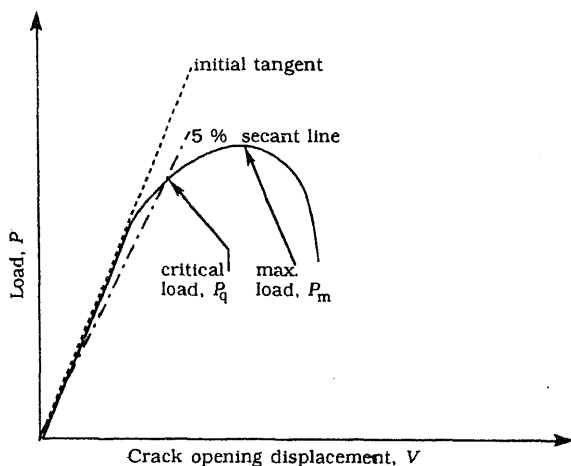


Figure 3. Schematic load displacement curve and the terminology related to a K_{Ic} test plot.

With the advent of high toughness materials, K_{Ic} was found to be inadequate to represent fracture toughness because linear elastic conditions are not preserved at the tip of cracks so that a crack in these materials may not start growing even at the maximum load. To characterize such high toughness materials, the concepts of J -integral and crack opening displacements have been introduced (Knott 1973).

3. Other fracture toughness parameters

3.1 J -Integral

A simplest definition of J -integral can be stated as *a measure of energy absorbed by a cracked body*. The J value, in a laboratory specimen, is calculated by measuring the area under the load-displacement curve, the test procedure being similar to that of a K_{Ic} test. The equation used is of the form:

$$J_I = A\alpha/(B(W-a)), \quad (4)$$

where A is the area under the load-displacement curve and α is a factor depending on the specimen geometry and is obtainable from handbooks. Like K_{Ic} , J_{Ic} indicates the critical fracture toughness value at which a fresh crack surface starts forming in a body and is a material property, having units of kJm^{-2} . The appropriate standard for J_{Ic} testing is ASTM (1992b).

3.2 Crack tip opening displacement

For a cracked body under stress, the crack tip opening displacement (CTOD, δ) is *the extent of opening at the crack tip*. On the application of stress to the component, the crack tip undergoes elastic opening, blunting and then the crack extends. The amount of opening at the start of crack propagation is known as critical crack tip opening displacement, δ_{Ic} . Experimentally, the CTOD is calculated from the opening measured at the crack mouth in a loaded specimen (BSI 1979; ASTM 1992c). The mouth opening displacement (MOD) is measured by a clip-on-gauge. The equation for calculating the CTOD is given in figure 4, which is a schematic of three-point bend specimen under load.

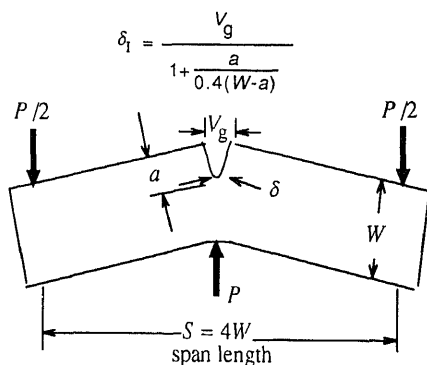


Figure 4. Three point bend specimen under load.

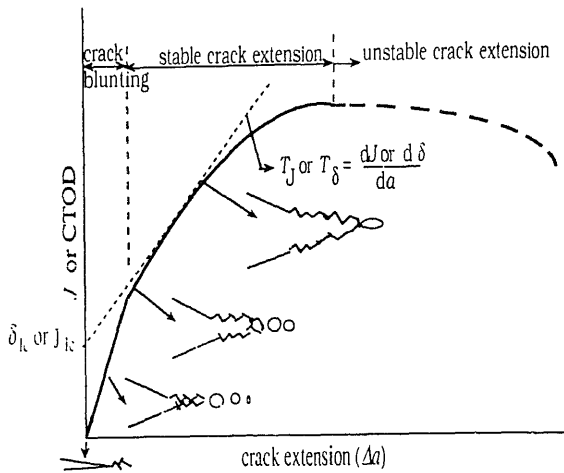


Figure 5. A schematic crack growth resistance curve.

There exist a number of inter-relations between K , J and δ , knowing any one, the other parameters can be calculated.

$$\delta_{Ic} = (J_{Ic}) / (2m\sigma_y) = (K_{Ic}^2) / (mE\sigma_y). \quad (5)$$

In the above equation, m is a constraint factor and depends on the strain hardening behaviour of the material.

The CTOD concept has gained popularity, particularly for assessment of weldments, because it is believed that the local crack tip environment is better represented by CTOD and in the heterogeneity associated with a weldment, the local environment may vary considerably.

3.3 Crack growth resistance curves

The parameter J is very useful for developing crack growth resistance curves, generally known as R -curves. A schematic of the R -curve is presented in figure 5.

These curves represent the complete characterization, i.e., initiation and propagation, of the flaw. The slope of the stable tearing regime is termed as tearing modulus, T_J , having units of MPa, and indicates the material's resistance to crack propagation. Once these curves are obtained from laboratory tests for a given material, J values could be computed for an existing crack in a component under service, and the behaviour of the crack, as to whether the flaw is stable or approaching instability can be predicted from the R -curve (Turner 1983).

4. Guidelines for fracture assessment

Several leading organizations have developed guidelines for assessment of defects in components, based on one of the fracture parameters discussed above. Some of these are: *An engineering approach for elastic-plastic fracture analysis* (Kumar et al 1984) by Electric Power Research Institute (EPRI) and *Guidance on methods for assessing the*

acceptability of flaws in fusion welded structures (Garwood 1985) by Central Electricity Generation Board (CEGB). The latter has been the most popular, with particular reference to weldments, and the British Standards Institution has published a document, PD 6493 (BSI 1991), to streamline procedures for fracture assessment. Salient features of the document are discussed here.

The PD 6493 guidelines are provided for three levels of assessment and are based on CTOD design curves. The levels are in the increasing complexity of the treatment. Level 1 is an initial screening level and provides a simplified method of checking whether particular flaws present a fracture problem, or whether the flaws can be considered safe without having to use the more complex assessment procedures. Level 2 is full treatment and is based on the use of an assessment diagram which combines consideration of fracture and local plastic collapse. It gives the user an opportunity to assess the safety margins required. The level 3 approach will permit greater accuracy but involves greater complexity and more material data. It is particularly appropriate where failure occurs by ductile tearing (high work hardening).

4.1 Information required for assessment

Before the treatment of three levels of assessment, the essential data required for this purpose can be listed as:

- (a) position and orientation of flaw (NDE);
- (b) structural and weld geometry, welding procedure (fabrication);
- (c) stresses and temperatures including transient (all loadings including those arising during transport, erection and testing, local loads, misalignments, structural discontinuities, membrane stress, bending stress, thermal and residual stress, peak stress);
- (d) material properties (yield and tensile strength, Young's modulus);
- (e) fatigue data ($S-N$ curves, Paris constants);
- (f) fracture toughness (K_{Ic} , CTOD, impact toughness);
- (g) high temperature behaviour of material (creep rupture, creep fatigue, creep crack propagation data);
- (h) Corrosion data (bulk corrosion, stress corrosion cracking i.e., K_{ISCC}).

Once the information as above is obtained (from laboratory tests, stress analysis, assumptions based on experience, service conditions and NDE), the assessment is carried out, at different levels, as discussed below.

4.2 Level 1, preliminary assessment

4.2a *Estimation of the acceptability of a known flaw:* Applied CTOD is calculated as:

$$\delta_I = (K_I^2 / \sigma_y) E = (\sigma_1^2 \pi a) / (\sigma_y E), \quad (6)$$

where a is the flaw length and σ_1 is the applied maximum tensile stress.

The flaw is acceptable if $\delta_r^{0.5}$ (ratio of applied CTOD, δ_I , to that of δ_{Ic} of the material) is less than 0.707 and S_r , plastic collapse ratio, (ratio of net section-stress, σ_n , to that of flow stress, σ_f , of the material) is less than 0.8. Since this is a level 1 approach, no additional safety factor is required.

4.2b *Estimation of acceptable flaw size:* The equivalent tolerable flaw parameter a_m is given as:

$$a_m = (\delta_{lc} E) / [2\pi(\sigma_1/\sigma_y)^2 \sigma_y]. \quad (7)$$

The relationship already includes a variable safety factor, averaging about 2. The flaw parameter, a_m , may represent a variety of flaw shapes and dimensions of equivalent severity. Having obtained the flaw parameter, equivalent part-thickness embedded flaw and surface flaw dimensions can be derived from the figure 6.

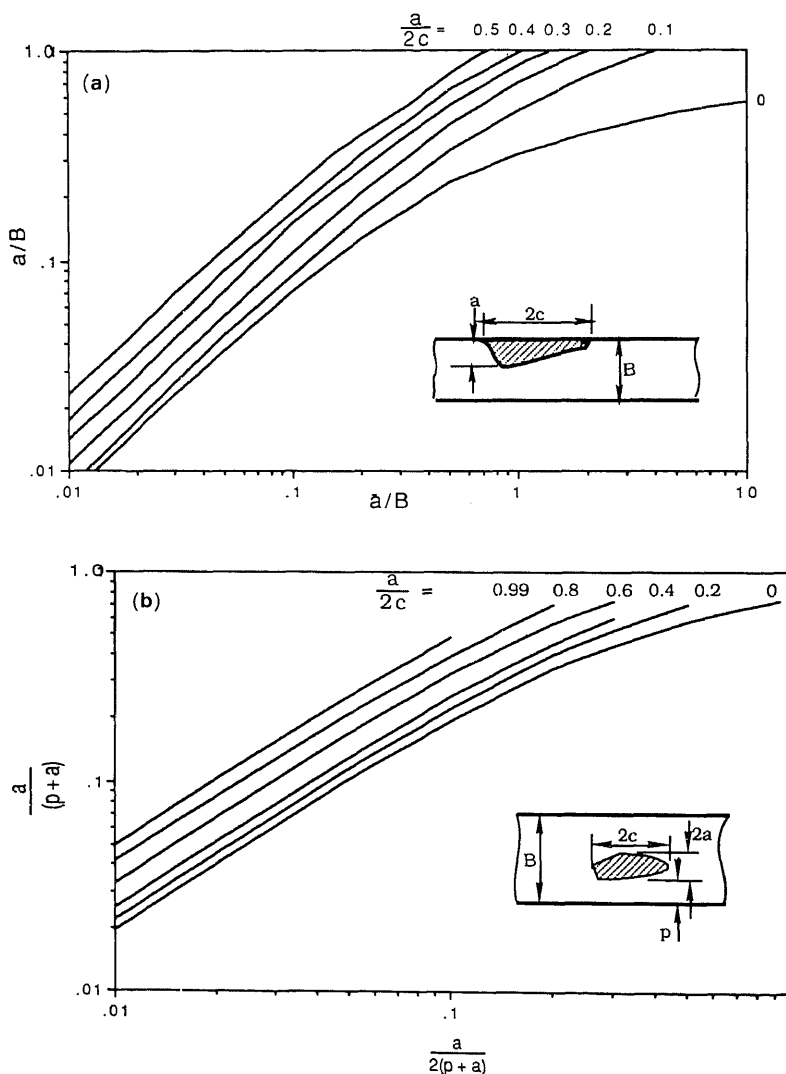


Figure 6. Relationship between actual flaw dimensions and the parameter \bar{a} for (a) surface and (b) embedded flaws.

4.3 Level 2, normal assessment

4.3a *Estimation of the acceptability of a known flaw:* In the level 1 assessment only primary stresses are considered. At level 2, secondary stress is also taken into account while calculating δ_I as per (6). Further, the parameter δ_r is calculated as:

$$\delta_r^{0.5} = (\delta_I / \delta_{Ic})^{0.5} + \rho \quad (8)$$

where ρ is a correction factor for plasticity interactions of the primary and secondary stresses.

The plastic collapse ratio, S_r , is calculated as previously. Using the level 2 assessment diagram shown in figure 7, the point represented by (δ_r^{\pm}, S_r) is marked on the plot. If the marked point lies within the assessment curve, then the flaw is acceptable. If the point lies on or outside the line, the flaw is not acceptable.

4.3b *Estimation of limiting flaw size:* The limiting flaw size a_m is defined by a computed point which lies on the failure assessment line given in figure 7. It may be obtained by plotting a series of calculated points for various sizes, and noting the flaw size at which the appraisal point falls on the assessment line.

4.4 Level 3, advanced assessment

The level 3 method makes use of assessment diagram derived from the stress/strain curve of the material. This allows advantage to be taken of any high work hardening characteristics of the material which may prevent failure. A partial safety factor may be applied depending on the consequence of failure. For example, the safety factor may be taken to be *moderate* if local failure does not cause complete structural collapse or it may be taken to be *severe* if there is risk of complete structural collapse resulting in severe hazard.

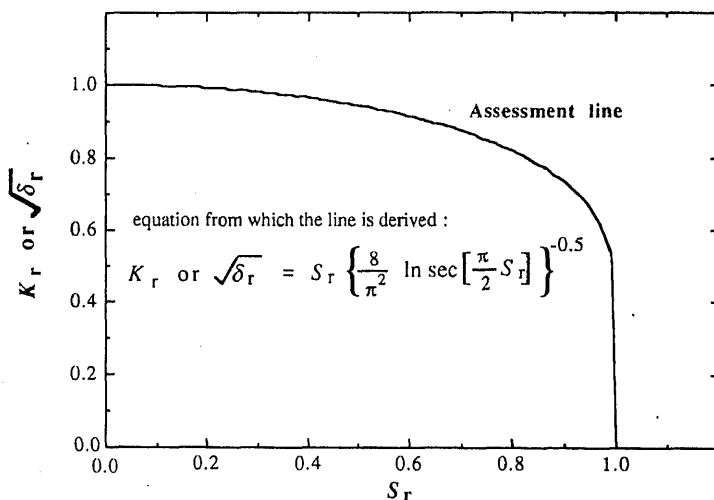


Figure 7. Estimation of acceptability of a known flaw (level 2).

4.4a *Assessment diagram*: The assessment diagram is constructed by plotting values of δ_r , calculated from:

$$\delta_r^{0.5} = \left[\frac{E \ln(1 + \varepsilon)}{\sigma(1 + \varepsilon)} + \frac{\sigma^3(1 + \varepsilon)^3}{2\sigma_y^2 E \ln(1 + \varepsilon)} \right]^{-0.5} \quad (9)$$

against L_r defined as the ratio $\sigma(1 + \varepsilon)/\sigma_y$, where σ, ε are stress and strain, respectively, of the structure or the component, and σ_y is the yield stress. The assessment diagram for level 3 is shown in figure 8. This failure analysis diagram can be adopted where the stress/strain curve is uncertain (e.g., HAZ regions) and for all materials which do not exhibit a yield discontinuity in the stress/strain curve.

4.4b *Estimation of acceptability of a known flaw*: When δ_{lc} , a single value of toughness of the material, is known, the parameter δ_r is calculated as per (8) as a component of the assessment point. Equation (9) is used for calculating $\delta_r^{0.5}$ while constructing the failure assessment diagram. The value of L_r is the ratio of net section stress to that of yield stress. Note that the denominator is the yield stress, as compared to the flow stress while calculating S_r in level 1 & 2 approaches. The resulting point (δ_r, L_r) is plotted on the failure assessment diagram. If the point lies within the assessment curve, then the flaw is acceptable, if the point lies on or outside the line, then the flaw is not acceptable.

4.4c *Estimation of limiting initial flaw size*: The limiting flaw size, a_{cr} , is that flaw size which touches the failure assessment line tangentially when a locus of all possible assessment points is drawn. All the other points on the locus lie outside the area bounded by the axes and the assessment line. This corresponds to the limiting load

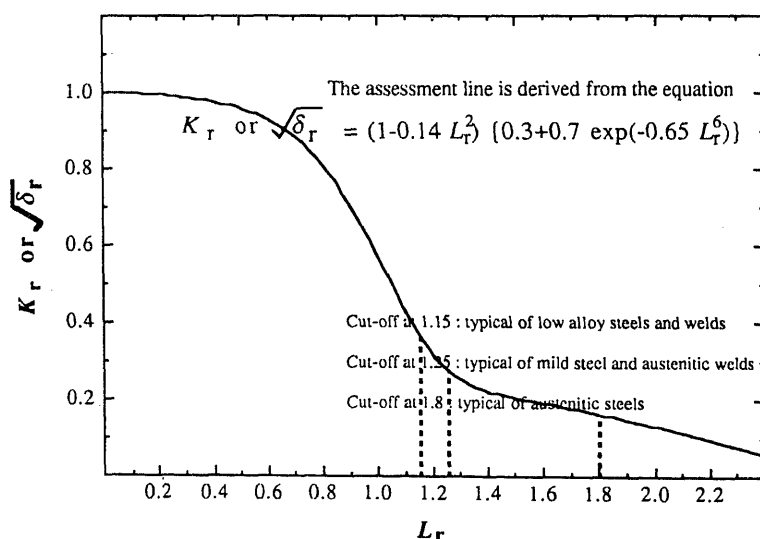


Figure 8. Level 3 failure assessment diagram when complete stress/strain data are available.

factor, F_I (ratio of limit load to that of applied load) equal to unity, and is most easily obtained from a plot of F as a function of initial flaw size.

5. Assessment for fatigue cracks

In components subjected to fatigue loading, flaws can originate from any of the existing defects e.g., stress concentrators, inclusions, misalignments, machining/welding defects etc. Most of the life of such components is spent at the crack initiation stage itself. Once the crack has initiated, it grows steadily and the crack growth in this stage can be represented by the Paris Law, which can be mathematically stated as:

$$da/dN = A(\Delta K)^n \quad (10)$$

where, da/dN is the crack growth per cycle, ΔK is the operating stress intensity range (difference between maximum and minimum operating stress intensity) and A and n are material constants obtained from laboratory tests. Schematically, the Paris Law is shown in figure 9.

In a laboratory test (ASTM 1992d), standard specimens from the material of interest are loaded in fatigue. During the test, the crack increment is monitored along with the number of cycles. ΔK is calculated from the specimen size, load levels and the crack length at a given instant. The Paris constants, A and n are calculated respectively, from

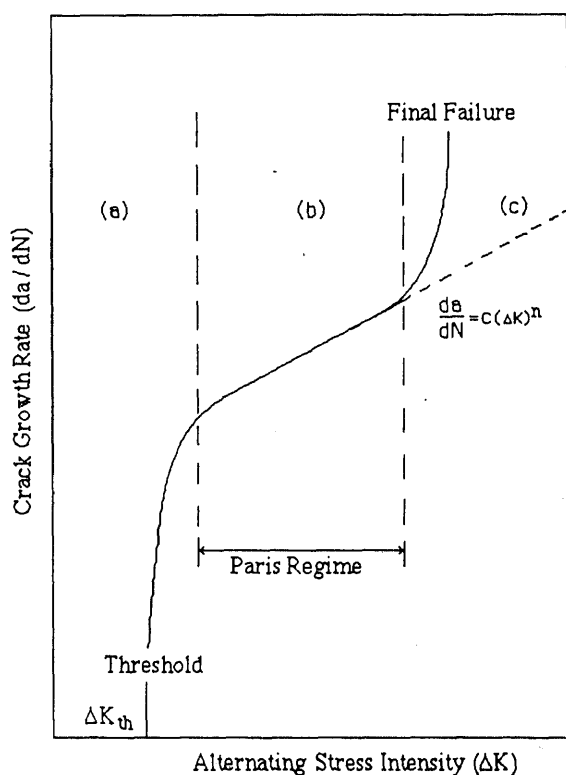


Figure 9. Schematic representation of fatigue crack growth rate data showing Paris regime.

the intercept and slope of the linear portion of the da/dN vs ΔK plot. From the plot in figure 9, it is seen that the fatigue crack growth rate curve has three distinct regimes. If the operating stress levels are below ΔK_{th} , the threshold stress intensity factor range, the component has infinite life. If the operating stresses are approaching K_c , as in regime III, the component has negligible life and needs immediate replacement. In regime II, which is also known as Paris regime, the crack grows in a steady state manner and the remaining life of the component can be predicted, by separating the variables and integrating for N

$$N_f = \int_0^N dN = \int_{a_i}^{a_{cr}} da / (A(\Delta K)^n). \quad (11)$$

In the above equation, N_f gives the total life (in terms of cycles), a_i is obtained from non-destructive examination of the component, the critical crack length, a_{cr} is obtained from (3).

Once the flaw dimensions and orientations are known using standard non-destructive examination methods, the flaws are resolved as per the direction of the acting stresses. Various guidelines on flaw resolutions and assumptions are described in PD 6493 (BSI 1991) and some stress analysis handbooks. The flaw, thus identified, the operating stress cycles and the limiting flaw dimension are the data required for fatigue assessment. Fatigue life is then calculated as per (11). Where the constants A and n are not available for a particular material, they may be taken as $A = 3 \times 10^{-13}$ and $n = 3$ (for da/dN units of mm/cycle; ΔK units of $\text{Nmm}^{-3/2}$) for all ferritic steels operating in air or other non-aggressive environments at temperatures up to 100°C . For structural ferritic steels operating in a marine environment, in the absence of specific corrosion-fatigue data, the crack growth constants may be taken as: $A = 2.3 \times 10^{-12}$ and $n = 3$. These values correspond to the upper bound values of all the published data. For carbon and carbon manganese steels, analysis of published data shows that ΔK_{th} (stress range below which crack does not grow) is about $63 \text{ Nmm}^{-3/2}$. In welded joints, if the residual stress (σ_R) is not available, it is assumed to be of yield strength magnitude. In the absence of data, on a particular material, ΔK_{th} of $63 \text{ Nmm}^{-3/2}$ may be assumed for weldments. Where the materials are non-ferrous and the specific data are not available, as a first approximation, the constants can be calculated as:

$$A = 3 \times 10^{-13} \left[\frac{E_{\text{steel}}}{E_{\text{matl.}}} \right]^3. \quad (12)$$

Similarly the threshold stress intensity factor can be obtained as:

$$\Delta K_{th} = \Delta K_{th(\text{steel})} \left[\frac{E_{\text{steel}}}{E_{\text{matl.}}} \right]. \quad (13)$$

6. Special requirements for assessing weldments

Fabrication by welding induces complex three-dimensional residual stresses that are caused by the heating and cooling effects on the parent metal adjacent to the weld pool. Proper fit-up of adjacent pieces, sequencing and positioning of the weld and preheating or postheating (stress relieving) of the weld assembly would minimize the residual stress. In weldments, the potential crack starters are internal imperfections, such as porosity, lack of fusion, trapped slag, weld toes, weld terminators (Signes *et al* 1967;

Fisher 1970; Watkinson *et al* 1970). However, the existence of tolerable imperfections cannot be avoided and in some cases, attempts to remove these imperfections may result in a condition worse than the original condition (Barsom & Rolfe 1987b).

When conducting fracture toughness tests on heat affected zone regions, considerable variability can occur due to location of the crack tip in different microstructural regions. It is necessary to carry out sectioning of specimens for tests on HAZ regions after testing to determine the precise location of the crack tip. In cases where the HAZ toughness cannot be assessed, it can be assumed to be the lower of the toughness value of the adjacent weld metal or parent metal.

For assessing as-welded assemblies, the tensile residual stresses may be assumed to be equal to yield-strength of the material, for flaws lying in a plane transverse to the welding direction. For structures subjected to postweld heat treatment, the level of residual stress may be assumed to be 30% of the yield-strength. The desirability of having appropriate accurate fracture toughness data cannot be emphasised too strongly, and it is vital that toughness data be obtained from weld procedure samples at the time of construction and recorded if there is any likelihood of flaw assessment being required at any later stage.

7. Concluding remarks

The stress situation in a flawed component under stress is quite complex as compared to a homogeneous component under identical stress. Lack of knowledge on behaviour of cracks in weldments has led to severe catastrophic failures in the past. Optimum decisions on retiring a component with a crack, or to continue in operation, could be based on fracture mechanics concepts. These concepts are particularly effective in dealing with integrity assessment of weldments wherein defects are most common. Fracture toughness evaluation has now been standardized by ASTM and BSI. The developments in this area are now at a stage where they are being used routinely in space and nuclear engineering components. Guidelines and a few specific software codes have also been evolved for fracture assessment by shop-floor inspection engineers with minimum exposure to principles of fracture mechanics.

References

- ASTM 1992a Test method for plane strain fracture toughness: E-399. *Annual book of ASTM standards* (Washington, DC: ASTM) vol. 03.01
- ASTM 1992b Standard test method for J_{IC} measure of fracture toughness: E-813. *Annual book of ASTM standards* (Washington, DC: ASTM) vol. 03.01
- ASTM 1992c Standard test method for crack tip opening displacement measurement of fracture toughness: E-1290. *Annual book of ASTM standards* (Washington, DC: ASTM) vol. 03.01
- ASTM 1992d Standard test method for measurement of fatigue crack growth rates: E-647. *Annual book of ASTM standards* (Washington, DC: ASTM) vol. 03.01
- ASW 1990 *American Society for Welding Handbook* (Miami, FL: ASW) vol. 1-3
- Barsom J M, Rolfe S T 1987a *Fatigue and fracture prevention and control in structures* (Englewood Cliffs, NJ: Prentice Hall) 6: 202
- Barsom J M, Rolfe S T 1987b *Fatigue and fracture prevention and control in structures* (Englewood Cliffs, NJ: Prentice Hall) 14: 446
- Bennett J A, Mindlin H 1973 Material aspects of failure of Point Pleasant bridge. *J. Test. Eval.* 1: 152-161

- BSI 1979 British Standards Institution. Methods for COD testing: BS-5762
- BSI 1991 British Standards Institution. Guidance on methods for assessing acceptability of flaws in fusion welded structures, PD: 6493 (UK: BSI)
- Broek D 1986 *Engineering fracture mechanics: Principles and fundamentals* (Amsterdam: Martineez-Noordhaf)
- Fisher J W 1970 Effect of weldments on the fatigue strength of steel beams. Transportation Research Board (USA), Report no. 102
- Garwood S J 1985 A CTOD method for the analysis of ductile materials. In *Proc. Fracture Mechanics: 18th symposium*, ASTM Standard Technical Publications 945
- Ghosh R N, Ranganath V R, Prasad K, Sinha A N 1990 Investigation on structural integrity of Horton sphere. National Metallurgical Laboratory. Report no. 11620024
- Kannien M F, Popelar C H 1985 *Advanced fracture mechanics* (New York: Oxford University Press) chap. 1
- Knott J F 1973 *Fundamentals of fracture mechanics* (London: Butterworths)
- Kumar V, German M D 1984 Advances in elastic-plastic fracture analysis. EPRI report no. 3607
- Lancaster J F 1980 *Metallurgy of welding* 3rd edn (London: George Allen and Unwin) chap. 4
- Ranganath V R, Kumar A N, Pandey R K 1991 Fracture toughness characterisation of a weldment in a microalloyed steel using resistance curves. *Mater. Sci. Eng.* A132: 153–160
- Rooke D P, Cartwright D J 1976 *Compendium of stress intensity factors* (London: HMSO)
- Signes, Baker R G, Harrison J D, Burdekin F M 1967 Factors affecting the strength of welded high strength steels. *Br. Welding J.* 14(3): 108–116
- Tada H, Paris P, Irwin G 1973 *The stress analysis of cracks handbook* (Hellertown: Del Res. Corp.)
- Turner C E 1983 Further developments of a J based design curve. In *Proc. Elastic-plastic fracture: 2nd symposium. Vol. 2: Fracture curves and engineering applications*. ASTM Standard Technical Publications 803
- Watkinson F, Bodger P H, Harrison J D 1970 The fatigue strength of welded joints in high strength steels and methods for improvement. *Proc. Conf. Fatigue of welded structures* (Brighton: Welding Inst.)
- Williams M L, Ellinger G A 1953 Investigation of structural failures of welded ships. *Welding J. (Miami)* 32: 498s–528s

Studies on fatigue crack growth for airframe structural integrity applications

R SUNDER

Structural Integrity Division, National Aerospace Laboratories, Bangalore 560017, India

Present address: Bangalore Integrated System Solutions, 99, 14th A cross, Malleswaram, Bangalore 560003, India

Abstract. A review is made of efforts at the National Aerospace Laboratories in the development of fatigue crack growth prediction technology for airframe applications. The research was focused on extension of rainflow techniques for crack growth analysis and development of accelerated crack growth calculation methods for spectrum loading. Fatigue crack closure forms a crucial element of modelling and fractographic techniques were developed for its study. These, combined with binary coded event registration enabled crack growth and closure mapping for part-through cracks in metallic materials. Experimental research on short cracks at notches led to discovery of the hysteretic nature of crack closure, which explains well-known history-sensitive local mean stress effects in notch root fatigue. Optical fractography of failures obtained under simulated service conditions revealed that short cracks do not exhibit any more scatter than long cracks at comparable growth rates. The nature of multi-site crack initiation and growth of small cracks at notches was investigated and the effort extended to lug joints that are widely used in airframe applications. Results from this work suggest the possibility of modelling crack growth from a size smaller than 50 microns through to failure, thereby accounting for a major fraction of total life.

Keywords. Fatigue crack growth; rainflow technique; airframe structural integrity; fractographic techniques.

1. Introduction

For many years *S-N* (stress-life) curves served as the major input in design to meet endurance requirements. The curves were established from experimental data obtained predominantly on rotating cantilever machines. These work-horses of early experimental research on metal fatigue were essentially restricted in application to constant amplitude high cycle fatigue. While the application value of such data is considerable in the case of some engineering components including axles and weldments in reversed

bending, the appearance of high performance structures such as airframes and automobiles imposed new requirements. The service load environment of many fatigue critical structures is often characterized by a mix of an extremely large number of small load cycles, which can cause the bulk of damage and a few overloads that can induce inelastic response and associated stress-strain hysteresis and residual stresses. The combination of Miner's rule (Miner 1945) and S - N curves can fail to account for the complex nature of fatigue damage under such conditions.

The advent of servohydraulic test technology and computer control introduced the capability to test materials and components under conditions that closely relate to actual service environment. The concept of servo feedback control made it possible to use displacement transducers for testing under axial strain control – an essential requirement to determine the relationship between strain amplitude and fatigue life in Low-Cycle Fatigue (LCF). Computer control made incremental strain testing easy – making it possible to determine the cyclic stress-strain curve from a single test. This curve is essential if one is to calculate fatigue life for a notched component under service loading. Finally, computer control also made it possible to validate life predictions through testing under simulated service load sequences. This was the framework for JoDean Morrow's pioneering work (Morrow 1968) on the notch root mean stress effect in LCF and the subsequent development of the Manson-Coffin-Smith-Watson-Topper relationships for fatigue life (Manson *et al* 1966; Topper *et al* 1970). Wetzel's modelling of the Masing relationship (Wetzel 1971), combined with the Neuber equation (Neuber 1961) relating applied elastic stress excursions to notch root inelastic stress-strain response provided the analytical foundation for extension of laboratory data obtained on smooth coupons in LCF to notched components under service loading (Dowling *et al* 1977). Today's industry standard procedures for fatigue analysis are based on these inputs: general engineering design for endurance including automotive design applications rely on fatigue analysis using the local stress-strain approach (LSS).

2. Why is fatigue crack propagation significant in fatigue analysis?

It has been long recognized that fatigue crack growth is the final stage leading to failure of the material through gradual and irreversible reduction in residual strength. The fraction of total fatigue life exhausted on crack propagation (FCP life) is known to depend on a number of variables (Schijve 1967). The assumed initial crack length plays an obvious role – if crack growth is tracked from a smaller crack length, one would account for a larger FCP life interval. High strength materials as a rule show a smaller fraction of FCP life as opposed to high toughness materials – while the former may be highly resistant to crack initiation, once a crack is formed, failure follows early. Briefly, this dichotomy is related to ductility: a given alloy system will exhibit reduction in ductility with increase in yield and ultimate strength; crack initiation life reduces with increased cyclic inelastic strain (irreversible slip-band formation is accelerated), while conversely, crack growth is restrained by the formation of a large plastic zone (whose size increases with reduced yield stress). This enhances resistance to fracture in two ways: energy dissipation occurs over a larger volume of material (Raju 1980) and crack tip blunting associated with local yield reduces local stress concentration (Christensen 1959). With increase in stress level, a larger fraction of total life is spent on FCP (when viewed from a given initial crack length to failure). In fact, recent studies on short crack

growth at notches revealed that crack growth at high stress level can commence without any incubation period (Newman *et al* 1992; Prakash *et al* 1994).

As finite geometry affects critical crack size, a large structural component will permit a larger crack than a smaller component, particularly in a thin section promoting plane-stress conditions with a proportional increase in critical crack size. It would follow that in many large built-up, thin-walled structures like airframes, a crack may initiate early at a stress raiser under conditions of plane strain, then propagate into a through crack that may grow for a substantial time, particularly if local stiffeners inhibit rapid increase of stress intensity with crack length (Poe 1971). One may note that airframe design requirements recommend the implementation of multiple-load path configuration, which in a deformation controlled situation will always lead to stress relaxation in a cracked element. *S-N* curves obtained on small round coupons are unlikely to provide useful inputs for estimating the endurance of such structural components.

Operational environment provides compelling reasons to address endurance from a crack growth viewpoint. Current accent in technology development is on the ability to monitor the condition of a structure in service. New design standards call for repair, overhaul and eventual retirement for cause, rather than on the basis of calendar years or hours of service. There is no practical way to track exhaustion of life to crack initiation. Indeed, there is no parameter that can be said to represent damage in the stage of crack initiation. The one exception to this rule may be the observation that residual compressive stresses induced as part of the manufacturing process tends to relax prior to crack initiation. Crack size on the other hand serves as a direct indication of damage. By defining an inspection interval based on conservative estimates of FCP life to failure and after defining initial crack size based on inspection capability, modern airframes are operated safely for over thirty calendar years or 60 to 120 thousand hours of useful service.

The origin of design, operation and retirement based on assessment of residual strength in the presence of cracks goes back to the sixties. The United States Air Force which happens to be the world's largest operator of aircraft was the first to recognize the significance of residual strength and life in the presence of cracks. Plagued by a series of catastrophic wing failures on B-47 aircraft in 1958, a programme was initiated to formulate new design standards for airframes (Lincoln 1994). Within ten years, MilSpec 1651A was evolved as the "USAF Aircraft Structural Integrity Program" (ASIP). This standard relies on fracture mechanics criteria for design purposes and is widely used in contemporary aircraft design. The success of ASIP has led to the evolution of similar standards for aeroengines (ENSIP).

The past 30 years have seen many advances in understanding the mechanics and mechanisms of fatigue crack growth. Over this period, the discipline of Fracture Mechanics has developed with analytical and numerical tools that handle cracks of virtually any size and shape in both isotropic as well as anisotropic materials including composites and ceramics. The appearance of Transmission and Scanning Electron Microscopy (TEM and SEM) together with computer-controlled servohydraulic load frames contributed greatly to better understanding of mechanisms that control the growth of a fatigue crack under both simple as well as complex load sequences.

This paper is an attempt to review research effort on FCP at National Aerospace Laboratories (NAL) over the past 15 years in a few selected areas which appear to be of practical significance:

- Nature of cumulative fatigue damage in FCP under random loading, representative of service conditions, including the contribution of individual cycles to overall fatigue damage,
- Phenomenon of fatigue crack closure, which effectively renders a fatigue crack closed even under tensile loading and is responsible for stress ratio effects and also for load interaction effects, and,
- Growth of small, part-through cracks at notches that occupies a sizable portion of total fatigue life.

3. Rainflow cycle counting in cumulative fatigue damage analysis

Laboratory test data to characterize material resistance to fatigue are obtained under constant amplitude loading. Service load environment on the other hand is random in nature. Fatigue analysis for an arbitrary load sequence is complicated by the absence of complete fatigue cycles that characterized laboratory test conditions during data generation, thereby violating an important similarity criterion. Consider the sequence of loads shown in figure 1 along with the simulated notch root inelastic stress-strain response. We find that the small load excursions 1-3, 5-7 and 10-12 constitute closed fatigue cycles – as indicated by the closed hysteresis loops in the stress-strain plot. Fatigue damage for these cycles can be computed both in terms of exhaustion of fatigue life in crack initiation and in terms of crack extension using available expressions based on laboratory test data for constant amplitude loading. While these cycles are of the same applied magnitude, the stress-strain simulation clearly indicates different local mean stress for each of these cycles due to the effect of superposed overload and underload. Local stress/strain amplitude however will always be identical and load history insensitive, given a stable and symmetric cyclic stress strain curve. In the event notch response would have been totally elastic, local mean stress due to the three cycles would also be identical and load history insensitive. Let us now consider excursions 3-5 and 8-10. While they appear to be complete fatigue cycles when viewed as applied load, clearly, the associated

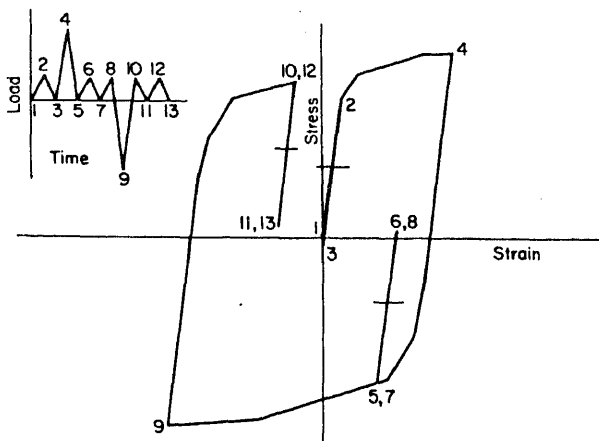


Figure 1. Arbitrary sequence of loads and simulated notch root stress-strain.

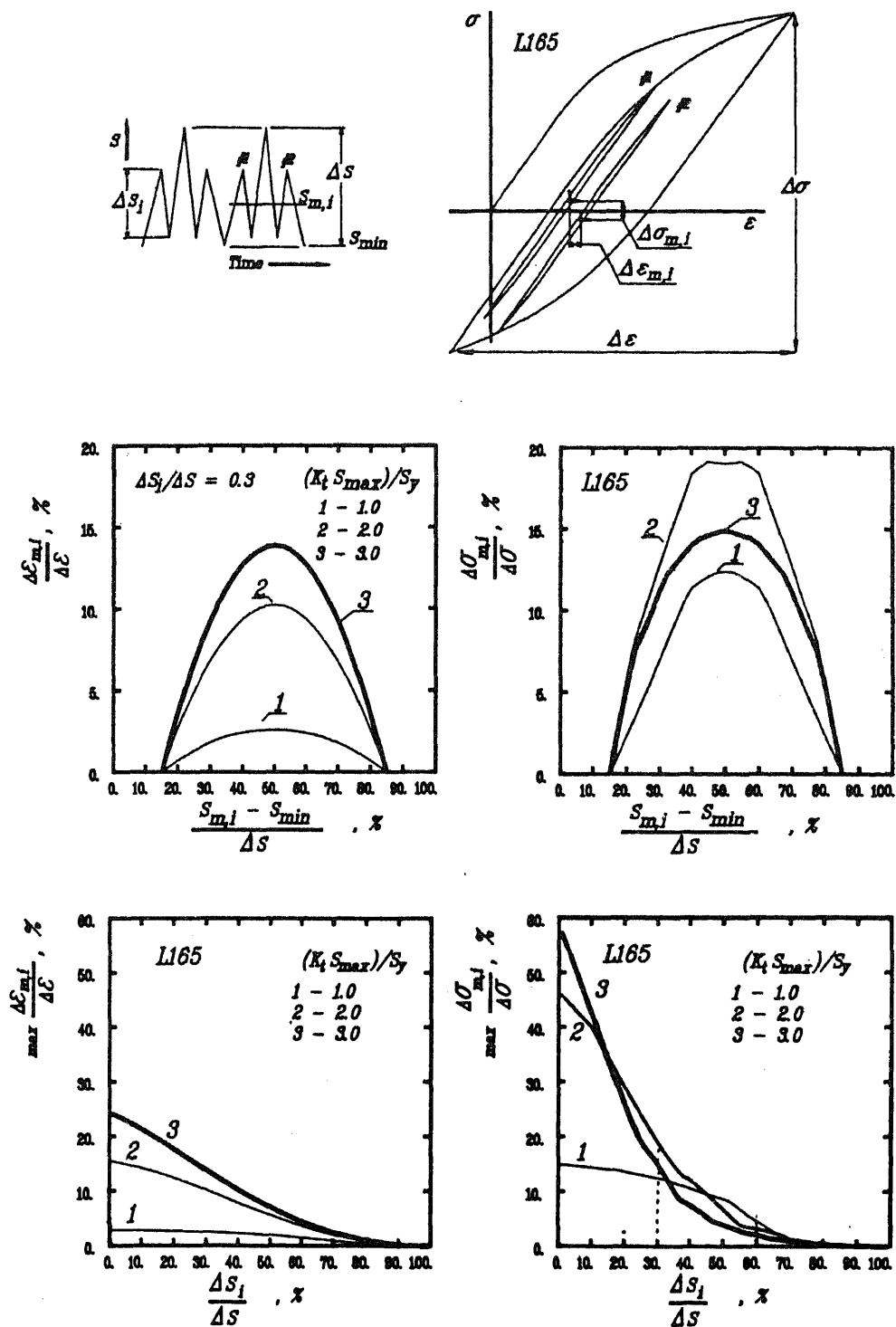


Figure 2. Effect of minor stress range and stress ratio on envelope of notch root mean stress variation (Sunder *et al* 1984).

stress-strain excursions indicate they are not. Obviously, one cannot compute fatigue damage for these load excursions. However, should there be one more load excursion starting from 13 and meeting or crossing the load level at 4, the hysteresis loop spanning the points 9 and 4 would close, permitting damage estimates due to the load cycle 4-9-4.

The association of closed stress-strain hysteresis loops with closed fatigue cycles forms the basis for the rainflow cycle counting method invented by Endo (Endo *et al* 1967). It provides the framework for extending constant amplitude test data to random service load sequences by reducing any given arbitrary load sequence into a table of closed fatigue cycles. ASTM Standard E-1049-85 incorporates rainflow as a recommended procedure for analysis of arbitrary load-time histories.

The rainflow method is essentially based on LCF/LSS concepts. It may be noted that given stable cyclic stress-strain properties and absence of creep, rainflow counted cycles will be notch response insensitive. For this reason, cycle counting performed even on a nondimensionalised load sequence will be valid. As shown in figure 1, the notch root stress and strain amplitude corresponding to counted applied load cycles can be directly computed through Neuber analysis, without recourse to cycle-by-cycle simulation of notch root stress-strain response. Further, Dowling & Khosrovaneh (1989) have shown that history-dependent variation in local mean stress-strain will occur within a pre-defined envelope that is controlled by the largest load cycle in a given sequence. Another study showed, that the extent of this variation for individual cycles in the rainflow table will be inversely proportional to their amplitude - small cycles will see greater history dependence than large cycles (see figure 2) (Sunder 1992). It follows, that given a rainflow table, upper and lower bound fatigue life can be determined without recourse to cycle-by-cycle simulation of notch root stress-strain. For many spectra of practical interest, fatigue life estimates can be accelerated without losing the effect of load history. This illustrates the potential of the rainflow method in 'digesting' complex load histories.

4. Validity of rainflow for crack growth analysis

The nature of fatigue damage accumulation by way of fatigue crack extension is not analogous to notch root damage accumulation as handled by the LCF/LSS approach. Therefore, the concept of rainflow cycle counting cannot be automatically extended to fracture mechanics handling of fatigue crack growth. The fatigue crack tip moves as the crack extends. It leaves behind a wake that causes crack closure (a detailed consideration of the closure phenomenon is forthcoming), effectively truncating the applied load sequence below a certain level. Finally, crack extension is assumed to occur only in the rising portion of a load cycle, while notch root reversed slip accumulation occurs equally on both the rising as well as falling half of an applied load cycle.

An experimental study was performed at NAL to examine the validity of rainflow for crack growth analysis (Sunder *et al* 1984). Typical results appear in figure 3. Figure 3a shows one of the load sequences used in the study. It consists of a number of small cycles embedded within a large cycle on the rising half (segment A) and falling half (segment B). When rainflow counted, segments A and B are identical (though when viewed as rising excursions only, the two are very different). Further, the rainflow counted cycles in the two segments are applied as separate blocks of cycles (segments C and D). As

shown by the fractograph in figure 3b, each of these segments leaves behind a discernible striation whose quantitative analysis in figure 3c and 3d clearly demonstrates that:

- segments A and B result in identical crack extension, and,
- crack extension from individual counted cycles in a segment adds up to match the overall crack extension in the segment

In contrast, conventional crack growth computation on the premise that the crack grows during any rising load interval (rainflow is neglected) would have indicated that:

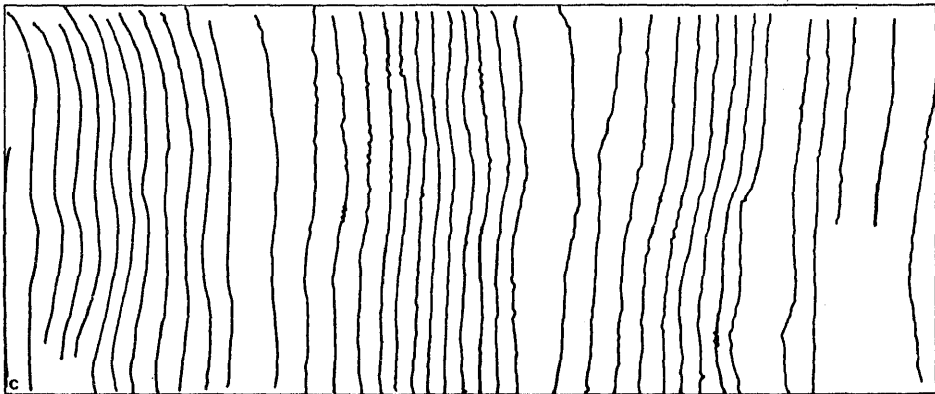
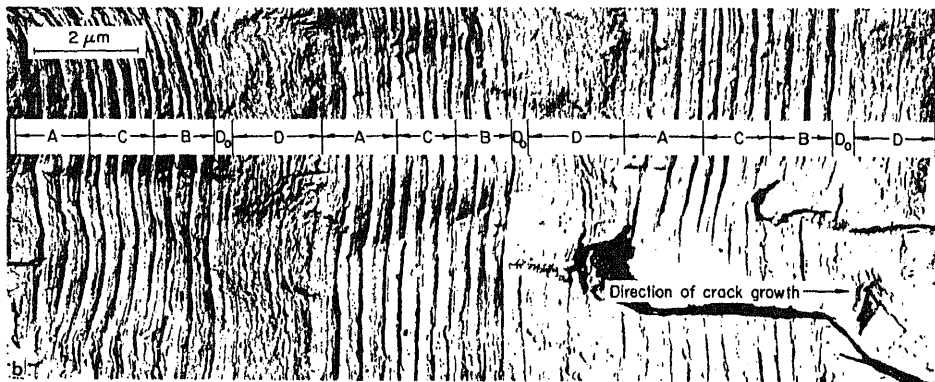
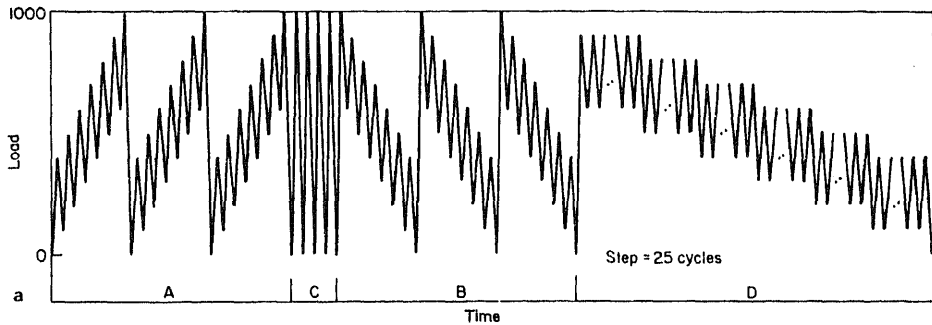


Figure 3. (Continued)

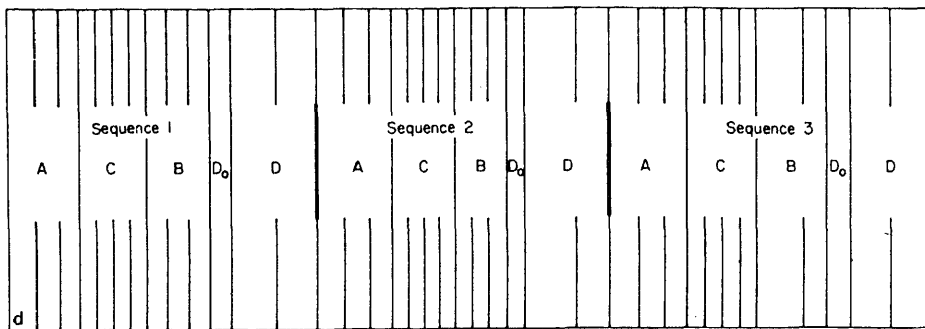


Figure 3. Typical results from fractographic validation of cycle counting techniques (Sunder *et al* 1984). (a) One block of load sequence. This sequence was repeated to failure. (b) Typical fractograph, showing crack extension in individual segments of load sequence. Repetition of segments removes ambiguity in striation measurement. (c) Digitized fractograph and (d) Equivalent fractograph for quantification of striation spacing which correlate with estimates from rainflow cycle counting.

- crack extension in B will be greater than in A, and,
- cumulative crack extension from individual Rainflow counted cycles will be greater than estimates for A and B based on rising load excursions.

Thus, fractographic evidence appears to back up the validity of rainflow cycle counting for fracture mechanics analysis. A similar conclusion would follow if fatigue crack growth is viewed from energy balance considerations (Raju 1980). Figure 4 shows a schematic of crack tip response to cyclic loading, with the associated stress-strain hysteresis loops. Note that the effect of fatigue crack closure is also shown. It was pointed out earlier, that for rainflow on the applied load sequence to be valid for notch root inelastic stress-strain, the cyclic stress-strain curve has to be stable. In a similar fashion, for rainflow analysis on applied load sequence to be valid for the associated stress-intensity sequence, crack extension over the sequence should be negligible when compared to crack tip plastic zone size. This condition may not be satisfied at higher growth rates, particularly under transport aircraft spectrum loading (Sunder *et al* 1984). The restriction is illustrated by figure 5 with a schematic of loads in a full flight (ground-air-ground cycle). The overload seen in the middle of the flight will close into a full rainflow counted cycle only when combined with the rising load excursion before the first small cycle and the falling excursion after the last small cycle. The crack extension during the intervening small cycles can be considerable, requiring rainflow to be carried out on the stress intensity, rather than load sequence. Such an exercise would have to be iterative in nature: to determine stress intensity sequence, crack growth has to be tracked, which strictly speaking, requires prior rainflow analysis.

5. Applications of rainflow to crack growth analysis and testing

As shown in the preceding sections, fatigue analysis can be performed exclusively on the rainflow cycle count table, without recourse to cycle-by-cycle estimates. The advantages of this option are obvious from the viewpoint of computation speed. Even more

Fatigue crack growth prediction for airframe applications

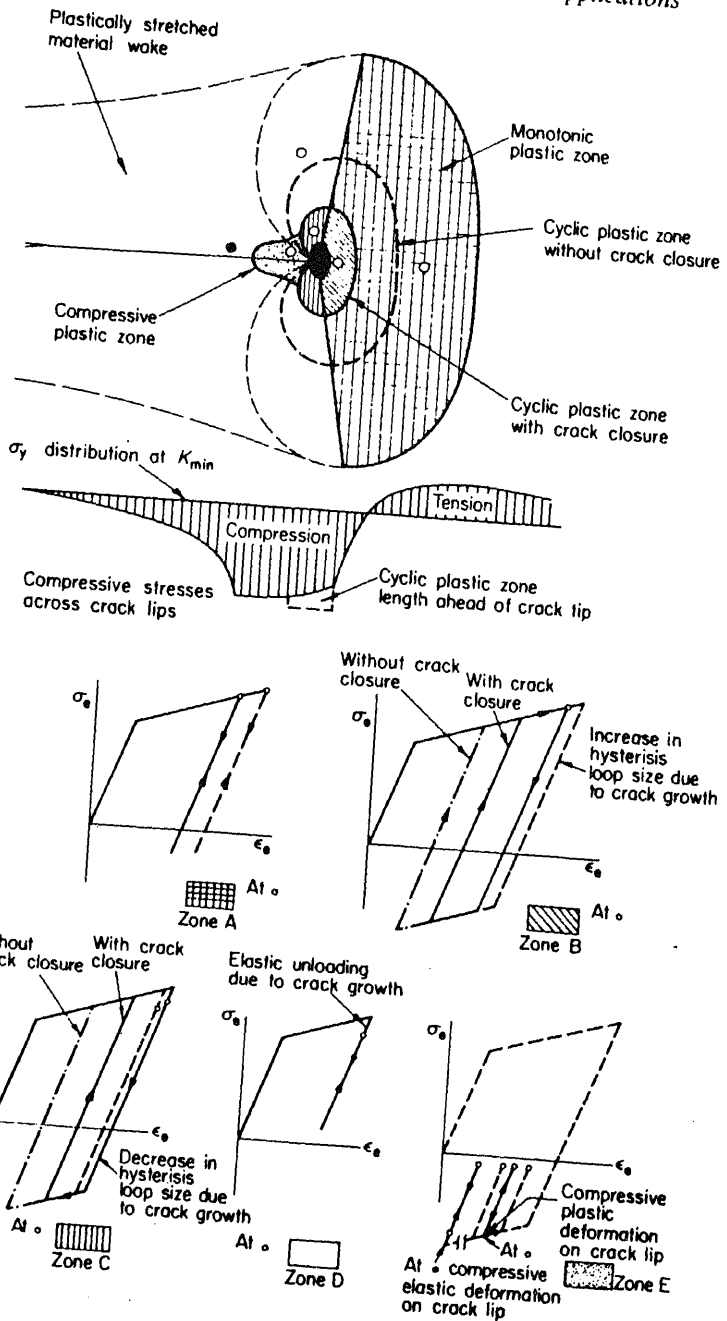


Figure 4. Schematic of crack tip cyclic stress-strain response (Raju 1980).

so in the case of crack growth analysis, whose computation time would otherwise be determined by crack growth rate. Proceeding on the premise that fatigue crack closure is the significant load interaction mechanism, it would follow that average crack growth rate for a sequence of 'n' arbitrary loads can be determined from its rainfall

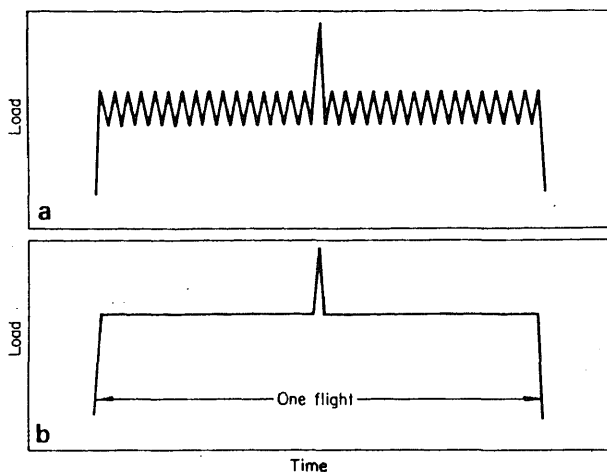


Figure 5. (a) Load excursions in a typical flight. (b) Major cycle.

cycle count from the following adaptation of the Elber equation for crack growth rate (Elber 1971):

$$(da/dN)_{av} = (C/n) \sum_{i=1}^n \Delta K_{eff,i}^m \quad (1)$$

where, $\Delta K_{eff,i}$ is effective stress intensity range computed for the i th rainflow counted cycle. In the summation, crack length is assumed to be constant.

6. Cumulative damage in fatigue crack growth

Equation (1) was used as the basis for an accelerated fatigue crack growth prediction method, that is described in (Sunder 1992). By operating on the table of Rainflow counted cycles, rather than on the source load sequence, cycle-by-cycle estimates are replaced by calculations on the rainflow table, which is considerably shorter. Crack growth analysis is thereby highly accelerated. Even so, the quality of predictions was found to be comparable or superior to the best available methods as indicated by the results in table 1. The predictions listed in the table are for data used in a Round-Robin exercise involving a variety of aircraft wing load spectra. The results are for a 6 mm thick Al-Cu alloy sheet material. As a rule, spectrum load fatigue crack growth predictions are better for larger material thickness. Spectrum load crack growth rate estimates are shown in figure 6 along with experimental data obtained at NAL on 7.5 mm 8090-T8771 Al-Li alloy plate stock and 1.6 mm thick 8090C-T81 sheet material.

It is likely that for thinner sections down to 1 mm, characteristic of airframe skin applications, prediction quality would have been worse. This may be attributed to the influence of other load interaction mechanisms, notably crack-front incompatibility (Schijve 1974; Zuidema & Blaauw 1988), which are known to occur at smaller crack lengths in thinner material, thereby affecting growth in its early stages. Nevertheless, the sound analytical background of predictions based on rainflow, their compatibility with the LSS/LCF approach and the accelerated computations, thanks to the assumption of

Table 1. Assessment of crack growth life prediction quality for a number of airframe load spectra (Chang & Hudson 1981). Results in columns 5–11 are from different models *considered in the Round-Robin. Column 12 shows results from linear cumulative damage analysis.

Load spectrum	Reference stress (MPa)	Crack propagation life (cycles)	Ratios of predicted crack growth life to test life 5–11										Average error of 5–11(+ / –)	Lowest K_{re} (MPa m ^{1/2})
			JC(1)	JC(2)	CMH	JN(1)	JN(2)	WSJ	JR	LCD	RS			
Fighter (air-air)	138	115 700	1.21	1.46	2.13	1.01	1.20	1.18	1.84	1.27	1.19	0.43	14.45	
Fighter (air-air)	207	58 585	0.76	0.91	1.35	0.67	0.71	0.97	1.26	0.85	0.87	0.27	20.98	
Fighter (air-air)	276	18 612	0.79	0.93	1.36	0.64	0.66	1.06	1.39	0.89	0.94	0.30	27.97	
Fighter (air-ground)	138	268 908	1.13	1.37	1.47	1.47	1.48	1.27	1.85	1.09	1.32	0.24	12.25	
Fighter (air-ground)	207	95 642	0.77	0.96	1.04	0.89	0.96	0.94	1.38	0.81	1.01	0.21	17.53	
Fighter (air-ground)	276	36 367	0.64	0.80	0.82	0.65	0.72	0.82	1.24	0.70	0.87	0.22	24.10	
Fighter (ins.-navig.)	207	380 443	0.74	1.39	1.25	2.52	1.47	1.55	2.13	0.73	1.38	0.64	15.88	
Fighter (ins.-navig.)	276	164 738	0.58	1.12	0.94	1.47	1.06	1.35	1.75	0.62	1.13	0.41	21.17	
Fighter composite	138	218 151	1.06	1.33	1.97	1.17	1.14	1.24	1.84	1.09	1.20	0.38	14.13	
Fighter composite	207	65 627	0.79	1.01	1.42	0.78	0.85	1.01	1.49	0.87	1.00	0.31	20.98	
Fighter composite	276	22 182	0.77	0.98	1.42	0.69	0.74	1.03	1.53	0.88	1.02	0.34	27.97	
Transport composite	96.6	1 359 000	1.78	1.31	—	0.76	1.02	1.08	2.65	3.00	1.23	0.73	12.26	
Transport composite	135.24	279 000	1.53	1.14	—	1.25	0.76	0.92	2.25	1.81	1.01	0.51	17.96	
Mean (Accuracy):			0.96	1.13	1.38	1.07	0.98	1.11	1.74	1.12	1.09			
Standard deviation (consistency):			0.36	0.22	0.42	0.33	0.28	0.20	0.42	0.63	0.16			

* LCD – linear cumulative damage model; RS – author's prediction model

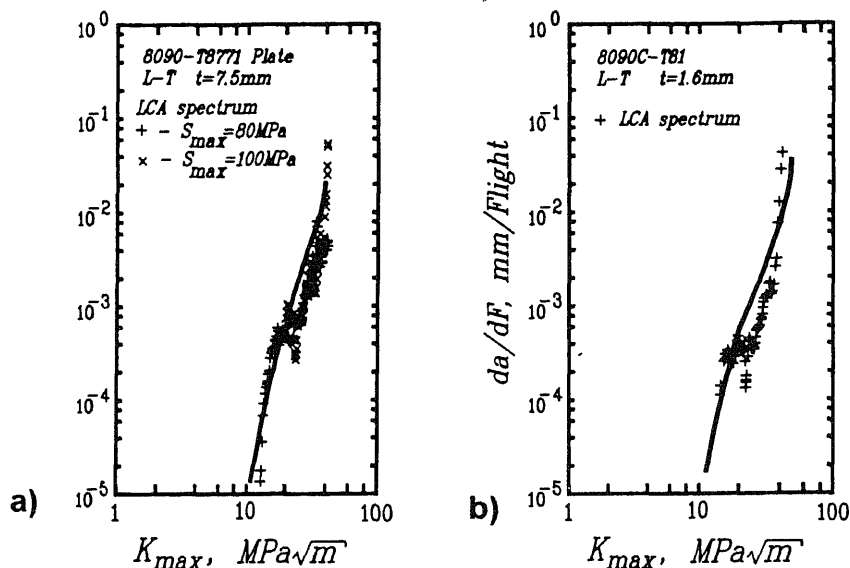


Figure 6. Experimental crack growth rates under Light Combat Aircraft (LCA) spectrum loading (curve) compared with experimental data (points). (a) 7.5 mm thick 8090-T8771 Al-Li plate material, (b) 1.6 mm thick 8090C-T81 sheet material.

a constant closure stress, renders them suitable for engineering application. The discovery of hysteresis in crack closure (whose description is forthcoming) and its implementation in the prediction model extended the scope of the analysis to short cracks at notches, thereby spanning a much larger fraction of total fatigue life.

When fatigue crack growth estimates are performed directly on the rainflow cycle count, it is possible to study the cumulative nature of fatigue damage, including the contribution of individual fatigue cycles to crack growth. Such an exercise was performed for a variety of load spectra (Sunder 1992). Figure 7 shows typical results from a cumulative damage analysis for crack growth under the FALSTAFF and TWIST load spectra. FALSTAFF is a fighter aircraft wing loading standard, dominated by manoeuvre loading, while TWIST applies to transport aircraft and is characterized by a large number of gust loads.

The nondimensionalised Range-Damage versus Exceedance (RDE) diagrams in figure 7 demonstrate qualitative differences between the two spectra. Each curve is identified by an encircled number. Curve 1 is the applied load range exceedance. It shows what percentage of the load cycles in the load spectrum exceeds a given applied stress range. Note that information on stress ratio of individual load cycles is lost in this curve. However, the concerned data are accounted for in damage analysis. Curve 2 shows exceedance of effective stress range, assuming linear cumulative damage (load interaction is ignored). It accounts for crack closure in individual load cycles as experienced under constant amplitude conditions. Curve 3 represents exceedance of effective stress range, after accounting for load interaction – it is assumed that closure in the largest cycle of the rainflow cycle will dominate. Curve 2 is usually above 3, indicating that damage under spectrum loading is retarded due to load interaction. Note however, that in the case of the TWIST spectrum, there are locations, where

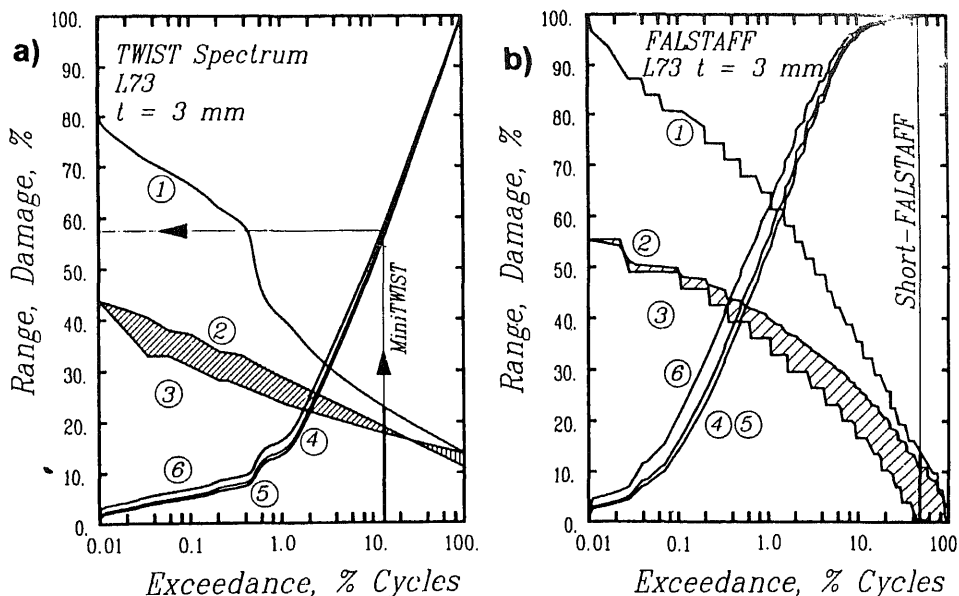


Figure 7. Range, damage-exceedance (RDE) diagrams for L73 Al-Cu sheet material under TWIST (a) and FALSTAFF (b) load spectra. Shown in figures are cumulative damage content of MiniTWIST and ShortFALSTAFF load spectra, when compared to full sequences.

curve 3 goes over curve 2, indicating the reverse. Finally, curve 3 represents damage exceedance.

In the case of the FALSTAFF spectrum, curve 4 shows that just 10% of the (largest) load cycles account for about 98% of all the damage. 90% of the (smaller) cycles could have been excluded from analysis without any impact on crack growth estimates. This explains why the Short-FALSTAFF spectrum widely used in tests gives the same results as the full spectrum (Schuetz 1989). The reverse holds true for the TWIST spectrum. We find that 10% of the cycles account for about 50% of total damage. While the FALSTAFF damage curve asymptotically approaches the 100% mark, the TWIST curve approaches peak value in a log-linear fashion. It would follow, that for the TWIST spectrum (and many other transport aircraft spectra as well), the large number of small cycles contribute significantly to damage. Figure 7a explains why the Mini-TWIST spectrum will provide retarded crack growth rates as observed in the literature (Schuetz 1989).

The RDE diagram provides a simple format to assess the fatigue damage potential of a load spectrum, without cumbersome cycle-by-cycle analysis and shows potential for application in endurance/durability studies as well as in testing.

7. Realtime application of rainfall

Experience shows that the fatigue process is load-history sensitive. In other words, should there be a need to evaluate endurance of a structural component, fatigue testing

must be performed under a load sequence closely simulating the service environment. Computer controlled servohydraulic test systems permit such testing. The time of such testing however increases with test duration and an important question arises as to whether the load spectrum can be truncated to omit load cycles that may not anyway contribute much by way of fatigue damage. The RDE diagrams shown in figure 7 provide the analytical framework for omitting cycles from a load spectrum. This was the basis for the derivation of the Mini-LCA spectrum from the full LCA spectrum. As shown by the RDE diagram and crack growth rates in figure 8, while the Mini-LCA spectrum contains only 10% of the load cycles, it causes the same fatigue damage as the full LCA spectrum—crack growth rate data from the two fall into a single scatter band.

The Mini-LCA spectrum is an example of rainflow and RDE diagram based spectrum editing prior to a test. If cycle omission criteria can be specified prior to or even in the course of a test, an on-line rainflow analysis can be performed by the test application program on load sequence segments before their application on the test specimen (Sunder 1989). An example of a 'variable' criterion is omission stress intensity range, which will cause different number of cycles to be omitted depending on crack size. Figure 9 shows a schematic of how a source load sequence may be edited. Note that the sequence in figure 9e cannot be condensed any further because the rainflow algorithm will not see any more closed cycles. Thus, rainflow when implemented on a flight-by-flight basis will guarantee that at least the most severe cycle will be applied on the test coupon – irrespective of the specified omission criteria.

The application program 'pipelines' test code into the microprocessor-based test controller (Sunder 1985; Sunder & Venkatesh 1990). Thus, while the test controller is

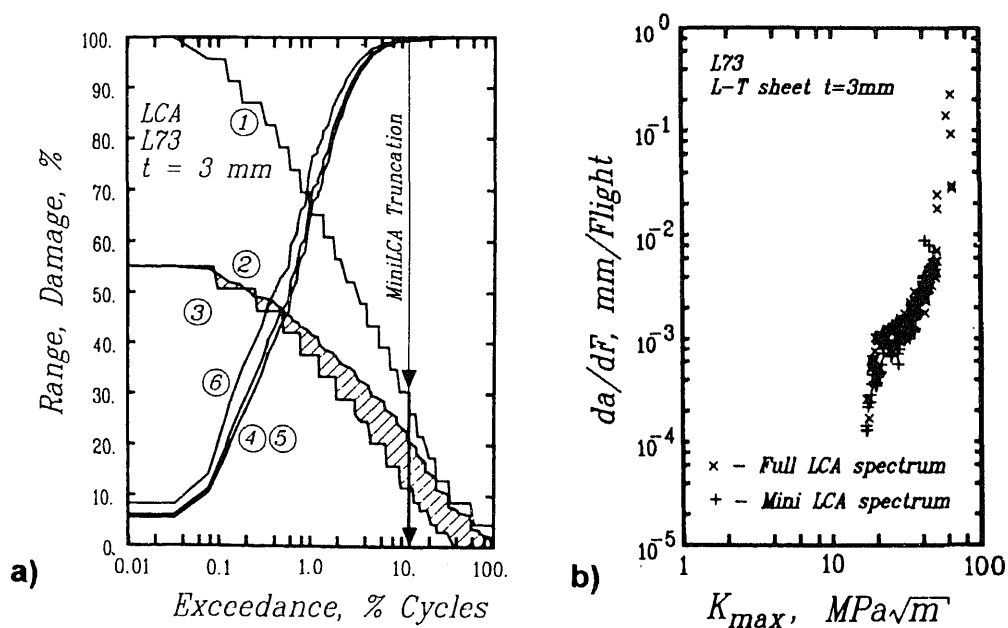


Figure 8. (a) RDE diagram for crack growth in LCA spectrum and L73 Al-Cu sheet material. Line shows the basis for derivation of MiniLCA Spectrum. (b) Fatigue crack growth rates under full LCA and MiniLCA spectrum loading.

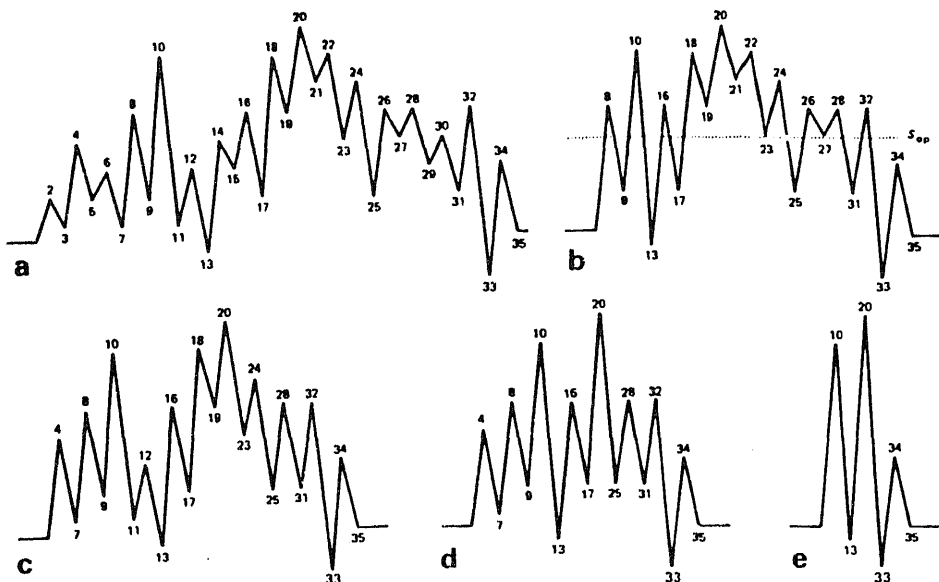


Figure 9. Consequences of on-line rainflow-based spectrum editing (Sunder 1989): (a) initial load sequence, (b) cycles below crack closure load omitted, and (c, d, e) cycles of progressively larger range omitted. Sequence cannot be condensed any further.

busy applying a segment of the load sequence, the host computer performs on-line rainflow to prepare the next segment. The speed with which the cycles are omitted is much faster than the speed with which the load frame can apply the remaining load cycles. To the observer, the test appears to proceed uninterrupted.

The scheme for on-line spectrum editing has been standard after 1984 in all spectrum load tests at NAL. It is used to accelerate pre-cracking (all minor cycles are deleted) and for accelerated data generation. It has also been used in iterative tests to determine effective crack closure level and threshold stress intensity valid for spectrum loading as shown in figure 10 (Sunder 1989). The principle behind closure stress determination is that a fatigue crack will not extend due to load cycles applied while it is fully closed. Their omission will therefore not retard crack growth. Starting from a high level, by selecting progressively decreasing omission levels in successive tests, a particular level will be identified associated with no further acceleration in crack growth rate. This is the effective closure level for the given load spectrum. Effective threshold stress intensity range is determined in a similar fashion. Progressively smaller omission ranges are specified for stress intensity. While the range is above a certain threshold, crack growth rate will accelerate. Below this point, crack growth rates will not see any change. This value is treated as the effective threshold stress intensity for the spectrum.

As shown in figure 10 (top), the crack closure value determined from iterative testing is 2.5 g or about 28% of maximum stress, which compares well with estimates using other techniques for the same material. On the other hand, it was surprising to find that threshold stress intensity range was effectively near zero. This is a significant observation and may explain why even very small load cycles are damaging in transport spectra, by their

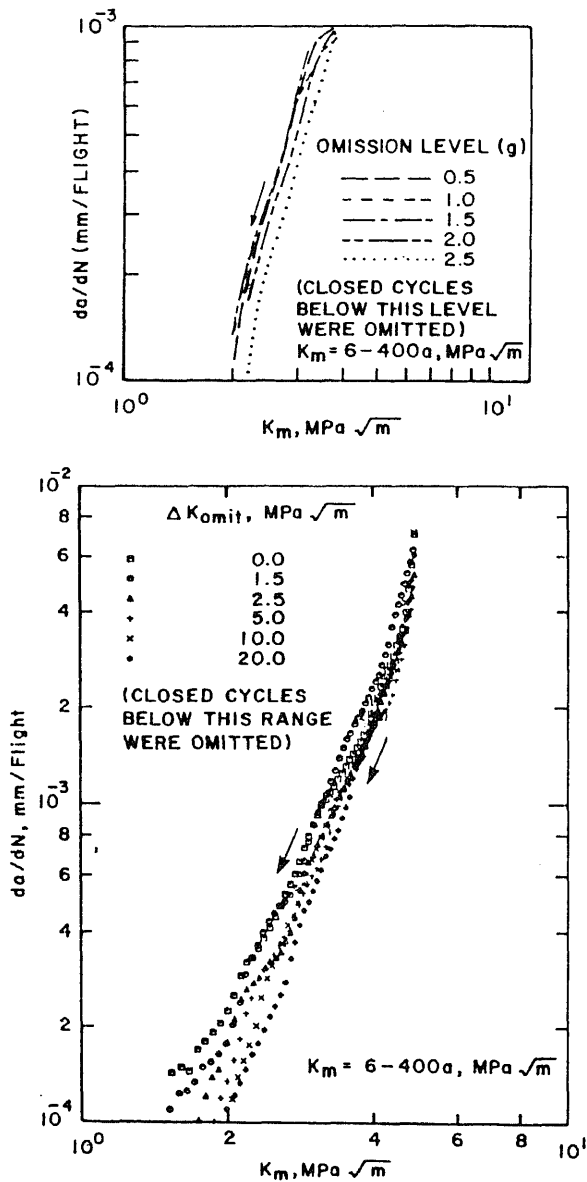


Figure 10. Results from tests on aluminium-alloy sheet specimens with on-line spectrum editing (Sunder 1987): (top) tests with different omission level, and (bottom) tests with different omission ΔK . All tests used the same linearly decreasing 1-g related K -function listed in the figures. Spectrum clipped at 6g.

shear number. It would follow that threshold studies under constant amplitude loading may yield unconservative results when used in estimates of spectrum load crack growth.

8. Fatigue crack closure

Linear elastic fracture mechanics (LEFM) suggests that the slope of applied load versus crack opening displacement (COD) depends only on Young's Modulus and crack

length. This implies a linear load versus COD relationship. In experiments on 2024-T3 Al-alloy sheet centre cracked specimens, Elber (1971) discovered that the slope in the load versus COD relationship remains linear only over a certain upper fraction of load level. Below this load level, the slope increases, implying a diminishing crack length. This effect was attributed to fatigue crack closure, whereby, the stretched wake formed by the advancing crack tip closes even under tensile loading, with the near tip fracture surfaces transferring load in bearing. The area of closure increases with unloading, as indicated by the increasing slope in the load versus COD curve. A closed crack obviously does not see damage due to fatigue cycling. Elber (1971) thereby proposed the effective stress range concept, whereby it is assumed that crack growth occurs only a due to the portion of the applied load cycle when the crack is open. While Elber's (1971) observations were on closure due to plasticity, more forms of closure were reported by subsequent research, such as oxide induced closure, roughness effects, etc. (Suresh *et al* 1981; Ritchie & Suresh 1982; Suresh & Ritchie 1982). It may be fair to say that fatigue crack closure has seen more publications than research on any other phenomenon in FCP, indicating the attention it has attracted from researchers the world over.

For a given material and thickness, crack closure stress ratio, S_{cl}/S_{max} , increases with stress ratio. Elber's discovery thereby explained for the first time, how mean stress affects sub-critical fatigue crack growth rate. Up to this point, mean stress effects were correlated by a suitable approximating equation. In principle, it could be argued that existing approximations were adequate considering that crack closure stress required experimental determination anyway. The same does not hold true however for random load conditions, typical of service environment. It was observed that crack opening stress, S_{op} , remains more or less constant under random loading (Elber 1976; Schijve 1979), effectively eliminating the effect of a large component of fatigue loading. S_{op} would be controlled by the crack tip deformations due to the larger loads, explaining the effect of overloads on FCP under variable amplitude loading. The ability of fatigue crack closure to explain load interaction effects and the increasing power of analytical tools to model crack closure under variable amplitude loading have made the phenomenon a popular choice in life prediction models (de Koning 1981; Newman 1981; Dougherty *et al* 1992; Vormwald *et al* 1992).

The significance of fatigue crack closure in practical applications makes S_{op} an important variable in experimental and analytical studies. Yet, even after about 25 years of research and hundreds of publications on the subject, the engineering community does not have a standard procedure for its experimental determination – unlike other mechanical properties such as yield stress, K_{1c} , J_{1c} etc. It may be noted that even a universally accepted definition of S_{cl} is lacking. The measured value of S_{cl} using Elber's COD gauge depends on the location of the gauge with respect to the crack tip. More precise laser interferometry based measurements using indents near the crack tip have also shown the same effect. Many other techniques have been proposed for measuring crack closure. These include ultrasound, DC-potential drop (DCPD), acoustic emission etc. Being diagnostic in nature, these techniques cannot avoid the subjective element of data interpretation. This introduces inaccuracies and discrepancies in estimates, which are rather unacceptable, considering the power relationship between crack growth rate, da/dN and effective range, ΔK_{eff} .

Proceeding on the assumption that da/dN is in fact controlled exclusively by ΔK_{eff} , it would follow that the crack closure phenomenon must also manifest itself in striation

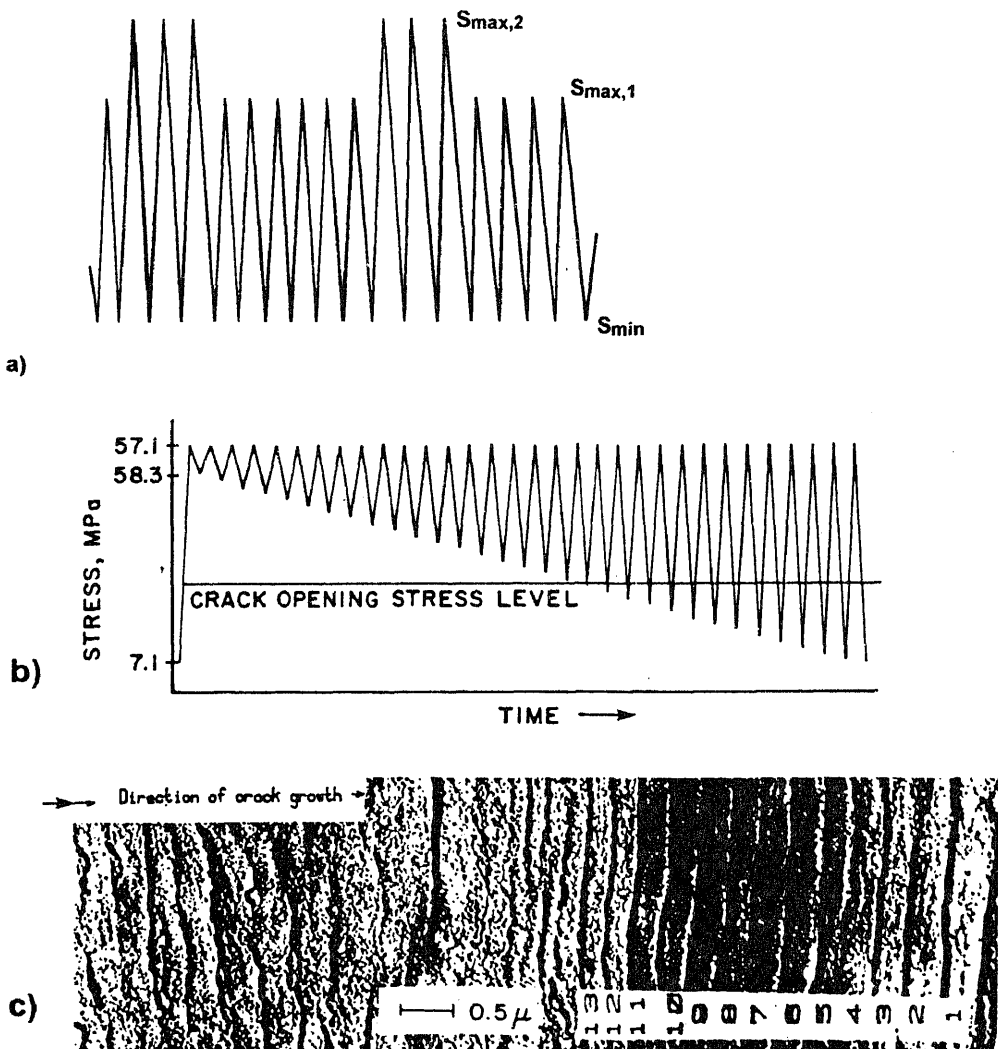


Figure 11. Load sequences used for fractographic assessment of crack closure. (a) Constant S_{min} and varying S_{max} (Pelloux *et al* 1980), (b) constant maximum stress and varying minimum stress (Sunder & Dash 1982), (c) striation pattern obtained from load sequence in (b).

patterns on the fracture surface. In many materials, individual load cycles form a striation on the fracture surface. The striation spacing indicates crack extension per cycle. Consider the simple load sequence in figure 11a in the framework of the Elber equation for crack growth rate:

$$\frac{da}{dN} = C \Delta K_{eff}^m \quad (2)$$

Cycles 1 and 2 have the same S_{\min} , but $S_{\max,2}$ exceeds $S_{\max,1}$. In the event of absence of crack closure, the striation spacing ratio, s_r , for the two cycles will be given by:

$$s_r = \left[\frac{S_{\max,1} - S_{\min,1}}{S_{\max,2} - S_{\min,2}} \right]^m \quad (3)$$

In the presence of crack closure (3) is rewritten as:

$$s_r = \left[\frac{S_{\max,1} - S_{cl}}{S_{\max,2} - S_{cl}} \right]^m \quad (4)$$

Given s_r from electron fractography, S_{cl} can be determined from (4). This idea formed the basis for an experimental study by Pelloux *et al* (1980). The technique proposed by them relies on the validity of the exponent, m . This material constant is determined from experimental macro crack growth rate data, which need not coincide with striation spacings if other crack-extension mechanisms are involved, along with striation formation. In fact, Pelloux *et al* obtained S_{cl} estimates assuming different values for the exponent.

The shortcoming in the above technique was overcome by Sunder & Dash (1982), who proposed a different type of load sequence that is schematically described in figure 11b. A programmed load sequence with constant S_{\max} and S_{\min} varying gradually from cycle to cycle is used in the test. Assuming S_{cl} is constant over this block of cycles, at the cycles with S_{\min} less than S_{cl} will leave behind equally spaced striations. By simply counting the number of equally spaced striations in a load block, one can directly determine S_{cl} (see typical striation pattern in figure 11c). The technique is based on the hypothesis that only fatigue crack closure can explain equally spaced striations from the type of load sequence shown in figure 11b. It is not sensitive to the exponent, m , or in fact, even the nature of the growth rate equation. Besides, the method offers the possibility of determining S_{cl} with a known degree of error – equal to the difference in S_{\min} between successive cycles. On the other hand, it must be noted that in actual practice, there is an element of subjectivity in counting off equally spaced striations. Another disadvantage with the technique is that it requires a specially designed load sequence and cannot be easily adapted to a particular sequence of interest to the user. The material must be conducive to striation formation and finally, the technique provides best results with TEM, which is a rather cumbersome exercise.

The above method for crack closure assessment has been used in a number of studies on the crack closure phenomenon. It confirmed for example, that crack closure close to the surface of the specimen is greater than in the mid-thickness region, where plane strain conditions prevail (see figure 12) (Sunder & Dash 1982).

9. Crack closure development in notch root corner cracks

One of the major advantages of the fractographic technique for closure measurement is that estimates are local in nature. This feature was exploited in a study which involved application of a 'closure block' along with a binary coded load block that 'punches' the cycle count onto the fracture surface (Anandan & Sunder 1987). The technique of binary coding was demonstrated in earlier work, where in alphanumeric information

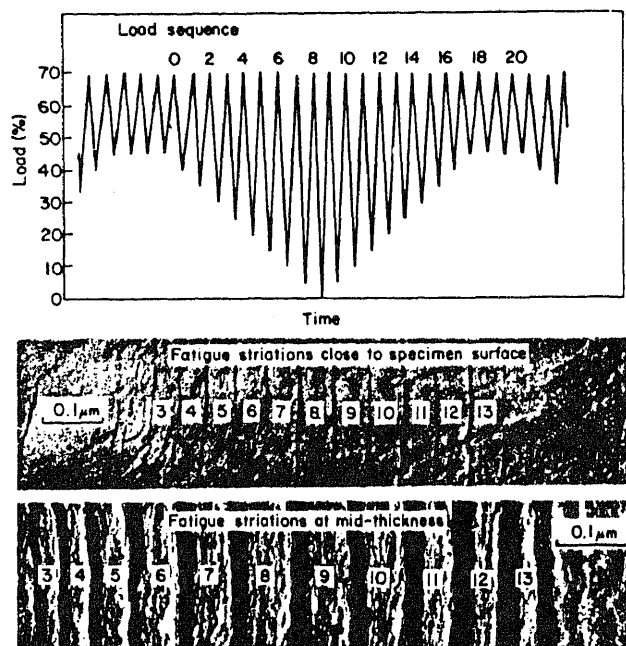


Figure 12. More equally spaced striations are found near the surface than at the mid-thickness area, indicating less closure at mid-thickness (Sunder & Dash 1982).

was fractographically encoded into a striation pattern (see figure 13) (Sunder 1983). This opened up the possibility of introducing event markers on the fracture surface, which can be identified during subsequent fractography, thus permitting crack front and crack closure mapping for part-through cracks.

A fractographic study on closure development was performed on a keyhole type of SENT specimen, with a corner crack emanating out of a 0.25 mm deep crack initiator (Anandan & Sunder 1987). The tests were conducted after application of various levels of prior static overload to examine how notch root residual stresses will affect the evolution of crack front and associated S_{cl} values. Some results appear in figure 14. Note the higher levels of S_{cl} close to the notch surface. S_{cl} varied by almost 50% depending on location. The binary coded striation patterns were used to decode the cycle count and thereby build up the crack front shape and map the growth of the corner crack at the notch root. It was found that residual compressive stresses caused by prior static tensile overload reduce the 'local mean stress' along the notch surface (see figure 15). This retards local crack front progress because of reduced effective stress as indicated by increased closure stress levels.

The Jo Dean Morrow and Smith–Watson–Topper equations for LCF based fatigue damage (Morrow 1968; Topper *et al* 1970) account for residual stress effects by introducing a local mean stress correction factor. While this correction is empirical in nature, the notch root stress strain response to applied elastic loading is simulated by the Local Stress–Strain (LSS) method, that is based on Neuber conversion (Neuber 1961) and Masing model (Wetzel, 1971). As demonstrated by the data in figure 15, the same Neuber conversion can be used to determine notch root stress ratio and associated S_{cl} values to provide a fracture mechanics based explanation for reduced

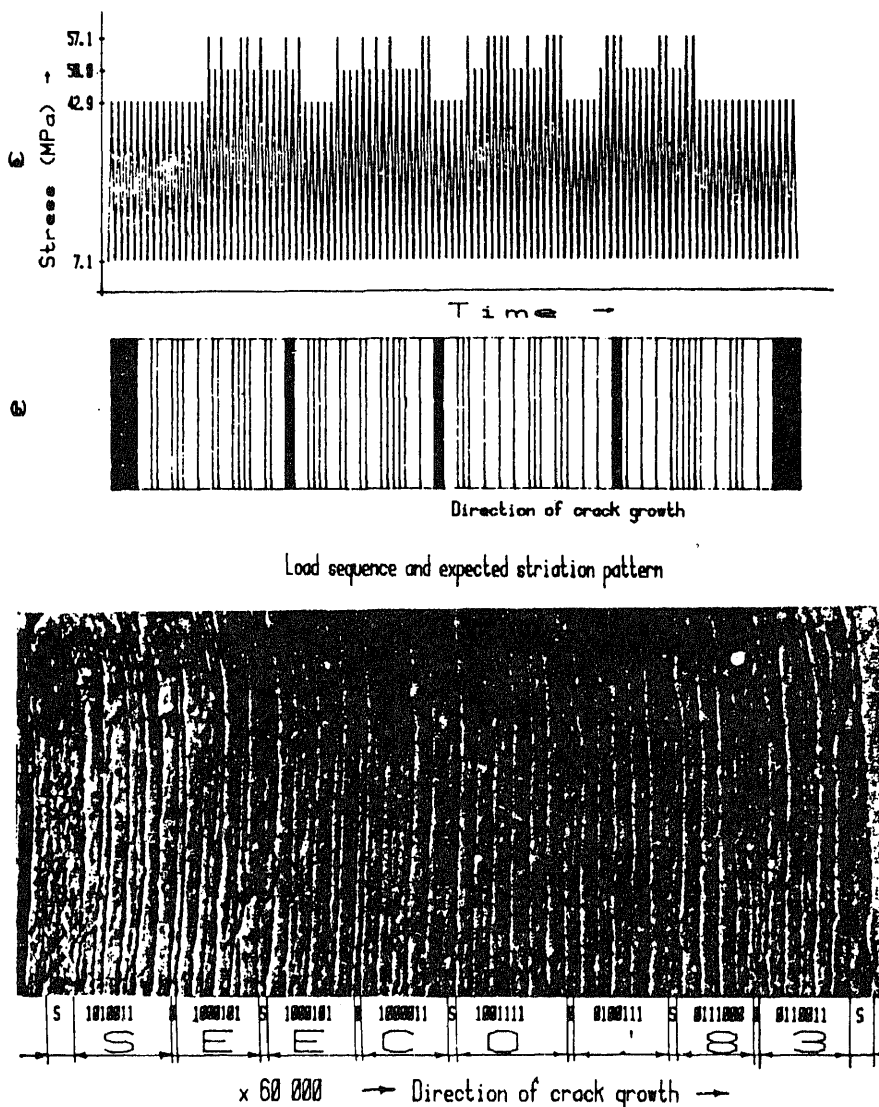


Figure 13. Binary coded load sequence (a) and striation pattern (b) representing the character string "SEECO'83" (Sunder 1983). The same technique was used to punch the load cycle count onto the fracture surface for event registration purposes.

fatigue damage in the presence of compressive residual stresses: local stress ratio is lower than applied stress ratio, the fatigue crack remains closed over a larger portion of the load cycle and crack growth is retarded by the reduced effective stress intensity range. These results are for fairly large cracks, at least a fraction of a millimeter in size. Subsequent research whose description is forthcoming showed that the same conclusion holds true for much smaller cracks that can form at the very commencement of fatigue cycling.

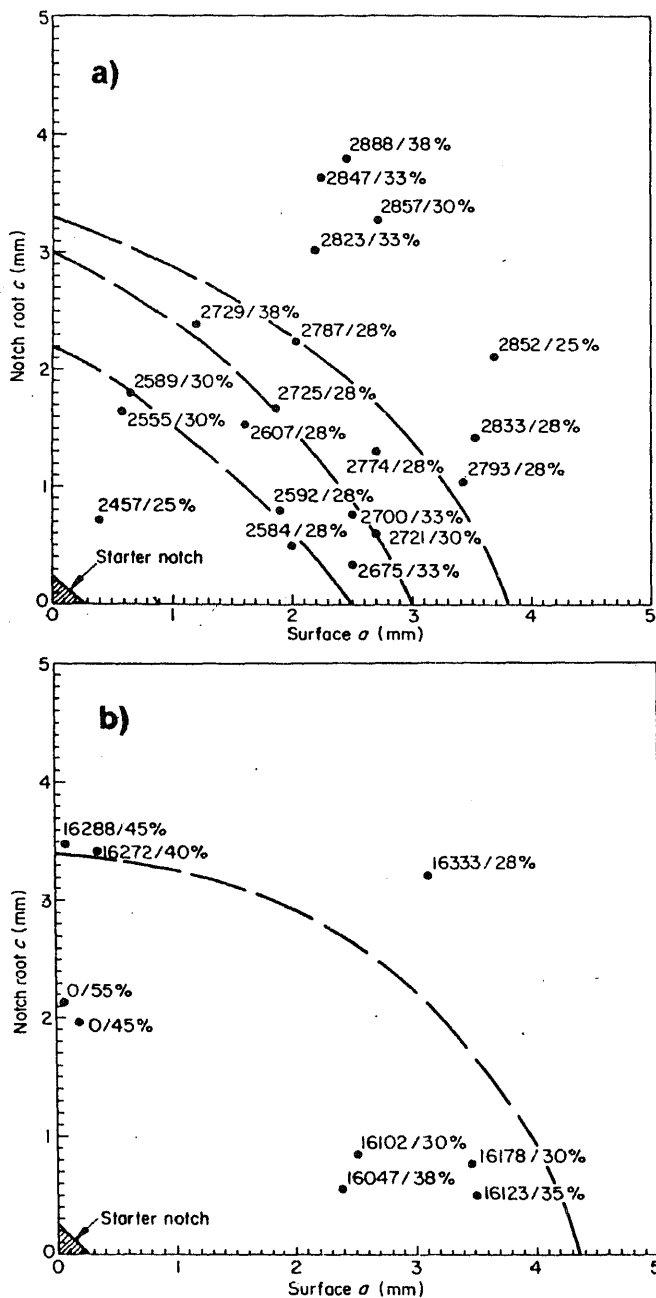


Figure 14. Fractographically determined crack opening stress levels for a key hole notch specimen without prior overload (a) and after 100% prior tensile overload (b) (Anandan & Sunder 1987).

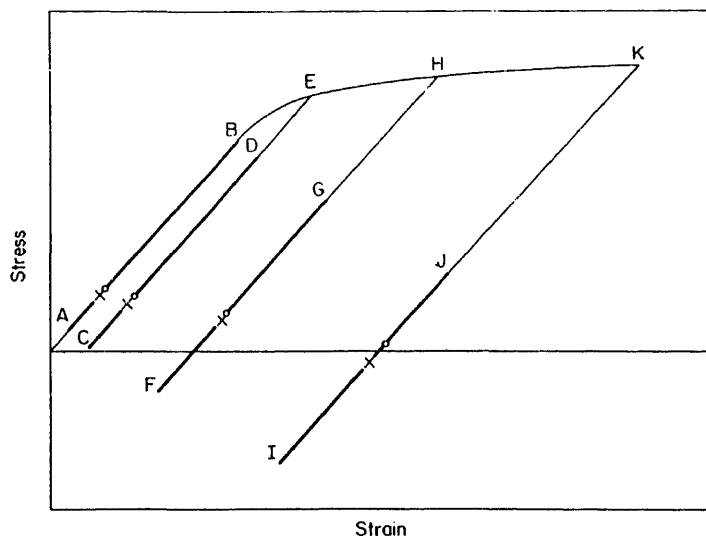


Figure 15. Tensile overload of different magnitude (E,H,K) leaves behind progressively greater compressive residual stress that reduce local stress ratio. As a consequence, the crack is closed over a larger fraction of the load cycle, leading to retarded growth. Crosses are fractographically estimated notch root S_{op} , circles are from literature data for given stress ratio (Anandan & Sunder 1987).

10. Hysteresis in fatigue crack closure

Consider the arbitrary load sequence and associated notch root stress-strain response shown in figure 16. Cycles A, B and cycles C, D are of the same applied magnitude. Yet, because of the notch root stress strain hysteresis, larger loads applied between these similar cycles induce residual stress that change their local mean stress and strain. As a consequence of this load interaction, cycles B and D have a lower mean stress than cycles A and C respectively. When interpreted from a fracture mechanics viewpoint, crack extension in cycles B, D should be less than in A, C respectively.

Experiments were conducted to investigate crack closure behaviour under conditions of varying local mean stress (Sunder 1991). Testing was on L165 Al-Cu alloy coupons with a central hole, with natural crack initiation under the test sequence shown in figure 17. This sequence contains a number of smaller cycles superposed on a major cycle. The simulated notch root stress-strain response to this sequence is also shown in the figure. The cycles on the rising and falling half of the major cycle are equal in magnitude and applied stress ratio. An attempt was made to determine crack closure stress, S_{cl} for each of these cycles. This was done by introducing into each of them, a suitable crack closure block that was described earlier, to give the rather complex load sequence which appears in a typical fractograph shown in figure 18. These experiments revealed that under variable amplitude inelastic notch root stress-strain, the crack will not open at a constant applied stress level in individual cycles. This phenomenon can be explained on the premise that crack closure stress, S_{cl} is distinct from and always greater than crack opening stress, S_{op} . S_{cl} and S_{op} for the major cycle in

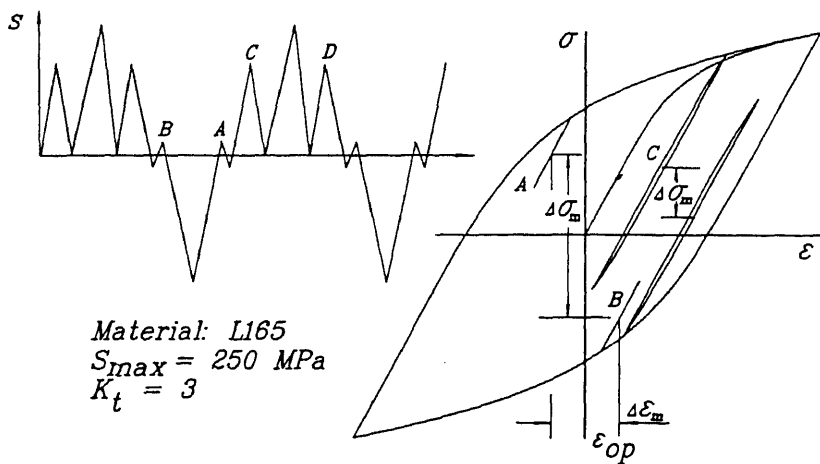


Figure 16. Notch root stress strain response to a complex load sequence.

a sequence will form an interval over which $S_{op,i}$ in individual embedded cycles will fall. Fatigue crack extension is controlled by the rising segment of the load excursion between S_{op} and S_{max} . S_{cl} while being of academic interest under constant amplitude loading, acts as an upper bound for S_{op} in smaller embedded cycles.

Hysteretic crack closure behaviour is schematically explained in figure 19. In the case of a long crack under elastic loading, S_{op} and S_{cl} are similar (figure 19a). $S_{op,i}$ in individual cycles under complex loading will not therefore see substantial variation. In

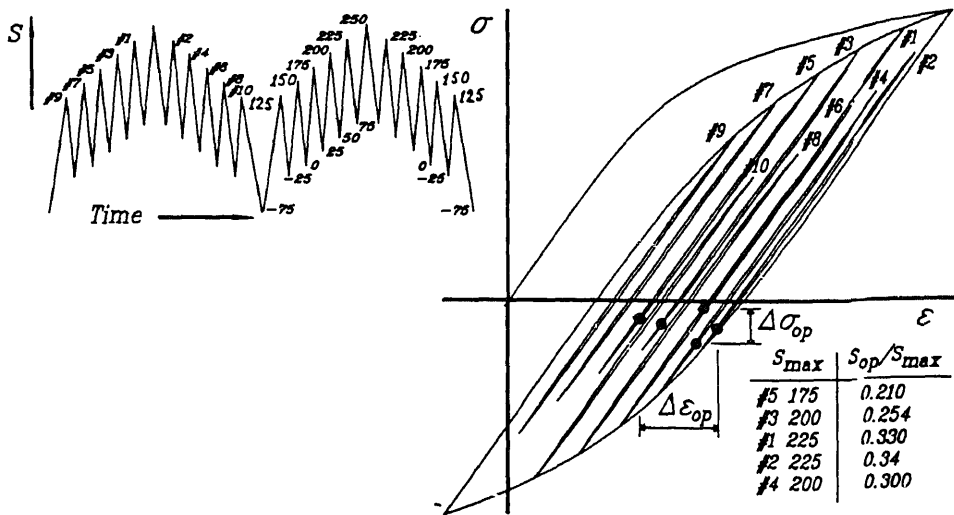


Figure 17. Load sequence with many embedded cycles on rising and falling half. This sequence was modified suitably for fractographic estimates of S_{op} in the embedded cycles (also see figure 18).



Figure 18. Typical fractograph from notch root area obtained from load sequence shown in the picture. This sequence was built around the root sequence shown in figure 17.

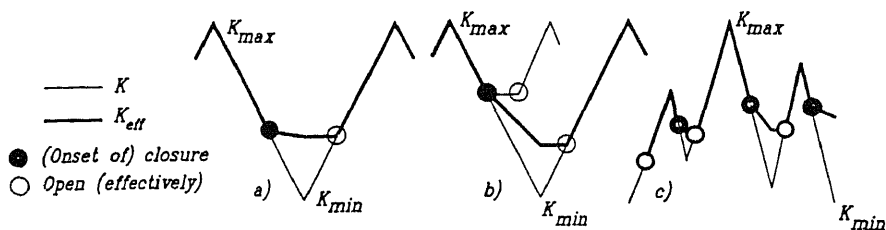


Figure 19. Schematic of hysteretic crack opening and closure under constant amplitude elastic (a) and inelastic (b) loading, and under arbitrary loading (c).

contrast, consider the case in figure 19b, showing closure response for a notch root crack under conditions of local cyclic inelasticity. The onset of closure (S_{cl}) occurs at a stress level much higher than S_{op} . This is due to the stress excursion from S_{cl} down to S_{min} , which lowers the stress at which the crack will open. The significance of this difference can be understood if we consider the possibility of applied stress not falling below S_{cl} , but rather, going up once again towards S_{max} . In this event, the crack would open immediately (see figure 19b). Figure 19c shows the interplay between closure and opening stress under a complex load sequence, that can be described by a 'linear hysteretic' model (Sunder 1991).

The hysteretic nature of S_{op} variation is qualitatively similar (in terms of its influence on damage due to crack extension) to that expected from load history effects on notch root local mean stress variation (in terms of damage estimates from LCF/LSS considerations). This provides a fracture mechanics foundation to explain well-known history sensitive local mean stress effects that were so far modelled empirically. It may also be noted that in the absence of hysteresis in crack closure, one would not be able to explain (from a fracture mechanics viewpoint), why notch root fatigue damage is load history sensitive.

11. Fractographic characterization of crack closure hysteresis

The work described in the preceding sections highlights the qualitative similarity between the hysteretic nature of notch root mean stress and notch root crack closure stress variation under complex loading. In an effort to develop a procedure for crack growth calculations under spectrum loading, a study was conducted to estimate S_{op} and S_{cl} values for Al-Cu alloy 2014-T6511 (L168 or HE15AST) under a variety of test conditions (Sunder *et al* 1993a).

Figure 20 provides a summary of experimental results at $R = -0.3$. This is representative of stress ratio of the major cycle in most aircraft wing lower surface load spectra. Clearly, S_{op} and S_{cl} are barely different for long cracks under elastic loading. But as crack size diminishes and stress level increases, the difference between the two increases substantially. While S_{cl} varies only marginally, S_{op} appears to fall rapidly below zero stress when the notch root sees cyclic inelastic loading. It follows that a fatigue crack can in principle be open in compression and implies that an assumption that negative stress intensity can be ignored may be unconservative. Indeed, experiments at $R = -3.3$ confirmed that a notch root crack can be open over a large portion of

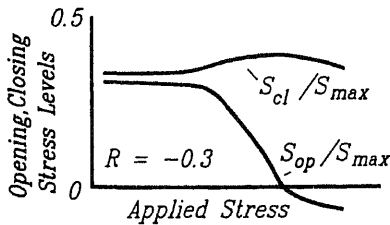


Figure 20. Schematic summary of measured closure and opening loads versus stress range at $R = -0.3$ in 6 mm thick L168 extruded bar stock (Sunder *et al* 1993a).

a compressive load cycle (Sunder *et al* 1993a). All these experiments used the specially designed load sequence and estimates of S_{op} and S_{cl} based on the number of equally based striations.

The S_{op} and S_{cl} values obtained in the above study along with laboratory data on crack growth rate in laboratory coupons under constant amplitude loading and the proposed hysteretic model for crack closure variation formed the basis for the framework for notch root short crack growth calculations (see figure 21). The influence of notch root cyclic inelasticity on crack driving force was accounted for by introducing a correction factor on stress intensity. In this manner, the cyclic stress-strain response of the material forms an essential input for crack growth computations. Calculations were made for notch root crack growth under various conditions of the FALSTAFF load spectrum, starting from an initial crack size of under 30 microns. These results are summarized in figure 22 and appear to support the application of fracture mechanics in fatigue crack growth analysis starting from extremely small and barely detectable crack sizes through to failure.

Figure 23 provides a schematic of how load interaction effects can be interpreted in the light of experimental observations and modelling described in the previous sections. Figure 23a shows a programmed load sequence with periodic overloads and

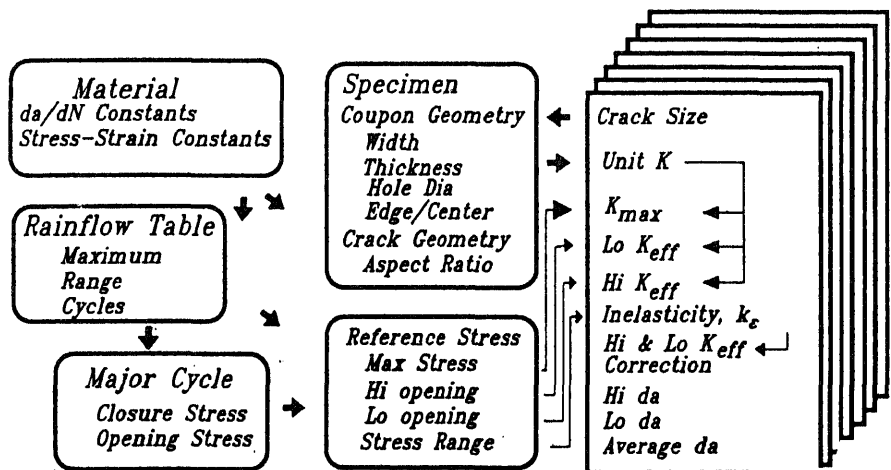


Figure 21. Framework of notch root fatigue crack growth rate analysis (Sunder *et al* 1993b)

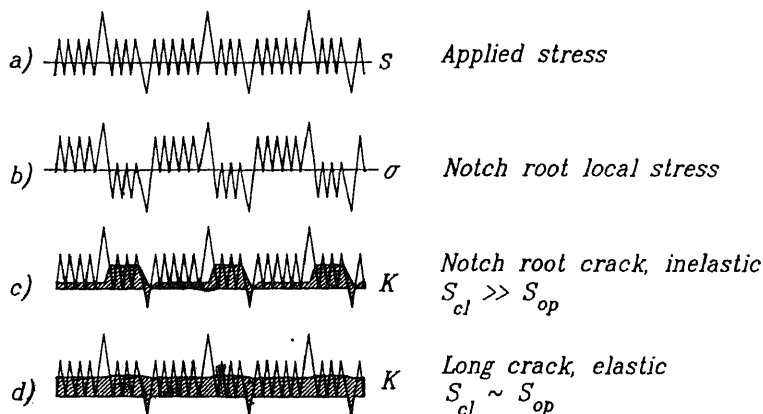


Figure 22. Schematic of load interaction effects in crack initiation, short and long crack growth (Sunder, 1991).

underloads superposed on a baseline sequence of small load cycles. If the notch root does not see inelastic strain under these stresses, notch root stress strain will see a scaled, but linear response, indicating total absence of load interaction effects. Figure 23b shows notch root inelastic stress-strain response. The beneficial effect of overload is seen by way of reduced mean stress in the following small cycles, while the underloads are followed by increased local mean stress. This is the basis for the load history effects as simulated by the Manson-Coffin-Topper equations in the LCF/LSS method. Figure 23c shows crack closure response for a notch root crack. We find that as a consequence of crack closure hysteresis, fatigue damage due to crack growth is affected in much the same way as fatigue damage from LCF/LSS considerations in figure 23b. Finally, figure 23d shows long crack elastic response, indicating little cycle-by-cycle sensitivity to load sequence. This observation may appear to contradict observations of retarded crack growth after an overload. It must be noted that the present discussion is restricted to cycle-by-cycle effects, while periodic overloads do introduce transient phenomena, with crack closure varying as the crack grows into and out of the overload plastic zone. Such transients are related to crack increment, rather than cycling and require due consideration in the event of large duration load spectra and high crack growth rates.

Considering that short cracks can initiate very early in life, it is indeed possible that much of what has been hitherto modelling effectively through LCF/LSS approach, may in fact fall within the framework of a fracture mechanics approach. The associated 'damage mechanics' concept was proposed by Newman *et al* (1992). However, the question of hysteresis in crack closure was not addressed in their work.

The crack closure concepts presented in the present paper and their extension to random load conditions through rainflow considerations has recently been confirmed using high resolution laser interferometry studies of crack tip displacements under specially designed load sequences (Ashbaugh *et al* 1994). The study included a comprehensive finite element analysis of the problem which provided data that closely tie up with previous fractographic observations as well as the laser interferometry measurements. These

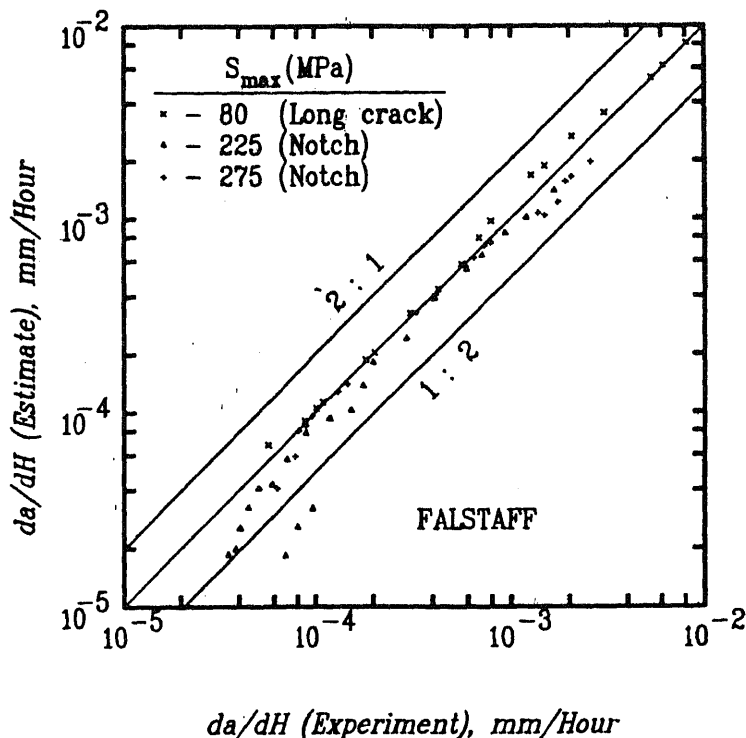


Figure 23. Summary of crack growth rate calculations for long and short cracks. Short crack data extend down to about 40 micron crack size (Sunder *et al* 1993b).

measurements were performed with reference to microscopic indents about 150 microns apart and about 50 to 100 microns ahead of the crack tip. Displacement over this gauge length versus applied load excursion is shown in figure 24. Note that displacement is shown in relative terms as a deviation from the unloading load versus COD slope. The load sequence contains five rainflow counted cycles, two each on the rising and falling half of the major cycle. Clearly, S_{op} in the embedded cycles is greater than in the case of the major cycle as would also follow from the hysteretic closure model. The closure of the data loops also confirms earlier fractographic observations (Sunder *et al* 1984) on the validity of rainflow for fatigue crack growth. Finally, it appears to underline the relevance of energy balance considerations to fatigue damage through crack tip stress-strain hysteresis as explained in figure 4 (Raju 1980).

The preceding sections provide an indication about the value of fractography in understanding the nature of fatigue crack growth under complex loading. Described below is another application of quantitative fractography.

12. Notch root short crack growth under spectrum loading

The evaluation of short crack growth rate predictions under spectrum loading (figure 23) posed the requirement of obtaining reliable experimental data (down to

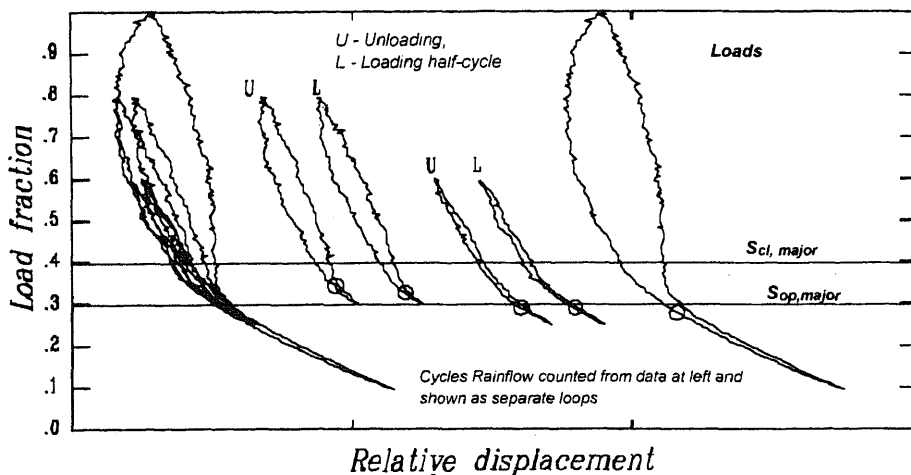


Figure 24. Relative crack opening displacement versus load in a complex sequence shown at top right. Data from laser interferometry over entire sequence shown at left. Small circles indicate Sop in individual counted cycles (Ashbaugh *et al* 1994).

crack size of under 50 microns) that could be used as a reference. As such cracks have to initiate naturally (artificially initiated cracks would have an unacceptably large initial size), they cannot be tracked by conventional instrumentation, particularly when multi-site initiation is possible. Available data from the literature have largely been obtained using surface replica technique (Newman & Edwards 1988). In our studies, an attempt was made to characterize short crack growth rates through optical fractography.

The basis for fractographic crack growth rate estimation is the correlation between crack extension per cycle and striation spacing. Striations in turn can be due to a single cycle or due to a group of cycles. Figure 3 showed examples of both. The FALSTAFF load spectrum which was used in the study is a randomized load sequence. It was adapted for fractography by conversion into a programmed load sequence (Sunder *et al* 1993a). To ensure equivalence of the two, the sequence was first reduced to a rainflow cycle count. A total of 18 large cycles of different magnitude were identified in the spectrum. The remaining cycles were broken into 18 similar blocks. One each was attached to each one of the major cycles. Care was taken to space the two largest cycles apart in such a manner that they could be easily identified on the fracture surface. The resultant programmed load sequence (shown in figure 25) was checked for equivalence with the original FALSTAFF sequence, first analytically, then, after minor adjustments, experimentally, to ensure that the two sequences provided the same growth rates on a long crack that could be monitored visually, through instrumentation (from unloading compliance) and fractographically (to ensure that fractographic estimates under programmed loading conform to visual observations). These results appear in figure 26.

The fractographically determined crack growth rate curve was integrated 'backwards from the failure point' down to the smallest possible crack size (ranging from 10

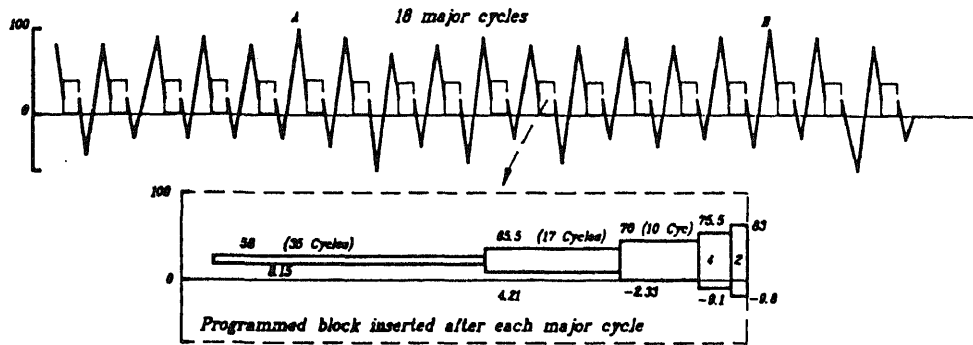


Figure 25. Programmed FALSTAFF load sequence used in fractographic studies on notch root crack growth (Sunder *et al* 1993a)

to 50 microns, depending on the clarity of pictures). This gave the crack propagation life. Life to formation of the small crack was then estimated as the difference between endurance and crack propagation life. As a consequence, the fractographic technique provided the opportunity to examine aspects of early crack growth that could not be addressed using conventional methods. This procedure was used in experiments on a number of notched coupons at different stress levels. Later, the same procedure was used to study crack growth in a lug joint, whose description is forthcoming.

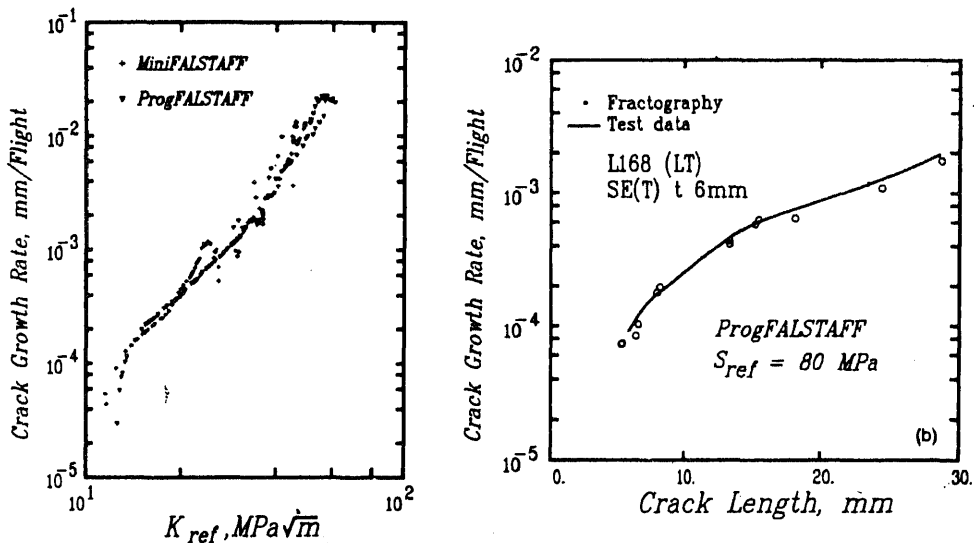


Figure 26. Long crack growth rates under randomized MiniFALSTAFF and programmed FALSTAFF (left), Fractographic and visual observations of crack growth rate under programmed FALSTAFF (right) (Sunder *et al* 1993a).

The study provided many significant observations (Prakash *et al* 1994; Sunder *et al* 1994):

- Surface replica based measurements provide an exaggerated measure of scatter in growth rate. Short crack growth rates do not exhibit more scatter than long cracks at comparable growth rates. This is illustrated by the data in figure 27. The scatter seen in replica based data is obviously related to shortcomings in the technique and also to the possibility that there indeed may be some discontinuity in crack extension as registered on the specimen surface.
- Number of naturally initiating cracks increases with applied stress level. Figure 28 summarizes this effect from tests on coupons of two thicknesses. These data are for the FALSTAFF spectrum. It is possible that the relationship will depend on the load spectrum under consideration as crack formation is likely to be accelerated by the larger cycles in the spectrum. In case of the TWIST spectrum, the larger cycle accounts for less damage as indicated by the RDE diagram in figure 7. It would

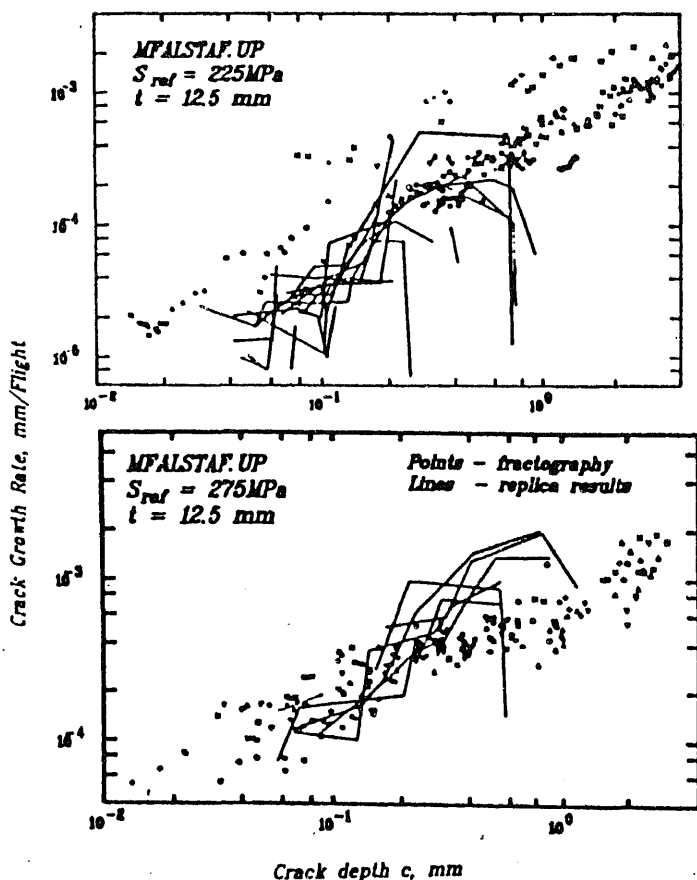


Figure 27. Replica and fractography based crack growth rate estimates for naturally initiating multiple cracks at two different stress levels (Sunder *et al* 1994).

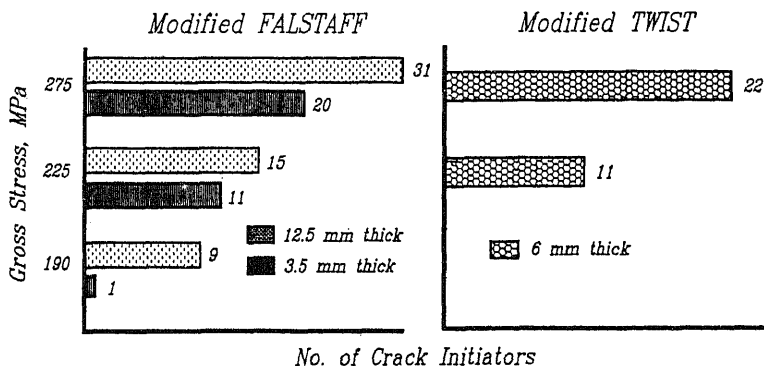


Figure 28. Effect of stress level on number of crack initiating sites. Data for two different specimen thicknesses (Sunder & Prakash 1994).

follow that in case of TWIST, fewer initiation sites will be associated with the same stress level when compared to FALSTAFF.

- Artificially initiated fatigue cracks behave differently from naturally initiating ones (see figure 29). Experiments on edge-notched coupons showed that naturally initiating cracks grow faster than artificially initiated ones. This was related to the crack initiator behaving as a blunt secondary notch inside the primary notch, when compared to a much sharper crack tip. It would follow that to be of practical value, short crack experiments must involve natural crack initiation.
- Multiple natural cracks do not initiate simultaneously. On the other hand, cracks that form early will accelerate the formation and growth of new cracks due to stress redistribution along the notch surface. This is illustrated by the results in figure 29. Thus, the slowest crack on the fracture surface was possibly the dominant one, having formed earlier than the others. It was noted that for purpose of life calculations, consideration of the dominant crack alone is likely to provide satisfactory estimates.

13. Fatigue crack growth in lugs under spectrum loading

Advances in fracture mechanics and in our understanding of fatigue crack growth mechanisms have largely been based on laboratory testing of coupons with standard stress intensity solutions. Many fatigue failures on airframes occur at joints and fasteners, which represent a fairly complex geometry.

In a recent new application of fractography, lug joints with different degree of interference fit were tested to failure under both constant amplitude as well as programmed FALSTAFF loading conditions (Sunder & Prakash 1994). The fracture surface was then studied to determine growth rates down to crack size below 50 microns. The measurements were performed with an optical microscope equipped with digital imaging technology. The constant amplitude growth rates were then compared with data from standard laboratory coupons to derive a stress intensity calibration. These data appear in figure 30. They appear to indicate shortcomings in available

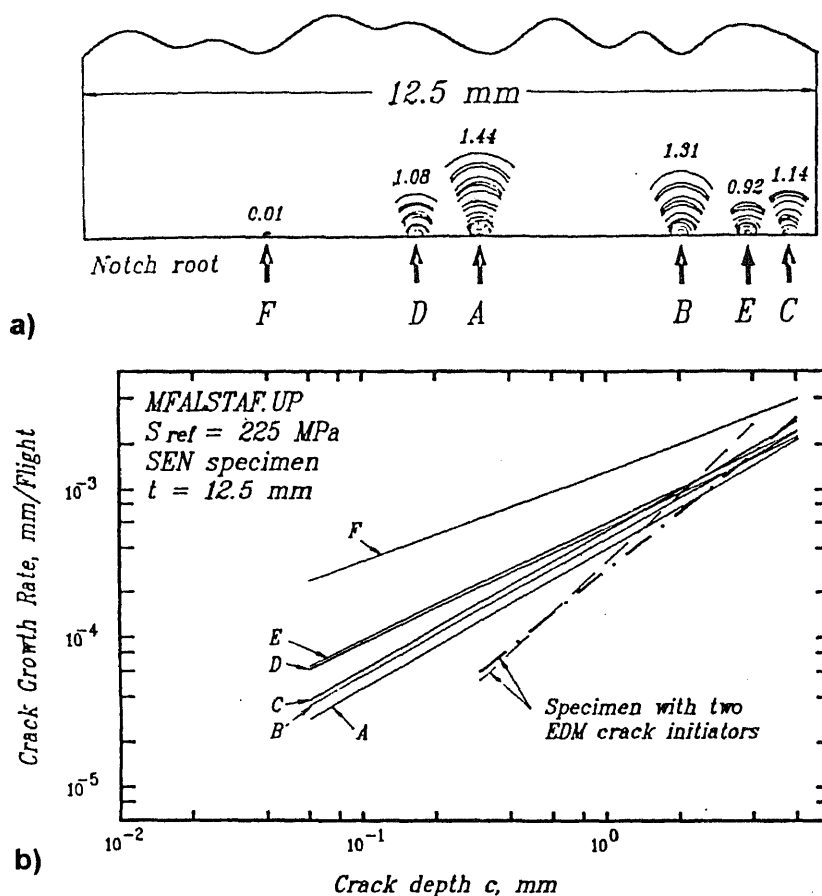


Figure 29. Reconstructed intermediate crack front mapping from multiple sites A–F (a), and (b) crack growth rates for individual cracks. ‘A’ was the dominant crack having appeared first, while B–F exhibit accelerated growth rates. Two discontinuous lines in (b) show the lower growth rates for artificially initiated cracks (Sunder & Prakash 1994).

analytical solutions for stress intensity in lugs, particularly when small cracks are involved (about 150 microns and less). On the other hand, the data also indicated that irrespective of the degree and nature of the interference fit, crack growth rate appear to fall into a single scatter band above a crack size of about 150 microns. While this observation requires verification for other stress levels, one may conclude that given a suitable stress intensity calibration, fracture mechanics can handle the durability as well as damage tolerance of joints and fasteners.

14. Concluding remarks

The research described in this paper was aimed at improving fatigue life prediction technology in engineering application. While the materials and load spectra studied are

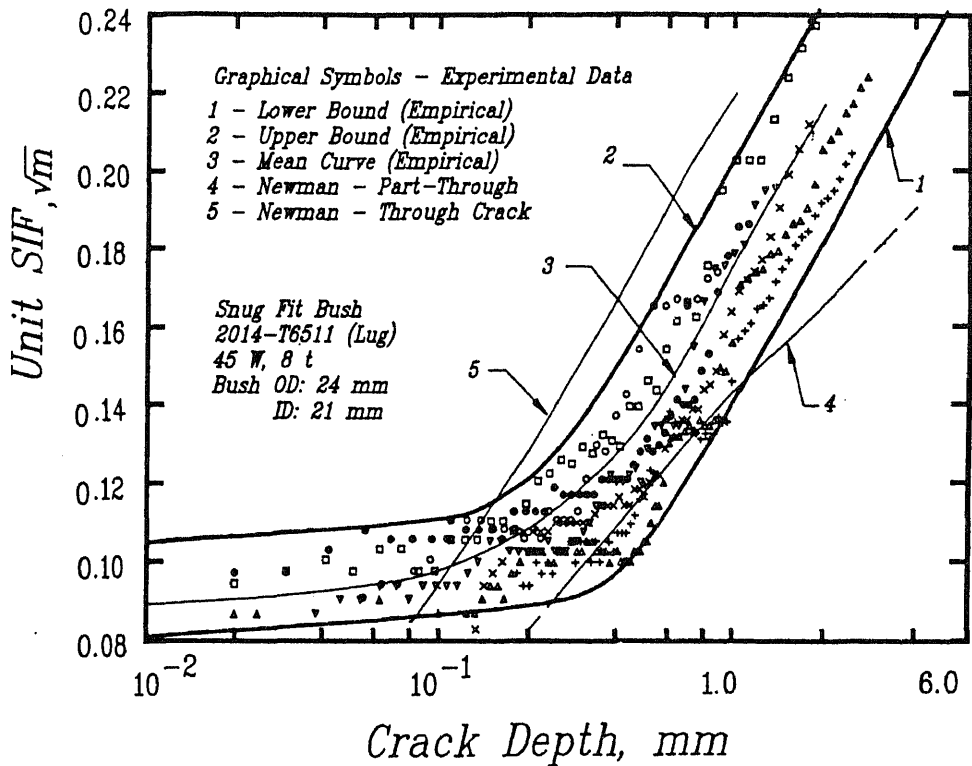


Figure 30. Calibrated stress intensity versus crack depth for a part-through crack growing out of the lug notch root. Calibration obtained under constant amplitude loading (Sunder & Prakash 1994).

specific to airframe structural application, they may be relevant to many other fatigue critical structures and machinery. The complexity of metal fatigue in engineering application may be attributed to a number of factors, including:

- Stress distribution in a builtup structure, particularly at stress raisers and its response to dynamic loading conditions,
- cumulative damage under random load conditions, typical of service environment, and,
- effects of environment, creep and residual stress variation that may change initially assumed mechanical properties and response.

The work described in this paper relates to the second aspect, which centres around the extrapolation of test data obtained on laboratory coupons under constant amplitude loading to real components subject to a random load environment:

- Difference between an arbitrary load sequence and constant amplitude loading from the viewpoint of cumulative damage.

The rainflow cycle counting technique bridges this difference. While it was discovered in a low-cycle fatigue framework, its validity for crack growth analysis

has been demonstrated through electron fractography of failures obtained under specially designed programmed load sequences. In view of its mechanistic basis, the rainflow technique could be developed for accelerated fatigue life analysis and testing.

- Sensitivity of both crack initiation as well as crack propagation to load history (load interaction effects). Experience shows these can account for more than an order of magnitude variation in fatigue life.

Most life prediction models account for history effects by simulating the effect of mean stress. A hypothetical material, whose fatigue response is insensitive to mean stress, is also likely to be insensitive to load history effects. Fatigue crack closure has been identified as the means through which mean stress affects crack growth. The experimental research described in this paper provided a better understanding on crack closure distribution across the crack front in through as well as short, part-through cracks.

A significant outcome of recent research has been the discovery of hysteresis in fatigue crack closure. This discovery provides the link between fracture mechanics and low-cycle fatigue considerations of fatigue damage under complex loading and may lead to a unified consideration of the fatigue problem.

A central feature of the research described in the paper is its interdisciplinary approach. All the experiments involved specially designed loading that required extensive use of custom-built test automation. Computer controlled testing at NAL saw much progress over the past 15 years and the technology is currently being commercialized. Most experiments were followed up by electron and optical fractography, which in recent years has gained from the appearance of cost effective PC-based image enhancement and processing techniques.

Further work is recommended in the area of natural crack formation under service loading. While fracture mechanics appears to be able to handle cracks as small as 20 microns, high endurance applications (particularly engine components and automobile suspension) require better understanding of how a crack of that size forms – of course under a randomized load environment. The problem holds exciting avenues of research in the area of fasteners, which appear to often determine the quality of structural integrity assurance. Finally, load monitoring technology for built-up structures combined with NDE and life prediction technology have potential application in life extension schemes in view of aging problems and growing cost of new installations.

15. Scope of analytical effort

Analytical modeling in solid and fluid mechanics including fracture mechanics proceeds from first principles and basic material constants. Fatigue life prediction in contrast is essentially restricted to extrapolation of laboratory data obtained either under constant amplitude or random loading to other sequences, stress levels and crack geometries. Laboratory coupon level testing for data generation is therefore required for every new material and its variation including processing. National Aerospace Laboratories have been actively involved in material test data generation for design as well as type certification purposes. A few thousand tests have been performed over the past six years to determine the LCF and FCP constants for a variety of Al-Cu, Al-Li, steel and titanium alloys used in airframe applications. Such testing contributed to type

approval of a number of indigenous materials for airframe materials and to the qualification of imported candidate materials for use in aircraft development programmes.

Stringent requirements on air worthiness and structural integrity require laboratory level full-scale testing to demonstrate the quality of a new design or modification of operating aircraft. All the preceding analyses including residual life predictions are intended to ensure a high degree of probability that the design as a total system will survive certification testing under conditions that closely simulate real operation over the stipulated service life. This concept is now followed by the highly competitive auto industry in view of the high costs of retrofits under warranty and liability clauses. In the years to come, it is likely that other industries in the country, including energy, chemical industries, rail transportation and consumer durable sector will follow the same trend. Thus, in the years to come, testing will continue to play a major role in qualifying the durability and damage tolerance of materials and structures, while analytical effort will be expected to optimize design and make testing more cost effective.

The work described in this paper enjoyed the strong support of Dr S R Valluri, Prof R Narasimha and Dr K N Raju. Financial support for the effort was provided by Aeronautical Research & Development Board, Aeronautical Development Agency and Department of Science and Technology. The author would like to place on record the considerable effort of professional colleagues from many countries, who contributed by way of peer review and encouragement to the documentation in international literature of the reported research. The support over the years from colleagues from the Materials Science Division, Structures Division, Engineering Services and Graphic Arts at NAL is gratefully acknowledged. Finally, the author is indebted to colleagues in the Structural Integrity Division for their active involvement and unstinting support in the studies reported in this paper.

References

- Anandan K, Sunder R 1987 Closure of part through cracks at the notch root. *Int. J. Fatigue* 9: 217-222
- Ashbaugh N E, Dattaguru B G, Khobeib M, Nicholas T, Prakash R V, Seshadri B, Sunder R 1994 Experimental and finite element study of crack closure Parts 1 & 2. *J. Fatigue Fracture Eng. Mater. Struct* (submitted)
- Christensen R H 1959 *Metal fatigue* (New York: McGraw-Hill)
- Chang J B, Hudson C M (eds) 1981 Methods and models for predicting fatigue crack growth under spectrum loading. ASTM STP 748
- de Koning A U 1981 A simple crack closure model for prediction of fatigue crack growth rates under variable amplitude loading. ASTM STP 743 pp. 384-412
- Dougherty D J, de Koning A U, Hillberry B M 1992 Modeling high crack growth rate under variable amplitude loading. ASTM STP 1122 pp. 214-233.
- Dowling N E, Brose W R, Wilson W K 1977 Notched member fatigue life predictions by the local strain approach. *Fatigue under complex loading: Analyses and experiments* (Warrendale, PA: Society of Automotive Engineers) vol. AE-6, pp. 55-84
- Dowling N E, Khosrovaneh A K 1989 Simplified analysis of helicopter fatigue loading spectra ASTM STP 1006 pp. 150-171
- Elber W 1971 The significance of fatigue crack closure (Philadelphia: American Society for Testing and Materials) ASTM STP 486, p. 230

- Elber W 1976 Equivalent constant-amplitude concept for crack growth under spectrum loading. ASTM STP 595 pp. 236-250
- Endo T, Mitsunaga K, Nakagawa H 1967 Fatigue of metals subjected to varying stress prediction of fatigue lives. Paper presented at Kyushu District Meeting of the Japanese Society of Mechanical Engineers, JSME, Kyushu
- Lincoln J W, 1994 Overview of the structural integrity process, an assessment of fatigue damage and crack growth prediction techniques. AGARD Report 797, Paper LP
- Manson S S, Freche J C, Ensign, C R 1966 Application of a double linear damage rule to cumulative fatigue. Fatigue crack propagation. ASTM STP 415, pp. 384-412
- Miner M A 1945 Cumulative damage in fatigue *Trans, ASME, J. Appl. Mech.* 12: A159-164
- Morrow J 1968 Fatigue properties of metals. Fatigue design handbook Soc. of Automotive Eng. §3-2
- Neuber H 1961 Theory of stress concentration for shear-strained prismatical bodies with arbitrary nonlinear stress-strain law. *Trans. ASME, J. Appl. Mech.* 28: 544-550
- Newman J C 1981 A crack closure model for predicting fatigue crack growth under aircraft spectrum loading. ASTM STP 748 pp. 53-84
- Newman J C, Edwards P R 1988 Short crack growth behaviour in an aluminum alloy - An AGARD cooperative test programme. AGARD Report 732
- Newman J C Jr, Phillips E P, Swain M H, Everett R A Jr, 1992 Fatigue mechanics: An assessment of a unified approach to life prediction. Advances in fatigue lifetime predictive techniques (eds) M R Michell, R W Landgraf, ASTM STP 1122 pp. 5-27
- Pelloux R M N, Faral M, McGee W M 1980 Fractographic measurements of crack tip closure. *Fracture Mechanics: Twelfth Conf.* ASTM STP 700, pp. 35-48
- Poe C C 1971 Fatigue crack propagation in stiffened panels. ASTM STP 486, pp. 79-97
- Prakash R V, Sunder R, Mitchenko E I 1994 A study of naturally initiating notch root fatigue cracks under spectrum loading. NAL Project Document SN 9406. National Aerospace Laboratories Bangalore
- Raju K N 1980 *Energy balance considerations in ductile fracture and fatigue crack growth*, PhD thesis, Indian Institute of Science, Bangalore
- Ritchie R O, Suresh S 1982 Some considerations on fatigue crack closure induced by fatigue fracture morphology. *Metall. Trans* A13: 937-940
- Schijve J 1967 Significance of fatigue cracks in micro-range and macro-range. Fatigue crack propagation. ASTM STP 415, pp. 415-459
- Schijve J 1974 Fatigue damage accumulation and incompatible crack front orientation *Eng. Fracture Mech.* 6: 245-252
- Schijve J 1979 Prediction methods for fatigue crack growth in aircraft material. Report LR-282, Delft University of Technology, Delft
- Schuetz W 1989 Standardised stress-time histories - An overview. (eds) J M Potter, R T Watanabe, ASTM STP 1006, pp. 3-16
- Sunder R 1983 Binary coded event registration on fatigue fracture surfaces. *Proc. SEECO'83* (ed) B Dabell (London: Society of Environmental Engineers) p. 197
- Sunder R 1985 System for automated crack growth testing under random loading. *Int. J. Fatigue* 7: 3-12
- Sunder R 1989 Compilation of procedures for fatigue crack propagation testing under complex load sequences. (eds) J M Potter R T Watanabe, ASTM STP 1006 pp. 211-230
- Sunder R 1991 Notch root crack closure under cyclic inelasticity. Project Document PDST 9132 National Aeronautical Laboratory (Also 1993 *J. Fatigue Fracture Eng. Mater. Struct.*) 16: 677-692
- Sunder R 1992a Rainflow applications in accelerated cumulative fatigue analysis. *The rainflow method in fatigue* (eds) Y Murakami (Oxford: Butterworth Heinemann) pp. 67-76
- Sunder R 1992b Near-threshold fatigue crack growth prediction under spectrum loading (eds) M R Mitchell, R W Landgraf, pp. 161-175
- Sunder R 1992c Contribution of individual load cycles to crack growth under aircraft spectrum loading (eds) M R Mitchell, R W Landgraf, ASTM STP 1122, pp. 176-190
- Sunder R 1993 Contribution of individual spectrum load cycles to damage in notch root crack initiation. *Short and long crack growth* (eds) M R Mitchell, R W Landgraf, ASTM STP 1211, pp. 19-29

- Sunder R, Dash P K 1982 Measurement of fatigue crack closure through electron microscopy. *Int. J. Fatigue* 4: 97-105
- Sunder R, Prakash R V 1994 A study of fatigue crack growth in lugs under spectrum loading. Project Document SN 9407. National Aerospace Laboratories Bangalore (submitted for publication in ASTM STP).
- Sunder R, Prakash R V, Mitchenko E I 1993a Fractographic study of notch fatigue crack closure and growth rates (eds) J E Masters, L N Gilbertson, ASTM STP 1203 pp. 113-131
- Sunder R, Prakash R V, Mitchenko E I 1993b Calculation of spectrum load notch root crack growth rate under elastic and inelastic conditions. (eds) M R Mitchell, R W Landgraf (Philadelphia: American Society for Testing and Materials) ASTM STP 1211, pp. 30-44
- Sunder R, Prakash R V, Mitchenko E I 1994 Growth of artificially and naturally initiating notch root cracks under FALSTAFF spectrum loading. AGARD Report 797, Paper 10
- Sunder R, Seetharam S A, Bhaskaran T 1984 Cycle counting for fatigue crack growth analysis. *Int. J. Fatigue* 6: 147-156
- Sunder R, Venkatesh C S 1990 Dedicated microprocessor based controller for fatigue testing. (eds) A A Braun, N E Ashbaugh, F M Smith. ASTM STP 1092, pp. 68-82
- Suresh S, Ritchie R O 1982 A geometric model for fatigue crack closure induced by fracture surface roughness. *Metall. Trans.*
- Suresh S, Zamiski G F, Ritchie R O 1981 Oxide induced crack closure: An explanation for near threshold corrosion fatigue crack growth behavior. *Metall. Trans.*, A12: 1435-1443
- Topper T H, Sandor B I 1970 Effects of mean stress and prestrain on fatigue damage summation. Effects of environment and complex load history on fatigue life ASTM STP 462, pp. 93-104
- Vormwald M, Heuler P, Seeger T 1992 A fracture mechanics based model for cumulative damage assessment as part of fatigue life prediction. ASTM STP 1122, pp. 28-43
- Wetzel R M 1971 *A method for fatigue damage analysis*, Ph D thesis, Department of Civil Engineering, Univ. of Waterloo, Ontario
- Zuidema J, Blaauw H S 1988 Slant fatigue crack growth in Al-2024 sheet material. *Eng. Fracture Mech.* 29: 401-413



Mechanisms and modelling of creep in superalloys

M McLEAN¹, L M PAN¹ and R N GHOSH²

¹Department of Materials, Imperial College of Science, Technology & Medicine, Prince Consort Road, London SW7 2BP, UK

²National Metallurgical Laboratory, Jamshedpur 831 007, India

Abstract. The characteristics of creep deformation of nickel-base superalloys are reviewed and the implications for the micromechanisms controlling the behaviour are considered. The development of a model of the creep deformation that is compatible with the physical mechanisms is traced, first in an isotropic form and later incorporating full crystallographic anisotropy. The validity of the model and its ability to be extrapolated to more complex loading conditions are evaluated against a wide range of experimental measurements.

Keywords. Crystallographic anisotropy; nickel base superalloy; crystal rotation; shape change; low cycle fatigue; isotropic/anisotropic model; single crystal turbine blade.

1. Introduction

The development of nickel-base superalloys and the evolution of the gas turbine engine have been closely related, each having a history that stretches only about fifty years (Betteridge & Shaw 1987). Indeed, the gas turbine is still by far the largest engine making use of these materials and the continual drive to improve engine efficiency has lead to very rapid changes in alloy composition and microstructure. More importantly, the technology pull aspect of the development has meant that new variants of superalloys have been very rapidly introduced into service.

A wide range of different alloy compositions and processing technologies have been developed for specific requirements in both different parts of gas turbines and for engines used for different applications. Thus, for example, in aero engines there is a requirement for materials with high creep strength capable of operating at high temperatures for use as turbine blades, whereas other materials with high yield and fatigue strengths capable of operating at high stresses and low temperatures are required for turbine disks. Similarly there are important differences in the requirements for materials for use in marine environments, for electricity generation and for civilian and military aircraft. However, alloys have been developed that suit all of these applications giving a wide range of compositions and processing routes. This has largely been achieved in an empirical manner and it is arguable that the development of new nickel-based alloys is becoming increasingly difficult because of the maturity of the technology.

Concentrating on the blade applications where creep behaviour is of particular importance we note that alloy microstructures have been controlled in addition to alloy composition in order to achieve optimum properties. The current state of the art for the most advanced turbine blade alloys is to produce these materials in single crystal form which leads to a high level of anisotropy of properties (Duhl 1987). Although the alloy strengths have probably been optimised to a level which is going to be difficult to exceed, it is unlikely that the full potential of these materials is yet being achieved. This is because there is as yet an inadequate understanding of the variation in relevant mechanical behaviour as a function of operating conditions and crystallographic anisotropy. Even if it were, the design procedures currently available cannot yet incorporate full time-dependent, anisotropic plasticity. Computer-aided design is developing very rapidly as computer power becomes cheaper and more readily available. However, these engineering developments can only be effective if there is a parallel improvement in the understanding and representation of material behaviour. Although the technology of alloy production is mature, engineering aspects of the use of single crystal superalloys are at a very early stage of development.

This paper will review current understanding of the factors influencing the creep behaviour of superalloys with particular emphasis on single crystal materials. It will describe the evolution of a model of anisotropic creep in single crystal superalloys that is expressed as constitutive laws which may be incorporated into finite element calculations of component behaviour. The paper will also indicate how the model has been validated and point to possible future directions.

2. Creep behaviour of solid solutions and superalloys

There is an extensive literature reporting studies of creep behaviour of a wide range of materials and of theoretical interpretation and modelling relating to these results (Wilshire & Evans 1987, 1990, 1993). Concepts of the mechanisms of creep deformation have largely been derived from studies on simple metals and solid solution alloys, there is now a very good understanding of the micromechanisms controlling creep in these materials (Langdon 1985). However, there are some very significant differences in the creep behaviour of nickel-base superalloys compared to that of simpler metallic materials. To highlight a few of these differences:

- Plastic pre-strain of superalloys accelerates the creep rate whereas it hardens most solid solution alloys (Dyson *et al* 1976).
- There is very little difference in creep curves of superalloys produced under constant load and constant stress conditions whereas these tests give large differences in most solid solution alloys (Loveday & Dyson 1990).
- Nickel-based superalloys exhibit very little, indeed probably no, steady state creep but are dominated by a tertiary creep regime of increasing creep rate. Solid solution alloys generally have an extensive steady state regime.
- Tertiary creep in nickel-base superalloys is exhibited in conditions of both tensile and compressive loading indicating that it cannot be due to cracking or cavitation. In solid solution alloys tertiary creep is generally associated with cavitation damage and is only apparent when there is a significant component of tensile loading (Tilley & Harrison 1973).

In view of these important differences it is essential to reconsider the mechanisms controlling creep deformation in multi-phase systems such as superalloys. The conventional models of recovery-controlled creep leading to a steady state behaviour that evolves into a tertiary regime when cavitation develops describes simple metals very well. However, they are not appropriate for superalloys, or indeed for many other microstructurally complex alloys. Dyson & McLean (1983), Henderson & McLean (1983), Dyson (1988) and Ion *et al* (1986) have, over a number of years, developed a model which attributes the characteristic softening of nickel-based superalloys to a progressive increase in the density of mobile dislocations that accumulate with increasing plastic strain. This can be thought of as being the result of inhibition of extensive glide of dislocations that encounter particles of the gamma prime precipitate. Insufficient dislocations are produced to provide a significant level of dislocation hardening and most new dislocations created remain mobile. Other factors that can contribute to the characteristic tertiary creep, such as loss of internal load bearing area due to the development of grain boundary cavities or reduction in load bearing cross-section during deformation (Ashby & Dyson 1984), which are common to most other materials, are relatively unimportant in single crystal superalloys and will not be considered here.

It has been possible to develop a relatively simple set of equations based on these concepts that adequately describe the creep behaviour of isotropic nickel-based alloys. More recently Ghosh *et al* (1990) and Pan *et al* (1993) have extended the approach to account for the material anisotropy in single crystal superalloys. This has taken the isotropic model as its starting point but recognises that even at high temperatures deformation results from dislocations moving on a few slip systems of well-defined crystallinity. Consequently, the model has been reframed in term of shear stresses and shear strains on these allowed slip systems and the total anisotropic deformation has been computed by summing the shear displacements from all active slip systems. This paper will briefly review the model and will compare its predictions with a range of validity experiments.

3. Isotropic model

The model has been expressed in the formalism of continuum damage mechanics (Kachanov 1958) in which the creep rate $\dot{\epsilon}$ is written as a function of state variables (or damage parameters) that represent the current condition of the material, in particular of the structural and microstructural features that control the strength of the material. If it is possible to derive equations describing the evolution of these state variables (S_1, S_2, S_3) then the creep behaviour can be determined by integration of a set of coupled differential equations:

$$\begin{aligned}\dot{\epsilon} &= f(\sigma, T, S_1, S_2, \dots), \\ \dot{S}_1 &= g(\sigma, T, S_1, S_2, \dots), \\ \dot{S}_2 &= h(\sigma, T, S_1, S_2, \dots).\end{aligned}\tag{1}$$

The problem is to identify the explicit forms of these equations that are compatible with the known micromechanisms of deformation so that these can be evaluated quantitatively from standard creep data to allow extrapolation to complex loading conditions.

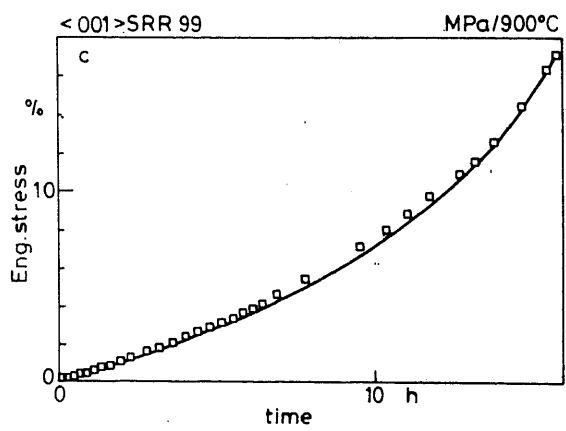
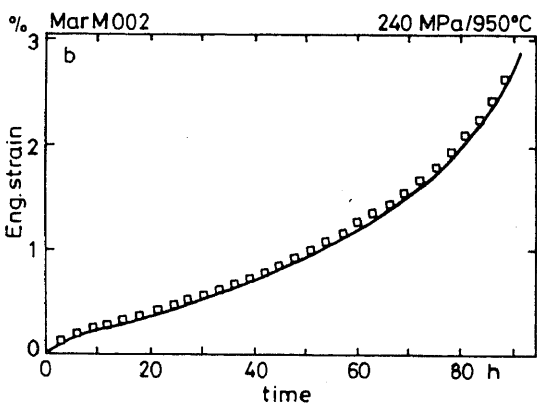
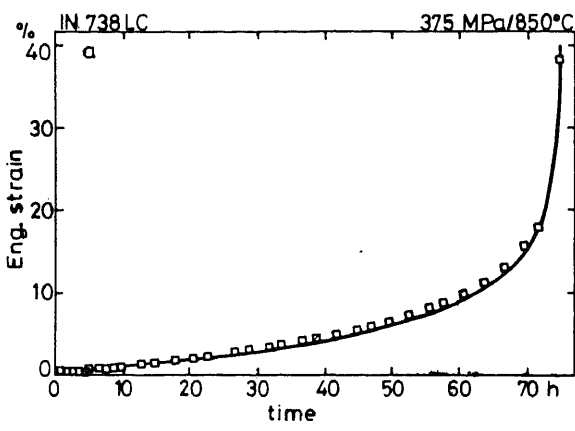


Figure 1. Examples of the fit of the isotropic model to creep curves for three different nickel base superalloys.

Dyson & McLean (1990) have given a comprehensive review of the isotropic model, so only the principal point will be given here. When cavitation and change of external material cross section can be neglected, the isotropic creep behaviour can be represented by a set of three equations involving two state variable S , ω and four constants $\dot{\epsilon}_i$, H , S_{ss} , C .

$$\begin{aligned}\dot{\epsilon} &= \dot{\epsilon}_i(1 - S)(1 + \omega), \\ \dot{S} &= H\dot{\epsilon}_i(1 - (S/S_{ss})), \\ \dot{\omega} &= C\dot{\epsilon}.\end{aligned}\quad (2)$$

S is a dimensionless representation of an internal stress that progressively increases to a steady state value S_{ss} leading to primary creep. The increasing density of mobile dislocations ρ is expressed through $\omega = (\rho - \rho_i)/\rho_i$ where the subscript i indicates the initial value.

Dyson & McLean (1990) describe a procedure for analysing a creep curve to evaluate the constants $\dot{\epsilon}_i$, H , S_{ss} , C and this has been successfully applied to several materials and been shown to be particularly appropriate to nickel-base superalloys. Figure 1 compares several creep curves for nickel-base superalloys with the curves generated using equation set (2). This is not a particularly demanding test of the model since other more empirical approaches can provide equally accurate fitting of the shapes of individual creep curves. However, the differential form of equation set (2) allows the creep strains that develop during variations in stress and/or temperature to be evaluated quite easily. Figure 2 compares the measured creep strain during cyclic loading with a prediction using model constants evaluated from constant stress tests.

Ghosh & McLean (1992) have extended this model to incorporate a wider range of loading conditions. In particular they show that strain-controlled deformation can be taken into account by the addition of one further equation into equation set (2). This represents the contribution of stress relaxation during variations in applied stress. If we represent the total and elastic contributions to strain by ϵ_T , ϵ_E respectively, while the creep component has no subscript, the additional equation is:

$$\dot{\sigma} = E\dot{\epsilon}_E = E(\dot{\epsilon}_T - \dot{\epsilon}). \quad (3)$$

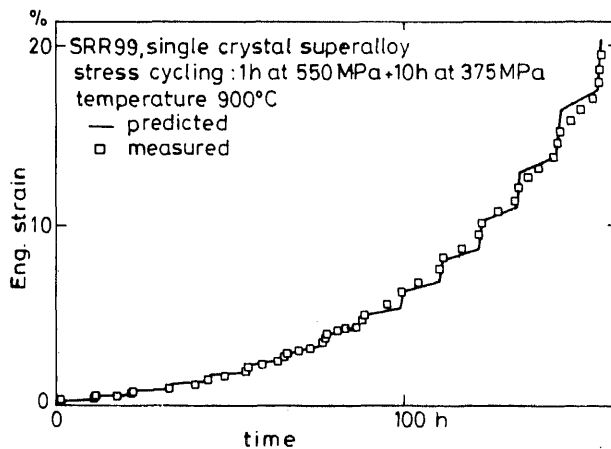


Figure 2. Comparison of the measured creep curves obtained under conditions of cyclic creep for the single crystal superalloy SRR99 axially stressed along the $\langle 001 \rangle$ direction with the model prediction based on a database of constant stress creep tests.

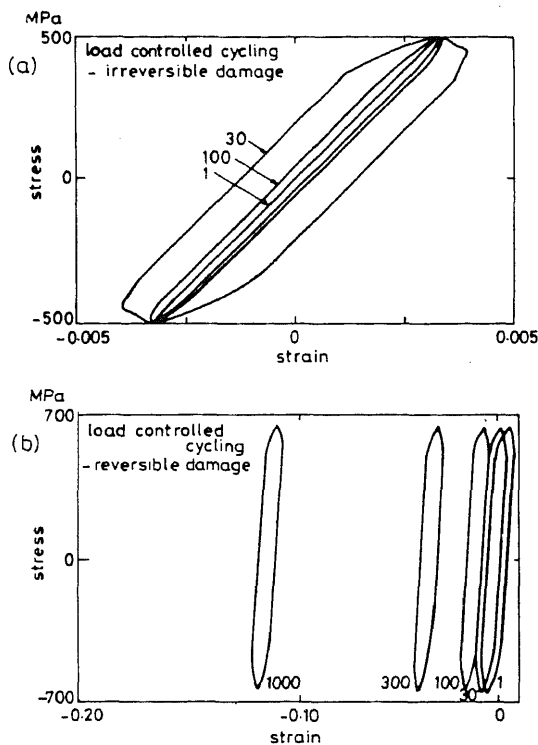


Figure 3. Predictions of the low cycle behaviour of IN738LC during constant load cycles based on model parameters established from a database of constant stress creep tests. The two predictions are for simulations of (a) irreversible growth of damage and (b) for damage that grows in tensile stresses but heals in compressive stresses.

Integration of the combination of equation set (2) and (3) subject to appropriate boundary conditions allows the simulation of several types of axial deformation: constant strain rate, stress relaxation, strain or load controlled low cycle fatigue. Ghosh & McLean (1992) considered *inter alia* the consequences of reversible and irreversible damage; i.e. damage that grew under tension but healed under compressive loads, compared to damage that continued to grow irrespective of the direction of loading. Figure 3 illustrates the different predictions for these two types of damage for load-controlled LCF. For irreversible damage the plastic strain range progressively increases, while for reversible damage the strain range remains constant but the loops are progressively displaced giving a ratcheting of the material.

4. Anisotropic model

Extension of the model to account for anisotropic creep of single crystals by Ghosh *et al* (1990), and Pan *et al* (1993) considers deformation to be restricted to specific slip systems and to occur at a rate $\dot{\gamma}$ that depends on the resolved shear stress τ , temperature T and equivalent state variables to those introduced in the isotropic model. For the k th slip system:

$$\dot{\gamma}^k = \dot{\gamma}_i^k (1 - S)(1 + \omega)$$

$$\dot{S} = H \dot{\gamma}_i^k (1 - (S/S_{ss}))$$

The total displacement ε_{ij} is obtained by summing all N components of shear on the allowed slip directions $\{n_1 n_2 n_3\} \langle b_1 b_2 b_3 \rangle$

$$\varepsilon_{ij} = \sum_{k=1}^N \gamma^k b_i^k n_j^k \quad (5)$$

The subscripts i, j take values 1, 2 or 3 representing the three cube axes and k identifies one of the N slip vectors being considered. Having constructed the strain matrix, anisotropic deformation is completely defined. An arbitrary crystal direction $[x_1 x_2 x_3]$ will transform to a new orientation $[X_1 X_2 X_3]$ in the small strain approximation:

$$\begin{bmatrix} X_1 \\ X_2 \\ X_3 \end{bmatrix} = \begin{bmatrix} 1 + \varepsilon_{11} & \varepsilon_{12} & \varepsilon_{13} \\ \varepsilon_{21} & 1 + \varepsilon_{22} & \varepsilon_{23} \\ \varepsilon_{31} & \varepsilon_{32} & 1 + \varepsilon_{33} \end{bmatrix} \cdot \begin{bmatrix} x_1 \\ x_2 \\ x_3 \end{bmatrix} \quad (6)$$

Strain in that direction is given by the magnitudes of the initial and final vectors, $\varepsilon = (\bar{X} - \bar{x})/\bar{x}$. If the constants of the creep equation are known, this allows the calculations of:

- crystal rotations during creep;
- strain in any direction;
- changes in material shape during deformation.

There is a considerable body of evidence in the literature that dislocation activity in nickel-base superalloys is largely restricted to octahedral planes even at high temperature (Caron *et al* 1988). There have also been reports of cube slip, in addition to elements of octahedral to cube cross-slip. In our analysis we allow the possibility of activity on $\{111\} \langle \bar{1}10 \rangle$ and $\{100\} \langle 011 \rangle$. We have discounted the possibility of a $\{111\} \langle \bar{2}11 \rangle$ system for the reasons detailed by Ghosh *et al* (1990).

For certain orientations which are symmetrically oriented with respect to the active slip vectors there is no change in crystal orientation or of specimen shape as a result of deformation. In these cases the tensile and shear formulations of the model are totally equivalent. Moreover, for axial loading along $\langle 001 \rangle$ there is no resolved shear stress on the cube planes, so deformation only results from octahedral slip. This allows the parameters of equation set (4) relating to $\{111\} \langle \bar{1}10 \rangle$ deformation to be evaluated from a creep database of $\langle 001 \rangle$ specimens using simple geometrical transformations of the parameters of the tensile formulation. Similarly, the parameters for cube slip can be determined by analysis of $\langle 111 \rangle$ specimens.

Figure 4 shows the optimum fit of the model to a creep curve for a $\langle 001 \rangle$ specimen tested in tension under constant stress conditions; the tensile and shear formulations give identical predictions. The creep curve calculated for $\langle 111 \rangle$ assuming that only octahedral slip is operative is also shown; this predicts a significantly longer life than for $\langle 001 \rangle$ whereas a shorter life is measured as shown. The model also provides a good representation of $\langle 111 \rangle$ creep curves by establishing the parameters for cube shear creep.

Having established the model parameters for both octahedral and cube shear creep as functions of stress and temperature by analysis of creep databases for $\langle 001 \rangle$ and $\langle 111 \rangle$ specimens respectively it is straightforward to calculate the deformation that results for arbitrary crystal orientations and applied stresses.

The model can also be combined with a representation of the anisotropy of elastic constants to include aspects of stress relaxation needed to account for arbitrary loading

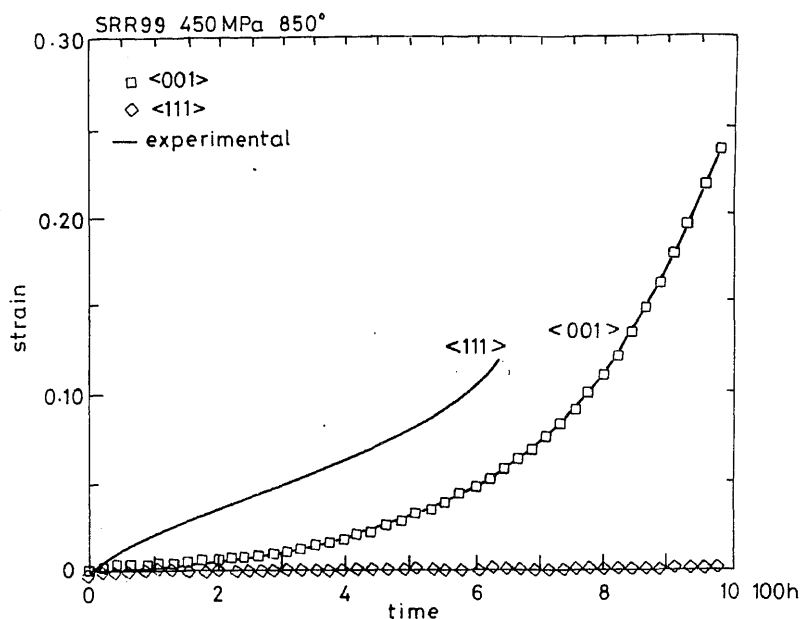


Figure 4. Comparison of the experimental and calculated creep curves for $\langle 001 \rangle$ and $\langle 111 \rangle$ oriented specimens of SRR99 tested at 450 MPa/850°C assuming that only $\{111\}\langle 110 \rangle$ glide operates.

conditions and arbitrary orientations (Pan *et al* 1993). For axial loading along the $\langle hkl \rangle$ direction the Young's modulus can be expressed in terms of the components of the compliance tensor S .

$$E_{\langle hkl \rangle} = [S_{11} + \{S_{44} - 2(S_{11} - S_{12})\}(h^2k^2 + k^2l^2 + l^2h^2)]^{-1}. \quad (7)$$

Using a time-stepping sequence, the creep strain in the $\langle hkl \rangle$ is computed and combined with the equation to determine the stress under strain-controlled conditions.

$$\sigma = E_{\langle hkl \rangle}(\varepsilon_T - \varepsilon). \quad (8)$$

4.1 Validation of anisotropic model

The model can provide an acceptable representation of a database of uniaxial creep results for the symmetrical $\langle 001 \rangle$ orientation, as indicated in figure 5, but this is not a particularly demanding test since equally good fits can be obtained by empirical models. The more demanding tests are to assess the ability of the model to extrapolate successfully from creep data for simple orientations to predict:

- creep behaviour for arbitrary complex orientations being able to account for variations in the form and magnitude of the anisotropy of creep as functions of stress and temperature;
- changes in orientation with creep strain;
- shape distortions of creep test specimens during deformation;

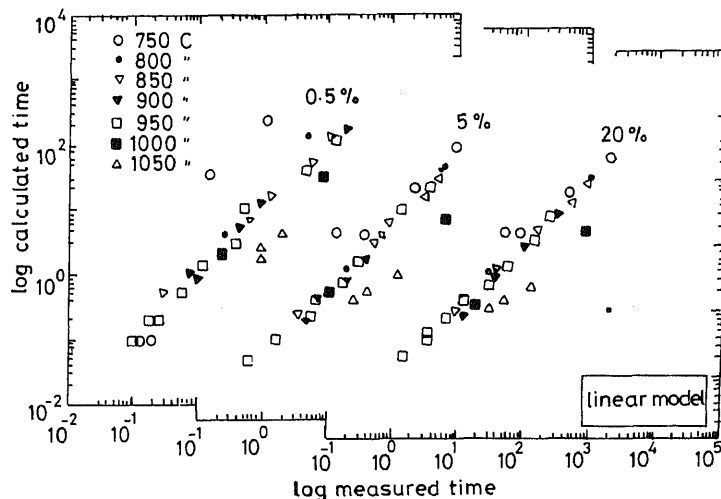


Figure 5. Comparison of the measured and calculated times to (a) 0.5%, (b) 5% and (c) 25% elongations for SRR99.

- material response to a range of stress and strain controlled deformation for both simple and complex orientations.

All these aspects have been evaluated experimentally.

4.1a Anisotropy of creep: Figures 6a–c show the predicted and measured tensile creep curves for $\langle 001 \rangle$ and $\langle 111 \rangle$ orientations of the alloy SRR99 for three different stresses at 850°C in which the observed changes in relative creep strength are successfully reproduced bearing in mind the intrinsic scatter in creep data (Ghosh *et al* 1990). It is also possible to calculate the creep curves for arbitrary orientations but this is not a particularly demanding test.

4.1b Orientation changes: Uniaxially stressed specimens of simple symmetric orientations are not predicted to exhibit any change in orientation during creep deformation, and none are observed. However, in the case of complex orientations and/or multiaxial stresses where some slip systems are disproportionately activated there can be an expectation of quite large lattice rotations. Unfortunately, the increase in dislocation density with accumulating creep strain makes the accurate determination of crystal orientation by conventional X-ray techniques extremely difficult. Electron back-scatter patterns produced in a scanning electron microscope gives precise orientations with high spatial resolution (Dingley 1984). A series of fractured creep specimens, all of which exhibited a considerable degree of necking, have been examined using this technique to relate the change in orientation along the specimen length to the local strain as measured by the reduction in area. Figure 7 compares the measured changes in the axial orientation with those calculated by the model using parameters established from the creep database for $\langle 001 \rangle$ and $\langle 111 \rangle$ orientations (McLean *et al* 1992). There is clearly a high level of agreement between prediction and measurement of rotations that do not correlate with those predicted by the operation of a single slip system.

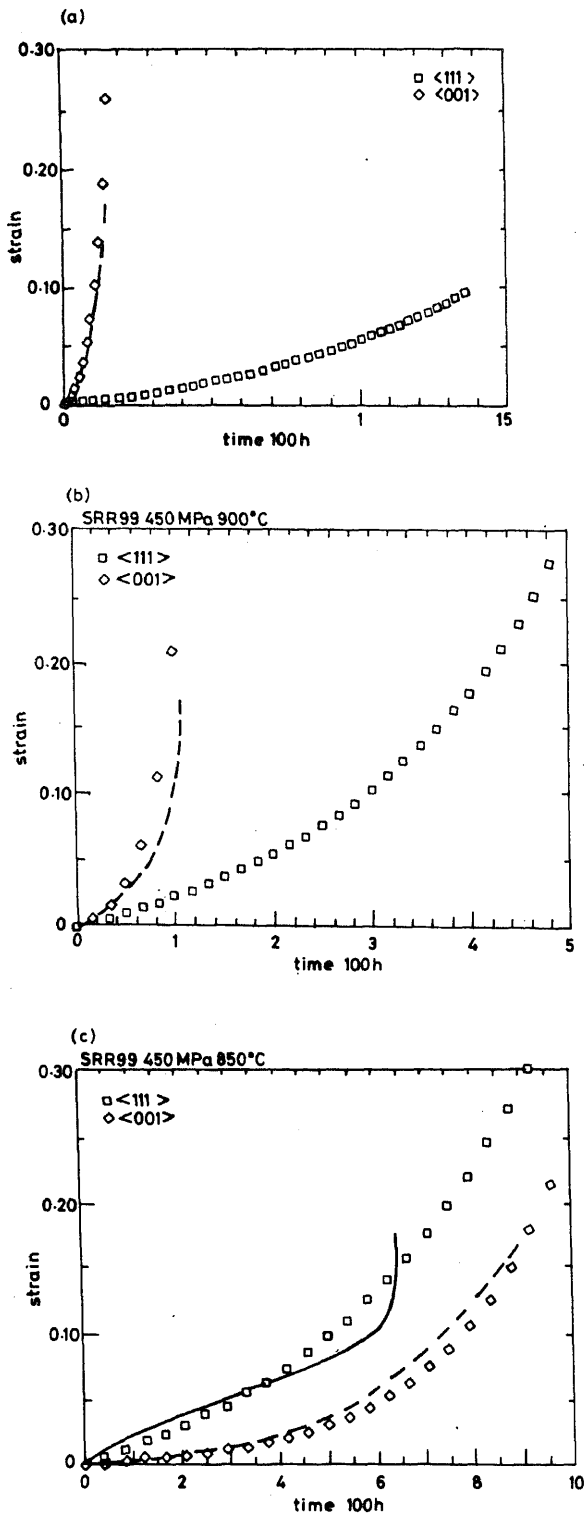


Figure 6. Measured and calculated creep curves for SRR99 with $\langle 001 \rangle$ and $\langle 111 \rangle$ orientations tested in tension at various temperatures (850, 900 and 950°C) and a stress of 450 MPa showing the variation in relative creep performance.

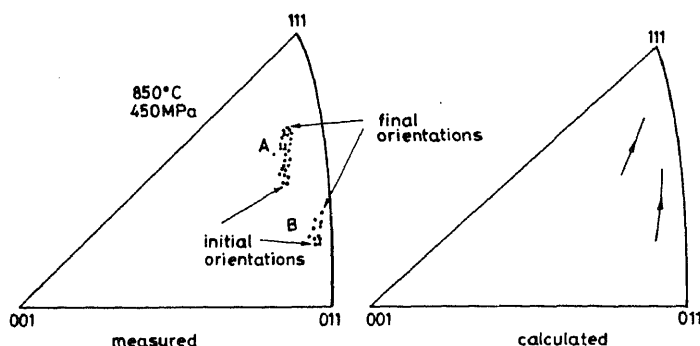


Figure 7. Crystal rotations during creep deformation of SRR99 of different complex orientations tested at 850°C/450 MPa: (a) experimental measurements using electron back-scatter patterns and (b) model predictions.

4.1c Shape changes: The diameters of a series of creep specimens were accurately determined as functions of specimen rotation and reduction in area along the length of the necked specimens, carefully correlating the measurements with the crystallographic orientation of the specimens (Pan *et al* 1994, 1995). The measured and calculated cross-sections are shown in figure 8 as opposite halves of the same figure since planar symmetry is expected. Clearly, for the example shown, there is close agreement between measurements and model prediction for the orientation shown. In this case the model predicts a predominance of cube slip. Indeed these measurements combined with those of the orientation changes provide incontrovertible evidence of shear on cube planes on a macroscopic scale. This does not necessarily imply that there is extensive dislocation activity on cube planes at a microscopic level.

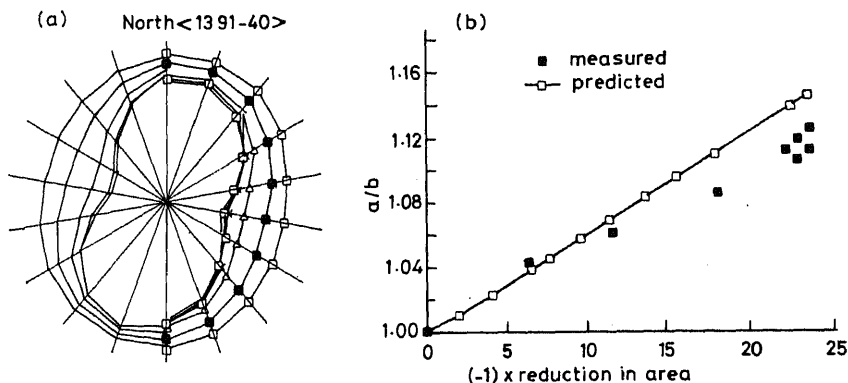


Figure 8. Comparisons of measured and predicted cross-sections of creep specimens of SRR99 at various reductions in area along the necked test-piece: (a) composite polar plots showing measurements (right) and calculations (left) and (b) ratio of maximum/minimum diameters as a function of reduction in area.

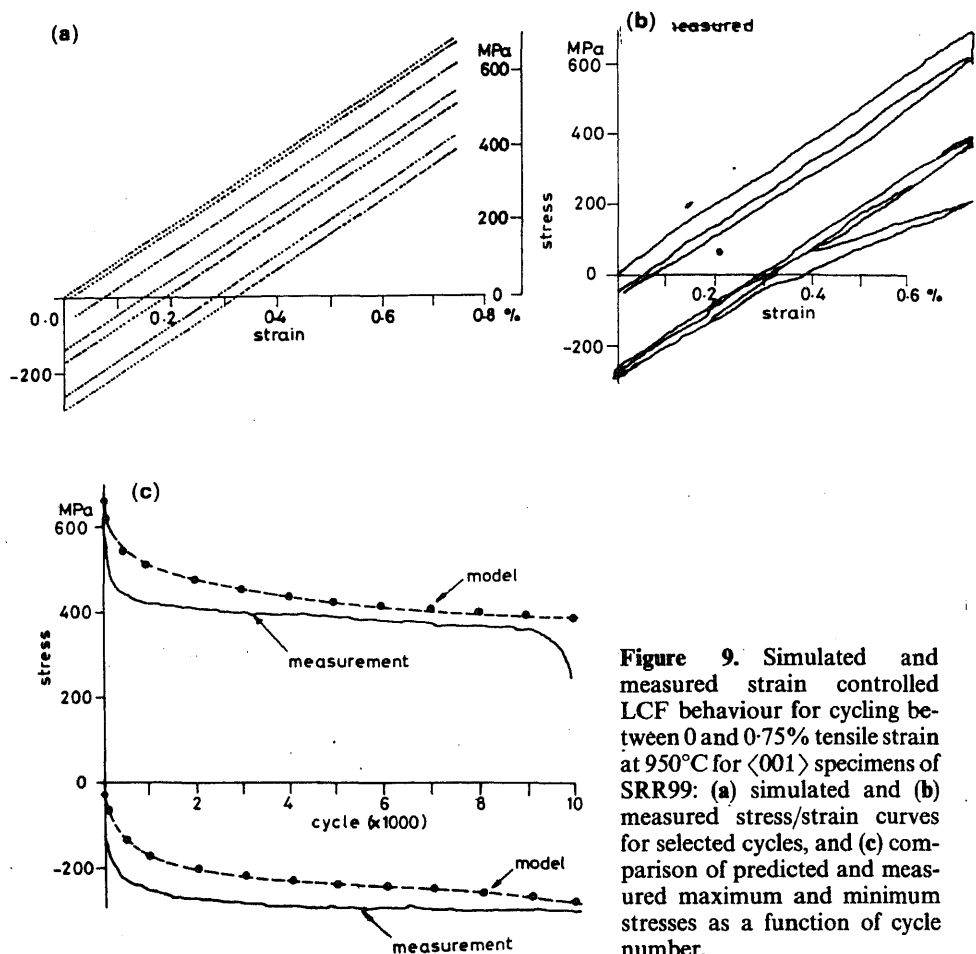


Figure 9. Simulated and measured strain controlled LCF behaviour for cycling between 0 and 0.75% tensile strain at 950°C for $\langle 001 \rangle$ specimens of SRR99: (a) simulated and (b) measured stress/strain curves for selected cycles, and (c) comparison of predicted and measured maximum and minimum stresses as a function of cycle number.

4.1d Low cycle fatigue: The results of a series of high strain, elevated temperature low cycle fatigue tests for SRR99 have been compared with simulations using model parameters derived from a creep database (Pan *et al* 1994). A typical example, for strain controlled cycle between strain limits of 0 and 0.75% tensile strain at 950°C, is shown in figure 9. Each cycle taken individually exhibits largely elastic deformation, but there is a shakedown of stresses reducing the maximum tensile stress and placing the unloading cycle into compression. This is consistent with there being some relaxation of the elastic tensile stress due to creep. The model calculations reproduce the observed behaviour to an acceptable degree of accuracy, particularly in view of the large difference in strain rates associated with the low cycle fatigue tests and with the creep tests forming the database.

5. Conclusions

A physics-based model of creep deformation in nickel-base superalloys has been developed, first in an isotropic form and later to account for the full crystallographic

anisotropy of single crystal superalloys, that successfully represents the principal characteristics of creep in these materials. The model has been validated against both direct creep data and a number of more indirect measures of creep deformation. Comparisons of measurements with model predictions of orientation and shape changes and of the effects of cyclic loading provide particularly demanding tests of the model that are successfully achieved.

Much of the work described in this review has been funded by the Defence Research Agency and creep data and specimens for examination were supplied by Dr M R Winstone of DRA.

References

- Ashby M F, Dyson B F 1984 Creep damage mechanics and micromechanisms. *Advances in fracture research* (eds) S R Valluri, D M R Taplin, P Rama Rao, J F Knott, R Dubey (Oxford: Pergamon) vol. 1, pp. 3–30
- Betteridge W, Shaw S W K 1987 Development of superalloys. *Mater. Sci. Technol.* 3: 682–694
- Caron P, Ohta Y, Nakagawa Y G, Khan T 1988 *Superalloys* (eds) D N Duhl *et al* (Warrendale, PA: The Metallurgical Society) p. 215
- Dingley D J 1984 *Proc. Conf. "Scanning Electron Microscopy – II"* Chicago, p. 569
- Duhl D N 1987 *Superalloys – II* (eds) C T Sims *et al* (New York: Wiley)
- Dyson B F, Loveday M S, Rodgers M J 1976 Grain boundary cavitation under various states of applied stress. *Proc. R. Soc. London A349*: 245–259
- Dyson B F, McLean M 1983 Particle coarsening, σ_0 and tertiary creep *Acta Metall. Mater.* 31: 17–27
- Dyson B F 1988 Creep and fracture of metals: Mechanisms and mechanics. *Rev. Phys. Appl.* 23: 605
- Dyson B F, McLean M 1990 Creep deformation of engineering alloys: Developments from physical modelling. *ISIJ* 30: 802–811
- Ghosh R N, Curtis R V, McLean M 1990 Creep deformation of single crystal superalloys – modelling the crystallographic anisotropy. *Acta. Metall. Mater.* 38: 1977–1992
- Ghosh R N, McLean M 1992 High temperature deformation in engineering alloys – Modelling for strain or load control. *Acta. Metall. Mater.* 40: 3075–3083
- Henderson P J, McLean M 1983 Microstructural contribution to friction stress and recovery kinetics during creep of nickel-base superalloys IN 738 LC. *Acta. Metall. Mater.* 31: 1203–1219
- Ion J C, Barbosa A, Ashby M F, Dyson B F, McLean M 1986 The modelling of creep for engineering design – I. NPL Report DMA A115, National Physical Laboratory, Teddington
- Kachanov L M 1958 Time of the rupture process under creep conditions. *Izv. Akad. Nauk. SSR* 8: 26
- Langdon T E 1985 In *Dislocations and properties of real materials*, Book No. 323 (London: The Institute of Materials) p. 221
- Loveday M S, Dyson B F 1990 In *Proc. 4th Int. Conf. on Creep and Fracture of Engineering materials and structures* (London: The Institute of Materials) p. 947
- McLean M, Ghosh R N, Curtis R V, Basu-Conlin U, Winstone M R 1992 Anisotropy of high temperature deformation of single crystal superalloys. In *Superalloys* (eds) S Antolovitch *et al* (Warrendale, PA: The Metallurgical Society) pp. 609–618
- Pan L M, Ghosh R N, McLean M 1993 Extension of an anisotropic creep model to general high temperature deformation of a single crystal superalloy. *Proc. of EuroMat 93, Paris* (to be published)

- Pan L M, Ghosh R N, McLean M 1994 Load and strain controlled deformation of a single crystal superalloy – Modelling and validation. *Proc. of ICSMA 6*, Sendai, Japan (The Japanese Institute of Metals) pp 583–586
- Pan L M, Scheibli I, Shollock B A McLean M 1995 Asymmetric creep deformation of a single crystal superalloy. *Acta Metall. Mater.* 43: 1375–1384
- Tilley G P, Harrison G F 1973 *J. Strain Anal.* 8: 124
- Wilshire B, Evans R W (eds) 1987, 1990, 1993 *Proc. Swansea conferences on creep and fracture of engineering materials and structures* (London: Institute of Materials)

Life-assessment technology for fossil power plants

R VISWANATHAN

Electric Power Research Institute, 3412 Hillview Avenue, Palo Alto, California 94303, USA

Abstract. During the last decade, construction of new fossil power plants has come to a virtual halt in the United States. The main factors responsible for this situation are: (1) industry perception of the existence of sufficient reserve margins, (2) uncertainty in forecasting load growth, (3) cost of borrowing for new plant construction, (4) siting and licensing problems for new plants, and (5) the applicability of more stringent environmental standards for new plants. Unfortunately, by the year 2000 it is estimated that nearly 20% of all the fossil units will be more than 40 years old, and almost 44% will be more than 30 years old. Based on historical trends, nearly half of all fossil plants have been retired before their fortieth year and three quarters before serving 50 years. In the future this trend is unlikely because of the shrinking reserve margins and the long lead time for new capacity addition. If the life of these aging plants can be extended by 20–30 years, utilities can have a viable low-cost alternative to building new plants while at the same time circumventing some of the regulatory, siting and licensing constraints. In view of this, plant life extension has become an integral part of the planning strategy for many US utilities. A critical component of the Electric Power Research Institute's (EPRI) efforts in formulating life extension strategies for fossil power plants is the development of techniques to assess the current condition of high-temperature components. These techniques are necessary not only for assessment of the remaining life, but also for avoiding catastrophic failures and forced outages, for setting up inspection intervals and for optimizing the operating procedures. The components that are being addressed at present are boiler pressure parts, steam pipes and steam turbine rotors. This paper will provide a brief overview of current concerns and areas of research where significant progress has been made to address these concerns from a phenomenological point of view.

Keywords. Life-assessment technology; fossil power plants; life extension strategies.

1. Introduction

Components operating at elevated temperatures can fail due to excessive deformation, bursting under pressure, or cracking under pure creep or creep-fatigue conditions.

Failure by cracking may further be viewed as consisting of three stages: crack initiation, crack propagation, and final failure of the component once the crack reaches a critical size. Life-assessment techniques are, therefore, aimed at quantifying uniform or localized incipient damage prior to crack initiation, the rate at which cracks grow, and the critical crack size that will lead to final failure. Eventual failure of the component can occur either by leakage or rupture at the operating temperature or by rapid brittle fracture at lower temperatures during start-up/shutdown transients. In the latter case, the critical size of the crack is defined by the fracture toughness of the material. Since embrittlement phenomena occurring in service can reduce the toughness of the material, knowledge of fracture toughness in the service-exposed condition is necessary.

Based on worldwide experience during the last five years, a three-level approach for life assessment has evolved. In this approach, simple calculational techniques are used in the first level, followed by nondestructive and destructive tests in the next two levels. The focus of research has been mainly to reduce the uncertainties and hence the conservatism in each of the levels of assessment. This article is an overview of advances during the last five years in refining the assessment procedures under each of these levels, with special emphasis on results of work sponsored by the Electric Power Research Institute (EPRI). A more complete review of the extensive body of relevant literature may be found in Viswanathan (1989). While this paper will review advancements from a generic technology point of view, specific techniques applicable to individual components such as turbine rotors, steam pipes, headers and tubes may be found in other key overview papers (Becker *et al* 1987; Harris *et al* 1993; Viswanathan & Wells 1993; Wells & Viswanathan 1993; Viswanathan *et al* 1994).

2. Calculation techniques

In the calculational procedures, plant records and the time-temperature history of the component are reviewed. The creep or creep-fatigue life fraction consumed is calculated using assumed material properties and damage rules. This procedure is usually inaccurate due to errors in assumed history, in the material properties, and in the damage rules. The temperature-history information may be refined by supplemental nondestructive or destructive examinations such as microstructural studies, hardness measurements, and oxide-scale measurements. The uncertainties in material properties can be reduced by building a database, particularly with respect to service-retrieved components taking into account the environmental effects. The limitations of the damage rules have also been explored based on extensive laboratory studies.

2.1 Life fraction rule for creep

The Life Fraction Rule (LFR) states that at failure

$$\sum t_i/t_r = 1, \quad (1)$$

where t_i is the time spent at a given stress and temperature, and t_r is the rupture life for the same test conditions. When the damage fractions incurred under different sets of stress-temperature conditions add up to unity, failure is presumed to occur. Hart (1976), Woodford (1979), and Bolton *et al* (1980) have demonstrated that the LFR is

valid for temperature changes but not for stress changes. In a multiclient project recently completed at ERA Technology, an extensive body of long-time data has been generated, with the specific intent of verifying the LFR for varying temperature conditions (Brear & McCarthy 1989) and the results have been analysed in detail by Viswanathan (Viswanathan & Gehl 1992). Two heats of a 0.5Cr-0.5Mo-0.25V steel were evaluated: a pipe-grade steel with a predominantly ferritic microstructure and relatively high ductility (15% elongation) under long-term service conditions, designated MG, and a cast turbine casing steel with a bainitic microstructure and low ductility (3.5% elongation), designed FW. In addition, a ductile tubing steel of 2 1/4Cr-1Mo steel designated heat RG was also evaluated.

Specimens from heat MG were subjected to creep damage fractions of 0.25, 0.45, 0.63, and 0.82 at 575°C at a stress of 69.5 MPa; specimens from heat FW were also subjected to similar levels of initial creep damage by testing at 550°C and 84.9 MPa. The predamaged samples were then subjected to accelerated rupture testing at higher temperatures, holding the stress at the same level as in the initial creep damage tests.

Results of the accelerated stress rupture tests on heat MG at 69.5 MPa for the virgin condition and for the predamaged conditions are shown in figure 1. The target values of remaining life at 575°C based on the LFR are also indicated. If the LFR is valid, the temperature vs. time-to-rupture lines should be parallel to the virgin material line and should pass through the respective target values. This is clearly not the case; linear

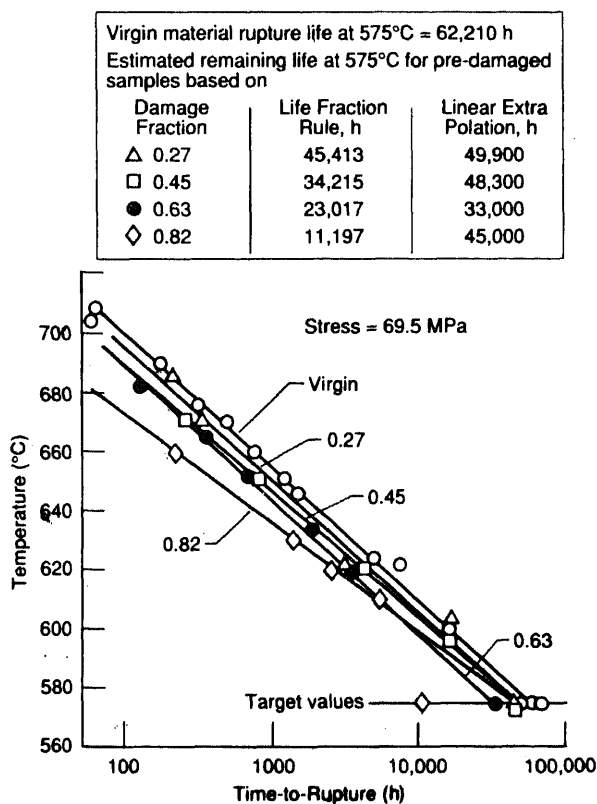


Figure 1. Stress rupture curves for heat MG in the virgin condition and after prior creep damage to various life fractions.

extrapolation of the accelerated-test data predicted remaining lives at 575°C in excess of the target value in every case. For the 0.82 predamaged samples, the accelerated-test results grossly over-predicted the remaining life compared to the calculated value based on the LFR.

The trend, for the brittle cast FW (see figure 2) is exactly opposite to that observed for the ductile heat MG. With the exception of the 0.45 predamaged sample, for all other samples, the predictions from the accelerated tests fell short of the target values calculated from the LFR.

A third heat of 2 1/4 Cr-1 Mo steel (designated RG) in the normalized and tempered condition was used for the program. Tube samples of the steel were pressurized to an equivalent stress of 116 MPa (16.6 ksi) and tested to creep life fractions of 0.5 and 0.72 at 525°C (975°F), the mean rupture life being 45,475 h in the burst tests. From the interrupted test tubes, chordal samples were machined and subjected to accelerated tests, uniaxially at a constant stress of 16.6 ksi (116 MPa), at a number of temperatures in the range of 550 to 650°C (1025°F to 1200°F). Some tests were also carried out at 525°C (975°F) to enable comparison of the actual remaining life at 525°C (975°F) with those predicted by the LFR and from isostress extrapolation. Results of these rupture tests are shown in figure 3. The uniaxial rupture life for the virgin material was shorter than the burst test lives (30,094 h vs 45,475 h) indicating that the mean diameter hoop stress formula resulted in an overestimation of the equivalent stress. For the pre-damaged samples, the actual remaining test lives at 525°C agreed very closely with

Virgin material rupture-life at 550°C = 67,726 h

Estimated remaining life at 550°C for pre-damaged samples based on

	Damage fraction	Life fraction rule, (h)	Linear extrapolation, (h)
△	0.26	50,132	32,000
□	0.45	37,260	62,000
●	0.63	25,066	18,000
◇	0.91	12,871	10,000

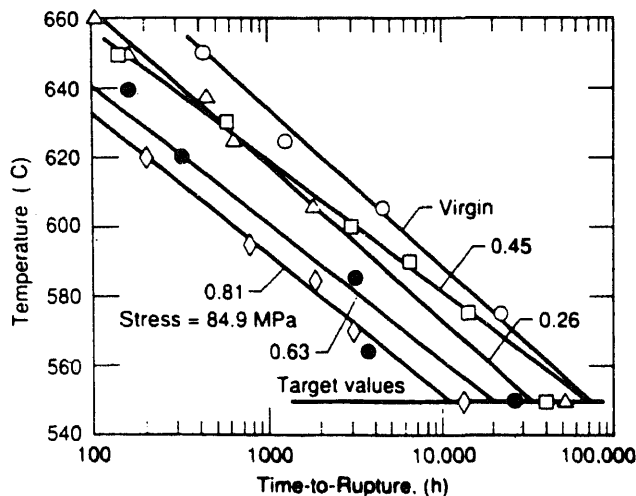


Figure 2. Stress rupture curves for heat FW in the virgin condition and after prior creep damage to various life fractions.

Virgin material rupture life at 525°C and 115.8 MPa is 30,094 h in uniaxial test and 45475 h in biaxial tests. Estimated remaining life at 525°C for predamaged samples based on

	Damage fraction	Life fraction rule, (h)	Linear extrapolation, (h)	Actual, (h)
●	Virgin, biaxial	—	—	45,475
○	Virgin, uniaxial	—	30,094	33,100
△	0.50	16,350	19,217	20,920
□	0.72	9,268	14,856	14,473

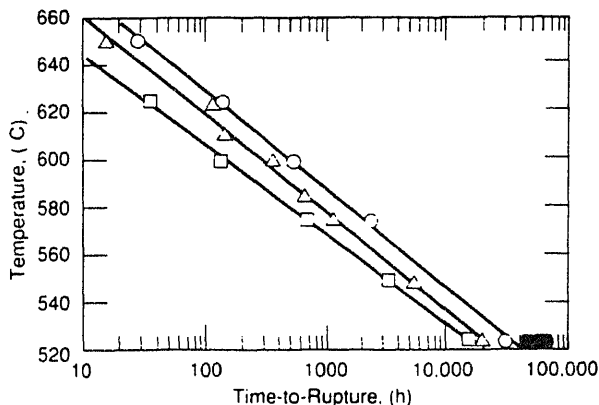


Figure 3. Results of tube burst tests and uniaxial accelerated isostress rupture tests on samples machining from tubes previously subjected to 0.5 and 0.72 life fraction creep damage, 2 1/4 Cr-Mo steel (Heat RG).

those estimated from the remaining life fraction using the life fraction rule and from linear extrapolation of the accelerated test results.

A correlation between the expected life based on the LFR and the observed life for the three heats (figure 4) shows that for the brittle material, the actual life is always shorter than the expected life while the opposite is true for the ductile heat MG. For the ductile heat RG of 2 1/4 Cr-1 Mo steel, the expected life agrees closely with the observed life in the accelerated tests.

The difference in behaviour between the brittle and ductile cases is believed to result from differences in damage mechanisms. Prior creep damage in the brittle case consisted of "mechanical damage" with extensive formation of creep cavities. In the ductile case, damage was "metallurgical" damage consisting of microstructural changes. In the brittle steel, subsequent testing by temperature acceleration presumably resulted in rapid linkup of cavities, leading to premature failure; in the ductile steel, on the other hand, temperature acceleration presumably led to recovery of some of the metallurgical damage, resulting in increased life.

The correlation between prior expended life fraction and remaining life fraction measured in the accelerated tests shown in figure 5 may be used as a modified basis for LFR. For a ductile material, the LFR may be used for a conservative prediction of remaining life. For a brittle material, a value of < 1 as defined by the lower-bound envelope in figure 6 may be used as a conservative failure criterion.

For a ductile material, the implications of the above results to actual situations in which the LFR is invoked are as follows: When LFR is used to calculate cumulative damage under conditions where the average metal temperature increases with service

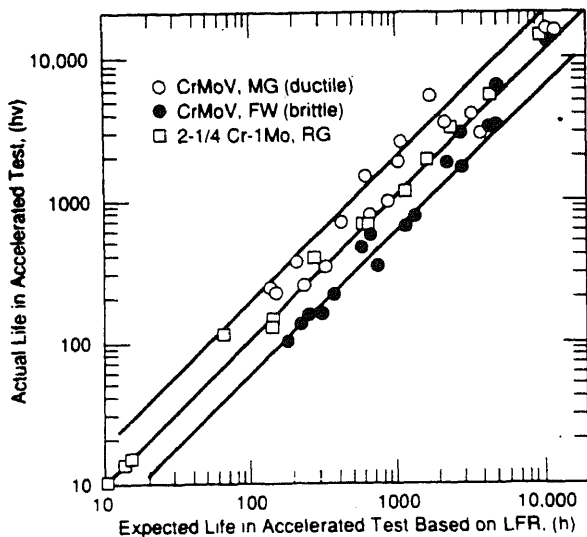


Figure 4. Correlation between expected life based on life fraction rule and actually observed life in post exposure accelerated test.

time (e.g., superheater tubes), failure will always occur at $\Sigma t_i/t_r > 1$. Hence, $\Sigma t_i/t_r = 1$ should be used as a conservative failure criterion. The same reasoning may be applied to situations where periodic temperature excursions occur.

In all life-fraction calculations, the virgin material behaviour (minimum or mean of the International Organization for Standardization's [ISO's] Larson-Miller data) is used as the reference condition for calculating the t_r . In reality, as the component softens, the applicable Larson-Miller curve is continuously changing in such a way

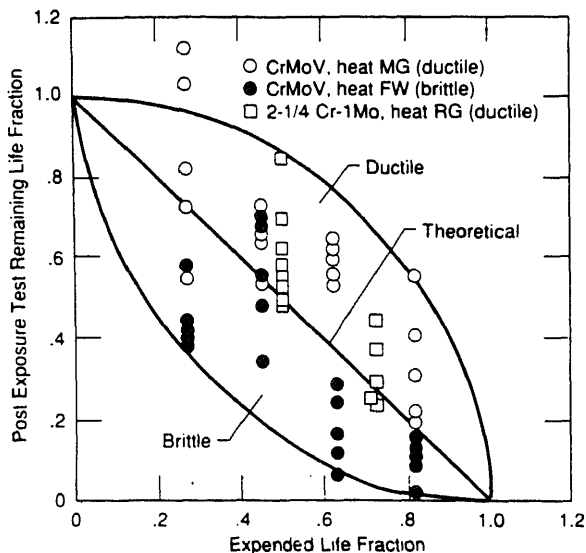


Figure 5. Expended life fraction under service conditions vs. the remaining life fraction as determined from post exposure accelerated tests for 3 heats of steel.

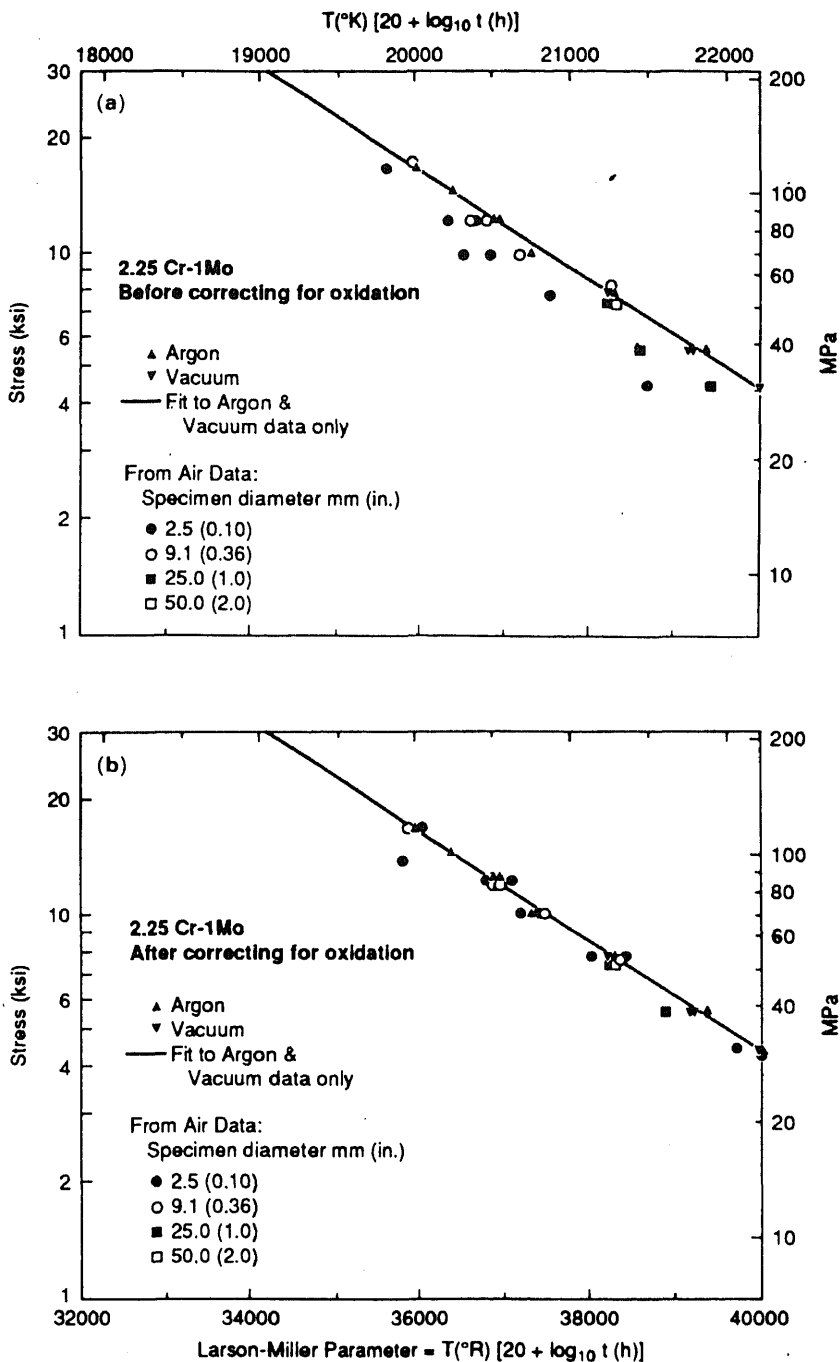


Figure 6. Larson-Miller stress rupture curve for 2-1/4 Cr-1 Mo steel specimens of different sizes, before (a) and after (b) correcting for oxidation effects associated with specimen size.

that the actual cumulative damage can be more than that calculated by using the virgin material curve. Application of the LFR could be improved by taking the softening reactions into account.

2.2 *Linear damage rule for creep fatigue*

A variety of rules have been enunciated for calculating total damage when both creep and fatigue damage are present in a component. The most popular among these is the linear damage rule, in which the life fractions consumed in creep (t/t_r) and fatigue (N/N_f) are added as follows:

$$\Sigma(N/N_f) + \Sigma(t/t_r) = D. \quad (2)$$

Differing approaches to calculating N/N_f , t/t_r and the value of D at failure have led to alternate rules which have been extensively discussed earlier (1989).

An extensive critique of damage rules as they apply to fossil plant components has been published by Viswanathan (1992, 1993). Detailed review of literature shows that there are divergent opinions regarding which damage approach provides the best basis for life prediction. It is quite clear that a number of variables, such as test temperature, strain range, frequency, time and type of hold, waveform, ductility of the material, and damage characteristics, affect the fatigue life. The conclusions drawn in any investigation may therefore apply only to the envelope of material and test conditions used in that study. The validity of any damage approach has to be examined with reference to the material and service conditions relevant to a specific application. Broad generalizations based on laboratory tests, which often may have no relevance to actual component conditions, do not appear to be productive. Thus, one should use a tailored, case-specific approach for any given situation.

One of the major problems in evaluating the applicability of different life-prediction methods is that in many cases it is necessary to use all the available data in deriving the life-prediction method and thus it is possible to examine only the accuracy with which a given method describes the data. There also is a scarcity of instances in which service experience has been compared with specific life-prediction methods. In general, the available methods are utilized only to predict the lives of samples tested under laboratory conditions. Validation against component test data in the laboratory and in-service monitoring of actual equipment would lead to more confidence in the use of the various rules.

Results from most studies show that even the best of the available methods can predict life only to within a factor of 2 to 3. Some of the cited reasons for these inaccuracies have already been discussed. Some additional reasons are: failure of the methods to model changing stress-relaxation and creep characteristics caused by strain softening or hardening, use of monotonic creep data instead of cyclic creep data, and lack of sufficiently extended-duration test data. None of the damage rules available today is entirely based on sound mechanistic principles. They are all phenomenological in nature, involving empirical constants that are material-dependent and difficult to evaluate. Extrapolation of the rules to materials and conditions outside the envelope covered by the specific investigation often results in unsuccessful life predictions. Material behaviour under isothermal LCF conditions in the laboratory often turns out to be totally irrelevant to material behaviour under thermochemical fatigue cycles involving in-phase or out-of-phase thermal cycles in the field. For application to service

components, the stress-strain variation for each type of transient and its time dependence must be known with accuracy. Such calculations are difficult and expensive to perform. Because of these limitations and the simplicity of the linear-damage summation using the life-fraction rule, the latter approach continues to enjoy widespread popularity in engineering applications.

2.3 Oxidation and specimen size correction

The effect of oxidation on rupture life is relevant in several aspects of remaining-life assessment, particularly for heavy-section components with wall thickness values exceeding 25 mm. Rupture life databases used in original design, such as the ISO, ASTM, and National Research Institute for Metals' (NRI) databases, are based on test data generated on small specimens with diameters of 6–10 mm. When these data are utilized in remaining-life-fraction calculations, conservative results are obtained. In addition, when standard ASTM specimens of 10 mm or less diameter extracted from heavy-walled piping are tested in air for remaining-life assessment, the resulting values are likely to be conservative. Results of isostress rupture tests conducted at elevated temperatures may need to be corrected for oxidation effects.

An extensive study of oxidation correction factors (CFs) for 2.25 Cr–1 Mo steels has been published by Nakashiro *et al* (1991). Oxidation correction factors were developed based on oxidation kinetics derived from literature and based on loss of diameter actually observed on samples. Using the correction factor, the original NRI Larson–Miller plot based on 6 mm diameter specimens was revised to reflect the behaviour of standard 10 mm specimens. This study was, however, confined to tubing applications; specimen sizes beyond 10 mm were not addressed.

An alternate approach for developing OCFs consisted of rupture testing specimens of varying size (2.5–50 mm) (Brear 1994). Selective tests were also carried out on 9 mm-diameter specimens in argon. Preliminary results from one heat of 2.25 Cr–1 Mo steel (heat BSH) have shown that the rupture life in air is increased by increasing the specimen size from 2.5 to 9 mm with a further increase of life in argon as shown in figure 6a. Foulds & Viswanathan (1994) have analysed these data and developed a methodology for rationalizing the specimen size effect. In the method, the following phenomenological aspects of creep/rupture were utilized:

$$\dot{\epsilon} t_r = C \text{ (Monkman Grant Law),} \quad (3)$$

where the constant C may vary from test to test and need not be of known value.

$$\dot{\epsilon} = B \sigma^n \exp(A/T) \text{ (Norton Law)} \quad (4)$$

where the values of the constants B and A need not be known. ' n ' may be measured easily over short test duration and

$$\int_0^{t_r} (\dot{\epsilon} dt) / C = 1 \quad (5)$$

where $\dot{\epsilon}$ is time-dependent and specimen-size dependent as a function of oxide formation. The equation is based on the assumption that the Robinson Life Fraction Rule applies to the test specimen when one test specimen is represented by multiple, individual test specimens with a reducing size in time.

The resulting closed form after integrating and solving for t_R (in vacuum) is:

$$t_R(\text{corrected}) = r_0^{2n} \left[\frac{1.6}{k(1-n)} \left\{ r_0 - \left(\frac{kt_r}{1.6} \right)^{1/2} \right\}^{2(1-n)} - \frac{3.2r_0}{k(1-2n)} \left\{ r_0 - \left(\frac{kt_r}{1.6} \right)^{1/2} \right\}^{1-2n} + \frac{1.6r_0^{2(1-n)}}{k(1-n)(1-2n)} \right] \quad (6)$$

where k is the parabolic constant for oxide growth in air, t_R is the predicted vacuum test life, t_r is the measured air test rupture time, and r_0 is the initial specimen radius. The constants 1.6 and 3.2 arise from a Pilling–Bedworth assumption of 2.0.

When (6) is applied to the data shown in figure 6 all the data collapse onto a single line, regardless of specimen size as shown in figure 6b.

3. Nondestructive techniques for characterizing damage

Conventional nondestructive evaluation (NDE) methods fail to detect incipient damage, which can be a precursor to crack initiation and subsequent rapid failure. Several improved NDE techniques have recently been developed for estimating life consumption. These include strain-monitoring techniques, microstructural techniques, hardness-based techniques, and oxide-scale measurement techniques for superheater/reheater tubes.

3.1 Strain monitoring

Strain measurements are often employed to detect creep damage. Gross changes such as header swelling and rotor bore expansion have been monitored in the past. Frequently, due to unknown variations in the original dimensions, changes in dimensions cannot be determined with confidence. Dimensional measurements fail to provide indications of highly damaging and localized creep strains such as those in the heat-affected zones of welds and regions of stress concentrations in the base metal. Cracking can frequently occur without manifest overall strain. Furthermore, the critical strain accumulation preceding fracture can vary widely with a variety of operational material parameters, and with stress state. To enable measurement of localized strains, an "off-line" condition surveillance system has been developed. The system uses the replication principle to evaluate localized strains and life consumption (Cane & Bissall 1986). A surface grid is scribed at the region of interest and preserved by means of an oxidation-resistant coating. A hard replica of high stability is used to duplicate the grid. Biaxial strain assessment is then made by high-resolution measurement of the replicas taken at successive plant inspection shutdowns. A predictive strain-rate lifetime model approach is used to establish "fitness for service." No field experience with this technique has been reported.

3.2 Hardness-based techniques for creep damage assessment

The changes of hardness in low-alloy steels as a function of time and temperature have been extensively quantified, so that hardness changes can be used to estimate the

operating temperature (Askins 1989; Ellis *et al* 1989). Correlations have also been established between tensile (hence hardness) and the Larson–Miller rupture relationships for low-alloy steels. These correlations enable selection of the appropriate Larson–Miller plot corresponding to a given hardness level, which can be used to calculate the remaining life.

Current procedures do not recognize that the Larson–Miller parameter for rupture decreases with in-service aging. A model that explicitly takes into account the decreased rupture life due to softening has recently been developed for 2.25Cr–1Mo steels by Grunloh & Ryder (1989). The effect of aging on creep rupture endurance is modelled by the incorporation of the ultimate tensile strength at room temperature (UTS) into the second-degree polynomial shown in (7), which was derived by analysis of a large body of data, shown in figure 7.

$$\text{LMP}_{(\text{rupture})} = 40,975 + 57(\text{UTS}) - 5,225(\log \sigma) - 2,450(\log \sigma)^2. \quad (7)$$

In this equation, time, temperature, and stress are in units of hours, R (deg. Rankine), and ksi (1 ksi = 6.89 MPa), respectively. The effect of aging is taken into account by applying an aging correction factor to the original UTS, based on known kinetics of aging for the steel. Using temperature, applied stress, and starting UTS as input, a computer code calculates the LMP for rupture in the aged condition (and hence t_r) at 1,000 hour intervals. The incremental damage for each time step, and hence the cumulative damage t/t_r , can be calculated. Kimura and others developed a similar approach to calculate creep life consumption of CrMoV rotors (Kimura *et al* 1988) and casings (Fujiyama *et al* 1990).

Goto and others have proposed using hardness as a stress indicator in the remaining-life assessment of CrMoV rotors (Goto 1985; Kadoya *et al* 1985). They have quantified the effect of stress on the aging process so that by comparing the kinetics of hardness

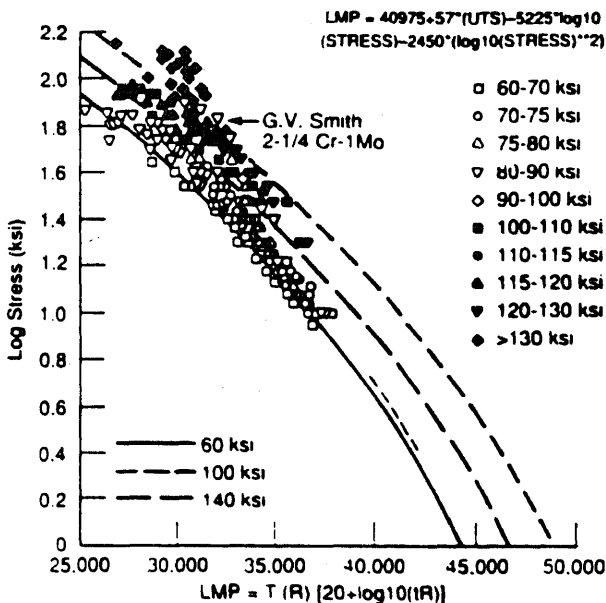


Figure 7. 2-1/4Cr-1Mo rupture data showing UTS dependence.

change in the rotor with that of thermally aged samples, the local stress can be determined. This value of stress and the known value of service temperature are used in conjunction with the Larson–Miller rupture plot to estimate t_r for the material in its current damage state.

In contrast, McGuire & Gooch (1989) show that the magnitude of the stress is unimportant once a “threshold stress level” has been exceeded. For all stress levels in the range 70–240 MPa, the hardness change in the stressed condition was found to be 21% higher compared to the change in the unstressed condition.

A creep model incorporating structural degradation as monitored by hardness changes has been proposed by Cane & Bissall (1986). By equating the kinetics of hardness change to the kinetics of interparticle spacing changes, the decrease in the threshold back stress for creep is modelled. Substitution of the threshold back stress in the Norton creep law yields an expression for secondary creep rate $\dot{\epsilon}$ in terms of hardness changes. By integrating the $\dot{\epsilon}$ between $t = 0$ and $t = t_r$, where t_r is the time to failure in terms of the time to reach an arbitrarily chosen critical strain, the remaining rupture life is predicted. The model is currently based on limited data and involves numerous assumptions that can only be justified by further research.

3.3 Hardness and low-cycle fatigue life

Considerable work has been carried out (Goto 1985; Kadoya *et al* 1985; Kimura *et al* 1988; Fujiyama *et al* 1990) in applying hardness for calculation of fatigue-life consumption in CrMoV rotor grooves. It has been observed that low-cycle fatigue damage results in strain softening and can be measured as a hardness decrease. The premise, therefore, is that if the fatigue curve corresponding to the current hardness (in service) could be defined, the fatigue-life fraction consumed could be calculated by entering the appropriate total strain range $\Delta\epsilon_t$ versus number of cycles to crack initiation (N_f) curve, as shown in figure 8 (Kimura *et al* 1988). These relationships have been quantified (Kimura *et al* 1988):

$$\Delta\epsilon_t = k_1 N_f^{\alpha_1} + k_2 N_f^{\alpha_2}, \quad (8)$$

where

$$\log k_1 = 2.59 \times 10^{-3} \text{ Hv} - 0.9 \quad \text{and} \quad k_2 = 22.0, \quad (9)$$

$$\alpha_1 = 1.64 \times 10^{-4} \text{ Hv} - 0.09 \quad \text{and} \quad \alpha_2 = 0.59, \quad (10)$$

$$\sigma_{yd} = 1.07 \text{ Hv} - 40.6. \quad (11)$$

where k_1 and α_1 are hardness-dependent constants, and σ_{yd} is the cyclic yield strength. For any given hardness of the steel, (8)–(11) can be used to calculate fatigue-life fraction consumed under different transients, and these fractions can be summed up to calculate the total fatigue-life expenditures using the procedures detailed by Kimura *et al* (1988).

3.4 Creep cavitation model

Metallographic methods have been developed that can correlate either cavitation evolution or changes in carbide spacings with creep-life expenditure. It has been

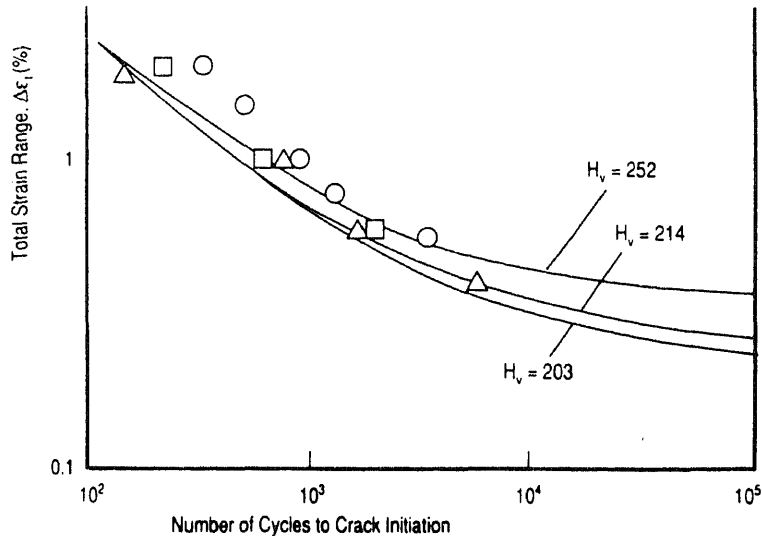


Figure 8. Estimation of low-cycle fatigue properties by hardness for a Cr-Mo-V rotor forging at 566°C. H_v = Vickers hardness number.

observed that, in boiler piping, cavitation is the principal damage mechanism at brittle zones, weld heat-affected zones, and high-stress regions in the base metal (Ellis *et al* 1988). In the other cases, carbide coarsening was found to be a better indicator of life consumption. A preliminary model based on carbide coarsening has also been developed (Askins 1989).

Neubauer & Wedel (1983) characterized cavity evolution in steels at four stages – isolated cavities, oriented cavities, linked cavities (microcracks), and macrocracks – and formulated recommendations corresponding to the four stages of cavitation. To provide a theoretical and quantitative basis for cavity evolution, Cane & Shammas (1984) used a constrained-cavity-growth model and proposed a relation between the number fraction of cavitated boundaries (parameter A) and the life fraction consumed using heat-specific constants. Values of these constants either had to be assumed or determined experimentally for each heat, thus restricting the usefulness of the model. Based on interrupted-creep tests on simulated heat-affected zone 1 Cr–0.5 Mo steels, Ellis and others concluded that the data had too much scatter to verify the life-prediction model of Cane. The data could nevertheless be used empirically, by plotting all the data together in the form of a scatterband whose lower limits are defined by (Ellis *et al* 1989).

$$A = 0.517(t/t_r) - 0.186. \quad (12)$$

In using the A parameter method, the specific procedure used to measure A is crucial. The A parameter is defined as the number fraction of cavitating grain boundaries encountered in a line parallel to the direction of maximum principal stress. To measure A reproducibly, the procedure needs to be standardized.

Since (12) was developed using two steels of widely different impurity concentrations, it is anticipated that the scatterband encompasses most 1 Cr–0.5 Mo steels in service.

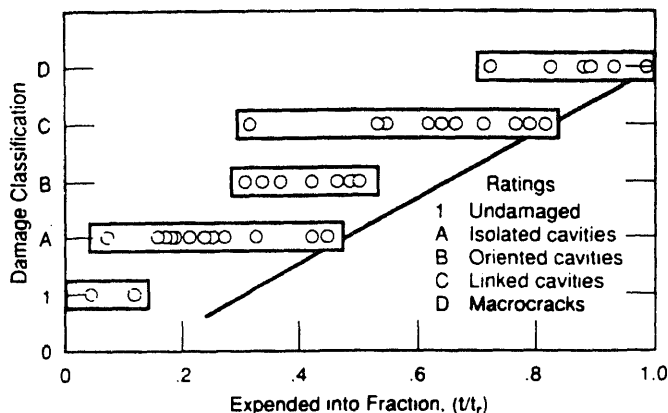


Figure 9. Correlation between damage classification and expended creep-life fraction for 1-1/4 Cr-1/2 Mo steels.

Limited data on heat-affected zone samples from 2.25 Cr-1 Mo steels also have shown that the cavitation behaviour can be described by (12). Extension of this correlation to weld metal, to steels with fine grain size, and to other steels, however, would lead to errors.

An alternate, easier-to-use method has also been proposed by Ellis *et al* (1989). The damage classifications have been correlated with life fractions, and thus a life-fraction range has been established for each class (see figure 9). The Wedel-Neubauer classifications of material condition (undamaged, class A, class B, class C, and class D) correspond roughly to expended-life-fraction (t/t_r) values of 0.27, 0.46, 0.65, 0.84, and 1, respectively, using the conservative lower-bound curve shown in figure 9. Since the expended life fraction corresponding to various damage classifications is known, the remaining life can be calculated using the relationship

$$t_{\text{rem}} = t((t_r/t) - 1) \quad (13)$$

where t is the service life expended. The remaining life corresponding to various damage classifications can be calculated to be $2.7t$, $1.17t$, $0.54t$, and $0.19t$ for undamaged material, isolated cavitation, oriented cavitation, and microcracking respectively. By applying a safety factor of three to the above values, the safe reinspection intervals can be established to be $0.9t$, $0.4t$, $0.18t$ respectively. This approach has been developed and applied by Paterson as shown in figure 10 (Paterson 1989). The figure clearly shows that the reinspection interval is not only a function of the current damage level, but also the service life elapsed, unlike in the Wedel and Neubauer approach, where the reinspection interval prescribed is independent of elapsed service life. For all combinations of damage classification and service life in regime B in the figure, the new approach results in increased inspection intervals. Several utilities that have adopted the approach have realized significant savings in inspection costs. (EPRI 1990).

The field replication data forming the basis of the Wedel-Neubauer recommendations have recently been reviewed (EPRI 1991). When these limited data were analysed, no consistent trends of cavitation evolution with operating time or with calculated creep life fraction consumed could be discerned. The laboratory data generated and analysed by Ellis and others appear to be the only available quantitative basis for setting inspection intervals.

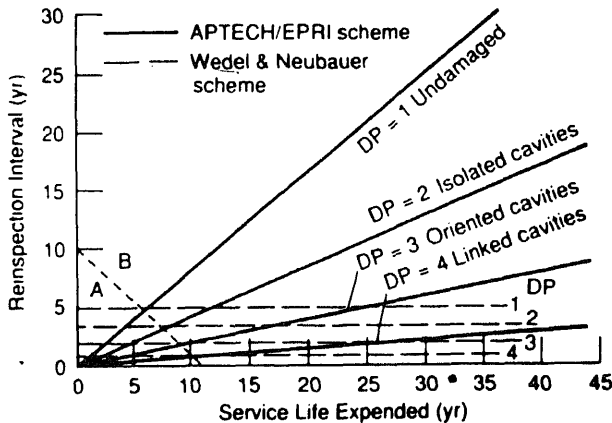


Figure 10. Service life versus reinspection interval for Ap-tech/EPRI remaining useful life method and the Neubauer-Wedel method.

The progress of creep cavitation as a function of creep life fraction expended in CrMoV rotor steels has been investigated by Goto. Additional data by Carlton *et al* (1987) show wide variations in behaviour due to differences in grain size, ductility, and impurity contents. The results of Goto agree reasonably well with those of McGuire and Gooch for expended life fractions up to about 0.75, but show larger values of A at higher life fractions. Comparisons of the behaviour of CrMoV rotor steels with CrMo piping steels suggests that the CrMo steels cavitate more readily and reach much larger values of the A parameter at failure compared to the CrMoV steels. It has also been noted that in CrMoV steels, cavitation is observed only at the end of second-stage and beginning of third-stage creep, unlike in CrMo steels where cavitation occurs during the second-stage creep (Lempp *et al* 1986). The relative insensitivity of the A parameter to expended creep life for rotor steels makes accurate determination of the A parameter crucial. For this reason, the damage classification as a function of expended life is shown in figure 11 using the lower bound curve. The life fractions consumed are estimated to be 0.3, 0.6, 0.85, and 1, respectively, for undamaged and classes A, B, and C damage. These values are larger compared to CrMo steels, indicating that for a given damage classification, life consumption is higher in CrMoV steels, compared to CrMo steels. Blade root fixings after blade removal may be amenable to the use of replication, and cavitation has been observed in rotors at these locations. More complex equipment required for replication of rotor bores has also been developed (Goto 1985; Kadoya *et al* 1985). However, creep cavitation in rotor bores has not been reported to date.

3.5 Analysis of carbides

Askins (1989) has attempted to utilize parameters such as matrix-solute compositions, ratios of carbide phases, and matrix-lattice parameters as quantitative indices of temperature during aging of 1Cr-0.5Mo steels. Their data indicate a rapid initial decline in matrix-solute content and an increase in the $M_{23}C_6/M_3C$ ratio with time and temperature of aging. Changes in the matrix-solute content were also found to be reflected in changes in lattice-parameter values. Although these general trends could be

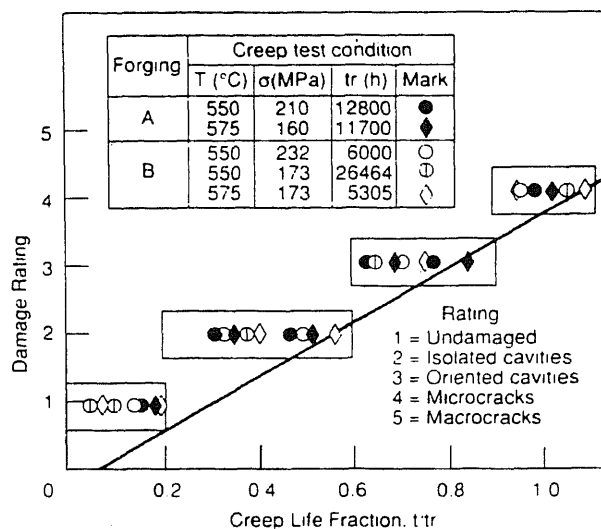


Figure 11. The correlation between damage classification and creep-life fraction for CrMoV rotor steels.

confirmed, excessive scatter in the results did not permit quantitative correlation of any of these parameters with aging history.

In 2.25Cr-1Mo steels, there have been several investigations showing that prolonged exposure at about 540°C causes an irreversible form of embrittlement known as "carbide-induced embrittlement" (Cheruvu 1981; Qu & Kuo 1981; Watanabe & Shoji 1994). The embrittlement is manifested as an increase in the fracture-appearance transition temperature (FATT) and is generally associated with the formation of M_6C molybdenum-rich carbides at the grain boundaries. The carbides act as sites for crack nucleation, promoting transgranular cleavage cracks at low temperatures. Carbide formation also results in softening of the steel since it depletes the matrix of the strengthening precipitate Mo_2C and the molybdenum in solid solution. The softening reaction is also manifested as decreased creep strength and rupture strength.

Carbide evolution in 2.25Cr-1Mo steel has been investigated by Stevens & Lonsdale (1984), Stevens & Flewitt (1985) and Munson (1990). In both studies, the amount of M_6C carbides as a percentage of the total weight percent of carbides increased with time and temperature. Plotted in terms of a Larson-Miller time-temperature parameter, the results (figure 12) show the family of curves from the Stevens and Flewitt study to be shifted laterally by a significant amount compared to that of Munson.

These studies suggest that although the evolution of M_6C may be used as a qualitative index of service temperature, wide variations may occur due to differences in initial microstructure and composition. Data in figure 12 also show that the kinetics of M_6C formation are considerably accelerated by phosphorus. Improved procedures for carbide extraction as well as a larger database on samples with various initial compositions and heat treatments are needed before the microstructural techniques can be used for plant-life assessment. Stevens & Flewitt (1985) also found that the evolution of the M_6C phase was unaffected by stress. Nakatani *et al* (1990) have developed

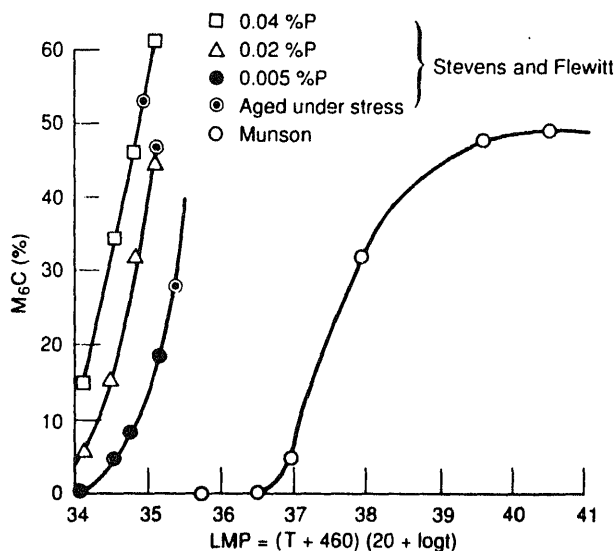


Figure 12. Evolution of M_6C in 2.25Cr-1Mo steel as a function of aging time and temperature. (In the equation for LMP, temperature is in degrees Fahrenheit and time is in hours.)

correlations between the percent M_6C and rupture-life reduction so that the percent M_6C in a service-exposed component could be used to deduce the creep-life fraction consumed.

The evolution of carbide phases in CrMoV rotor steels has been investigated on a single heat aged at 650°C by McGuire & Gooch (1989). The percentages of $M_{23}C_6$, M_7C_3 , and VC were found to increase appreciably with aging, with a decrease in M_3C . Most significantly, the average Fe:Cr ratio in the carbides decreased systematically with aging. Expansion of this database to more heats and aging conditions could open the door to the widespread use of the Fe:Cr ratio in carbides as an index of degradation in these steels.

4. Destructive tests

Destructive tests provide a direct measure of the current damage state of the material. They are the last resort in the assessment route, since the tests require removal of samples from operating components. There are limitations on the number of available samples and locations from which they can be taken. Periodic assessment of the remaining life is not possible. The costs of cutting out material, machining samples, and conducting tests can add up to a significant expenditure. These costs are further compounded by the plant outage during the extended period of evaluation and decision making. Despite these limitations, removal of core plug samples from headers and ring samples from bore or periphery of rotors is becoming increasingly common. Destructive testing generally includes tensile, impact, and creep/stress-rupture tests. Since the purpose and limitations of the tensile and impact tests are obvious, only the creep life evaluations are described here.

4.1 Creep tests

A procedure for estimating the current damage state by conducting stepped creep tests using a single specimen has been described in detail by Voorhees (1985). The procedure defines which stage of creep the material is in under service conditions but does not provide estimates of remaining life. The Monkman-Grant relationship for steels has also been in wide use and enables estimation of remaining life by determining the second-stage creep rate from creep tests. Improvements to this procedure have also been suggested by Castillo & Khouli (1986). The most common procedure, however, continues to be the use of isostress rupture tests.

The isostress rupture test procedure consists of conducting accelerated rupture tests at a temperature above the service temperature. The stress is kept as close as possible to the service stress value. The results are plotted as $\log t_r$ versus T and extrapolated linearly to the service temperature to estimate the remaining life. Results from recent research have identified the limitations of and possible refinements to the technique.

Results described earlier suggest that linear extrapolation of results from temperature-accelerated tests may yield optimistic predictions of remaining life under service conditions in the case of ductile materials; the reverse would be true for brittle materials. In either case, the predicted values are expected to be in agreement with the actual value within a factor of ± 2 .

This conclusion is in agreement with that of Melton (1983). Unfortunately, it is generally difficult to define a "brittle" and "ductile" class of materials since ductility can vary from heat to heat and with the test conditions. For our purposes, we can define a "brittle" steel as one prone to creep damage by cavitation, and a ductile material as one in which creep damage occurs primarily by softening. This is consistent with the observation by the ERA researchers that the ductile case MG showed no evidence of cavitation even at a life-fraction consumption of 0.82, while the brittle cast FW cavitated profusely. Using this definition, castings, coarse-grained heat-affected zones in welds, and fusion lines in welds may fit under the "brittle" category, while the base metal in forgings, piping, and tubes may fit in the "ductile" category. These observations are consistent with the recent results of Masuyama *et al* (1990) indicating differences in behaviour between ductile base metal and brittle heat-affected zones in 2.25Cr-1Mo steel. They further observed that in brittle heat-affected zones, both stress-accelerated and temperature-accelerated tests gave equivalent results that closely conformed to the LFR, while in the ductile base metal, only the temperature-accelerated isostress test results were in agreement with the LFR.

Since isostress tests are normally conducted in air, oxidation correction factors are also important. The extrapolated remaining-life values obtained from the accelerated tests should be corrected for oxidation effects. If tests are conducted in inert environments, no correction factor would be needed. A further refinement to the technique consists of using miniature specimens to minimize sample requirements. It has been demonstrated that miniature specimens (10 mm long, 3 mm diameter) tested in argon yield results representative of large specimens tested in air (Askins & Marchant 1988; Kadoya *et al* 1990).

4.2 Crack-growth studies

All of the techniques described so far relate to life prediction from a crack-initiation

point of view. For heavy-wall components, the initiation criteria have to be combined with crack-growth data to perform a fracture mechanics analysis of remaining life. Fatigue crack growth analysis procedures are well established. For creep-crack growth and creep-fatigue crack growth, however, methodologies and data needed for analysis have been gathered only during the last few years.

4.2a Creep crack growth: Extensive creep crack growth data pertaining to CrMo piping steels and CrMoV rotor steels have been collected, analysed, and consolidated (Saxena 1988; Saxena *et al* 1994). It has been observed that a crack-tip driving force parameter termed C_t , which takes time-dependent creep deformation into account, correlates much better with crack growth rates (da/dt) than the traditionally used elastic stress intensity factor K . The relation between da/dt and C_t can be expressed as

$$da/dt = bC_t^m. \quad (14)$$

To assess the remaining life of a component under creep-crack-growth conditions, two principal ingredients are needed: an appropriate expression for relating the driving force C_t to the nominal stress, crack size, material constants, and geometry of the component being analysed; and a correlation between this driving force and the crack-growth rate in the material, which has been established on the basis of prior data or by laboratory testing of samples from the component. Once these two ingredients are available, they can be combined to derive the crack size as a function of time. The general methodology for doing this is illustrated below, assuming C_t to be the driving crack-tip parameter.

The general expression for C_t given in (14) essentially reduces to the form

$$C_t = \sigma \varepsilon(A, n) a H(\text{geometry}, n), \quad (15)$$

where σ is the stress far from the crack tip, obtained by stress analysis; ε is the strain rate far from the crack tip, which is a function of the constants A and n in the Norton relation; a is the crack depth obtained from NDE measurements; and H is a tabulated function of geometry and the creep exponent n . The values of A and n are either assumed from prior data or generated by creep testing of samples. By assembling all the constants needed, the value of C_t can be calculated.

Once C_t is known, it can be correlated to the crack-growth rate through the constants b and m in (14). Combining (14) and (15) provides a first-order differential equation for crack depth (a) as a function of time (t). Theoretically, this equation can be solved by separating variables and integrating. However, the procedure is complicated by the time-dependency of C_t and the crack size dependence of the term H in (10). To circumvent this, crack-growth calculations are performed with the current values of da/dt (or \dot{a}), to determine the time increment required for incrementing the crack size by a small amount Δa (i.e., $\Delta t = \Delta a / \dot{a}$). This provides new values of a , t , and C_t , and the process is then repeated. When the value of a reaches the critical size a_c as defined by K_{IC} , J_{IC} , wall thickness, remaining ligament thickness, or any other appropriate failure parameter, failure is deemed to have occurred.

Although this procedure appears complex at first sight, the calculations are relatively easy, once the principles are understood. Computer programs have been developed to perform the entire analysis on personal computers. Among these, the *Steamline Inspection Code* and *PCPIPE* are in wide use in the United States. The only judgment involved is in selecting proper values for the constants A , n , b , and m , because large

scatter in creep and crack-growth data necessitates subjective choices. If actual creep and/or crack-growth tests could be performed, more accurate results could be obtained. Even if only the values of A and n in the Norton law could be pinned down by running creep tests in argon using the miniature samples described earlier, uncertainties could be reduced. A sample output may be in the form of crack depth versus time or a plot of crack size vs. remaining life, as illustrated in figure 13. This plot was generated for a thick-wall cylinder under internal pressure containing a longitudinal crack. The outside radius and wall thickness of the cylinder were assumed to be 45.7 cm and 7.62 cm, respectively, and the hoop stresses were calculated for internal pressures of 8.96 and 13.79 MPa. Materials properties in the degraded condition (hot region) as well as in the undegraded condition were considered. The results show that the remaining life is a function of the stresses as well as of prior degradation. Plots of this type could be used to determine remaining life or to set inspection criteria and inspection intervals.

Ainsworth *et al* (1987) have recently described a unified approach for structures containing defects. This approach incorporates structural failure by rupture, incubation behaviour preceding crack growth, and creep crack growth in a single framework. Service life is governed by a combination of time to rupture, time of incubation, and time of crack growth. All of these quantities are calculated using a reference stress that is specifically applicable to the geometry of the component and is derived analytically or based on scale-model tests. If the desired service life exceeds the calculated rupture time, retirement may be necessary.

In the opposite situation, further analysis is carried out to calculate the incubation time during which no crack growth is expected to occur. If the calculation indicates that the incubation time t_i is less than the desired service life, then a crack-growth analysis is performed to calculate the crack-growth life t_g . If the total life, $t_i + t_g$, is less than the desired service life, safe operation beyond that point would be considered undesirable. This approach seems promising and deserves further exploration.

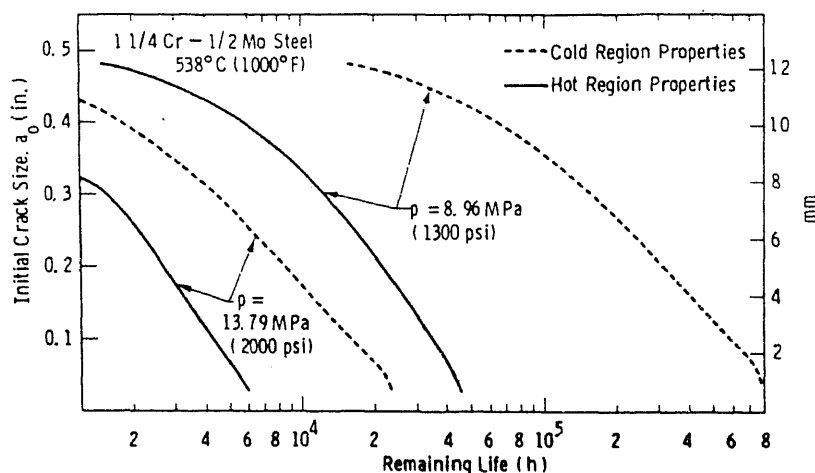


Figure 13. Remaining life as a function of initial crack size for an internally pressurized cylinder, illustrating a typical output from crack-growth analysis.

A number of variables affect the crack growth rate by modifying b , C_i , or m . The effect of these variables is summarized below (Saxena 1988; Saxena *et al* 1994).

- In-service degradation increases crack growth rate. In ductile CrMo steel base metal, the effect was attributable to increased C_i , while in brittle CrMoV rotor steels, the effect was attributable to an increased value of m . Widely divergent estimates of remaining life arise due to uncertainties in the crack growth coefficients b and m and in the Norton law coefficients A and n . Determination of component-specific A and n by miniature specimen creep tests on samples, and determination of b and m by creep crack growth, can greatly reduce the uncertainty in the remaining-life analysis.
- Crack growth rates at welds, fusion lines, and heat-affected zone materials are at least a factor of five higher compared to base metal.
- The presence of localized chains of inclusion, further assisted by segregation of impurities to interfaces such as grain boundaries and fusion lines, causes significant increases in creep crack growth rates.
- The presence of large amounts of impurities in the steel accelerates crack growth by increasing m .
- All material and experimental variables that reduce creep ductility result in higher crack growth rates.
- Temperature can have mixed effects on crack growth. In cases where the effect of temperature is merely to increase creep rate, the da/dt increases with increase in temperature due to increase in C_i . On the other hand, if a transition from a brittle to ductile condition is involved, increase in temperature may actually decrease the crack growth rates.
- Crack-tip constraint has a pronounced effect on crack growth. Assumptions regarding plane-stress or plane-strain conditions can have a pronounced effect on da/dt .
- Inclusion of primary creep, in addition to the secondary creep in calculation to the secondary creep in calculating C_i , results in larger values of da/dt and reduced remaining life.

4.2b Creep-fatigue crack growth: Major advances have been made in developing methodologies and data needed to treat crack growth under the combined effects of creep and fatigue at elevated temperatures. The loading conditions in elevated-temperature power generation components can often be simply represented by a trapezoidal wave shape consisting of a loading period, a hold time and an unloading period.

For these conditions, Saxena and coworkers (Saxena & Gieseke 1987; Gieseke & Saxena 1989; Yoon *et al* 1994) have suggested the following formulations for treating creep fatigue crack growth data. According to them the total crack growth rate during creep-fatigue loading can be partitioned into cycle-dependent and time-dependent components as follows:

$$[da/dn]_{\text{total}} = (da/dn)_{\text{fatigue}} + (da/dn)_{\text{hold}}, \quad (16)$$

where for trapezoidal loading $(da/dn)_{\text{fatigue}}$ corresponds to the crack growth rate associated with the loading/unloading portion of the cycle and $(da/dn)_{\text{hold}}$ corresponds to the crack growth rate associated with the hold period. The time-dependent crack growth occurs only under constant amplitude loading during C^* and C_i can be used in characterizing the crack growth rate during the hold period of the cycle, t_h . Due to

experimental limitations, it is difficult to obtain instantaneous values of da/dt and C_t during the hold period. However, average values of the crack growth rate and the C_t parameter can be accurately measured. The average da/dt and C_t are obtained as follows:

$$(da/dt)_{avg} = (1/t_h)(da/dN)_{hold} \quad (17)$$

and

$$(C_t)_{avg} = (1/t_h) \int_0^{t_h} C_t dt. \quad (18)$$

The $(da/dN)_{hold}$ is the crack growth during the hold period and is obtained by subtracting the cycle-dependent crack growth rate from the total crack growth rate.

The total crack growth rate is then given by

$$da/dN = C_{fatigue}(\Delta K)_{fatigue}^n + C_1 [(C_t)_{avg}]^q t_h \quad (19)$$

By comparing (20) with (16), it is readily seen that the first term in (19) given by the Paris Law represents the pure fatigue component and the second term represents the creep/creep fatigue component.

In test specimens, $(C_t)_{avg}$ can be determined from the measurements of load-line deflection as a function of time during the hold period. The value of $(C_t)_{avg}$ can be estimated by the following equation:

$$(C_t)_{avg} = [\Delta P(\Delta V_c)/BW t_h] (F'/F), \quad (20)$$

where ΔV_c is the change in load-line deflection during the hold period due to creep deformation, ΔP is the applied cyclic load, B and W are the thickness and width of the specimen, respectively, $F = K - a$ a calibration factor $= (K/P)BW^{1/2}$, and $F' = dF/d(a/W)$. Similarly, the $(da/dt)_{avg}$ can be determined by subtracting the pure fatigue crack growth component from the total da/dN per cycle as per (16) and dividing the resulting $(da/dN)_{hold}$ by t_h as per (17). The C_t average can be correlated with the (da/dt) average.

Figure 14b shows a plot of $(da/dt)_{avg}$ with $(C_t)_{avg}$ for 1.25 Cr–0.5 Mo steels for 538°C. The data include test results for a 98-second hold time, ten-minute hold time, and also the creep crack growth rate data (Yoon *et al* 1994). When plotted as a function of $(C_t)_{avg}$, the time rates of crack growth for these very different conditions fall on the same trend curve, in contrast when the crack growth per cycle is plotted as a function of ΔK (see figure 14a) different curves are obtained. The significance of the above trend with regard to predicting the hold-time effect in engineering components is obvious since creep crack growth data can be used to estimate creep-fatigue crack growth data and vice versa. It must be mentioned that if da/dN were correlated with ΔK , as has been done in the past (Saxena & Bassani 1984), the data for each hold time will follow a different trend as shown in figure 14a. In order to use this approach for predicting crack growth during hold time it is necessary to estimate the magnitude of $(C_t)_{avg}$ for components. An equation has been proposed to estimate the $(C_t)_{avg}$ for any geometry for a material deforming by elastic-cyclic plasticity and power-law creep (Yoon *et al* 1994). The details of this equation are given in the above reference and are outside of the scope of this overview. The applicability of this approach to steels other than Cr–Mo steels is yet to be explored.

There are additional concerns that must be addressed in order to develop total confidence in this approach. Currently, there is no provision to consider the interaction

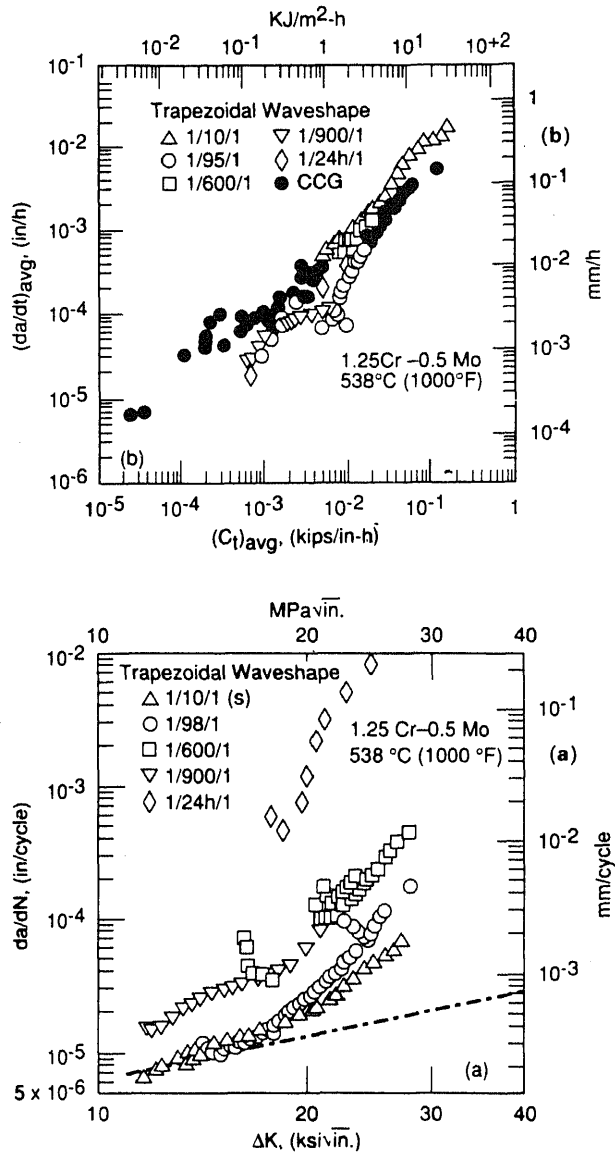


Figure 14. Comparison of creep-fatigue crack growth rates with (a) fatigue crack growth rate plotted using ΔK , and (b) creep crack growth data using $(C_t)_{avg}$.

between loading/unloading rates and the crack growth rate during hold time. During start-up, large transient thermal stresses often develop. Therefore, the hold period may be preceded by a fatigue cycle with a maximum stress considerably higher than the stress during hold. As yet, no methods are available considering such loading. Analytical expressions for estimating $(C_t)_{avg}$ need further numerical verification. Also, new expressions that consider primary creep deformation are needed. The crack growth data for verification of these concepts are currently limited to a single specimen geometry. Therefore, data on a different specimen geometry must be obtained.

5. Nondestructive evaluation of toughness

In heavy-section components, severe thermal stresses occurring during startup/shutdown transients can occasionally cause failures by rapid brittle fracture at relatively low temperatures. The crucial last step in remaining-life analysis of cracked components is, therefore, the determination of the critical crack size, based on a knowledge of the current toughness of the materials at the critical location. This toughness, generally expressed in terms of the plane-strain stress intensity for fracture (K_{IC}) determines the critical crack size for failure. The usual procedure involves estimation of the K_{IC} at low temperatures based on well-established correlations between the 50% ductile-to-brittle Fracture Appearance Transition Temperature (FATT) and K_{IC} . Considerable progress has been made in estimating the FATT of steels using relatively nondestructive techniques.

In Cr–Mo steels, operating at or above 538°C, the embrittlement mechanism of concern has been the carbide-induced embrittlement described earlier. An electrochemical polarization test has been developed by Watanabe & Shoji (1994) for measuring the increase in FATT due to embrittlement in such cases. In CrMoV rotor steels temper embrittlement is of greater concern. The most promising techniques in this case involve the use of phosphorus versus FATT correlation, picric acid etch (PAE) tests, small punch tests, and electrochemical tests.

5.1 Phosphorus-FATT correlations

Viswanathan & Gehl (1991) have performed an in-depth review of FATT data available on several CrMoV rotors that had been retired after 20 to 40 years of service as well as a few laboratory aged samples. The data population includes those from their work as well as additional data points from a recent paper by Seeley *et al* (1993). These samples were temper embrittled to varying degrees, the worst embrittlement occurring in the exposure temperature range of 370–425°C. The FATT in the embrittled condition could be correlated with the phosphorus content of the steel, as shown in figure 15. The D-grade rotor samples, which had been austenitized at 1,010°C and therefore had a coarser grain size compared to the C-grade rotor samples, exhibited slightly higher tendency to embrittle. Within limits of scatter, the post-service FATT could be estimated based on a knowledge of the phosphorus content alone.

5.2 Small punch testing

In the small punch test, a finished small punch (SP) specimen is placed between a 2.54 mm diameter hemispherical punch and a die. The punch displacement rate is controlled during the test, and a load versus deflection curve is thus developed where the area under the curve denotes the energy absorbed during the test. By conducting tests at different temperatures, a curve of absorbed energy versus temperature can be developed that is very similar in shape to that of a Charpy energy versus temperature curve, with the difference that the SP test curve is shifted laterally to lower temperatures along the temperature axis compared to the Charpy curve. The midpoint of the energy curve can be used to define a ductile-to-brittle transition temperature (T_{sp}). Foulds and others (Foulds *et al* 1991, 1993, 1994; Foulds & Viswanathan 1994)

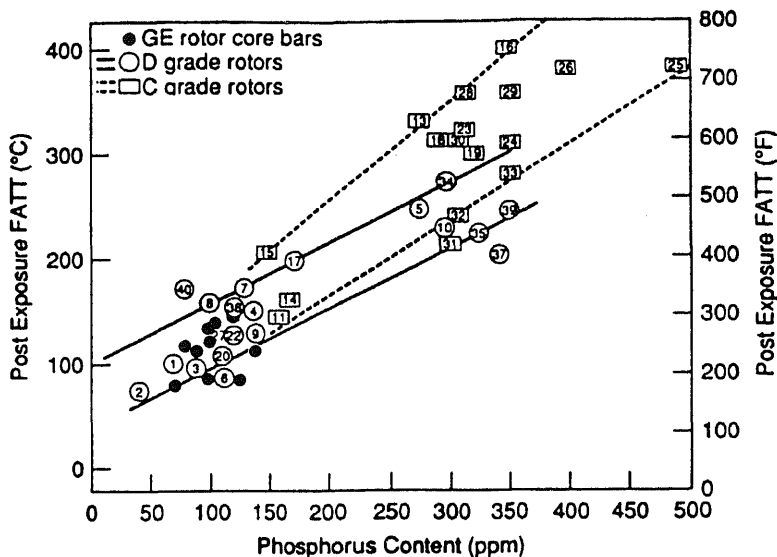


Figure 15. Variation of post exposure FATT (corrected for exposure temperature and location variations) with the phosphorus content of CrMoV rotor steel.

have successfully applied the test procedure to determine the T_{sp} for several retired rotor and disk samples. The T_{sp} values obtained correlated well with the Charpy FATT values as shown in figure 16.

The specimen needed for an SP test is only 0.508 mm thick with a diameter of 6.35 mm. Specimens of this size can be easily removed from critical locations in the rotor bar without affecting the rotor integrity by using a recently developed “scoop” device. If bore samples from the critical locations were unavailable, samples from other locations could be tested and the FATT values obtained could be corrected for location dependence using the approximations described by Viswanathan & Gehl (1991).

As stated earlier, the ultimate value of FATT in making run/repair/replace decisions is in the estimation of fracture toughness, K_{IC} , and the K_{IC} -dependent tolerable crack or defect size. A direct determination of K_{IC} can reduce the potential conservatism associated with the indirect FATT-to- K_{IC} estimation process. Recently, the Electric Power Research Institute (EPRI) has completed preliminary development of a non-empirical, purely analytical approach to using a single small punch test to directly determine K_{IC} (Foulds *et al* 1993, 1994). The procedure is material-independent, and requires no prior knowledge of material mechanical properties. The approach is based on the continuum material toughness concept wherein the criterion for fracture is defined and measured via the continuum stress-strain deformation properties of the material. The procedure specifically involves computing the “local” strain energy density accumulated at the location and time of crack initiation in the small punch test specimen using large-strain finite element analysis. Since the procedure also includes estimation of the material uniaxial tensile stress-strain behaviour from the small punch load-displacement curve, both the fracture toughness and the uniaxial tensile behaviour are determined from a single test. Details of the test and analysis procedures, and

5. Nondestructive evaluation of toughness

In heavy-section components, severe thermal stresses occurring during startup/shutdown transients can occasionally cause failures by rapid brittle fracture at relatively low temperatures. The crucial last step in remaining-life analysis of cracked components is, therefore, the determination of the critical crack size, based on a knowledge of the current toughness of the materials at the critical location. This toughness, generally expressed in terms of the plane-strain stress intensity for fracture (K_{IC}) determines the critical crack size for failure. The usual procedure involves estimation of the K_{IC} at low temperatures based on well-established correlations between the 50% ductile-to-brittle Fracture Appearance Transition Temperature (FATT) and K_{IC} . Considerable progress has been made in estimating the FATT of steels using relatively nondestructive techniques.

In Cr-Mo steels, operating at or above 538°C, the embrittlement mechanism of concern has been the carbide-induced embrittlement described earlier. An electrochemical polarization test has been developed by Watanabe & Shoji (1994) for measuring the increase in FATT due to embrittlement in such cases. In CrMoV rotor steels temper embrittlement is of greater concern. The most promising techniques in this case involve the use of phosphorus versus FATT correlation, picric acid etch (PAE) tests, small punch tests, and electrochemical tests.

5.1 Phosphorus-FATT correlations

Viswanathan & Gehl (1991) have performed an in-depth review of FATT data available on several CrMoV rotors that had been retired after 20 to 40 years of service as well as a few laboratory aged samples. The data population includes those from their work as well as additional data points from a recent paper by Seeley *et al* (1993). These samples were temper embrittled to varying degrees, the worst embrittlement occurring in the exposure temperature range of 370–425°C. The FATT in the embrittled condition could be correlated with the phosphorus content of the steel, as shown in figure 15. The D-grade rotor samples, which had been austenitized at 1,010°C and therefore had a coarser grain size compared to the C-grade rotor samples, exhibited slightly higher tendency to embrittle. Within limits of scatter, the post-service FATT could be estimated based on a knowledge of the phosphorus content alone.

5.2 Small punch testing

In the small punch test, a finished small punch (SP) specimen is placed between a 2.54 mm diameter hemispherical punch and a die. The punch displacement rate is controlled during the test, and a load versus deflection curve is thus developed where the area under the curve denotes the energy absorbed during the test. By conducting tests at different temperatures, a curve of absorbed energy versus temperature can be developed that is very similar in shape to that of a Charpy energy versus temperature curve, with the difference that the SP test curve is shifted laterally to lower temperatures along the temperature axis compared to the Charpy curve. The midpoint of the energy curve can be used to define a ductile-to-brittle transition temperature (T_{sp}). Foulds and others (Foulds *et al* 1991, 1993, 1994; Foulds & Viswanathan 1994)

in its application of a more cost-effective and nondestructive method for assessing the condition of tubing.

7. Summary

During the last decade major advances have been made in developing an overall strategy for assessing the remaining life of critical components operating at elevated temperatures. The strategy is based on a phased approach in which calculational, nondestructive and destructive evaluations are judiciously and sequentially linked to be most cost-effective. Research has been aimed at improving the accuracy of life prediction using all of these techniques in order to avoid undue conservatism and premature replacement of components. Key results of the research addressing both damage and crack growth phenomena under creep and creep-fatigue phenomena have been reviewed in this paper.

References

- Ainsworth R A, Chell G G, Coleman M C, Goodall I W, Gooch D G, Haigh J R, Neate G J 1987 CEBG assessment procedure for defects in plant operating in the creep range. *Fatigue Fracture Eng. Mater. Struct.* 10: 115-127
- Askins M C 1989 Remaining life estimation of boiler pressure parts. Vol. 4, Metallographic models for weld heat affected zones. EPRI Report CS-5588, EPRI, Palo Alto, CA, November
- Askins M C, Marchant K D 1988 Remaining Life Estimation of Boiler Pressure Parts, Vol. 2, Miniature Specimen Testing. EPRI Report CS-5588, EPRI, Palo Alto, CA: January
- Becker F L, Walker S M, Viswanathan R 1987 Guidelines for the evaluation of seam-welded steam pipes. EPRI Report CS-4774, Palo Alto
- Bolton C J, Dyson B F, Williams K R 1980 *Mater. Sci. Eng.* 46: 231-245
- Brear J M 1994 The effect of oxidation upon long-term stress rupture data of 1 CrMo and 2-25 Cr-1 Mo Steels. ERA Report 94-0504, EPRI project RP2253-4
- Brear J M, McCarthy P 1989 Residual life assessment methods. ERA Report 89-0230, EPRI Project RP2253-2
- Cane B J, Bissall A M 1986 Predictive assessment of damage in elevated temperature weldment. Paper presented at the EPRI Plant Maintenance Technology Conference, Houston, TX, 14-16 November
- Cane B J, Shammass M 1984 A method for remanent life estimation by quantitative assessment of creep cavitation on plant. Report TPRD/L2645/N84, Central Electricity Generating Board, UK
- Carlton R G, Gooch D J, Hawkes E M 1987 The central electricity generating board approach to the determination of remanent life of high temperature turbine rotors. I Mech E paper C300/87
- Castillo R, Koul A K, Toscano E N 1986 Lifetime prediction under constant load creep condition for a cast Ni-base superalloy. (ASME paper 85, GT241 presented at the International Gas Turbine Conference, Düsseldorf, Germany, 8-12 June
- Cheruvu N S 1989 Degradation of mechanical properties of steel components. *Metall. Trans. A* 20: 87-97
- Ellis F V, Henry J F, Shammass M S 1988 Remaining life estimation of boiler pressure parts. Vol. 1, Identification of relevant damage mechanisms. EPRI Report CS-5588, EPRI, Palo Alto, CA, November
- Ellis F V, Henry J F, Shammass M S 1989 Remaining life estimation of boiler pressure parts. Vol. 4, Metallographic models for weld heat affected zones. EPRI Report CS-5588, EPRI, Palo Alto, CA, November

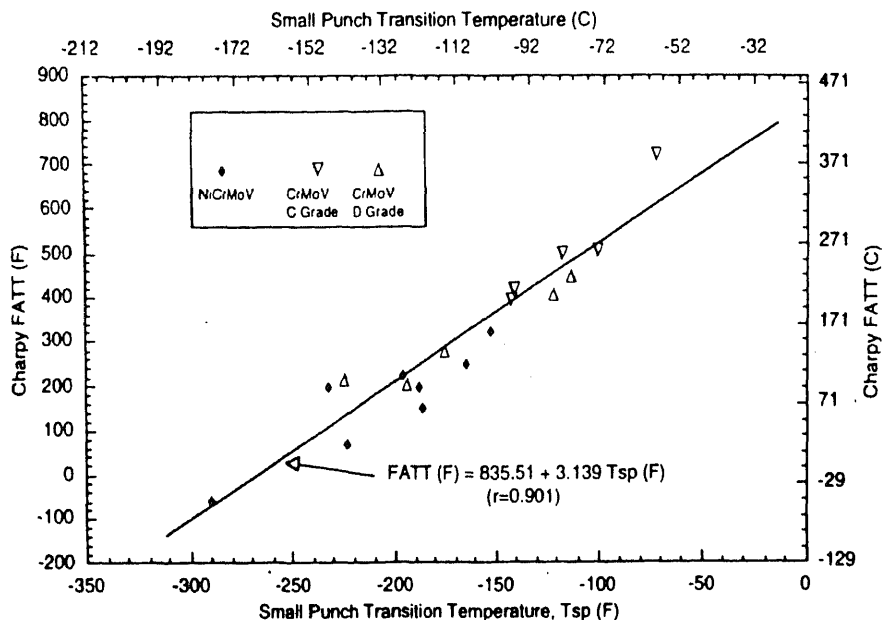


Figure 16. Correlation between Charpy transition temperature (FATT) and transition temperature measured from small punch tests (T_{sp}) for 1Cr1MoV and 2.5 to 3.5 NiCrMoV rotor and disk steels.

results are contained in Foulds *et al* (1993). Uniaxial tensile stress-strain curves are derived from the small punch test to an accuracy of typically $< 5\%$ of the stress at any strain. With regard to fracture toughness, K_{IC} prediction accuracy of the technique is about $\pm 25\%$. This level of accuracy can result in more than a factor-of-two increase over the FATT-estimated lower bound K_{IC} . This translates to roughly more than a factor-of-four increase in the tolerable crack/defect size in the rotor, and a significantly increased safe-life estimate.

6. Life-assessment for superheater tubes

The EPRI has developed a methodology that uses measurements of steamside oxide-scale thickness to predict the remaining creep life of high-temperature superheater/reheater tubing (Paterson & Rettig 1988; Viswanathan *et al* 1994). In addition, the validity of measuring the oxide-scale thickness ultrasonically has also been demonstrated by establishing a good correlation between ultrasonic measurements and direct measurements on tube samples removed from superheater assemblies from several fossil boilers. Comparison of uniaxial test results with tube burst tests results has also helped identify the correct formulas for computing the reference stress in tubing, replacing a more conservative formula used in the past. The kinetics of steam-side oxide-scale growth in heat-flux and nonheat-flux areas are also being measured in boilers. Cumulatively, these results have provided industry with the needed confidence

in its application of a more cost-effective and nondestructive method for assessing the condition of tubing.

7. Summary

During the last decade major advances have been made in developing an overall strategy for assessing the remaining life of critical components operating at elevated temperatures. The strategy is based on a phased approach in which calculational, nondestructive and destructive evaluations are judiciously and sequentially linked to be most cost-effective. Research has been aimed at improving the accuracy of life prediction using all of these techniques in order to avoid undue conservatism and premature replacement of components. Key results of the research addressing both damage and crack growth phenomena under creep and creep-fatigue phenomena have been reviewed in this paper.

References

- Ainsworth R A, Chell G G, Coleman M C, Goodall I W, Gooch D G, Haigh J R, Neate G J 1987 CEBG assessment procedure for defects in plant operating in the creep range. *Fatigue Fracture Eng. Mater. Struct.* 10: 115-127
- Askins M C 1989 Remaining life estimation of boiler pressure parts. Vol. 4, Metallographic models for weld heat affected zones. EPRI Report CS-5588, EPRI, Palo Alto, CA, November
- Askins M C, Marchant K D 1988 Remaining Life Estimation of Boiler Pressure Parts, Vol. 2, Miniature Specimen Testing. EPRI Report CS-5588, EPRI, Palo Alto, CA: January
- Becker F L, Walker S M, Viswanathan R 1987 Guidelines for the evaluation of seam-welded steam pipes. EPRI Report CS-4774, Palo Alto
- Bolton C J, Dyson B F, Williams K R 1980 *Mater. Sci. Eng.* 46: 231-245
- Brear J M 1994 The effect of oxidation upon long-term stress rupture data of 1 CrMo and 2-25 Cr-1 Mo Steels. ERA Report 94-0504, EPRI project RP2253-4
- Brear J M, McCarthy P 1989 Residual life assessment methods. ERA Report 89-0230, EPRI Project RP2253-2
- Cane B J, Bissall A M 1986 Predictive assessment of damage in elevated temperature weldment. Paper presented at the EPRI Plant Maintenance Technology Conference, Houston, TX, 14-16 November
- Cane B J, Shammas M 1984 A method for remanent life estimation by quantitative assessment of creep cavitation on plant. Report TPRD/L2645/N84, Central Electricity Generating Board, UK
- Carlton R G, Gooch D J, Hawkes E M 1987 The central electricity generating board approach to the determination of remanent life of high temperature turbine rotors. I Mech E paper C300/87
- Castillo R, Koul A K, Toscano E N 1986 Lifetime prediction under constant load creep condition for a cast Ni-base superalloy. (ASME paper 85, GT241 presented at the International Gas Turbine Conference, Düsseldorf, Germany, 8-12 June
- Cheruvu N S 1989 Degradation of mechanical properties of steel components. *Metall. Trans. A* A20: 87-97
- Ellis F V, Henry J F, Shammas M S 1988 Remaining life estimation of boiler pressure parts. Vol. 1, Identification of relevant damage mechanisms. EPRI Report CS-5588, EPRI, Palo Alto, CA, November
- Ellis F V, Henry J F, Shammas M S 1989 Remaining life estimation of boiler pressure parts. Vol. 4, Metallographic models for weld heat affected zones. EPRI Report CS-5588, EPRI, Palo Alto, CA, November

- EPRI 1990 Field metallography research leads to improved re-examination interval for creep damaged steam pipes. EPRI First Use Report B197, EPRI, Palo Alto, CA, December
- EPRI 1991 Development of a replica database for life assessment of balance-of-plant components. RTUV and Failure Analysis Associates, Interim Report, EPRI Project RP2253-10, EPRI, Palo Alto, CA, January
- Foulds J R, Jewett C W 1994 Miniature specimen test technique for toughness assessment. Final Report, EPRI RP1957-10, EPRI, Palo Alto, CA (in press)
- Foulds J R, Viswanathan R 1994 Small punch testing for determining the material toughness of low alloy steels. *ASME, J. Eng. Mater. Technol* 116: 457-464
- Foulds J R, Jewett C W, Viswanathan R 1991 Miniature specimen test technique for FATT. *Joint Power Generation Conference* (New York: ASME) 91JPGC-PWR 38
- Foulds J R, Woytowicz P J, Parnell T K, Jewett C W 1993 Fracture toughness by small punch testing. In *Proc. of the Third EPRI Turbo/Generator Conference* (Palo Alto, CA: EPRI)
- Foulds J R, Woytowicz P J, Parnell T K, Jewett C W 1994 Fracture toughness by small punch testing. Final Report on Project RP2426-38, EPRI, Palo Alto, CA
- Fujiyama K, Kimura K, Muramatsu M, Yamaha M 1990 Evaluation of creep properties of degraded CrMoV turbine cast steels through hardness measurement and its application to life assessment. *ISIJ International*, 30: 869-875
- Gieseke B, Saxena A 1989 Correlation of creep-fatigue crack growth rates using crack-tip parameters. *Advances in fracture research* (eds) K Salama *et al* (Elmsford, NY: Pergamon Press) pp. 189-196
- Goto T 1985 Study on residual creep life estimation using nondestructive material property tests. Mitsubishi Technical Bulletin, No. 169, Mitsubishi
- Grunloh H, Ryder R H 1989 General atomics, San Diego, CA, private communication of results from EPRI project RP2253-10
- Harris D A, Ryder R H, Schultz C 1993 BLESS: Boiler Life Evaluation and Simulation and System - A Computer Code for Reliability. Analysis of Headers and Piping. In *Reliability and risk in pressure vessels and piping* (eds) J Phillips *et al* (New York: ASME, PVP) 251: 17-26
- Hart R V 1976 *Met. Technol.* 3:
- Kadoya Y *et al* 1985 Material characteristics NDE system for high temperature rotors. Presented at the ASME/IEEE Joint Power Generation Conference, Paper No. 85-JPGC, PWR-10
- Kadoya Y, Goto T, Date S, Yamauchi T 1990 Assessment of remaining life of fossil power plant parts by means of miniature creep rupture test. *Iron Steel Inst. Jpn. Int.* 30: 853-860
- Kimura K, Fujiyama K F, Muramatsu M 1988 Creep and fatigue life prediction. *High-temperature creep-fat* (eds) R Ohtani M Ohnami, T Inow (Elsevier; Japan: Society of Materials Science)
- Lempp W, Kasik N, Feller U 1986 Paper presented at the Second International Symposium on the Nondestructive Characterization of Materials, Montreal
- Masuyama F, Nishimura N, Igari T 1990 Creep damage simulation test and creep life assessment system for elevated temperature plant components. *Iron Steel Inst. Jpn. Int.* 30: 885-895
- McGuire J, Gooch D J 1989 Metallographic techniques for residual life assessment of 1 CrMoV rotor forgings. *International Conference on Life Assessment and Extension*, Nederlands Inst. Voor Lastetechniek, The Hague, p. 116
- Melton K N 1983 The isostress extrapolation of creep rupture data. *Mater. Sci. Eng.* 59: 143-149
- Munson R 1990 Radian Corporation, Austin, TX, private communication
- Nakashiro M *et al* 1991 Evaluation of long term creep strength of 2.25 Cr-1 Mo heat transfer tube in actual service stress level range. *Iron Steel Inst. Jpn. Int.* 30: 823-828
- Nakatani H, Yokoyama T, Masuyama F, Nishimura N 1990 Metallurgical damage detection and life evaluation system for boiler pressure parts. Paper presented at the EPRI Conference on Predictive Maintenance of Fossil Plant Component, Boston, MA, October
- Neubauer B, Wedel V 1983 Restlife estimation of creeping components by means of replicas. *Advances in life prediction methods* (eds) D A Woodford, J R Whitehead (New York: ASME) pp. 307-314
- Paterson S R 1989 APTECH Engineering, Mountain View, CA, private communication
- Paterson S R, Rettig T W 1988 Remaining life assessment of superheater and reheater tubes. EPRI Report CS-5564, EPRI, Palo Alto, CA

- Qu Z, Kuo K H 1981 Embrittlement of $2\frac{1}{4}$ Cr MoV bolts after long exposure at 540°C. *Metall. Trans.* A12: 1333–1337
- Saxena A 1988 Limits of LEFM in the characterization of high-temperature fatigue crack growth. *Basic questions in fatigue* (eds) R P Wei, R Gangloff (Philadelphia, PA: ASTM) vol. 2, STP 924 pp. 27–40
- Saxena A 1994 Creep crack growth in CrMoV rotor steels. EPRI RP2481–5 report, EPRI, Palo Alto, CA, in press
- Saxena A, Bassani J L 1984 Time-dependent fatigue crack growth behavior at elevated temperature. *Fracture interaction of microstructure, mechanisms and mechanics* (Warrendale, PA: TMS) pp. 357–383
- Saxena A, Gieseke B 1987 Transients in elevated temperature crack growth. *Proceedings of MECAMAT – International Seminar on High Temperature Fracture Mechanism and Mechanics* vol. 3, pp. 19–36
- Saxena A, Han J, Banerji K 1988 Creep crack growth in boiler and steam pipe steels. EPRI Report CS-5583, EPRI, Palo Alto, CA, January
- Seeley R E, Kaplan A, Bullock G S, 1993 C-Grade CrMoV steel turbine rotor life assessment. *Proceedings, Third EPRI Turbine/Generator Conference* (Palo Alto, CA: EPRI)
- Stevens R A, Flewitt P E J 1985 The effect of phosphorus on the microstructure and creep strength of 2.25 Cr–1 Mo steel. SER/SSD/85/0020/R, Central Electricity Generating Board, UK, March
- Stevens R A, Lonsdale D 1984 Isolation and quantification of various carbide phases in 2.25Cr–1 Mo Steel. SER/SSD/84–0046/N, Central Electricity Generating Board, UK, June
- Viswanathan R 1989 *Damage mechanisms and life assessment of high temperature components* (Metals Park, Ohio: ASM)
- Viswanathan R 1992 Low cycle fatigue life prediction. In *LCF 3, Low cycle fatigue and elasto-plastic behavior of materials* (eds) K T Rie (London: Elsevier) pp. 695–721
- Viswanathan R 1993 Creep fatigue life prediction of fossil plant components. In *Creep, fatigue flaw evaluation and leak before break assessment* (eds) Y S Garud *et al* (ASME, PVP) 266: 33–51
- Viswanathan R, Gehl S 1991 A method for estimation of the fracture toughness of CrMoV rotor steels based on composition. *ASME J. Eng. Mater. Technol.* 113: 263–271
- Viswanathan R, Gehl S M 1992 Effect of aging on the creep rupture behavior of steels. *First International Conference on Microstructures and Mechanical Properties of Aging Materials* (eds) P K Liaw *et al* (Warrendale: TMS AIME) pp. 35–41
- Viswanathan R, Wells C H 1993 Life prediction of turbine generator rotors. In *Technology for the 90s – A decade of progress* (eds) M K Au Yang *et al* pp. 139–179 (New York: ASME)
- Viswanathan R, Patterson S R, Gounloh H 1994 Life assessment of superheater and reheater tubes in fossil boilers. *J. Press. Vessel Technol.* 116: 1–16
- Voorhees H 1985 *Metals handbook. 9th edn Mechanical testing* (Metals Parks, Ohio: ASM) vol. 8, p. 339
- Watanabe Y, Shoji T 1994 (private communication)
- Wells C H, Viswanathan R 1993 Life assessment of high energy piping. In *Technology for the 90s – A decade of progress* (Eds) M K Au Yang *et al* (New York: ASME) pp 179–217
- Woodford D A 1979 *J. Eng. Mater. Technol.* 101: 331–340
- Yoon K B, Saxena A, McDowell D L 1994 Influence of crack tip cyclic plasticity on creep-fatigue crack growth. *22nd ASTM National symposium on fracture mechanics* (Philadelphia, PA: ASTM) (in press)



Creep life extension of high temperature components under wall thinning conditions

R N GHOSH, S CHAUDHURI, N ROY and L CHATTOPADHYAY

National Metallurgical Laboratory, Jamshedpur 831 007, India

Abstract. Current methods of life extension of high temperature components have been examined. Importance of changing section size as a result of corrosion and erosion has been emphasized. A simple method based on the influence of service exposure on rupture strength of the material and the data collected on loss of section size during routine shut-down of plants has been suggested. Highlights of the computer software developed to assist such an exercise have been discussed. The outputs have been shown to compare fairly well with the results reported in literature.

Keywords. Stress rupture tests; service exposure; Cr–Mo/Cr–Mo–V steels; time–temperature parameter; rupture strength; corrosion/erosion rates; reference stress; rupture life.

1. Introduction

The high temperature components of power plants and petroleum refineries are usually designed on the basis that failure must not occur within a stipulated design life under the expected operating conditions during service. In the case of components like heater tubes or steam pipes, creep is the major life-limiting factor. At the design stage it is therefore necessary to know the stresses which the engineering material can sustain at the service temperature without creep failure within the planned operational life. Since most designs are based on an assumed life of 100,000 hours or even 250,000 hours (approximately 30 years), knowledge of long-term creep rupture properties for relevant steels is essential. Therefore expensive multi-laboratory long-term stress rupture test programmes have been conducted on a range of steels. At present we do have a database which could give a fairly good estimate of up to 250,000 h rupture strength for a variety of steels recommended for elevated temperature applications. However, the main problem with such data is the unusually large scatter of around $\pm 20\%$ of the stress level (Evans & Wilshire 1985). This is equivalent to an order of magnitude of scatter in the expected rupture life at any specified stress level. Since failure of components can lead to serious financial and safety problems, plant operation can be allowed only with a reasonable assurance that catastrophic failure will not occur. Therefore designs of high temperature components are based on the minimum assured level of rupture strength i.e. the lower limit of the scatter band. Yet most of the materials

used for construction will have stress rupture properties better than the lower limit of the scatter band. In addition a safety factor of 1.3 to 1.6 in stress is commonly used at the design stage. Therefore even at the end of the specified design life most large-scale plants have a significant built-in additional life. This is supported by the fact that a survey indicates that more than 93,000 MW of power is being generated by plants which are more than 50 years old (Paterson *et al* 1987).

Many of the plants installed in our country during the late 1950s and early 1960s are now approaching the end of their design life. With increasing capital costs for construction of new plants (which is currently around Rs. 4 cores/MW) considerable world-wide attention is being focussed on refurbishment and life extension of existing units. A three-stage procedure is being commonly followed (McNaughton *et al* 1986; Townsend 1987). Stage 1 looks at the design method in the light of the new long-term material data that may have become available since the plant was commissioned, whereas stage 2 involves *in situ* inspection of components using a variety of approaches such as measurement of dimension, nondestructive testing, surface metallography and chemical analysis, primarily to identify locations where stage 3 procedure should be undertaken. This stage involves stress rupture testing and microstructural examination of service-exposed material.

Microstructural studies offer only an additional qualitative information on the condition of components. It is the accelerated stress rupture tests on service-exposed material that provide a quantitative estimate of remanent life of a component. Acceleration is achieved by performing tests at higher than normal operating stress and temperature. Some of the experimental studies have shown that whilst temperature acceleration provides a reasonable estimate, stress acceleration may give a rather optimistic value (Wiegand *et al* 1975; Hart 1976). This is primarily because high temperature tests do not significantly modify the microstructures developed in steels during long-term plant exposures. However, in order to allow tests to be performed at higher than normal temperature range without significant oxidation, it is necessary to provide an inert atmosphere or vacuum. If such tests are performed in air, it is likely to provide an optimistic estimate of life.

In addition, section sizes of components change as a result of corrosion and erosion. Consequently, the operating stress that the component is subjected to increases with aging. Therefore data on loss of section size should also form an important input in the life assessment of aging high temperature components. The paper presents some of our experience on such an exercise.

2. Effect of service exposure on rupture strength

Accelerated stress rupture test data on a number of service exposed steam pipes were analysed using a menu-driven computer software developed at our laboratory (Chatopadhyay *et al* 1990). This provides a framework for analysing short-term test data using various parametric techniques to predict either long-term rupture strength or rupture lives under any user-specified operating conditions. Figure 1 shows a typical stress vs Larson-Miller parameter plot where test data on CrMoV steel having different extents of service exposures have been superimposed with data on virgin steel. Twenty has been used as the parametric constant for all sets of data so that a visual comparison can be made. The trend reveals that if any attempt is made to extrapolate

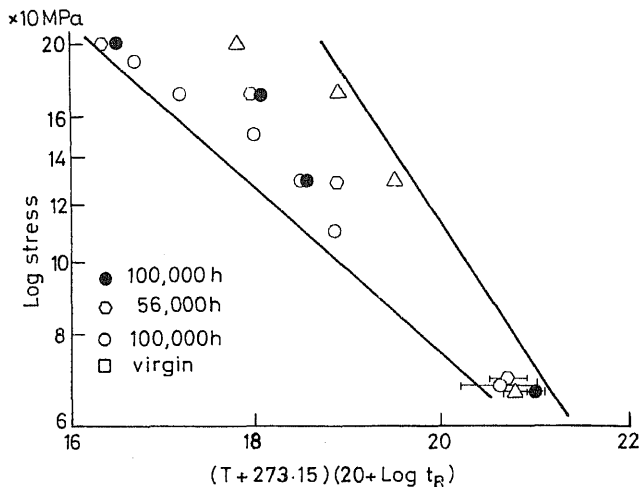


Figure 1. Stress rupture plots of virgin and service exposed Cr-Mo-V steel having different extents of service exposure.

beyond the domain of available test data it is likely to provide an unrealistic estimate of remaining life having no definite correlation with the extent of past service exposure. This aspect has been critically examined by Ghosh *et al* (1986). Table 1 presents a comparison of the life estimates arrived at by using three different time-temperature parameters for samples having different extent of service exposure. The inconsistency in life estimate is clearly as a result of extrapolation beyond the domain of available data.

However, if no attempt is made to extrapolate, rather only an estimate of upto 100,000 h rupture strength is attempted, results exhibit a definite correlation with the length of service exposure. Table 2 gives an estimate of 100,000 h rupture strength for four different sets of samples obtained by using three different time-temperature parameters. Irrespective of the method used the result demonstrates that the virgin sample has the highest rupture strength whereas the 100,000 h service exposed material has the lowest rupture strength. The table 2 includes two sets of samples having the same length of service exposure. The minor variation in their rupture strength could be as a result of different extent of damage accumulation possibly due to different average metal wall temperature.

Table 1. Remaining lives in hours of steam pipes at 550°C and 64 MPa obtained from an analysis of stress rupture data.

Service exposure (h)	Remaining lives (h) obtained by		
	LMP	SDP	MHP
100,000	91,000	97,000	89,000
100,000	46,000	56,000	50,000
56,000	184,000	199,000	105,400
Virgin	161,000	164,000	98,000

Table 2. 100,000 h rupture strength in MPa at 550°C obtained by three different parametric methods.

Service exposure (h)	Rupture strength		
	LMP	SDP	MHP
100,000	67.7	66.7	55.9
100,000	68.7	68.7	60.8
56,000	72.6	72.6	66.5
Virgin	97.1	97.1	102.0

Figure 2 represents the stress rupture test data on service exposed 5Cr- $\frac{1}{2}$ Mo steel heater tubes of Petroleum Refineries (Singh *et al* 1994). Irrespective of the service exposure all data lie above the minimum specified rupture strength plot for the same grade of steel. Rupture tests were carried out on virgin tube material as well. These also have been superimposed on figure 2. If one were to rely on short-term test data one may conclude from figure 2 that with service exposure the material becomes stronger whereas in reality it may not be so. This is primarily because stress rupture test data even on the same grade of material collected from various sources can exhibit large scatter. The material tested may also belong to different lots of products. Therefore in such cases it is more appropriate to conclude that both service-exposed and virgin material data lie within the same scatter band. This would imply that life assessment of components can still be made on the basis of the minimum specified rupture strength of this steel.

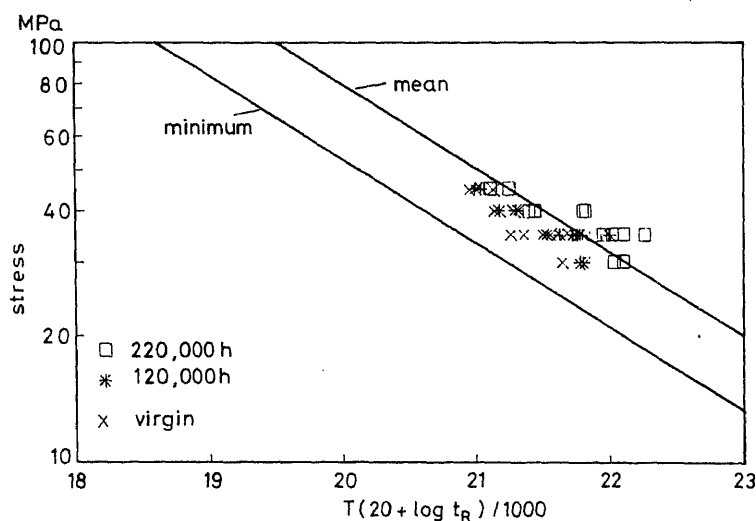


Figure 2. Stress rupture data of virgin and service exposed 5Cr-0.5Mo steel mostly lying above the minimum specified ASTM line.

3. Life estimation method

Even though in many instances the material properties of service-exposed components are found to be better than the minimum specified levels, component dimensions do change as a result of prolonged service. Most prominent amongst these is the loss of thickness due to either corrosion, erosion or oxidation. Pertinent standard codes do not consider these for life estimation. Only an additional thickness allowance is kept, based on past experience to take care of the likely loss of section size. Zarrabi (1993) has recently proposed a simple method of estimating boiler tube life in the presence of corrosion and erosion processes. This is based on the calculation of reference stress for the tube as a function of time assuming a constant thinning rate on either side of the tube wall. The time it takes to exceed the flow stress or the rupture strength gives an estimate of the life. Two types of failure mechanisms have been considered by Zarrabi (1993) viz. plastic collapse determined by flow stress and creep determined by rupture strength; the shorter of the two being the dominant mode. Use of reference stress, a concept popularized by Sim (1968), rather than equivalent stress is recommended as it has been found to provide accurate prediction of deformation behaviour. Recent experiments on $\frac{1}{2}\text{Cr}-\frac{1}{2}\text{Mo}-\frac{1}{2}\text{V}$ steel tubes have shown that rupture data also can be correlated with the reference stress. Expressions for reference stress (S) are now available for a host of component geometries (Boyle & Spense 1983). In the case of tubes it is given by:

$$S = \frac{3^{1/2}}{2} K \frac{P}{\ln\{(d+H)/(d-H)\}}, \quad (1)$$

where P is the average operating pressure, d is the mean tube diameter, H is the wall thickness at any instant t and K is a constant describing the nature of wall thinning e.g. uniform or localized. Kitching & Zarrabi (1981, 1982) have reported the values of K for various kinds of wall thinning. If it is uniform, $K = 1$.

Assuming that the tube thins down uniformly both from the inner as well as the outer surface at a constant rate Zarrabi (1993) has developed a computer code which could predict the life of boiler tubes under wall thinning condition. This requires a systematic representation of the stress rupture data in the form of specific equations rather than the tabular representation used in ISO/TR 7468 (1981). His program uses a mathematical form recommended by the Central Electricity Generating Board (CEGB), UK, for representing the master plot (Fielding 1979). The analysis revealed that in comparison to the θ projection method popularised by Evans *et al* (1985, 1992) this provides a conservative estimate of life for any given thinning rate.

Use of complex time-temperature parameter having several nonlinear terms to reduce the scatter in the master rupture plot do not necessarily provide realistic life estimates from short term test data. Very often such an analysis will require a large volume of test data. Data collected on the same material from different sources would add to the extent of scatter. In this context therefore it is worthwhile to examine how the predictions based on simpler forms of rupture parameter compare with those arrived at by Zarrabi (1993). CLIP (Chattopadhyay *et al* 1990) which is a user-friendly computer software developed at National Metallurgical Laboratory (NML) provides a simple framework for creep life prediction of engineering materials with the help of

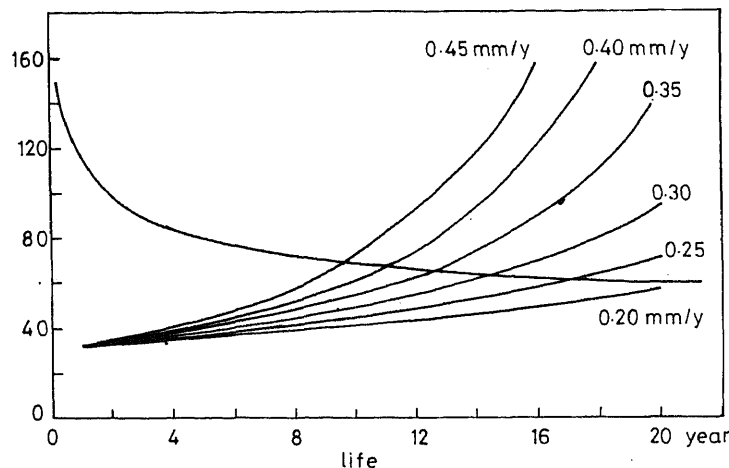


Figure 3. Rupture strength of 0.5Cr-0.5Mo-0.25V at 575°C has been plotted as function of time to rupture. Reference stresses as estimated from (1) have been superimposed for various assumed rates of wall thinning. The point of intersection with the rupture strength plot gives the estimate of life.

three commonly used time-temperature parameters, viz;

$$\text{Larson-Miller Parameter (LMP)} = T(C + \log t_r)$$

$$\text{Sherby-Dorn Parameter (SDP)} = \log t_r - b/T$$

$$\text{Manson-Heferd Parameter (MHP)} = (\log t_r - \log t_0)/(T - T_0)$$

where C , b , $\log t_0$ and T_0 are material constants. These can be estimated from an analysis of the master rupture plot using the method of least squares assuming that the master plot can be expressed as a polynomial function of $\log(\text{stress})$. The software provides the user an option to select its order. Usually an equation of order 3 or 5 is selected as it is sure to provide at least one real root. Use of equations of higher order is unnecessary as this does not improve predictive power of such representations significantly.

Using the software, rupture lives at different stresses at a given temperature can be computed. Figure 3 gives a typical plot of rupture stress vs life using Larson-Miller Parametric representation of master rupture curve for Cr-Mo-V steel. In order to estimate life of simple components such as heater tubes, operating stress as calculated by (1) can be superimposed on this figure. Assuming various rates of wall thinning this has been computed for a tube having an initial dimension and average operating pressure given in table 3. Subsequently this has been superimposed on figure 3. The point of intersection provides an estimate of the life.

4. Results and discussion

The method described above has been used to estimate the life of typical boiler tubes given in table 3. Figure 4 shows the dependence of tube life on thickness for various

Table 3. A typical boiler tube specification.

Original outer dia	d_0	50.00 mm
Original thickness	H_0	9.00 mm
Internal effective pressure	P	16.0 MPa
Effective temperature	T	575°C

grades of Cr–Mo steels using standard rupture data. It is clear that steels having higher amounts of Cr and Mo do not necessarily have longer rupture lives. 2.25 Cr–1 Mo steel has better creep resistance than 9Cr–1 Mo steel. It is only with Nb additions and reduced carbon content that creep resistance of 9Cr–1 Mo steel can be improved beyond that of 2.25 Cr–1 Mo steel.

Figure 5 compares the life estimates of tubes of different thicknesses made of Cr–Mo–V steel using the three different time–temperature parameters described above. The results reported by Zarrabi (1993) are also superimposed on the same plot. The life estimate plots in figure 4 and 5 are almost linear because the thinning rate has been assumed to be constant.

In order to show the influence of thinning rate on life estimates arrived at by various methods of representing the master rupture curve, calculations have been made for Cr–Mo–V steel tubes. Figure 6 depicts the effect of thinning rate on tube life. Results arrived at by using different parametric representations are indeed expected to differ. The difference is however more prominent at lower thinning rates. In our country, where generally coals with high ash content are in use, design should be based on a relatively higher rate of wall thinning. In such cases, however, the difference in life estimates using any of the parameters described above is likely to be marginal.

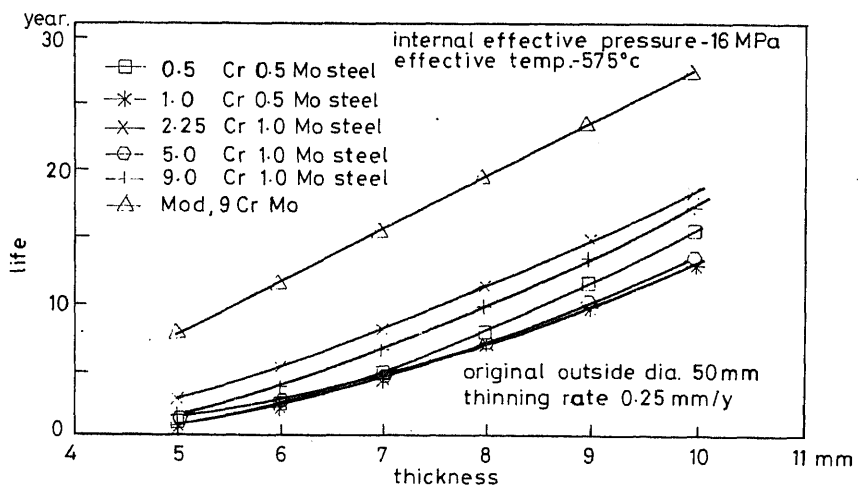


Figure 4. Creep life vs initial tube thickness plots for various grades of Cr–Mo/Cr–Mo–V steels have been compared. The thinning rates in all cases have been assumed to be constant

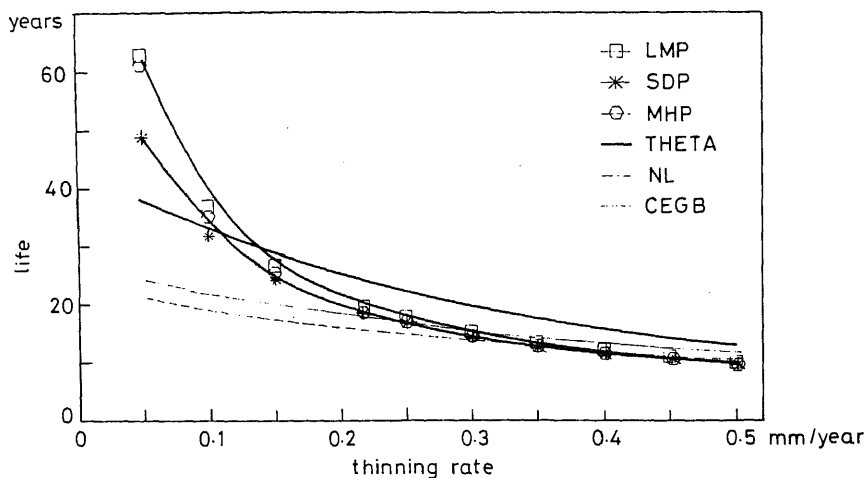


Figure 5. Creep life vs initial tube thickness plots obtained using different parametric functions have been compared. NL represents a functional plot using the natural logarithm of stress as suggested by Zarrabi (1993). See text for details about rest of the representations. The material corresponds to 0.5Cr-0.5Mo-0.25V.

Thinning of heater tubes can take place by any one or a combination of the following three mechanisms, viz; (i) creep strain accumulation, (ii) oxide scale growth at the inner wall in the presence of steam/water at high pressure and temperature, (iii) fire-side corrosion. Since the magnitude of creep strain that can be accommodated because of

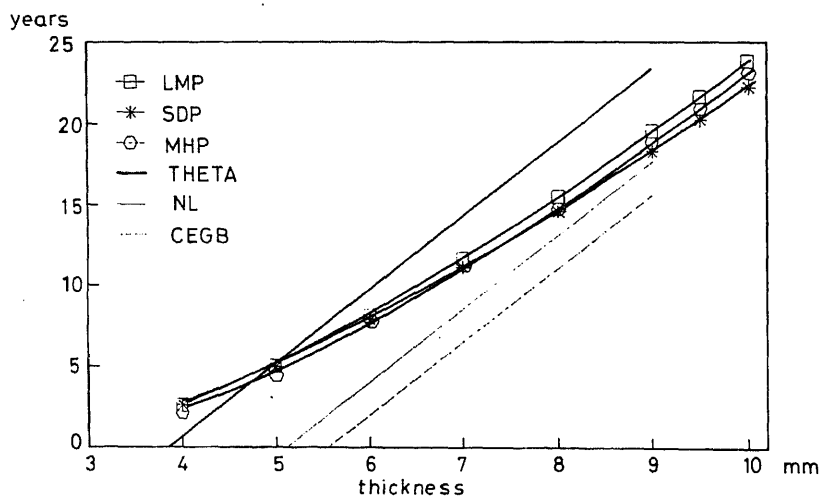


Figure 6. Creep life vs thinning plots for 0.5Cr-0.5Mo-0.25V steel obtained using different parametric functions have been compared. NL represents a functional plot using the natural logarithm of stress as suggested by Zarrabi (1993). See text for details about rest of the representation. The material corresponds to 0.5Cr-0.5Mo-0.25V.

design constraint is very limited, its contribution to wall thinning may be considered marginal. Excellent predictive models are now available for estimating loss of thickness due to oxide scale growth (Paterson & Rettig 1987). However major problems would arise in estimating loss of wall thickness due to fire-side corrosion. Besides, the actual extent of wall thinning is critically dependent on the actual operating conditions and environment. Since it is mandatory to shut down boilers for routine inspection every six months, wall thickness measurement could be carried out at specified locations to get a fairly accurate estimate of the kinetics of loss of the tube wall thickness. Such measurement would provide more reliable estimates of life as it corresponds to the actual operating conditions.

Although the method described assumes that the tube thins down at identical rates both from the inner and the outer walls it can easily be extended to cases where these are different. Work in this direction is in progress. However, a rough analysis indicates that for heater tubes having a low thickness to diameter ratio, as is commonly observed, life estimates will not be very much different. Therefore the procedure described above can safely be used for the evaluation of the life of tubular components of a boiler for any life extension exercise.

References*

- Boyle J T, Spence J 1983 *Stress analysis for creep* (London: Butterworths) p. 119
- Chattopadhyay L, Singh R, Ghosh R N 1990 CLIP - a menu driven software for creep life prediction of engineering materials. NML Report No. 03421139
- Evans R W, Wilshire B 1985 *Creep of metals and alloys* (London: Inst of Metals)
- Evans R W, Parker J D, Wilshire B 1992 *Int. J. Pressure Vessels Piping* 50: 147-160
- Fielding P J 1979 Polynomial representation of ISO data for creep rupture of various steels. CEEGB Rep. SSD/SE/M50/79
- Ghosh R N, Singh R, Kumar R 1986 *Int. Conf. on Creep* (Tokyo: Japan Soc. Mech. Eng.) pp. 391-385
- Hart R V 1976 *Met. Technol. (London)* 13: 1-7
- ISO/TR 7468 1981 (E). Int. Org. for Standardization. Summary of average stress rupture properties of wrought steels for boilers and pressure vessels, Switzerland, No. 150
- Kitching R, Zarrabi K 1981 *Int. J. Mech. Sci.* 23: 31-48
- Kitching R, Zarrabi K 1982 *Int. J. Pressure Vessels Piping* 10: 235-270
- McNaughton W P, Richman R H, Pillar C S, Perry L W 1986 Generic guidelines for life extension of fossil fuel power plants. Report CS 4778. Electric Power Research Institute, Palo Alto, CA
- Paterson S R, Rettig T W 1987 Remaining life estimation of boiler pressure parts - 2-1/2Cr Mo steel superheater and reheater tubes. Project Report RP 2253-5, Final Report. Electric Power Research Institute, Palo Alto, CA
- Paterson S R, Rettig T W, Clarke K J 1987 *Conf. Proc. life extension and assessment of fossil power plants* (eds) R B Dooley, R Viswanathan. EPRI, Palo Alto, CA, pp. 455-474
- Sim R G 1968 *Creep in structures*. Ph D thesis, Univ. of Cambridge
- Singh R, Ghosh R N, Chaudhuri S, Joarder A, Mitra A, Mohanty O N, Tarafder S 1994 Remaining life assessment of process heater tube of petroleum refineries. NML Internal Report
- Townsend R D 1987 In *Refurbishment and life extension of steam plant* (London: Inst. Mech. Eng.) p. 223
- Wiegand H, Granachar J, Sander M 1975 *Arch. Eisenhutenwesen* 45: 533-539
- Zarrabi K 1993 *Int. J. Pressure Vessels Piping* 53: 351-358

*These references are not in our usual format. Readers may please bear with us

ACADEMY PUBLICATIONS IN ENGINEERING SCIENCES

Volume 1. The Aryabhata Project (eds U R Rao, K Kasturirangan)

Volume 2. Computer Simulation (eds N Seshagiri, R Narasimha)

Volume 3. Rural Technology (ed. A K N Reddy)

Volume 4. Alloy Design (eds S Ranganathan, V S Arunachalam, R W Cahn)

... written by eminent scientists of India and abroad... Academy deserves all praise in bringing out these [papers]

Powder Metall. Assoc. India, Newslett.

Volume 5. Surveys in Fluid Mechanics (eds R Narasimha, S M Deshpande)

An informal and stimulating publication... (provides) a survey of many important topics in Fluid Mechanics... All the papers are of excellent technical content and most are very well written. Many include lengthy reference lists, which are as useful as the body of the paper... The publishing quality is very good...

IEEE J. Ocean Eng.

... The general level (of papers) is high... Several are likely to have wide appeal...

J. Fluid Mech.

Volume 6. Wood Heat for Cooking (eds K Krishna Prasad, P Verhaart)

... interesting and stimulating account of technical thinking on the wood stove problem up to date... excellent collection of valuable and thought-provoking investigations.

Rev. Projector (India)

Volume 7. Remote Sensing (eds B L Deekshatulu, Y S Rajan)

... Several contributions are specifically addressing topics of national interest, however, the majority of the papers is of general interest for a wide community. The book can serve not only as an inventory of the Indian activities, but also as a textbook on techniques and applications of remote sensing.

Photogrammetria

... particularly refreshing...

Int. J. Remote Sensing

Volume 8. Water Resources Systems Planning (eds M C Chaturvedi, P Rogers)

... well got up and very well printed... forms a valuable addition to our limited literature on Water Resources of India.

Curr. Sci.

Volume 9. Reactions and Reaction Engineering (eds R A Mashelkar, R Kumar)

... eighteen portraits of some major frontiers of research in CRE by a Micro-Who's Who of contemporary CRE researchers... good mix of theory and experiment that will provide many a good read for the specialist as well as the generalist researcher... "must-buy" for all research libraries, corporate or personal that contain CRE titles.

Can. J. Chem. Eng.

Volume 10. Reliability and Fault-Tolerance Issues in Real-Time Systems (ed. N Viswanadham)

... should help the reader to obtain a global view of the design of real-time systems with specifications in reliability and fault tolerance.

IEEE Control Syst. Mag.

Volume 11. Composite Materials and Structures (ed. K A V Pandalai)

... will surely find its place in libraries dealing with applied research.

Bull. Electrochem.

Volume 12. Developments in Fluid Mechanics and Space Technology (eds R Narasimha, A P J Abdul Kalam)

Volume 13. Advanced Ceramics (ed. E C Subbarao)

... presents a comprehensive view of advanced ceramics... should be of interest to students, research scientists, development engineers and to those engaged in the modern ceramic industry.

Ind. Ceram.

... most of the chapters put stress not only on the science, but also on the technological aspects.

Trans. Indian Ceram. Soc.

Volume 14. Modelling and Control of Stochastic Systems (eds N Viswanadham, V S Borkar)

Volume 15. Parallel and Real-Time Distributed Computing (ed. R K Shyamasundar)

Foreword

Structural mechanics deals with how engineering structures such as buildings, airplanes, vehicles, rotating machines etc. behave under external service loads and natural forces. Traditionally the subject has been divided into statics and dynamics. Thus structural dynamics is the study of civil, mechanical and aerospace engineering structures under dynamic forces due to earthquakes, wind turbulence, waves, jet noise, blade rotation, moving loads, mass imbalance and other causes. Many of these forces exhibit randomness and hence the need for stochastic structural dynamics. Over the years, the theory of linear systems under deterministic and stochastic inputs has been well developed. However owing to large displacements or inelastic material properties, structural systems exhibit nonlinearity. Nonlinearity in engineering dynamical systems is quite complicated to handle under either deterministic or stochastic inputs. Exact solutions are not common. Even when such solutions are available they refer to overly simplified systems under excitations which are often unrealistic. Thus a frontier area of research in structural dynamics has been the investigation of complex nonlinear systems under deterministic and stochastic excitations. The present issue of *Sādhanā* brings out some of the recent advances in this field. In all, in this issue there are twenty papers contributed by research workers from eight countries.

The first paper is a review on nonlinear random vibration. Manohar presents a detailed state-of-the-art review on exact and approximate approaches to nonlinear systems under random excitation. The response of nonlinear systems under the influence of white noise can be shown to be a Markov vector process. Hence the probability density of the response vector satisfies the Fokker-Planck-Kolmogorov (FPK) equation. However, exact solutions for the FPK equation are difficult to obtain. The paper by Anh discusses how the averaging method which is popular in deterministic problems can be used to integrate the FPK equation. The van der Pol oscillator has been the classical example of a nonlinear system exhibiting a basic limit cycle. Naess and Hegstad study this oscillator under a white noise excitation. They solve the associated FPK equation numerically by the path integral method. Experimental work in nonlinear random vibration is difficult and hence uncommon. Ibrahim and Lee have experimentally investigated the random response of a nonlinear beam under white noise excitation to verify the results of closure methods and numerical simulation. Heuer *et al* study the nonlinear vibration of shallow shells made up of composite materials under white noise excitations. The response is a diffusion process and hence using the FPK equation approach it is possible to arrive at some interesting results on the probability of snap buckling of the structure. Homology design, attempts at realizing the desired modes of vibration of structures with specified constraints. Nakagiri and Yoshikawa investigate such a problem for out of plane vibration of a planar frame under uncertain boundary conditions which introduces nonlinearity into the problem.

The next three papers investigate active control of structures under random inputs. Karmeshu and Schurz study the stability of simple linear and nonlinear elastic oscillators with distributed delays under stochastic seismic inputs. In practice, civil engineering structures such as tall buildings are hysteretic. Suzuki presents a method for optimal control of hysteretic structural systems under earthquake excitations, modelled in terms of white noise processes. The system and observation equations are handled in terms of Itô stochastic calculus. Approximate solution procedures based on linearization and closure techniques have been presented. Raju and Narayanan investigate the active control of a moving vehicle modelled as a two degree-of-freedom system with nonlinear suspensions. Equivalent linearization approximation has been used to arrive at a linear model of the problem for further analysis. Dynamics of offshore structures is a typical practical example wherein nonlinearity and stochasticity are present. Venkataramana and Kawano study the response of two models of offshore structures in random seas under seismic excitation. Nonlinearity enters through the hydrodynamic damping term. Datta *et al* study the nonlinear response of guyed towers, under random wave forces. These structures are extremely flexible with very low natural frequencies. This necessitates inclusion of second-order wave forces in the dynamic analysis.

In recent years the phenomenon of chaos in nonlinear oscillator is attracting considerable attention. There are six papers devoted to various aspects of chaos. Sekar and Narayanan present a state-of-the-art review. Namachchivaya *et al* study the bifurcation behaviour in two-degree-of-freedom shallow arches under periodic and stochastic excitations. Through the Melnikov method it is shown that chaos is possible. Schiehlen and Hu introduce a stability measure to study system sensitivity to initial conditions and other parameters. The concept is illustrated with the help of the Duffing oscillator. Popp *et al* study in some detail friction induced stick-slip oscillators. They investigate for a friction oscillator the bifurcation behaviour and routes to chaos. Bontempi and Casciati consider the nonlinear dynamics of a truss with several bars and nodes. It is demonstrated that the Kolmogorov entropy can be used as a tool to detect chaotic response. Chandiramani *et al* investigate the nonlinear flutter of a buckled composite panel. Their theory includes effects of in-plane edge restraints, initial imperfections, transverse shear and direct stresses in the model. Periodic solutions and bifurcations are found under a supersonic flow. They demonstrate that chaos is possible under certain conditions.

The last three papers address three different problems in nonlinear structural dynamics. Ghanem *et al* study the nonlinear oscillations of a two degree-of-freedom structural cylinder model in oscillatory flow. Hydrodynamic forces are imposed using available results from theoretical fluid mechanics. Higher order harmonic solutions are obtained using classical methods of nonlinear oscillations. Nonlinear mechanical systems are popularly analysed through equivalent linearization approximation. Fai Ma proposes a method for handling the equations of motion of linearized controlled structures. Such systems possess stiffness and damping matrices which are not necessarily symmetric. The method is an extension of classical modal analysis and hence appeals to structural engineers. Special approaches have been developed in the active control of space structures. One such method is by embedding piezoelectric materials in the panels so that sensing and actuating mechanisms become part of the structure. Reddy and Mitchell develop theories for laminated composite plates with piezoelectric laminae. These theories include coupling between the elastic, thermal and electrical

fields. The nonlinear equations of motion for in-plane and bending vibrations of such plates have been derived.

It has given me immense satisfaction to have worked on this special issue. I am grateful to the authors and to the reviewers for their cooperation. I thank the editorial board of *Sādhanā* for giving me this opportunity to bring out this special issue. As guest editor I enjoyed my interactions with the editorial office of the Indian Academy of Sciences.

June 1995
Roorkee

R N IYENGAR
Guest Editor



Methods of nonlinear random vibration analysis

C S MANOHAR

Department of Civil Engineering, Indian Institute of Science, Bangalore
560 012, India

Abstract. The various techniques available for the analysis of nonlinear systems subjected to random excitations are briefly introduced and an overview of the progress which has been made in this area of research is presented. The discussion is mainly focused on the basis, scope and limitations of the solution techniques and not on specific applications.

Keywords. Nonlinear systems; random excitations; nonlinear vibration; vibration analysis.

1. Introduction

Random vibration methods are extensively used in earthquake, wind, transportation and offshore structural engineering applications. Here, the uncertainties in specifying the forces acting on the structure are quantified using sophisticated load models based on the theory of probability and stochastic processes. Consequently, the response analysis of structures is also carried out in a probabilistic framework which eventually leads to the assessment of the safety of the structure. In order to maintain a consistent level of sophistication in modelling, the vibrating structure also needs to be modelled with care. This concern leads to questions on modelling nonlinear behaviour of the structural system and also on modelling uncertainties in specifying the structural parameters themselves. The questions of structural nonlinearity are particularly important while addressing the problem of failures and safety assessments, especially, since the nonlinear response is, at times, radically different from the one obtained using a simplified linear model. These questions offer considerable challenge to the analyst and are currently being actively pursued in vibration engineering research as evidenced by a continuous stream of publications in leading international journals. The present paper aims at presenting an overview of the research work in this field highlighting the developments which have taken place over the last decade. The emphasis is, therefore, to focus on the various techniques and methodologies, which have admittedly come to stay as powerful tools in dealing with problems encountered frequently in the area of nonlinear random vibrations.

The sources of nonlinearities in vibration problems can be categorized into four groups:

- Geometric nonlinearities arising out of large deformations;
- nonlinear elastic and dissipation properties of the structural material;

- topological causes as in the case of vibroimpact systems such as rocking blocks and systems with stoppers;
- fluid-structure interactions leading to nonlinear couplings.

Table 1 lists a few examples which have been studied in the literature in the context of nonlinear random vibration of engineering structures. In these problems closed form solutions are rarely possible. Moreover, there exists no single general analytical procedure which leads to acceptable solution under all circumstances. The influential factors in formulating the solution procedures are

- System degrees of freedom, nature of nonlinearity (that is, nonlinearity in mass, stiffness or damping and symmetry/asymmetry of nonlinearity), predominance of the nonlinearity in affecting the system behaviour, including quasiperiodicity and bifurcations, in the absence of random excitations,
- Stationarity/nonstationarity of excitation, probability distribution and strength of excitation,
- Excitation bandwidth in relation to system bandwidth,
- Mechanism of excitation, that is, external or parametric,
- Response variables of interest.

Accordingly, several approximate solution procedures have been developed which lead to acceptable solutions in specific problem domains. Mostly, the approximations are based on the Markovian nature of the response or on the proximity of the response probability density function (pdf) to Gaussian distributions. Many of the methods are ingenious extensions of deterministic nonlinear analysis procedures to stochastic problems. A discussion on the following methods is presented in the sequel: (i) Markov vector approach, (ii) Perturbation, (iii) Equivalent linearization, (iv) Equivalent non-linearization, (v) Closure, (vi) Stochastic averaging, (vii) Stochastic series solution and (viii) Digital simulations.

2. Markov vector approach

When the inputs arise from Gaussian white noise processes the response will be a diffusion process and the associated transitional pdf (tpdf) will satisfy the well-known Kolmogorov equations. The governing equations of motion in these situations can be cast in the form of equations of the Itô type as follows:

$$d\mathbf{X}(t) = f(\mathbf{X}(t), t)dt + G(\mathbf{X}(t), t)d\mathbf{B}(t), \quad (1)$$

under the initial conditions

$$\mathbf{X}(t_0) = \mathbf{Y}, \quad (2)$$

where, $\mathbf{X}(t) = n \times 1$ response vector, $f(\mathbf{X}(t), t) = n \times n$ matrix, $G(\mathbf{X}(t), t) = n \times m$ matrix, $\mathbf{B}(t) = m \times 1$ vector of the Brownian motion processes having the properties

$$\mathbf{E}[\Delta_j(t)] = \mathbf{E}[B_j(t + \Delta t) - B_j(t)] = 0, \quad (3)$$

$$\mathbf{E}[\Delta_i(t)\Delta_j(t)] = 2D_{ij}\Delta t, \quad (4)$$

and $\mathbf{Y} = n \times 1$ vector of initial conditions independent of $\mathbf{B}(t)$. Here $\mathbf{E}[\cdot]$ represents the mathematical expectation operator. The above representation of equations of motion

Table 1. Example of nonlinear engineering vibrating systems.

Nonlinear system	Model	Equation of motion	Reference
Frictional seismic base isolation system	Coloumb's oscillator	$\ddot{x} + \mu g \operatorname{sgn}(\dot{x}) + \omega^2 x = -\ddot{\mu}_g(t)$	Ahmadi & Su (1987)
Plate undergoing large amplitude vibrations	Duffing's oscillator	$\ddot{x} + 2\eta\omega\dot{x} + \omega^2 x + \alpha x^3 = f(t)$	Lin (1967)
Hysteretic structure	Bouc's oscillator	$m\ddot{x} + c\dot{x} + \alpha kx + (1 - \beta)kz = f(t)$ $\dot{z} = (1/\eta)[A\dot{x} - \nu(\beta \dot{x} z z ^{n-1}z - \gamma\dot{x} z ^n)]$	Wen (1989) Iyengar & Dash (1978)
Vibro-impact system	Rectangular rocking block	$I\ddot{\theta} + WR \sin(\alpha \operatorname{sgn} \theta - \theta)[1 + f(t)]$ $+ WR \cos(\alpha \operatorname{sgn} \theta - \theta)g(t) = 0$ $\dot{\theta}(t^*) = c\dot{\theta}(t^*); t^*: \theta(t^*) = 0.$	Spanos & Koh (1986) Iyengar & Manohar (1991)
Across wind oscillation of chimneys	Van der Pol's oscillator	$m\ddot{y} + c\dot{y} + ky = \alpha_1\dot{y} + \alpha_2\dot{y}^3 + f(t)$	Vickery & Basu (1983) Manohar & Iyengar (1991a, b)
Ship rolling in random seas	—	$\ddot{\phi} + \varepsilon^2 F(\dot{\phi}) + \omega^2 \phi [1 + k\varepsilon^2 \phi^2 + \varepsilon f(t)] = \varepsilon f(t)$	Roberts (1982)
Offshore structure under wave loads	Modified Morrison's model	$M\ddot{X} + C\dot{X} + KX = P(t)$ $P_i(t) = \frac{1}{2}C_D\rho A_i[u_i(t) - \dot{x}_i(t)] u_i(t) $ $- \dot{x}_i(t) + C_M\rho V_i\dot{u}_i(t) - \dot{C}_M\rho V_i\ddot{x}_i(t)$	Taylor & Rajagopalan (1982)

is fairly general in the sense that it allows for: (1) Multi-degree linear/nonlinear discrete systems, (2) external and parametric excitations, (3) nonstationary excitations, (4) nonwhite excitations, in which case, additional filters to model inputs as filtered white noise processes are to be appended to the system equations with a consequent increase in the size of the problem and (5) random initial conditions. The Kolmogorov equations satisfied by the response tpdf, $p(\mathbf{x}, t | \mathbf{y}, t_0)$ are

- the Chapman-Kolmogorov-Smoluckowski (CKS) integral equation

$$p(\mathbf{x}, t | \mathbf{y}, t_0) = \int_{-\infty}^{\infty} p(\mathbf{x}, t | \mathbf{z}, \tau) p(\mathbf{z}, \tau | \mathbf{y}, t_0) d\mathbf{z}, \quad (5)$$

- the forward equation or the Fokker-Planck-Kolmogorov (FPK) equation

$$\begin{aligned} \frac{\partial p(\mathbf{x}, t | \mathbf{y}, t_0)}{\partial t} = & - \sum_{j=1}^n \frac{\partial}{\partial x_j} [f_j(\mathbf{x}, t) p(\mathbf{x}, t | \mathbf{y}, t_0)] \\ & + \sum_{ij=1}^n \frac{\partial^2}{\partial x_i \partial x_j} [(GDG^T)_{ij} p(\mathbf{x}, t | \mathbf{y}, t_0)], \end{aligned} \quad (6)$$

- the backward equation

$$\frac{\partial p(\mathbf{x}, t | \mathbf{y}, t_0)}{\partial t_0} = - \sum_{j=1}^n f_j(\mathbf{y}, t) \frac{\partial p(\mathbf{x}, t | \mathbf{y}, t_0)}{\partial y_j} - \sum_{ij=1}^n [GDG^T]_{ij} \frac{\partial^2 p(\mathbf{x}, t | \mathbf{y}, t_0)}{\partial y_i \partial y_j}. \quad (7)$$

In these equations, the superscript T denotes the matrix transpose operation. The first of these equations represents the consistency condition for the response process to be Markov. Equation (7) is the adjoint of (6) and these two equations can be derived using (5) together with the equation of motion given by (1). It is of interest to note that the forward equation and backward equations are also satisfied by several other response probability functions of interest. Thus, for instance, the probability, $Q(t | \mathbf{y}, t_0)$, that first passage across a specified safe domain will not occur in the time interval $t_0 - t$ for trajectories in the phase plane starting at \mathbf{y} at $t = t_0$, can be shown to satisfy the backward Kolmogorov equation. The formulation of these equations leads to the exact response characterization of a limited class of problems and helps in formulating strategies for approximate analysis for a wider class of problems. The details of the derivation of these equations along with a discussion on the initial conditions, boundary conditions, well posedness, eigenvalues and eigenfunctions and the existence, uniqueness and stability of stationary solutions can be found in the works of Bharucha Reid (1960), Stratonovich (1963), Caughey (1963a, 1971), Feller (1966), Fuller (1969) and Roberts (1986a). A comprehensive treatment of the FPK equation and its application in physical sciences is available in the monographs by Risken (1989) and Horsthemke & Lefever (1984).

2.1 Exact solutions

The complete solution of the FPK equation is obtainable for all externally forced linear oscillators (Lin 1967) and for a class of first order nonlinear systems (Caughey & Dienes 1961; Stratonovich 1963; Atkinson & Caughey 1968; Atkinson 1973). In these solutions either the Fourier and Laplace transform techniques or the method of eigenfunction expansion is used. Methods based on group theory have also been developed (Bluman,

1971). The stationary solution, when it exists, can be found for all first order systems and for a limited set of higher order systems. A general class of systems for which exact stationary solution under external white noise excitation is possible is discussed by Caughey & Ma (1982a, 1982b). This set includes single degree of freedom (sdf) systems with nonlinear stiffness and a class of sdf and multi-degree of freedom (mdof) systems with nonlinear damping and stiffness. Dimentberg (1982) has obtained stationary pdf for a specific sdf system in which both parametric and external white noise excitations are present. This solution has been obtained through an inverse procedure (Dimentberg 1988a). Here an approximate solution is first obtained based on the method of stochastic averaging. This solution is substituted into the governing FPK equation for the original system. This equation would be exactly satisfied provided the system's parameters are related in a certain special way. Thus, this subset of parameters defines a class of systems for which the governing reduced FPK equation is solvable. The concept of detailed balance developed earlier by physicists (Gardiner 1983; Risken 1989), has been used by Yong & Lin (1987) and Langley (1988a) to obtain exact stationary solution for a class of sdf and mdof nonlinear systems under white noise excitations. In this method, the components of response vector \mathbf{Y} are classified as either even or odd depending upon their behaviour under a time reversal of t to $-t$. The even variables do not change their sign whereas the odd variables undergo a change of sign. These are denoted as

$$\tilde{x}_i = \varepsilon_i x_i, \quad \text{no summation on } i, \quad (8)$$

where $\varepsilon_i = 1$ for even variables and $\varepsilon_i = -1$ for odd variables. The state of detailed balance is defined as

$$p(\mathbf{x}, t | \mathbf{y}, t_0) = p(\tilde{\mathbf{y}}, t | \tilde{\mathbf{x}}, t_0), \quad t > t_0. \quad (9)$$

In the steady state, in terms of the drift coefficients A_i and diffusion coefficient B_{ij} this condition is given by

$$A_i(\mathbf{x})p(\mathbf{x}) + \varepsilon_i A_i(\tilde{\mathbf{x}})p(\mathbf{x}) - \frac{\partial}{\partial x_j} [B_{ij}(\mathbf{x})p(\mathbf{x})] = 0, \quad (10)$$

$$B_{ij}(\mathbf{x}) - \varepsilon_i \varepsilon_j B_{ij}(\tilde{\mathbf{x}}) = 0. \quad (11)$$

Here summation on repeated index is implied. When these conditions are satisfied, the stationary solution expressed as

$$p(\mathbf{x}) = C \exp[-U(\mathbf{x})], \quad (12)$$

can be obtained by solving the equation for $U(\mathbf{x})$, the generalized potential. The class of problems than can be solved using this method, is shown to include the problems considered by Caughey & Ma (1982a, b) and Dimentberg (1982). Furthermore, Lin & Cai (1988) and Cai & Lin (1988a) have shown that the exact stationary solution as in (12) can still be obtained even when one of the conditions for detailed balance, namely (11) is not satisfied. This class of systems has been termed as belonging to the class of generalized potential. More general class of exactly solvable FPK equations have been discussed by Zhu *et al* (1990) and To & Li (1991).

2.2 Approximate methods

For analysing problems possessing no exact solutions one has to take recourse to approximate methods. An iterative procedure based on the parametrix method for

studying existence and uniqueness of solutions of partial differential equations (Friedman 1964) has been used by a few authors (Caughey 1971; Mayfield 1973). It has been shown that both transient and steady state solutions can be obtained using this method. Also, the method is useful in improving approximate results obtained by other techniques. However, the method has not been used widely in random vibration studies (Roberts 1981). Payne (1968) used a combination of perturbation and eigenfunction expansion techniques to analyse nearly linear first order systems under white noise inputs. He has derived perturbation expansion for eigenvalues and eigenfunctions of the FPK equation up to $O(\varepsilon^2)$ and obtained the corresponding expression for response autocorrelation function. Here ε may be denoted as a smallness parameter associated with the nonlinearity. Iwan & Spanos (1978) have employed similar techniques to obtain nonstationary response envelope distribution of a linear sdof system. Johnson & Scott (1979, 1980) considered the first order system studied by Payne (1968) and extended his analysis to compute expansion terms up to $O(\varepsilon^7)$. Furthermore, they have also applied this method to second-order systems.

Atkinson (1973) has used an adjoint variational method to find the eigenvalues of the FPK operator. He has generated trial functions that are orthogonal to known stationary solution and has determined response power spectral density (psd) for the case of a Duffing oscillator, a bang-bang system and a system with nonlinear damping. Toland *et al* (1972) proposed a random walk analogy based on a discrete approximation to continuous Markov process, and obtained a recurrence relation for response probabilities. This technique is equivalent to using finite difference approximation on the FPK equation and is time consuming especially when the domain of integration is large. The eigenfunction expansion method is applicable when the time and space variables in the FPK equation can be separated which is generally possible when the drift and diffusion terms are time invariant. In a more general context, the methods of weighted residual have been employed by several authors. Thus, Bhandari & Sherrer (1968) have used the Galerkin technique to find the stationary response of sdof and a two degree of freedom system with polynomial nonlinearities. Wen (1975, 1976) has extended this analysis to nonstationary response analysis and studied the response of the Duffing oscillator and a hysteretic system. The use of the method in determining psd response and the first excursion failure probabilities of response has also been indicated. A similar technique has been used by Solomos & Spanos (1984) for obtaining the amplitude response of a linear sdof system under evolutionary random excitation. Another variant of the weighted residual technique, namely, the method of moments, has been used by Fujita & Hattori (1980) for the analysis of sdof systems with collisions under modulated white noise input. Langley (1985) has applied the finite element method to solve the two dimensional FPK equation associated with the stationary response of a Duffing oscillator and a ship rolling problem. The domain in the phase space to be covered by finite elements was estimated using an equivalent linearization solution. An improper selection of the extent of the domain is shown to result in negative values for response pdf. Bergman & Spencer (1992) have studied the transient solutions of the FPK equations of several second order nonlinear systems using finite element method.

Other discretization procedures based on path integral formalisms (Wehner & Wolfer 1983; Kapitanik 1985, 1986; Naess & Johnsen 1993) and cell mapping techniques (Sun & Hsu 1990) have also been developed. These methods are related to the iterative technique discussed by Crandall *et al* (1966) and are based on an assumption that

the tpdf over short time steps is Gaussian. Sun & Hsu have used a Gaussian closure approximation to evaluate the transitional probabilities, while, Naess and Johnsen have employed cubic **B**-splines to represent the tpdf. It is to be noted that although the analysis makes the short-time Gaussian approximation for the tpdf, the global non-Gaussian nature of the unconditional pdf is, nevertheless, captured by the analysis.

2.3 Generalizations and moment equations

Generalization of the FPK equation to non-diffusive Markov processes has been discussed by Pawula (1967). Here the inputs are modelled as white noise arising out of non-Gaussian processes. The response in such cases will still have the Markovian property but the equation of motion of the transitional pdf will have infinite number of terms. Tylikowski & Marowski (1986) have considered the response of a Duffing oscillator to Poissonian impulse excitation and have shown that the transitional pdf satisfies an integro-partial differential equation. The use of truncated generalized FPK equations in computing the lower order moments has been demonstrated by Risken (1989).

When response moments are of interest, the governing equations for the moments can be derived based on the FPK equation (Soong 1973). Thus, the moments of the function $h[\mathbf{X}(t), t]$ of the solution $\mathbf{X}(t)$ of (1) can be shown to be governed by the equation

$$\frac{d}{dt} \mathbf{E}[h(\mathbf{X}, t)] = \sum_{j=1}^n \mathbf{E} \left[f_j \frac{\partial h}{\partial x_j} \right] + \sum_{ij=1}^n \mathbf{E} \left[(GDG^T)_{ij} \frac{\partial^2 h}{\partial x_i \partial x_j} \right] + \mathbf{E} \left[\frac{\partial h}{\partial t} \right]. \quad (13)$$

By setting $h[\mathbf{X}(t), t] = X_1^{k_1} X_2^{k_2} X_3^{k_3} \dots X_n^{k_n}$ and choosing different values for k_i , one can derive equations for the most commonly used moments. These equations can be readily solved for the case of deterministic nonautonomous linear systems under white noise inputs. This forms the basis for obtaining approximate transient solutions using linearization procedures. In the case of linear oscillators with parametric white noise excitations, the response is non-Gaussian and the associated FPK equation is not solvable. However, the exact response moments can be obtained by solving the associated moment equations. In nonlinear problems these equations form an infinite hierarchy and an exact solution of moment equations also is not possible. Based on the principle of maximum entropy, Sobczyk & Trebicki (1990, 1992) and Chang (1991) have developed approximate stationary solutions of nonlinear systems under parametric and external noise excitations. This consists of employing pdf with undetermined coefficients which, in turn, are found by maximizing the entropy subject to the constraints of the pdf normalization and the moment equations which are obtained through the governing FPK equations. Roy & Spanos (1991) have utilized a perturbation solution scheme for the moment equations and have shown that the scheme overcomes the problem of infinite hierarchy. They have proposed Pade type transformations of the series which enables the analysis to be applicable even for strongly nonlinear systems. Furthermore, the same authors (Roy & Spanos 1993) have studied the response power spectral density of nonlinear systems by utilizing formal solutions of the FPK equation as discussed by Risken (1989) in conjunction with a power series expansion in terms of Pade approximants for the response spectra. The method requires the knowledge of the stationary response of the FPK equation.

As has been briefly indicated earlier, the Markov property of response has also been used in the study of first passage probabilities. Here, either the forward or the backward Kolmogorov equation is solved in conjunction with appropriate boundary conditions imposed along the critical barriers. Alternatively, starting from the backward Kolmogorov equation, one can also derive equations for moments of the first passage time, which, in principle, can be solved recursively. Thus, denoting by $\tilde{T}(\mathbf{y})$, the time required by the response trajectory of (1) initiated at the point $\mathbf{x} = \mathbf{y}$ in the phase space at time $t = t_0$ to cross a specified safe domain for the first time, the moments $M_k = E[\tilde{T}^k]$, $k = 1, 2, \dots, N$, can be shown to be governed by the equation

$$-\sum_{j=1}^n f_j(\mathbf{y}, t) \frac{\partial M_k}{\partial y_j} - \sum_{ij=1}^n (GDG^T)_{ij} \frac{\partial^2 M_k}{\partial y_i \partial y_j} + k M_{k-1} = 0 \quad (k = 0, 1, 2, \dots), \quad (14)$$

with the condition $M_0 = 1$. These equations are referred to as the generalized Pontriagin-Vitt (GPV) equations in the literature. Although no exact analytical solution exists for finding M_k , several approximations are available and they have been reviewed by Roberts (1986a). These methods include method of weighted residuals (Spanos 1983), random walk models (Toland & Yang 1971; Roberts 1978), finite difference method (Roberts 1986b), finite element method (Spencer & Bergman 1985) and cell mapping techniques (Sun & Hsu 1988).

2.4 Summary

The FPK equation approach is the only source of exact solutions in nonlinear random vibration problems. It also forms a powerful tool for approximate analysis. The application of the method is, however, limited to Markovian responses. The solution procedures are not tractable when dealing with large number of variables or with nonstationary inputs. Although the method is applicable when the input is a filtered white noise, this class of problems has not received much attention in the literature.

3. Perturbation method

This is a straightforward extension of the technique used in deterministic problems. The method is applicable when the equations of motion contain a small parameter characterizing the nonlinearity in the system. The solution is expanded in a power series in small parameter which leads to a set of linear differential equations which can further be solved sequentially. The method is applicable to both sdof and mdof systems under additive or multiplicative, stationary or nonstationary stochastic inputs. It was first used by Crandall (1963) to evaluate response moments of sdof and mdof systems with nonlinear stiffness under stationary Gaussian excitations. Shimogo (1963a, b) considered symmetric and asymmetric nonlinear systems under stationary random inputs and computed the response psd using an iterative technique, which, in essence, is identical to the perturbation method. Crandall *et al* (1964) and Khabbaz (1965) applied the method to systems with nonlinear damping and evaluated the response psd. They also indicated the possibility of the even ordered response moments and the psd function becoming negative for large values of the nonlinearity parameter. To a first order of approximation, the psd function obtained

using this method and the equivalent linearization technique have been shown to be identical (Crandall 1964). Manning (1975) has estimated the response of the Duffing oscillator to stationary excitation and has shown that by evaluating the response to second order of the nonlinearity parameter, it is possible to display the effects of nonlinear resonances in the response psd. The response of the Duffing oscillator to nonstationary random inputs has been studied by Soni & Surendran (1975). The application of the method to systems with random parametric excitation has been discussed by Soong (1973).

Perturbation method is well suited for polynomial nonlinearities and is useful in computing response moments and sometimes the psd function. Determination of the response pdf using this method is, however, not possible because of the non-Gaussian nature of the higher order corrections. Furthermore, obtaining second or higher order corrections involves cumbersome calculations and is not practicable. It can be noted that the method is asymptotic in nature and the accuracy markedly worsens with the increase in the value of the nonlinearity parameter.

4. Equivalent linearization

This method is by and large the most popular approach in nonlinear random vibration problems. It is extension of the well known harmonic linearization technique to stochastic problems and is applicable to both sdof and mdof systems under stationary or nonstationary inputs. The method consists of optimally approximating the nonlinearities in the given system by linear models so that the resulting equivalent system is amenable for solution. For evaluating the parameters in the equivalent system, an additional assumption that the response is Gaussian is generally made. This method was developed in 1950's in the context of random vibration problems (see Caughey 1963b for earlier references) and nonlinear stochastic controls (Booton 1954). The subsequent developments of the method in vibration problems may be found in the works of Spanos (1981a), Roberts & Spanos (1990) and Socha & Soong (1991) and those in the field of control in the work of Sinitsyn (1974).

Caughey (1963b) applied this technique to find stationary response of nonlinear sdof systems and a class of mdof systems under stationary inputs. The method was generalized to a wider class of mdof systems by Foster (1968), Iwan & Yang (1972) and Atalik (1974). When nonstationary response is of interest the equivalent parameters will be functions of time and accordingly the equivalent linear system will be time varying. For the case of Markovian responses Iwan & Mason (1980) and Wen (1980) have obtained the nonstationary response of mdof systems by solving numerically the moment equations derived from the governing FPK equation. Spanos (1980b) modified the method to deal with mdof systems having asymmetric nonlinearities in which case the response has a nonzero mean. When the inputs are nonwhite the solution of time varying equivalent linear system is generally difficult. Ahmadi (1980b) and Sakata & Kimura (1980) have suggested different schemes to deal with such problems. These schemes have also been extended to analyze the nonstationary response of asymmetric sdof and mdof systems to nonwhite inputs (Kimura & Sakata 1981, 1987). In the study of continuous nonlinear systems, linearization can be done after discretizing the equation of motion or at the level of partial differential equation itself. The latter class of problems have been studied by Iwan & Krousgrill (1983) and Iwan & Whirley (1993).

4.1 Extensions and improvements

The method is versatile, easy to implement and computationally efficient. It is applicable when the nonlinearities and the excitations are such that the response is unimodal and nearly Gaussian. This does not necessarily imply that the nonlinearity should be small. Crandall (1973) has demonstrated that for a first order system with cubic nonlinearities, the mean square response using this technique is fairly accurate even when nonlinearity parameter is of the order of 100. The method invariably leads to Gaussian response pdf and fails to display nonlinear resonances in the response psd. Furthermore, the method is not applicable to systems with parametric excitations.

Several modifications to the method have been proposed to overcome some of the above limitations. Crandall (1973) has obtained a nonlinear integral equation for the improved estimate for the stationary response autocorrelations. Generalization of the method for the case of nonlinear systems with both parametric and external white noise excitations has been suggested by Bruckner & Lin (1987a). Here the original Itô equation for the nonlinear system is optimally replaced by a linearized Itô equation so that the first and the second moments computed from the equivalent system has minimum mean square error. For evaluating equivalent parameters use is made of the higher order moment equations and no appeal to the Gaussianness of the response nor for invoking any other closure approximation is necessary. In the methods discussed above the nonlinear system of a given order is invariably replaced by an equivalent system of the same order. Iyengar (1988a) has explored the possibility of replacing a given nonlinear system by an equivalent linear system of a higher order. In his study the nonlinear terms of the given equation are substituted by new dependent variables. Additional equations which govern these new variables and which are nonlinear in nature are obtained by suitably differentiating the given nonlinear equation. The resulting higher order system of nonlinear equations is further analyzed using the usual linearization scheme. For the case of the Duffing oscillator under white noise excitation, the results obtained using this method are shown to be better than the usual linearization solution and in particular, the response psd obtained using this method is shown to display the effects of secondary resonance in the form of an additional peak at about three times the primary resonance frequency. Extensions of equivalent linearization procedures to allow for non-Gaussian nature of the response have also been proposed. Thus, Manohar & Iyengar (1990) considered the broad band excitation of the Van der Pol oscillator and replaced the nonlinear oscillator by a linear system excited by a non-Gaussian input. The non-Gaussian excitation allowed for the limit cycle oscillations of the system in the absence of the external noise. This enabled the correct prediction of bimodal pdf of the response displacement and velocity which the traditional linearization fails to predict (Zhu & Yu 1987). Pradlwarter *et al* (1988), Pradlwarter (1989) and Schueller *et al* (1991) have considered stochastic response of inelastic systems and have proposed a non-Gaussian linearization scheme which is based on the theoretical results shown by Kozin (1987) that linear systems exist which lead, at least for white noise excitations, exactly to the first statistical moments of the response of the respective true nonlinear systems. The method involves nonlinear transformation between nonlinear response and the linear response which has to be chosen based on physical considerations. Iyengar (1992) considered Duffing's oscillator under narrow band excitation and developed an equivalent linear system whose stiffness parameter is random in nature. This parameter is shown to be a function of response

envelope which is approximated as a random variable. While the response conditioned on the stiffness is Gaussian, the unconditioned response becomes non-Gaussian in nature.

4.2 Nonuniqueness of solutions and stochastic stability

The solution obtained using equivalent linearization is not necessarily unique in more than one sense. Firstly, the answers depend on criterion of equivalence adopted. While the most commonly used criterion requires that the mean square equation difference be minimized, other criteria involving alternative norms of differences or other averaging operators are also admissible (Spanos 1981a; Bolotin 1984). Recently Elishakoff & Zhang (1993) have applied several optimization schemes on a randomly driven first order nonlinear system and have shown that, when the differences are averaged with respect to a weight function, which, in turn, is taken to be a nonlinear function of the system potential energy, the estimate of the response variance coincides with the known exact solution. Casciati *et al* (1993) have considered second order nonlinear systems under broad band excitation and established the equivalence by requiring that the upcrossing rate of a specified critical level for the nonlinear and for the equivalent linear oscillator be equal. Obviously the success of this approximation depends upon the accuracy with which the upcrossing statistics are known.

Another source of nonuniqueness, which is, perhaps more subtle, arises within the framework of a specified equivalence criterion. Thus, the linearization technique when applied to nonlinear systems under combined harmonic and noise excitations (Iyengar 1986; Manohar & Iyengar 1991a), narrow band excitations (Richard & Anand 1983; Davies & Nandlall 1986; Davies & Rajan 1986; Jia & Fang 1987; Iyengar 1988b, 1989; Manohar & Iyengar 1991b; Roberts 1991; Kolioupoulos & Langley 1993) or for systems with multiple stable equilibrium states under broad band excitations (Langley 1988b; Fan & Ahmadi 1990) leads to multivalued response statistics. It may be noted in this context that Spanos & Iwan (1978) have earlier demonstrated the uniqueness of equivalent linear systems under certain conditions but not of the solutions generated by the equivalent systems.

The occurrence of multivalued response statistics apparently resemble the coexistence of multiple steady states encountered in the deterministic nonlinear oscillation problems. In random vibration context, however, it is important to note that stationary response statistics, when they exist, are necessarily unique. This follows from the fact that the steady solution of the governing FPK equation is always unique (Fuller 1969). The scope of this result includes all the nonlinear dynamical systems which are governed by equations of the form as given in (1) and, as has been noted in § 2, this class is fairly extensive. This fact was not recognized in some of the earlier studies on narrow band excitation of the Duffing oscillators (Davies & Nandlall 1986; Davies & Rajan 1986; Jia & Fang 1987). These authors used a stability analysis of moment equations and concluded that response statistics are multivalued and display the jump behaviour. Iyengar (1986, 1988b, 1989) suggested that the realisability of the multiple solutions must be decided based on the almost sure stochastic stability of the multiple solutions and not on the stability analysis of moment equations. His study showed that in regions of multiple solutions, the linearization solution based on the assumption of Gaussianity of the response is stochastically unstable and, therefore, not valid. Furthermore, simulation studies on response amplitude showed that the probability density function

is bimodal in regions where linearization predicts multiple solutions. The studies by Langley (1988b) and Fan & Ahmadi (1990) on broad band excitation of nonlinear systems show that mean square response predicted by the linearization technique may not be unique while the corresponding exact solutions are unique. The system considered in these studies had multiple stable equilibrium states and the random response had multimodal probability density functions. The question of possible relationship between the multiple solutions predicted by linearization and local behaviour of the sample functions has been considered by few authors (Dimentberg 1988b; Roberts 1991; Koliopoulos & Langley 1993). It is suggested that the multiple solutions correspond to local behaviours near the modes of the response pdf. The relationship between such local behaviour and global behaviour in an ensemble sense is not obvious and further research is clearly required to resolve this issue.

5. Equivalent nonlinearization

This method is conceptually similar to the method of equivalent linearization and can be viewed as a generalization leading to non-Gaussian estimates for the response. The method has been introduced by Caughey (1986). It consists of replacing the given nonlinear system by an equivalent nonlinear system which belongs to the class of problems which can be solved exactly. This method is related to the class of exactly solvable FPK equations and thus is applicable only to systems under white noise inputs. The criterion of replacement is again the minimization of the mean square error. The method leads to non-Gaussian stationary response pdf and estimates correctly the random response of limit cycle systems in which case, equivalent linearization fails. Cai & Lin (1988b) have developed a similar technique and have applied it to systems in which parametric excitations are also present. Here, the replacement oscillator belongs to the class of systems possessing generalized stationary potential and is selected on the basis that the average energy of dissipation remains unchanged. For a specific system, the solution obtained using this method is shown to be superior to that obtained by stochastic averaging. The application of the method to randomly excited hysteretic structures has also been developed (Cai & Lin 1990). The method has also been studied by Zhu & Yu (1989) who have chosen equivalent nonlinear systems which are energy dependent. They have indicated that the method is asymptotically exact and is equivalent to the method of stochastic averaging of the energy envelope. In a study on random response of limit cycle systems, Manohar (1989) has developed equivalent nonlinearization solutions for the randomly driven Van der Pol oscillator. In one scheme, the Van der Pol oscillator under white noise excitation is replaced by a Van der Pol-Rayleigh oscillator which can be solved exactly. This involves linearization of only a part of the original equation and the equivalent parameters are found based on minimization of mean square error. In an attempt to model the multimodal pdf of the response phase process, Manohar has applied a similar partial linearization procedure to the simplified equations for the response amplitude and phase processes which, in turn, were obtained using a second order stochastic averaging procedure. Furthermore, the same procedure was also used to investigate the effect of noise on frequency entrainment of harmonically driven Van der Pol oscillator (Manohar & Iyengar 1991a) and in the study of rocking of rigid blocks under random base motions (Iyengar & Manohar 1991). The scheme of partial linearization has also been studied recently by

Elishakoff & Cai (1993). To & Li (1991) have presented a systematic equivalent nonlinearization procedure which is again based on the broad class of exactly solvable FPK equations and utilizes calculus of variations to derive the optimal replacement system. In a study on systems with asymmetric nonlinearities, Spanos & Donley (1991) and Li & Kareem (1993) have developed equivalent systems with quadratic nonlinearities. The evaluation of the equivalent parameters is based on an approximate analysis of the equivalent systems using Volterra series representations (see § 8).

6. Closure approximations

In nonlinear random vibration problems the equations for response moments and correlations form an infinite hierarchy and exact solutions are not possible. This is true even for the class of systems for which exact response pdf is obtainable using the FPK equation. The closure problem consists of approximately replacing the infinite hierarchy of equations with a finite set so that estimates for the important lower order moments can be obtained.

6.1 Closure using assumed probability density function

The closure approximation can be made either in conjunction with an assumed response pdf or directly on the moment equations. Dashevskii (1967), Assaf & Zirkle (1976) and Crandall (1980, 1985) have employed a series representation for response pdf in terms of the Hermite polynomials. The series is truncated after a finite number of terms. The first term in the series has the form of a Gaussian pdf. The unknown coefficients of the series are related to the response cumulants, central moments or expectations of the Hermite polynomials in response variables. The equations needed to determine these coefficients are generated from the governing equation of motion. This procedure can be viewed as the generalization of equivalent linearization technique wherein the response was assumed to be Gaussian and the parameters in the distribution were determined using moment identities derived from equations of motion. Liu & Davies (1988) have applied Hermite polynomial approximation for the pdf and studied the nonstationary response of nonlinear second-order systems. Furthermore, the same authors (Davies & Liu 1992) have also studied the power spectrum of Duffing's oscillator using a similar procedure. Iyengar (1975) and Iyengar & Dash (1976, 1978) have developed a closure technique in which the response variables and input variables, either as they appear or after a transformation, are assumed to be jointly Gaussian. It is possible in this formulation to take into account non-Gaussian excitations and amplitude limited responses. The method handles nonlinear and stochastically time varying systems in a unified manner (Dash & Iyengar 1982).

6.2 Closure in terms of moments or cumulants

In the second approach, one directly deals with moment equations. Here the unknown higher order moments are approximated as functions of lower order moments, thereby truncating the hierarchy of these equations. Thus, Ibrahim (1978), Ibrahim *et al* (1985), Bolotin (1984) and Wu & Lin (1984) have considered different schemes for closing

hierarchy of moment equations. Appeal is generally made to the quasinormal approximation which connects are higher order moments to the lower order moments through relations that are strictly valid only for Gaussian variables. This can be expressed in terms of either the direct moments, central moments or cumulants. The quasinormal approximation using cumulants amounts to setting cumulants beyond a given order to zero. For a Gaussian random variable, it may be recalled, all the cumulants beyond order two vanish. Other closure schemes such as discarding the direct or central moments beyond an order or ignoring the correlations among the response variables have also been proposed (Soong 1973). Bellman & Richardson (1968), Wilcox & Bellman (1970) and Sancho (1970) have used a mean square closure technique in which the unknown higher order moment is expressed as an optimal linear combination of lower order moments.

6.3 *Limitations and improvements*

The closure methods are applicable to a wide class of systems and excitations. They have been extensively used in the response and stability analysis of sdof and mdof systems with parametric and nonparametric excitations. However, it has not been possible to justify closure approximations through analytical approaches. Most of the closure schemes are theoretically inconsistent at some level as they violate well-known identities and inequalities of probability theory. Thus, for example, the moment closure scheme of setting direct moments beyond order n to zero violates the inequality $E[x^{2n}] > E[x^n]^2$. The cumulant closure violates the theorem due to Marcinkiewicz (Gardiner 1983) which states that the cumulant generating function cannot be a polynomial of order higher than two, that is, either all but the first two cumulants vanish or there are an infinite number of nonvanishing cumulants.

Bellman & Richardson (1968) have derived a condition under which the truncated equations obtained using the mean square closure technique preserves moment properties. No similar results are available for other closure schemes. Although it has been demonstrated with a specific example that the accuracy of closure scheme systematically improves as the order of approximation is increased, examples to counter this are also readily available (Crandall 1985). Instances of the estimated pdf becoming negative have also been encountered (Crandall 1985). Sun & Hsu (1987) have applied second, fourth, and sixth-order cumulant neglect schemes to a specific problem for which exact stationary solution is available and they have delineated regions where the schemes yield acceptable results. In certain parameter regions the fourth- and sixth-order schemes are shown to predict erroneous behaviour including a faulty jump in the response. Fan & Ahmadi (1990) have considered a system with multiple stable equilibrium driven by white noise excitation. They have shown that the stationary response statistics generated by Gaussian closure and non-Gaussian cumulant neglect closure techniques are not unique and are dependent on initial conditions. This contradicts the uniqueness property of the stationary solutions of the FPK equation (see §4.1). Pawleta & Socha (1992) have compared approximate nonstationary solutions obtained using closure approximations with the corresponding exact solutions for the case of parametrically excited linear systems and have shown that near stability boundaries the approximations are not acceptable.

The second-order cumulant neglect and the Gaussian closure techniques are similar to equivalent linearization method and are consistent closure schemes. However, they

yield acceptable results only when the response has features of Gaussian variables. For example, when applied to random vibration of self-excited systems (Bolotin 1984) they lead to drastically wrong results (Zhu & Yu 1987; Manohar & Iyengar 1990) (see § 4.1). Recently Grigoriu (1991) has developed a consistent closure procedure which is based on an estimator of the response pdf that consists of superposition of specified kernels weighted by undetermined parameters. These unknown parameters are determined based on the criterion that the moment equations are optimally satisfied up to a specified closure level.

7. Stochastic averaging methods

In these methods the response of lightly damped systems to broad band excitation is approximated by a diffusion process. The coefficients of the associated FPK equation are derived based on an appropriate averaging of the equations of motion. The appeal of these methods lies in the fact that they often reduce the dimensionality of the problem and significantly simplify the solution procedures. On account of this advantage they are also applied to systems wherein the response is already Markov. Different versions of the method are available and are widely used in the problems of response prediction, stability analysis and the first passage and fatigue failure analyses. Extensive surveys of related literature have been published (Ibrahim 1985; Roberts & Spanos 1986; Roberts 1986a; Zhu 1988).

7.1 *Averaging of amplitude and phase*

The method was originally proposed by Stratonovich (1963, 1967) as a generalization of the deterministic averaging method developed earlier by Bogoliubov and Mitropolsky (1961). He considered sdof nonlinear systems under random excitation and showed that when the relaxation time of the oscillator is large compared to the correlation time of the excitation, the response can be approximated by a diffusion Markov process. Subsequently, Khasminskii (1966) provided a rigorous mathematical proof for Stratonovich's arguments. The necessary requirements for applying the method are satisfied if the system is lightly damped and the excitation power spectrum is slowly varying in the neighbourhood of the system's natural frequency. The response in such a case will be a narrow band process with slowly varying amplitude and phase. The averaging procedure is a combination of temporal and ensemble averaging and it aims at eliminating rapid oscillations from the dominant slowly varying components and also at replacing randomly fluctuating components by equivalent delta correlated processes. This results in a pair of Itô differential equations for amplitude and phase which will have to be analysed using the FPK equation. In many cases the equation for amplitude gets uncoupled from that of the phase thus enabling the determination of the stationary distribution of the amplitude process. In fact this is the main advantage of this method. In order to determine the stationary pdf of displacement and velocity variables, the knowledge of joint pdf of amplitude and phase is essential. But it is in general difficult to obtain this pdf. However under the assumption that amplitude and phase are independent it is still possible to obtain an approximation to pdf of displacement and velocity.

Stratonovich used this method to examine the response of sdof self-excited systems to parametric and nonparametric excitations. Subsequently, the method has been generalized to include mdof systems and nonstationary inputs and widely used in

random vibration studies (Roberts & Spanos 1986). The method has also formed the basis for the study of first passage failures (Roberts 1986a) and stability analysis (Ibrahim 1985). For problems wherein the time varying nature of the system such as deterministic excitations or nonstationary inputs needs to be preserved, Lin (1986) has proposed that the temporal averaging in Stratonovich's procedure may be dispensed with. Heuristic arguments for relaxing restrictions on time constants of input and response for problems of stability analysis have also been given.

7.2 *Quasistatic averaging*

A variation of the standard stochastic averaging method, known as the method of quasistatic averaging, has also been developed by Stratonovich (1967). The method is applicable to problems in which the correlation time of the excitation greatly exceeds the relaxation time of the system. This requirement is contrary to the one stipulated for the applicability of the standard stochastic averaging method. The method consists of only temporal averaging. The ensemble averaging with its attendant Markovian approximation is dispensed with. In applying this method, envelope representation is used for both the input and the response processes. During temporal averaging the amplitude and phase angle are approximated as random variables and hence as constants. This finally leads to a nonlinear memoryless transformation relating the input and the output amplitudes and phase angles. Thus the solution of the given random differential equation is converted to a problem in nonlinear transformation of random variables. The method has been used in the study of nonlinear systems under narrow band excitations by several authors (Lennox & Kuak 1976; Sato *et al* 1985; Richard & Anand 1983; Iyengar 1986).

7.3 *Averaging of energy envelope*

The stochastic averaging method is found to give acceptable results for systems with nonlinear damping. In fact when damping is amplitude dependent and the excitation is white noise, the method leads to the known exact solutions (Roberts 1976). However, for a system with nonlinear stiffness, such as Duffing's oscillator, the solution does not display the effects of nonlinearity. In such cases a higher order averaging procedure needs to be used (Stratonovich 1967; Ibrahim 1985). This, however, involves cumbersome calculations. A simpler alternative is to examine whether a one dimensional Markovian approximation can be obtained for the energy envelope of the response. This was originally proposed by Stratonovich (1963) who considered systems under white noise inputs and reduced the two dimensional Markovian vector consisting of a slowly varying energy envelope and a rapidly varying displacement component to a one dimensional Markovian approximation for the energy envelope. This method has further been developed by Roberts (1976, 1978) and generalized to incorporate nonwhite inputs (Roberts 1982), parametric excitations (Zhu 1983) and nonstationary inputs (Red-Horse & Spanos 1992). Here, the averaging is carried out over a period equal to the undamped natural period of the system, which, now depends on the energy of the response. The results obtained using this method also agree with the available exact solutions. Zhu & Lin (1991) and Zhu *et al* (1994) have considered systems with correlated Gaussian excitations and have included the additional contributions to damping and stiffness made by the Wong-Zakai correction

terms. These additions are incorporated into the definition of the energy envelope and the consequent new results are shown to be improvements over earlier averaging results. Another version of stochastic averaging is also available (Sunahara *et al* 1977). In this a deterministic averaging is carried out directly on the coefficients of the governing FPK equation. This method has been shown to be equivalent to the averaging of the amplitude or the energy envelope of the response (Zhu 1988).

7.4 *Combination of averaging with other methods*

The method of stochastic averaging has also been used in combination with other methods of random vibration analysis. Thus, Iwan & Spanos (1978) proposed a combination of equivalent linearization and stochastic averaging to analyze systems with nonlinear stiffness. For the case of the Duffing oscillator under white noise input, the method improves the results obtained using averaging of response amplitude but does not lead to the exact solutions. Furthermore, Ariaratnam (1978) has questioned the consistency of approximations made in this analysis. Stratonovich (1967) has used equivalent linearization technique to solve simplified equations obtained using stochastic averaging. Bruckner & Lin (1987b) have adopted a complex form of stochastic averaging which eases the application of non-Gaussian closure technique to the simplified equations and is particularly useful in analyzing nonlinear mdof systems. In the study of nonlinear systems under combined harmonic and random excitations or when a higher order averaging in Cartesian co-ordinates is done, the resulting simplified equations do not get uncoupled, and, in general, are unsolvable within the framework of the Markov process theory. Under such situations Manohar & Iyengar (1990, 1991a) have proposed combining averaging with equivalent nonlinearization technique. This procedure is shown to give satisfactory results for the case of Van der Pol's oscillator under broad band and combined harmonic and white noise excitations.

7.5 *Method of stochastic normal forms*

An alternative way of reducing the dimensionality of the problem using modern bifurcation theories, *viz*, center manifold theory (Guckenheimer & Holmes 1983), has been developed by Sri Namachchivaya & Lin (1991). The method consists of eliminating certain response variables which are asymptotically stable as being unimportant with the essential behaviour of the system restricted to the dynamics of the remaining critical variables. The differences between this method and the traditional averaging arise in carrying out the 'temporal' part of the averaging, while, the ensemble averaging, with the consequent Markovian approximation, remains essentially the same. In fact, the equivalence of this method with a higher order stochastic averaging has been demonstrated (Sri Namachchivaya & Leng 1990). The approach has been employed in the study of the effects of noise on bifurcations in nonlinear systems and for specific cases, the method is shown to be more generally applicable than the stochastic averaging (Sri Namachchivaya 1991; Leng *et al* 1992).

7.6 *System stochasticity problems*

Although, the averaging methods are widely used in vibration problems, the idea of

applying them to problems of spatial variability is novel. Thus, the usefulness of the averaging method in the study of stochastic boundary value problems has been investigated by Manohar & Iyengar (1993, 1994) in the context of the determination of the eigensolutions of stochastic wave equations. Here, the given boundary value problem is converted into a set of initial value problems and, these are, in turn, simplified by averaging over spatial domain. The results obtained on the pdf of the eigensolutions using this approximation is found to compare very well with digital simulation results.

7.7 Summary

The methods of stochastic averaging enhance the scope of the FPK equation approach in random vibrations. The different versions of this method are mathematically well founded (Zhu 1988). This is in contrast to other approximate techniques discussed earlier. The other merit of these methods is that they lead to non-Gaussian estimates for the response.

8. Stochastic series solutions

A widely used method in deterministic problems is the one based on the representation of the solution in an infinite series. Here an unknown function is expanded in a set of known functions. A few studies based on the extension of this concept to stochastic problems are available in random vibration literature. Thus, Iyengar & Dash (1976) have considered a linear sdof system with both parametric and external random excitations. The parametric excitation is taken to be a nonwhite process. The response is expanded in a power series in the random coefficient process. The unknown coefficients in this series are taken to be deterministic and are determined based on the minimization of the mean square error in an interval of time. Ahmadi and his coworkers (Ahmadi 1980a; Jahedi & Ahmadi 1983; Orabi & Ahmadi 1987a, 1987b, 1988) have used the Weiner-Hermite functions in the study of the Duffing oscillator under stochastic excitation. These functions are a set of statistically orthogonal functions and form a complete random basis for expanding a given random process. See the book by Schetzen (1980) for a systematic account of the Volterra and Wiener theories of nonlinear systems. In the solution both the input and the response processes are expanded in a set of these functions. The orthogonality property further leads to a set of nonlinear coupled integro-differential equations for the unknown kernels in the expansion. These equations have been further solved using an iterative technique. For a Gaussian random process the series consists of only one term and thus the higher order terms in the series are non-Gaussian corrections. Thus the method systematically leads to non-Gaussian estimates for response statistics. However, it is not possible to obtain the expressions for the non-Gaussian pdf with this method. Using a single term in the expansion has been shown to be equivalent to the technique of equivalent linearization (Ahmadi & Orabi 1987). Recently, Ghanem & Spanos (1993) have studied random response of second order nonlinear systems using series expansions for both the excitation and response processes which consist of unknown deterministic functions of time which are weighted by known set of orthogonal random variables.

The excitations are represented exactly using the Karhunen–Loeve expansions. Following the concept of Galerkin expansions, the response is also expanded using the same basis random variables which are used for representing the excitation. This leads to a set of deterministic ordinary differential equations for the unknown functions which can be solved numerically. The method has been applied to the response analysis of Duffing's oscillator subjected to filtered white noise excitation yielding satisfactory results.

9. Digital simulation technique

For problems which are beyond the reach of exact or approximate analysis, the digital simulation technique forms the only means of solution. This technique is also useful in checking the validity of approximate analysis procedures. Here one follows a sample function approach in which the problem is handled largely in a time domain deterministic framework. The application of this method consists of three steps: (i) Simulation of random inputs, (ii) discretization of the stochastic model and generation of response, and (iii) statistical processing of samples of response. Thus, at every stage, the method requires the availability of efficient computers. The basic tool for generating random inputs is the pseudo-random number generator which is a deterministic algorithm that produces a set of numbers which are statistically indistinguishable from uniformly distributed random numbers (Chambers 1967). Scalar and vector random variables of specified distributions can be obtained by suitably transforming the uniformly distributed random numbers (Ripley 1987). Comprehensive reviews on generation of random processes and fields using spectral representations and discrete time series models are available respectively, in the works of Shinozuka & Deodatis (1991) and Spanos & Mignolet (1989). In the response analysis numerical schemes such as Runge–Kutta or predictor–corrector algorithms are used to solve the equations of motion. The method has been widely used in nonlinear response analysis (see, for example, Lutes & Shah 1973; Vaicatis *et al* 1974, Spanos 1980a, 1981b, Zhu *et al* 1993, Manohar & Iyengar 1990) and in first passage problems (Crandall *et al* 1966; Roberts 1976; Pi *et al* 1971; Spanos 1983; Iyengar & Manohar 1991). It has also been extensively used in problems of system stochasticity, parametric excitations and stochastic stability analyses (Shinozuka & Deodatis 1991).

The simulation technique has vast scope and is uniformly applicable to nonlinear and parametric response analysis of sdof and mdof systems. However, in order to obtain reliable estimates of response variables, sufficiently large size of samples should be used in the analysis. This fact makes the method significantly expensive. This is particularly true in response analysis involving estimation of rare events and in the study of large mdof systems. The method is well suited for stationary response analysis where assumption of ergodicity is admissible. Spanos (1981a) has estimated that the cost of simulation studies is typically 100 to 1000 times that of an approximate analysis using equivalent linearization. It has been found that the cost of simulation increases linearly with sample size while the accuracy improves in proportion to the square root of sample size (Spanos & Lutes 1987). Nevertheless, given the strides made over the last few years in computer technology, one can readily foresee the broadening of the scope of digital simulation techniques in engineering stochastic analyses.

10. Summary and conclusions

Various methods for stochastic response analysis have been outlined in the previous sections. Exact solutions are obtainable from the FPK equation approach but are scarce. It is generally necessary to take recourse to one of the several approximate procedures available. Many of the approximations are based on the assumption that the response process is nearly Gaussian distributed and/or is Markovian or nearly Markovian in nature. The approximate techniques based on the FPK equation are applicable to Markovian responses and are largely confined to lower order systems. The perturbation method is applicable to weakly nonlinear systems under weak stochastic inputs. They are useful in getting non-Gaussian estimates for response moments but are cumbersome and relatively inefficient. Equivalent linearization is useful for systems with Gaussian inputs and is applicable over a wide range of nonlinearity. The method leads to Gaussian estimates for the response and hence is suited for problems where the excitation and the system are such that the response is unimodal and nearly Gaussian. When applied to systems with multimodal response probability densities, the method leads to nonunique response statistics and requires careful interpretation. The method is not applicable for evaluating parametric responses. Equivalent nonlinearization methods are based on the class of exactly solvable FPK equations and are limited to systems driven by white noise excitations. The closure schemes are an improvement over equivalent linearization as they can take into account parametric excitations and can lead to non-Gaussian estimates for the response. The methods are however mathematically not well founded. The perturbation, equivalent linearization and closure methods are all fairly general and are applicable to both transient and steady state analysis of sdof and mdof systems. Stochastic averaging methods are applicable to lightly damped systems with parametric and external broad band inputs. They are mathematically well founded and in the case of systems under white noise for which the FPK equations are solvable, the methods lead to the exactly known solutions. These methods reduce the dimensionality of the problem and widen the scope of the FPK equation approach. Their applicability, however, is largely limited to sdof systems. Digital simulation technique is universally applicable and leads to estimates of the response to any desired level of accuracy. The method relies on the availability of a fast computer and is quite expensive, especially, in the study of large scale systems and in the analysis of rare events.

The above methods have been applied in the past to study a variety of nonlinear problems such as structures undergoing large amplitude vibrations, yielding systems, self-excited systems, hysteretic systems, vibroimpact systems and rocking of blocks. The developments of these methods are characterized by two conflicting objectives. Firstly, the methods are expected to be viable when applied to large-scale engineering structures, while, on the other hand, they need to capture correctly, the qualitative behaviour of nonlinear systems. The linearization and closure methods are, perhaps, the only feasible analytical methods which can be used in conjunction with computational structural models for studying large scale mdof systems. One of the major drawbacks of these methods, however, lies in their inability to capture correctly the interactions between equilibrium states of the unforced system and external random excitations. It has been noted by Andronov and others as far back as in 1933 (Bolotin 1967; Kozin 1969) that, for systems under white noise excitations, the most probable response states correspond to the stable equilibrium states of the unforced system (also

see Kapitanaiik 1986). Similar behaviour can be expected in the study of the random response of systems exhibiting complicated bifurcation patterns such as those associated with jumps, limit cycles, nonlinear resonances and entrainments. It is important to recognize that corresponding to multiple stable solutions of the unforced system, the stochastic response probability density functions can be multimodal. Evidently, the linearization and closure techniques are ill equipped to model these nonlinear features satisfactorily. On the other hand, the averaging and FPK equation based approaches are mathematically well founded and perform well when applied to simple systems displaying the above mentioned complicated response patterns, but are, however, of limited use in analysing large scale structures. Thus, methods to overcome these limitations still need to be developed.

References

- Ahmadi G 1980a A note on the Wiener-Hermite representations of the earthquake ground acceleration. *Mech. Res. Commun.* 7: 7-11
- Ahmadi G 1980b Mean square response of a Duffing oscillator to a modulated white noise excitation by the generalized method of equivalent linearization. *J. Sound Vib.* 71: 9-15
- Ahmadi G, Orabi I I 1987 Equivalence of single term Wiener-Hermite and equivalent linearization techniques. *J. Sound Vib.* 118: 307-311
- Ahmadi G, Su L 1987 Response of a frictional base isolator to random earthquake excitations. From *Seismic engineering: Recent advances in design, analysis, testing and qualification methods*. Book No. G00374 (ed) T H Liu, A Marr (New York: ASME) PVP-vol. 127, pp 399-404
- Ariaratnam S T 1978 Discussion on the paper by W D Iwan and P T D Spanos. *J. Appl. Mech.* 45: 964-965
- Assaf Sh A, Zirkle L D 1976 Approximate analysis of nonlinear stochastic systems. *Int. J. Control* 23: 477-492
- Atalik T S 1974 *Stationary random response of nonlinear multidegree of freedom systems by a direct equivalent linearization technique*. Ph D thesis, Duke University
- Atkinson J D 1973 Eigenfunction expansion for randomly excited nonlinear systems. *J. Sound Vib.* 30: 153-172
- Atkinson J D, Caughey T K 1968 Spectral density of piecewise linear first order systems excited by white noise. *Int. J. Nonlinear Mech.* 3: 137-156
- Bellman R E, Richardson J M 1968 Closure and preservation of moment properties. *J. Math. Anal. Appl.* 23: 639-644
- Bergman L A, Spencer B F Jr 1992 Robust numerical solution of the transient Fokker-Planck equation for nonlinear dynamical systems. *Proceedings of IUTAM symposium on Nonlinear Stochastic Mechanics*, Turin, Italy, pp 49-60
- Bhandari R G, Sherrer R E 1968 Random vibrations in discrete nonlinear dynamic systems. *J. Mech. Eng. Sci.* 10: 168-174
- Bharucha Reid A T 1960 *Elements of theory of Markov processes and their applications* (New York: McGraw-Hill)
- Bluman G W 1971 Similarity of the one dimensional Fokker-Planck equation. *Int. J. Nonlinear Mech.* 6: 143-153
- Bogoliubov N N, Mitropolsky Y A 1961 *Asymptotic methods in the theory of nonlinear oscillations* (New York: Gordon and Breach)
- Bolotin V V 1967 Statistical aspects in the theory of structural stability. In *Dynamic stability of structures* (ed.) G Hermann (Oxford: Pergamon) 67-81
- Bolotin V V 1984 *Random vibration of elastic systems* (Hague: Martinus Nijhoff)
- Booton R C 1954 The analysis of nonlinear control systems with random inputs. *IRE Trans. Circuit Theory* 1: 32-34
- Bruckner A, Lin Y K 1987a Generalization of the equivalent linearization method for nonlinear random vibration problems. *Int. J. Nonlinear Mech.* 22: 227-235

- Brucker A, Lin Y K 1987b Application of complex stochastic averaging to nonlinear random vibration problems. *Int. J. Nonlinear Mech.* 22: 237–250
- Cai G Q, Lin Y K 1988a On exact stationary solutions of equivalent nonlinear stochastic systems. *Int. J. Nonlinear Mech.* 23: 315–325
- Cai G Q, Lin Y K 1988b A new approximate solution technique for randomly excited nonlinear oscillators. *Int. J. Nonlinear Mech.* 23: 409–420
- Cai G Q, Lin Y K 1990 On randomly excited hysteretic structures. *J. Appl. Mech.* 57: 442–448
- Casciati F, Faravelli L, Hasofer A M 1993 A new philosophy for stochastic equivalent linearization. *Probab. Eng. Mech.* 8: 179–185
- Caughey T K 1963a Derivation and application of Fokker–Planck equation to discrete nonlinear dynamic systems subjected to white random excitation. *J. Acoust. Soc. Am.* 35: 1683–1692
- Caughey T K 1963b Equivalent linearization techniques. *J. Acoust. Soc. Am.* 35: 1706–1711
- Caughey T K 1971 Nonlinear theory of random vibration. In *Advances in applied mechanics* (ed.) C S Yih (New York: Academic Press) 11: 209–243
- Caughey T K 1986 On the response of nonlinear oscillators to stochastic excitation. *Probab. Eng. Mech.* 1: 2–10
- Caughey T K, Dienes J K 1961 Analysis of a nonlinear first order system with white noise input. *J. Appl. Phys.* 32: 2476–2479
- Caughey T K, Ma F 1982a The exact steady state solution of a class of nonlinear stochastic systems. *Int. J. Nonlinear Mech.* 17: 137–142
- Caughey T K, Ma F 1982b The steady state response of a class of dynamical systems to stochastic excitation. *J. Appl. Mech.* 49: 629–632
- Chambers R P 1967 Random number generation on digital computers. *IEEE Spectrum* (February): 48–56
- Chang R J 1991 Maximum entropy approach for stationary response of nonlinear oscillators. *J. Appl. Mech.* 58: 266–271
- Crandall S H 1963 Perturbation techniques for random vibration of nonlinear systems. *J. Acoust. Soc. Am.* 35: 1700–1705
- Crandall S H 1964 The spectrum of random vibration of a nonlinear oscillator. *Proceedings 11th International Congress on Applied Mechanics*, Munich
- Crandall S H 1973 Correlations and spectra of nonlinear system response. *Nonlinear Vib. Prob.* 14: 39–53
- Crandall S H 1980 Non-Gaussian closure for random vibration of nonlinear oscillators. *Int. J. Nonlinear Mech.* 15: 303–313
- Crandall S H 1985 Non-Gaussian closure techniques for stationary random vibration. *Int. J. Nonlinear Mech.* 20: 1–8
- Crandall S H, Khazzaz G R, Manning J E 1964 Random vibration of an oscillator with nonlinear damping. *J. Acoust. Soc. Am.* 36: 1330–1334
- Crandall S H, Chandiramani K L, Cook R G 1966 Some first passage problems in random vibration. *J. Appl. Mech.* 33: 532–538
- Dash P K, Iyengar R N 1982 Analysis of randomly time varying systems by Gaussian closure technique. *J. Sound Vib.* 83: 241–251
- Dashevskii M L 1967 Approximate analysis of the accuracy on nonstationary nonlinear systems using the method of semi-invariants. *Autom. Remote Control* 28: 1673–1690
- Davies H G, Nandall D 1986 Phase plane for narrow band random excitation of a Duffing oscillator. *J. Sound. Vib.* 104: 277–283
- Davies H G, Rajan S 1986 Random superharmonic response of a Duffing oscillator. *J. Sound. Vib.* 111: 61–70
- Davies H G, Liu Q 1992 The response spectrum of a nonlinear oscillator. *J. Appl. Mech.* 59: 459–462
- Dimentberg M F 1982 An exact solution to a certain nonlinear random vibration problem. *Int. J. Nonlinear Mech.* 17: 231–236
- Dimentberg M F 1988a Discussion on paper by Y Yong and Y K Lin. *J. Appl. Mech.* 55: 498–499
- Dimentberg M F 1988b Statistical dynamics of nonlinear and time-varying systems (Taunton: Research Studies Press)
- Elishakoff I, Cai G Q 1993 Approximate solution for nonlinear random vibration problems by partial stochastic linearization. *Probab. Eng. Mech.* 8: 233–237

- Elishakoff I, Zhang X 1993 An appraisal of different stochastic linearization procedures. *J. Sound. Vib.* 152: 370–375
- Fan G, Ahmadi G 1990 On loss of accuracy and non-uniqueness of solutions generated by equivalent linearization and cumulant-neglect methods. *J. Sound Vib* 137: 385–401
- Feller W 1966 *An introduction to probability theory and its applications* (New Delhi: Wiley Eastern) vol. 2
- Foster E T Jr 1968 Semilinear random vibrations in discrete systems. *J. Appl. Mech.* 35: 560–564
- Friedman A 1964 *Partial differential equations of parabolic type* (Englewood Cliffs N J: Prentice Hall)
- Fujita T, Hattori S 1980 Nonstationary random vibration of a nonlinear system with collision. *Bull. JSME* 23: 1857–1864
- Fuller A T 1969 Analysis of nonlinear stochastic systems by means of the Fokker–Planck equation. *Int. J. Control* 9: 603–655
- Gardiner C W 1983 *Handbook of stochastic methods for physics, chemistry and natural sciences* (New York: Springer-Verlag)
- Ghanem R, Spanos P D 1993 A stochastic Galerkin expansion for nonlinear random vibration analysis. *Probab. Eng. Mech.* 8: 255–264
- Grigoriu M 1991 A consistent closure method for nonlinear random vibration. *Int. J. Nonlinear Mech.* 26: 857–866
- Guckenheimer J, Holmes P J 1983 *Nonlinear oscillators, dynamical systems and bifurcations of vector fields* (New York: Springer-Verlag)
- Horsthemke W, Lefever R 1984 *Noise induced transitions theory and applications in physics, chemistry and biology* (Berlin: Springer-Verlag)
- Ibrahim R A 1978 Stationary response of a randomly parametric excited nonlinear system. *J. Appl. Mech.* 45: 910–916
- Ibrahim R A 1985 *Parametric random vibration* (Hertfordshire New York: Research Studies Press/John Wiley and Sons)
- Ibrahim R A, Soundararajan A, Heo H 1985 Stochastic response of nonlinear system based on a non-Gaussian closure. *J. Appl. Mech.* 52: 965–970
- Iwan W D, Krousgrill C M 1983 Equivalent linearization for continuous dynamical systems. *J. Appl. Mech.* 50: 415–420
- Iwan W D, Mason A B Jr 1980 Equivalent linearization for systems subjected to non-stationary excitation. *Int. J. Nonlinear Mech.* 15: 71–82
- Iwan W D, Spanos P T D 1978 Response envelope statistics for nonlinear oscillators with random excitation. *J. Appl. Mech.* 45: 170–174
- Iwan W D, Whirley R G 1993 Nonstationary equivalent linearization of nonlinear continuous systems. *Probab. Eng. Mech.* 8: 273–280
- Iwan W D, Yang I M 1972 Application of statistical linearization techniques to nonlinear multidegree of freedom systems. *J. Appl. Mech.* 39: 545–550
- Iyengar R N 1975 Random vibration of a second order nonlinear elastic system. *J. Sound Vib.* 40: 155–165
- Iyengar R N 1986 A nonlinear system under combined periodic and random excitation. *J. Stat. Phys.* 44: 907–920
- Iyengar R N 1988a Higher order linearization of nonlinear random vibration. *Int. J. Nonlinear Mech.* 23: 385–391
- Iyengar R N 1988b Stochastic response and stability of the Duffing oscillator under narrow band excitation. *J. Sound. Vib.* 126: 255–263
- Iyengar R N 1989 Response of nonlinear systems to narrowband excitation. *Struct. Safety* 6: 177–185
- Iyengar R N 1992 Approximate analysis of nonlinear systems under narrow band random excitation, *Proceedings of IUTAM symposium on Nonlinear Stochastic Mechanics, Turin, Italy*, pp. 309–320
- Iyengar R N, Dash P K 1976 Random vibration analysis of stochastic time varying systems. *J. Sound. Vib* 45: 69–89
- Iyengar R N, Dash P K 1978 Study of the random vibration of nonlinear systems by the Gaussian closure technique. *J. Appl. Mech.* 45: 393–399
- Iyengar R N, Manohar C S 1991 Rocking response of rectangular blocks under random noise base excitation. *Int. J. Nonlinear Mech.* 26: 885–892

- Jahedi A, Ahmadi G 1983 Application of Wiener-Hermite expansion to nonstationary random vibration of a Duffing oscillator. *J. Appl. Mech.* 50: 436-442
- Jia W, Fang T 1987 Jump phenomena in coupled Duffing oscillators under random excitation. *J. Acoust. Soc. Am.* 81: 961-965
- Johnson J P, Scott R A 1979 Extension of eigenfunction expansion solutions of a Fokker-Planck equation; 1: First order systems. *Int. J. Nonlinear Mech.* 14: 315-324
- Johnson J P, Scott R A 1980 Extension of eigenfunction expansion solutions of a Fokker-Planck equation; 2: Second order system. *Int. J. Nonlinear Mech.* 15: 41-56.
- Kapitanaik T 1985 Stochastic response with bifurcations to nonlinear Duffing's oscillator. *J. Sound Vib.* 102: 440-441
- Kapitanaik T 1986 A property of a stochastic response with bifurcation of a nonlinear system. *J. Sound Vib.* 107: 177-180
- Khabbaz G R 1965 Power spectral density of the response of a nonlinear system to random excitation. *J. Acoust. Soc. Am.* 38: 847-850
- Khasminskii R Z 1966 A limit theorem for the solutions of differential equations with random right hand sides. *Theory Probab. Appl.* 11: 390-406
- Kimura K, Sakata M 1981 Nonstationary responses of a non-symmetric nonlinear system subjected to wide class of random excitation. *J. Sound Vib.* 76: 261-272
- Kimura K, Sakata M 1987 Nonstationary response analysis of a nonsymmetric nonlinear multidegree of freedom system to nonwhite random excitation. *Proceedings of KSME/JSME Vibration Conference*, Seoul, Korea, 180-189
- Koliopoulos P K, Langley R S 1993 Improved stability analysis of the response of a Duffing oscillator under filtered white noise. *Int. J. Nonlinear Mech.* 28: 145-155
- Kozin F 1969 A survey of stability of stochastic systems. *Automatica* 5: 95-112
- Kozin F 1987 The method of statistical linearization for nonlinear stochastic vibrations. In *Nonlinear stochastic dynamic engineering systems, IUTAM symposium*, Innsbruck (eds) F Ziegler, G I Schueller, pp. 45-56
- Langley R S 1985 A finite element method for the statistics of nonlinear random vibration. *J. Sound. Vib.* 101: 41-54
- Langley R S 1988a Application of the principle of detailed balance to the random vibration of nonlinear oscillators. *J. Sound Vib.* 125: 85-92
- Langley R S 1988b An investigation of multiple solutions yielded by the equivalent linearization method. *J. Sound Vib.* 127: 271-281
- Leng G, Sri Namachchivaya N S, Talwar S 1992 Robustness of nonlinear systems perturbed by external random excitation. *J. Appl. Mech.* 59: 1015-1022
- Lennox W C, Kuak Y C 1976 Narrow band excitation of a nonlinear oscillator. *J. Appl. Mech.* 43: 340-344
- Li Y, Kareem A 1993 Multivariate Hermite expansion of hydrodynamic drag loads on tension leg platforms. *J. Eng. Mech.* 119: 91-112
- Lin Y K 1967 *Probabilistic theory of structural dynamics* (New York: McGraw-Hill)
- Lin Y K 1986 Some observations on the stochastic averaging method. *Probab. Eng. Mech.* 1: 23-27
- Lin Y K, Cai G Q 1988 Exact stationary response solution for second order nonlinear systems under parametric and external white noise excitations: Part II. *J. Appl. Mech.* 55: 702-705
- Liu Q, Davies H G 1988 Application of non-Gaussian closure to the nonstationary response of a Duffing oscillator. *Int. J. Nonlinear Mech.* 23: 241-250
- Lutes L D, Shah V S 1973 Transient random response of bilinear oscillators. *J. Eng. Mech.* 99: 715-734
- Manning J E 1975 Response spectra for nonlinear oscillators. *J. Eng. Ind.* 97: 1223-1226
- Manohar C S 1989 *Random vibrations of limit cycle systems and stochastic strings*. Ph D thesis, Department of Civil Engineering, Indian Inst. Sci., Bangalore
- Manohar C S, Iyengar R N 1990 Random vibration of a limit cycle system, Report No. 1-1990, Structural Engineering Laboratory, Indian Inst. Sci., Bangalore
- Manohar C S, Iyengar R N 1991a Entrainment of Van der Pol's oscillator in presence of combined periodic excitation and noise. *Int. J. Nonlinear Mech.* 26: 679-786
- Manohar C S, Iyengar R N 1991b Narrow band random excitation of a limit cycle system. *Arch. Appl. Mech.* 61: 133-141

- Manohar C S, Iyengar R N 1993 Probability distribution of the eigenvalues of systems governed by stochastic wave equation. *Probab. Eng. Mech.* 8: 57–64
- Manohar C S, Iyengar R N 1994 Free vibration analysis of stochastic strings. *J. Sound Vib.* 176(1): 35–48
- Mayfield W W 1973 A sequence solution to the Fokker–Planck equation. *IEEE Trans. Inf. Theory* IT19: 165–175
- Naess A, Johnsen J M 1993 Response statistics of nonlinear, compliant offshore structures by the path integral solution method. *Probab. Eng. Mech.* 8: 91–106
- Orabi I I, Ahmadi G 1987a A functional series expansion method for response analysis of nonlinear systems subjected to random excitations. *Int. J. Nonlinear Mech.* 22: 451–465
- Orabi I I, Ahmadi G 1987b Nonstationary response analysis of a Duffing oscillator by the Wiener–Hermite expansion method. *J. Appl. Mech.* 54: 434–440
- Orabi I I, Ahmadi G 1988 Response of the Duffing oscillator to a non-Gaussian random excitation. *J. Appl. Mech.* 55: 740–743
- Pawleta H, Socha L 1992 Cumulant neglect closure of nonstationary solutions of stochastic system. *J. Appl. Mech.* 57: 776–779
- Pawula R F 1967 Generalization and extension of the Fokker–Planck–Kolmogorov equations. *IEEE Trans. Inf. Theory* IT-13: 33–41
- Payne H J 1968 An approximate method for nearly linear, first order stochastic differential equations. *Int. J. Control* 7: 451–463
- Pi H N, Ariaratnam S T, Lennox W C 1971 First passage time for the snap-through of a shell-type structure. *J. Sound Vib.* 14: 375–384
- Pradlwarter H J 1989 Non-Gaussian linearization: An efficient tool to analyze nonlinear MDOF systems. *Proceedings, SMiRTM* 10: 19–30
- Pradlwarter H J, Schueller G I, Chen X W 1988 Consideration of non-Gaussian response properties by use of stochastic equivalent linearization. *Proceedings, 3rd International conference on recent advances in structural dynamics*, Southampton, pp. 737–752
- Red-Horse J R, Spanos P D 1992 A generalization to stochastic averaging in random vibration. *Int. J. Nonlinear Mech.* 27: 85–101
- Richard K, Anand G V 1983 Nonlinear resonance in strings under narrow band random excitation, Part I: Planar response and stability. *J. Sound Vib.* 86: 85–98
- Ripley B D 1987 *Stochastic simulation* (New York: Wiley)
- Risken H 1989 *Fokker–Planck equation: Methods of solution and applications* 2nd edn (Berlin: Springer Verlag)
- Roberts J B 1976 First passage probability for nonlinear oscillators. *J. Eng. Mech.* 102: 851–866
- Roberts J B 1978 The energy envelope of a randomly excited nonlinear oscillator. *J. Sound Vib.* 60: 177–185
- Roberts J B 1981 Response of nonlinear mechanical systems to random excitation. Part I: Markov Methods. *Shock Vib. Dig.* 13(4): 17–28
- Roberts J B 1982 A stochastic theory for nonlinear ship rolling in irregular seas. *J. Ship Res.* 26: 229–245
- Roberts J B 1986a First passage probabilities for randomly excited systems: Diffusion methods. *Probab. Eng. Mech.* 1: pp. 66–81
- Roberts J B 1986b First passage time for randomly excited nonlinear oscillators. *J. Sound Vib.* 109: 33–50
- Roberts J B 1991 Multiple solutions generated by statistical linearization and their physical significance. *Int. J. Nonlinear Mech.* 26: 945–960
- Roberts J B, Spanos P T D 1986 Stochastic averaging: An approximate method of solving random vibration problems. *Int. J. Nonlinear Mech.* 21: 111–134
- Roberts J B, Spanos P T D 1990 *Random vibration and statistical linearization* (Chichester: John Wiley and Sons)
- Roy R V, Spanos P D 1991 Pade-type approach to nonlinear random vibration analysis. *Probab. Eng. Mech.* 6: 119–128
- Roy R V, Spanos P D 1993 Power spectral density of nonlinear system response: the recursion method. *J. Appl. Mech.* 60: 358–365
- Sakata M, Kimura K 1980 Calculation of the nonstationary mean square response of a nonlinear system subjected to nonwhite excitation. *J. Sound Vib.* 73: 333–343

- Sancho N G F 1970 On the approximate moment equations of a nonlinear stochastic differential equation. *J. Math. Anal. Appl.* 29: 384–391
- Sato K, Yamamoto S, Kamada O, Takatsu N 1985 Jump phenomena in gear system to random excitation. *Bull. JSME*, 28: 1271–1278
- Schetzen M 1980 *The Volterra and Wiener theories of nonlinear systems* (New York: John Wiley and Sons)
- Schueller G I, Pradlwarter H J, Bucher C G 1991 Efficient computational procedures for reliability estimates of mdof systems. *Int. J. Nonlinear Mech.* 26: 961–974
- Shimogo T 1963a Nonlinear vibrations of systems with random loading. *Bull. JSME* 6: 44–52
- Shimogo T 1963b Unsymmetrical nonlinear vibration of systems with random loading. *Bull. JSME* 6: 53–59
- Shinozuka M, Deodatis G 1991 Simulation of stochastic processes by spectral representation. *Appl. Mech. Rev.* 44: 191–203
- Sinitsyn I N 1974 Methods of statistical linearization (survey). *Autom. Remote Control* 35: 765–776
- Sobczyk K, Trebicki J 1990 Maximum entropy principle in stochastic dynamics. *Probab. Eng. Mech.* 5(3):
- Sobczyk K, Trebicki J 1992 Analysis of stochastic systems via maximum entropy principle. *Proceedings of IUTAM symposium on Nonlinear Stochastic Mechanics*, Turin, Italy pp. 485–497
- Socha L, Soong T T 1991 Linearization in analysis of nonlinear stochastic systems. *Appl. Mech. Rev.* 44: 399–422
- Solomos G P, Spanos P T D 1984 Oscillator response to nonstationary excitation. *J. Appl. Mech.* 51: 907–912
- Soni S R, Surendran K 1975 Transient response of nonlinear systems to stationary random excitation. *J. Appl. Mech.* 42: 891–893
- Soong T T 1973 *Random differential equations in science and engineering*. (New York: Academic Press)
- Spanos P T D 1980a Numerical simulations of a Van der Pol oscillator. *Comput. Math. Appl.* 6: 135–145
- Spanos P T D 1980b Formulation of stochastic linearization for symmetric or asymmetric mdof nonlinear systems. *J. Appl. Mech.* 47: 209–211
- Spanos P T D 1981a Stochastic linearization in structural dynamics. *Appl. Mech. Rev.* 34: 1–8
- Spanos P T D 1981b Monte Carlo simulations of response of nonsymmetric dynamic system to random excitations. *Comput. Struct.* 13: 371–376
- Spanos P T D 1983 Survival probability of nonlinear oscillator subjected to broad band random disturbances. *Int. J. Nonlinear Mech.* 17: 303–317
- Spanos P T D 1986 Analysis of block random rocking. *Soil Dyn. Earthquake Eng.* 5: 178–184
- Spanos P T D, Iwan W D 1978 On the existence and uniqueness of solutions generated by equivalent linearization. *Int. J. Nonlinear Mech.* 13: 71–78
- Spanos P T D, Lutes L D 1987 A primer of random vibration techniques in structural engineering. *Shock Vib. Dig.* 19(4): 3–9
- Spanos P D, Mignolet M P 1989 ARMA Monte Carlo simulation in probabilistic structure analysis. *Shock Vib. Dig.* 21(11): 3–14
- Spanos P D, Donley M G 1991 Equivalent statistical quadrization for nonlinear systems. *J. Eng. Mech.* 117: 1289–1310
- Spencer B F, Bergman L A 1985 The first passage problem in random vibration for a simple hysteretic oscillator. Technical Report AAE 85–8, University of Illinois, Urbana
- Sri Namachchivaya N S 1991 Co-dimension two bifurcations in the presence of noise. *J. Appl. Mech.* 58: 259–265
- Sri Namachchivaya N S, Leng G 1990 Equivalence of stochastic averaging and stochastic normal forms. *J. Appl. Mech.* 57: 1011–1017
- Sri Namachchivaya N S, Lin Y K 1991 Method of stochastic normal forms. *Int. J. Nonlinear Mech.* 26: 931–944
- Stratonovich R L 1963, 1967 *Topics in the theory of a random noise* (New York: Gordon and Breach) vols. 1 and 2
- Sun J Q, Hsu C S 1987 Cumulant neglect closure method for nonlinear systems under random excitations. *J. Appl. Mech.* 54: 649–655

- Sun J Q, Hsu C S 1988 First-passage time probability of nonlinear stochastic systems by generalized cell mapping method. *J. Sound Vib.* 124: 233–248
- Sun J Q, Hsu C S 1990 The generalized cell mapping method in nonlinear random vibration based upon short-time Gaussian approximation. *J. Appl. Mech.* 57: 1018–1025
- Sunahara Y, Asakura T, Marita Y 1977 On the asymptotic behaviour of nonlinear stochastic dynamical systems considering initial states. In *Stochastic problems in dynamics* (ed.) B L Clarkson (London: Pitman) pp 138–175
- Taylor R E, Rajagopalan A 1982 Dynamics of offshore structures, Part I: Perturbation analysis. *J. Sound Vib.* 83: 401–416
- To C W S, Li D M 1991 Equivalent nonlinearization of nonlinear systems to random excitation. *Probab. Eng. Mech.* 6: 184–192
- Toland R H, Yang C Y 1971 Random walk model for first passage probability. *J. Eng. Mech.* 97: 791–906
- Toland R H, Yang C Y, Hsu C K C 1972 Nonstationary random vibration of nonlinear structures. *Int. J. Nonlinear Mech.* 7: 395–406
- Tylikowski A, Marowski W 1986 Vibration of a nonlinear single degree of freedom system due to Poissonian impulse excitation. *Int. J. Nonlinear Mech.* 21: 229–238
- Vaicatis R, Dowell E H, Ventres C S 1974 Nonlinear panel response by a Monte Carlo approach. *AIAA J.* 12: 685–691
- Vickery B J, Basu R I 1983 Across wind vibrations of structures of circular cross section Part I: Development of a mathematical model for two dimensional condition. *J. Wind Eng. Ind. Aerodyn.* 12: 49–97
- Wehner M F, Wolfer W G 1983 Numerical evaluation of path-integral solutions to Fokker–Planck equations. *Phys. Rev. A* 27: 2663–2670
- Wen Y K 1975 Approximate method for nonlinear random vibration. *J. Eng. Mech.* 101: 389–401
- Wen Y K 1976 Method for random vibration of hysteretic system. *J. Eng. Mech.* 102: 249–263
- Wen Y K 1980 Equivalent linearization for hysteretic systems under random excitation. *J. Appl. Mech.* 47: 150–154
- Wen Y K 1989 Methods of random vibration for inelastic structures. *Appl. Mech. Rev.* 42(2): 39–52
- Wilcox R M, Bellman R 1970 Truncation and preservation of moment properties for Fokker–Planck moment equations. *J. Math. Anal. Appl.* 32: 532–542
- Wu W F, Lin Y K 1984 Cumulant neglect closure for nonlinear oscillators under parametric and external excitations. *Int. J. Nonlinear Mech.* 19: 349–362
- Yong Y, Lin Y K 1987 Exact stationary response solution for second order nonlinear systems under parametric and external white noise excitation. *J. Appl. Mech.* 54: 414–418
- Zhu W Q 1983 Stochastic averaging of the energy envelope of nearly Lyapunov systems. In *Random vibrations and reliability. Proceedings of IUTAM Symposium* (ed.) K Hennig Frankfurt (Berlin: Akademie-Verlag) pp 347–357
- Zhu W Q 1988 Stochastic averaging methods in random vibrations. *Appl. Mech. Rev.* 41: 189–199
- Zhu W Q, Lin Y K 1991 Stochastics averaging of energy envelope. *J. Eng. Mech.* 117: 1890–1905
- Zhu W Q, Yu J S 1987 On the response of Van der Pol oscillator to white noise excitation. *J. Sound. Vib.* 117: 421–431
- Zhu W Q, Yu J S 1989 The equivalent nonlinear system method. *J. Sound Vib.* 129: 385–395
- Zhu W Q, Cai G Q, Lin Y K 1990 On exact stationary solutions of stochastically perturbed Hamiltonian systems. *Probab. Eng. Mech.* 5: 84–87
- Zhu W Q, Lu M Q, Wu Q T 1993 Stochastic jump and bifurcation of a Duffing oscillator under narrow-band excitation. *J. Sound Vib.* 165: 285–304
- Zhu W Q, Yu M Q, Lin Y K 1994 On improved stochastic averaging procedure. *Probab. Eng. Mech.* 9: 203–212



Higher order averaging method of coefficients in Fokker-Planck equation

NGUYEN DONG ANH

Institute of Mechanics, Vien Co, 224 Doi Can, Hanoi, Vietnam

Abstract. Two methods of integrating the first-order averaged Fokker-Planck (FP) equation used in the theory of random oscillations are proposed for the non-autonomous cases. Further, since the effect of some nonlinear terms is lost during the first-order averaging procedure, the procedures for obtaining higher approximate solutions to the FP equation are developed. It is shown that these procedures involve the classical first-order averaging method of coefficients in FP equation. The Duffing and Van der Pol oscillations are considered.

Keywords. Averaging; FP equation; random vibration; white noise.

1. Introduction

Over many years the well-known averaging method, originally given by Krylov and Bogoliubov and then developed by Mitropolskii (Bogoliubov & Mitropolskii 1963), has proved to be a very useful tool for investigating deterministic weakly nonlinear vibration problems. The advantage of this method is that it reduces the dimension of the response coordinates. In the field of random vibration the averaging method was extended by Stratonovich (1963) and had a mathematically rigorous proof by Khasminskii (1963).

It should be noted that although the general higher order averaging procedure was already described for deterministic differential equations (Mitropolskii 1971), principally only the first-order averaging method has been applied in practice. Recently, a systematical application of the first-order averaging method to arbitrary order differential equations subjected to deterministic and random excitations was presented (Mitropolskii *et al* 1992). It is well-known, however, that the effect of some nonlinear terms such as cubic stiffness is lost during the first-order averaging procedure. Thus, the latter is not sufficient to describe the effect of those nonlinear terms. In order to overcome this insufficiency, the procedures for obtaining higher approximate solutions to the Fokker-Planck (FP) equation are developed in the paper. It is shown that the presented procedures involve, in particular, the first-order stochastic averaging method (SAM) of coefficients in FP equation.

2. SAM of coefficients in FP equation

Consider the equation of motion of a single-degree-of-freedom mechanical system

$$\ddot{x} + \omega^2 x = \varepsilon f(x, \dot{x}, \omega t, \varepsilon) + (\varepsilon^{1/2}) \sigma \xi(t), \quad (1)$$

wherein the symbols have their customary meaning, σ is a constant, f is a nonlinear function in x and \dot{x} and periodic in ωt with period 2π , and ε is a small positive parameter. The random excitation $\xi(t)$ is a Gaussian white noise process of unit intensity

$$E(\xi(t)\xi(t+\tau)) = \delta(\tau), \quad (2)$$

where $E(\cdot)$ denotes the expectation operator. Equation (1) may be considered as the following system of Ito stochastic differential equations,

$$dx(t) = \dot{x} dt, \quad (3)$$

$$d\dot{x}(t) = [\varepsilon f - \omega^2 x] dt + (\varepsilon)^{1/2} \sigma dn(t), \quad (4)$$

where $n(t)$ is the Wiener process and

$$E(n(t)n(t')) = \min\{t, t'\}. \quad (5)$$

The solution of the corresponding linear system (1), ($\varepsilon = 0$), has the form

$$x(t) = a \cos \phi, \quad (6)$$

$$\dot{x}(t) = -a\omega \sin \phi, \phi = \omega t + \theta, \quad (7)$$

where a and θ are constants. In the case where $\varepsilon \neq 0$, according to the classical approach of the averaging method the state coordinates (x, \dot{x}) are to be transformed to the pair of (a, θ) by the change (6) and (7).

In order to obtain the amplitude and phase Ito differential equations let these equations be written in the form

$$\begin{aligned} da(t) &= K_1(a, \phi, \omega t, \varepsilon) dt + \beta(a, \phi, \omega t, \varepsilon) dn(t), \\ d\theta(t) &= K_2(a, \phi, \omega t, \varepsilon) dt + \gamma(a, \phi, \omega t, \varepsilon) dn(t), \end{aligned} \quad (8)$$

where K_1, β, K_2, γ are unknown functions of $a, \phi, \omega t$ and ε . For a given function $F(t, a, \phi)$ the Ito differential rule (Gikhman *et al* 1982) gives

$$dF = [\partial F / \partial t + (l_1 + l_2)F] dt + l_3 F dn(t), \quad (9)$$

wherein the operators l_1, l_2 , and l_3 denote

$$\begin{aligned} l_1 &= K_1 \frac{\partial}{\partial a} + K_2 \frac{\partial}{\partial \phi}, l_3 = \beta \frac{\partial}{\partial a} + \gamma \frac{\partial}{\partial \phi}, \\ l_2 &= \frac{1}{2} \beta^2 \frac{\partial^2}{\partial a^2} + \beta \gamma \frac{\partial^2}{\partial a \partial \phi} + \frac{1}{2} \gamma^2 \frac{\partial^2}{\partial \phi^2}. \end{aligned} \quad (10)$$

Differentiating (6) with respect to time and using (9) yields

$$dx(t) = [-a\omega \sin \phi + (l_1 + l_2)(a \cos \phi)] dt + l_3 (a \cos \phi) dn(t). \quad (11)$$

On the other hand, substituting (7) into (3) gives

$$dx(t) = [-a\omega \sin \phi] dt. \quad (12)$$

Further, differentiating (7) with respect to t and using (9) yields

$$d\dot{x}(t) = [-a\omega^2 \cos \phi + (l_1 + l_2)(-a\omega \sin \phi)] dt + l_3(-a\omega \sin \phi) dn(t). \quad (13)$$

Comparing (11) with (12) and (13) with (4) gives the following relations

$$(l_1 + l_2)(a \cos \phi) = 0, \quad (14)$$

$$l_3(a \cos \phi) = 0, \quad (15)$$

and

$$(l_1 + l_2)(-a\omega \sin \phi) = \varepsilon f(a, \phi, \omega t, \varepsilon), \quad (16)$$

$$l_3(-a\omega \sin \phi) = (\varepsilon)^{1/2} \sigma. \quad (17)$$

where

$$f(a, \phi, \omega t, \varepsilon) = f(x, \dot{x}, \omega t, \varepsilon), \quad \text{with } x = a \cos \phi, \quad \dot{x} = -a\omega \sin \phi. \quad (18)$$

Noting (10), the explicit forms of (15), (17) and (14), (16) are, respectively,

$$\begin{aligned} \beta \cos \phi - \gamma a \sin \phi &= 0, \\ -\beta \omega \sin \phi - \gamma a \omega \cos \phi &= (\varepsilon)^{1/2} \sigma, \end{aligned} \quad (19)$$

and

$$\begin{aligned} K_1 \cos \phi - K_2 a \sin \phi &= \beta \gamma \sin \phi + \frac{1}{2} \gamma^2 a \cos \phi, \\ K_1 \sin \phi + K_2 a \cos \phi &= -\beta \gamma \cos \phi + \frac{1}{2} \gamma^2 a \sin \phi - \frac{\varepsilon}{\omega} f(a, \phi, \omega t, \varepsilon). \end{aligned} \quad (20)$$

Therefore, one gets from (19) and then from (20)

$$\begin{aligned} \beta &= -\frac{(\varepsilon)^{1/2}}{\omega} \sigma \sin \phi, \quad \gamma = -\frac{(\varepsilon)^{1/2}}{a\omega} \sigma \sin \phi, \\ K_1 &= -\frac{\varepsilon}{\omega} f(a, \phi, \omega t, \varepsilon) \sin \phi + \frac{\varepsilon}{2a\omega^2} \sigma^2 \cos \phi, \\ K_2 &= -\frac{\varepsilon}{a\omega} f(a, \phi, \omega t, \varepsilon) \cos \phi - \frac{\varepsilon}{a^2 \omega^2} \sigma^2 \sin \phi \cos \phi. \end{aligned} \quad (21)$$

Hence, (3), (4) are transformed into the amplitude and phase differential equations (8) where K_1, β, K_2, γ are given in (21). The FP equation, written for the probability density function $W(a, \theta, t)$ corresponding to the system (8), has the form

$$\begin{aligned} \frac{\partial W}{\partial t} &= -\varepsilon \left\{ \frac{\partial}{\partial a} (K_1 W) + \frac{\partial}{\partial \theta} (K_2 W) \right. \\ &\quad \left. - \frac{1}{2} \left[\frac{\partial^2}{\partial a^2} (K_{11} W) + 2 \frac{\partial^2}{\partial a \partial \theta} (K_{12} W) + \frac{\partial^2}{\partial \theta^2} (K_{22} W) \right] \right\}, \quad (22) \end{aligned}$$

where

$$\begin{aligned}K_{11}(a, \phi) &= \frac{\sigma^2}{\omega^2} \sin^2 \phi, \\K_{12}(a, \phi) &= \frac{\sigma^2}{a\omega^2} \sin \phi \cos \phi, \\K_{22}(a, \phi) &= \frac{\sigma^2}{a^2\omega^2} \cos^2 \phi.\end{aligned}\tag{23}$$

Khasminskii (1963) proved that when $\varepsilon \rightarrow 0$ the solution of Cauchy's problem of (22) approaches the solution of the following averaged FP equation

$$\begin{aligned}\frac{\partial W}{\partial t} = -\varepsilon \left\{ \frac{\partial}{\partial a} (\langle K_1 \rangle W) + \frac{\partial}{\partial \theta} (\langle K_2 \rangle W) \right. \\ \left. - \frac{1}{2} \left[\frac{\partial^2}{\partial a^2} (\langle K_{11} \rangle W) + 2 \frac{\partial^2}{\partial a \partial \theta} (\langle K_{12} \rangle W) + \frac{\partial^2}{\partial \theta^2} (\langle K_{22} \rangle W) \right] \right\},\end{aligned}\tag{24}$$

where $\langle \cdot \rangle$ is the averaging operator with respect to time or to phase ϕ ,

$$\langle \cdot \rangle = \frac{1}{2\pi} \int_0^{2\pi/\omega} (\cdot) dt = \frac{1}{2\pi} \int_0^{2\pi} (\cdot) d\phi.\tag{25}$$

In the non-autonomous case, where the function f in (1) contains explicitly the time ωt , the averaged coefficients $\langle K_1 \rangle$, $\langle K_2 \rangle$ are functions in a and θ . Thus, the solution to (24) is still a difficult problem. In Mitropolskii *et al* (1992) and Anh (1985), two methods for investigating the stationary solution $W(a, \theta)$ of (24) are proposed.

2.1 Method of auxiliary function

The method transforms the FP equation (24) into a partial differential equation for an auxiliary function $u(a, \theta)$

$$\frac{\partial}{\partial \theta} M \left(a, \theta, \frac{\partial u}{\partial a}, \frac{\partial u}{\partial \theta}, u \right) = \frac{\partial}{\partial a} N \left(a, \theta, \frac{\partial u}{\partial a}, \frac{\partial u}{\partial \theta}, u \right),\tag{26}$$

where M and N are known functions of indicated arguments. After finding the function $u(a, \theta)$, the stationary probability density function $W(a, \theta)$ can be found by the quadrature

$$\begin{aligned}W(a, \theta) = \exp \left\{ \int M \left(a, \theta, \frac{\partial u}{\partial a}, \frac{\partial u}{\partial \theta}, u \right) da \right. \\ \left. + \int N \left(a, \theta, \frac{\partial u}{\partial a}, \frac{\partial u}{\partial \theta}, u \right) d\theta \right\}.\end{aligned}\tag{27}$$

However, the effectiveness of the use of (26) is that its trivial or simple solutions correspond to the nontrivial exact solution (27) of the FP equation (24). Hence, one gets a method to determine sufficient conditions for the integrability of the last equation: to impose sufficient conditions on the coefficients $\langle K_i \rangle$ and $\langle K_{ij} \rangle$, $i, j = 1, 2$; so that (26) admits some definite solution $u(a, \theta)$, under which the particular exact solution (27) of the FP equation (24) can be found in quadratures.

Consider, for example, the following simple auxiliary function

$$u(a, \theta) = 0.$$

Equation (26) takes the form

$$\begin{aligned} \frac{\partial}{\partial \theta} \left\{ \frac{2}{\langle K_{11} \rangle} \left(\langle K_1 \rangle - \frac{1}{2} \frac{\partial \langle K_{11} \rangle}{\partial a} \right) \right\} = \\ \frac{\partial}{\partial a} \left\{ \frac{2}{\langle K_{22} \rangle} \left(\langle K_2 \rangle - \frac{1}{2} \frac{\partial \langle K_{22} \rangle}{\partial \theta} - \frac{\langle K_{12} \rangle}{\partial a} \right) - \right. \\ \left. \frac{4 \langle K_{12} \rangle}{\langle K_{11} \rangle \langle K_{22} \rangle} \left(\langle K_1 \rangle - \frac{1}{2} \frac{\partial \langle K_{11} \rangle}{\partial a} \right) \right\}. \end{aligned} \quad (28)$$

Thus, if the coefficients $\langle K_j \rangle$, $\langle K_{ij} \rangle$, $i, j = 1, 2$, of drift and diffusion satisfy the condition (28), then the FP equation (24) has the exact solution

$$\begin{aligned} W(a, \theta) = \exp \left\{ 2 \int \left[\frac{\langle K_1 \rangle}{\langle K_{11} \rangle} - \frac{1}{2 \langle K_{11} \rangle} - \frac{\langle K_{11} \rangle}{\partial a} \right] da \right. \\ \left. + 2 \int \left[\frac{1}{\langle K_{22} \rangle} \left(\langle K_2 \rangle - \frac{1}{2} \frac{\partial \langle K_{22} \rangle}{\partial \theta} - \frac{\partial \langle K_{12} \rangle}{\partial a} \right) - \right. \right. \\ \left. \left. - \frac{4 \langle K_{12} \rangle}{\langle K_{11} \rangle \langle K_{22} \rangle} \left(\langle K_1 \rangle - \frac{1}{2} \frac{\partial \langle K_{11} \rangle}{\partial a} \right) \right] d\theta \right\}. \end{aligned} \quad (29)$$

In the case of external white noise excitation, one has

$$\begin{aligned} \langle K_{11} \rangle &= \langle (\sigma^2/\omega^2) \sin^2 \phi \rangle = \frac{\sigma^2}{2\omega^2}, \\ \langle K_{12} \rangle &= \langle (\sigma^2/\omega^2) \sin \phi \cos \phi \rangle = 0 \\ \langle K_{22} \rangle &= \langle (\sigma^2/a^2 \omega^2) \cos^2 \phi \rangle = \frac{\sigma^2}{2\omega^2 a^2}. \end{aligned} \quad (30)$$

Then the condition (28) is simplified

$$\frac{\partial}{\partial \theta} \langle K_1 \rangle = \frac{\partial}{\partial a} (a^2 \langle K_2 \rangle), \quad (31)$$

and the corresponding solution (29) takes the form

$$W(a, \theta) = \exp \{ (4\omega^2/\sigma^2) \int [\langle K_1 \rangle da + a^2 \langle K_2 \rangle d\theta] \}. \quad (32)$$

A class of mechanical systems, for which the condition (28) is fulfilled, has been indicated in Mitropolskii *et al* (1992).

2.2 Method of expansion in a quasicyclic coordinate

First, the FP equation (24) is transformed to the form

$$\frac{\partial \langle K_1 \rangle}{\partial a} + \frac{\partial \langle K_2 \rangle}{\partial \theta} - \frac{1}{2} \frac{\partial^2 \langle K_{11} \rangle}{\partial a^2} - \frac{\partial^2 \langle K_{12} \rangle}{\partial a \partial \theta}$$

$$\begin{aligned}
& -\frac{1}{2} \frac{\partial^2 \langle K_{22} \rangle}{\partial \theta^2} + \left(\langle K_1 \rangle - \frac{\partial \langle K_{11} \rangle}{\partial \theta} - \frac{\partial}{\partial \theta} \langle K_{12} \rangle \right) \frac{\partial \Phi}{\partial a} \\
& + \left(\langle K_2 \rangle - \frac{\partial \langle K_{22} \rangle}{\partial \theta^2} - \frac{\partial \langle K_{12} \rangle}{\partial a} \right) \frac{\partial \Phi}{\partial \theta} - \frac{\langle K_{11} \rangle}{2} \left[\left(\frac{\partial \Phi}{\partial a} \right)^2 + \frac{\partial^2 \Phi}{\partial a^2} \right] \\
& - \langle K_{12} \rangle \left[\frac{\partial^2 \Phi}{\partial a \partial \theta} + \frac{\partial \Phi}{\partial a} \frac{\partial \Phi}{\partial \theta} \right] - \frac{\langle K_{22} \rangle}{2} \left[\frac{\partial^2 \Phi}{\partial \theta^2} + \left(\frac{\partial \Phi}{\partial \theta} \right)^2 \right] = 0, \quad (33)
\end{aligned}$$

where

$$\phi(a, \theta) = \ln W(a, \theta). \quad (34)$$

In many cases, the coefficients of drift and diffusion are polynomials in the amplitude a with integral powers and with coefficients depending on θ . The amplitude a may thus play the role of a quasicyclic coordinate. According to the method of expansion in series in terms of the quasicyclic coordinate, one can also find the solution of (33) in $\partial \Phi / \partial a$ in the form of a polynomial containing integral powers of the amplitude a :

$$\frac{\partial \phi}{\partial a} = a^{-\tau} + \sum_{i=0}^{\infty} i \mu_i(\theta) a^{i-1}. \quad (35)$$

Then one has

$$W(a, \theta) = Ca^{\tau} \exp \left\{ \sum_{i=0}^{\infty} \mu_i(\theta) a^i \right\}. \quad (36)$$

Substituting (35) in to (33), and equating the coefficients of the same powers of a , one obtains a closed system of separable differential equations for the successive determination of all the unknown coefficients $\mu_i(\theta)$. The arbitrary integration constants must be chosen from the condition for the functions $\mu_i(\theta)$ to be periodic. The problem of the convergence of the series (36) is not easy, however, it does not arise in cases when one admits an exact solution of the form

$$\mu_i(\theta) = \Psi_i(\theta), \quad i = 0, 2, \dots, N; \quad \mu_l(\theta) = 0, \quad l \geq N + 1. \quad (37)$$

Then we obtain

$$W(a, \theta) = Ca^{\tau} \exp \left\{ \sum_{i=0}^{\infty} \Psi_i(\theta) a^i \right\}. \quad (38)$$

This property will be shared by many mechanical systems (Mitropolskii *et al* 1992).

Example 1. The Van der Pol system to periodic and white noise excitations

$$\ddot{x} + \omega^2 x = \varepsilon(1 - \gamma x^2) \dot{x} + \varepsilon P \cos \omega t + \sqrt{\varepsilon} \sigma \xi(t). \quad (39)$$

The corresponding coefficients of drift and diffusion are to be found

$$\begin{aligned}
K_1 &= a \sin^2 \phi - a^3 \gamma \cos^2 \phi \sin^2 \phi - \frac{P}{\omega} \cos \omega t \sin \phi + \frac{\sigma^2}{2\omega^2} \cos^2 \phi a^{-1}, \\
K_2 &= \sin \phi \cos \phi - a^2 \gamma \cos^3 \phi \sin \phi - \frac{P}{a\omega} \cos \omega t \cos \phi - \frac{\sigma^2}{\omega^2} \sin \phi \cos \phi a^{-2}, \\
K_{11} &= \frac{\sigma^2}{\omega^2} \cos^2 \phi, \quad K_{12} = \frac{\sigma^2}{\omega^2} \sin \phi \cos^2 \phi a^{-1}, \quad K_{22} = \frac{\sigma^2}{\omega^2} \cos^2 \phi a^{-2}. \quad (40)
\end{aligned}$$

Hence one gets, noting $\omega t = \phi - \theta$,

$$\begin{aligned}\langle K_1 \rangle &= \frac{\sigma^2}{4\omega^2} a^{-1} + \frac{a}{2} - \frac{\gamma}{8} a^3 - \frac{P}{2\omega} \sin \theta, \\ \langle K_2 \rangle &= -\frac{P}{2\omega} \cos \theta a^{-1}, \\ \langle K_{11} \rangle &= \frac{\sigma^2}{2\omega^2}, \quad \langle K_{12} \rangle = 0, \quad \langle K_{22} \rangle = \frac{\sigma^2}{2\omega^2} a^{-2}.\end{aligned}\quad (41)$$

It is easy to show that the averaged coefficients (41) satisfy the condition of integrability (31). Thus, substituting (41) into (32) yields the following probability density function $W(a, \theta)$ of the Van der Pol system (39)

$$W(a, \theta) = Ca \exp \left\{ -\frac{2\omega P}{\sigma^2} \sin \theta a + \frac{\omega^2}{\sigma^2} a^2 - \frac{\gamma \omega^2}{8\sigma^2} a^4 \right\}, \quad (42)$$

where C is a normalization constant.

The solution (42) can also be obtained by using the method of expansion in a quasicyclic coordinate. Thus, let

$$W(a, \theta) = Ca \exp \{ \mu_0(\theta) + \mu_1(\theta)a + \mu_2(\theta)a^2 + \dots \}. \quad (43)$$

Substituting (43), (41) into FP equation (24) and equating the coefficients of $a^{-2}, a^{-1}, a^0, \dots$ we obtain the following system of separable equations for the unknown $\mu_0(\theta), \mu_1(\theta), \mu_2(\theta), \dots$ (a prime denotes differentiation with respect to θ),

$$\begin{aligned}\mu_0'' + \mu_0' &= 0, \quad \mu_1'' + \mu_1 = 0, \\ \mu_2'' + 4\mu_2 &= \frac{4\omega^2}{\sigma^2} - (\mu_1^2 + \mu_1'^2) - \frac{2\omega P}{\sigma^2} (\mu_1 \sin \theta + \mu_1' \cos \theta), \\ \mu_3'' + 9\mu_3 &= -2(2\mu_1\mu_2 + \mu_1'\mu_2') - \frac{2\omega P}{\sigma^2} (2\mu_2 \sin \theta + \mu_2' \cos \theta) + \frac{2\omega^2}{\sigma^2} \mu_1, \\ \mu_4'' + 16\mu_4 &= -(4\mu_2^2 + \mu_2'^2) - 2(3\mu_1\mu_3 + \mu_1'\mu_3') - \frac{2\omega^2\gamma}{\sigma^2} - \\ &\quad \frac{2\omega P}{\sigma^2} (3\mu_3 \sin \theta + \mu_3' \cos \theta) + \frac{4\omega^2}{\sigma^2} \mu_2.\end{aligned}\quad (44)$$

It can be shown that the system (44) has the solution

$$\begin{aligned}\mu_0(\theta) &\equiv 0, \quad \mu_n(\theta) \equiv 0, \quad n \geq 5, \\ \mu_1(\theta) &= -\frac{2\omega P}{\sigma^2} \sin \theta, \quad \mu_2(\theta) = \frac{\omega^2}{\sigma^2}, \quad \mu_4(\theta) = -\frac{\gamma \omega^2}{8\sigma^2}.\end{aligned}\quad (45)$$

Substituting (45) into (43) yields (42) again.

The probability density function (42) has extremums at the points (a, θ) , where

$$\begin{aligned}\frac{\partial W}{\partial a} &\equiv \frac{\sigma^2}{a} + 2\omega^2 a - \frac{\gamma \omega^2}{2} a^3 - 2\omega P \sin \theta = 0, \\ \frac{\partial W}{\partial \theta} &\equiv -2\omega P a \cos \theta = 0.\end{aligned}\quad (46)$$

Hence, we get the most probable value of the amplitude

$$\left[\frac{\sigma^2}{a} + 2\omega^2 a - \frac{\gamma\omega^2}{2} a^3 \right]^2 = 4\omega^2 P^2. \quad (47)$$

For $\sigma \rightarrow 0$, $P \rightarrow 0$ the value (47) tends to the known value of the amplitude of self-oscillations of the Van der Pol system.

If the mechanical system is autonomous, the averaged corresponding coefficients of drift $\langle K_1 \rangle$, $\langle K_2 \rangle$ depend only on a . Thus, the stationary probability density function of amplitude $W_0(a)$ can be found from the equation

$$\frac{\partial}{\partial a} [\langle K_1 \rangle W_0(a)] - \frac{1}{2} \frac{\partial^2}{\partial a^2} [\langle K_{11} \rangle W_0(a)] = 0. \quad (48)$$

It is known that in many cases of interest the averaged FP equation (48) is not sufficient for analysis of nonlinear terms in the original equation (1).

3. Higher approximate solutions to FP equation

We consider only the autonomous case of (1) and suppose the considered system has a stationary response. Using the transformation

$$x = a \cos \phi, \quad \dot{x} = -a\omega \sin \phi, \quad (49)$$

and the Ito formula we reduce (1) to the form

$$\begin{aligned} da &= \varepsilon K_1(a, \phi, \varepsilon) dt - ((\varepsilon)^{1/2}/\omega) \sigma \sin \phi dn(t), \\ d\phi &= [\omega + \varepsilon K_2(a, \phi, \varepsilon)] dt - ((\varepsilon)^{1/2}/\omega a) \sigma \cos \phi dn(t). \end{aligned} \quad (50)$$

The corresponding FP equation for the stationary probability density function $W(a, \phi)$ takes the form

$$\begin{aligned} \omega \frac{\partial W}{\partial \phi} &= -\varepsilon \left\{ \frac{\partial}{\partial a} (K_1 W) + \frac{\partial}{\partial \phi} (K_2 W) \right. \\ &\quad \left. - \frac{1}{2} \left[\frac{\partial^2}{\partial a^2} (K_{11} W) + 2 \frac{\partial^2}{\partial a \partial \phi} (K_{12} W) + \frac{\partial^2}{\partial \phi^2} (K_{22} W) \right] \right\}, \end{aligned} \quad (51)$$

where the coefficients of drift and diffusion are given in (21). Denote

$$\Phi(a, \phi) = \ln W(a, \phi), \quad \Phi_0(a) = \ln W_0(a). \quad (52)$$

It is easy to show

$$\begin{aligned} \frac{\partial W}{\partial a} &= \frac{\partial \Phi}{\partial a} W, \quad \frac{\partial^2 W}{\partial a^2} = \left[\frac{\partial^2 \Phi}{\partial a^2} + \left(\frac{\partial \Phi}{\partial a} \right)^2 \right] W, \\ \frac{\partial^2 W}{\partial a \partial \phi} &= \left[\frac{\partial^2 \Phi}{\partial a \partial \phi} + \frac{\partial \Phi}{\partial a} \frac{\partial \Phi}{\partial \phi} \right] W. \end{aligned} \quad (53)$$

For the given functions $K_j(a, \phi)$, $K_{ij}(a, \phi)$, $K_{ij} = K_{ji}$, $i, j = 1, 2$, the operators $[K_i, K_{ij}] \mathcal{L}$ and $[K_i, K_{ij}] l$ are defined as follows

$$\begin{aligned}
 [K_i, K_{ij}] \mathcal{L}(W) &= \frac{\partial}{\partial a}(K_i W) + \frac{\partial}{\partial \phi}(K_{ij} W) \\
 &\quad - \frac{1}{2} \left[\frac{\partial^2}{\partial a^2}(K_{i1} W) + \frac{2\partial^2}{\partial a \partial \phi}(K_{i2} W) + \frac{\partial^2}{\partial \phi^2}(K_{22} W) \right], \\
 [K_i, K_{ij}] l(W) &= \left(\frac{\partial K_i}{\partial a} + \frac{\partial K_i}{\partial \phi} - \frac{1}{2} \frac{\partial^2 K_{i1}}{\partial a^2} - \frac{\partial K_{i2}}{\partial a \partial \phi} - \frac{1}{2} \frac{\partial^2 K_{22}}{\partial \phi^2} \right) \\
 &\quad + \left(K_i - \frac{\partial K_{i1}}{\partial a} - \frac{\partial K_{i2}}{\partial \phi} \right) \frac{\partial W}{\partial a} + \left(K_{ij} - \frac{\partial K_{22}}{\partial \phi} - \frac{\partial K_{i2}}{\partial a} \right) \frac{\partial W}{\partial \phi} \\
 &\quad - \frac{1}{2} \left\{ K_{i1} \left(\frac{\partial^2 W}{\partial a^2} + \left(\frac{\partial W}{\partial a} \right)^2 \right) \right. \\
 &\quad \left. + 2K_{i2} \left(\frac{\partial^2 W}{\partial a \partial \phi} + \frac{\partial W}{\partial a} \frac{\partial W}{\partial \phi} \right) + K_{22} \left(\frac{\partial^2 W}{\partial \phi^2} + \left(\frac{\partial W}{\partial \phi} \right)^2 \right) \right\}. \quad (54)
 \end{aligned}$$

Calculations show that operators $[K_i, K_{ij}] \mathcal{L}$, $[K_i, K_{ij}] l$ have the following properties

$$[K_i, K_{ij}] \mathcal{L}(\alpha W + \beta W_1) = \alpha [K_i, K_{ij}] \mathcal{L}(W) + \beta [K_i, K_{ij}] \mathcal{L}(W_1), \quad (55a)$$

$$\alpha [K_i, K_{ij}] \mathcal{L}(W) = [\alpha K_i, \alpha K_{ij}] \mathcal{L}(W) = [K_i, K_{ij}] \mathcal{L}(\alpha W), \quad (55b)$$

$$[K_i + R_i, K_{ij} + R_{ij}] \mathcal{L}(W) = [K_i, K_{ij}] \mathcal{L}(W) + [R_i, R_{ij}] \mathcal{L}(W), \quad (55c)$$

$$[K_i, K_j] \mathcal{L}(W_1 W) = [K_i W_1, K_{ij} W_1] \mathcal{L}(W), \quad (55d)$$

$$[K_i, K_{ij}] \mathcal{L}(W) = W [K_i, K_{ij}] l(W), \quad (55e)$$

$$\langle [K_i, K_{ij}] \mathcal{L}(W_0(a)) \rangle = [\langle K_i \rangle, \langle K_{ij} \rangle] \mathcal{L}(W_0(a)), \quad (55f)$$

where

$$W(a, \phi), \quad W_1(a, \phi), \quad R_i(a, \phi), \quad R_{ij}(a, \phi), \quad R_{ij} = R_{ji}, \quad i, j = 1, 2,$$

are arbitrary functions of a and ϕ , $W_0(a)$ is a function in a , α and β are constants. Using now the operator $[K_i, K_{ij}] \mathcal{L}$, the FP equation (51) can be rewritten in the form

$$\omega \frac{\partial W}{\partial \phi} = -\varepsilon [K_i, K_{ij}] \mathcal{L}(W). \quad (56)$$

Suppose that

$$K_i(a, \phi, \varepsilon) = K_{i0}(a, \phi) + R_{i1}(a, \phi)\varepsilon + R_{i2}(a, \phi)\varepsilon^2 + \dots, \quad i = 1, 2. \quad (57)$$

We seek the solution of (56) in the form

$$W = W_0 + \varepsilon W_1 + \varepsilon^2 W_2 + \dots \quad (58)$$

Substituting (57), (58) into (56) and noting the properties (55) yields

$$\begin{aligned}
 \omega \left[\frac{\partial W_0}{\partial \phi} + \varepsilon \frac{\partial W_1}{\partial \phi} + \varepsilon^2 \frac{\partial W_2}{\partial \phi} + \dots \right] = \\
 -\varepsilon \{ [K_{i0}, K_{ij}] \mathcal{L}(W_0) + \varepsilon [K_{i0}, K_{ij}] \mathcal{L}(W_1) + [R_{i1}, 0] \mathcal{L}(W_0) + \dots \}
 \end{aligned}$$

Comparing the coefficients of like powers of ε one obtains

$$\varepsilon^0: \omega \frac{\partial W_0}{\partial \phi} = 0, \quad (59)$$

$$\varepsilon^1: \omega \frac{\partial W_1}{\partial \phi} = -[K_{i0}, K_{ij}] \mathcal{L}(W_0), \quad (60)$$

$$\varepsilon^2: \omega \frac{\partial W_2}{\partial \phi} = -[K_{i0}, K_{ij}] \mathcal{L}(W_1) - [R_{i1}, 0] \mathcal{L}(W_0). \quad (61)$$

From (59) it follows

$$W_0 = W_0(a), \quad (62)$$

then (60) yields

$$\omega \frac{\partial W_1}{\partial \phi} = -[K_{i0}, K_{ij}] \mathcal{L}(W_0(a)). \quad (63)$$

The arbitrary integration function $W_0(a)$ must be chosen from the condition for the function W_1 to be periodic. Thus, one gets from (63)

$$\langle [K_{i0}, K_{ij}] \mathcal{L}(W_0(a)) \rangle = 0, \quad (64)$$

$$\omega \frac{\partial W_1}{\partial \phi} = -\{[K_{i0}, K_{ij}] \mathcal{L}(W_0(a)) - \langle [K_{i0}, K_{ij}] \mathcal{L}(W_0(a)) \rangle\} \quad (65)$$

Taking into account the property (55f), one can rewrite (64) in the form

$$[\langle K_{i0} \rangle, \langle K_{ij} \rangle] \mathcal{L}(W_0(a)) = 0, \quad (66)$$

which is identical to (48). Hence, it is shown that the averaged FP equation (48) may be obtained by equating to zero the averaged value of the coefficient of power ε in the original FP equation (51). Further, using (66) and (55e) one gets from (65)

$$\omega \frac{\partial W_1}{\partial \phi} = -W_0(a) [K_{i0}, K_{ij}] l(\Phi_0(a)). \quad (67)$$

Expand $[K_{i0}, K_{ij}] l(\Phi_0(a))$ into a Fourier series as K_i, K_{ij} are periodic functions in ϕ with period 2π (see (21))

$$\begin{aligned} [K_{i0}, K_{ij}] l(\Phi_0(a)) = 2 \sum_{n=1} \{ \langle [K_{i0}, K_{ij}] l(\Phi_0(a)) \sin n\phi \rangle \sin n\phi \\ + \langle [K_{i0}, K_{ij}] l(\Phi_0(a)) \cos n\phi \rangle \cos n\phi \}. \end{aligned} \quad (68)$$

Substituting (68) into (67) yields

$$W_1(a, \phi) = W_0(a) (W_{11}(a, \phi) + W_{10}(a)), \quad (69)$$

where $W_{10}(a)$ is an arbitrary integration function of a , and

$$\begin{aligned} W_{11}(a, \phi) = -\frac{2}{\omega} \sum_{n=1} \frac{1}{n} \{ \langle [K_{i0}, K_{ij}] l(\Phi_0(a)) \cos n\phi \rangle \sin n\phi - \\ \langle [K_{i0}, K_{ij}] l(\Phi_0(a)) \sin n\phi \rangle \cos n\phi \}. \end{aligned} \quad (70)$$

Substituting (69) into (61) and noting (55a), (55d) yields

$$\begin{aligned} \omega \frac{\partial W_2}{\partial \phi} = & -[K_{i0} W_{11}, K_{ij} W_{11}] \mathcal{L}(W_0(a)) - [K_{i0} W_0(a), K_{ij} W_0(a)] \\ & \times \mathcal{L}(W_{10}(a)) - \frac{\partial}{\partial a}(R_{11} W_0(a)) - \frac{\partial}{\partial \phi}(R_{21} W_0(a)). \end{aligned} \quad (71)$$

Therefore it follows

$$\begin{aligned} & \langle [K_{i0} W_{11}, K_{ij} W_{11}] \mathcal{L}(W_0(a)) + [K_{i0} W_0(a), K_{ij} W_0(a)] \\ & \times \mathcal{L}(W_{10}(a)) - \frac{\partial}{\partial a}(R_{11} W_0(a)) - \frac{\partial}{\partial \phi}(R_{21} W_0(a)) \rangle = 0 \end{aligned} \quad (72)$$

or noting (55f),

$$\begin{aligned} & [\langle K_{i0} W_{11} \rangle, \langle K_{ij} W_{11} \rangle] \mathcal{L}(W_0(a)) + [\langle K_{i0} W_0(a) \rangle, \langle K_{ij} W_0(a) \rangle] \\ & \times \mathcal{L}(W_{10}(a)) - \frac{\partial}{\partial a}(\langle R_{11} \rangle W_0(a)) = 0. \end{aligned} \quad (73)$$

In the explicit form, (73) takes the form

$$\begin{aligned} & \langle K_{i0} W_{11} \rangle W_0(a) - \frac{1}{2} \frac{\partial}{\partial a} \{ \langle K_{11} W_{11} \rangle W_0(a) \} + \langle K_{i0} W_0(a) \rangle W_0(a) \\ & - \frac{1}{2} \frac{\partial}{\partial a} \{ \langle K_{11} W_0(a) \rangle W_{10}(a) \} - \frac{\partial}{\partial a} - \frac{\partial}{\partial a} (\langle R_{11} \rangle W_0(a)) = 0. \end{aligned} \quad (74)$$

Using (48) one gets from (74),

$$\begin{aligned} & \langle K_{i0} W_{11} \rangle - \frac{1}{2} \frac{\partial}{\partial a} \langle K_{11} W_{11} \rangle - \frac{1}{2} \langle K_{11} W_{11} \rangle \frac{\partial \Phi_0(a)}{\partial a} \\ & - \frac{1}{2} \langle K_{11} \rangle \frac{\partial W_{10}}{\partial a} - \frac{\partial \langle R_{11} \rangle}{\partial a} - \langle R_{11} \rangle \frac{\partial \Phi_0(a)}{\partial a} = 0 \end{aligned}$$

So one obtains

$$\begin{aligned} W_{10}(a) = & \int \left[\frac{1}{\langle K_{11} \rangle} 2 \langle K_{i0} W_{11} \rangle - \frac{\partial}{\partial a} \langle K_{11} W_{11} \rangle \right. \\ & \left. - \langle K_{11} W_{11} \rangle \frac{\partial \Phi_0(a)}{\partial a} - 2 \frac{\partial}{\partial a} \langle R_{11} \rangle - 2 \langle R_{11} \rangle \frac{\partial \Phi_0}{\partial a} \right] da. \end{aligned} \quad (75)$$

Substituting (75) into (71) and noting that

$$[K_{i0} W_0, K_{ij} W_0] \mathcal{L}(W_{10}) = [K_{i0} W_{10}, K_{ij} W_0] \mathcal{L}(W_0),$$

one gets from (71)

$$W_2(a, \phi) = W_0(a) W_{22}(a, \phi), \quad (76)$$

where

$$\begin{aligned} W_{22}(a, \phi) = & -\frac{1}{\omega} \int \left\{ [K_{i0} W_{11} + K_{i0} W_{10}, K_{ij} W_{11} + K_{ij} W_{10}] l(\Phi_0(a)) \right. \\ & \left. - \frac{\partial R_{11}}{\partial a} - R_{11} \frac{\partial \Phi_0}{\partial a} - \frac{\partial R_{21}}{\partial \phi} \right\} d\phi. \end{aligned} \quad (77)$$

According to SAM, the second approximate solution to the FP equation (51) is defined as

$$W(a, \phi) = W_0(a) \{1 + \varepsilon(W_{10}(a) + W_{11}(a, \phi))\}, \quad (78)$$

and the improved second approximate solution is

$$W(a, \phi) = W_0(a) \{1 + \varepsilon(W_{10}(a) + W_{11}(a, \phi)) + \varepsilon^2 W_{22}(a, \phi)\}, \quad (79)$$

where $W_0(a)$, $W_{10}(a)$, $W_{11}(a, \phi)$ and $W_{22}(a, \phi)$ are found from (48), (75), (70) and (77), respectively. It is seen that the solution (79) might be negative, however, this difficulty arises very often in truncated series expanding the probability density function.

Example 2 – Duffing oscillator: Apply now the proposed procedure to the Duffing oscillator subjected to white noise excitation

$$\ddot{x} + \omega^2 x = -2\epsilon h \dot{x} - \epsilon \gamma x^3 + \sqrt{\epsilon} \sigma \xi(t), \quad h, \gamma > 0. \quad (80)$$

From (80) and (21) one gets

$$\begin{aligned} K_1(a, \phi) &= \frac{\sigma^2}{4a\omega^2} - ha + \left(ha + \frac{\sigma^2}{4a\omega^2}\right) \cos 2\phi + \frac{\gamma}{4\omega} a^3 \sin 2\phi + \frac{\gamma}{8\omega} a^3 \sin 4\phi, \\ K_2(a, \phi) &= \frac{3\gamma}{8\omega} a^2 - \left(h + \frac{\sigma^2}{2a^2\omega^2}\right) \sin 2\phi + \frac{\gamma}{2\omega} a^2 \cos 2\phi + \frac{\gamma}{8\omega} a^2 \cos 4\phi, \\ K_{11}(a, \phi) &= \frac{\sigma^2}{2\omega^2} - \frac{\sigma^2}{2\omega^2} \cos 2\phi, \quad K_{12}(a, \phi) = \frac{\sigma^2}{2a\omega^2} \sin 2\phi, \\ K_{22}(a, \phi) &= \frac{\sigma^2}{2a^2\omega^2} + \frac{\sigma^2}{2a^2\omega^2} \cos 2\phi. \end{aligned} \quad (81)$$

The corresponding averaged FP equation (48) is

$$\frac{\partial}{\partial a} \left[\left(\frac{\sigma^2}{4a\omega^2} - ha \right) W_0(a) \right] - \frac{1}{2} \frac{\partial^2}{\partial a^2} \left[\frac{\sigma^2}{2\omega^2} W_0(a) \right] = 0, \quad (82)$$

which gives the solution

$$W_0(a) = Ca \exp \left\{ -\frac{2h\omega^2}{\sigma^2} a^2 \right\}. \quad (83)$$

It is seen that the solution (83) corresponds to the linear case of the system (80), ($\gamma = 0$), and does not include the effect of the nonlinear term γx^3 .

Further, substituting (81), (83), (54) into (68) yields

$$[K_i, K_{ij}] l(\Phi_0(a)) = -\frac{\gamma h \omega}{2\sigma^2} a^4 \{2 \sin 2\phi + \sin 4\phi\}. \quad (84)$$

Then, from (67) one gets

$$W_{11}(a, \phi) = -W_0(a) \frac{\gamma h a^4}{2\sigma^2} \left\{ \cos 2\phi + \frac{1}{4} \cos 4\phi \right\} \quad (85)$$

Further, using (81), (83), and (85) one gets from (75)

$$W_{10}(a) = \frac{-3\gamma ha^4}{8\sigma^2}. \quad (86)$$

Hence, the second approximate solution to the FP equation (51) for the Duffing case (80) takes the form

$$W(a, \phi) = Ca \exp \left\{ -\frac{2h\omega^2}{\sigma^2} a^2 \right\} \left[1 - \frac{\varepsilon\gamma h}{8\sigma^2} a^4 (3 + 4 \cos 2\phi + \cos 4\phi) \right]. \quad (87)$$

The condition

$$\int_0^\infty \int_0^{2\pi} W(a, \phi) da d\phi = 1 \quad (88)$$

gives

$$C = (2h\omega^2/\pi\sigma^2)(1 + (3\varepsilon\gamma\sigma^2/16h\omega^4)). \quad (89)$$

From (87) one gets the probability density function $W(a)$, $W(\phi)$, respectively.

$$W(a) = \frac{4h\omega^2}{\sigma^2} \left(1 + \frac{3\varepsilon\gamma\sigma^2}{16h\omega^4} \right) \left(a - \frac{3\varepsilon\gamma h}{8\sigma^2} a^5 \right) \exp \left\{ -\frac{2h\omega^2}{\sigma^2} a^2 \right\},$$

$$W(\phi) = \frac{1}{2\pi} \left(1 + \frac{3\varepsilon\gamma\sigma^2}{16h\omega^4} \right) \left[1 - \frac{\varepsilon\gamma\sigma^2}{16h\omega^4} (3 + 4 \cos 2\phi + \cos 4\phi) \right]. \quad (90)$$

Thus, in particular, one has

$$\langle a^2 \rangle = \frac{\sigma^2}{2h\omega^2} - \varepsilon \frac{3\gamma\sigma^4}{16h^2\omega^6}. \quad (91)$$

Hence, using the second approximate solution, the effect of the nonlinear term γx^3 is obtained in the formulae (87), (90), and (91). It is seen from (91), that the nonlinear term γx^3 reduces the mean square of the amplitude. This effect cannot be found from the first stochastic averaging.

4. A modified procedure

A similar procedure can be applied to the function $\Phi(a, \phi)$ by imposing

$$\Phi = \Phi_0 + \varepsilon\Phi_1 + \varepsilon^2\Phi_2 + \dots \quad (92)$$

Noting (52), (55e) one gets from (56) the following equation for Φ :

$$\omega \frac{\partial \Phi}{\partial \phi} = -\varepsilon [K_i, K_{ij}] I(\Phi). \quad (93)$$

Substituting (57), (92) into (93) and comparing the coefficients of like powers of ε yields

$$\omega \frac{\partial \Phi_0}{\partial \phi} = 0, \quad (94)$$

$$\omega \frac{\partial \Phi_1}{\partial \phi} = -[K_{i0}, K_{ij}]l(\Phi_0), \quad (95)$$

$$\begin{aligned} \omega \frac{\partial \Phi_2}{\partial \phi} = & - \left(K_{10} - \frac{\partial K_{11}}{\partial a} - \frac{\partial K_{12}}{\partial \phi} \right) \frac{\partial \Phi_1}{\partial a} - \left(K_{20} - \frac{\partial K_{22}}{\partial \phi} - \frac{\partial K_{12}}{\partial a} \right) \frac{\partial \Phi_1}{\partial \phi} \\ & + \frac{1}{2} K_{11} \left(\frac{\partial^2 \Phi_1}{\partial a^2} + 2 \frac{\partial \Phi_0}{\partial a} \frac{\partial \Phi_1}{\partial a} \right) + K_{12} \left(\frac{\partial^2 \Phi_1}{\partial a \partial \phi} + \frac{\partial \Phi_0}{\partial a} \frac{\partial \Phi_1}{\partial \phi} \right) \\ & + \frac{1}{2} K_{22} \frac{\partial^2 \Phi_1}{\partial \phi^2} - \frac{\partial R_{11}}{\partial a} - \frac{\partial R_{21}}{\partial \phi} - R_{11} \frac{\partial \Phi_0}{\partial a}, \dots \end{aligned} \quad (96)$$

As an illustration apply the procedure to the autonomous Van der Pol system (39), ($P = 0$). In this case the coefficients K_1, K_2 of drift do not depend on ε and are obtained from (40) by putting $P = 0$. Equation (94) yields $\Phi_0 = \Phi_0(a)$ and (95) gives, in particular,

$$[\langle K_{i0} \rangle, \langle K_{ij} \rangle]l(\Phi_0(a)) = 0. \quad (97)$$

Substituting (40) ($P = 0$) and (54) into (97) yields

$$\Phi_0(a) = \ln C + \ln a + \frac{\omega^2}{\sigma^2} a^2 - \frac{\gamma \omega^2}{8\sigma^2} a^4, \quad (98)$$

$$W_0(a) = Ca \exp \left\{ \frac{\omega^2}{\sigma^2} a^2 - \frac{\gamma \omega^2}{8\sigma^2} a^4 \right\}. \quad (99)$$

Substituting (40) ($P = 0$) and (99) into (54) one gets from (95)

$$\begin{aligned} \Phi_1(a, \phi) = & \frac{\gamma}{32\omega\sigma^2} (12\sigma^2 a^2 + 4\omega^2 a^4 - \gamma \omega^2 a^6) \sin 2\phi \\ & + \frac{\gamma\omega}{64\sigma^2} (\gamma a^6 - 4a^4) \sin 4\phi + \Phi_{10}(a). \end{aligned} \quad (100)$$

Substituting (100) and (40) ($P = 0$) into (96) after averaging a particular solution for $\Phi_{10}(a)$ is obtained,

$$\Phi_{10}(a) = 0 \quad (101)$$

Thus, the probability density function $W(a, \phi)$ of amplitude and phase of the autonomous Van der Pol system (39), ($P = 0$), takes the form

$$\begin{aligned} W(a, \phi) = & Ca \exp \left\{ \frac{\omega^2}{\sigma^2} a^2 - \frac{\gamma \omega^2}{8\sigma^2} a^4 + \frac{\varepsilon \gamma}{32\omega\sigma^2} (12\sigma^2 a^2 + 4\omega^2 a^4 - \gamma \omega^2 a^6) \right. \\ & \left. \times \sin 2\phi + \frac{\varepsilon \gamma \omega}{64\sigma^2} (\gamma a^6 - 4a^4) \sin 4\phi + \varepsilon^2 \dots \right\}, \end{aligned} \quad (102)$$

where C is a normalization constant.

5. Conclusion

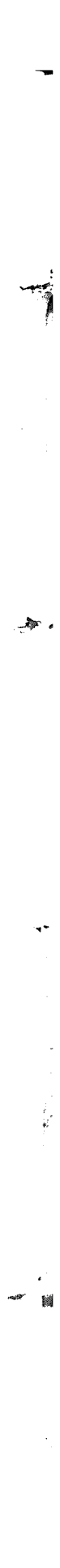
The stochastic averaging method is a useful tool for analysis of nonlinear random vibrations. Therefore, the development of SAM has attracted interest from investigators.

Furthermore, it has been observed that the effect of many nonlinear perturbations cannot be described by using the first approximate solution of SAM. It is shown in this paper that this difficulty may be overcome by considering higher approximate solutions of SAM.

Support from the fundamental research project in natural sciences is gratefully acknowledged.

References

- Anh N D 1985 On the study of random oscillations in non-autonomous mechanical systems using the FPK equation. *Prikl. Mat. Mekh.* 49: 392–397 (translated from the Russian by Pergamon Journals Ltd)
- Bogoliubov N N, Mitropolskii Iu A 1963 *Asymptotic methods in the theory of nonlinear oscillations* (Moscow: Nauka) (in Russian)
- Gikhman I I, Skorokhod A V 1982 *Stochastic differential equations and applications* (Kiev: Naukova - Dumka) (in Russian)
- Khasminskii R 1963 Principle of averaging for parabolic and elliptic differential equations and for Markov processes with small diffusion. *Theor. Prob. Appl.* 8: 1–21 (in Russian)
- Mitropolskii Iu A 1971 *Averaging method in nonlinear mechanics* (Kiev: Naukova – Dumka) (in Russian)
- Mitropolskii Iu A, Dao N V, Anh N D 1992 *Nonlinear oscillations in systems of arbitrary order* (Kiev: Naukova – Dumka) (in Russian)
- Stratonovitch R 1963 *Topics in the theory of random noise* (New York: Gordon & Breach) Vol. 1



Transient and stationary response statistics of van der Pol oscillators subjected to broad band random excitation

A NAESS¹ and B K HEGSTAD²

¹ Faculty of Civil Engineering, The Norwegian Institute of Technology, Rich. Birkelands v la, N-7034 Trondheim, Norway

² Faculty of Physics and Mathematics, The Norwegian Institute of Technology, A. Getz v 1, N-7034 Trondheim, Norway

Abstract. The joint probability density function of the state space vector of a white noise excited van der Pol oscillator satisfies a Fokker–Planck–Kolmogorov (FPK) equation. The paper describes a numerical procedure for solving the transient FPK equation based on the path integral solution (PIS) technique. It is shown that by combining the PIS with a cubic *B*-spline interpolation method, numerical solution algorithms can be implemented giving solutions of the FPK equation that can be made accurate down to very low probability levels. The method is illustrated by application to two specific examples of a van der Pol oscillator.

Keywords. Nonlinear vibration; stochastic excitation; random response; van der Pol oscillator.

1. Introduction

The van der Pol oscillator has been extensively studied over the last several decades, and it has come to play the role as one of the archetypes of a nonlinear oscillator. Its dynamic properties relative to deterministic harmonic excitation are by now well mapped out. The available literature on the van der Pol oscillator is voluminous. A guide to this literature is provided by Hayashi (1964), Andronov *et al* (1987) and Hagedorn (1988).

While the reported work on the van der Pol oscillator is extensive, only a very small part of it deals with the probabilistic aspects of this oscillator, in particular the response statistics when the oscillator is subjected to stochastic excitation, see e.g. Caughey (1959), Stratonovich (1967), Piszczek (1977), Spanos (1979), Zhu & Yu (1987). The purpose of the present paper is to contribute to the study of the response statistics of the van der Pol oscillator when it is subjected to stationary Gaussian white noise.

Due to its particular nonlinear properties, the dynamic analysis of the van der Pol oscillator does not easily lend itself to the various perturbation, linearization or similar techniques. At present there seems to be basically two methodologies available for studying the response statistics of substantially nonlinear dynamic systems subjected to

random forcing. One is the time domain Monte Carlo simulation method. The other is based on the theory of Markov processes. In this paper we shall deal exclusively with methods of the second class. In this class, the methods are based on the assumption that the forcing term can be obtained by filtering white noise processes. It is then often possible to rewrite the equation of motion in terms of a Markov vector process whose probability density function satisfies the Fokker–Planck–Kolmogorov (FPK) equation, also referred to as the forward Kolmogorov equation, and the backward Kolmogorov equation (Risken 1989; Wong & Hajek 1985). Solving one of the these equations would provide an extensive probabilistic characterization of the response process. However, it has turned out that these partial differential equations are in fact quite difficult to solve. Considerable effort has been invested in setting up numerical procedures for this purpose, see for instance Wehner & Wolfer (1983), Langley (1985) and Bergman & Spencer (1992).

2. The dynamic model

The equation of motion for a van der Pol oscillator driven by white noise can be written as follows, after suitable rescaling if necessary,

$$\ddot{X}(t) + 2\zeta[X(t)^2 - 1]\dot{X}(t) + X(t) = (2D)^{1/2}N(t). \quad (1)$$

Here ζ and D are positive parameters, determining specific versions of the oscillator. $N(t)$ denotes a standard, stationary Gaussian white noise, that is, $E[N(t)] = 0$ and $E[N(t)N(t + \tau)] = \delta(\tau)$.

The response behaviour of the oscillator depends decisively on the numerical values of the parameters of the problem. Already van der Pol (1927) observed that (1) would give rise to limit cycle oscillations that are almost sinusoidal functions of time when ζ is small compared to 1.0, while large values of ζ would result in oscillations approaching a square wave. These highly nonlinear oscillations are often referred to as relaxation oscillations.

The relaxation oscillation behaviour is in fact also reflected to a certain extent in the random response of a van der Pol oscillator to stochastic excitation. Early contributions to the study of white noise excited van der Pol oscillators were given by Stratonovich (1967), Caughey (1959) and Piszczek (1977). They developed approximation methods for deriving information on the stationary response statistics.

Numerical simulations have also been used to study the random response of the van der Pol oscillator, see e.g. Spanos (1979). Applying a generalized cell mapping technique (Hsu 1987) based on Monte Carlo simulation, Chiu & Hsu (1986) gave results for the steady-state probability density function of the van der Pol oscillator for a range of damping parameters ζ . This technique was further developed by Sun & Hsu (1990), to yield rather complete probabilistic information on the steady-state behaviour of the oscillator for specific values of the parameters. Recently, Zhu & Yu (1987) presented a critical review of previous work, pointing out that the stochastic averaging method used by Stratonovich, yields reasonable approximations of the response of a white noise excited van der Pol oscillator provided that $\zeta \ll 1$.

The key to the calculation of the response statistics of the white noise driven van der Pol oscillator is the fact that the joint PDF of the state space vector $[X, \dot{X}]^T$ satisfies a Fokker–Planck–Kolmogorov (FPK) equation. However, no general closed form

solution is known for the case of the van der Pol oscillator. It is therefore necessary to develop numerical solution strategies that apply to this particular oscillator. This has in fact turned out to be a rather demanding task. Langtangen (1991) and Bergman & Spencer (1992) report work on the development of finite element methods. The last paper presents results from the application of such methods to the van der Pol oscillator.

In the present paper an alternative solution strategy will be described. This is based on the concept of a path integral, which can be exploited to provide a formal solution to the FPK equation. The path integral solution (PIS) hinges on the property that the associated Markov diffusion process may be assumed to behave locally like a Brownian motion. This makes it possible to express the transition probability densities (TPD) of the Markov process in closed form for a short time step. The Markov character can then be invoked to build a global (in time) solution from local (in time) TDPs.

The PIS technique has been used as a basis for developing numerical solution methods for the FPK equation of nonlinear dynamic models driven by white noise by Wehner & Wolfer (1983) and Naess & Johnsen (1991, 1992). Naess & Johnsen have shown that the PIS technique can be used to provide accurate solutions down to very low probability levels for a wide range of nonlinear oscillators.

3. The path integral solution

Let the vector process $\mathbf{Z}(t) = [Z_1(t), Z_2(t)]^T$ (T as superindex denotes transposition) be defined by $Z_1(t) = X(t)$ and $Z_2(t) = \dot{X}(t)$. The equation of motion (1) can then be rewritten as

$$d\mathbf{Z}(t) = \mathbf{m}[\mathbf{Z}(t)]dt + \mathbf{Q}dB(t). \quad (2)$$

Here

$$\mathbf{m}[\mathbf{Z}(t)] = \begin{bmatrix} Z_2(t) \\ -2\zeta[Z_1(t)^2 - 1]Z_2(t) - Z_1(t) \end{bmatrix}, \quad (3)$$

$$\mathbf{Q} = \begin{bmatrix} 0 \\ (2D)^{1/2} \end{bmatrix}. \quad (4)$$

$B(t)$ denotes a standard, real Brownian motion, cf. Risken (1989) or Wong & Hajek (1985). Equation (2) will be interpreted as an Itô stochastic differential equation. The solution $\mathbf{Z}(t)$ to (2) is a Markov vector process whose TPD $p(z, t|z', t')$ is defined by the equation

$$\text{Prob}\{\mathbf{Z}(t) \in A | \mathbf{Z}(t') = z'\} = \int_A \int p(z, t|z', t') dz, \quad (5)$$

where $A \subseteq \mathbf{R}^2$ is some event, $z, z' \in \mathbf{R}^2$, $dz = dz_1 dz_2$. $\text{Prob}\{B|\Gamma\}$ denotes the conditional probability of B given Γ . It can be shown that the TPD $\dot{p} = p(z, t|z', t')$ ($t > t' \geq 0$) of the van der Pol oscillator satisfies the FPK equation,

$$\frac{\partial p}{\partial t} = 2\zeta(z_1^2 - 1)p - z_2 \frac{\partial p}{\partial z_1} + [2\zeta(z_1^2 - 1)z_2 + z_1] \frac{\partial p}{\partial z_2} + D \frac{\partial^2 p}{\partial z_2^2}, \quad (6)$$

with initial condition $p(z, t'|z', t') = \delta(z - z') - \delta(z_1 - z'_1)\delta(z_2 - z'_2)$.

Since clearly $\text{Prob}\{\mathbf{Z}(t) \in \mathbf{R}^2 | \mathbf{Z}(t') = \mathbf{z}'\} = 1$, the TPD satisfies the following normalization condition

$$\int_{-\infty}^{\infty} \int_{-\infty}^{\infty} p(\mathbf{z}, t | \mathbf{z}', t') d\mathbf{z} = 1 \quad (7)$$

Let $f(\mathbf{z}, t)$ denote the PDF of the random vector $\mathbf{Z}(t)$. If $f(\mathbf{z}, t') = w(\mathbf{z})$ for some initial PDF $w(\mathbf{z})$, then it is recognized from (6) and the relation,

$$f(\mathbf{z}, t) = \int_{-\infty}^{\infty} \int_{-\infty}^{\infty} p(\mathbf{z}, t | \mathbf{z}', t') w(\mathbf{z}') d\mathbf{z}', \quad (8)$$

that $f(\mathbf{z}, t)$ itself is a solution of (6) satisfying the initial condition $f(\mathbf{z}, t') = w(\mathbf{z})$.

The steady-state or stationary solutions $f_s(\mathbf{z})$ of (6), if they exist, are those solutions of (6) which satisfy $\partial f / \partial t = 0$, or

$$f_s(\mathbf{z}) = \lim_{t \rightarrow \infty} f(\mathbf{z}, t) = \lim_{t \rightarrow \infty} p(\mathbf{z}, t | \mathbf{z}', t') \quad (9)$$

To derive the PIS appropriate for the van der Pol oscillator, one may proceed in a manner similar to the derivations in Risken (1989). It can then be shown that the TPD for small values of $\tau (= t - t')$ is given by the following expression, which is correct up to terms of order τ^2 .

$$p(\mathbf{z}, t + \tau | \mathbf{z}', t) = \delta(\mathbf{z}_1 - \mathbf{z}'_1, -\mathbf{z}'_2 \tau) [1/2(\pi D \tau)^{1/2}] \times \exp\{- (1/4D\tau)[\mathbf{z}_2 - \mathbf{z}'_2 + 2\zeta(\mathbf{z}'_1{}^2 - 1)\mathbf{z}'_2 \tau + \mathbf{z}'_1 \tau]^2\}. \quad (10)$$

It may be noted that the expression for the TDP given by (10) is not unique, cf. Risken (1989).

Having obtained an explicit expression for the TDP for a short time step, one can now invoke the Markov property. This allows a TPD over a time interval of arbitrary length to be expressed in terms of a product of short-time TPDs. By dividing a given time interval (t', t) into N small time intervals of length $\tau = (t - t')/N$, it is found that $(t_j = t' + j\tau, t = t^N, \mathbf{z} = \mathbf{z}^{(N)}, t' = t_0, \mathbf{z}' = \mathbf{z}^{(0)})$

$$p(\mathbf{z}, t | \mathbf{z}', t') = \int_{\mathbf{R}^{2(N-1)}} \dots \int \prod_{j=1}^N p(\mathbf{z}^{(j)}, t_j | \mathbf{z}^{(j-1)}, t_{j-1}) d\mathbf{z}^{(1)} \dots d\mathbf{z}^{(N-1)}. \quad (11)$$

Similarly, with an initial PDF $f(\mathbf{z}', t') = w(\mathbf{z}')$, the PDF $f(\mathbf{z}, t)$ will be given by

$$f(\mathbf{z}, t) = \int_{\mathbf{R}^{2N}} \dots \int \prod_{j=1}^N p(\mathbf{z}^{(j)}, t_j | \mathbf{z}^{(j-1)}, t_{j-1}) w(\mathbf{z}^{(0)}) d\mathbf{z}^{(0)} \dots d\mathbf{z}^{(N-1)}. \quad (12)$$

Hence, by combining (10) with (11) or (12), a formal (approximate) solution of the FPK equation can be written down. Equations (11) and (12), which are often referred to as PIS, constitute the core of the numerical solution procedure to be described subsequently. It is realized that a numerical solution according to this method, automatically provides the evolution in time of the (conditional) PDF of the Markov process $\mathbf{Z}(t)$ from given start conditions in terms of an initial density $f(\mathbf{z}', t') = w(\mathbf{z}')$, including the degenerate case $f(\mathbf{z}', t') = \delta(\mathbf{z}' - \mathbf{z}_0)$, for some starting point \mathbf{z}_0 . We may therefore study directly how the response statistics develops in time from specified initial conditions until the oscillator reaches the steady-state response behaviour.

Obviously, the closer the initial PDF is to the stationary PDF, the faster the oscillator settles down to the steady-state behaviour.

It is also worth noting how the PIS relates to the physics of the dynamic model, which is expressed through the coefficient vectors $\mathbf{m}(\cdot)$ and \mathbf{Q} , cf. (2). The evolution in time of the PDF as expressed by the PIS, is seen to be directly determined by these coefficients in an explicit manner. This fact is a very important advantage of the PIS method, and reveals its fundamental physical significance.

4. Numerical implementation

The Chapman-Kolmogorov equation expressed as

$$p(z^{(j)}, t_j | z', t') = \int_{-\infty}^{\infty} \int_{-\infty}^{\infty} p(z^{(j)}, t_j | z^{(j-1)}, t_{j-1}) p(z^{(j-1)}, t_{j-1} | z', t') dz_1^{(j-1)} dz_2^{(j-1)}, \quad (13)$$

constitutes the basis for the iterative numerical implementation of the PIS.

The numerical estimates of the TPDs are calculated on a discrete set of grid points in state space. In an effort to retain accuracy with a relatively coarse grid, the expected smoothness of the TPDs was invoked. This would justify the introduction of an interpolation and smoothing procedure. For the purpose at hand, it was found that application of cubic *B*-splines (de Boor 1978) offered the desired accuracy and smoothness. This procedure was used as follows. At each time step $t_{j-1} \rightarrow t_j$, $p(z^{(j-1)}, t_{j-1} | z', t')$ is represented as a cubic *B*-spline series in the following manner,

$$p(z^{(j-1)}, t_j | z', t') = \sum_{k_1=1}^{M_1} \sum_{k_2=1}^{M_2} \Gamma^{(j-1)}(k_1, k_2) B_{k_1}(z_1^{(j-1)}) B_{k_2}(z_2^{(j-1)}), \quad (14)$$

M_i = number of grid points for the i th state variable z_i . Assuming that each set $\{B_{k_i}(\cdot)\}_{k_i=1}^{M_i}$, $i=1,2$ is a basis of cubic *B*-splines associated with the knot sequence (de Boor 1978) determined by the grid points for the i th variable z_i , it can be shown that $\{B_{k_1}(\cdot) B_{k_2}(\cdot)\}_{k_1=1}^{M_1} \{k_2=1}^{M_2}$ constitutes a basis of cubic *B*-splines for two-dimensional problems. $\{\Gamma^{(j-1)}(k_1, k_2)\}_{k_1=1}^{M_1} \{k_2=1}^{M_2}$ is the set of interpolation coefficients associated with time t_{j-1} .

The representation of $p(z^{(j-1)}, t_{j-1} | z', t')$ by *B*-splines makes it possible to retain high numerical accuracy even with a fairly coarse basic grid if $p(z^{(j-1)}, t_{j-1} | z', t')$ is not too singular. By substituting from (14) into (13), we obtain

$$p(z^{(j)}, t_j | z', t') = \sum_{k_1=1}^{M_1} \sum_{k_2=1}^{M_2} \Gamma^{(j-1)}(k_1, k_2) \times \int_{-\infty}^{\infty} \int_{-\infty}^{\infty} p(z^{(j)}, t_j | z^{(j-1)}, t_{j-1}) B_{k_1}(z_1^{(j-1)}) B_{k_2}(z_2^{(j-1)}) dz_1^{(j-1)} dz_2^{(j-1)}. \quad (15)$$

It is seen from (10) that the TPDs do not depend on absolute time, but only on the time increment. Markov processes whose TPDs have this property, are called homogeneous. It follows that

$$p(z^{(j)}, t_j | z^{(j-1)}, t_{j-1}) = p(z^{(j)}, \tau | z^{(j-1)}, 0), \quad j=1,2,\dots \quad (16)$$

which holds for any $t_j - t_{j-1} = \tau \geq 0$.

From (15) and (16) it is seen that for a fixed value of the time increment τ , each of the integrals on the right hand side of (15) needs to be calculated only once, and can be stored for repeated use. That is, the following parameters are calculated initially and stored

$$B_{k_1, k_2}^{l_1, l_2} = \int_{-\infty}^{\infty} \int_{-\infty}^{\infty} p(z_{(l_1, l_2)}^{(j)}, \tau | z_1^{(j-1)}, 0) B_{k_1}(z_1^{(j-1)}) B_{k_2}(z_2^{(j-1)}) dz_1^{(j-1)} dz_2^{(j-1)}. \quad (17)$$

Here, the index $l_i, i = 1, 2$, refers to grid point number l_i for the state space variable z_i . It may be noted here that due to the properties of the TPD for small time increments τ , the tensor $B_{k_1, k_2}^{l_1, l_2}$ has a strongly banded character with the elements decreasing rapidly away from the main diagonal $k_1 = l_1, k_2 = l_2$. This has important implications for the efficiency of the computer program. Let $p_{l_1, l_2}^{(j)} = p(z_{(l_1, l_2)}^{(j)}, t_j | z', t')$. Then (15) can be rewritten as

$$p_{l_1, l_2}^{(j)} = \sum_{k_1=1}^{M_1} \sum_{k_2=1}^{M_2} \Gamma^{(j-1)}(k_1, k_2) B_{k_1, k_2}^{l_1, l_2}. \quad (18)$$

Having calculated the TPD $p(z^{(j)}, t_j | z', t')$ at the grid points by using (18), a spline interpolation is again carried out and a new set of interpolation coefficients $\{\Gamma^{(j)}(k_1, k_2)\}_{k_i=1}^{M_i}$ are calculated. This provides an updated representation of the TPD for time step j , cf. (14). For each time step, the normalization condition (7) is checked. That is, if for the chosen grid domain $(a_1, b_1) \times (a_2, b_2)$,

$$\begin{aligned} & \int_{a_2}^{b_2} \int_{a_1}^{b_1} p(z^{(j)}, t_j | z', t') dz_1^{(j)} dz_2^{(j)} \\ &= \sum_{k_1=1}^{M_1} \sum_{k_2=1}^{M_2} \Gamma^{(j)}(k_1, k_2) \prod_{i=1}^2 \int_{a_i}^{b_i} B_{k_i}(x) dx = q_j, \end{aligned} \quad (19)$$

and $q_j \neq 1.0$ within the desired accuracy, then the following replacement is made to restore the correct normalization.

$$\Gamma^{(j)}(k_1, k_2)^{\text{new}} \leftarrow q_j^{-1} \Gamma^{(j)}(k_1, k_2)^{\text{old}}. \quad (20)$$

This normalization check and replacement strategy contributes to producing a very stable and accurate numerical procedure provided a proper choice of time step, grid size and grid domain has been made.

5. Numerical examples

In the numerical calculations, appropriate choices have to be made for the grid domains and their discretizations as well as the corresponding time increments. At present such choices are made mostly on the basis of experience and trial and error. We shall not enter a detailed discussion of this part of the subject, but rather concentrate on the results themselves. More detailed discussions of the numerics of some of the case studies presented here are given in Naess & Hegstad (1994).

As previously stated, the parameter ζ plays a crucial role in determining the dynamic behaviour of the van der Pol oscillator. For small values of ζ (compared to 1.0), which

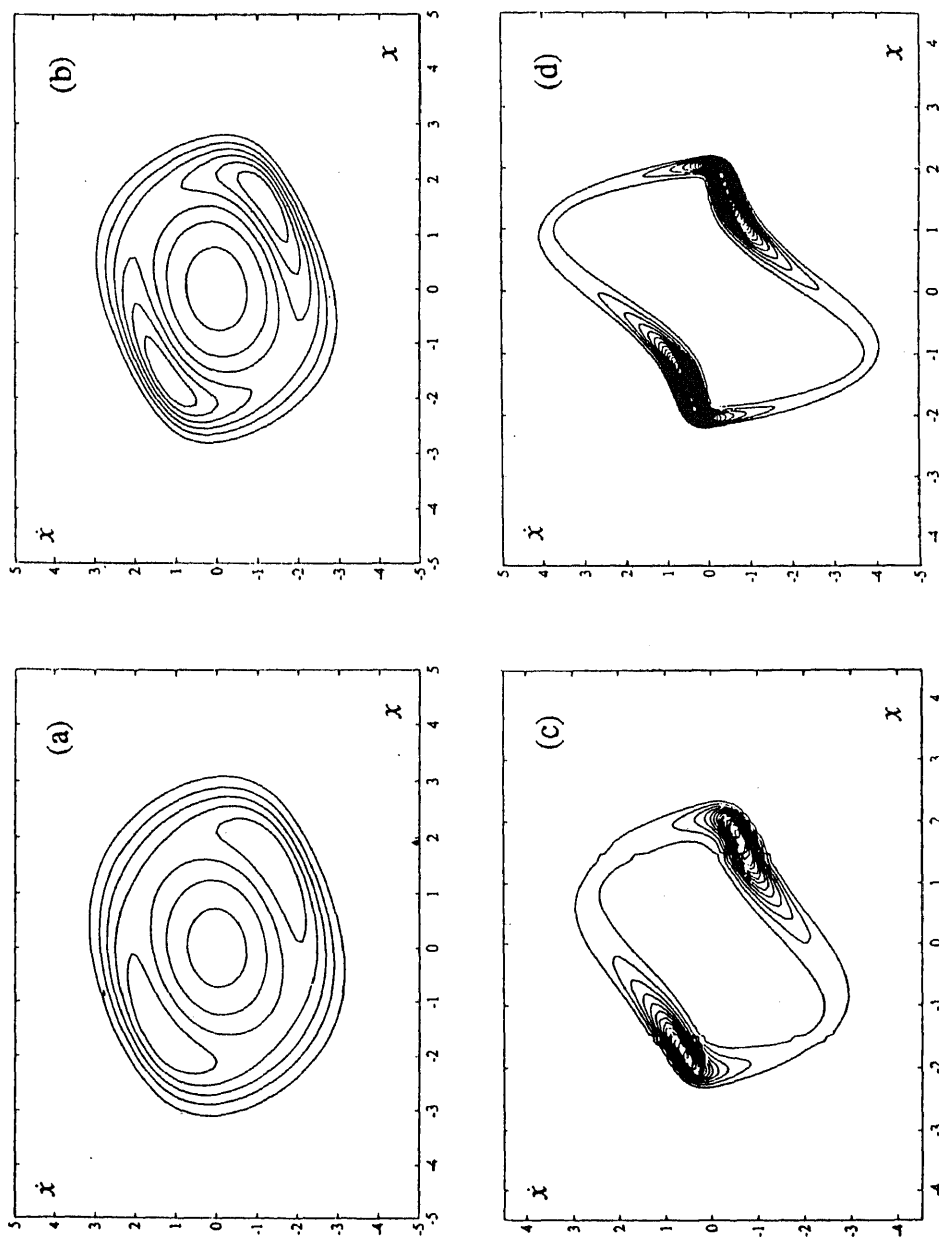


Figure 1. Contour plots of the PDF of the state space vector of oscillator response for $D = 0.1$ and various ζ -values. $\zeta = 0.05$ (a), 0.1 (b), 0.5 (c), 1.0 (d).

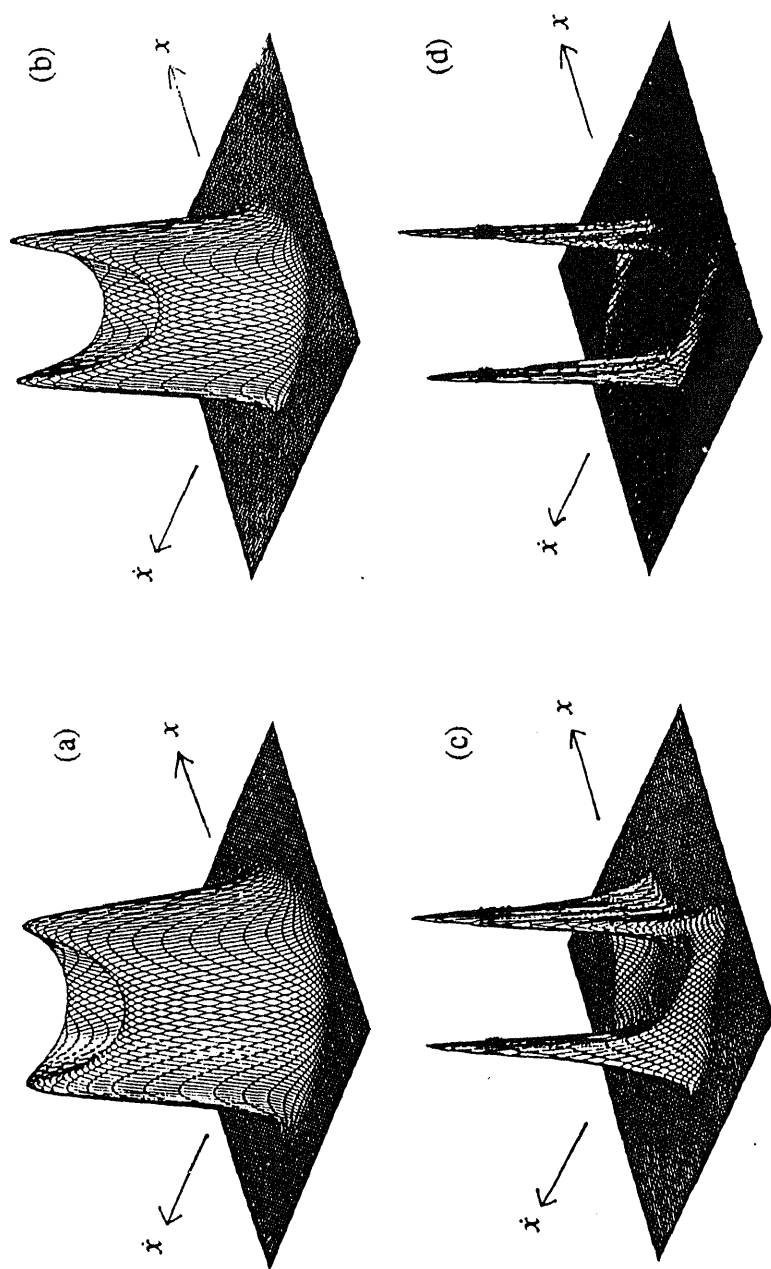


Fig. 2. Three-dimensional plots of the PDF of the state space vector of oscillator response for $D = 0.1$ and various ζ -values. $\zeta = 0.05$ (a), 0.1 (b), 1.0 (c), 5.0 (d).

corresponds to an almost linear oscillator with natural frequency close to unity, the time history of the response to harmonic excitation is almost sinusoidal when the driving frequency is in the neighbourhood of unity (harmonic entrainment), cf. Hayashi (1964). In contrast, for large values of ζ , the response time history approaches a square wave. To study how this property is carried through when the excitation is random, we have done computations for a set of conditions with a constant excitation level, specifically $D = 0.1$, and with increasing ζ -values from 0.05 to 1.0.

To get a clear qualitative picture of how the response statistics change with increasing values of the ζ -parameter, the results for the stationary PDFs from the calculations are presented both as contour plots in figure 1 and as three-dimensional plots in figure 2. From these figures it is clearly recognized how the response changes from a somewhat diffuse sinusoidal behaviour for small ζ , to a much more focussed limit cycle behaviour approaching that of a square wave. To wit, from figures 1d and 2d it is seen that for $\zeta = 1.0$, the oscillator spends most of its time at large excursions and small velocities, which is precisely what is to be expected for an almost square wave.

To provide more quantitative results for the stationary response statistics of the van der Pol oscillator, plots of the marginal PDFs for displacement and velocity are given in figures 3 and 4, respectively. As a partial verification, the calculated PDF of

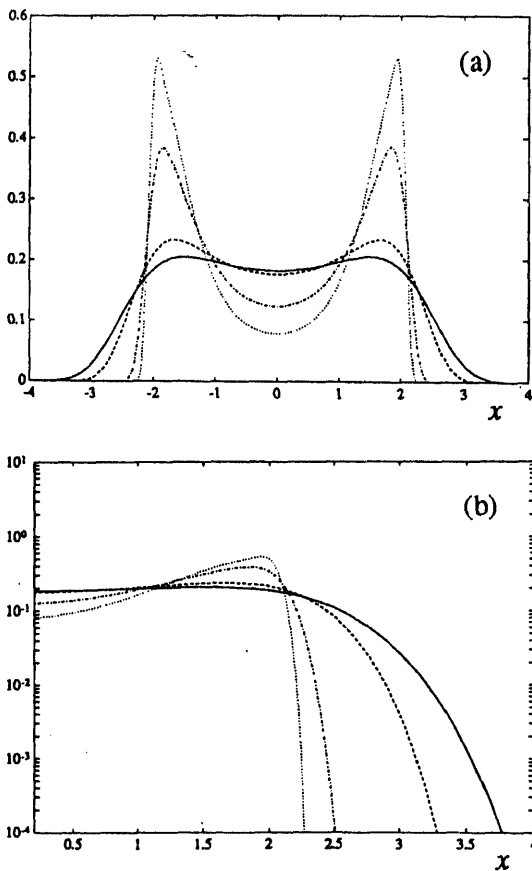


Figure 3. (a) Linear and (b) logarithmic plots of the marginal PDFs of oscillator displacement response for $D = 0.1$ and various ζ -values. $\zeta = 0.05$ (—), 0.1 (---), 0.5 (-·-·-), 1.0 (···).

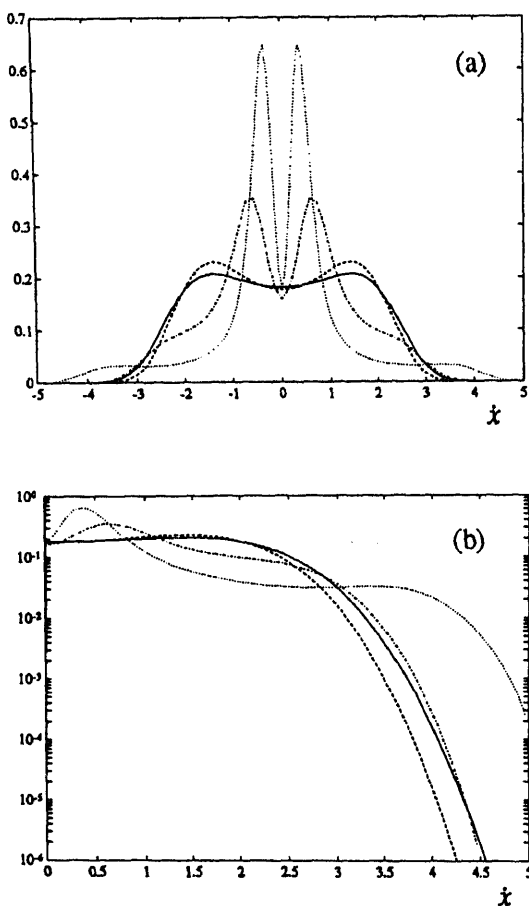


Figure 4. (a) Linear, and (b) logarithmic plots of the marginal PDFs of oscillator velocity response for $D = 0.1$ and various ζ -values. $\zeta = 0.05$ (—), 0.1 (---), 0.5 (-.-.), 1.0 (···).

displacement response for the van der Pol oscillator is compared to the results of Monte Carlo simulations for two case studies by Naess & Hegstad (1994), and the agreement was found to be good.

As previously stated, one of the remarkable features of the PIS technique is the high accuracy that can be retained down to very low probability levels. This property has been substantiated in several earlier papers, cf. Naess & Johnsen (1991, 1992 and 1993). A principal experience from this work is that if proper numerical procedures are followed, the obtained results are very reliable. To the extent that this conclusion has general validity, it is very important. It allows us to provide accurate results relevant for extreme response analyses of nonlinear oscillators where no *a priori* results are available. This cannot easily be done by Monte Carlo simulations since it requires at present either extrapolation or a prohibitive amount of CPU time.

It is also interesting to have a look at the transient behaviour of the oscillator. We have chosen to study the case with parameter values $\zeta = 1.0$ and $D = 0.1$. In figure 5 it is shown how the PDF of the state space vector develops in time after being released from the point $(2.0, 2.0)$. That is, the initial PDF is a delta function located at this starting point. It is seen that the oscillator almost immediately locks on to the limit cycle

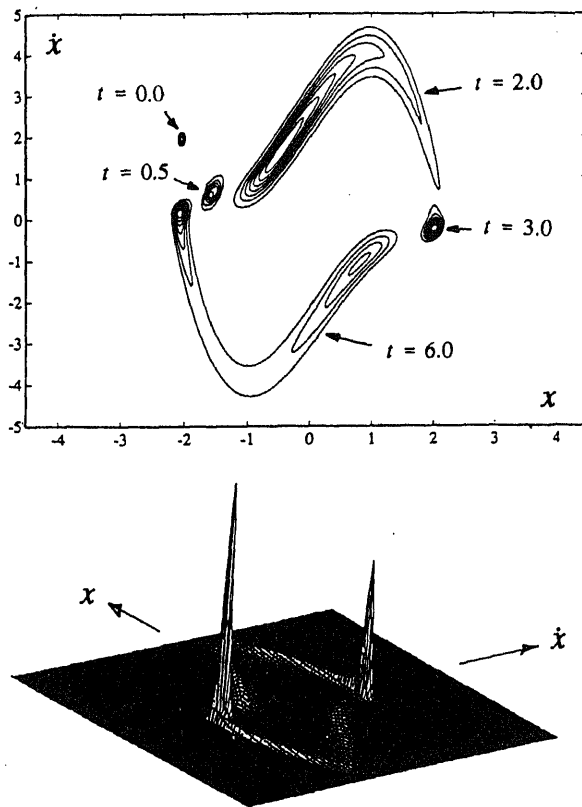


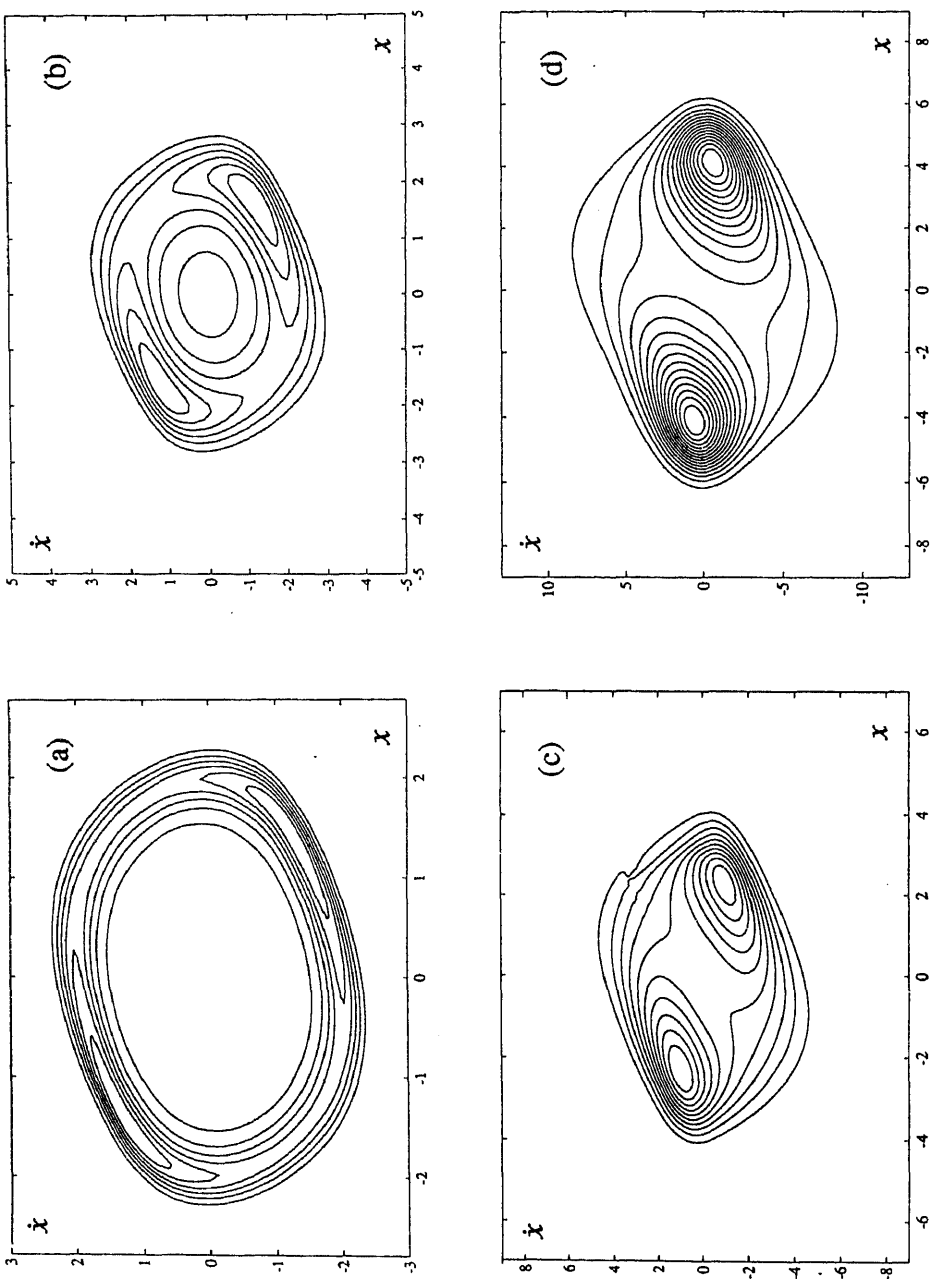
Figure 5. Transient behaviour of the PDF of the state space vector of oscillator response for $D = 0.1$ and $\zeta = 1.0$.

oscillations. Numerical studies of situations where the transient behaviour is known, indicates that the PIS method provides accurate estimates also of the transient response statistics.

In the last series of numerical results, the effect of increasing excitation level is illustrated. The ζ -parameter is kept constant at the value 0.1, while the excitation level runs through the values $D = 0.01, 0.1, 1.0$ and 10.0 . The results are given in figures 6 and 7. As could be expected, when the excitation level is very low, the oscillator displays an almost linear behaviour. However, as the excitation level increases, the nonlinear, square wave character of the system comes more to the forefront, although the oscillations are much less focussed on a limit cycle behaviour than would be the case with larger values of the ζ -parameter.

6. Conclusions

The paper has described a general numerical technique for calculating the response statistics of nonlinear oscillators subjected to broad band random excitation. By application to a white noise excited van der Pol oscillator, it has been demonstrated that detailed information about the statistics of this system can be obtained by implementing the so-called path integral solution (PIS) method. It is pointed out that



6. Contour plots of the PDF of the state space vector of oscillator response for $\zeta = 0.1$ and various D -values. $D = 0.01$ (a); 0.1 (b), 1.0 (c),

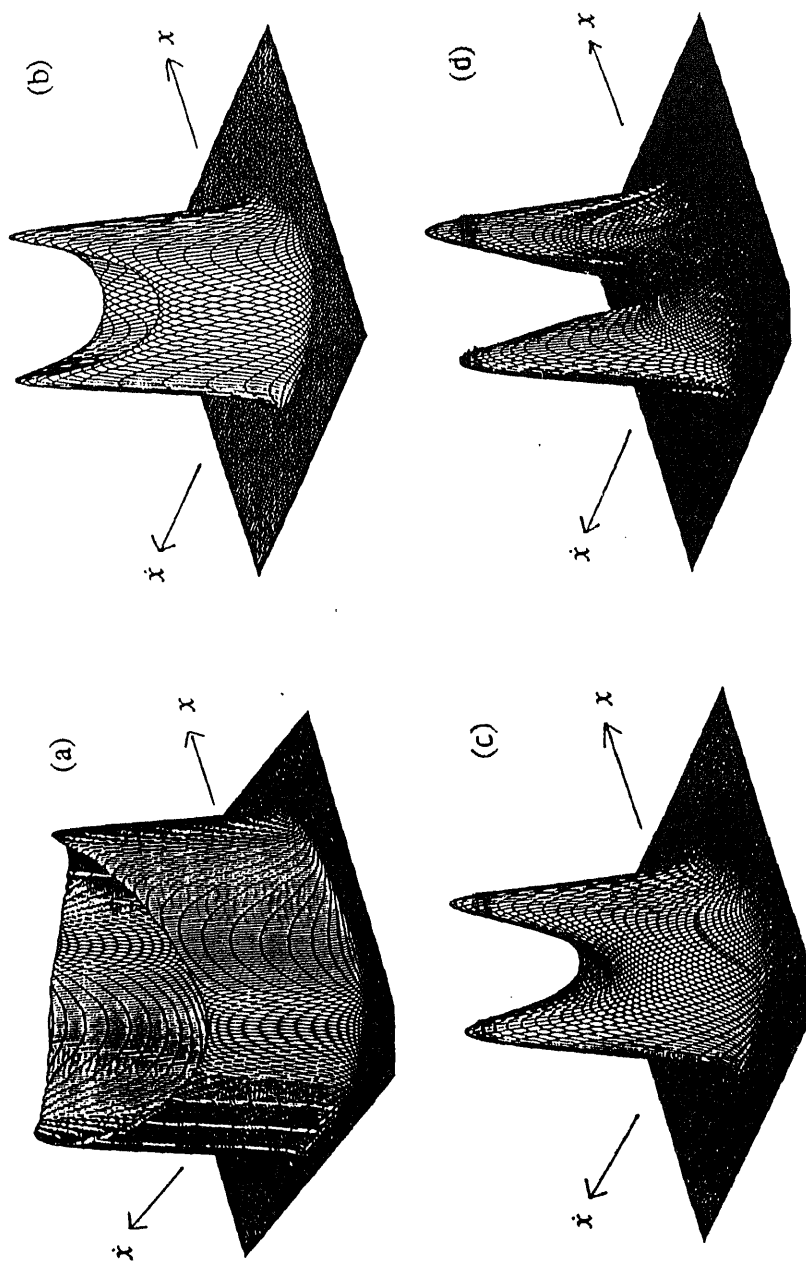


Figure 7. Three-dimensional plots of the PDF of the state vector of oscillator response for $\zeta = 0.1$ and various D -values. $D = 0.01$ (a), 0.1 (b), 1.0 (c) 10.0 (d).

the PIS method provides a very robust numerical solution technique that allows accurate calculation of both transient and stationary response statistics up to response levels beyond reach for most other solution procedures.

References

- Andronov A A, Vitt A A, Khaikin S E 1987 *Theory of oscillators*, (New York: Dover)
- Bergman L A, Spencer B F Jr 1992 Robust numerical solution of the transient Fokker-Planck equation for nonlinear dynamical systems. *Proc. IUTAM Symposium on Nonlinear Stochastic Mechanics*, Turin, Italy (eds) N Bellomo, F Casciati (Berlin, Heidelberg: Springer-Verlag)
- Caughey T K 1959 Response of van der Pol's oscillator to random excitation. *J. Appl. Mech.* 26: 345-348
- Chiu H M, Hsu C S 1986 A cell mapping method for nonlinear deterministic and stochastic systems - Part II Examples of application. *ASME J. Appl. Mech.* 50: 953-962
- de Boor C 1978 *A practical guide to splines* (New York: Springer-Verlag)
- Hagedorn P 1988 *Non-linear oscillations* 2nd edn (Oxford: Clarendon)
- Hayashi C 1964 *Non-linear oscillations in physical systems* (New York: McGraw-Hill)
- Hsu C S 1987 *Cell-to-cell mapping - A method of global analysis for nonlinear systems* (New York: Springer-Verlag)
- Langley R S 1985 A finite element method for the statistics of nonlinear random vibration. *J. Sound Vib.* 101: 41-54
- Langtangen H P 1991 A general numerical solution method for Fokker-Planck equations with applications to structural reliability. *Probabilistic Eng. Mech.* 6: 33-48
- Naess A, Hegstad B K 1994 Response statistics of van der Pol oscillators excited by white noise. *Nonlinear Dyn.* 5: 287-297
- Naess A, Johnsen J M 1991 Direct numerical simulation of the response statistics on nonlinear dynamic systems. *Proc. Scandinavian Forum for Stochastic Mechanics I*, Lund Institute of Technology, Swedish Council for Building Research, D7: 1991
- Naess A, Johnsen J M 1992 Response statistics of nonlinear dynamic systems by path integration. *Proc. IUTAM Symposium on Nonlinear Stochastic Mechanics*, Turin, Italy (eds) N Bellomo, F Casciati (Berlin, Heidelberg: Springer-Verlag)
- Naess A, Johnsen J M 1993 Response statistics of nonlinear, compliant off-shore structures by the path integral solution method. *Probabilistic Eng. Mech.* 8: 91-106
- Piszczyk K 1977 Influence of random disturbances on determined nonlinear vibration. *Stochastic problems in dynamics* (ed.) B L Clarkson (London: Pitman)
- Risken H 1989 *The Fokker-Planck equation* 2nd edn. (Berlin: Springer-Verlag)
- Spanos P T D 1979 Numerical simulations of a van der Pol oscillator. *Comput. Math. Appl.* 6: 135-145
- Stratonovich R L 1967 *Topics in the theory of random noise* (New York: Gordon and Breach) vol. 2
- Sun J Q, Hsu C S 1990 The generalized cell mapping method in nonlinear random vibration based upon short-time Gaussian approximation. *ASME J. Appl. Mech.* 57: 1018-1025
- van der Pol B 1927 Forced oscillations in a circuit with nonlinear resistance (reception with reactive triode). *Philos. Mag.* 7: 65-80
- Wehner M F, Wolfer W G 1983 Numerical evaluation of path integral solutions to Fokker-Planck equations. *Phys. Rev. A* 27: 2663-2670
- Wong E, Hajek B 1985 *Stochastic processes in engineering systems* (New York: Springer-Verlag)
- Zhu W O, Yu J S 1987 On the response of van der Pol oscillator to white noise excitations. *J. Sound Vib.* 117: 421-431

Random excitation of nonlinear elastic structures with internal resonances

R A IBRAHIM and B H LEE

Department of Mechanical Engineering, Wayne State University, Detroit, MI 48202, USA

Abstract. The influence of random vibration on the design of mechanical components has been restricted to the linear theory of small oscillations. However, this theory is inadequate and fails to predict the complex response characteristics which may be observed experimentally and can only be predicted by employing the nonlinear theory. This paper presents a brief overview of the basic nonlinear phenomena associated with nonlinear random vibration.

An example of a clamped-clamped beam under filtered white noise excitation in the neighbourhood of 1:1 internal resonance condition is considered. Three approaches are employed to examine the response and stochastic bifurcation of the beam coupled modes. These are the Fokker-Planck equation together with closure schemes, Monte Carlo simulation, and experimental testing. The analytical results are compared with those determined by Monte Carlo simulation. It is found that above a critical static buckling load the analytical results fail to predict the snap-through phenomenon, while both Monte Carlo simulation and experimental results reveal the occurrence of snap-through. The bifurcation of second mode is studied in terms of excitation level, internal detuning and damping ratios. It is found that below the critical load parameter, the response statistics do not significantly deviate from normality. Above the critical value, where snap-through takes place, the response is strongly non-Gaussian.

Keywords. Random excitation; nonlinear elastic structures; internal resonances; complex response characteristics.

1. Introduction

The nonlinear random vibration of structural elements is one of the serious problems of great concern to the designers of mechanical systems. This problem mainly deals with the stochastic stability/bifurcation and response statistics. The stochastic stability analysis of the equilibrium position is usually carried out on the basis of a linearized approximation to the system equations of motion. If the equilibrium is unstable in a stochastic sense, the linearized equations do not provide a unique bounded solution.

On the other hand, if the system's inherent nonlinearities are included in the mathematical modelling, the solution trajectories which emanate from an unstable equilibrium often end up in bounded limit cycles. Moreover, the nonlinear modelling also allows the designer to predict a wide range of complex response characteristics such as multiple solutions, jump phenomena, internal resonance, and chaotic motion. The system nonlinearity is dictated by several factors including the system's geometry, boundary conditions, and material characteristics. The geometry and boundary conditions can result in inertia and stiffness nonlinearities. For example in a clamped-clamped beam the nonlinearity is mainly governed by the mid-plane stretching, while for a cantilever beam the nonlinearity can include inertia and curvature depending on the mode in question. These continuous elastic elements are usually described by partial differential equations of the form

$$\mathcal{L}(w(z, t)) = U(z, t), \quad (1)$$

together with the appropriate boundary conditions, where \mathcal{L} is a linear/nonlinear operator, $w(z, t)$ is the structure deflection in a function of space coordinate z and time t , and $U(z, t)$ is a random excitation field. To develop methods for evaluating the nonlinear response to stochastic excitation, an approximate solution of the nonlinear partial differential equation can be obtained by expanding the response coordinate $w(z, t)$ in terms of a finite number of eigenfunctions

$$w(z, t) = \sum_{j=1}^n \phi_j(z) q_j(t), \quad (2)$$

where $\phi_j(z)$ is the eigenfunction of mode j of the eigenvalue problem obtained by setting nonlinearities and nonconservative forces to zero, and $q_j(t)$ is the corresponding generalized coordinate. The partial differential equation (1) can now be reduced to a system of n nonlinear coupled ordinary differential equations in $q_j(t)$ using the Ritz-Galerkin approach (Kantorovich & Krylov 1958). The random excitation field $U(z, t)$ can also be expanded in terms of the system normal modes $\phi_j(z)$

$$U(z, t) = \sum_{j=1}^n \phi_j(z) \xi_j(t), \quad (3)$$

where ξ_j is the generalized force associated with mode j . Introducing relations (2) and (3) into (1) and applying Galerkin's method results in a set of nonlinear ordinary differential equations of the general form

$$\{\ddot{q}\} + [C(t)]\{\dot{q}\} + [[K] + [\xi_0(t)]]\{q\} + \{\psi(q, \dot{q}, \xi(t))\} = \bar{K}\{\xi(t)\} \quad (4)$$

where $[C(t)]$ and $[K]$ are the linear damping and stiffness matrix coefficients, ξ_0 represents the parametric random component, and the vector ψ represents all nonlinear terms due to material and structural nonlinearities. \bar{K} is a constant coefficient.

In problems concerning structure failure, one of the most important questions is whether the solution, which is the system response to a random perturbation, remains bounded for all time. In the case of parametric excitation, a more refined question is whether the equilibrium solutions, if they exist, are asymptotically stable. The method of stochastic Liapunov functions has been proven to be effective for stochastic ordinary differential equations (ODE's) to a partial differential equation (PDE) setting. For stochastic ODE's the Liapunov method for stability has been systematically developed

by Khas'minskii (1980), and by many others (see for example Kushner 1967, and Pinsky 1974). The Liapunov method for stochastic PDE's was initiated by Chow (1982) to treat a class of parabolic problems. Stochastic stability can be examined in terms of one of the stochastic modes of convergence such as mean square stability, almost sure stability. Recently, mathematicians established a measure of exponential growth of system's response known as the Liapunov exponent for nonlinear dynamical systems and for parametrically excited linear systems.

1.1 Single mode random excitation

The random response of a clamped-clamped beam has been extensively examined within the framework of one mode excitation. Nonlinear systems described by one mode excitation are usually modelled by the nonlinear differential equation

$$\ddot{q} + 2\xi\omega_n\dot{q} + \omega_n^2 q + \varepsilon\psi(q, \dot{q}, \ddot{q}) = \xi(t) \quad (5)$$

where $\xi(t)$ is an external excitation and ψ may include nonlinear stiffness, damping and inertia terms and ε is a small parameter. The case of nonlinear stiffness has received an extensive amount of investigation. The equation of motion of this case is known as a Duffing oscillator. The early study of single mode response under random excitation goes back to the work of Lyon *et al* (1961). They considered $\xi(t)$ as a narrow band Gaussian process derived from a wide band excitation of a resonant filter centred at frequency ω_1 .

$$\ddot{\xi} + 2\xi_f\omega_1\dot{\xi} + \omega_1^2\xi = W(t), \quad (6)$$

where $W(t)$ is a white noise. The purpose of their study was to find out if the well-known jump phenomenon can occur under narrow band random excitation. The response was studied by using the quasi-linearization method and by experimental testing. The results revealed multivalued response characteristics which have the same general appearance as those for sinusoidal forcing except that the peaks are much sharper. The same feature has been observed by Lennox & Kuak (1976). They used quasi-static method with small but finite bandwidth. However, their method does not allow one to investigate the influence of bandwidth. Fang & Dowell (1987) analysed the response of a Duffing oscillator to a narrow band random excitation by numerical simulation. Their results showed that multi-valued mean square responses can occur for mono-level excitations having very narrow bandwidths. As the bandwidth increases, the multi-valued responses give way to single valued responses. Similar results were obtained using many different approaches, such as, averaging method (Roberts & Spanos 1986; Davies & Rajan 1988; Davies & Liu 1990, 1992), stochastic linearization (Dimentberg 1971; Iyengar 1989; Roberts & Spanos 1990; Roberts 1991), probabilistic linearization technique (Iyengar 1992), numerical simulation (Davies & Rajan 1988; Iyengar 1989, 1992; Davies & Liu 1990, 1992), and experimental testing (Lyon *et al* 1961). An alternative approach has been proposed by Davies & Nandlall (1986). They modelled the excitation as the response of a lightly-damped second order filter to white noise. Thus the four-dimensional Fokker-Planck-Kolmogorov (FPK) equation can be written for the response. An approximate, time-dependent solution based on a Gaussian closure scheme was obtained from the four-dimensional FPK equation. The result was smoothed time histories for the mean square displacement and velocity. When

plotted in a phase plane, the solution showed two stable attractors and a saddle point for the case in which the excitation had very narrow bandwidth, in a certain frequency range. This behaviour is related to the well-known jump phenomenon. As the bandwidth of the excitation increased, the phase plane was reduced to a single stable attractor (sink), indicating the elimination of the jump phenomenon.

The FPK equation for a Duffing oscillator to filtered excitation has been solved numerically by Kapitaniak (1985) using the path-integral method. He presented the stationary probability density function of the stochastic process as bimodal. Davies & Liu (1990) investigated the same system via averaging method and numerical simulation. They showed that the probability density function obtained for narrow bandwidth excitation has multi-local maxima (multifurcation) with random jumps. Also, for wider bandwidth excitation the probability density function shows only a single local maxima. Similar result was obtained by Iyengar (1992) using numerical simulation. Koliopoulos & Bishop (1993) studied a method for the prediction of response statistics of nonlinear oscillators subjected to narrow band random noise based on a quasi-harmonic assumption. They showed that the method can easily incorporate the possible jumps of the system via the input-response amplitude curve. This curve defines critical input values which define the region of possible jumps. In this case the probability density of the response amplitude exhibits two peaks.

Iyengar (1986, 1988) has presented a stochastic stability analysis of a nonlinear hardening-type oscillator subjected to narrow band random excitation. He showed that only one statistical moment is stable and, hence, the multivalued predictions of the equivalent linearization analysis do not correspond to the real behaviour of the system. Koliopoulos & Langley (1993) improved the stability analysis for the same system. They showed that when jumps between competing response states occur, the choice of an appropriate value for the kurtosis of the response is crucial for a reliable estimation of the local statistical moments and for a more accurate stochastic stability analysis than the equivalent linearization method. Furthermore, a modification is proposed which takes into account the influence of certain nonlinear terms in the variational equation for the case of strong nonlinearities.

1.2 Multi-mode random excitation

The case of multi-degree-of-freedom system involves new problems in addition to those encountered for single mode excitation. The new problems mainly arise due to the nonlinear modal interaction which is only significant if the normal mode frequencies are commensurable, i.e. when the normal mode frequencies are governed by the internal resonance condition $\sum k_i \omega_i = 0$, where k_i are integers, and ω_i are the system's natural frequencies. Under this condition, the mode which is directly excited interacts with other modes in the form of energy exchange. This type of modal interaction is referred to as autoparametric (Minorsky 1962). In the absence of internal resonances, the response is only dominated by the directly excited modes. The energy sharing in random vibration of nonlinearly coupled modes is believed to be first addressed by Newland (1965). The random response of two degree-of-freedom systems with autoparametric coupling was examined by Ibrahim & Roberts (1976, 1977), Schmidt (1977a, b), Ibrahim & Heo (1986), Soundararajan & Ibrahim (1988), Li & Ibrahim (1989), Ibrahim *et al* (1990), and Nayfeh & Serhan (1991). These authors considered

different nonlinear coupled oscillators such as coupled beams, liquid sloshing interaction with elastic support, shallow arches, strings and hinged-clamped beams. For systems governed by quadratic nonlinearity it was found that the Gaussian closure scheme leads to nonstationary response statistics while the non-Gaussian closure gives a stationary response to a white noise excitation. Systems with cubic nonlinearity exhibit complex response characteristics in the neighbourhood of the condition of internal resonance. It was reported that unbounded response statistics take place at certain regions above and below the exact internal resonance. For regions well remote from the exact internal resonance condition the system experienced linear response behaviour. These results were qualitatively verified experimentally by Roberts (1980), Ibrahim & Sullivan (1990), and Ibrahim *et al* (1990). In some cases the experimental results revealed an uncertain region of excitation level over which the coupled mode may or may not interact with the directly excited mode.

Ibrahim & Li (1988) and Li & Ibrahim (1990) considered the nonlinear interaction of a three degree-of-freedom structural system subjected to a wide-band random excitation. The nonlinearity of this system resulted in different critical regions of internal resonance. The response statistics were predicted by using Gaussian and non-Gaussian closure schemes, and Monte Carlo simulation. While the non-Gaussian closure predicted multiple solutions in the neighbourhood of exact internal resonance, the Monte Carlo simulation yields only one branch of the stationary solution corresponding to a zero set of initial conditions. This implies the existence of domains of attraction corresponding to the stationary attractors of the system.

Nonlinear continuous systems, not governed by internal resonance conditions, such as beams and plates subjected to random excitation, can exhibit new phenomena not found in discrete nonlinear systems. Mei & Wentz (1982), Moyer (1988) and Reinhall & Miles (1989) showed a new response behaviour which takes the form of a definite widening response spectra, as well as a shift, of the resonance peak as the excitation level is increased. These features can only be predicted using Monte Carlo simulation or experimental testing. All well-known analytical methods failed to predict these phenomena. This motivated Ibrahim *et al* (1993) to study the stochastic bifurcation of a clamped-clamped beam under wide band random excitation in the neighbourhood of the internal resonance condition $\omega_3 = \omega_1 + 2\omega_2$, which is mainly governed by the value of pre-applied axial static load. They used Gaussian and non-Gaussian closures, Monte Carlo simulation and experimental testing. The nonlinear response is represented by the first three modes. In the neighbourhood of the critical bifurcation parameter (axial static load/Euler buckling load) the Monte Carlo simulation yields strong nonstationary mean square response for the asymmetric mode which is not directly excited. Experimental and Monte Carlo simulation exhibit nonlinear features similar to those observed by Mei & Wentz (1982) and others as described previously. The estimated probability density functions, from numerical simulation, displayed significant deviation from normality. Furthermore, the response revealed non-zero mean under zero mean excitation. This non-zero mean was attributed to the fact that the straight beam is under initial axial load. It was also reported that large initial conditions resulted in numerical instability and only small initial conditions were used to generate bounded solutions.

This paper presents an example which is an extension of the work of Ibrahim *et al* (1993) to examine the stochastic behaviour of a buckled clamped-clamped beam in the neighbourhood of 1:1 internal resonance. In this case the treatment will be confined to

the nonlinear interaction of the first two modes. The excitation is considered narrow band which is generated from a linear second order shaping filter subjected to a white noise. The filter central frequency is selected to be close to the natural frequency of the excited mode. Three different approaches will be employed. These are the closure schemes, Monte Carlo simulation and experimental testing.

2. Example

2.1 Analytical model and analysis

Figure 1 shows a clamped-clamped beam which is buckled due to an axial load $P > P_{cr}$, where P_{cr} is the Euler buckling load. Under this load the beam will have a static deflection $U_0(x)$. The base excitation is assumed as a filtered white noise process. The motion of the beam is governed by the nonlinear partial differential equation, which is derived by using Hamilton's principle;

$$m \frac{\partial^2 U(x, t)}{\partial t^2} + EI \frac{\partial^4 (U(x, t) + U_0(x))}{\partial x^4} + P \frac{\partial^2 (U(x, t) + U_0(x))}{\partial x^2} - \frac{EA}{2L} \frac{\partial^2 (U(x, t) + U_0(x))}{\partial x^2} \int_0^L \left\{ \frac{\partial (U(x, t) + U_0(x))}{\partial x} \right\}^2 dx = -m \frac{\partial^2 Y(t)}{\partial t^2}, \quad (7)$$

where $U(x, t)$ is the beam deflection at position x and time t measured from $U_0(x)$; E is Young's modulus of the beam; I is the area moment of inertia in bending; and A is the cross-sectional area of the beam. The static axial load P exceeds the Euler buckling load P_{cr} , i.e.:

$$P = P_{cr} + \frac{EA}{2L} \int_0^L \left(\frac{\partial U_0(x)}{\partial x} \right)^2 dx. \quad (8)$$

The deflection of the beam is expanded into n modes,

$$U_0(x) + U(x, t) = \tilde{C} V_0 \left(\Phi_1(x) + \sum_{i=1}^n \tilde{q}_i(t) \Phi_i(x) \right), \quad (9)$$

where V_0 is the initial deflection of the beam at $x = L/2$; $\tilde{C} = 1/\Phi_1(L/2)$; $\tilde{q}_i = q_i/h$, $q_i(t)$ are the generalized coordinates; and $\Phi_1(x)$ are the corresponding shape functions which

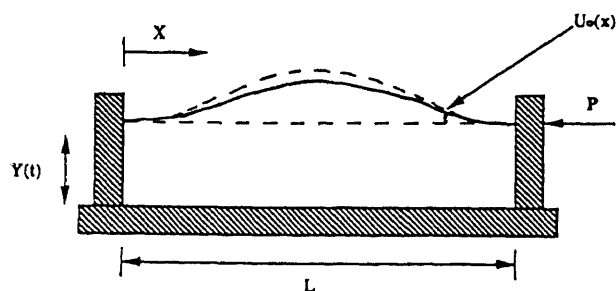


Figure 1. Schematic diagram of initially buckled beam.

are selected from the linear eigenvalue problem of a clamped-clamped beam:

$$\Phi_i(x) = A_i [\cos(\beta_i x) - \cosh(\beta_i x)] + [\sin(\beta_i x) - \sinh(\beta_i x)], \quad (10)$$

where $A_i = -[\sin(\beta_i L) - \sinh(\beta_i L)]/[\cos(\beta_i L) - \cosh(\beta_i L)]$, and $\beta_i L = 4.730041$, 7.85305 , and 10.995608 , for $i = 1, 2$, and 3 , respectively.

Applying Galerkin's method to (7) for the first two modes and introducing a linear viscous damping, the equations of motion in non-dimensional form are

$$\begin{aligned} Q_1'' + 2\zeta_1 r Q_1 + r^2 Q_1 + \varepsilon r^2 (1.5 Q_1^2 + 1.804 Q_2^2) \\ + \varepsilon^2 r^2 (1.804 Q_1 Q_2^2 + 0.5 Q_1^3) = -f_a Z(\tau), \\ Q_2'' + 2\zeta_2 Q_2 + Q_2 + \varepsilon r^2 (3.74 Q_1 Q_2) \\ + \varepsilon^2 r^2 (1.8687 Q_1^2 Q_2 + 6.74 Q_2^3) = 0, \end{aligned} \quad (11a)$$

where the excitation $Z(\tau)$ is generated from the second-order linear shaping filter

$$Z'' + 2\zeta_f r_f Z' + r_f^2 Z = \varepsilon^2 W(\tau), \quad (11b)$$

where

$$\begin{aligned} \tau = \omega_2 t, \quad r = \frac{\omega_1}{\omega_2}, \quad \varepsilon = \frac{b}{L}, \quad r_f = \frac{\omega_f}{\omega_2}, \quad f_a = 1.32/V_0, \\ \omega_0^2 = 720.0756 EI/(mL^4), \quad \omega_1^2 = \omega_0^2 (V_0/h)^2, \quad \omega_2^2 = 2.76089 \omega_0^2, \\ Z(\tau) = \frac{L \ddot{Y}(t)}{b \omega_2^2} \approx \frac{-L \omega_f^2 Y(\tau)}{b \omega_2^2}, \quad \text{and} \quad Q_i(\tau) = \frac{L}{b} \tilde{q}_i(t), \quad i = 1, 2 \end{aligned}$$

and a prime denotes differentiation with respect to τ . $W(\tau)$ is a zero mean and stationary Gaussian white noise. $Z(\tau)$ is the response process of the linear filter (11b) whose bandwidth and centre frequency are controlled by the parameters ζ_f and r_f . The quadratic nonlinear terms in (11a) are due to the curvature resulting from the static deflection, whereas the cubic nonlinear terms are due to the mid-plane stretching. The first two mode natural frequencies give rise to the internal resonance condition at $V_0/h = 1.66$ ($r = 1$) as shown in figure 2. In this paper, the dynamic response of the system in the neighbourhood of the internal resonance condition $r = 1$ is considered.

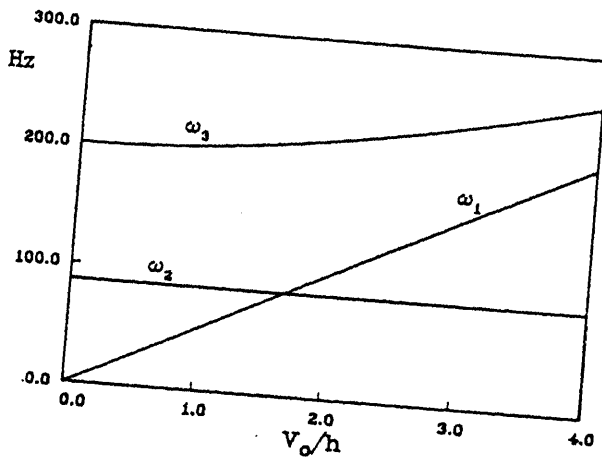


Figure 2. Effect of static deflection on the beam natural frequencies.

The departure from the exact internal resonance is expressed by the internal detuning parameter Δ , defined by the relationship:

$$r = 1 + \varepsilon^2 \Delta. \quad (12)$$

The external excitation is assumed Gaussian white noise process whose correlation time is much smaller than any characteristic period of oscillation of the system. In this case the response can be approximated by a Markov state vector which is established through the coordinate transformation:

$$\{Q_1, Q'_1, Q_2, Q'_2, Z, Z'\} = \{X_1, X_2, X_3, X_4, X_5, X_6\} = \mathbf{X}.$$

If the random process $W(\tau)$ is replaced by the formal derivative of the Brownian process $B(\tau)$, i.e., $W(\tau) = \sigma dB(\tau)/d\tau$, where $\sigma^2 = 2D$, equations (11) can be transformed into the Itô type equations

$$\begin{aligned} dX_1 &= X_2 d\tau, \quad dX_3 = X_4 d\tau, \quad dX_5 = X_6 d\tau, \\ dX_2 &= \{-2\zeta_1 r X_2 - r^2 X_1 - \varepsilon r^2 (1.5 X_1^2 + 1.80 X_3^2) \\ &\quad - \varepsilon^2 r^2 (1.804 X_1 X_3^2 + 0.5 X_1^3) - f_a X_5\} d\tau, \\ dX_4 &= \{-2\zeta_2 X_4 - X_3 - \varepsilon r^2 (3.74 X_1 X_3) - \varepsilon^2 r^2 (1.8687 X_1^2 X_3 + 6.74 X_3^3)\} d\tau, \\ dX_6 &= (-2\zeta_f r_f X_6 - r_f^2 X_5) d\tau + \varepsilon^2 \sigma dB(\tau). \end{aligned} \quad (13)$$

The joint probability density $p(\mathbf{X}, \tau)$ of the response coordinates is described by the Fokker-Planck equation

$$\frac{\partial p(\mathbf{X}, \tau)}{\partial \tau} = - \sum_{i=1}^6 \frac{\partial}{\partial X_i} [a_i(\mathbf{X}, \tau) p(\mathbf{X}, \tau)] + \frac{1}{2} \sum_{i=1}^6 \sum_{j=1}^6 \frac{\partial^2}{\partial X_i \partial X_j} b_{ij}(\mathbf{X}, \tau) p(\mathbf{X}, \tau), \quad (14)$$

where the coefficients a_i and b_{ij} are the drift and diffusion coefficients, defined by the relationships

$$a_i(X, \tau) = \lim_{\Delta\tau \rightarrow 0} \frac{1}{\Delta\tau} E[X_i(\tau + \Delta\tau) - X_i(\tau)], \quad (15)$$

$$b_{ij}(X, \tau) = \lim_{\Delta\tau \rightarrow 0} \frac{1}{\Delta\tau} E[\{X_i(\tau + \Delta\tau) - X_i(\tau)\} \{X_j(\tau + \Delta\tau) - X_j(\tau)\}].$$

In view of the system nonlinearity, it is not possible to solve the system Fokker-Planck equation for the response probability density. Instead, one may derive a general first-order differential equation for the response dynamic moments. This equation is obtained by multiplying both sides of (14) by the scalar function, $\Phi(\mathbf{X}) = X_1^{k_1} X_2^{k_2} X_3^{k_3} X_4^{k_4} X_5^{k_5} X_6^{k_6}$, and integrating by parts over the entire state space $-\infty < \mathbf{X} < \infty$. Then the general first-order differential moment equation;

$$\begin{aligned} m_{k_2, k_3, k_4, k_5, k_6} &= k_1 m_{k_1-1, k_2+1, k_3, k_4, k_5, k_6} \\ &+ k_2 \{-2\zeta_1 r m_{k_1, k_2, k_3, k_4, k_5, k_6} - r^2 m_{k_1+1, k_2-1, k_3, k_4, k_5, k_6} \\ &\quad - \varepsilon r^2 (1.5 m_{k_1+2, k_2-1, k_3, k_4, k_5, k_6} + 1.804 m_{k_1, k_2-1, k_3+2, k_4, k_5, k_6}) \\ &\quad - \varepsilon^2 r^2 (1.804 m_{k_1+1, k_2-1, k_3+2, k_4, k_5, k_6} + 0.5 m_{k_1+3, k_2-1, k_3, k_4, k_5, k_6}) \end{aligned}$$

$$\begin{aligned}
& -f_a m_{k_1, k_2-1, k_3, k_4, k_5+1, k_6} \} + k_3 m_{k_1, k_2, k_3-1, k_4+1, k_5, k_6} \\
& + k_4 \{ -2\zeta_2 m_{k_1, k_2, k_3, k_4, k_5, k_6} - m_{k_1, k_2, k_3+1, k_4-1, k_5, k_6} \\
& - \varepsilon^2 (3.74 m_{k_1+1, k_2, k_3+1, k_4-1, k_5, k_6}) - \varepsilon^2 r^2 (1.8687 m_{k_1+2, k_2, k_3+1, k_4-1, k_5, k_6} \\
& + 6.74 m_{k_1, k_2, k_3+3, k_4-1, k_5, k_6}) \} + k_5 m_{k_1, k_2, k_3, k_4, k_5-1, k_6+1} \\
& + k_6 (-2\zeta_f r_f m_{k_1, k_2, k_3, k_4, k_5, k_6} - r_f^2 m_{k_1, k_2, k_3, k_4, k_5+1, k_6-1}) \\
& + \frac{1}{2} k_6 (k_6 - 1) \varepsilon^4 \sigma^2 m_{k_1, k_2, k_3, k_4, k_5, k_6-2}, \quad (16)
\end{aligned}$$

where

$$\begin{aligned}
m_{k_1, k_2, k_3, k_4, k_5, k_6} &= E[X_1^{k_1} \dots X_6^{k_6}] \\
&= \int_{-\infty}^{\infty} \dots \int_{-\infty}^{\infty} \Phi(X_1^{k_1} X_2^{k_2} X_3^{k_3} X_4^{k_4} X_5^{k_5} X_6^{k_6}) p(X, \tau) dX_1 \dots dX_6. \quad (17)
\end{aligned}$$

Equation (16) constitutes an infinite set of coupled moment equations. In order to solve for the response statistics, these equations must be truncated by an appropriate closure scheme. Gaussian and the first-order non-Gaussian closure schemes are considered. The Gaussian closure is carried out by setting third- and fourth-order cumulants to zero and expressing third- and fourth-order moment in terms of first- and second-order moments. In this case, the Gaussian closure requires to generate 27 coupled first-order differential moment equations. The first-order non-Gaussian closure

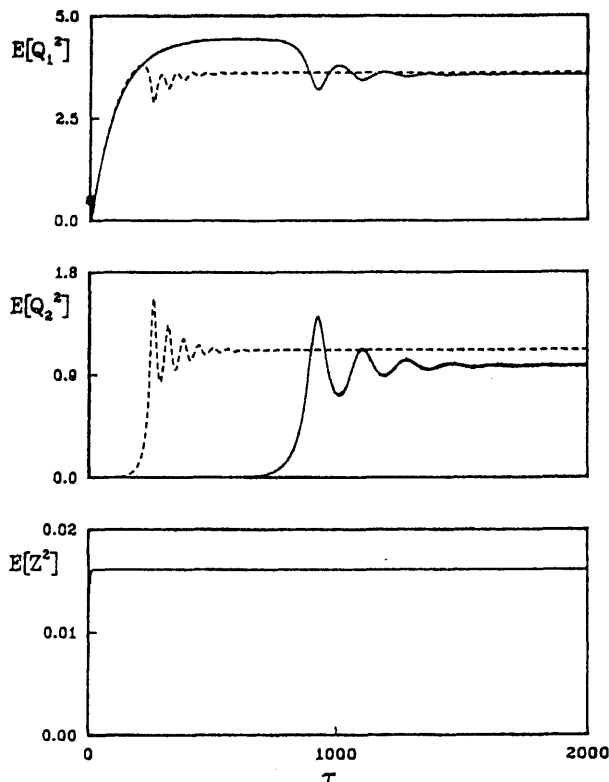


Figure 3. Time-history records of mean square according to — Gaussian, and --- non-Gaussian closures.

is carried out by setting fifth- and sixth-order cumulants to zero. For the present problem one needs to generate 6 equations for the first-order moment, 21 equations for the second-order, 56 equations for third-order, and 126 equations of fourth-order, with a total of 209 first order differential equations. The solution of the differential equations are numerically solved by using the IMSL DIVPAG subroutine (Adams-Moulton or Gear numerical integration method). The numerical integration is performed with double precision using time increment $\Delta\tau = 0.2$ and integration accuracy 0.1D-03.

The first mode is excited by a filtered white noise whose centre frequency is very close to the first mode natural frequency ($r_f \approx r$). The bandwidth of this random process is selected such that it does not excite any other higher modes. The system response is then governed mainly by the first mode. However, the second mode can be excited through nonlinear modal interaction near internal resonance condition. Figure 3 shows time history records of the mean square responses as obtained by Gaussian and non-Gaussian closures for internal detuning $\Delta = -4.0$. These values of Δ correspond to $r = 0.99$. These solutions are obtained for excitation spectral density $(\varepsilon^2\sigma)^2 = 0.0125$, damping ratios $\zeta_1 = \zeta_2 = 0.005$, and filter parameter $\zeta_f = 0.2$. The figure shows that the non-Gaussian solution is slightly higher than the Gaussian solution. For the same initial conditions the two schemes yield different transient periods. Different excitation levels, internal detuning parameter, and filter parameters may result in unimodal response. Accordingly, the stochastic bifurcation of the second mode of the two solutions depends to a great extent on excitation level and system parameters such as system damping ratios and internal detuning parameter Δ . The

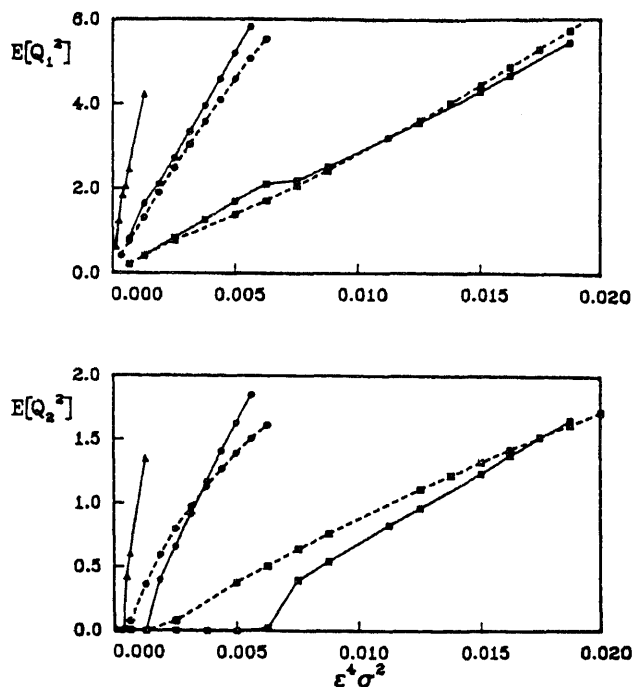


Figure 4. Effect of excitation level on response mean squares for different filter damping ratios: $\zeta_f = 0.05$ -- Δ -- Gaussian; $\zeta_f = 0.1$ -- \circ -- Gaussian, -- \bullet -- non-Gaussian; $\zeta_f = 0.2$ -- \square -- Gaussian, -- \blacksquare -- non-Gaussian.

bifurcation behaviour also depends on the damping ratio of the linear shaping filter equation which is related to the bandwidth of the filtered excitation. Figure 4 shows that the second mode bifurcation takes place at different excitation levels due to different damping ratios of the linear shaping filter. If the damping ratio of the linear shaping filter increases, relatively higher excitation level is required for the second mode bifurcation. For very small filter damping ratio, such as $\zeta_f = 0.05$, the non-Gaussian closure was found to encounter numerical instability.

The effect of internal detuning parameter Δ on the response mean square, as determined by the two closures, is shown in figure 5 for damping ratios $\zeta_1 = \zeta_2 = 0.005$, excitation level $(\varepsilon^2 \sigma)^2 = 0.005$ and filter damping ratio $\zeta_f = 0.2$. This figure demonstrates that in the neighbourhood of exact internal detuning the energy is transferred from the externally excited mode to the second mode. It is found that mixed mode interaction takes place over a wider internal detuning parameter for the non-Gaussian closure solution than the range of the Gaussian solution. It is seen that the mean squares are not symmetric about exact internal resonance condition due to the presence of cubic nonlinearity.

The dependence of the mean square response on the excitation level is shown in figure 6 for internal detuning parameter $\Delta = -4$ ($r = 0.99$) and three different system damping ratios $\zeta_1 = \zeta_2 = 0.003, 0.005$, and 0.007 . The damping ratio of linear shaping filter has a fixed value of $\zeta_f = 0.2$. It is seen that if the system damping ratios increase, the second mode requires a higher excitation level to bifurcate. For the same system damping ratios, the Gaussian closure solution yields second mode bifurcation at

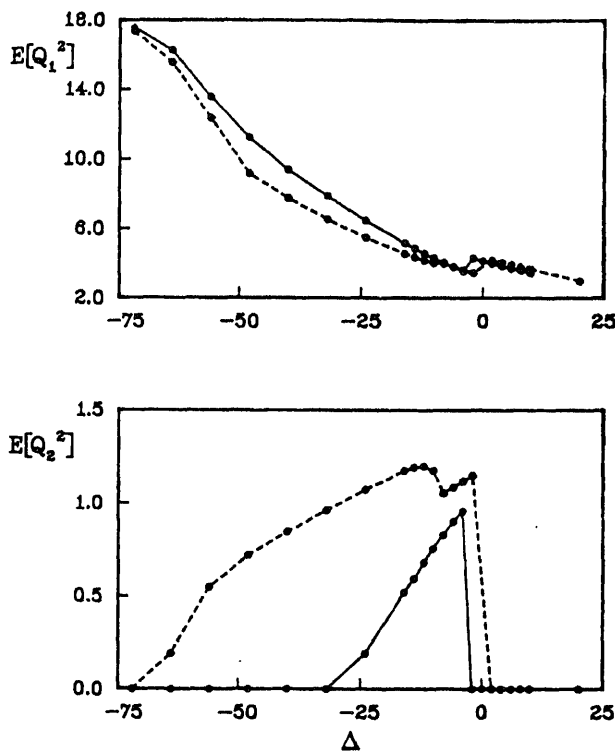


Figure 5. Dependence of mean square response on the internal detuning; --○-- Gaussian closure, --●-- non-Gaussian closure.

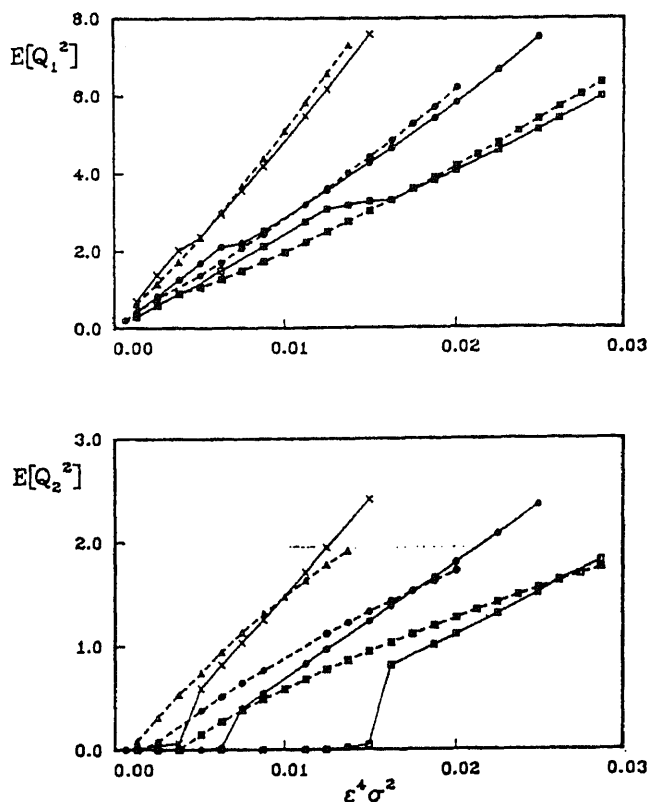


Figure 6. Mean square response vs excitation level for different system damping ratios $\zeta_1 = \zeta_2 = 0.003$ --- \times --- Gaussian, --- Δ --- non-Gaussian; $\zeta_1 = \zeta_2 = 0.005$ --- \circ --- Gaussian, --- \bullet --- non-Gaussian; $\zeta_1 = \zeta_2 = 0.007$ --- \square --- Gaussian, --- \blacksquare --- non-Gaussian.

a higher excitation level than the level due to the non-Gaussian closure. At relatively low excitation level the response is unimodal and the first mode mean square is governed by a linear relationship with the excitation level.

The bifurcation boundaries for three different system damping ratios on the $\sigma^2 - \Delta$ plane showing the separation between single and mixed mode responses are plotted in figures 7 and 8. Figures 7 and 8 are obtained for $\varepsilon = 0.005$, $\zeta_f = 0.2$, and for three different system damping ratios, $\zeta_1 = \zeta_2 = 0.003, 0.005$, and 0.007 as solved by Gaussian and non-Gaussian closures, respectively. It is obvious that as the system damping ratio increases, the region of two mode interaction shrinks. Furthermore, the two mode interaction occurs in the non-Gaussian solutions at less excitation power spectral density level than the level of the Gaussian solution. For $\Delta > -2$, both solutions predict only unimodal response of the directly excited mode.

2.2 Monte Carlo simulation

Numerical simulation of nonlinear vibration problems requires an extensive number of

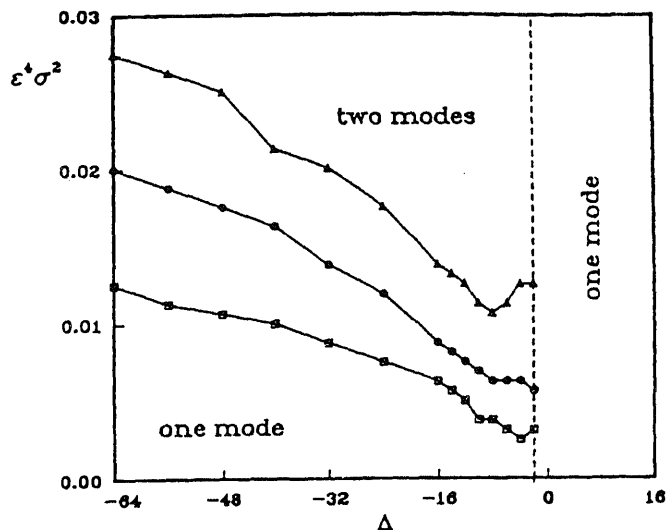


Figure 7. Bifurcation diagram according to Gaussian closure: $\zeta_1 = \zeta_2 = 0.007$
 $-\Delta-$, $\zeta_1 = \zeta_2 = 0.005$ $--\circ--$, $\zeta_1 = \zeta_2 = 0.007$ $--\square--$.

numerical integration of the actual equations of motion in order to establish an adequate ensemble record of the response characteristics. The number of excitation records is dictated by the system complexity and the convergence of response statistics to a stationary state. The method first requires the system equations of motion to be

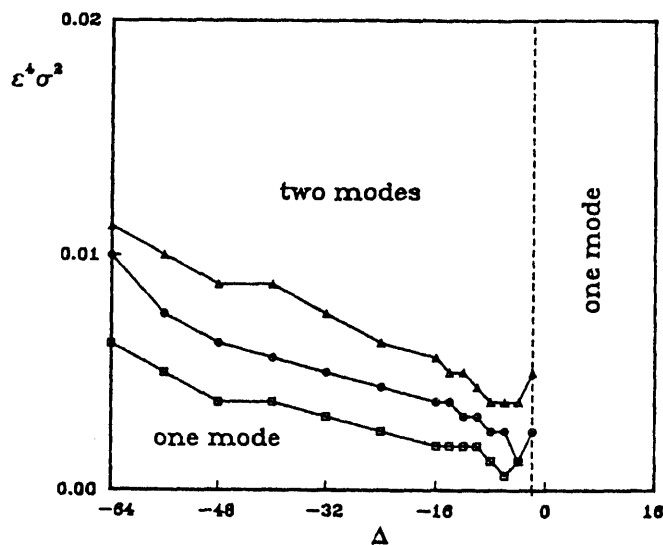


Figure 8. Bifurcation diagram according to non-Gaussian closure: $\zeta_1 = \zeta_2 = 0.007$
 $-\Delta-$, $\zeta_1 = \zeta_2 = 0.005$ $-\circ-$, $\zeta_1 = \zeta_2 = 0.007$ $-\square-$.

written in the state vector form

$$\begin{aligned}
 X'_1 &= X_2, & X'_3 &= X_4, & X'_5 &= X_6, \\
 X'_2 &= -2\zeta_1 r X_2 - r^2 X_1 - \varepsilon r^2 (1.5 X_1^2 + 1.804 X_3^2) \\
 &\quad - \varepsilon^2 r^2 (1.804 X_1 X_3^2 + 0.5 X_1^3) - f_a X_5, \\
 X'_4 &= -2\zeta_2 X_4 - X_3 - \varepsilon r^2 (3.74 X_1 X_3) - \varepsilon^2 r^2 (1.8687 X_1^2 X_3 + 6.74 X_3^3) \\
 X'_6 &= -2\zeta_f r_f X_6 - r_f^2 X_5 + W(\tau).
 \end{aligned} \tag{18}$$

The first mode is excited by a filtered white noise random excitation $X_5(\tau)$ whose central frequency is very close to the first mode natural frequency. The bandwidth of the random process $X_5(\tau)$ depends on damping ratio of the shaping filter ζ_f . To estimate the mean square response five hundred records of the white noise $W(\tau)$ are simulated and a sequence of 25,000 random numbers are sampled for a single record by using the IMSL subroutine DRNNOR [random number generation from a normal distribution using an inverse Cumulative Distribution Function (CDF) technique]. The six coupled differential equations (18) are then numerically solved by the IMSL DIVPAG subroutine. Response statistics such as, auto-correlation function, probability density function, and

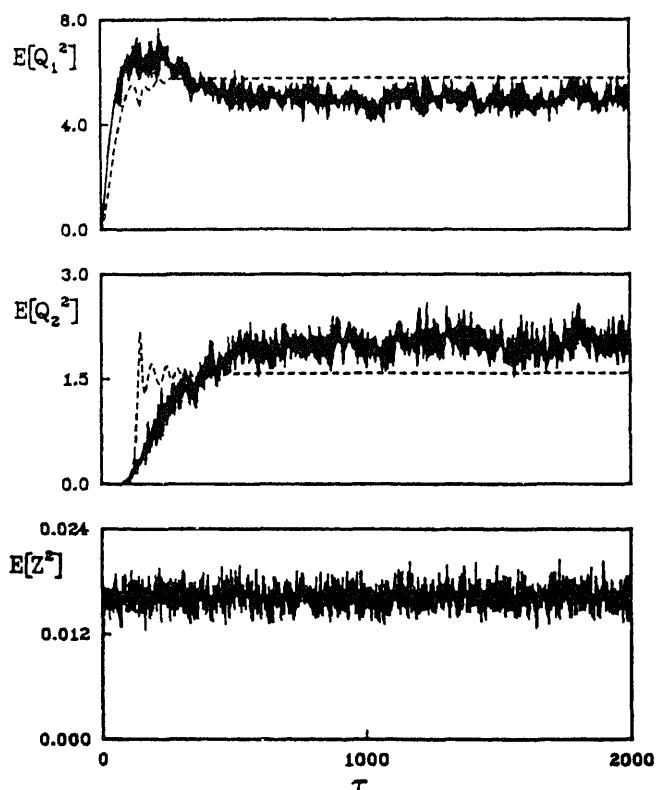


Figure 9. Time history records of mean square responses according to — Monte Carlo simulation, and --- non-Gaussian closure.

power spectral density function are estimated using the ILS (Interactive Laboratory System) software and other subroutines.

The mean square response and filtered excitation time history records are shown in figure 9 for $\zeta_f = 0.1$, $\zeta_1 = \zeta_2 = 0.005$, $(\varepsilon^2 \sigma)^2 = 0.00625$, and $\Delta = -4$ ($r = 0.99$). This figure also includes the mean square responses as determined by the non-Gaussian closure scheme (shown by dashed curves) for comparison. It is seen that both numerical simulation and non-Gaussian closure solution are in good agreement. The fluctuation exhibited by the Monte Carlo simulation records may be attributed to a statistical error of the ensemble averaging. As shown in the closure results, second mode bifurcation is mainly governed by system parameters and excitation level. However, Monte Carlo simulation predicted mixed mode interaction at relatively higher excitation level than the level predicted by closure schemes. Due to space limitations these results are not shown in this paper. The time history records obtained from Monte Carlo simulation are processed to estimate other statistical parameters including autocorrelation function, power spectra, and probability density function. The power spectra are determined from the Fourier transform of the autocorrelation functions using the ILS software with Hanning window algorithm. Because the system is tuned at exact 1:1 internal resonance and the central frequency of the

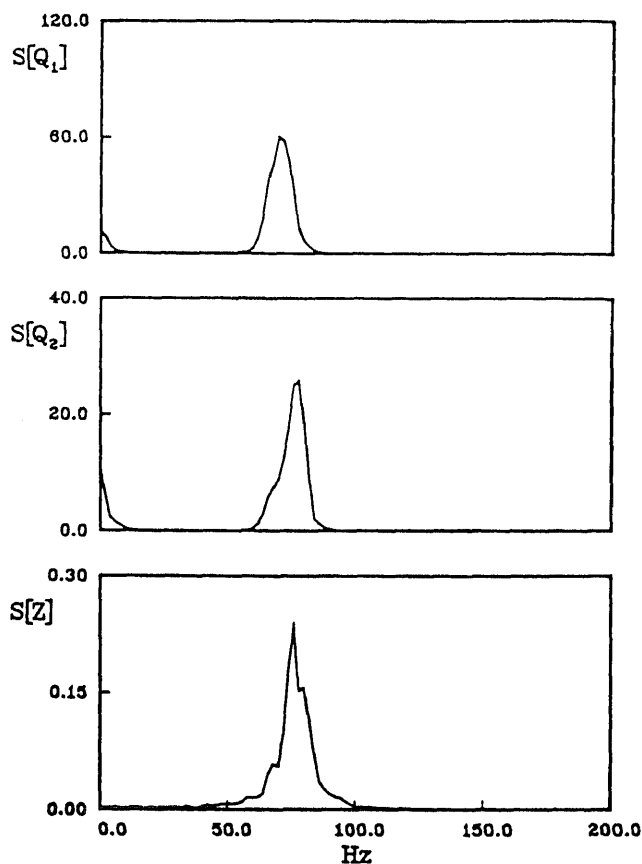


Figure 10. Estimated power spectra (same parameters as of figure 9).

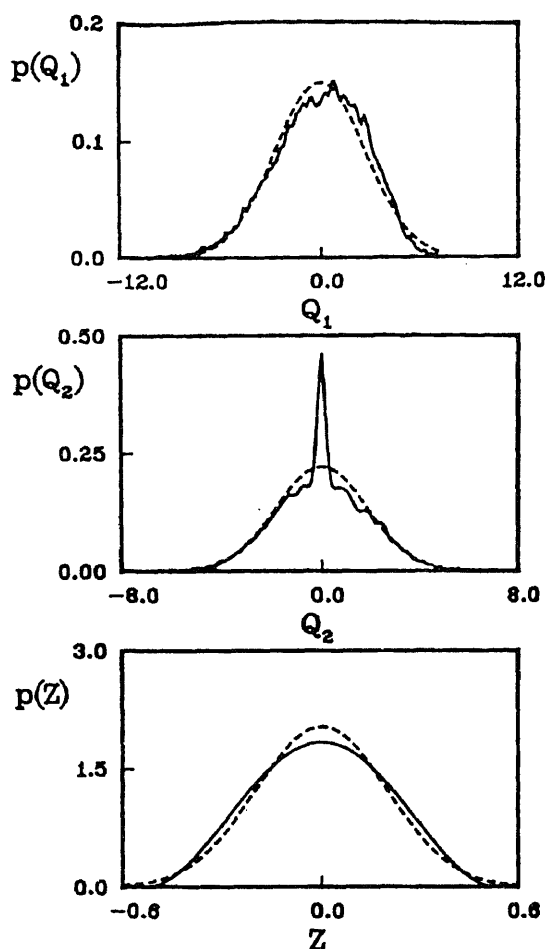


Figure 11. Estimated probability densities according to Monte Carlo simulation.

filtered excitation is close to the first mode natural frequency, the response spectra are localized at the normal mode natural frequencies as shown in figure 10. It is also observed that there is sharp spike at zero frequency which implies a non-zero mean for the response processes under zero mean random excitation.

The probability density functions of the filtered excitation and response time history records are estimated and shown in figure 11 for $\zeta_f = 0.05$, $\zeta_1 = \zeta_2 = 0.005$, $(\varepsilon^2 \sigma)^2 = 0.00625$, and $\Delta = -4$. The figure includes the corresponding Gaussian density function, shown by the dashed curve, as reference for measuring the deviation of the response from normality. It is seen that the filtered excitation is Gaussian since it is generated from a linear constant coefficient filter, while the response coordinates demonstrate significant deviation from Gaussianity characterized by multi-maxima. Depending on the value of the filter damping ratio, different response probability density functions are obtained. For small damping ratios $\zeta_f = 0.05$ and 0.1 the probability density functions of the first and the second modes response exhibit multi maxima. The transition from multi maxima to one maximum density of the second mode response is found to take place for relatively higher filter damping ratio $\zeta_f > 0.15$.

This implies that the deviation from Gaussianity and the degree of nonlinear interaction between the two modes become more significant as the filtered excitation bandwidth becomes narrower.

3. Experimental investigation

3.1 Experimental model and equipment

Experimental random vibration tests of nonlinear structures are scarce and valuable. They are valuable in exploring new phenomena not predicted from theory. They are particularly important where different theoretical approaches lead to different results for the same problem. They also provide physical insight into a number of complex dynamic phenomena and in identifying systems' modal parameters. In the experimental tests we consider a beam of spring steel with 0.254 m length and 0.0127×0.00005 m cross-section. Figure 12 shows a schematic diagram of the instrumentation used in the lab. The beam is clamped at both ends and mounted on a platform directly bolted to the armature of a 2669N (600-lb) thrust VTS electromagnetic shaker. The excitation signal of the shaker is detected using a piezoelectric Bruel & Kjaer model 4383 accelerometer which is mounted on the shaker. The beam response is measured using two 350 Ohm strain gauges (CEA-06-250UW 350 type) in a two arm bridge. The signals from both transducers are amplified and digitized using an analog-digital converter system. The input signal to the shaker is generated by a random noise generator (HP-3565S system) and is amplified before it goes to the shaker.

The r.m.s. acceleration and frequency of the shaker output are adjusted according to pre-selected values. This is done by incorporating a combination of frequency band shaping filters and a buffer amplifier with step input attenuator between the random

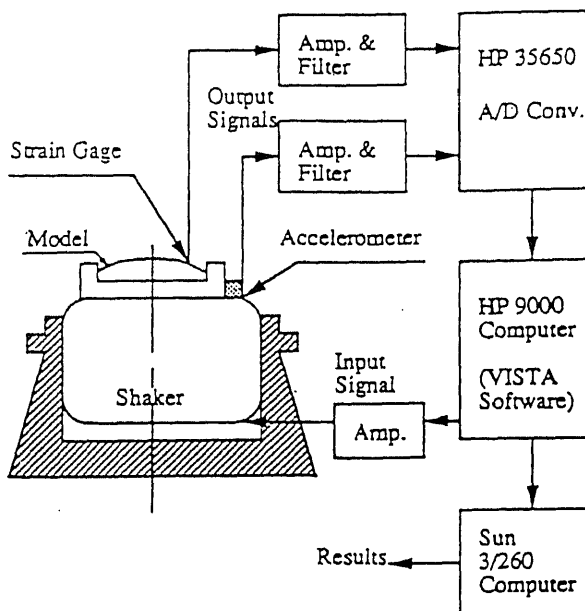


Figure 12. Experimental equipment and set-up.

noise generator and the shaker. The random excitation is generated by using a HP VISTA module of the HP-3565S system and amplified through a Techtron Model 7550 power amplifier. The response signal on the other hand is amplified by a Micro-Measurements Model 2310 signal conditioning amplifier. The excitation and response signals are read by a Hp-3565 Spectrum Analyzer and the data are transferred to a Sun 3/260 computer. Statistical parameters of the response and excitation are estimated by using the ILS (Interactive Laboratory System) software. In addition to the subroutines available in the ILS software, a FORTRAN program is written by the authors to estimate the probability density functions.

3.2 Experimental results

Several attempts were made to buckle the beam with initial static deflection by exerting an initial axial load higher than the Euler buckling load at one end of the beam. These attempts were carried out to reach an initial static deflection V_0 close to the theoretical critical value $V_0/h = 1.66$ which corresponds to 1:1 internal resonance condition. The closest value achieved during the tests is in the vicinity of $V_0/h = 1.86$. Accordingly, it was not possible to satisfy the condition of exact internal resonance. The damping ratio ζ_1 was measured from the free vibration tests and was found to be 0.003. The first two natural frequencies of the beam were measured from the response spectra and were found to be $\omega_1 = 80$ Hz and $\omega_2 = 110$ Hz. The excitation of the actual tests was then specified to have a centre frequency close to 75 Hz and bandwidth of 100 Hz. It was observed that there was a critical excitation level below which the beam oscillates about one potential well (one of the buckled positions). Above this critical level, the beam was observed to oscillate between the two wells where the snap-through took place.

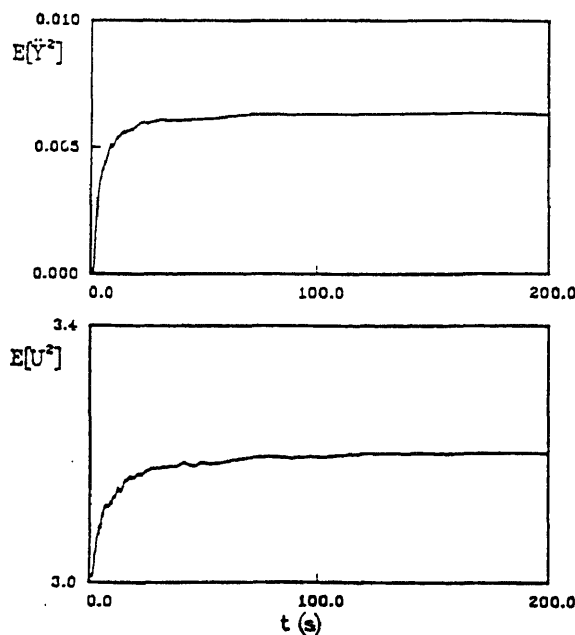


Figure 13. Experimental mean square time histories.

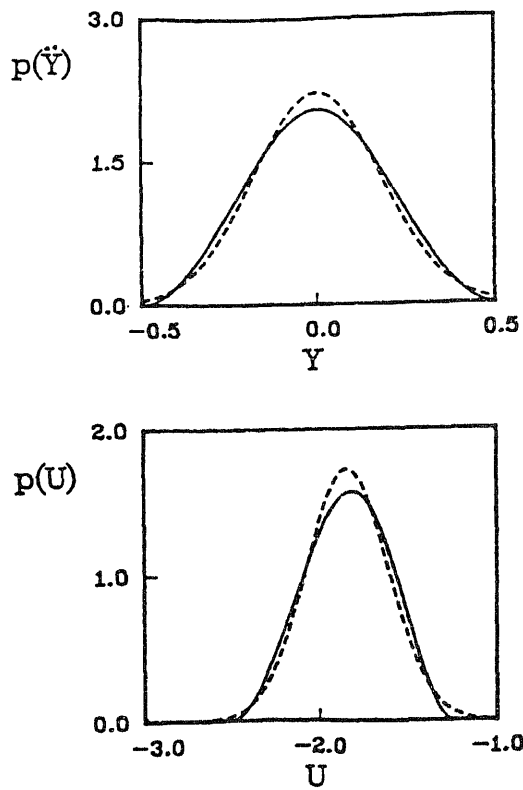


Figure 14. Measured probability densities of the shaker and beam response (dotted curves show Gaussian densities).

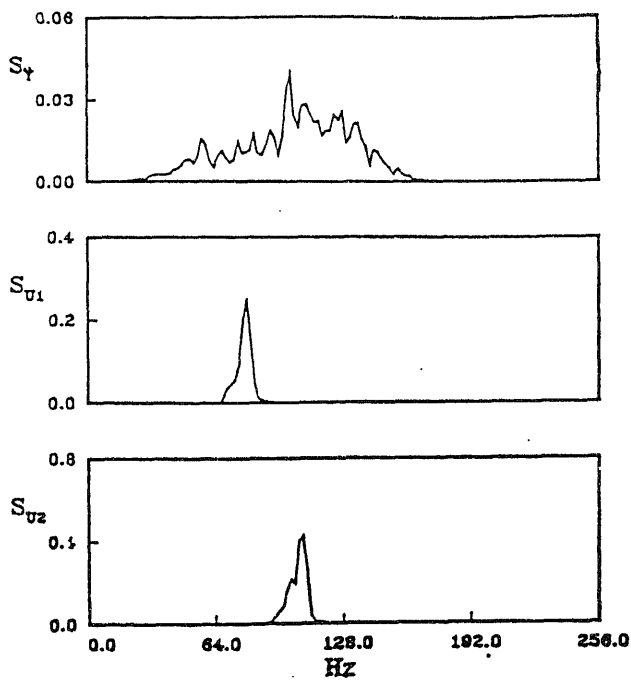


Figure 15. spectra.

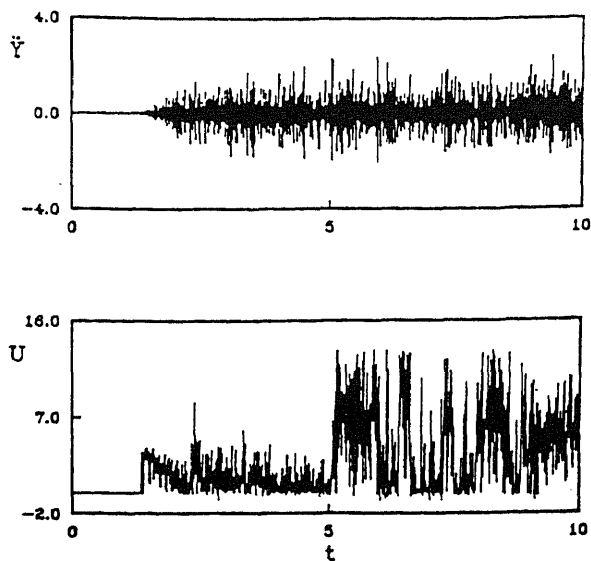


Figure 16. Time history records showing the snap-through.

However, for a long test duration, it was difficult to identify the excitation level due to the inevitable uncertainty at the beam boundary conditions.

Figure 13 shows time history records of the mean squares of the shaker acceleration and the beam deflection. The excitation level of this case is below the critical level. It is seen that the beam mean square reaches a stationary value and the oscillations take place about one buckled position. The probability density function of the response exhibits slight deviation from the Gaussian distribution as shown in figure 14. The response

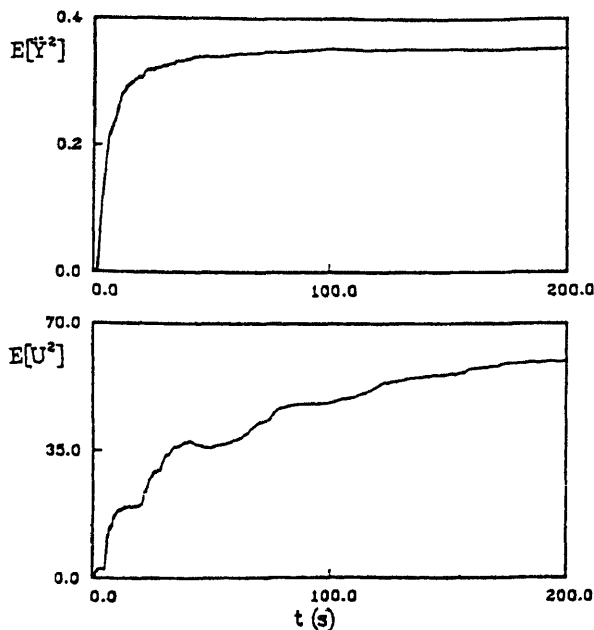


Figure 17. Time history records of mean squares (corresponding to snap-through).

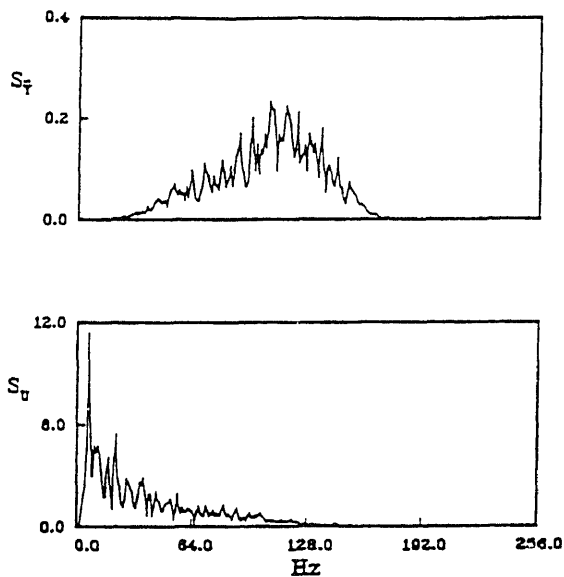


Figure 18. Measured power spectra corresponding to snap-through case.

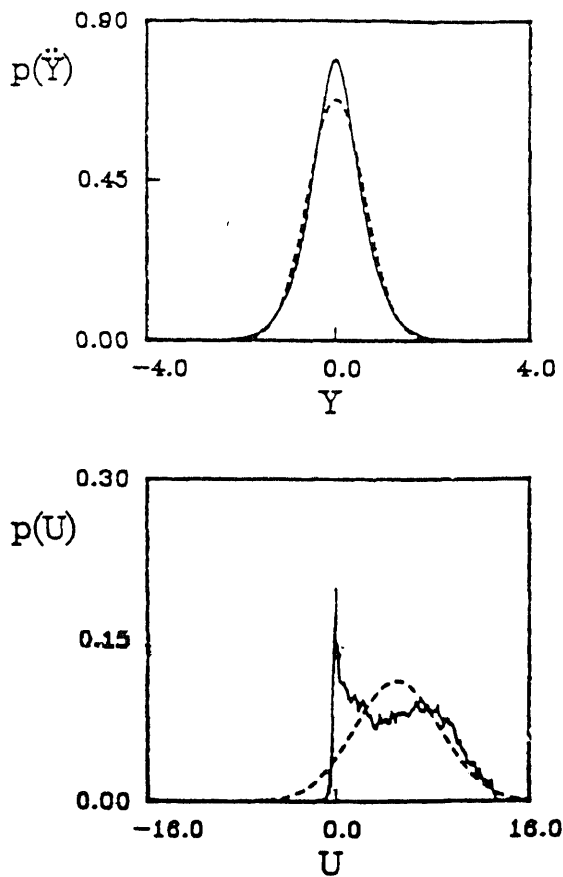


Figure 19. Measured probability densities (dotted curves are the corresponding Gaussian).

signal is decomposed into two components corresponding to the first two modes through an ideal band-pass filter with cut-off frequencies 30-95 Hz and 95-220 Hz, respectively. Each filtered signal was processed to estimate the corresponding power spectral density functions. Figure 15 shows the power spectra of the excitation and the first two modes. It is seen that each mode spectrum is centred around its natural frequency and the spectrum level of the second mode is higher than that of the first mode.

Under relatively higher excitation level the snap-through phenomenon was observed as shown in the time history records of figure 16. The response signals are found to fluctuate between two potential wells in an irregular manner. The time history records of the mean squares of the excitation and the beam response are shown in figure 17 and it is clear that the beam response does not achieve stationarity during the test period. The power spectra of the shaker and beam response are estimated and displayed in figure 18. The response spectrum is not concentrated at a single frequency but rather is spread over a wide frequency band. The same feature has been predicted numerically and the beam response is mainly characterized by chaotic motion. The corresponding probability density is shown in figure 19 which exhibits two peaks corresponding to the two wells of the buckled beam. The straight position is unstable in all tests as predicted numerically. These experimental results are reported for qualitative comparison and no quantitative comparison with the analytical or numerical results is made. The reason is that, during each test, the initially given conditions such as the axial load and the initial static deflection do not remain constant due to the inevitable slipping effect at the beam ends.

4. Conclusions

Nonlinear random vibration is important in the design stage of mechanical systems. Several complex characteristics owe their origin to nonlinear effects. The theory of nonlinear random vibration is limited in predicting these characteristics. Numerical simulation as well as experimental tests are important in exploring other phenomena such as snap-through and stochastic chaos. Under a filtered white noise excitation, the nonlinear response and stochastic bifurcation of a clamped-clamped beam have been studied in the neighbourhood of 1:1 internal resonance. The mean square responses show that the bifurcation of the second mode response depends on the excitation level, system damping ratios, internal detuning parameter, and the damping ratio of filter equation. The damping ratio of the filter equation is related to the bandwidth of filtered excitation. The response bifurcation is examined at different excitation levels, detuning ratios, and damping ratio of the linear filter equation. The range of two-mode interaction predicted by non-Gaussian closure is wider than that by Gaussian closure. Monte Carlo simulation is found to be in good agreement with the analytical results in predicting the second mode bifurcation boundary. The effect of damping ratio of the linear filter on the response statistics is found to reduce the interaction between the two modes.

This research is supported by a grant from the National Science Foundation under grant number MSS-9203733 and by additional funds from the Institute for Manufacturing Research at Wayne State University.

References

- Chow P L 1982 Stability of nonlinear stochastic evolution equations. *J. Math. Anal. Appl.* 400–419
- Davies H G, Liu Q 1990 The response envelope probability density function of a Duffing oscillator with random narrow band excitation. *J. Sound Vib.* 139: 1–8
- Davies H G, Liu Q 1992 On the narrow band random response distribution function of a non-linear oscillator. *Int. J. Non-Linear Mech.* 27: 805–816
- Davies H G, Nandlall D 1986 Phase plane for narrow band random excitation of a Duffing oscillator. *J. Sound Vib.* 104: 277–283
- Davies H G, Rajan S 1988 Random superharmonic and subharmonic response: Multiple time scaling of a Duffing oscillator. *J. Sound Vib.* 126: 195–208
- Dimentberg M F 1971 Oscillations of a system with nonlinear cubic characteristics under narrow band random excitation. *Mech. Solid.* 6: 142–146
- Fang T, Dowell E H 1987 Numerical simulations of jump phenomena in stable Duffing systems. *Int. J. Non-Linear Mech.* 22: 267–274
- Ibrahim R A, Heo H 1986 Autoparametric vibration of coupled beams under random support motion. *ASME J. Vib. Acoust. Stress, Reliab. Design* 108: 421–426
- Ibrahim R A, Li W 1988 Structural modal interaction with combination internal resonance under wide band random excitation. *J. Sound Vib.* 123: 473–495
- Ibrahim R A, Roberts J W 1976 Broad band random excitation of a two degree-of-freedom system with autoparametric coupling. *J. Sound Vib.* 44: 335–348
- Ibrahim R A, Roberts J W 1977 Stochastic stability of the stationary response of a system with autoparametric coupling. *Z. Angew. Math. Mech.* 57: 643–649
- Ibrahim R A, Sullivan D G 1990 Experimental investigation of structural autoparametric interaction under random excitation. *AIAA J.* 28: 338–344
- Ibrahim R A, Yoon Y J, Evans M G 1990 Random excitation of nonlinear coupled oscillators. *Nonlinear Dyn.* 1: 91–116
- Ibrahim R A, Lee B H, Afaneh A H 1993 Structural modal multifurcation with internal resonance, Part II: Stochastic approach. *ASME J. Vib. Acoust.* 115: 193–201
- Iyengar R N 1986 Stochastic response and stability of the Duffing oscillator under narrow band excitation. *J. Sound Vib.* 126: 255–263
- Iyengar R N 1988 Higher order linearization in nonlinear random vibration. *Int. J. Non-Linear Mech.* 23: 385–391
- Iyengar R N 1989 Response of nonlinear systems to narrow band excitation. *Struct. Safety* 6: 177–185
- Iyengar R N 1992 Approximate analysis of nonlinear systems under narrow band random inputs. *Nonlinear Stochastic Mechanics, IUTAM Symposium (Turin)* (eds) N Bellomo, F Casciati (Berlin: Springer-Verlag)
- Kantorovich L V, Krylov V I 1958 *Approximate methods of higher analysis* (Amsterdam: Nordhoff)
- Kapitaniak T 1985 Stochastic response with bifurcation to nonlinear Duffing's oscillators. *J. Sound Vib.* 102: 440–441
- Khas'minskii R Z 1980 *Stochastic stability of differential equations* (Amsterdam: Sijthoff Noordhoff)
- Koliopoulos P K, Bishop S R 1993 Quasi harmonic analysis of the behaviour of hardening Duffing oscillator subjected to filtered white noise. *Nonlinear Dyn.* 4: 279–288
- Koliopoulos P K, Langley R S 1993 Improved stability analysis of the response of a Duffing oscillator under filtered white noise. *Int. J. Non-Linear Mech.* 28: 145–155
- Kushner H 1967 *Stochastic stability and control* (New York: Academic Press)
- Lennox W C, Kuak Y C 1976 Narrow band excitation of a nonlinear oscillator. *J. Appl. Mech.* 43: 340–344
- Li W, Ibrahim R A 1989 Principal internal resonances in 3-DOF systems subjected to wide-band random excitation. *J. Sound Vib.* 130: 305–321
- Li W, Ibrahim R A 1990 Monte Carlo simulation of coupled nonlinear oscillators under random excitations. *ASME J. Appl. Mech.* 57: 1097–1099

- Lyon R H, Heckl M, Hazelgrove C B 1961 Response of hard-spring oscillator to narrow band excitation, *J. Acoust. Soc. Am.* 33: 1404–1411
- Mei C, Wentz K R 1982 Analytical and experimental nonlinear response of rectangular panels to acoustic excitation. *AIAA 23rd Structures, Structural Dynamics and Materials Conference*, New Orleans, LA, 514–520
- Minorsky N 1962 *Nonlinear oscillation* (New York: Van Nostrand)
- Moyer E T Jr 1988 Time domain simulation of the response of geometrically nonlinear panels subjected to random loading. *Proc. 29th AIAA Structures, Structural Dynamics and Materials Conference*, Paper No. 88–2236, pp. 210–218
- Nayfeh A H, Serhan S J 1991 Response moments of dynamic systems with modal interactions. *J. Sound. Vib.* 151: 291–310
- Newland D E 1965 Energy sharing in random vibration of nonlinearly coupled modes. *J. Inst. Math. Appl.* 1: 199–207
- Pinsky M 1974 Stochastic stability and the Dirichlet problem. *Commun Pure Appl. Math.* 27: 311–350
- Reinhall P G, Miles R N 1989 Effect of damping and stiffness on the random vibration of nonlinear periodic plates. *J. Sound Vib.* 132: 33–42
- Roberts J B 1991 Multiple solutions generated by statistical linearization and their physical significance. *Int. J. Non-Linear Mech.* 26: 945–959
- Roberts J B, Spanos P T D 1986 Stochastic averaging: An approximate method of solving random vibration problems. *Int. J. Non-linear Mech.* 21: 111–134
- Roberts J B, Spanos P T D 1990 *Random vibrations and statistical linearization* (New York: John Wiley & Sons)
- Roberts J W 1980 Random excitation of a vibratory system with autoparametric interaction. *J. Sound Vib.* 69: 101–116
- Schmidt G 1977a Probability densities of parametrically excited random vibration. In *Stochastic problems in dynamics* (ed.) B L Clarkson (London: Pitman) pp. 197–213
- Schmidt G 1977b Vibrating mechanical systems with random parametric excitation. In *Theoretical and applied mechanics* (ed.) W T Koiter (Amsterdam: North-Holland) pp. 439–450
- Soundarajan A, Ibrahim R A 1988 Parametric and autoparametric vibrations of an elevated water tower, Part III: Random response. *J. Sound Vib.* 121: 445–462

Nonlinear deterministic and random response of shallow shells

R HEUER¹, H IRSCHIK² and F ZIEGLER¹

¹Civil Engineering Department, Technical University of Vienna, Wiedner Hauptstraße 8-10/E201, Austria, A-1040

²Institute of Technical Mechanics and Foundations of Mechanical Engineering, Johannes-Kepler-University Linz, Linz-Auhof, Austria, A-4040

Abstract. Deterministic and random vibrations are considered for the case of shear deformable shallow shells composed of multiple perfectly bonded layers. The nontrivial generalization of the flat plate vibrations is expressed by the fact of "small amplitude" vibrations existing about the curved equilibrium position together with the snap-through and snap-buckling type large amplitude vibrations about the flat position. The geometrically nonlinear vibrations are treated by applying Berger's approximation to the generalized von Karman-type plate equations considering hard hinged supports of the straight boundary segments of skew or even more generally shaped polygonal shells. Shear deformation is considered by means of Mindlin's kinematic hypothesis and a distributed lateral force loading is applied. Application of a multi-mode expansion in the Galerkin procedure to the governing differential equation, where the eigenfunctions of the corresponding linear plate problem are used as space variables, renders a coupled set of ordinary time differential equations for the generalized coordinates with cubic and quadratic nonlinearities. For reasons of convergence, a light viscous modal damping is added. The nonlinear steady-state response of shallow shells subjected to a time-harmonic lateral excitation is investigated and the phenomenon of primary resonance is studied by means of the "perturbation method of multiple scales". The use of a nondimensional formulation and introduction of the eigen-time of the basic mode of the associated linearized problem provides a unifying result with respect to the planform of the shell. Within the scope of random vibrations, it is assumed that the effective forces can be modelled by uncorrelated, zero-mean wide-band noise processes. Considering the set of modal equations to be finite, the Fokker-Planck-Kolmogorov (FPK) equation for the transition probability density of the generalized coordinates and velocities is derived. Its stationary solution gives the probability of eventual snapping after a long time has elapsed. However, the probability of first occurrence follows from the (approximate) integration of the nonstationary FPK equation. The probability of first dynamic snap-through is derived for a single mode approximation with the influence of higher modes taken into account. Using the two-mode expansion, the probability distribution of the asymmetric snap-buckling is also evaluated.

Keywords. Nonlinear vibrations; shallow shells; primary resonance; snap-through; snap buckling; Fokker–Planck equation

1. Introduction

Von Karman's nonlinear plate equations represent the starting point of several modified theories for plate and shell structures. Recent reviews of nonlinear plate problems are given by Sathyamoorthy (1987) and Chia (1988). Within the scope of static applications, von Karman's nonlinear theory, originally derived for flat plates, was generalized by Marguerre (1950) to include the effect of initial imperfections, and in von Karman & Tsien (1941) it was extended to cylindrical shell problems. Extensive literature surveys on the topic of nonlinear free vibrations of shallow shells are elaborated by Leissa & Kadi (1971). Evensen (1972) gives a review on nonlinear natural and forced oscillations of thin-walled circular cylindrical shells, where existing disagreements as to whether the shell behaves as a hard or a soft spring, and whether the type of behaviour depends upon the boundary conditions and/or the shell being open or closed, are discussed.

Following a procedure developed by the authors, Heuer *et al* (1990, 1992), for flat and for buckled isotropic plates (of polygonal planform), Heuer (1994) derived a similar unifying representation of the influence of large amplitudes on forced vibrations of shallow shells with a generally shaped polygonal planform. Shells composed of multiple transversely isotropic elastic layers are considered. Equations of motion according to the dynamic version of the von Karman–Tsien theory, compare von Karman & Tsien (1941), modified by the kinematic hypothesis of Mindlin (1951) are the starting point. The edges are assumed to be simply supported and the in-plane displacements are constrained such that the approximation of Berger (1955) holds. Based on the concept of Jones & Klein (1968) a correspondence of the laminated shell to a moderately thick homogeneous shell is found. A multi-mode approach and the Galerkin procedure are subsequently applied to approximately solve the boundary value problem. The result of the projection is a set of nonlinearly coupled ordinary differential equations. A unifying result with respect to polygonal planform is achieved by the time transformation to the linear eigentime of the associated linearized plate problem.

As an illustration of deterministic oscillations, the nonlinear steady-state response of shallow shells and panels subjected to a time-harmonic lateral excitation is investigated. With respect to the phenomenon of primary resonance, a single-term approximation is used, and the solution of the corresponding problem is obtained by means of the "perturbation method of multiple scales" according to Nayfeh & Mook (1979).

Furthermore, shallow shells excited by random forces are considered. In that case where the generalized forces can be modelled by uncorrelated, zero-mean white noise processes, and a finite set of modal equations suffices, the Fokker–Planck–Kolmogorov (FPK) equation for the stationary transition probability density of the generalized coordinates and velocities is derived. Up to now, the FPK equation was used to determine the transition probability density function of the response of rather simple structures like strings (Ariaratnam 1962), beams (Herbert 1964), rectangular plates (Herbert 1965), and shallow arches (Ariaratnam & Sankar 1968; Sankar & Ariaratnam 1971a, b; Sun & Hsu 1989). The authors recently extended that classical approach to

more complex plane and shallow structures with polygonal boundaries (Heuer *et al* 1992, 1993a, b). Their strategy is applied in this paper to shallow shells when forced by random pressure loads. Nonlinear vibrations of shallow arches and buckled beams in the elastic range have been considered by Seide (1986), Penketgorn *et al* (1989), Locke & Mei (1990), Abou-Rayyan & Nayfeh (1993) by means of either simulation techniques or with the closure scheme and also by discretization with FEM.

2. Multimodal approach for nonlinear vibrations of shallow shells

Geometrical nonlinearity is considered by means of the kinematic assumptions for the midsurface strains of the shallow shell according to von Karman & Tsien (1941). Taking into account the effect of shear, the distribution of strain through the thickness of the shell is assumed according to the Reissner–Mindlin first order shear deformation theory, see Reissner (1985) and Mindlin (1951). Using these kinematic assumptions when setting up the strain energy, the contributions due to the in-plane, bending, and shear deformation become, respectively:

$$U_m = \frac{1}{2} D \int_A I_e^2 dA, \quad (1)$$

$$U_b = \frac{1}{2} K \int_A \left\{ \left[\Psi_{x,x}^2 + \Psi_{y,y}^2 + \frac{1}{2} (\Psi_{x,y} + \Psi_{y,x})^2 \right] + \nu \left[2\Psi_{x,x}\Psi_{y,y} - \frac{1}{2} (\Psi_{x,y} + \Psi_{y,x})^2 \right] \right\} dA, \quad (2)$$

$$U_s = \frac{1}{2s} D \int_A \left[(w_{,x} + \Psi_x)^2 + (w_{,y} + \Psi_y)^2 \right] dA, \quad (3)$$

where w denotes the deflection and Ψ_x, Ψ_y are the cross-sectional rotations. I_e stands for the first invariant of the midsurface strain tensor. The contribution of the second invariant is neglected in (1) following Berger (1955): Berger's assumption is a reasonable well-behaving approximation for structures with immovable in-plane boundary conditions. It renders exact results in the case of a shallow shell strip and has been confirmed for circular plates by Schmidt (1974) using a perturbation technique and the von Karman equations. Immovable in-plane boundary conditions are considered throughout the paper. In (1)–(3), A denotes the shell area projected onto the (x, y) -plane, $D, K, 1/s$ denote the effective stiffness in the case of symmetrically laminated shells composed of transversely isotropic layers,

$$(D, K) = \sum_{k=1}^N \int_{z_{k-1}}^{z_k} [E_k/(1-\nu_k^2)](1, z^2) dz, \quad \nu = \frac{1}{K} \sum_{k=1}^N K_k \nu_k, \quad (4)$$

$$1/s = \kappa^2 \sum_{k=1}^N \int_{z_{k-1}}^{z_k} G_{ek} dz, \quad (5)$$

and ν is an effective Poisson's ratio. The shear factor κ^2 is commonly set to 1.2.

Considering the lateral pressure loading p perpendicular to the shallow shell surface and neglecting rotatory as well as in-plane inertia, the field equations of this shear-deformable Berger-type shallow shell theory have been derived by Heuer (1994) using

Hamilton's principle. For thermally stressed and buckled plates see Heuer *et al* (1990, 1992, 1993a). As a result, the deflection turns out to be governed by the single fourth-order differential equation, μ is the averaged mass per unit of area:

$$K(1 + sn)\Delta\Delta w - n[\Delta w - 2(H - Ks\Delta H)] - Ks\mu\Delta\ddot{w} + \mu\ddot{w} = p - Ks\Delta p, \quad (6)$$

where n characterizes a time variant isotropic in-plane force, that is constant throughout the plate domain and is related to the deflection by the averaging integral

$$n = -D \left[\frac{1}{2A} \int_A w(\Delta w - 4H) dA \right], \quad (7)$$

H is the initial Gaussian curvature of the shallow shell.

Shallow shells with straight edges and with boundary conditions of the hard hinged type are considered,

$$\Gamma: w = 0, \Delta w = 0. \quad (8)$$

In a multimodal approach, the deflection and the lateral force loading of the shell are expanded into the orthogonal set of eigenfunctions w_j^* of the corresponding linearized flat plate problem where $n = 0$;

$$w(\mathbf{x}, t) = \sum_{j=1}^N c_j q_j^*(t) w_j^*(\mathbf{x}), p(\mathbf{x}, t) = \sum_{j=1}^N c_{pj} f_{pj}^*(t) w_j^*(\mathbf{x}), \quad (9)$$

The coefficients c carry the appropriate dimensions and may be chosen freely. The superscript (*) stands for nondimensional quantities. In Irschik (1985) it has been shown, that the eigenfunctions of those shear deformable simply supported plates with polygonal planform are governed by a set of second-order Helmholtz-differential equations with homogeneous Dirichlet's boundary conditions,

$$\Delta w_j^* + \alpha_j w_j^* = 0, j = 1, 2, \dots, N \quad (10)$$

$$\Gamma: w_j^* = 0. \quad (11)$$

For homogeneous shear deformable plates, the eigenvalues are directly proportional to the linear natural frequencies by

$$\omega_{jLo}^p = \left[K\alpha_j^2 / \mu(1 + Ks\alpha_j) \right]^{1/2}. \quad (12)$$

Using (9) as a Ritz-approximation for the solution of (6) and running through the Galerkin procedure give the set of coupled non-linear ODEs; a light linear viscous modal damping is added at this stage of discretization, λ_j^* :

$$q_j^{*''} + 2\lambda_j^* q_j^{*'} + \sum_{k=1}^N a_{jk}^* q_k^{*2} + \sum_{k=1}^N b_{jk}^* q_k^{*3} + q_j^* \sum_{k=1}^N d_{jk}^* q_k^* + q_j^* \sum_{k=1}^N e_{jk}^* q_k^{*2} = f_{pj}^* p_j^*, j = 1, \dots, N, \quad (13)$$

where

$$a_{jk}^* = \left\{ K\alpha_j^2 \delta_{jk} + \frac{4D\theta_k^* c_k}{R_0^2 \beta_j^* c_j} (\theta_j^* - Ks\delta_j^* / R_0^2) \right\} / \left[\mu(1 + Ks\alpha_j) \omega_{1Lo}^p \right], \quad (14)$$

$$b_{jk}^* = \frac{4D\alpha_k\beta_k^*c_k^2}{R_0\beta_j^*c_j}(\vartheta_j^* - Ks\delta_j^*/R_0^2)/\mu(1 + Ks\alpha_j)\omega_{1Lo}^2, d_{jk}^* = \frac{2D\alpha_j\vartheta_k^*c_k}{R_0\mu\omega_{1Lo}^2}, \quad (15)$$

$$e_{jk}^* = D\alpha_j\alpha_k\beta_k^*c_k^2/(2\mu\omega_{1Lo}^2), p_j^* = c_{pj}/(\mu c_j\omega_{1Lo}^2), \quad (16)$$

$$\beta_j^* = \frac{1}{A} \int_A w_j^{*2} dA, \vartheta_j^* = \frac{R_0}{A} \int_A Hw_j^* dA, \delta_j^* = \frac{R_0^3}{A} \int_A \Delta Hw_j^* dA. \quad (17)$$

R_0 stands for a characteristic length and δ_{jk} represents the Kronecker delta.

The non-dimensional form of (13) has been derived by scaling the time with the fundamental natural frequency of the linearized plate problem,

$$t^* = \omega_{1Lo}^p t, \quad (18)$$

where

$$(\cdot)' = \frac{\partial}{\partial t^*}.$$

Structures having the same similarity numbers result in an identical nondimensional response being sure or random. Any possibly non-regular polygonal planform of the shell enters only via the parameters α_j and β_j^* of the simple linear boundary value problems as determined by (10) and (11). Thus, only these linear eigenvalue problems have to be solved.

3. Steady-state motion at primary resonances

In this section, the behaviour of shallow shells subjected to a time-harmonic lateral excitation is examined. In order to investigate the phenomenon of primary resonance the forcing frequency is selected in the neighbourhood of an eigenfrequency of the linear structure. For a qualitative study, a single-term approximation is used as starting point, and the governing equation (13) becomes in that case

$$q^{*''} + 2\lambda^* q^{*'} + \tilde{a}^{*2} q^* + \tilde{b}^* c^* q^{*2} + \tilde{e}^* c^{*2} q^{*3} = (p^*/c^*) \cos(\Omega^* t^*). \quad (19)$$

The non-dimensional parameters,

$$\tilde{a}^* = a_{11}^{*1/2}, \tilde{b}^* = (b_{11}^* + d_{11}^*)/c^*, \tilde{e}^* = e_{11}^*/c^{*2}, c^* = c_1/R_0, \quad (20)$$

are determined by means of the expressions according to (14)–(17), and they are independent of the dimensionless amplitude c^* .

In the case of primary resonance the forcing frequency is set

$$\Omega^* = \tilde{a}^* + \varepsilon^2 \sigma^*, \quad (21)$$

where the detuning parameter σ^* quantitatively describes the nearness of Ω^* to the linear eigenfrequency. For steady-state response, the "perturbation method of multiple scales" according to Nayfeh & Mook (1979) is applied to obtain in a straight forward manner the following nonlinear frequency response equation:

$$\left(\frac{\Omega^*}{\tilde{a}^*}\right) = 1 + \frac{3}{8} g^* \left(\frac{c^*}{\tilde{a}^*}\right)^2 \pm \left[\left(\frac{p^*}{2c^* \tilde{a}^{*2}}\right)^2 - \left(\frac{\lambda^*}{\tilde{a}^*}\right)^2 \right]^{1/2}, \quad (22)$$

where

$$g^* = e^* - \frac{10}{9} \left(\frac{b^*}{\tilde{a}^*}\right)^2, \quad (23)$$

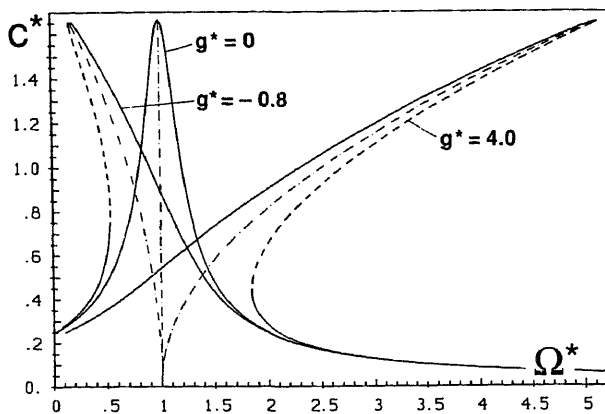


Figure 1. Nonlinear frequency response function according to (22) for three nonlinearity parameters $g^* = -0.8, 0, 4.0$; $p^* = 0.5$, $\lambda^* = 0.15$, $\tilde{a}^* = 1$; — stable and --- unstable portions, ··· backbone curves.

represents the influence of large deflection on the frequency response function (FRF). According to the sign of g^* the shell behaves as a hard spring ($g^* > 0$) or as a soft spring ($g^* < 0$) and, as g^* approaches zero, the problem becomes linear. Figure 1 shows this nonlinear influence. Here, all the FRFs are displayed for shells with given damping ratio $\lambda^* = 0.15$, the loadfactor is $p^* = 0.5$, dependent on the parameter values $g^* = -0.8, 0, 4.0$. The bending deformation of the resonance curves leads to multi-valued amplitudes and the entire solution splits into stable and unstable branches. At those points where the tangent is vertical the well-known jump phenomenon, which indicates dynamic snap-through of the shell, occurs.

4. Nonlinear random vibrations

In the present analysis it is assumed that the initial curvature of the shallow shell is proportional to the basic eigenmode of the linearized plate problem,

$$H = \frac{1}{2} C \alpha_1 w_1^*, \quad (24)$$

where $C \alpha_1$ measures the intensity of initial curvature. In that case (13) turns out to be given by

$$q_j^{*''} + 2\lambda_j^* q_j^{*'} + a_j^* q_j^* + \delta_{1j} \sum_{k=1}^N b_{jk}^* q_k^{*2} + 2b_{1j}^* q_1^* q_j^* + q_j^* \sum_{k=1}^N e_{jk}^* q_k^{*2} = f_{pj}^*, \quad (25)$$

where

$$a_j^* = \alpha_j^{*2} [(1 + s^*) / (1 + s^* \alpha_j^*)] + C^{*2} D^* \beta_1^* (1 + s^*) \delta_{1j}, \quad (26)$$

$$d_{1j}^* = \frac{1}{2} C^* D^* (\beta_1^*) \alpha_j^* (1 + s^*), \quad e_{jk}^* = \frac{1}{2} D^* \alpha_j^* \alpha_k^* (1 + s^*), \quad (27)$$

with the following similarity numbers:

$$a_j^* = \alpha_j / \alpha_1, \quad s^* = K s \alpha_1, \quad D^* = D R_0^2 / K, \quad C^* = C / R_0, \quad \beta_1^* = \frac{1}{A} \int_A w_1^{*2} dA. \quad (28)$$

To finally derive the simple form of (25), the following choice must be made but without

loss of generality:

$$c_j^2 = R_0^2/\beta_j^*, c_{pj} = c_j \alpha_1^2 K/(1+s^*). \quad (29)$$

The lateral force load is split into the static and the dynamic part,

$$f_{pj}^* = f_{js}^* + f_{jd}^*, \quad (30)$$

where f_{js}^* is assumed to be given and deterministic, while $f_{jd}^*(t)$ is characterized by a stochastic process. By definition, a generalized potential function

$$V^* = -f_{js}^* q_j^* + \frac{1}{2} \sum_{k=1}^N (a_j^* + 2b_{j1}^* q_1^*) q_j^{*2} + \frac{1}{4} \sum_{k=1}^N \sum_{k=1}^N c_{jk}^* q_j^{*2} q_k^{*2}, \quad (31)$$

transforms the coupled modal (25) to the dynamically driven set of ODEs

$$q_j^{*''} + 2\lambda_j^* q_j^{*'} + (\partial V^*/\partial q_j^*) = f_{jd}^*. \quad (32)$$

It is this standard form of (32) that makes the application of the classical FPK formulation of the theory of nonlinear random vibrations possible. This approach, however, until recently was restricted in applications to simple structures, like one-span beams or arches and rectangular plates or cylindrical panels. The nondimensional form of (25), when properly interpreted has no restrictions of validity with respect to geometry of the planform or the "order of elasticity" of rather complexes structures, like shallow composite shells erected above a non-regular polygonal planform.

The stochastic modal dynamic loads $f_{jd}^*(t)$ are approximated by uncorrelated zero-mean Gaussian white noise processes with the autocorrelation, we omit subsequently the superscript (*),

$$\langle f_{jd}(t) f_{kd}(t+\tau) \rangle = 2D_j \delta(\tau) \delta_{jk}, \quad (33)$$

while a given deterministic static force load f_{1s} is considered to be correlated to the first mode with static amplitude q_{1s} .

In this classical case the transition probability density $p(q_1 \dots q_N, q'_1 \dots q'_N)$ of the system with potential restoring force and light linear modal damping is a solution of the FPK-equation with the initial conditions

$$\sum_j \frac{\partial}{\partial q'_j} \left[\left(\frac{\partial V}{\partial q_j} + 2\lambda_j q'_j \right) p \right] - \sum_j \frac{\partial}{\partial q_j} (q'_j p) + \sum_j D_j \frac{\partial^2 p}{\partial q_j'^2} = \frac{\partial p}{\partial t}, \quad (34)$$

$$\lim_{t \rightarrow 0+} p(q_1 \dots q_N, q'_1 \dots q'_N, t) = \delta(q_1 - q_{1s}) \delta q_2 \dots \delta q_N \delta q'_1 \dots \delta q'_N.$$

The stationary solution of (34) in a mechanical setting has been derived by Caughey (1963),

$$p(q_1 \dots q_N, q'_1 \dots q'_N) = \bar{B} \exp \left\{ -\frac{1}{\bar{K}} \left(\frac{1}{2} \sum_j q_j'^2 + V \right) \right\}, \quad (35)$$

with the additional assumption of constant ratios of intensities and light damping,

$$D_j/(2\lambda_j) = \bar{K} = \text{const. for all } j. \quad (36)$$

Multiple integration over the velocity space gives the n -dimensional probability density function of the generalized coordinates

$$p(q_1 \dots q_N) = \exp \{ -V/\bar{K} \}, \quad (37)$$

where B is determined through normalization,

$$\int_{-\infty}^{+\infty} \dots \int_{-\infty}^{+\infty} p(q_j \dots q_n) \Pi dq_j = 1 \Rightarrow B. \quad (38)$$

The mean-square response of the j th modal deflection equals the second moment that results from the cross moments by putting $j = k$,

$$\langle q_j q_k \rangle = \int_{-\infty}^{+\infty} \dots \int_{-\infty}^{+\infty} q_j q_k p(q_j \dots q_n) \prod_j dq_j. \quad (39)$$

Considering the nonlinear vibrations of flat plates, the influence of the higher modes upon $\langle q_1^2 \rangle$ has been studied in detail in Heuer *et al* (1992).

As an extension of these results, figure 2 illustrates the influence of the initial curvature and shape, measured by C , (19), of shallow shells with $\alpha_j/\alpha_1 = j^2$, $j = 1, 2, \dots$, upon $\langle q_1^2 \rangle$. The influence of five modes is taken into account. A convergence study of the nonlinear mean-square response in the parameter space of figure 2 has been performed. It was found that all the higher modes $N \geq 5$ alter these results by less than one half of a promille. That means their contribution to the mean-square value is negligible. These results refer to a shell with polygonal boundary, without any deterministic lateral load, when vibrating about the undeformed configuration.

It is well known, however, that the vibrations about the static equilibrium position of shallow shells may show snap-through behavior. The probability of first occurrence of snap-through in a time interval T has been approximately determined by Ariaratnam & Sankar (1968) for SDOF-systems of the form

$$q_1'' + 2\lambda_1 q_1' + \partial V/\partial q_1 = f_{1d}. \quad (40)$$

Using (31) with $N = 1$ and (32), the potential V can be identified as

$$V(q_1) = \frac{e_{11}}{4} q_1^4 + b_{11} q_1^3 + \frac{a_1}{2} q_1^2 - f_{1s} q_1. \quad (41)$$

Assuming the intensities in (36) to be sufficiently small,

$$\bar{K} \ll h, h = V(q_{1B}) - V(q_{1A}), \quad (42)$$

where B refers to the intermediate barrier of unstable equilibrium position. Where the potential takes on its maximum, and A indicates the initial (stable) equilibrium configuration q_{1s} , the following approximation has been derived by Ariaratnam &

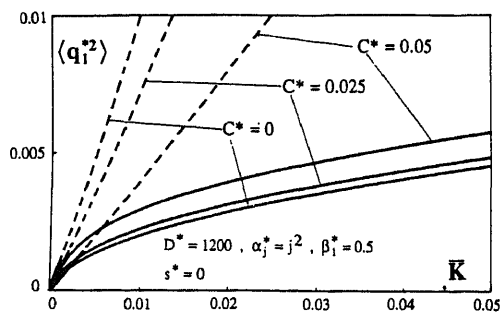


Figure 2. Linear (---) and nonlinear (—) nondimensional mean-square response $\langle q_1^2 \rangle$ as a function of \bar{K} according to (37) and (39). The graph is valid for shallow shells with $\alpha_j^* = j^2$, $j = 1, 2, \dots, N$, regardless of their special polygonal plan-form. $C^* = C/R_0$.

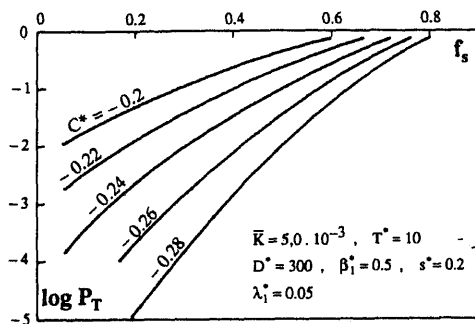


Figure 3. Probability of first occurrence of snap-through P_T as a function of $f_s = f_{1s}/\max f_{1s}$ for various values of C^* . The graph is independent of the special skew planform of the shallow shell, $C^* = C/R_0$.

Sankar (1968):

$$P_T = (T/2\pi)(-V_A''/V_B'')^{1/2}[(\lambda_1^2 - V_B'')^{1/2} - \lambda_1] \exp(-h/\bar{K}). \quad (43)$$

In the present case

$$V'' \equiv \frac{\partial^2 V}{\partial q_1^2} = (3e_{11}q_1^2 + 6b_{11}q_1 + a_1) \left| \begin{array}{l} q_1 = q_{1A}, \\ q_1 = q_{1B} \end{array} \right. \quad (44)$$

and $\partial V/\partial q_1 = 0$ renders the equilibrium positions $q_{1A} < q_{1B} < q_{1C}$ that exist under the action of f_{1s} . Snapping occurs with probability P_T from q_{1A} to q_{1C} . Equation (43) is evaluated and the result is plotted in figure 3 for shear deformable shallow shells. The probability P_T of snap-through is presented as a function of the static force load ratio $f_s = f_{1s}/\max f_{1s}$, where $\max f_{1s}$ is the static snap-through load. Note, that the SDOF-approximation of (40)–(44) gives a unifying formulation for simply supported shallow shells of arbitrary polygonal planform.

As was pointed out by Ashwell (1962), see also Irschik (1986) and Ziegler & Rammerstorfer (1989), the loss of stability of the static equilibrium position may be accompanied by a bifurcation to a higher mode. For nonlinear random vibrations, this so-called snap-buckling has been studied in detail by Sankar & Ariaratnam (1971a, b) starting with a two-mode approximation of the form

$$q_1'' + 2\lambda_1 q_1' + \partial V/\partial q_1 = f_{1d}. \quad (45)$$

$$q_1'' + 2\lambda_2 q_2' + \partial V/\partial q_2 = 0$$

This set of equations can be matched to the current more general formulation of (31) with $N = 2$, by putting

$$V(q_1, q_2) = \frac{1}{4}(e_{11}q_1^4 + e_{22}q_2^4) + b_{11}q_1^3 + \frac{1}{2}(a_1q_1^2 + a_2q_2^2) + q_1q_2^2(b_{12} + (e_{11}/2)q_1) - f_{1s}q_1, \quad (46)$$

to render the class of systems of shallow shells. Again sufficiently small levels of excitation are assumed

$$\bar{K} \ll h_1, h_1 = V(q_{1B}, q_{2B}) - V(q_{1A}, 0). \quad (47)$$

The value of the generalized coordinate at the equilibrium point A is consequently taken from the single-mode analysis. The coordinates of the saddle-point B_1 are the roots of the static equations resulting from equation (45), see figure 4,

$$\partial V/\partial q_1 = 0, \partial V/\partial q_2 = 0, \quad (48)$$

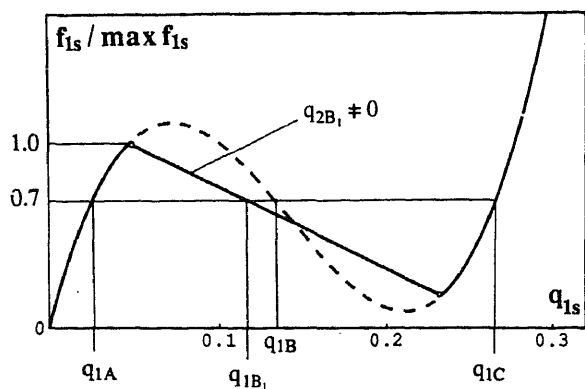


Figure 4. Static force deflection curve, snap-buckling problem; $D^* = 300$, $\beta_1^* = 0.5$, $s^* = 0.2$.

and are given by the following expressions, where $q_{2B_1}^2 \geq 0$

$$q_{1B_1} = e_{22}(f_{1s} + a_2 b_{12}/e_{22})/(a_1 e_{22} - 2b_{12}^2 - a_2 e_{12}), \quad (49)$$

$$q_{2B_1} = [-(a_2 + 2b_{12}q_{1B_1} + e_{12}q_{1B_1}^2)/e_{22}]^{1/2}. \quad (50)$$

Sankar & Ariaratnam (1971a), in a detailed analysis, derived the following approximation for the probability of first snap-buckling within the time interval T :

$$\bar{P}_T = \frac{T}{2\pi} \cos^2 \phi \left[-\frac{(V_{11})_A}{(V_{11})_{B_1}} \right]^{\frac{1}{2}} \{ [\lambda^2 - (\bar{V}_{11})_{B_1}]^{1/2} - \lambda \} \exp\left(-\frac{h_1}{K}\right), \quad (51)$$

where

$$(V_{11})_A = \frac{\partial^2 V}{\partial q_1^2} \bigg|_{q_1=q_{1A}}, \quad (\bar{V}_{11})_{B_1} = \frac{\partial^2 \bar{V}}{\partial s_1^2} \bigg|_{s_1=s_{1B_1}, s_2=s_{2B_1}}, \quad (52)$$

$$(\bar{V}_{11})_{B_1} = \frac{1}{2}[(V_{11})_{B_1} + (V_{22})_{B_1}] - \frac{1}{2}\{[(V_{11})_{B_1} - (V_{22})_{B_1}]^2 + 4(V_{12})_{B_1}^2\}^{1/2}, \quad (53)$$

$$(V_{ij})_{B_1} = \frac{\partial^2 V}{\partial q_i \partial q_j} \bigg|_{q_1=q_{1B_1}, q_2=q_{2B_1}}, \quad i, j = 1, 2, \quad (54)$$

and a transformation to the principal coordinates s_1, s_2 has been performed by means of Mohr's circle:

$$\begin{Bmatrix} q_1 \\ q_2 \end{Bmatrix} = \mathbf{D}(\phi) \begin{Bmatrix} s_1 \\ s_2 \end{Bmatrix}, \quad (55)$$

with the angle of rotation ϕ

$$\tan 2\phi = 2(V_{12})_{B_1}/[(V_{11})_{B_1} - (V_{22})_{B_1}]. \quad (56)$$

Figure 5 shows the probability of first occurrence of snap-buckling of a shallow shell with $\alpha_2^* = 13/5$ (that holds e.g. for a shell above a right-angled isosceles triangular base with hard hinged supports) as a function of the load ratio $\bar{f}_s = f_{1s}/\max f_{1s}$. The maximum load according to the static equations (49) and (50), $\max f_{1s}$, results from the condition $q_{2B_1}^2 = 0$.

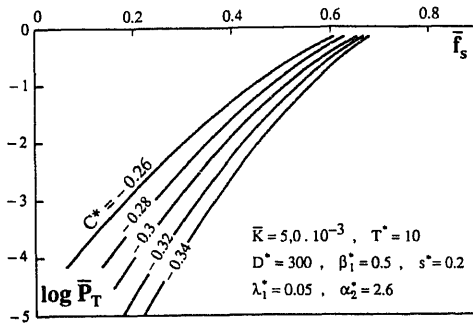


Figure 5. Probability of first occurrence of snap-buckling \bar{P}_T , (51) as a function of $\bar{f}_s = \bar{f}_{1s}/\max \bar{f}_{1s}$, for various values of C^* . The graph is valid for shear deformable shallow shells with $\alpha_2^* = 13/5$, e.g. right-angled isosceles triangular shell. $C^* = C/R_0$.

5. Conclusion

It has been shown that even complex structures like non-regularly shaped shallow shells designed with composite materials, forced by lateral loads can be projected onto the space of the linear modes of the associated flat plates. The resulting set of coupled nonlinear ODEs is transformed and finally brought in a nondimensional form that is of the classical type of dynamic equations with potential restoring force.

Approximating a random environment by physical white noise processes makes the classical analysis of the resulting Markov process by means of the FPK equation possible. Approximate values of the probabilities of snap-through and snap-buckling vibrations are calculated in the parameter space. In the case of single mode approximations the results are general. Taking into account the influence of higher modes restricts the results to a class of structures having a definite sequence of the linear natural frequencies divided through the basic frequency.

List of symbols

$a_{jk}^*, b_{jk}^*, d_{jk}^*, e_{jk}^*$	coefficients of differential equations (13);
D	effective stretching stiffness;
E_k	Young's modulus of the k th layer;
G_{ck}	transverse shear modulus of the k th layer;
H	mean curvature
I_2, II_e	invariants of the mid-surface strain tensor;
K	effective bending stiffness;
n	Berger's in-plane force;
P_T	probability of first occurrence of snap-through in a time interval T ;
\bar{P}_T	probability of first occurrence of snap-buckling in a time interval T ;
P	lateral force loading;
q_j^*	generalized coordinates of shell deflection;
$p(q_1 \dots q_N, q'_1 \dots q'_N)$	transition probability density;
$\langle q_j^2 \rangle$	mean-square response of the j th generalized coordinate;
$1/s$	shear rigidity;

U_b	bending energy;
U_m	membrane energy;
U_s	strain energy due to shear deformation;
V	potential function;
w	mid-surface deflection;
w_j^*, α_j	Helmholtz-eigenfunctions and -eigenvalues;
κ^2	shear factor;
μ	mass density per unit shell area;
ν_k	Poisson's ratio of the k th layer;
Ψ_x, Ψ_y	cross-sectional rotations.

References

- Abou-Rayán A M, Nayfeh A H 1993 Stochastic response of a buckled beam to external and parametric random excitations, *34th AIAA/ASME/ASCE/AHS/ASC-Conference*, La Jolla, CA, Paper 93-1425-CP, pp. 1030-1040
- Ariaratnam S T 1962 Response of a loaded nonlinear string to random excitation. *J. Appl. Mech.* 29: 483-485
- Ariaratnam S T, Sankar T S 1968 Dynamic snap-through of shallow arches under stochastic loads. *AIAA J.* 6: 798-802
- Ashwell D G 1962 Nonlinear problems. In *Handbook of engineering mechanics* (ed.) W Flügge (New York: McGraw Hill) pp. 45-7 - 45-9
- Berger H M 1955 A new approach to the analysis of large deflection of plates. *J. Appl. Mech.* 22: 465-472
- Caughey T K 1963 Derivation and application of the Fokker-Planck equation to discrete nonlinear dynamic systems subjected to white random excitation *J. Acoust. Soc. Am.* 35: 1683-1692
- Chia C Y 1988 Geometrically nonlinear behavior of composite plates: A review. *Appl. Mech. Rev.* 41: 439-451
- Evensen D A 1972 Nonlinear vibrations of circular cylindrical shells. In *Proc. Symp. on Thin-Shell Structures: Theory, experiments, and design*, Pasadena, California (eds) Y C Fung, E E Sechler (Englewood Cliffs, N J: Prentice-Hall) pp. 133-155
- Herbert R E 1964 Random vibrations of a nonlinear elastic beam. *J. Acoust. Soc. Am.* 36: 2090-2094
- Herbert R E 1965 Random vibrations of plates with large amplitudes. *J. Appl. Mech.* 32: 547-552
- Heuer R 1994 Large flexural vibrations of thermally stressed layered shallow shells. *Nonlinear Dynamics* 5: 25-38
- Heuer R, Irschik H, Ziegler F 1990 Multi-modal approach for large natural flexural vibrations of thermally stressed plates. *Nonlinear Dynamics* 1: 449-458
- Heuer R, Irschik H, Ziegler F 1992 Large amplitude random vibrations of polygonal plates *Proceedings of the IUTAM-Symposium on Nonlinear Stochastic Mechanics*, Torino (eds) N Bellomo, F Casciati (Berlin: Springer-Verlag) pp. 285-296
- Heuer R, Irschik H, Ziegler F 1993a Nonlinear random vibrations of thermally buckled skew plates. *Probabilistic Eng. Mech.* 8: 265-271
- Heuer R, Irschik H, Ziegler F 1993b Randomly forced nonlinear vibrations of layered skew plates and shallow shells. *34th AIAA/ASME/ASCE/AHS/ASC-Conference*, La Jolla CA, Paper 93-1625-CP, pp. 2809-2816
- Irschik H 1985 Membrane-type eigenmotions of Mindlin plates. *Acta Mech.* 55: 1-20
- Irschik H 1986 Large thermoelastic deflections and stability of simply supported polygonal panels. *Acta Mech.* 59: 31-46
- Jones R M, Klein S 1968 Equivalence between single-layered and certain multilayered shells. *AIAA J.* 6: 2295-2300
- von Karman Th, Tsien H S 1941 The buckling of thin cylindrical shells under axial compression. *J. Aeronaut. Sci.* 8: 303-312

- Leissa A W, Kadi A S 1971 Curvature effects on shallow shell vibrations *J. Sound Vib.* 16: 173–187
- Locke J, Mei C C 1990 Finite element, large-deflection random response of thermally buckled beams, *AIAA J.* 28: 2125–2131
- Marguerre K 1950 Knick- und Beulvorgänge. In *Neuere Festigkeitsprobleme des Ingenieurs* (ed.) K Marguerre (Berlin: Springer-Verlag) pp. 229–235
- Mindlin R D 1951 Influence of rotatory inertia and shear on flexural motions of isotropic, elastic plates. *J. Appl. Mech.* 18: 31–38
- Nayfeh A H, Mook D T 1979 *Nonlinear oscillations* (New York: Wiley)
- Penketgorn T, Rojiani K B, Plaut R H 1989 Snap-through of a shallow arch under random loading. *Probabilistic Eng. Mech.* 4: 114–119
- Reissner E 1985 Reflections on the theory of elastic plates. *Appl. Mech. Rev.* 38: 1453–1464
- Sankar T S, Ariaratnam S T 1971a Snap-buckling of shell-type structures under stochastic loading. *Int. J. Solids Struct.* 7: 655–666
- Sankar T S, Ariaratnam S T 1971b Instability of stochastically loaded shallow arches in nonsymmetric modes. *Int. J. Solids Struct.* 7: 1305–1316
- Sathyamoorthy M 1987 Nonlinear vibration analysis of plates: A review and developments. *Appl. Mech. Rev.* 40: 1553–1561
- Schmidt R 1974 On Berger's method in the nonlinear theory of plates. *J. Appl. Mech.* 41: 521–523
- Seide R 1986 Snap-through of initially buckled beams under uniform random pressure. In *Random vibrations-status and recent developments* (eds) I Elishakoff, R H Lyon (Amsterdam: Elsevier) pp. 403–414
- Sun J-Q, Hsu C S 1989 Random vibration of hinged elastic shallow arch. *J. Sound Vib.* 132: 299–315
- Ziegler F, Rammerstorfer F G 1989 Thermoelastic stability. In: *Thermal stresses III.* (ed.) R B Hetnarski (Amsterdam: North-Holland) ch. 2, pp. 108–189



Homology design of vibration mode shape under uncertain boundary conditions

SHIGERU NAKAGIRI and NOBUHIRO YOSHIKAWA

Institute of Industrial Science, University of Tokyo, 7-22-1, Roppongi, Minato-ku, Tokyo 106, Japan

Abstract. A methodology is proposed for homology design to realize such a vibration mode shape that satisfies a certain geometrical relation before and during vibration. The formulation is based on the finite element eigenvalue and sensitivity analyses so that a governing equation for the design variables is derived under the condition that the homology constraint holds while the eigenvalue problem is satisfied.

The nonlinear effect of uncertain boundary conditions on the homologous mode shape is examined through convex model of the uncertainties. The worst case of the disturbed mode shape due to the uncertainties is estimated employing the Lagrange multiplier method.

The numerical example of out-of-plane vibration of a planar lattice frame displays the validity of the proposed method for homology design. The worst case of the disturbed mode shape is discussed when rotational stiffness of the boundary fluctuates.

Keywords. Vibration mode shape; homology design; finite element sensitivity analysis; Moore–Penrose generalized inverse; uncertain boundary condition; convex model.

1. Introduction

Structures have been regarded basically as carriers of external loads in the field of structural mechanics. Static structures such as bridge and pressure vessels are not expected to perform any function or motion actively, other than to serve as passive bases to carry loads. Integrity and safety have long been pursued as the primary aim of structural design even in mobile structures such as aircraft, ship and automobile.

In modern times, dimensional accuracy and excellent performance are demanded for precision instruments and smart machinery in order to fulfil the mission assigned to the structures on the premises that their stiffness and strength are ensured. The quality of mission and performance nowadays is a major concern of adaptive structures, deployable structures and large flexible spacecraft. For instance, high accuracy in shape

control is required for the antenna mirror of a huge radio telescope at any tilting angle to achieve high resolution for radio wave collection, while the parabolic shape of the antenna is likely to be deformed by its self-weight. This is an example where the deformation should be kept under control as well as stresses.

Hoerner proposed the concept of homologous deformation in the design of huge radio telescopes and stated that the deformation of a structure shall be called homologous, if a given geometrical relation holds, for a given number of structural points, before, during and after the deformation (Hoerner 1967). His idea was adopted in practice to construct a huge radio telescope (Morimoto *et al* 1982). A finite element formulation was proposed for the homology design of the frame structure under static loading based on the condition that the solution of the equilibrium equation with a rectangular stiffness matrix exists (Hangai & Guan 1989). A different formulation of homology design, with less computational effort than the formulation by Hangai, by means of avoiding the tiresome calculation of the sensitivities of the Moore–Penrose generalized inverse, was made (Yoshikawa & Nakagiri 1993).

This paper deals with a methodology of the homology design to control vibration mode shape at a single eigenmode as the first step for dynamic homology design of flexible structures. It discusses the nonlinear effect of the uncertainties, involved in the structural system, on the homologous mode shape. The methodology is based on the finite element sensitivity analysis of vibration eigenvalue problem. Use is made of the convex model to estimate the worst case of the disturbed homologous mode shape due to the uncertainties (Ben-Haim & Elishakoff 1990). The validity of the proposed methodology is examined by the numerical examples concerned with a planar lattice frame.

2. Statement of the problems

Suppose we have a baseline design of an elastic structure, and that the linear undamped eigenvalue problem of the vibration is given by (1) after the geometrical boundary conditions are duly processed,

$$([\bar{K}] - \bar{\lambda}[\bar{M}])\{\bar{\phi}\} = \{0\}, \quad (1)$$

where $[K]$ and $[M]$ denote $N \times N$ symmetric stiffness matrix and consistent mass matrix, λ the eigenvalue, and $\{\phi\}$ the corresponding eigenvector of the eigenmode concerned, respectively. The symbol of upper bar indicates a current baseline design. The constraint for the prescribed homologous mode shape can be expressed in the following form by using a constraint matrix $[C]$,

$$\{\phi_h\} = [C]\{\phi_i\}, \quad (2)$$

where the subscripts h and i stand for J homologous components and $I (= N - J)$ independent components of the eigenvector, respectively. We call the mode shape homologous if a certain geometrical relation holds in a part or whole of the mode shape of a structure before and during harmonic vibration, similar to the definition of homologous deformation stated by Hoerner. If the eigenvector obtained from (1) satisfies the constraint relation of (2), the baseline itself realizes homology design. Usually, (2) is not satisfied, and the baseline design should be changed so that (2) holds for the eigenvector of the structure after design change. The first problem in this study is to find a way to change the baseline design so that the homologous mode shape is realized.

The eigenvalue and eigenvector are subjected to the material constants, dimensions and boundary conditions of the structure. Then the homologous mode shape, if feasible, is likely to be disturbed by the fluctuation of the aforementioned influential factors. The second problem is how to estimate the worst case of the homologous mode shape disturbed by uncertain fluctuations in the boundary conditions.

3. Finite element formulation of homology design

3.1 Derivation of governing equation of design variables

The constraint matrix $[C]$ should be adequately constituted, since the way to express the homologous mode constraint is not unique even for an identical homologous mode shape. In this paper, the ingredients of the matrix $[C]$ are supposed to be constant under the assumption that the constraint is linear. In order to find the homology design which satisfies (2), we choose M design variables α_m corresponding to design parameters p_m in the following form.

$$p_m = \bar{p}_m(1 + \alpha_m). \quad (3)$$

It is assumed that the change in the stiffness matrix arising from the design change can be expressed by the first-order approximation of the Taylor series expansion in the vicinity of a current baseline design, as given below. The subscript m indicates the m -th design variable, and the superscript I the first-order. The first-order sensitivity of the stiffness matrix $[K_m^I]$ can be easily evaluated by taking the derivative of the stiffness matrix with respect to α_m .

$$[K] = [\bar{K}] + \sum_{m=1}^M [K_m^I] \alpha_m. \quad (4)$$

The change in the mass matrix is approximated in the same form as above. When we express the change in the eigenvector in the following form,

$$\{\phi\} = \{\bar{\phi}\} + \sum_{m=1}^M \{\phi_m^I\} \alpha_m, \quad (5)$$

and that of the eigenvalue in the same form, we can evaluate the sensitivities of the eigenpair λ_m^I and $\{\phi_m^I\}$ by the conventional method of sensitivity analysis (Fox & Kapoor 1968).

In the framework of the first-order approximation, the sensitivities of the eigenpair thus obtained ensure that the eigenvalue problem in the form of (1) is satisfied even after the design change. Substituting the relevant parts of the eigenvector of (5) into (2), we have (6), and its summarized form is expressed as (7),

$$\sum_{m=1}^M (\{\phi_{hm}^I\} - [C]\{\phi_{im}^I\}) \alpha_m = [C]\{\bar{\phi}_i\} - \{\bar{\phi}_h\}, \quad (6)$$

$$[A]\{\alpha\} = \{b\}, \quad (7)$$

where $[A]$ is a $J \times M$ rectangular matrix and $\{\alpha\}$ the unknown vector consisting of M design variables. This is the governing equation of the design variables of the homology design for mode shape.

3.2 Determination of design variables

The unknown vector $\{\alpha\}$ can be solved through (7) by use of the Moore–Penrose generalized inverse of the rectangular matrix $[A]$ (Rao & Mitra 1971). The solution $\{\alpha\}$ exists when the following equation is satisfied,

$$([I] - [A][A]^-)\{b\} = \{0\}, \quad (8)$$

where $[I]$ denotes a $J \times J$ identity matrix. The symbol on the right shoulder ($-$) indicates the Moore–Penrose generalized inverse. The general solution $\{\alpha\}$ is given by

$$\{\alpha\} = [A]^- \{b\} + ([I] - [A]^- [A])\{h\}, \quad (9)$$

where the first term on the right hand side is called the particular solution, and the second one the complementary solution, respectively. In (9), $[I]$ indicates an $M \times M$ identity matrix, and $\{h\}$ stands for an arbitrary vector. The particular solution results in the minimal norm of $\{\alpha\}$, owing to the property of the Moore–Penrose generalized inverse.

We determine the design variables only by the particular solution of (9), that is, set the arbitrary vector $\{h\}$ equal to a null vector, so as to minimize the design change from the current baseline design in the sense that the norm of the design variables is minimal. It is necessary for the completion of the homology design to renew the baseline design and repeat the finite element eigenvalue analysis and sensitivity analysis for the renewed baseline design in order to cope with the deficiency of the first-order approximation employed in the formulation until (2) holds exactly. Equation (6) indicates that no design change takes place further because $\{\alpha\} = \{0\}$ after (2) is satisfied exactly.

4. Convex approach to estimate disturbed mode shape due to uncertain boundary conditions

4.1 Sensitivity analysis of homologous mode shape

Suppose that (10) represents the eigenvalue problem which affords the homologous mode shape $\{\phi_a\}$ as aimed at and corresponding to eigenvalue λ_a ,

$$([K_a] - \lambda_a [M_a])\{\phi_a\} = \{0\}, \quad (10)$$

where $[K_a]$ and $[M_a]$ denote the $N \times N$ stiffness matrix and mass matrix obtained by the homology design respectively. In this section we examine the nonlinear effect of the uncertain degree of boundary constraint on the homologous mode shape. The following formulation deals with the fluctuation of $[K_a]$ due to L uncertain factors f_i , which stand for the degree of boundary constraint and are supposed to be independent of each other. The fluctuation of a factor f_i is expressed in the (11) with uncertain variable ε_i whose mean value is assumed to be equal to zero,

$$f_i = f_i^* (1 + \varepsilon_i), \quad (11)$$

where the asterisk indicates the mean value hereafter. It is assumed that the fluctuation of $[K_a]$ in the vicinity of the mean values of the uncertain factors can be approximated in the first-order form of (12). This causes a nonlinear effect on the uncertain fluctuation of the eigenvector of the homologous mode shape $\{\phi_a\}$. The first-order approximation

of the eigenvector change is given by (13) below, its sensitivity being evaluated in the similar manner with that for $\{\phi_m^I\}$,

$$[K_a] = [K_a^*] + \sum_{i=1}^L [K_{ai}^I] \varepsilon_i, \quad (12)$$

$$\{\phi_a\} = \{\phi_a^*\} + \sum_{i=1}^L \{\phi_{ai}^I\} \varepsilon_i. \quad (13)$$

Equation (13) enables us to express the first-order approximation of the uncertain deviation vector of the mode shape $\{V\}$ from the homologous mode shape as given below,

$$\{V\} = [C]\{\phi_{ia}\} - \{\phi_{ha}\} = [S]\{\varepsilon\}, \quad (14)$$

where the sensitivity matrix $[S]$ consists of the sensitivities of the eigenvector with respect to the uncertain variables, and $\{\varepsilon\}$ denotes uncertain variable vector.

4.2 Worst case estimated by convex model

Now that the uncertain deviation vector is approximated in the first-order form, an index to indicate the magnitude of the disturbance caused by the uncertainties can be devised somehow. The weighted sum of the absolute value of the aforementioned deviation vector is a candidate for linear definition. Instead of it, we define an index Δ in a similar manner with the definition of standard deviation, namely, the square root of the squared sum of the difference between a vector component and the mean value of the components. The square of the index is summarized in the following form,

$$\Delta^2 = \{\varepsilon\}^T [D] \{\varepsilon\}, \quad (15)$$

where the deviation matrix $[D]$ is derived mainly by taking the product of sensitivity matrix $[S]$ in a proper way, and superscript T indicates transpose of the matrix.

The magnitude of the deviation index Δ is dependent on the uncertain variable vector. The aim of this study is not to discuss how widely the deviation index spreads, but to formulate a convex approach for the estimation of its maximal value, namely, its worst case for a given set of the uncertain variables. In the convex models of uncertainty (Ben-Haim & Elishakoff 1990), we do not define any probabilistic measure for the uncertain variables, but define a domain in which conceivable uncertain variables are confined. In other words, we specify a domain where the uncertain variables are expected to exist, no matter how scarce our knowledge of the uncertain variables. In case this domain is a convex hull, the maximal value of any convex function of the uncertain variables lies on the domain boundary. This property enables us to search the worst case of the deviation index for the convex hull. We deal with the case where the uncertain variables are confined to a convex hull expressed as a hyperellipse in L -dimensional space as follows,

$$e^2 \{\varepsilon\}^T [\Omega] \{\varepsilon\} \leq 1. \quad (16)$$

The convexity of the domain is ensured when the matrix $[\Omega]$ in (16) is positive-definite. The matrix $[\Omega]$ is employed to prescribe the characteristics of the uncertain variables. We call it characteristic matrix. The constant e in the above equation is introduced to

set the expanse of the domain which is to be determined by our knowledge about the uncertainties.

The worst case of the deviation index can be searched easily by the Lagrange multiplier method applied to the following functional in which v denotes the Lagrange multiplier.

$$\Pi = \{\varepsilon\}^T [D] \{\varepsilon\} + v(e^2 \{\varepsilon\}^T [\Omega] \{\varepsilon\} - 1). \quad (17)$$

The stationary conditions of the functional with respect to the uncertain variable vector and Lagrange multiplier give rise to the following.

$$\frac{\partial \Pi}{\partial \{\varepsilon\}^T} = 2([D] + ve^2 [\Omega]) \{\varepsilon\} = \{0\}, \quad (18)$$

$$\frac{\partial \Pi}{\partial v} = e^2 \{\varepsilon\}^T [\Omega] \{\varepsilon\} - 1 = 0. \quad (19)$$

Equation (18) constitutes an eigenvalue problem defined by the matrices $[D]$ and $[\Omega]$ for the eigenvalue $\mu = ve^2$ and (19) is the normalizing condition of the eigenvector. Once the eigenvalue problem of (18) is solved, we obtain the eigenvalue μ and corresponding eigenvector $\{\psi\}$, which indicate the worst case of the deviation index as given below,

$$\Delta^2 = \{\psi\}^T [D] \{\psi\} = ve^2 \{\psi\}^T [\Omega] \{\psi\} = -v = \mu/e^2, \quad (20)$$

and the set of the uncertain variables, from which the worst case arises. It is needless to say that the maximal eigenvalue is to be computed in the L th mode in the eigenvalue analysis. Equation (20) means that the eigenvalue μ represents the essential sensitivity of the deviation index with respect to the magnitude of the uncertain variables.

5. Numerical example

5.1 Homology design for mode shape

The formulations of the homology design and worst case search are examined through numerical example concerned with out-of-plane vibration of a planar lattice frame simply-supported at four points as shown in figure 1. The lattice is discretized into finite elements. Each section is represented by a bending finite element with torsion. The cross-section of all elements is circular and 50 mm in diameter in the initial baseline design. The Young's modulus, modulus of rigidity, Poisson's ratio and mass density of

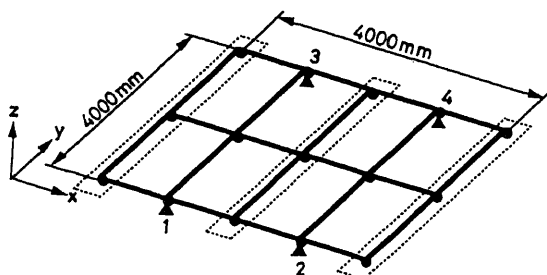


Figure 1. Planar lattice frame simply-supported at four points.

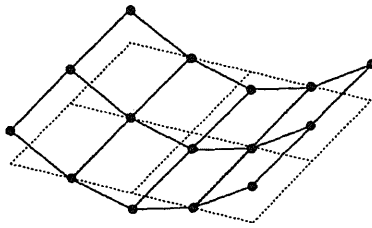


Figure 2. First mode shape of lattice of initial design.

the material are set equal to 70.0 GPa, 26.9 GPa, 0.3 and $3.0 \times 10^3 \text{ kg/m}^3$, respectively. The geometrical boundary conditions at the supports are represented by virtual springs attached to the nodes, whose spring constant is expressed as sEI/l^3 for the deflection constraint, and the one for the rotation constraint as cEI/l , respectively. In these expression, EI and l denote the flexural rigidity and section length of 1,000 mm of the beam element in the initial design, respectively. The case of $s = c = 0$ indicates free support, while $s = c = \infty$ indicates fixed support. Simply-supported condition in the finite element analysis can be expressed by $s > 50.0$ and $c = 0$. The natural frequency of the first mode is 4.571 Hz for the initial design for nearly simply-supported conditions with the inputs of $s = 100.0$ and $c = 0.1$, and the saddle-shape mode is shown in figure 2.

Suppose that an optical system is to be mounted on the central rib encircled by a broken line in figure 1, and the deflection arising from the saddle-shape mode should be eliminated to keep accurate collimation of the optical axis. This elimination can be achieved by homology design to set a homologous mode shape of the three ribs in the y -direction straight and parallel to the undeformed state.

Figure 3 illustrates the mode shape obtained by the homology design, in which 22 design variables are assigned to the diameter of all the section members. The baseline design has to be renewed three times until the three ribs are made sufficiently straight. The eigenvector is normalized as $\{\phi\}^T \{\phi\} = 1$. In carrying out the design change, the Moore–Penrose generalized inverse $[A]^-$ is calculated on the basis of the eigenvalue analysis related to $[A][A]^T$ (Rao & Mitra 1971). It is shown in the figure that the saddle-shape mode is eliminated, and the lattice is deformed not like a plate but like a beam, when viewed in the y -direction, as is aimed at. Figure 4 depicts the section diameter determined after the homology design is achieved. The natural frequency is decreased to 1.557 Hz. A simple way to keep the ribs straight is to make the flexural rigidity of the ribs enormously large, and this inevitably causes considerable increase in the lattice weight. On the other hand, the homology design results in weight increase by only 76.2% of the initial weight. This implies that homology design is capable of realizing the objective mode shape with slight increase in structure weight.

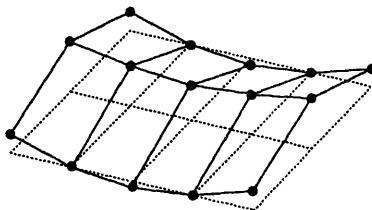


Figure 3. First mode shape obtained by homology design.

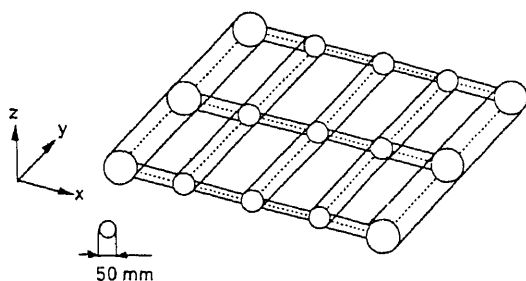


Figure 4. Changes in diameter required for homology design.

5.2 Convex analysis of disturbed mode shape

The nonlinear effect of the boundary constraint coefficient for rotation c on the first natural frequency is depicted in figure 5, for which the value s is kept equal to 100.0. The dotted line in the figure indicates the natural frequency calculated by $s = 100.0$ and $c = 0.0$. The uncertain fluctuation of the boundary conditions of nearly simple support is simulated by taking the coefficient c as an uncertain factor, and the worst case of the disturbed homologous mode shape can be estimated by the formulation given in § 4.2.

Table 1 summarizes the result of the worst case estimation by means of the convex approach. The mean values of the fluctuating coefficients c for the four supports are set equal to 0.1, the deterministic value s being kept constant at 100.0. These inputs enable us to evaluate the deviation matrix $[D]$ duly. The fluctuation of c is assumed to arise from a common cause for all the four supports and is uncorrelated with the other. Then we assume that the characteristic matrix $[\Omega]$ is given in the form of an identity matrix. Solving the eigenvalue problem of (18), we obtain the value of μ/e^2 as is listed in the second column of table 1 for $e = 1.0$ together with the corresponding eigenvector components, which are so normalized that the norm is equal to unity, in the fourth through seventh columns. The worst case estimated by the convex approach is given the maximal eigenvalue of 0.1633×10^{-2} (deviation index equal to 0.04041) with regard to $e = 1.0$. On the other hand, the value of Δ^2 calculated from the disturbed mode shape for $\varepsilon_1 = 0.4877$, $\varepsilon_1 = 0.5036$ and so on for $e = 1.0$ is 0.1711×10^{-2} as is listed in the third column. The agreement between the two values proves that the estimation by the convex approach based on the first-order approximation is satisfactory even for rather

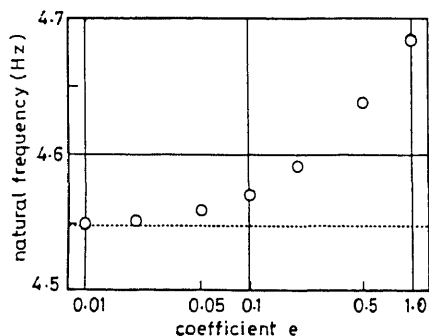


Figure 5. Nonlinear increase of natural frequency with rotation constraint.

Table 1. Worst case estimated by convex model.

Mode	$\mu/e^2 (\times 10^{-2})$	$\Delta^2 (\times 10^{-2})$	ε_1	ε_2	ε_3	ε_4
1	0.1633	0.1711	0.4877	0.5036	-0.5097	-0.4987
2	0.0673	0.0828	-0.4783	0.4720	0.5223	-0.5249
3	0.0008	0.0054	-0.5165	-0.4920	-0.5107	-0.4800
4	0.0000	0.0048	0.5163	-0.5305	0.4545	-0.4954

large fluctuation of $e = 1.0$. When we know the expanse of the ellipse is less, for example $e = 2.0$, we can estimate the deviation index as equal to $0.02021 = 0.04041/2.0$.

6. Concluding remarks

Success of homology design is decided by adequate setting of the initial design, judicious choice of the design parameters and proper formulation. The validity of the proposed methodology for homology design and estimation of the worst case of the disturbed mode shape is demonstrated by the numerical example concerned with a single mode shape of the out-of-plane vibration of a planar frame for which the homology design is possible. The possibility of the homology design which controls the multiple mode shapes should be examined, and a pertinent formulation would be demanded in the future when homology design in the field of forced vibration and random vibration is desired. The convex model of uncertainties seems to be useful as a device to formulate robust homology design in the future because the model affords us to estimate the worst case in a straightforward way. It is desired to establish the means to form the characteristic matrix methodically and realistically based on the knowledge about uncertainties such as variance and correlation.

List of symbols

$[A]$	coefficient matrix;
$\{b\}$	calculated vector;
$[C]$	matrix representing homologous mode constraint;
c	coefficient for rotation constraint;
$[D]$	deviation matrix;
EI	flexural rigidity of beam element;
e	coefficient indicating expanse of uncertainty domain;
f_i	uncertainty factor;
$\{h\}$	arbitrary vector;
$[I]$	identity matrix;
$[K]$	stiffness matrix;
l	length of beam element;
$[M]$	mass matrix;
p_m	design parameter;
$[S]$	sensitivity matrix;
s	coefficient for deflection constraint;
$\{\alpha\}$	design variables vector;

α_m	design variable;
ε_n	uncertainty variable;
λ	eigenvalue;
μ	eigenvalue (worst case);
v	Lagrange multiplier;
$\{\phi\}$	eigenvector;
ψ	eigenvector (worst case);
$[\Omega]$	characteristic matrix.

Subscripts

$[a]$	achieved homology design;
h	homologous;
i	independent;
m	m th variable;

Superscripts

I	first-order;
$(-)$	Moore–Penrose generalized inverse;
$(\overline{-})$	(overbar) current baseline design;
$(*)$	indicating mean value;

References

- Ben-Haim Y, Elishakoff I 1990 *Convex models of uncertainty in applied mechanics* (Amsterdam: Elsevier) chap. 2
- Fox R L, Kapoor M P 1968 Rate of change of eigenvalues and eigenvectors. *AIAA J.* 6: 2426–2429
- Hangai Y, Guan F I 1989 Structural shape analysis with the constraint condition of homologous deformation. *J. Struct. Constr. Eng., Trans. Arch. Inst. Jpn.* 405: 97–102 (in Japanese)
- Hoerner S 1967 Homologous deformation of tilttable telescope. *Proc. Am. Soc. Civ. Eng.* 93 (ST3): 461–485
- Morimoto M, Kaifu N, Takizawa Y, Aoki K, Sakakibara O 1982 Homology design of large antenna. Mitsubishi Electric Corp., Technical Report, Vol. 56, No. 7: 495–502 (in Japanese)
- Rao C R, Mitra S K 1971 *Generalized inverse of matrices and its applications* (New York: John Wiley & Sons) chap. 3
- Yoshikawa N, Nakagiri S 1993 Homology design of frame structure by finite element method. *Theoretical and Applied Mechanics, Proc. the 42nd Japan National Congress for Applied Mechanics* (eds) M Hori, S Kobayashi (Tokyo: University Press) vol. 42, pp. 43–51

Effects of distributed delays on the stability of structures under seismic excitation and multiplicative noise

KARMESHU¹ and HENRI SCHURZ²

¹School of Computer and Systems Sciences, Jawaharlal Nehru University, New Delhi 110 067, India

²Institute of Applied Analysis and Stochastics, Mohrenstr. 39, Berlin 10117, Germany

Abstract. The effect of seismic excitation and multiplicative noise (arising from environmental fluctuations) on the stability of a single degree of freedom system with distributed delays are investigated. The system is modelled in the form of a stochastic integro-differential equation interpreted in Stratonovich sense. Both deterministic stability and stochastic moment stability are examined for the system in the absence of seismic excitation. The model is also extended to incorporate effects of symmetric nonlinearity. The simulation of stochastic linear and nonlinear systems is carried out by resorting to numerical techniques for the solution of stochastic differential equations.

Keywords. Stochastic stability; weak and strong time delay; random oscillations; seismic excitation; stochastic differential equations; numerical methods; implicit Euler, Mil'shtein and balanced methods.

1. Introduction

The technique of vibration suppression by active control of civil engineering structures has drawn considerable attention in recent years (Abdel-Rohman 1987; Chung *et al* 1988; Pu & Kelly 1990; Yang *et al* 1990; Agrawal *et al* 1993; Zhang *et al* 1993). The purpose of applying the control is to reduce the damage caused by unexpected disturbances like earthquakes, wind and dynamic excitations. The main emphasis of the work done on the control design concerns instability of structures due to unavoidable time delay, unless it could be compensated properly, e.g. see Agrawal *et al* (1993). Time delay arises on account of a number of factors such as the time taken in data acquisition from sensors located at different parts of the structure or unsynchronized application of control forces. Even if the time delay is negligible, the structure could be destabilized due to excitations by the control force.

A number of attempts have been made to treat the system as a linear optimal feedback control problem. These studies have been restricted to SDOF (single-degree of freedom) and n -DOF controlled structures with constant time delay described by

linear differential equations. An important aspect which has been generally ignored in modelling of such systems is the neglect of stochastic effects. It is well-known that parametric noise can destabilize a linear system which is otherwise stable, see Kozin (1969). Arnold (1974), Karmeshu & Bansal (1975), Karmeshu (1976) or Ariaratnam & Srikantiah (1978). Moreover, the delay magnitude varies from one sensor to another and from one actuator to another, as already mentioned in Abdel Rohman (1987). It may be useful to examine the effect of continuous and nonconstant time delay instead of fixed time lags.

The object of this paper is to investigate the effects of seismic excitations and multiplicative noise on the stability of an SDOF system with distributed delays. The paper consists of six sections. Section 2 contains the formulation of the model. The resulting stochastic differential equation (SDE) with multiplicative noise is interpreted in the Stratonovich sense. Section 3 is concerned with the stability analysis of the deterministic linear system. Sections 4 and 5 are devoted to the stochastic analysis of the linear system with weak and strong delay. Mean square stability of the system without seismic excitation is also investigated. Section 6 deals with the numerical simulation for transient solution of the linear stochastic model. Effects of nonlinearity in the stochastic SDOF system are contained in § 7. Finally, the last section summarizes the observed effects and ends with concluding remarks. In the appendices numerical methods for the solution of SDEs and results on mean square stability used for robust and reliable simulations have been outlined.

2. Formulation of the models with distributed delays

The model considered here is based on distributed delays instead of fixed discrete time delay. The displacement $x(t)$ of an SDOF structure follows the integro-differential equation

$$\ddot{x} + \omega^2 x + 2\zeta\omega\dot{x} + g_1 \int_0^t K_1(t-s)x(s)ds + g_2 \int_0^t K_2(t-s)\dot{x}(s)ds = 0, \quad (1)$$

where ω, ζ, g_1, g_2 are nonnegative real parameters. The parameters g_1 and g_2 represent feedback gains of the displacement and velocity of the oscillations, whereas ω and ζ natural frequency and damping ratio coefficients respectively. $K_1(t)$ and $K_2(t)$ are absolutely integrable weight functions specifying the distributed delays. For simplicity, it is also supposed that these functions are normalized, i.e.

$$\int_0^\infty |K_1(u)|du = 1 \text{ and } \int_0^\infty |K_2(u)|du = 1. \quad (2)$$

Equation (1) can be interpreted as a distributed delay version of the SDOF system with discrete delay considered by Agrawal *et al* (1993).

When the system is subjected to seismic excitations and environmental fluctuations, (1) modifies to the form

$$\ddot{x} + \omega^2 x + 2\zeta\omega\dot{x} + g_1 \int_0^t K_1(t-s)x(s)ds + g_2 \int_0^t K_2(t-s)\dot{x}(s)ds = F(x, \dot{x}, t),$$

where $F(x, \dot{x}, t)$ reflects stochastic perturbation forces which can be decomposed as

$$F(x, \dot{x}, t) = \sigma_1 x(t) \xi_1(t) + \sigma_2 \dot{x}(t) \xi_2(t) + \sigma_3 \ddot{z}(t). \quad (4)$$

The first two terms on the right side of (4) correspond to stochastic environmental perturbations, and the last term represents a ground level acceleration corresponding to seismic excitations. The random environmental perturbations per unit displacement and per unit velocity are modelled by the independent white noise processes $\xi_1(t)$ and $\xi_2(t)$. σ_i , ($i = 1, 2$) give the magnitude of the fluctuations incorporated in (4). The first two terms express state-dependent noise. Such terms are called multiplicative noise.

Several attempts to model seismic excitations have been made, e.g. Shinozuka (1967, 1972) or Kozin (1977). Following Bolotin (1960), seismic excitation can be modelled as the nonstationary process

$$\ddot{z}(t) = I(t) \xi_3(t), \quad (5)$$

where $\xi_3(t)$ is a white noise process being independent of $\xi_1(t)$ and $\xi_2(t)$. $I(t)$ is supposed to be of the form

$$I(t) = \exp(-\alpha t) - \exp(-\beta t), \quad 0 < \alpha < \beta, \quad (6)$$

with its parameters α and β .

The resulting integro-differential equation (3) can be interpreted in many different ways due to the variety of stochastic integration calculus. Two major interpretations have crystallized, namely Itô and Stratonovich calculus. These two are also related to each other in the sense that the results of one of them can be obtained from the other via a transformation formula, see e.g. Arnold (1974). Here we have adopted the Stratonovich interpretation as it is preferable for modelling physical phenomena, cf. Wong & Zakai (1965). Thus, from now on we make use of the terms 'Stratonovich interpretation' and 'Itô prescription'.

Additionally, when effects of symmetric nonlinearities are to be incorporated, see Moon (1987), the equation of motion takes the form

$$\ddot{x} + \omega^2 x + 2\zeta\omega\dot{x} + g_1 \int_0^t K_1(t-s)x(s)ds + g_2 \int_0^t K_2(t-s)\dot{x}(s)ds + \gamma x^3 = F(x, \dot{x}, t). \quad (7)$$

Note that in the absence of external excitations, displacement and velocity feedback gains, (7) has the form of the well-known Duffing equation, cf. Iyengar (1986), Moon (1987). To analyse the model we need specific forms of the weight functions $K_1(t)$ and $K_2(t)$. For the sake of simplicity we shall especially examine the case $K_1(t) = K_2(t) = K(t)$ in this paper. The main attention is drawn to the two forms

$$K(t) = v \exp(-vt) \text{ and} \quad (8)$$

$$K(t) = v^2 t \exp(-vt). \quad (9)$$

In consonance with similar approaches in population ecology, e.g. MacDonald (1978), the form (8) is termed as 'weak delay' and (9) as 'strong delay'. At first we consider the case incorporating weak delay.

Weak delay: Writing $x_1(t)$ for the displacement $x(t)$ as well as $x_2(t)$ for the velocity $\dot{x}(t)$

of the vibration, system (7) is equivalently described by the set

$$\begin{aligned}\dot{x}_1 &= x_2, \\ \dot{x}_2 &= -(\omega^2 x_1 + 2\zeta\omega x_2 + g_1 x_3 + g_2 x_4 + \gamma x_1^3) + \sigma_1 x_1 \xi_1(t) + \sigma_2 x_2 \xi_2(t) \\ &\quad + \sigma_3 I(t) \xi_3(t), \\ \dot{x}_3 &= -vx_3 + vx_1, \\ \dot{x}_4 &= -vx_4 + vx_2.\end{aligned}\tag{10}$$

Thus, the stochastic integro-differential equation (7) has been replaced by a set of four coupled differential equations.

Strong delay: In a similar way we now introduce the system with strong delay. Using the symbols $x_1(t) = x(t)$ and $x_2(t) = \dot{x}(t)$, the stochastic integro-differential equation can be rewritten as

$$\begin{aligned}\dot{x}_1 &= x_2, \\ \dot{x}_2 &= -(\omega^2 x_1 + 2\zeta\omega x_2 + g_1 x_3 + g_2 x_5 + \gamma x_1^3) + \sigma_1 x_1 \xi_1(t) + \sigma_2 x_2 \xi_2(t) \\ &\quad + \sigma_3 I(t) \xi_3(t), \\ \dot{x}_3 &= -vx_3 + vx_4, \\ \dot{x}_4 &= -vx_4 + vx_1, \\ \dot{x}_5 &= -vx_5 + vx_6, \\ \dot{x}_6 &= -vx_6 + vx_2.\end{aligned}\tag{11}$$

Thus, the original systems with both weak and strong delay have artificially blown up to very specific sets of coupled stochastic differential equations without time delay. This appearance is due to the special kernel structure of the distributed lag.

3. Stability analysis of the deterministic linear model

When stochastic perturbation forces as well as cubic nonlinearity are absent the equation of motion simplifies to (1). Its Laplace transformation gives the characteristic equation

$$H(\Delta) = \Delta^2 + \omega^2 + 2\zeta\omega\Delta + g_1 \bar{K}_1(\Delta) + g_2 \Delta \bar{K}_2(\Delta) = 0,\tag{12}$$

where $\bar{K}_i(\Delta)$ is the Laplace transform of $K_i(t)$ ($i = 1, 2$). The stability of the linear system described by (1) requires that all roots of (12) have negative real parts. Assume that $K_1(t) = K_2(t) = K(t)$.

Now we examine the two cases corresponding to weak and strong delay.

Weak delay: In the case $K(t) = v \exp(-vt)$, (12) becomes

$$(\Delta + v)(\Delta^2 + 2\zeta\omega\Delta + \omega^2) + v(g_2\Delta + g_1) = 0.\tag{13}$$

Applying Routh-Hurwitz criterion, e.g. see May (1974), (13) possesses roots with negative real parts iff $2\zeta\omega + v > 0$, $v(\omega^2 + g_1) > 0$ and

$$(2\zeta\omega + v)(2\zeta\omega + g_2) + 2(\zeta\omega^3/v) > g_1.\tag{14}$$

Strong delay: Suppose $K(t) = v^2 t \exp(-vt)$. Then (12) reduces to

$$(\Delta^2 + 2v\Delta + v^2)(\Delta^2 + 2\zeta\omega\Delta + \omega^2) + v^2(g_2\Delta + g_1) = 0. \quad (15)$$

Proceeding as above, the stability conditions are $\zeta\omega + v > 0$,

$$v^2(\omega^2 + g_1) > 0 \quad \text{and} \quad \frac{\omega^2}{v} + 4\zeta\omega + v > \frac{\eta^2 + \omega^2 + g_1}{\eta}, \quad (16)$$

where

$$\eta = \frac{2\omega^2 + 2v\zeta\omega + g_2 v}{2(\zeta\omega + v)}.$$

A cursory comparison of inequalities (14) and (16) shows that stability conditions in case of weak delay are more likely to be satisfied than those for strong delay.

4. Stochastic analysis of the linear system with weak delay

While neglecting effects of nonlinearity ($v = 0$), the system under seismic excitation and environmental fluctuations is governed by the set (11) of linear SDEs. Let the triplet $(W^1(t), W^2(t), W^3(t))$ represent three mutually independent Wiener processes driving the considered dynamics. Then the system governing the stochastic process $X(t) = (x_1(t), \dots, x_d(t))^T$ with $d = 4$ can be written in the form

$$dX(t) = \underline{A}X(t)dt + B^1 X(t) \circ dW^1(t) + B^2 X(t) \circ dW^2(t) + C dW^3(t), \quad (17)$$

where \underline{A}, B^1, B^2 are the real $d \times d$ -matrices, and C the d -dimensional real vector corresponding to system (11). Here $()^T$ denotes the transpose of the inscribed vector or matrix. Equation (17) is interpreted in Stratonovich sense.

For the purpose of more convenient mathematical handling, we transform system (17) to its equivalent Itô form (cf. Arnold 1974; Kloeden & Platen 1992),

$$dX(t) = AX(t)dt + B^1 X(t)dW^1(t) + B^2 X(t)dW^2(t) + C dW^3(t), \quad (18)$$

It turns out that the only difference between the matrices \underline{A} and A rests with the element $a_{2,2} = \underline{a}_{2,2} + \frac{1}{2}\sigma_2^2$. The system matrices of the drift and diffusion parts have the following form

$$A = (a_{i,j})_{i,j=1\dots 4} = \begin{pmatrix} 0 & 1 & 0 & 0 \\ -\omega^2 & -2\zeta\omega + \frac{1}{2}\sigma_2^2 & -g_1 & -g_2 \\ v & 0 & -v & 0 \\ 0 & v & 0 & -v \end{pmatrix},$$

$$B^1 = (b_{i,j}^1)_{i,j=1\dots 4} \quad \text{with} \quad b_{i,j}^1 = \begin{cases} \sigma_1 & \text{if } i=2, j=1 \\ 0 & \text{else} \end{cases}$$

$$B^2 = (b_{i,j}^2)_{i,j=1\dots 4} \quad \text{with} \quad b_{i,j}^2 = \begin{cases} \sigma_2 & \text{if } i=j=2 \\ 0 & \text{else} \end{cases}$$

and

$$C = (0 \ \sigma_3 I(t) \ 0 \ 0)^T. \quad (19)$$

The solution process $X(t)$ is a diffusion process, and accordingly a detailed description of the probabilistic behaviour of the model can be obtained in terms of the probability density $p = p(x_1, x_2, x_3, x_4; t)$ given by the Fokker-Planck equation (FPE). The FPE corresponding to (18) has the form

$$\begin{aligned} \frac{\partial p}{\partial t} = & -\frac{\partial}{\partial x_1}[x_2 p] - \frac{\partial}{\partial x_2} \left[\left\{ -\omega^2 x_1 + \left(\frac{1}{2} \sigma_2^2 - 2\zeta\omega \right) x_2 - g_1 x_3 - g_2 x_4 \right\} p \right] \\ & - \frac{\partial}{\partial x_3} [v(x_1 - x_3)p] - \frac{\partial}{\partial x_4} [v(x_2 - x_4)p] \\ & + \frac{1}{2} \frac{\partial^2}{\partial x_2^2} [(\sigma_1^2 x_1^2 + \sigma_2^2 x_2^2 + \sigma_3^2 I^2(t))p]. \end{aligned} \quad (20)$$

The complete solution of this FPE being subject to appropriate boundary conditions seems to be impossible. Accordingly, one has to be content with the evolution of moments of the process $X(t)$. It is pertinent to emphasize that in the presence of seismic excitation the transient solution of process $X(t)$ is very crucial. However, before embarking on a detailed numerical analysis of the stochastic system, we first study the stability behaviour of the system in the moment sense in the absence of seismic excitation.

Moment stability of the system without seismic excitation. While examining the asymptotical behaviour the term of seismic excitation can be neglected. Modelling with the approach of Bolotin (1960) this term is damped out exponentially fast, and hence it plays no role for the long-term behaviour of the system.

When seismic excitation is absent, SDE (18) reduces to

$$dX(t) = AX(t)dt + B^1 X(t)dW^1(t) + B^2 X(t)dW^2(t). \quad (21)$$

Taking expectation, the system of first moments $Y^i(t) = E X^i(t)$ follows the equation

$$dY(t) = dEX(t) = AEX(t)dt = AY(t)dt. \quad (22)$$

Obviously, system (21) is asymptotically stable in the mean sense iff the real parts of all eigenvalues of the matrix A are negative. The characteristic polynomial c of A expanded in z is

$$\begin{aligned} c_A(z) &= \det(A - zU_4) \\ &= (z + v)(z^3 + (2\zeta\omega - \frac{1}{2}\sigma_2^2 + v)z^2 + ((g_2 + 2\zeta\omega - \frac{1}{2}\sigma_2^2)v + \omega^2)z \\ &\quad + v(\omega^2 + g_1)), \end{aligned} \quad (23)$$

where U_4 represents the unit matrix in $\mathbb{R}^{4 \times 4}$.

Using Routh-Hurwitz criterion, we find that the system has stable first moments if

$$2\zeta\omega + v > \frac{1}{2}\sigma_2^2$$

and

$$(2\zeta\omega + v - \frac{1}{2}\sigma_2^2)(\omega^2 + 2\zeta\omega v + g_2 v - \frac{1}{2}\sigma_2^2 v) > (\omega^2 + g_1)v. \quad (24)$$

It may be noted that multiplicative fluctuations characterizing the displacement have no influence on the stability of first moments. On the other hand multiplicative fluctuations affecting random velocity make the conditions for stability more stringent than those for the deterministic case, i.e. when $\sigma_2 = 0$ [cf. (14)].

The analysis of evolution and asymptotic behaviour of the second moments are more difficult and tiring than the above for the first moments. For this purpose we follow Arnold (1974). One obtains

$$\dot{Q}(t) = AQ + QA^T + B^1 Q B^{1T} + B^2 Q B^{2T}, \quad (25)$$

for the second moment matrix $Q(t) = (EX^1(t)X^j(t))_{i,j=1\dots 4}$. Analysing the deterministic system (25) one gains the desired assertions for the stability of SDE (21) in mean square sense. We introduce the notations

$$\begin{aligned} p_1 &= q_{1,1}, & p_2 &= q_{1,2}, & p_3 &= q_{1,3}, & p_4 &= q_{1,4}, & p_5 &= q_{2,2}, \\ p_6 &= q_{2,3}, & p_7 &= q_{2,4}, & p_8 &= q_{3,3}, & p_9 &= q_{3,4} & \text{and} & p_{10} &= q_{4,4}. \end{aligned}$$

With this notation one finds the vector differential equation equivalent to (25)

$$\dot{p} = Sp, \quad (26)$$

where $p(t)$ is the corresponding $d'(d' + 1)/2 = 10$ - dimensional vector of second moments. The elements of matrix S are received from (25) using the symmetry of the second moment matrix $Q(t)$. For the decision on mean square stability one encounters the characteristic polynomial $c_s(z) = \det(S - zU_{10})$ of degree 10 where U_{10} represents the unit matrix in $\mathbb{R}^{10 \times 10}$. An application of computer packages like MAPLE for symbolic computations provides unwieldy expressions running into several pages. Thus there is no hope of getting an exact analysis of roots of the polynomial as functions of system parameters. Therefore one has to resort to numerical computations for specific parameters, as discussed in § 6.

5. Stability analysis of the linear system with strong delay

Proceeding on similar lines, one can carry out moment stability analysis of the system with strong delay. The system is governed by a set of linear SDEs (13) while assuming $\gamma = 0 = \sigma_3$. After rewriting the system in its equivalent Itô form one obtains the drift matrix

$$A = (a_{i,j})_{i,j=1\dots 6} = \begin{pmatrix} 0 & 1 & 0 & 0 & 0 & 0 \\ -\omega^2 & -2\zeta\omega + \frac{1}{2}\sigma_2^2 & -g_1 & 0 & -g_2 & 0 \\ 0 & 0 & -v & v & 0 & 0 \\ v & 0 & 0 & -v & 0 & 0 \\ 0 & 0 & 0 & 0 & -v & v \\ 0 & v & 0 & 0 & 0 & -v \end{pmatrix}, \quad (27)$$

which establishes the qualitative mean behaviour of the linear system. Its characteristic polynomial is

$$\begin{aligned} c_A(z) &= \det(A - zU_6) \\ &= (z + v)^2((z + v)^2(z^2 - z(-2\zeta\omega + \frac{1}{2}\sigma_2^2) + \omega^2) + zv^2g_2 + v^2g_1). \end{aligned} \quad (28)$$

This can be rewritten as

$$c_A(z) = (z + v)^2(z_4 + 2b_1z^3 + vb_2z^2 + 2vb_3z + b_4),$$

where

$$b_1 = \zeta\omega + \nu - \sigma_2^2/4, \quad (29)$$

$$b_2 = (\omega^2/\nu) + 4\zeta\omega + \nu - \sigma_2^2, \quad (30)$$

$$b_3 = \omega^2 + \nu\zeta\omega + \frac{1}{2}g_2\nu - \frac{1}{4}\sigma_2^2\nu \quad (31)$$

and

$$b_4 = \nu^2(\omega^2 + g_1). \quad (32)$$

Necessary and sufficient conditions for negative real parts of the roots of polynomial (28) are

$$b_1 > 0, \quad b_3 > 0, \quad b_4 > 0, \quad b_2 > (b_3/b_1) + (b_1/b_3)(\omega^2 + g_1), \quad (33)$$

see May (1974). We note that in the presence of velocity-dependent noise (i.e. $\sigma_2 > 0$) conditions (29) and (30) become more stringent.

One can obtain the differential matrix equation for the second moment matrix by a procedure similar to the previous section. However, in order to derive conditions for mean square stability of the system, one has to resort to numerical computations, which we omit here.

6. Numerical simulation for the linear model with weak delay

In the presence of seismic excitation and environmental fluctuations the knowledge about the transient solution of the vector process $X(t)$ is of paramount importance. For carrying out transient analysis we have to simulate sample paths of the system. A brief outline of the numerical procedure is given in appendices A and B. It would be of great interest to have an estimate of the frequency with which the sample paths cross the boundaries of the deterministic solution of the system. It would be equally interesting to study the duration time for which the sample paths remain outside the boundaries or above some critical values. In view of these goals we resort to the numerical solution of stochastic systems.

Another important aspect relates to the numerical computation and visualization of the evolution of first and second moments of variables of interest. In linear systems we have two alternatives, namely the direct statistical estimation of the moments from the stochastic system or the solution of the corresponding ordinary differential equation system. Of course, in linear models the latter could be without additive noise. However, to incorporate seismic excitations in the nonlinear model we make use of numerical techniques and statistical estimation procedures.

6.1 Numerical simulation of sample paths and first moments

It is recommended to implement the implicit Euler method with drift implicitness 0.5 or a balanced method with simple correction by a scalar factor depending locally on the current Wiener process increments. This enables us to integrate fairly accurate stochastically stiff systems and guarantees numerical stability of moments, particularly mean square stability, cf. Schurz (1993). These procedures provide us with very robust approximate solutions.

For gaining insight into the evolution of components of the system without seismic excitation, we resort to the implicit Euler method with implicitness $\rho = 0.5$ and

equidistant time step size $\Delta = t_{n+1} - t_n = 0.001$. This method employs the scheme

$$Y_{n+1} = (U - \rho A \Delta)^{-1} (U + (1 - \rho) A \Delta + B^1 \Delta W_n^1 + B^2 \Delta W_n^2) Y_n \quad (34)$$

$$(n = 0, 1, 2, \dots)$$

starting with $Y_0 = X(0)$ at time t_0 for the linear system without additive noise. $\Delta W_n = W(t_{n+1}) - W(t_n)$ denotes the current Wiener process increment, whereas Y_{n+1} gives the value of the approximate solution at time $t_{n+1} = t_0 + n\Delta$. Once again U represents the unit matrix. The parameter values for the simulation of the model with weak delay are

$$X(0) = (1, 0, 0, 0); \quad \omega = 5; \quad \zeta = 0.1514; \quad g_1 = 11.85; \quad g_2 = 4.87; \quad (35)$$

$$v = 0.1; \quad \sigma_1 = 5; \quad \sigma_2 = 1.4 \quad \text{and} \quad \sigma_3 = 0.$$

Figure 1 visualizes a plot of the components of the random oscillator with weak delay. Obviously, the components are more or less rapidly damped out. For the corresponding first moments one observes the same pattern. The damping seems to be slightly slower than that in the deterministic model, and from a critical value of σ_2 onwards the damping gives place to instability (not due to numerics!) with increasing amplitudes (amplification). Furthermore, for this parameter choice (35) we know that the linear homogeneous equation has a mean square stable, and hence a mean stable equilibrium solution (We checked it with MAPLE). This fact is demonstrated in figure 2.

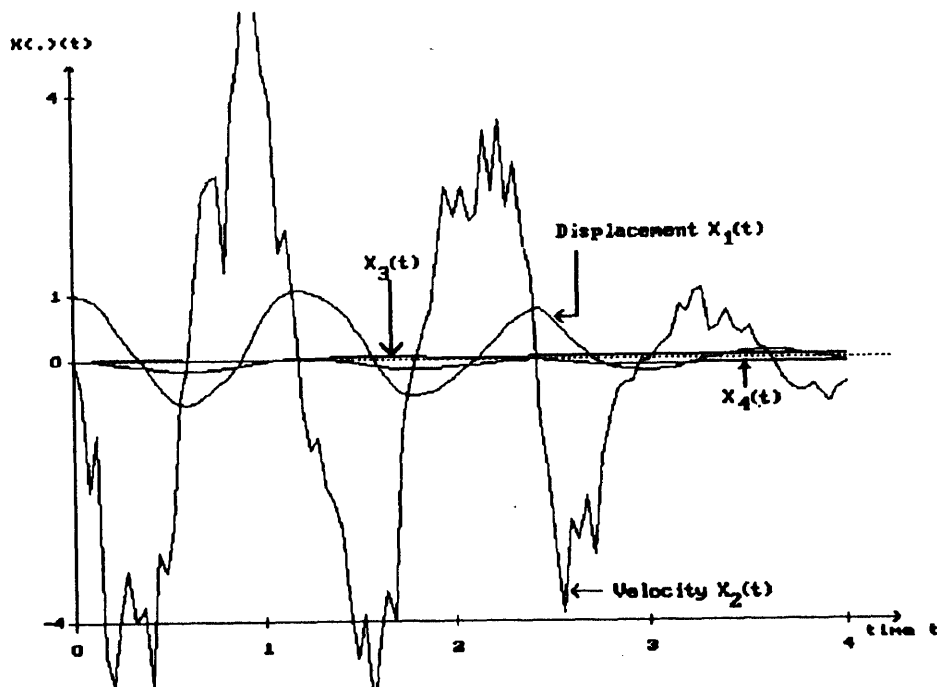


Figure 1. Pathwise evolution of components without seismic excitation.

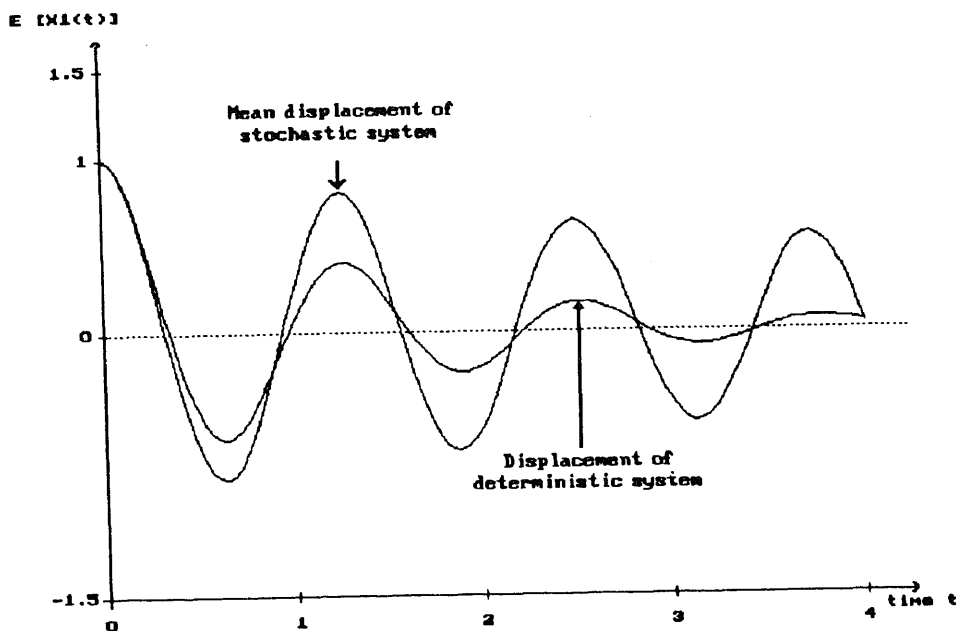


Figure 2. Comparison of displacements without seismic excitation.

The plot of this figure compares the mean displacement of the stochastic system with the displacement of the deterministic one. In figure 2 it is shown that an amplification in the mean sense is caused by multiplicative noise forces. The value of the parameter σ_2 plays the decisive role in establishing this amplification process. However, the phase of the mean oscillations does not seem to change under these noise forces. For producing figure 2 we have applied the same Euler method (34) with implicitness and step size as in figure 1.

Finally, we have carried out some simulations for the system with weak delay in the presence of seismic excitation using the same setup (35). The new parameters are

$$\sigma_3 = 0.9; \quad \alpha = 1 \quad \text{and} \quad \beta = 2.$$

For further simplification, we make use of balanced methods circumventing the costly inversion of correction matrices in the implicit Euler methods. Balanced methods introduced by Mil'shtein *et al* (1992) give an alternative means of controlling the numerical moment behaviour (for details see appendix). We suggest the balanced method

$$Y_{n+1} = c_n^{-1} \cdot ((Uc_n + A\Delta + B^1 \Delta W_n^1 + B^2 \Delta W_n^2) Y_n + C \Delta W_n^3), \quad (36)$$

$$(n = 0, 1, 2, \dots)$$

for the numerical solution of the linear system. Its correction factor c_n is simply a real number and chosen with

$$c_n = 1 + \|A\| \Delta + (1 + \|B^1\|^2) |\Delta W_n^1| + (1 + \|B^2\|^2) |\Delta W_n^2|.$$

Consequently, this numerical method simply represents a locally and appropriately corrected Euler method. Furthermore, it gives more numerical stability (visible with large step sizes and other parameter choices).

Results concerning the temporal evolution of estimated first moment of the displacement are shown in figure 3, along with the corresponding deterministic evolution. The presence of seismic excitation leads to a shift in the phase of the stochastic displacement compared with the deterministic one, as seen in this figure. The results depicted in the figures above can be considered as reliable. For confirming the presented results, we repeated the numerical integration and estimation with smaller step sizes several times.

Corresponding numerical studies could also be executed on computers for the model with strong delay, but this is omitted as the computational effort increases considerably. However, comparison studies between models with weak and strong delay would be of great interest.

6.2 Numerical simulation of exit frequencies

In order to answer the questions pertaining to the frequency with which the sample paths cross the boundaries of the deterministic solution and the duration of remaining outside the boundaries, we make use of sample pathwise simulation of the linear system with weak delay and seismic excitation. For this purpose 1000 simulations are carried out. Figure 4 shows the proportion of sample paths of the displacement remaining outside the interval $[-0.5, +0.5]$ for increasing time t .

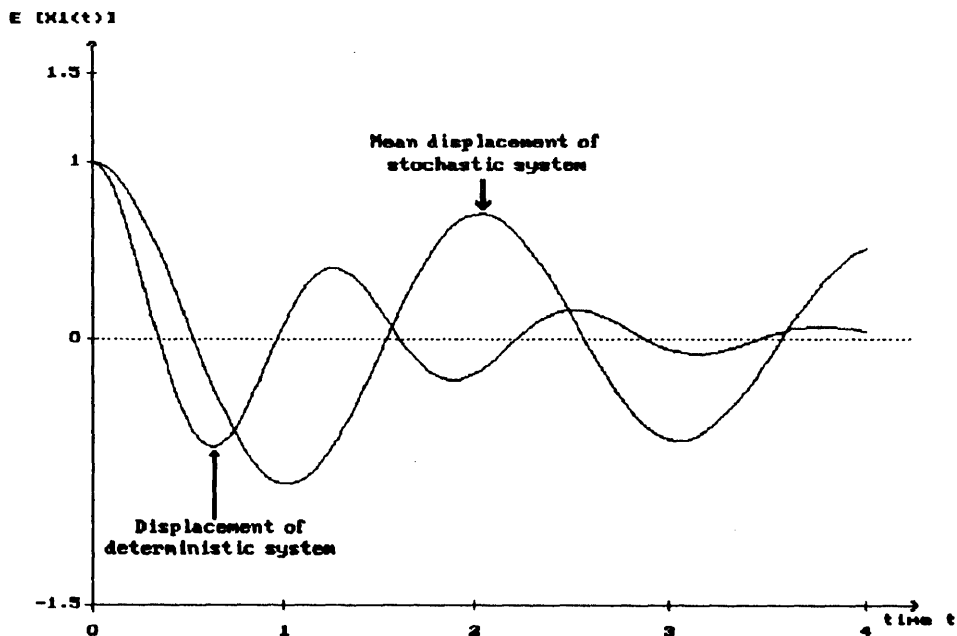


Figure 3. Evolution of deterministic and mean displacement with seismic excitation.

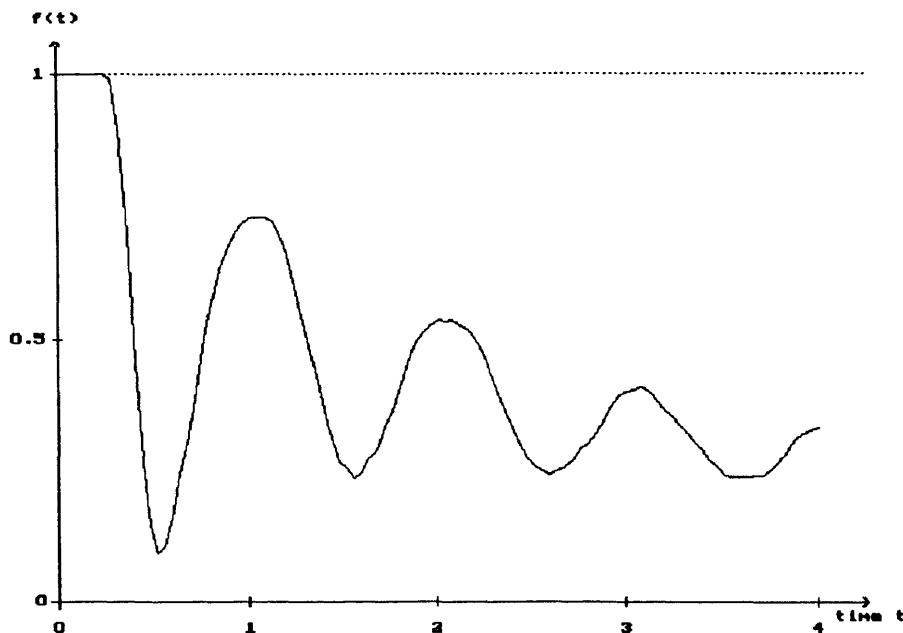


Figure 4. Temporal evolution of the relative exit frequency.

7. Effects of feedback and stochasticity under cubic nonlinearity ($\gamma > 0$)

In this section we briefly discuss some effects coming in through the nonlinear term $x_1^3(t)$ in the model system, i.e. $\gamma \neq 0$. Up to a certain level of γ we can treat this case as a perturbation of the corresponding linear system. Thus, for very small parameters γ , it would not affect decisively the dynamical behaviour. This is dramatically changing with increasing γ . For practical simulations we recommend using only balanced methods with appropriate weights. To some extent they guarantee the most numerically stable behaviour which is possible. Now we draw the attention to several special cases in the presence of cubic nonlinearity.

7.1 A deterministic nonlinear oscillator with small feedback

At first we numerically examine the deterministic dynamical behaviour in the phase plane of the first two components. Under small feedback parameters (g_1, g_2) the system behaves like a stable nonlinear oscillator in the vicinity of the equilibrium point zero. Thus we can expect a spiralization process of the corresponding flow converging to its steady state (equilibrium zero) in the phase plane. This effect is demonstrated in figure 5. As already mentioned, the system without distributed delays undergoes the movement of the well-known Duffing oscillator. This oscillator possesses one to three steady states (equilibria) depending on the system parameters (the sign in front of ω_2 establishes its number). In our model we observe the presence of only one steady state which is stable because of the positivity of ω^2 . The qualitative behaviour seems to be the same under small feedback, as seen in the figure.

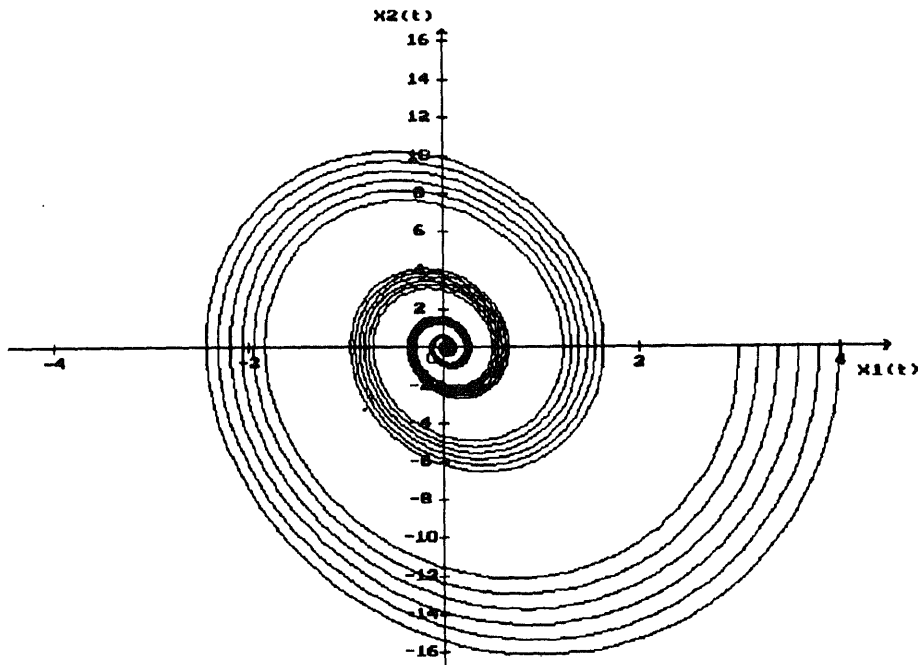


Figure 5. Phase diagram of the deterministic nonlinear system with small feedback.

7.2 A deterministic nonlinear oscillator with large feedback

A change of feedback parameters g_1 and g_2 as well as the exponential rate ν cause several effects. It turns out that the spiralization and attraction process of the obtained flow are decisively influenced by them, e.g. the clustering process, the speed and direction of attraction. This fact is seen in figure 6. Beyond critical values for the feedback gains it even leads to a destabilization of the dynamical system, whereas the increasing value of ν causes further stiffness of the system (simultaneous appearance of slowly and rapidly varying components).

7.3 A stochastic nonlinear oscillator with distributed delays

Now we incorporate stochasticity. Experiments show that the speed of attraction is damped in the presence of stochastic terms. Noise as well as cubic nonlinearity effect an amplification of the system when it is moving far from the equilibrium point. Furthermore the built-in stochasticity destabilizes the spiralization process (form, duration and convergence) depending on its intensity parameters in the phase plane. However, under small noise an attraction of the flow can be studied cf. figure 7. The following figure visualizes the dynamical behaviour in terms of a stochastic flow in the phase plane. The paths for several initial values are plotted with respect to the same random noise output.

In contrast to our specific model setup, the general noisy Duffing oscillator is a well-studied example of a bistable random oscillator with three steady states (the zero

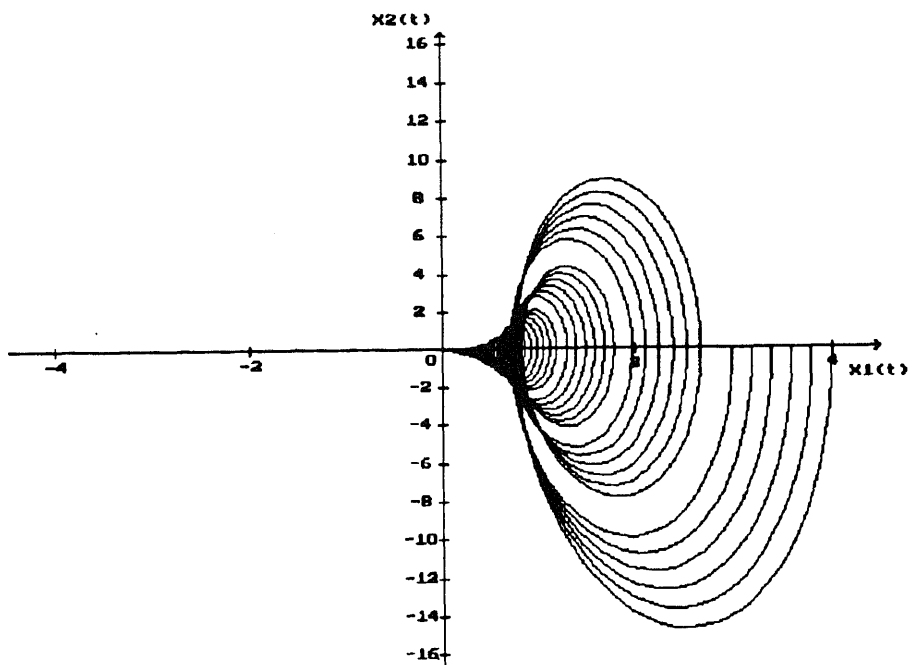


Figure 6. Phase diagram of the deterministic system with large feedback.

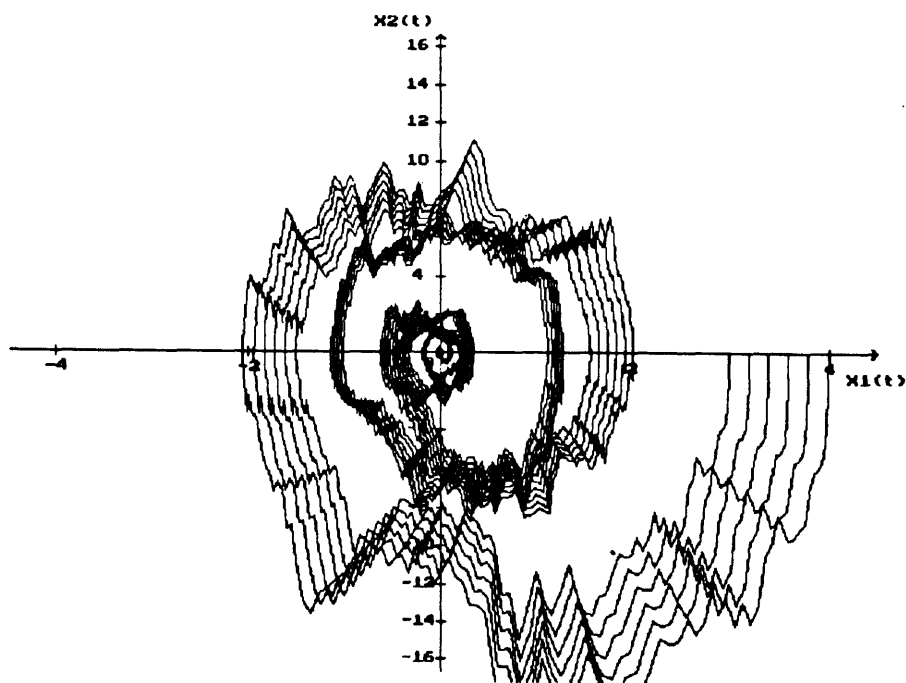


Figure 7. Phase diagram of a noisy nonlinear system with delay.

point is unstable!). This physical object leads to a chaotic movement between two attraction regions and a symmetric change of clustered trajectories (tunnelling). In our model the parameter σ_1 determines the nearness to this behaviour, however processes of attraction and separation alternate. With growing σ_1 one observes a significant change between separation and attraction periods around different points, finally the movement of the oscillator becomes more and more chaotic.

For the same parameter setup as in § 6 the system has still a stable behaviour under cubic nonlinearity with parameter $\gamma = 1$. This picture is confirmed by figure 8. There we estimated the mean square evolution of the nonlinear system. As seen the amplitudes decrease monotonically. However, this process is damped with growing influence of seismic excitation and nonlinearity. Thus, one can expect serious instabilities, both in estimation procedures for the mean evolution and in the displacement.

As we have already seen, the nonlinearity can have several effects. It is important to take into consideration such terms. By varying parameters σ_1 and σ_2 one could expect a significant change in the long-term behaviour of solutions, but varying σ_3 affects the transient behaviour. This process which is often called bifurcation undergoes a pitch-fork bifurcation within the framework of the Duffing oscillator. The point where just this effect occurs seems to be of great interest. Such bifurcation points indicate some structural instability in general. Corresponding bifurcation diagrams should show that bifurcation is related to the emergence of new solutions and a change in the stability behaviour. Stable and unstable steady states (equilibria) may occur in our seismic models. For a discussion of the stochastic bifurcation theory see the papers from the school of Arnold (1974) or in Horsthemke & Lefever (1984). However, this theory for

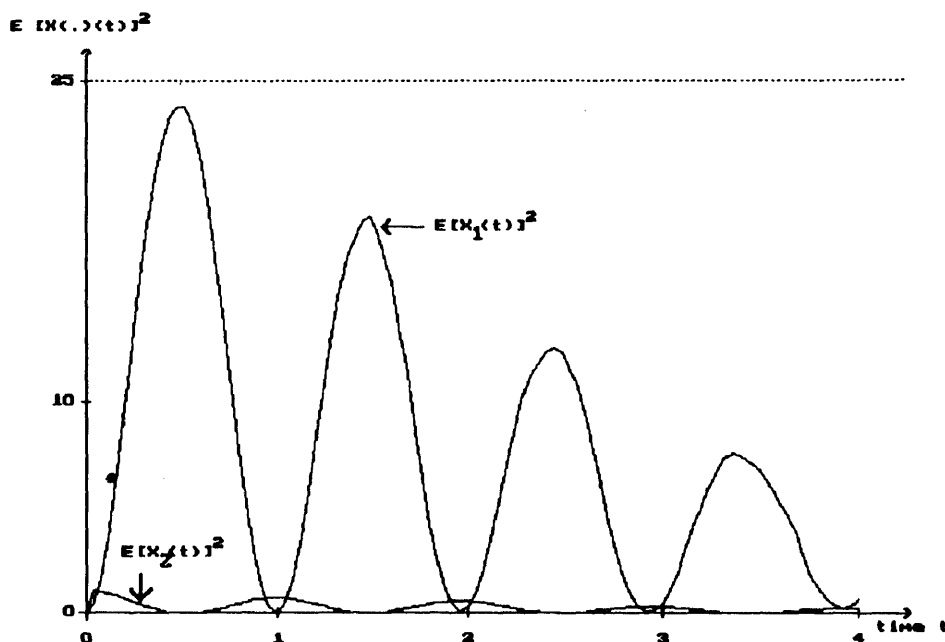


Figure 8. Mean square evolution of the components X_1 and X_2 with delay and seismic excitation ($\gamma = 1$).

higher-dimensional systems is still in its infancy and reliable numerical methods to detect steady states and to notice the qualitative aspects of stochastic dynamical systems are urgently required.

8. Conclusions

The paper has examined and visualized some effects of nonconstant weak and strong time delay on seismic structures. Additionally we have introduced stochasticity, through several noise sources in seismic models. In this paper we examine the stochastic dynamical systems governing the seismic structures. It would be useful to understand more accurately their behaviour, before one introduces active controls in them. The form of stochasticity introduced here not only serves the purpose of expressing uncertainty in the process but also allows an interpretation of random perturbations in system parameters.

The paper demonstrates that Stratonovich noise destabilizes the temporal behaviour of seismic structures, although this aspect is not new in the general theory of stochastic dynamical systems. The same effect was observed in both linear and nonlinear models. Incorporating stochasticity and cubic nonlinearity leads to a significant amplification of the system components. Up to a certain level of stochasticity the damping and attraction process is somewhat delayed and beyond that level even serious instabilities can occur. Seismic excitations following the specification (6) due to Bolotin (1960) mainly effect a change in the transient system behaviour and a shift in the phase between displacement and velocity of the oscillations.

For solving the model equations for seismic structures, numerical techniques must be carefully chosen. They are useful in indicating qualitative characteristics of these dynamical systems, e.g. stability of an equilibrium point, and provide the user with reliable results. Numerical simulations should employ implicit Euler methods, or more generally some appropriately chosen balanced methods. They are able to control fairly well the behaviour of the simulated dynamical system, at least up to the mean square level.

Appendix A. Numerical methods for solving SDE's

The development of stochastic numerical techniques began with some examinations to generate the simplest numerical solutions in the early fifties. At this stage, of its infancy, one already knows about the Euler scheme and its convergence to the exact solution. Meanwhile there are many contributions on this subject. Mil'shtein (1974) has done pioneering work in this field. Further contributions by himself followed in the eighties, e.g. see the book (Mil'shtein 1988). Furthermore, we want to point to the paper of Wagner & Platen (1978), which laid the foundations for a general calculus for numerical analysis of stochastic differential equations. They developed the stochastic Taylor formula, a counterpart of the deterministic Taylor formula, which leads to systematic numerical methods of a higher convergence order. Finally, it led to the development of a 'new field' in the eighties. These investigations and more are given in the monograph of Kloeden & Platen (1992). For a more experimental and computer-oriented approach, Kloeden *et al* (1994) have recently published a book. The French school, see e.g. Pardoux & Talay (1985) or Talay (1982, 1989, 1990), has made important contributions to the subject. An alternative approach to stochastic numerical methods

mentioned here was given by Kushner (1989). He constructs Markov chain approximations in order to treat efficiently stochastic control problems, such as the heavy traffic problem. This appendix follows the approach of Artemiev, Mil'shtein, Kloeden and Talay. For further sophisticated reviews and interesting facts see the papers of Artemiev, Clark and Cameron, Newton, Rümelin, Shkurko, Strittmatter and many others. However, we are only able to present some basic facts on this subject, and do not claim any completeness.

In contrast to the deterministic calculus, the stochastic integration depends on the choice of intermediate points. By varying this choice one gains different integral notions. Two of them turn out to be very effective. One is the Itô integral, which has more mathematical meaning due to convenient properties, whereas the other, the Stratonovich integral, is more appropriate for practical modelling (cf. Wong & Zakai 1965). Both versions can be transformed to each other in a natural way. Now, for the sake of simplicity, we only consider the Itô type of stochastic differential equations. These equations are often driven by a stochastic process having independent identically Gaussian distributed increments. The Wiener process $W(t)$ with zero mean and $\mathbb{E}[W(t)]^2 = t$ represents such a process. Although very erratic, this stochastic process is appropriate for modelling (at least in mean square sense). Several applications rely on this noise source. Now, let there be given an m -dimensional Wiener process $(W^j(t))_{j=1,\dots,m}$ which drives the Itô differential equation

$$dX(t) = a(t, X(t))dt + \sum_{j=1}^m b^j(t, X(t))dW^j(t), \quad (37)$$

starting at $X(0) = x_0 \in \mathbb{R}^d$ on the time interval $[0, T]$. Solutions $\{X(t): t \geq 0\}$ of (37) exist and are unique under the assumptions of Lipschitz continuity and of 'appropriate' polynomial boundedness of the functions $a_i(\cdot)$ and $b_i^j(\cdot)$ ($i = 1 \dots d$, $j = 1 \dots m$). The simplest method generating such solutions numerically is the Euler-Maruyama method (for short Euler method). These solutions are constructed by

$$Y_{n+1} = Y_n + a(Y_n)\Delta_n + \sum_{j=1}^m b^j(Y_n)\Delta W_n^j; \quad (n = 0, 1, 2, \dots). \quad (38)$$

Here Y_{n+1} denotes the value of the approximate solution using integration step size $\Delta_n = t_{n+1} - t_n$ at time point t_{n+1} . With $\Delta W_n^j = W^j(t_{n+1}) - W^j(t_n)$ we denote the current j th increment of the Wiener process $W^j(t)$ which can be generated as a standard Gaussian random variable multiplied by $\Delta_n^{1/2}$. At least for 'small enough' step sizes Δ_n , appropriate convergence theorems justify the application of method (38) to (37) to obtain an approximate solution depending on the practical purpose. In case of pathwise approximation (strong) one requires that a constant $K = K(T) > 0$ (T terminal time) exists such that

$$\forall t_n: \mathbb{E} \|X(t_n) - Y(t_n)\| \leq K(T) \cdot \Delta^n, \quad (39)$$

where $\Delta = \sup \Delta_n < +\infty$. In contrast to that, for momentwise approximation (weak) it is sufficient to demand only the existence of positive constants $K = K(T, g)$ such that

$$\forall t_n: \|\mathbb{E}(g(X(t_n)) - g(Y(t_n)))\| \leq K(T, g) \cdot \Delta^\beta, \quad (40)$$

with respect to a class of 'sufficiently smooth' functions g (often $g \in C_p^\infty$). The weak convergence has more practical utility because one is mostly interested in the calculation

of moments only. In those cases one may even simplify the generation of the random variables ΔW_n^j in (38). For equidistant approximations, it turns out to take any independent identically distributed random variables $\xi_{j,n}$ instead of ΔW_n^j which satisfy the moment relation

$$|\mathbb{E}\xi| + |\mathbb{E}\xi^3| + |\mathbb{E}\xi^5| + |\mathbb{E}\xi^2 - \Delta| + |\mathbb{E}\xi^4 - 3\Delta^2| \leq C \cdot \Delta^3,$$

for some constant $C > 0$. Thus we keep the weak convergence order β of numerical methods, at least up to the order $\beta = 2 \cdot 0$. For example, this is true for three-point distributed random variables ξ with

$$\mathbb{P}(\xi = \pm(3\Delta)^{1/2}) = 1/6 \quad \text{and} \quad \mathbb{P}(\xi = 0) = 2/3.$$

Moreover, for method (38) one can take simpler random variables other than the above. Choosing noise increments $\xi_{j,n}$ satisfying

$$|\mathbb{E}\xi| + |\mathbb{E}\xi^3| + |\mathbb{E}\xi^5| + |\mathbb{E}\xi^2 - \Delta| \leq C \cdot \Delta^2 \quad (41)$$

for some constant $C > 0$, e.g. two-point distributed random variables ξ with

$$\mathbb{P}(\xi = \pm \Delta^{1/2}) = \frac{1}{2},$$

the weak convergence order $\beta \leq 1$ of numerical methods is achieved, cf. Kloeden & Platen (1992). These simplifications in the generation of random variables save time and computational effort, but the same procedure cannot be applied to the scheme (38) approximating pathwise solution of (37) under the requirement (39). The method (38) possesses strong convergence order $\gamma = 0.5$ and weak convergence order $\beta = 1.0$. For proofs, see e.g. Kloeden & Platen (1992).

Mil'shtein has done one of the first trials of systematic construction of numerical methods and proved the convergence of the well-known Mil'shtein methods (with $\gamma = 1.0$ and $\beta = 1.0$). In general, corresponding higher order methods are derived from the stochastic Taylor expansion, resulting from iterative application of Itô's lemma by appropriate truncation. This approach suggested first in Wagner & Platen (1978) is described in Mil'shtein (1988) or in Kloeden & Platen (1992). For further details, see Artemiev (1993), Clark & Cameron (1980), Newton (1991), Pardoux & Talay (1985), Talay (1982, 1989, 1990) or Kloeden *et al* (1991, 1994).

As in deterministic analysis, asymptotic stability and the already mentioned convergence together give reasonable robust solutions. For the sake of guaranteeing stable numerical behaviour, in our experiments we used slightly changed schemes based on the Euler method. Stability guarantees that small initial perturbations have no marked influence on the dynamical behaviour. In deterministic analysis one suggests implicit methods, i.e. such methods which also involve locally the new value of the approximation. These methods ensure numerically stable behaviour. In stochastic analysis too there are such methods. However, the variety of stability concepts here is large, cf. Kozin (1969). We suggest following the concept of moment stability. For a brief exposition on mean square stability, i.e. the stability of second moments, see appendix B. To some extent, stochastically stable behaviour can be guaranteed by following the family of implicit Euler methods envisaged by the scheme

$$Y_{n+1} = Y_n + \{\rho a(Y_{n+1}) + (1 - \rho)a(Y_n)\}\Delta_n + \sum_{j=1}^m b^j(Y_n)\Delta W_n^j; \quad (n = 0, 1, 2, \dots) \quad (42)$$

with fixed implicitness parameter $\rho \in [0, 1]$. Of course, for the application of these methods the corresponding system (42) must be locally resolvable. An alternative means to control the stochastic stability behaviour is given by the balanced methods. Following Mil'shtein *et al* (1992) these methods possess the form

$$Y_{n+1} = Y_n + a(Y_n)\Delta_n + \sum_{j=1}^m b^j(Y_n)\Delta W_n^j + \sum_{j=0}^m c^j(t_n, Y_n)(Y_n - Y_{n+1})|\Delta W_n^j|, \quad (43)$$

where $c^j(.,.)$ are bounded $d \times d$ -matrices and $\Delta W_n^0 = \Delta_n (n = 0, 1, 2, \dots)$. For their existence and convergence it is convenient to require that the matrices

$$M(t, x) := U + \sum_{j=0}^m \alpha_j c^j(t, x) \quad (44)$$

are invertible. Additionally the norms of their inverses must be uniformly bounded for all pairs $(t, x) \in [0, T] \times \mathbb{R}^d$ and sequences of non-negative real numbers $(\alpha_j)_{j=0,1,\dots,m}$ with $\alpha_0 \in [0, \delta]$. Strong convergence of order $\gamma = 0.5$ has been established in Mil'shtein *et al* (1992). Furthermore, one immediately concludes the weak convergence of order $\beta = 0.5$ for general models of type (37).

In particular, methods (42) and (43) are appropriate to integrate systems interpreted as physically stiff. Stiffness often occurs in physical phenomena, e.g. in stochastic mechanics. One encounters stiffness if there are two dynamical components in the system where one is moving rapidly and very erratically while the other is relatively slow. Generally speaking, the methods (42) are recommended to moment stability and in such cases where the deterministic part plays the decisive role in the dynamics. In cases where the stochastic aspect is more important one should rather adopt some appropriately chosen balanced methods. They can even be implemented more simply and can achieve better control on the dynamical behaviour of numerical solutions. The problem of choosing the weight matrices c^j in the balance methods (43) is circumvented by the simple choice of $c^j = \alpha_j \|b^j\| U$ with positive scalars α_j in case of finite norms. Note that these methods are especially constructed to treat more accurately systems with linear multiplicative noise or with diffusion vectors having only bounded linear-polynomial growth (more cannot be expected in general, because of the assumptions guaranteeing their strong convergence!). However, the knowledge about them is still inadequate.

With the methods (42) and (43) we have obtained reasonable results for our random oscillators. In this paper corresponding higher order methods are deliberately avoided. Extensive studies concern their stability. Furthermore, higher order methods would not be always applicable to nonlinear models. They require 'too much smoothness, boundedness' of the drift and diffusion coefficients $a^i(\cdot)$, $b_i^j(\cdot)$ and 'additional information' on the noise (multiple Itô integrals with respect to the Wiener process). Their generation involves massive systems and sets of multiple integrals. Sometimes these methods cause explosions in their numerical solutions close to zero (due to unbounded derivatives of drift and diffusion), else they do not show stable behaviour (see Schurz 1993). As of now we cannot recommend higher order methods for nonlinear models, for visualizing stochastic dynamics and for studying their characteristics (such as Lyapunov exponents). However, in specific models they can be very useful.

with fixed implicitness parameter $\rho \in [0, 1]$. Of course, for the application of these methods the corresponding system (42) must be locally resolvable. An alternative means to control the stochastic stability behaviour is given by the balanced methods. Following Mil'shtein *et al* (1992) these methods possess the form

$$Y_{n+1} = Y_n + a(Y_n)\Delta_n + \sum_{j=1}^m b^j(Y_n)\Delta W_n^j + \sum_{j=0}^m c^j(t_n, Y_n)(Y_n - Y_{n+1})|\Delta W_n^j|, \quad (43)$$

where $c^j(\cdot, \cdot)$ are bounded $d \times d$ -matrices and $\Delta W_n^0 = \Delta_n$ ($n = 0, 1, 2, \dots$). For their existence and convergence it is convenient to require that the matrices

$$M(t, x) := U + \sum_{j=0}^m \alpha_j c^j(t, x) \quad (44)$$

are invertible. Additionally the norms of their inverses must be uniformly bounded for all pairs $(t, x) \in [0, T] \times \mathbb{R}^d$ and sequences of non-negative real numbers $(\alpha_j)_{j=0,1,\dots,m}$ with $\alpha_0 \in [0, \hat{\alpha}]$. Strong convergence of order $\gamma = 0.5$ has been established in Mil'shtein *et al* (1992). Furthermore, one immediately concludes the weak convergence of order $\beta = 0.5$ for general models of type (37).

In particular, methods (42) and (43) are appropriate to integrate systems interpreted as physically stiff. Stiffness often occurs in physical phenomena, e.g. in stochastic mechanics. One encounters stiffness if there are two dynamical components in the system where one is moving rapidly and very erratically while the other is relatively slow. Generally speaking, the methods (42) are recommended to moment stability and in such cases where the deterministic part plays the decisive role in the dynamics. In cases where the stochastic aspect is more important one should rather adopt some appropriately chosen balanced methods. They can even be implemented more simply and can achieve better control on the dynamical behaviour of numerical solutions. The problem of choosing the weight matrices c^j in the balance methods (43) is circumvented by the simple choice of $c^j = \alpha_j \|b^j\| U$ with positive scalars α_j in case of finite norms. Note that these methods are especially constructed to treat more accurately systems with linear multiplicative noise or with diffusion vectors having only bounded linear-polynomial growth (more cannot be expected in general, because of the assumptions guaranteeing their strong convergence!). However, the knowledge about them is still inadequate.

With the methods (42) and (43) we have obtained reasonable results for our random oscillators. In this paper corresponding higher order methods are deliberately avoided. Extensive studies concern their stability. Furthermore, higher order methods would not be always applicable to nonlinear models. They require 'too much smoothness, boundedness' of the drift and diffusion coefficients $a^i(\cdot)$, $b_i^j(\cdot)$ and 'additional information' on the noise (multiple Itô integrals with respect to the Wiener process). Their generation involves massive systems and sets of multiple integrals. Sometimes these methods cause explosions in their numerical solutions close to zero (due to unbounded derivatives of drift and diffusion), else they do not show stable numerical behaviour (e.g. see Schurz 1993). As of now we cannot recommend higher methods for solving general nonlinear models, for visualizing stochastic dynamics or for estimating their qualitative characteristics (such as Lyapunov exponents which describe the long-term behaviour). However, in specific models they can be very effective. For example, if one can make use

stable iff

$$\exists c_1, c_2 > 0 \forall t_0 \geq 0 : \mathbb{E} \|X_t(x_0, t_0)\|^2 \leq c_1 \|x_0\|^2 \exp(-c_2(t - t_0)). \quad (47)$$

For results on exponential stability, see the works of Sasagawa (1981) and Khas'minskij (1980). Further contributions on stability and different concepts can be found in Arnold (1974), Kozin (1969) or Kushner (1967). For sophisticated approaches, see e.g. the papers of Baxendale (1985) or the collection of papers in Arnold & Wihstutz (1986). The following theorem forms the base for further consideration of corresponding discrete systems.

Theorem B.1. Assume that the matrix-valued functions $A(t)$ and $B^j(t)$ in (45) are bounded on $[t_0, \infty]$. Then, for exponential stability of the null solutions in the mean square sense it is necessary that for any, and sufficient that for a particular symmetrical, positive definite, continuous and bounded $d \times d$ -matrix $C(t)$ with $x^T C(t)x \geq k_1 |x|^2$ ($k_1 > 0$) for all $t \geq 0$ the matrix differential equation

$$\frac{dD(t)}{dt} + A^T(t)D(t) + D(t)A(t) + \sum_{j=1}^m B^{jT}(t)D(t)B^j(t) = -C(t), \quad (48)$$

possesses a matrix solution $D(t)$ with the same properties as the matrix $C(t)$.

This theorem and its proof can be found in a more general form in Khas'minskij (1980). The present formulation is from Arnold (1974). Similar to the above definition one can introduce the notion of mean square stability of the null solution for numerical methods.

DEFINITION B.2

A numerical solution $(Y_n)_{n \in \mathbb{N}}$ with fixed step size Δ starting in y_0 at time t_0 has an (asymptotically) mean square stable null solution iff

$$\exists \delta > 0 \forall t_0 \geq 0 \forall y_0 \in \mathbb{R}^d \|y_0\| < \delta : \lim_{n \rightarrow \infty} \mathbb{E} \|y_n\|^2 = 0, \quad (49)$$

where we understand that the limit in (49) is taken only at discrete times t_n .

In contrast to stability analysis for continuous time systems, the stability analysis for numerical methods is still in its initial stage. A somewhat discrete counterpart to the above theorem is stated below for implicit Euler and Mil'shtein methods. For the construction and convergence of implicit Mil'shtein methods see Kloeden & Platen (1992) and Kloeden *et al* (1994). Let $P_n^{\rho, M}$ denote the matrix of second moments $\mathbb{E} Y_n^i Y_n^j$ in the implicit Mil'shtein method for (45) at time t_n , and $P_n^{\rho, E}$ that for the corresponding implicit Euler method (42) using the same step size Δ and implicitness $\rho \in [0, 1]$. It is not hard to verify that from the stability of matrix sequences P_n^ρ follows the stability in mean square sense, as required in (49), and vice versa. Thus one can draw further inference about the behaviour of the sequence $(P_n^\rho)_{n=0,1,2,\dots}$ for both the implicit methods. The following result is stated for autonomous systems, i.e. for systems with time-independent drift and diffusion parts.

Theorem B.2. Assume that both the discrete systems start with the same positive definite matrix P_0 of second moments for the autonomous form of SDE (45). Then the mean

square evolution of both discrete systems is given by the corresponding operators \mathcal{L}_ρ^E and \mathcal{L}_ρ^M mapping from the space of positive definite $d \times d$ -matrices into itself, and the following relations hold

$$(i) \quad P_{n+1}^{\rho,E} = (\mathcal{L}_\rho^E)^n(P_0) \leqslant_{(+)} (\mathcal{L}_\rho^M)^n(P_0) = P_{n+1}^{\rho,M}, \quad \text{i.e.}$$

$$\forall x \in \mathbb{R}^d: x^T P_{n+1}^{\rho,E} x \leqslant x^T P_{n+1}^{\rho,M} x: n = 0, 1, 2, \dots,$$

$$(ii) \quad \forall S \in \mathbb{R}^{d \times d}, S \text{ positive definite solution of (48), } \forall \rho \geqslant 0.5:$$

$$\mathcal{L}_\rho^E S <_{(+)} S, \text{ hence the eigenvalues of } \mathcal{L}_\rho^E \text{ are smaller than unity.}$$

$$(iii) \quad \rho = 0.5 \Rightarrow$$

The implicit Euler method possesses a mean square null solution iff the null solution is mean square stable for the continuous time system.

$$(iv) \quad \forall S \in \mathbb{R}^{d \times d}, S \text{ positive definite, } \forall \rho_1, \rho_2, 0 \leqslant \rho_1 \leqslant \rho_2: \mathcal{L}_{\rho_2} S \leqslant_{(+)} \mathcal{L}_{\rho_1} S$$

where \mathcal{L}_ρ is the mean square operator of the implicit Euler or Mil'shtein method, respectively.

These are the results of the paper by Schurz (1993) where one also finds the proofs. In B.2.(i) matrix inequalities are to be understood in terms of positive definiteness of the difference matrix.

Remarks: The results on mean square stability in implicit Euler and Mil'shtein methods are very effective. As a conclusion, the half-implicit Euler method ($\rho = 0.5$) can be considered as a stability indicator of the continuous time system to be solved numerically by this method. This method possesses a mean square stable null solution iff the null solution is mean square stable for the corresponding continuous time system (see B.2.(iii)). Through B.2.(iv) the 'monotonic nesting' of mean square stability domains has been discovered. Thus the most mean square stable method (within the class $0 \leqslant \rho \leqslant 1$) is the fully drift-implicit method, i.e. the numerical method with implicitness $\rho = 1$. This holds for both the family of implicit Euler methods and the family of implicit Mil'shtein methods.

If one is not interested in indicating stability, one could also apply balanced methods to achieve control on the discrete dynamical behaviour. As an advantage of the balanced methods, the costly inversion of correction matrices is not really necessary. One can use balanced methods with scalar corrections, e.g. in case of bounded norms of drift $a(\cdot)$ and diffusion $b^j(\cdot)$ take

$$Y_{n+1} = Y_n + w_n^{-1} \left(a(Y_n) \Delta_n + \sum_{j=1}^m b^j(Y_n) \Delta W_n^j \right), \quad (50)$$

where $w_n = 1 + \alpha_0 \|a(\cdot)\| \Delta_n + \sum_{j=1}^m \alpha_j \|b^j(\cdot)\| |\Delta W_n^j|$ with nonnegative real parameters $(\alpha_j)_{j=0,1,\dots,m}$. It is not hard to verify that there exist balanced methods (50) which provide mean square stable numerical solutions. Moreover, with (50) one can state numerical methods which possess a more mean square stable null solution than any of the implicit Euler or implicit Mil'shtein methods for bilinear systems. The only disadvantage of balanced methods is that they reduce slightly the weak convergence order and could be too stable (not applicable as stability indicator) for general continuous time systems. Apart from these drawbacks the balanced methods seem to

be the richest and most robust class of numerical methods so far. For results concerning them, see Schurz (1994).

Higher order Taylor methods, methods with higher convergence order and those derived from the stochastic Taylor formula do not seem to be appropriate to achieve stability. For example, theorem B.2.(i) shows that the implicit Mil'shtein method is worse than the corresponding implicit Euler method as regards mean square stability. This indicates that one has to introduce terms carefully in the numerical method to achieve higher convergence order and stable behaviour simultaneously. However, the drawbacks of higher order methods still exist. There is no appropriate stochastic control on their stability behaviour up to now.

Part of the work was done during the visit of the second author to the Jawaharlal Nehru University, New Delhi in December 1993, for which the authors would like to thank the University.

References

- Abdel-Rohman M 1987 Time-delay effects on actively damped structures. *J. Eng. Mech.* 113: 1709–1719
- Agrawal A K, Fujino Y, Bhartia B K 1993 Instability due to time delay and its compensation in active control of structures. *Earthquake Eng. Struct. Dyn.* 22: 211–224
- Ariaratnam S T, Srikantiah T K (1978) Parametric instabilities in elastic structures under stochastic loading *J. Struct. Mech.* 6: 349–365
- Arnold L 1974 *Stochastic differential equations* (New York: Wiley)
- Arnold L, Wihstutz V (eds) 1986 Lyapunov exponents. *Proc. Workshop, Bremen 1984 In Springer Lectures in Mathematics* No. 1186 (Berlin: Springer)
- Artemiev S S 1993 Certain aspects of application numerical methods for solving SDE systems. *Bull. Novosibirsk Comput. Numer. Anal.* 1: 1–16
- Baxendale P H 1985 Moment stability and large deviations for linear stochastic differential equations. *Taniguchi Symp. PMMP Katata*, pp. 31–54
- Bolotin V V 1960 Statistical theory of seismic design of structures. *Proc. 2nd WEEE Japan*, pp. 13–65
- Chung L L, Reinhorn A M, Soong T T 1988 Experiments on active control of seismic structures. *J. Eng. Mech.* 114: 241–256
- Clark J M C, Cameron R J 1980 The maximum rate of convergence of discrete approximations for stochastic differential equations. *Springer Lecture Notes in Control and Information Sci.* (Berlin: Springer) 25: 162–171
- Gard C T 1988 *Introduction to stochastic differential equations* (Basel: Marcel Dekker)
- Gardiner C W 1983 *Handbook of stochastic methods* (Berlin: Springer)
- Horsthemke W, Lefever R 1984 Noise induced transitions. *Springer Series in Synergetics* (Berlin: Springer)
- Iyengar R N 1986 A nonlinear system under combined periodic and random excitation *J. Stat. Phys.* 44: 907–920
- Karmeshu 1976 Motion of a particle in a velocity dependent random force *J. Appl. Probab.* 13: 684–695
- Karmeshu, Bansal N K 1975 Stability of moments in a single neutronic system with stochastic parameters. *Nucl. Sci. Eng.* 58: 321–327
- Khas'minskij R Z 1980 *Stochastic stability of differential equations* (Alphen aan den Rijn: Sijthoff & Noordhoff)
- Kloeden P E, Platen E 1992 *Numerical solution of stochastic differential equations Applications of mathematics* (Berlin: Springer) vol. 23

- Kloeden P E, Platen E, Schurz H 1994 *Numerical solution of stochastic differential equations through computer experiments* (Springer Unixtext)
- Kloeden P E, Platen E, Schurz H 1991 The numerical solution of nonlinear stochastic dynamical systems: A brief introduction. *Int. J. Bifurcation Chaos* 1: 277–286
- Kozin F 1969 A survey of stability of stochastic systems *Automatika* 5: 95–112
- Kozin F 1977 An approach to characterizing, modelling and analysing earthquake excitation records. *CISM Lecture Notes* (Springer) 225: 77–109
- Kushner H 1967 *Stochastic stability and control* (New York: Academic Press)
- Kushner H 1989 Numerical methods for stochastic control problems in continuous time, LCDS-Report No. 89–11 Brown Univ., Rhode Island
- MacDonald N 1978 Time lags in biological models. *Lecture Notes in Biomathematics* (ed.) S Levin (Berlin: Springer) vol. 27
- May R M 1974 *Stability and complexity in model ecosystem* (Princeton: University Press)
- Mil'shtein G 1974 Approximate integration of stochastic differential equations. *Theor. Probab. Appl.* 19: 557–562
- Mil'shtein G 1988 *The numerical integration of stochastic differential equations* (Sverdlovsk: Uralski Univ. Press)
- Mil'shtein G, Platen E, Schurz H 1992 Balanced implicit methods for stiff stochastic systems: An introduction and numerical experiments, Preprint No. 33, IAAS - Berlin
- Mil'shtein G N, Tretjakov M V 1993 Numerical solution of differential equations with colored noise *J. Stat. Phys.* (submitted)
- Moon F C 1987 *Chaotic vibrations* (New York: John Wiley)
- Newton N J 1991 Asymptotically efficient Runge–Kutta methods for a class of Itô and Stratonovich equations. *SIAM J. Appl. Math.* 51: 542–567
- Pardoux E, Talay D 1985 Discretization and simulation of stochastic differential equations. *Acta Appl. Math.* 3: 23–47
- Pu J P, Kelly J M 1990 Active control and seismic isolation *J. Eng. Mech.* 117: 2221–2236
- Sasagawa T 1981 On the exponential stability and instability of linear stochastic systems. *Int. J. Contr.* 33: 363–370
- Schurz H 1993 Mean square stability for discrete linear stochastic systems, Preprint No. 72, IAAS - Berlin
- Schurz H 1994 Asymptotical mean square stability of an equilibrium point of some linear numerical solutions (Preprint, IAAS - Berlin Submitted)
- Shinozuka M 1972 Monte-Carlo solution of structural dynamics *J. Comput. Struct.* 2: 855–874
- Talay D 1982 *Analyse Numérique des Equations Differentielles Stochastiques*, Thèse 3ème cycle, Univ. Provence
- Talay D 1989 Approximation of upper Lyapunov exponents of bilinear stochastic differential equations, INRIA-Report No. 965, France
- Talay D 1990 Simulation and numerical analysis of stochastic differential systems: A review, Rapports de Recherche, No. 1313, INRIA, France
- Wagner W, Platen E 1978 Approximation of Itô integral equations, (Preprint) *Z. Ing. Math. Mech., Acad. of Sci. GDR, Berlin*
- Wong E, Zakai M 1965 On the relation between ordinary and stochastic differential equations. *Int. J. Eng. Sci.* 3: 213–229
- Wedig W 1987 Stochastische Schwingungen - Simulation, Schätzung und Stabilität. *Z. Ang. Math. Mech.* 67: T34–T42
- Yang J N, Akbarpour A, Askar G 1990 Effect of time delay on control of seismic-excited buildings *J. Struct. Eng.* 116: 2801–2814
- Zhang L, Yang C Y, Chajes M J, Cheng A H-D 1993 Stability of active-tendon structural control with time delay. *J. Eng. Mech.* 119: 1017–1024

Stochastic control of hysteretic structural systems

YOSHIYUKI SUZUKI

Disaster Prevention Research Institute, Kyoto University, Gokasho, Uji,
Kyoto 611, Japan

Abstract. A method of stochastic optimal control of hysteretic structural systems under earthquake excitations is presented. Stochastic estimation and control problems are formulated in the form of Itô stochastic differential equations on the basis of the theory of continuous Markov processes. The conditional moment equations given observation data are derived for nonlinear filtering, and are closed by introducing appropriate analytical form of the conditional probability density functions of the state variables. Under the assumption that the admissible controls are expressed as functions of the conditional moment functions the Bellman equation is derived. If the spatial variables of the Bellman equation are defined by a part of the full set of conditional moment functions appearing in the closed moment equations, the resulting Bellman equation is coupled with conditional moment equations both for filtering and for prediction. The Gaussian and non-Gaussian stochastic linearization techniques combined with simple solution techniques to the Bellman equation are examined to solve the Bellman equation or extended Riccati equations without prediction procedures.

Keywords. Stochastic optimal control; stochastic estimate; hysteretic structure; stochastic linearization.

1. Introduction

In the last two decades there has been a growing interest in the active structural control with the increase of demand to ensure not only the structural safety but also the serviceability of civil and building structures subjected to intense earthquake and wind excitations (e.g. Yao 1972, Yang 1975, Leipholz & Abdel-Rohman 1986). Since there are many uncertainties and randomness in modelling input excitations and nonlinear controlled structural systems, the control force is to be stochastically determined on the basis of observation data of output responses of the actual structural system. Moreover, since the observations are partially made on a few limited points of the structural system and are contaminated by noise, the stochastic optimal control based on the stochastic estimate is to be explored to obtain a reliable controlled structural system (Kushner 1967; Jazwinski 1970). The stochastic estimate-based optimal control problem has been investigated vigorously in the field of control engineering in the recent past. It has been well recognized that the stochastic optimal estimate under the

minimum error variance criterion and the stochastic optimal control associated with the quadratic cost functional could be separately solved for linear dynamic systems (Wonham 1968). As for nonlinear dynamic systems, however, the stochastic estimation and optimal control problems may not always be solved independently. As far as the hysteretic structural systems are concerned, further theoretical and computational method would be explored to materialize the idea of the structural control for actual structural systems.

The objective of this paper is to find a reasonable method for the stochastic estimate-based optimal control of hysteretic structural systems on the basis of the theory of continuous Markov vector processes (Gikhman & Skorokhod 1972). First, both system and observation equations of controlled hysteretic structural systems are expressed in the form of the Itô stochastic differential equations. The fundamental equations governing the time variations of the conditional probability density functions and the conditional moment functions given an observation data from an initial time to the current time are derived. In order to evaluate the conditional expectations of nonlinear functions appearing in the conditional moment equations and to close them, the approximate conditional probability density function of the state variables is discussed. On the other hand, if the performance criterion is given by the conditional expectation of a cost functional given an initial condition and if the admissible control is supposed to belong to a class of functions of conditional moment functions for stochastic estimates, the Bellman equation may be derived according to Bellman's optimality principle (Bellman 1957).

For a general class of nonlinear dynamic systems including hysteretic structural systems, if the admissible control is restricted to a class of functions of a set of conditional moment functions which is a part of the full set of those appearing in the approximate conditional probability density function, the Bellman equation is not closed and has to be solved simultaneously with the stochastic estimate solution procedure including prediction, since the Bellman equation is conditioned at the end time of control. From both analytical and computational aspects, one of the most readily available procedures for the above problems might be the stochastic linearization technique which combined the stochastic estimation with optimal control of nonlinear dynamic systems (Sunahara 1970, 1987). For a practical point of view, in order to deal with the stochastic estimate-based optimal control of hysteretic multi-degree-of-freedom structural systems, simplified, approximate procedures, to which are combined the Gaussian and non-Gaussian stochastic linearization in nonlinear filter dynamics with simple solution techniques to the Bellman equation, are discussed.

2. Formulation of stochastic estimation and control problems

2.1 Basic equations for stochastic estimate-control

The basic equations for stochastic estimation and optimal control problems of nonlinear structural systems may be expressed as the following pair of system and observation equations:

$$dZ_t = F_t^c(Z_t)dt + G_t dW_t, \quad (1)$$

$$dY_t = H_t^c(Z_t)dt + R_t dV_t, \quad (2)$$

where

$$F_t^c(Z_t) = F_t(Z_t) + B_t C_t(S_t), \quad (3)$$

$$H_t^c(Z_t) = H_t(Z_t) + D_t C_t(S_t). \quad (4)$$

In the above equations, Z_t and Y_t are, respectively, n -dimensional state and k -dimensional output vectors, $F_t(Z_t)$ and $H_t(Z_t)$ are, respectively, n - and k -dimensional vector-valued nonlinear functions of time t and state vector Z_t , G_t , R_t , B_t and D_t are $n \times m$, $k \times l$, $n \times s$ and $k \times s$ matrix-valued functions of t , and W_t and V_t are, respectively, normalized system and observation noises which are supposed to be independent vector Wiener processes as follows:

$$E \begin{bmatrix} dW_t \\ dV_t \end{bmatrix} [dW_t^T dW_t^T] = \begin{bmatrix} I & 0 \\ 0 & I \end{bmatrix} dt, \quad (5)$$

where the superscript T denotes the transpose of vector or matrix, and I is the identity matrix. The s -dimensional vector-valued admissible control function $C_t(S_t)$ is described in terms of a vector-valued stochastic estimate S_t .

Here the stochastic estimate S_t is given as collections of conditional moment functions given an observation y_t during the time interval $[t_0, t]$, the admissible control function $C_t(S_t)$ is then a measurable function with respect to y_t . Hence, if the functions $F_t(Z_t)$ and $H_t(Z_t)$ are mathematically well-defined as single-valued nonlinear functions of t and Z_t , the system equation given by (1) is the Itô nonlinear vector stochastic differential equation, and the simultaneous equations consisting of the system and observation equations given by (1) and (2) are also the Itô stochastic differential equations.

2.2 Controlled hysteretic structural systems

In modelling the hysteretic structural systems, it is required to describe hysteretic characteristics in well-defined differential forms in terms of relevant state variables in order to formulate the system and observation equations in the form of the Itô stochastic differential equations. The hysteretic restoring force is in general expressed as

$$\phi = rx + (1-r)z, \quad (6)$$

where ϕ is the dimensionless hysteretic characteristic, x is the deformation nondimensionalized by a reference yield deformation, z is the dimensionless hysteretic component, r is a weight of linear component x to ϕ , and both z and ϕ are normalized to have unit initial rigidities. For the bilinear hysteretic model the hysteretic component z is, in particular, expressed in the following differential form (Kobori *et al* 1976):

$$\dot{z} = \dot{x} [1 - U(\dot{x})U(z - \delta) - U(-\dot{x})U(z + \delta)] \equiv g(\dot{x}, z), \quad (7)$$

where $\delta > 0$, δ is a dimensionless yield deformation, the overdot means derivative with respect to time and $U(\cdot)$ denotes the Heaviside unit step function. The unified differential form of the general hysteretic constitutive laws is given for a class of piecewise linear hysteresis including degrading or stiffening property (Suzuki & Minai 1988a) for curved hysteresis (Wen 1976, Baber & Wen 1981). By making use of the differential forms of hysteretic constitutive laws and by defining the whole state vector

Z_t representing the controlled hysteretic structural system subjected to earthquake excitations, the state space equation of the whole dynamic system may be written in the form

$$\dot{Z}_t = F_t(Z_t) + B_t C_t(S_t) + N_t, \quad (8)$$

where N_t is an input excitation vector.

In the case where the input excitation is measurable with observation noise in addition to the structural responses, the observation equation is expressed as the following Itô stochastic differential equation:

$$d {}_E Y_t = N_t dt + {}_E R_t d {}_E V_t, \quad (9)$$

where ${}_E \dot{Y}_t$ is the measured input excitation, ${}_E R_t$ is a time-dependent matrix and ${}_E V_t$ is a normalized Wiener process representing observation noise. From (8) and (9) the system equation is then expressed as

$$dZ_t = [F_t(Z_t) + C_t B_t(S_t)] dt + d {}_E Y_t - {}_E R_t d {}_E V_t. \quad (10)$$

By setting $G_t = -{}_E R_t$ and $dW_t = d {}_E V_t$ and by replacing $F_t(Z_t) + C_t B_t(S_t) + {}_E \dot{Y}_t$ with $F_t^c(Z_t)$, (10) is reduced to the form of (1).

3. Stochastic estimate of nonlinear dynamic systems

It is well-known that the optimal estimator under the minimum error variance criterion is given by the conditional expectation of the state vector Z_t at the estimation time τ given observation data y_t in a time interval $[t_0, t]$ (Jazwinski 1970). That is

$$\langle Z_\tau \rangle_t = \int_{R^n} dZ_\tau Z_\tau p_\tau(Z_\tau | y_t), \quad t \geq \tau, \quad (11)$$

where $p_\tau(Z_\tau | Y_t)$ is the conditional probability density function of filtering, prediction or smoothing according to the case where $\tau = t$, $\tau > t$ or $\tau < t$ and R^n denotes the n -dimensional full state space. Since it is difficult to determine directly the conditional probability density functions, the conditional moment equations are solved numerically in a nonstationary state to evaluate the time-dependent conditional probability density function as well as conditional statistics of state variables including the optimal estimator. By defining an arbitrary twice differentiable and integrable function of the state vector Z_τ as $\phi(Z_\tau)$, the conditional expectation of $\phi(Z_\tau)$ and its differential with respect to τ are respectively given by

$$\langle \phi(Z_\tau) \rangle_t = \int_{R^n} dZ_\tau \phi(Z_\tau) p_\tau(Z_\tau | y_t), \quad (12)$$

and

$$d_\tau \langle \phi(Z_\tau) \rangle_t = \int_{R^n} dZ_\tau \phi(Z_\tau) d_\tau p_\tau(Z_\tau | y_t). \quad (13)$$

In order to obtain the time evolution of $\langle \phi(Z_\tau) \rangle_t$ with time parameter τ it is necessary to determine the differential form $d_\tau p_\tau(Z_\tau | y_t)$ of the conditional probability density function. For controlled nonlinear dynamic systems the filtering and prediction problems are essential. The filtering problem is discussed herein for the sake of simplicity.

Since the solution process Z_t to (1) and the joint solution process (Z_t, Y_t) to (1) and (2) are continuous Markov vector processes, the associated Kolmogorov differential operators are given as (Minai & Suzuki 1987)

$$L_Z^* \varphi_t = \frac{1}{2} ((G_t G_t^T)_{\kappa\nu} \varphi_t)_{,\kappa\nu} - (F_{t\kappa}^c \varphi_t)_{,\kappa}, \quad (14)$$

and

$$L_Z \varphi_t = \frac{1}{2} ((G_t G_t^T)_{\kappa\nu} \varphi_{t,\kappa\nu} + F_{t\kappa}^c \varphi_{t,\kappa}). \quad (15)$$

In the above equations, φ_t is considered as a scalar-valued function of t and Z_t and L_Z^* and L_Z are forward and backward operators. It is noted that in these equations the summation and differentiation conventions are used, the subscripts κ and ν attached directly to vectors and matrices denote the specified element and those following the comma represent partial differentiations with respect to the specified elements of the state vector Z_t . By making use of these differential operators the differential form of the conditional probability density function is given by

$$dp_t(Z_t|y_t) = L_Z^* p_t(Z_t|y_t) dt + \tilde{H}_t(Z_t)(R_t R_t^T)^{-1} p_t(Z_t|y_t) dv_t, \quad (16)$$

where

$$dv_t = dY_t - \langle H_t^c(Z_t) \rangle_t dt, \quad (17)$$

$$\tilde{H}_t(Z_t) = H_t(Z_t) - \langle H_t(Z_t) \rangle = \tilde{H}_t^c(Z_t). \quad (18)$$

Substituting (16) into (13) and taking account the independence of dv_t and Z_t yields

$$d\langle \phi(Z_t) \rangle_t = \langle L_Z \phi(Z_t) \rangle_t dt + \langle \phi(Z_t) \tilde{H}_t^T(Z_t) \rangle_t (R_t R_t^T)^{-1} p_t(Z_t|y_t) dv_t. \quad (19)$$

In particular, the first order conditional moment, namely the optimal estimator of filtering is written as

$$d\langle Z_t \rangle_t = \langle F_t^c(Z_t) \rangle_t dt + K_t dv_t, \quad (20)$$

in which

$$K_t = \langle \tilde{Z}_t \tilde{H}_t^T(Z_t) \rangle_t (R_t R_t^T)^{-1}, \quad (21)$$

$$\tilde{Z}_t = Z_t - \langle Z_t \rangle_t, \quad (22)$$

where \tilde{Z}_t is the estimation error vector. The differential form which governs the conditional expectation of a scalar-valued function $\phi(\tilde{Z}_t)$ of the error vector is given as follows:

$$d\langle \phi(\tilde{Z}_t) \rangle_t = \langle L_{\tilde{Z}} \phi(\tilde{Z}_t) \rangle_t dt + \left\{ \langle \phi(\tilde{Z}_t) \tilde{H}_t^T(Z_t) \rangle_t (R_t R_t^T)^{-1} - \left\langle \frac{\partial^T}{\partial \tilde{Z}_t} \phi(\tilde{Z}_t) \right\rangle_t K_t \right\} dv_t, \quad (23)$$

where

$$L_{\tilde{Z}} \varphi_t = \frac{1}{2} G'_{t\kappa\nu} \varphi_{t,\kappa\nu} + F'_{t\kappa} \varphi_{t,\kappa\nu}, \quad (24)$$

$$G'_t = G_t G_t^T + K_t R_t R_t^T K_t^T, \quad (25)$$

$$F'_t = \tilde{F}_t(Z_t) - K_t \tilde{H}_t(Z_t), \quad (26)$$

$$\tilde{F}_t(Z_t) = F_t(Z_t) - \langle F_t(Z_t) \rangle_t = \tilde{F}_t^c(Z_t). \quad (27)$$

By defining the higher order conditional central moment function as

$$\tilde{M}(l_1, l_2, \dots, l_n; t) = \left\langle \prod_{i=1}^n \tilde{Z}_{ii}^{l_i} \right\rangle_t, \quad \text{for } \sum_{i=1}^n l_i \geq 2, \quad (28)$$

the higher order conditional central moment equation is derived from (22) as

$$\begin{aligned} d\tilde{M}(l_1, l_2, \dots, l_n; t) = & \sum_{i=1}^{n-1} \sum_{j=i+1}^n l_i l_j G'_{ij} \left\langle \tilde{Z}_{ii}^{-1} \tilde{Z}_{ij}^{-1} \prod_{s=1}^n \tilde{Z}_{ts}^{l_s} \right\rangle_t dt \\ & + \frac{1}{2} \sum_{i=1}^n l_i (l_i - 1) G'_{iii} \left\langle \tilde{Z}_{ii}^{-2} \prod_{s=1}^n \tilde{Z}_{ts}^{l_s} \right\rangle_t dt \\ & + \sum_{i=1}^n l_i \left\langle F'_{ii}(Z_t) \tilde{Z}_{ii}^{-1} \prod_{s=1}^n \tilde{Z}_{ts}^{l_s} \right\rangle_t dt \\ & + \sum_{i=1}^k \left\langle \tilde{H}_i(Z_t) \prod_{s=1}^n \tilde{Z}_{ts}^{l_s} \right\rangle_t (R_t R_t^T)^{-1} dv_t, \end{aligned} \quad (29)$$

with

$$\tilde{M}(l_1, l_2, \dots, l_n; t) = 0 \quad \text{for } \sum_{i=1}^n l_i = 1,$$

$$\tilde{M}(0, 0, \dots, 0; t) = 1.$$

In order to evaluate the conditional expectations in the right-hand sides of (21) and (29) and to close the conditional moment equations given by (21) and (29), the time-dependent joint conditional probability density function is definitely required. An approximate probability density function expressed in the form of a finite mixed type orthogonal series expansion depending on the property and range of each state variable may be efficient. Such approximate probability density functions have been utilized in the stochastic response analyses, reliability analyses and stochastic estimation (Suzuki & Minai 1985, 1988b, 1989; Minai & Suzuki 1987). With the cooperation of the appropriate conditional probability density function the closed set of conditional moment equations can be written in the following vector-matrix form:

$$dS_t^N = P_t^c(S_t^N)dt + Q_t(S_t^N)dv_t, \quad (30)$$

where the set S_t^N denotes the full set of the conditional moment functions which are needed to prescribe the approximate conditional probability density function, and P_t^c and Q_t are considered as the drift vector and diffusion matrix, respectively.

4. Stochastic estimate-based optimal control

The stochastic optimum control of a nonlinear dynamic system may be formulated as the minimizing problem of a prescribed cost functional subject to the constraints of the system and observation equations in order to find the optimum control function expressed in terms of the stochastic estimate S_t . A typical cost functional is given by

$$J(u_s, y_0) = E \left\{ \Phi_T(Z_T) + \int_{t_0}^T L_s(Z_s, u_s) ds \mid y_0 \right\}, \quad (31)$$

where u_s is a vector-valued control function, T is the end time of control, and $L_s(Z_s, u_s)$ and $\Phi_T(Z_T)$ are a real-valued nonnegative convex cost density function and concentrated

cost function at T , respectively. The initial observation y_0 may be equivalent to the initial condition Z_0 of the state vector. Here the control function is confined to be a function of stochastic estimate S_t which is the full set S_t^N of the conditional moment functions or its subset, that is

$$u_t = C_t(S_t), \quad (32)$$

for $S_t \subseteq S_t^N$. The minimum value function associated with the cost functional defined by (31) is written in the following form:

$$V_t(y_0) = \min_{\substack{C_s(S_s) \\ s \in [t_0, T]}} E \left\{ \Phi_T(Z_T) + \int_{t_0}^T L_s(Z_s, u_s) ds \mid y_0 \right\}, \quad (33)$$

for $t_0 \leq t < T$. By supposing that the minimum value function $V_t(y_t)$ is denoted as $V_t(S_t^N)$ and the admissible control function is given by $C_t(S_t^N)$, the Bellman equation which governs the minimum value function as well as the optimality law of control is derived in the following form:

$$\min_{C_t(\xi)} \left[\langle L_t(Z_t, C_t(\xi)) \rangle_t \Big|_{S_t^N = \xi} + \left(\frac{\partial}{\partial t} + L_\xi \right) V_t(\xi) \right] = 0, \quad (34)$$

with the end condition

$$V_t(\xi) = \langle \Phi_T(Z_T) \rangle_T \Big|_{S_t^N = \xi}, \quad (35)$$

where

$$L_\xi \varphi_t = \frac{1}{2} (Q_t(\xi) (R_t R_t^T) Q_t^T(\xi))_{\kappa\nu} \varphi_{t,\kappa\nu} + P_{t\kappa}^c(\xi) \varphi_{t,\kappa}, \quad (36)$$

which is the Kolmogorov backward differential operator associated with (30).

In this case, since $S_t = S_t^N$, the Bellman equation (34) is closed in the sense that all the coefficient functions are determined as the definite functions of time, and the optimal control function $C_t^*(S_t^N)$ and the minimal value of the cost function $V_0(S_0^N)$ may be obtained by solving (34) backward independently from the stochastic estimation procedure (Wonham 1968).

In the case where the admissible control functions are defined as functions of a subset S_t' of S_t^N and the minimum value function is supposed to be expressed as $V_t(S_t')$ which may contain unknown coefficient functions, the same derivation procedure as that of (34) may bring formally the following equation:

$$\min_{C_t(\xi)} \left[\langle L_t(Z_t, C_t(\xi)) \rangle_t \Big|_{S_t' = \xi} + \left(\frac{\partial}{\partial t} + L_\xi \right) V_t(\xi) \right] = 0, \quad (37)$$

with the end condition

$$V_t(\xi) = \langle \Phi_T(Z_T) \rangle_T \Big|_{S_t' = \xi}, \quad (38)$$

in which L_ξ takes the same form as in (36), but is a formal backward differential operator concerning the following stochastic differential equation:

$$dS_t' = P_t^c(S_t') dt + Q_t(S_t') dv_t. \quad (39)$$

For nonlinear system and observation equations, it is clear that (37) is not closed, in general, for the case where $S_t = S_t' \subset S_t^N$. In order to complete the Bellman equation given by (37) the unknown coefficient functions, which may depend on the complementary set of

S_t^N with respect to S_t^N , are to be determined in cooperation with both filtering and prediction procedures.

The Bellman equation given by (34) or (37) may concern with the optimal control law and determination of the minimal value function. In the Bellman equation the control function appears in the first term and drift term of $L_\xi V_t(\xi)$. But dividing the coefficient function $P_t^c(\xi)$ appearing in L_ξ into two parts,

$$P_t^c(\xi) = {}^1P_t(\xi) + {}^2P_t(\xi), \quad (40)$$

where ${}^1P_t(\xi)$ is independent of the control function whereas ${}^2P_t(\xi)$ depends on the control function, the optimality law of control may be given by

$$\frac{\partial}{\partial C_t} \langle L_t(Z_t, C_t(\xi)) \rangle_t |_{S_t = \xi} + \frac{\partial}{\partial C_t} {}^2P_t(\xi) \frac{\partial}{\partial \xi} V_t(\xi) = 0 \quad (41)$$

As indicated in (1) to (4), (20) and (29), the explicit form ${}^2P_t(\xi)$ is $B_t C_t(\xi)$ which is concerned only with the first order conditional moment equations. If the vector-valued optimal control function $C_t^*(\xi)$ is found from (41) in terms of the minimum value function or its derivatives, substitution of this optimal control function into (34) or (37) may yield the reduced Bellman equation which is a nonlinear partial differential equation governing the minimum value function $V_t(\xi)$. By solving the reduced Bellman equation backward to obtain $V_t(\xi)$ and by replacing ξ with S_t , the optimal control function is determined as a function of conditional moment functions concerning filtering. Further substitution of the optimum control function in (1) to (4) completes the system and observation equations of the controlled structural system.

As a simple but most practical performance criterion, consider the case where the cost functional is a quadratic form and $S_t = \langle Z_t \rangle_t$. That is, the cost functional is written as

$$J(u_s, y_0) = E \left\{ Z_T^T \psi Z_T + \int_{t_0}^T (Z_s^T M_s Z_s + u_s^T N_s u_s) ds | y_0 \right\}, \quad (42)$$

and an admissible control function belongs to a class of functions of the optimal estimator as follows:

$$u_s = C_s(\langle Z_t \rangle_t), \quad (43)$$

where M_s and N_s are $n \times n$ nonnegative and $s \times s$ positive definite weight matrices for the state and control vectors, respectively, ψ is an $n \times n$ concentrated weight matrix at the end time of control. For this special case, the solution to the optimality condition given by (42) is determined as

$$C_t^*(\xi_1) = -\frac{1}{2} N_t^{-1} B_t^T \frac{\partial}{\partial \xi_1} V_t(\xi_1), \quad (44)$$

and the Bellman equation is reduced to

$$\begin{aligned} \frac{\partial}{\partial t} V_t(\xi_1) + \xi_1^T M_t \xi_1 + \text{tr}[M_t \langle \tilde{Z}_t \tilde{Z}_t^T \rangle_t] + {}^1P_t^T(\xi_1) \frac{\partial}{\partial \xi_1} V_t(\xi_1) \\ + \frac{1}{2} \text{tr} \left[Q_t(\xi_1) (R_t R_t^T) Q_t^T(\xi_1) \frac{\partial}{\partial \xi_1} \frac{\partial}{\partial \xi_1} V_t(\xi_1) \right] \\ - \frac{1}{4} \frac{\partial^T}{\partial \xi_1} V_t(\xi_1) B_t N_t^{-1} B_t^T \frac{\partial}{\partial \xi_1} V_t(\xi_1) = 0, \end{aligned} \quad (45)$$

with the end condition

$$V_T(\xi_1) = \xi_1^T \psi \xi_1 + \text{tr}[\psi \langle \tilde{Z}_T \tilde{Z}_T^T \rangle_T], \quad (46)$$

where

$${}^1P_t^T(\xi_1) = \langle F_t(Z_t) \rangle_t |_{\langle Z_t \rangle_t = \xi_1}, \quad (47)$$

$$Q_t(\xi_1) = K_t |_{\langle Z_t \rangle_t = \xi_1} = \langle \tilde{Z}_t \tilde{H}_t^T(Z_t) \rangle_t |_{\langle Z_t \rangle_t = \xi_1} (R_t R_t^T)^{-1}. \quad (48)$$

In the above equations, ξ_1 is the n -dimensional spatial vector corresponding to the first order conditional moment functions, $\partial/\partial \xi_1$ means the gradient operator with respect to ξ_1 and $\text{tr}[\cdot]$ means the trace of matrix.

The reduced Bellman equation and the end condition given by (45) and (46) contain undetermined coefficient functions. If the approximate conditional probability density function is described in terms of the conditional moment functions up to the N th order to solve the stochastic estimation, the order N is generally larger than one which is the highest order in S_t for this special case. Therefore the undetermined functions, which are expressed in terms of the higher order conditional moment functions of the order from 2 to N , may be determined by means of the stochastic estimation including both filtering and prediction scheme. By referring to the solution technique for linear quadratic systems, the Bellman equation for the nonlinear quadratic systems may be converted to extended Riccati equations if the coefficient functions in the Bellman equation could be expressed by polynomials or by expanding them in a finite power series of the spatial variables.

5. Simplified, approximate solution procedures

In applying the stochastic estimate-based optimal control techniques in the preceding sections to large complex structural systems such as hysteretic multi-degree-of-freedom structural systems, it may be necessary to simplify the whole procedure, specifically the closure technique of the conditional moment equations and the solution method for the reduced Bellman equation or its associated extended Riccati equations.

As a practical method, the stochastic linearization of nonlinear functions appearing in the system and observation equations is considered. The vector-valued nonlinear function $F_t(Z_t)$ in (3) is linearized as follows:

$$F_t(Z_t) \cong f_t Z_t + f_t^0, \quad (49)$$

where f_t and f_t^0 are, respectively, $n \times n$ matrix and n -vector linearization coefficients. These coefficients are determined so that the conditional expectation of the square norm of n -vector difference between the actual nonlinear function and the equivalent linear function is minimized (Sunahara 1987). That is

$$\min_{f_t, f_t^0} \langle \|\varepsilon_t\|^2 \rangle_t, \quad (50)$$

where

$$\varepsilon_t = F_t(Z_t) - (f_t Z_t + f_t^0). \quad (51)$$

Then the linearization coefficients f_i and f_i^0 are given by

$$f_i = \langle \tilde{F}_i(Z_i) \tilde{Z}_i^T \rangle_i \langle \tilde{Z}_i \tilde{Z}_i^T \rangle_i^{-1}, \quad (52)$$

$$f_i^0 = \langle F_i(Z_i) \rangle_i - \langle \tilde{F}_i(Z_i) \tilde{Z}_i^T \rangle_i \langle \tilde{Z}_i \tilde{Z}_i^T \rangle_i^{-1}. \quad (53)$$

The stochastic linearization under Gaussian assumption is effective for weakly nonlinear dynamic systems. In this case the coefficient f_i is especially given by

$$f_i = \left\langle \frac{\partial}{\partial Z_i} F_i^T(Z_i) \right\rangle_i^T. \quad (54)$$

In the same way, the nonlinear function $H_i(Z_i)$ in (4) is linearized as $h_i Z_i + h_i^0$.

In particular, consider the nonlinear function $g_i(\dot{x}_i, z_i)$, given by (7), which appears in the differential representation of the bilinear hysteretic constitutive law. Here the suffix i means the i th bilinear hysteretic component and $g_i(\dot{x}_i, z_i)$ is linearized in terms of \dot{x}_i and z_i . Since the range of the hysteretic component z_i is $[-\delta_i, \delta_i]$, it is evident that the probability density function of z_i is quite dissimilar to the normal density function whereas the probability distributions of the displacement x_i and velocity \dot{x}_i are relatively close to the normal distribution. A non-Gaussian linearization is to be performed to take account of the non-Gaussian property of z_i . The conditional joint probability density function $p_i(\dot{x}_i, z_i | y_i)$ may be approximated by the following form (Kobori *et al* 1976; Suzuki & Minai 1989):

$$p_i(\dot{x}_i, z_i | y_i) = D_i w_N(\dot{x}_i, z_i | y_i), \quad (55)$$

$$D_i(\cdot) = [U(z_i + \delta_i) - U(z_i - \delta_i) + \delta(z_i + \delta_i) \int_{-\infty}^{-\delta_i} d\zeta_i + \delta(z_i - \delta_i) \int_{\delta_i}^{\infty} d\zeta_i](\cdot), \quad (56)$$

where D_i denotes the folding operator which is introduced to take account of the spikes of the probability density function concerning the state variable z_i at the boundaries and w_N is the joint normal density function. In this case the conditional expectations including the nonlinear term g_i can be expressed in terms of the conditional moment functions up to the second order. It is noted that the covariance matrix prescribing the normal probability density function is different from the conditional covariance matrix with respect to \dot{x}_i and z_i , and the transformation between them is needed.

If the admissible control function is described as a function of the optimal estimator, the linearized system and observation equations are written as

$$dZ_i = \{f_i Z_i + f_i^0 + B_i C_i(\langle Z_i \rangle_i)\} dt + G_i dW_i, \quad (57)$$

$$dY_i = \{h_i Z_i + h_i^0 + D_i C_i(\langle Z_i \rangle_i)\} dt + R_i dV_i, \quad (58)$$

where as in (5) W_i and V_i are assumed to be incrementally uncorrelated normalized Wiener processes. The conditional moment equations for filtering are closed within the second order, and are obtained simply from (20) and (29) as follows:

$$d\langle Z_i \rangle_i = \{f_i \langle Z_i \rangle_i + f_i^0 + B_i C_i(\langle Z_i \rangle_i)\} dt + \langle \tilde{Z}_i \tilde{Z}_i^T \rangle_i h_i^T (R_i R_i^T)^{-1} dv_i, \quad (59)$$

$$d\langle \tilde{Z}_i \tilde{Z}_i^T \rangle_i = \{f_i \langle \tilde{Z}_i \tilde{Z}_i^T \rangle_i + \langle \tilde{Z}_i \tilde{Z}_i^T \rangle_i f_i^T + G_i G_i^T - \langle \tilde{Z}_i \tilde{Z}_i^T \rangle_i h_i^T (R_i R_i^T)^{-1} h_i \langle \tilde{Z}_i \tilde{Z}_i^T \rangle_i\} dt, \quad (60)$$

where

$$dv_i = dY_i - \{h_i \langle Z_i \rangle_i + h_i^0 + D_i C_i(\langle Z_i \rangle_i)\} dt. \quad (61)$$

The functional form of $V_t(\xi_1)$ for the linearized system can be expressed in the quadratic form

$$V_t(\xi_1) = \xi_1^T \alpha_t \xi_1 + 2\xi_1^T \beta_t + \gamma_t. \quad (62)$$

The associated Riccati equations are given by

$$\dot{\alpha}_t + M_t + f_t^T \alpha_t + \alpha_t f_t - \alpha_t B_t N_t^{-1} B_t^T \alpha_t = 0, \quad (63)$$

$$\dot{\beta}_t + \alpha_t f_t^0 - \alpha_t B_t N_t^{-1} B_t^T \beta_t = 0, \quad (64)$$

$$\begin{aligned} \dot{\gamma}_t + \text{tr}[M_t \langle \tilde{Z}_t \tilde{Z}_t^T \rangle_t] + \text{tr}[\langle \tilde{Z}_t \tilde{Z}_t^T \rangle_t h_t^T (R_t R_t^T)^{-1} h_t \langle \tilde{Z}_t \tilde{Z}_t^T \rangle_t \alpha_t] \\ + 2(f_t^0)^T \beta_t - \beta_t^T B_t N_t^{-1} B_t^T \beta_t = 0, \end{aligned} \quad (65)$$

with the end conditions

$$\alpha_T = \Psi, \quad (66)$$

$$\beta_T = 0, \quad (67)$$

$$\gamma_T = \text{tr}[\Psi_T \langle \tilde{Z}_T \tilde{Z}_T^T \rangle_T]. \quad (68)$$

The optimal control function is given by

$$C_t^*(\langle Z_t \rangle_t) = -N_t^{-1} B_t^T (\alpha_t \langle Z_t \rangle_t \beta_t). \quad (69)$$

It is noted that the linearization coefficients f_t , f_t^0 , h_t and h_t^0 are to be determined on the basis of stochastic estimate. Hence, in order to solve the Riccati equations given by (63) through (65) in the backward direction from the specified end time T to the current time, the linearization coefficients as well as the conditional moment functions $\langle Z_t \rangle_t$ and $\langle \tilde{Z}_t \tilde{Z}_t^T \rangle_t$ are to be determined in the future time interval (t, T) through filtering and prediction.

To avoid the prediction procedure the Riccati equations given by (63) and (64) are solved in quasi-stationary state in which the time-rate terms are neglected. This approximation may be supported by the slowly varying excitation and system parameters and fast converging properties of α_t and β_t with respect to time. Under the quasi-stationary assumption, the matrix α_t is reduced to the solution to the following time-dependent nonlinear algebraic equation:

$$M_t + f_t^T \alpha_t + \alpha_t f_t - \alpha_t B_t N_t^{-1} B_t^T \alpha_t = 0, \quad (70)$$

If the solution α_t to (70) is obtained, the quasi-stationary solution β_t and the associated solution γ_t to (65) are successively given by

$$\beta_t = (\alpha_t B_t N_t^{-1} B_t^T - f_t^T)^{-1} \alpha_t f_t^0, \quad (71)$$

$$\begin{aligned} \gamma_t = \text{tr}[\psi \langle \tilde{Z}_T \tilde{Z}_T^T \rangle_T] + \int_t^T \{ \text{tr}[M_s \langle \tilde{Z}_s \tilde{Z}_s^T \rangle_s] \\ + \text{tr}[\langle \tilde{Z}_s \tilde{Z}_s^T \rangle_s h_s^T (R_s R_s^T)^{-1} h_s \langle \tilde{Z}_s \tilde{Z}_s^T \rangle_s \alpha_s] \\ + 2(f_s^0)^T \beta_s - \beta_s^T B_s N_s^{-1} B_s^T \beta_s \} ds. \end{aligned} \quad (72)$$

The optimal control function is determined from (69) by making use of the solutions to the quasi-stationalized Riccati equations.

The above mentioned method for stochastic estimate-based optimal control has the advantage of the simplicity in the analytical and computational procedures. On

the other hand, the method may be inapplicable to the case of strongly nonlinear dynamic systems, since the stochastic linearization may not be available, especially the Gaussian assumption of the conditional probability density function may no longer be valid, and since the slowly varying and rapid convergence properties of the solution to the Riccati equations, may be lost in this case. From the practical point of view, however the combined method based on the stochastic linearization and quasi-stationalization techniques may be sufficiently effective since most cases of structural control may aim at suppressing the dynamic responses within or around the elastic limit deformations.

6. Concluding remarks

The stochastic estimate-based optimal control for hysteretic structural systems has been presented from a methodological point of view. The stochastic estimate and optimal control system may be described as a closed-loop system consisting of a nonlinear dynamic system including hysteretic characteristics subjected to the optimal control forces and stochastic excitations, an observer with a stochastic estimation scheme to identify the full state of system and excitations and a controller having a stochastic optimization scheme to minimize a prescribed cost function. The system and observation equations are expressed in the form of the Itô stochastic differential equations on the basis of the theory of continuous Markov vector processes. The admissible control functions are supposed to belong to a class of functions of stochastic estimates, which mean a set of conditional moment functions given observation data, and the cost function is assumed to be the conditional expectation of an integral type functional with a concentrated cost at the end time of control given initial data.

For a general class of nonlinear dynamic systems, if the admissible control functions are defined as functions of the full set of conditional moment functions appearing in the approximate conditional probability density function, the Bellman equation as well as the reduced Bellman equation are closed in the sense that they could be solved independently of the stochastic estimation procedure. Otherwise the Bellman equation is coupled with the conditional moment equations for filtering and prediction. As a rule, the coefficient functions appearing in the Bellman equation or reduced Bellman equation could be expressed as analytic functions of the conditional moment functions. For a general class of nonlinear dynamic systems including hysteretic structural systems, however, the solution to the Bellman equation may not be obtained without any approximation. A possible solution procedure to this problem is to approximate the coefficient functions in the Bellman equation by polynomials or by a finite power series expansion of the spatial variables corresponding to a set of conditional moment functions, the reduced Bellman equation is then converted to the associated extended Riccati equations which are, in general, to be simultaneously solved with the conditional moment equations for filtering and prediction. Only for the case of the closed Bellman equation, the associated extended Riccati equations are solved independently of the conditional moment equations as in the case of linear quadratic systems.

From a practical point of view, in order to apply the stochastic estimate-based optimal control scheme to large complex structural systems, an approximate procedure based on the stochastic linearization and quasi-stationalization techniques has

been discussed and found to be effective for a class of weakly nonlinear dynamic systems (Kawamoto *et al* 1990). For strongly nonlinear dynamic systems the more accurate approximate methods are to be explored on the basis of higher order conditional moment equations than second. If the excitation is measurable with observation noise, the measured excitation term is added to the drift term of the system equation and its noise term is replaced by the observation noise of excitation. This slight modification maintains almost the same solution procedures as in the case of stochastic excitations. The observation of excitation is effective to simplify the stochastic estimation procedure since it is not necessary to identify dynamic systems generating the excitation.

The main concerns of the present paper have been in the formulation of the stochastic estimate-based optimal control of nonlinear dynamic systems including hysteretic structural systems, and the solution techniques of the conditional moment equations concerning the observer and of the Bellman equation or the extended Riccati equations associated with the controller. There might remain, however, a number of matters to be further examined from analytical and computational aspects, for example stochastic modeling of excitations and structural system, effective non-Gaussian closure methods for conditional moment equations depending on the properties of nonlinear functions in system and observation equations, and appropriate solution techniques for the Bellman equation or the extended Riccati equations under constraint performance criteria.

References

- Baber T T, Wen Y K 1981 Random vibration of hysteretic, degrading systems. *J. Eng. Mech. ASCE* 107: 1069–1087
- Bellman R F 1957 *Dynamic programming* (Princeton, NJ: University Press)
- Gikhman I I, Skorokhod 1972 *Stochastic differential equations* (Berlin: Springer-Verlag)
- Jazwinski A H 1970 *Stochastic processes and filtering theory* (New York: Academic Press)
- Kawamoto Y, Suzuki Y, Minai R 1990 Stochastic control of hysteretic structures. Reports of Architectural Institute of Japan, Kinki Sub-division, pp 441–444 (in Japanese)
- Kobori T, Minai R, Suzuki Y 1976 Stochastic seismic response of hysteretic structures. *Bull. Disaster Prevention Res. Inst.* 26: 55–70
- Kushner H J 1967 *Stochastic stability and control* (New York: Academic Press)
- Leipholtz H H E, Abdel-Rohman M 1986 *Control of structures* (Dordrecht: Martinus Nijhoff)
- Minai R, Suzuki Y 1987 Stochastic estimates of nonlinear dynamic systems. *Proceedings of U.S.-Japan Joint Seminar. Lecture Notes in Engineering* (eds) Y K Lin, R Minai (Berlin: Springer-Verlag) pp 204–230
- Sunahara Y 1970 An approximate method of state estimation for nonlinear dynamical systems. *J. Basic Eng., ASME* 92: 385–393
- Sunahara Y 1987 Recent trends of estimation-control theory of nonlinear stochastic systems and its applications. *Proceedings of the Second IFAC Symposium: Stochastic control* (eds) N K Sinha, L A Telksnys (Oxford: Pergamon) pp 1–6
- Suzuki Y, Minai R 1985 Seismic reliability analysis of hysteretic structures based on stochastic differential equations. *Proceedings of the Fourth International Conference on Structural Safety and Reliability* 25: 177–186
- Suzuki Y, Minai R 1988a Application of stochastic differential equations to seismic reliability analysis of hysteretic structures. *Probabilistic Eng. Mech.* 3: 43–52
- Suzuki Y, Minai R 1988b Seismic damage and reliability analysis of hysteretic multi-degree-of-freedom structures. *Proceedings of the Ninth World Conference on Earthquake Engineering* 8: 773–778

- Suzuki Y, Minai R 1989 Seismic reliability analysis of hysteretic structural systems. *Computational mechanics of probabilistic and reliability analysis* (eds) W K Liu, T Belytschko (Lausanne: Elmepress International) pp 510–541
- Wen Y K 1976 Method for random vibration of hysteretic systems *J. Eng. Mech. ASCE* 102: 249–263
- Wonham W M 1968 On the separation theorem of stochastic control. *SIAM J. Control* 6: 312–326
- Yang J N 1975 Application of optimal control theory to civil engineering structures. *J. Eng. Mech. ASCE* 101: 819–838
- Yao J T P 1972 Concept of structural control. *J. Struct. Eng., ASCE* 98: 1567–1574

Active control of non-stationary response of a two-degree of freedom vehicle model with nonlinear suspension

G V RAJU¹ and S NARAYANAN²

¹Department of Mechanical Engineering, SRKR Engineering College, Bhimavaram 534 202, India

²Department of Applied Mechanics, Indian Institute of Technology, Madras 600 036, India

Abstract. Active control of non-stationary response of a two-degree of freedom vehicle model with nonlinear passive suspension elements is considered in this paper. The method of equivalent linearization is used to derive an equivalent linear model and optimal control laws are obtained by using stochastic optimal control theory based on full state information. Velocity squared quadratic damping and hysteretic type of stiffness nonlinearities are considered. The effect of the nonlinearities on the active system performance is studied. The performance of active suspensions with nonlinear passive elements is found to be superior to the corresponding passive suspension systems.

Keywords. Nonlinear vehicle model; stochastic linearization; optimal control; nonstationary response.

1. Introduction

In recent years considerable interest has been generated in the use of active vehicle suspensions which can improve the performance of the vehicle compared to the passive suspension systems. Many of the works reported in the literature are concerned with the active control of the stationary response of vehicle models with a constant velocity traverse. There are many situations in which the response of the vehicle becomes non-stationary, examples being (a) when it traverses a nonhomogeneous road profile at constant or variable velocity, (b) when the vehicle traverses a homogeneous rough road with variable velocity, and (c) when the vehicle traversing a smooth road suddenly encounters a homogeneous rough road at constant velocity. The problem of control of non-stationary response of linear single degree of freedom (sdf) and two-degree of freedom (2-dof) vehicle models with active suspensions including full state and partial state feedback in the cases (b) and (c) mentioned above has been treated by Narayanan & Raju (1990, 1991).

The suspension systems of a large class of road vehicles consist of a combination of coil and/or leaf springs and dampers. Normally in the vibration analysis of vehicle

systems, these are modelled as linear springs and dampers for simplicity of analysis. In reality, however, the force-deformation characteristics of these springs exhibit non-linear behaviour especially of the hysteretic type. Therefore, for a realistic vehicle dynamic model it is necessary to take into consideration the nonlinearities in the passive suspension systems. In vehicular vibration problems nonlinearities in the suspensions have been taken into consideration in the vibration analysis by Kirk & Perry (1970), Kirk (1971), Yadav & Nigam (1978), in the context of landing gear response to runway unevenness, and by Rill (1983), Harrison & Hammond (1986a), Narayanan (1987), and El Madany (1987) in the context of response of road vehicles to random road undulations. All these works considered only passive suspensions. The active control of non-stationary response of a single degree of freedom vehicle model with nonlinear passive suspension elements has been considered for the first time by Narayanan & Raju (1991).

In this paper, the active control of non-stationary response of a 2-dof quarter car vehicle model with nonlinear passive elements such as quadratic dampers and hysteretic type stiffness elements, due to variable velocity traverse is considered. The method of equivalent linearization is used to derive the linearized equations of motion for the vehicle model. The hysteretic nature of the suspension spring is modelled by a modified Bouc's (1967) model in which the restoring force of the spring is assumed to be a combination of pre-yielding and hysteretic components. The stochastic optimal control theory is applied to the linearized vehicle model in the deriving optimal control law based on full state information. Since the equivalent linear spring and damping coefficients of the linearized model are functions of the response statistics of the vehicle, an iterative scheme is required in computing the optimal control gains and response statistics. The performance of the active system is compared with that of a passive system in terms of ride comfort, suspension stroke, roadholding and control efforts.

2. Road input model

Taking into account the rolling contact of the tyre with the road surface, the variable $h(s)$ representing the road input displacement in space domain, is governed by the second order filter in spatial domain given by (Harrison & Hammond 1986a)

$$h''(s) + (\alpha + \beta)h'(s) + \alpha\beta h(s) = \Gamma w(s), \quad (1)$$

where the number of primes denotes the order of differentiation with respect to the space variable s representing the traverse along the rough road, and α and β respectively are the cutoff wave numbers of the road profile and rolling contact filters, σ^2 is the variance of true road profile and $w(s)$ is the spatial white noise excitation with autocorrelation function given by

$$E[w(s_2)w(s_1)] = \mathbf{Q}\delta(s_2 - s_1), \quad (2)$$

where \mathbf{Q} is the intensity of the white noise taken to be unity, $\delta(\cdot)$ is the Dirac delta function and $\Gamma = \beta\sigma(2\alpha)^{1/2}$.

Defining $h_1(s) = h(s)$ and $h_2(s) = h'(s)$, (1) can be put in state variable form in the space domain as

$$h_1'(s) = h_2(s), \quad (3a)$$

$$h_2'(s) = -(\alpha + \beta)h_2(s) - \alpha\beta h_1(s) + \Gamma w(s). \quad (3b)$$

Considering s as a function of time, the variables $h_1(s)$ and $h_2(s)$ which are functions of the space variable s can be regarded as functions of time, that is, $h_1(s(t)) = \tilde{h}_1(t)$, $h_2(s(t)) = \tilde{h}_2(t)$. It is assumed that the functional form of s is restricted such that $\dot{s}(t) \geq 0$ and $\dot{s}(t)$ vanishes only at isolated times t_i .

Noting that $d(\cdot)/ds = (dt/ds) \cdot (d(\cdot)/dt)$, one can express (3a) & (3b) in the form

$$\dot{\tilde{h}}_1(t) = \dot{s}(t) \tilde{h}_2(t), \quad (4a)$$

$$\dot{\tilde{h}}_2(t) = -\dot{s}(t)(\alpha + \beta) \tilde{h}_2(t) - \dot{s}(t) \alpha \beta \tilde{h}_1(t) + (\dot{s}(t))^{1/2} \Gamma w_1(t). \quad (4b)$$

In (4b) the delta function property $\delta(s(t)) = \delta(t - t_i)/|\dot{s}(t)|$ (Zadeh & Desoer 1963), has been made use of with the parameterized white noise process $w(s(t))$ being equivalent in a covariance sense to the white noise process $w_1(t)/(\dot{s}(t))^{1/2}$ (Harrison & Hammond 1986b), with autocorrelation function $E[w_1(t_1)w_1(t_2)] = Q\delta(t_2 - t_1)$.

For variable velocity traverse of the vehicle, (4a) and (4b) are with time varying coefficients. Consequently the road input $\tilde{h}_1(t)$ becomes non-stationary and so also the response statistics of the vehicle model.

3. Vehicle equations of motion

The 2-dof quarter car vehicle model with quadratic damping and hysteretic stiffness between the sprung and unsprung masses is shown in figure 1. M is the sprung mass, m is the unsprung mass, c is the coefficient of linear viscous damping, c_1 is the coefficient of nonlinear quadratic damper, α_1 and k are the hysteretic suspension spring parameters, and k_t is the tyre stiffness.

The dynamics of the nonlinear 2-dof vehicle model can be represented by the equations of motion:

$$M\ddot{y}_1 + c\dot{q} + c_1|\dot{q}|\dot{q} + \alpha_1 kq + (1 - \alpha_1)kz - u = 0, \quad (5)$$

$$m\ddot{y}_2 - c\dot{q} - c_1|\dot{q}|\dot{q} - \alpha_1 kq - (1 - \alpha_1)kz + k_t(y_2 - \tilde{h}_1) + u = 0, \quad (6)$$

where $q = y_1 - y_2$ is the relative displacement between the sprung and unsprung masses, y_1 and y_2 respectively, are absolute displacements of the sprung and unsprung

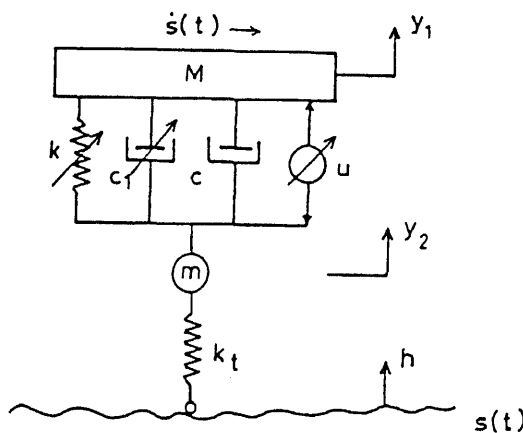


Figure 1. Two-degree of freedom nonlinear vehicle model.

masses, \tilde{h}_1 is the filtered road input displacement to the vehicle model, and u is the control force. The parameter z representing the hysteretic displacements is given by the nonlinear differential equation (Wen 1980),

$$\dot{z} = -\gamma|\dot{q}|z|z|^{n-1} - \eta\dot{q}|z|^n + A\dot{q}. \quad (7)$$

In the above equation γ , η , A and n are parameters fitting the force-displacement characteristic of the hysteretic system. Parameters γ and η control the shape of the hysteretic loop, A the restoring force amplitude, and n the smoothness of transition from elastic to plastic response. In further analysis the exponent n is assumed to be unity without loss of generality. In the absence of hysteretic stiffness the equations of motion are obtained by setting $\alpha_1 = 1$ in (5) and (6). If the quadratic damping is absent we set $c_1 = 0$ in (5) and (6).

4. Equivalent linear system

A multidegree of freedom nonlinear dynamic system can be represented in the form,

$$\mathbf{M}\ddot{\mathbf{X}} + \mathbf{C}\dot{\mathbf{X}} + \mathbf{K}\mathbf{X} + \mathbf{g}(\mathbf{X}, \dot{\mathbf{X}}) = \mathbf{f}(t), \quad (8)$$

where \mathbf{X} is the state vector which includes z , the hysteretic displacement given by (7), and $\mathbf{g}(\mathbf{X}, \dot{\mathbf{X}})$ is the vector containing nonlinear elements. Let the system of equations (8) be replaced by the equivalent linear system of equations represented by

$$\mathbf{M}\ddot{\mathbf{X}} + \mathbf{C}^*\dot{\mathbf{X}} + \mathbf{K}^*\mathbf{X} = \mathbf{f}(t), \quad (9)$$

where

$$\mathbf{C}^* = \mathbf{C} + \mathbf{C}' \text{ and } \mathbf{K}^* = \mathbf{K} + \mathbf{K}', \quad (10)$$

\mathbf{C} and \mathbf{K} representing, respectively, the linear part of damping and stiffness matrices, and \mathbf{C}' and \mathbf{K}' are obtained by minimizing the mean square error $E[\mathbf{e}^T \mathbf{e}]$ where the vector \mathbf{e} is defined by

$$\mathbf{e} = \mathbf{g}(\mathbf{X}\dot{\mathbf{X}}) - \mathbf{C}'\dot{\mathbf{X}} - \mathbf{K}'\mathbf{X}. \quad (11)$$

Assuming the excitation vector $\mathbf{f}(t)$ to be a zero mean Gaussian random vector and since the system of equations (8) is linear, the response of the equivalent linear system can also be considered Gaussian. Under this condition, using the results of Iwan & Yang (1972), and Atalik & Utku (1976), it can be shown that the elements of the matrices \mathbf{C}' and \mathbf{K}' are given by

$$\mathbf{C}'_{ij} = E[\partial \mathbf{g}_i / \partial \dot{\mathbf{X}}_j], \quad (12)$$

$$\mathbf{K}'_{ij} = E[\partial \mathbf{g}_i / \partial \mathbf{X}_j]. \quad (13)$$

Using the above results the linearized equations of motion of the 2-dof vehicle model can be obtained as

$$M\ddot{y}_1 + (c + c_{eq})\dot{q} + \alpha_1 kq + (1 - \alpha_1)kz - u = 0, \quad (14)$$

$$m\ddot{y}_2 - (c + c_{eq})\dot{q} - \alpha_1 kq - (1 - \alpha_1)kz + k_t(y_2 - \tilde{h}_1) + u = 0, \quad (15)$$

$$\dot{z} + c_h\dot{q} + k_h z = 0, \quad (16)$$

where

$$c_{eq} = 2(2/\pi)^{1/2} c_1 \sigma_{\dot{q}}, \quad (17)$$

$$c_h = (2/\pi)^{1/2} [\gamma(E(\dot{q}_z)/\sigma_q) + \eta\sigma_2] - A, \quad (18)$$

$$k_h = (2/\pi)^{1/2} [\eta(E(\dot{q}_z)/\sigma_z) + \gamma\sigma_q]. \quad (19)$$

5. Optimal control of linearized vehicle model

Defining an augmented state vector as,

$$\mathbf{X}_a(t) = [x_1 \ x_2 \ x_3 \ x_4 \ x_5 \ x_6 \ x_7]^T,$$

where

$$x_1 = y_1, \ x_2 = \dot{y}_1, \ x_3 = y_2, \ x_4 = \dot{y}_2, \ x_5 = z, \ x_6 = \tilde{h}_1, \ x_7 = \tilde{h}_2,$$

the linearized equations of motion of the vehicle, [(14)–(16)], and the equations representing the filtered road input, (4a, b), can be combined to yield

$$\dot{\mathbf{X}}_a(t) = \mathbf{F}(t)\mathbf{X}_a(t) + \mathbf{G}(t)\mathbf{U}(t) + \mathbf{D}(t)\mathbf{W}(t), \quad (20)$$

where

$$\mathbf{F}(t) = \begin{bmatrix} \mathbf{F}_x & \mathbf{D}_x \\ \mathbf{0} & \mathbf{F}_D \end{bmatrix}, \quad \mathbf{G}(t) = \begin{bmatrix} \mathbf{G}_x \\ \mathbf{0} \end{bmatrix}, \quad \mathbf{D}(t) = \begin{bmatrix} \mathbf{0} \\ \mathbf{D}_d \end{bmatrix}, \quad (21)$$

$$\mathbf{F}_x(t) = \begin{bmatrix} 0 & 1 & 0 & 0 & 0 \\ -\frac{\alpha_1 k}{M} & -\frac{c + c_{eq}}{M} & \frac{\alpha_1 k}{M} & \frac{c + c_{eq}}{M} & \frac{(\alpha_1 - 1)k}{M} \\ 0 & 0 & 0 & 1 & 0 \\ \frac{\alpha_1 k}{m} & \frac{c + c_{eq}}{m} & -\frac{\alpha_1 k + k_t}{m} & -\frac{c + c_{eq}}{m} & \frac{(1 - \alpha_1)k}{m} \\ 0 & -c_h & 0 & c_h & -k_h \end{bmatrix},$$

$$\mathbf{D}_x(t) = \begin{bmatrix} 0 & 0 & 0 & k_t/m & 0 \\ 0 & 0 & 0 & 0 & 0 \end{bmatrix}^T, \quad \mathbf{F}_D(t) = \begin{bmatrix} 0 & \dot{s}(t) \\ -\alpha\beta\dot{s}(t) & -(\alpha + \beta)\dot{s}(t) \end{bmatrix},$$

$$\mathbf{G}_x(t) = [0 \ 1/M \ 0 \ -1/m \ 0]^T, \quad \mathbf{D}_d(t) = [0 \ \beta\sigma(2\alpha\dot{s}(t))^{1/2}]^T. \quad (22)$$

Optimal control law based on full state feedback is obtained by minimizing a weighted sum of the mean square values of sprung mass acceleration (J_1), suspension stroke (J_2), roadholding (J_3) and control forces (J_4) with corresponding weighting factors ρ_1 , ρ_2 , ρ_3 , and ρ_4 . Thus the performance index can be expressed as

$$J = E \left[\int_{t_0}^{t_1} (\rho_1 J_1 + \rho_2 J_2 + \rho_3 J_3 + \rho_4 J_4) dt \right]. \quad (23)$$

The overall performance index can be expressed in the standard form as (Kwakernaak & Sivan 1972)

$$J = E \left[\mathbf{X}_a(t_1) \mathbf{S}_1 \mathbf{X}_a^T(t_1) + \int_{t_0}^{t_1} [\mathbf{X}_a^T(t) \mathbf{U}^T(t)] \begin{bmatrix} \mathbf{A}(t) & \mathbf{N}(t) \\ \mathbf{N}^T(t) & \mathbf{B}(t) \end{bmatrix} \begin{Bmatrix} \mathbf{X}_a(t) \\ \mathbf{U}(t) \end{Bmatrix} dt \right], \quad (24)$$

where $E[\cdot]$ denotes expectation operator, $A(t)$ is symmetric positive semi-definite, $B(t)$ is positive definite, $S_1 = S(t_1)$ is symmetric final state weighting matrix, and $[t_0, t_1]$ is control period. The matrices $A(t)$, $N(t)$ and $B(t)$ which are functions of system parameters and the weighting factors are given in Raju (1991).

The optimal control law based on full state information has the form (Kwakernaak & Sivan 1972),

$$U(t) = -C(t)X_a(t), \quad (25)$$

in which $C(t)$ is the control gain vector given by

$$C(t) = B^{-1}[N^T + G^T S]. \quad (26)$$

$S(t)$ is symmetric and is the solution of the matrix differential Riccati equation

$$\begin{aligned} -\dot{S} = & S(F - GB^{-1}N^T) + (F - GB^{-1}N^T)^T S \\ & - SGB^{-1}G^T S + (A - NB^{-1}N^T), \end{aligned} \quad (27)$$

with the terminal condition $S(t_1)$.

The mean square value of the state $P(t) = E[X_a(t)X_a^T(t)]$ is given by the solution of the matrix differential Lyapunov equation

$$\dot{P}(t) = (F - GC)P(t) + P(t)(F - GC)^T + DQD^T, \quad (28)$$

with initial conditions $P(t_0)$.

In the problem considered here the system matrix $F(t)$ is a function of response statistics of the vehicle and the Riccati equation in turn is a function of system matrix $F(t)$. This means that in order to be able to solve the Riccati equation, the response statistics of the vehicle should be known *a priori*. This problem is overcome by an iterative procedure described in the sequel.

Iterative procedure

In this scheme control gains corresponding to the linear vehicle model are first computed over the entire period of control. These control gains are used in obtaining the response statistics of the nonlinear vehicle model. Then using the current response statistics of the nonlinear vehicle model, control gains are computed again over the period of control. This iterative procedure is repeated until the values of control gains and the response statistics at any particular time converge to a specified degree of accuracy. In the example considered here convergence was achieved with respect to the control gains and response statistics within 4 iterations.

6. Evaluation of performance measures

The mean square values of the sprung mass acceleration J_1 , suspension deflection J_2 , tyre deflection J_3 , and control force J_4 can be evaluated from the following relations.

$$J_1 = \sum_{i=1}^7 \sum_{j=1}^7 \{F(2,i) - C(i)/M\} \{F(2,j) - C(j)/M\} P_{ij}, \quad (29)$$

$$J_2 = P_{11} - 2P_{13} + P_{33}, \quad (30)$$

$$J_3 = P_{33} - 2P_{36} + P_{66}, \quad (31)$$

$$J_4 = \sum_{i=1}^7 \sum_{j=1}^7 C(i) C(j) P_{ij}. \quad (32)$$

7. Initial conditions

The initial conditions required in solving the Lyapunov equation (28) are obtained as in Raju & Narayanan (1991). The case of the vehicle starting from rest and moving with constant acceleration is considered in this study. The initial conditions for this case are given in the sequel.

For the homogeneous filtered road profile,

$$E[\tilde{h}_1^2] = \sigma^2 \beta / (\alpha + \beta) = P_{66}(0), \quad (33)$$

$$E[\tilde{h}_2^2] = \sigma^2 \alpha \beta^2 / (\alpha + \beta) = P_{77}(0). \quad (34)$$

Other initial conditions are

$$P_{11}(0) = P_{13}(0) = P_{16}(0) = P_{36}(0) = \sigma^2 \beta / (\alpha + \beta). \quad (35)$$

Since the zero-lag covariance matrix $\mathbf{P}(t)$ is symmetric

$$P_{13}(0) = P_{31}(0), P_{16}(0) = P_{61}(0), P_{63}(0) = P_{36}(0). \quad (36)$$

All other $P_{ij}(0)$ are identically equal to zero.

8. Results and discussion

The optimal control problem of the non-stationary response of a nonlinear 2-dof vehicle model is solved for the variable velocity run, corresponding to constant acceleration.

The numerical data used for the vehicle and road profile model are, $M = 267$ kg, $m = 36.6$ kg, $k = 18.7$ kN/m, $c = 1398$ Ns/m, $c_1 = 1000$ Ns/m, $k_t = 184$ kN/m, $\alpha = 0.15$ m, $\beta = 2.0$, $\sigma^2 = 75.69 \times 10^{-6}$ m².

The values of the parameters for the hysteretic type suspension spring model are chosen as $\alpha_1 = 0.2$, $\eta = \gamma = 0.5$, $A = 1.5$ and $n = 1.0$. The weighting factors used in the performance index are $\rho_1 = 1.0$, $\rho_2 = 10^3$, $\rho_3 = 10^4$, $\rho_4 = 10^{-6}$.

To bring out clearly the influence of different types of nonlinearities on the performance of passive and active systems, the results are plotted for the passive and active systems for the cases of (i) only quadratic damping, (ii) only hysteretic spring and (iii) a combination of both quadratic damping and hysteretic spring. The curves corresponding to these three cases in the case of passive suspension are respectively designated by (a), (b) and (c) and in case of corresponding active suspensions by (d), (e), and (f) where the active system is obtained based on full state feedback.

The performance with respect to ride comfort, for the cases (a)–(f) are shown in figure 2. From the figure it is clear that the active suspension can substantially improve the ride quality as compared to the corresponding passive system. Also while in the case of the passive systems, the suspension with quadratic damping performs better than that with hysteretic spring or a combination of both, in the case of active systems the

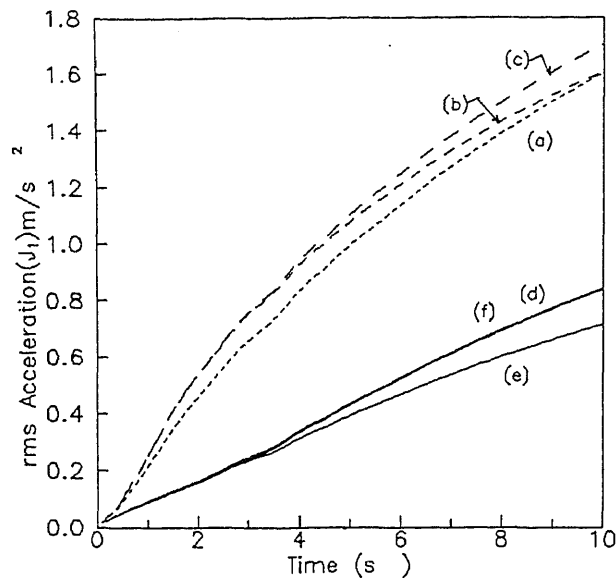


Figure 2. Ride performance of nonlinear passive (---) and active (—) systems. Passive (a) quadratic (b) hysteretic (c) quad. and hysteretic (d), (e) and (f) corresponding active systems.

performance with only the hysteretic spring (case (e)) is better in comparison to the cases (d) or (f).

The performance of the vehicle with respect to rms stroke response (figure 3) is somewhat reversed between the active and passive systems. In all the three cases the rms stroke response is worse for the active suspensions than for the passive suspensions. However, when this performance criterion (stroke response) is compared separately for

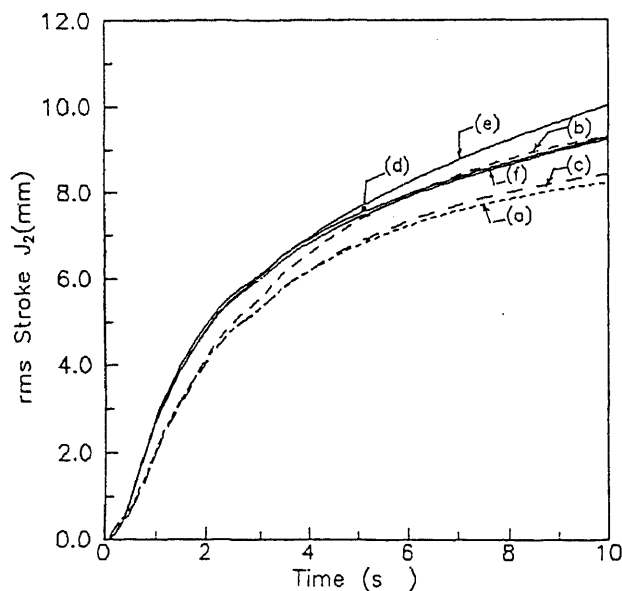


Figure 3. rms stroke response of nonlinear passive (---) and active (—) systems.

the passive and active suspension schemes with respect to the type of nonlinearities present it is observed that the performance is better with only quadratic damping ((a) and (d)), followed by the use of both quadratic damping and hysteretic stiffness ((c) and (f)). The performance with nonlinearity corresponding to hysteretic spring alone ((b) and (e)) is below that for the cases (a) and (d), and (e) and (f).

The performance with respect to roadholding (figure 4) behaviour is similar to the case of suspension stroke for the different forms of nonlinearities in the suspension. In this case also the performances of the active suspensions are poor compared to the passive suspensions. Also, the performance of the active suspension with the only hysteretic spring type of nonlinearity (case (e)) is worse than the other two active schemes (d) and (f). In the case of passive suspensions the types of nonlinearities do not influence the performance with respect to roadholding very much. The poor performance of the active suspensions in comparison with the passive suspensions with respect to roadholding and suspension stroke may be attributed to the relatively large weightage for the term corresponding to the ride comfort in the overall performance index.

The overall performance index for the active control schemes and for the passive suspensions corresponding to the three types of nonlinearities considered for the passive device is plotted in figure 5. Even though, the performance of the active systems is better or worse than the corresponding passive suspensions with respect to individual performance criterion considered separately, with respect to the overall performance of the vehicle the active suspensions perform much better than the corresponding passive suspensions for all the cases of nonlinearities. The nature of variation of overall performance index with respect to time in figure 5 is almost similar to the variation of the rms acceleration in figure 2. This corroborates to the fact that the ride comfort criterion is weighted relatively more in the performance index than the roadholding and suspension stroke criteria.

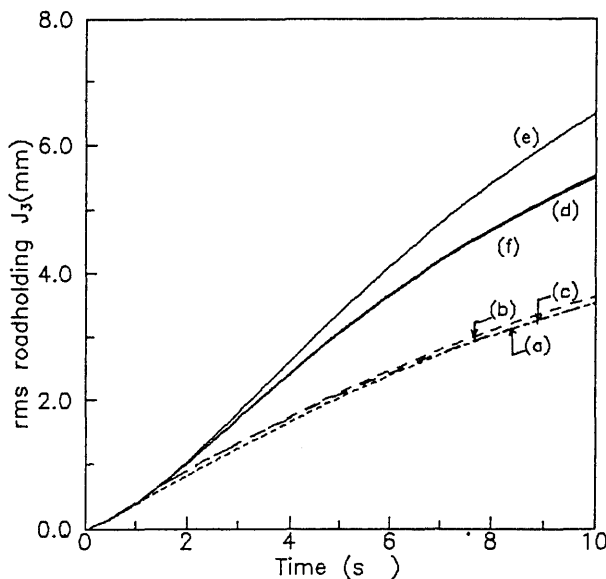


Figure 4. Roadholding performance of nonlinear passive (---) and active (—) systems.

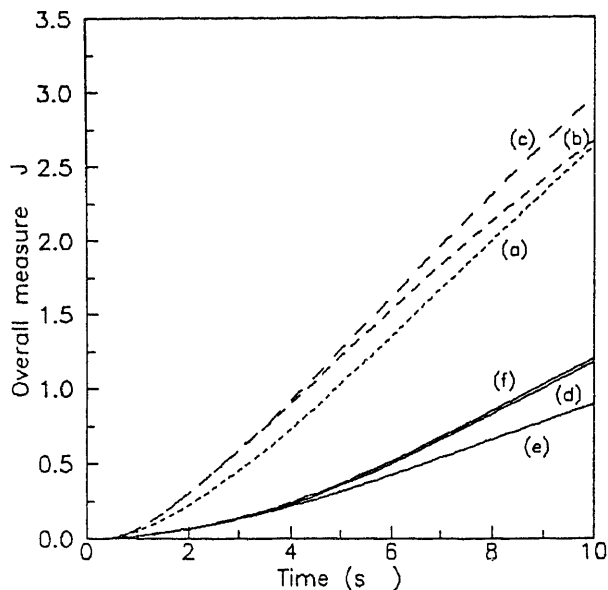


Figure 5. Overall performance of nonlinear passive (---) and active (—) systems.

The control force effort of the active schemes with full state feedback corresponding to the three nonlinear suspensions is shown in figure 6. The control force requirement for the case (e) of only hysteretic spring nonlinearity is the least as time increases, even though it is slightly more for initial times than for the case (d) of only the quadratic damping nonlinearity.

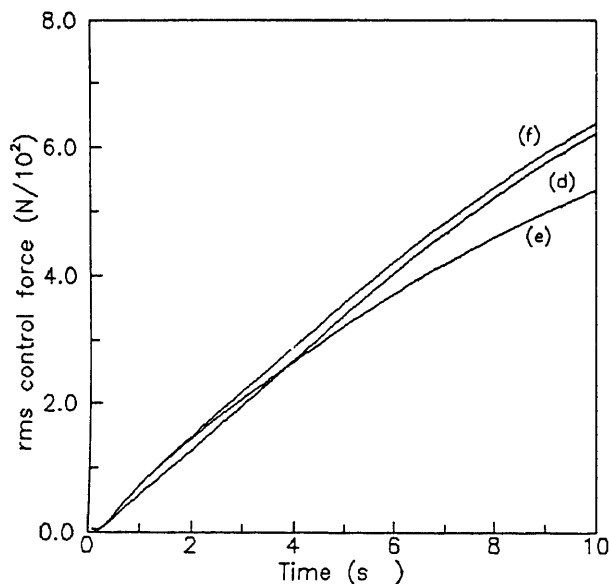


Figure 6. Control expenditure (J_4) for nonlinear active systems with full state feedback.

9. Conclusions

Active control of non-stationary response of an accelerating 2-dof vehicle model with nonlinear passive elements of the quadratic type, hysteretic spring type, and a combination of quadratic damping and hysteretic spring has been considered along with the equivalent linearization method in formulating the application of linear stochastic optimal control theory of time varying systems to the problem. It has been demonstrated that with the active control scheme with the full state feedback one can control the non-stationary response of the nonlinear vehicle model very effectively.

References

- Atalik T S, Utku S 1976 Stochastic linearization of multi degree of freedom nonlinear systems. *Earthquake Eng. Struct. Dyn.* 4: 411–420
- Bouc R 1967 Forced vibration of mechanical systems with hysteresis. *Proceedings of 4th Conference on Nonlinear Oscillations*, Prague, Czechoslovakia
- El Madany M M 1987 Nonlinear ride analysis of heavy trucks. *Comput. Struct.* 25: 69–82
- Harrison R F, Hammond J K 1986a Approximate, time domain, nonstationary analysis of stochastically excited, nonlinear systems with particular reference to the motion of vehicles on rough ground. *J. Sound Vib.* 105: 361–371
- Harrison R F, Hammond J K 1986b Evolutionary (frequency/time) spectral analysis of the response of vehicles moving on rough ground by using covariance equivalent modelling. *J. Sound Vib.* 107: 29–38
- Iwan W D, Yang I M 1972 Application of statistical linearization techniques to nonlinear multi-degree of freedom systems. *Trans. ASME, J. Appl. Mech.* 545–550
- Kirk C L 1971 The random heave and pitch response of aircraft to runway roughness. *Aeronaut. J. R. Aeronaut. Soc.* 75: 476–483
- Kirk C L, Perry P J 1970 Analysis of taxiing induced vibrations in aircraft by the power spectral density method. *Aeronaut. J. R. Aeronaut. Soc.* 75: 182–193
- Kwakernaak H, Sivan R 1972 *Linear optimal control systems* (New York: John Wiley and Sons)
- Narayanan S 1987 Nonlinear and non-stationary random vibration of hysteretic systems with application to vehicle dynamics. In *Proc. IUTAM Symposium on Nonlinear Stochastic Dynamic Engineering Systems*, Innsbruck, Austria (eds) F Ziegler, G I Schuëller (Berlin: Springer-Verlag)
- Narayanan S, Raju G V 1990 Stochastic optimal control of non-stationary response of a single degree of freedom vehicle model. *J. Sound Vib.* 141: 649–673
- Narayanan S, Raju G V 1992 Active control of non-stationary response of vehicles with nonlinear suspensions. *Vehicle Syst. Dyn.* 21: 73–87
- Raju G V 1991 *Active control concepts in non-stationary vehicle response*. Ph D thesis, Indian Institute of Technology, Madras
- Raju G V, Narayanan S 1991 Optimal estimation and control of non-stationary response of a two-degree of freedom vehicle model. *J. Sound Vib.* 149: 413–428
- Rill G 1983 *Instationäre Fahrzeugschwingungen bei Stochastischer Erregung*. Ph D thesis, Institute B for Mechanics, University of Stuttgart, Stuttgart
- Wen Y K 1980 Equivalent linearization for hysteretic systems under random excitation. *Trans. ASME J. Appl. Mech.* 47: 150–154
- Yadav D, Nigam N C 1978 Ground induced nonstationary response of vehicle. *J. Sound Vib.* 61: 117–126
- Zadeh L A, Desoer C A 1963 *Linear system theory – The state space approach* (New York: McGraw-Hill)



Nonlinear dynamics of offshore structures under sea wave and earthquake forces

K VENKATARAMANA and KENJI KAWANO

Department of Ocean Civil Engineering, Kagoshima University,
Korimoto 1-21-40, Kagoshima City 890, Japan

Abstract. A study of dynamic response of offshore structures in random seas to inputs of earthquake ground motions is presented. Emphasis is placed on the evaluation of nonlinear hydrodynamic damping effects due to sea waves for the earthquake response. The structure is discretized using the finite element method. Sea waves are represented by Bretschneider's power spectrum and the Morison equation defines the wave forcing function. Tajimi–Kanai's power spectrum is used for the horizontal ground acceleration due to earthquakes. The governing equations of motion are obtained by the substructure method. Response analysis is carried out using the frequency-domain random-vibration approach.

It is found that the hydrodynamic damping forces are higher in random seas than in still water and sea waves generally reduce the seismic response of offshore structures. Studies on the first passage probabilities of response indicate that small sea waves enhance the reliability of offshore structures against earthquakes forces.

Keywords. Offshore structure, dynamic response, nonlinear hydrodynamic damping, first passage probability.

1. Introduction

The analysis and design of offshore structures is a complicated process and requires several assumptions and approximations. The structures have to resist hostile environment and must stand on soils whose properties may be predicted only to an approximate degree of accuracy. The loads acting on offshore structures in a typical ocean environment are many such as wind, waves, tides, currents, ice, earthquakes, temperature loads, operational loads and so on. It is necessary to design an offshore structure such that it can respond to moderate environmental loads without damage and is capable of resisting severe environmental loads without seriously endangering the occupants. The various offshore structures presently in use are jacket-type fixed platforms, submersible or semisubmersible type floating platforms, steel or concrete gravity platforms, guyed towers, tension leg platforms, storage tanks, submersible pipe lines etc. The choice of a particular type of offshore structure depends on environmental

and geotechnical conditions, functional objectives, safety requirements, and economical and political considerations. Most of the offshore structures located in 30 m to 200 m depth for oil and gas exploration purposes are jacket-type platforms. These platforms usually consist of space frame structures with piles driven through their legs.

Offshore structures may be analyzed using static or dynamic analysis methods. Static analysis methods are sufficient for structures which are rigid enough to neglect the dynamic forces associated with the motion under the time-dependent environmental loadings. On the other hand, structures which are flexible due to their particular form and which are to be used in deep sea must be checked for dynamic loads. Dynamic analysis is particularly important for waves of moderate heights as they make the greatest contribution to fatigue damage and reliability of offshore structures. The dynamic analysis methods may be based on either deterministic approach or stochastic approach. In the deterministic approach, time records of dynamic loads are used to calculate the time-dependent structural responses. In the stochastic approach, dynamic loads are treated as random processes and are represented by their spectral densities. The structural responses are also expressed accordingly. Thus, in the deterministic approach, all calculations are carried out mostly in the time domain whereas in the stochastic approach, they are carried out mostly in the frequency domain. Stochastic methods have become increasingly popular as they are better suited to study the long-term behaviour of offshore structures for a range of sea states.

For offshore structures assembled by slender members, evaluation of wave forces is one of the most important steps in any dynamic analysis. Rigorous mathematical solution has yet to be developed and the empirical force model proposed by Morison *et al* (1950) is widely used. Morison equation is an approximate solution to a complex problem. Numerous researchers have investigated the validity and applicability of this equation. It appears preferable to attempt to improve this equation rather than formulate a new one (Bea & Lai 1978). Morison equation was originally proposed for stationary cylindrical piles in waves. This equation is generalized for a non-stationary structure by considering the relative motion between the water particle and the structure. Since the motion of water particles in the ocean have statistical characteristics, wave forces are also represented with stochastic processes namely with a Gaussian and ergodic process. Using the power spectral density function for the variations of wave heights, power spectral density functions of wave forces can be easily determined through the spectral approach. Weigel *et al* (1957) observed that close proportionality exists between measured wave force and sea surface spectral densities. Borgman (1967) confirmed their results and proposed a spectral method of formulation of wave forces due to random wave action on vertical piles fixed at sea bottom. Deo & Narasimhan (1988) have proposed a generalized spectral method of formulation of wave forces due to multi-directional random waves on inclined members of offshore structures. Once the wave forces are expressed in the spectral form, dynamic analysis can be carried out using the principles of random vibration and the structural responses may be determined. Foster (1970) developed a stochastic model for dynamic analysis of fixed-base offshore towers. One of the major problems involved in the stochastic analysis is the efficient modelling of nonlinear hydrodynamic drag and damping forces. The studies by Malhotra & Penzien (1970a, 1970b) provided an improved method for stochastic dynamic analysis of offshore structures. A linearization technique was proposed in these studies to tackle the nonlinear hydrodynamic drag and damping forces, the essence of which is to alter damping coefficients in an optimal manner. The applicability of

this linearization technique for random waves in comparison with other possible procedures have been discussed by Dao & Penzien (1982), and Gudmestad & Connor (1983). Eatock Taylor & Rajagopalan (1983) showed that this linearization technique is found to predict good responses only when the structural velocities are quite small compared to water particle velocities. Nonlinear dynamic analysis methods have been proposed by Laya *et al* (1984) and Jain & Dutta (1987) to deal with larger structural velocities under regular or random waves.

For a typical offshore structure located in a seismically active region, earthquake loading should also be considered in the dynamic analysis. Earthquake motions are generated through numerous random phenomena and are essentially random in nature. Several methods are available for the dynamic analysis of structures on land subjected to earthquake ground motions. However, these methods cannot be directly applied to offshore structures due to the presence of surrounding water and sea waves. Dynamic analysis is complicated due to the fact that hydrodynamic forces are coupled to the dynamic response. Penzien *et al* (1972) have presented a stochastic method of analysis of fixed-base offshore towers due to random sea waves and strong motion earthquakes. They observed that the hydrodynamic drag effects become important with increasing tower period or water depth. Bea (1979) developed the design criteria for offshore platforms subjected to these loads and compared his results with onshore building structures. Anagnostopoulos (1982) carried out studies on the evaluation of modal solutions of offshore platforms. All these investigations treat the effects of wave and earthquake forces independently assuming that they do not act simultaneously. But in normal seas subjected to earthquake ground motions, there may be wind generated waves of at least 1 m to 3 m heights. Therefore, it is important to investigate whether the earthquake response of offshore structures is significantly affected by these sea waves.

This paper discusses the dynamic response of offshore structures in random seas subjected to earthquake ground motions. Emphasis is placed on the evaluation of nonlinear hydrodynamic damping effects of sea waves for the seismic response. The input ground acceleration is horizontal and is expressed by Tajimi-Kanai's power spectrum for the stationary filtered white noise. The dynamic equations of motion are derived using the substructure method and the response analysis is carried out using the frequency-domain random-vibration approach. Numerical results are presented for various combinations of typical sea states and earthquake ground motions. The response quantities are compared using the principles of first passage probabilities across specific barriers.

2. Dynamic response analysis method

Figures 1 and 2 show the elevations of offshore structure models with pile-soil foundation systems. The wave force is expressed using the Morison equation and the nonlinear relative-velocity squared drag term is replaced by an equivalent linearized drag term assuming that the probability density function for the relative particle velocity is Gaussian. In the present problem, relative velocity is the difference between the water particle velocity due to wave motion and the structural velocity due to wave motion as well as due to earthquake motion. The linearized Morison equation has the form:

$$\{F_a\} = [C_M]\{\dot{v}_a\} - [C_A]\{\ddot{u}_a\} + [\bar{C}_D]\{\{v_a\} - \{\dot{u}_a\}\}, \quad (1)$$

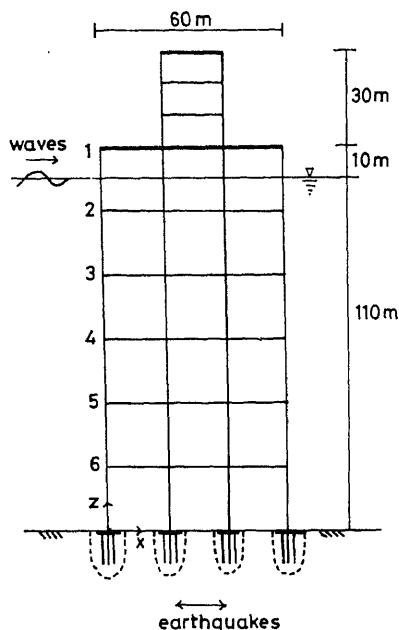


Figure 1. Analytical model of offshore structure: Model A.

where

$$[C_M] = [\kappa \rho C_m V \mathbf{I}], [C_A] = [\kappa \rho (C_m - 1) V \mathbf{I}],$$

$$[\bar{C}_D] = [\kappa \rho C_d (A/2)(8/\pi)^{1/2} \sigma_r \mathbf{I}], \quad r = v_a - \dot{u}_a,$$

in which ρ is the mass density of water, V is the volume of the displaced water, A is the area projected in the direction of flow, C_m is the inertia coefficient, C_d is the drag coefficient, $\{u_a\}$ is the displacement vector of the structure, $\{v_a\}$ is the water particle velocity vector

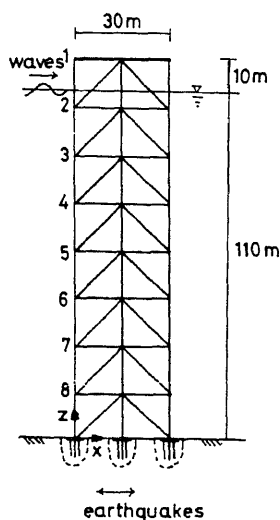


Figure 2. Analytical model of offshore structure: Model B.

and $\{\ddot{v}_a\}$ is the water particle acceleration vector at the undeflected structure coordinate locations, σ_r is the rms value of the relative particle velocity which is obtained by an iterative procedure.

Dynamic response characteristics of the structure depends on the vibrational behaviour of the structure as well as on the dynamic characteristics of the foundation-soil system. In the present study, the equation of motion is obtained by the substructure method in which the structure-pile-soil system is hypothetically divided into two substructures: the structure and the pile-soil foundation. The equation of motion for the total system is obtained by combining equations of motion for the structure subsystem and for the pile-soil subsystem, and by satisfying the compatibility conditions of displacements and the equilibrium conditions of forces at base nodal points. The nodal points except at the base have three degrees of freedom: horizontal displacement, vertical displacement, and rotational displacement in plane. The soil-structure interaction is idealized as a system of spring-dashpot element. The dynamic stiffness coefficient of the pile-soil foundation is obtained by the impedance method. The total displacement of the structure is treated as the sum of the dynamic displacement of the structure for the rigidly supported base condition, and the quasi-static displacement due to the interactions with the foundation. The dynamic displacement of the structure is treated as a linear combination of the first few vibration modes for the rigidly supported base condition which have significant effects on the response. The quasi-static displacement is expressed as the superposition of a few generalized displacements.

The equation of motion for the structure-pile-soil system is finally expressed as (Venkataramana *et al* 1989):

$$\begin{bmatrix} [I] & [\tilde{M}_{ap}] \\ [\tilde{M}_{pa}] & [\tilde{M}_p] \end{bmatrix} \begin{Bmatrix} \{\ddot{q}\} \\ \{\ddot{u}_p\} \end{Bmatrix} + \begin{bmatrix} [\kappa 2\beta_{fj}\omega_{fj} \nabla] & [\tilde{C}_{ap}] \\ [\tilde{C}_{pa}] & [\tilde{C}_p] \end{bmatrix} \begin{Bmatrix} \{\dot{q}\} \\ \{\dot{u}_p\} \end{Bmatrix} + \begin{bmatrix} [\kappa\omega_{fj}^2 \nabla] & 0 \\ 0 & [\tilde{K}] \end{bmatrix} \begin{Bmatrix} \{q\} \\ \{u_p\} \end{Bmatrix} = \begin{bmatrix} [P_a] \\ [P_b] \end{bmatrix}_w \begin{Bmatrix} \{\ddot{v}_a\} \\ \{\ddot{v}_b\} \end{Bmatrix} - \begin{bmatrix} [P_a] \\ [P_b] \end{bmatrix}_e \{\ddot{u}_g\}, \quad (2)$$

where

$$\begin{bmatrix} [P_a] \\ [P_b] \end{bmatrix}_w = \begin{bmatrix} [\Phi]^T [C_M] & [\Phi]^T [\bar{C}_D] \\ [G]^T [L]^T [C_M] & [G]^T [L]^T [\bar{C}_D] \end{bmatrix},$$

$$\begin{bmatrix} [P_a] \\ [P_b] \end{bmatrix}_e = \begin{bmatrix} [\Phi]^T [\tilde{M}_{aa}] [L] [G] \\ [G]^T [L]^T [\tilde{M}_{aa}] [L] + [M_{bb}] \end{bmatrix} [G],$$

$$\{u_a^c\} = [\Phi] \{q\},$$

in which the subscript *a* denotes the unrestrained nodal points above the base, the subscript *b* denotes the nodal points at the base, the subscript *p* denotes the pile-soil foundation, the subscripts *w* and *e* denote the wave and earthquake respectively, *q* is the modal displacement vector for dynamic displacements, Φ is the undamped eigenvector (mode shape) for the structure with rigidly supported base condition, ω_{fj} is the corresponding natural frequency for the *j*th vibration mode of the structure with rigidly supported base condition, β_{fj} is the corresponding damping ratio which includes both the structural damping and the hydrodynamic damping and \ddot{u}_g is the seismic ground acceleration.

Equation (2) contains a nonproportional damping matrix and hence complex eigenvalue analysis must be carried out for exact response analysis. However, when the

lower natural frequencies are well separated, the modal coupling effects due to off-diagonal terms are negligible. Therefore a simplifying approximation is made in the present study by considering only the diagonal terms of the damping matrix.

The response quantities in (2) can be expressed as a linear combination of generalized coordinates $\{y\}$ using a new eigenvector $[\Psi]$ for the structure-pile-soil system. Therefore, (2) can be transformed as

$$\{\ddot{y}\} + [\kappa 2\beta_j \omega_j] \{\dot{y}\} + [\kappa \omega_j^2] \{y\} = [\Psi]^T \left[\begin{matrix} [P_a] \\ [P_b] \end{matrix} \right]_w \left\{ \begin{matrix} \{\dot{v}_a\} \\ \{v_a\} \end{matrix} \right\} - [\Psi]^T \left[\begin{matrix} [P_a] \\ [P_b] \end{matrix} \right]_e \{\ddot{u}_g\}, \quad (3)$$

where

$$\left\{ \begin{matrix} \{q\} \\ \{u_p\} \end{matrix} \right\} = [\Psi] \{y\},$$

in which ω_j is the natural frequency for j th vibration mode of the structure-pile-soil system, β_j is the corresponding damping ratio which includes the structural damping, the radiation damping through the pile-soil foundation and the hydrodynamic damping.

Responses may be obtained from (3) by substituting for water particle velocities, water particle accelerations and ground accelerations. But, these variables take random values and require the application of random vibration approach. Assuming that the sea waves have stochastic properties of the zero-mean Gaussian process, they are represented by the one dimensional power spectrum of the Bretschneider type which is a function of statistically known mean wave height \bar{H} and mean wave period \bar{T} . The associated wave kinematics are computed by small amplitude wave theory. On the other hand, the seismic characteristics of the ground motion for stationary conditions are represented by Tajimi-Kanai's expression for power spectrum of ground acceleration.

Using the assumptions of stationary process and independent random process of sea wave and input ground acceleration, the power spectrum of generalized modal forces can be obtained by the summation of each power spectrum. The variance of the modal responses is then expressed as

$$E \left[\left\{ \begin{matrix} \{q\} \\ \{u_p\} \end{matrix} \right\} \left\{ \begin{matrix} \{q\} \\ \{u_p\} \end{matrix} \right\}^T \right] = \int_{-\infty}^{\infty} [\Psi][H(\omega)][S_{FF}(\omega)][H(\omega)^*][\Psi]^T d\omega, \quad (4)$$

in which $[H(\omega)]$ is the complex frequency response function and $[H(\omega)^*]$ is its conjugate. Using the results of (4), the relative response of superstructure is determined by transforming the modal response due to the modal matrix of the superstructure.

The duration times of earthquake ground motions and sea waves are very different. Therefore the responses due to these forces and their inter-relationships may be better interpreted using the principles of first passage probabilities. The reliability $L(\lambda)$ of the structure corresponds to the probability of response $x(t)$ not exceeding the value of a critical barrier λ and is given as (Vanmarcke 1975):

$$L(\lambda) = \exp \left[-\frac{1}{\pi} (\alpha_2/\alpha_0)^{1/2} t_0 \exp \left(-\frac{\gamma^2}{2} \right) \times \left\{ 1 - \exp \left(-(\pi/2)^{1/2} q_x \gamma \right) \right\} / \left\{ 1 - \exp \left(-\frac{\gamma^2}{2} \right) \right\} \right], \quad (5)$$

where

$$\alpha_i = \int_0^\infty \omega^i G_x(\omega) d\omega \quad (i = 0, 1, 2)$$

in which t_0 is the duration of the input excitation, γ is the ratio of the critical barrier and the rms response, $G_x(\omega)$ is the power spectral density function of the response and q_x is the bandwidth parameter which represents the degree of dispersion of the spectral density function about its central frequency.

3. Numerical results and discussions

The dynamic response analysis is carried out for model A and model B shown in figures 1 and 2 respectively. Model A has a lower fundamental frequency compared to that of model B. The depth of water is 110 m from mean sea level. The main members have an outer diameter of 2.8 m and a thickness of 27 mm. Each leg of the tower rests on a pile-soil foundation. The structural members as well as the piles in the foundation are made of steel. Table 1 shows the details of pile-soil foundation. The shear wave velocity V_s in the soil is assumed to be 100 m/sec. The natural frequencies and vibrational mode shapes are computed by eigenvalue analysis. The values of natural frequencies are shown in table 2 for up to the third mode of vibration. The structural damping for the first vibration mode of the structure subsystem is assumed to be 2%. When the soil-structure interaction is considered, by incorporating the pile-soil foundation in the offshore structure model, the structural and radiation damping is found to be 1.35% for model A and 1.95% for model B.

Figure 3 shows the example of Bretschneider's wave energy spectrum for mean wave height of 3 m, and mean wave periods of 5 s and 7 s. Higher frequency components have smaller energy while lower frequency components have greater energy. Figure 4 is a plot of Tajimi-Kanai's ground acceleration spectrum for rms ground accelerations of 30 gal (moderate earthquakes) and 100 gal (severe earthquakes). Marine soil is usually soft and therefore a characteristic ground frequency of 10 rad/s and damping ratio of 0.6 are assumed. It is seen that sea wave motion is a narrow band process whereas earthquake ground motion is relatively a broad band process. The dominant peak frequencies of these two types of loadings are also well separated.

The Morison equation is used to compute the hydrodynamic forces due to the surrounding water and sea waves. The values of the inertia coefficient C_m and the drag

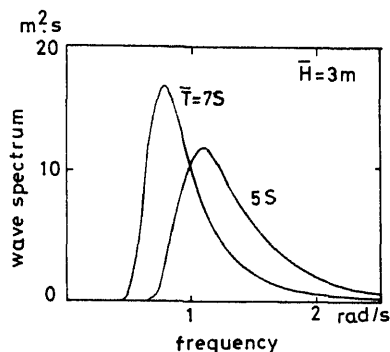


Figure 3. Wave energy spectrum.

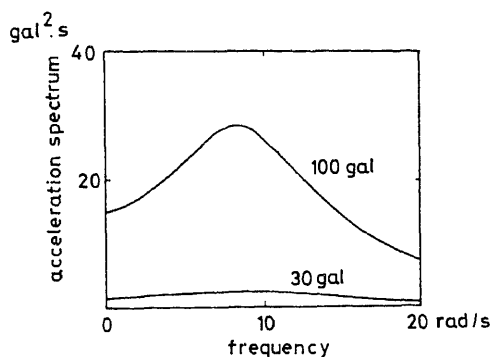


Figure 4. Ground acceleration spectrum.

coefficient C_d are assumed to be 2.0 and 1.0 respectively. The linearized drag term is computed by a cyclic procedure by altering the damping coefficients in an optimal manner. In the present study, reasonable convergence was attained in about three cycles of iteration.

Figures 5 and 6 show the rms response displacement at node 1 (top node) of models A and B respectively, and the response is plotted against rms ground acceleration. The response due to earthquake input generally increases with the increase in ground acceleration. When sea waves are neglected, hydrodynamic damping has a small effect on the response and the response increases linearly with the increment in the input ground acceleration. For rms acceleration of earthquake motions over about 30 gal, the displacement responses due to earthquake forces in random seas are lower than those due to earthquake forces in still water. The differences of these responses have an increasing tendency for an increase of the mean wave height and the mean wave period. However, the probability of the simultaneous occurrence of the severe earthquake motions and very strong sea waves is very small. In moderate wave conditions, which correspond to mean wave heights under about 3 m, the probability that the offshore

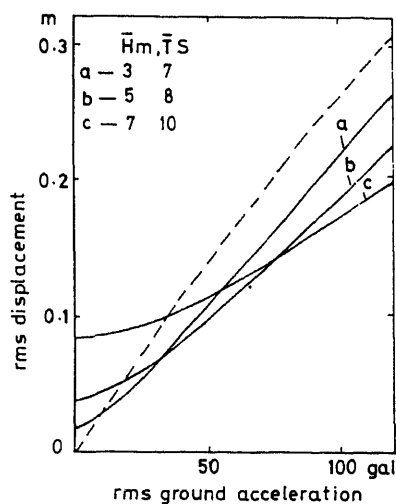


Figure 5. RMS displacement at node 1 for model A (--- earthquakes in still water; — earthquakes in a random sea).

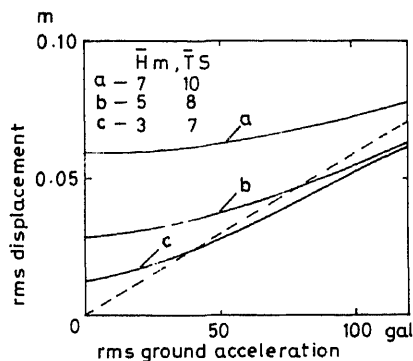


Figure 6. RMS displacement at node 1 for model B (--- earthquakes in still water; — earthquakes in a random sea).

structure is hit by severe earthquake motions is considerable. Also, when the offshore structure is subjected to earthquake motions under about 20 gal, the responses due to simultaneous loadings of earthquake motions and sea wave forces are generally larger than those due to earthquake motions only.

The response characteristics are very sensitive to the intensity of earthquake motions and sea wave forces. Further, in the absence of sea waves, nonlinear hydrodynamic damping forces which are proportional to the square of structural velocities are relatively small. On the other hand, if sea waves are included, the hydrodynamic damping forces are now proportional to the square of the relative velocities between the waves and the structure. Since the wave velocities are very much higher than the structure. Since the wave velocities are very much higher than the structural velocities, nonlinear hydrodynamic damping forces become larger than those without waves. Examples of hydrodynamic damping ratios for the first vibration mode of the structure-pile-soil system are shown in table 3 for mean wave height of 3 m, mean wave period of 7 s and rms ground acceleration of 30 gal.

Figures 7 to 10 show the rms response displacement at node 1 for sea waves of mean heights ranging from 3 m to 7 m in situations of specified earthquake forces. When rms ground acceleration is 30 gal, responses due to simultaneous loadings of earthquake motion and small sea waves give generally smaller evaluations than those due to earthquake motions in still water. But, when the earthquake motions are severe, the

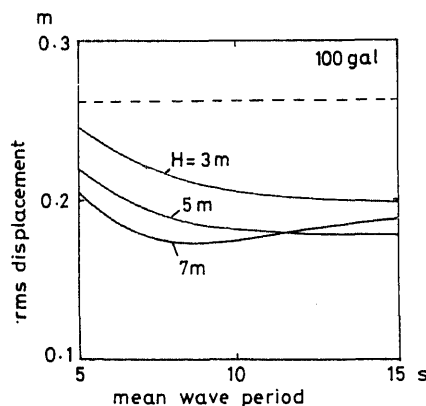


Figure 7. RMS displacement at node 1 for model A (--- earthquakes in still water; — earthquakes in a random sea).

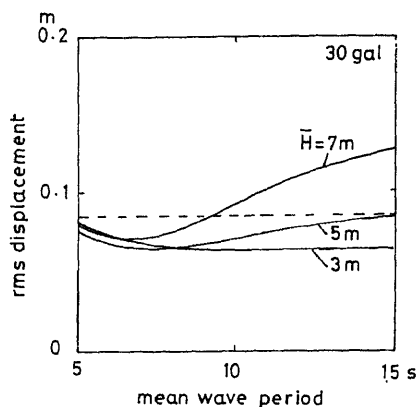


Figure 8. RMS displacement at node 1 for model B (--- earthquakes in still water; — earthquakes in a random sea).

responses due to wave and earthquake loadings are very much smaller than those due to earthquake forces in still water, even for large wave conditions. Therefore the responses are mainly controlled by the earthquake forces, the proximity of the excitation frequency to the fundamental frequency of the offshore structure system and the nonlinear hydrodynamic damping due to sea waves.

The reliabilities on the first passage of responses, which are functions of the duration times of sea waves and earthquake ground motions, are calculated using Vanmarcke's expression (5), and are plotted in figure 11 for model A and in figure 12 for model B. The numbers in the figures indicate the rms ground accelerations. As a rough estimate, $3.5\sigma_x$, where σ_x is the response displacement at node 1 and 3.5 is the peak factor, is used as the mean extreme response or barrier level λ . The duration time t_0 is expressed in multiples of the first natural period T_0 . The reliabilities of the structure for earthquake forces are generally higher when sea waves are included in the analysis since the hydrodynamic forces reduce the response values.

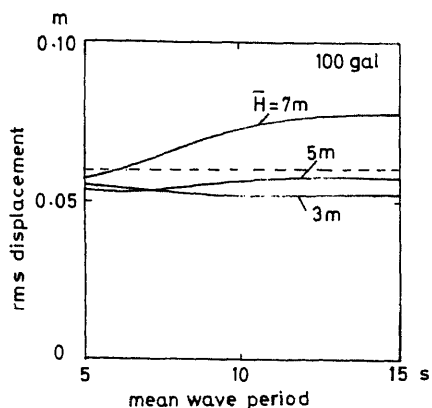


Figure 9. RMS displacement at node 1 for model A (--- earthquakes in still water; — earthquakes in a random sea).

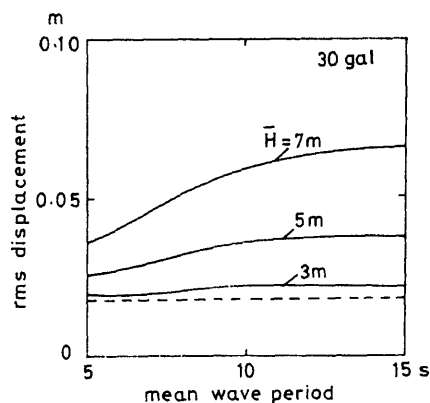


Figure 10. RMS displacement at node 1 for model B (--- earthquakes in still water; — earthquakes in a random sea).

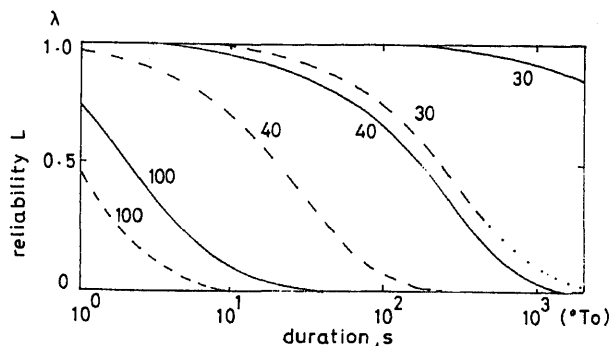


Figure 11. Reliabilities on level crossing of response displacement: Model A (--- earthquakes in still water; — earthquakes in a random sea).

The two loads considered in the present research are the wave and earthquake loads. Sea wave is a narrow-band steady-state process of several hours duration and earthquake is a broad-band transient process occurring for a few minutes. Comparing only the rms response of structure due to these loads is not sufficient for understanding the mechanism of hydrodynamic damping effects of sea waves on the seismic response. Therefore a first passage probability analysis, which takes into account the differences in their duration times, is carried out in this paper. Of course, one may question the validity of such an approach. But this method will serve as a tool for understanding the basic concepts and for realizing the extent of damping effects of sea waves on the earthquake response evaluation.

4. Conclusions

The dynamic response analysis of offshore structures in random seas have been carried out for the input of earthquake loadings. Two types of models are considered for numerical study: one is a relatively flexible structure and the other is a relatively rigid structure. The results of analysis indicate that responses due to earthquake motions vary with the intensity of the input ground acceleration. In the absence of sea waves, the effects of nonlinear hydrodynamic damping are small. When sea waves are considered, hydrodynamic damping forces are proportional to the square of the relative velocities between the waves and the structure. Since the wave velocities are very much higher

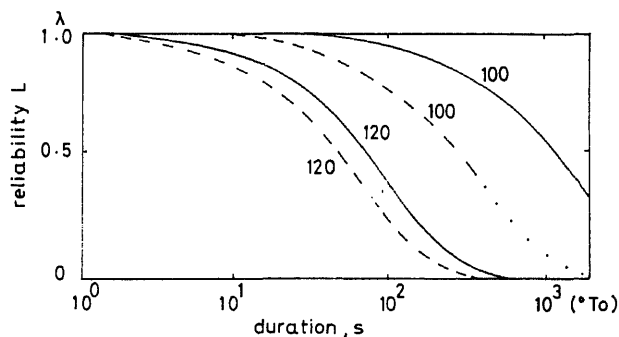


Figure 12. Reliabilities on level crossing of response displacement: Model B (--- earthquakes in still water; — earthquakes in a random sea).

than the structural velocities, these damping forces become larger than those without waves.

In the present paper, the results are mainly based on frequency-domain analysis. As a next step, time-domain analysis is being carried out. The findings of that study will be published later.

References

- Anagnostopoulos S A 1982 Wave and earthquake response of offshore structures: Evaluation of modal solutions. *J. Struct. Div., Am. Soc. Civ. Eng.* 108(ST10): 2175–2191
- Bea R G 1979 Earthquake and wave design criteria for offshore platforms. *J. Struct. Div., Am. Soc. Civ. Eng.* 105(ST2): 401–419
- Bea R G, Lai N W 1978 Hydrodynamic loadings on offshore structures. *Offshore Technology Conference*, Houston, Paper OTC 3064, 155–188
- Borgman L E 1967 Spectral analysis of ocean wave forces on piling. *J. Waterways Harbors Div., Am. Soc. Civ. Eng.* 93(WW2): 129–156
- Dao B V, Penzien J 1982 Comparison of treatments of nonlinear drag forces acting on fixed offshore platforms. *Appl. Ocean Res.* 4(2): 66–72
- Deo M K, Narasimhan S 1988 Generalized estimation of wave force spectra, *J. Waterway, Port, Coastal Ocean Eng.* 114: 175–190
- Eatock T R, Rajagopalan A 1983 Load spectra for slender offshore structures in waves and currents, *Earthquake Eng. Struct. Dyn.* 11: 831–842
- Foster Jr E T 1970 Model for nonlinear dynamics of offshore towers, *J. Eng. Mech. Div., Am. Soc. Civ. Eng.* 96(EM1): 41–67
- Gudmestad O T, Connor J J 1983 Linearization methods and the influence of current on the nonlinear hydrodynamic drag force. *Appl. Ocean Res.* 5(4): 184–194
- Jain A K, Dutta T K 1987 Nonlinear dynamic analysis of offshore towers in frequency domain. *J. Eng. Mech. Div., Am. Soc. Civ. Eng.* 113: 610–625
- Laya E J, Connor J J, Shyamsunder S 1984 Hydrodynamic forces on flexible offshore structures, *J. Eng. Mech. Div., Am. Soc. Civ. Eng.* 110: 433–448
- Malhotra A K, Penzien J 1970a Nondeterministic analysis of offshore structures, *J. Eng. Mech. Div., Am. Soc. Civ. Eng.* 96(EM6): 985–1003
- Malhotra A K, Penzien J 1970b Response of offshore structures to random wave forces, *J. Struct. Div., Am. Soc. Civ. Eng.* 96(ST10): 2155–2173
- Morison J R, O'Brien M P, Johnson J W, Schaaf S A 1950 The force exerted by surface waves on piles. *Pet. Trans., AIME* 189: 149–154
- Penzien J, Kaul M K, Berge B 1972 Stochastic response of offshore towers to random sea waves and strong motion earthquakes. *Comput. Struct.* 2: 733–756
- Vanmarcke E H 1975 On the distribution of the first-passage time for normal stationary random processes. *J. Appl. Mech.* 42: 215–220
- Venkataramana K, Yamada Y, Yoshihara S, Iemura H, Kawano K 1989 Stochastic response of offshore structures to sea wave and earthquake excitations with fluid–structure–soil interaction. Research Report, Dept. of Civil Eng., Kyoto Univ., 89-ST-01, 97–141
- Wiegel R L, Beebe K E, Moon J 1957 Ocean wave forces on circular cylindrical piles, *J. Hydraulics Div., Am. Soc. Civ. Eng.* 83(HY2): Proc. Paper 1199

Stochastic response of guyed tower under second-order wave force

T K. DATTA, R S BISHT and A K JAIN

Civil Engineering Department, Indian Institute of Technology, Hauz Khas,
New Delhi 110 016, India

Abstract. Guyed towers have low natural frequencies compared with generally encountered wave frequencies. They are therefore highly susceptible to low frequency second-order wave forces resulting from the non-linear phenomenon in the integrated fluid pressure on the submerged structure. A simplified approach is presented here to obtain the second-order wave forces encountered in random sea state for offshore guyed towers using a simulation procedure. Nonlinear response of a guyed tower to second-order and first-order wave forces, and a combination of the two are obtained in time domain. The time histories of responses and the wave forces are analysed to investigate their stochastic characteristics.

Keywords. Offshore guyed tower; second-order wave force; drift force; nonlinear vibrations; stochastic characteristics.

1. Introduction

The basic feature of a guyed tower platform is that it is designed to move with the waves, in at least some of its degrees of freedom. The system opposes wave forces predominantly by inertial effects. This is in contrast to the fixed platform which opposes wave forces primarily by the stiffness effect in the structure-foundation system. By their very nature, guyed towers have low fundamental frequency and, therefore, are susceptible to excitation at much lower frequencies than those of waves. Analysis of these structures for first-order wave forces would then invariably predict very low responses. The effect of second-order wave forces, which have generally significant energy content at low frequencies, on the response of such platforms must be included in their overall analysis.

Investigation of the second-order drift forces, exciting low frequency responses, has been extensively conducted for floating structures like buoys, semisubmersibles etc. Potential theory was used to derive the second-order drift forces by Pinkster (1979), Pinkster & Huijsmans (1982), Standing *et al* (1981), Chakrabarti & Cotter (1984), Eatock Taylor (1986) and Karppinen (1979), where the wave drift forces were defined as the second-order term in the integrated fluid pressure on the submerged body and was found to be proportional to the square of the wave amplitude. Salvesen *et al* (1982), Wahab (1974), Pijfers & Brink (1977) and Ferretti & Berta (1980) studied the slowly varying motion caused by

the second-order viscous drift force due to interaction between current, wind and wave force. The drift force was defined as the mean value of the total force over a wave period and was derived by using Morison's equation. The time histories of wave drift force for random waves were generated with the help of the square of the slowly varying wave envelope (hence, second order) and the drift force operator (i.e. drift force coefficient plotted against frequency of encounter).

Peak mooring forces were analysed by Hsu & Blenkarn (1970) which were caused by the vessel's slow drift oscillation in a random sea. They calculated the wave drift force based on conservation of momentum principles and the concept of "radiation stress" introduced by Longuet-Higgins & Steward (1964). Remery & Hermans (1971) also investigated the slow drift oscillations of a moored object in random seas. The drift force was calculated as a function of the square of the reflected and scattered wave elevation. The reflection coefficient was determined from experimental tests on a rectangular barge in head waves.

Kim & Yue (1989) have presented a new method for predicting slowly varying wave drift excitations in multidirectional seas. The method retains the assumption of narrow bandedness in frequency but treats the wave directional spreading exactly. Naess (1989) has emphasised the importance of estimating the extreme values of the combined first order and slow drift response of an offshore structure, subjected to a stationary irregular sea wave. The study indicates a strong coupling between the first order and the slow drift response. Kato *et al* (1990) presented an approximate solution for calculating the power spectral density function of total responses including first-order as well as second-order motions. Also, they showed that there exists a coupling between the first- and second-order responses. Grue (1988) has examined wave drift damping and low frequency oscillations of a moored elliptic cylinder. For long incoming waves he has obtained positive damping. But for short incoming waves damping forces were found to be negative. Langley (1987) has derived probability density function for low frequency second-order forces and motions using a method which represents the random sea state as a sum of regular waves. Grue & Palm (1986) have analysed the influence of a uniform current on slowly varying forces and displacements and the results show that current may have a great impact on the slowly varying motion of a moored body.

Jain & Datta (1991) have carried out investigations on articulated towers for the response due to viscous drift forces. They have calculated the slowly varying drift force by assuming that the drift force is proportional to the product of the square of the wave envelope and the drift force coefficient in regular waves.

Herein, a simplified method for obtaining the second-order wave force, encountered in the nonlinear oscillation of guyed tower in random sea states, is determined by a procedure similar to that proposed by Pijfer & Brink (1977). The guyed tower is analysed in time domain for the second-order wave force, first-order wave force and a combination of the two. The time histories of the nonlinear response as well as the wave force are analysed for a particular sea state in order to highlight the stochastic behaviour of the guyed tower in low frequency oscillation.

2. Analysis

2.1 Guyed tower model

The Exxon guyed offshore tower model has been considered to carry out the present

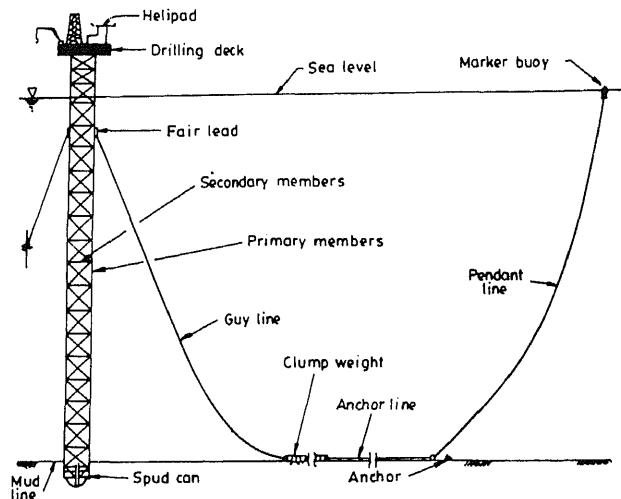


Figure 1. Schematic Exxon prototype guyed tower.

investigations. The tower is shown in figure 1. The bottom of the tower is provided with a restricted rotational restraint. For the present study the tower has been idealized as an equivalent uniform shear beam with a rotational spring at the base of the tower as shown in figure 2. Varying degrees of rotational movement of the tower may be achieved by varying the rotational spring stiffness. The guylines have been idealized by a nonlinear spring. The contribution of buoyancy to the restoring force in these structures is generally small when compared with that from the guyline stiffness, and is, therefore neglected in this study (Dutta 1984). Further, it is assumed that the dynamics of the guylines does not significantly influence the global tower motion. Thus, the stiffness of the nonlinear spring is obtained from a separate static analysis of the guylines under its own weight and current induced forces. The typical force excursion relationship of the guylines, for the example problem is shown in figure 3.

The offshore tower is discretized into a number of plane 2D beam elements. At each node, the dynamic degrees of freedom consist of sway translations and in plane rotations. The equation of motion in structural co-ordinates takes the form

$$[M]\{\ddot{x}\} + [C]\{\dot{x}\} + [K]\{x\} = F(t). \quad (1)$$

In the mass matrix $[M]$, added mass of the element is considered up to still water level. The effect of variable added mass due to the instantaneous position of the tower is assumed to be negligible and is ignored in the formulation of the problem. The damping matrix $[C]$ of the system is assumed to be a linear combination of (constant) mass and stiffness matrices; $\{\ddot{x}\}$, $\{\dot{x}\}$ and $\{x\}$ are, respectively the vectors of structural acceleration, velocity and displacement. The stiffness matrix $[K]$ is made time invariant by considering in it only the initial tangent stiffness of the nonlinear spring representing the guy system. As a result of this, correction to the resistive force at any instant of time is required and it is incorporated in the right-hand side load vector $F(t)$. The equations of motion are finally uncoupled using normal mode theory and an iterative technique. As a result, the damping matrix $[C]$ need not be explicitly known. Modal damping ratios are only required for the solution of equation of motion. $F(t)$ depends upon the type of analysis being performed. For the first order wave force analysis, $F(t)$ is due to

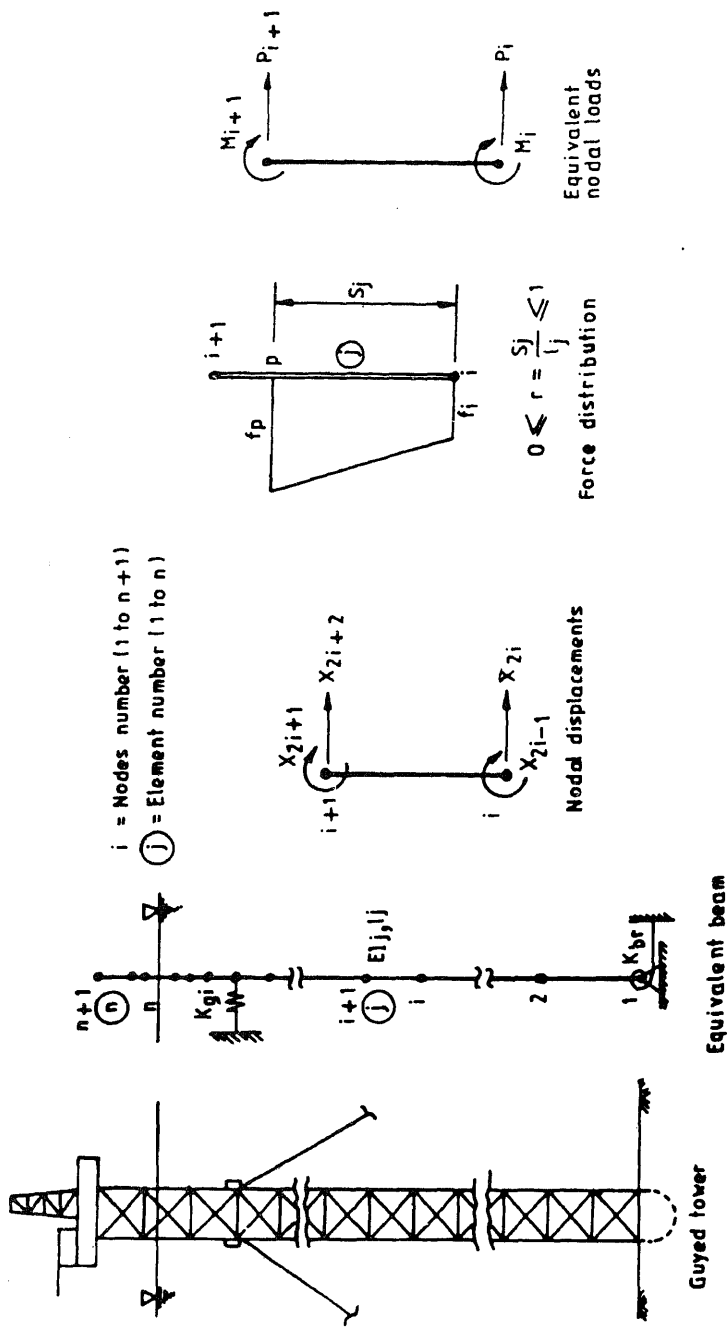


Figure 2. Finite element model of guyed tower.

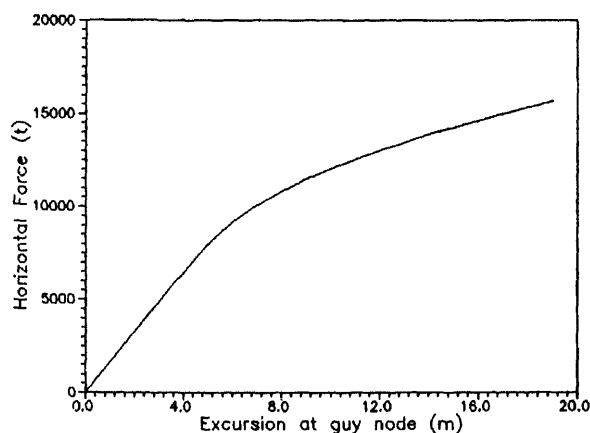


Figure 3. Force excursion relationship for prototype guyed tower.

the hydrodynamic loading calculated based on inertia and drag effects produced by the water particle kinematics. For the second order wave force analysis, the time history of $F(t)$ is simulated by considering low frequency wave forces resulting from nonlinear phenomenon in the integrated fluid pressure acting on the structure. For complete analysis, $F(t)$ is a combination of first-order and second-order wave forces. It is to be noted that the first-order wave force $F(t)$ depends on both structural velocity (due to nonlinear drag) and structural displacement (due to nonlinear force excursion relationship of guylines) apart from the water particle kinematics. The second-order wave force depends upon the nonlinear response of the guyed tower in regular waves of different periods as explained later. Thus (1) becomes highly non-linear especially where first- and second-order wave forces are considered together.

2.2 Simulation of second-order wave forces

The time histories of the drift forces are obtained using a method proposed by Pijfers & Brink (1977). According to this method, a mean hydrodynamic force at various nodes is calculated, which is the time average of all hydrodynamic forces acting on the structure, obtained through the Morison's concept. The wave drift force is then defined as the mean force in consequence of the waves and can be calculated by subtracting the true current force from the hydrodynamic force. The method is based on the assumption that the wave spectrum is sufficiently narrow. A random, long crested sea may then be written as an amplitude modulated signal:

$$\delta(t) = \text{Re } \Omega(t) = \text{Re } [R(t)\{\exp i \Gamma(t)\}], \quad (2)$$

where, $\delta(t)$ = wave amplitude, $R(t)$ = slowly varying wave envelope, $\Omega(t)$ = a complex variable whose real part provides the wave amplitude $\Gamma(t)$ the phase angle, equal to $\omega_c t + \varepsilon(t)$, where ω_c is the central frequency of the narrow band spectrum and $\varepsilon(t)$ is a slowly varying phase angle.

The above formulation leads to the expression for a momentary frequency of the spectrum as:

$$\dot{\Gamma}(t) = \omega_c + \dot{\varepsilon}(t). \quad (3)$$

The slowly varying drift force is then calculated assuming that the drift force is proportional to the product of the square of the wave envelope $R(t)$ and the drift force coefficient in regular waves at the momentary frequency $\dot{\Gamma}(t)$. The drift force $D_i(t)$ at any node i of the tower is then given by

$$D_i(t) = 0.5 \beta_w g C_i(\dot{\Gamma}) R^2(t). \quad (4)$$

Evaluation of the value of $D_i(t)$, (5), requires the time histories of $R^2(t)$, $\dot{\Gamma}(t)$ and drift force coefficient C_i at each momentary frequency $\dot{\Gamma}(t)$

2.3 Determination of time histories of $R^2(t)$ and $\dot{\Gamma}(t)$

The wave envelope R is the modulus of a complex variable *i.e.*

$$R^2 = (\text{Re } \Omega)^2 + (\text{Im } \Omega)^2. \quad (5)$$

Also,

$$\Gamma = \tan^{-1} [\text{Im } \Omega / \text{Re } \Omega], \quad (6)$$

and

$$\begin{aligned} \dot{\Gamma} &= [(\text{Re } \Omega)^* (\dot{\text{Im}} \Omega) - (\text{Im } \Omega)^* (\dot{\text{Re}} \Omega)] / [(\text{Re } \Omega)^2 + (\text{Im } \Omega)^2] \\ &= (1/R^2) [(\text{Re } \Omega)^* (\dot{\text{Im}} \Omega) - (\text{Im } \Omega)^* (\dot{\text{Re}} \Omega)]. \end{aligned} \quad (7)$$

The irregular wave amplitude $\delta(t)$ is defined as $\text{Re } \Omega(t)$ and is given by the sum of a large number of regular waves, *i.e.*

$$\delta(t) = \text{Re } \Omega(t) = \sum_n A_n \cos(\omega_n t + \Theta_n), \quad (8)$$

in which A_n is obtained according to the well-known formula;

$$A_n = [2 S_\delta(\omega_n) \Delta\omega_n]^{1/2}. \quad (9)$$

$S_\delta(\omega_n)$ is the spectral density ordinate of the wave spectrum at frequency ω_n ; Θ_n is the random phase angle between 0 and 2π radians; ω_n is the randomly varying frequency and $\Delta\omega_n$ is the frequency interval. Since $\delta(t)$ is considered as $\text{Re } \Omega(t)$, the imaginary part of $\Omega(t)$ is found to be

$$\text{Im } \Omega(t) = \sum_n A_n \sin(\omega_n t + \Theta_n). \quad (10)$$

The time derivatives of $\text{Re } \Omega$ and $\text{Im } \Omega$ are therefore,

$$\dot{\text{Re}} \Omega = - \sum_n A_n \omega_n \sin(\omega_n t + \Theta_n), \quad (11)$$

$$\dot{\text{Im}} \Omega = \sum_n A_n \omega_n \cos(\omega_n t + \Theta_n). \quad (12)$$

Using (8)–(12), the time histories of $R^2(t)$ and $\dot{\Gamma}(t)$ can be determined from (5) and (7).

2.4 Determination of drift force coefficient

The drift force coefficient C_i at any given momentary frequency $\dot{\Gamma}$ is obtained from the plot of C_i vs σ_e , where σ_e is the frequency of encounter. For a given regular wave of

amplitude δ_a and frequency σ , the drift force coefficient C_i is given by

$$C_i = \bar{D}_i / (0.5 \beta_w g \delta_a^2), \quad (13)$$

where \bar{D}_i is the mean drift force and is found by subtracting the true current force from the mean hydrodynamic force i.e.

$$\bar{D}_i = \bar{F}_i - F_c, \quad (14)$$

where F_c is current force due to constant current profile across the depth, \bar{F}_i is mean hydrodynamic force and i is the node number.

The frequency of encounter is given by:

$$\sigma_e = \sigma(1 + \sigma \dot{U}_c / g). \quad (15)$$

The mean hydrodynamic force \bar{F}_i at node i is obtained by determining the mean hydrodynamic forces over one period of encounter T i.e.

$$\bar{F}_i = (1/T) \int_0^T f_i(t) dt, \quad (16)$$

$f_i(t)$ = hydrodynamic force at node i .

The hydrodynamic force $f_i(t)$ is calculated from Morison's equation viz.

$$\begin{aligned} f_i(t) = & 0.5 \beta_w C_d D_d |\tilde{U}_i| (\tilde{U}_i) + 0.25 C_m \beta_w \pi D_m^2 \dot{\tilde{U}}_i \\ & - 0.25 \pi \beta_w (C_m - 1) D_m^2 \ddot{\tilde{X}}_i. \end{aligned} \quad (17)$$

The relative velocity \tilde{U} comprises mass transport velocity, V_{mi} , water particle velocity, \dot{U}_i , the current velocity \dot{U}_c and structural velocity \dot{X}_i and is given by

$$\tilde{U}_i = V_{mi} + \dot{U}_i + \dot{U}_c - \dot{X}_i, \quad (18)$$

In which V_{mi} , in deep water, according to Stokes theory, is given by

$$V_{mi} = \delta_a^2 K \sigma \exp(-2Ky), \quad (19)$$

where K is the wave number and y is a function of the water depth.

Since the computation of $f_i(t)$ as given by (17) requires \dot{X}_i and \ddot{X}_i , the response of the tower is to be obtained for different combinations of the regular wave of amplitude δ_a and frequency σ . The response analysis of the guyed tower for regular waves of amplitude δ_a and frequency σ is performed by (1) in time domain using the Newmark β method. Because of the dependence of $F(t)$ on structural velocity and displacement, the equation of motion is solved by numerical integration using iteration at each time step to tackle all the nonlinearities. The efficiency of the analysis is augmented by the use of the normal mode theory (Bathe & Wilson 1976).

2.5 Simulation of the first-order wave force

For a given random sea state the time history of first-order wave force at any node is obtained by using (17). The time histories of water particle kinematics \dot{U}_i and \ddot{U}_i are obtained from the PSDFs of water particle kinematics using the Monte Carlo simulation technique (8).

2.6 Response analysis

The responses of the guyed tower for the first-order and second-order wave forces and

Table 1. Details of the idealised guyed tower.

Deck height	480 m
Mean sea level	457 m
Height at guy node	442 m
Guy diameter	9 cm
Number of guys	20
Guy system initial tension	1680 kN
EI	50000 GNm
Deck weight	69000 kN
Structural weight	3790 kN/m
Base restraint	20 GNm/rad
Effective drag diameter	35.05 m
Effective inertial diameter	5.79 m
C_d	0.90
C_m	2.00
Structural critical damping ratio	2%
Height at node 17	447 m
Structure's fundamental frequency	0.2689 rad/s
Structure's second frequency	1.3260 rad/s

for the combination of the two are obtained in time domain using Newmark's β method with iteration required at each time step to tackle the nonlinearities (Datta & Jain 1988). The equations of motions are solved in normal coordinates thereby decoupling the equations of motion. The details of the method are available in the reference cited above.

3. Numerical results and discussion

The details of the idealised guyed tower are given in table 1. The tower is analysed for a random sea state with $H_{1/3} = 15.0$ m and $T_z = 9.0$ s. The sea state is characterised by the one-sided Pierson Moskowitz (P-M) spectrum and has been simulated for a duration

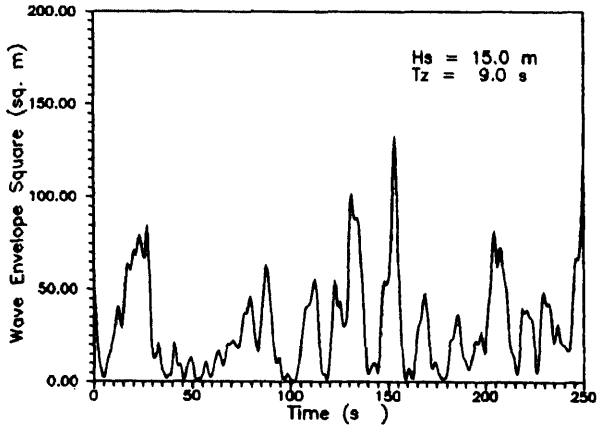


Figure 4. Time history of wave envelope square.

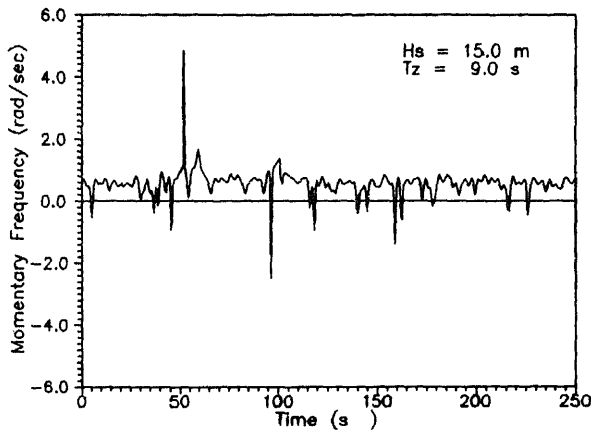


Figure 5. Time history of momentary frequency.

of about 17.5 minutes. Typical time histories of wave envelope square $R^2(t)$ and the momentary frequency $\dot{\Gamma}(t)$ for the sea state are shown in figures 4 and 5.

Figure 6 shows the variation of the drift force coefficient with encounter frequency computed at node 17 of the tower which is the node just above the fairlead point (very near to the mean sea level). The nonlinearly varying drift force coefficients do not differ significantly for different wave amplitudes up to an encounter frequency equal to 1.0 rad/s. Since the oscillation of the tower is predominantly guided by the low frequency response, the range of instantaneous frequencies generally falls within 1.0 rad/s. Therefore the values of drift force coefficient $C_i(\dot{\Gamma})$ for any value of $\dot{\Gamma}_i(t)$ may be obtained from any of the curves corresponding to wave amplitudes $\delta_a = 1$ m, 2 m and 3 m.

Figure 7 shows the power spectral density function (PSDF) of second order wave force at node 17. The PSDF has significant energy at lower frequencies, as expected. On the other hand, the low frequency contents of the PSDF of the first-order wave force are small (figure 8).

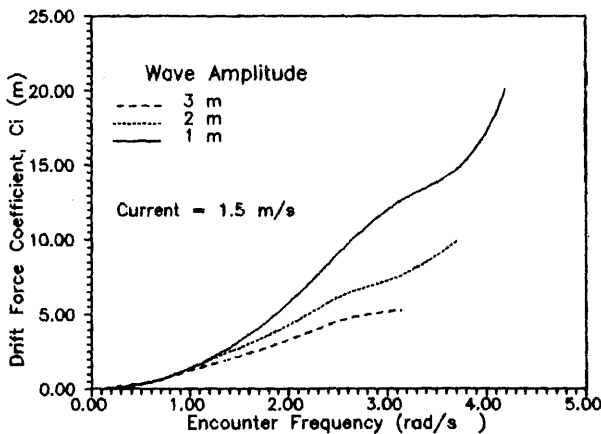


Figure 6. Variation of drift force coefficient (at node 17).

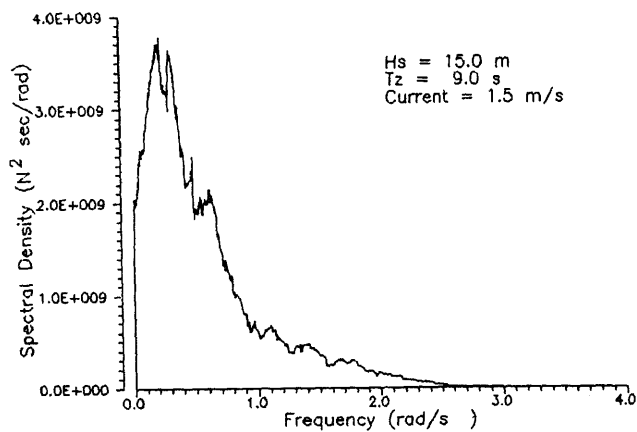


Figure 7. PSDF of 2nd order wave force (at node 17).

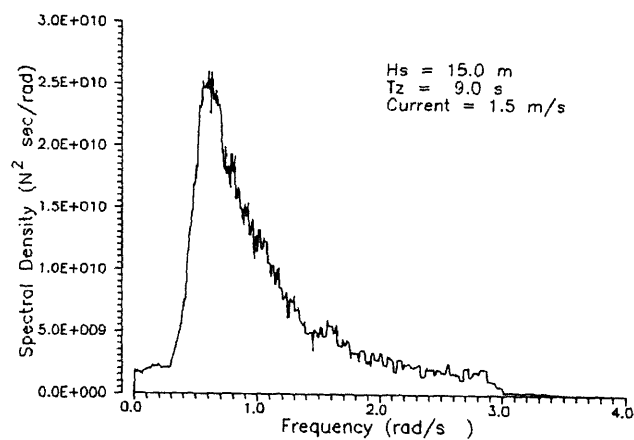


Figure 8. PSDF of 1st order wave force (at node 17).

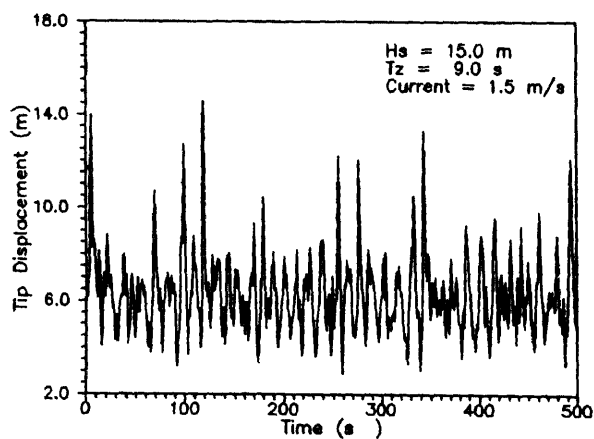


Figure 9. Time history of tip displacement due to 1st order wave forces.

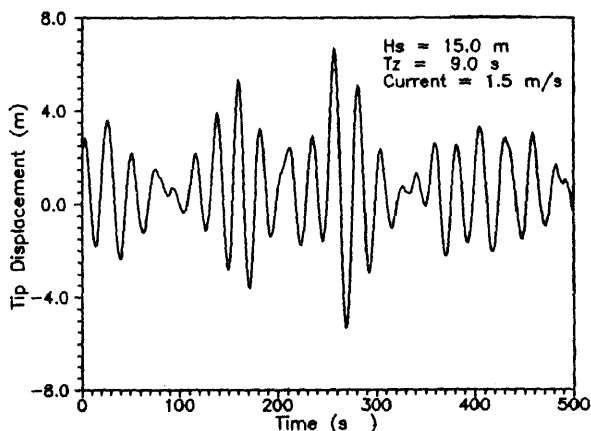


Figure 10. Time history of tip displacement due to 2nd order wave forces.

The PSDFs of tip displacements and the corresponding time histories of response due to first- and second-order wave forces are shown in figures 9–12. Low frequency excitation of the structure at the fundamental frequency due to a second-order wave force is evident from the plot of PSDF shown in figure 12. It is interesting to note that the frequency contents of the response spectrum due to a second-order wave force are practically insignificant in the vicinity of predominant wave frequency. On the other hand, the response characteristics due to the first-order wave force are such that the spectrum has large frequency content at the predominant wave frequency. Low frequency contents of the spectrum are not large.

Figure 13 shows the PSDF of tip displacement due to the combined first and second order wave forces. The spectrum is characterised by two peaks, one occurring near the fundamental frequency of the structure (0.269 rad/s) and the other at the predominant wave frequency (0.7 rad/s). The first peak shows the low frequency resonating effect due to the second order wave force while the second peak is predominantly the effect of the first-order wave force. Comparing figures 12 and 13, it is seen that the response peak (the first peak in figure 13) due to the second-order wave force is reduced when first- and

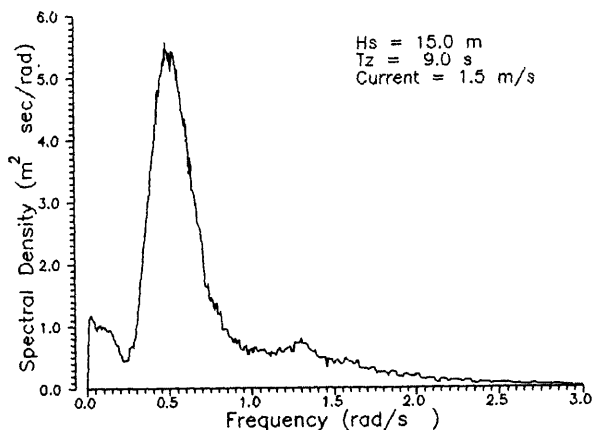


Figure 11. PSDF of tip displacement due to 1st order wave force.

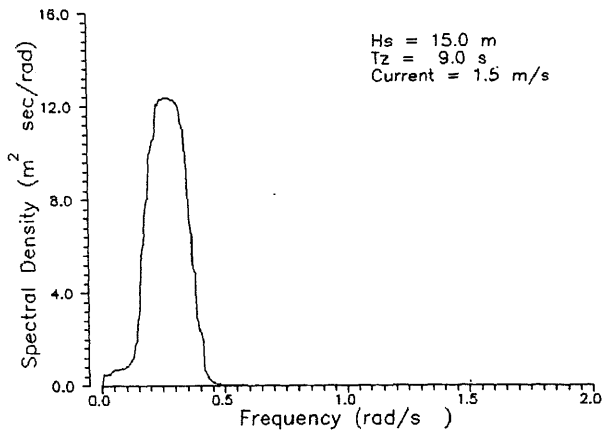


Figure 12. PSDF of tip displacement due to 2nd order wave force.

second-order wave forces are considered together. This reduction is presumably caused by nonlinear hydrodynamic damping associated with the first-order wave forces.

Table 2 compares the mean square values of the tip displacements due to the two wave forces and their combinations. The response due to the second-order wave force alone is quite significant (about 26% of that due to the first-order one). If the effect of the second-order wave force is not taken into consideration, the overall response is underestimated by about 13%. The difference in the overall response, however, depends upon the amount of hydrodynamic damping present in the first-order wave force.

Figure 14 shows the cumulative distribution function (CDF) of the first order wave force, the second-order wave force and the combination of the two at node 17. It is seen that the CDFs of the forces deviate from the normal distribution, especially near the tail ends. This clearly shows the effect of nonlinearities on the distribution of the hydrodynamic forces. The CDFs of responses corresponding to different types of wave forces are shown in figure 15. Distributions deviate considerably from the Gaussian distribution near the ends, because of considerable non-linearities present in the wave

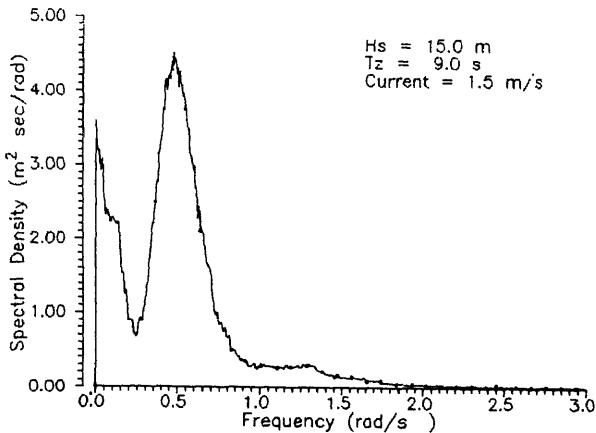


Figure 13. PSDF of tip displacement due to combined 1st & 2nd order wave forces.

Table 2. Comparison of mean square values of tip displacement response for different sea states.

Sea states	First order (m^2)	Second order (m^2)	Combined wave force (m^2)
$H_s = 15.0\text{ m}$ $T_z = 9.0\text{ s}$	6.492	1.705	7.476

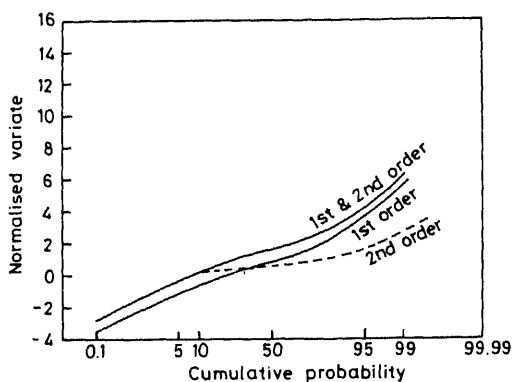


Figure 14. Distribution of wave forces (in Gaussian plot).

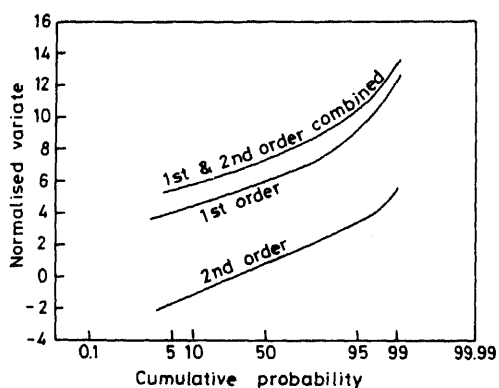


Figure 15. Distribution of tip displacement responses (in Gaussian plot).

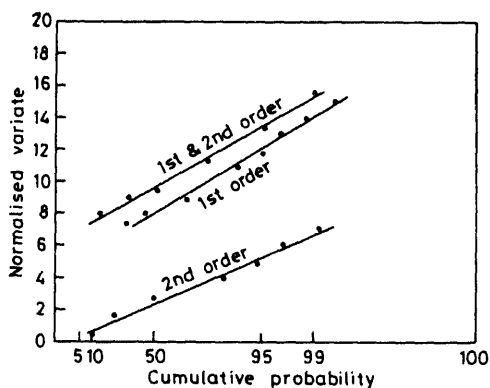


Figure 16. Distribution of positive peaks of tip displacement response (in Rayleigh plot).

forces. However, the distribution of positive peaks of the responses (figure 16) tend to (mildly) follow Rayleigh distribution.

4. Conclusions

A simplified approach for obtaining the second-order wave force in the random sea state is presented for offshore guyed towers. The responses due to first- and second-order wave forces, and their combination are obtained in time domain considering hydrodynamic nonlinearity and the nonlinearity present in the restoring force provided by the guy lines. The responses of the tower are analysed to investigate their statistical characteristics. The results of the numerical study lead to the following conclusions.

- (a) The second order drift force has significant energy at the low frequency range.
- (b) The response due to the second-order wave force only shows resonating effect at the structures's fundamental frequency and could be quite significant.
- (c) When the second-order wave force is combined with the first-order wave force, the low frequency response caused by the effect of the second-order wave force is reduced because of hydrodynamic damping associated with the first-order wave force effect.
- (d) Both first-order and second-order wave forces are non-Gaussian due to significant nonlinearity present in the integrated fluid structure system.
- (e) The distributions of the responses are non-Gaussian. However, the peak distribution tends to (mildly) follow Rayleigh distribution.

References

- Bathe K J, Wilson E L 1976 *Numerical methods in finite element analysis* (Englewood Cliffs, N J: Prentice-Hall)
- Chakrabarti S K, Cotter D C 1984 Interaction of wave with a moored semi-submersible. *Proc. 3rd Offshore Mech. and Arctic Engineering Symp.*, New Orleans pp. 119–127
- Datta T K, Jain A K, 1988 Nonlinear surge response of tension leg platform to random waves. *Eng. Struct.* 10: 204–210
- Dutta A 1984 *Dynamic behaviour of offshore guyed towers*. Ph D thesis, Dept of Civil Eng., Indian Institute of Technology, Delhi
- Eatock Taylor R 1986 Low frequency behaviour of compliant offshore systems. *Keynote Addresses in Proceedings, 3rd Indian Conf. on Ocean Engineering* (Bombay: Indian Inst. Technol.) pp. 17–55
- Ferretti C, Berta N 1980 Viscous effect contribution to the drift forces on floating structures. *International Symposium on Ocean Engineering and Shiphandling* (Gothenburg: University Press)
- Grue J 1988 Wave drift damping and low-frequency oscillations of an elliptic cylinder in irregular waves: *Appl. Ocean Res.* 10: 10–19
- Grue J, Palm E 1986 The influence of a uniform current on slowly varying forces and displacements. *Appl. Ocean Res.* 8: 232–239
- Hsu F H, Blenkarn K A 1970 Analysis of peak mooring forces caused by slow vessel drift oscillation in random seas. paper no. OTC 1159, I135–I145
- Jain A K, Datta T K 1991 Response of articulated towers to viscous drift forces. *Int. Shipbuilding Progr.*, 38: 315–331
- Karppinen T 1979 An approach to computing the second order steady forces on semi-submersible structures. Report No. 16 *Helsinki University of Technology, Ship Hydrodynamics Laboratory*.

- Kato S, Kinoshita T, Takase 1990 Statistical theory of total second order responses of moored vessels in random seas. *Appl. Ocean Res.* 12: 2-13
- Kim M H, Yue D K P 1989 Slowly varying wave drift forces in short-crested irregular seas. *Appl. Ocean Res.* 11: 2-18
- Langley R S, 1987 A statistical analysis of low frequency second order forces and motions. *Appl. Ocean Res.* 9: 163-170
- Longuet-Higgins M S, Steward R W 1964 Radiation stresses in water waves; a physical discussion. *Deep Sea Res* 11: 529-536
- Naess A 1989 Prediction of extremes of combined first-order and slow-drift motions of offshore structures. *Appl. Ocean Res.* 11: 100-110
- Pijfers J G L, Brink A W 1977 Calculated drift forces of two semi-submersible platform types in regular and irregular waves. paper no. OTC 2977 155-161
- Pinkster J A 1979 Mean and low frequency wave drifting forces on floating structures. *Ocean Eng.* 6: 593-615
- Pinkster J A, Huijsmans R H M 1982 The low frequency motions of a semi-submersible in waves, *Proc. 3rd International Boss Conference, MIT*, pp. 447-466
- Remery G F M, Hermans A J (1971) The slow drift oscillations of a moored object in random seas. paper no OTC 1500 II 829-836
- Salvesen N, Von Kerczek C H, Yue D K, Stern F 1982 Computation of nonlinear surge motions of tension leg platforms. paper no. OTC 4394 199-215
- Standing R G, DaCunha N M C, Matten R B 1981 Slowly varying second order wave forces: theory and experiments. Report No. R138, National Maritime Inst.
- Wahab R 1974 Wave induced motions and forces on a floating structure. Report No. 1865, Netherland Ship Research Centre, TNO, Delft



Chaos in mechanical systems – A review

P SEKAR and S NARAYANAN

Machine Dynamics Laboratory, Department of Applied Mechanics,
Indian Institute of Technology, Madras 600 036, India

Abstract. In this paper, a review of the various developments in the field of chaotic dynamics with specific emphasis on chaos in structural and mechanical systems is presented. The paper discusses some known chaotic systems such as the Lorenz, Rössler, Ueda and Henon attractors as well as chaos in Duffing and Van der Pol oscillators. The paper also covers chaos in piecewise linear systems, impacting oscillators and flow induced vibrating systems. Topics such as bifurcations and routes to chaos, different ways of characterising chaos, domains of attraction and control of chaos are also discussed.

Keywords. Chaos; bifurcations; nonlinear systems; strange attractors.

1. Introduction

Nonlinear dynamical systems are encountered in many areas of science and engineering, such as in chemical kinetics, celestial mechanics, fluid flow problems, structural dynamics and mechanical vibration. Because of the numerous interesting phenomena exhibited by nonlinear systems and also because of the lack of a general method of analysis for all nonlinear systems, the theory of nonlinear oscillations have fascinated physicists, mathematicians and engineers for a long time.

Recent years have witnessed a significant increase in research efforts in understanding chaotic motions of nonlinear dynamical systems in many fields of science and engineering. Chaos may be described as bounded random like motion exhibited by deterministic nonlinear systems characterised by their sensitivity to initial conditions. Not all nonlinear systems exhibit chaos, nor does chaos occur for all combinations of system parameters and initial conditions for a given system. In fact no general conditions have as yet been clearly established to *a priori* identify chaos for a given set of parameters and initial conditions. Chaotic behaviour is represented by highly irregular motion and the power spectrum of the associated time history is continuous. In many cases of chaotic motion, the phase plane plot shows a complicated pattern without being closed and the Poincaré map which is the stroboscopic projection of phase trajectories sampled at equal intervals of time (usually equal to the period of excitation) shows the existence of a strange attractor where the phase points tend to occupy certain regions of phase space for dissipative systems. In the case of regular periodic motion of the system the Poincaré map contains a single point for period 1 and two points for

period 2 motion *etc.* The most reliable way of characterising chaos is through Lyapunov exponent which is a measure of the sensitivity of the system behaviour to initial conditions.

Even though such irregular behaviour of nonlinear systems had been alluded to in the pioneering works of Poincaré (1921), Birkhoff (1927), Andronov *et al* (1966) and Lyapunov (1949), it is only in the last two decades that a systematic study of chaos has been carried out aided by the massive power of computing provided by present day computers and sophisticated graphic facilities.

In this paper, we present a review of the literature in the area of chaotic vibrations in nonlinear dynamical systems. As the subject has grown rapidly in the last decade, the literature available is very vast and covers many different systems like convective flows, aeroelastic systems, nonlinear electrical circuits, feedback control devices, mechanical systems with clearances and backlashes, rotating machines, nonlinear acoustic systems *etc.* The literature is abound in the numerical aspects of characterising chaotic motions in terms of phase plane diagrams, Poincaré maps, time histories, and associated power spectra, Lyapunov exponents and fractal dimensions. It also covers many of the theoretical and mathematical concepts, especially the geometric theory of nonlinear differential equations, which are used to predict the existence of chaos for a set of system parameters as well as investigate the different routes to chaos by use of bifurcation theory and stability analysis which also help to understand the phenomenon of chaos. There are papers which employ conventional methods of nonlinear analysis like the averaging and harmonic balance methods to approximately predict certain bifurcation behaviour leading to chaos. Some other works are devoted to experimental methods to demonstrate chaos in physical nonlinear systems. In addition to the vast literature available on the identification of chaos in various systems, control of chaos is also drawing considerable attention.

It is a formidable task to review the entire literature on the subject in view of the sheer magnitude of the information available. Therefore we confine our literature survey mainly to those concerning chaos in mechanical and structural systems.

Important developments in this area can be found in the books by Guckenheimer & Holmes (1983), Lichtenberg & Liberman (1983), Iooss & Joseph (1980), Arnold (1983), Kubiček & Mareck (1983), Berge *et al* (1984), Hao Bai-Lin (1984), Thompson & Stewart (1986), Moon (1992), Devaney (1987), Hsu (1987), Seydel (1988), Cvitanović (1989), Baker & Gollub (1990), Parker & Chua (1989), Wiggins (1990), Kapitaniak (1991) and also in the papers by Takens (1980), Ott (1981), Holmes & Moon (1983), Salam *et al* (1983), Mees & Sparrow (1987), Grebogi *et al* (1987), Dowell (1988a, b), Holmes (1990a, 1990b), Ott *et al* (1990), Argyris (1991), Thompson & Soliman (1991), Stewart & Ueda (1991) and Thompson (1992).

1.1 Early history

Though the ideas, methods and rigorous mathematical theories regarding chaos have crystallised only in the last two decades as an important discipline in many mathematical, physical and engineering fields, Poincaré (1921) was aware of the existence of irregular motions in nonlinear systems and their sensitivity to initial conditions even at the beginning of this century. The foundation laid by Poincaré on the geometrical theory of nonlinear systems was strengthened by Birkhoff (1927) who was also aware of aperiodic motions in nonlinear systems as were Van der Pol & Van der Mark (1927)

who had also observed random like behaviour in experiments with nonlinear electrical circuits.

Lorenz (1963) a student of Birkhoff, was one of the earliest to observe chaotic behaviour in the study of atmospheric turbulence and its effects on long range weather predictions. He considered a simplified version of the convective equation in non-dimensional form as

$$\dot{x} = \sigma(y - x), \quad \dot{y} = \rho x - y - xz, \quad \dot{z} = xy - \beta z, \quad (1)$$

where the overdot denotes differentiation with respect to nondimensional time and σ and ρ are related to the Prandtl number and Rayleigh number respectively and β a geometric factor. Even in this simple form (1), which were derived by some scheme of modal approximations of the governing nonlinear partial differential equations (Navier–Stokes equations) with xz and xy being the nonlinear terms for the parameter values of $\sigma = 10$, $\rho = 28$, $\beta = 8/3$, Lorenz observed chaotic behaviour.

Lorenz equations are invariant under the symmetry $(x, y, z) \rightarrow (-x, -y, z)$ and over a large region of parameter space, there are three unstable stationary points: the origin of the phase space, $(0, 0, 0)$, $((\beta(\rho - 1))^{1/2}, (\beta(\rho - 1))^{1/2}, (\rho - 1))$, $(-(\beta(\rho - 1))^{1/2}, -(\beta(\rho - 1))^{1/2}, (\rho - 1))$ which are mapped onto each other by the symmetry. The origin is a saddle point while the other two equilibrium points are unstable foci. The location and the type of equilibrium points for a range of parameter values are concisely discussed by Thompson & Stewart (1986). Much of our present understanding of these equations and their solutions are summarized in the excellent book by Sparrow (1982).

Originally it was hoped that these equations describe the Rayleigh–Bernard flow of a fluid between heated plates. That no longer seems likely because of the poor convergence properties of the modal expansion. But the equations have retained interest for their possible prototypical value (Dowell 1988a). For parameters specified above, this system of equations exhibits chaotic behaviour and the corresponding phase space plot is given in figure 1. Such behaviour is termed as strange attractor to distinguish the motion from classic limit cycle motions, forced periodic motions as well

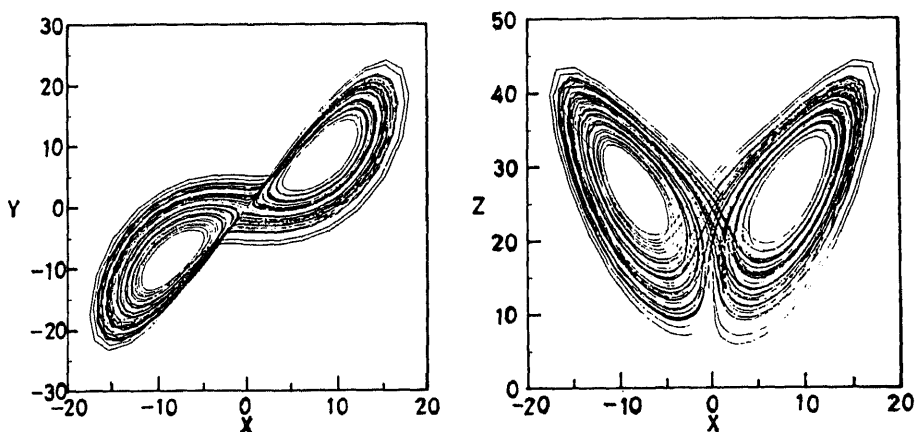


Figure 1. Lorenz attractor.

as fixed equilibrium points to which the system eventually comes to rest. The Lorenz model may be considered as a self excited autonomous system exhibiting chaos and had led to the oft repeated condition that there should be at least three variables for the existence of chaos in an autonomous system.

1.2 Structure of the paper

This paper is organised into eleven sections. In §2 we discuss the dynamics relating to some of the celebrated chaotic attractors in the literature. Section 3 discusses various types of nonlinearities which are of the Duffing and Van der Pol type of oscillators, nonlinear pendulum and systems with dry friction and associated chaotic phenomena encountered in mechanical systems. Section 4 is devoted to the dynamical systems where the nonlinearities arise due to piecewise linear functions such as those encountered in impacting systems. Chaos in flow induced problems is discussed in §5. Various types of bifurcations and the different routes to chaos are presented in §6. Section 7 deals with the control of chaos. The computational methods for obtaining periodic solutions are discussed in §8. In §9, various methods of obtaining the domains of attraction of coexistent solutions are presented. The various methods of characterisation of chaos are presented in §10. The paper ends with some of the important conclusions which are presented in §11.

2. Some other chaotic attractors

Chaos and the various phenomena associated with nonlinear systems have been found to occur both in continuous time dynamical systems represented by differential equations as well as discrete time dynamical systems represented by maps. While in the review we concentrate mainly on continuous time systems we also make some references to maps. Some of the strange attractors other than the Lorenz attractor which are quite extensively studied in the literature on chaos are the Rössler, Ueda, double scroll and Henon attractors.

2.1 Rössler attractor (spiral chaos)

Rössler (1976) introduced asymmetry into the Lorenz system and obtained equations of the following form

$$\dot{x} = -(y + z), \quad \dot{y} = x + ay, \quad \dot{z} = b + z(x - c). \quad (2)$$

Using the equations Rössler explained the dynamics of chemical reactions in a stirred tank. This apparently simple nonlinear autonomous system has only a single nonlinear term xz . For negligibly small values of z and for $0 < a < 2$ the system possesses an unstable focus at the origin and hence the trajectories spiral outwards and will eventually be attracted to infinity if the nonlinear term is absent. But as z increases the effect of nonlinearity becomes predominant and the trajectories are confined within a bounded attractor. The constant c acts as threshold for switching of the nonlinear term. For some values of the parameters a , b , and c , it can happen that only a periodic attractor is obtained. However, for substantial ranges of parameter values no such

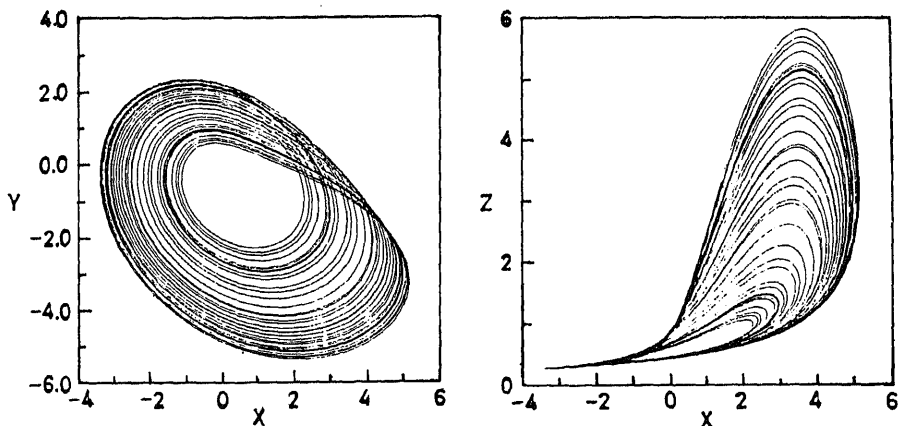


Figure 2. Rössler attractor.

periodic attractor exists and in these ranges all trajectories eventually resemble figure 2. Figure 2 represents the phase plane plot for the following parameter values: $a = 0.398$, $b = 2$, $c = 4$. Any two trajectories starting at nearby points on this attracting set will diverge exponentially, which is primary evidence of chaotic motion (Thompson & Stewart 1986).

2.2 Ueda's (Japanese) attractor

Even though Ueda obtained aperiodic solutions during an analog computer simulation of a forced self oscillatory system as early as 1961 he could publish his results only after he met Professor Hiromu Momota and Professor David Ruelle (Ueda 1985). It was generally believed that multiple equilibrium points are required for a system to exhibit chaos. But for the first time Ueda (1979) observed a strange chaotic behaviour in a single well potential problem with the origin as the only equilibrium point of centre type. Ueda (1979, 1985) studied a nonlinear electrical circuit which is governed by the following differential equation

$$\ddot{x} + c\dot{x} + x^3 = f \cos(t). \quad (3)$$

It has been found that for the parameter ranges $f = 9.9 - 13.3$ for $c = 0.1$ and $c = 0.0 - 0.31$ and for $f = 12.0$, the Duffing equation in the above form exhibits chaotic behaviour. A typical strange attractor is given in figure 3 and Ruelle calls this as the Japanese attractor.

2.3 Double scroll attractor

A simple autonomous electrical circuit known as Chua's Matsumoto (1984) is given below,

$$\dot{x} = \alpha(y - h(x)), \quad \dot{y} = x - y + z, \quad \dot{z} =$$

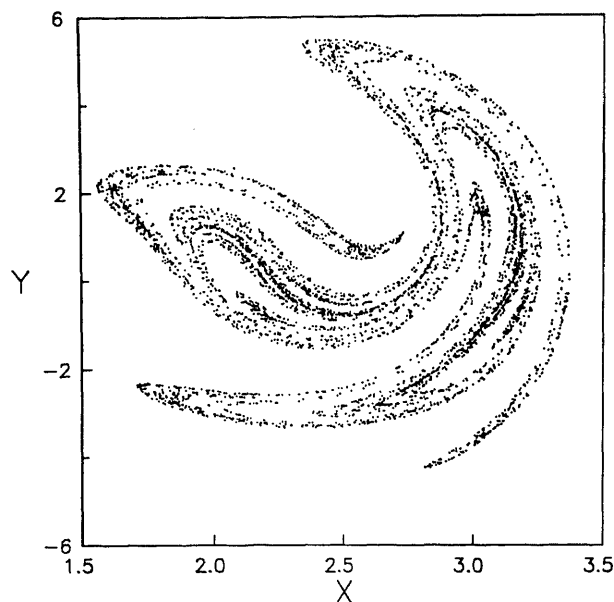


Figure 3. Ueda's attractor.

where $h(x)$ is the piecewise linear function given by

$$h(x) = \begin{cases} m_1 x + (m_0 - m_1) & x > 1, \\ m_0 x & |x| \leq 1, \\ m_1 x - (m_0 - m_1) & x < -1. \end{cases}$$

The phase trajectories of this system of equations also exhibit chaotic behaviour and has been extensively analysed. For parameters $\alpha = 9.0$, $\beta = 100/7$, $m_0 = -1/7$ and $m_1 = 2/7$, (4) show chaotic behaviour and the corresponding phase plane plots are shown in figure 4. The existence of chaos in double scroll attractor has been explained using the Shilnikov theorem (Shilnikov 1970).

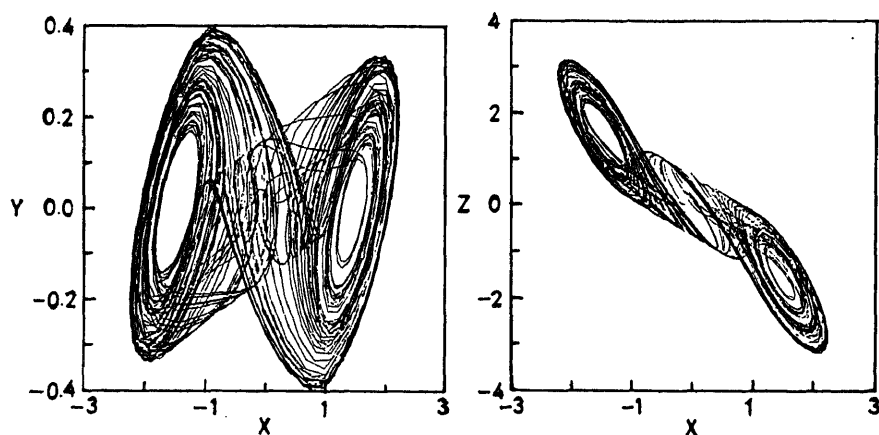


Figure 4. Double scroll attractor.

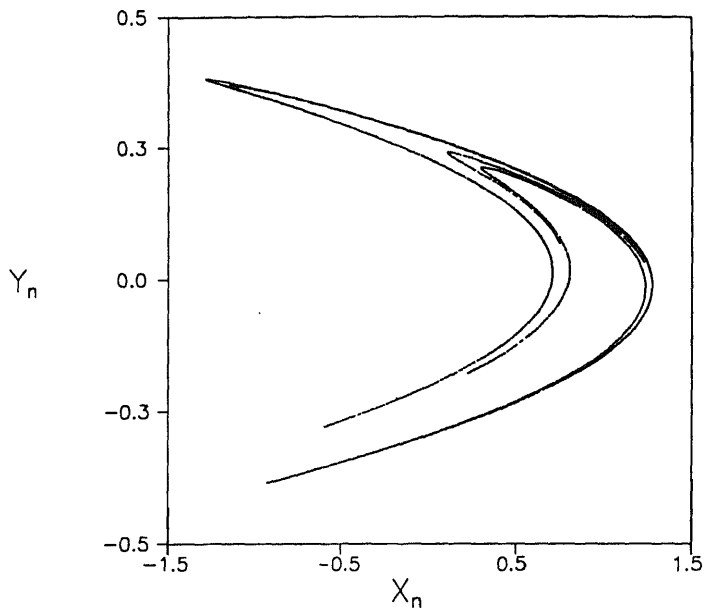


Figure 5. Henon attractor.

2.4 Henon attractor

Henon (1976) studied a two-dimensional quadratic map of the following form.

$$\begin{aligned} X_{n+1} &= 1.0 - aX_n^2 + Y_n, \\ Y_{n+1} &= bX_n. \end{aligned} \quad (5)$$

It possesses a saddle point at $(0, 0)$ and a fixed point at $(b - 2, b^2 - 2b)$. For $b = 0.3$ and ' a ' small this fixed point is a sink. As ' a ' increases it undergoes a sequence of period doubling bifurcations of periods, 2, 4, 8, 16, ... Ultimately this sequence of bifurcation culminates in chaos. The mapping as given in (5) has been studied extensively and possesses a strange attractor for a range of values of a and b . For $a = 1.4$ and $b = 0.3$ this system of mapping equations exhibit chaos and the corresponding strange attractor is shown in figure 5.

3. Structural systems and chaos

3.1 Structural systems and nonlinearities

Presence of nonlinearities is essential for a dynamical system to exhibit chaotic behaviour. Structural and mechanical systems also exhibit certain measure of nonlinearity in their dynamic behaviour. In most cases, when the motions are small the system dynamics could be adequately represented by linear models. Modern structural design practice like optimum designs, fully stressed and limit state designs, post buckling behaviour, which utilizes material to its fullest load carrying capacity and the

use of composite materials, greater speeds of operation of machinery and lighter constructions, extreme environments like earthquakes, heavy storms, ocean wave turbulence, fluid flow etc. have led to many of these systems operating in the nonlinear range. In these situations, the geometric or material nonlinearities become significant and dominate system behaviour. In mechanical systems, these nonlinearities are generally manifested in the stiffness and damping terms and have to be taken into account in the dynamic analysis. In mechanical systems the nonlinearities are usually associated with the presence of clearance, impact, preload, dry friction, hysteresis, fluid flow, dissimilar compression and tension behaviour etc (Schmidt & Tondl 1986).

In structural dynamical systems, there are a number of examples which exhibit chaotic behaviour. Some of them are (1) oscillations of beams with nonlinear restraints (Moon & Shaw 1983; Gudmundson 1989), (2) forced vibrations of a buckled beam (Holmes 1979; Moon 1980), (3) nonlinear flutter of plates under combined axial load and fluid flow (Dowell 1982), (4) parametrically forced pendulum (McLaughlin 1981; Leven *et al* 1985), (5) mechanisms with dry friction (Popp & Stelter 1989; Narayanan & Jayaraman 1991), (6) gear trains with clearance and impacts (Kunert & Pfeiffer 1989; Kahraman & Singh 1990b; Sato *et al* 1991), (7) heat exchanger tubes subjected to external flow (Païdoussis & Li 1992), (8) fluid conveying pipes with large flow velocity and loose baffles (Païdoussis & Moon 1988a), (9) rolling element bearings with clearance (Mevel & Guyader 1993), (10) vehicle systems (Kaas-Petersen & True 1985; Meijaard & De Pater 1989; Palkovics & Venhovens 1992), (11) large amplitude oscillations of arches, cables, strings (Johnson & Bajaj 1989; Szemplinska-Stupnicka *et al* 1989; Molteno & Tufillaro 1990; O'Reilly & Holmes 1992; Perkins 1992; Thomsen 1992), (12) rotor dynamics (Ehrich 1992), (13) rolling motion and capsizing of ships (Nayfeh & Hydeir 1986; Virgin 1987; Nayfeh & Sanchez 1988; Thompson *et al* 1990; Kan & Taguchi 1993), (14) slider crank mechanism (Peurach & Tongue 1991), (15) time delay systems (Plaut & Hsieh 1987; Tsuda *et al* 1992), (16) helicopter blade dynamics (Flowers & Tongue 1992), (17) structural cracks with fractal geometry (Theocaris & Panagiotopoulos 1993), (18) machinery acoustics (Moon & Broschart 1991).

3.2 Chaos in Duffing type nonlinearities

Duffing (1918) introduced a nonlinear oscillator which contains a positive cubic term. This equation in different forms has been used to model the dynamics of many systems in various fields of science and engineering.

3.2a Chaos in buckled beam (two-well potential): The equation of motion of the buckled beam in its first mode under harmonic excitation as derived by Tseng & Dugundji (1971) results in a Duffing's equation with negative linear stiffness and positive cubic stiffness and is of the form:

$$\ddot{x} + c\dot{x} - \alpha x + \beta x^3 = f \cos(\omega t), \quad \text{with } \alpha, \beta > 0. \quad (6)$$

The unperturbed form of the equation contains three equilibrium points; one at the origin of the phase space which is an unstable saddle point, and the other two symmetrically placed on either side of the origin at $(+(\alpha/\beta)^{1/2}, 0)$ $(-(\alpha/\beta)^{1/2}, 0)$ being centres.

Ever since Holmes (1979) presented his results of the dynamics of the harmonically excited buckled beam and showed the existence of chaotic and strange attractor

behaviour for certain parameter values by analog and digital computer studies, the Duffing's equation in this form has become one of the most celebrated models in the study of chaos as it represents a simple system bringing out most of the important features of chaotic behaviour. Chaos has been explained in these systems in terms of the solution jumping erratically from phase plane orbits about one equilibrium point to orbits about the other equilibrium point as the magnitude of the harmonic force is increased for a given frequency of excitation. Chaos in harmonically excited buckled beams has also been experimentally demonstrated by Moon & Holmes (1979) and Moon (1980) where magnetic forces were used to buckle a cantilever beam and the support was excited to introduce the external harmonic excitation. Moon & Li (1985a) observed fractal looking boundary which is correlated with the appearance of homoclinic orbits in the Poincaré map. Stable and unstable manifolds and the basin boundary for such a system is given in figure 6. Moon & Li (1985b) calculated the dimension of the strange attractor and observed that higher damping results in a smaller dimensional attractor.

Dowell & Pezeshki (1986, 1988) have shown, by means of a shell plot, the extreme sensitivity of the system to initial conditions as the harmonic force was increased with the periodic motion about the left equilibrium point changing to a periodic motion about the right equilibrium point even for negligibly small differences in initial conditions with attendant loss of predictability about the system. Similar explanation has also been provided by Tongue (1986). Tang & Dowell (1988a) have considered the effects of the higher modes on the chaotic motion of a buckled beam under external harmonic excitation and computed the threshold force required for chaotic motions. They compared their numerical results with experiments on a magnetically buckled beam similar to that of Moon (1980). Good qualitative agreement between numerical and experimental results were reported by them based on the inclusion of three modes in their analysis. Hanagud *et al* (1989) studied the motion of a simply supported buckled beam subjected to base excitation. Periodic and chaotic behaviour are obtained as the amplitude of base excitation is varied. A case with intermediate support with clearance is also investigated.

The route to chaos in this case is through a cascade of period doubling bifurcations as the magnitude of the external force is varied for a given frequency. One important feature of this period doubling bifurcation is that the ratio of the difference between the critical values of the parameter at which successive period doubling bifurcations take place for a cycle to that of the next cycle approaches a universal limit equal to 4.669201. This universal behaviour was shown to be true by Feigenbaum (1978) in the context of

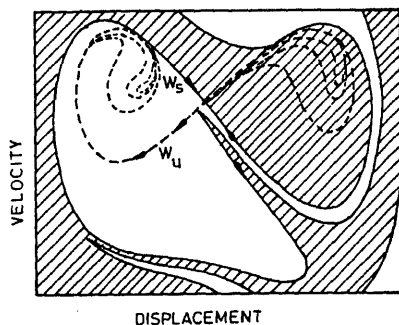


Figure 6. Stable and unstable manifolds of the Poincaré map superimposed on the basin boundary (Moon & Li 1985b).

chaos of iterative maps and the ratio is known as the Feigenbaum number, while the period doubling sequence is known as the Feigenbaum sequence. The period doubling sequence is one of the most observed pre-chaotic phenomenon. Feigenbaum has analysed the noninvertible one-dimensional map $x_{n+1} = F(x_n)$ depending on a parameter λ . He has shown that the family F has an infinite sequence of period doubling bifurcations of periodic orbits as the parameter λ is varied. When λ becomes greater than or equal to σ chaos occurs, where

$$\sigma = \lim_{n \rightarrow \infty} \sigma_n = [\lambda_n - \lambda_{n-1}] / [\lambda_{n+1} - \lambda_n] = 4.669201. \quad (7)$$

It should be pointed out that because σ is independent of the exact nature of the function F , this universal constant can be found for physical systems governed by differential equations. This question was discussed by Tousi & Bajaj (1985) where weak nonlinear and harmonically forced, two-degree of freedom systems have been studied by both averaging and shooting methods (Aprille & Trick 1972). Awrejcewicz (1991) considered a similar equation in an attempt to identify the route to chaos in driven mechanical oscillators. Using the shooting method he showed four sequences of period doubling bifurcations and each new solution was stable over an interval smaller than the interval of the previous member of the sequence. At the end chaos was obtained. Further he addressed the compatibility of the results with Feigenbaum constant (σ). He also presented two sequences of period doubling bifurcations in which one converged to σ while the other oscillated: $\sigma_n = 8.076; 3.305; 18.154$. This kind of oscillation in the Feigenbaum constant was also observed by Tousi & Bajaj (1985).

Another physical system in which chaos occurs is in the case of flutter of a buckled plate (Holmes 1977; Holmes & Marsden 1978; Dowell 1982). Dowell considered the von Karman nonlinear plate equations under axial compressive force with fluid flow on one side and used Galerkin modal expansion to get a two mode representation of the equation of motion which very much resembled the two well potential oscillator. He showed how the motions in the two modes interacted in a subtle way to generate chaos essentially through a Duffing's equation mechanism, the motion in one mode providing excitation to other. Brunsden *et al* (1989) have proposed a method for the prediction of the power spectra of chaotic motions by considering them as random superpositions of deterministic structures as single excursion around a homoclinic orbit. They showed good agreement between their predictions and the power spectra obtained by numerical simulations of the buckled beam equation and experimental results. Bispectral analysis of a buckled beam subjected to two harmonic excitations is performed and the results indicate that varying the relative phase angle of the high frequency term can result in the system moving in and out of chaos (Pezeshki *et al* 1991).

Criterion for the existence of chaos for the two-well potential problem such as the buckled beam has been established in the parameter space (frequency–amplitude of harmonic excitation) based on the Melnikov function (Guckenheimer & Holmes 1983; Moon 1980) which has come to be known as the Melnikov–Holmes criterion (Melnikov 1963). The criterion is based on the observation that the intersection of stable and unstable manifolds of the saddle point led to chaos. Holmes (1984) has shown that the intersection of stable and unstable manifolds leads to a horse-shoe map. The Melnikov function is a measure of the distance between stable and unstable manifolds in the phase space when the distance between them is small. Melnikov

function for (6) is given by (Holmes 1979),

$$f_M = \frac{4}{3} \left[\frac{c\alpha^{3/2}}{\pi\omega(2\beta)} \right] \sinh \frac{\pi\omega}{2\alpha^{1/2}}, \quad (8)$$

and when f exceeds f_M the sensitivity to initial conditions increases whereby the system exhibits chaotic behaviour.

Dowell & Pezeshki (1986, 1988) based on physical arguments and numerical studies have concluded that a necessary condition for chaos to occur in such double well potential problems is the intersection of stable limit cycle about the left or right equilibrium point and the unstable limit cycle of the saddle point. This is illustrated in figure 7. The forcing amplitude corresponding to the intersection of stable and unstable limit cycle and the Melnikov's value do not differ much. This observation by Dowell has been discussed critically by Szemplinska-Stupnicka (1992). Dowell (1991) made an attempt to give theoretical reasons for results obtained by the previous computer studies. Dowell & Pezeshki (1988) and Dowell (1991) state that "in order to have steady state chaos one must have near stable and unstable limit cycles in the phase space..." This becomes both necessary and sufficient condition for chaos. The term "steady state chaos" used here means large amplitude cross well motion which can be viewed as irregular hoppings between oscillations around two stable equilibria.

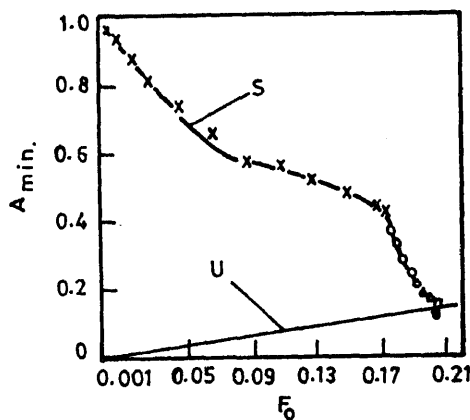
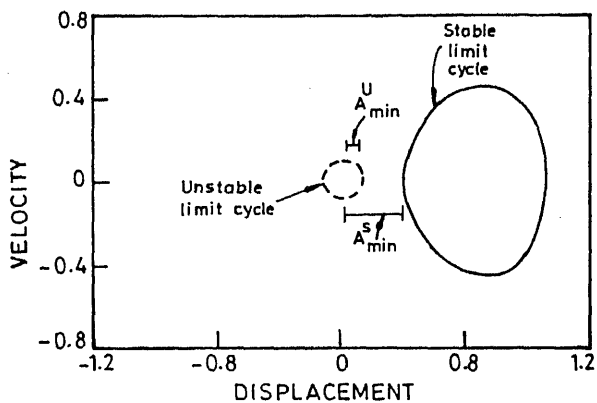


Figure 7. Stable and unstable limit cycles (Dowell & Pezeshki 1988).

Szemplinska-Stupnicka (1992) argues that for the problem of "necessary and sufficient conditions for steady state chaos" to occur, "criteria of chaos" still remain a point of contention in current investigations by pointing out the two contradictory assumptions considered by Dowell (1991). Rudowski & Szemplinska-Stupnicka (1987), Szemplinska-Stupnicka (1988a, 1989), Szemplinska-Stupnicka & Rudowski (1992) used approximate analytical method (harmonic balance method) and obtained analytical expressions for various bifurcation curves and the regions of chaos in the two dimensional plane consisting of the excitation force and frequency. Figure 8 illustrates the stable and unstable manifolds before, after and during intersection and also the corresponding response curves. Period doubling and saddle node bifurcation boundaries and the regions of chaos are shown in figure 9.

Higuchi & Dowell (1991) studied the effect of a mean load f_0 in addition to the harmonic excitation. Awrejcewicz (1991) studied the effect of constant term in the external excitation using shooting method. For $c = 0.25$, $f = 0.4$, $\alpha = 1.0$ and $\omega = 1.0$ he obtained the $1/2$ subharmonic solutions for the range of mean load $f_0 (0.4657 > f_0 > 0.0918)$. For $f_0 = 0.12$ the system exhibited chaos in which the strange attractor formed two line attractors which are well separated. As f_0 is decreased from 0.0918 and when it reaches 0.04657 one of the eigenvalues of the corresponding monodromy matrix penetrates the $+1$ boundary of the unit circle while the other remains inside. Shooting method fails for further changes in parameter value. For these

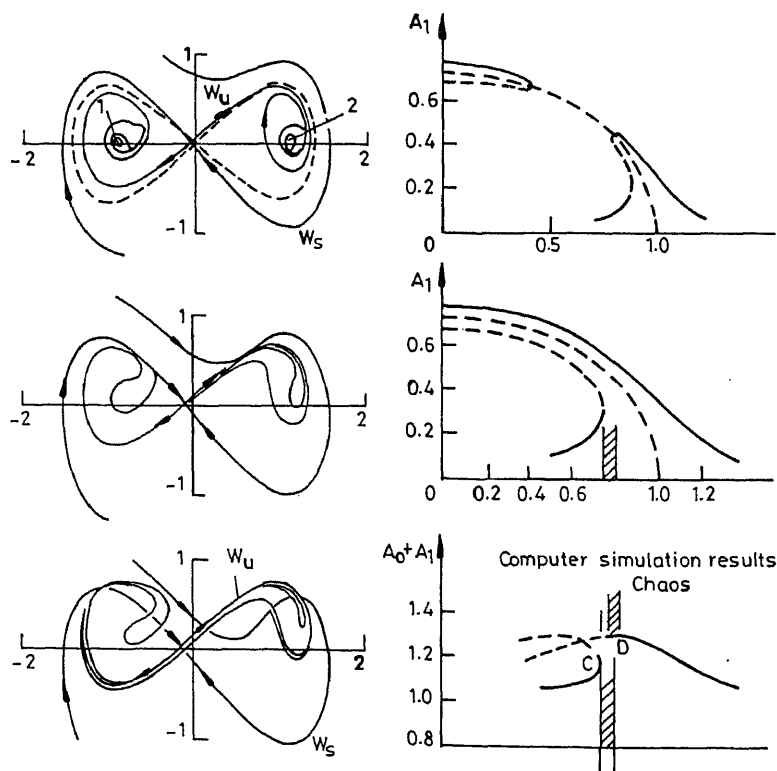


Figure 8. Invariant and response curves (Holmes 1979; Szemplinska-Stupnicka & Rudowski 1992).

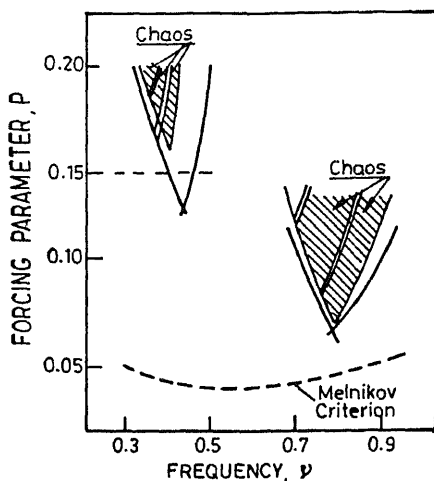


Figure 9. Bifurcation boundaries and regions of chaos (Szemplinska-Stupnicka & Rudowski 1992).

parameter combinations the oscillator possesses a strange attractor which is the closure of the unstable manifolds. This possibility of the violent birth of a strange chaotic attractor has been shown by Neimark (Butenin *et al* 1976). Gottwald *et al* (1992) conducted an experiment with a slider kept on a structure with the surface of two well potential excited by a harmonic force. Using this experimental mimicry, they constructed strange attractors for various parameter values. Baren (1994) studied Bernoulli–Euler, Rayleigh and Timoshenko models of a buckled beam using Melnikov's method.

Wiggins (1987) and Ide & Wiggins (1989) investigated quasiperiodically forced buckled beam equation. Using Melnikov analysis the homoclinic bifurcation sets in a five parameter space (c, f_1, f_2, ω_1 and ω_2) were obtained. By proper manipulation of the parameters the bifurcations sets were indicated in a two dimensional plane. It was also indicated how homoclinic bifurcation sets for an arbitrary number of frequencies may be obtained. Parthasarathy (1992) studied the same system with external and parametric excitations and obtained the bifurcation sets. Yagasaki (1990, 1991) and Yagasaki *et al* (1990) studied the motion of a buckled beam subjected to external and parametric type quasiperiodic excitations by applying averaging method as given by Holmes (1980). The existence of homoclinic orbits was proved and the homoclinic bifurcation curves were presented.

Iyengar (1992) investigated a buckled beam equation with random initial conditions. In the regimes wherein the solution is periodic, the solutions are insensitive to at least small changes in initial conditions. The variance or second central moment of the ensemble response is derived with the initial conditions of the state variables which are specified as random variables with small variances. In the limit as the variances of the initial conditions go to zero, if the response variances also tend to zero with time, the solution of the original dynamical system is nonchaotic. Otherwise the solution will be chaotic. Kunert & Pfeiffer (1991) adequately described the strange attractor of the buckled beam equation in terms of the probability distribution of the state space variables. To approximate these probability distributions an additional stochastic excitation of small intensity was taken into account. This not only reduced the problems concerning numerical convergence of the solution but was also more realistic

because a finite level of noise would be present anyway. Due to the additional noise excitation the calculation of probability density could be achieved directly by the solution of Fokker–Planck equation, if the excitation was white noise.

3.2b Hardening spring (single-well potential): It is very likely that chaotic motions occur in systems with multiple well potential as compared to single well potential. Since the year 1979 when distinctly new types of steady state solutions called “randomly transitional phenomena”, or chaotic motions were reported by Ueda (1979), it has become clear that our knowledge about properties and behaviour of the class of system is far from being complete. While the chaotic motion in systems having three positions of equilibrium, studied extensively by theoretical and experimental methods can be intuitively explained by physical arguments, the arguments fail in systems having single well potential (Szemplinska-Stupnicka 1986). The equation of motion of a single well potential system is given as

$$\ddot{x} + c\dot{x} + \alpha x + \beta x^3 = f \cos(\omega t), \quad \text{with } \alpha, \beta > 0. \quad (9)$$

Ueda (1979, 1980) considered the oscillations of a resonance circuit containing a saturable inductor. For parameters $c = 0.1$, $\alpha = 0.0$, $\beta = 1.0$, $f = 12.0$ and $\omega = 1.0$, (9) exhibits chaos. Szemplinska-Stupnicka (1987) also showed chaotic behaviour in a similar system and offered an explanation in terms of the instability of period three motion with respect to an aperiodic motion providing a sharp route to chaos. She also considered the effect of the static component of excitation. The period doubling sequence was predicted reasonably well by approximate harmonic balance analysis and considering the stability of period 1 motion with respect to the $1/2$ subharmonic motion by means of Floquet's theory. Novak & Frehlich (1982) studied hardening Duffing system by harmonic balance and stability analysis and obtained period doubling route to chaos in certain range of forcing parameter. Sato *et al* (1983) observed global scaling properties for the bifurcation in parameter space in Duffing and generalised Duffing equations using numerical simulations. The scaling properties were discussed in terms of a one-dimensional map. Similar observations in the parameter space can possibly be observed for double well potential problem in the parametric space diagrams given by Szemplinska-Stupnicka & Rudowski (1992). Tongue (1986) has also demonstrated the presence of chaos in the system of Ueda's type. He has offered an explanation that for large values of exciting force the system behaved in a manner similar to a multi-well potential oscillator. The importance of step length for numerical integration was also highlighted. Fang & Dowell (1987) by extensive numerical integration obtained multiple steady state periodic solutions like period 4 and period 6 and dual periodic responses for certain range of parameters. The chaotic motion also possessed dual solution. It has been suggested by them that the transition to chaos is through a sequence of dual periodic responses, period doubling sequence, almost periodic motion with a large period.

3.2c Softening spring (inverted double-well potential): The equation of motion of an oscillator with softening type (symmetric) of nonlinearity is given as below:

$$\ddot{x} + c\dot{x} + \alpha x - \beta x^3 = f \cos(\omega t), \quad \text{with } \alpha, \beta > 0. \quad (10)$$

Huberman & Crutchfield (1979) investigated such a system and found that for parameters $c = 0.4$, $\alpha = 1.0$, $\beta = 4.0$, $f = 0.115$ and for a small range of ω in the region

$0.525 < \omega < 0.53$ the system exhibited chaos. The problem was also studied by other authors notably by Steeb *et al* (1983), Turcher (1982), Rätty *et al* (1984a, 1984b), Szemplinska-Stupnicka (1988b) and Van Dooren (1988). It has been observed that chaos occurs at frequencies in the region of the principal resonance and the route to chaos is initially through a symmetry breaking bifurcation for a period 1 motion in the neighbourhood of $\omega = 0.53$ leading to two asymmetric period 1 motions being the dual of each other followed by a sequence of period doubling bifurcations of the dual periodic motions as the forcing frequency ω is decreased. Szemplinska-Stupnicka (1988b) has applied approximate analytical techniques (harmonic balance method) to predict the symmetry breaking bifurcation and the subsequent period doubling bifurcations by considering the stability of periodic motions with respect to the other periodic motions by using Floquet theory. Similar analysis has been carried out by Van Dooren (1988) also. Nayfeh & Sanchez (1989) analysed a similar system using multiple time scales, analog and numerical simulations in a two parameter space consisting of the frequency and amplitude of excitation. The basin boundary metamorphoses were studied using cell mapping method. Virgin & Cartee (1991) used multiple time scale and harmonic balance methods to obtain response curves and escape boundaries.

3.3 Chaos in pendulum (sinusoidal potential well)

The forced pendulum is a typical nonlinear system having sinusoidal potential well. The system with linear damping subjected to harmonic excitation is represented by the following equation,

$$\ddot{x} + c\dot{x} + \sin(x) = f \sin(\omega t). \quad (11)$$

The forced pendulum is isomorphic to many other familiar nonlinear systems, such as Josephson junctions and the phase locked loop configuration of a voltage controlled oscillator. It is essential to note that at the outset the seemingly simple situation of a forced pendulum is quite complex due to the fact that the space of variables is large. The interplay between the driving force and the natural modes of the pendulum causes chaos. Huberman *et al* (1980) obtained the response curves for a range of normalised frequency and also presented the bifurcation diagram with left side boundary indicating period doubling phenomena and right side boundary obtained from fold bifurcation values. This particular form of the bifurcation diagram is typical of a softening system. D'Humieres *et al* (1982) summarise the important results of their study as follows: (a) Prior to going chaotic the pendulum is found to break its spatial symmetry and oscillate with a larger amplitude to one side than the other. (b) The period doubling cascade is found to be a generic phenomenon for the forced pendulum. It occurs in the oscillating states of the pendulum and also in the rotating regime where the pendulum rotation frequency is phaselocked to the driving frequency. (c) Another chaotic state commonly observed appears to be related to random transitions between two phase-locked states that have become unstable. (d) A third kind of chaotic behaviour arises when the driving frequency is much smaller than the low amplitude resonance frequency of the pendulum. If the amplitude of the driving force becomes larger than the critical value at which the pendulum begins to rotate, the motion is a combination of positive and negative rotations in between which the pendulum undergoes damped oscillations. A two-dimensional state diagram with driving amplitude and normalized frequency is presented and various types of phaselocked regions and intermittent

regions are indicated. The phaselocked regions and the frequency response curves are shown in figure 10. Pederson & Davidson (1981) have also given similar qualitative picture by using numerical simulations. Although period doubling is found to be fairly common in the phaselocked states of the pendulum, it does not always manifest itself in complete bifurcation cascades. Intermittent behaviour between two unstable phaselocked states is also commonly observed. Koch & Leven (1985) investigated a parametrically forced pendulum and obtained the boundaries of subharmonic and homoclinic bifurcations on the basis of Melnikov method and second order averaging methods. It is shown that as the parameter is varied, repeated resonances of successively higher periods occur culminating in homoclinic orbits. For some selected parameter sets, the theoretical predictions are tested by numerical calculations and good agreement is found between them. Leven *et al* (1985) conducted experiments on parametrically harmonically excited pendulums to study the periodic and chaotic type motions. Period doubling route to chaos is identified with increasing driving amplitude and decreasing damping force. The coexistence of different periodic solutions as well as periodic and chaotic solutions is demonstrated and various transitions between them are studied. Transient chaos is also observed in the system. The transition from metastable chaos to sustained chaotic behaviour is also investigated. Hatwal *et al* (1983) obtained periodic and chaotic motions of a pendulum hinged to a mass of a harmonically excited nonlinear single degree of freedom (sdf) system. This system is taken as an example of an autoparametric system. They used numerical, analytical and experimental methods for this study. Miles (1988) investigated the motion of the pendulum with a single harmonic term in the solution and obtained the frequency response curves for various values of the amplitude of excitation. The symmetry breaking bifurcation boundaries are also presented in the parametric plane consisting of the damping and the amplitude of excitation. The results are compared with those obtained by Bryant who expands the solution in a truncated Fourier series which is given in one of the appendices of the same paper.

3.4 Chaos in Thompson's escape equation

Thompson (1989) constructed an asymmetric potential well and considered the

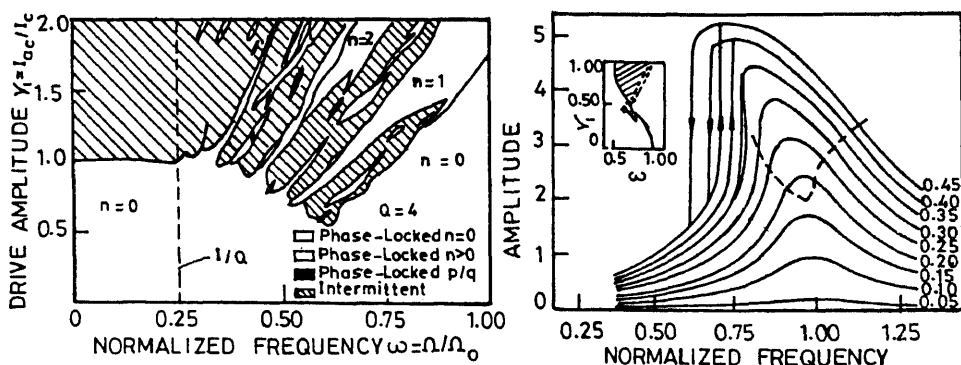


Figure 10. Phase locked regions and response curves (D'Humieres *et al* 1982).

following escape equation

$$\ddot{x} + c\dot{x} + x - x^2 = f \sin \omega t. \quad (12)$$

This model has been used to explain the capsizing of ships, offshore vessels, etc. By extensive numerical methods, Thompson (1989) constructed flip and fold bifurcation boundaries. Numerical path following techniques have been used to trace the bifurcation curves. For this purpose, PATH package (Kass-Petersen 1987a) and AUTO software (Deodol 1986) have been used. The results have been presented in three-dimensional figures consisting of frequency and amplitude of excitation and the response. Regions of chaos boundary escape are also given. The frequency response curves are given in figure 11. The boundaries of bifurcations, regions of chaos and the regions of escape are given in figure 12. Melnikov analysis is performed and the bifurcation line based on Melnikov analysis is also marked along with numerical results. The route to chaos is through period doubling and also by saddle node bifurcations. The system undergoes chaotic oscillations before it gets attracted to

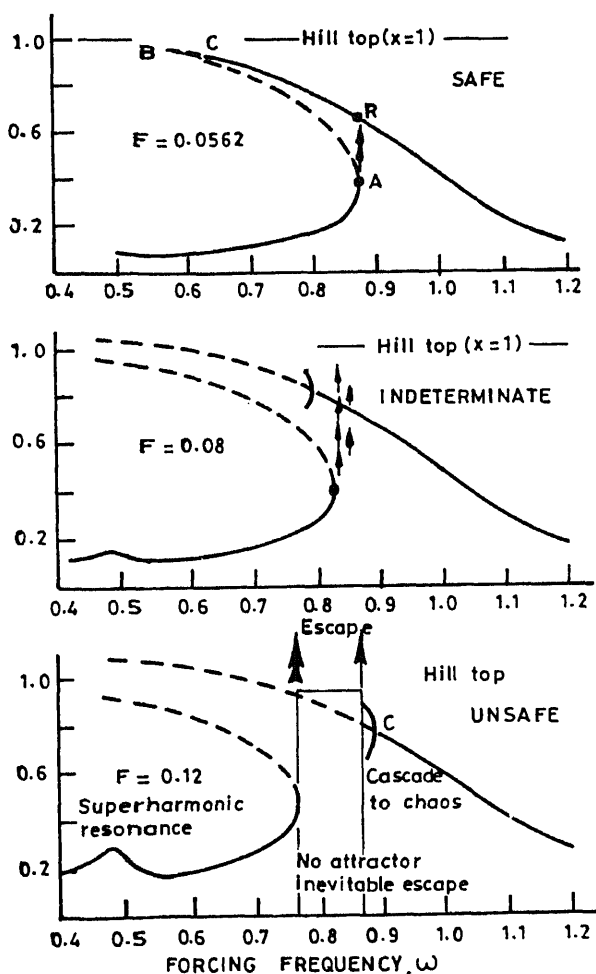


Figure 11. Frequency response curves (Thompson & Soliman 1991).

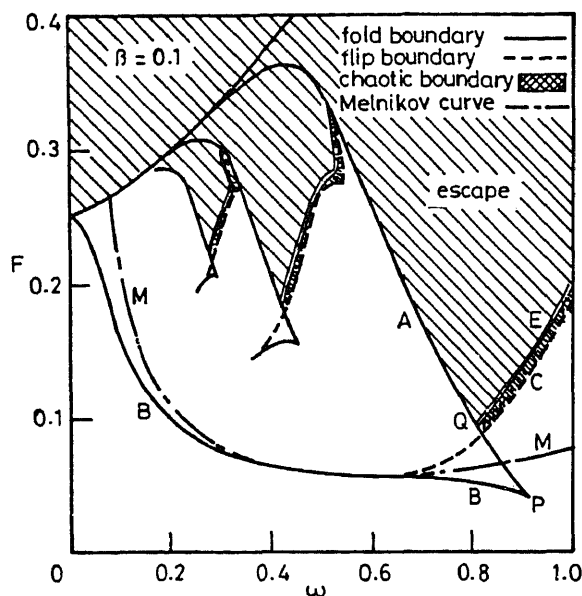


Figure 12. Bifurcations and escape boundaries and regions of chaos (Thompson 1989).

infinity. Initial condition maps are constructed for various parameter combinations. The loss of engineering integrity and basin erosion are discussed. It is noted that as the excitation force increases and reaches the Melnikov values, the probability that the system gets attracted to infinity increases steadily. Virgin (1988) used harmonic balance method in conjunction with stability analysis to obtain approximate boundaries of flip and fold bifurcations. This escape equation has been thoroughly studied by Thompson and his co-workers (Thompson *et al* 1987; Soliman & Thompson 1989; Thompson & Soliman 1990; Lansbury & Thompson 1990; Soliman 1993). Very recently a new phenomenon of indeterminate bifurcation was identified in this system and it attracted a lot of attention (Thompson & Soliman 1991; Soliman 1993).

Soliman & Thompson (1992a, 1992b) studied parametrically excited Thompson's equation and showed the possibility of indeterminate subcritical and transcritical bifurcations leading to chaos. Szemplinska-Stupnicka (1993) has analysed Thompson's escape equation using harmonic balance method and the results compare very well with those obtained by Thompson and his co-workers.

3.5 Chaos in Van der Pol type nonlinearities

The Van der Pol oscillator is another celebrated nonlinear system like the Duffing's oscillator. The equation of motion of the harmonically excited Van der Pol's oscillator is given in the form

$$\ddot{x} + \mu(x^2 - 1)\dot{x} + x = f \sin \omega t. \quad (13)$$

Without the external excitation it represents a self-excited autonomous system having a limit cycle and has been used to model many oscillatory phenomena in which the damping is a function of displacement such as vortex induced vibration of bluff bodies (Hartlen & Currie 1970; Iwan & Blevins 1974) and also with dry friction characteristics

(Tondl 1985). Guckenheimer & Holmes (1983) have indicated the possibility of mild chaotic behaviour of this system for small μ in a narrow range of control parameters f and ω . For large values of μ , Cartwright & Littlewood (1945), Levinson (1949), and Hayashi (1964), showed the possibility of steady state subharmonic responses with two different multiples of exciting frequencies ω . Levinson concluded that the transient response could become very complicated before the motion settled to one of the steady state periodic motions. Such behaviour in the parlance of chaotic dynamics is called transient chaos. But it has been observed that the forced Van der Pol's oscillator does not exhibit steady state chaos.

A combination of the Van der Pol–Duffing oscillator is also extensively studied in the literature and has been shown to exhibit chaotic behaviour. Ueda & Akamatsu (1981) have shown that for $\mu = 0.2$, $f = 17.0$ and $\omega = 4.0$ the system possesses strange attractor. Steeb & Kunick (1987) have considered the general form of nonlinear stiffness with x^n term and showed that for $n = 1$ the system does not possess strange attractor and for $n = 3, 5$, etc. the system exhibits chaotic behaviour. Chaos was confirmed by the positive value of Lyapunov exponent and decaying auto correlation function. Steeb *et al* (1983) observed chaos in a self excited system. Steeb *et al* (1986) have also studied a limit cycle system with two forcing frequencies which are incommensurate and confirmed the presence of chaos by computing the Lyapunov exponents. Awrejcewicz (1989) and Awrejcewicz & Mrozowski (1989) have also considered a similar problem describing a mechanical oscillator with the excitation term proportional to square of the frequency of excitation. They also studied the effect of dry friction through bifurcation and stability analysis and showed that chaotic behaviour for certain parameter ranges in the neighbourhood of Hopf bifurcation. Holmes & Rand (1980) considered an autonomous Van der Pol–Duffing oscillator and obtained bifurcation curves and had shown the type of phase plane trajectories in all the regions of two dimensional parameter plot. Xu *et al* (1985) obtained the initial condition maps for two degree of freedom coupled autonomous oscillator by using simple cell mapping method (Hsu 1987). Kapitaniak & Wojewoda (1990) and Kapitaniak *et al* (1990) investigated a Van der Pol oscillator for a quasiperiodic force represented by $f \cos(\omega t) \cos(\Omega t)$. For a fixed value of $\Omega = 2.464$, various types of attractors are found as ω is varied. For $\omega = 1.848$ the Poincaré map shows a periodic attractor, for $\omega = 1.614$ a two frequency quasiperiodic attractor, for $\omega = 1.401$ a strange non-chaotic attractor and for $\omega = 1.395$ a chaotic strange attractor appears in the Poincaré map. The strange non-chaotic attractors can be quantified on the basis of the frequency spectrum which usually consists of many more harmonic components. These are also characterised by determining the maximum Lyapunov exponent. The word strange refers to the geometrical structure of the attractor. An attractor which is not

- a finite set of points
- a limit cycle (a closed curve)
- a smooth (piecewise smooth) surface (for example, torus)
- bounded by a piecewise smooth closed surface volume

is called a strange attractor. An attractor is chaotic if at least one of the Lyapunov exponents of the system is positive. Strange non-chaotic attractor is one which is geometrically strange, but for which typical orbits have non-positive Lyapunov exponents.

Natsiavas (1991) studied a single degree of freedom oscillator with symmetric piecewise linear stiffness and piecewise damping of Van der Pol type (negative damping

around mean position) and observed periodic, quasiperiodic and chaotic solutions. Jump and beating phenomena and coexistence of subharmonic and quasiperiodic solutions are observed. Qin *et al* (1989) used analog simulation to study the driven Van der Pol oscillator and obtained quasiperiodic, Farey sequence, period doubling bifurcations and period adding sequence in chaos area. Brindley *et al* (1991) proposed an analytical method for predicting the boundaries of region in parameter space within which a strange non-chaotic attractor exists for quasiperiodically forced Van der Pol equation. The boundaries are obtained using conditions for Hopf bifurcation and the existence of quasiperiodic solutions. Belogortsev (1992) derived an analytical expression for the double Poincaré mapping for a weakly nonlinear quasiperiodic Van der Pol oscillator under two periodic forcing and obtained some analytical results about the quasiperiodic response of the oscillator. It has been shown that this mapping plays the same significant role as the averaged equations in the theory of the periodically forced Van der Pol oscillator. The bifurcation portrait in a two-dimensional parameter plane consisting of amplitude of exciting force f and the detuning parameter is shown. The regions of chaos are also indicated.

3.6 Chaos in dry friction-damped systems

Vibrating systems with Coulomb or dry friction damping can be considered as a piecewise linear system with discontinuous damping. Shaw (1986) considered the dynamics of a linear single degree of freedom vibrating system with dry friction damping. As the system is linear in each regime, Poincaré return maps can be effectively used to perform the bifurcation analysis. Popp & Stelter (1989) have analytically and experimentally showed chaotic behaviour of a single and a two degree freedom system under harmonic excitation with dry friction damping. Intermittency-I and period doubling bifurcations are observed. Awrejcewicz & Mrozowski (1989) have also considered chaotic motions of simple mechanical system with dry friction terms. However, in their analysis the basis system was of Duffing type. Grabec (1986) modelled friction in cutting tools and found self excited chaos in a four dimensional phase space. Feeny & Moon (1989) applied autocorrelation function based on symbolic equations to a chaotic dry friction oscillator to estimate the largest Lyapunov exponent. The friction problem is well suited for symbolic dynamics since two states of motion can be identified: sticking and slipping. This study is done for an experimental oscillator and for a numerical model.

Narayanan & Jayaraman (1989a, 1991) and Jayaraman (1991) investigated the response of a single degree of freedom spring mass system characterised by Duffing type stiffness and kept in moving belt. The dynamics of the system was governed by the following differential equation

$$\ddot{x} - g\beta(\dot{x} - v) + g\beta(\dot{x} - v)^3 + g\mu \operatorname{sgn}(\dot{x} - v) + \gamma_1 x + \gamma_3 x^3 = f \cos \omega t. \quad (14)$$

This system is analysed for the following system parameter $\alpha = 0.05$, $\beta = 0.02$, $\gamma_1 = 0.0$, $\gamma_3 = 10000$, $\mu = 0.6$, and $v = 1.0$. The frequency of excitation ω is varied from 2 to 30. In this range of frequencies many windows of chaos are obtained through extensive numerical simulations. The route to chaos is through a cascade of period doubling. The approximate periodic solutions are obtained using harmonic balancing and the frequency response plots are obtained. The stability of periodic solutions with respect to the subharmonics is investigated by using Floquet theory. The presence of chaos is

confirmed by the positive Lyapunov exponent. Initial condition maps are obtained through interpolated cell mapping approach as given by Tongue & Gu (1988a).

3.7 Chaos in hysteretically damped systems

It is well known that for the most important structural materials, the mechanical behaviour under cyclic loading at high amplitudes is inelastic. The restoring force versus displacement diagram in general shows hysteretic loops with decreasing slopes representing energy dissipation and material damage (Sozen 1974; Wen 1989). This behaviour can be adequately represented by Bouc's model (Barber & Wen 1981). Yang *et al* (1991) demonstrated the possibility of chaotic vibrations in hysteretically damped systems using numerical methods. Chaos is confirmed by the presence of positive Lyapunov exponent. Phase plane plots and Poincaré maps are also constructed. Probability density function and power spectral density plots are also presented. Sato *et al* (1989) also used point mapping method to study a similar system and observed jump phenomenon and chaotic behaviour.

3.8 Chaos in maps

In addition to differential flow a large body of literature is available for discrete maps also. The one-dimensional quadratic map $[x_{i+1} \rightarrow \alpha x_i - x_i^2]$ also exhibits a variety of bifurcation phenomena encountered in nonlinear systems. Period doubling as well as crises type of bifurcation are pointed out in this map (Grebogi *et al* 1982, 1983). For $\alpha < -0.25$ no fixed point of the map exists. At $\alpha = -0.25$ a tangent bifurcation occurs at which a stable and an unstable fixed point are created. It is well known that as α is increased past -0.25 , the stable fixed point undergoes period doubling which culminates in chaos at $\alpha = 1.40095$.

4. Chaos in piecewise linear/impacting systems

Chaotic vibrations have been obtained in many mechanical systems having piecewise linear characteristics such as in impact oscillator problems and systems with clearances and backlashes. Holmes (1982) has studied the vertical motion of a ball bouncing on a massively sinusoidally vibrating table. The impact motion is analysed using a simple difference equation satisfying a simple impact rule involving the coefficient of restitution. Flip and fold bifurcations have been found to occur and the values of bifurcation parameters have been obtained. For large velocities and coefficient of restitution (r) close to unity it has been established that chaotic motions occur. The stable and unstable manifolds have been generated and it has been observed that they intersect prior to the occurrence of chaotic motion. The strange attractor is found on the unstable manifolds of the saddle point. The horseshoes for 1 curves are also discussed. The tangling of stable and unstable manifolds in the presence of horseshoe map is given in figure 13. Tufano & Athanasopoulos (1983a) have studied the dynamics of a bilinear oscillator using modern dynamical systems theory (as the

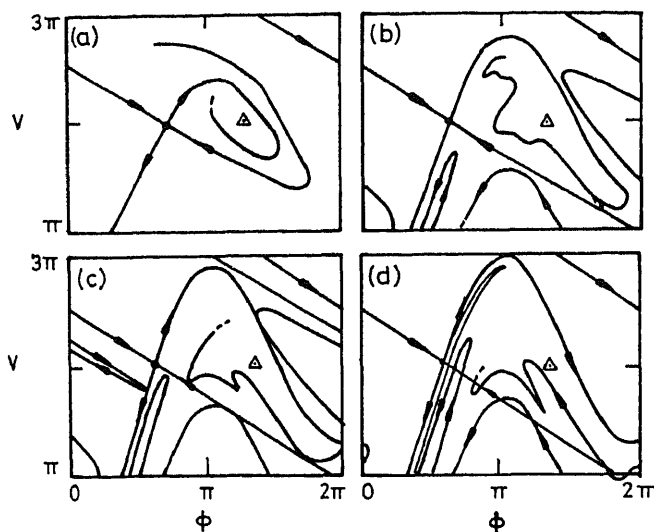


Figure 13. Stable and unstable manifolds (Holmes 1982).

maps are used). The flip bifurcation curves are drawn for periodic orbits of the impact oscillator. The flip bifurcation curves have been drawn using centre manifold calculations. Shaw & Holmes (1983b) analysed a linear oscillator subjected to a harmonic excitation hitting against a rigid stop with very low or zero coefficient of restitution (r). As the value of r is zero, the mass returns with zero velocity after hitting the stop. This facilitates study of the dynamics of the system using a one dimensional map. The physical model with zero coefficient of restitution and the frequency response curves for single impact orbits are shown in figure 14. Period doubling bifurcation diagrams for periods 1, 2, 3, 4 and 5 are given with frequency of excitation ω as the bifurcation parameter. However, finite dissipation cases are also treated by considering 2D map as a singular perturbation of the 1D map.

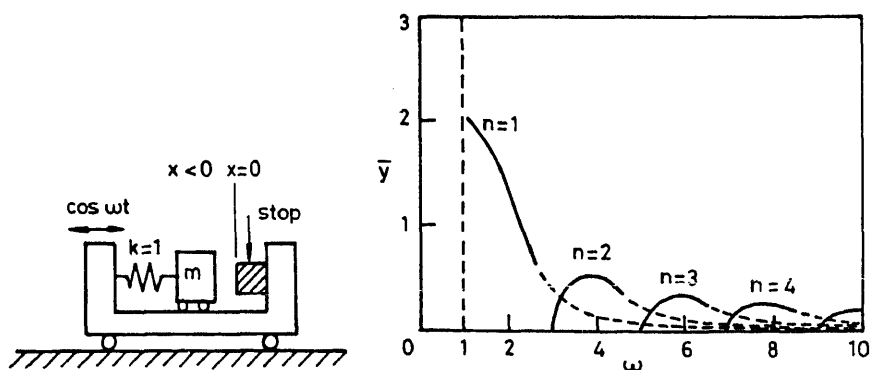


Figure 14. The physical model and response curves of an impact oscillator with large dissipation (Shaw & Holmes 1983b).

Thompson *et al* (1983) analysed a bilinear oscillator representing the motion of the offshore mooring tower and found that the system undergoes a series of flip bifurcations before attaining chaos. Using Poincaré return maps Shaw (1985) analysed the periodic motions of a linear sdf oscillator with two symmetrically placed rigid stops about the equilibrium position under harmonic excitation. Frequency response curves for various amplitude of excitation ($\beta = 1, 2, 3$), coefficient of restitution ($r = 0.5, 0.7, 0.9$) for various periodic orbits ($n = 1, 3, 5$) in the range of exciting frequencies ($\omega = 0-10$) have been presented. The frequency response curves exhibit a hardening type non-linearity for all orbits studied. For periodic orbits with $n = 1, 3$ and 5 , saddle node bifurcation curves have been drawn in β - ω plane. Using digital simulation homoclinic tangling of invariant curves is observed and chaotic motions are encountered. The chaotic motions were confirmed by the presence of a strange attractor and sensitivity to the initial conditions.

Kotera & Yamanashi (1986) investigated the influence of coefficient of restitution and the coefficient of damping on the chaotic motion of an impact oscillator. Chow & Shaw (1986) and Shaw & Rand (1989) analysed a second order linear differential equation with negative linear stiffness representing the small motion of inverted pendulum impacting against rigid stops on both sides. Using Poincaré return maps single sided and symmetric double sided impact motions were studied. The saddle node and flip bifurcation curves have been given in parameter planes β - α and β - ω . For both types of motion Melnikov calculations have been performed to get the parameter ranges above which one can expect intersection of invariant curves. Shaw & Shaw (1989) performed a similar study on the motion of the above system mounted on a linear sdf system. Bifurcation diagram and the explicit expressions for invariant curves are obtained. Moore & Shaw (1990) conducted experiments on normal and inverted pendulums and compared the results with those obtained analytically. It was observed that the inverted pendulum exhibits ten different steady state responses for the same driving amplitude and frequency. Isomäki *et al* (1988) have obtained domains of attraction of various coexisting solutions of an impact oscillator. Mahfouz & Badrakhan (1990) used numerical methods to investigate the different piecewise models with setup springs and clearances. Bifurcation diagrams and the various regions of steady state responses including chaos are presented.

Moon & Li (1990) conducted experiments on space truss structure and observed chaotic behaviour. In connection with the study of space truss structures Li *et al* (1990), modelled two truss members with smooth pin and play as a zero stiffness oscillator and analysed the system by employing a simple impact rule. For small harmonic forcing amplitude the symmetric and asymmetric periodic solutions are obtained using Poincaré return maps. Saddle node and pitch fork bifurcations are found for both types of solution, while flip bifurcations are found for the asymmetric periodic solutions. Bifurcations diagrams with driving amplitude as the bifurcation parameter are given. Using digital simulation strange attractors are obtained. It is quite surprising that this work was motivated by the question of whether the source of chaos was the large number of elements in the experimental truss or whether chaos would result from forcing a small structure which was held together by pin joints. Heiman *et al* (1987, 1988) studied the periodic and chaotic motions of a secondary mass moving in an inclined slot in a harmonically moving primary mass using the Poincaré return mapping. Stability boundaries for various types of motions are obtained for $r = 0.1, 0.5$ and 0.9 . Period doubling bifurcations are studied using the return maps. Whiston

(1987) analysed the steady state vibroimpacting responses of harmonically excited linear oscillators by using a modern dynamical systems approach allied with numerical simulation. The homoclinic tangling of invariant curves have been presented with very high resolution. The results are discussed in an engineering context. Whiston (1992) discussed the non-differentiable nature of the vibro impact dynamics which can lead to breakdown of the global stable manifold theorem applicable to smooth dynamical systems. An extensive study is made on the various aspects of the stable and unstable manifolds as they are very important to understand the structure of the strange attractor and the creation of horseshoe maps which leads to chaos. Chaos is also observed in impact oscillators designed for the purpose of vibration control (Sharif-Bakhtiar & Shaw 1988; Shaw & Tung 1988; Karyeacis & Caughey 1989). Natsiavas & Babcock (1988) modelled the motion of an unanchored fluid tank as a piecewise linear oscillator and studied the same under harmonic excitation. Chaotic responses are obtained by numerical simulation for a range of parameter values.

Sato *et al* (1991) investigated the motion of gear pair considering it as a piecewise linear oscillator with time dependent tooth stiffness and backlash using point mapping method. Using a stability analysis the saddle node bifurcation and flip bifurcation sets are obtained for a range of frequency and forcing amplitude parameters. Kahraman & Singh (1990a, 1990b) studied the impact dynamics of a gear pair considering the system as a piecewise linear one using digital simulation and concluded that for certain combinations of parameters the system exhibits chaos. The dynamics of single degree of freedom system with clearance and continuous nonlinearities were studied by Kahraman & Singh (1992). Kozol & Brach (1991) analysed the vertical motion of a ball impacting against a rocking table and found that for certain frequency range the ball motion becomes chaotic. Grazing incidence of an impact oscillator can also cause chaotic motion (Nordmark 1991; Ivanov 1993). Peterka & Vacik (1992) have studied a simple impact oscillator and presented the regions in parameter plane in which various types of periodic motions occur. The transition from periodic to chaotic motion in an impact oscillator is discussed. Raghothama (1993) investigated the dynamics of spur gear pair with clearance type of nonlinearity by using both numerical numeric-analytical methods and obtained various types of bifurcations which lead to chaos. Periodic solutions are obtained by incremental harmonic balancing method. However, chaotic and quasiperiodic solutions are obtained by numerical simulations. A three-degree of freedom model representing a gear-bearing system is also considered. A cam mechanism with clearance induced piecewise nonlinearity is also investigated and the possibility of chaotic behaviour is established. Vaishali (1994) investigated roller bearing system with clearance and Hertzian type contact nonlinearity and constructed parametric space diagram indicating the regions of various types of steady state response. Period doubling and quasiperiodic route to chaos are identified using numerical simulation.

5. Flow-induced vibration and chaos

5.1 External flow

In flow-induced vibration problems such as aeroelastic flutter, vortex induced and galloping oscillations, vibrations due to fluid elastic instability, the aero/fluid dynamic

forces including the vibrations are almost invariably non-conservative and nonlinear functions of structural motion leading to a complex and wide variety of dynamical characteristics of coupled fluid-structure interaction problems. In addition to the nonlinear nature of fluid forces, if the structure is inherently nonlinear and also excited by external forces, the dynamics becomes still more complex and it is natural to expect chaotic behaviour in such systems. Holmes & Marsden (1978) and Dowell (1982) have shown the existence of chaos in the flutter of nonlinear plates subjected to in-plane compressive loads and fluid flow on one side. Holmes (1977) and Holmes & Marsden (1978) have also considered in great detail and by use of bifurcation theory and centre manifold theorem, the bifurcation behaviour and stability of motions corresponding to transition to divergence and flutter of nonlinear plates. Huang *et al* (1990) have studied the dynamic response of a two degree freedom model of offshore structures in a steady current and regular wave environment. The hydrodynamic forces on the structure are modelled by modified Morison equations and an additional nonlinear symmetric hardening spring is included in the model. Period doubling route to chaos is identified in this system. Liaw (1988) has observed a subharmonic route to chaos in the dynamical behaviour of articulated towers subjected to hydrodynamic forces. The sensitivity to the initial conditions is also discussed.

Chaotic motions of an autonomous two dimensional aerofoil with cubic pitching stiffness in incompressible flow are investigated by Zhao & Yang (1990). Phase plane diagrams are constructed confirming chaotic behaviour and a period doubling route is discerned. A two step approximate analysis by coupling the limit cycle amplitude of the flutter motion for one of the equations and treating it as an excitation to the other oscillator, the route to chaos for the aerofoil system is presented. Simiu & Cook (1991) have considered the chaotic motions of the harmonically forced single degree of freedom square prism in a fluid flow and two degree of freedom autonomous elastically coupled two square prisms in fluid flow. They have shown chaotic motions in a range of system parameters through a quasiperiodic route. Simiu & Cook (1992) presented a number of empirical fluid-elastic models to study the dynamical behaviour of bluff bodies.

Narayanan & Jayaraman (1993) and Jayaraman & Narayanan (1990c) considered a nonlinear oscillator with Duffing type of nonlinearity of the hardening type subjected to harmonic excitation and fluid forces. The physical model and the corresponding piecewise linear stiffness function are shown in figures 15 and 16. The flow-induced force is described by a polynomial of relative velocity between the structure and fluid and given by Blevins (1977). By numerical simulations the various periodic and chaotic solutions are obtained. Using approximate analysis (harmonic balancing in conjunction with Floquet analysis) the period 1 and period 2 solutions are obtained (Narayanan

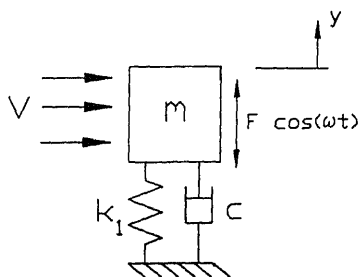


Figure 15. A square prism in cross flow.

& Jayaraman 1993). Period doubling route to chaos is identified. Chaos is confirmed by the presence of positive Lyapunov exponent. Initial condition maps for periodic and their dual periodic orbits are obtained by interpolated cell mapping (Jayaraman & Narayanan 1990a). Sekar & Narayanan (1994) used the Fast Galerkin method to obtain some of the initial periodic orbits. Fast Galerkin method in conjunction with the stability analysis is used to investigate the same problem and the various periodic orbits and their bifurcation points are predicted very accurately. Narayanan & Sekar (1994) investigated a harmonically excited sdf oscillator subjected to fluid flow using the fast Galerkin and numerical methods. A bilinear stiffness function is assumed (figure 16). Period doubling, mode locking phenomenon and crises are found to occur in this system. Bifurcation boundaries and bifurcation diagrams with flow velocity as the bifurcation parameter are presented. Chaos is confirmed by the existence of positive Lyapunov exponent. A general theory for the analytical investigation of tube arrays in cross flow is given by Chen (1987). Païdoussis (1987) discussed flow-induced instabilities of cylindrical structures. Païdoussis & Li (1992) investigated the chaotic dynamics of heat-exchanger tubes impacting on loose supports using delay differential equations. Both the ends of the tubes are assumed to be clamped while the intermediate support is assumed to be having certain amount of clearance. Symmetric and asymmetric ($x = 0.5$ and 0.45) cases are studied. The model representing the physical system is shown in figure 17. Using numerical simulation the critical velocity of fluid flow beyond which irregular impacting motion occurs is determined. The intermediate support is assumed as a cubic stiffness and also a trilinear stiffness. The impacting motion is studied by Poincaré return maps. Chaos is confirmed by positive Lyapunov exponents. Period doubling and Hopf bifurcations are found to occur. Païdoussis *et al* (1993) have studied the response of heat exchanger tubes under the excitation of an experimentally determined nonlinear fluid force using a two degree of freedom analytical model for rotated triangular array of cylinders. Complex tube dynamics are predicted due to the nonlinearities introduced by impact/sliding at the tube supports.

5.2 Internal flow

Numerous studies have been conducted on the dynamics of flexible tubes conveying fluid. Chaotic motions in nonlinear pipes conveying fluid have been reported in the

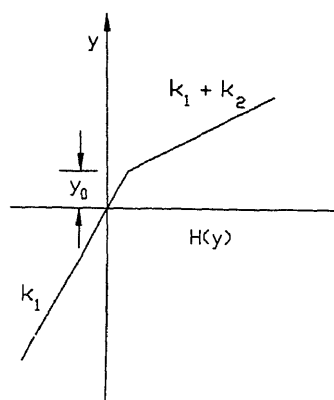


Figure 16. Piecewise linear stiffness function.

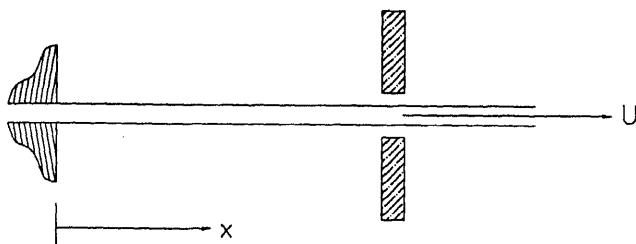


Figure 17. A constrained pipe conveying fluid.

recent literature. The bifurcation behaviour and the stability of motion of nonlinear pipes conveying fluid are treated in the works of Bajaj *et al* (1980), Bajaj & Sethna (1982, 1984) and Thompson & Lunn (1981). The bifurcation to subharmonic and combination harmonic types of resonances of nonlinear pipes conveying fluid with harmonic flow velocity fluctuations are given by Sri Namachchivaya (1989), Sri Namachchivaya & Tein (1989). The fluid-conveying cantilevered pipe has become a classical problem for the study of all autonomous nonconservative dynamical systems because of the simplicity with which it can be modelled analytically and the relative ease with which reliable experiments may be conducted (Païdoussis & Li 1993).

Tang & Dowell (1988b) were perhaps the first to consider chaotic vibrations in a cantilevered pipe conveying fluid in the presence of magnetically generated potential wells. They have used a pipe with an inset steel strip and two equispaced permanent magnets on either side, exerting strong nonlinear forces on the pipe and buckling it into one of the two potential wells on either side of the pipe similar to buckled beam experiment of Moon. Increasing flow velocity sufficiently above the critical value for flutter about the buckled state, the pipe develops chaotic oscillations. The autonomous system without external force was considered theoretically while the nonautonomous system with an external harmonic excitation was treated theoretically and experimentally. Once again chaos was obtained for sufficiently high amplitudes of harmonic excitation and the threshold value force was strongly dependent on the flow velocity. They also considered the influence of damping and the number of degrees of freedom used in their model and found that the character of the dynamics was sensitive to both. Païdoussis & Moon (1988a, b) considered the motion of a linear cantilevered pipe conveying fluid with nonlinear boundary conditions in the form of motion limiting constraints similar to those used in impacting systems. They constructed phase plane diagrams, Poincaré maps, calculated the autocorrelation and power spectral density functions and Lyapunov exponents confirming the chaotic behaviour. Markrides & Edelstein (1992) studied the oscillations of cantilevered tube conveying fluid in the presence of motion limiting constraints using finite element method. Quasiperiodic route to chaos was observed for increased flow velocity and for stiffness parameter associated with the motion limiting stops.

A detailed account of investigation on the pipes conveying fluid is given in a recent review paper by Païdoussis & Li (1993). Païdoussis *et al* (1992) have observed chaos in cantilevered pipe conveying fluid with motion limiting stops when the flow velocity is sufficiently high. The dimensions of the chaotic attractors are calculated using delay embedding technique. Païdoussis *et al* (1991) have analysed a constrained pipe conveying fluid using numerical simulations and compared the simulation with the experimental results.

Jayaraman & Narayanan (1990b), Jayaraman (1991) and Jayaraman & Narayanan (1993) investigated pipes conveying fluid considering it as an sdf and 2-dof (degree of freedom) system with parametric excitations and identified chaotic behaviour. Fundamental and parametric resonances were treated by multiple time-scale methods. Transient chaos is also observed. Stability regions for trivial and nontrivial boundaries and initial condition maps are obtained. Period doubling route to chaos is identified in the system. Dual responses for periodic and chaotic motions are also presented.

6. Bifurcations and routes to chaos

For a nonlinear dynamical system possessing chaotic behaviour, the nature of transition from periodic motion to chaos, as a control parameter is varied, is of importance both in terms of confirming its deterministic status as well as in anticipating chaotic behaviour if it exhibits similar prechaotic behaviour. The stability of periodic solutions can be determined by using Floquet theory (Arnold 1983). The eigenvalues of the monodromy matrix can be obtained and by plotting these eigenvalues in the unit circle one can obtain the stability information of the periodic orbit (Hsu 1974). If all the eigenvalues (Floquet multipliers) lie inside the unit circle it indicates the solution is stable. The eigenvalues can leave the unit circle in three ways and are shown in figure 18 (Arnold 1983).

6.1 Types of bifurcations (*flip and fold*)

When one of the eigenvalues leaves the unit circle through -1 boundary, the system undergoes period-doubling bifurcation otherwise called flip bifurcation (intermittency type II), in which the original periodic orbit becomes unstable and a new periodic orbit with twice the original period gets generated. Successive such bifurcations result in the

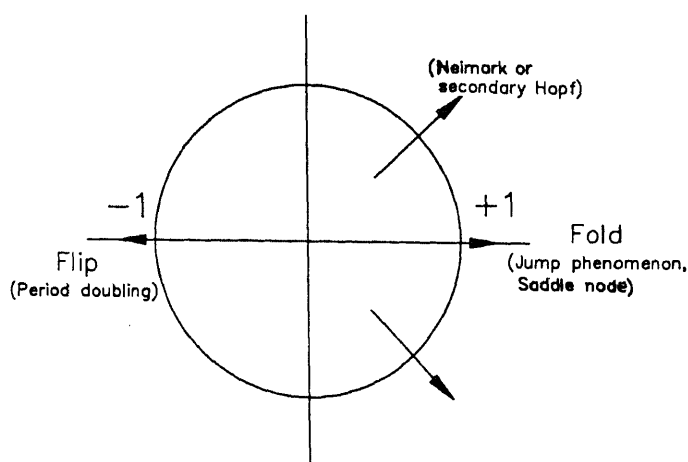


Figure 18. Nature of bifurcations and leaving of Floquet multipliers from unit circle (Arnold 1983).

familiar period doubling route to chaos which has a quantitative universal constant called the Feigenbaum constant (Feigenbaum 1978).

If one of the eigenvalues penetrates the $+1$ boundary of the unit circle it indicates birth or annihilation of a new periodic orbit. A saddle node bifurcation indicates that a saddle and a node merge and the frequency becomes incommensurate leading to birth of quasiperiodic solution which is generally characterised by a closed curve in the Poincaré map. Before this bifurcation the response contains combination harmonic frequencies indicating the modelocking phenomenon and after the bifurcation the frequencies become incommensurate indicating the drifting of phase points leading to quasiperiodic response. It also indicates a jump phenomenon in which the orbit jumps from a resonant to a nonresonant branch (or vice-versa) of the response curve in which a vertical tangency is reached indicating an exchange of stability. Sometimes a periodic orbit gets destroyed and a sudden explosion of the size of the attractor occurs (intermittency-I). This kind of sudden growth of the size of the attractor which normally results in chaos is called crisis (Grebogi *et al* 1982, 1983a). Kleczka *et al* (1989) and Bajaj (1991) discussed interior and boundary crises.

If the complex conjugate eigenvalue leaves the unit circle radially, it is known as the Hopf bifurcation whereby a fixed point bifurcates to a limit cycle and further change in the control parameter results in quasiperiodic orbit (intermittency-III). This kind of bifurcation is called a Neimark bifurcation (named after the Russian mathematician) or secondary Hopf bifurcation.

A symmetry breaking bifurcation which always precedes the period doubling bifurcation is indicated when one of the eigenvalues touches the $+1$ boundary of the unit circle from inside and travels backwards. Symmetric solutions characterised by odd harmonic components will become asymmetric by the introduction of even harmonic components after symmetry breaking bifurcation. Thompson (1992) classified generic co-dimension-one attractor bifurcations in dissipative systems and presented them in table form.

6.2 Ruelle–Takens route to chaos – T^3 , torus bifurcation

An important route to chaos in mechanical system is through quasiperiodic motions and their subsequent instabilities. The precursor to such a route is the existence of Hopf bifurcation such as occurring in flutter problems when a static equilibrium position becomes unstable and bifurcates into a periodic limit cycle motion as a control parameter is varied. Further Hopf bifurcations and consequent simultaneous existence of coupled limit cycles with incommensurate frequencies lead to quasiperiodic motions. When the quasiperiodic motion becomes unstable chaos occurs in a finite sequence of bifurcations.

The theory of quasiperiodic route to chaos with finite sequence of Hopf bifurcations was first observed by Ruelle & Takens (1971) and later elaborated by Newhouse *et al* (1978) as a model for turbulence. It challenged for the first time the mechanism proposed by Landau (Landau & Lipschitz 1971) which required an infinite sequence of Hopf bifurcations for the generation of turbulence. In fact they showed that quasiperiodic motion with three incommensurate frequencies being the result of the three successive Hopf bifurcations suffice for the generation of chaos. This route is also called as torus 3 bifurcation or T^3 bifurcation. The route to chaos through quasiperiodic motion with three incommensurate

frequencies has been used to explain the behaviour of Rayleigh–Bernard convection (Gollub & Benson 1979).

6.3 T^2 , torus bifurcation

Though the quasiperiodic route to chaos through torus T^3 bifurcations with a strange attractor is a more familiar one it is not the only quasiperiodic route to chaos. Curry & Yorke (1977) and Berge *et al* (1984) have discussed another quasiperiodic route to chaos, where chaos occurs directly from a quasiperiodic regime with only two incommensurate frequencies without the appearance of a third frequency. In this route before the eventual departure of the trajectories from the torus T^2 - and its destruction leading to chaos, frequency synchronisation (mode locking) takes place when the incommensurate frequencies in the T^2 motion become commensurate.

The quasiperiodic route to chaos either by T^3 or T^2 torus bifurcations have been discussed in the literature by Curry (1978), Gollub & Benson (1980), Grebogi *et al* (1983b), Ostlund *et al* (1983), Fein *et al* (1985), Gwinn & Westervelt (1986), Sano & Savada (1983) and Stavans *et al* (1985). The quasiperiodic route to chaos has also been discovered in the chaotic motion of nonlinear spring to harmonic motion (Johnson & Bajaj 1989; Molteno & Tufillaro 1990) in the coupled Van der Pol–Duffing oscillator with Coulomb damping under harmonic excitation (Awrejcewicz 1989; Awrejcewicz & Mrozowski 1989) in the self-excited forced autonomous square prisms considered as a two-degree of freedom system (Simiu & Cook 1991), in a two-degree of freedom nonlinear oscillator with cubic nonlinearities in stiffness terms and subjected to harmonic excitation (Cheng 1991). The problems of gear meshing with profile error excitation which represent mechanical systems also exhibit chaotic behaviour through quasiperiodic route to chaos (Kahraman & Singh 1990b, Raghothama 1993). Quasiperiodic route to chaos is identified in roller bearing systems with Hertzian type contact nonlinearity (Mével & Guyader 1993; Vaishali 1994).

6.4 Intermittent route to chaos

Another route to chaos in which long periods of periodic motions are interspersed with sudden bursts of chaotic motions is called the intermittent route to chaos. As the control parameter is varied the chaotic bursts become more frequent and longer. Evidence of such intermittent chaos has been provided by Manneville & Pomeau (1980) in the Rayleigh–Bernard convection model for turbulence. Simiu & Cook (1991) have also observed intermittent chaos in their analysis of chaos of coupled square prisms.

6.5 Transient chaos

Sometimes chaotic motions appear for some parameter changes but eventually settle to a periodic or quasiperiodic attractor after a short time. This phenomenon is called transient chaos and has been discussed in the works of Grebogi *et al* (1983a). Such transient chaos is possible when a weak and unstable chaotic attractor coexists with a stable periodic attractor. While motion may begin on the chaotic attractor, as the trajectories wander it may get locked onto the periodic attractor. Both intermittent and transient forms of chaos perhaps exist in a large class of nonlinear dynamical systems, but have not been reported widely in the literature because of their transient nature.

7. Control of chaos

There is a lot of evidence for the presence of chaos in nonlinear dynamical systems. On occasions, chaos is a beneficial feature as it enhances mixing in chemical reactions and provides a vigorous mechanism for transporting heat and/or mass. However, in many situations, chaos may be an undesirable phenomenon which may lead to irregular operations and cause fatigue failure in mechanical systems, temperature oscillations in thermal systems and increased drag in flow systems. In such situations the chaotic attractor may be controlled. The chaotic attractor typically has embedded within it an infinite number of unstable periodic orbits (Holmes 1979; Takens 1980; Ueda 1985; Auerbach *et al* 1987; Lathrop & Kostelich 1989; Pawelzik 1991; Schwartz & Triandaf 1992).

7.1 OGY method

Making use of the above observation, Ott *et al* (1990) demonstrated how one can convert a chaotic attractor to a periodic attractor by stabilising any one of the large number of unstable periodic orbits that are typically embedded in the chaotic attractor. This method utilizes delay coordinate embedding and so is applicable to experimental situations in which *a priori* analytical knowledge of the system dynamics is not available. The approach is as follows: some of the unstable low periodic orbits that are embedded in the chaotic attractor are located. These orbits are examined and one which gives improved performance is selected. Finally, a small time dependent parameter perturbation is made so as to stabilize the selected unstable periodic orbit. The Henon map is taken as an example to demonstrate the control procedure.

Ditto *et al* (1990) implemented the Ott, Grebogi and Yorke (OGY) method to a periodically driven physical system (magnetoelastic ribbon) converting its chaotic motion into period-1 and period-2 orbits. The power of the method is highlighted. Singer *et al* (1991) demonstrated by using both experimental and theoretical results, how low energy feedback control signals can be successfully used to suppress chaotic flow in a thermal convection loop. Using the OGY method, Hunt (1991) converted chaotic orbits of the diode resonator into stable orbits with periods up to 23 drive cycles long. In addition to stabilizing already existing low-period orbits the method allows small alterations in the attractor thus permitting previously nonexistent periodic orbits to be stabilized. It is an analog technique and therefore can be very fast, making it applicable to a wide variety of systems.

Mehta & Henderson (1991) implemented the OGY method and showed how a chaotic system is able to generate a desired aperiodic orbit by making only small temporal perturbations to an available set of system parameters. In their method the chaotic system is modified by generating aperiodic orbits within some bounded region, or perhaps by generating even different chaotic trajectories. Tél (1991) extended the OGY method to control transient chaos and presented the novel features of the control process: the time needed to achieve control is constant, independent of the maximum perturbation, number of trajectories controlled depends on the maximum perturbation and follows a power law. Dressler & Nitché (1992) and Nitché & Dressler (1992) applied the OGY method to control systems whose attractor is constructed by delay coordinates. They have brought out the important fact that whenever delay coordinates are used, the experimental surface of section map depends not only on the actual parameter but also on the preceding one. In order to bring out this dependence two modifications are introduced which lead to a better

performance of the control. To compare their control abilities these algorithms are applied to simulations of the Duffing oscillator. Romeiras *et al* (1992) extended the OGY method, allowing for a more general choice of the feedback matrix and implementation to higher dimensional system. Kapitaniak (1993) devised a way of analytically controlling chaos using the OGY method and the quantitative behaviour of the Feigenbaum period doubling sequence. Shinbrot (1993) discussed the merits of the OGY method and reviewed various other methods of controlling chaos.

7.2 Other methods

Other methods of controlling chaos are due to Hübler (1989), Jackson (1990), Braiman & Goldhirsch (1991), Bandyopadhyay *et al* (1992) and Chen & Dong (1992, 1993). The control of chaos is achieved by modifying the chaotic system by appending a linear spring mass system to the original chaotic systems (Narayanan & Jayaraman 1989b). However, the combined system also exhibits chaos in certain range of parameters. Blazejczyk *et al* (1993) presented a review on control of chaos.

8. Computation of periodic solutions

The analysis of nonlinear systems include (a) location of periodic solutions, (b) stability of periodic solutions, (c) local analysis: that is the study of bifurcation of periodic solutions as the system parameters are varied, and (d) global analysis: determination of the domains of attraction of all periodic motions and strange attractors. This section presents the various methods of obtaining periodic solutions.

8.1 Frequency domain method

In this method, the solution is expressed as a truncated Fourier series. Since, systems with piecewise linear or nonlinear stiffness or damping characteristics are in general strongly nonlinear, the conventional solution procedures such as harmonic balance, multiple time scales, averaging methods etc. cannot be successfully used to determine the steady state solutions. However, strong nonlinear systems may be analyzed by numerical-analytic methods such as Incremental Harmonic Balance Method (IHB), Fast Galerkin Method (FG), Alternate Frequency/Time domain method (AFT) etc.

Cesari (1963) obtained steady state solutions of nonlinear dynamical equations by using a trigonometric polynomial expansion, which is equivalent to a truncated Fourier series. Urabe (1965) gives the mathematical justification for the trigonometric polynomial expansion and Urabe & Reiter (1966) show how the Fourier coefficients may be computed at each iteration while employing Newton–Raphson procedure, with a discrete Fourier transform, once the nonlinear functions are evaluated in time domain. Mickens (1988) obtained the bounds on the periodic coefficients of nonlinear differential equations. Van Dooren (1973) used Urabe's approach to obtain the combination harmonic of differential type of a damped two degree of freedom system with quadratic and cubic nonlinearities. Samoilenko & Ronto (1979) developed a matrix method in which the matrices relating the time and frequency domain are formed. These matrices can be considered as a discrete Fourier transform in matrix

form. Tamura *et al* (1981) developed a matrix method to obtain higher order approximation for steady state solutions using complex Fourier series expansion. The elements of the corresponding Jacobian matrix are obtained by taking advantage of its special structure. Kondou *et al* (1986) developed a general computer-oriented formulation of the harmonic balance method. The stability of periodic solutions is also considered. The fast Galerkin method is proposed by Ling & Wu (1987) which uses FFT to implement Urabe's method. Cameron & Griffin (1989) developed the alternating frequency/time domain method by implementing the FG method in an efficient manner. The harmonic components of the nonlinear terms are obtained by using FFT while that of the linear terms are obtained by direct substitution of the equations obtained from the assumed solution. They have also reduced the number of nonlinear algebraic equations obtained by harmonic balancing to half by expressing cosine and sine terms in complex form. Ling (1990) discusses the merits of the FG method. Buonomo (1992) has developed a trigonometric collocation method to obtain periodic solutions of nonlinear oscillators. The nonlinear algebraic equations in terms of the undetermined coefficients of the solutions is solved by the Newton–Raphson method. The explicit expressions for elements of the corresponding Jacobian matrix are derived. Cardona *et al* (1994) developed a multiharmonic method in conjunction with FFT algorithm and Newton–Raphson procedure which is similar to the one developed by Tamura *et al* (1981). In addition to the solution methodology, various other issues like initial approximate solutions, convergence, errors due to truncation of higher harmonics etc. are also addressed by Tamura *et al* (1981).

Maezawa (1961) and Maezawa & Furukawa (1973) obtained harmonic and superharmonic responses of an sdf oscillator with bilinear and trilinear stiffness subjected to external harmonic excitation using the Fourier series expansion. Maezawa *et al* (1980) obtained the steady state solutions of an sdf system with bilinear restoring force, subjected to a general periodic excitation by expanding the solution in a Fourier series. In their analysis the duration of contact of the mass with the spring of higher stiffness is assumed and the corresponding steady state solution is obtained. Stability of periodic solutions is investigated using Hill's determinant approach.

IHB method is capable of accommodating multiple harmonic components and thereby handles strong nonlinearities without much difficulty. It is ideally suited for parametric studies since it can step from a known state of vibration to a neighbouring state which corresponds to an incremental change in one of the governing parameters of the system (Lau *et al* 1981, 1982). Lau *et al* (1983) developed a procedure to obtain the combination harmonic solutions with little modification of the IHB method. Pierre & Dowell (1985) studied the dynamic instability of plates with geometrical nonlinearities using IHB method. Few special algorithms have been given for tracing the stability boundaries especially for linear viscous damping case. Pierre *et al* (1985) obtained frequency response curves for an sdf and 2 dof dry friction nonlinear systems by modifying the original IHB method. As the dry friction elements introduce a signum function in the equation of motion, the evaluation of derivatives and the Galerkin integrals (in which Dirac delta function appears) causes considerable difficulties. The integration is reduced to a summation and is evaluated by finding the zeros of the function. The effect of number of harmonics on the accuracy of the solution is discussed. Ferri (1986) shows that the FG method and the IHB method are theoretically the same, since the Galerkin approximation and incrementation are employed in both the methods. In the IHB method, incrementation process is followed by the

Galerkin approximation while the reverse is true in the case of the FG method. This observation had earlier been made by Neuman & Sen (1972). Wei & Pierre (1989) used a Galerkin–Newton–Raphson procedure to solve dry friction damped nearly periodic structures. Wong *et al* (1991) extended the IHB method to bilinear stiffness systems and obtained periodic, subharmonic and superharmonic responses and compared their results with those obtained by Maczawa *et al* (1980). This procedure appears to be more involved as compared to the FG method since the integral evaluation requires a separate routine to find the zeros of a function involving heaviside step function. It appears that the concept developed and used by Pierre *et al* (1985) to evaluate the integrals arising from damping nonlinearity is applied by Wong *et al* (1991) for the case of stiffness nonlinearity. It has also been extended to a general piecewise linear stiffness function with multiple number of restraining springs (Lau & Zhang 1992).

Choi & Noah (1988) employed a multi-harmonic balancing procedure to solve an unsymmetrical piecewise linear sdf system. Kim & Noah (1991) proposed a modified harmonic balance/Fourier transform approach to determine the steady state periodic solutions and applied the same to an unsymmetrical piecewise linear single degree of freedom system subjected to harmonic excitation. This procedure of obtaining the approximate periodic solutions can be considered as an efficient implementation of the method proposed by Urabe & Reiter (1966). But the estimation of error involved in the approximate solutions is not considered in their analysis. The stability of the solutions is investigated by constructing the monodromy matrix of the periodic system. Bouc & Defilippi (1987) applied Urabe's method for multidimensional random vibration problems for stationary solutions. Leung & Fung (1989a) constructed bifurcation curves and the regions of chaos for a Duffing's oscillator with zero linear stiffness by using the IHB method and compared them with those obtained by Ueda (1985). Parametric diagrams indicating the regions of periodic and chaotic solutions are constructed for a Duffing oscillator with positive and negative linear stiffnesses. Chaos is confirmed when all periodic solutions become unstable. The elements of the corresponding Jacobian matrix (or the tangent matrix) are obtained in a special way which facilitates the parameter unfolding. Cheung *et al* (1990) presented the formulation of the IHB method for multidegree freedom system with cubic nonlinearity. An incremental arc length approach combined with a cubic extrapolation technique is adopted to trace the response curves automatically.

Lau & Yuen (1991) used IHB method to obtain limit cycle solutions of a single degree of freedom and 2 degrees of freedom nonlinear autonomous self-excited systems. In these cases a large number of harmonics (in 10s) have to be assumed while expressing the periodic solutions because the periodicity is not known exactly. Choi & Lou (1991) developed a new iterative procedure for obtaining the steady state periodic solutions of piecewise nonlinear single degree of freedom oscillator. This method iteratively utilizes the FFT procedure and harmonic balancing to change the nonlinear algebraic equations obtained through harmonic balancing to a sequence of linear algebraic equations thereby getting exact linearisation. During each iteration the constant coefficient of the solution is adjusted in such a way as to make the constant coefficient of the nonlinear stiffness function zero. The stability boundaries are determined by constructing the Hill's determinant for the linearised system. The frequency domain method has been used to obtain the steady state vibration of the beams, arches etc. in conjunction with finite element method (Leung & Fung 1989, 1990a, 1990b; Lewandowski 1992). Leung

(1989) used the same procedure to construct the amplitude-frequency relation (backbone curve) of the nonlinear natural vibration of a beam. Oravsky (1990) has developed a matrix method to evaluate the multiharmonic components of periodic solutions by expressing the set of equations of motion in first order form. The Floquet theory is used to obtain the stability of periodic solutions. Kanarachos & Spentzas (1992) developed a method based on Galerkin approximation of nonlinear differential equations by expressing the solution in a truncated Fourier series form. The resulting nonlinear algebraic equations are solved by Powell's minimisation method. Atadan & Huseyin (1984), Huseyin & Lin (1991) Huseyin & Wang (1991) developed an intrinsic harmonic balancing method which utilises the advantages of both multiple time scale and harmonic balance methods. The power of the method in both the determination of periodic solutions as well as the bifurcation analysis is demonstrated in a series of papers for both autonomous and non-autonomous, parametric and external excitations. However, non-analytical nonlinearities cannot be treated in the present form.

The IHB method introduces considerable difficulties because the evaluation of integrals arising out of Galerkin process is problem dependent. To avoid these difficulties Narayanan & Sekar (1993, 1994) developed a fast incremental harmonic balance method in which the integrals are identified as Fourier coefficients and are calculated using FFT. The corresponding elements of the Jacobian matrix (tangent matrix) obtained during Newton–Raphson method is also obtained using FFT. Hence, this method is suitable for problems having both analytical and nonanalytical nonlinearities. This method is demonstrated for systems containing deviating arguments also. The response of systems with multiple harmonic excitations which could be incommensurate is also dealt with.

8.2 Time domain method

This method requires a numerical integration procedure. The differential equations are reduced to first order form and the solution may be obtained by Runge–Kutta, Adams–Moulton etc. methods (Parker & Chua 1989). Tongue (1987a) and Reinhall *et al* (1989) have discussed the implications of selection of the step length for integration on the solution of nonlinear differential equations.

8.2a Brute force method/point mapping method: In this method, differential equations governing the dynamics of the system are integrated using any one of the numerical integration procedures. Some of these methods are Runge–Kutta method, Adams–Bashforth method, Adams–Moulton method and Gear method. The equations are mapped successively using the differential equations with initial conditions obtained by the previous mapping step. The periodicity is checked once the solution is attracted to some attractor (Flashner & Hsu 1983).

8.2b Shooting method: In this method the differential equations are integrated with the specified initial conditions along with the linearised equations with unit matrix as the initial conditions for one period of solution assumed. The shoots are obtained from the solution of the linearised equations and are added to the current initial conditions to get the new initial conditions. This procedure is continued till the solution is attracted to a particular attractor. Unstable solutions can also be obtained. Aprile &

Trick (1972) initially proposed such a method and it is applied to many problems (Chua & Lin 1975). Modifications of the shooting method may be found in Schwartz (1983), Meijaard (1991) and Foale & Thompson (1991). Tsuda *et al* (1992) used shooting method for equations with deviating argument.

Kaas-Petersen (1987b) presented an algorithm to get periodic and biperiodic solutions with a use of Poincaré map. Stability analysis and continuation of solutions with a change in the control parameter are also incorporated. Kleczka *et al* (1990) and Kleczka *et al* (1991) demonstrate a methodology for the analysis of local bifurcations with codimension one (expression for Poincaré map with one system parameter) of nonlinear dynamical systems using a combination of analytical and numerical methods. Bifurcation analysis is performed with use of center manifold theory and symbolic manipulation of variables. Any of the general purpose computer algebra programs like MACSYMA, MATHEMATICA, MAPLE or REDUCE etc. can be used for symbolic computation. Bursal & Tongue (1992) developed a hybrid symbolic-numerical method for integrating ordinary differential equations based on Taylor's series concept.

9. Domains of attraction

Unlike linear systems, nonlinear systems can exhibit multiple solutions for the same set of system parameters. The type of solution to which the system eventually gets attracted depends on the initial conditions. The set of initial conditions which leads the system to a particular attractor is called the domain of attraction. There are instances in which periodic and chaotic solutions coexist. Hence, delineation of all the domains of attraction is very important to understand the system behaviour. In this section we review the various methods of obtaining the domains of attraction of all steady state solutions for a given set of system parameters of a dynamical system. The first approach is the direct way of getting the domains of attraction by sweeping the whole region of interest of the phase space by numerical simulation. Analog computers are also used to determine the domains of attraction (Bajkowski & Szemplinska-Stupnicka 1975; Tondl 1985).

9.1 Invariant curves method

The second approach involves backward mapping of all the points of the boundary of a sufficiently small region around a stable periodic attractor. The region is constructed such that the forward mapping of all the points in the boundary is contained within the region. By repeatedly applying the backward mapping it is possible to get larger and larger domains of attraction (Levinson 1944; Hayashi *et al* 1969; Hsu 1977; Hsu *et al* 1977). Point mapping method or shooting method may also be used to obtain the periodic solutions. Flashner & Guttalu (1988) used a combined point mapping/stability analysis procedure to locate the periodic orbits and also to determine the domains of attraction.

The third approach is based on the concept that the boundary of the domain of attraction is nothing but the stable manifolds of the saddle point for particular system parameters. If the stable (sometimes referred as ω branch, W^s branch or inset) and unstable manifold (sometimes referred as α branch, W^u branch or outset) of the saddle point intersects, the domain of attraction becomes fractal.

Once the periodic solution is obtained its stability analysis can be performed. If the eigenvalues of the stability matrix is less than unity in modulus then the solution is a stable one. If the absolute value of one of the eigenvalues is more than one while the other one is less than one then the point is a repeller (saddle). In certain circumstances (if the initial condition lies on the unstable manifold itself) the saddle point may be located by backward integration. It may be mentioned here that the eigenvector directions coincide with stable and unstable manifolds as they approach the saddle point. A very small straight line segment can be taken near the saddle point along the eigenvector direction such that the two ends of the segment are the arbitrarily selected initial conditions and the mapped values for that initial conditions. For stable manifold we must use backward mapping while forward mapping should be used for unstable manifold. A large set of points can be taken along the segment. For simplicity these points can be taken in a linear fashion (Troger 1979; Thompson *et al* 1987; Foale & Thompson 1991). This procedure is called the ladder of starts for obvious reason. Ling (1986) has selected an arbitrary length (normally less than 0.01) of the line segment and arranged the points such that the distances between neighbouring points form a geometric series. These points can be mapped repeatedly to get the invariant curves in the entire region of interest. The initial line segment should be short enough (there is no general procedure to select the starting point as this depends on the problem of interest) to avoid a deviation from the real invariant manifold so it is sometimes not sufficient to map it only once. In such situations a spline extrapolation may be used to arrange the mapped points to lie on the manifolds. Alexander (1989) developed a computer oriented automatic procedure to produce the invariant manifolds. A modified Powell hybrid procedure is used to locate the saddle point. Higher order saddles are also dealt with. A pseudo computer code is given. Li & Moon (1990) use the method of ladder of starts to draw the invariant manifolds of three well potential problem. First the saddle point of the unperturbed system is located and to locate the saddle point of the perturbed system the perturbed system is linearised about the unperturbed saddle point and the resulting linearised system is integrated to obtain the deviation of the original saddle point.

9.2 Cell mapping methods

Nonlinear dynamical systems can exhibit hysteresis (multiple solutions) behaviour for certain combinations of parameters. Hence, it is very essential to obtain the various attractors and the corresponding domains of attraction. Cell mapping methods can be used for this purpose. An excellent account of the cell mapping procedures is presented in the book by Hsu (1987).

9.2a Simple cell mapping (SCM): In cell mapping the concept of complete time trajectories is discarded and the state space is considered as a collection of cells. Each cell is identified by its cell vector. In SCM all the phase space within any given cell is considered to map to the same target cell (Hsu 1980). Once the mapping is obtained the cells may be mapped repeatedly till they are attracted to a particular attractor. An unravelling algorithm is given in Hsu & Guttalu (1980). As the state space is discretised into a finite number of cells one may get some spurious attractors depending upon the size of the cells. This difficulty is solved to some extent in generalised cell mapping

method. Kreuzer (1985) analysed chaotic systems using cell mapping approach. Xu *et al* (1985) obtained domains of attraction of 2-degree of freedom self-excited nonlinear systems which required enormous amount of computing power. This problem is solved in a different way to obtain the domains of attraction by Levitas *et al* (1992). In their approach the n -dimensional initial condition space is reduced to n number of $(n - 1)$ dimensional cross-section spaces and these are further discretised into a large number of cells. The mapping of each cell is obtained by noting the terminal cell of the trajectory starting with the centre of each cell after the trajectory had made a specified number of intersections on the $(n - 1)$ dimensional cross-sectional spaces. Using SCM, domains of attractions are obtained and compared with those obtained by Xu *et al* (1985). Henon's method may be used for getting exact return maps (Henon 1982). Pezeshki & Dowell (1987) obtained initial condition maps for the buckled beam by numerical integration. Lam *et al* (1982) identify the spurious attractors and overcome this problem by integrating the original set of differential equations with the attractors obtained by SCM as initial conditions. They have proposed a parallel processing approach for SCM. This procedure appears to be more efficient than reducing the cell size. Nordmark (1993) has developed a computer-oriented interactive program to obtain the domains of attraction in which he reduces the cell size where it is really required.

9.2b Generalized cell mapping (GCM): In GCM a given cell has a finite number of target cells which are found by integrating a finite number of initial conditions within the initial cell and observing in which target cells they terminate. Based on the distribution of these cells that mapped to a given target cell, a probabilistic mapping is constructed which allows one to study the system steady state attractors and their domains of attraction via Markov chain theory (Hsu 1982; Hsu *et al* 1982). The GCM has been used to calculate the maximum Lyapunov exponent (Kim & Hsu 1986). Bestle & Kreuzer (1986) developed an efficient algorithm for solving systems with a large number of cells using GCM.

9.2c Interpolated cell mapping (ICM): In SCM and GCM only a finite number of terminal trajectories are possible. To relax this constraint, Tongue (1987b) and Tongue & Gu (1988a) developed an interpolated cell mapping approach in which the exact location of the trajectory is obtained using linear interpolation of the neighbouring cell centres. This method is found to be very efficient in determination of the domains of attraction. Tongue & Gu (1988b) presented the theoretical basis for the validity of the interpolated cell mapping approach. Jayaraman & Narayanan (1990a) have used this method to obtain the domains of attraction of the Duffing oscillator with Coulomb friction and a square prism kept in a fluid flow. Tongue & Gu (1988c) presented a second order interpolated cell mapping procedure which improved the results of the linear interpolated cell mapping procedure. Tongue & Smith (1989) have demonstrated how Lyapunov exponents may be evaluated using the interpolated cell mapping procedure.

9.2d Fuzzy cell mapping (FCM): Sun & Hsu (1990) analysed a first order nonlinear system by assuming that a parameter of the system is described by a fuzzy set theory as given by Zadeh (1965).

The other methods of obtaining the domains of attraction are due to Varosi *et al* (1987), Schichtel & Beckmann (1991), and Eschenazi *et al* (1989). Varosi *et al* (1987)

discretise the entire phase space by a large number of simplices of appropriate size and by using barycentric coordinates a piecewise linear approximation for the Poincaré maps is obtained. Eschenazi *et al* (1989) use relative rotation rates of the periodic orbits with respect to other orbits thereby locating the repellers and trace the invariant manifolds and the basin boundary. The idea of relative rotation rates of periodic orbits is used to study the bifurcational precedences (McRobie 1992). Schichtel & Beckmann (1991) use Poincaré return maps to locate the repellers and by constructing invariant manifolds the domain of attraction is obtained.

10. Characterisation of chaos

Chaotic behaviour is confirmed by many different ways depending upon the problem and situation. Both qualitative and quantitative methods are available to characterise chaotic behaviour. Unclosed phase plane plots, presence of strange attractor in the Poincaré map, continuous power spectrum, irregular time history, intersection of stable and unstable manifolds, fractal basin boundary, Feigenbaum sequence of bifurcations indicate chaos. Chaos is mostly confirmed by the presence of positive Lyapunov exponent and fractional dimension of the strange attractors.

10.1 Lyapunov exponents

This analysis is very similar to the Floquet theory for the consideration of the linear stability of a periodic motion and has the same inspiration as the linear analysis of motion in vicinity of a trajectory. While in the Floquet theory, one is concerned as to the motion after one period of a closed orbit, in the computation of Lyapunov exponents, this restriction is not there. Lyapunov exponents are the average exponential rates of divergence or convergence of neighbouring trajectories in phase space. Presence of at least one positive Lyapunov exponent indicates chaos with the magnitude of the exponent reflecting the time scale on which the system dynamics becomes unpredictable. Negative Lyapunov exponents signify closeness of neighbouring trajectories and hence periodic motion (Shaw 1981; Eckmann & Ruelle 1985).

Shimada & Nagashima (1979) developed a numerical procedure to calculate k -dimensional Lyapunov exponents using Oseledec's multiplicative ergodic theorem (Oseledec 1968). The nonlinear equations are integrated with the specified initial conditions along with the linearised (perturbed) equations with unit matrix as the initial conditions. To avoid overflow error which arises mainly due to the stretching and folding of phase space volume, Shimada & Nagashima (1979) applied Gram-Schmidt-Reorthogonalisation (GSR) procedure to the vectors of linearised flow of the system. Kim & Hsu (1986) obtained the largest Lyapunov exponent by generalised cell mapping. Wolf *et al* (1985) presented a computer code to generate Lyapunov exponents using the procedure given by Nagashima and Shimada. They have also presented another method and the corresponding code for evaluating the Lyapunov exponents from a time history obtained from experimental measurements. The sum of the Lyapunov exponents is the time averaged divergence of the phase velocity: hence any dissipative dynamical system will have *at least* one negative exponent, the sum of all the exponents is negative which indicates the boundedness of the solution. In a three dimensional continuous dissipative dynamical system, the only possible spectra, and

the attractors they describe are as follows, $(+, 0, -)$, a strange attractor; $(0, 0, -)$, a limit cycle; and $(-, -, -)$ a fixed point (Wolf *et al* 1985). The Lyapunov dimension d_L is calculated as follows (Farmer *et al* 1983; Frederickson *et al* 1983),

$$d_L = j + \sum_{i=1}^j \frac{\lambda_i}{|\lambda_{j+1}|},$$

where λ_j is the largest Lyapunov exponent and j is defined as

$$\sum_{i=1}^j \lambda_i > 0; \quad \sum_{i=1}^{j+1} \lambda_i < 0.$$

The relation between Lyapunov exponents and the material coordinates are discussed by Berger & Rokni (1987) and Rokni & Berger (1991).

10.2 Dimension

The definitions and the calculations of various dimensions are discussed in Moon (1992). The various dimensions include correlation, capacity information, information and Lyapunov dimension. Correlation dimension was developed by Grassberger & Procaccia (1983a, 1983b) and it has been the most widely applied dimension measure, largely because of the ease with which it can be computed. Efficient box counting methods are also available to calculate the correlation dimension (Liebovitch & Toth 1989). Attractors can be reconstructed using delay coordinates (Packard *et al* 1980). Takens (1980) has given a sound mathematical foundation for delay embedding procedure. Broomhead & King (1986) have given a detailed procedure to select the optimum delay time and the embedding dimension.

11. Conclusions

Different mechanical systems which can exhibit chaotic behaviour are reviewed. Discussion focusses on typical mechanical systems which are generally described by piecewise linear differential equations like impacting or clearance systems, systems consisting of dry friction type damping elements, pipes conveying pulsating fluid, and systems which are exposed to fluid flow. Work on typical nonlinear models like a two-well potential system which is applicable to two stable state systems like buckled beam is reviewed. Models that are relevant for ship dynamics, which are characterised by potential well with escape, are given. Other models like pendulum, Duffing and Van der Pol type systems are also included. The different types of bifurcations and the routes to chaos which normally occur in various systems are presented. A short review about the literature available on the various ways of controlling chaos is also dealt with.

The development of various methods of obtaining the periodic orbits and their relevance for the bifurcation analysis is extensively reviewed especially for frequency domain method. Cell mapping methods for initial condition maps and the construction of invariant curves are also discussed. Discussion on characterising chaos like Lyapunov exponents, calculation of dimension of attractors is also included.

References

- Alexander N A 1989 Production of computational portraits of bounded invariant manifolds. *J. Sound Vib.* 117: 219–232
- Andronov A A, Vitt A A, Khaikin S C 1966 *Theory of oscillators* (Oxford: Pergamon)
- Aprille T J, Trick T N 1972 A computer algorithm to determine the steadystate responses of nonlinear oscillators *IEEE Trans. Circuit Theory* 19: 354–360
- Argyris J H 1991 An adventure in chaos. *Comput. Methods Appl. Mech. Eng.* 91: 997–1091
- Arnold V I 1983 *Geometrical methods in the theory of ordinary differential equations* (Berlin: Springer-Verlag)
- Atadan A S, Huseyin K 1984 An intrinsic method of harmonic analysis of nonlinear oscillators. *J. Sound Vib.* 95: 525–530
- Auerbach D, Cvitanovic' P, Eckmann J P, Gunaratne G 1987 Exploring chaotic motion through periodic orbits. *Phys. Rev. Lett.* 58: 2387–2389
- Awrejcewicz J 1989 Two kinds of evolution of strange attractors for the example of a particular nonlinear oscillator. *J. Appl. Math. Phys.* 40: 375–386
- Awrejcewicz J 1991 Three routes to chaos in simple sinusoidally driven oscillators. *Z. Angew. Math. Mech.* 71: 71–79
- Awrejcewicz J, Mrozowski 1989 Bifurcations and chaos of a particular van der Pol Duffing oscillator. *J. Sound Vib.* 132: 89–100
- Bajaj A K 1991 Examples of boundary crises phenomenon in structural dynamics. *Int. Ser. Numer. Math.* 97: 27–36
- Bajaj A K, Sethna P R 1982 Bifurcations in three dimensional motion of articulated tubes. Part 2. Nonlinear analysis. *ASME J. Appl. Mech.* 49: 612–618
- Bajaj A K, Sethna P R 1984 Flow induced bifurcations in three-dimensional oscillatory motions of continuous tubes. *SIAM J. Appl. Math.* 44: 270–286
- Bajaj A K, Sethna P R and Lundgren T S 1980 Hopf bifurcation phenomenon in tubes carrying fluid. *SIAM J. Appl. Math.* 39: 213–230
- Bajkowski J, Szemplinska-Stupnicka W 1975 Domains of attraction of the secondary periodic and combination resonances in nonlinear two-degree of freedom system. *VII Internationale Konferenz über Nichtlineare Schwingungen* vol. 1.1, pp. 55–69 (Berlin: Akademik-Verlag)
- Baker G L, Gollub J P 1990 *Chaotic dynamics: an introduction*
- Bandyopadhyay J, Ravi Kumar V, Kulkarni B D, Deshpande P B 1992 On dynamic control of chaos: A study with reference to a reacting system. *Phys. Lett.* A166: 197–204
- Barber T T, Wen Y K 1981 Random vibration of hysteretic degrading systems. *ASCE J. Eng. Mech.* 107: 1069–1087
- Baren D D 1994 Mathematical models used in studying chaotic vibration of buckled beams. *Mech. Res. Commun.* 21: 184–196
- Belogortsev A B 1992 Analytical approach to the torus bifurcation in quasiperiodically forced van der Pol oscillator. *Phys. Lett.* A61: 352–356
- Berge P, Pomeau Y, Vidal Ch 1984 *Order within chaos* (New York: John Wiley & Sons)
- Berger B S, Rokni M 1987 Lyapunov exponents and continuum kinematics *Int. J. Eng. Sci.* 25: 1079–1089
- Bestle D, Kreuzer E 1986 An efficient algorithm for global analysis of nonlinear systems. *Comput. Methods Appl. Mech. Eng.* 59: 1–9
- Birkhoff G G 1927 *Dynamical systems* (Providence, RI: Am. Math. Soc.)
- Blazejczyk B, Kapitaniak T, Wojewoda J, Brindley J 1993 Controlling chaos in mechanical systems. *Appl. Mech. Rev.* 46(7): 385–391
- Blevins R D 1977 *Flow induced vibrations* (New York: Von-Nostrand Reinhold)
- Bouc R, Defilippi M 1987 A Galerkin multiharmonic procedure for nonlinear multidimensional random vibration. *Int. J. Eng. Sci.* 25: 723–733
- Braiman Y, Goldhirsch I 1991 Taming chaotic dynamics with weak periodic perturbations. *Phys. Rev. Lett.* 66: 2545–2548
- Brindley J, Kapitaniak T, El Naschie M S 1991 Analytical conditions for strange chaotic and nonchaotic attractors of the quasiperiodically forced Van der Pol equation. *Physica D* 51: 28–38

- Broomhead D S, King G P 1986 Extracting qualitative dynamics from experimental data. *Physica D* 20: 217–236
- Brunsden V, Cortell J, Holmes P J 1989 Power spectra of chaotic vibrations of a buckled beam. *J. Sound Vib.* 130: 1–25
- Buonomo A 1992 A collocation algorithm for calculating the periodic solutions of nonlinear oscillators. *Int. J. Circuits Theory Appl.* 20: 107–116
- Bursal E H, Tongue B H 1992 A hybrid symbolic-numerical method for integrating ordinary differential equations. *J. Sound Vib.* 152: 295–304
- Butenin I W, Neimark I I, Fufai N A 1976 *Introduction into nonlinear oscillations* (Moskwa: Nauka) (in Russian)
- Cameron T M, Griffin J H 1989 An alternating frequency/time domain method for calculating the steadystate response of nonlinear dynamic systems. *ASME J. Appl. Mech.* 56: 149–154
- Cardona A, Coune T, Lerusse A, Geradin M 1994 A multiharmonic method for nonlinear vibration analysis. *Int. J. Numer. Methods Eng.* 37: 1593–1608
- Cartwright M L, Littlewood J E 1945 On nonlinear differential equations of the second order I. The equation is $\ddot{y} + k(1 - y^2)\dot{y} + y = b\lambda k \cos(\lambda t + a)$. *J. London Math. Soc.* 20: 180–189
- Cesari L 1963 Functional analysis and periodic solutions of nonlinear differential equations. *Contrib. Differ. Equ.* 1: 149–187
- Chen G, Dong X 1992 On feedback control of chaotic dynamical systems. *Int. J. Bifurcation Chaos* 2: 407–411
- Chen G, Dong X 1993 On feedback control of chaotic continuous-time systems. *IEEE Trans. Circuits Syst.* 40: 591–601
- Chen S S 1987 A general theory for dynamic instability of tube arrays in cross flow. *J. Fluids Struct.* 1: 35–53
- Cheng C 1991 Invariant torus bifurcation series and evolution of chaos exhibited by a forced nonlinear vibration system. *Int. J. Non-Linear Mech.* 26: 105–116
- Cheung Y K, Chen S H, Lau S L 1990 Application of the incremental harmonic balance method to cubic nonlinear systems. *J. Sound Vib.* 140: 273–286
- Choi Y S, Noah S T 1988 Forced periodic vibration of unsymmetric piece-wise linear systems. *J. Sound Vib.* 121: 117–126
- Choi H S, Lou J Y K 1991 Nonlinear behavior and chaotic motions of an SDOF system with piece-wise nonlinear stiffness. *Int. J. Non-Linear Mech.* 26: 461–473
- Chow S N, Shaw S W 1986 Bifurcations of subharmonics. *J. Differ. Equ.* 65: 304–320
- Chua L O, Lin P M 1975 *Computer-aided analysis of electronic circuits. Algorithm and computational techniques* (Englewood Cliffs, NJ: Prentice-Hall)
- Civitanovic' P 1989 *Universality in chaos* 2nd edn (New York: Adams Hilger)
- Curry L O 1978 A generalised Lorenz system. *Commun. Math. Phys.* 60: 193–204
- Curry J M, Yorke J A 1977 *The structure of attractors in dynamical systems: Springer Notes in Mathematics* 668. *A transition from Hopf bifurcation to chaos* (Berlin: Springer Verlag)
- D'Humieres D, Beasley M R, Huberman B A, Libchaber A 1982 Chaotic states and routes to chaos in the forced pendulum. *Phys. Rev. A* 26: 3483–3496
- Devaney R L 1987 *Introduction to chaotic dynamical systems* (New York: Addison-Wesley)
- Ditto W L, Raueo S N, Spano M L 1990 Experimental control of chaos. *Phys. Rev. Lett.* 65: 3211–3214
- Doedel E 1986 AUTO: Software for continuation and bifurcation problems in ordinary differential equations. Report, Department of Applied Mathematics, California Institute of Technology
- Dowell E H 1982 Flutter of buckled plate as an example of chaotic motion of a deterministic autonomous system. *J. Sound Vib.* 85: 333–344
- Dowell E H 1988a Chaotic oscillations in mechanical systems. *Comput. Mech.* 1: 199–216
- Dowell E H 1988b Chaotic oscillations in mechanical systems. *Comput. Struct.* 30: 171–184
- Dowell E H 1991 A chaotic scenario. *J. Sound Vib.* 144: 179–180
- Dowell E H, Pezeshki C 1986 On the understanding of chaos in Duffing equation including a comparison with experiment. *ASME J. Appl. Mech.* 53: 5–9
- Dowell E H, Pezeshki C 1988 On necessary and sufficient conditions for chaos to occur in Duffing's equation: An heuristic approach. *J. Sound Vib.* 121: 195–200
- Dressler U, Nitsche G 1992 Controlling chaos using time delay coordinates. *Phys. Rev. Lett.* 68: 1–4

- Duffing G 1918 *Erzwungene Schwingungen bei Veränderlicher Eigenfrequenz und ihre technische Bedeutung*. Ph D thesis Sammlung Vieweg, Braunschweig
- Eckmann J P, Ruelle D 1985 Ergodic theory of chaos and strange attractors. *Rev. Mod. Phys.* 57: 617–656
- Ehrich F 1992 Observations of subcritical superharmonic and chaotic response in rotordynamics. *ASME J. Vib. Acoust.* 114: 93–100
- Eschenazi E, Solari H G, Gilmore R 1989 Basin of attraction in driven dynamical systems. *Phys. Rev. A* 39: 2609–2627
- Fang T, Dowell E H 1987 Numerical simulations of periodic and chaotic responses in a stable Duffing system. *Int. J. Non-Linear Mech.* 22: 401–425
- Farmer J D, Ott E, Yorke J A 1983 The dimension of chaotic attractors. *Physica D* 7: 153–180
- Feeny B F, Moon F C 1989 Autocorrelation on symbol dynamics for a chaotic dry-friction oscillator. *Phys. Lett. A* 141: 397–400
- Feigenbaum M J 1978 Quantitative universality for a class of nonlinear transformations. *J. Stat. Phys.* 19: 25–52
- Féin A P, Heutmaker M S, Gollub J P 1985 Scaling and transition from quasi-periodicity to chaos in hydrodynamic systems. *Phys. Scr.* T9: 79–84
- Ferri A A 1986 On the equivalence of the incremental harmonic balance method and the harmonic balance – Newton–Raphson method. *ASME J. Appl. Mech.* 53: 455–457
- Flashner H, Guttalu R S 1988 A computational approach for studying domain of attraction. *Int. J. Non-Linear Mech.* 23: 279–295
- Flashner H, Hsu C S 1983 A study of nonlinear periodic systems via the point mapping method. *Int. J. Numer. Meth. Eng.* 19: 185–215
- Flowers G T, Tongue B H 1992 Chaotic dynamical behaviour in a simplified rotor blade lag model. *J. Sound Vib.* 156: 17–26
- Foale S, Thompson J M T 1991 Geometrical concepts and computational techniques of nonlinear dynamics. *Comput. Methods Appl. Mech. Eng.* 89: 381–394
- Frederickson P, Kaplan J L, Yorke E D, Yorke J A 1983 The Lyapunov dimension of strange attractors. *J. Differ. Equ.* 49: 185–207
- Gollub J P, Benson S V 1979 *Phase locking in the oscillations leading to turbulence in pattern formation* (ed.) H Haken (Berlin: Springer Verlag)
- Gollub J P, Benson S V 1980 Many routes to turbulent convection. *J. Fluid Mech.* 100: 449–470
- Gottwald J A, Virgin L N, Dowell E H 1992 Experimental mimicry of Duffing's equation. *J. Sound Vib.* 158: 447–467
- Grabec I 1986 Chaos generated by the cutting process. *Phys. Lett. A* 117: 384–386
- Grassberger P, Procaccia I 1983a Measuring the strangeness of strange attractors. *Physica D* 9: 189–208
- Grassberger P, Procaccia I 1983b Characterisation of strange attractors. *Phys. Rev. Lett.* 50: 346–349
- Grebogi C, Ott E, Yorke J A 1982 Chaotic attractors in crisis. *Phys. Rev. Lett.* 48: 1507–1510
- Grebogi C, Ott E, Yorke J A 1983a Crises, sudden changes in chaotic attractors and transient-chaos. *Physica D* 7: 181–200
- Grebogi C, Ott E, Yorke J A 1983b Are three frequency quasiperiodic orbit to be expected in typical dynamical systems? *Phys. Rev. Lett.* 51: 339–342
- Grebogi C, Ott E, Yorke J A 1987 Basin boundary metamorphoses: changes in accessible boundary orbits. *Physica D* 24: 243–262
- Guckenheimer J, Holmes P J 1983 *Non-linear oscillations, dynamical systems and bifurcations of vector fields* (New York: Springer Verlag)
- Gudmundson P 1989 On the accuracy of the harmonic balance method concerning vibrations of beams with nonlinear supports. *Ing. Archiv.* 59: 333–344
- Gwinn E G, Westervelt R M 1986 Scaling structure of attractors at the transition from quasi-periodicity to chaos in electronic transport in Ge. *Phys. Rev. Lett.* 59: 157–160
- Hanagud S, Abhyankar N S, Chander R 1989 Studies in chaotic vibrations of buckled beams. *Appl. Mech. Rev.* 42: S100–S107
- Hao Bai-Lin (ed.) 1984 *Chaos* (Singapore: World Scientific)
- Hartlen R J, Currie I G 1970 Lift oscillator model of vortex induced *Mech.* 96: 577–591

- Hatwal H, Mallik A K, Ghosh A 1983 Forced nonlinear oscillations of an autoparametric systems. Part II – Chaotic response. *ASME J. Appl. Mech.* 50: 663–668
- Hayashi C 1964 *Nonlinear oscillations in physical systems* (New York: McGraw Hill)
- Hayashi C, Ueda Y, Kawakami H 1969 Transformation theory as applied to the solutions of nonlinear differential equations of the second order. *Int. J. Non-Linear Mech.* 4: 235–255
- Heiman M S, Bajaj A K, Sherman P J 1988 Periodic motions and bifurcations in dynamics of an inclined pair. *J. Sound Vib.* 124: 55–78
- Heiman M S, Sherman P J, Bajaj A K 1987 On the dynamics and stability of an inclined impact pair. *J. Sound Vib.* 114: 535–547
- Henon M 1976 A two-dimensional mapping with a strange attractor. *Commun. Math. Phys.* 50: 69–77
- Henon M 1982 On the numerical computation of Poincaré maps. *Physica D* 5: 412–414
- Higuchi K, Dowell E H 1991 Effect of constant transverse force on chaotic oscillations of sinusoidally excited buckled beam. *Int. J. Non-Linear Mech.* 26: 419–426
- Holmes P 1990a Nonlinear dynamics, chaos, and mechanics. *ASME Appl. Mech. Rev.* 43: Part 2, S23–S39
- Holmes P 1990b Poincaré, celestial mechanics, dynamical systems theory and chaos. *Phys. Rep.* 193: 137–163
- Holmes P J 1977 Bifurcations to divergence and flutter in flow induced oscillations: A finite dimensional analysis. *J. Sound Vib.* 53: 471–503
- Holmes P J 1980 Averaging and chaotic motions in forced oscillations. *SIAM J. Appl. Math.* 38: 65–80. Errata and addenda *SIAM J. Appl. Math.* 40: 167–168
- Holmes P J, Rand D A 1980 Phase portraits and bifurcations of the nonlinear oscillator: $\ddot{x} + (\alpha + \gamma x^2)\dot{x} + \beta x + \delta x^3 = 0$. *Int. J. Non-Linear Mech.* 15: 449–458
- Holmes P J, Moon F C 1983 Strange attractors and chaos in nonlinear mechanics. *J. Appl. Mech.* 50: 1021–1032
- Holmes P J 1979 A nonlinear oscillator with a strange attractor. *Philos. Trans. R. Soc. London* 292: 419–448
- Holmes P J 1982 The dynamics of repeated impacts with a sinusoidally vibrating table. *J. Sound Vib.* 84: 173–189
- Holmes P J 1984 Bifurcation sequences in horseshoe maps: Infinitely many routes to chaos. *Phys. Lett.* A104: 299–302
- Holmes P J, Marsden J 1978 Bifurcation to divergence and flutter in flow induced oscillations: An infinite dimensional analysis. *Automatika* 14: 367–384
- Hsu C S 1974 On approximating a general linear periodic system. *J. Math. Anal. Appl.* 45: 234–251
- Hsu C S 1977 On nonlinear parametric excitation problems. *Adv. Appl. Mech.* 17: 245–301
- Hsu C S 1980 A theory of cell-to-cell mapping dynamical systems. *ASME J. Appl. Mech.* 48: 931–939
- Hsu C S 1982 A probabilistic theory of nonlinear dynamical systems based on the cell state space concept. *ASME J. Appl. Mech.* 49: 895–902
- Hsu C S 1987 *Cell-to-cell mapping: A method of global analysis for nonlinear systems* (Berlin: Springer-Verlag)
- Hsu C S, Guttalu R S 1980 An unravelling algorithm for global analysis of dynamical systems. *ASME J. Appl. Mech.* 48: 940–948
- Hsu C S, Yee H C, Cheng W H 1977 Determination of global regions of asymptotic stability for difference dynamical systems. *ASME J. Appl. Mech.* 44: 147–153
- Hsu C S, Guttalu R S, Zhu W H 1982 A method of analysing generalised cell mapping. *ASME J. Appl. Mech.* 48: 885–894
- Huang Y M, Bajaj A K, Krousgrill C M 1990 Complex inline and whirling response of structures to oscillating flow. *J. Sound Vib.* 136: 491–505
- Huberman B, Crutchfield J P 1979 Chaotic states of anharmonic systems in periodic fields. *Phys. Rev. Lett.* 43: 1743–1747
- Huberman B, Crutchfield J P, Packard N 1980 Noise phenomena in Josephson junctions. *Appl. Phys. Lett.* 37: 750–752
- Hübler A 1989 *Helv. Phys. Acta* 62 291
- Hunt E R 1991 Stabilizing high period orbits in a chaotic system: The diode resonator. *Phys. Rev. Lett.* 67: 1953–1955

- Huseyin K, Lin R 1991 An intrinsic multiple scale harmonic balance method for nonlinear vibration and bifurcation problems. *Int. J. Non-Linear Mech.* 26: 727–740
- Huseyin K, Wang S 1991 An extension of the intrinsic harmonic balancing method to the analysis of forced vibration. *J. Sound Vib.* 148: 361–363
- Ide K, Wiggins S 1989 The bifurcation to homoclinic tori in the quasiperiodically forced Duffing oscillator. *Physica D*34: 169–182
- Iooss G, Joseph D D 1980 *Elementary stability and bifurcation theory* (New York: Springer-Verlag)
- Isomäki H M, J von Boehm, Rätty R 1988 Fractal basin boundaries of an impacting particle. *Phys. Lett. A*126: 484–490
- Ivanov A P 1993 Stabilisation of an impact oscillator near grazing incidence owing to resonance. *J. Sound Vib.* 162: 562–565
- Iwan W D, Blevins R D 1974 A model for vortex induced oscillations of structures. *ASME J. Appl. Mech.* 41: 581–586
- Iyengar R N 1992 Stochastic characterization of chaos in a nonlinear system. *Phys. Lett. A*154: 357–360
- Jackson E A 1990 On the control of complex dynamical systems. *Physica D*50: 341–366
- Jayaraman K 1991 *Chaotic vibrations of some nonlinear mechanical systems*. Ph D thesis, Indian Institute of Technology, Madras
- Jayaraman K, Narayanan S, 1990a Interpolated cell mapping for nonlinear dynamical systems. *National Conference on Computational Techniques in Continuum Mechanics, Madras*
- Jayaraman K, Narayanan S 1990b Chaotic oscillations of pipes conveying pulsating fluid. *Proc. of International Conference on Advances in Structural Testing, Analysis and Design, India, Vol II*: 966–971
- Jayaraman K, Narayanan S 1990c Periodic and chaotic oscillations of a harmonically excited square prism in fluid flow. *Proc. of National Seminar on Aerospace Structures, India* pp. 181–191
- Jayaraman K, Narayanan S 1993 Chaotic oscillations in pipes conveying pulsating fluids Part I: Numerical simulation of multi periodic and chaotic motions, Part II – Stability analysis by multiple time scale and harmonic balancing. *Nonlinear Dynamics* (communicated)
- Johnson J M, Bajaj A K 1989 Amplitude modulated and chaotic dynamics in resonant motion of strings. *J. Sound. Vib.* 128: 87–107
- Kaas-Petersen C 1987a Path User's Guide Report May 1987 Leeds University Centre for nonlinear studies
- Kaas-Petersen C 1987b Computation, continuation and bifurcation of torus solutions for dissipative maps and ordinary differential equations. *Physica D*25: 288–306
- Kaas-Petersen C, True H 1985 Periodic, bi-periodic and chaotic dynamical behaviour of railway vehicles. *Proc. 9th IAVSD Symposium Linköping*, 208–221
- Kahraman A, Singh R 1990a Nonlinear dynamics of a spur gear pair *J. Sound Vib.* 142: 49–75
- Kahraman A, Singh R 1990b Nonlinear dynamics of a gear rotor system with multiple clearances. *J. Sound Vib.* 144: 469–506
- Kahraman A, Singh 1992 Dynamics of an oscillator with both clearance and continuous nonlinearities. *J. Sound Vib.* 151: 180–185
- Kan M, Taguchi H 1993 Chaos and fractals in nonlinear roll and capsize of a damaged ship. *International Workshop on Physical and Mathematical Modelling of Vessel's stability in a seaway. OTRADNOYE'93, Kaliningrad, Russia*
- Kanarachos A E, Spentzas C N 1992 A Galerkin method for the steadystate analysis of harmonically excited nonlinear system. *Mech. Mach. Theory* 27: 661–671
- Kapitaniak T 1991 *Chaotic oscillations in mechanical systems* (Manchester: University Press)
- Kapitaniak T 1993 Analytical method of controlling chaos in Duffing's oscillator. *J. Sound Vib.* 163: 182–187
- Kapitaniak T, Ponce E, Wojewoda J 1990 Route to chaos via strange nonchaotic attractors. *J. Phys. A*23: L383–L387
- Kapitaniak T, Wojewoda J 1990 Strange nonchaotic attractors of a quasiperiodically forced van der Pol's oscillator. *J. Sound Vib.* 138: 162–169
- Karyeacis M P, Caughey T K 1989 Stability of a semi-active impact damper: Part I – Global behavior 930–940. Part-II-Periodic solutions. *ASME J. Appl. Mech.* 56: 926–929

- Kim M C, Hsu C S 1986 Computation of the largest Lyapunov exponent by the generalised cell mapping. *J. Stat. Phys.* 45: 49–61
- Kim Y B, Noah S T 1991 Stability and bifurcation analysis of oscillators with piece-wise linear characteristics: A general approach. *ASME J. Appl. Mech.* 58: 545–553
- Kleczka M, Kleczka W, Kreuzer E 1990 Bifurcation analysis: A combined numerical and analytical approach. *Continuation and bifurcations: Numerical techniques and applications* (eds) D Roose *et al* (Amsterdam: Kluwer) pp. 123–137
- Kleczka M, Kreuzer E, Wilmers C 1989 Crisis in mechanical systems. *Proc. of IUTAM Symposium on Nonlinear Dynamics and Engineering Systems* (ed.) W Schiehlen pp 141–148 (Berlin: Springer Verlag)
- Kleczka M, Kreuzer E, Wilmers C 1991 Combined analytical-numerical analysis of nonlinear dynamical systems. *Int. Ser. of Numer. Math.* 97: 199–203
- Koch B P, Leven R W 1985 Subharmonic and homoclinic bifurcations in a parametrically forced pendulum. *Physica D* 15: 1–13
- Kondou T, Tamura H, Sueoka A 1986 On a method of higher approximation and determination of stability criterion for steady oscillations in nonlinear systems. *Bull. JSME* 29: 525–532
- Kotera T, Yamanashi H 1986 Chaotic behavior in an impact vibration system 2nd Report: Influence of damping coefficient and coefficient of restitution. *Trans. JSME* 52: 1883–1886
- Kozol J E, Brach R M 1991 Two-dimensional vibratory impact with chaos. *J. Sound Vib.* 148: 319–327
- Kreuzer E 1985 Analysis of chaotic systems using the cell mapping approach. *Ing.-Archiv.* 55: 285–294
- Kubiček M, Marek M 1983 *Computational methods in bifurcation theory and dissipative structures* (New York: Springer-Verlag)
- Kunert A, Pfeiffer F 1989 Stochastic models for rattling in gearboxes. *Proc. of IUTAM Symposium on Nonlinear Dynamics and Engineering Systems* (ed.) W Schiehlen (Berlin: Springer Verlag) pp. 173–180
- Kunert A, Pfeiffer F 1991 Description of chaotic motion by an invariant distribution as the example of driven Duffing oscillator. *Int. Ser. Numer. Math.* 97: 225–230
- Lam K Y, Liaw C Y, Chan E S 1992 Parallel determination of basins of attraction. *Computational methods in engineering: advances and applications* (Singapore: World Scientific) pp. 1223–1227
- Landau L, Lipschitz E 1971 *Mechanics of fluids* (Moscow: Mir Publications)
- Lansbury A N, Thompson J M T 1990 Incursive fractals: a robust mechanism of basin erosion preceding the optimal escape from a potential well. *Phys. Lett.* A150: 355–361
- Lathrop D P, Kostelich E J 1989 Characterisation of an experimental strange attractor by periodic attractors. *Phys. Rev.* A40: 4028–4031
- Lau S L, Cheung Y K, Wu S Y 1981 Amplitude incremental variation principle for nonlinear vibration of elastic systems. *ASME J. Appl. Mech.* 48: 959–964
- Lau S L, Cheung Y K, Wu S Y 1982 A variable parameter incrementation method for dynamic stability of linear and nonlinear elastic system. *ASME J. Appl. Mech.* 49: 849–853
- Lau S L, Cheung Y K, Wu S Y 1983 Incremental harmonic balance method with multiple time scales for aperiodic vibration of nonlinear systems. *ASME J. Appl. Mech.* 50: 871–876
- Lau S L, Yeun S W 1991 Hopf bifurcation and limit cycle analysis by incremental harmonic balance method *Comput. Methods Appl. Mech. Eng.* 91: 1109–1121
- Lau S L, Zhang W S 1992 Nonlinear vibrations of piecewise linear systems by incremental harmonic balance method. *Trans. ASME J. Appl. Mech.* 59: 153–160
- Leung A Y T 1989 Nonlinear natural vibration of beams by selective coefficient increment. *Comput. Mech.* 5: 73–80
- Leung A Y T, Fung F C 1989a Construction of chaotic regions. *J. Sound Vib.* 131: 445–455
- Leung A Y T, Fung F C 1989b Nonlinear steadystate vibration of frames by finite element method. *Int. J. Numer. Meth. Eng.* 28: 1599–1618
- Leung A Y T, Fung F C 1990a Nonlinear steadystate vibration and dynamic snap through of shallow arch beams. *Earthquake Eng. Struct. Dyn.* 19: 409–430
- Leung A Y T, Fung F C 1990b Geometrical nonlinear vibration of spinning structures. *J. Sound Vib.* 139: 43–62
- Leven R W, Pompe B, Wilke C and Koch B P 1985 Experiments on periodic and chaotic motions of parametrically forced pendulum. *Physica D* 16: 371–384

- Levinson N 1944 Transformation theory of nonlinear differential equations of the second order. *Ann. Math.* 45: 723–737
- Levinson N 1949 A second order differential equation with singular solution. *Ann. Math.* 50: 127–153
- Levitas J, Weller J T, Singer J 1992 Poincaré-like simple cell mapping for global analysis of nonlinear dynamical systems. *Comput. Meth. Eng.: Advances and Applications* (Singapore: World Scientific) pp 909–914
- Lewandowski R 1992 Nonlinear steadystate vibration of structures by harmonic balance/finite element method. *Comput. Struct.* 44: 287–296
- Li G X, Moon F C 1990 Criteria for chaos of a three well potential oscillator with homoclinic and heteroclinic orbits. *J. Sound Vib.* 136: 17–34
- Li G X, Rand R H, Moon F C 1990 Bifurcations and chaos in a forced zero-stiffness impact oscillator. *Int. J. Non-Linear Mech.* 25: 417–432
- Liaw C Y 1988 Bifurcations of subharmonics and chaotic motions of articulated towers. *Eng. Struct.* 10: 117–124
- Lichtenberg A J, Lieberman M A 1983 *Regular and stochastic motion* (New York: Springer Verlag)
- Liebovitch L S, Toth T 1989 A fast algorithm to determine fractal dimensions by box counting. *Phys. Lett.* A141: 386–390
- Ling F H 1986 A numerical study of the applicability of the Melnikov's method. *Phys. Lett.* A119: 447–452
- Ling F H 1990 An alternating frequency/time domain method for calculating the steadystate response of nonlinear dynamical systems – Discussion/Authors closure. *ASME J. Appl. Mech.* 57: 251–252
- Ling F H, Wu X X 1987 Fast Galerkin method and its application to determine periodic solutions of nonlinear oscillators. *Int. J. Non-Linear Mech.* 22: 89–98
- Lorentz E N 1963 Deterministic nonperiodic flow. *J. Atmos. Sci.* 20: 130–141
- Lyapunov A M 1949 *Problème Général de la Stabilité du mouvement* (Princeton: University Press)
- Maezawa S 1961 Steady forced vibration of unsymmetrical piece-wise linear system. *Bull. JSME* 4: 201–229
- Maezawa S, Furukawa S 1973 Superharmonic resonance in piecewise linear oscillator. *Bull. Jpn. Soc. Mech. Eng.* 16: 931–941
- Maezawa S, Kumano H, Minakuchi Y 1980 Forced vibrations in an unsymmetrical piece-wise linear system excited by general periodic force function. *Jpn. Soc. Mech. Eng.* 23: 68–75
- Mahfouz I A, Badrakhan F 1990 Chaotic behaviour of some piecewise linear systems. Part I. Systems with setup spring or with unsymmetric elasticity. 289–328, Part II – Systems with clearance. *J. Sound Vib.* 143: 253–288
- Makrides G A, Edelstein W S 1992 Some numerical studies of chaotic motions in tubes conveying fluid. *J. Sound Vib.* 152: 517–530
- Manneville P, Pomeau Y 1980 Different ways to turbulence in dissipative dynamical systems. *Physica D* 1: 219–226
- Matsumoto T 1984 A chaotic attractor from Chua's circuit. *IEEE Trans. Circuits Sys.* 33: 1055–1058
- McLaughlin J B 1981 Period doubling bifurcations and chaotic motion for a parametrically forced pendulum. *J. Stat. Phys.* 24: 375–388
- McRobie F A 1992 Bifurcational precedences in the braids of periodic orbits of spiral 3-shoes in driven oscillators. *Proc. R. Soc. London A* 438: 545–569
- Mees A, Sparrow C 1987 Some tools for analysis chaos. *Proc. IEEE* 75: 1058–1070
- Mehta N J, Henderson R M 1991 Controlling chaos to generate aperiodic orbits. *Phys. Rev.* A44: 4861–4865
- Meijaard J P 1991 Direct determination of periodic solutions of the dynamical equations of flexible mechanisms and manipulators. *Int. J. Numer. Meth. Eng.* 32: 1691–1710
- Meijaard J P, De Pater A D 1989 Railway vehicle systems dynamics and chaotic vibrations. *Int. J. Non-Linear Mech.* 24: 1–17
- Melnikov V K 1963 On the stability of the center for time periodic perturbations. *Trans. Moscow Math. Soc.* 12: 1–57
- Mevel B, Guyader J L 1993 Routes to chaos in ball bearings. *J. Sound Vib.* 162: 471–487
- Mickens R E 1988 Bounds on the coefficients for the periodic solutions of nonlinear oscillator equations. *J. Sound Vib.* 124: 199–203
- Miles J 1988 Resonance and symmetry breaking for the pendulum. *Physica D* 31: 252–266

- Molteno T C A, Tuffillaro N B 1990 Torus doubling and chaotic string vibrations. *J. Sound Vib.* 137: 327–330
- Moon F C 1980 Experiments on chaotic motions of a forced nonlinear oscillator: Strange attractors. *ASME J. Appl. Mech.* 47: 638–644
- Moon F C 1992 *Chaotic and fractal dynamics* (New York: Wiley)
- Moon F C, Broschart T 1991 Chaotic sources of noise in machine acoustics. *Arch. Appl. Mech.* 61: 438–448
- Moon F C, Holmes P J 1979 A magneto elastic strange attractor. *J. Sound Vib.* 65: 275–296
- Moon F C, Li G X 1985a Fractal basin boundaries and homoclinic orbits for periodic motion in a two-well potential. *Phys. Rev. Lett.* 55: 1439–1443
- Moon F C, Li G X 1985b The fractal dimension of two well potential strange attractors. *Physica D* 17: 99–108
- Moon F C, Li G X 1990 Experimental study of chaotic vibrations in a pin jointed space truss structure. *Am. Inst. Aeronaut. Astronaut. J.* 28: 915–921
- Moon F C, Shaw S W 1983 Chaotic vibrations of a beam with nonlinear boundary conditions. *Int. J. Non-Linear Mech.* 18: 465–477
- Moore D B, Shaw S W 1990 The experimental response of an impacting pendulum system. *Int. J. Non-Linear Mech.* 25: 1–16
- Narayanan S, Jayaraman K 1989a Chaotic motions in nonlinear systems with Coulomb damping. *Proc. of IUTAM Symp. on Nonlinear Dyn. Eng. Sys.* (ed.) W Schiehlen (Berlin: Springer Verlag) 217–224
- Narayanan S, Jayaraman K 1989b Control of chaotic oscillation by vibration absorber. *ASME Design Technical Conference – 12th Biennial Conference on Mechanical Vibration and Noise DE-18.5*, 391–394
- Narayanan S, Jayaraman K 1991 Chaotic vibration in nonlinear oscillator with Coulomb damping. *J. Sound Vib.* 146: 1–17
- Narayanan S, Jayaraman K 1993 Chaotic oscillations of a square prism in fluid flow. *J. Sound Vib.* 166: 87–101
- Narayanan S, Sekar P 1993 Bifurcation and chaos of coupled systems by fast incremental harmonic balancing. *IUTAM Symposium on Nonlinearity and Chaos in Engineering Dynamics*, London.
- Narayanan S, Sekar P 1994 *Nonlinearity and chaos in engineering dynamics* (eds) J M T Thompson, S R Bishop 29: 365–375
- Narayanan S, Sekar P 1995 Periodic and chaotic responses of a sdf system with piecewise linear stiffness subjected to combined harmonic and flow induced excitations. *J. Sound Vib.* 26: 281–298
- Natsiavas S 1991 Dynamics of piece-wise linear oscillator with van der Pol type damping. *Int. J. Non-Linear Mech.* 26: 349–366
- Natsiavas S, Babcock C D 1988 Behaviour of unanchored fluid filled tanks subjected to ground excitation. *Trans. ASME J. Appl. Mech.* 55: 654–659
- Nayfeh A H, Khdeir A A 1986 Nonlinear rolling of ships in regular beam seas. *Int. Shipbuild. Prog.* 33: 40–49
- Nayfeh A H, Sanchez N E 1988 Chaos and dynamic instability in the rolling motion of ships. *Proceedings of the 17th Symposium on Naval Hydrodynamics*, The Hague
- Nayfeh A H, Sanchez N E 1989 Bifurcations in a forced softening Duffing oscillator. *Int. J. Non-Linear Mech.* 24: 483–497
- Neuman C P, Sen A 1972 Galerkin procedure, quasi-linearisation and nonlinear boundary value problems. *J. Optim. Theory Appl.* 9: 433–437
- Newhouse S, Ruelle D, Takens T 1978 Occurrence of strange axiom A attractor near quasi-periodic flows on T^m , $m \geq 3$. *Commun. Math. Phys.* 64: 35–40
- Nitsche G, Dressler U 1992 Controlling chaotic dynamical systems using time delay coordinates. *Physica D* 58: 153–164
- Nordmark A B 1991 Non-periodic motion caused by grazing incidence in an impact oscillator. *J. Sound Vib.* 145: 279–297
- Nordmark A B 1993 A computer implementation for the interactive study of dynamical systems by cell mappings. *IUTAM Symposium on Nonlinearity and Chaos in Engineering Dynamics*, London (ed.) J M T Thompson
- Novak S, Frehlich R G 1982 Transition to chaos in the Duffing oscillator. *Phys. Rev.* A26: 3660–3663

- O'Reilly O, Holmes P J 1992 Nonlinear, nonplanar and nonperiodic vibrations of a string. *J. Sound Vib.* 153: 413–435
- Oravsky V 1990 Determination of periodic solutions and their stability for nonlinear systems by a new matrix method. *XII International Conference on Nonlinear Oscillations*
- Oseledec V I 1968 A multiplicative ergodic theorem: Lyapunov characteristic numbers for dynamical systems. *Trans. Moscow Math. Soc.* 12: 1–57
- Ostlund S, Rand D, Sethna J, Siggia E 1983 Universal properties of the transition from quasi-periodicity to chaos in dissipative systems. *Physica D8*: 303–342
- Ott E 1981 Part-I. Strange attractors and chaotic motions of dynamical systems. *Rev. Mod. Phys.* 53: 655–672
- Ott E, Grebogi C, Yorke J A 1990 Controlling chaos. *Phys. Rev. Lett.* 64: 1196–1199
- Packard N H, Crutchfield J P, Farmer J D, Shaw R S 1980 Geometry from a time series. *Phys. Rev. Lett.* 45: 712–715
- Païdoussis M P 1987 Flow induced instabilities of cylindrical structures. *Appl. Mech. Rev.* 40: 163–175
- Païdoussis M P, Li G X 1992 Dynamics of cross flow induced vibrations of heat exchanger tubes impacting on loose supports. *J. Sound. Vib.* 152: 305–326
- Païdoussis M P, Li G X 1993 Pipes conveying fluid. A model dynamical problem. *J. Fluids Struct.* 7: 137–204
- Païdoussis M P, Moon F C 1988a Nonlinear and chaotic fluid elastic vibrations of a flexible pipe conveying fluid. *J. Fluids Struct.* 2: 567–591
- Païdoussis M P, Moon F C 1988b Nonlinear and chaotic fluid elastic vibrations of a flexible pipe conveying fluid. *Proc. Int. Symp. on Flow induced vibration and noise, ASME Nonlinear Interaction Effects and Chaotic motions* (eds) M M M P Paidoussis, R J Hansen pp. 107–133
- Païdoussis M P, Cusumano J P, Copeland G S 1992 Low dimensional chaos in a flexible tube conveying fluid. *Trans. ASME J. Appl. Mech.* 59: 196–205
- Païdoussis M P, Li G X, Rand R H 1991 Chaotic motions of a constrained pipe conveying fluid: Comparison between simulation, analysis and experiment. *Trans. ASME J. Appl. Mech.* 58: 559–565
- Païdoussis M P, Price S J, Mureithi 1993 Nonlinear and chaotic dynamics of a two-degree of freedom analytical model for a rotated triangular array in cross flow *J. Fluids Struct.* 7: 497–520
- Palkovics L, Venhovens P J Th 1992 Investigation on stability and possible chaotic motions in the controlled wheel suspension system. *Veh. Syst. Dyn.* 21: 269–296
- Parker T S, Chua L O 1989 *Practical numerical algorithms for chaotic systems* (New York: Springer-Verlag)
- Parthasarathy S 1992 Homoclinic bifurcation sets of the parametrically driven Duffing oscillator. *Phys. Rev. A46*: 2147–2150
- Pawelzik K 1991 Unstable periodic orbits and prediction. *Phys. Rev. A43*: 1808–1812
- Pederson N F, Davidson A 1981 Chaos and noise rise in Josephson junctions. *Appl. Phys. Lett.* 39: 830–832
- Perkins N C 1992 Modal interactions in the nonlinear response of elastic cables under parametric/external excitation. *Int. J. Non-Linear Mech.* 27: 233–250
- Peterka F, Vacik J 1992 Transition to chaotic motion in mechanical systems with impacts. *J. Sound Vib.* 154: 95–115
- Peurach J, Tongue B H 1991 Chaotic response of a slider crank mechanism. *ASME J. Vib. Acoust.* 113: 69–73
- Pezeshki C, Dowell E H 1987 An examination of initial condition maps for the sinusoidally excited buckled beam modelled by the Duffing's equation. *J. Sound Vib.* 117: 219–232
- Pezeshki C, Elgar S, Krishna R C 1991 An examination of multi frequency excitation of the buckled beam. *J. Sound Vib.* 148: 1–9
- Pierre C, Dowell E H 1985 A study of dynamic instability of plates by extended incremental harmonic balance method. *ASME J. Appl. Mech.* 52: 693–697
- Pierre C, Ferri A A, Dowell E H 1985 Multiharmonic analysis of dry friction damped systems using incremental harmonic balance method. *ASME J. Appl. Mech.* 52: 958–964
- Plaut R H, Hsieh J C 1987 Chaos in mechanism with time delays under parametric and external excitation. *J. Sound Vib.* 114: 73–90

- Poincaré H 1921 *The foundation of science: Science and method* (New York: The Science Press)
- Popp K, Stelter P 1989 Nonlinear oscillations of structures induced by dry friction. *Proc. of IUTAM Symposium on Nonlinear Dynamics and Engineering Systems* (ed.) W Schiehlen (Berlin: Springer Verlag) pp 233–240
- Qin G R, Gong D C, Li R, Wen X D 1989 Rich bifurcation behaviors of the driven van der Pol oscillator. *Phys. Lett.* A141: 412–416
- Raghothama A 1993 *Bifurcation and chaos in gear and cam mechanisms with clearance type nonlinearities*. MS thesis, Indian Institute of Technology, Madras
- Räty R, Isomaki H M, von Boehm J 1984a Chaotic motion of a classical anharmonic oscillator. *Acta Polytech. Scand.* 85: 1–30
- Räty R, von Boehm J, Isomaki H M 1984b Absence of inversion symmetric limit cycles of even periods and chaotic motion of Duffing oscillator. *Phys. Rev. Lett.* A103: 289–291
- Reinhall P J, Caughey T K, Storti D W 1989 Order and chaos in a discrete Duffing oscillator: Implications on numerical integration. *Trans. ASME J. Appl. Mech.* 56: 162–167
- Rokni M, Berger B S 1991 Chaotic motion of a two link mechanism. *J. Sound Vib.* 147: 349–351
- Romeiras F J, Grebogi C, Ott E 1992 Controlling chaotic dynamical systems. *Physica D* 58: 165–192
- Rössler O E 1976 Different types of chaos in two simple differential equations. *Z. Naturforsch.* A31: 1664–1670
- Rudowski J, Szemplinska-Stupnicka W 1987 On an approximate criterion for chaotic motion in a model of a buckled beam. *Ingen.-Arch.* 57: 243–255
- Ruelle D, Takens F 1971 On the nature of turbulence. *Commun. Math. Phys.* 20: 167–192
- Salam F M A, Marsden J E, Varaiya P P 1983 Chaos and Arnold diffusion in dynamical systems. *IEEE Trans. Circuits Syst.* CAS 30: 697–708
- Samoilenko A M, Ronto N I 1979 *Numeric-analytic methods of investigating periodic solutions*
- Sano M, Sawada Y 1983 Transition from quasi-periodicity to chaos in a system of coupled nonlinear oscillators. *Phys. Lett.* A97: 73–76
- Sato S, Sano M, Sawada Y 1983 Universal scaling property in bifurcation structure of Duffing's and of generalised Duffing's equation. *Phys. Rev.* A28: 1654–1658
- Sato K, Yamamoto S, Fujishiro S 1989 On the dynamic response of the hysteretic system. *Comput. Mech.* 5: 241–254
- Sato K, Yamamoto S, Kawakami T 1991 Bifurcation sets and chaotic states of a gear system subjected to harmonic excitation. *Comput. Mech.* 7: 173–182
- Schichtel T, Beckmann P E 1991 The use of first return maps in the computation of basin boundaries in three dimensional phase space. *Phys. Lett.* A156: 163–168
- Schmidt G, Tondl A 1986 *Nonlinear vibrations* (Cambridge: University Press)
- Schwartz I B 1983 Estimating regions of existence of unstable periodic orbits using computer based techniques. *SIAM J. Numer. Anal.* 20: 106–120
- Schwartz I B, Triandaf I 1992 Tracking unstable orbits in experiments. *Phys. Rev.* A46: 7439–7444
- Sekar P, Narayanan S 1994 Periodic and chaotic motions of a square prism in cross flow. *J. Sound Vib.* 170: 1–24
- Seydel R 1988 *From equilibrium to chaos: Practical bifurcation and stability analysis* (New York: Elsevier)
- Sharif-Bakhtiar M, Shaw S W 1988 The dynamic response of a centrifugal pendulum vibration absorber with motion limiting stops. *J. Sound Vib.* 126: 221–235
- Shaw R 1981 Strange attractors, chaotic behaviour and information flow. *Z. Naturforsch.* A36: 80–112
- Shaw S W, Holmes P J 1983a A periodically forced piece-wise linear oscillator. *J. Sound Vib.* 90: 129–155
- Shaw S W, Holmes P J 1983b A periodically forced impact oscillator with large dissipation. *ASME J. Appl. Mech.* 50: 849–857
- Shaw S W 1985 The dynamics of a harmonically excited system having rigid amplitude constraints. Part-I: Subharmonic motions and local bifurcations 459–464 Part-2: Chaotic motions and global bifurcations. *ASME J. Appl. Mech.* 52: 453–458
- Shaw S W 1986 On the dynamic response of a system with dry friction. *J. Sound Vib.* 108: 305–325

- Shaw S W, Rand R H 1989 The transition to chaos in a simple mechanical system. *Int. J. Non-Linear Mech.* 24: 41–56
- Shaw J, Shaw S W 1989 The onset of chaos in a two degree of freedom impacting system. *Trans. ASME J. Appl. Mech.* 56: 168–174
- Shaw S W, Tung P C 1988 The dynamic response of a system with preloaded compliance. *ASME J. Dyn. Sys. Control.* 110: 278–283
- Shilnikov L P 1970 A contribution to the problem of the structure of an extended neighbourhood of a rough equilibrium state of saddle-focus type. *Math. USSR Sbornik.* 10: 91–102
- Shimada I, Nagashima T 1979 A numerical approach to ergodic problem of dissipative dynamical systems. *Prog. Theor. Phys.* 61: 1605–1615
- Shinbrot T 1993 Using small perturbations to control chaos. *Nature (London)* 363: 411–417
- Simiu E, Cook G R 1991 Chaotic motions of self-excited forced and autonomous square prisms. *ASCE J. Eng. Mech.* 117: 241–259
- Simiu E, Cook G R 1992 Empirical fluid-elastic models and chaotic galloping: a case study. *J. Sound Vib.* 154: 45–66
- Singer J, Wang Y Z, Bau H H 1991 Controlling a chaotic system. *Phys. Rev. Lett.* 66: 1123–1125
- Soliman M S 1993 Jumps to resonance: Long chaotic transients, unpredictable outcome and the probability of restabilisation. *ASME J. Appl. Mech.* 60: 669–676
- Soliman M S, Thompson J M T 1989 Integrity measures quantifying the erosion of smooth and fractal basins of attraction. *J. Sound Vib.* 135: 453–475
- Soliman M S, Thompson J M T 1992a Indeterminate subcritical bifurcations in parametric resonance. *Proc. R. Soc. London* A438: 511–518
- Soliman M S, Thompson J M T 1992b Indeterminate transcritical bifurcations in parametrically excited systems. *Proc. R. Soc. London* A439: 601–610
- Sozen M A 1974 Hysteresis structural elements. *Proc. Conf. Appl. Mech. Earthquake Sys. ASME Annu. Meeting AMD.* 8: 66–98
- Sparrow C 1982 *The Lorenz equations* (New York: Springer-Verlag)
- Sri Namachchivaya N 1989 Nonlinear dynamics of supported pipe conveying pulsating fluid. Part I: Subharmonic resonance. *Int. J. Non-Linear Mech.* 24: 185–196
- Sri Namachchivaya N, Tien W M 1989 Nonlinear dynamics of supported pipe conveying pulsating fluid. Part II: Combination resonance. *Int. J. Non-Linear Mech.* 24: 197–208
- Stavens J, Heslot F, Libchaber A 1985 Fixed winding number of the quasiperiodic route to chaos in a convective fluid. *Phys. Rev. Lett.* 55: 596–599
- Steeb W H, Erig W, Kunik A 1983 Chaotic behaviour and limit cycle behaviour of anharmonic systems with periodic external perturbations. *Phys. Lett.* A93: 267–270
- Steeb W H, Kunik A 1987 Chaos in limit cycle systems with external periodic excitations. *Int. J. Non-Linear Mech.* 22: 349–361
- Steeb W H, Louw J A, Kapitaniak T 1986 Chaotic behaviour of an anharmonic oscillator with two external periodic forces. *J. Phys. Soc. Jpn.* 55: 3279–3280
- Stewart H B, Ueda Y 1991 Catastrophes with indeterminate outcome. *Proc. R. Soc. London* 432: 113–123
- Sun J Q, Hsu C S 1990 Global analysis of nonlinear dynamical systems with fuzzy uncertainties by the cell mapping method. *Comput. Methods Appl. Mech. Eng.* 83: 109–120
- Szemplinska-Stupnicka W 1986 The $1/2$ subharmonic resonance and its transition to chaotic motion in a nonlinear oscillator. *Int. J. Non-Linear Mech.* 21: 401–409
- Szemplinska-Stupnicka W 1987 Secondary resonances and approximate models of routes to chaotic motion in nonlinear oscillators. *J. Sound Vib.* 113: 155–172
- Szemplinska-Stupnicka W 1988a The refined approximate criterion for chaos in a two state mechanical system. *Ing.-Archiv.* 58: 354–366
- Szemplinska-Stupnicka W 1988b Bifurcations of harmonic solution leading to chaotic motion in the softening type Duffing's oscillator. *Int. J. Non-Linear Mech.* 23: 257–277
- Szemplinska-Stupnicka W 1989 The approximate criteria for chaos in multi well potential vibrating systems. *Proc. of IUTAM Symp. on Nonlinear Dyn. and Eng. Sys.* (ed.) W Schiehlen (Berlin: Springer-Verlag)
- Szemplinska-Stupnicka W 1992 A discussion on necessary and sufficient conditions for steady-state chaos. *J. Sound Vib.* 152: 369–372

- Szemplinska-Stupnicka W 1993 On analytical estimate of safe impulsive velocity in the driven escape oscillator. *IUTAM Symposium on Nonlinearity and Chaos in Engineering Dynamics* (ed.) J M T Thompson
- Szemplinska-Stupnicka W, Plaut R H, Hsieh J C 1989 Period doubling and chaos in unsymmetric structures under parametric excitation *ASME J. Appl. Mech.* 56: 947–952
- Szemplinska-Stupnicka W, Rudowski J 1992 Local methods in predicting occurrence of chaos in two-well potential systems: superharmonic frequency region. *J. Sound Vib.* 152: 57–72
- Takens F 1980 Detecting strange attractors in turbulence. In *Lecture notes in mathematics* (eds) D A Rand, L S Young (Berlin: Springer)
- Tamura H, Tsuda Y, Sueoka A 1981 Higher approximation of steady oscillations in nonlinear systems with single degree of freedom (suggested multi-harmonic balance method). *Bull. JSME.* 24: 1616–1625
- Tang D M, Dowell E H 1988a On the threshold force for chaotic motions for a forced buckled beam. *ASME J. Appl. Mech.* 55: 190–196
- Tang D M, Dowell E H 1988b Chaotic oscillations of a cantilevered pipe conveying fluid. *J. Fluids Struct.* 2: 263–283
- Tél T 1991 Controlling transient chaos. *J. Phys.* A24: L1359–L1368
- Theocaris P S, Panagiotopoulos P D 1993 Cracks of fractal geometry with unilateral contact and friction interface conditions. *Int. J. Fract.* 60: 293–310
- Thomsen J J 1992 Chaotic vibrations of non-shallow arches. *J. Sound Vib.* 153: 239–258
- Thompson J M T 1989 Chaotic phenomena triggering the escape from a potential well. *Proc. R. Soc. London* A421: 195–225
- Thompson J M T 1992 Global unpredictability in nonlinear dynamics, capture, dispersal and indeterminate bifurcations. *Physica* D58: 260–272
- Thompson J M T, Bishop S R, Leung L M 1987 Fractal basins and chaotic bifurcations prior to escape from a potential well. *Phys. Lett.* A121: 116–120
- Thompson J M T, Bokaian A R, Ghaffari R 1983 Subharmonic resonances and chaotic motions of a bilinear oscillator. *IMA J. Appl. Math.* 31: 207–234
- Thompson J M T, Lunn T S 1981 Static elastic formulations of a pipe conveying fluid. *J. Sound Vib.* 77: 127–132
- Thompson J M T, Rainey R C T, Soliman M S 1990 Ship stability criteria based on chaotic transients from incursive fractals. *Philos. Trans. R. Soc. London* A332: 149–167
- Thompson J M T, Soliman M S 1990 Fractal control boundaries of driven oscillators and their relevance to safe engineering design. *Proc. R. Soc. London* A428: 1–13
- Thompson J M T, Soliman M S 1991 Indeterminate jumps to resonance from a tangled saddle-node bifurcation. *Proc. R. Soc. London* A432: 101–111
- Thompson J M T, Stewart H B 1986 *Non-linear dynamics and chaos* (New York: John Wiley & Sons)
- Tondl A 1985 Analysis of a self excited system with a dry friction. *Int. J. Non-Linear Mech.* 20: 471–479
- Tongue B H 1986 Existence of chaos in a one degree of freedom system. *J. Sound Vib.* 110: 69–78
- Tongue B H 1987a Characteristics of numerical simulations of chaotic systems. *ASME J. Appl. Mech.* 54: 695–699
- Tongue B H 1987b On obtaining global nonlinear system characteristics through interpolated cell mapping. *Physica* D28: 401–408
- Tongue B H, Gu K 1988a Interpolated cell mapping of dynamical systems. *ASME J. Appl. Mech.* 55: 461–466
- Tongue B H, Gu K 1988b A theoretical basis for interpolated cell mapping. *SIAM J. Appl. Math.* 18: 1206–1214
- Tongue B H, Gu K 1988c A higher order method of interpolated cell mapping. *J. Sound Vib.* 125: 169–179
- Tongue B H, Smith D 1989 Lyapunov exponents by means of interpolated cell mapping. *ASME J. Appl. Mech.* 56: 691–696
- Tousi S, Bajaj A K 1985 Period doubling bifurcations and modulated motion in forced mechanical systems. *ASME J. Appl. Mech.* 52: 446–452
- Troger H 1979 On point mappings for mechanical systems possessing homoclinic and heteroclinic points. *ASME J. Appl. Mech.* 46: 468–469

- Tseng W Y, Dugundji J 1971 Nonlinear vibrations of a buckled beam under harmonic excitation. *ASME J. Appl. Mech.* 56: 691–696
- Tsuda Y, Tamura H, Seouka A, Fujii T 1992 Chaotic behavior of a nonlinear vibrating system with a retarded argument. *JSME Int. Ser. III* 35: 259–267
- Tufillaro N B, Abano A M 1986 Chaotic dynamics of a bouncing ball. *Am. J. Phys.* 54: 939–944
- Turcher H 1982 Bistability and Feigenbaum bifurcation of driven anharmonic oscillator. *Phys. Lett.* A30: 385–388
- Ueda Y 1979 Randomly transitional phenomena in the system governed by Duffing's equation. *J. Stat. Phys.* 20: 181–196
- Ueda Y 1980 Steady motions exhibited by Duffing's equation. *Picture book of regular and chaotic motions, new approaches to nonlinear dynamics* (ed) P J Holmes (SIAM) pp 311–322
- Ueda Y 1985 Random phenomena resulting from nonlinearity in the system described by Duffing's equation. *Int. J. Non-Linear Mech.* 20: 481–491
- Ueda Y, Akamatsu N 1981 Chaotically transitional phenomena in the forced negative resistance oscillator. *IEEE Trans. Circuits Syst.* 28: 217–223
- Urabe M 1965 Galerkin's procedure for nonlinear periodic systems. *Arch. Ration. Mech. Anal.* 20: 120–152
- Urabe M, Reiter 1966 Numerical computation of nonlinear forced oscillations by Galerkin's procedure. *J. Math. Anal. Appl.* 14: 107–140
- Vaishali A G 1994 Bifurcation and chaos in a rotor-bearing system with clearance. M. Tech. Thesis, Indian Institute of Technology, Madras
- Van der Pol B, Van der Mark J 1927 Frequency demultiplication. *Nature (London)* 120: 363–364
- Van Dooren R 1973 Differential tones in a damped mechanical system with quadratic and cubic nonlinearities. *Int. J. Non-Linear Mech.* 8: 575–583
- Van Dooren R 1988 On the transition from regular to chaotic behaviour in the Duffing's oscillator. *J. Sound Vib.* 123: 327–339
- Varosi F, Grebogi C, Yorke J A 1987 Simplicial approximation of Poincaré maps of differential equations. *Phys. Lett.* A124: 59–64
- Virgin L N 1987 The nonlinear rolling response of a vessel including chaotic motions leading to capsize in regular waves. *Appl. Ocean Res.* 9: 89–95
- Virgin L N 1988 On the harmonic response of an oscillator with unsymmetric restoring force. *J. Sound Vib.* 126: 157–165
- Virgin L N, Cartee L A 1991 A note on the escape from a potential well. *Int. J. Non-Linear Mech.* 26: 449–452
- Wei S T, Pierre C 1989 Effects of dry friction damping on the occurrence of localized forced vibration in nearly periodic structures. *J. Sound Vib.* 129: 397–416
- Wen Y K 1989 Methods of random vibration for inelastic structures. *Appl. Mech. Rev.* 42: 39–52
- Whiston G S 1987a The vibro-impact response of a harmonically excited and preloaded one dimensional linear oscillator. *J. Sound Vib.* 115: 303–319
- Whiston G S 1987b Global dynamics of a vibro impacting linear oscillator. *J. Sound Vib.* 118: 395–424
- Whiston G S 1992 Singularities in vibroimpact dynamics. *J. Sound Vib.* 152: 427–460
- Wiggins S 1987 Chaos in the quasiperiodically forced Duffing oscillator. *Phys. Lett.* A124: 138–142
- Wiggins S 1990 *Introduction to applied nonlinear dynamical and chaos*. (New York: Springer Verlag)
- Wolf A, Swift J B, Swinney H L, Vastano A 1985 Determining Lyapunov exponents from a time series. *Physica D* 16: 285–317
- Wong C W, Zhang W S, Lau S L 1991 Periodic forced vibration of unsymmetrical piece-wise linear systems by incremental harmonic balance method. *J. Sound Vib.* 149: 91–105
- Xu J X, Guttalu R S, Hsu C S 1985 Domains of attraction for multiple limit cycles of coupled van der Pol equations by simple cell mapping. *Int. J. Non-Linear Mech.* 20: 507–517
- Yagasaki K 1990 Second order averaging and chaos in quasiperiodically forced weakly nonlinear oscillators. *Physica D* 44: 445–458
- Yagasaki K 1991 Chaos in a weakly nonlinear oscillator with parametric and external resonances. *ASME J. Appl. Mech.* 58: 244–250
- Yagasaki K, Sakata M, Kimura K 1990 Dynamics of a weakly nonlinear system subjected to combined parametric and external excitation. *ASME J. Appl. Mech.* 57: 209–217

- Yang C Y, Chang A H D, Roy R V 1991 Chaotic and stochastic dynamics for a nonlinear structural system with hysteresis and degradation. *Probab. Eng. Mech.* 6: 193–203
- Zadeh L A 1965 Fuzzy sets. *Inf. Control* 8: 338–353
- Zhao L C, Yang Z C 1990 Chaotic motions of an airfoil with nonlinear stiffness in incompressible flow. *J. Sound Vib.* 138: 245–254

Some aspects of chaotic and stochastic dynamics for structural systems

N SRI NAMACHCHIVAYA, M M DOYLE and N MALHOTRA

Nonlinear Systems Group, Department of Aeronautical and Astronautical Engineering, University of Illinois at Urbana-Champaign, Urbana, IL 61801, USA

Abstract. In this paper, the bifurcation behaviour of an externally excited four-dimensional nonlinear system is examined. Throughout this paper, a two-degree-of-freedom shallow arch structure under either a periodic or a stochastic excitation will be considered. For the case when the excitation is periodic, the local and global behaviour is examined in the presence of principal *subharmonic resonance* and *1:2 internal resonance*. The method of averaging is used to obtain the first order approximation of the response of the system under resonant conditions. A standard Melnikov type perturbation method is used to show analytically that the system may exhibit chaotic dynamics in the sense of Smale horseshoe for the 1:2 internal resonance case in the absence of dissipation. In the case of stochastic excitation, the stability of the stationary solution is examined by determining the *maximal Lyapunov exponent* and *moment Lyapunov exponent* in terms of system parameters. An asymptotic method is used to obtain explicit expressions for various exponents in the presence of weak dissipation and noise intensity. These quantities provide almost-sure stability boundaries in parameter space. When the system parameters lie outside these boundaries, it is essential to understand the nonlinear behaviour. The method of stochastic averaging is applied to obtain a set of approximate Itô equations which are then examined to describe the local bifurcation behaviour.

Keywords. Nonlinear dynamics; Melnikov analysis; Lyapunov exponent; global stochastic bifurcations; arch structures.

1. Introduction

The study of nonlinear dynamics is of great interest to engineers due to the wide range of applicability of nonlinear phenomena, such as existence of limit cycles, hysteretic effects, period-doubling bifurcations and complex dynamics, in mechanical and structural systems. This paper deals with the study of such nonlinear effects in structural problems which arise mainly due to geometric nonlinearities. The local

bifurcation analysis of nonlinear structural/mechanical systems is well understood when the input to the system is deterministic. However, the global dynamics of these problems, including possible chaotic behaviour, is the subject of much of the current research. There is a great deal of literature on the computational results that have appeared in the study of chaotic dynamics of both structural and mechanical systems. However, these methods do not provide a great insight into the nature of the complicated dynamics that is present in these nonlinear systems. The perturbative Melnikov method presented in this paper detects such complicated dynamics due to global bifurcations. A detailed discussion of the higher dimensional Melnikov analysis is given by Wiggins (1988). In the first part of this paper, both the local and global behaviour of deterministic systems are considered. As an application, the dynamics of a shallow arch subjected to time-dependent loading are examined.

In addition to deterministic excitations, practical engineering systems generally experience random loading conditions due to environmental disturbances, inherent noise, unmodelled dynamics, etc. Various methods are available for evaluating the stability and local bifurcation behaviour of these stochastic systems. However, global techniques for analysing such nonlinear random dynamical systems are not so well developed. There is a great deal of research in progress in the mathematical aspects of global analysis and the limited results available are not yet applicable to engineering problems. Thus, only stability and local stochastic bifurcation results are presented here. Most of the analysis in this paper is based on the general results of the authors on Lyapunov exponents, moment Lyapunov exponents and stochastic bifurcations. These results are applied to a certain class of structural problems.

In §2, a brief discussion of the physical problem, a shallow arch subjected to time-dependent loading, is presented along with various assumptions used in obtaining a set of Lagrangian equations of motion. Section 3 contains results of global bifurcations in the presence of 1:2 internal and subharmonic resonance. The stability of the stationary solutions under the influence of random excitation is studied in §4 in which results on Lyapunov exponents and moment Lyapunov exponents are presented. Finally, §4.2 contains results on stochastic bifurcations.

2. Equations of motion

Shallow arch structures subjected to various load conditions have been investigated by many authors in the past. Dynamic behaviour of the arch structures under impulsive loading was examined by Mettler (1962), Lock (1965), Humphrey (1966) and Hsu (1969). Recently Sri Namachchivaya & Doyle (1988) and Tien *et al* (1994) studied bifurcation behaviour and chaotic dynamics of a shallow arch subjected to small amplitude periodic excitation. In this study the dynamic response of a shallow arch is investigated. The shallow arch is assumed to be subjected to a lateral loading $p(x, t)$, as shown in figure 1.

The equation of motion governing the lateral deflection $w(x, t)$ of this arch can be derived using the energy method, and is given as:

$$mw_{tt} + \beta w_t + EIw_{xxxx} - EA h(w, t)(\bar{w}_{xx} + w_{xx}) = p(x, t), \quad (1)$$

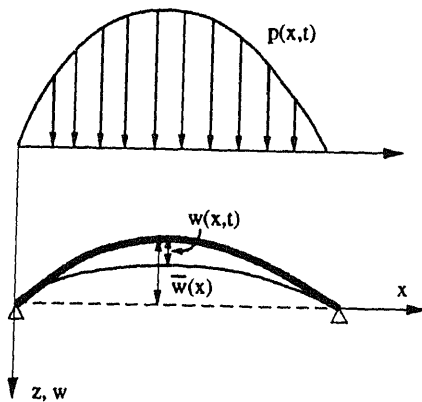


Figure 1. Geometry of the shallow arch structure subjected to lateral loading $p(x, t)$.

where

$$h(w, t) = (1/l) \left[u(l, t) + \int_0^l \left(\frac{1}{2} w_x^2 + \bar{w}_{xx} w_{xx} \right) dx \right],$$

$$\bar{w}(x) = -q_0 \sin(\pi x/l),$$

$$p(x, t) = (p_0 + f(t)) \sin(\pi x/l).$$

Here, q_0 is the initial rise parameter, p_0 is the static loading and $f(t)$ is time-dependent part of the lateral loading. The spatial function $\bar{w}(x)$ represents the initial deflection of the unloaded arch. The arch is subjected to the following boundary conditions

$$w = 0, \quad w_{xx} = 0 \quad \text{at} \quad x = 0, l.$$

The Galerkin method is used to reduce the equation of motion to the ordinary differential equations by selecting appropriate shape functions. The transverse motion $w(x, t)$ of the arch is approximated by the following expression:

$$w(x, t) = q_1(t) \sin(\pi x/l) + q_2(t) \sin(2\pi x/l). \quad (2)$$

The non-dimensional equations of motion describing the evolution of the amplitudes of two fundamental modes can be written in $(Q_1 = q_1 - q_0, Q_2 = q_2)$ coordinates as

$$\begin{aligned} \ddot{Q}_1 + \beta_1 \dot{Q}_1 + Q_1 + Q_1(Q_1^2 - q_0^2 + 4Q_2^2) + (q_0 - \lambda_0) &= f(t), \\ \ddot{Q}_2 + \beta_2 \dot{Q}_2 + 16Q_2 + 4Q_2(Q_1^2 - q_0^2 + 4Q_2^2) &= 0, \end{aligned} \quad (3)$$

where β_1 and β_2 are the viscous damping parameters for the first and second mode, respectively, and λ_0 represents the non-dimensional loading parameter. The details of this derivation and the definitions of non-dimensional variables and parameters can be found in Tien (1992).

This study deals with the dynamic response, stability and bifurcation behaviour of a system described by (3). Here $f(t)$ is either a time periodic function or a white noise process. The first part of the paper deals with the global behaviour of the periodically forced shallow arch system in the presence of 1:2 internal and principal subharmonic resonance.

3. Deterministic Analysis

Resonances have long been known to cause complex or chaotic behaviour in both dissipative and Hamiltonian dynamical systems. Since these resonances provide near-integrable structure in the governing equations, one can use certain analytical methods to study their global behaviour. To this end, in this section, consider (3) in the presence of parametric subharmonic and internal resonances. Here it is assumed that the external forcing is periodic, i.e. $f(t) = \rho \cos vt$ where ρ and v represent the amplitude and frequency of the harmonic excitation, respectively. In the absence of any external excitation (i.e., $f(t) = 0$), the system (3) permits single mode constant solutions ($Q_1(t) = Q_{10}$, $Q_2(t) = 0$). Tien *et al* (1994) considered small perturbations in the neighbourhood of $(Q_{10}, 0)$ and obtained nonlinear variational equations corresponding to the forced equations of motion (3). In this investigation, a more realistic approach is taken. First, the single mode time-dependent solutions for the forced case are obtained using a power series expansion. Next, the nonlinear variational equations governing the small perturbations are obtained near the time-dependent single mode solutions. The external forcing appears as a parametric term in these perturbation equations. By using the method of averaging (Bogoliubov & Mitropolsky 1961), the first order approximation of the response of these perturbation equations is obtained in the presence of 1:2 internal resonance and the principal subharmonic resonance.

3.1 Scaling and averaged equations

In order to investigate the dynamics of the arch for 1:2 internal resonance, the damping terms are ignored and the external forcing amplitude is assumed to be small as compared to other terms, i.e.,

$$\mu = \varepsilon\gamma, \quad \beta_1 = \beta_2 = 0, \quad (4)$$

where ε is a small parameter ($0 < \varepsilon \ll 1$). As mentioned previously, the equations of motion (3) permit $(Q_1(t) = \eta(t), Q_2(t) = 0)$ as one of the solutions. The following expansion of $\eta(t)$ is assumed

$$\eta(t) = \eta_0 + \varepsilon\eta_1 + \varepsilon^2\eta_2 + O(\varepsilon^3). \quad (5)$$

In order to obtain variational equations about this solution, small perturbations x_1 and x_2 in the neighbourhood of single mode solutions $(\eta(t), 0)$, are considered, i.e.

$$Q_1 = \eta(t) + \varepsilon x_1, \quad Q_2 = 0 + \varepsilon x_2. \quad (6)$$

The nonlinear variational equations governing the perturbations can be written as:

$$\begin{aligned} \ddot{x}_1 + \omega_1^2 x_1 + \varepsilon[6\eta_0\eta_1 x_1 + \eta_0(3x_1^2 + 4x_2^2)] \\ + \varepsilon^2[3x_1(\eta_1^2 + 2\eta_0\eta_2) + \eta_1(3x_1^2 + 4x_2^2) + x_1^3 + 4x_1x_2^2] + O(\varepsilon^3) = 0, \\ \ddot{x}_2 + \omega_2^2 x_2 + \varepsilon[8\eta_0\eta_1 x_2 + 8\eta_0x_1x_2] \\ + \varepsilon^2[4x_2(\eta_1^2 + 2\eta_0\eta_2) + 8\eta_1x_1x_2 + 4(x_1^2x_2 + 4x_2^3)] + O(\varepsilon^3) = 0, \end{aligned} \quad (7)$$

where $\omega_1^2 = 3\eta_0^2 + (1 - q_0^2)$ and $\omega_2^2 = 4[\eta_0^2 + (4 - q_0^2)]$. Here η_0 is governed by a third order algebraic equation and η_1, η_2 etc. can be explicitly obtained in terms of known

parameters and time. This yields

$$\begin{aligned}\eta_0^3 + (1 - q_0^2)\eta_0 + (q_0 - \lambda_0) &= 0, \\ \eta_1 &= b_1 \cos(vt), \\ \eta_2 &= b_2 + b_3 \cos(vt) + b_4 \cos(2vt),\end{aligned}\quad (8)$$

where $b_1 = \gamma/(w_1^2 - v^2)$ and b_2, b_3 and b_4 can be similarly expressed in terms of unknown quantities. The Hamiltonian corresponding to (7) can be expressed as

$$\begin{aligned}H(\mathbf{x}_p, \mathbf{x}_q) &= H_0 + \varepsilon H_1 + O(\varepsilon^2) \\ &= \frac{1}{2}[x_{p1}^2 + x_{p2}^2 + \omega_1^2 x_{q1}^2 + \omega_2^2 x_{q2}^2] \\ &\quad + \varepsilon[\eta_0 x_{q1}^3 + 4\eta_0 x_{q1}^2 x_{q2} + \eta_0 \eta_1 (3x_{q1}^2 + 4x_{q2}^2)] + O(\varepsilon^2),\end{aligned}\quad (9)$$

where $x_{q1} = x_1, x_{q2} = x_2, x_{p1} = \dot{x}_1$ and $x_{p2} = \dot{x}_2$. The steady state behaviour and bifurcation analysis of the system is best described when the following canonical change of variables is introduced:

$$\begin{aligned}x_{qi} &= (2a_i)^{1/2} \cos(\omega_i t + (\phi_i/\omega_i)), \quad \dot{x}_{pi} = -\omega_i (2a_i)^{1/2} \sin(\omega_i t + (\phi_i/\omega_i)), \\ \forall i &= 1, 2.\end{aligned}\quad (10)$$

The following detuning parameters are introduced in order to examine the dynamics of the system in the presence of principal subharmonic resonance and 1:2 internal resonance.

$$\omega_1^2 = \frac{1}{4}(v^2 - \varepsilon\sigma_1), \quad \omega_2^2 = \frac{1}{16}(v^2 - \varepsilon\sigma_2),\quad (11)$$

where σ_1 is the measure of deviation of the forcing frequency from twice the natural frequency of the first mode, and $(\sigma_2 - \sigma_1)$ represents the deviation from the 1:2 internal resonance. At this stage, the method of averaging (Bogoliubov & Mitropolsky 1961) is applied to simplify the system. The averaged equations in the canonical variables can be expressed as

$$\begin{aligned}\dot{a}_1 &= \varepsilon \left[\frac{6}{v} a_1 b_1 \eta_0 \sin(2\theta_1) + \frac{4}{v} (2a_1)^{1/2} a_2 \eta_0 \sin(\theta_1 - 2\theta_2) \right] + O(\varepsilon^2), \\ a_1 \dot{\theta}_1 &= \varepsilon \left[-\frac{1}{(4v)} \sigma_1 a_1 + \frac{3}{v} a_1 b_1 \eta_0 \cos(2\theta_1) \right. \\ &\quad \left. + \frac{2}{v} (2a_1)^{1/2} a_2 \eta_0 \cos(\theta_1 - 2\theta_2) \right] + O(\varepsilon^2), \\ \dot{a}_2 &= \varepsilon \left[-\frac{16}{v} (2a_1)^{1/2} a_2 \eta_0 \sin(\theta_1 - 2\theta_2) \right] + O(\varepsilon^2), \\ a_2 \dot{\theta}_2 &= \varepsilon \left[-\frac{1}{(2v)} \sigma_2 a_2 + \frac{8}{v} (2a_1)^{1/2} a_2 \eta_0 \cos(\theta_1 - 2\theta_2) \right] + O(\varepsilon^2),\end{aligned}\quad (12)$$

where $\theta_i = \phi_i/\omega_i$. In order to analyse the trivial equilibrium solutions, the averaged equations can be transformed to the rectangular coordinates. One finds that the trivial solution ($a_1 = 0, a_2 = 0$) may lose its stability only through a simple bifurcation and may give rise to one or two coupled mode nontrivial equilibrium branches or one single

and one coupled mode solution branches. For a detailed account of the stability and bifurcation analysis, one is referred to Malhotra & Sri Namachchivaya (1995).

3.2 Analytical investigation of chaotic dynamics

In order to examine the possibility of the chaotic dynamics in the system, the higher dimensional Melnikov analysis is employed. The details of the framework of this method can be found in Wiggins (1988). Originally this method is due to Melnikov (1963) who considered a two-dimensional non-autonomous system with a completely integrable unperturbed part and small ($O(\varepsilon)$) time periodic terms. The non-resonant higher dimensional Melnikov method assumes the homoclinic structure of the unperturbed system along with arbitrary perturbations. Generically, certain invariant sets may persist under perturbations. Thus, the knowledge of the global dynamics of the unperturbed integrable system can be used to develop a measure of the distance between the stable and unstable manifolds of that invariant set in the perturbed system. This measure is called the *Melnikov function*, which provide crucial information on the possibility of the presence of chaotic behaviour in certain classes of nonlinear systems.

3.2a Reduction to the standard form: Consider the following canonical transformation in order to reduce the averaged system of equations to the form appropriate for applying the higher dimensional Melnikov theory as described in Wiggins (1988):

$$q_1 = \left(\frac{\phi_1}{\omega_1} - 2 \frac{\phi_2}{\omega_2} \right), \quad q_2 = 2 \frac{\phi_2}{\omega_2}, \quad p_1 = a_1 \omega_1, \quad p_2 = \frac{1}{2}(a_2 + 4a_1)\omega_2. \quad (13)$$

This transformation leads to the following set of equations in (p_1, q_1, p_2, q_2) coordinates:

$$\begin{aligned} \dot{p}_1 &= \varepsilon \left[\frac{32\eta_0}{v^{3/2}}(p_1)^{1/2}(p_2 - p_1) \sin q_1 + \frac{6b_1\eta_0}{v} p_1 \sin 2(q_1 + q_2) \right] + O(\varepsilon^2), \\ \dot{q}_1 &= \varepsilon \left[-\frac{\sigma_1}{4v} + \frac{\sigma_2}{v} + \frac{16\eta_0(p_2 - 3p_1)}{v^{3/2}(p_1)^{1/2}} \cos(q_1) \right. \\ &\quad \left. + \frac{3b_1\eta_0}{v} \cos 2(q_1 + q_2) \right] + O(\varepsilon^2), \\ \dot{p}_2 &= \varepsilon \left[\frac{6b_1\eta_0}{v} p_1 \sin 2(q_1 + q_2) \right] + O(\varepsilon^2), \\ \dot{q}_2 &= \varepsilon \left[-\frac{\sigma_2}{v} + \frac{32\eta_0}{v^{3/2}}(p_1)^{1/2} \cos q_1 \right] + O(\varepsilon^2). \end{aligned} \quad (1)$$

In these equations, the effect of excitation is present through the terms involving η coefficient, b_1 , since $b_1 = \gamma/(\omega_1^2 - v^2)$. Thus, (14) attains the desired form if the time rescaled and the forcing terms are assumed to be small compared to the nonlinear terms. For this purpose, the variables and parameters are rescaled in the following manner:

$$\gamma = \varepsilon\gamma', \quad t = t'/\varepsilon, \quad p_1 = p'_1/A^2, \quad p_2 = p'_2/A^2, \quad ($$

where $A = (16\eta_0 v^{-3/2})$ and t' denotes the slow time. For convenience, the prime (') is dropped from the rescaled variables and parameters. The rescaled equations up to $O(\varepsilon)$ can now be written as:

$$\begin{aligned}\dot{p}_1 &= 2p_1^{1/2}(p_2 - p_1) \sin q_1 + \varepsilon[2\mu p_1 \sin 2(q_1 + q_2)], \\ \dot{q}_1 &= \mu_1 + \mu_2 + p_1^{-1/2}(p_2 - 3p_1) \cos q_1 + \varepsilon[\mu \cos 2(q_1 + q_2)], \\ \dot{p}_2 &= \varepsilon[2\mu p_1 \sin 2(q_1 - q_2)], \\ \dot{q}_2 &= -\mu_2 + 2p_1^{1/2} \cos q_1,\end{aligned}$$

where

$$\mu_1 = -\frac{\sigma_1}{4v}, \quad \mu_2 = \frac{\sigma_2}{v}, \quad \mu = \frac{3}{v}b_1\eta_0.$$

In (16), the dot indicates differentiation with respect to t' . The objective is to study the global dynamics associated with this system. As a first step, the structure of the unperturbed system (obtained by setting $\varepsilon = 0$) is examined. This can be expressed as:

$$\begin{aligned}\dot{p}_1 &= 2p_1^{1/2}(p_2 - p_1) \sin q_1, \\ \dot{q}_1 &= \mu_1 + \mu_2 + p_1^{-1/2}(p_2 - 3p_1) \cos q_1, \\ \dot{p}_2 &= 0, \\ \dot{q}_2 &= -\mu_2 + 2p_1^{1/2} \cos q_1.\end{aligned}\tag{17}$$

It is clear that the first two equations are completely independent of q_2 , and $p_2 = p_{20} = \text{constant}$. Therefore, it is sufficient to study the phase flow in (p_1, q_1) coordinates only. The canonical transformations (13) and the periodicity of q_1 suggests that the range of interest in (p_1, q_1) coordinates is: $0 < p_1 \leq p_{20}$ and $0 \leq q_1 \leq 2\pi$. The Hamiltonian corresponding to the two-dimensional (p_1, q_1) vector field is given as:

$$\hat{H}(p_1, q_1) = (\mu_1 + \mu_2)p_1 + 2p_1^{1/2}(p_2 - p_1) \cos q_1.\tag{18}$$

It is obvious that the orbits in (p_1, q_1) phase space depend only on the three parameters (p_{20}, μ_1, μ_2) . The fixed points of the reduced vector field, in the range of interest, are given as follows:

$$(p_{20}, \hat{q}_1), (p_{20}, 2\pi - \hat{q}_1), (p_1^+, 0), (p_1^-, 2\pi), (p_1^+, \pi),$$

where

$$\begin{aligned}\hat{q}_1 &= \cos^{-1}[\sigma/2(p_{20})^{1/2}] \\ p_1^\pm &= (1/18)[\sigma^2 + 6p_{20} \pm \sigma(\sigma^2 + 12p_{20})^{1/2}], \\ \sigma &= (\mu_1 + \mu_2).\end{aligned}$$

The linear stability analysis indicates that the phase flow has qualitatively different behaviour in region III as compared with regions I and II (figure 2). These three regions are defined in the following manner:

$$\begin{aligned}\text{I: } &\{(\sigma, p_{20}) | \sigma \geq 0, (\sigma^2 - 4p_{20}) < 0\}, \\ \text{II: } &\{(\sigma, p_{20}) | \sigma \geq 0, (\sigma^2 - 4p_{20}) < 0\} \\ \text{III: } &\{(\sigma, p_{20}) | (\sigma^2 - 4p_{20}) > 0\}.\end{aligned}$$

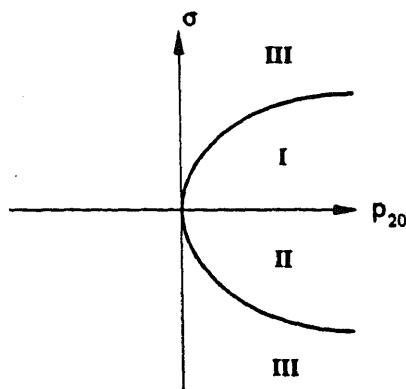


Figure 2. Various global bifurcation sets (I, II, III) in $(p_{20} - \sigma)$ parameter space.

One can easily check that the equilibrium points (p_{20}, \hat{q}_1) and $(p_{20}, 2\pi - \hat{q}_1)$ are *saddle points* in regions I and II, and the equilibrium points $(p_1^+, 0)$, $(p_1^+, 2\pi)$ and (p_1^-, π) exist as *centre points* anywhere in (σ, p_{20}) parameter space. One also notices that there are no saddle points in region III, thus there do not exist any homoclinic/heteroclinic connections in region III. The phase portraits corresponding to these global bifurcation sets (I and II) are shown in figure 3. These phase portraits indicate the existence of a heteroclinic cycle ($A-A'$) connecting the two saddle points (p_{20}, \hat{q}_1) and $(p_{20}, 2\pi - \hat{q}_1)$. The condition for the existence of this heteroclinic cycle is given as:

$$p_{20} \geq \frac{\sigma^2}{4}. \quad (20)$$

Furthermore, it will be shown numerically that chaotic behaviour is not possible for this system when the system parameters lie outside of region I and II.

3.2b The Melnikov function: The next step is to determine whether the heteroclinic cycle would break under small perturbations, and if it does break, whether the stable and unstable manifolds of these heteroclinic connections (A and A') intersect transversely. This information is obtained by calculating the Melnikov function M (Wiggins 1988) defined by

$$M = \int_{-\infty}^{\infty} \left[\frac{\partial \bar{H}}{\partial p_1} g^{p_1} + \frac{\partial \bar{H}}{\partial q_1} g^{q_1} + \frac{\partial \bar{H}}{\partial p_2} g^{p_2} \right] dt - \frac{\partial \bar{H}}{\partial p_2} \Big|_{(p_{20}, \hat{q}_1)} \int_{-\infty}^{\infty} g^{p_2} dt, \quad (21)$$

where the integrand has been evaluated at any arbitrary point on the heteroclinic cycle. In the above expression, g^{p_1} , g^{q_1} , g^{p_2} and g^{q_2} are the $O(\epsilon)$ terms in the four-dimensional perturbed system given by (16),

$$g^{p_1} = 2\mu p_1 \sin 2(q_1 + q_2),$$

$$g^{q_1} = \mu \cos 2(q_1 + q_2),$$

$$g^{p_2} = 2\mu p_1 \sin 2(q_1 + q_2),$$

$$g^{q_2} = 0,$$

(22)

and the Hamiltonian (\bar{H}) corresponding to the four-dimensional unperturbed phase

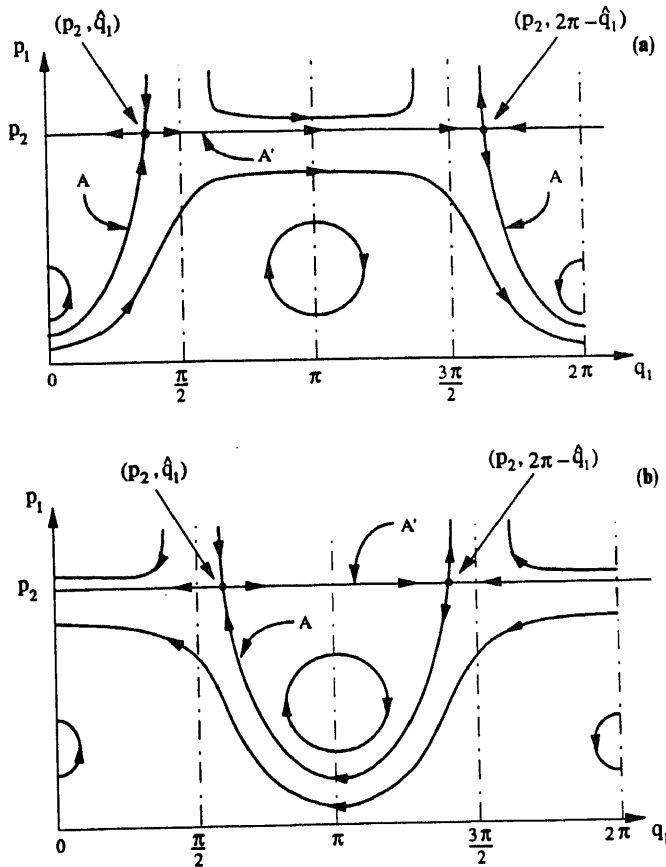


Figure 3. (a) Unperturbed phase flow in (p_1, q_1) phase space in region I (i.e. $\sigma > 0$).
 (b) Unperturbed phase flow in (p_1, q_1) phase space in region II (i.e. $\sigma < 0$).

space is given as:

$$\bar{H}(p_1, q_1, p_2, q_2) = \sigma p_1 + 2p_1^{1/2}(p_2 - p_1) \cos q_1 - \mu_2 p_2. \quad (23)$$

On substituting (22) and (23) in (21), the Melnikov function for this system can be expressed as follows:

$$\begin{aligned} M = \int_{-\infty}^{\infty} [& \{ \sigma + p_1^{-1/2}(p_2 - 3p_1) \cos q_1 \} \{ 2\mu p_1 \sin 2(q_1 + q_2) \} \\ & - \{ 2p_1^{1/2}(p_2 - p_1) \sin q_1 \} \{ \mu \cos 2(q_1 + q_2) \} \\ & + \{ -\mu_2 + 2p_1^{1/2} \cos q_1 \} \{ 2\mu p_1 \sin 2(q_1 + q_2) \}] dt \\ & - \mu_1 \int_{-\infty}^{\infty} [2\mu p_1 \sin 2(q_1 + q_2)] dt. \end{aligned} \quad (24)$$

3.2c Time parametrized expressions for heteroclinic orbits: In order to evaluate the Melnikov function, the explicit expressions for the heteroclinic orbits are required. The

heteroclinic orbit A' is the horizontal line connecting the two saddle points as shown in figure 3. This orbit is described by the following set of equations:

$$\begin{aligned} p_1(t) &= p_{20}, \\ \dot{q}_1(t) &= \sigma - 2(p_{20})^{1/2} \cos q_1(t), \\ p_2(t) &= p_{20}, \\ \dot{q}_2(t) &= -\mu_2 + 2(p_{20})^{1/2} \cos q_1(t). \end{aligned} \quad (25)$$

To evaluate the Melnikov function for the heteroclinic orbit A' , one does not require the explicit expressions for $q_1(t)$ and $q_2(t)$. On substituting $p_1(t) = p_{20}$ in (24) and further simplifying the integrand, the Melnikov function assumes the following form

$$\begin{aligned} M_{A'}^{I,II} &= \int_{-\infty}^{\infty} [\{\sigma - 2(p_{20})^{1/2} \cos q_1\} \{2\mu p_{20} \sin 2(q_1 + q_2)\} \\ &\quad + \{-\mu_1 - \mu_2 + 2p_{20}^{1/2} \cos q_1\} \{2\mu p_{20} \sin 2(q_1 + q_2)\}] dt. \end{aligned} \quad (26)$$

Using $\sigma = (\mu_1 + \mu_2)$ in (26), it is trivial to show $M_{A'}^{I,II} = 0$, which means the $O(\varepsilon)$ distance between the stable and unstable manifolds of A' is always zero and, hence, it can be concluded that the heteroclinic orbit A' does not break at order $O(\varepsilon)$ perturbation.

The parametrized expression describing the heteroclinic orbit A can be obtained as

$$\bar{H}(p_1, q_1) = \bar{H}(p_{20}, \hat{q}_1),$$

which implies,

$$p_1(t) = \sigma^2/4 \cos^2 q_1(t). \quad (27)$$

Substituting this in the unperturbed equations for \dot{q}_1 and \dot{q}_2 , explicit expressions for $q_1(t)$ and $q_2(t)$ can be obtained. Hence, the heteroclinic orbit A can be described by

$$\begin{aligned} p_1(t) &= \frac{\sigma^2}{4} + \left(p_{20} - \frac{\sigma^2}{4}\right) \tanh^2 \left(\left(p_{20} - \frac{\sigma^2}{4}\right)^{1/2} t \right), \\ q_1(t) &= \tan^{-1} \left[\frac{2}{\sigma} \left(\left(p_{20} - \frac{\sigma^2}{4}\right)^{1/2} \tanh \left(\left(p_{20} - \frac{\sigma^2}{4}\right)^{1/2} t \right) \right] + q_{10}, \\ p_2(t) &= p_{20}, \\ q_2(t) &= \mu_1 t + q_{20}, \end{aligned} \quad (28)$$

where q_{10} is the initial value of $q_1(t)$. For region I ($0 \leq \sigma < 2(p_{20})^{1/2}$), $q_{10} = 0$ and for region II ($-2(p_{20})^{1/2} < \sigma \leq 0$), $q_{10} = \pi$. q_{20} is the initial value of $q_2(t)$ and is used as another parameter. Using these expressions in (24), and after some algebraic manipulation, the Melnikov function for the heteroclinic orbit A can be obtained as

$$\begin{aligned} M_A^{I,II} &= 2\mu \sin 2q_{20} \int_{-\infty}^{\infty} (p_1(t))^{1/2} \{p_{20} - p_1(t)\} \cos(q_1(t) + 2\mu_1 t) dt \\ &\quad + 2\mu \cos 2q_{20} \int_{-\infty}^{\infty} (p_1(t))^{1/2} \{p_{20} - p_1(t)\} \sin(q_1(t) + 2\mu_1 t) dt. \end{aligned} \quad (29)$$

One observes that the integrand associated with the second integral in this expression is an odd function of t , and thus the contribution due to this part is zero. The first integral

can be computed easily using (27) and (28) to give

$$M_A^{I,II} = C(\mu_1, \mu_2, \mu, p_{20}) \sin 2q_{20}, \quad (30)$$

where

$$C(\mu_1, \mu_2, \mu, p_{20}) = 2\mu_1(\mu_2 - \mu_1)\mu\pi \csc\left(\frac{\mu_1\pi}{(p_{20} - (\sigma^2/4))^{1/2}}\right). \quad (31)$$

It is worth mentioning that C depends on the system parameters μ_1, μ_2, μ and p_{20} , and is, in general, non-zero. Hence, under the circumstances when C is non-zero, the Melnikov function ($M_A^{I,II}$) will have a simple zero with respect to q_{20} at $q_{20} = n\pi/2$. In this case, the heteroclinic orbit A may break under small perturbation with transversal intersection and the system may exhibit chaotic dynamics in the sense of Smale Horseshoe.

3.2d Numerical results: In order to examine the effect of small perturbations on the dynamics of the unperturbed system in more detail, one often resorts to numerical simulations. As noted previously, in the absence of any perturbations, the system dynamics can be studied completely in (p_1, q_1) phase space (figure 4a). The introduction

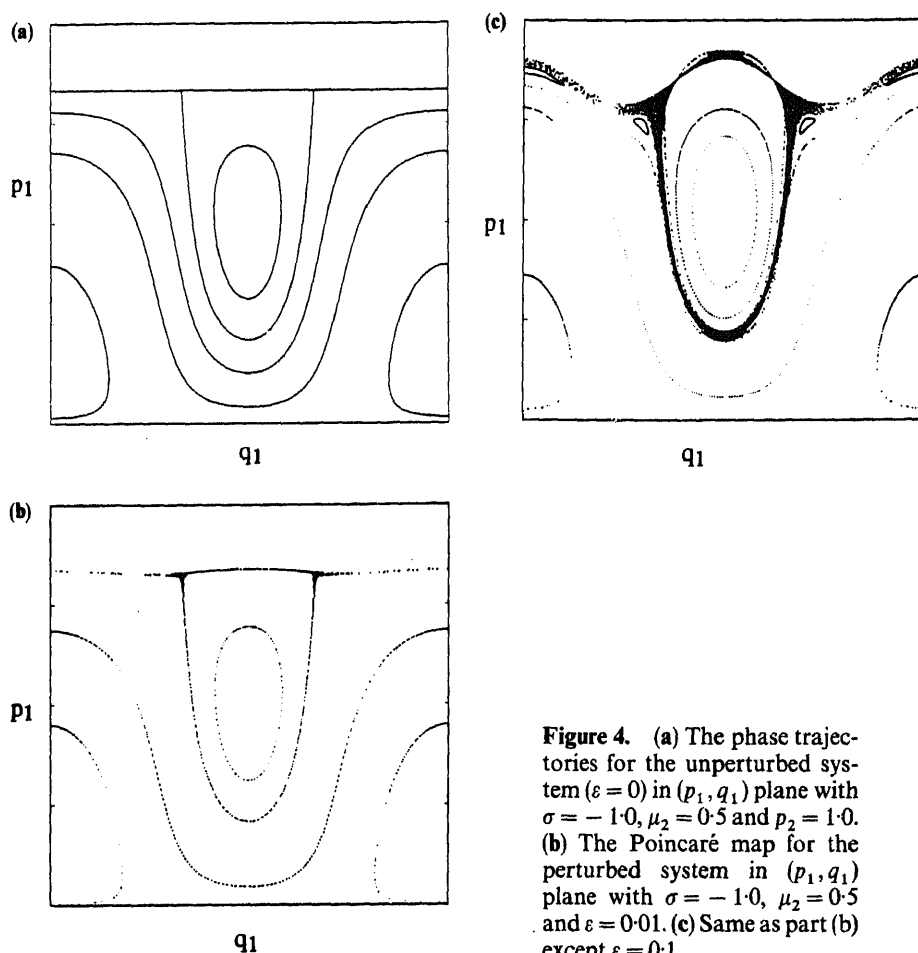


Figure 4. (a) The phase trajectories for the unperturbed system ($\varepsilon = 0$) in (p_1, q_1) plane with $\sigma = -1.0$, $\mu_2 = 0.5$ and $p_2 = 1.0$. (b) The Poincaré map for the perturbed system in (p_1, q_1) plane with $\sigma = -1.0$, $\mu_2 = 0.5$ and $\varepsilon = 0.01$. (c) Same as part (b) except $\varepsilon = 0.1$.

of small perturbation couples the dynamics of all the variables (p_1, q_1, I, θ) and in four-dimensional phase space the dynamics can be very complicated. Although the analysis considered earlier provides some insight into the global dynamics of the perturbed system, it does not generally yield the complete picture. However, the trajectories in the four-dimensional phase space can be numerically computed on a two-torus. Using the fact that $q_2 \in T^1$ is a phase variable with period π , three-dimensional Poincaré maps can be constructed in (p_1, q_1, p_2) phase space, with $q_2 = q_{20} \bmod \pi$, where q_{20} can be set to zero without loss of generality. Furthermore, the momentum p_2 varies very slowly for small perturbations. Thus, the Poincaré map can be easily represented in (p_1, q_1) space.

Figure 4b shows a Poincaré map in (p_1, q_1) space for $\sigma = -1.0$, $\mu_2 = 0.5$, and $\varepsilon\mu = 0.01$. In this diagram, one finds that most of the periodic orbits of the unperturbed system survive as quasi-periodic orbits with non-commensurable frequencies on a 2-torus, while the initial conditions taken very close to the unperturbed heteroclinic orbit lead to chaotic dynamics in the perturbed system. As the perturbation strength ($\varepsilon\mu$) is increased to 0.1, the extent of the chaotic attractor increases and various small secondary regions appear in a symmetric fashion about the $q_1 = 0$ axis (figure 4c). These secondary regions are small islands of quasi-periodic motion embedded in the layer of stochastic motion. The global dynamics of this system were studied for various values of the system parameters. It was observed that for a given perturbation strength the extent of the chaotic layer is rather small for non-zero values of the detuning parameter σ as compared to the case where $\sigma = 0$. The number, location and appearance of the secondary regions are also sensitive to the values of the detuning parameters. The influence of small perturbations arising from dissipation effects was also examined. It was found that even a very small damping causes the secondary regions to disappear, and the quasi-periodic orbits and chaotic attractor shrink towards the trivial solution. For additional details on the nature of trajectories in the perturbed system, one is referred to Malhotra & Sri Namachchivaya (1995).

To summarise, in this section the conditions on system parameters for which the shallow arch system can exhibit chaotic dynamics under small harmonic excitations are explored. It is shown that in the absence of any dissipation and excitation, the averaged system corresponding to the nonlinear variational equations can have heteroclinic connections for certain values of system parameters. The higher dimensional Melnikov's method is used to show that one of the heteroclinic orbits may break under small time periodic excitations. Under these conditions, the averaged system may have Smale Horseshoe type chaos whenever the system parameters σ and p_{20} lie inside the domains I and II. Using a standard theorem, these results can be extended for the original system. It must be noted that the existence of a simple zero of the Melnikov function only provides the necessary condition for chaos to occur. The applicability of this method is restricted to this class of problems in the sense that one cannot examine the effect of perturbations arising from the dissipation effects. Numerical simulations were also performed to confirm the predictions made in the analysis and to further explore the effect of small perturbations on the periodic and heteroclinic orbits. These simulations reveal very exciting details of the underlying structure of the quasi-periodic orbits and chaotic regions in the perturbed system.

4. Stochastic analysis

This section examines the response, stability and bifurcations of nonlinear structural

systems under stochastic excitations. There has been considerable research in this area both from mathematical and engineering points of view. In this section, a review of recent results pertaining to two-degree-of-freedom structural systems and some new results on moment Lyapunov exponents are presented. This section is divided into three parts dealing with Lyapunov exponents, moment Lyapunov exponents and stochastic bifurcations. The first two sections address the stability aspects and the final section deals with the nonlinear response of stochastic systems.

The stability of a linear stochastic system can be defined in several ways. The weakest definition is that of stability in distribution. A more conservative estimate of the stability boundary is described by stability in probability. Thus, if a system is stable in probability, it is also stable in distribution. The other commonly used definitions of stochastic stability are stability in the r th mean and almost-sure stability, or stability with probability one. If a dynamical system excited by noise is stable according to either of these definitions, it is stable in distribution and in probability, as well. It is well known that, for a linear system with stochastic parametric excitation, the Lyapunov exponents are analogous to the real part of the eigenvalue. Stability in the almost-sure sense is determined by the sign of the maximal Lyapunov exponent.

However, r th mean and almost-sure stability do not imply each other, i.e. a system can be almost surely stable while its 2nd moments grow exponentially. Kozin & Sugimoto (1977), with extensions by Arnold (1991), established a characterization between moment stability and almost-sure stability for linear Itô stochastic differential equations when the process is ergodic on the entire surface of the n -sphere. It was shown that the region of sample stability is the limit of the regions of r th moment stability for r approaching zero. In this section, both Lyapunov exponents and moment Lyapunov exponents obtained for the two-degree-of-freedom arch problem using asymptotic methods will be presented.

When the steady state motion of the nonlinear system is unstable, either in the mean square or almost sure sense, the nonlinearities act as limiters of the response and give rise to a new steady state motion. In order to examine such bounded motions, the response of the system beyond the bifurcation point must be examined. Section 4.2 examines such behaviour.

4.1 Asymptotic linear results

The systems under consideration consist of multiplicative two-degree-of-freedom systems. Such systems are encountered in the study of mechanical systems subjected to fluctuating loading or imposed displacements as well as in the investigation of the stability of steady state motions of nonlinear dynamical systems. Consider, for example,

$$\begin{aligned}\ddot{y}_1 + 2\zeta\omega_1\dot{y}_1 + \omega_1^2 y_1 + f(y_1, y_2) &= w(t), \\ \ddot{y}_2 + 2\zeta\omega_2\dot{y}_2 + \omega_2^2 y_2 + y_2 g(y_1, y_2) &= 0,\end{aligned}\tag{32}$$

where $f(0, 0) = 0$, $\partial f / \partial y_2(y_1, 0) \neq 0$, and $w(t)$ is a white noise process. Then the stability of the solution ($y_1 = \xi(t)$, $y_2 = 0$) is governed by a set of variational equations defined by

$$\ddot{\xi} + 2\zeta\omega_1\dot{\xi} + \omega_1^2 \xi + f(\xi, 0) = 0.$$

The maximal Lyapunov exponent for a general four-dimensional system with two critical modes parametrically perturbed by a small intensity real noise process is approximated

by Sri Namachchivaya & Van Roessel (1993) and Doyle & Sri Namachchivaya (1994) using a perturbation approach. In these studies, the natural frequencies are assumed to be non-commensurable and the infinitesimal generator associated with the noise process is assumed to have an isolated simple zero eigenvalue.

4.1a Maximal Lyapunov exponent: The focus of this section is to approximate the maximal Lyapunov exponents for a two-dimensional system perturbed by a small intensity multiplicative real noise process. Consider linear oscillatory systems described by equations of motion of the form

$$\ddot{q}_i + \omega_i^2 q_i + \varepsilon^2 2\zeta\omega_i \dot{q}_i + \varepsilon \sum_{j=1}^2 k_{ij} q_j f(\xi(t)) = 0, \quad i, j = 1, 2,$$

where the q_i 's are generalized coordinates, ω_i is the i th natural frequency, and $\varepsilon\zeta$ represents a small viscous damping coefficient. The term $\xi(t)$ is a small intensity real noise process. In this section, an asymptotic expansion for the maximal Lyapunov exponent under the real noise assumption is calculated, and readers are referred to Pinsky & Wihstutz (1991), Sri Namachchivaya & Van Roessel (1993) and Doyle & Sri Namachchivaya (1994) for general calculations of these quantities.

The method outlined in the last two references above applies to systems of the form

$$\dot{x} = Ax + \varepsilon f(\xi(t))Bx, \quad x \in \mathbb{R}^4. \quad (33)$$

Appropriate scaling of the matrix A yields

$$A = A_0 - \varepsilon^2 A_1,$$

where

$$A_0 = \begin{bmatrix} 0 & \omega_1 & 0 & 0 \\ -\omega_1 & 0 & 0 & 0 \\ 0 & 0 & 0 & \omega_2 \\ 0 & 0 & -\omega_2 & 0 \end{bmatrix} \quad \text{and} \quad A_1 = \begin{bmatrix} \delta_1 & 0 & 0 & 0 \\ 0 & \delta_1 & 0 & 0 \\ 0 & 0 & \delta_2 & 0 \\ 0 & 0 & 0 & \delta_2 \end{bmatrix}.$$

The matrix B is described by $B = [b_{ij}]$. For convenience, the following notation is employed

$$H_{ij}^{\pm} = b_{2i-1,2j} \pm b_{2i,2j-1} \quad \text{and} \quad J_{ij}^{\pm} = b_{2i,2j} \pm b_{2i-1,2j-1}.$$

The quantities δ_1 and δ_2 are damping parameters. In this analysis, it is assumed that the frequencies ω_1 and ω_2 are non-commensurable. The results presented in this paper are obtained under very general conditions on the noise term. The term $\xi(t)$ is a small intensity real noise process defined on a smooth connected one-dimensional Riemannian manifold M (with or without boundary). The smooth function $f: M \rightarrow \mathbb{R}$ is assumed to have zero mean.

Before proceeding, a brief description of some of the results of Oseledec's Multiplicative Ergodic Theorem (Oseledec (1968)), as related to four-dimensional systems, is necessary. Consider the linear stochastic system in (33) under the assumption that $\xi(t)$ is ergodic. According to the Multiplicative Ergodic Theorem, the Lyapunov exponent

of the solution of (33), $x(t; x_0)$, for the initial condition $x_0 (x_0 \neq 0)$ is

$$\lambda(x_0) = \lim_{t \rightarrow \infty} \frac{1}{t} \log \|x(t; x_0)\|, \quad (34)$$

where $\lambda(x_0)$ takes on one of r fixed or non-random values $\lambda_1 < \dots < \lambda_r$. Which λ_i is realized depends on the initial condition x_0 . The multiplicities of the Lyapunov exponents sum to the dimension of the system, n (in this case, $n = 4$). Associated with each λ_i there exists a random linear invariant subspace E_i , known as an Oseledec space, such that $E_1 \oplus E_2 \oplus \dots \oplus E_r = \mathbf{R}^n$, with

$$\lim_{t \rightarrow \pm \infty} \frac{1}{t} \log \|x(t; x_0)\| = \lambda_i \quad \text{iff} \quad x(t; x_0) \in E_i.$$

The dimension of each Oseledec space E_i is given by the multiplicity of the associated Lyapunov exponent, λ_i .

Let G denote the infinitesimal generator of $\xi(t)$, i.e.

$$G(\xi) = \mu_i(\xi) \frac{\partial}{\partial \xi_i} + \frac{1}{2} \sigma_{ij}^2(\xi) \frac{\partial^2}{\partial \xi_i \partial \xi_j},$$

and, as in Sri Namachchivaya & Van Roessel (1993), assume that G has an isolated simple zero eigenvalue. This implies that $u \equiv \text{constant}$ is the only solution of $Gu = 0$. Consequently, the adjoint operator G^* must also have an isolated simple zero eigenvalue. The results obtained from this analysis are applicable when the manifold M is of arbitrary dimension.

By the usual transformation i.e.

$$x_{2i-1} = r_i \cos \phi_i, \quad x_{2i} = r_i \sin \phi_i \quad \text{and} \quad \rho_i = \ln(r_i),$$

amplitude and phase equations of the form

$$\dot{\rho}_i = \varepsilon^2 [\bar{p}_i(\phi)] + \varepsilon [p_i(e^{(\rho_j - \rho_i)}, \phi)] f(\xi(t)), \quad (35)$$

$$\dot{\phi}_i = [\omega_i + \varepsilon^2 \bar{h}_i(\phi)] + \varepsilon [h_i(e^{(\rho_j - \rho_i)}, \phi)] f(\xi(t)), \quad (36)$$

are obtained. In this form, the amplitude and phase equations are coupled by the presence of terms of the form $e^{(\rho_j - \rho_i)}$ for $i \neq j$. Since $e^{(\rho_j - \rho_i)}$ is always positive, one can introduce a one-to-one mapping $e^{(\rho_j - \rho_i)} = \tan \theta$, $\theta \in [0, \pi/2]$. Thus, applying the following transformations to the original system,

$$x_1 = e^\rho \cos \phi_1 \cos \theta, \quad x_2 = -e^\rho \sin \phi_1 \cos \theta,$$

$$x_3 = e^\rho \cos \phi_2 \sin \theta, \quad x_4 = -e^\rho \sin \phi_2 \cos \theta,$$

yields the following set of equations for the amplitude ρ , phase variables (ϕ_1, ϕ_2, θ) and noise process ξ :

$$\dot{\rho} = \varepsilon f(\xi) q_1(\phi_1, \phi_2, \theta) + \varepsilon^2 \bar{q}_1(\theta),$$

$$\dot{\phi}_i = \omega_i + \varepsilon f(\xi) h_i(\phi_1, \phi_2, \theta) + \varepsilon^2 \bar{h}_i(\phi_1, \phi_2, \theta),$$

$$\dot{\theta} = \varepsilon f(\xi) q_2(\phi_1, \phi_2, \theta) + \varepsilon^2 \bar{q}_2(\theta),$$

$$d\xi = \mu(\xi) dt + \sigma(\xi) \circ dW_t,$$

where q_i , \tilde{q}_i and h_i are given in terms of H_{ij}^{\pm} , J_{ij}^{\pm} and $\delta_i(i, j = 1, 2)$. Given the structure of the A_1 matrix, it can be shown that $h_i \equiv 0$ for $i = 1, 2$.

The processes $(\phi_1, \phi_2, \theta, \xi)$ are independent of the amplitude ρ and form a diffusive Markov process with associated generator

$$L^\varepsilon = L^0 + \varepsilon L^1 + \varepsilon^2 L^2,$$

where, in general

$$L^0 = \sum_{i=1}^2 \omega_i \frac{\partial}{\partial \phi_i} + G(\xi),$$

$$L^1 = f(\xi) \left[q^2 \frac{\partial}{\partial \theta} + \sum_{i=1}^2 h_i \frac{\partial}{\partial \phi_i} \right],$$

$$L^2 = \tilde{q}_2 \frac{\partial}{\partial \theta} + \sum_{i=1}^2 \tilde{h}_i \frac{\partial}{\partial \phi_i}.$$

For this particular A_1 matrix, $L^2 = \tilde{q}_2(\partial/\partial\theta)$; we also define the function $Q^\varepsilon(\phi_1, \phi_2, \theta, \xi)$ such that

$$Q^\varepsilon = Q^0 + \varepsilon Q^1 + \varepsilon^2 Q^2.$$

In the present analysis, one can write Q^ε in terms of $f(\xi)$, q_1 and \tilde{q}_1 as follows:

$$Q^\varepsilon(\phi_1, \phi_2, \theta, \xi) = \varepsilon f(\xi) q_1(\phi_1, \phi_2, \theta) + \varepsilon^2 \tilde{q}_1(\theta).$$

Then, according to Oseledec's multiplicative ergodic theorem (Oseledec 1968), assuming the operator L^ε to be ergodic, the maximal Lyapunov exponent is given by

$$\lambda^\varepsilon = \langle Q^\varepsilon, p^\varepsilon \rangle = \int_0^{\pi/2} \int_M \int_0^{2\pi} \int_0^{2\pi} Q^\varepsilon p^\varepsilon d\phi_1 d\phi_2 d\xi d\theta,$$

where p^ε is the unique ergodic invariant measure associated with the generator L^ε , i.e. p^ε solves the Fokker–Planck equation given by

$$L^{\varepsilon*} p^\varepsilon = 0,$$

provided L^ε is hypoelliptic.

A formal expansion of the invariant measure is constructed, i.e.

$$p^\varepsilon = p^0 + \varepsilon p^1 + \cdots + \varepsilon^N p^N + \cdots.$$

Substituting this expansion and the expansion for L^ε into the Fokker–Planck equation yields the following sequence of Poisson equations to be solved for p^0, p^1, p^2, \dots :

$$L^{0*} p^0 = 0,$$

$$L^{0*} p^1 = -L^{1*} p^0,$$

$$L^{0*} p^2 = -L^{1*} p^1 - L^{2*} p^0.$$

This yields the following asymptotic expression for the maximal Lyapunov exponent (see Doyle & Sri Namachchivaya (1994) for proof):

$$\begin{aligned} \lambda^\varepsilon = & \langle Q^0, p^0 \rangle + \varepsilon [\langle Q^1, p^0 \rangle + \langle Q^0, p^1 \rangle] \\ & + \varepsilon^2 [\langle Q^2, p^0 \rangle + \langle Q^1, p^1 \rangle + \langle Q^0, p^2 \rangle] + \cdots. \end{aligned}$$

Since $Q^0 = 0$, the expression for the maximal Lyapunov exponent reduces to

$$\lambda^\varepsilon = \varepsilon \langle Q^1, p^0 \rangle + \varepsilon^2 [\langle Q^2, p^0 \rangle + \langle Q^1, p^1 \rangle] + \dots,$$

where p^0 and p^1 satisfy the Poisson equations above with the periodic boundary conditions

$$p^0(\phi_1, \phi_2, \theta, \xi) = p^0(\phi_1 + 2\pi, \phi_2, \theta, \xi) = p^0(\phi_1, \phi_2 + 2\pi, \theta, \xi),$$

$$p^1(\phi_1, \phi_2, \theta, \xi) = p^1(\phi_1 + 2\pi, \phi_2, \theta, \xi) = p^1(\phi_1, \phi_2 + 2\pi, \theta, \xi).$$

Solving the $O(1)$ Poisson equation with appropriate boundary conditions and considering the non-commensurability condition on the natural frequencies yields

$$p^0(\xi, \theta) = v(\xi) F(\theta) / 4\pi^2,$$

where $v(\xi)$ is the invariant measure satisfying $G^*v = 0$. Note that for arbitrary $F(\theta)$, the inner product $\langle Q^1, p^0 \rangle = 0$ due to the periodic boundary conditions on ϕ_1 and ϕ_2 and the zero mean assumption on $f(\xi)$. The maximal Lyapunov exponent, up to $O(\varepsilon^2)$, reduces to

$$\lambda^\varepsilon = \varepsilon^2 [\langle Q^2, p^0 \rangle + \langle Q^1, p^1 \rangle].$$

Using the solvability condition for the $O(\varepsilon)$ Poisson equation, one can show that a unique solution for p_1 exists. The $O(\varepsilon)$ Poisson equation itself yields an expression for p_1 in terms of p_0 . The term $F(\theta)$ in the expression for p_0 can be determined with the aid of the $O(\varepsilon^2)$ solvability condition. Evaluating the solvability condition yields the following ordinary differential equation for $F(\theta)$:

$$-\frac{d}{d\theta} [\Phi(\theta) F(\theta)] + \frac{1}{2} \frac{d^2}{d\theta^2} [\Psi^2(\theta) F(\theta)] = 0, \quad (37)$$

where

$$\Psi^2(\theta) = A \cos^2 2\theta + B \cos 2\theta + C,$$

$$\Phi(\theta) = -\frac{1}{2}(\tilde{\lambda}_1 - \tilde{\lambda}) \sin 2\theta + \Psi^2(\theta) \cot 2\theta.$$

This is indeed the diffusion equation in θ . This describes the stochastic coupling between ρ_1 and ρ_2 in (35).

Throughout the remainder of this paper, the following notation will be used:

$$\alpha_{ij} = \frac{1}{8} [(H_{ij}^{-2} + J_{ij}^{+2}) S(\Omega^-) + (H_{ij}^{+2} + J_{ij}^{-2}) S(\Omega^-)],$$

$$\beta_i = \frac{1}{8} (H_{ii}^{+2} + J_{ii}^{-2}) S(2\omega_i),$$

$$\mu = \frac{1}{8} [H_{12}^+ H_{21}^+ + J_{12}^- J_{21}^-] S(\Omega^+) - (H_{12}^- H_{21}^- + J_{12}^+ J_{21}^+) S(\Omega^-),$$

$$\gamma_1 = \frac{1}{4} (H_{21}^- J_{12}^+ + H_{12}^- J_{21}^+) \Gamma(\Omega^-),$$

$$\gamma_2 = \frac{1}{4} (H_{21}^+ J_{12}^- + H_{12}^+ J_{21}^-) \Gamma(\Omega^+),$$

$$\gamma = \frac{1}{16} (J_{11}^+ - J_{22}^+)^2 S(0) + \frac{1}{4} (\beta_1 + \beta_2) - \frac{1}{4} (\alpha_{12} + \alpha_{21}) - \frac{1}{2} \mu.$$

The sine and cosine spectrums are defined, respectively, as

$$\Gamma(\omega) = 2 \int_0^\infty R(T) \sin \omega T dT \quad \text{and} \quad S(\omega) = 2 \int_0^\infty R(T) \cos \omega T dT,$$

where $R(T)$ is the autocorrelation of $f(\xi)$, i.e.

$$R(T) = \int_M f(\xi) K(\xi, T) d\xi,$$

and $\Omega^\pm = \omega_1 \pm \omega_2$. Employing this notation yields

$$A = -\gamma,$$

$$B = -\frac{1}{2}(\alpha_{12} - \alpha_{21}) = -\frac{1}{2}\alpha^-,$$

$$C = \gamma + \frac{1}{2}(\alpha_{12} + \alpha_{21}) = \gamma + \frac{1}{2}\alpha^+,$$

$$\lambda_i = -\delta_i + \beta_i \text{ and } \tilde{\lambda}_i = \lambda_i + \gamma_i,$$

where λ_1 and λ_2 are the Lyapunov exponents for the case when the modes in (33) are decoupled.

Equation (37) can be rewritten as

$$\frac{d}{d\theta} \left\{ -\Phi(\theta)F(\theta) + \frac{1}{2} \frac{d}{d\theta} [\Psi^2(\theta)F(\theta)] \right\} = 0. \quad (38)$$

Let $A_{sr}(\theta)$ be the term in the brackets. Then, $A_{sr}(\theta)$ must be constant with respect to θ , i.e. $A_{sr}(\theta) = A_{sr}$. By examining (38), one can see that there may be singularities in the open interval $(0, \pi/2)$. All possible singular cases must be considered when attempting to solve this expression for $F(\theta)$. The location of the singular points and the behaviour of the diffusion process in the presence of these singularities is studied by Doyle & Sri Namachchivaya (1994). The white noise case was studied separately by Sri Namachchivaya et al (1994). The results of the white noise case can also be obtained as the limiting case of the above real noise results.

4.1b Moment Lyapunov exponents for white and real noise cases: Although sample solutions may be stable with probability one, the mean square response of the system for the same parameter values may grow exponentially. A concise formulation of the relation between almost-sure sample stability and the p th mean stability is presented by Arnold (1991). More extensive coverage for real and white noise cases was given by Arnold & Wihstutz (1986). In this section, asymptotic expansions for the moment Lyapunov exponent, the exponential rate of growth or decay of the p th mean, under the white and real noise assumptions are calculated and the readers are referred to Doyle et al (1995) for general calculations of these quantities.

For the structural problem under consideration, the oscillators of (32) are decoupled yielding two single-degree-of-freedom systems. Thus, in determining the moment stability of the four-dimensional system, one may calculate the moment Lyapunov exponents for each oscillator individually. In the present analysis, the moment Lyapunov exponents for a general two-dimensional linear system excited by white or real noise are approximated. These results will be applied to the shallow arch problem in §4.1c.

By definition the moment Lyapunov exponent is given by

$$g(p) := \lim_{t \rightarrow \infty} \frac{1}{t} \log E|x(t, x_0)|^p, \quad p \in \mathbb{R}, \quad x_0 \in \mathbb{R}^2 - \{0\}, \quad (39)$$

where $g(p)$ is a smooth convex function with $g(0) = 0$ and $g'(0) = \lambda$ and the sign of $g(p)$ defines the exponential stability ($g(0) < 0$) or instability ($g(0) > 0$) of the p th moment.

In order to calculate the moment Lyapunov exponent in the white noise case, consider the first-order equations after an appropriate transformation, i.e.,

$$dx = A x dt + \sum_{i=1}^2 B^i x \circ dW_i(t), \quad x \in \mathbf{R}^4, \quad (40)$$

where

$$A = \begin{bmatrix} -\delta & -\omega \\ \omega & -\delta \end{bmatrix}, \quad B^i = [b_{jk}^{(i)}],$$

and W_i are independent unit variance Wiener processes. Projecting the first order equations onto a circle, i.e.,

$$\begin{aligned} \rho &= \ln \|x\|, \quad \theta = \tan^{-1}(x_2/x_1), \\ \dot{\rho} &= q_0(\theta) + \sum_{i=1}^2 \sigma_i q_i(\theta) \circ dW_i(t), \end{aligned} \quad (41)$$

$$\dot{\theta} = h_0(\theta) + \sum_{i=1}^2 \sigma_i h_i(\theta) \circ dW_i(t), \quad (42)$$

one can define the moment Lyapunov exponent $g(p)$ as the principal eigenvalue of the problem on S^1 (see, for example, Arnold 1991).

$$L(p)\phi(p) = g(p)\phi(p), \quad \forall p \in \mathbf{R}, \quad (43)$$

where

$$L(p) = \mathcal{L} + p\mathcal{X} + p\mathcal{Z} + \frac{p^2}{2}\mathcal{R}, \quad (44)$$

$$\begin{aligned} \mathcal{L} &= h_0 \frac{\partial}{\partial \theta} + \sum_{i=1}^2 \left(h_i \frac{\partial}{\partial \theta} \right)^2, \\ \mathcal{Z} &= q_0 \frac{\partial}{\partial \theta} + \sum_{i=1}^2 q_i \frac{\partial}{\partial \theta}, \\ \mathcal{X} &= \sum_{i=1}^2 q_i h_i \frac{\partial}{\partial \theta}. \end{aligned} \quad (45)$$

In general, the solution of $g(p)$ to all orders of p is difficult to calculate. However, using the convex and analytic properties of $g(p)$ one can write

$$g(p) = g(0) + pg'(0) + (p^2/2)g''(0) + O(p^3), \quad (46)$$

and the associated eigenvalue problem reduces to (Arnold & Wihstutz 1986)

$$L\psi = \lambda - \mathcal{Z}, \quad L\eta = g''(0) - 2(\mathcal{X} + \mathcal{Z} - \lambda)\psi - \mathcal{R}, \quad (47)$$

where

$$\psi := \frac{\partial \phi}{\partial p} \Big|_{p=0}, \quad \eta := \frac{\partial^2 \phi}{\partial p^2} \Big|_{p=0}.$$

Explicit calculation of various coefficients yields

$$h_0 = \omega, \quad q_0 = -\delta,$$

$$h_i = \frac{1}{2}(b_{21}^i - b_{12}^i) + \frac{1}{2}(b_{22}^i - b_{11}^i)\sin(2\theta) + (b_{21}^i + b_{12}^i)\cos(2\theta),$$

$$q_i = \frac{1}{2}(b_{11}^i + b_{22}^i) + \frac{1}{2}(b_{12}^i + b_{21}^i)\sin(2\theta) + (b_{11}^i - b_{22}^i)\cos(2\theta).$$

Assuming that σ is of the order ε i.e., $\sigma_i \rightarrow \varepsilon\sigma_i$, one can obtain the asymptotic expansions of the maximal Lyapunov exponent and $g''(0)$ as

$$\lambda_\varepsilon = -\delta + \varepsilon^2 \frac{\sigma^2}{8} \sum_{i=1}^2 [(b_{22}^i - b_{11}^i)^2 + (b_{21}^i - b_{12}^i)^2],$$

$$g''(0) = \varepsilon^2 \frac{\sigma^2}{8} \sum_{i=1}^2 [2(b_{11}^i + b_{22}^i)^2 + (b_{11}^i - b_{22}^i)^2 + (b_{12}^i + b_{21}^i)^2].$$

Thus, the quadratic expansion of $g(p)$ is

$$\begin{aligned} g_\varepsilon(p) = & -p\delta + \varepsilon^2 \frac{\sigma^2}{8} \sum_{i=1}^2 [(b_{22}^i - b_{11}^i)^2 + (b_{21}^i - b_{12}^i)^2]p \\ & + \varepsilon^2 \frac{p^2 \sigma^2}{16} \sum_{i=1}^2 [2(b_{11}^i + b_{22}^i)^2 + (b_{11}^i - b_{22}^i)^2 + (b_{12}^i + b_{21}^i)^2]. \end{aligned}$$

For the real noise case, consider the linear system of equations

$$\dot{x} = Ax + \varepsilon f(\xi(t))Bx, \quad x \in \mathbb{R}^2, \quad (48)$$

$$d\xi = X_0(\xi)dt + \sum_{i=1}^2 X_i(\xi) \circ dW_i, \quad (49)$$

where A and B are as defined for (40). The following procedure for calculating the moment Lyapunov exponent is based heavily on the perturbation method presented in §4.1a. Projecting the equations of motion onto the circle yields

$$\dot{\rho} = q(\theta) = q_0(\theta) + \varepsilon f(\xi)q_1(\theta),$$

$$\dot{\theta} = \omega + \varepsilon f(\xi)h_1(\theta),$$

$$d\xi = X_0(\xi)dt + \sum_{i=1}^2 X_i(\xi) \circ dW_i,$$

and the moment Lyapunov exponent $g(p)$ solves (43) with

$$L(p) = L^\varepsilon + pq(\theta),$$

where L^ε is the generator of the Markov diffusion process involving θ and ξ . We expand this generator as in §4.1a. For the two-dimensional case, this operator becomes $L^\varepsilon = L^0 + \varepsilon L^1$ with

$$L^0 = G(\xi) + \omega \frac{\partial}{\partial \theta}, \quad L^1 = f(\xi)h_1(\theta) \frac{\partial}{\partial \theta}.$$

The associated eigenvalue problem and corresponding solvability conditions are

$$L\psi = \lambda - q(\theta),$$

$$\text{solvability: } \lambda = \langle \mu(\xi), q(\theta) \rangle,$$

$$L\eta = g''(\theta) - 2(q(\theta) - \lambda)\psi,$$

$$\text{solvability: } g''(0) = 2\langle \mu(\xi), (q(\theta) - \lambda)\psi \rangle,$$

where ψ and η are as defined for (47). In the above expressions, $\mu(\xi) = \mu(\xi)_0 + \varepsilon\mu(\xi)_1 + \varepsilon^2\mu(\xi)_2 + \dots = \mu^\varepsilon(\xi)$ is the unique ergodic invariant measure associated with the generator L^ε , i.e. $\mu^\varepsilon(\xi)$ solves the Fokker-Planck equation given by

$$L^{\varepsilon*} \mu^\varepsilon(\xi) = 0,$$

provided L^ε is hypoelliptic. $\lambda = \lambda^\varepsilon$ is the maximal Lyapunov exponent which may be calculated using the method of §4.1a.

Expanding the equations for ψ and η in powers of ε yields the following set of Poisson equations.

$$L_0 \psi_0 = \lambda_0,$$

$$L_0 \psi_1 = \lambda_1 - q_1 f(\xi) - L_1 \psi_0,$$

$$L_0 \psi_2 = \lambda_2 - q_2 - L_1 \psi_1 - L_2 \psi_0,$$

$$L_0 \eta_0 = V_0 - 2(q_0 - \lambda_0) \psi_0,$$

$$L_0 \eta_1 = V_1 - 2[(q_0 - \lambda_0) \psi_1 - (\lambda_1 - q_1 f(\xi)) \psi_0] - L_1 \eta_0,$$

$$L_0 \eta_2 = V_2 - 2[(q_0 - \lambda_0) \psi_2 - (\lambda_1 - q_1 f(\xi)) \psi_1 - (\lambda_2 - q_2) \psi_0] - L_1 \eta_1 - L_2 \eta_0.$$

The quantities V_0 , V_1 and V_2 are the terms in the asymptotic expansion for $g''(0)$, i.e. $g''(0) = V_0 + \varepsilon V_1 + \varepsilon^2 V_2$. The solvability condition for the $O(\varepsilon)$ Poisson equation for η_0 yields $V_0 = 0$. Using the fact that $q_0 = -\delta$, one can easily verify that $\lambda_0 = -\delta$ and $\lambda_1 = 0$. Employing these results and the $O(\varepsilon)$ equations for ψ_0 and η_0 implies

$$\psi_0 = 1 \quad \text{and} \quad \eta_0 = \text{const.}$$

The Poisson equations reduce to

$$L_0 \psi_1 = -q_1 f(\xi),$$

$$L_0 \psi_2 = \lambda_2 - q_2 - L_1 \psi_1,$$

$$L_0 \eta_1 = V_1 - 2q_1 f(\xi),$$

$$L_0 \eta_2 = V_2 - 2[q_1 f(\xi) \psi_1 + (q_2 - \lambda_2)] - L_1 \eta_1.$$

The solvability conditions for the last two equations yield

$$V_1 = 2\langle \mu_0, q_1 f(\xi) \rangle,$$

$$V_2 = 2\langle \mu_0, (\lambda_2 - q_2) + q_1 f(\xi) \psi_1 \rangle + 2\langle \mu_1, q_1 f(\xi) \rangle.$$

Due to the zero mean assumption on $f(\xi)$, $V_1 = 0$. This yields $g''(0) = \varepsilon^2 V_2$.

Define

$$\beta = (b_{12} + b_{21})^2 + (b_{22} - b_{11})^2 \quad \text{and} \quad \kappa = 2(b_{22} + b_{11})^2.$$

Employing these quantities in the expression for V_2 yields

$$g''(0) = \varepsilon^2 \left\{ \frac{\beta}{8} S(2\omega) + \frac{\kappa}{8} S(0) \right\}.$$

Recall the fact that

$$g'(0) = \lambda = \lambda_0 + \varepsilon^2 \lambda_2 = -\delta + \frac{\varepsilon^2}{8} \beta S(2\omega).$$

Solving for the terms in the expression for V_2 then yields the following expression for $g''(0)$

$$g''(0) = \frac{1}{8} \{ \beta S(2\omega) + \kappa S(0) \}.$$

Finally, the moment Lyapunov exponent is given by

$$g(p) = -\delta p + \frac{\varepsilon^2 p}{16} \{ p \kappa S(0) + (p+2) \beta S(2\omega) \}. \quad (50)$$

Detailed calculations of the moment Lyapunov exponents for two-dimensional systems under real noise excitation are given by Doyle *et al* (1995).

4.1c Shallow arch under stochastic excitation: In this section, the results obtained previously are applied to study the dynamics of the shallow arch structure when the time-dependent portion of the lateral loading is white noise, i.e. $f(t) = w(t)$. In this case, the stationary solutions of (3) are given by $Q_1 = \xi(t)$ and $Q_2 = 0$. Perturbing the equations of motion about this solution by substituting

$$Q_1 = \xi(t) + \eta_1(t) \text{ and } Q_2 = 0 + \eta_2(t)$$

yields the following set of linearized perturbation equations:

$$\ddot{\eta}_i + \omega_i^2 \eta_i - \delta_i \dot{\eta}_i + \sum_{j=1}^2 k_{ij} \eta_j f(\xi(t)) = 0, \quad (51)$$

where $k_{11} = 3$, $k_{22} = 4$ and $k_{ij} = 0$, for $i \neq j$, and $f(\xi(t)) = \xi(t)^2$. Since $f(\xi(t))$ results from the nonlinearities in the original equations, it can be assumed to be of $O(\varepsilon)$, i.e. $f(\xi(t)) \rightarrow \varepsilon f(\xi(t))$. Furthermore, the dissipation may be rescaled as $\beta_i \rightarrow \varepsilon^2 \beta_i$. Using this rescaling, (51) can be brought to the form of (33) with

$$A_0 = \begin{bmatrix} 0 & \omega_1 & 0 & 0 \\ -\omega_1 & 0 & 0 & 0 \\ 0 & 0 & 0 & \omega_2 \\ 0 & 0 & -\omega_2 & 0 \end{bmatrix}, \quad A_1 = \begin{bmatrix} 0 & 0 & 0 & 0 \\ 0 & \beta_1 & 0 & 0 \\ 0 & 0 & 0 & 0 \\ 0 & 0 & 0 & \beta_2 \end{bmatrix},$$

and

$$B = \begin{bmatrix} 0 & 0 & 0 & 0 \\ -k_{11}/\omega_1 & 0 & 0 & 0 \\ 0 & 0 & 0 & 0 \\ 0 & 0 & -k_{22}/\omega_2 & 0 \end{bmatrix}.$$

These equations describe a set of uncoupled oscillators, i.e. there is no θ process coupling the modes at the linear level. In this case, as stated in section 4.1a, the Lyapunov exponents are given by

$$\lambda_i = \varepsilon^2 \left\{ -\delta_i + \frac{1}{8} \left(\frac{k_{ii}}{\omega_i} \right)^2 S(\omega_i) \right\}, \quad i = 1, 2.$$

The maximal Lyapunov exponent is then

$$\lambda^* = \max(\lambda_1, \lambda_2).$$

In order to calculate the results pertaining to the original problem of the shallow arch, make use of (51) along with the appropriate parameters. It is obvious that for the arch problem, the linear variational equations about the stationary solutions are decoupled as

shown in (51). For each degree of freedom, the parametric coefficients can be expressed as $b_{21}^i = -k_{ii}/\omega_i$ and the remaining b_{ij} 's are identically zero where the superscript i indicates the first or second mode. The moment Lyapunov exponents of the i th oscillator for the white and real noise cases can be written as

$$g_i(p) = \varepsilon^2 p \left\{ -\delta + (2+p) \frac{\sigma^2}{16} \left(\frac{k_{ii}}{\omega_i} \right)^2 \right\},$$

and

$$g_i(p) = \varepsilon^2 p \left\{ -\delta + (2+p) \frac{S(2\omega_i)}{16} \left(\frac{k_{ii}}{\omega_i} \right)^2 \right\},$$

respectively.

4.2 Nonlinear results based on averaging

The aim of this section is to shed some light on the so called *stochastic bifurcation*. The questions that must be answered are, (i) What are the hypotheses for the occurrence of stochastic bifurcation? and (ii) What does one see as an outcome of the bifurcation phenomena, both mathematically and physically? There has been considerable work in this line from both theoretical and physical points of view. The effects of stochastic perturbations on a dynamical system exhibiting Hopf bifurcation have been studied by Graham (1982), Baris *et al* (1982) and Sri Namachchivaya (1988, 1990) to name a few. The original nonlinear equation cannot be solved explicitly unless there are some assumptions made with respect to the nonlinearities and the noise terms. These assumptions are based on the physics of the problem and the phenomena that one is interested in observing. To this end, this section will focus on the effects of noise on systems that are close to certain bifurcation points.

The method of averaging involves the convergence of a parameterized sequence of processes to a limit process in some weak sense under strong mixing conditions on the noise process. The so called method of averaging, which was obtained on a physical basis by Stratonovich has been widely used to approximate physical processes with certain smoothness, differentiability, and mixing conditions by a diffusive Markov process. A mathematically rigorous proof of the main results was given by Khas'minskii (1968). Since then several authors have developed the averaging theory in various directions using various assumptions. This method has some advantages because the limit process obtained by this procedure is more tractable mathematically due to two main reasons namely (i) it approximates a real noise with strong mixing conditions by a Markov diffusive process, (ii) and due to the averaging procedure the averaged equations have a S^1 symmetry which allows one to examine the amplitudes by themselves and a reduction in the dimension of the system. However, the disadvantage of this procedure is the weak convergence to the limit process. This allows one only to compare the original system with the averaged system from the point of view of the distributions.

4.2a Nonlinear stationary response: In this section, some of the results of Sri Namachchivaya (1990) and Arnold *et al* (1995) that are available based on the method of stochastic averaging are summarized. This will provide some general trend of the actual behaviour. We shall first recast the original equations in the first order form

$$\dot{x} = A_0 x + \sum_{i=1}^2 \sigma_i \xi_i A_i x + F(x), \quad x \in \mathbb{R}^2, \quad (52)$$

where

$$A_0 = \begin{bmatrix} \delta' \eta & \omega \\ -\omega & \delta' \eta \end{bmatrix}, \quad (53)$$

where η is a system parameter, the matrices A_i are assumed symmetric and ξ_1 and ξ_2 are assumed independent stationary noise processes with zero mean. The method of averaging allows more general processes provided the dependence between $\xi(\omega, t)$ and $\xi(\omega, t + \tau)$ becomes weaker in some sense with increasing τ where ξ_i are taken to be real processes. Using an appropriate linear transformation $x \rightarrow Sx$ where

$$S = \begin{bmatrix} \cos(\omega t) & -\sin(\omega t) \\ \sin(\omega t) & \cos(\omega t) \end{bmatrix}, \quad (54)$$

in (52) and making an appropriate scaling for the noise and dissipative terms yields a set of equations in so called standard form

$$\dot{x} = \varepsilon f(x, \xi, t), \quad (55)$$

where explicit form of f is omitted and can be easily calculated using this transformation.

The method of stochastic averaging can be applied to the above equations, provided the noise processes are stationary with zero mean and correlation functions satisfy the strong mixing conditions. Thus by applying the results of Khas'minskii (1968) the solution of this equation can be uniformly approximated in a weak sense on the time interval of $O\left(\frac{1}{\varepsilon^2}\right)$ by a Markov process which is continuous w.p.1 and satisfies the following Stratonovich equations

$$\begin{aligned} dx = & [(\lambda_0 - R \|x\|^2)Ix + (m_\phi^0 - S \|x\|^2)Jx]dt + (\sigma_{aa}^0)^{1/2}Ix \circ dW_1(t) \\ & - (\sigma_{\phi\phi}^0)Jx \circ dW_2(t) \end{aligned} \quad (56)$$

where

$$\lambda_0 := \delta + \frac{1}{8} \sum_i \beta_i S_i(2\omega), \quad m_\phi^0 = \omega' \eta - \frac{1}{8} \sum_i \beta_i \Gamma_i(2\omega),$$

$$\begin{aligned} R = & \frac{1}{16\omega} \{ F_{2,x_1x_2} (F_{2,x_1x_1} + F_{2,x_2x_2}) - F_{1,x_1x_2} (F_{1,x_1x_1} + F_{1,x_2x_2}) \\ & - F_{1,x_2x_2} F_{2,x_2x_2} + F_{1,x_1x_1} F_{2,x_1x_1} \} \\ & + \frac{1}{16} \{ F_{1,x_1x_1x_1} + F_{1,x_1x_2x_2} + F_{2,x_1x_1x_2} + F_{2,x_2x_2x_2} \}, \end{aligned}$$

$$\begin{aligned} S = & \frac{1}{32\omega} \{ (2F_{1,x_1x_2} - F_{2,x_2x_2} - 3F_{2,x_1x_1})(F_{2,x_2x_2} + F_{2,x_1x_1}) \\ & - (3F_{1,x_2x_2} + F_{1,x_1x_1} - 2F_{2,x_1x_2})(F_{1,x_2x_2} + F_{1,x_1x_1}) \\ & + \frac{1}{3} [(2F_{1,x_1x_2} + F_{2,x_1x_1} - F_{2,x_2x_2})(F_{2,x_2x_2} - F_{2,x_1x_1} - F_{2,x_1x_2}) \\ & - (F_{1,x_2x_2} - F_{1,x_1x_1} + 2F_{2,x_1x_2})(F_{1,x_2x_2} - F_{1,x_1x_1} + F_{2,x_1x_2})] \} \\ & + \frac{1}{16} \{ F_{1,x_2x_2x_2} + F_{1,x_1x_1x_2} - F_{2,x_1x_2x_2} - F_{2,x_1x_1x_1} \}, \end{aligned}$$

$$\sigma_{aa}^0 = \frac{1}{8} \sum_i [\kappa_i S_i(0) + \beta_i S_i(2\omega)], \quad \sigma_{\phi\phi}^0 = \frac{1}{8} \sum_i \beta_i S_i(2\omega),$$

$$\kappa_i = 2(A_{i22} + A_{i11})^2, \quad \beta_i = (A_{i12} + A_{i21})^2 + (A_{i22} - A_{i11})^2,$$

and F_{i,x_j,x_k} denotes $(\partial^2 F_i / \partial x_j \partial x_k)(0,0)$. The stationary density function for the nonlinear problem can be written as $p(x_1, x_2) = p(r, \phi) |J|$ where $J = 1/r$. Thus, an explicit expression for the density function in terms of x_1 and x_2 is

$$p(x_1, x_2) = 2 \frac{\Lambda}{\Gamma(v)} (x_1^2 + x_2^2)^{v-1} \exp[-\Lambda(x_1^2 + x_2^2)],$$

provided v is positive. In the above expression,

$$\alpha = g'(0) = \lambda_0, \quad \gamma = g''(0) = \sigma_{aa}^0, \quad \Lambda = \frac{R}{\sigma_{aa}^0}.$$

It is clear from the expression that the change in the shape of the density function depends on v , thus on the quantities $g'(0)$ and $g''(0)$. The above results indicate that for $v < 0$, although the probability density may exist, it is not normalizable. For $0 < v < 1$, a normalizable probability density exists with infinite value at the origin. At $v = 1$, the density exhibits a finite maximum at the origin with value 2Λ . For values of $v > 1$, there is a maximum value of the probability density away from zero. These are similar to the amplitude equations discussed by Stratonovich (1967).

4.2b Stability of stationary solutions: Let us assume that the stationary solution of x is given by $\eta(t)$. Then the linear variational equations about the stationary solution are obtained by putting $x = \eta(t) + u$, as

$$\begin{aligned} du = & [(\lambda_0 - 2R\|\eta\|^2)Iu + (m_\phi^0 - 2S\|\eta\|^2)Ju + (\eta_1^2 - \eta_2^2)Mu - 2\eta_1\eta_2Nu]dt \\ & + (\sigma_{aa}^0)^{1/2}Iu \circ dW_1(t) - (\sigma_{\phi\phi}^0)^{1/2}Ju \circ dW_2(t), \end{aligned} \quad (57)$$

where

$$N = \begin{bmatrix} -R & S \\ S & R \end{bmatrix}, \quad M = \begin{bmatrix} S & R \\ R & -S \end{bmatrix}, \quad J = \begin{bmatrix} 0 & 1 \\ -1 & 0 \end{bmatrix}.$$

In order to determine the almost-sure stability of $\eta(t)$ one can examine the sign of the top Lyapunov exponent of the above equations. To this end projecting the above equations on to a circle, by letting

$$\rho = \ln \|u\| \text{ and } \theta = \tan^{-1}(u_2/u_1)$$

yields

$$d\rho = q_0(\eta, \theta)dt + (\sigma_{aa}^0)^{1/2} \circ dW_1(t),$$

$$d\theta = h_0(\eta, \theta)dt + (\sigma_{\phi\phi}^0)^{1/2} \circ dW_2(t),$$

where

$$q_0(\eta, \theta) = \lambda_0 - 2R\|\eta\|^2$$

$$- (R^2 + S^2)^{1/2} \{(\eta_1^2 - \eta_2^2)\cos(2\theta + 2\chi) + 2\eta_1\eta_2\sin(2\theta + 2\chi)\},$$

$$h_0(\eta, \theta) = -m_\phi^0 - 2S\|\eta\|^2$$

$$- (R^2 + S^2)^{1/2} \{(\eta_1^2 - \eta_2^2)\sin(2\theta + 2\chi) - 2\eta_1\eta_2\cos(2\theta + 2\chi)\},$$

and $2\chi = \tan^{-1}(S/R)$. Since the averaged equations governing the stationary solution $x = \eta(t)$ has an S^1 symmetry, letting $\eta_1 = r \cos \theta$ and $\eta_2 = r \sin \theta$ and $\psi = \theta - \phi + \chi$ yields

$$d\rho = [\lambda_0 - 2Rr^2 - r^2(R^2 + S^2)^{1/2} \cos(2\psi)]dt + (\sigma_{aa}^0)^{1/2} \circ dW_1(t),$$

$$d\psi = [Sr^2 + r^2(R^2 + S^2)^{1/2} \sin(2\psi)]dt,$$

$$dr = [\lambda_0 r - Rr^3]dt + (\sigma_{aa}^0)^{1/2} r \circ dW_1(t),$$

$$d\phi = [-\rho(2\omega) + Sr^2]dt + (\sigma_{\phi\phi}^0)^{1/2} \circ dW_1(t).$$

It is clear that the Lyapunov exponents are given by

$$\lambda = \lambda_0 - 2RE[r^2] - (R^2 + S^2)^{1/2} E[r^2 \cos(2\psi)],$$

and depending on the joint invariant measure $p(r, \phi)$ one can either obtain the maximum or the minimum of the Lyapunov exponent. But due to the S^1 symmetry of the averaged equations the amplitude process by itself is a Markov diffusive process, and the stationary density is given by

$$p(r) = 2(\Lambda/\Gamma(v))r^{2v-1} \exp[-\Lambda r^2], \quad v = \alpha/\gamma,$$

provided v is positive where v and Λ are as defined previously.

However, the stationary states of the fictitious angle ψ for a given value of the amplitude r are given by the angle

$$\bar{\psi} = \sin^{-1}[-S/(R^2 + S^2)^{1/2}] + n\pi, \quad n = 0, 1, 2, \dots,$$

and the stability of the stationary states is given by the sign of $\cos(2\bar{\psi})$. The sign of the constants R and S define the location of the fixed points on the circle. In general, for the deterministic case, it is clear that for a stable periodic orbit it is essential to keep $R > 0$. For convenience, if one assumes $S \geq 0$, then there are four distinct points on the circle, namely:

$$\bar{\psi}_{s,1} = \frac{\pi}{2} + \psi^0, \quad \bar{\psi}_{s,2} = \frac{3\pi}{2} + \psi^0, \quad \bar{\psi}_{u,1} = \pi - \psi^0, \quad \bar{\psi}_{u,2} = 2\pi - \psi^0.$$

It is obvious for all initial values, except for those values of $\psi = \bar{\psi}_{u,1}$, the flow on the circle will reach either one of the two stable fixed point $\bar{\psi}_{s,1}$. It is well known that the stationary measure $p(r, \psi) := p(r)p(\psi|r)$ where $p(r)$ is marginal and $p(\psi/r)$ is the conditional density. Thus one can define

$$p(r, \psi) = \begin{cases} p(r)\{\frac{1}{2}\delta_{\bar{\psi}_{s,1}} + \frac{1}{2}\delta_{\bar{\psi}_{s,2}}\} & \psi \in [0, 2\pi)/\{\bar{\psi}_{u,i}\}, \quad i = 1, 2, \\ p(r)\{\frac{1}{2}\delta_{\bar{\psi}_{u,1}} + \frac{1}{2}\delta_{\bar{\psi}_{u,2}}\} & \psi = \bar{\psi}_{u,i}, \quad i = 1, 2. \end{cases}$$

The Lyapunov exponents are then

$$\lambda_{1,2} = \lambda_0 - 2RE[r^2] - E[r^2](\pm R),$$

where the negative sign corresponds to the maximal exponent since it is calculated from the invariant measure associated with the stable fixed point. By evaluating the expected value of the amplitude process, i.e. $E[r^2] = \lambda_0/R$, it is obvious that the Lyapunov exponents for the trivial and nontrivial solutions respectively, are

$$\lambda_1^0 = \lambda_2^0 = \lambda_0, \quad \lambda_1^1 = 0, \quad \lambda_2^1 = -2\lambda_0,$$

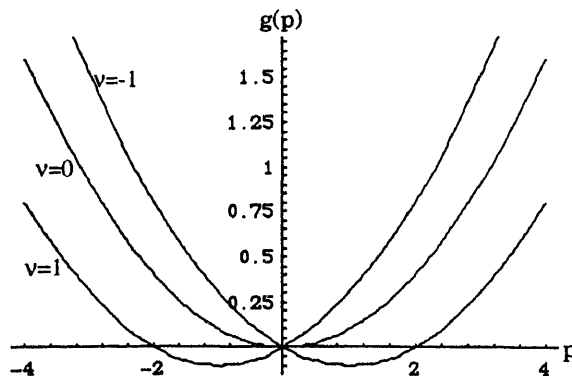


Figure 5. The moment Lyapunov exponent $g(p)$ for $v=1$.

where $\lambda_0 := \beta + \kappa(2\omega)$. The sum of the Lyapunov exponents can be calculated using the trace formula from the Stratonovich equation for the perturbation u

$$\Sigma = \lambda_1 + \lambda_2 = 2(\lambda_0 - 2RE[\|\eta\|^2]) = -2\lambda_0,$$

which matches the sum of the individual exponents obtained from the invariant measures. This implies that the bifurcating solution is asymptotically stable. Such results have been obtained by Sri Namachchivaya (1990) by perturbing the amplitude equation itself.

4.3 Discussion of results

As indicated earlier, the linear problem has been solved using asymptotic and averaging methods while the nonlinear problem has been solved only by method of stochastic averaging. The results presented in the stochastic part of this paper based on these two methods will be discussed and compared in this section only for systems in \mathbb{R}^2 .

The results in \mathbb{R}^2 are shown in figures 5–8. Figures 5 and 6 show the moment Lyapunov and Lyapunov exponents obtained using asymptotic methods while figures 7 and 8 depict the results obtained using averaging. Due to symmetry in x_1 and x_2 , the stationary density is shown only as a function of x_1 . The top Lyapunov exponent for

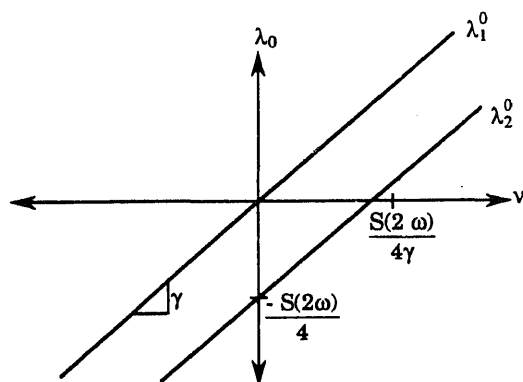


Figure 6. Lyapunov exponents λ_1^0 and λ_2^0 : asymptotic results.

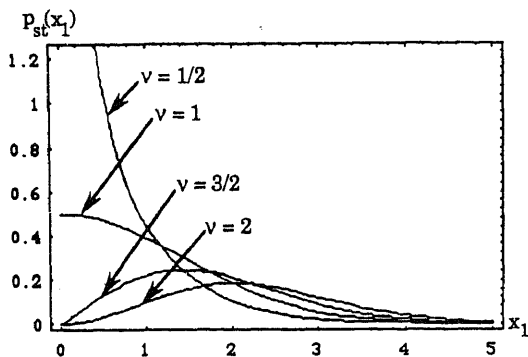


Figure 7. Stationary probability density function $p(x_1, x_2)$.

the trivial solution of the averaged system, λ_1^0 , is identical to that of the original system using the asymptotic analysis. However, the second Lyapunov exponent of the averaged system is the same as the top Lyapunov exponent due to the existence of S^1 symmetry in the averaged equations. This symmetry of the averaged system erroneously predicts that the Lyapunov exponents will cross the imaginary axis simultaneously. However, the asymptotic results, from the trace formula, accurately predict two distinct crossings with $\lambda_1^0 + \lambda_2^0 = -2\delta$. For consistency, λ_1^0 and λ_2^0 obtained from the asymptotic analysis can be expressed in terms of the parameter ν as

$$\lambda_1^0 = \nu g''(0) \quad \text{and} \quad \lambda_2^0 = \nu g''(0) - \beta S(2\omega)/4.$$

The moment Lyapunov exponents are the same for the averaged and original equations. Although the moment Lyapunov exponents are obtained from the linear problem, it has been shown that they play an important role in predicting the parameter value necessary for the existence of a normalizable density function for the nonlinear response. The relationship between the parameter value at which the stationary density attains a finite maximum and the zero of the moment Lyapunov exponent evaluated at $-d$, where d is the dimension of the problem, was first shown by Baxendale (1990) and Arnold (1984). It is interesting to note that the value of $\nu = 1$ at which the density first has a finite maximum corresponds to the value of ν for which $g(-2) = 0$. In addition, a nontrivial normalizable density is shown to exist for positive ν . Since the trivial solution is asymptotically stable for $\nu < 0$, one expects a nontrivial

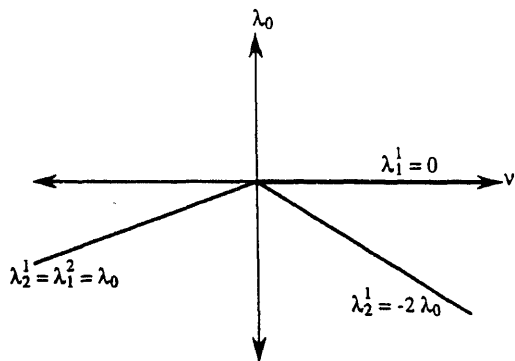


Figure 8. Lyapunov exponents λ_1^0 and λ_2^0 : averaging results.

solution to exist only for $\nu > 0$. This indicates that the densities obtained from averaging preserve these transitions in the system behaviour although some other details may be lost due to averaging (see Arnold *et al* 1995, for details). It is clear from the analysis that, for the deterministic system, a Hopf bifurcation takes place at $\delta = 0$. However, the perturbed system shows a bifurcation of a nontrivial measure from the trivial measure $\mu = \delta_0$ (where δ_0 denotes the Dirac measure at the origin) takes place at $\nu = 0$ ($\delta = \beta S(2\omega)/8$). This new measure displays a peak away from the origin only for $\nu > 1$ ($\delta < -\kappa S(0)/8$). This second transition can be predicted from the moment Lyapunov exponent is evaluated at $-d$ and this corresponds to Baxendale's large deviation phenomenon.

It is obvious from the moment Lyapunov exponent diagram, figure 5, that there are parameter values (for example, $\nu = -1$) at which $\lambda_1^0 < 0$ indicating that the system is sample stable while $g(p) > 0$ for large p (for example, $p > 2$) indicating the p th mean response is unstable. This implies that, although $|x(t; x_0)| \rightarrow 0$ as $t \rightarrow \infty$ with probability one with an exponent rate λ_1^0 , there is a small probability that $|x(t; x_0)|$ is large. This makes the expected value of this rare event large for large value of p and results in the p th mean instability.

5. Conclusions

In the first part of this paper, global bifurcations that are present in the presence of internal and parametric resonances for a shallow arch structure under periodic forcing are examined. It is found that, in the neighbourhood of 1:2 internal resonance in the absence of dissipation, the shallow arch exhibits a typical KAM phase portrait. The analysis of similar structural problems in the presence of 1:1 internal resonance and dissipation indicates Selnikov-type behaviour in the response. These results are presented by Malhotra & Sri Namachchivaya (1995).

The second half of this paper examines the response, stability and bifurcation behaviour of structural systems subjected to white or real noise excitation. The maximal Lyapunov exponent and moment Lyapunov exponent are approximated using a perturbation approach. This approach is described in more detail in Arnold *et al* (1986), Doyle & Sri Namachchivaya (1994) and Doyle *et al* (1995). The behaviour of the bifurcated solution is examined using the method of stochastic averaging.

The practice of examining just the qualitative changes in a family of stationary density functions of the Fokker-Planck equation (for example, the transition from a single peak to double peak or crater type density function) is not enough to understand stochastic bifurcations. This is primarily due to the fact that solutions of the Fokker-Planck equation measure the proportion of time spent in a volume element by the one-point motion. These have little to do with the asymptotic behaviour and its stability which are obtained from two-point motions, hence the Lyapunov exponents. Thus, one needs to establish a procedure for finding nontrivial invariant measures for the original nonlinear problem without averaging and determine their stability properties.

The authors would like to acknowledge the support of the Air Force of Scientific Research through grant 93-0063 monitored by Dr Spencer Wu and the National Science Foundation through grant MSS-PYI-90-57437.

References

- Arnold L 1984 A formula connecting sample and moment stability of linear stochastic systems. *SIAM J. Appl. Math.* 44: 793–802
- Arnold L 1991 Bifurcation in random systems: A survey. In *Nonlinear and random vibrations* (Oberwolfach: Math. Forsch. Inst.)
- Arnold L, Papanicolaou G, Wihstutz V 1986 Asymptotic analysis of Lyapunov exponent and rotation number of the random oscillator and applications. *SIAM J. Appl. Math.* 46: 427–450
- Arnold L, Sri Namachchivaya N, Schenk K L 1995 Towards the understanding of stochastic bifurcations: A case study. *Int. J. Bifurcation Chaos* (to appear)
- Arnold L, Wihstutz V 1986 *Lyapunov exponents: A survey. vol. 1186 Lecture notes in mathematics* (Berlin: Springer-Verlag) pp. 1–26
- Baris F, Mansour M M, Van den Broeck C 1982 Asymptotic properties of coupled nonlinear Langevin equations in the limit of weak noise. Part II: Transition to a limit cycle. *J. Stat. Phys.* 28: 577–587
- Baxendale P H 1990 *Invariant measures for nonlinear stochastic differential equations. vol. 1486 Lecture notes in mathematics* (Berlin: Springer-Verlag) pp. 123–140
- Bogoliubov N, Mitropolsky Y A 1961 *Asymptotical methods in the theory of nonlinear oscillations* (New York: Gordon and Breach)
- Doyle M M, Sri Namachchivaya N 1994 Almost-sure asymptotic stability of a general four dimensional dynamical system driven by real noise *J. Stat. Phys.* (to appear)
- Doyle M M, Sri Namachchivaya N, Arnold L 1995 Moment Lyapunov exponents for general two dimensional systems driven by white and real noise. *Dyn. Stability Syst.* (submitted)
- Graham R 1982 Hopf bifurcations with fluctuating control parameter. *Phys. Rev. A* 25: 3234–3258
- Hsu C S 1969 Stability of shallow arches against snap-through under time-wise step loads. *AIAA J.* 35: 31–39
- Humphrey J S 1966 On dynamic snap bucking of shallow arches. *AIAA J.* 4: 878–886
- Khas'minskii R Z 1968 On the principles of averaging for Itô stochastic differential equations. *Kybernetika* 4: 260–279
- Kozin F, Sugimoto S 1977 Relations between sample and moment stability for linear stochastic differential equations. In *Proceedings of Conference on Stochastic Differential Equations and Applications* (ed.) J D Mason (New York: Academic Press) pp. 145–162
- Lock M H 1965 The snapping of a shallow sinusoidal arch under a step pressure load. Tech. Rep. TRD-469 (5240–10–16), Air Force Systems Command, Los Angeles
- Malhotra N, Sri Namachchivaya N 1995 Global dynamics of shallow arch structures. (In preparation)
- Melnikov M H 1963 On the stability of the center for time periodic perturbations. *Trans. Mosc. Math. Soc.* 12: 1–57
- Mettler E 1962 Dynamic buckling. In *Handbook of engineering mechanics* (New York: McGraw-Hill)
- Oseledec V I 1968 A multiplicative ergodic theorem Lyapunov characteristic numbers for dynamical systems. *Trans. Mosc. Math. Soc.* 19: 197–231
- Pinsky M A, Wihstutz V 1991 Lyapunov exponents for white and real noise driven two-dimensional systems. *Lect. Appl. Math.* 27: 201–213
- Sri Namachchivaya N 1988 Hopf bifurcation in the presence of both parametric and external stochastic excitation. *ASME J. Appl. Mech.* 55: 923–930
- Sri Namachchivaya N 1990 Stochastic bifurcation. *Appl. Math. Comput.* 38: 101–159
- Sri Namachchivaya N, Doyle M M 1988 Chaotic motion of a shallow arch. In *Proceeding of 29th Structures, Structural Dynamics and Materials Conference* (AIAA) pp. 198–209
- Sri Namachchivaya N, Van Roessel H J 1993 Maximal Lyapunov exponent and rotation numbers for two coupled oscillators driven by real noise. *J. Stat. Phys.* 71: 549–567
- Sri Namachchivaya N, Van Roessel H J, Talwar S 1994 Asymptotic analysis of the Lyapunov exponent and rotation number of two degree of freedom stochastic systems. *ASME J. Appl. Mech.* (to appear)
- Stratonovich R L 1967 *Topics in the theory of random noise* (New York: Gordon and Breach) vol. 2

- Tien W M 1992 *Chaotic and stochastic dynamics of structural systems*. Ph D thesis, University of Illinois at Urbana-Champaign
- Tien W M, Sri Namachchivaya N, Bajaj A K 1994a Nonlinear dynamics of a shallow arch under periodic excitation, part I: 1:2 internal resonance. *Int. J. Nonlinear Mech.* (to appear)
- Tien W M, Sri Namachchivaya N, Malhotra N 1994b Nonlinear dynamics of a shallow arch under periodic excitation, part II: 1:1 internal resonance. *Int. J. Nonlinear Mech.* (to appear)
- Wiggins S 1988 *Global bifurcations and chaos* (New York: Springer-Verlag)

Analysis of nonlinear structural dynamics by the concept of stability measure

W SCHIEHLEN and B HU

Institute B of Mechanics, University of Stuttgart, D-70550 Stuttgart, Germany

Abstract. Engineering structures may collapse under dynamic loading, resulting in large displacement motions. The generation of the equations of motion, and an approach for the stability assessment of nonlinear vibrations are presented. The Duffing oscillator is used as an example for the application of the method presented.

Keywords. Multibody systems; stability assessment; Duffing oscillator.

1. Introduction

Mechanical systems like collapsing engineering structures can be modelled properly as multibody systems for dynamical analysis, see Sedlacek & Neuenhaus (1993). The complexity of the dynamical equations called for the development of computer-aided formalisms a quarter of a century ago. The theoretical background is today available from a number of textbooks authored e.g. by Wittenburg (1977), Schiehlen (1986), Roberson & Schwertassek (1988), Nkravesh (1988), Haug (1989) and Shabana (1989).

In addition, a number of commercially distributed computer codes were developed, a summary of which is given in the *Multibody Systems Handbook* edited by Schiehlen (1990). The computer codes available show different capabilities; some of them generate only the equations of motion in numerical or symbolical form, respectively, some of them provide numerical integration and simulation codes, too. Moreover, there are also extensive software systems in the market which offer graphical data input, animation of body motions and automated signal data analysis.

For the analysis of nonlinear systems in recent years new mathematical tools have been developed, see e.g. Holmes & Guckenheimer (1983), Moon (1983), Schiehlen (1993a) and Kreuzer & Schmidt (1993). However, these sophisticated tools are restricted mostly to low dimensional systems hardly found in structural dynamics. Therefore, the concept of stability assessment is introduced, see Schiehlen (1993b). In this paper this concept is applied to the Duffing oscillator representing a wide range of dynamic systems with progressive restoring forces.

2. Modelling of multibody systems

According to the free body diagram of a mechanical system, first, all constraints are omitted and the system of p bodies holds $6p$ degrees of freedom. The position of the system is given relative to the inertial frame by the 3×1 translation vector

$$\mathbf{r}_i = [r_{i1} \ r_{i2} \ r_{i3}]^T, \quad i = 1(1)p, \quad (1)$$

of the centre of mass C_i and the 3×3 rotation tensor

$$\mathbf{S}_i = \mathbf{S}_i(\alpha_i, \beta_i, \gamma_i), \quad (2)$$

written down for each body. The rotation tensor \mathbf{S}_i depends on three angles $\alpha_i, \beta_i, \gamma_i$ and corresponds with the direction cosine matrix relating the inertial frame I and the body-fixed frame i to each other. The $3p$ translational coordinates and the $3p$ rotational coordinates (angles) can be summarized in a $6p \times 1$ position vector

$$\mathbf{x} = [r_{11} \ r_{12} \ r_{13} \ r_{21} \ \cdots \ \alpha_p \ \beta_p \ \gamma_p]^T. \quad (3)$$

Equations (1) and (2) read now

$$\mathbf{r}_i = \mathbf{r}_i(\mathbf{x}), \quad \mathbf{S}_i = \mathbf{S}_i(\mathbf{x}). \quad (4)$$

Secondly, the q holonomic, rheonomic constraints are added to the mechanical system given explicitly by

$$\mathbf{x} = \mathbf{x}(\mathbf{y}, t), \quad (5)$$

where the $f \times 1$ position vector

$$\mathbf{y} = [y_1 \ y_2 \ y_3 \ \cdots \ y_f]^T \quad (6)$$

is used summarizing the f generalized coordinates of the system. The number of generalized coordinates corresponds to the number of degrees of freedom, $f = 6p - q$, with respect to the system's position. Then, translation and rotation of each body follow from (4) and (5) as

$$\mathbf{r}_i = \mathbf{r}_i(\mathbf{y}, t), \quad \mathbf{S}_i = \mathbf{S}_i(\mathbf{y}, t), \quad (7)$$

and the velocities are found by differentiation with respect to the inertial frame:

$$\mathbf{v}_i = \dot{\mathbf{r}}_i = \frac{\partial \mathbf{r}_i}{\partial \mathbf{y}} \dot{\mathbf{y}} + \frac{\partial \mathbf{r}_i}{\partial t} = \mathbf{J}_{Ti}(\mathbf{y}, t) \dot{\mathbf{y}} + \bar{\mathbf{v}}_i(\mathbf{y}, t), \quad (8)$$

$$\boldsymbol{\omega}_i = \dot{\mathbf{s}}_i = \frac{\partial \mathbf{s}_i}{\partial \mathbf{y}} \dot{\mathbf{y}} + \frac{\partial \mathbf{s}_i}{\partial t} = \mathbf{J}_{Ri}(\mathbf{y}, t) \dot{\mathbf{y}} + \bar{\boldsymbol{\omega}}_i(\mathbf{y}, t), \quad (9)$$

The $3 \times f$ Jacobian matrices \mathbf{J}_{Ti} and \mathbf{J}_{Ri} defined by (8) and (9) characterize the virtual translational and rotational displacement of the system, respectively. They are also needed later for the application of d'Alembert's principle. The infinitesimal 3×1 rotation vector \mathbf{s}_i used in (9) follows analytically from the corresponding infinitesimal skew-symmetrical 3×3 rotation tensor. However, the matrix \mathbf{J}_{Ri} can also be found by a geometrical analysis of the angular velocity vector $\boldsymbol{\omega}_i$ with respect to the angles $\alpha_i, \beta_i, \gamma_i$, see e.g. Schiehlen (1986).

The accelerations are obtained by a second differentiation with respect to the inertial frame:

$$\mathbf{a}_i = \mathbf{J}_{Ti}(\mathbf{y}, t) \ddot{\mathbf{y}} + \frac{\partial \mathbf{v}_i}{\partial \mathbf{y}} \dot{\mathbf{y}} + \frac{\partial \mathbf{v}_i}{\partial t}, \quad (10)$$

$$\boldsymbol{\alpha}_i = \mathbf{J}_{Ri}(\mathbf{y}, t) \ddot{\mathbf{y}} + \frac{\partial \boldsymbol{\omega}_i}{\partial \mathbf{y}} \dot{\mathbf{y}} + \frac{\partial \boldsymbol{\omega}_i}{\partial t}. \quad (11)$$

For scleronomic constraints the partial time-derivatives in (8), (9) and (10), (11) vanish.

For the application of Newton's and Euler's equations to multibody systems the free body diagram has to be used again. Now the rigid bearings and supports are replaced by adequate constraint forces and torques as discussed later in this section.

Newton's and Euler's equations read for each body in the inertial frame

$$m_i \dot{\mathbf{v}}_i = \mathbf{f}_i^e + \mathbf{f}_i^r, \quad i = 1(1)p, \quad (12)$$

$$\mathbf{I}_i \dot{\boldsymbol{\omega}}_i + \tilde{\boldsymbol{\omega}}_i \mathbf{I}_i \boldsymbol{\omega}_i = \mathbf{l}_i^e + \mathbf{l}_i^r, \quad i = 1(1)p. \quad (13)$$

The inertia is represented by the mass m_i and the 3×3 inertia tensor \mathbf{I}_i with respect to the center of mass C_i of each body. The external forces and torques in (12) and (13) are composed by the 3×1 applied force vector \mathbf{f}_i^e and torque vector \mathbf{l}_i^e due to springs, dampers, actuators, weight etc. and by the 3×1 constraint force vector \mathbf{f}_i^r and torque vector \mathbf{l}_i^r . All torques are related to the centre of mass C_i . The applied forces and torques, respectively, depend on the motion by different laws and they may be coupled to the constraint forces and torques in the case of friction.

The proportional forces are characterized by the system's position and time functions

$$\mathbf{f}_i^e = \mathbf{f}_i^e(\mathbf{x}, t). \quad (14)$$

For example, conservative spring and weight forces as well as purely time-varying forces are proportional forces.

The proportional differential forces depend on the position and the velocity,

$$\mathbf{f}_i^e = \mathbf{f}_i^e(\mathbf{x}, \dot{\mathbf{x}}, t). \quad (15)$$

A parallel spring-dashpot configuration is a typical example for this kind of forces.

The Newton-Euler equations of the complete system are summarized in matrix notation by the following vectors and matrices. The inertia properties are written in the $6p \times 6p$ diagonal matrix

$$\bar{\mathbf{M}} = \text{diag}\{m_1 \mathbf{E} \ m_2 \mathbf{E} \ \dots \ \mathbf{I}_1 \ \dots \ \mathbf{I}_p\}, \quad (16)$$

where the 3×3 identity matrix \mathbf{E} is used. The $6p \times 1$ force vectors \mathbf{q}^c , \mathbf{q}^e , \mathbf{q}^r representing the Coriolis forces, the ideal applied forces and the constraint forces, respectively, are given by the following scheme,

$$\bar{\mathbf{q}} = [\mathbf{f}_1^T \ \mathbf{f}_2^T \ \dots \ \mathbf{l}_1^T \ \dots \ \mathbf{l}_p^T]^T. \quad (17)$$

Further the $6p \times 6p$ matrix $\bar{\mathbf{J}}$ is introduced as a global matrix;

$$\bar{\mathbf{J}} = [\mathbf{J}_{T1}^T \ \mathbf{J}_{T2}^T \ \dots \ \mathbf{J}_{R1}^T \ \dots \ \mathbf{J}_{Rp}^T]^T. \quad (18)$$

Now, the Newton–Euler equations can be represented as follows for holonomic systems in the inertial frame

$$\bar{\mathbf{M}}\bar{\mathbf{J}}\ddot{\mathbf{y}} + \bar{\mathbf{q}}^c(\mathbf{y}, \dot{\mathbf{y}}, t) = \bar{\mathbf{q}}^e(\mathbf{y}, \dot{\mathbf{y}}, t) + \bar{\mathbf{q}}^r. \quad (19)$$

Holonomic systems with proportional or proportional–differential forces result in *ordinary* multibody systems.

The equations of motion of holonomic systems are found according to d'Alembert's principle by premultiplication of (19) with $\bar{\mathbf{J}}^T$ as

$$\mathbf{M}(\mathbf{y}, t)\ddot{\mathbf{y}} + \mathbf{k}(\mathbf{y}, \dot{\mathbf{y}}, t) = \mathbf{q}(\mathbf{y}, \dot{\mathbf{y}}, t). \quad (20)$$

Here, the number of equations is reduced from $6p$ to f , the $f \times f$ inertia matrix $\mathbf{M}(\mathbf{y}, t)$ is completely symmetrized $\mathbf{M}(\mathbf{y}, t) = \bar{\mathbf{J}}^T \bar{\mathbf{M}} \bar{\mathbf{J}} > 0$, and the constraint forces and torques are eliminated. The remaining $f \times 1$ vector \mathbf{k} describes the generalized Coriolis forces and the $f \times 1$ vector \mathbf{q} includes the generalized applied forces.

In addition to the mechanical representation (20) of a multibody system, there exists also the possibility to use the more general representation of dynamical systems in the state space, i.e.,

$$\dot{\mathbf{x}} = \mathbf{f}(\mathbf{x}, t), \quad (21)$$

where \mathbf{x} means the $n \times 1$ state vector composed of generalized coordinates and velocities, and t the time, respectively.

3. Stability assessment

The dynamical equations of multibody systems describing non autonomous nonlinear oscillations are represented in a canonical form as

$$\dot{\mathbf{x}} = \mathbf{f}(\mathbf{x}, t), \quad \mathbf{x}(t_0) = \mathbf{x}_0 \quad (22)$$

following from (21). Here \mathbf{x} is the $n \times 1$ state vector, \mathbf{f} an $n \times 1$ vector function and t means the time. At initial time t_0 the initial state \mathbf{x}_0 is given. It is assumed that $\mathbf{f}(\mathbf{0}, t) = \mathbf{0}$ represents an equilibrium position $\mathbf{x} = \mathbf{0}$. Due to the nonlinearity of the system, there may exist additional equilibrium $\mathbf{x} = \mathbf{x}^*$.

The stability in the sense of Ljapunov characterizes the qualitative behaviour of the equilibrium position $\mathbf{x} = \mathbf{0}$ of the dynamical system (22). For the stability definition the absolute value norm of a vector is used. The time-variant norm of the $n \times 1$ state vector

$$\mathbf{x}(t) := [x_1(t) \cdots x_n(t)]^T, \quad t \in [t_0, \infty) \quad (23)$$

is defined as

$$\|\mathbf{x}(t)\| := \max_{1 \leq i \leq n} |x_i(t)|. \quad (24)$$

The time-interval norm reads as

$$\|\mathbf{x}(t)\|_T := \max_{t \in [t_0, t_0 + T]} \|\mathbf{x}(t)\| \quad (25)$$

where time T may approach infinity,

$$\|\mathbf{x}(t)\|_{\infty} := \lim_{T \rightarrow \infty} \|\mathbf{x}(t)\|_T. \quad (26)$$

These definitions are also valid for matrices, e.g.,

$$\|\mathbf{A}\| := \max_{1 \leq i \leq n} \sum_{j=1}^n |a_{ij}|. \quad (27)$$

The dynamical system (22) is called stable (in the sense of Ljapunov) if for every positive $\varepsilon > 0$ there exists a positive number $\delta = \delta(\varepsilon) > 0$ such that for all initial conditions bounded by

$$\|\mathbf{x}_0\| < \delta = \delta(\varepsilon) \quad (28)$$

the corresponding trajectories $\mathbf{x}(t)$ remain bounded for all t :

$$\|\mathbf{x}(t)\| < \varepsilon. \quad (29)$$

The dynamical system (22) is asymptotically stable if it is stable and for all bounded initial conditions (28) the corresponding trajectory tends to zero

$$\lim_{t \rightarrow \infty} \|\mathbf{x}(t)\| = 0. \quad (30)$$

If the dynamical system (22) is not stable it will be called unstable.

Based on these definitions, there exists a large literature on stability problems, and quite a number of textbooks, e.g., Hahn (1967) and Müller (1977). However, the stability analysis provides only a qualitative answer. For engineering applications some quantitative global information on the dynamical behaviour is of interest. This can be obtained by a stability assessment.

From the stability definitions in the sense of Ljapunov the following local and global stability measures are defined.

The local stability measure

$$S1(\mathbf{x}_0, t_0) := \frac{\|\mathbf{x}_0\|}{\|\mathbf{x}(t)\|_{\infty}} \quad (31)$$

characterizes the ratio between a given initial state \mathbf{x}_0 and the corresponding maximal displacement of the trajectory. The local stability measure $S1$ depends on \mathbf{x}_0 and t_0 .

The global stability measure

$$S2(r, t_0) := \min_{\mathbf{x}_0 \in \{\mathbf{x} : \|\mathbf{x}\| = r\}} S1(\mathbf{x}_0, t_0) \quad (32)$$

is defined for a subspace of the initial conditions' state space. The global stability measure $S2$ characterizes the maximal displacement of all trajectories starting out of the initial conditions' subspace which is by definition a hyper-cube with respect to the equilibrium point $\mathbf{x} = \mathbf{0}$.

By definition it yields

$$0 \leq S1 \leq 1, \quad 0 \leq S2 \leq 1. \quad (33)$$

In a numerical analysis the integration interval is limited. Then, the local stability measure (31) and the global stability measure (32) have to be replaced by

$$S1_T(\mathbf{x}_0, t_0) := \frac{\|\mathbf{x}_0\|}{\|\mathbf{x}(t)\|_T} \quad (34)$$

$$S2_T(r, t_0) := \min_{\mathbf{x}_0 \in \{\mathbf{x} \mid \|\mathbf{x}\| = r\}} S1_T(\mathbf{x}_0, t_0). \quad (35)$$

For autonomous systems

$$\dot{\mathbf{x}} = \mathbf{f}(\mathbf{x}), \quad \mathbf{x}(t_0) = \mathbf{x}_0 \quad (36)$$

the initial time can be chosen as $t_0 = 0$ without any restriction to the generality.

There is a direct relation between the stability and the above defined stability measures. For an unstable system one may choose a series of initial conditions satisfying $\|\mathbf{x}_{0_1}\| > \|\mathbf{x}_{0_2}\| > \dots > \|\mathbf{x}_{0_n}\|$. Then it yields

$$\lim_{n \rightarrow \infty} \|\mathbf{x}_{0_n}\| = 0 \quad \text{and} \quad \lim_{n \rightarrow \infty} S1(\mathbf{x}_{0_n}, t_0) = 0. \quad (37)$$

On the other hand, if the local stability measure $S1$ has the nonzero minimum s , then

$$\|\mathbf{x}(t)\|_\infty \leq \frac{1}{s} \|\mathbf{x}_0\|. \quad (38)$$

This means $\|\mathbf{x}(t)\|_\infty \rightarrow 0$ for $\|\mathbf{x}_0\| \rightarrow 0$, i.e., the system is stable in the sense of Ljapunov.

Usually the components of the state vector, $x_1(t), \dots, x_n(t)$, have different units. For the applications of the stability measures it is necessary that all components have the same unit. This can be achieved by standardizing operations.

The stability measures defined characterize dynamical systems of arbitrary dimension by a scalar number. Therefore, they are especially well suited for the multibody system analysis. More sophisticated geometric measures of analysis are usually restricted to two or at most three dimensions. The above defined stability measures may be applied to linear systems, too, see Schiehlen & Hu (1995).

4. The Duffing oscillator

The Duffing oscillator represents a wide range of dynamic systems with progressive restoring forces. The equation of motion of the Duffing oscillator with a negative stiffness modelling a vertical Euler beam support column loaded over its buckling point reads as

$$\ddot{x} + d\dot{x} - x + x^3 = a \cos \omega t. \quad (39)$$

This equation describes a damped, periodically forced nonlinear and nonautonomous vibrating buckled beam. It is used here as an example for the application of the method presented. If not mentioned otherwise, the parameter of this Duffing equation are chosen as follows,

$$d = 0.15, \quad a = 0.3, \quad \omega = 1.$$

The Duffing oscillator has a very complex dynamical behaviour. Figure 1 shows a typical steady-state chaotic trajectory in the phase plane. It turns out that there is an attractive chaotic region.

According to the definitions of the stability measure, it is proved that the local stability measure $S1$ and the global stability measure $S2$ are periodic with respect to the initial time t_0 ,

$$S1(x_0, \dot{x}_0, t_0) = S1(x_0, \dot{x}_0, t_0 + 2\pi/\omega), \quad (40)$$

$$S2(r, t_0) = S2(r, t_0 + \pi/\omega). \quad (41)$$

Moreover, the local stability measure has one symmetry, i.e.

$$S1(x_0, \dot{x}_0, t_0) = S1(-x_0, -\dot{x}_0, t_0 + \pi/\omega). \quad (42)$$

An overall view of the stability measures is gained after the calculation of all initial conditions. Using a drawing technique for colour postscript figures developed by Schaub (1990), one can graphically represent the local stability measure $S1$, see figure 2. It shows clearly that the local stability measure $S1$ is more sensitive to initial displacements than to initial velocities. Moreover, figure 3 and figure 4 show the influence of initial time t_0 on the local stability measure $S1$. Then, a more detailed analysis has to be performed in the parameter region found from the stability measures. Using the result on the stability measure $S1$, the global stability measure $S2$ can also be evaluated and the influence of initial time t_0 on the stability measures can be more easily seen (figure 5).

Numerical results indicate that the initial time t_0 does not play an important role in the stability measures of the Duffing oscillator for the small initial conditions and large initial conditions. However, in the middle range of the initial conditions the stability measures are sensitive to the initial time t_0 , see figure 5. Sometimes, the Duffing

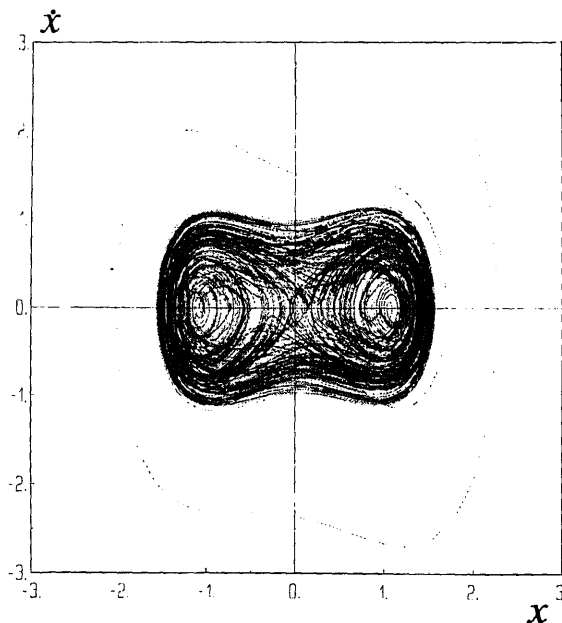


Figure 1. The phase curve of the Duffing oscillator for the initial time $t_0 = 0$ and the initial condition $x_0 = \dot{x}_0 = 2$.

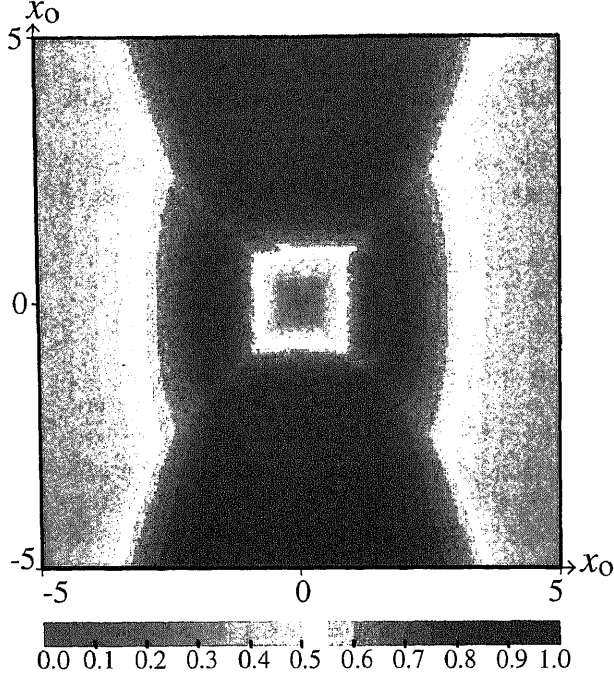


Figure 2. The local stability measure $S1_T$ of the Duffing oscillator at the initial time $t_0 = 0$ for $T = 200$, $-5 \leq x_0 \leq 5$ and $-5 \leq \dot{x}_0 \leq 5$.

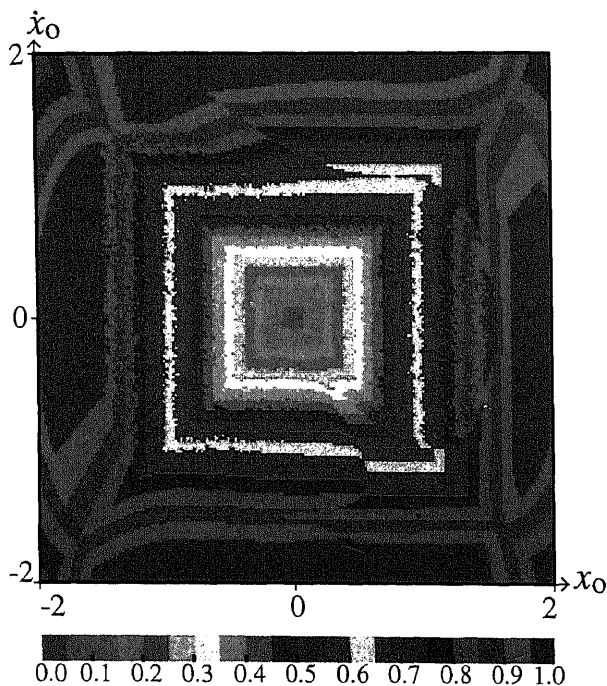


Figure 3. The local stability measure $S1_T$ of the Duffing oscillator at the initial time $t_0 = \pi/4$ for $T = 200$, $-2 \leq x_0 \leq 2$ and $-2 \leq \dot{x}_0 \leq 2$.

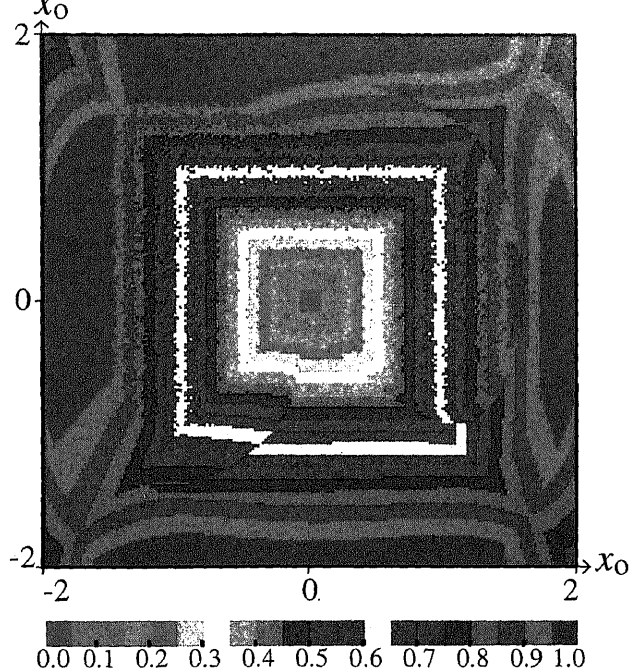


Figure 4. The local stability measure $S1_T$ of the Duffing oscillator at the initial time $t_0 = \pi/2$ for $T = 200$, $-2 \leq x_0 \leq 2$ and $-2 \leq \dot{x}_0 \leq 2$.

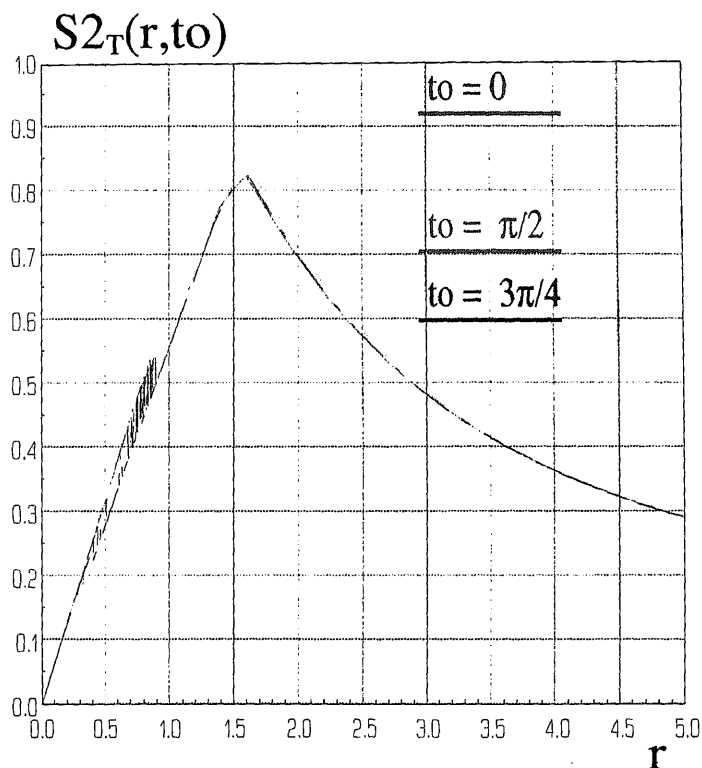


Figure 5. The global stability measure $S2_T$ of the Duffing oscillator at different initial time t_0 for $T = 200$.

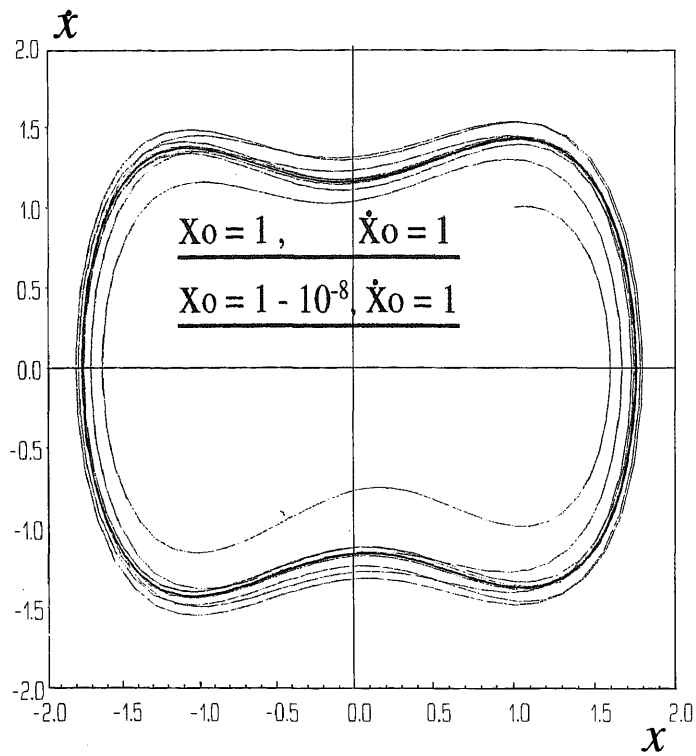


Figure 6. The phase curves of the Duffing oscillator for the initial time $t_0 = 0$ and the initial conditions $x_0 = \dot{x}_0 = 1$ and $x_0 = 1 - 10^{-8}, \dot{x}_0 = 1$.

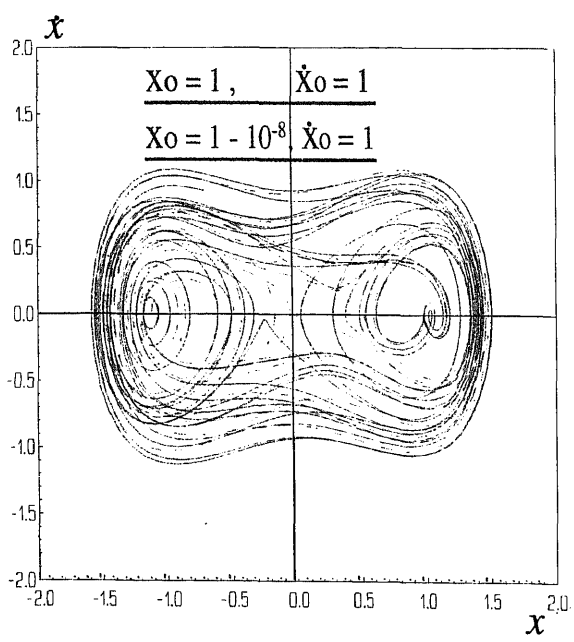


Figure 7. The phase curves of the Duffing oscillator for the initial time $t_0 = \pi/2$ and the initial conditions $x_0 = \dot{x}_0 = 1$ and $x_0 = 1 - 10^{-8}, \dot{x}_0 = 1$.

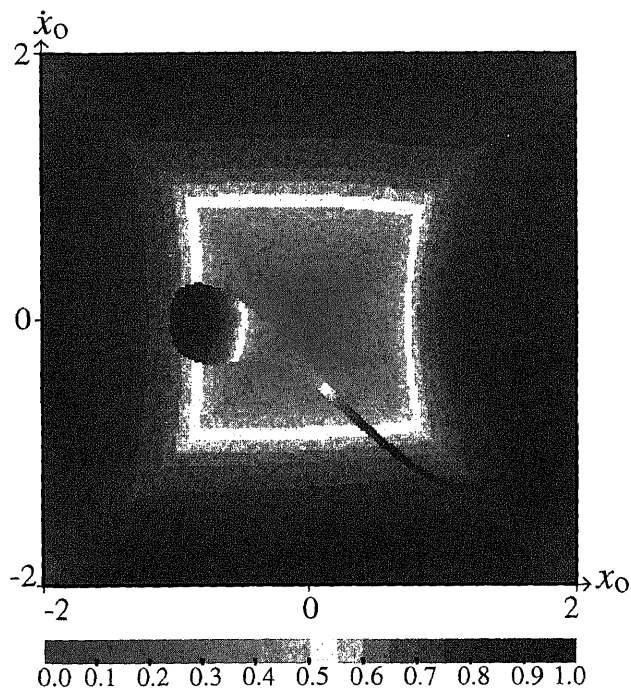


Figure 8. The local stability measure $S1_T$ of the Duffing oscillator at the initial time $t_0 = 0$ for $\omega = 0$, $T = 200$, $-2 \leq x_0 \leq 2$ and $-2 \leq \dot{x}_0 \leq 2$.

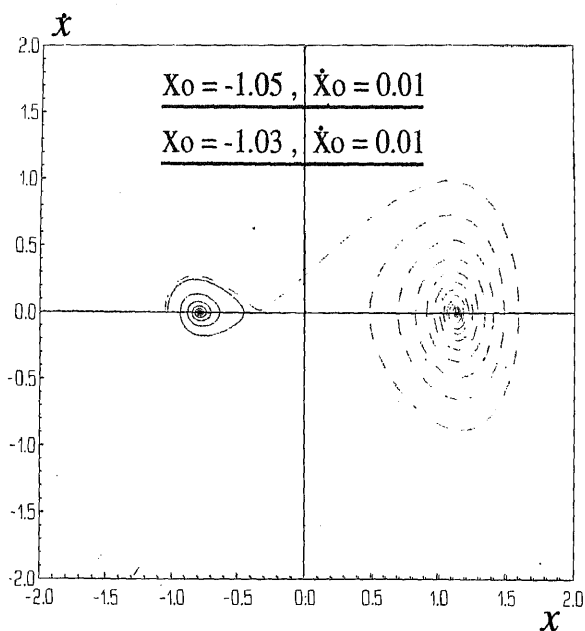


Figure 9. The phase curves of the Duffing oscillator for the initial time $t_0 = 0$ and the initial conditions $x_0 = -1.05$, $\dot{x}_0 = 0.01$ and $x_0 = -1.03$, $\dot{x}_0 = 0.01$.

oscillator even shows highly different dynamical characteristics. For example, the phase curves for two slightly different initial conditions, $(1, 1)$ and $(1 - 10^{-8}, 1)$, with different initial times $t_0 = 0$ and $t_0 = \pi/2$, are incredibly different. For the initial time $t_0 = 0$, the Duffing oscillator shows a periodical limit cycle, figure 6. However, the motion for the initial time $t_0 = \pi/2$ at the same initial condition is chaotic, see figure 7.

In addition, the influence of the frequency of the excitation on the stability measures is shown in figure 8, where the frequency is chosen zero. From the phase curves in figure 9, one can more easily understand the curious green hole in figure 8. Again, the stability measures proved to be valuable in identifying critical parameters.

5. Conclusion

Engineering structures may result in highly nonlinear equations of motion, but in applications only bounded motions are acceptable. The approach of stability measures allows the systematic computation of a basin of bounded motions for systems of arbitrary dimension. Then, the sensitivity of the systems under consideration to initial conditions and parameters can be investigated in more detail. The stability measures are not related to the frequency of the system response, they consider the absolute value of all state variables often important in the engineering design of mechanical systems. Some fundamental phenomena have been analysed for the Duffing oscillator representing structures with progressive stiffness.

References

- Hahn W 1967 *Stability of motion* (Berlin: Springer-Verlag)
- Haug E J 1989 *Computer-aided kinematics and dynamics of mechanical systems* (Boston: Allyn and Bacon)
- Holmes P, Guckenheimer J 1983 *Nonlinear oscillations, dynamical systems and bifurcations of vector fields* (New York: Springer)
- Kreuzer E, Schmidt G (eds) 1993 *1st European Nonlinear Oscillation Conference* (Berlin: Academic-Verlag)
- Moon F C 1983 *Chaotic vibrations: An introduction for applied scientists and engineers* (New York: Wiley)
- Müller P C 1977 *Stabilität und Matrizen* (Berlin: Springer-Verlag)
- Nikravesh P E 1988 *Computer-aided analysis of mechanical systems* (New Jersey: Prentice-Hall)
- Roberson R E, Schwertassek R 1988 *Dynamics of multibody systems* (Berlin: Springer-Verlag)
- Shabana A 1989 *Dynamics of multibody systems* (New York: Wiley)
- Schaub S 1990 *Interpolationsverfahren für Zellabbildungsmethoden*. Diplomarbeit DIPL-30, Stuttgart; Institut B für Mechanik
- Schiehlen W 1986 *Technische Dynamik* (Stuttgart: Teubner)
- Schiehlen W (ed.) 1990 *Multibody systems handbook* (Berlin: Springer-Verlag)
- Schiehlen W (ed.) 1993a *Advanced multibody system dynamics – Simulation and software tools* (Dordrecht: Kluwer)
- Schiehlen W 1993b Nonlinear oscillations in multibody systems – Modeling and stability assessment. In *1st European nonlinear oscillation conference* (eds) E Kreuzer, G Schmidt (Berlin: Academic-Verlag) pp. 85–106
- Schiehlen W, Hu B 1995 Amplitude bounds of linear free vibrations. *J. Appl. Mech.* 62: 231–233
- Sedlacek G, Neuenhaus D 1993 Simulation of failure scenarios for movable steel structures. In *Advanced multibody system dynamics* (ed.) W Schiehlen (Dordrecht: Kluwer) pp. 277–296
- Wittenburg J 1977 *Dynamics of systems of rigid bodies* (Stuttgart: Teubner)

Dynamical behaviour of a friction oscillator with simultaneous self and external excitation

K POPP, N HINRICHS and M OESTREICH

Institute of Mechanics, University of Hannover, Appelstraße 11, D-30167 Hannover, Germany

Abstract. Friction-induced self-sustained oscillations, also known as stick-slip vibrations, occur in mechanical systems as well as in everyday life. In engineering applications these vibrations are undesirable and should be avoided. In the present paper it is shown how the very robust limit cycles of stick-slip vibrations can be broken up by a harmonic disturbance. Based on a simple model of a friction oscillator with simultaneous self and external excitation the resulting bifurcation behaviour and the routes to chaos are investigated for a wide range of system parameters. The influence of different types of friction characteristics is elaborated and the admissibility of smoothing procedures is examined by comparing results gained for non-smooth and smoothed friction characteristics.

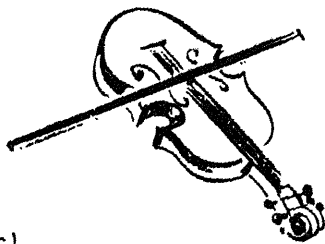
Keywords. Friction oscillator; stick-slip vibrations; self-excitation; bifurcations; chaos; non-smooth systems.

1. Introduction

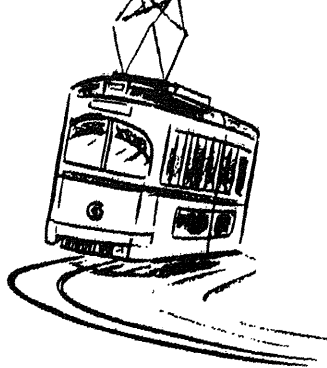
Self-sustained oscillations due to dry friction, also known as stick-slip vibrations, appear in everyday life as well as in engineering systems. Figure 1 shows some examples. The sound of bowed instruments, creaking doors or squeaking chinks and the squealing noise of tramways in narrow curves are caused by stick-slip vibrations. Other engineering examples are rattling joints of a robot, grating brakes or chattering machine tools.

The explanation of the stick-slip phenomenon can be found in textbooks, e.g. Kauderer (1958), Magnus (1961) or Hagedorn (1984). Since we are dealing with self-sustained oscillations, the vibration system encounters an energy source, an oscillator, and a switching mechanism triggered by the oscillator, which controls the energy flow from the source to the vibrating system, cf. figure 2.

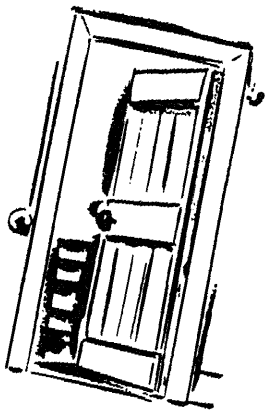
If the energy flow into the vibration system is greater (less) than the dissipation during one period, then the vibration amplitude will increase (decrease). If the energy input and output is balanced during each period, then an isolated periodic motion occurs, which is known to be a limit cycle. Let us take the violin as an example. Obviously, the energy source is represented by the motion of the bow and the oscillator



(c)



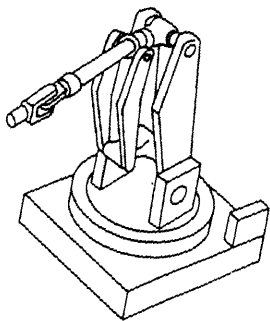
(d)



(e)



(f)



(g)

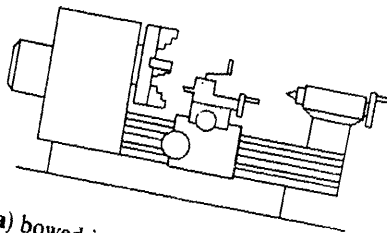
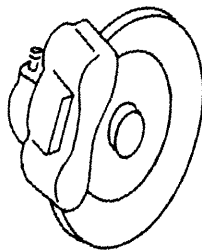


Figure 1. Examples of stick-slip vibrations: (a) bowed instruments, (b) squealing
 railways in narrow curves, (c) squeaking doors, (d) squealing chalks, (e) rattling
 joints of robots, (f) grating brakes, (g) chattering machine tools.

the string. But how is the energy transferred from the bow to the string, or in
 is, what is the switching mechanism for the energy flow? Here, the dry
 bow and strings comes into play (this is why the

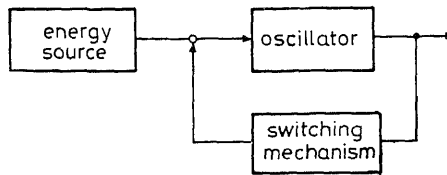


Figure 2. Block diagram of a self-sustained vibration system.

colophony). Essential is a friction force with a decreasing characteristic for increasing relative velocities of the rubbing surfaces. This will be explained by means of the simple friction oscillator shown in figure 3, which has been used as a model for bowed

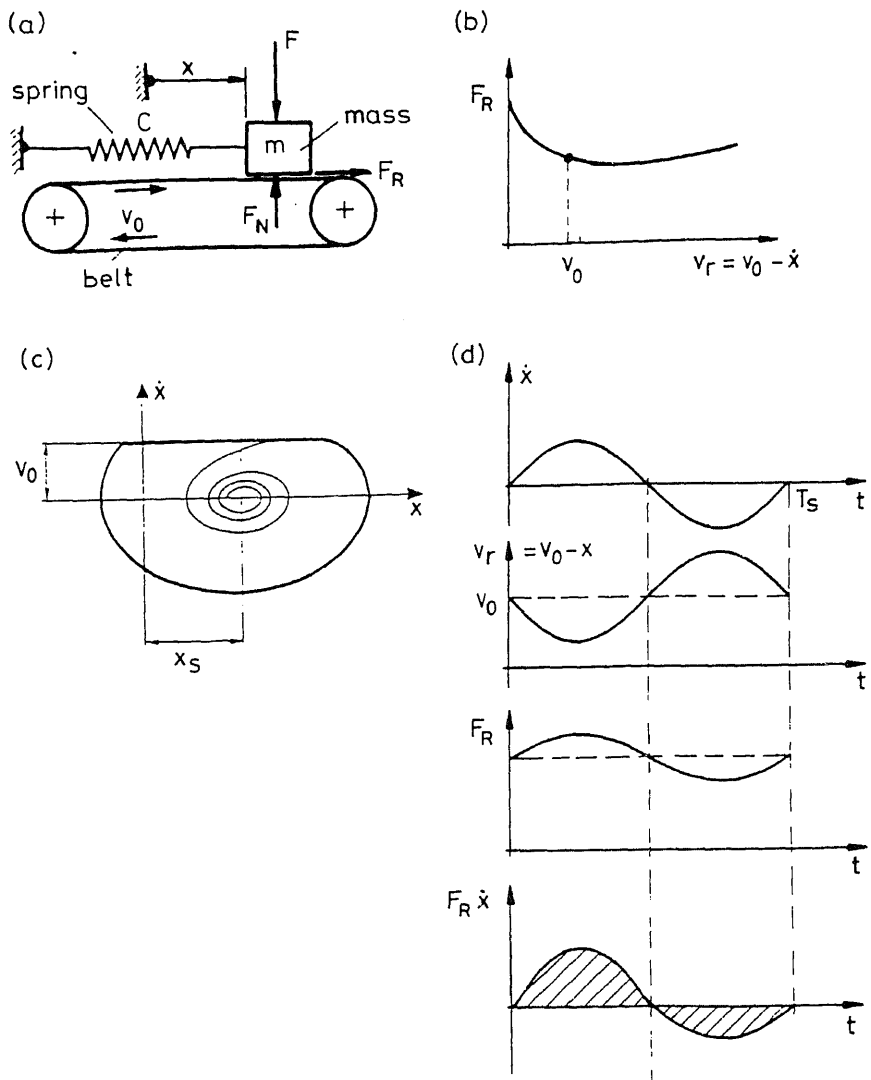


Figure 3. Friction oscillator: (a) mechanical model, (b) friction force characteristic, (c) limit cycle, (d) time histories of motion, friction force and input power.

instruments. The energy source is a moving belt with speed $v_0 = \text{constant}$, driving the mass of the discrete spring-mass oscillator. The friction force F_R depends on the relative velocity $v_r = v_0 - \dot{x}$ between belt and mass. The friction force characteristic $F_R = F_R(v_r)$ is shown in figure 3b. Since the limit value of the static friction force $F_R(v_r \rightarrow 0)$ is greater than the kinetic friction force $F_R(v_r \neq 0)$, the friction force characteristic decreases for small values of v_r . This has been observed e.g. by Conti (1875), Galton (1878), Franke (1882), Bochet (1961) and Kraft (1967). If the belt velocity is adjusted so that the friction force shows a negative slope for the equilibrium state $x = x_s$, $\dot{x} = 0$, then this state becomes unstable. Thus, the amplitude grows and the trajectory in the x, \dot{x} -phase plane fast reaches a limit cycle, cf. figure 3c, where clearly the slip mode $A \rightarrow B$ and the stick mode $B \rightarrow A$ can be distinguished. The physical reason for the instability is an energy transfer from the belt to the mass. This is qualitatively shown in figure 3d by a sequence of time histories of one period duration. Assuming a small mass motion around the equilibrium position with a sinusoidal velocity results in a sinusoidal fluctuation of the relative velocity $v_r = v_0 - \dot{x}$ around the mean value v_0 . Due to the force characteristic the corresponding friction force is larger for smaller values of v_r than for larger values. Thus, the product $F_R \dot{x}$ which denotes the mechanical power input on the mass shows larger positive than negative values. Hence, a positive energy input, $\Delta E_{in} = \int_0^{T_s} F_R \dot{x} dt > 0$, results during each period T_s , which in turn leads to increasing vibration amplitudes until the limit cycle is reached.

Figure 4 shows three different types of friction characteristics, in the following denoted by I, II, III, and the corresponding phase portraits. Here, the friction coefficient $\mu(v_r) = |F_R(v_r)|/F_N$, i.e. the friction force F_R related to the normal force F_N in the contact area, has been plotted. Friction characteristic I is due to Coulomb's friction law and consists of a static friction coefficient $\mu(v_r = 0) = \mu_0$ and a smaller constant kinetic friction coefficient $\mu(v_r \neq 0) = \mu$. So, the transition from stick ($v_r = 0$) to slip ($v_r \neq 0$) is not continuous. Friction characteristic II is similar to that shown in figure 3 and has been explained earlier. Here, the transition from static to kinetic friction is continuous but not differentiable. Friction characteristic III follows from II by a smoothing procedure so that the characteristic is continuous and differentiable, however, there is no pronounced static friction any more and $\mu(v_r = 0) = 0$ holds. The smoothing is done by multiplication of the non-smooth characteristic with a smoothing function $g(v_r)$, where

$$g(v_r) = (2/\pi) \arctan(c_1 v_r) \quad (1)$$

has been chosen. The slope g' of the function g for $v_r = 0$ is given by

$$g' = \left. \frac{dg(v_r)}{dv_r} \right|_{v_r=0} = \frac{2}{\pi} c_1, \quad (2)$$

so that the slope is proportional to c_1 . The angle α between the vertical axis and the tangent to the smoothing function g in the origin is defined by

$$\alpha = \arctan \frac{1}{g'}. \quad (3)$$

The three corresponding phase portraits are qualitatively similar. Since characteristic I has no negative slope for the equilibrium state, this state does not become unstable and in its neighbourhood exist periodic solutions in a pure slip mode in contrast to the solutions for characteristic II and III, where self-excitation takes place. However, for initial conditions far away from the equilibrium state, in any case all trajectories ultimately

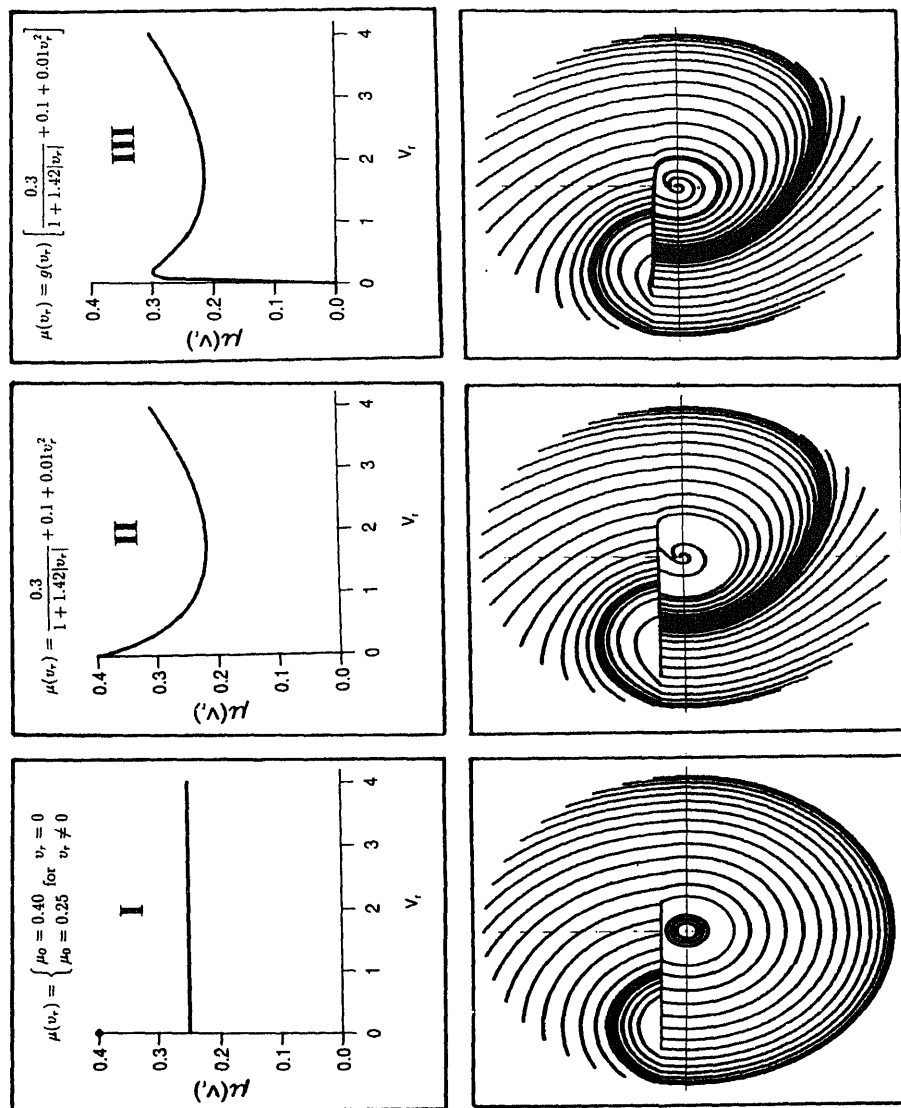


Figure 4. (a) Friction characteristics I, II, III, (b) corresponding phase portraits for pure self excitation.

reach the limit cycle. (In case of characteristic I it is better to say limit curve instead of limit cycle, since other periodic solutions exist, but this distinction shall not be made in the following.) The limit cycle for characteristics I and II consists of a horizontal line due to the stick mode whereas for characteristic III there is no line representing constant velocity since there exists no real stick mode. The differences in the friction characteristics are also reflected in the transition from stick to slip and slip to stick in the corresponding limit cycles. The slope of the limit cycle in the transition points is non-smooth (smooth) for both points for characteristic I (III), whereas for characteristic II the slope is smooth for the transition from stick to slip and non-smooth for the slip to stick transition. Comparing the three phase portraits we find the interesting result that all trajectories starting outside the limit cycle behave in a similar manner independent of the underlying friction characteristic. This robustness is important, since in applications the friction characteristic may vary considerably or is not known at all.

In engineering applications stick-slip vibrations are undesirable and should be avoided since they debase precision of motion and safety of operation or create noise. In the present paper it is investigated how the very robust limit cycle of stick-slip vibrations can be broken up by a harmonic disturbance. Thus, the simple self-sustained friction oscillator of second order shown in figure 3a is extended to a third order system by subjecting the left end of the spring to a harmonic external excitation and the corresponding dynamical behaviour is investigated. It is well known that self-excited one-degree-of-freedom vibration systems with external excitation can exhibit rich bifurcational behaviour and also chaos. There exists a fast growing literature on such systems with smooth nonlinearities, e.g. Guckenheimer & Holmes (1983), Abraham & Shaw (1982), Thompson & Stewart (1986), Kunick & Steeb (1986), Neimark & Landa (1987), Moon (1987, 1992). But also in case of self-excitation due to the *non-smooth* nonlinearity of dry friction chaotic behaviour has been found, cf. Popp *et al* (1985), Grabec (1988), Fingberg (1989, 1990), Popp & Stelter (1990), Stelter & Popp (1989), Stelter (1990), Stelter & Sestro (1991), Popp (1991, 1992). In the following investigation, results will be shown for all three friction characteristics I, II, III. Special attention will be paid to the admissibility of smoothing procedures, which will be examined by comparing bifurcation diagrams gained for non-smooth and smoothed friction characteristics. The benefit of smoothed friction characteristics is the possibility to apply common bifurcation theory and its numerical realization in readily available computer codes, cf. Seydel (1983, 1993). However, there is a growing need for mathematical tools for the analysis of non-smooth nonlinear systems.

2. Model of a friction oscillator with simultaneous self- and external excitation

The mechanical model of the friction oscillator with simultaneous self- and external excitation is shown in figure 5. The following notation is used: mass m , spring constant c , displacement of mass $x(t)$, excitation $u(t) = u_0 \cos \Omega t$, excitation frequency Ω , belt speed v_0 , relative velocity $v_r = v_0 - \dot{x}$. The equation of motion reads

$$m\ddot{x}(t) + cx(t) = F_R(v_r) + cu_0 \cos \Omega t, \quad (4)$$

where the friction force F_R depends on the relative velocity v_r and the normal force F_N ($F_N \geq 0$). During the slip mode ($v_r \neq 0$) holds

$$F_R(v_r) = \mu(v_r) F_N \operatorname{sgn}(v_r), \quad (5)$$

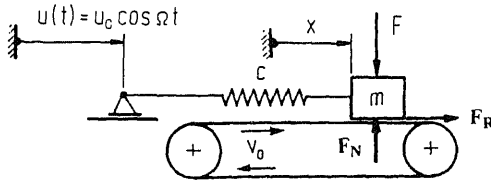


Figure 5. Mechanical model of a friction oscillator with simultaneous self- and external excitation.

whereas for the stick mode ($v_r = 0$) the friction force reads

$$F_R = c(x(t) - u_0 \cos \Omega t), \quad (6)$$

and is bounded by

$$|F_R| \leq \mu_0 F_N. \quad (7)$$

The static and kinetic friction coefficients follow from figure 4. However, for friction characteristic III no distinct stick mode occurs, thus, (5) holds for the complete motion.

For the static equilibrium with $u_0 = 0$ from (4) the static displacement follows

$$x = x_s = \frac{F_R(v_r = v_0)}{c} = \mu(v_r = v_0) \frac{F_N}{c}. \quad (8)$$

The equation of motion can be normalized using

$$\tau = \omega_0 t, \quad \omega_0 = (c/m)^{1/2}, \quad \eta = \Omega/\omega_0, \quad (*)' = [d(*)/d\tau] = [(\dot{(*)})/\omega_0], \quad v_r = v_0 - \omega_0 x'. \quad (9)$$

From (4) and (9) it follows

$$x''(\tau) + x(\tau) = [F_R(v_r)/c] + u_0 \cos \eta \tau. \quad (10)$$

The corresponding system of autonomous differential equations reads

$$\begin{aligned} x'_1 &= x_2, \\ x'_2 &= -x_1 + [F_R(v_r)/c] + u_0 \cos \eta x_3, \\ x'_3 &= \eta, \end{aligned} \quad (11)$$

where $x_1 = x(\tau)$, $x_2 = x'(\tau)$, $x_3 = \eta \tau$.

For friction characteristics II and III, numerical solutions have been performed on the basis of (11) using the Advanced Continuous Simulation Language, ACSL (1991). For friction characteristics I, however, the general solution can be given analytically. For both solution methods special attention has to be paid to the exact determination of the transition states from stick to slip and from slip to stick.

3. Solution methods

3.1 Point-mapping approach

As mentioned before, for friction characteristic I an analytic solution can be formulated for the stick and the slip modes. The exact states of transition from one mode to the other have to be calculated and implemented as initial values for the analytic solution of the corresponding modes.

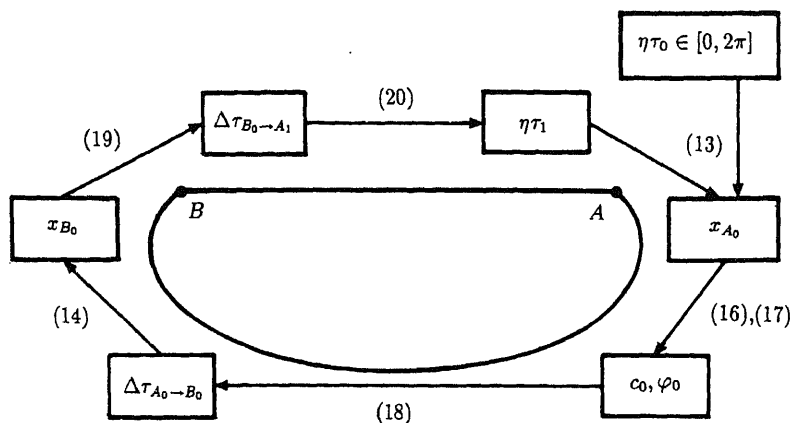


Figure 6. Schematic diagram for the point-mapping approach.

The system behaviour is calculated following the procedure shown in figure 6: Starting with the stick mode ($v_r = 0, \dot{x} = v_0$) from (6) and (7) it follows

$$|x(\tau) - u_0 \cos \eta \tau| \leq x_0, \quad x_0 = \mu_0 (F_N / c). \quad (12)$$

The equality sign in (12) holds if the spring force reaches the maximum friction force for the stick mode which characterizes the transition point A . With the choice of the excitation angle $\eta\tau_0 \in [0, 2\pi]$ from

$$|x_{A_0} - u_0 \cos \eta \tau_0| = x_0 \quad (13)$$

it follows the displacement x_{A_0} where slip initiates. Here, x_{A_i} in each cycle i is bounded by $x_0 - u_0 \leq x_{A_i} \leq x_0 + u_0$.

For the subsequent slip mode $A \rightarrow B$ ($v_r \neq 0, \mu(v_r) = \mu = \text{constant}$) to the next transition point B the corresponding solution reads

$$x(\tau) = c_0 \cos(\tau - \varphi_0) + [u_0 / (1 - \eta^2)] \cos \eta \tau + x_s, \quad x_s = \mu (F_N / c), \quad (14)$$

$$v_r = v_0 - \omega_0 x' \geq 0, \quad (15)$$

where c_0 and φ_0 can be determined from the initial conditions for $\tau_0 = \tau_{A_0}$ ($x(\tau_0) = x_{A_0}, x'(\tau_0) = v_0 / \omega_0$):

$$c_0 = \left[\left(x_{A_0} - x_s - \frac{u_0}{1 - \eta^2} \cos \eta \tau_{A_0} \right)^2 + \left(-\frac{v_0}{\omega_0} - \frac{u_0 \eta}{1 - \eta^2} \sin \eta \tau_{A_0} \right)^2 \right]^{1/2}, \quad (16)$$

$$\varphi_0 = -\arctan \left[\left(\frac{v_0}{\omega_0} + \frac{u_0 \eta}{1 - \eta^2} \sin \eta \tau_{A_0} \right) / \left(x_{A_0} - x_s - \frac{u_0}{1 - \eta^2} \cos \eta \tau_{A_0} \right) \right] + \tau_{A_0} \bmod 2\pi. \quad (17)$$

Now (14) holds till the mass velocity reaches the belt velocity again, so that the equality sign of (15) is valid. Substituting the derivative of (14) into (15) an implicit equation for the normalized time $\Delta\tau_{A_0 \rightarrow B_0}$ of the motion from A to B is given:

$$\begin{aligned} x'(\tau_{B_0}) &= -c_0 \sin(\tau_{A_0} + \Delta\tau_{A_0 \rightarrow B_0} - \varphi_0) \\ &\quad - [u_0 \eta / (1 - \eta^2)] \sin(\eta \tau_{A_0} + \eta \Delta\tau_{A_0 \rightarrow B_0}) = v_0 / \omega_0. \end{aligned} \quad (18)$$

With the solution $\Delta\tau_{A_0 \rightarrow B_0}$ of (18) the displacement x_{B_0} of point B , where the transition from the slip mode to the stick mode takes place, can be calculated from (14).

Now the mass again sticks on the belt and moves with it until the restoring spring force reaches the maximum friction force acting on the mass. From

$$|v_0 \Delta\tau_{B_0 \rightarrow A_1} - u_0 \cos(\eta(\tau_{B_0} + \Delta\tau_{B_0 \rightarrow A_1}))| = x_0 - x_{B_0}, \quad (19)$$

the time $\Delta\tau_{B_0 \rightarrow A_1}$ is given implicitly. The corresponding displacement x_{A_1} of the transition point A at the time

$$\tau_1 = \tau_0 + \Delta\tau_{A_0 \rightarrow B_0} + \Delta\tau_{B_0 \rightarrow A_1}, \quad (20)$$

can be calculated as mentioned above using (13). Hence, the iterative procedure starts again. So, with the help of (13)–(20) a sequence of the states x_{A_i} and x_{B_i} can be calculated.

In contrast to a similar mapping approach used by Guckenheimer & Holmes (1983) for the analysis of a jumping ball on a vertically moving surface, here the point-mapping is given in implicit form. Thus, for solving the implicit equations a suitable Newton method has to be chosen.

3.2 Numerical integration

For friction characteristics II and III, where the kinetic friction coefficient is not constant, other solution methods have to be chosen. The system behaviour for these characteristics has been calculated by numerical integration of (11). For the system with characteristic II also an exact determination of the points of transition from stick to slip A and from slip to stick B is necessary. Passing those points during integration demands starting a special routine that determines the exact states of transition by iteration. For the smoothed friction characteristic III no distinct stick mode occurs. Smoothing the friction characteristic results in stiff system equations for small values of the relative velocity. In this case appropriate integration routines and/or special stepsize control has to be used. In this work the numerical integration has been done using the program package ACSL. With the supplied language element SCHEDULE an easy and sufficient implementation of the iteration to the transition points from one mode to another is possible. With the help of stepsize control algorithms the integration steps are adjusted dynamically in order to keep the error in each state variable below a prescribed value. At this point it should be mentioned that solving the system equations utilizing the point-mapping approach (if possible) leads to an enormous saving of CPU-time in the order of factor 1000.

3.3 Numerical bifurcation analysis

For smooth nonlinear systems like the friction oscillator with friction characteristic III program packages for the bifurcation analysis can be applied. Here, several computer codes are available, for instance BIFPACK (Seydel 1993), AUTO (Doedel 1981) and PATH (Kaas-Petersen 1987). The results of § 4.3 have been obtained with BIFPACK, a program for continuation, bifurcation and stability analysis.

For the task continuation and branch switching the system equation (10) can be reformulated into a boundary-value problem as follows. Periodic oscillations obey the

boundary conditions

$$x(0) = x(T), \quad x'(0) = x'(T), \quad (21)$$

where T denotes the period and satisfies

$$T = n2\pi/\eta, \quad \text{with } n \in \mathbb{N}, \quad (22)$$

so that $u(\tau = 0) = u(\tau = T)$ holds.

As a consequence of (22) the integration of the system equation (10) for one period requires an adapted integration interval $0 \leq \tau \leq T$ whenever η is changed. Shifting the dependence of η to the right-hand side of the differential equation, the integration interval is transformed to unity length (Seydel 1983).

We introduce the normalized time ξ

$$\xi = (1/T)\tau, \quad (23)$$

so that $0 \leq \xi \leq 1$ holds for one period and use the derivative

$$\frac{d(*)}{d\xi} = T \frac{d(*)}{d\tau}. \quad (24)$$

With the notation $y_1(\xi) = x_1(\tau)$, $y_2(\xi) = x_2(\tau)$ and $y_3(\xi) = \eta$, so that y_3 represents the bifurcation parameter, the system of autonomous differential equations reads

$$\begin{aligned} \frac{dy_1}{d\xi} &= n2\pi \frac{y_2}{y_3}, \\ \frac{dy_2}{d\xi} &= n \frac{2\pi}{y_3} \left[-y_1 + u_0 \cos(2\pi n\xi) + g(v_r) \frac{F_R(v_r)}{c} \right], \\ \frac{dy_3}{d\xi} &= 0. \end{aligned} \quad (25)$$

Here, $g(v_r)$ denotes the smoothing function (1) and $v_r = v_0 - \omega_0 y_2$. The boundary conditions now read as follows:

$$\begin{aligned} y_1(0) - y_1(1) &= 0, \\ y_2(0) - y_2(1) &= 0, \\ y_3(0) &= \eta. \end{aligned} \quad (26)$$

The Jacobian matrix can be determined analytically from (25). Now the required input, cf. (25) and (26), for the use of BIFPACK is available.

The following work done by BIFPACK can be summarized as follows (Seydel 1983):

- First the initial (and final) values y_1 and y_2 of the periodic trajectories for a fixed number n have to be calculated, so that the boundary conditions are satisfied. This can be done by using shooting methods:

An initial guess for y_1, y_2 leads after the integration for the interval $0 \leq \xi \leq 1$ to a nonzero residual vector

$$\begin{bmatrix} y_1(0) - y_1(1) \\ y_2(0) - y_2(1) \end{bmatrix} = \mathbf{r}(y_1(0), y_2(0)). \quad (27)$$

- Detecting the initial values y_1, y_2 of a periodic orbit requires a vanishing residual vector $\mathbf{r}(y_1(0), y_2(0))$. So, a combination of an integrator, which determines the initial and final states for a set of guessed initial values, with a Newton method, that approximates the zero crossing of the residual vector calculated from the output of the integrator serves as simplest shooting method. In professional multiple shooting methods the integration interval is subdivided several times, so that better convergence of the Newton method can be obtained.
- For a suitable next step of the bifurcation parameter a predictor-method calculates an initial guess for the corresponding initial state, and the multiple shooting method leads to the determination of the periodic orbit.
- Path tracing repeats the procedure described above again and again. During continuation turning points can be approximated on the basis of a suitable test function. Additional subroutines carry out the stability analysis for calculated periodic orbits.

Thus, efficient methods are placed at the users disposal, that – compared to classical numerical integration – supply additional information like unstable branches and the detection of branch points.

4. System behaviour for different friction characteristics

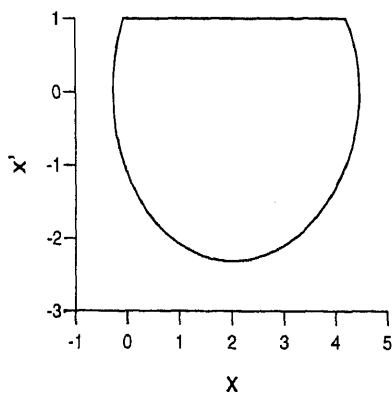
In this chapter the system behaviour of the friction oscillator with simultaneous self- and external excitation for the different friction characteristics I, II and III is elaborated.

4.1 Friction characteristic I

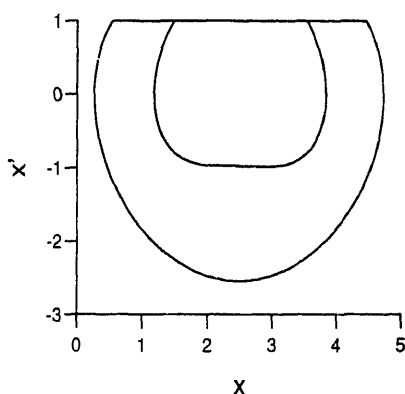
4.1a State space behaviour: The system behaviour for a fixed set of bifurcational parameters $u_0, F_N/c$ and η is represented by the phase trajectories. Figure 7 shows different types of phase trajectories, where the velocity v of the mass is shown as a function of the displacement x . In contrast to the system without external excitation represented by the phase portraits shown in figure 4 the system with external excitation can exhibit one-periodic solutions (figure 7a), two-periodic solutions (figure 7b), higher-periodic solutions and also chaotic system behaviour (figure 7c). As an interesting detail one can see that for large amplitudes u_0 of the excitation short interruptions of the stick mode become possible. Pushed by spring forces the mass overtakes the belt (figure 7d) or slows down reentering the stick mode after a small wiggle (figure 7e). In the following we confine ourselves to small excitation amplitudes u_0 , so that interruptions of the stick mode as mentioned above can be excluded. For this restriction (13) of the point-mapping approach can be simplified by assuming $x_{A_i} > u_0 \cos(\eta\tau)$.

The trajectory of a solution with high periodicity in the three-dimensional state space $M = \mathbb{R}^2 \times S^1$ is presented by a flattened torus (figure 8). One can distinguish the circular ring area on top of the torus characterizing the stick mode with constant velocity of the mass ($v_r = v_0 - \omega_0 x' = 0$) and the remaining surface for the slip mode. The thick line represents the trajectory of the one-periodic motion of figure 7a. After one rotation around the centre axis of the torus, i.e. after one period of the excitation

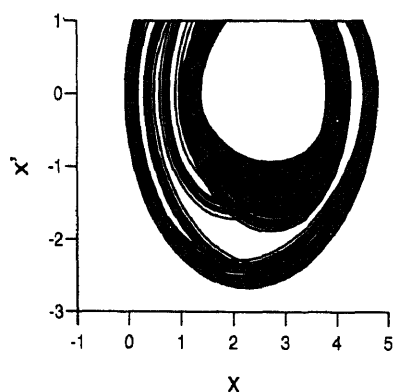
(a)



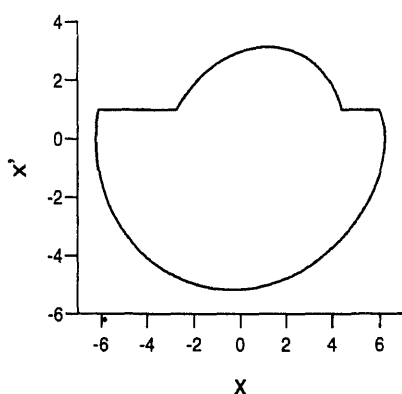
(b)



(c)



(d)



(e)

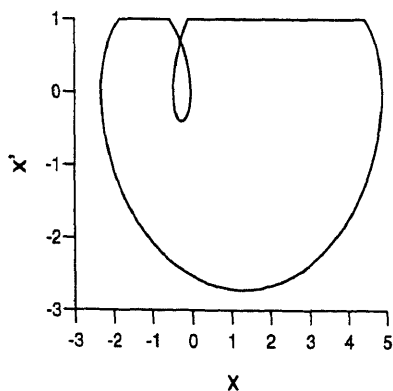


Figure 7. Phase plane plots for
 (a) $\eta = 0.75$, $F_N/c = 10$, $u_0 = 0.5$,
 (b) $\eta = 2.15$, $F_N/c = 10$, $u_0 = 0.5$,
 (c) $\eta = 1.97$, $F_N/c = 10$, $u_0 = 0.5$,
 (d) $\eta = 0.5$, $F_N/c = 10$, $u_0 = 4.0$,
 (e) $\eta = 0.41$, $F_N/c = 5$, $u_0 = 2.6$.

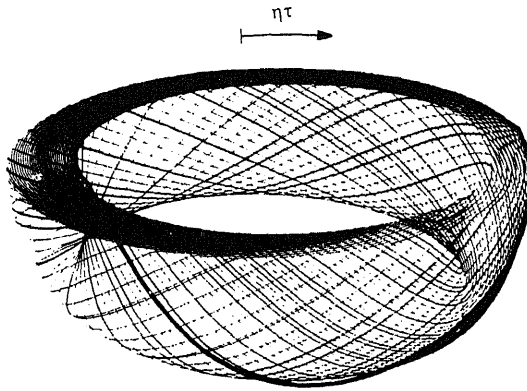


Figure 8. Trajectory in the three-dimensional phase space for $\eta = 0.6$, $F_N/c = 10$, $\mu_0 = 0.5$, and a one-periodic solution for $\eta = 0.75$, $F_N/c = 10$, $u_0 = 0.5$.

($n = 1$), the trajectory has also rotated once ($p = 1$) around the body of the torus and returned to its initial state. The ratio of revolutions along and around the torus is called the winding number W , here it yields $W = n/p = 1/1$.

One way to visualize the geometric structure of the attractor is the Poincaré-map P , where a projection on a hyperspace Σ of the state space M is chosen that fulfills the transversality and recurrence conditions for the trajectories, e.g. Kunick & Steeb (1986). For the friction oscillator the choice of Σ can be done in a simple, illustrative way: The Poincaré-map can be carried out by determining the intersection points of the trajectories on the torus M with a plane Σ transversal to the torus corresponding to $\eta\tau = \text{constant}$. In other words, the trajectory is flashed stroboscopically with the frequency of the excitation. In figure 9a the trajectory of the chaotic solution (figure 7c) in the three-dimensional state space is shown together with the plane Σ . From figure 9b it can be seen, that the attractor of the chaotic motion exhibits a Cantor-set-like structure.

4.1b Bifurcational behaviour: For a more global examination of the bifurcational behaviour of the system, representative points of the trajectory for each set of bifurcation parameters have been extracted. In the bifurcation diagram the displacement x_A (transition from stick to slip) and x_B (transition from slip to stick) is plotted as a function of the bifurcation parameters η (figure 10a) and F_N/c (figure 10b). For clarity, once again the phase plane plot of a one-periodic solution is shown. In this figure one can also distinguish one-periodic, higher-periodic and chaotic solutions. For increasing values of F_N/c (figure 10b) the length of the stick line grows, so the distance between the points x_A and x_B becomes larger. However, the interval where the transition from stick to slip takes place, given by $x_0 - u_0 \leq x_{A_i} \leq x_0 + u_0$, remains constant.

In order to gain further insight it is useful to characterize the phenomena which change the system behaviour.

4.1c Winding number: From figure 8 it seems obvious that the number n of rotations of the trajectory around the centre axis of the torus, i.e. the number of excitation periods, and the number p of revolutions around the body of the torus is different for different system parameters. Evaluating the winding number, e.g. Devaney (1986),

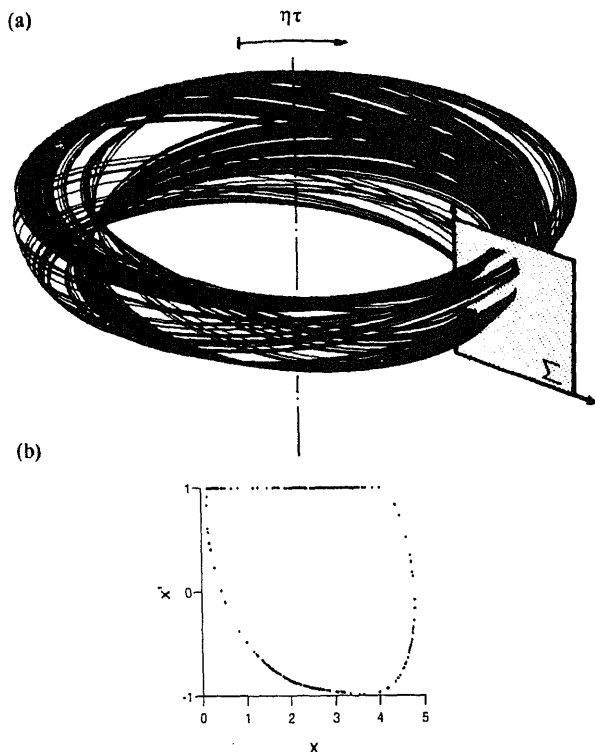


Figure 9. Chaotic trajectory in the three-dimensional phase space for $\eta = 1.97$, $F_N/c = 10$, $u_0 = 0.5$. (b) Corresponding Poincaré-map.

defined by

$$W = \lim_{j \rightarrow \infty} \frac{\eta(\tau_j - \tau_0)}{2\pi j}, \quad (28)$$

leads to the interesting result shown in figure 11. An increase of the bifurcation parameter η changes the bifurcational behaviour and results apparently in a monotonic increase of the winding number. Regions of the same periodicity yield a constant winding number. In the case of a regular system behaviour the winding number is rational and given by the ratio $W = n/p$. Irregular system behaviour leads to an irrational winding number. The behaviour of the winding number for changing system parameters as shown in figure 11b is called a devil's staircase and has also been found in other dynamical systems, e.g. Devaney (1986), Parlitz & Lauterborn (1987). A diagram showing the inverse period $1/p$ versus the frequency ratio η is given in figure 12 and visualizes the self-similarity of the devil's staircase.

The similarity of the results for the winding number to those of the well-known circle map e.g. Devaney (1986), Hale & Kocak (1991), leads to the question whether for the friction oscillator also a one-dimensional map can be given.

4.1d A one-dimensional map: From the point-mapping approach (cf. figure 6) one can define the map H in the following way:

$$H: S^1 = [0, 2\pi] \ni \eta\tau = \eta\tau_0 \mapsto H(\eta\tau) = \eta\tau_1 \in [0, 2\pi] = S^1. \quad (29)$$

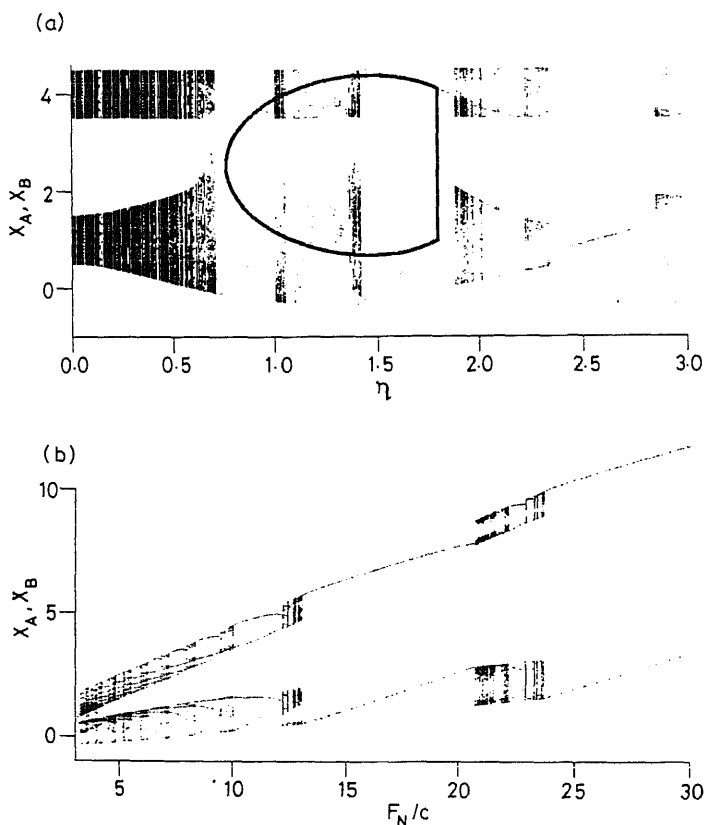


Figure 10. Bifurcation diagram with variation of parameters (a) η for $F_N/c = 10$ and $u_0 = 0.5$, (b) F_N/c for $\eta = 2.1$ and $u_0 = 0.5$.

For this one-dimensional mapping approach also a more illustrative explanation can be given: The limit curve of the flattened top of the torus (figure 13) is given *a priori* by (13) for all values $\eta\tau$. Starting the solution procedure at any limiting point $\eta\tau_0$, after some time $\eta\tau_1$ the trajectory will return to one point of the limiting curve. So, the H -map plots the arrival point $\eta\tau_1$ as a function of the start point $\eta\tau_0$.

Figure 14 shows the graph of $H(\eta\tau)$ for a one-periodic motion. This way of description may be used to gain further insight into the different kinds of changes in the system behaviour by means of a graphical analysis. First, one has to draw the diagonal $D = \{(x, x) \mid x \in \mathbb{R}\}$. A vertical line from the start value of the iteration $(\eta\tau_0, 0)$ to the graph of H crosses the graph at $(\eta\tau_0, H(\eta\tau_0) = \eta\tau_1)$. Then a horizontal line from this point to D meets the diagonal at $(\eta\tau_1, \eta\tau_1)$. So, a vertical line to the graph followed by a horizontal line back to D yields the image of the point $\eta\tau_i$ under H on the diagonal. An orbit is given by drawing line segments repeatedly vertically from D to the graph and then horizontally from the graph to D . For the given set of parameters this procedure yields the following result: The orbit runs into a stable fix point representing the one-periodic motion. The intersection points I_{HD} of the curve $H(\eta\tau)$ with the diagonal D can be used as indicators for one-periodic motions. If $|H'(I_{HD})| < 1$, the fix point is stable, otherwise it is unstable, cf. Leven *et al* (1982). Besides one- and higher-

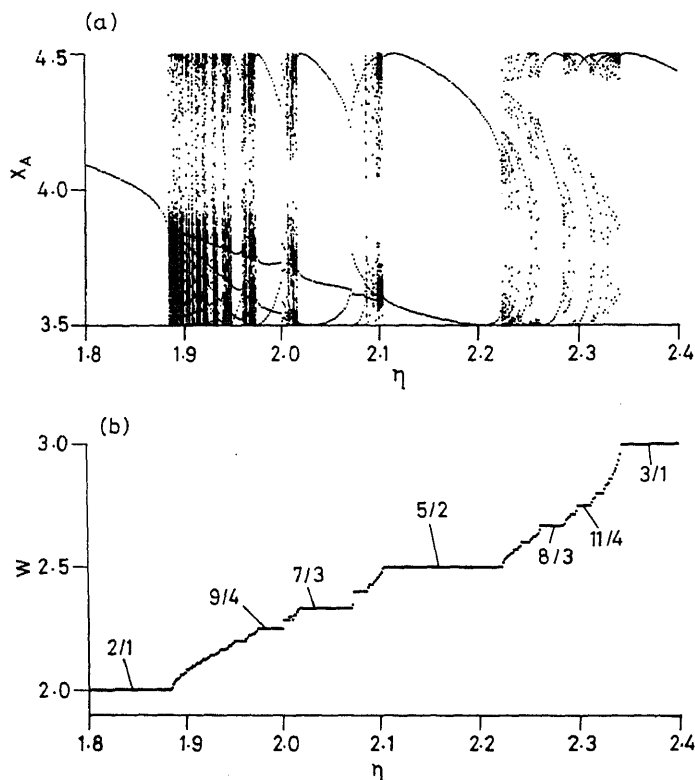


Figure 11. (a) Bifurcation diagram for $F_N/c = 10$ and $u_0 = 0.5$ with variation η , (b) corresponding winding number showing a devil's staircase.

motions chaotic system behaviour also can be analysed utilizing the H -map. In the following it shall be pointed out how the transition from regular motion to chaos takes place. This scenario is called routes to chaos.

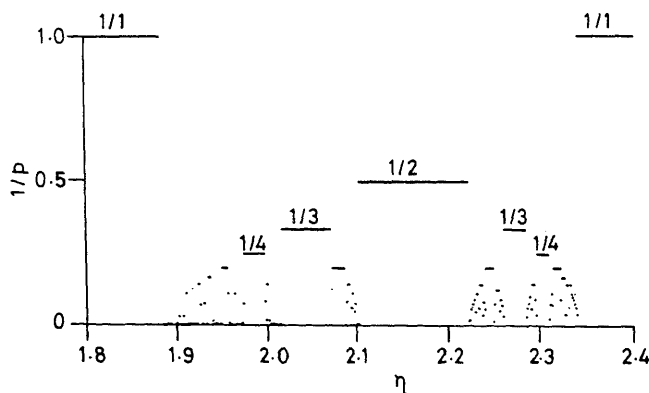


Figure 12. Diagram showing the inverse $1/p$ of the period p of the oscillation versus the frequency ratio η for $F_N/c = 10$ and $u_0 = 0.5$ (compare figure 11).

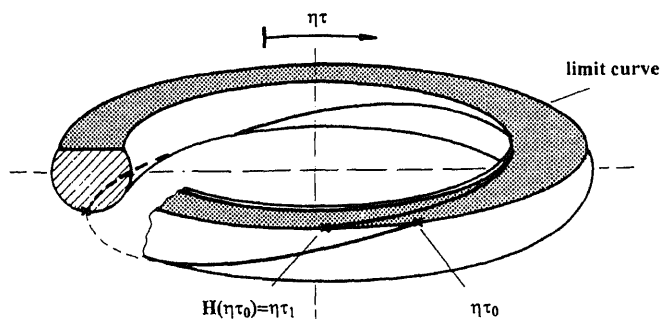


Figure 13. Visualization of the definition of the map $H(\eta\tau)$.

4.1e Intermittency: One route to chaos is intermittency. This phenomenon is characterized by intervals of apparently periodic motion interrupted by aperiodic bursts. This behaviour was first observed by Manneville & Pomeau (1980) for the Lorenz equation, where for a critical bifurcational value η_c the stable periodic motion disappears and chaos initiates. The phenomenon intermittency can be understood intuitively if we look at some suitable parts of the H -map. Figure 15a shows the situation for $\eta < \eta_c$. We can distinguish two fixed points represented by the two intersections of the H -map with the diagonal. One of them is stable, the other is unstable. For $\eta = \eta_c$ the graph of the H -map becomes tangential to the diagonal. In figure 15b, which shows the situation for $\eta > \eta_c$, these two fixed points have disappeared in a saddle-node bifurcation. Following the iteration procedure in figure 15b near the diagonal, each iteration results in a small change of $H(\eta\tau)$. In this region the solution seems to be stable, but after some iterations the seemingly stationary behaviour will be interrupted by sudden bursts. Evaluating the system response in time domain for $\eta < \eta_c$ (figure 15c) and $\eta > \eta_c$ (figure 15d) and the corresponding phase plane plots (figure 15e and figure 15f) the route to chaos via intermittency can be summarized as follows.

With increasing frequency ratio η the curve $H(\eta\tau)$ moves away from the diagonal. After a saddle node bifurcation no further stable fix points exist and a chaotic motion starts, characterized by seemingly periodic motions interrupted by sudden bursts.

4.1f Period doubling: Period doubling in nonlinear system has been observed in all branches of physics, chemistry and biology as well as in many technical problems. Also,

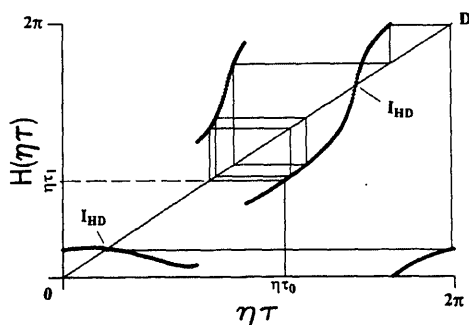


Figure 14. Graphical analysis for the H -map with $\eta = 1.55$, $F_N/c = 10$ and $u_0 = 0.5$.

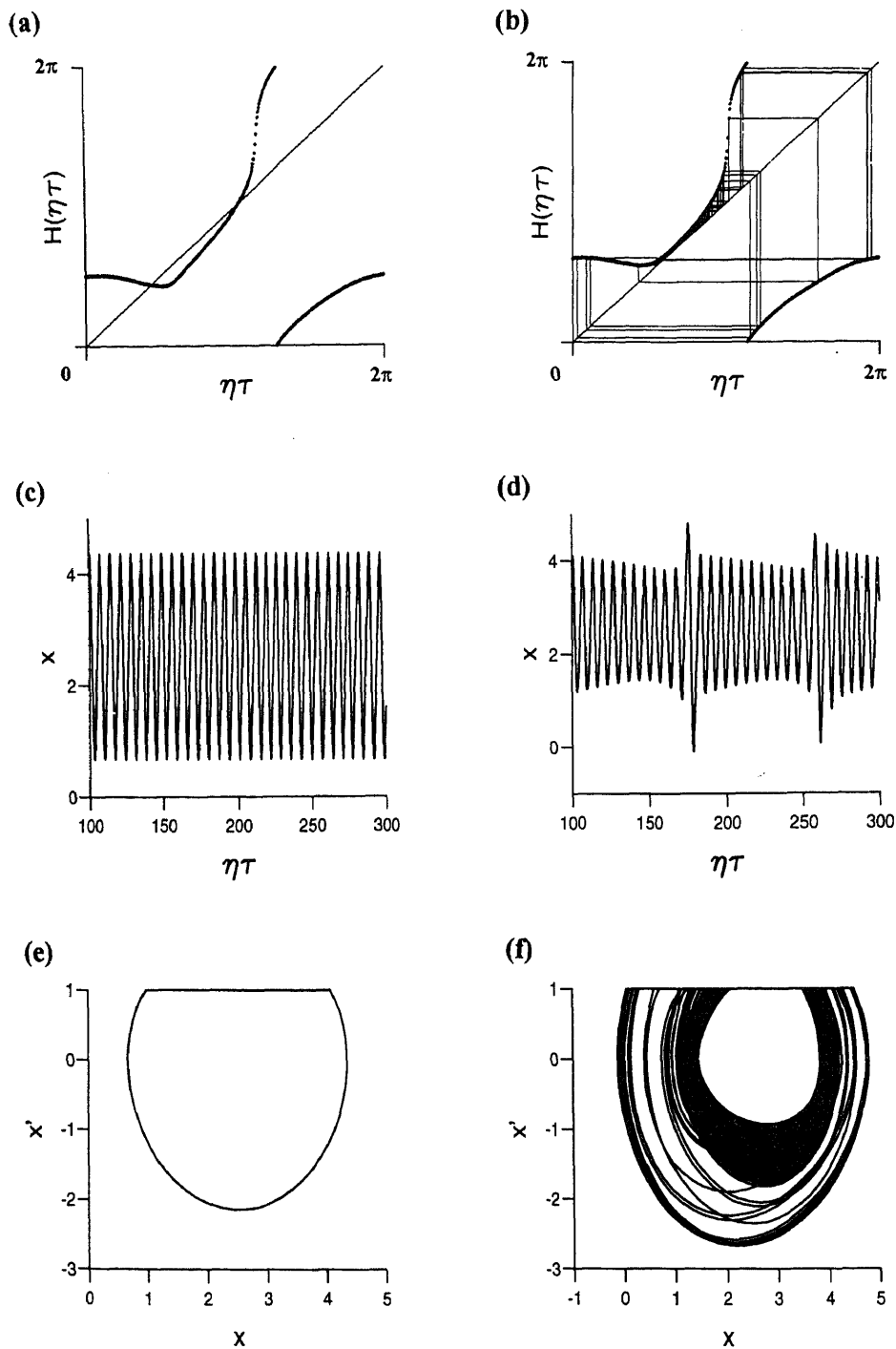


Figure 15. Visualization of intermittency for $F_N/c = 10$, $u_0 = 0.5$ and $\eta = 1.8$ (left), $\eta = 1.9$ (right): (a), (b) H -map, (c), (d) time history of displacement x , (e), (f) phase plane plot.

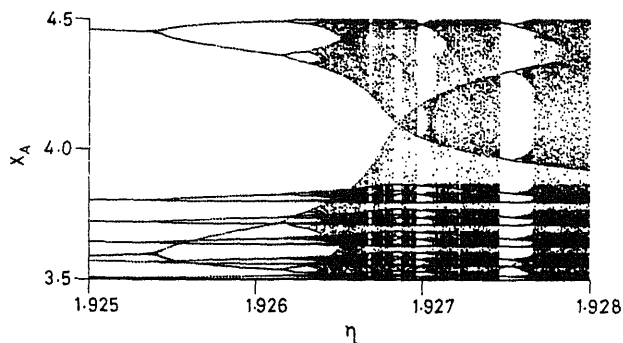


Figure 16. Bifurcation diagram with variation of the frequency ratio η showing period doubling for $F_N/c = 10$ and $u_0 = 0.5$.

for the friction oscillator period doubling cascades can be found (figure 16). For $\eta = 1.925$ the system exhibits a seven-periodic motion. For increasing η the system undergoes a bifurcation with a change to a periodic motion with twice the period of the original oscillation. The seven-periodic orbit becomes unstable and a stable 14-periodic orbit appears. Thereafter, a period doubling sequence occurs leading finally to chaos. One can also distinguish periodic windows. Those periodic windows undergo period doubling bifurcations, again leading to chaotic motion.

4.2 Friction characteristic II

For friction characteristic II also the system exhibits one-periodic (figure 17a), two-periodic (figure 17b) or higher-periodic solutions (figure 17c). Because of the smooth transition of the friction characteristic from stick to slip the phase trajectory is smooth at the transition point *A*. The different types of motion can also be distinguished by the power spectrum of the time series. For the periodic motions the fundamental frequency Ω and the corresponding higher harmonics are visible as sharp peaks (figure 18a, b). For the chaotic time series, the energy of the oscillator splits up to a broad band of frequencies. Thus, the onset of broad-band spectra can serve as an indicator of chaotic motion.

The investigation of the bifurcational behaviour for friction characteristic II leads to similar results to those presented for friction characteristic I, e.g. figure 19 shows two bifurcation diagrams where the parameters η (figure 19a) and (F_N/c) (figure 19b) have

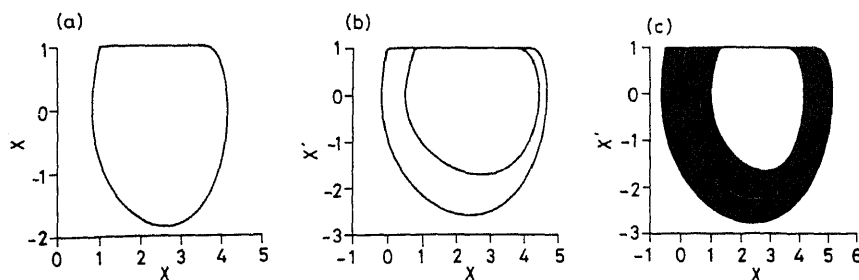


Figure 17. Phase plane plots ($F_N/c = 10$, $u_0 = 0.5$) for (a) $\eta = 0.94$, (b) $\eta = 1.15$, (c) $\eta = 1.05$.

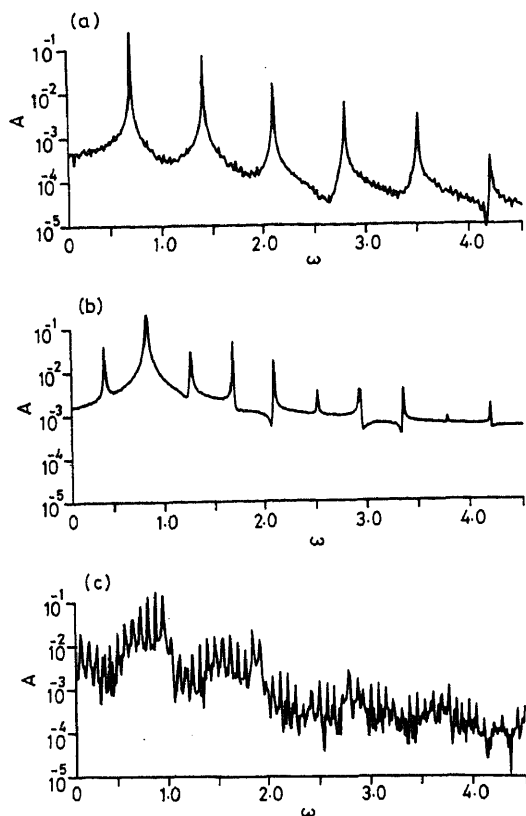


Figure 18. Frequency spectra ($F_N/c = 10$, $u_0 = 0.5$) for (a) $\eta = 0.94$, (b) $\eta = 1.15$, (c) $\eta = 1.05$.

been varied. The results can be compared to those shown in figure 10. Here, a self-similarity appears as follows: At each side of the one-periodic solution in figure 19b, periodic orbits with period two can be found. Each of these periodic motions again is surrounded by two periodic orbits of period three, and so on. As can be seen, the intervals of periodic system behaviour in the bifurcation diagram are interrupted by chaotic parameter regions.

4.3 Comparison of the results for friction characteristics I and II

Comparing the results gained for the different friction characteristics shows that the global bifurcational behaviour is independent of the kind of investigated friction characteristic. The bifurcational behaviour given by bifurcation diagrams with variation of η and F_N/c is qualitatively similar (cf. figures 10 and 19). The described phenomena seem to be robust with respect to the kind of friction characteristic used. It should also be mentioned that the more local phenomena like period doubling and intermittency described in § 4.1 can be found for both types of friction characteristics. In order to give an overview of the solution depending on the bifurcational parameters η and F_N/c , corresponding parameter maps have been calculated, cf. figures 20a and b. Here, the periodicity of the solution is visualized by a colour code. Regions of one-periodic orbits are marked in blue, regions of five- or higher-periodic orbits

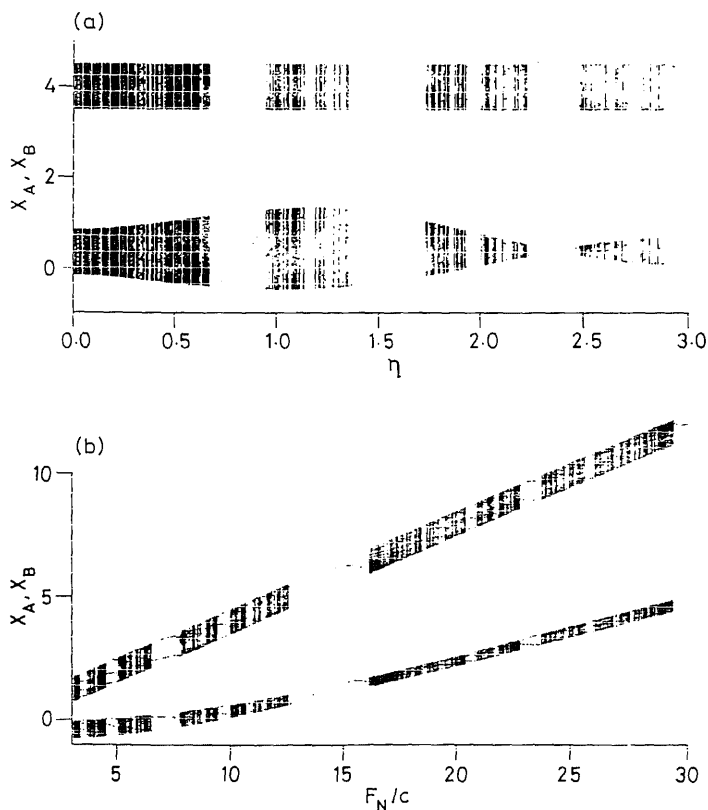


Figure 19. Bifurcation diagram with variation of (a) η for $F_N/c = 10$ and $u_0 = 0.5$, (b) F_N/c for $\eta = 2.1$ and $u_0 = 0.5$.

including chaos are represented in red. In this diagram the results shown in figures 10 and 19 are marked by solid lines. For each value η (F_N/c) on the horizontal (vertical) line the periodicity can be read with the help of the given colour code. Thus, by means of these parameter maps the system behaviour can be found for any set of parameters with a fixed excitation amplitude $u_0 = 0.5$ within the plotted range.

Comparing the two parameter maps obviously the general structure of the tongues for one-periodic motions is similar. For small values of η the limit curves of the lowest two blue regions are nearly identical. For high values of η and F_N/c the tongues of high periodic motions disappear for friction characteristic I. However, within the investigated parameter range the blue regions of one-periodic orbits for friction characteristic I are larger than those for characteristic II, whereas the red intervals of high periodic orbits are larger for characteristic II than that for I. The number of tongues characterizing orbits of equal periodicity is smaller for characteristic I than that for II. Another interesting difference between the results for the two friction characteristics can be observed e.g. for a constant value $F_N/c = 10$ and $\eta > 3$. Between the regions of one-periodic and high-periodic orbits for friction characteristic I there are two-, three-, and then four-periodic solutions without higher-periodic solutions in between, in contrast to the results for friction characteristic II.

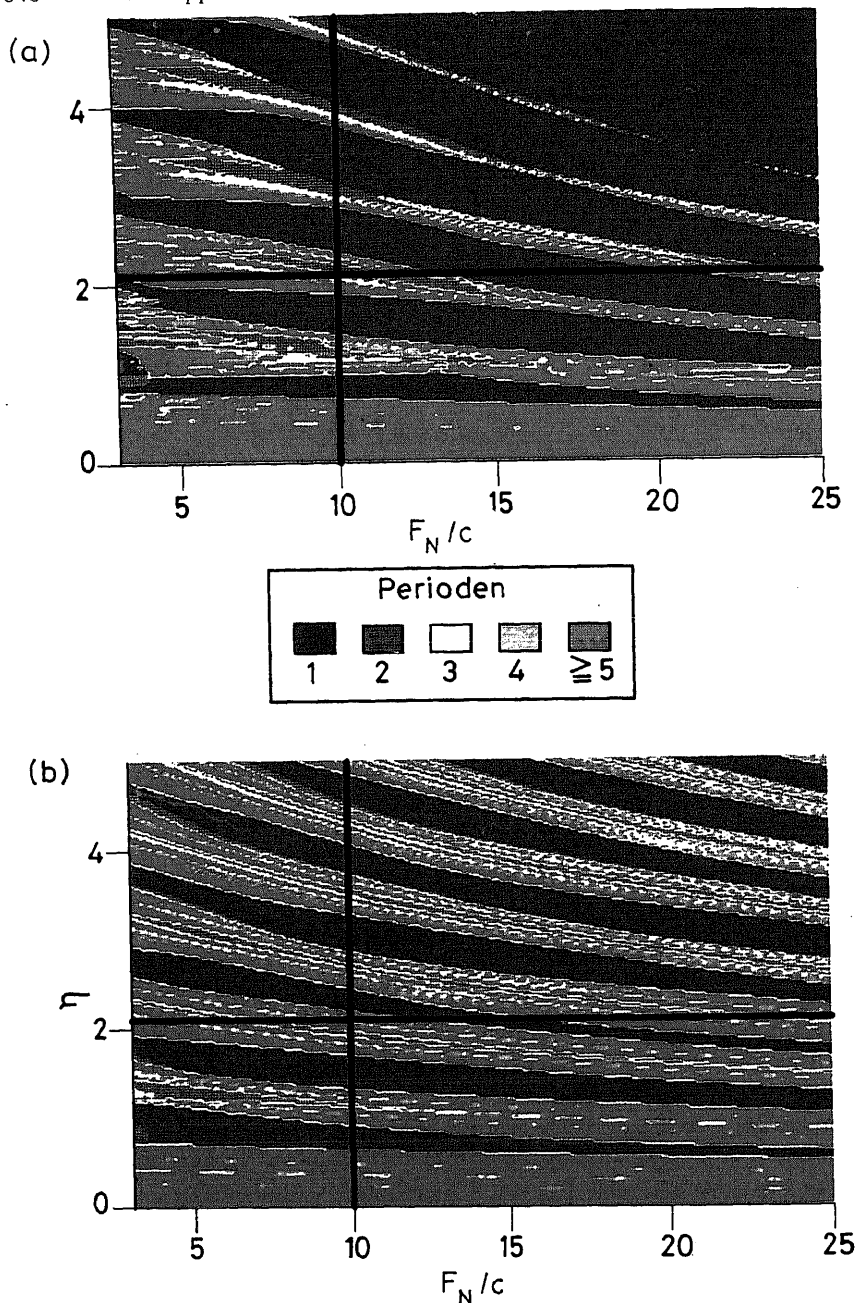


Figure 20. Parameter maps depending on η and F_N/c for $u_0 = 0.5$ for (a) friction characteristic I, (b) friction characteristic II.

4.4 Friction characteristic III

As shown before, the smoothing procedure gives a significant change of the friction characteristic. For increasing values of the argument c_1 of the smoothing function (cf. (1)), i.e. decreasing slope angle α of the smoothed characteristic, it becomes obvious

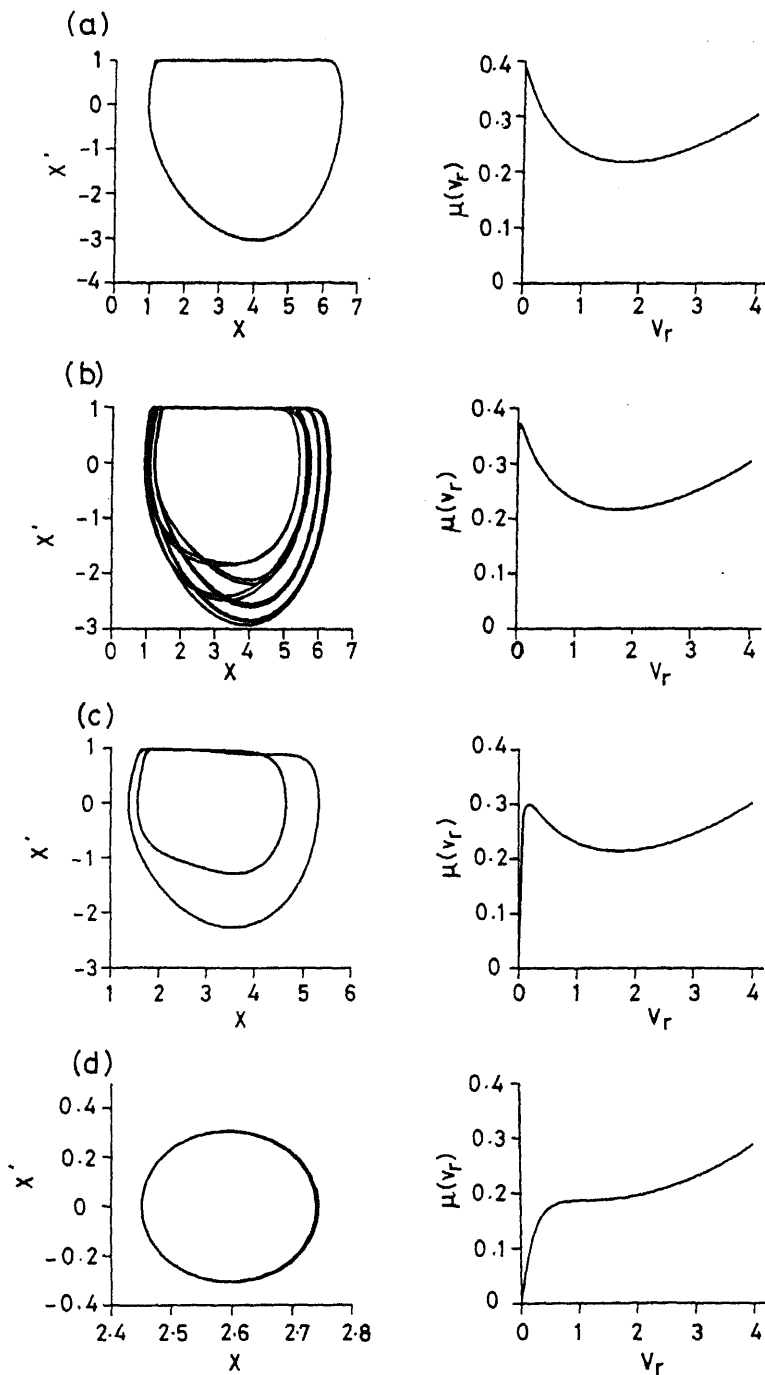


Figure 21. Phase plane plots with $\eta = 2.1$, $F_N/c = 15$ and $u_0 = 0.5$ for different smoothed friction characteristics: $\alpha = 0.03^\circ$ (a), 0.4° (b), 7.0° (c), 50.0° (d).

that the stick mode does not exist any more (figure 21), and the transition from stick to slip and vice versa becomes smooth. Now, for a fixed set of parameters but varying slope angle α , one-periodic and higher-periodic orbits can be found. Increasing α reduces the diameter of the closed curve representing the trajectory in the phase plane. Also the maximal velocity of the mass reduces. For high values of α the smoothed friction characteristic behaves monotonously and only periodic motions can be observed.

In the following it will be investigated whether the smoothed characteristic III is a good approximation of the original characteristic II. If the smoothing procedure is valid then the question arises, which argument c_1 or which angle α should be chosen? For a small angle α the bifurcation diagram (figure 22a) gives a good approximation of the original non-smooth friction characteristic (figure 19b). As mentioned before the transition point x_A from stick to slip for friction characteristic III does not exist any more. Thus, in the bifurcation diagrams the points $x(v=0)$ are shown, where the transition from positive to negative mass velocity takes place. Increasing the angle α results in a shift of the periodic solutions to higher values of F_N/c (figure 22b and c). The bifurcational behaviour depending on F_N/c and the slope angle α is shown in the parameter map (figure 23). This plot can be interpreted in the following way: For very small values of the angle α the solution approximates very well the bifurcational behaviour of friction characteristic II shown in figure 19 (compare the parameter regions of the one-, two-, and

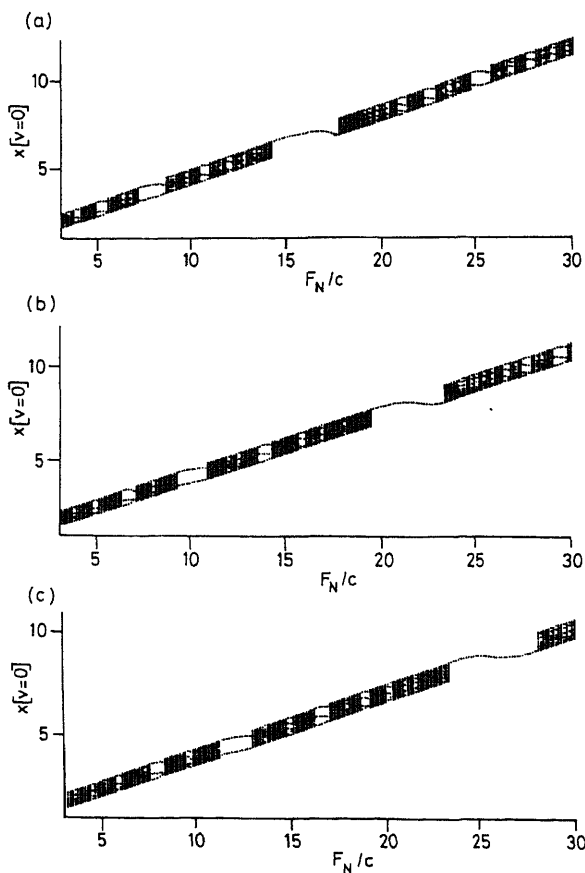


Figure 22. Bifurcation diagram with variation of F_N/c for $\eta = 2.1$, $u_0 = 0.5$ (a) $c_1 = 1000$, $\alpha = 0.1^\circ$, (b) $c_1 = 45$, $\alpha = 2.0^\circ$, (c) $c_1 = 20$, $\alpha = 4.5^\circ$.

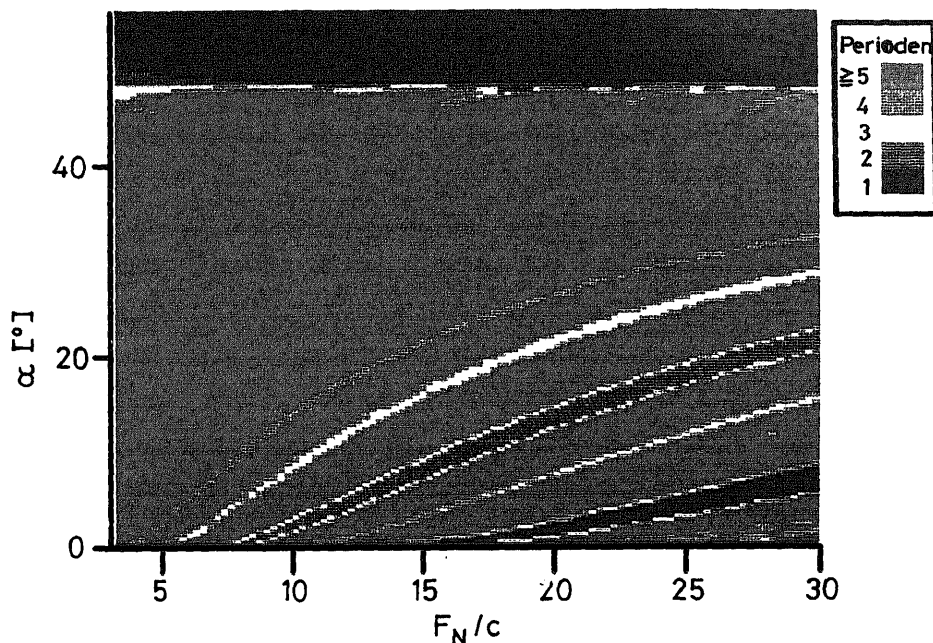


Figure 23. Parameter map depending on F_N/c and α for $\eta = 2.1$ and $u_0 = 0.5$.

three-periodic orbits). With increasing slope angle α corresponding regions of periodic solutions shift to higher values of F_N/c , but the basic structure remains. For high values of the angle α ($> 50^\circ$) this structure is destroyed. As a simple explanation for this a look at the smoothed friction characteristic shows that for all relative velocities the slope of the characteristic is positive, cf. figure 21d. With this validation of the smoothing procedure for stiff smoothing functions further insight into the bifurcational behaviour can be obtained applying numerical bifurcation analysis.

4.5 Bifurcation analysis for friction characteristic III

As described in § 3.3 in the parameter regions of periodic solutions of known winding numbers and with a guess for the initial values $y_1(0)$, $y_2(0)$ path following can be done by means of BIFPACK. Compared to numerical integration additional information can be given by the detection of branch points and the branch tracing for unstable periodic solutions. As a consequence of the chosen kind of normalisation, cp. (23), for a winding number $W = n/p$ there are n initial state vectors leading to the same periodic trajectory. In the phase portraits (figure 24a) the corresponding initial values $y_1(0)$, $y_2(0)$ for a one-periodic solution with $n = 3$ are marked by crosses. The plot of the excitation function (figure 24b) and the system response (figure 24c) in time domain show the different periods T/n with $n = 3$ and T , respectively. The results of the path-following procedure are given in figure 25a, where $y_1[u(t) = 1]$ is plotted versus η . Here, turning points are also detected and marked by crosses. The bifurcation diagram based on numerical simulations plotted in the same manner, cp. figure 25b, shows similar results for stable periodic solutions. However, in contrast to the bifurcation diagram (figure 19a), the periodic solutions with $W = n/p$ are represented by n points.

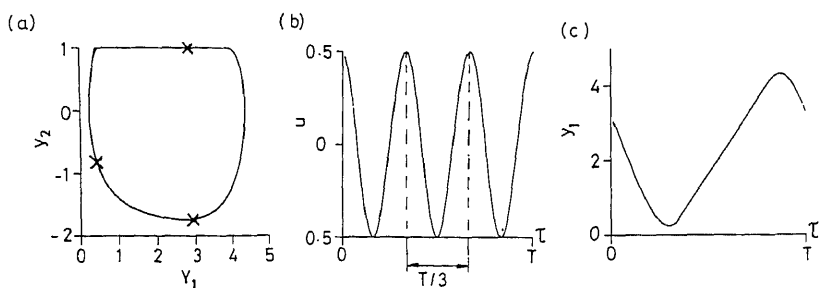


Figure 24. Influence of the winding number: (a) phase plane plot for $\eta = 2.4$, $F_N/c = 10$, $u_0 = 0.5$, $\eta = 3$, (initial states y_1, y_2 marked by crosses), (b) time history of the excitation with period $T/3$, (c) time history of the system response with period T .

In summary, for periodic solutions there is good agreement of the bifurcation parameters found by BIFPACK compared to numerical simulations. Additional information is given by BIFPACK with respect to the determination of unstable branches and the detection of branch points.

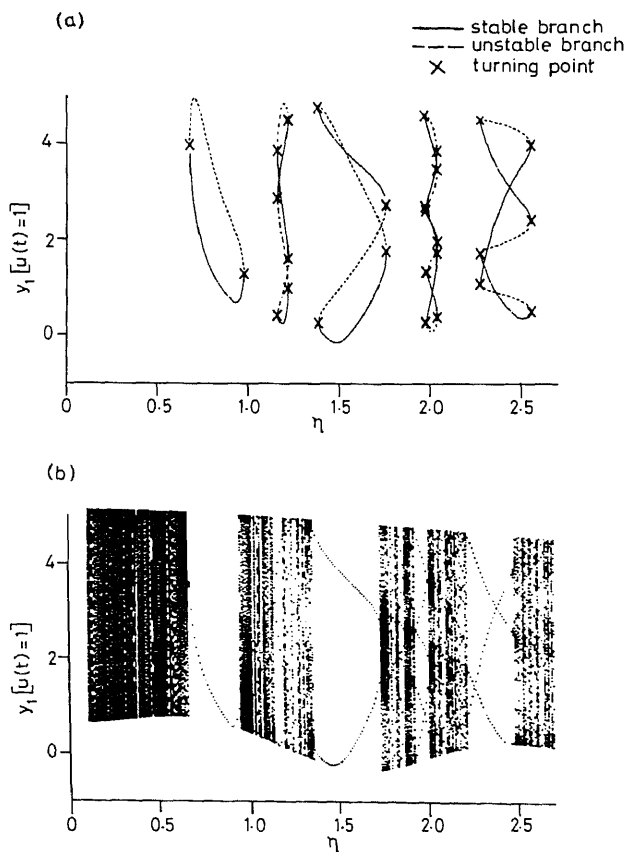


Figure 25. Bifurcation analysis for $F_N/c = 10$ and $u_0 = 0.5$: (a) using BIFPACK, showing stable and unstable branches as well as turning points, (b) numerical simulation.

5. Conclusions

This paper deals with friction-induced vibrations. Therefore, the friction characteristic plays an important role. Since in reality this characteristic is not known exactly, three different models of friction characteristics have been investigated, two of them are non-smooth. Thus, we have to cope with non-smooth dynamics. This is presently a challenge for dynamists and mathematicians.

The friction characteristics chosen allow to build up self-sustained stick-slip vibrations, which are undesired in technical applications. It has been shown that the very robust limit cycle of stick-slip motion can be broken up by an external harmonic disturbance. The resulting friction oscillator with simultaneous self- and external excitation shows rich bifurcational behaviour which has been analysed using different methods. A first general result is, that the bifurcation diagrams and bifurcation maps for the different non-smooth friction characteristics are qualitatively similar, thus, the bifurcation phenomena are robust. Furthermore, the results for non-smooth friction characteristics can be approximated very well by a smoothed characteristic, if the initial slope is very steep. As a consequence, beside numerical simulation methods computer codes for conventional bifurcation analysis can also be applied. A comparison of corresponding results shows good agreement with respect to the bifurcation parameters leading to periodic motions. However, behaviour other than the periodic cannot be investigated by such codes. The most promising is the third method developed and demonstrated in this paper, which is a point-mapping approach superior to the other methods with respect to computing time. This approach gives insight into the periodic as well as the chaotic behaviour. The way of mapping considered clearly shows the intermittency route and the period doubling route to chaos. Evaluating the winding number a devil's staircase has been found. The mapping approach together with the analysis of the winding number gives deep insight into the general dynamical behaviour, although the model under consideration is based on a non-smooth mathematical description.

The authors are grateful to Prof. A Mielke, Institute of Applied Mathematics, University of Hannover, for his helpful discussions and valuable suggestions.

References

- Abraham R H, Shaw C D 1982 *Dynamics – the geometry of behaviour. Part 1: Periodic behaviour* (Santa Cruz: Aerial Press)
- Abraham R H, Shaw C D 1983 *Dynamics – the geometry of behaviour. Part 2: Chaotic behaviour* (Santa Cruz: Aerial Press)
- ACSL (Advanced Continuous Simulation Language) 1991 *Reference manual*, edn 10-0 (Concorde, MA: Mitchell & Gauthier)
- Bochet B 1961 Nouvelles Recherches Experimentelles sur le Frottement et Glissement. *Mines Cabur* 19: 27–120
- Conti P 1875 Sulla Resistanza die Attrito. *Accad. Lincei* 11 (16)
- Devaney R L 1986 *An introduction to chaotic dynamical systems* (Menlo Park, CA: Benjamin Cummings)

- Doedel F J 1981 AUTO: A program for the bifurcation analysis of autonomous system. *Congr. Numer.* 30: 265–285
- Feeny B F, Moon F C 1993 Bifurcation sequences of a Coulomb friction oscillator. *Nonlinear Dyn.* 4: 25–37
- Fingberg U 1989 Squealing noise of railway wheels. A wheel-rail-squealing-noise model. *Proc. Polish-German Workshop on Dyn. Problems in Mech. Syst.*, Madralin, Poland (Polska Akademia Nauk.) pp. 111–122
- Fingberg U 1990 A model of wheel-rail squealing noise. *J. Sound Vib.* 143: 365–377
- Franke J 1882 Über die Abhängigkeit der gleitenden Reibung von der Geschwindigkeit. *Civ. Ing.*
- Galton I 1878 The action of brakes. On the effect of brakes upon railway trains. *Engineering* 25: 469–472
- Grabec I 1988 Explanation of random vibrations in cutting on grounds of deterministic chaos. *Robotics and Computer-Integrated Manufacturing* 14: 129–134
- Guckenheimer J, Holmes P 1983 *Nonlinear oscillations, dynamical systems, and bifurcation of vector fields* (New York, Berlin, Heidelberg: Springer-Verlag)
- Hagedorn P 1984 *Nichtlineare Schwingungen*. Wiesbaden: Akademische Verlagsgesellschaft
- Hale J, Kocak H 1991 *Dynamics and bifurcations* (Berlin, Heidelberg, New York: Springer-Verlag)
- Jahnke M 1987 *Nichtlineare Dynamik eines Reibschwingers*. IfM, Diplomarbeit, Universität Hannover
- Kaas-Petersen C 1987 *PATH-User's Guide* (Leeds: University of Leeds)
- Kauderer H 1958 *Nichtlineare Mechanik* (Berlin: Springer-Verlag)
- Kraft K 1967 Der Einfluß der Fahrgeschwindigkeit auf den Haftwert zwischen Rad und Schiene. *Archiv für Eisenbahntechnik* 22: 58–67
- Kunick A, Steeb W H 1986 *Chaos in dynamischen Systemen* (Mannheim, BI)
- Leven R W, Koch B P, Pompe B 1982 *Chaos in dissipativen Systemen* (Berlin: Akademie-Verlag)
- Magnus K 1961 *Schwingungen* (Stuttgart: Teubner)
- Manneville P, Pomeau Y 1980 Intermittent transition to turbulence in dissipative dynamical systems. *Commun. Math. Phys.* 74: 189–197
- Moon F C 1987 *Chaotic vibrations* (New York: John Wiley & Sons)
- Moon F C 1992 *Chaotic and fractal dynamics* (New York: John Wiley & Sons)
- Neimark J J, Landa P S 1987 *Stochastic and chaotic vibrations* (Moscow: Nauka) (in Russian)
- Parlitz U, Lauterborn W 1987 Period-doubling cascades and devil's staircases of the driven van der Pol oscillator. *Phys. Rev. A* 36: 1428–1434
- Popp K 1991 Chaotische Bewegungen beim Reibschwinger mit simultaner Selbstund Fremderregung. *Z. Angew. Math. Mech.* 71: T71–T73
- Popp K 1992 Some model problems showing stick-slip motion and chaos. *Trans. ASME Friction-induced Vib., Chatter, Squeal Chaos* DE-49: 1–12
- Popp K, Stelter P 1990a Nonlinear oscillations of structures induced by dry friction. In *Proceedings of IUTAM Symposium on nonlinear dynamics in engineering systems*. (Berlin: Springer-Verlag) pp. 233–240
- Popp K, Stelter P 1990b Stick-slip vibrations and chaos. *Philos. Trans. R. Soc. London A*: 89–105
- Popp K, Schneider E, Irretier H 1985 Noise generation in railway wheels due to rail-wheel contact forces. *Proc. 9th IAVSD-Symp.*, Linköping, pp. 448–466
- Seydel R 1983 *From equilibrium to chaos; practical bifurcation and stability analysis* (Amsterdam: Elsevier)
- Seydel R 1993 BIFPACK – A program package for continuation, bifurcation and stability analysis. Mathematische Institute der Julius-Maximilians-Universität Würzburg, Version 2.4
- Sparrow C 1982 *The Lorenz equation: bifurcations, chaos, and strange attractors*. *Applied Mathematical Sciences* 41 (New York: Springer-Verlag)
- Stelter P 1990 *Nichtlineare Schwingungen reibungsregelter Strukturen*. VDI R. 11 Nr. 137, Düsseldorf
- Stelter P 1992 Nonlinear vibrations of structures induced by dry friction. *Nonlinear Dyn.* 3: 329–345
- Stelter P, Popp K 1989 Chaotic behaviour of structures excited by dry friction forces. *Proc. Workshop on Rolling Noise Generation*, Berlin (ed.) M Hedel
- Stelter P, Sestro W 1991 Bifurcations in dynamics systems with dry friction. *Int. Ser. Numer. Math.* 97: 343–347
- Thompson J M T, Stewart H B 1986 *Nonlinear dynamics and chaos* (Chichester: Wiley)

Computation of the Kolmogorov entropy for MDOF systems

F BONTEMPI¹ and F CASCIATI²

¹ Polytechnic of Milan, P.zza L. da Vinci 32, 20133-Milan, Italy

² University of Pavia, Via Abbiategrasso 211, 27100-Pavia, Italy

Abstract. The dynamics of a truss structure with several bars and nodes is investigated. The bars are made of some nonlinear material and the truss structure shows large displacements under some time-dependent loads. The resulting equations are an example of a model which governs the motion of a general MDOF structure after some discretization procedure, like FEM. Attention is focused on the response strangeness met during the numerical integration of the motion equations. As a principal tool of investigation, one uses the Kolmogorov entropy, the value of which is able to detect the sensitivity to initial conditions. The material can present either nonlinear elastic softening or elasto-plastic behaviour.

Keywords. Bifurcation diagram; chaotic motion; Kolmogorov entropy; truss structure.

1. Introduction

Deep studies have been developed, during the last decade, on the understanding of the so-called chaotic behaviour of a nonlinear dynamic system, i.e. the sensitivity of the motion to the values which specify system parameters, external disturbances and, especially, initial conditions (Lichtenberg & Liebermann 1983; Wedig 1988; Baker & Gollub 1990). With reference to the dynamical systems of interest within structural engineering, one has a variety of methods for detecting chaos and they have been recently summarized in some doctoral theses (Kapitaniak 1990; Kunert 1992; Bontempi 1993) among others. Two parallel analyses can be conducted in order to make the study redundant and, hence, more reliable; in the first one the larger value of the Lyapunov exponent is computed (Benettin *et al* 1980; Wolf *et al* 1984; Wedig 1987, 1988); the second approach assesses the value of the Kolmogorov entropy (Hamilton & Brumer 1982; Termonia 1984). In the first case a positive value means chaos or stochasticity (Bontempi *et al* 1991), while regular behaviour is denoted by a non-positive value; in the second case regularity is just expressed by a null value (Bontempi & Casciati 1994).

The previous algorithms are easily implemented for structures with a few degrees of freedom. The objective of this paper is to show how large structural systems can be managed toward a Kolmogorov entropy computation. This is done with reference to

a multi-degree-of-freedom plane truss-structure for the analysis of which both material and geometric nonlinearities are incorporated.

2. Definition of the system

In this paper reference is done to the truss structure of figure 1. Each node has two degrees of freedom but the symmetry of the structure makes possible to write the equations of motion by considering six of the ten nodes. Let \mathbf{q} be the vector of the unknown displacements $\{q_1, q_2, \dots, q_6, \dot{q}_1, \dot{q}_2, \dots, \dot{q}_6\}$. The geometrical constraints are imposed by two hinges in the nodes 1 and 2 and two horizontal supports at nodes 5 and 6. There is a single harmonic vertical force $F(t) = A \cdot \sin(\omega \cdot t)$ along q_6 , the values of the parameters being $\omega = 1.13$ and $A = 0.275$. All the bars have area $S = 10$. With reference to figure 2, the material constitutive law requires the following parameters to be assigned

- E = the modulus of the initial elastic range = 1;
- σ_y = the yielding stress = 0.01.

This paper studies the sensitivity of the motion to changes in the values of the hardening modulus H , for different natures of the constitutive relation – nonlinear elastic or elasto-plastic. The general equation of motion is written as

$$\mathbf{M} \cdot \ddot{\mathbf{q}} + \mathbf{C} \cdot \dot{\mathbf{q}} + \mathbf{R}(\mathbf{q}, \dot{\mathbf{q}}) = \mathbf{F}(t), \quad (1)$$

in which \mathbf{M} = mass matrix, \mathbf{C} = damping matrix (both of them are diagonal matrices: $M_{ii} = 1$, $C_{ii} = 0.02$, $i = 1, 6$). The nonlinear restoring force vector is denoted by $\mathbf{R}(\mathbf{q}, \dot{\mathbf{q}})$ and the force vector $\mathbf{F}(t)$ has the only one non-zero component: $F_6(t) = F(t) = A \cdot \sin(\omega \cdot t)$.

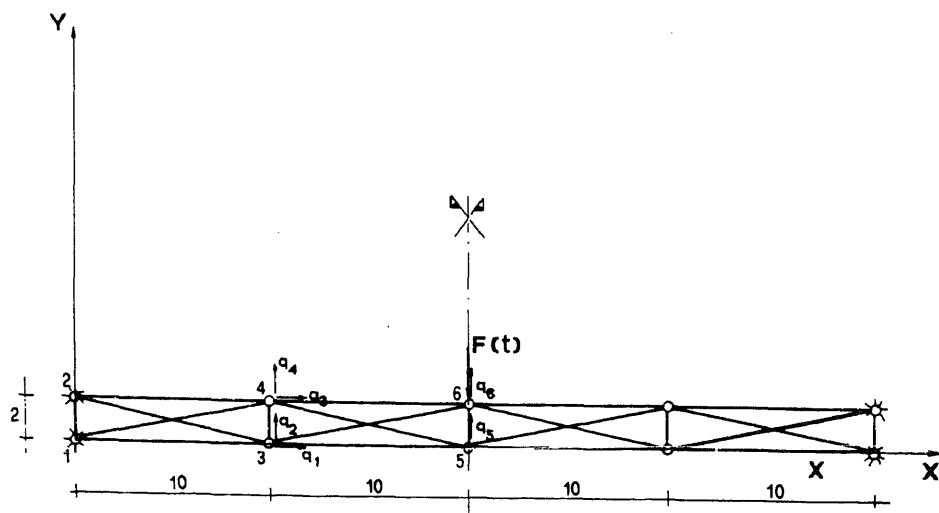


Figure 1. Geometry of the truss structure considered through the paper as reference example.

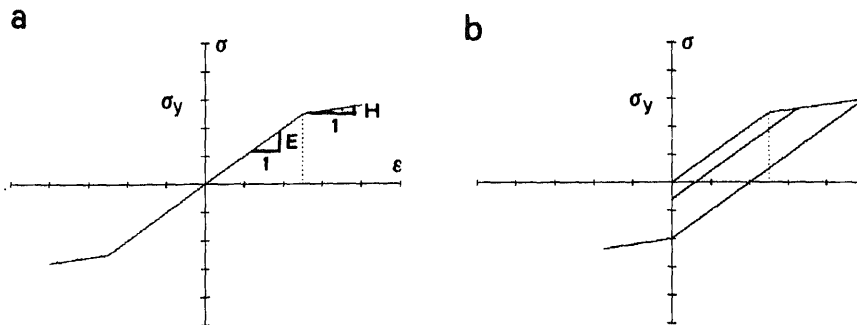


Figure 2. Definition of the constitutive relation: (a) nonlinear elastic; (b) elasto-plastic.

One adopts an updated Lagrangian formulation (Bathe 1982) in order to allow the geometrical effects, i.e. large displacements; in this way the stiffness matrix of the single bar is computed on the basis of the updated coordinates of the nodes of the structure. In particular, the transformation matrix from the local to the global coordinate system takes into account the variation of the inclination of the single bar.

The integration method is the Newmark one (Bathe 1982; Argyris & Mlejnek 1991), with the choice $\beta = 0.5$ and $\gamma = 0.25$. The integration time step is $\Delta T = T_F/100$ (T_F denotes the period of the external excitation: $T_F = 2\pi/\omega$). The six natural oscillation periods for the truss structure are $T_1 = 1.96$, $T_2 = 1.99$, $T_3 = 3.18$, $T_4 = 3.20$, $T_5 = 20.2$, $T_6 = 72.12$, the lower periods correspond to axial behaviour, while the higher ones characterize a flexural behaviour of the whole structure. Therefore the truss structure behaves essentially as a slender beam, with two main possibilities to deform itself, roughly as a single sinusoidal wave or as a half sinusoidal wave.

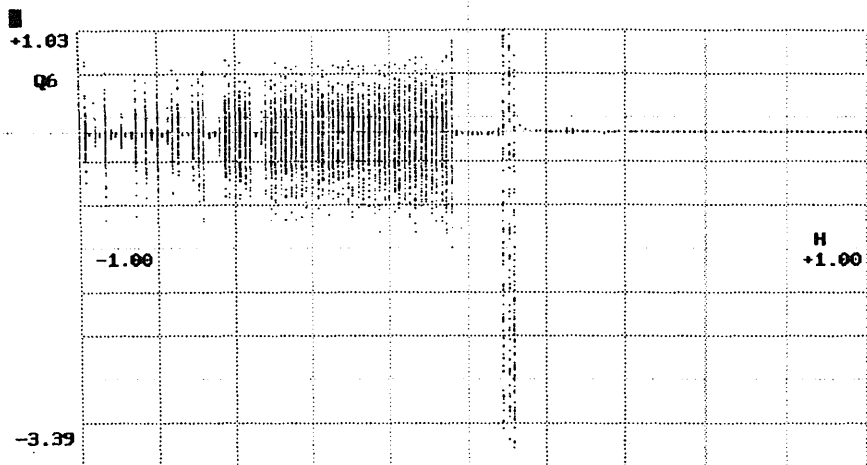
3. Bifurcation diagrams

As a first synthetic tool for understanding the dynamics of this MDOF structure, one builds the bifurcation diagram (Baker & Gollub 1990); in this way the dependence on the nature of the constitutive law (i.e. nonlinear elastic or elasto-plastic) and on the value of the hardening parameter H is detected.

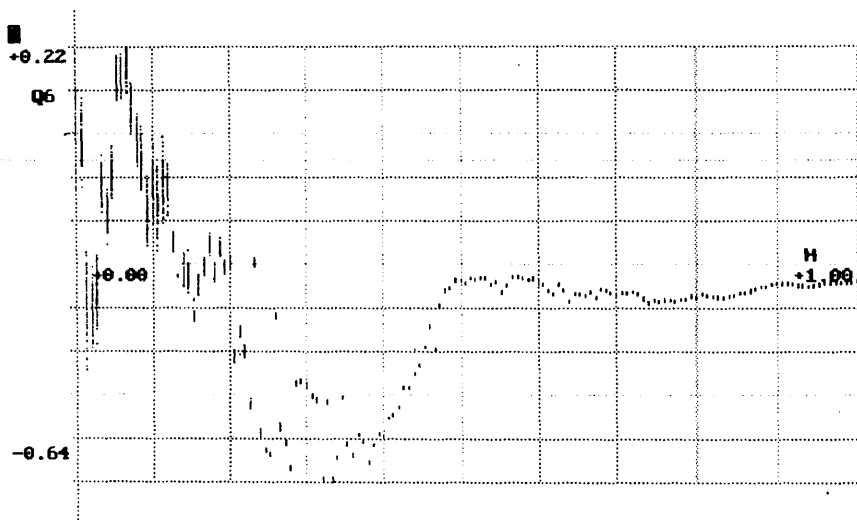
Consider (1) and select the kind of material and the nature of the displacements (either infinitesimal (small displacements) or finite (large displacements)); the four cases of table 1 arise.

Table 1. Different kinds of dynamic problems to be investigated.

	Small displacements	Large displacements



a



b

Figure 3. Bifurcation diagram for large displacements: (a) the nonlinear elastic case (LE); (b) the elasto-plastic case (LP).

For them, the bifurcation diagrams are built in the following manner:

- the variability range for the parameter H , the influence of which must be studied, selected: $\Delta H = H_{\max} - H_{\min}$;
- $N_H + 1$ values of the parameter H are allocated in this range: $H_k = H_{\min} - \Delta H/N_H \cdot k$, $k = 0, \dots, N_H$ (here $N_H = 150$);

- for each value H_k one integrates the equation of motion; after the transient period T_{tr} (numerical experience suggests $T_{tr} = 100 \cdot T_F$), one extract from the vector \mathbf{q} , at each time instant $t_h = T_{tr} + h \cdot T_{sn}$, $h = 1, \dots, N_s$ (here $N_s = 100$), the component q_6 , and specify a point (H_k, q_6) in a diagram with abscissa H and ordinate q_6 . The choice of the time period T_{sn} is critical, because it determines the appearance of the diagram, in the presence of a periodic force of period T_F , the natural choice turns out to be $T_{sn} = T_F$.

The interval $\Delta H = H_{\max} - H_{\min}$ of the hardening parameter was selected to be $[-1, 1]$ for the nonlinear elastic case and $[0, 1]$ for the elasto-plastic case. The effect of the softening branch (i.e. the situation $H < 0$) can be observed only in the former case.

The results obtained in the large displacement case are shown in figure 3:

- in the nonlinear elastic case (figure 3a), the strangeness of the motion (that characterizes quasiperiodic or aperiodic (i.e. chaotic) oscillations) appears in the softening area;
- in the elasto-plastic case (figure 3b), the motion appears strictly periodic for $H \geq 0.3$, while it is sometimes strange for $0 \leq H \leq 0.3$.

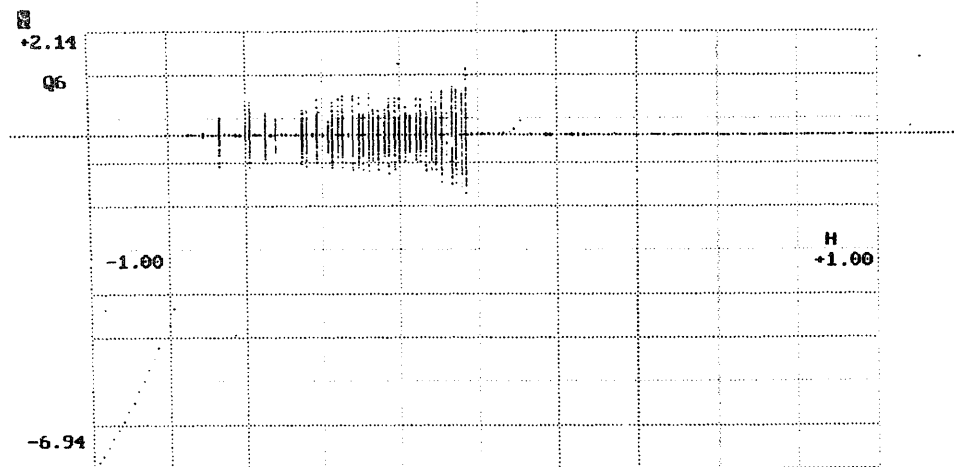
Figure 4 shows the same cases for small displacements. For the elastic case, no chaotic situation is shown in the hardening branch; some strangeness remains in the elasto-plastic case. Clearly, deeper computations are necessary to declare this case truly chaotic: in fact the time integration of elasto-plastic structures presents special features (Bontempi & Casciati 1995). In this paper, however, attention is focused on the measure of the irregular behaviour, irregularity that can also result from numerical inaccuracies.

4. Some simulations and the definition of the embedding phase space

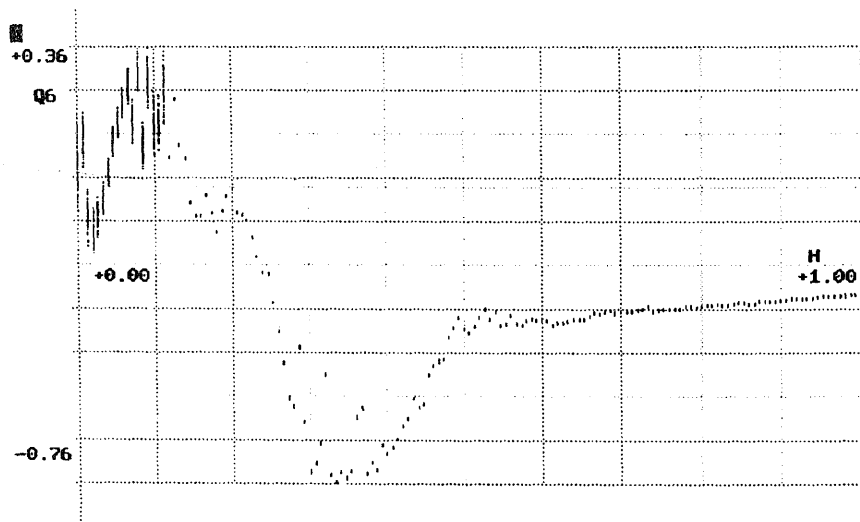
Some numerical simulations show the kind of motion the structure develops and provide quantitative measures of the strangeness (i.e. the chaoticity). The appearances of these simulations for the selected material law and for the fixed values of the hardening parameter H are represented in figures 5 and 6 in terms of time history and of the projection of the Poincaré section in the plane (q_6, \dot{q}_6) . The transient is left, to show that, in some cases, one has transient chaos.

Essentially, the aim of these simulations is to define the dimension n_e of the *embedding phase space* (Jackson 1991). Instead of working in the true phase space of dimension n (for the structure studied here, $n = 12$), a single time series could be able to give the main aspects of the dynamics of the structure in the reconstructed phase space of dimension $n_e < n$, in which the system dynamics can be embedded. With n_e known, this is done by replacing at each instant $t_k (t_k = t_0 + k \cdot \Delta T, k = 1, \dots)$ the true representative vector of the system $\mathbf{y}(t_k)$, the $2 \cdot n$ components of which are $q_i(t_k)$ and $\dot{q}_i(t_k)$, with vector $\mathbf{z}(t_k)$ of n_e components

$$\mathbf{z}(t_k) = \begin{pmatrix} z_{k+0 \cdot \Delta k} \\ z_{k+1 \cdot \Delta k} \\ z_{k+2 \cdot \Delta k} \\ \vdots \end{pmatrix}, \quad (2)$$



a



b

Figure 4. Bifurcation diagram for small displacements: (a) nonlinear elastic behaviour (SE); (b) elasto-plastic behaviour (SP).

with

$$z_k = q_6(t_k), \quad k = 1, \dots \quad (3)$$

Equation (3) represents the time series extracted from the time history of a particular degree of freedom of the structure (here just $q_6(t)$).

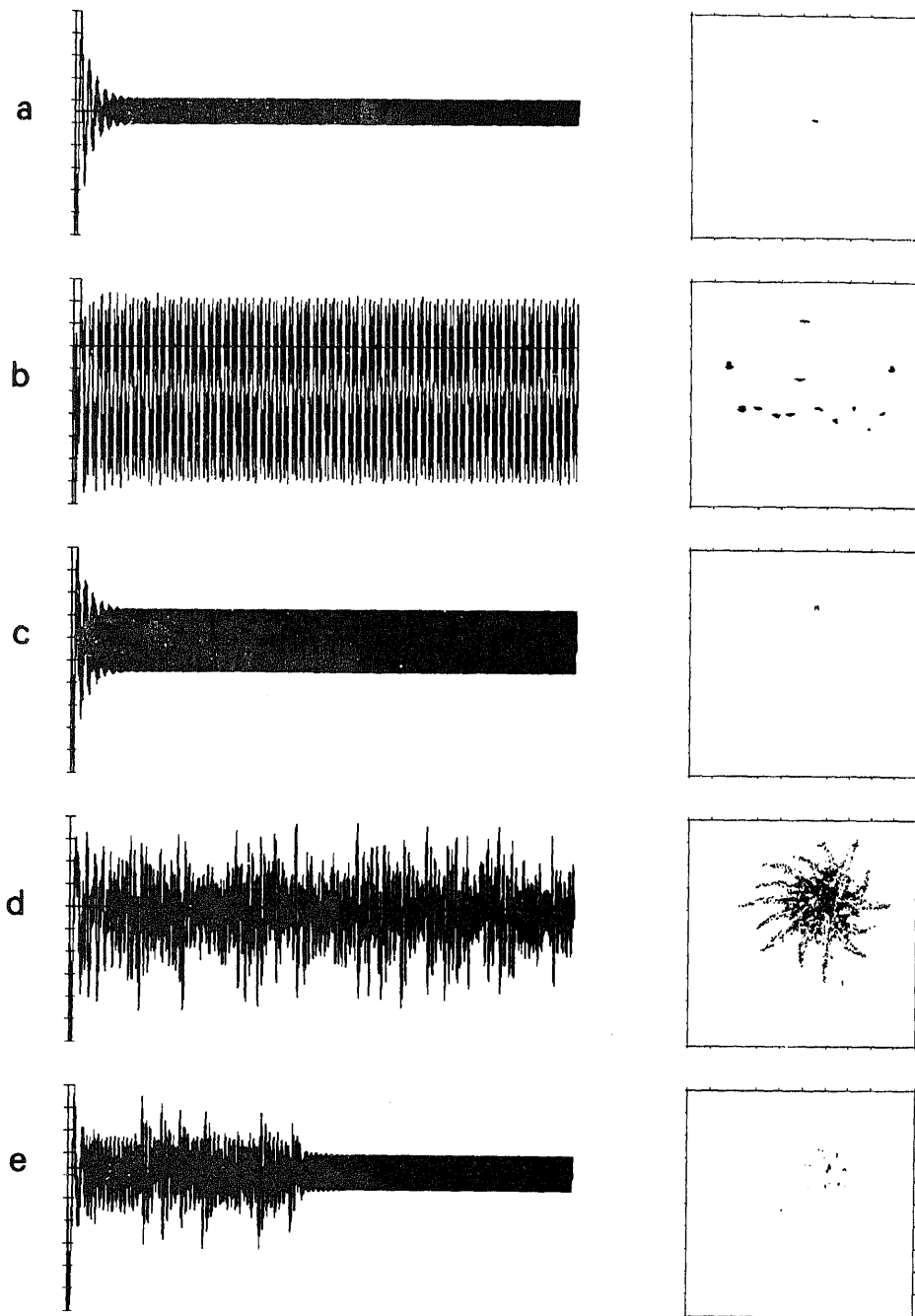


Figure 5. Some simulations for the nonlinear elastic case with large displacements (on the left side the time history and, on the right side, the projected Poincaré sections extracted from the pair of degrees of freedom $\{q_6, \dot{q}_6\}$): $H = 1.0$ (a), 0.1 (b), 0.0 (c), -0.2 (d), -0.5 (e).

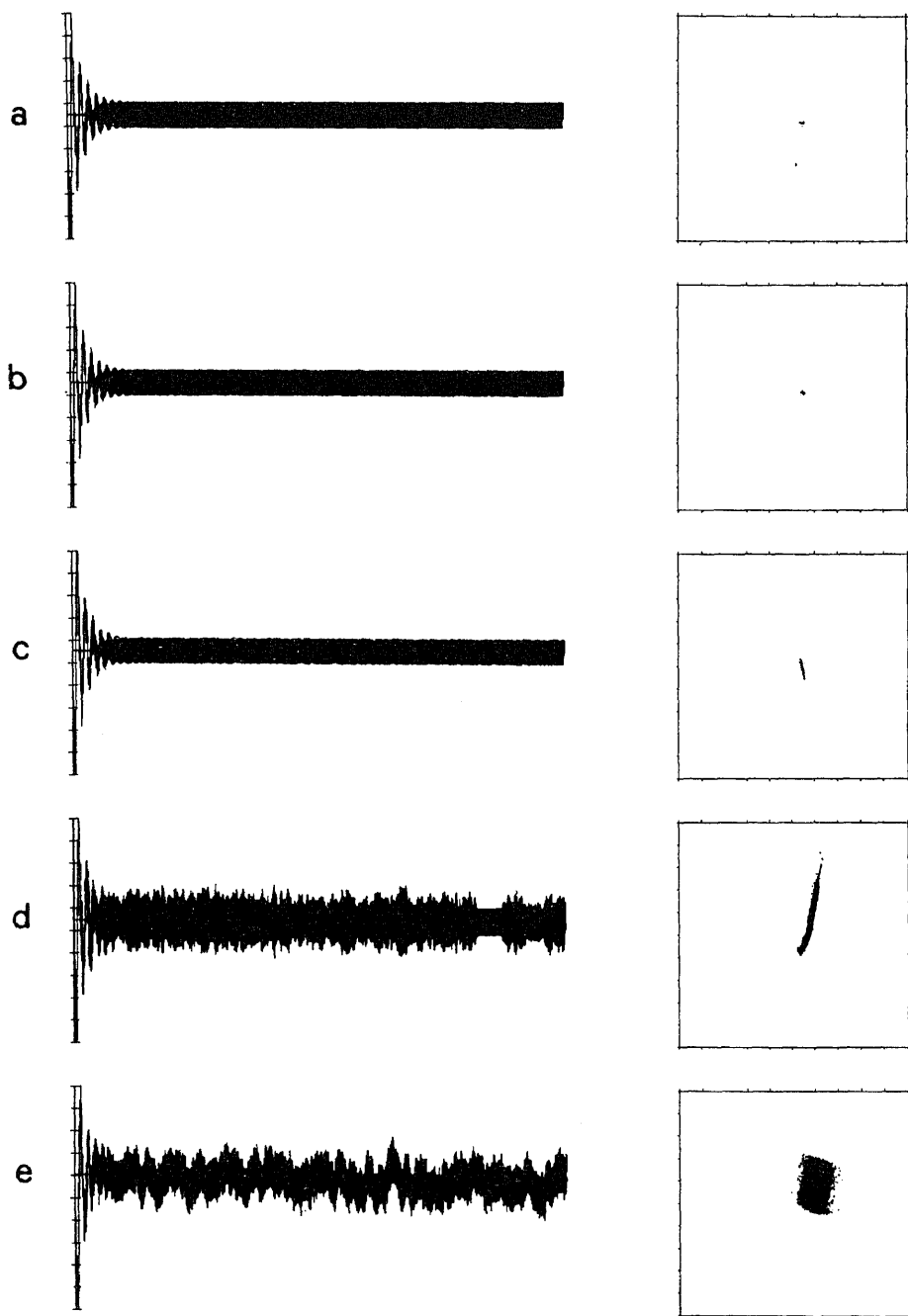


Figure 6. Some simulations for the elasto-plastic case with large displacements (on the left side the time history and, on the right side, the projected Poincaré sections extracted from the pair of degrees of freedom $\{q_6, \dot{q}_6\}$): $H = 1.0$ (a), 0.3 (b), 0.2 (c), 0.1 (d), 0.0 (e).

Table 2. Summary of the quantitative measures for the simulations in the non-linear elastic case (large displacements).

H	$d_G(2)$	$d_G(3)$	$d_G(4)$	$d_G(5)$	$d_G(6)$	K	λ_{\max}
1.0	1.93	1.90	2.20	2.47	2.28	0.00	-0.29
0.1	1.85	2.03	2.37	2.30	2.07	0.04	0.02
0.0	1.78	1.99	2.13	2.39	2.37	0.00	-0.98
-0.2	2.09	3.02	3.36	3.45	3.49	0.30	0.35
-0.5	1.86	1.89	2.14	2.08	2.38	0.03	0.02

The vector $\mathbf{z}(t_k)$ is therefore obtained from an ordered set of values of the same displacement, each of them sampled with a convenient time delay $T_s = \Delta k \cdot \Delta T$. The choice of the time delay T_s should be guided by the fact that there must exist a topological correspondence between the true representation in the original phase space and the one in the reconstructed phase space. Numerical experience shows that an optimal value of Δk separates cases of excessive correlation from cases too scattered (Jackson 1991). In the present example the optimal value was $\Delta k = 20$; this means a time delay $T_s = 20 \cdot \Delta T = 20 \cdot T_F/100 = T_F/5$.

The problem is how to determine the dimension n_e . This is realized by

- selecting a dimension n_e for the reconstructed phase space (i.e. the system dynamics is represented by (2) with $n_e = n_c$);
- computing the dimension of correlation of the underlying attractor of the system:

$$d_G(n_c) = \lim_{R \rightarrow 0} [\lg_2(C(R, n_c))/\lg_2(R)], \quad (4)$$

where $C(R, n_c)$ is the correlation function, i.e. the fraction of points of the attractor which are not farther away than R from a sampling point of the attractor itself (Baker & Gollub 1990).

Repeating the previous steps for different increasing values n_c , the embedding dimension n_e can be regarded as the smallest integer greater than all the attractor dimensions $d_G(n_c)$ previously computed.

In tables 2 and 3 one has some quantitative measures obtained from the time series of (3), for large displacements. The first row of both the tables corresponds to the

Table 3. Summary of the quantitative measures for the simulations in the elastoplastic case (large displacements).

H	$d_G(2)$	$d_G(3)$	$d_G(4)$	$d_G(5)$	$d_G(6)$	K	λ_{\max}
1.0	1.93	1.90	2.20	2.47	2.28	0.00	-0.29
0.3	1.91	2.19	2.30	2.44	1.99	0.47	0.52
0.2	2.00	2.12	2.25	2.62	2.27	0.84	0.83
0.1	1.90	2.11	2.40	2.58	2.58	0.70	0.81
0.0	2.00	2.51	2.54	2.51	2.55	0.48	0.51

perfectly linear elastic case. The first five columns of these tables give the numerical values of the correlation dimension $d_G(n_c)$, with increasing value of n_c from 2 to 6. From these measures of the dimension of the attractor, one realizes the possibility of working in a phase space with embedding dimension $n_e = 4$ (this is in agreement with the observation that the structure has two principal natural modes).

The last two columns of the two tables show the values computed in the embedding space of the Kolmogorov entropy K and of the maximum Lyapunov exponents λ_{\max} . The latter one is computed by standard procedures (Wolf *et al* 1984), while K is assessed by the procedure illustrated in the next section.

5. The computation of the Kolmogorov entropy

A quantitative evaluation of the behaviour of a dynamical system can be obtained partitioning its phase space. This operation is conducted through a grid of boxes $V_i, i = 1, \dots, N_{\text{box}}$ of characteristic size ε , which is indicative of the capacity to measure the status of the system (1) in the phase space. The numerical quantities extracted through the partition of the phase space are only approximated. This approximation increases as the number of boxes increases (i.e. the size ε decreases). The number N_{box} of boxes, however, is clearly related to the computational effort. Also the extension of the region of the phase space considered for the partition depends on analogous computational considerations, despite the fact that it is necessary to extend the partition beyond the points of the phase space visited from the system during its motion.

The first elementary measure to characterize the dynamics of the system is just the number of boxes N_{box} which are visited during the motion. A more significant information is given by the *probability mass function*,

$$p_i(t) = \int_{V_i} p(\mathbf{y}, t) \cdot dV_i, \quad (5)$$

of finding the status of the system in the i th box of volume V_i . In (5) $p(\mathbf{y}, t)$ denotes the probability density function in the phase space. This allows one to study systems with many attractors, with external noise and/or with sensitivity to the initial conditions.

Related to the form of the probability mass function, there is a quantity that measures the disorder connected with the motion of the system. This quantity is the *entropy* of the system (Lichtenberg & Liebermann 1983; Baker & Gollub 1990). Mathematically, it is defined by the relation:

$$I(t) = - \sum_i p_i(t) \cdot \lg_2(p_i(t)), \quad (6)$$

where the summation covers all the visited boxes (i.e. where $p_i \neq 0$). It is clear that, numerically, this expression depends on the discretization of the phase space. Also, this quantity is a function of the time because the quantities $p_i(t)$ are continuously varying in time. The average velocity of variation of the entropy, over the (*diffusion*) period required for the system to reach a stationary status, is called the *Kolmogorov entropy* (Baker & Gollub 1990; Casciati 1993)

$$K(t) = \langle \partial I(t) / \partial t \rangle. \quad (7)$$

It has the physical meaning of the velocity with which one loses information about the status of the dynamical system in the phase space. It is to remark again that this loss of predictability can result also from numerical inaccuracies. In this case, a positive K warns against numerical difficulties in the integration procedure.

In the presence of a high number of degrees of freedom, for computing the entropy $I(t)$, and, hence, K , one must afford the partition of a high dimensional phase space. For a space of dimension n , the partition with boxes of side ε of the cube of side L which contains the attractor, requires a number of boxes

$$N_{\text{box}} \propto [L/\varepsilon]^n. \quad (8)$$

with $L/\varepsilon = 10$ as a minimum, (8) leads to $N_{\text{box}} \propto 10^n$. The advantage of operating in the embedding space (with $n_e \ll n$) turns out to be evident. Following this idea, a computational technique has been conceived and implemented. It is based on the *renormalization of the Gibbs set* (Bontempi 1993; Casciati 1993), whose evolution is built from the knowledge of a single variable of the dynamical system (in this paper from (3)). One assigns a characteristic size ε and proceeds along the following steps:

- a reference point $\mathbf{z}(t_i)$ is selected in the embedding space;
- at the instant t_i , all the points $j \neq i$ of the series (2) that are within a single box of side ε centred around the point i are considered to form the Gibbs set; note that these points j should refer to times well different from the one of the point i , i.e. $i \gg j$ or $i \ll j$, because otherwise one considers points that are just the positions assumed by the reference point during its diffusion interval. These points are initially disposed in a single box of side ε : therefore the entropy of this set is zero since the set is perfectly ordered;
- the evolution of the Gibbs set is followed until an instant $t_f = t_i + \Delta \bar{T}$, sufficient to expand the Gibbs set (but such that the size of the Gibbs set remains lower than $0.1 \cdot D$, D being the maximum size of the attractor in the embedding space. In other words, $\Delta \bar{T}$ (here = $T_F/2$) must be lower than the diffusion time interval necessary for the system to reach the stationary status);
- at this point, one considers a *local* partitioning of the phase space with a grid of just one or two boxes along each dimension, around the position reached for the reference point. The number of boxes necessary to contain the deformed Gibbs set is then roughly only

$$N_{\text{box}} \propto 2^{n_e}. \quad (9)$$

One computes $p_i(t_f)$ and then $I(t_f)$. The Kolmogorov entropy K during the interval of time $t_f - t_i = \Delta \bar{T}$ is just

$$K = I(t_f)/(t_f - t_i); \quad (10)$$

Repeating the previous steps, along the evolution of the reference point (that means switching from $\mathbf{z}(t_i)$ to $\mathbf{z}(t_f)$), one obtains an approximation of K as soon as the measure stabilizes. In particular the second step corresponds to a renormalization; it is the trick by which only local partition of the embedding space (instead of a global one) is necessary.

A complete study of the behaviour of the structure of figure 1, is shown in figure 7 for the nonlinear elastic material law, and in figure 8 for the elasto-plastic case. In both cases, the top of the figure shows the effect of the presence of large displacements, while the bottom gives results within small displacements. As already emphasized, the embedding space dimension is $n_e = 4$, according to the results in tables 2 and 3. The main remark coming from these pictures concerns the spread of the irregular motion region along the design variable (H in the case under investigation).

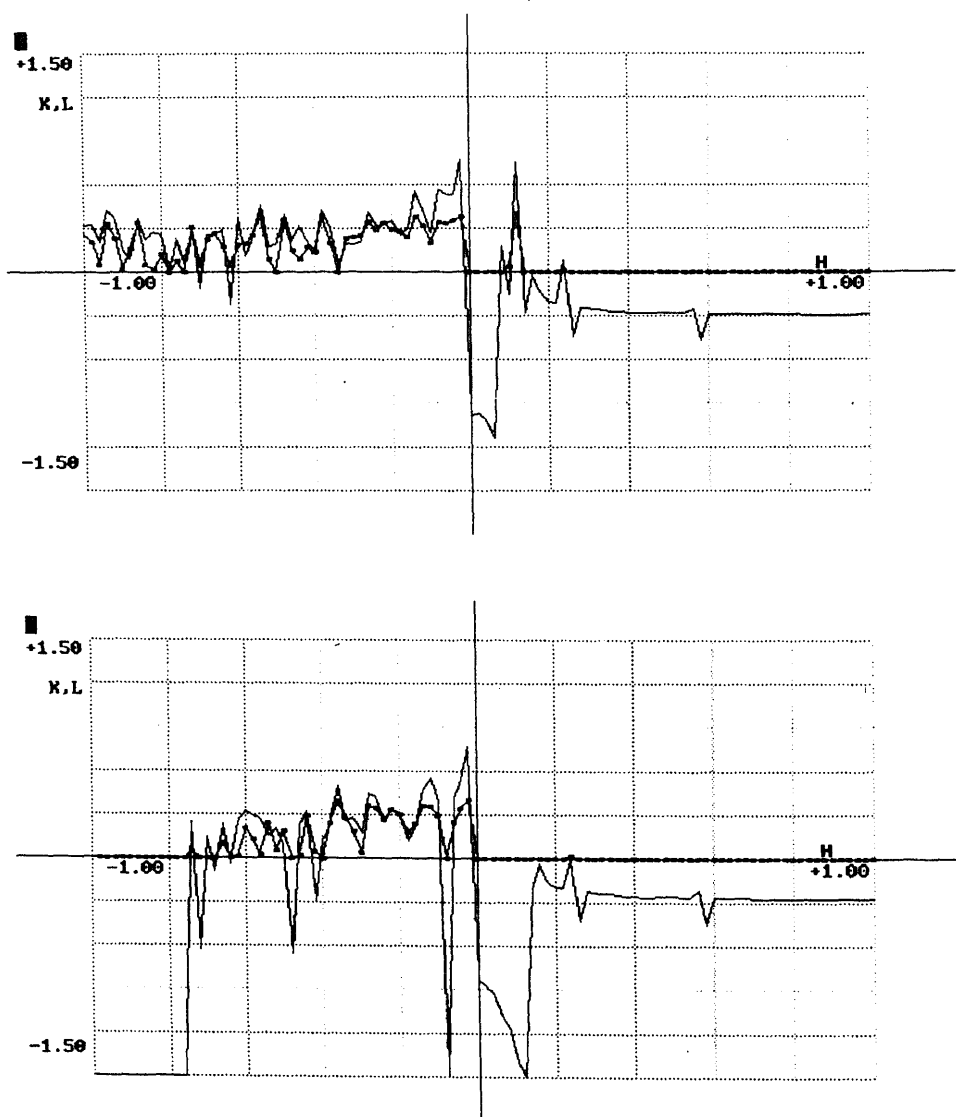


Figure 7. Spectrum of the Kolmogorov entropy and of the maximum Lyapunov exponent for the nonlinear elastic case: *top*, with large displacements (LE); *bottom*, small displacements (SE).

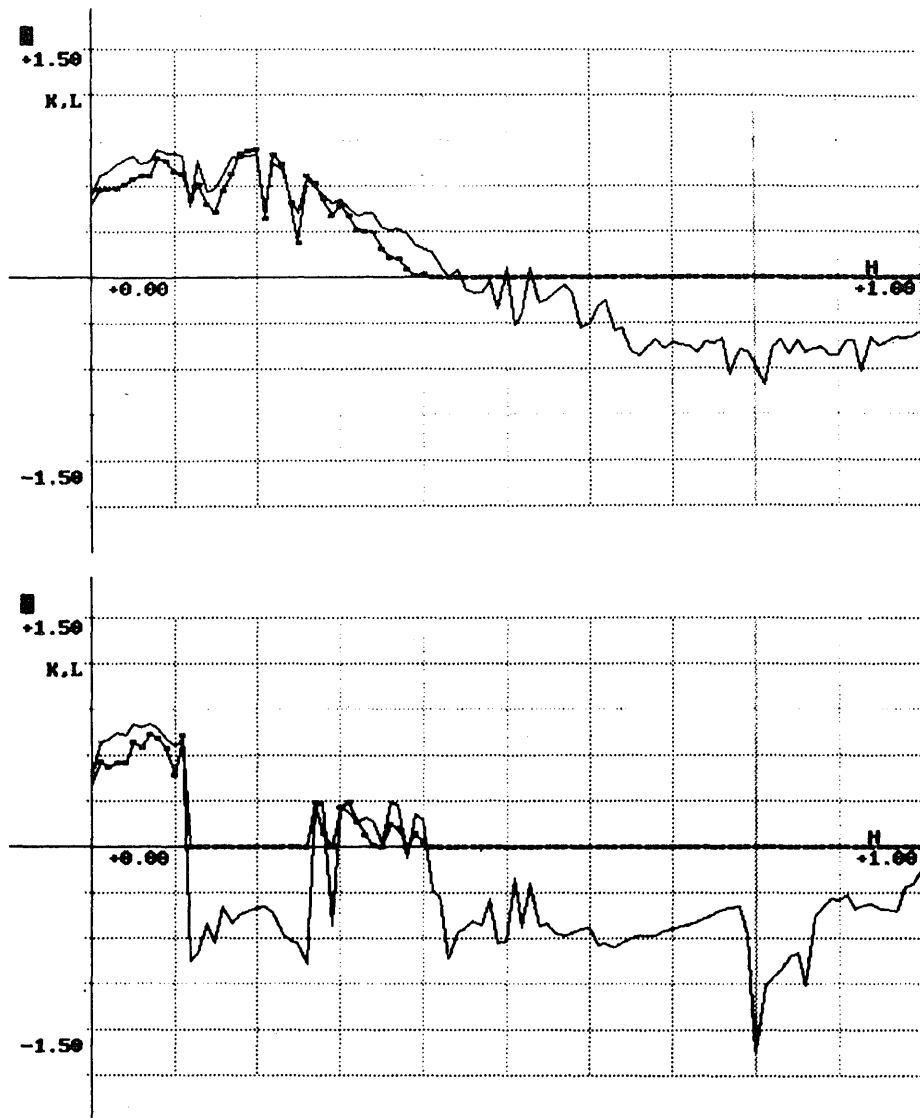


Figure 8. Spectrum of the Kolmogorov entropy and of the maximum Lyapunov exponent for the elasto-plastic case: *top*, with large displacements (LP); *bottom*, small displacements (SP).

6. Conclusions

This paper proposes an operative approach to the assessment of the Kolmogorov entropy for multi-degree-of-freedom systems. The value of the Kolmogorov entropy, permits one to reach conclusions on the predictability (whose loss can be due either to numerical inaccuracies or a truly chaotic behaviour) of the vibration of the structural system under investigation. The idea is to make available an approach parallel to the

standard computation of the maximum Lyapunov exponent. Its need is two-fold; from one side two alternative algorithms form a redundant, and hence more reliable, tool of investigation; from the other side the calculation of the Lyapunov exponents still suffers numerical problems.

The algorithm for the computation of the Kolmogorov entropy is based essentially on two concepts: (1) the Gibbs set (i.e. a collection of trajectories of the system to study) and (2) the embedding phase space (i.e. the reduced phase space in which the dynamics of the system can be represented). Both these ingredients are obtained from the time history of just a single *leading* degree of freedom of the structure. Clearly, an exact computation of the Kolmogorov entropy for MDOF systems would require a multi-variate analysis; in this sense, the algorithm proposed provide only an approximation of K . Anyway, consider a set of similar structures characterized by different values of the parameters that define the geometry, the material and the excitation. For the same choice of the leading degree of freedom, the associated time histories are always sufficient to detect predictability. For the structure considered in this paper, the numerical effort to compute the Kolmogorov entropy was approximately five times the one required by the computation of the maximum Lyapunov exponent.

This research has been supported by grants from the Italian Ministry of University and Scientific and Technological Research (MURST).

References

- Argyris J, Mlejnek H P 1991 *Dynamics of structures. Text on computational mechanics* (Amsterdam: North-Holland) vol. 5
- Baker G L, Gollub J P 1990 *Chaotic dynamics. An introduction* (Cambridge: University Press)
- Bathe K J 1982 *Finite element procedures in engineering analysis*, (Englewood Cliffs, NJ: Prentice-Hall)
- Benettin G, Galgani L, Giorgilli A, Strelcyn J M 1980 Lyapunov characteristic exponents for smooth dynamical systems and for Hamiltonian systems; method for computing all of them. Part 1: Theory. *Meccanica* 14: 9–20
- Benettin G, Galgani L, Giorgilli A, Strelcyn J M 1980 Lyapunov characteristic exponents for smooth dynamical systems and for Hamiltonian systems; A method for computing all of them. Part 2: Numerical application. *Meccanica* 14: 21–30
- Bontempi F 1993 *Transition to chaos in structural dynamics problems*. Ph D thesis, Politecnico di Milano (in Italian)
- Bontempi F, Casciati F 1994 Chaotic motion and stochastic excitation. *Nonlinear Dynamics*, 6: 179–191
- Bontempi F, Casciati F 1995 Discussion of the chaotic behaviour of an elastic-plastic structure (to appear)
- Bontempi F, Casciati F, Faravelli L 1991 Chaotic motion versus stochastic excitation. *Chaos, Soliton & Fractals* 1: 491–500
- Casciati F (ed.) 1993 *Dynamic motion: Chaotic and stochastic behaviour*. (Berlin: Springer Verlag) CISM Series 340
- Hamilton I, Brumer P 1982 Relaxation rates for two-dimensional deterministic mappings. *Phys. Rev. A* 25: N6
- Jackson A 1991 *Perspectives in nonlinear dynamics* (Cambridge: University Press) vol. 2
- Kapitaniak T 1990 *Chaos in systems with noise* (Singapore: World Scientific)
- Kunert A 1992 *Dynamik spielbehafteter Maschinenteile* (Dusseldorf: VDI Verlag) (in German)

- Lichtenberg A J, Lieberman M A 1983 *Regular and stochastic motion* (New York: Springer Verlag)
- Termonia Y 1984 Kolmogorov entropy from a time series. *Phys. Rev. A*29: 1612–1614
- Wedig W 1987 Lyapunov exponents of stochastic systems and related bifurcation problem. *Euromech 229, Nonlinear applied dynamics*, Stuttgart
- Wedig W 1988 Vom Chaos zur Ordnung (GAMM – Mitteilungen) vol. 2: pp. 3–31 (in German)
- Wolf A, Swift J B, Swinney H L, Vastano J A 1984 Determining Lyapunov exponents from a time series. *Phys. Rev. A*29: 285–317



Nonperiodic flutter of a buckled composite panel

NARESH K CHANDIRAMANI¹, RAYMOND H PLAUT² and
LIVIU I LIBRESCU¹

¹Department of Engineering Science and Mechanics, and

²Department of Civil Engineering, Virginia Polytechnic Institute and State University, Blacksburg, VA 24061, USA

Abstract. The nonlinear vibrations of a composite panel subjected to uniform edge compression and a high-supersonic coplanar flow is analysed. Third-order piston theory aerodynamics is used and the effects of in-plane edge restraints, small initial geometric imperfections, transverse shear deformation, and transverse normal stress are considered in the structural model. Periodic solutions and their bifurcations are determined using a predictor–corrector type Shooting Technique, in conjunction with the Arclength Continuation Method for the static state. It is demonstrated that third-order aerodynamic nonlinearities are destabilizing, and hard flutter oscillations (both periodic and quasiperiodic) of the buckled panel are obtained. Furthermore, chaotic motions of an uncompressed panel, as well as a buckled-chaotic transition, and chaos via period-doubling are possible, and the associated Lyapunov exponents are computed. A coexistence of the buckled state with flutter motion may also occur. Results indicate that edge restraints parallel to the flow do not significantly affect the immediate post-critical response, and that a higher-order shear deformation theory is required for a moderately thick/flexible-in-transverse-shear composite panel.

Keywords. Panel flutter; non-periodic motion, chaos; shear deformation; laminated composite plates.

1. Introduction

For the panel flutter problem, it is well-known that at post-critical flow speeds the induced membrane forces limit the oscillation amplitudes, thus preventing immediate panel failure. However, aerodynamic nonlinearities are more pronounced and usually destabilizing at high-supersonic speeds, and may cause the panel to experience hard flutter (i.e., a violent transition from equilibrium to finite motions). The application of in-plane compression (e.g., due to aerodynamic heating) can significantly alter the dynamic behavior of the panel (especially when the Euler bucking load is exceeded), as could the restraining of edges from in-plane motion. Thus, transitions to various

periodic and nonperiodic motions may occur for small variations of the control parameters (i.e., compressive load and flow speed). Furthermore, composite structural components, which are preferred in aerospace applications due to their high stiffness/strength to weight ratio, are usually characterized by weak rigidities in transverse shear.

When considering the aerodynamically nonlinear analysis of panels for various edge restraint conditions, Bolotin (1963) obtained hard (dangerous) and soft (benign) flutter scenarios, Librescu (1965) determined the nature of the flutter boundary, and McIntosh (1973) obtained nonsymmetric limit cycles and the critical loads yielding amplitude-sensitive instability. Holmes (1977) showed that a buckled equilibrium may coexist with flutter about the flat state, and that the transition from a buckled state to non-sinusoidal (periodic) flutter [see also Dowell (1966, 1984) and Shiau & Lu (1992)] occurs via a sudden jump.

Dowell (1982) showed that chaotic motions [also obtained by Shiau & Lu (1992) for composite panels, and by Yuen & Lau (1991)] may be suppressed by increasing the static pressure load. Chaos via period-doubling and intermittency was observed by Dowell (1984) while increasing the compressive load [cf. Swinney (1983) and Seydel (1988) for chaos scenarios]. Aperiodic motions and coexistence of many stable and unstable limit cycles were discovered by Yuen & Lau (1991). When penetrating the chaotic regime by increasing the compression, Dowell & Virgin (1990) observed a temporal loss of correlation (i.e., temporal chaos) followed by one that is spatial also (i.e., spatio-temporal chaos due to prominent higher modes). Zhao & Yang (1990) demonstrated that chaos is more likely for supersonic flow over a buckled panel than incompressible flow past an airfoil. For a fluttering plate undergoing a pull-up manoeuvre, Sipcic (1990) and Sipcic & Morino (1991) increased the manoeuvre load factor and obtained chaotic responses via intermittency, torus-bifurcation, period-doubling, and a jump phenomenon.

The primary forcing-flutter resonance problem was studied by Dzygadlo (1970). Kuo *et al* (1973) obtained higher flutter speeds (beyond which forcing-flutter and pure-forced response may coexist) when considering forcing-flutter interaction. The effect of the chord-to-length ratio on modal convergence and flutter amplitudes of a cantilevered plate was studied by Weiliang & Dowell (1991). Barai & Durvasula (1994) analysed the effects of shear deformation, ply orientation, and aspect ratio on the critical speeds of hybrid composite panels, for which they found that piston theory was the most appropriate aerodynamic model. Finite element method based analyses were done by Rao & Rao (1980), Han & Yang (1983), and Sarma & Varadan (1988) for various in-plane and out-of-plane boundary conditions, by Gray *et al* (1991) who presented results indicating the destabilizing effect of third-order piston theory aerodynamics, and by Liaw & Yang (1993) for laminated panels possessing structural uncertainties and subjected to uniform and non-uniform compression.

In the present study, the nonlinear dynamic response of a flat, laminated panel subjected to a high-supersonic gas flow of arbitrary orientation is analyzed. The model incorporates the combined effects of geometric and aerodynamic nonlinearities, transverse shear deformation, in-plane edge loads and edge restraints, and small initial geometric imperfections (e.g., manufacturing defects). Arclength continuation is used to determine the static state, periodic motions about which are obtained by a shooting technique that affords a systematic investigation of bifurcating motions as well. Direct numerical integration is considered for nonperiodic states, which are characterized using Lyapunov exponents.

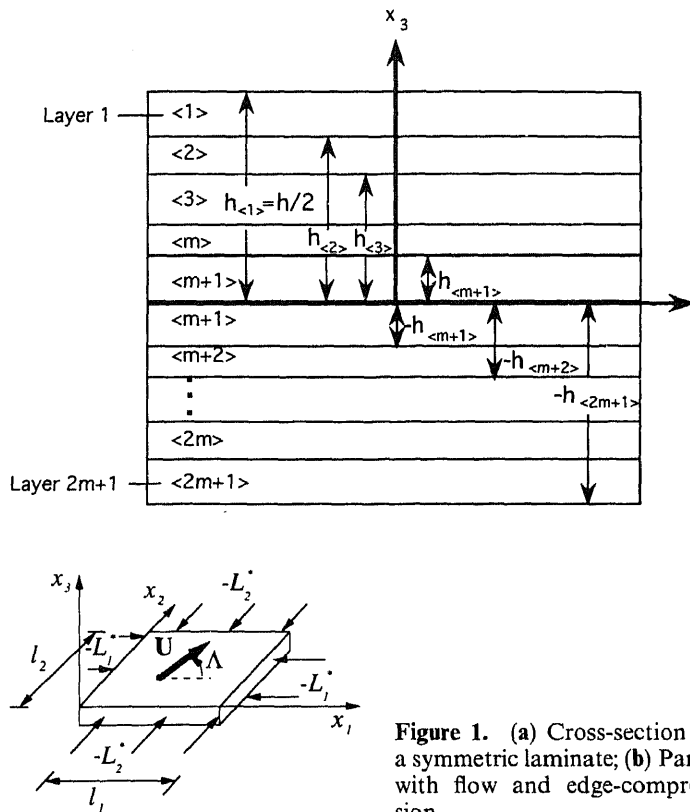


Figure 1. (a) Cross-section of a symmetric laminate; (b) Panel with flow and edge-compression.

2. Panel flutter equations

Consider a flat rectangular panel ($l_1 \times l_2$) of thickness h , symmetrically laminated with $2m + 1$ transversely isotropic layers (Librescu 1975) having their plane of isotropy parallel to the mid-plane. Furthermore, (x_3, x_ω) are orthogonal Cartesian axes, and the undeformed mid-plane ($x_3 = 0$) contains x_ω ($\omega = 1, 2$) (cf. figure 1).

The governing equations are obtained by following Librescu & Reddy (1989), Librescu & Stein (1991), Chandiramani (1993), and Chandiramani *et al* (1994), and by considering quasi-steady, third-order piston theory aerodynamics (e.g., Bolotin (1963)). Thus, for a shear-deformable, simply-supported panel subjected to a high-supersonic flow, the HSDT (higher-order shear deformation theory) equations describing the large lateral motion $u_3[x_\omega, t]$ (measured from the initially unstressed, imperfect state $\hat{u}_3[x_\omega]$) are

$$\begin{aligned}
 & (\bar{b} + \bar{c})C_{,\omega\omega\pi\pi} + 0.5(u_{3,\omega\omega}u_{3,\pi\pi} + 2u_{3,\omega\omega}\hat{u}_{3,\pi\pi} - u_{3,\omega\pi}u_{3,\omega\pi} - 2u_{3,\omega\pi}\hat{\mu}_{3,\omega\pi}) + \\
 & 2\delta_H\bar{d}(u_{3,\pi\omega\omega}u_{3,\pi} + u_{3,\pi\omega\omega}\hat{u}_{3,\pi} + \hat{u}_{3,\pi\omega\omega}u_{3,\pi} + u_{3,\pi\omega}u_{3,\pi\omega} + 2u_{3,\pi\omega}\hat{u}_{3,\pi\omega}) = 0 \\
 & Du_{3,\omega\omega\alpha\alpha} - \varepsilon_{\alpha\omega}\varepsilon_{\beta\rho}[C_{,\omega\rho}\{u_{3,\alpha\beta} + \hat{u}_{3,\alpha\beta}\} - S(C_{,\omega\rho}\{u_{3,\alpha\beta} + \hat{u}_{3,\alpha\beta}\}),_{\pi\pi}] - \\
 & \mathcal{A}[u_3 + \hat{u}_3] + S\mathcal{A}[u_3 + \hat{u}_3]_{,\alpha\alpha} + m_0[\ddot{u}_3 + c\dot{u}_3 - T(\dot{u}_{3,\alpha\alpha} + c\dot{u}_{3,\alpha\alpha})] = 0
 \end{aligned}$$

where

$$\begin{aligned} \mathcal{A}[\cdot] = & -\kappa\rho_\infty\delta_f\left\{\frac{1}{c_\infty}\left[\frac{\partial[\cdot]}{\partial t}+U_\infty\cos\Lambda\frac{\partial[\cdot]}{\partial x_1}+U_\infty\sin\Lambda\frac{\partial[\cdot]}{\partial x_2}\right]\right. \\ & +\frac{\kappa+1}{4}\delta_fM^2\left[\cos^2\Lambda\left(\frac{\partial[\cdot]}{\partial x_1}\right)^2+\sin^2\Lambda\frac{\partial[\cdot]}{\partial x_1}\frac{\partial[\cdot]}{\partial x_2}+\sin^2\Lambda\left(\frac{\partial[\cdot]}{\partial x_2}\right)^2\right] \\ & +\frac{\kappa+1}{12}M^3\left[\cos^3\Lambda\left(\frac{\partial[\cdot]}{\partial x_1}\right)^3+3\cos^2\Lambda\sin\Lambda\left(\frac{\partial[\cdot]}{\partial x_1}\right)^2\frac{\partial[\cdot]}{\partial x_2}\right. \\ & \left.\left.+3\cos\Lambda\sin^2\Lambda\frac{\partial[\cdot]}{\partial x_1}\left(\frac{\partial[\cdot]}{\partial x_2}\right)^2+\sin^3\Lambda\left(\frac{\partial[\cdot]}{\partial x_2}\right)^3\right]\right\}. \end{aligned}$$

Equations (1)_{1,2} expressed in terms of the Airy's stress function $C[x_\omega, t]$ and the transverse deflection u_3 are referred to herein as the von-Kármán-type compatibility and transverse force equilibrium equations, respectively (see Librescu and Stein 1991), while $\mathcal{A}[\cdot]$ denotes the nonlinear aerodynamic operator whose expression (1)₃ is consistent with high supersonic flight Mach numbers. Here, \hat{u}_3 is assumed small relative to u_3 , and $\delta_H = 1$ for the HSdT. Furthermore, ε_{aw} , c , κ , p_∞ , c_∞ , U_∞ , Λ , and $M (= U_\infty/c_\infty)$ are the 2D permutation symbol, viscous structural damping coefficient, polytropic gas coefficient, undisturbed air pressure, speed of sound, flow speed, coplanar flow angle (cf. figure 1b), and flight Mach number, respectively, and $\delta_f = 0$, $\delta_f = 2$ [$\delta_f = \hat{\delta}_f = 1$] when flow occurs past both faces (upper face only). This affords a consistent representation of either one-sided or two-sided high-supersonic flow which is modelled through the presence of aerodynamically nonlinear terms in u_3 (see (1)_{2,3}). The coefficients m_0 , \tilde{b} , \tilde{c} , \tilde{d} , D , S , and T are given in Chandiramani (1993), and the Einsteinian summation convention is implied for repeated Greek indices (which range over values 1, 2). Terms containing the coefficients S and T represent static and dynamic contributions, respectively, arising from transverse shear deformation of the composite panel, whereas D and m_0 denote the panel bending rigidity and mass per unit area, respectively. The classical plate theory (CPT) equations are obtained by considering an infinite transverse shear rigidity and $\delta_H = 0$ in (1)_{1,2}.

Considering the representations $\{u_3, \hat{u}_3\}^T = \sum_{m,n=1}^\infty \{A_{mn}(t), \hat{A}_{mn}\}^T \sin m\pi x_1/l_1 \sin n\pi x_2/l_2$ (which satisfy the out-of-plane boundary conditions), solving (1)₁ for C (cf. Chandiramani 1993, Chandiramani et al 1994), and then using Galerkin's method for (1)₂, the nondimensional panel flutter equations read

$$\begin{aligned} \ddot{a}_{rs} + [\varepsilon_S + \varepsilon_A \mathcal{G}_{rs}] \dot{a}_{rs} + \mathcal{R}_{rs} a_{rs} - [\mathcal{P}_{rs} \delta_{M1} L_1^* + \mathcal{Q}_{rs} \delta_{M2} L_2^*] (a_{rs} + \hat{a}_{rs}) \\ + \delta_f \lambda \left[\cos \Lambda \sum_{p=1}^k \mathcal{U}_{rsp} (a_{ps} + \hat{a}_{ps}) + \sin \Lambda \sum_{q=1}^l \mathcal{W}_{rsq} (a_{rq} + \hat{a}_{rq}) \right] \\ - \sum_{m=1}^k \sum_{n=1}^l [\mathcal{Z}_{rsmn} + \mathcal{Y}_{rsmn}] (a_{rs} a_{mn}^2 + \hat{a}_{rs} a_{mn}^2 + 2a_{rs} a_{mn} \hat{a}_{mn}) \\ - \sum_{p=1}^k \sum_{q=1}^l \sum_{m=1}^k \sum_{n=1}^l \sum_{i=1}^k \sum_{j=1}^l \mathcal{D}_{rspqmni} \\ \times (a_{pq} a_{mn} a_{ij} + \hat{a}_{pq} a_{mn} a_{ij} + a_{pq} \hat{a}_{mn} a_{ij} + a_{pq} a_{mn} \hat{a}_{ij}) \end{aligned}$$

$$\begin{aligned}
& + \delta_f \lambda^3 \sum_{p=1}^k \sum_{q=1}^l \sum_{m=1}^k \sum_{n=1}^l \sum_{i=1}^k \sum_{j=1}^l \mathcal{F}_{rspqmnij} \\
& \quad \times (a_{pq} a_{mn} a_{ij} + \hat{a}_{pq} a_{mn} a_{ij} + a_{pq} \hat{a}_{mn} a_{ij} + a_{pq} a_{mn} \hat{a}_{ij}) \\
& + \hat{\delta}_f \lambda^2 \sum_{m=1}^k \sum_{n=1}^l \sum_{i=1}^k \sum_{j=1}^l \mathcal{G}_{rsmnij} (a_{mn} a_{ij} + \hat{a}_{mn} a_{ij} + a_{mn} \hat{a}_{ij}) = 0, \\
& \sum_{r,s}^l, r = 1 \rightarrow k, s = 1 \rightarrow l,
\end{aligned} \tag{2}$$

where the coefficients are defined in Chandiramani (1993), and \nexists_α implies no summation over the index α . The tracer $\delta_{M\omega}$ equals 1 (0) when the edges $x_\omega = 0, l_\omega$ are movable [immovable/partially restrained] in the in-plane direction normal to the edge, and $\mathcal{G}_{rsmnij}[\mathcal{Y}_{rsmnij}]$ is 0 if the edges along the $x_1[x_2]$ direction are movable. Furthermore, $a_{mn}(=A_{mn}/h)$, $\hat{a}_{mn}(=\hat{A}_{mn}/h)$, L_ω^* , λ , ε_S , ε_A , and τ are the dimensionless modal- and imperfection-amplitudes, applied edge loads (positive in tension), flow speed, structural- and aerodynamic-damping coefficients, and time (henceforth replaced by t for convenience), respectively (cf. appendix A). The (4×1) and (2×2) cases of modal truncation were considered using *MACSYMA* ($k \times l$ truncation implies k chordwise and l spanwise modes).

3. Flutter response

For temporally constant edge loads, considering the representation $a_{ij}[t] = \tilde{a}_{ij} + \bar{a}_{ij}[t]$ and (2) yields the static aeroelastic equilibrium equations and the equations describing the motion of the panel $\bar{a}_{ij}[t]$ about its static equilibrium state \tilde{a}_{ij} . Introducing the state vectors \mathbf{y} and \mathbf{z} of dimension N and $2N$, respectively ($N = kl$), these two systems of equations have the form

$$\tilde{\mathbf{f}}[\mathbf{y}; \lambda, L_\alpha^*] = 0, \dot{\mathbf{z}} = \tilde{\mathbf{f}}[\mathbf{z}; \lambda, L_\alpha^*] \tag{3}$$

The components of $\mathbf{y}[\mathbf{z}]$ are $\tilde{a}_{ij}[\bar{a}_{ij}$ and $\dot{\bar{a}}_{ij}]$. For the (4×1) case, $\mathbf{y} \equiv \{\tilde{a}_{11}, \tilde{a}_{21}, \tilde{a}_{31}, \tilde{a}_{41}\}^T$ and $\mathbf{z} \equiv \{\bar{a}_{11}, \bar{a}_{21}, \bar{a}_{31}, \bar{a}_{41}, \dot{\bar{a}}_{11}, \dot{\bar{a}}_{21}, \dot{\bar{a}}_{31}, \dot{\bar{a}}_{41}\}^T$, and for the (2×2) case, $\mathbf{y} \equiv \{\tilde{a}_{11}, \tilde{a}_{12}, \tilde{a}_{21}, \tilde{a}_{22}\}^T$ and $\mathbf{z} \equiv \{\bar{a}_{11}, \bar{a}_{12}, \bar{a}_{21}, \bar{a}_{22}, \dot{\bar{a}}_{11}, \dot{\bar{a}}_{12}, \dot{\bar{a}}_{21}, \dot{\bar{a}}_{22}\}^T$. Furthermore, the $N-[2N-]$ dimensional vector $\tilde{\mathbf{f}}[\tilde{\mathbf{f}}][\mathbf{z}]$ is a nonlinear function of $\mathbf{y}[\mathbf{z}]$.

3.1 Determination of static equilibrium state and its stability

The arclength continuation method (ACM, e.g., Seydel 1988, Nayfeh & Balachandran 1994) is used to solve (3)₁. Varying one of the control parameters, e.g., λ , parametrizing (3)₁ in terms of the arclength s along a solution branch, and considering the Euclidean arclength normalization, one obtains

$$\tilde{\mathbf{f}}[\mathbf{y}[s]; \lambda[s]] = 0, (y_1 - y_1^*)^2 + \dots + (y_N - y_N^*)^2 + (\lambda - \lambda^*)^2 - ds^2 = 0, \tag{4}$$

where $(\mathbf{y}^*, \lambda^*)$ and (\mathbf{y}, λ) denote solutions for parameter values s^* and $s(=s^* + ds)$, respectively. The continuation scheme is initiated by solving (3)₁ for a specified λ . Thereafter, the solution branch is generated by considering $\mathbf{y}^* = \mathbf{y}$ and $\lambda^* = \lambda$ for each subsequent arclength step of specified size (ds), and solving (4) for (\mathbf{y}, λ) using the

Newton-Raphson method. The direction of continuation is governed by the initial guess provided for any one unknown, e.g., λ . A good initial guess for λ is $\lambda^* \pm ds$, with the choice $+/ -$ determining the continuation direction which is suitably altered in order to negotiate a turning point.

The Jacobian $\mathbf{J}_1 \equiv \nabla_{\mathbf{y}} \tilde{\mathbf{f}}$, where $\nabla_{\mathbf{y}}(\cdot) \equiv [\partial(\cdot)/\partial y_1, \dots, \partial(\cdot)/\partial y_N]$, is singular (with rank $N - 1$) at turning points and branch points. Moreover, the $(N + 1) \times N$ 'augmented matrix' $\tilde{\mathbf{A}} \equiv [\nabla_{\mathbf{y}} \tilde{\mathbf{f}} | \partial \tilde{\mathbf{f}} / \partial \lambda]$ has rank $N [< N]$ at a turning point (branch point). Thus, by monitoring the eigenvalues of both \mathbf{J}_1 and the matrices formed by eliminating the i th column ($i = 1 \rightarrow N$) of $\tilde{\mathbf{A}}$, the passing of turning points and branch points is detected. Branch points did not occur in the examples of this study.

The local stability of the static equilibrium state is determined from the eigenvalues of the Jacobian $\mathbf{J}_2 \equiv \nabla_{\mathbf{z}} \tilde{\mathbf{f}}|_{\mathbf{z}=0}$, whereby if every (any) eigenvalue resides in the left-[right-] half complex plane the state is asymptotically stable (unstable). As the control parameter (or arclength parameter) is varied, a Hopf bifurcation occurs at $(\mathbf{y}_0, \lambda_0)$ if \mathbf{J}_2 has a simple pair of pure imaginary eigenvalues (undergoing a transverse crossing of the imaginary axis) and no other eigenvalues with zero real part. At the bifurcation point, the static equilibrium state loses its asymptotic stability and a periodic solution of $(3)_2$ is born (e.g., Seydel 1988), i.e., flutter ensues. A supercritical (subcritical) Hopf bifurcation is characterized by stable (unstable) periodic solutions beyond (before) the bifurcation point, yielding soft (hard) flutter. The control parameter values at the Hopf bifurcation are termed the critical or flutter values.

3.2 Dynamic solutions and bifurcation behavior

The amplitudes of flutter oscillation about the static equilibrium state may be obtained by a direct numerical integration (NIM1) of the initial value problem (IVP) defined by $(3)_2$ and some initial conditions. However, convergence to a steady state is often very slow and strongly influenced by the choice of initial conditions. Thus, when seeking a periodic solution (i.e., the state and period T) of the autonomous system $(3)_2$, a shooting technique (NIM2) is considered (e.g., Parker & Chua (1989), Nayfeh & Balachandran (1994)). This consists of a predictor and a Newton-Raphson type corrector. An initial condition \mathbf{v} (a $2N$ -dimensional vector) that lies on the limit cycle (periodic solution) is sought, whereby the IVP is transformed into the two-point BVP

$$\dot{\mathbf{z}} = \tilde{\mathbf{f}}[\mathbf{z}; \lambda, L_x^*], \mathbf{z}[0; \mathbf{v}] = \mathbf{v}, \mathbf{z}[T; \mathbf{v}] = \mathbf{v}, \text{ where } \mathbf{z} = \mathbf{z}[t; \mathbf{v}]. \quad (5)$$

The corrections $(\delta \mathbf{v}, \delta T)$ to an initial guess (\mathbf{v}_0, T_0) are governed by the periodicity condition $\mathbf{z}[T_0 + \delta T; \mathbf{v}_0 + \delta \mathbf{v}] = \mathbf{v}_0 + \delta \mathbf{v}$. Introducing $(5)_1$ into the linearized equations obtained after a Taylor expansion of this condition, and augmenting the result with the Mees criterion which requires that $\delta \mathbf{v}$ be normal to $\tilde{\mathbf{f}}$, one obtains

$$\begin{aligned} \tilde{\mathbf{f}}[\mathbf{z}[T_0; \mathbf{v}_0]; \lambda, L_x^*] \delta T + [\nabla_{\mathbf{v}} \mathbf{z}[T_0; \mathbf{v}_0] - \mathbf{I}] \delta \mathbf{v} &= \mathbf{v}_0 - \mathbf{z}[T_0; \mathbf{v}_0], \\ \tilde{\mathbf{f}}^T[\mathbf{z}[T_0; \mathbf{v}_0]; \lambda, L_x^*] \delta \mathbf{v} &= \mathbf{0}. \end{aligned} \quad (6)$$

In the linear algebraic system (6), \mathbf{I} is the identity matrix and $\nabla_{\mathbf{v}} \mathbf{z}$ is the Jacobian of \mathbf{z} with respect to \mathbf{v} . Differentiating $(5)_1$ with respect to \mathbf{v} , one obtains $\nabla_{\mathbf{v}} \dot{\mathbf{z}} = \nabla_{\mathbf{v}} \tilde{\mathbf{f}}$ which, upon consideration of $(5)_4$, yields a system of linear ODE's in $\partial z_i / \partial v_j$. Further, integration of $(5)_1$ subject to $(5)_2$, followed by differentiation with respect to \mathbf{v} , yields the

initial conditions for $\nabla_v \mathbf{z}$. The IVP thus obtained reads

$$\frac{d}{dt}(\nabla_v \mathbf{z}) = \nabla_z \bar{\mathbf{f}} \nabla_v \mathbf{z}, \quad \nabla_v \mathbf{z}[0; \mathbf{v}] = \mathbf{I}. \quad (7)$$

Thus, periodic solutions are obtained by the following algorithm.

Step 1-Predictor: Obtain $\mathbf{z}[T_0; \mathbf{v}_0]$ and $\nabla_v \mathbf{z}[T_0; \mathbf{v}_0]$ by numerically integrating the IVP defined by the $(2N)^2 + 2N$ ODE's (5)₁ and (7)₁ and associated initial conditions (5)₂ and (7)₂.

Step 2-Corrector: Using $\mathbf{z}[T_0; \mathbf{v}_0]$ and $\nabla_v \mathbf{z}[T_0; \mathbf{v}_0]$, solve (6) to obtain the corrections $\delta \mathbf{v}$ and δT . If $|\delta \mathbf{v}|$ and $|\delta T|$ are below a specified tolerance, the algorithm has converged onto a limit cycle with period $T = T_0$ and containing the state $\mathbf{v} = \mathbf{v}_0$. Otherwise, the updated, initial guesses, i.e., $\delta \mathbf{v} + \mathbf{v}_0 \rightarrow \mathbf{v}_0$ and $\delta T + T_0 \rightarrow T_0$, are used and the algorithm is repeated.

The stability of a periodic solution $\bar{\mathbf{z}}[t]$ is ascertained from the eigenvalues of $\nabla_v \mathbf{z}[T_A; \mathbf{v}_0]$ (i.e., the Floquet multipliers, cf. appendix B). At bifurcation values of the control parameters, the nature of the non-decaying (oscillatory) disturbance \mathbf{z}^* (which yields a bifurcating solution $\mathbf{z} = \bar{\mathbf{z}} + \mathbf{z}^*$) is governed by how the critical Floquet multiplier $\tilde{\lambda}_k$ leaves the unit circle in the complex plane. This determines the type of bifurcation that may occur (e.g., Seydel 1988, Nayfeh & Balachandran 1994).

A stable limit cycle possessing inversion symmetry (appendix B) undergoes a *symmetry breaking bifurcation* when $\tilde{\lambda}_k$ leaves the unit circle through $+$. Beyond the bifurcation point, stable, symmetry broken (unsymmetric) and unstable, symmetric limit cycles coexist, and their periods are locally preserved. A stable, symmetric [unsymmetric] limit cycle undergoes a *tangent bifurcation* when $\tilde{\lambda}_k$ leaves the unit circle through $-1[+1]$. At the bifurcation point (also called a turning point), a stable and unstable limit cycle branch merge. Beyond the bifurcation point, the solution jumps to another state which could be a dynamic one (periodic or nonperiodic). A stable, unsymmetric limit cycle undergoes a *period-doubling bifurcation* when $\tilde{\lambda}_k$ leaves the unit circle through -1 . Beyond the bifurcation point, stable, period-doubled and unstable, periodic solutions coexist, and locally the period of the former is twice that of the latter. A *secondary Hopf (Niemark) bifurcation* occurs when two complex conjugate Floquet multipliers leave the unit circle transversely. This implies a Hopf bifurcation of a stable periodic solution, which introduces an additional frequency into the bifurcating solution which is two-period quasiperiodic (phase-locked) if the two frequencies are commensurate (incommensurate). Stable, quasiperiodic (QPM) and unstable, periodic solutions usually coexist beyond the bifurcation point.

It is noted that the NIM2 cannot be used to obtain nonperiodic (i.e., quasiperiodic or chaotic) solutions, and its convergence is sensitive to the initial guess and the step size of numerical integration (especially when multiple periodic solutions coexist). The numerical integration was performed using the fifth and sixth order Runge-Kutta-Verner method (IMSL-DVERK).

3.3 Characterization of motion

The Lyapunov exponents, which measure the average exponential rates of divergence or convergence of nearby phase space trajectories, were calculated using the algorithm

and program of Wolf *et al* (1985). In this method, primary and neighboring trajectories, evolving from points at the center and surface, respectively, of an infinitesimal $2N$ -dimensional hypersphere, are obtained from the IVP (5)_{1,2} and (7). The generation of principal axes (of the hypersphere) is ensured by choosing initial conditions (7)₂, and their evolution (i.e., stretching or contraction) is computed at each specified Lyapunov time step. A Gram–Schmidt re-orthonormalization of the principal axes is done at each Lyapunov time step in order to prevent a divergence in their magnitudes. The j th Lyapunov exponent is defined as $\hat{\lambda}_j = \lim_{t \rightarrow \infty} (1/t) \log_2(d_j[t]/d_j[0])$ ($j = 1 \rightarrow 2N$), where $d_j[t]$ is the length of the j th principal axis.

The value of $\hat{\lambda}_j$ depends upon the Lyapunov time step and Runge–Kutta integration time step, and a long-time integration is required to obtain an acceptable value of $\hat{\lambda}_j$. An autonomous system (e.g., (3)₂) possesses one zero exponent (except for a stable equilibrium point), and a dissipative system (e.g., (3)₂) is characterized by $\sum_{j=1}^{2N} \hat{\lambda}_j < 0$.

Stable equilibrium points possess all negative exponents, periodic solutions have one zero and $2N - 1$ negative exponents, K -period quasiperiodic motion (i.e., with K incommensurate frequencies) possesses K zero and $2N - K$ negative exponents, whereas a chaotic attractor has at least one positive exponent (indicating an exponential expansion in the corresponding principal direction). The Lyapunov (Kaplan–Yorke) dimension d_L is calculated using $d_L \equiv m + (\hat{\lambda}_1 + \hat{\lambda}_2 + \dots + \hat{\lambda}_m)/|\hat{\lambda}_{m+1}|$ where, after ordering the exponents as $\hat{\lambda}_1 \geq \hat{\lambda}_2 \geq \dots \geq \hat{\lambda}_{2N}$, m is defined as the largest integer satisfying $\hat{\lambda}_1 + \hat{\lambda}_2 + \dots + \hat{\lambda}_m \geq 0$ (e.g., Seydel 1988, Parker & Chua 1989). Thus, d_L is equal to 0, 1, and K for a point, periodic, and K -periodic attractor, respectively. A chaotic attractor possesses a non-integer d_L .

4. Discussion of results

Unless stated otherwise, an aerodynamically nonlinear, 4×1 mode analysis is performed for a square panel with movable edges and $l_1/h = 50$, and subjected to flow past both faces with $\Lambda = 0^\circ$. A three layered composite panel ($i = 1, 2, 3$, where indices 1 and 3 represent the outer layers) is considered. The data used are: $p_\infty = 7.092 \times 10^5 \text{ N.m}^{-2}$; $c_\infty = 3.299 \times 10^2 \text{ m.s}^{-1}$; $\kappa = 1.4$; $\varepsilon_S/\varepsilon_A = 0.1$ (assumed); $h = 2.54 \text{ cm}$; $h_{\langle 2 \rangle} = 0.5 h_{\langle 1 \rangle}$ (i.e., the thickness of the core layer is twice that of the face layers, cf. figure 1a); $\hat{a}_{11} = 0.2$, (remaining $\hat{a}_{ij} = 0$); $\rho_{\langle i \rangle} = 3.064 \times 10^3 \text{ kg.m}^{-3}$; $E_{\langle 1 \rangle} = E_{\langle 3 \rangle} = 1.01 \times 10^{12} \text{ N.m}^{-2}$; $E_{\langle 1 \rangle}/E_{\langle 2 \rangle} = 10$; $E_{\langle i \rangle}/E'_{\langle i \rangle} = 5$; $E_{\langle i \rangle}/G'_{\langle i \rangle} = 40$; and $\mu_{\langle i \rangle} = \mu'_{\langle i \rangle} = 0.25$. Here $E_{\langle i \rangle}$ and $\mu_{\langle i \rangle}$ are the Young's modulus and Poisson's ratio in the plane of isotropy, respectively, whereas $E'_{\langle i \rangle}$, $\mu'_{\langle i \rangle}$, and $G'_{\langle i \rangle}$ are the Young's modulus, Poisson's ratio, and shear modulus in the planes normal to the plane of isotropy, respectively, and $\langle i \rangle$ denotes the i^{th} layer.

The following notation is used. Periodic motions are denoted as SS-stable symmetric, SB-symmetry broken, SN-stable nonsymmetric, Pn-period- n , US-unstable symmetric, and UN-unstable nonsymmetric, whereas QPM denotes quasiperiodic motions. The maximum z_1 for which $z_5 = 0$ is termed the flutter amplitude $(z_1)_{\text{max}}$.

4.1 Results using linear and nonlinear aerodynamics

A 2×2 mode, HSDT analysis of a rectangular ($\phi \equiv l_1/l_2 = 0.5$) panel with $\Lambda = 30^\circ$ is performed, Figure 2 considers linear aerodynamics and $l_1/h = 24$. Figure 2a shows that

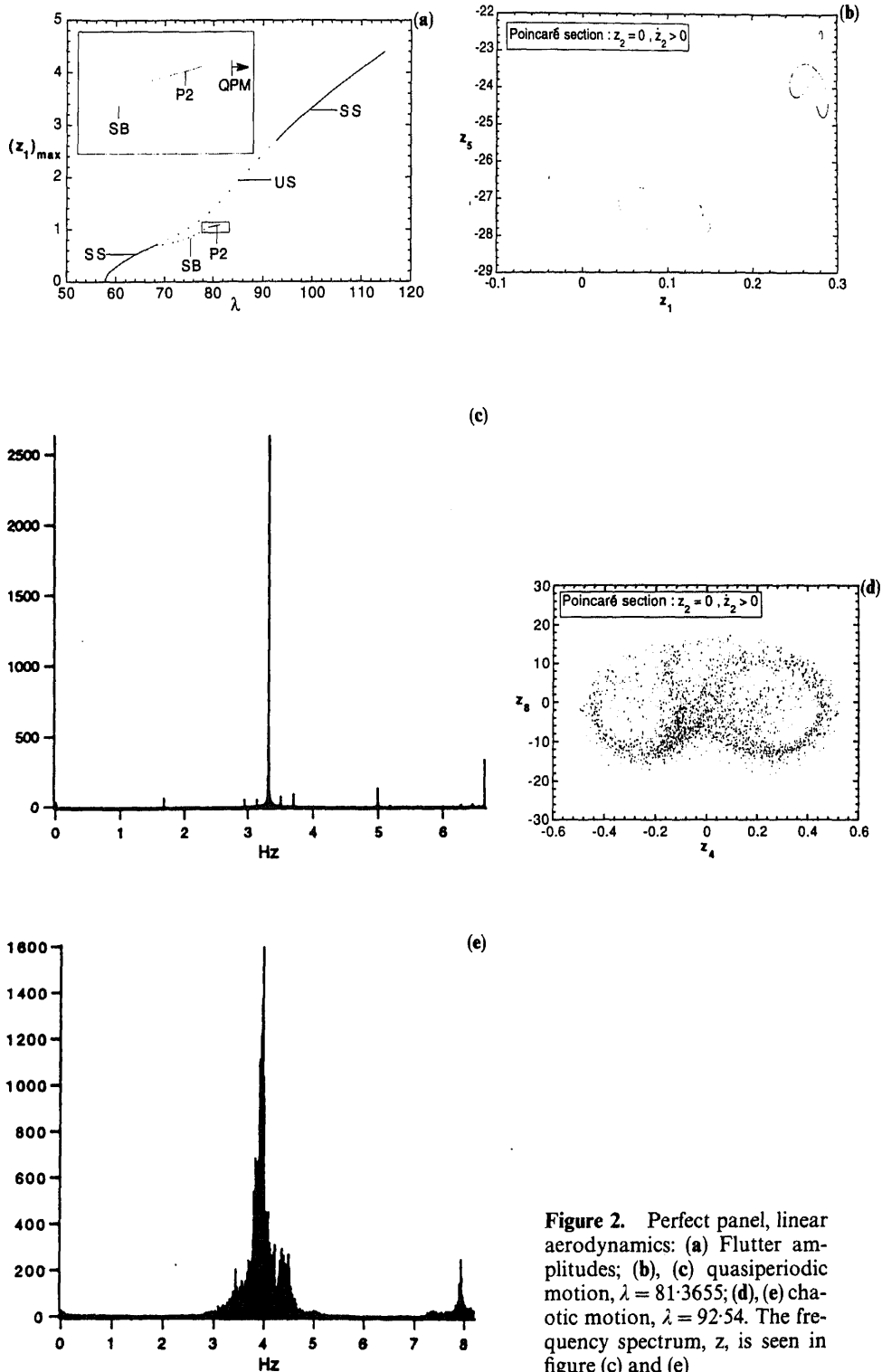


Figure 2. Perfect panel, linear aerodynamics: (a) Flutter amplitudes; (b), (c) quasiperiodic motion, $\lambda = 81.3655$; (d), (e) chaotic motion, $\lambda = 92.54$. The frequency spectrum, z , is seen in figure (c) and (e)

Table 1. Lyapunov exponents and dimension d_L .

<i>cf.</i>	$\hat{\lambda}_1$ $\hat{\lambda}_5$	$\hat{\lambda}_2$ $\hat{\lambda}_6$	$\hat{\lambda}_3$ $\hat{\lambda}_7$	$\hat{\lambda}_4$ $\hat{\lambda}_8$	Comment	d_L	Motion
Figure 2b $\lambda = 81.3655$	0.2187E-03 -0.6230E-01	-0.1688E-04 -0.1028E+00	-0.3989E-02 -0.2415E+00	-0.6216E-01 -0.2415E+00	$\hat{\lambda}_1 \approx 0$, $\hat{\lambda}_2 \approx 0$	≈ 2.00	2-period QPM
Figure 2d $\lambda = 92.54$	0.8308E+00 -0.7561E-01	0.2289E-01 -0.1349E+00	0.4776E-04 -0.2146E+00	-0.3047E-01 -0.1112E+01	$\hat{\lambda}_3 \approx 0$	7.36	chaotic
Figure 5b $L_1^* = -6.235$	0.9138E+00 -0.5223E+00	0.3802E+00 -0.9506E+00	0.1059E-02 -0.1205E+01	-0.1167E+00 -0.1769E+01	$\hat{\lambda}_3 \approx 0$	5.69	chaotic
Figure 6c $\lambda = 36.9456$	0.1907E+01 -0.4089E+00	-0.1439E-05 -0.4165E+00	-0.4013E+00 -0.7038E+00	-0.4085E+00 -0.2837E+01	$\hat{\lambda}_2 \approx 0$	6.38	chaotic
Figure 6d $\lambda = 34.8739$	0.1579E+01 -0.4286E+00	0.5187E+00 -0.6644E+00	0.9115E-04 -0.1415E+01	-0.2209E+00 -0.2638E+01	$\hat{\lambda}_3 \approx 0$	6.55	chaotic
Figure 7b $L_1^* = -15.928$	0.2005E-03 -0.4328E+00	-0.1669E-04 -0.4329E+00	-0.3942E+00 -0.8025E+00	-0.3944E+00 -0.8028E+00	$\hat{\lambda}_1 \approx 0$, $\hat{\lambda}_2 \approx 0$	≈ 2.00	2-period QPM
Figure 7b $L_1^* = -15.968$	0.6388E-03 -0.4359E+00	0.7795E-04 -0.4360E+00	-0.3956E+00 -0.6264E+00	-0.3958E+00 -0.9703E+00	$\hat{\lambda}_1 \approx 0$, $\hat{\lambda}_2 \approx 0$	≈ 2.00	2-period QPM

the flutter motion undergoes a symmetry-breaking bifurcation followed by a period-doubling and subsequently a bifurcation to quasiperiodic motion at $\lambda = 81.3654$ (2-period QPM, cf. table 1 for $\lambda = 81.3655$). The Poincaré section in figure 2b verifies this transition from P2 motion to QPM by indicating a transformation of two discrete points into two closed loops. Figure 2c displays the associated frequency spectrum. This contains sidebands around the fundamental frequency and its higher- and sub-harmonics, thus indicating the presence of additional, incommensurable frequencies. At $\lambda = 92.64$ (i.e., the second symmetry-breaking bifurcation point), the US solution regains its stability. For $\lambda = 92.54$, a phase trajectory (not included) indicating bounded, nonperiodic motion between the US and two neighboring unstable-SB limit cycles is obtained. Furthermore, the emerging pattern in figure 2d, the broadbanded frequency spectrum in figure 2e, and data in table 1 indicate that this motion is chaotic. This scenario for chaos conforms to the conjecture that chaotic motion could emerge when all coexisting equilibria (static or dynamic) are unstable (e.g., Dowell 1984).

Figure 3 displays results for flow past the upper face (i.e., second- and third-order aerodynamic nonlinearities present, cf. Case I) and past both faces (i.e., only third-order aerodynamic nonlinearities present, cf. Cases II and III). The P2 motion for Case I ($l_1/h = 100$) undergoes a bifurcation to QPM. For Case II ($l_1/h = 100$), the SB solution bifurcates to QPM, and the SS branch (occurring after the US solution regains its stability) approaches a turning point ($\lambda \approx 160.45$) beyond which a jump in response is expected. A subcritical Hopf bifurcation occurs at $\lambda = \lambda_F = 74.49$ for Case III ($l_1/h = 50$). This implies that hard flutter motion occurs when $\lambda > \lambda_F$, and could also occur for $\lambda < \lambda_F$ if the flat panel is appropriately disturbed.

4.2 Flutter of compressed and buckled panels

A uniaxially compressed panel is considered ($L_1^* < 0$). Stability boundaries for an imperfect panel are shown in figure 4a. As the control parameters are varied, starting from $L_1^* = \lambda = 0$ (i.e., the initially imperfect state), the stable configuration changes continuously. For low values of $-L_1^*$, a Hopf bifurcation occurs at the stability boundary and flutter ensues. At high values of $-L_1^*$ (i.e., the region marked with dots), the loss of stability results in a jump either to flutter or a new buckled state (snap-through). Depending upon the loading path (aerodynamic and compressive) considered, multiple flutter speeds are possible within a certain range of L_1^* . Furthermore, for a given flow speed, the CPT overpredicts the critical compressive load, and is insensitive to transverse shear flexibility variations, whereas the HSDT yields a lower critical compressive load for a panel with greater transverse shear flexibility. For the

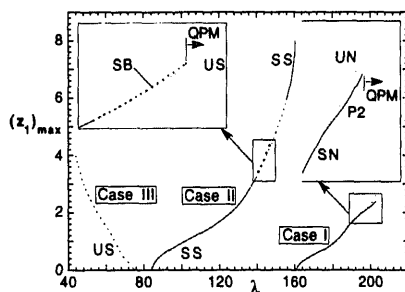


Figure 3. Flutter of perfect panel per face, flow past $l_1/h = 100$ bifurcation

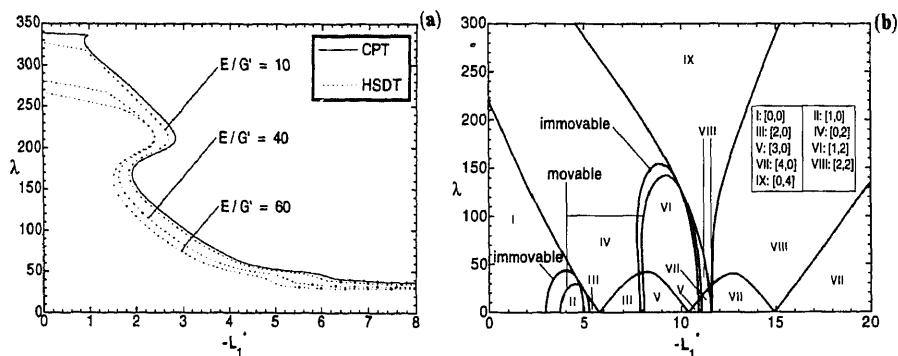


Figure 4. Stability boundaries: (a) imperfect panel; (b) perfect panel.

perfect panel, the stability of the trivial state $\{0\}$ was studied, and associated stability boundaries are shown in figure 4b. Based on $[R, C]$, where R and C are the number of real and complex eigenvalues of J_2 residing in the right-half complex plane, respectively, the $\lambda - L_1^*$ plane is divided into regions I-IX. The trivial solution is stable in I and undergoes divergence instability when crossing into II, and flutter instability (as the result of a Hopf bifurcation $H\{0\}$) when crossing into IV. However, as will be seen later, this is not the only mechanism for the onset of flutter. Buckled equilibria exist in II and III. Figure 4b reveals that restraining the edges parallel to the flow lowers the divergence

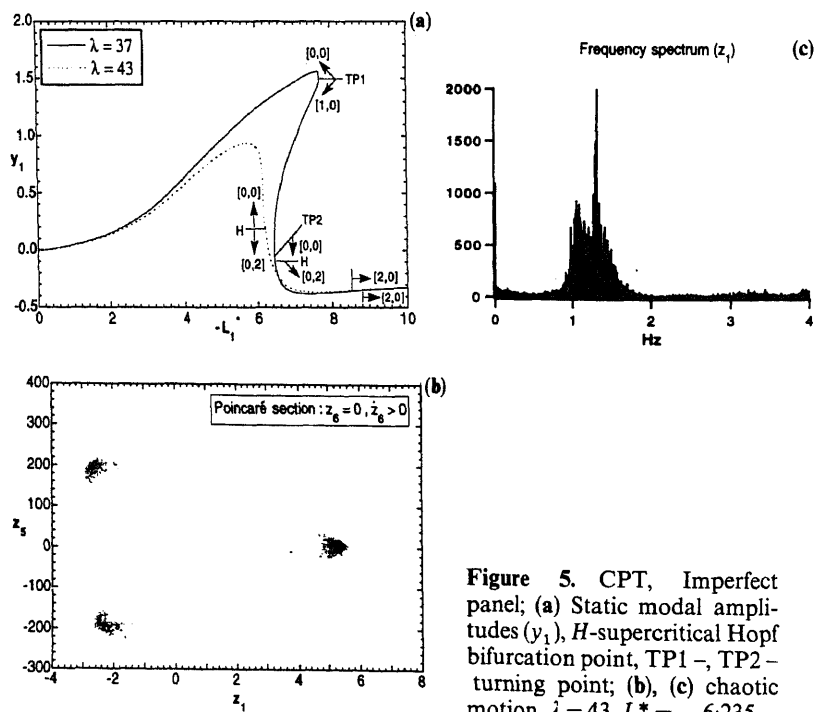


Figure 5. CPT, Imperfect panel; (a) Static modal amplitudes (y_1), H -supercritical Hopf bifurcation point, TP1 - TP2 - turning point; (b), (c) chaotic motion, $\lambda = 43$, $L_1^* = -6.235$.

Table 2. Motion past H ($\lambda = 43$, cf. figure 5a).

$-L_1^*$	T	$(z_1)_{\max}$	Motion type	Stability
0.620518E+01	0.5005E+00	0.25023E-03	SN	Stable
0.621268E+01	0.5117E+00	0.87581E-01	UN	Unstable
0.621268E+01	0.1023E+01	0.15611E+00	P2	Stable
0.621338E+01	0.1028E+01	0.17596E+00	P2	Unstable
0.621338E+01	0.2056E+01	0.17604E+00	P4	Stable
0.621349E+01	0.2057E+01	0.17770E+00	P4	Unstable
0.621349E+01	0.4115E+01	0.17773E+00	P8	Stable

compressive load and increases the flow speed required for flattening (which occurs when crossing from II into I), whereas it does not visibly affect the flutter speed.

For the imperfect panel, the region in the $\lambda - L_1^*$ plane where the transition from Hopf-bifurcation instability to jump-type instability occurs was studied (i.e., transition to the region marked with dots in figure 5a). The variation of the static solution (y_1) with L_1^* is shown in figure 5a. As the compressive load is increased, with $\lambda = 43$, initially the deformation increases and then the panel tends to flatten until a Hopf bifurcation (H) occurs, resulting in soft flutter about the equilibrium state. The motion begins as an SN limit cycle, then undergoes a sequence of period-doubling bifurcations resulting in P2 up to P8 motion (cf. table 2), and finally becomes chaotic (cf. figure 5b and c, and table 1 for $L_1^* = -6.235$ which is well past the P8 motion value). Thus, chaotic motion has resulted after a period-doubling sequence. For $\lambda = 37$, motion about TP1 and motion past H (cf. tables 3 and 4, respectively) indicate that for a range of L_1^* , the static state coexists with either periodic or quasiperiodic motions, i.e., the panel can remain buckled or can flutter. A similar observation was made by Holmes (1977) for a perfect panel undergoing cylindrical bending.

For the perfect panel, the region in the $\lambda - L_1^*$ plane where the divergence and flutter boundaries meet was studied (cf. figure 4b). Figure 6a shows the static solution (y_1) for $L_1^* = -5.5$, -5.8 , and -6.2 when λ is varied. It also shows the stable motion ($(z_1)_{\max}$) past $H\{0\}$ for $L_1^* = -5.5$ (for $L_1^* = -5.8$, cf. table 5). For $L_1^* = -5.5$, as λ is increased the buckled panel gradually flattens out and then flutters beyond $H\{0\}$. It is seen that for $L_1^* = -5.8$ (cf. table 5 which reveals a period-doubling sequence) there exists a range of λ for which the panel can either remain buckled or flutter about $\{0\}$. Increasing λ for $L_1^* = -5.8$, when passing the TP a sudden transition from the buckled state to periodic

Table 3. Stable motion about TP1 at $L_1^* = -7.712$ (cf. figure 5a).

$-L_1^*$	T	$(z_1)_{\max}$	Motion type
0.7602E+01			QPM
0.7712E+01	0.2774E+00	0.5599E+00	SN
0.7912E+01			QPM

Table 4. Stable motion past $H(\lambda = 37, \text{cf. figure 5a})$.

$-L_1^*$	T	$(z_1)_{\max}$	Motion type
0.643286E+01	0.6604E+00	0.1350E-03	SN
0.643415E+01	0.1343E+01	0.3968E-01	P2
0.643418E+01	0.2688E+01	0.5965E-01	P4
0.643419E+01	0.5379E+01	0.6017E-01	P8

motion about $\{0\}$ occurs. The motion, shown in figure 6b for $\lambda = 36.8456$, consists of the panel snapping back and forth, and vibrating about multiple unstable equilibria (similar limit cycles were obtained by Sipcic & Morino 1991). This is followed by chaotic motion when $\lambda = 36.9456$ (cf. figure 6c and table 1). For $L_1^* = -6.2$, a buckled-chaos transition was observed when passing the TP (cf. figure 6d and table 1 for $\lambda = 34.8739$).

Next, L_1^* is varied with λ held constant. For $\lambda = 24$ and $-L_1^*$ increasing, the buckled state (cf. figure 7a) undergoes a sudden transition to QPM (cf. figure 7b and table 1)

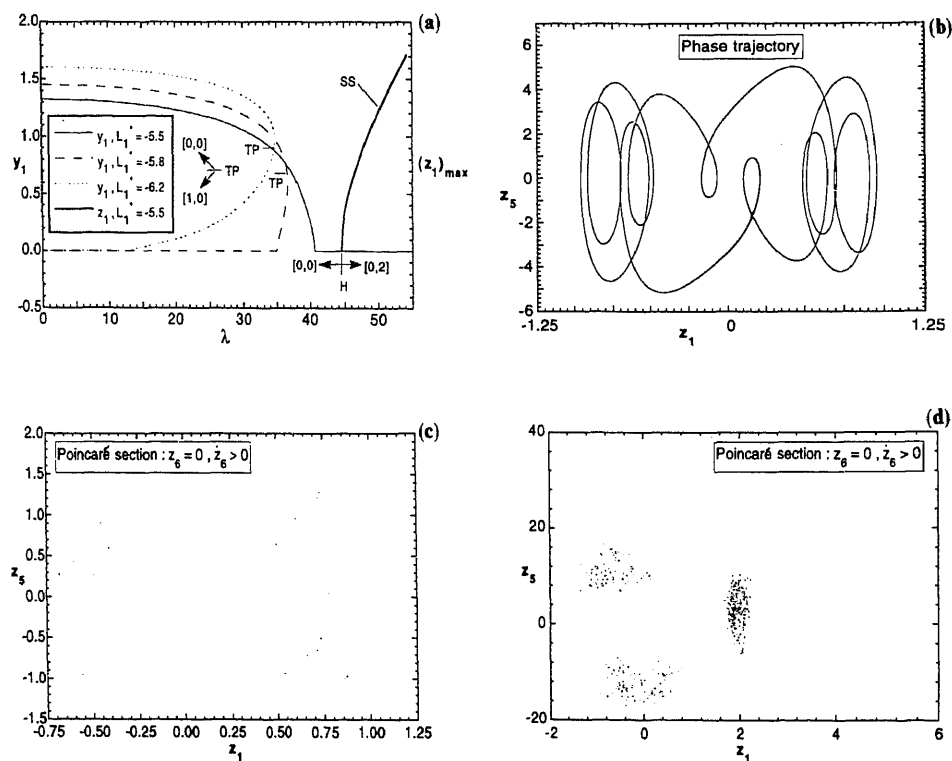
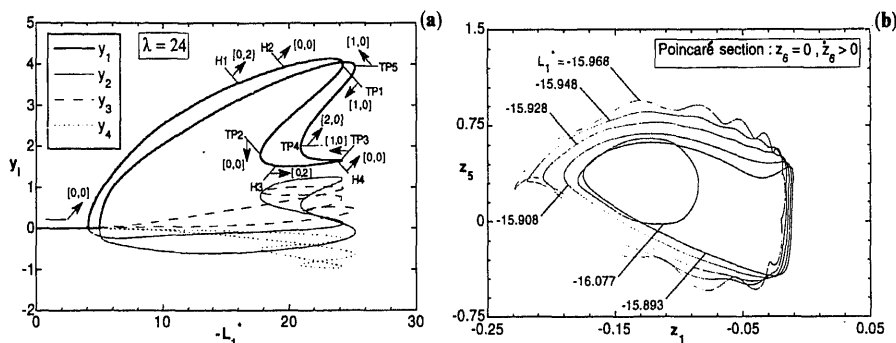


Figure 6. CPT, perfect panel; (a) Static (y_1) and dynamic ($(z_1)_{\max}$) modal amplitudes, H -supercritical Hopf bifurcation point, TP – turning point; (b) $L_1^* = -5.8$, periodic motion past TP , $\lambda = 36.8456$; (c) $L_1^* = -5.8$, chaotic motion past TP , $\lambda = 36.9456$; (d) $L_1^* = -6.2$, chaotic motion past TP , $\lambda = 34.8739$.

Table 5. Stable motion past $H\{0\}$ ($L_1^* = -5.8$, cf. figure 6a).

λ	T	$(z_1)_{\max}$	Motion type
0.351134E+02	0.1752E+01	0.6123E-02	SS
0.352254E+02	0.1652E+01	0.6768E-01	SB
0.352494E+02	0.3309E+01	0.5316E-01	P2
0.352531E+02	0.6619E+01	0.5916E-01	P4
0.352539E+02	0.1324E+02	0.6049E-01	P8
0.352540E+02	0.2648E+02	0.6076E-01	P16

**Figure 7.** HSDT, perfect panel; (a) Static modal amplitudes, $H1$ – $H3$ (subcritical), $H4$ (supercritical)–Hopf bifurcation point, $TP1$ – $TP5$ –turning point; (b) hard flutter motion (QPM) about $H1$ (cf. table 7 also).

about the nontrivial equilibrium state when passing $H1$ (subcritical, cf. table 6). The appearance of wrinkles in the Poincaré sections suggests the possibility of chaos via Torus–Bifurcation (cf. Swinney 1983) in the neighborhood of $L_1^* = -15.968$. Further increasing $-L_1^*$ results in shrinkage of the Poincaré section (cf. figure 7b) and eventually a transition from QPM to periodic motion (SN), followed by a sequence of period doubling and then QPM (cf. table 7). As $-L_1^*$ is decreased, QPM continues prior to $H1$, with the Poincaré section reducing in size (cf. figure 7b) until all motion suddenly ceases when $-L_1^* < 15.893$, i.e., the fluttering panel snaps back to the buckled state. These results show that hard flutter occurs about $H1$. The motion about $H\{0\}$ (supercritical, occurs at $L_1^* = -4.979$) and about $H4$ (supercritical), not included here, consists of a period-doubling sequence and reveals the coexistence of flutter motion with the buckled state. For $\lambda = 27$ (HSDT), the buckled panel experiences a transition

Table 6. Unstable motion prior to $H1$ (cf. figure 7a).

$-L_1^*$	T	$(z_1)_{\max}$	Motion type
0.1592E+02	0.9226E-01	0.7868E-03	UN
0.1587E+02	0.9513E-01	-0.4812E-01	UN

Table 7. Stable motion past $H1$ (cf. figure 7a, b).

$-L_1^*$	T	$(z_1)_{\max}$	Motion type
0.1607E+02			QPM
0.1617E+02	0.9983E-01	-0.1401E+00	SN
0.1647E+02	0.2021E+00	-0.1437E+00	P2
0.1681E+02	0.4110E+00	-0.1792E+00	P4
0.1683E+02			QPM

to chaos at $L_1^* = -4.965$ (chaotic at $L_1^* = -4.975$ also) which is similar to that for the case in figure 6c.

Results for a compressed, perfect panel with edges $x_2 = 0$, l_2 either movable or immovable, and edges $x_1 = 0$, l_1 movable are shown in figure 8. As the compressive load is increased with $\lambda = 40$, the restrained panel buckles, then suddenly flattens out (beyond the TP), and subsequently flutters about $\{0\}$. The unrestrained panel remains flat prior to experiencing flutter. Moreover, the edge restraint has no visible effect on the amplitudes of periodic motion in the vicinity of $H\{0\}$ and on the associated critical speed. This is so because the compression induced by the edge restraints is normal to the flow.

5 Conclusions

The nonlinear dynamic response arising from a high-supersonic flow over a uniformly compressed, shear-deformable, composite panel was studied. Third-order piston theory aerodynamics was considered along with small geometric imperfections and various in-plane boundary conditions. Periodic and nonperiodic motions were obtained using the shooting technique (NIM2) and direct numerical integration, respectively, in conjunction with arclength continuation for the static state. The results permit the following conclusions.

- Flutter of a compressed panel occurs either due to a Hopf bifurcation instability or as a jump from stable equilibrium to motion. Within the regions in the $\lambda - L_1^*$ plane

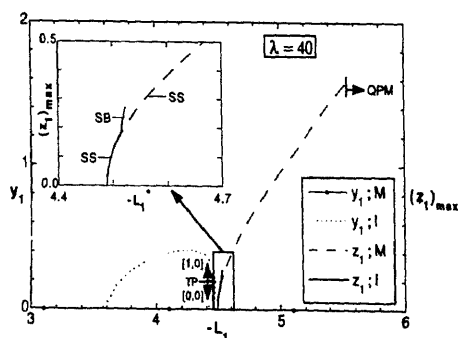


Figure 8. Effect of edge restraint on response, perfect panel, HSDT, edges $x_1 = 0$, l_1 movable (M), $x_2 = 0$, l_2 movable (M) or immovable (I), TP—turning point.

considered, it was found that periodic or quasiperiodic dynamic states may coexist with the stable static state, i.e., the panel could remain buckled or could flutter. For compressed panels, chaotic motions were obtained for imperfect panels via the period-doubling scenario, and also for perfect panels where a sudden transition from the buckled state to one of chaos (followed by complicated periodic motion) occurred. A chaotic response in the form of bounded nonperiodic motion between three unstable periodic solutions was observed for the uncompressed panel. Moreover, hard flutter motions (quasiperiodic and periodic) about the nontrivial equilibrium state can also occur.

- The restraining of edges parallel to the flow does not visibly affect the flutter speed and immediate post-critical response of perfect panels. However, the possibility of buckling prior to flutter is greater for restrained panels.
- The presence of aerodynamic nonlinearities, especially third-order ones, may cause hard flutter oscillations as well as a jump in dynamic response.
- The critical loads predicted by the HSDT [CPT] are lower (unchanged) for a panel with greater transverse shear flexibility. Moreover, the HSDT generally yields lower critical loads than the CPT.

Appendix A

Definitions of non-dimensional quantities

$$L_{\omega}^{*} \equiv \frac{L_{\omega}^{**} l_1^2}{\pi^2 D}, \lambda \equiv l_1^3 \frac{\kappa p_{\infty} U_{\infty}}{D c_{\infty}}, \tau \equiv \left(\frac{D}{m_0 l_1^4} \right)^{1/2} t, \varepsilon_S \equiv c \left(\frac{m_0 l_1^4}{D} \right)^{1/2},$$

$$\varepsilon_A \equiv \frac{\kappa p_{\infty}}{c_{\infty}} \frac{l_1^2}{(m_0 D)^{1/2}} \quad (A1)$$

Appendix B

Floquet theory and stability of the periodic solution

Applying a perturbation solution $\mathbf{z}^*[t]$ to a periodic solution $\bar{\mathbf{z}}[t]$ with period T , the following linearized disturbance equations are obtained from (3)₂:

$$\dot{\mathbf{z}}^*[t] = \hat{\mathbf{A}}[t; \lambda, L_{\alpha}^*] \mathbf{z}^*[t], \text{ where } \hat{\mathbf{A}}[t; \lambda, L_{\alpha}^*] = \nabla_{\mathbf{z}} \bar{\mathbf{f}}|_{\mathbf{z}=\bar{\mathbf{z}}}. \quad (1)$$

The period of $\hat{\mathbf{A}}$ is $T_A = T$ except when $\bar{\mathbf{f}}$ contains only odd nonlinearities and the limit cycle is symmetric (i.e., inversion symmetry implying $\bar{\mathbf{z}}[t] = -\bar{\mathbf{z}}[t + 0.5T]$), in which case $T_A = T/2$. One possible fundamental matrix solution of (B1), i.e., $\mathbf{Z}^*[t]$, is defined by the matrix IVP:

$$\dot{\mathbf{Z}}^* = \hat{\mathbf{A}}[t; \lambda, L_{\alpha}^*] \mathbf{Z}^*, \mathbf{Z}^*[0] = \mathbf{I}. \quad (B2)$$

Then, from Floquet theory one concludes that if \mathbf{Z}^* possesses distinct eigenvalues $\tilde{\lambda}_j$ (the Floquet multipliers), the system is asymptotically stable (unstable) if every (any) Floquet multiplier lies outside (inside) the unit circle whose centre is at the origin of the complex plane.

is seen that $\tilde{\Phi}$ is identical to $\nabla_z \mathbf{z}[T_A; \mathbf{v}_0]$. Hence, after a periodic solution is obtained by the shooting technique, its stability is ascertained as a by-product by determining the eigenvalues of $\nabla_z \mathbf{z}[T_A; \mathbf{v}_0]$ (e.g., Seydel 1988, Nayfeh & Balachandran 1994). Furthermore, for an autonomous system it can be shown that when $T_A = T[T_A = T/2]$, i.e., for an unsymmetric [symmetric] limit cycle, one of the Floquet multipliers is $+1 [-1]$.

Appendix

List of symbols

$A_{mn}[t], \hat{A}_{mn}$	amplitudes of lateral motion and lateral imperfection;
$a_{mn}[t], \hat{a}_{mn}$	nondimensional amplitudes of lateral motion and lateral imperfection;
$\tilde{a}_{mn}, \bar{a}_{mn}[t]$	static and dynamic components of $a_{mn}[t]$;
$\tilde{b}, \tilde{c}, \tilde{d}, S$	structural coefficients given in Chandiramani (1993);
$C[x_\omega, t]$	Airy stress function associated with in-plane stress resultants;
$c, \varepsilon_S, \varepsilon_A$	viscous structural damping coefficient, and non-dimensional structural and aerodynamic damping coefficients;
h, l_1, l_2, ϕ	thickness, length, width, and aspect ratio of panel;
$\mathbf{J}_1, \mathbf{J}_2$	Jacobian matrices for determining bifurcation and stability behavior of static state (\mathbf{y});
L_ω^*, λ	nondimensional edge-load and flow speed parameters;
m_0, D	mass per unit area and bending rigidity of panel;
s	arclength parameter;
U_∞, M, Λ	flow speed, Mach number, and coplanar flow angle;
$u_3[x_\omega, t], \hat{u}_3[x_\omega]$	lateral motion and lateral imperfection;
$\mathbf{y}, \mathbf{z}[t]$	state vectors associated with $\tilde{a}_{mn}, \bar{a}_{mn}[t]$;
$\tilde{\mathbf{z}}[t], \mathbf{z}^*[t]$	periodic solution of \mathbf{z} and corresponding applied disturbance tracers associated with HSDT, in-plane edge restraints, one-sided flow and two-sided flow;
$\delta_H, \delta_{M\omega}, \delta_f, \hat{\delta}_f$	polytropic gas coefficient, undisturbed air pressure, and speed of sound;
$\kappa, p_\infty, c_\infty$	Lyapunov exponents and associated dimension, initial condition and period associated with limit cycle;
$\hat{\lambda}_j, d_L$	material properties of i th layer, i.e., density; Young's modulus and Poisson's ratio in the plane of isotropy; Young's modulus, shear modulus, and Poisson's ratio in planes normal to the plane of isotropy;
\mathbf{v}, T	monodromy matrix and its eigenvalues (Floquet multipliers).
$\rho_{(i)}, E_{(i)}, \mu_{(i)}$	
$E'_{(i)}, G'_{(i)}, \mu'_{(i)}$	
$\tilde{\Phi}, \tilde{\lambda}_k$	

References

- Barai A, Durvasula S 1994 Flutter of hybrid laminated flat panels with simply supported edges in supersonic flow. *J. Sound Vib.* 169: 373–386
- Bolotin V V 1963 *Nonconservative problems of the theory of elastic stability* (New York: Macmillan)
- Chandiramani N K 1993 *Nonlinear flutter of composite shear-deformable panels in a high-supersonic flow* PhD dissertation, Virginia Polytechnic Institute and State University, Blacksburg

- Chandiramani N K, Librescu L I, Plaut R H 1994 Flutter of geometrically-imperfect shear-deformable composite panels using nonlinear aerodynamics. *J. Sound Vib.* (accepted)
- Dowell E H 1966 Nonlinear oscillations of a fluttering plate. *AIAA J.* 4: 1267–1275
- Dowell E H 1982 Flutter of a buckled plate as an example of chaotic motion of a deterministic autonomous system. *J. Sound Vib.* 85: 333–344
- Dowell E H 1984 Observation and evolution of chaos for an autonomous system. *J. Appl. Mech.* 51: 664–673
- Dowell E H, Virgin L N 1990 On spatial chaos, asymptotic modal analysis, and turbulence. *J. Appl. Mech.* 57: 1094–1097
- Dzygadlo Z 1970 Local analysis of nonlinear forced vibration of a plate of finite length in plane supersonic flow. *Proc. Vib. Probl.* 11: 353–368
- Gray C E, Mei C, Shore C P 1991 Finite element method for large-amplitude two-dimensional panel flutter at hypersonic speeds. *AIAA J.* 29: 290–298
- Han A D, Yang H T Y 1983 Nonlinear panel flutter using high-order triangular finite elements. *AIAA J.* 21: 1453–1461
- Holmes P J 1977 Bifurcations to divergence and flutter in flow-induced oscillations. *J. Sound Vib.* 53: 471–503
- Kuo C C, Morino L, Dugundji J 1973 Nonlinear interaction of panel flutter with harmonic forcing excitation. *AIAA J.* 11: 419–420
- Liaw D G, Yang H T Y 1993 Reliability and nonlinear supersonic flutter of uncertain laminated plates. *AIAA J.* 31: 2304–2311
- Librescu L 1965 Aeroelastic stability of orthotropic heterogeneous thin panels in the vicinity of the flutter critical boundary - Part I. *J. Méc.* 4: 51–76
- Librescu L 1975 *Elastostatics and kinetics of anisotropic and heterogeneous shell type structures* (Leyden: Noordhoff International Publishers)
- Librescu L, Reddy J N 1989 A few remarks concerning several refined theories of anisotropic composite laminated plates. *Int. J. Eng. Sci.* 27: 515–527
- Librescu L, Stein M 1991 A geometrically nonlinear theory of transversely isotropic laminated composite plates and its use in the postbuckling analysis. *Thin-Walled Struct.* 11: 177–201
- McIntosh S C 1973 Effect of hypersonic nonlinear aerodynamic loading on panel flutter. *AIAA J.* 11: pp 29–32
- Nayfeh A H, Balachandran B 1994 *Applied nonlinear dynamics: Analytical, computational, and experimental methods* (New York: John Wiley)
- Parker T S, Chua L O 1989 *Practical numerical algorithms for chaotic systems* (New York: Springer-Verlag)
- Rao K S, Rao G V 1980 Large amplitude supersonic flutter of panels with ends elastically restrained against rotation. *Comput. Struct.* 11: 197–201
- Sarma B S, Varadan T K 1988 Nonlinear panel flutter by finite element method. *AIAA J.* 26: 566–574
- Seydel R 1988 *From equilibrium to chaos: Practical bifurcation and stability analysis* (New York: Elsevier)
- Shiau L C, Lu L T 1992 Nonlinear flutter of two-dimensional simply supported symmetric composite laminated plates. *J. Aircraft* 29: 140–145
- Sipic S R 1990 The chaotic response of a fluttering panel: The influence of maneuvering. *Nonlinear Dyn.* 1: 243–264
- Sipic S R, Morino L 1991 Dynamic behavior of fluttering two-dimensional panels on an airplane in pull-up maneuver. *AIAA J.* 29: 1304–1312
- Swinney H L 1983 Observations of order and chaos in nonlinear systems. *Physica D* 7: 3–15
- Weiliang Y, Dowell E H 1991 Limit cycle oscillation of a fluttering cantilever plate. *AIAA J.* 29: 1929–1936
- Wolf A, Swift J B, Swinney H L, Vastano J A 1985 Determining Lyapunov exponents from a time series. *Physica D* 16: 285–317
- Yuen S W, Lau S L 1991 Effects of in-plane load on nonlinear panel flutter by incremental harmonic balance method. *AIAA J.* 29: 1472–1479
- Zhao L C, Yang Z C 1990 Chaotic motions of an airfoil with nonlinear stiffness in incompressible flow. *J. Sound Vib.* 138: 245–254



Coupled in-line and transverse flow-induced structural vibration: Higher order harmonic solutions

R GHANEM¹, P SPANOS² and S SWERDON²

¹Department of Civil Engineering, The Johns Hopkins University, Baltimore, MD 21218, USA

²Department of Civil Engineering, George R Brown School of Engineering, Rice University, Houston, TX 77251, USA

Abstract. Coupling of in-line and transverse flow-induced vibration can be significant in several structural engineering applications. In this study, a particular model already proposed in the literature is adopted. The relevant equations of this model feature nonlinearities and coupling between the two components of motion. The level of coupling depends on the relative properties of the flow and the structure. A harmonic balance technique is used to obtain an equivalent coupled system of linear equations. Higher order harmonics can be readily treated, yielding a quite general formulation which can be tailored to match the available computational resources. A parametric study is conducted using the proposed technique, and insight regarding the significance of the coupling of the two components of motion on the overall structural response is obtained. The proposed technique is applicable to any other refined model of coupling of in-line and transverse flow-induced vibration which may become available based on theoretical or experimental fluid mechanics developments.

Keywords. Offshore structures; vibrations; harmonic balance; vortex dynamics.

1. Introduction

The mechanics of wave forces on structures is an important aspect of engineering. Of these, vortex-induced oscillations is probably one of the most difficult to quantify. Theoretical justifications of vortex-induced oscillations have proceeded hand in hand with experimental verifications (Griffin *et al* 1973; Blevins 1990). A comprehensive review of the state-of-the-art on this topic was presented by Sarpkaya (Sarpkaya 1979). Some structures can be viewed as undergoing oscillations which are governed, in the in-line direction (parallel to the flow) by Morrison's equation (Blevins 1990). This equation, by

itself, cannot account for the observed transverse oscillations along a direction perpendicular, or transverse, to the flow. The magnitude of these transverse oscillations can be such that ignoring them may yield unconservative estimates of the associated structural loads. This problem can be remedied by including vortex-induced forces in the equations governing the motion of the structure. The inclusion of these forces results in two coupled differential equations which must be solved simultaneously. The numerical integration of these equations, although not trivial, is possible using specialized numerical analysis tools (Griffin *et al* 1973). In many instances, however, the cost of computation is significant, and a quick good estimate of the behavior of the structure is more valuable than an accurate result which may require unavailable numerical codes. This fact has prompted a number of researchers to seek approximations to the solution of the coupled system of equations using various techniques. The most important of these simplifications involve transposing the problem to the frequency domain. Invariably, this procedure has been carried out either by linearizing the equations of motion (Rajabi *et al* 1984) after uncoupling them, or by linearizing the equations in the in-line direction and neglecting the motion in the transverse direction (Chen & Lin 1989; Spanos & Chen 1980). Obviously these simplifications are incapable of capturing the nonlinear nature of the structural system which may involve oscillations at sub-harmonic frequencies. Furthermore, these approximations neglect the effect of the coupling between the in-line and transverse oscillations; this simplification has not been validated experimentally.

In this paper, an approximate technique is presented for the solution of the coupled equations governing the motion of a structure which is modelled as a two-degree-of-freedom system. The approximation involves an expansion in higher order harmonics, thus permitting a useful representation of nonlinear effects. Also, the coupling between the two components of motion is included, and its effect is investigated by comparing the results to corresponding results associated with the uncoupled equations.

2. Equations of motion

Figure 1 shows a two-degree-of-freedom model of a vibrating structure subjected to

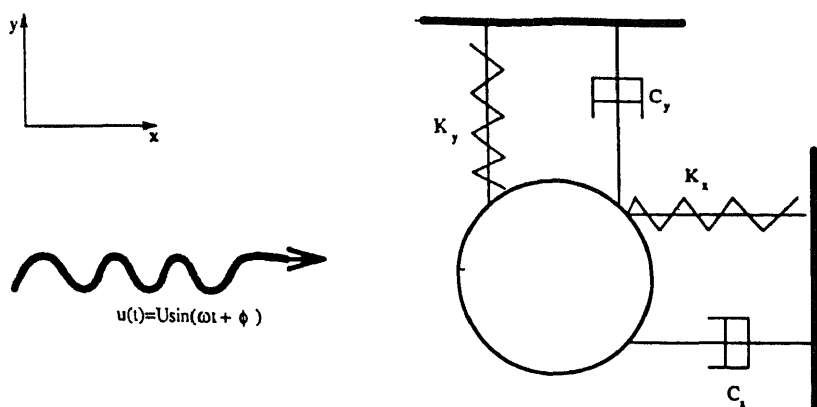


Figure 1. Two-degree-of-freedom model of an offshore structure.

loads produced by oscillatory flow. The structure is represented by a cylindrical component whose planar motion is restrained by two viscous dampers and two linear springs. The current velocity is assumed to be zero, and the cylinder is subjected to an oscillating flow of magnitude U . This does not affect the development of the general solution technique. In addition to this externally applied flow, vortex and flow-induced oscillations will develop in the form of excitations which are nonlinear functions of the response in both the in-line and the transverse directions. The motion of this simplified model is governed by the equations

$$m_0 \ddot{x} + 2\xi_0 \omega_0 m_0 \dot{x} + \omega_0^2 m_0 x = f_x(t), \quad (1)$$

and

$$m_0 \ddot{y} + 2\xi_0 \omega_0 m_0 \dot{y} + \omega_0^2 m_0 y = f_y(t). \quad (2)$$

In the above equations x and y denote the motion of the structure in the x and y directions respectively, while $f_x(t)$ and $f_y(t)$ denote the resultant forces acting, respectively, along these directions. The excitations $f_x(t)$ and $f_y(t)$ are composed of a drag component f_D , an added mass component, f_I , and a component f_V which is due to vortex shedding at a frequency ω_v . The combined excitations can be written as (Rajabi *et al* 1984; Dailey *et al* 1987)

$$\begin{aligned} f_x(t) &= f_{xD} + f_{xI} + f_{xV} \\ &= \frac{1}{2} C_D \rho D ((\dot{u} - \dot{x})^2 + \dot{y}^2)^{1/2} (\dot{u} - \dot{x}) + C_M \rho A (\ddot{u} - \ddot{x}) + \rho A \ddot{x} \\ &\quad - \frac{1}{2} C_L \rho D ((U_v - \dot{x})^2 + \dot{y}^2)^{1/2} |\dot{y}| \cos(\omega_v t), \end{aligned} \quad (3)$$

and

$$\begin{aligned} f_y(t) &= f_{yD} + f_{yM} + f_{yV} \\ &= -\frac{1}{2} C_D \rho D ((\dot{u} - \dot{x})^2 + \dot{y}^2)^{1/2} \dot{y} + (1 - C_M) \rho A \ddot{y} \\ &\quad + \frac{1}{2} C_L \rho D ((U_v - \dot{x})^2 + \dot{y}^2)^{1/2} |U_v - \dot{x}| \cos(\omega_v t), \end{aligned} \quad (4)$$

where

$$\dot{u} = \omega U (-\sin(\omega t) + \cos(\omega t)) \quad (5)$$

denotes the water particle velocity which is assumed, without loss of generality, to be in the x direction. In the above equations C_D denotes a drag coefficient, C_M denotes an added mass coefficient and C_L denotes a coefficient. Furthermore, the symbols ρ , D , and A denote the density of the fluid, the cross-sectional area of the immersed cylinder, and its diameter, respectively. It will prove practical for the subsequent development to use the nondimensional time τ defined by the equation

$$\tau = \omega t. \quad (6)$$

It will also prove expedient to define the following normalized coefficients

$$C_A = C_M - 1, \quad (7)$$

$$\xi_N = \xi_0 (m_0/m)^{1/2}, \quad (8)$$

$$\omega_N = \omega_0 (m_0/m)^{1/2}, \quad (9)$$

$$\beta = \omega/\omega_N, \quad (10)$$

$$m = m_0 + C_A \rho A, \quad (11)$$

$$\mu = U/D, \quad (12)$$

and

$$U_v = \omega U. \tag{13}$$

Furthermore, let the function $v(t)$ be represented by the equation

$$v(t) = \cos(t) - \sin(t). \tag{14}$$

Using the above notation, and denoting differentiation with respect to τ by a prime, the equation of motion in the x direction becomes

$$x'' + 2\xi_0(\omega_0/\omega)x' + (\omega_0/\omega)^2x = f_x(t)/(m_0\omega^2). \tag{15}$$

Substituting equation (3) for $f_x(t)$ gives

$$\begin{aligned} x'' + 2\xi_0\frac{\omega_0}{\omega}x' + \left(\frac{\omega_0}{\omega}\right)^2x &= \frac{1}{2}\frac{C_D\rho D}{m_0}((u' - x')^2 + y'^2)^{1/2}(u' - x') \\ &+ \frac{C_M\rho A}{m_0}(u'' - x'') + \frac{\rho A}{m_0}x'' - \frac{1}{2}\frac{C_L\rho D}{m_0}((U_v - x')^2 + y'^2)^{1/2}|y'|\cos\left(\frac{\omega_v}{\omega}\tau\right), \end{aligned} \tag{16}$$

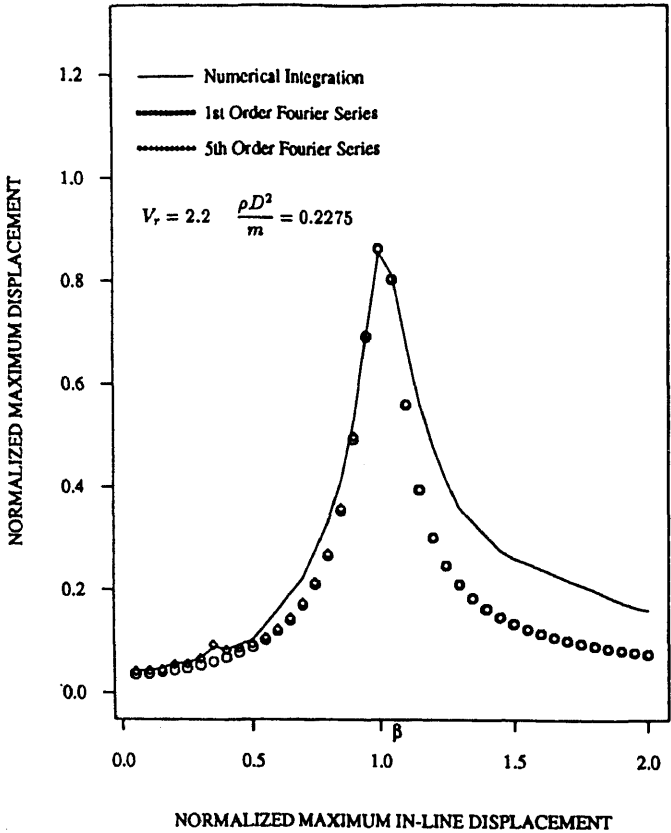


Figure 2. Maximum value of the normalized in-line displacement; $V_r = 2.2$, $\rho D^2/m = 0.2275$.

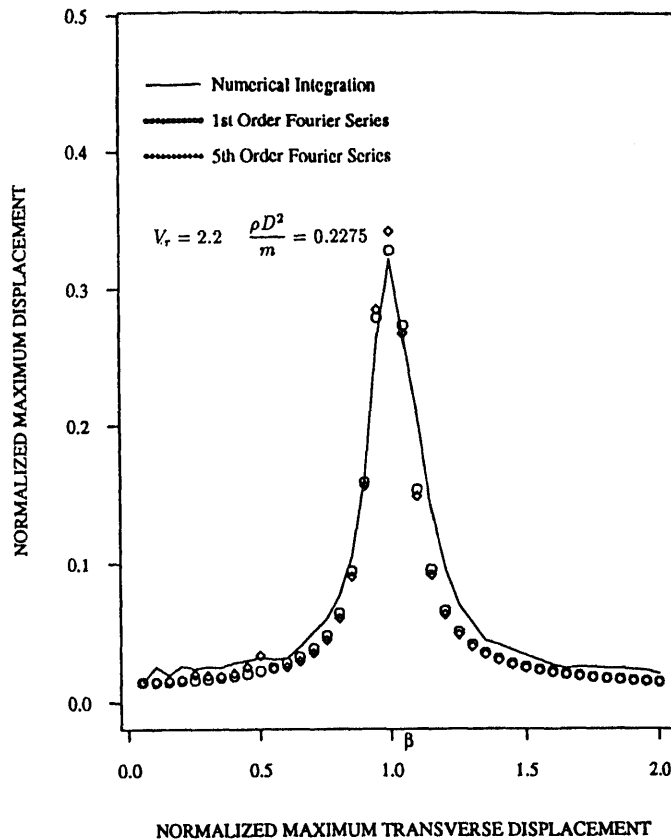


Figure 3. Maximum value of the normalized transverse displacement; $V_r = 2.2$, $\rho D^2/m = 0.2275$.

or equivalently

$$\begin{aligned}
 x'' & \left(1 + \frac{C_A \rho A}{m_0} \right) + 2\xi_0 \frac{\omega_0}{\omega} x' + \left(\frac{\omega_0}{\omega} \right)^2 x \\
 & = \frac{1}{2} \frac{C_D \rho D}{m_0} ((u' - x')^2 + y'^2)^{1/2} (u' - x') + \frac{C_M \rho A}{m_0} u'' \\
 & \quad - \frac{1}{2} \frac{C_L \rho D}{m_0} ((U_v - x')^2 + y'^2)^{1/2} |y'| \cos \left(\frac{\omega_v}{\omega} \tau \right), \quad (17)
 \end{aligned}$$

Dividing both sides of the equation by the inertia term $(1 + (C_A \rho A/m_0))$, and dividing again by D , yields the following equation

$$\begin{aligned}
 \frac{x''}{D} + 2 \frac{\xi_N x'}{\beta D} + \frac{1}{\beta^2} \frac{x}{D} & = \frac{1}{2} \frac{1}{(1 + (C_A \rho A/m_0))} \frac{C_D \rho D^2}{m_0} \\
 & \times \left[\left(\mu v(\tau) - \frac{x'}{D} \right)^2 + \left(\frac{y'}{D} \right)^2 \right]^{1/2} \left(\mu v(\tau) - \frac{x'}{D} \right)
 \end{aligned}$$

$$\begin{aligned}
& + \frac{1}{(1 + (C_A \rho A / m_0))} \frac{C_M \rho A}{m_0} \mu \dot{v}(\tau) - \frac{1}{2(1 + (C_A \rho A / m_0))} \frac{C_L \rho D^2}{m_0} \\
& \times \left(\left(\mu - \frac{x'}{D} \right)^2 + \left(\frac{y'}{D} \right)^2 \right)^{1/2} \left| \frac{y'}{D} \right| \cos \left(\frac{\omega_v}{\omega} \tau \right).
\end{aligned} \quad (18)$$

Noting that

$$m_0 \left(1 + \frac{C_A \rho A}{m_0} \right) = m, \quad (19)$$

the above equation of motion in the x direction simplifies to

$$\begin{aligned}
\frac{x''}{D} + 2 \frac{\xi_N}{\beta} \frac{x'}{D} + \frac{1}{\beta^2} \frac{x}{D} &= \frac{1}{2} \frac{C_D \rho D^2}{m} \left(\left(\mu v(\tau) - \frac{x'}{D} \right)^2 + \left(\frac{y'}{D} \right)^2 \right)^{1/2} \\
&\times \left(\mu v(\tau) - \frac{x'}{D} \right) + \frac{C_M \rho A}{m} \mu \dot{v}(\tau) \\
&- \frac{1}{2} \frac{C_L \rho D^2}{m} \left(\left(\mu - \frac{x'}{D} \right)^2 + \left(\frac{y'}{D} \right)^2 \right)^{1/2} \left| \frac{y'}{D} \right| \cos \left(\frac{\omega_v}{\omega} \tau \right).
\end{aligned} \quad (20)$$

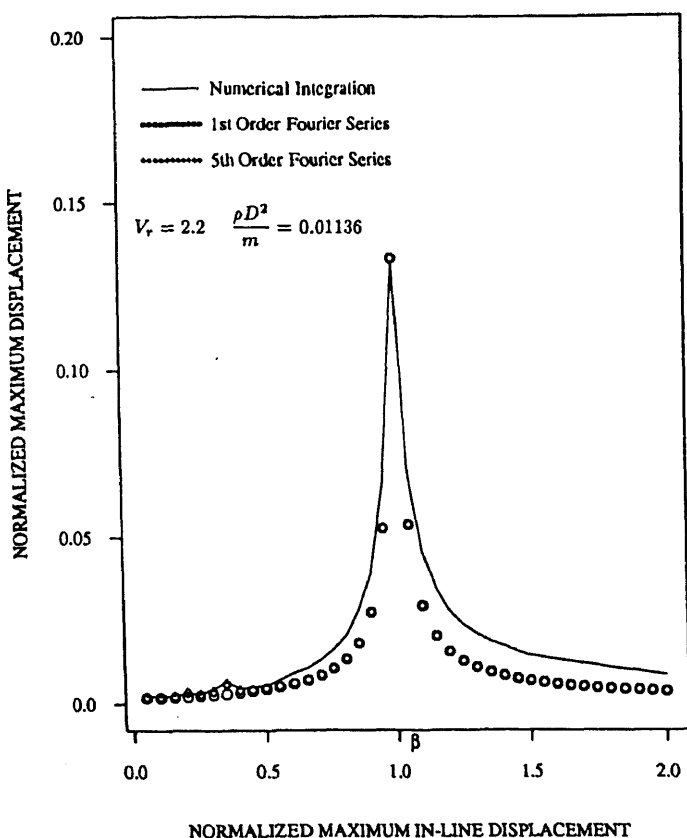


Figure 4. Maximum value of the normalized in-line displacement; $V_r = 2.2$, $\rho D^2 / m = 0.01136$.

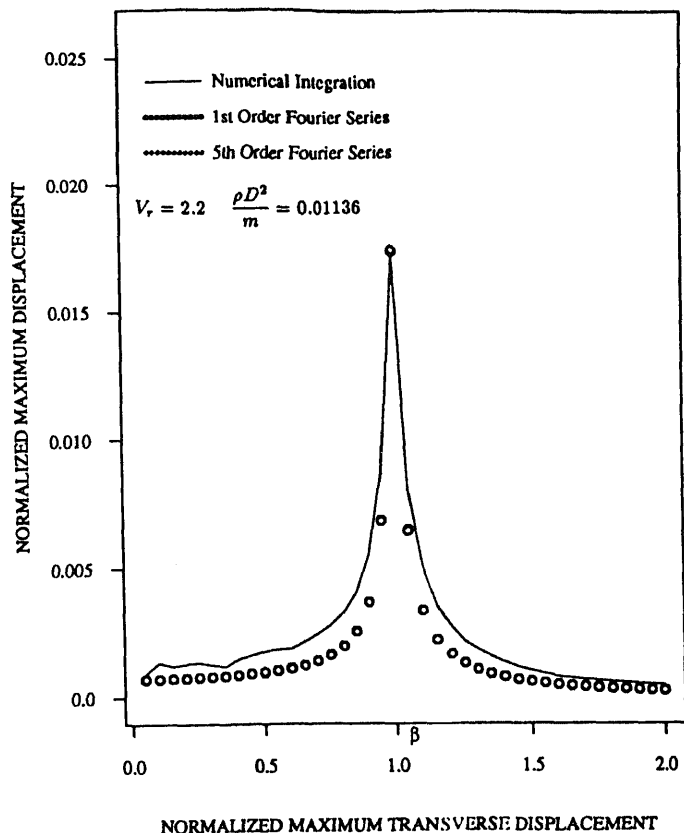


Figure 5. Maximum value of the normalized transverse displacement; $V_r = 2.2$, $\rho D^2/m = 0.01136$.

In a similar fashion, the wave forces in the y direction can be expressed in the following form, featuring a drag, an inertia, and a vortex term

$$\begin{aligned}
 f_y(t) &= f_{yD} + f_{yI} + f_{yV} \\
 &= -\frac{1}{2} C_D \rho D ((\dot{u} - \dot{x})^2 + \dot{y}^2)^{1/2} \dot{y} + (1 - C_M) \rho A \ddot{y} \\
 &\quad + \frac{1}{2} C_L \rho D ((U_v - \dot{x})^2 + \dot{y}^2)^{1/2} |U_v - \dot{x}| \cos(\omega_v t). \quad (21)
 \end{aligned}$$

Repeating the normalization procedure applied to (1), (2), governing the motion in the y direction, is transformed into the following normalized nondimensional form

$$\begin{aligned}
 \frac{y''}{D} + 2 \frac{\xi_N y'}{\beta D} + \frac{1}{\beta^2} \frac{y}{D} &= -\frac{1}{2} \frac{C_D \rho D^2}{m} \left(\left(\mu v(\tau) - \frac{x'}{D} \right)^2 + \left(\frac{y'}{D} \right)^2 \right)^{1/2} \left(\frac{y'}{D} \right) \\
 &\quad + \frac{1}{2} \frac{C_L \rho D^2}{m} \left(\left(\mu - \frac{x'}{D} \right)^2 + \left(\frac{y'}{D} \right)^2 \right)^{1/2} \left| \mu - \frac{x'}{D} \right| \cos \left(\frac{\omega_v}{\omega} \tau \right). \quad (22)
 \end{aligned}$$

Of special interest in analysing offshore structures subjected to vortex-induced vibration is the condition of locking. This phenomenon corresponds to the case where the frequency of vortex-induced oscillations coincides with the fundamental frequency of vibration of the structure, in which case,

$$\omega_v = \omega_0. \tag{23}$$

3. Solution of the equations of motion

The equations of motion developed in the previous section can be rewritten as

$$\begin{cases} \frac{x''}{D} + \frac{2\xi_N}{\beta} \frac{x'}{D} + \frac{1}{\beta^2} \frac{x}{D} = F_x, \\ \frac{y''}{D} + \frac{2\xi_N}{\beta} \frac{y'}{D} + \frac{1}{\beta^2} \frac{y}{D} = F_y. \end{cases} \tag{24}$$

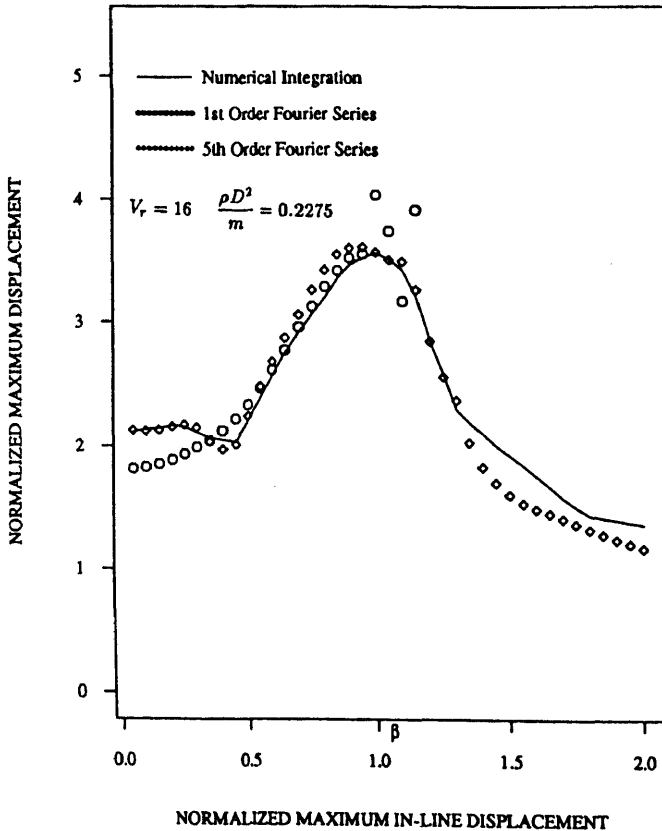


Figure 6. Maximum value of the normalized in-line displacement; $V_r = 16$, $\rho D^2/m = 0.2275$.

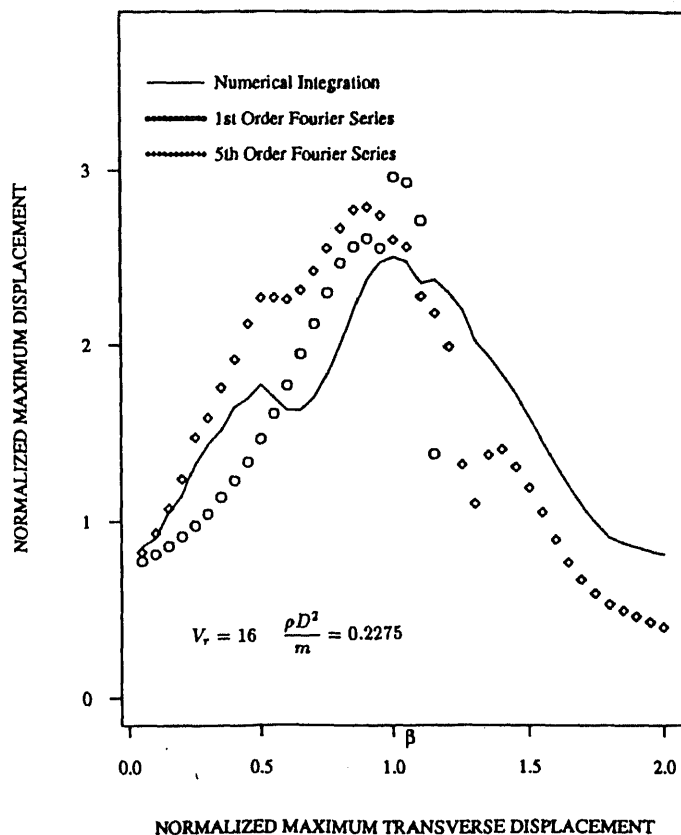


Figure 7. Maximum value of the normalized transverse displacement; $V_r = 16$, $\rho D^2/m = 0.2275$.

A solution will be sought to the problem by resorting to the harmonic balance technique. This requires expanding the response functions $x(t)$ and $y(t)$ in a Fourier series of the form

$$\frac{x(\tau)}{D} = x_0 + \sum_{i=1}^{\infty} [x_{2i-1} \sin(i\tau) + x_{2i} \cos(i\tau)], \quad (25)$$

$$\frac{y(\tau)}{D} = y_0 + \sum_{i=1}^{\infty} [y_{2i-1} \sin(i\tau) + y_{2i} \cos(i\tau)]. \quad (26)$$

The functions F_x and F_y are also expanded into their respective Fourier series in the form

$$F_x(\tau) = f_0^{(x)} + \sum_{i=1}^{\infty} [f_{2i-1}^{(x)} \sin(i\tau) + f_{2i}^{(x)} \cos(i\tau)], \quad (27)$$

$$F_y(\tau) = f_0^{(y)} + \sum_{i=1}^{\infty} [f_{2i-1}^{(y)} \sin(i\tau) + f_{2i}^{(y)} \cos(i\tau)]. \quad (28)$$

Substituting the last four equations back into the differential equations of motion

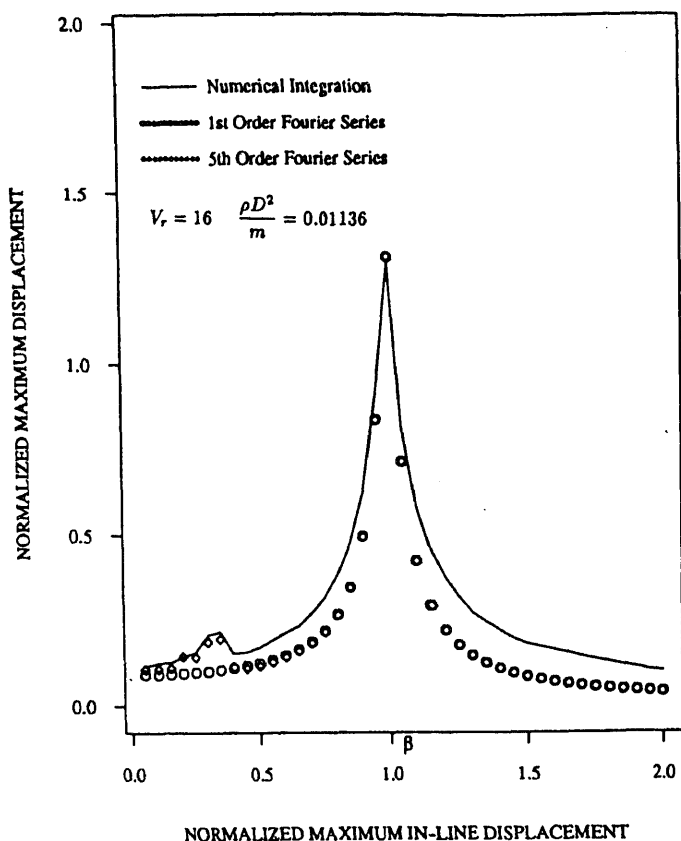


Figure 8. Maximum value of the normalized in-line displacement; $V_r = 16$, $\rho D^2/m = 0.01136$.

results in equations of the following form involving coefficients of same order in the expansions for $x(t)$

$$\begin{aligned}
 & \frac{1}{\beta^2} x_0 + \sum_{i=1}^{\infty} -i^2 x_{2i-1} \sin(i\tau) + i x_{2i-1} (2\xi_N/\beta) \cos(i\tau) + x_{2i-1} (1/\beta^2) \sin(i\tau) \\
 & - i^2 x_{2i} \cos(i\tau) - i x_{2i} (2\xi_N/\beta) \sin(i\tau) + x_{2i} (1/\beta^2) \cos(i\tau) \\
 & = f_0^{(x)} + \sum_{i=1}^{\infty} [f_{2i-1}^{(x)} \sin(i\tau) + f_{2i}^{(x)} \cos(i\tau)], \quad (29)
 \end{aligned}$$

Equating coefficients of sin and cos on both sides of the above equation results in the following algebraic equations for the Fourier coefficients of $x(t)$

$$\begin{cases} ((1/\beta^2) - i^2) x_{2i-1} - 2i(\xi_N/\beta) x_{2i} = f_{2i-1}^{(x)}, \\ 2i(\xi_N/\beta) x_{2i-1} + ((1/\beta^2) - i^2) x_{2i} = f_{2i}^{(x)}. \end{cases} \quad (30)$$

These can be solved in closed form to yield the following expression for the Fourier

coefficients

$$\begin{cases} x_0 = \beta^2 f_0^{(x)}, \\ x_{2i-1} = \frac{f_{2i-1}^{(x)}((1/\beta^2) - i^2) + f_{2i}^{(x)} 2i(\xi_N/\beta)}{((1/\beta^2) - i^2)^2 + (2i(\xi_N/\beta))^2}, \\ x_{2i} = \frac{f_{2i}^{(x)}((1/\beta^2) - i^2) - f_{2i-1}^{(x)} 2i(\xi_N/\beta)}{((1/\beta^2) - i^2)^2 + (2i(\xi_N/\beta))^2}. \end{cases} \quad (31)$$

A similar treatment for the equations in the transverse direction results in the following equations for the Fourier coefficients of $y(t)$

$$\begin{cases} y_0 = \beta^2 f_0^{(y)}, \\ y_{2i-1} = \frac{f_{2i-1}^{(y)}((1/\beta^2) - i^2) + f_{2i}^{(y)} 2i(\xi_N/\beta)}{((1/\beta^2) - i^2)^2 + (2i(\xi_N/\beta))^2}, \\ y_{2i} = \frac{f_{2i}^{(y)}((1/\beta^2) - i^2) - f_{2i-1}^{(y)} 2i(\xi_N/\beta)}{((1/\beta^2) - i^2)^2 + (2i(\xi_N/\beta))^2}. \end{cases} \quad (32)$$

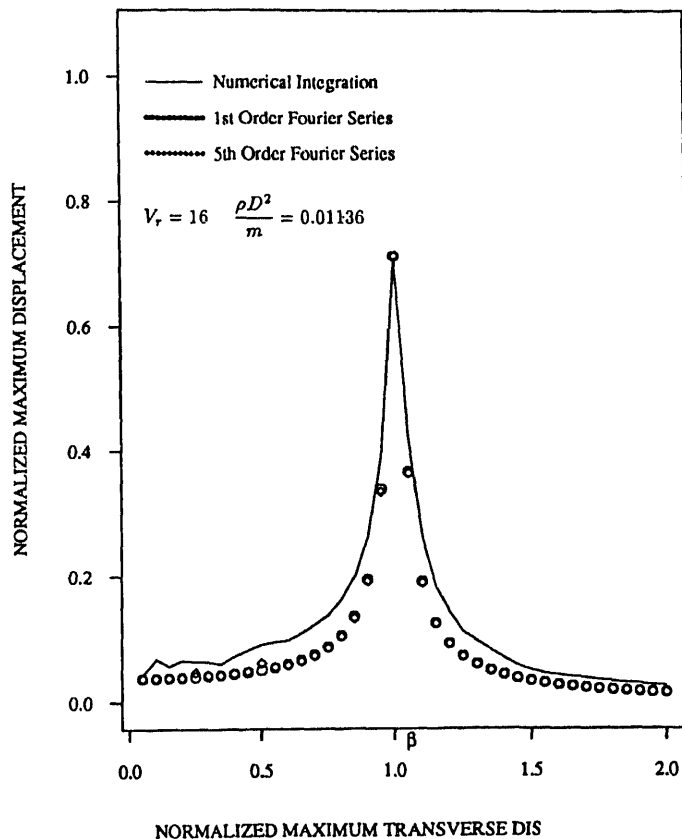


Figure 9. Maximum value of the normalized transverse displacement $\rho D^2/m = 0.01136$.

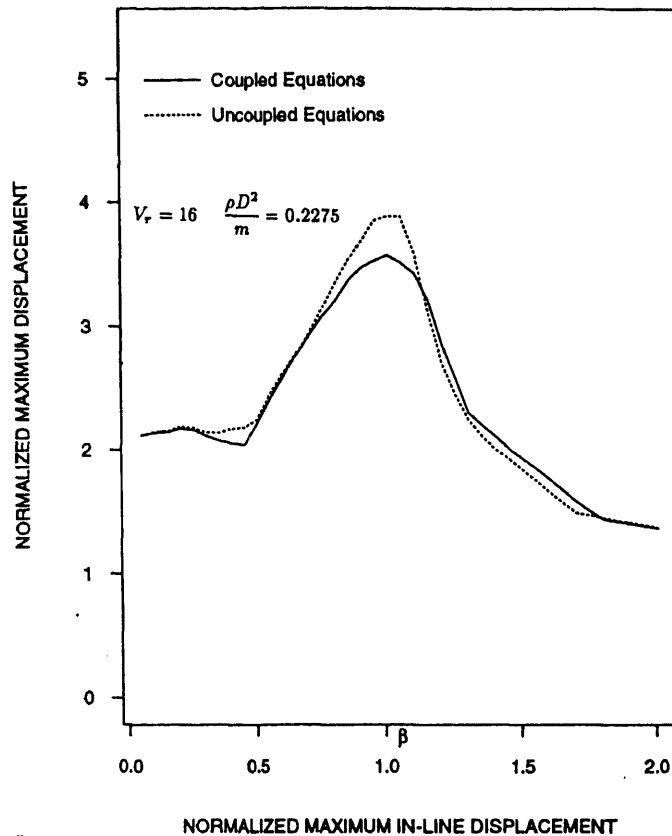


Figure 10. Coupled vs. uncoupled predictions; maximum value of the normalized in-line displacement; $V_r = 16$, $\rho D^2/m = 0.2275$.

Obviously, in the above expressions, $f_i^{(x)}$ and $f_i^{(y)}$ denote the Fourier coefficients of the functions F_x and F_y which themselves are nonlinear functions of $x(t)$ and $y(t)$. Therefore, in the implementation of the above procedure, an iterative scheme is followed whereby previous estimates of $x(t)$ and $y(t)$ are used in evaluating the numerical values of $f_i^{(x)}$ and $f_i^{(y)}$. The iteration is continued until a predetermined convergence tolerance has been achieved. In the numerical results shown in the next section, the norm

$$\|\varepsilon_k\| = \left(\sum_{i=0}^N (x_i^{(k)^2} + y_i^{(k)^2} - x_i^{(k-1)^2} - y_i^{(k-1)^2}) / \sum_{i=0}^N (x_i^{(k)^2} + y_i^{(k)^2}) \right)^{1/2}, \quad (33)$$

of the approximation error is used in establishing the convergence criterion. In the above expression, $x_i^{(k)}$ denotes the i th Fourier coefficients as obtained at the k th iteration.

For comparison, the results obtained from the coupled equations of motion are compared to those obtained using the uncoupled equations. These are obtained from (20) and (22) by neglecting the effect of the vortex-induced forces along the in-line direction, and by neglecting the contribution of the in-line motion to the transverse motion. The

uncoupled equations are given, in their normalized form, by the expressions

$$\frac{x''}{D} + 2\frac{\xi_N x'}{\beta D} + \frac{1}{\beta^2} \frac{x}{D} = \frac{1}{2} \frac{C_D \rho D^2}{m} \left(\left(\mu v(\tau) - \frac{x'}{D} \right)^2 \right)^{1/2} \left(\mu v(\tau) - \frac{x'}{D} \right) + \frac{C_M \rho A}{m} \mu v(\tau), \quad (34)$$

and

$$\frac{y''}{D} + 2\frac{\xi_N y'}{\beta D} + \frac{1}{\beta^2} \frac{y}{D} = -\frac{1}{2} \frac{C_D \rho D^2}{m} \left| \frac{y'}{D} \right| \left(\frac{y'}{D} \right) + \frac{1}{2} \frac{C_L \rho D^2}{m} \mu^2 \cos \left(\frac{\omega_v}{\omega} \tau \right). \quad (35)$$

4. Numerical results

A parametric study was carried out to assess the range of validity of the proposed approximation scheme. Different values of the reduced velocity coefficients V_r were considered, as well as different values of the mass ratio coefficient $M_r = m/\rho D^2$. The reduced velocity coefficients can be readily related to the coefficient μ appearing in the equations of motion using the relation

$$V_r = (2\pi/\omega_N)(U_v/D) = 2\pi\beta\mu. \quad (36)$$

Values of V_r equal to 16 and 2.2, were used in the parametric study. These values correspond to situations selected from offshore engineering applications where vortex-induced oscillations are expected to occur ($V_r = 16$), and situations where they are not expected to occur ($V_r = 2.2$) (Blevins 1990). Furthermore, values of $1/M_r$ equal to 0.01136 and 0.2275 were used, being representative of a heavy structure, and a less heavy structure, respectively. Also, a value of ξ_N equal to 0.02 was used as representative of the amount of structural damping present in a lightweight structure. The value of the other coefficients were: $C_D = 1.45$, $C_L = 1$ and $C_M = 1.25$.

In the numerical implementation of the procedure described in the previous section, convergence problems were encountered with the iterative procedure as described above. For a value of V_r equal to 16, the iterative algorithm failed to converge. This was due to a relatively large amplitude of oscillations. The problem was circumvented by adding the following term to both sides of each of the equations of motion,

$$\frac{1}{2} \rho C_D D E_0 \dot{x}, \quad E_0 = (1/T) \int_0^T |\dot{u} - \dot{x}| dt, \quad T = 2\pi/\omega. \quad (37)$$

The effect of this additional damping was to reduce the magnitude of the terms used in evaluating the components $f_i^{(x)}$ and $f_i^{(y)}$, while having no net effect on the final result. The nondimensional form of the above term is

$$(C_D/4\pi)(\rho D^2/m) \int_0^{2\pi} |u' - x'| d\tau x'. \quad (38)$$

Once this artificial damping was introduced into the governing equations, convergence to within a value of $\|e\|$ equal to 0.001 was achieved within three to five iterations, requiring a fraction of the time needed for the numerical integration of the equations of motion. The approximate technique was carried out for orders of the Fourier expansion equal to 1, 2, 3, 4, and 5, respectively. Only results pertaining to the first order and fifth order approximations are displayed in this paper. Furthermore, the

results shown herein relate to the maximum value of the displacement within one period. The magnitude of this parameter is deemed an important indicator reflecting the maximum level of stresses to be expected on the structure. Figures 2 and 3 show the results corresponding to a value of V_r equal to 2.2, and $\rho D^2/m$ equal to 0.2275. Both in-line and transverse displacements are featured. Figures 4 and 5 show the results corresponding to a value of V_r equal to 2.2 and a $\rho D^2/m$ equal to 0.01136. Note the quite good agreement between the time integration results and the approximate harmonic balance results. Figures 6–9 show the results corresponding to a value of V_r equal to 16. In this case, good results are obtained for a value of $\rho D^2/m$ equal to 0.01136. Note that even the secondary peak at a value of β equal to 0.35 was successfully identified. For a value of $\rho D^2/m$ equal to 0.2275, quite good results are again obtained for the in-line displacement. For the displacement in the transverse direction, however, the results, although acceptable, are not of the same quality as those for the other cases. It should be noted, in this context, that for this particular case, the results associated with the uncoupled equations differ substantially from the results associated with the coupled equations. Noticeable differences between coupled and uncoupled results were also observed for the cases corresponding to the in-line displacement with V_r equal to 16 and $\rho D^2/m$ equal to 0.2275, and for the

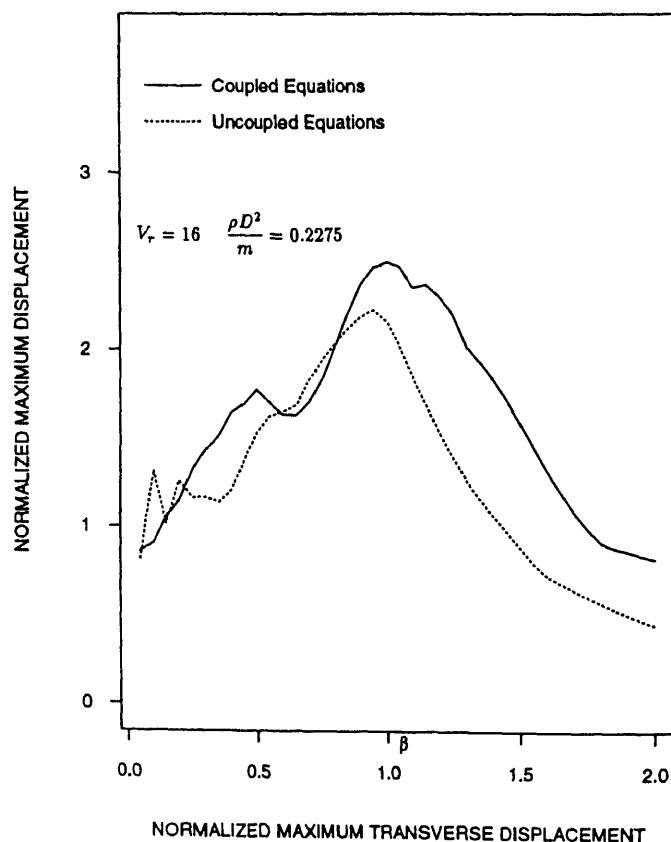


Figure 11. Coupled vs. uncoupled predictions; maximum value of the normalized transverse displacement; $V_r = 16$, $\rho D^2/m = 0.2275$.

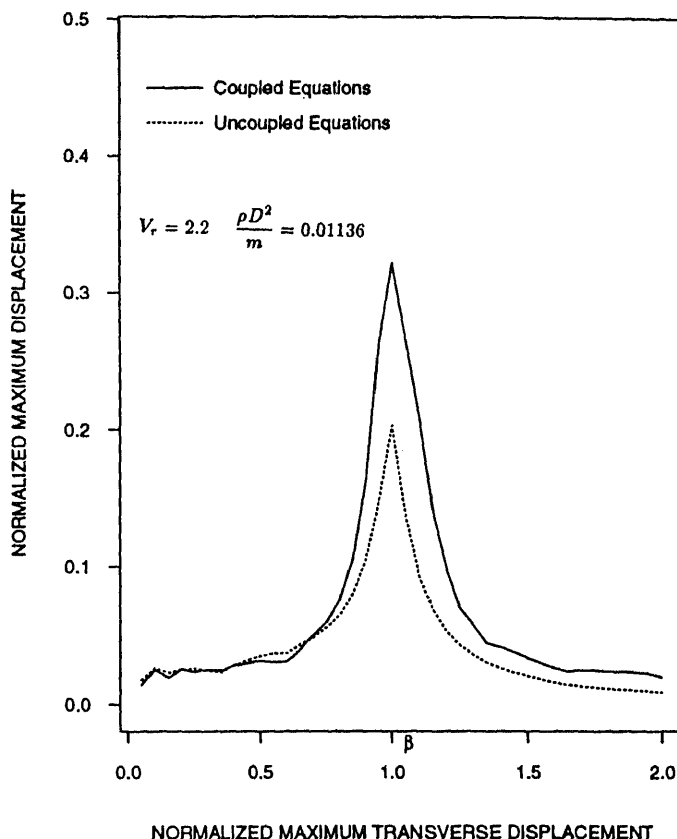


Figure 12. Coupled vs. uncoupled predictions; maximum value of the normalized transverse displacement; $V_r = 16$, $\rho D^2/m = 0.01136$.

transverse displacement with V_r equal to 2.2 and $\rho D^2/m$ equal to 0.2275. The results corresponding to these three cases are shown in figures 10–12. These differences are such that a design approach based on the uncoupled equations of motion may prove unreliable.

5. Conclusions

An approximate technique is presented for evaluating the response of structures modelled as two-degree-of-freedom systems. The effect of vortex-induced oscillations is taken into consideration, as well as the coupling of the equations associated with the various hydrodynamic loads on the structure. Linearization of the equations of motion is circumvented through the development of an iterative algorithm which implements a Fourier series of the response along each direction; Fourier series of arbitrary order can be readily incorporated. The computer time required to implement the proposed technique is a fraction of the time required to integration. This fact makes the proposed method well suited for small personal computers that are limited in their access to

software. The accuracy demonstrated by the numerical examples suggests that the technique may still be quite appealing even in a more sophisticated setting. Furthermore, using both the proposed technique and numerical integration, the effect of the coupling in the equations of motion was investigated. It was shown that the results associated with the uncoupled equations can be significantly different from those associated with the coupled equation. This fact suggests that caution should be exercised by researchers and practitioners who base their professional recommendations on one of the many available techniques that rely on the uncoupled form of the equations of motion. Finally, although the proposed technique was implemented for a simplified two-degree-of-freedom model of a structure, its extension to deal with multi-degree-of-freedom systems can be readily accomplished. The results from the present investigation can be regarded as warranting a research endeavor in that direction.

List of symbols

A	cross-sectional area of cylinder;
C_A	$C_M - 1$;
C_D	drag coefficient;
C_L	lift coefficient;
C_M	added mass coefficient;
D	diameter of cylinder;
E_0	energy of one period;
$f_i^{(x)}(t)$	i th Fourier coefficient of $f_x(t)$;
$f_i^{(y)}(t)$	i th Fourier coefficient of $f_y(t)$;
$f_{jD}(t)$	drag force in direction j ;
$f_{jV}(t)$	vortex force in direction j ;
$f_x(t)$	total force in direction x ;
$f_y(t)$	total force in direction y ;
m_0	mass of cylinder;
m	effective mass;
T	period of oscillations;
t	time;
U	wave amplitude;
U_v	ωU ;
$u(t)$	sinusoidal displacement field of water particles;
$v(t)$	$-\sin(t) + \cos(t)$;
V_r	reduced velocity;
$x(t)$	in-line displacement of cylinder;
$x_i(t)$	i th Fourier coefficient of $x(t)$;
$y(t)$	transverse displacement of cylinder;
$y_i(t)$	i th Fourier coefficient of $y(t)$;
β	non-dimensional frequency of oscillation;
μ	non-dimensional water elevation;
ξ_0	damping ratio;
ξ_N	normalized damping ratio;
ω	frequency of wave forces;

ω_0	natural frequency of cylinder;
ω_v	frequency of vortex oscillations;
ε_k	error in iterations;
ρ	density of fluid;
τ	nondimensional time.

References

- Blevins R D 1990 *Flow-induced vibration* 2nd edn (New York: Van Nostrand Reinhold)
- Chen Y H, Lin F M 1989 General drag-force linearization for nonlinear analysis of marine risers. *Ocean Eng.* 16: 265–280
- Dailey J E, Weidler J B, Hanna S, Zedan M, Yeung J 1987 Pile fatigue failures. III: Motions in seas. *ASCE, J. Waterway, Port, Coastal, Ocean Eng.* 113: 233–250
- Griffin O, Skop R, Koopmann G 1973 The vortex-excited resonant vibrations of circular cylinders. *J. Sound Vib.* 31: 235–249
- Rajabi F, Zedan M F, Mangiavacchi A 1984 Vortex shedding induced dynamic response of marine risers. *ASME, J. Energy Resources Technol.* 106: 214–221
- Sarpkaya T 1979 Vortex-induced oscillations. *ASME, J. Appl. Mech.* 46: 241–258
- Spanos P, Chen T 1980 Response of a dynamic system to flow-induced load. *Int. J. Non-Linear Mech.* 15: 115–126



Analysis of the equations of motion of linearized controlled structures

FAI MA

Department of Mechanical Engineering, University of California, Berkeley, California 94720, USA

Abstract. The linearized equations of motion of controlled structures possess coefficient matrices that lack the familiar properties of symmetry and definiteness. A method is developed for the efficient analysis of linearized controlled structures. This constructive method utilizes equivalence transformations in Lagrangian coordinates and does not require conversion of the equations of motion to first-order forms. Compared with the state-space approach, this method can offer substantial reduction in computational effort and ample physical insight. However, it is often necessary to draw upon some type of decoupling approximation for fast solution. Many numerical techniques involve discretized equations resembling those of linearized controlled structures. These numerical techniques can also be greatly streamlined if the method of equivalence transformations is incorporated.

Keywords. Linearized control structures; equivalence transformation; classical modal analysis; Lagrangian coordinates.

1. Introduction

A time-honoured procedure for the approximate solution of nonlinear mechanical systems is linearization, or in some cases piecewise linearization. The linearized equation of motion of an n -degree-of-freedom controlled structure can be written as

$$A\ddot{q} + B\dot{q} + Cq = f(t), \quad (1)$$

where A , B and C are arbitrary square matrices of order n . Embedded in these real coefficient matrices are the control gains, and as a result they need not possess any of the familiar properties of symmetry or definiteness. The Lagrangian coordinate q and the generalized excitation $f(t)$ are n -dimensional vectors. The various ways in which equations of the above type can arise have been discussed by Soong (1990) and other authors. These equations tend to manifest on a widespread scale in recent years, owing mostly to the increasing use of control devices in structures. Development of a fast method for the analysis of such equations is thus much deserving.

In theory, it is always possible and in fact customary to investigate a linearized controlled structure with the state-space approach, whereby the second-order equation

(1) is recast into a first-order system of dimension $2n$. After conversion into a first-order form, a large variety of numerical techniques are then available for subsequent analysis. But the state-space method has never appealed to structural engineers. An inordinate amount of computational effort is usually given as a reason. More importantly, there is serious absence of physical insight in tackling a first-order equation recast from the Lagrangian formulation. The reluctance to employ state-space techniques has led to the development of a whole array of special techniques for analysing subclasses of linearized controlled structures in the Lagrangian coordinate q . Some of these developments have been reported by Huseyin & Leipholz (1973), Fawzy & Bishop (1976), Inman (1983), and Caughey & Ma (1993).

Equations of the type (1) are coincident with those governing linear nonconservative vibrations, which have drawn relatively scant attention in classical theory. To be sure, it would be preferable if classical modal analysis could somehow be modified to treat systems with nonsymmetric coefficients. That might indeed be assumed in some earlier investigations. A literature survey in the testing of aircraft flutter and in the stressing of ship hulls, for example, reveals rather occasional use of terms such as logarithmic decrements, modes, or natural frequencies. But the meanings of these terms are not clear. When does a linearized controlled structure possess classical normal modes? What are the natural frequencies of a system with nonsymmetric coefficients? A theoretical basis, on which these concepts can be properly explored, is greatly desired.

Were system (1) symmetric and definite, the coefficient of acceleration would be a positive-definite mass matrix M , and the coefficients of velocity and displacement would respectively be positive-semidefinite damping and stiffness matrices D and K . In this case, (1) would take the familiar form

$$M\ddot{q} + D\dot{q} + Kq = f(t). \quad (2)$$

In linear nonconservative vibrations, the difference between the matrices B and D is sometimes accounted for by gyroscopic forces, and that between C and K by circulatory forces (Müller & Schiehlen 1985). Hence $B = 0$ implies an undamped nongyroscopic structure, and so on. While this type of terminology may not be applicable to linearized controlled structures, it will be convenient to adhere to such terminology. Applications in which A is not symmetric are given, for example, by Schmitz (1973) as well as Soom & Kim (1983).

The purpose of this article is to expound a fast method for the analysis of linearized controlled structures. This constructive method utilizes equivalence transformations in Lagrangian coordinates, and does not involve conversion of the equations of motion to first-order forms. As will be evident, the method represents a direct extension of classical modal analysis. The same method can certainly be applied to the analysis of linear nonconservative vibrations. The organization of this article is as follows. In §2, it is shown that a controlled structure in which $B = 0$ can be completely decoupled by an equivalence transformation. In addition, the meaning of natural frequencies will be clarified. Equivalence transformation is applied to a general linearized structure in §3. There, comparison is made with classical modal analysis of viscously damped systems. An illustrative example is given in §4, in which practical implications of the method are also discussed. A summary of findings is provided in §5. The terms, *linearized controlled structures* and *linear nonconservative vibrations*, will be used interchangeably in exposition.

2. Undamped nongyroscopic structures

Consider a linearized controlled structure in which $B = 0$. The equation of motion is

$$A\ddot{q} + C\dot{q} = f(t). \quad (3)$$

This system can be decoupled if and only if there exist two nonsingular matrices U and V such that VAU , VCU are diagonal. Two square matrices P and Q , related by $P = VQU$, are said to be connected by an equivalence transformation. An equivalence transformation between P and Q preserves the rank of the matrices. If $V = U^{-1}$, the equivalence transformation is called a similarity transformation. In the event that $V = U^T$, the equivalence transformation is a congruence transformation. The classical modal transformation is an example of congruence transformation. A congruence transformation is also a similarity transformation if U is an orthogonal matrix. Equivalence transformations that are neither similarity nor congruence transformations are rarely used in structural analysis. Nevertheless, in what follows, it will be shown that a linearized controlled structure in which $B = 0$ can be decoupled by equivalence transformation in practically every situation.

Let u be a column vector of order n and α be a scalar constant. If

$$q = u e^{\alpha t}, \quad (4)$$

is a homogeneous or complementary solution to (3), the generalized eigenvalue problem

$$Cu = \lambda Au \quad (5)$$

must be satisfied, where $\lambda = -\alpha^2$. Eigenvalue problems of this kind were traditionally addressed in the abstract theory of matrix pencils. Emphasis was usually placed on symmetric and definite pencils. As a consequence, results applicable to the above eigenvalue problem are scattered and rather incomplete. An extension based on the presentation of Zurmühl & Falk (1984) will be made here. Associated with eigenvalue problem (5) is the adjoint eigenvalue problem

$$C^T v = \lambda A^T v. \quad (6)$$

As (5) and (6) lead to the same characteristic determinant, the corresponding eigenvalues are identical.

At this point, the two assumptions underlying this investigation must be reviewed. First, it is required that A is nonsingular. This is a common assumption made in earlier investigations. Technically speaking, there is no practical loss of generality in accommodating this assumption. Should the coefficient matrix A be singular, at least one acceleration term can be removed from the formulation. A linearized controlled structure is termed degenerate if its coefficient of acceleration A is singular. The eigenvalue problem (5) possesses n eigenvalues if and only if A is nonsingular. Thus, the implicit assumption that a system is not degenerate ensures the existence of a full set of eigenvalues. The second requirement presumes independence of the eigenvectors associated with eigenvalue problem (5). An eigenvalue problem is termed defective if it does not possess a full complement of independent eigenvectors. Experience indicates that an eigenvalue problem (5) possessing physical significance is invariably not defective. And the assumption that there is a full complement of independent eigenvectors

can be made without fail in almost every application. A sufficient condition under which problem (5) is not defective is for the associated eigenvalues to be distinct. However, this is only a sufficient and not a necessary condition. In addition, the eigenvalue problem (5) is not defective if and only if its adjoint problem (6) is not defective. Henceforth, without practical loss of generality, it will be assumed that a linearized controlled structure is not degenerate or defective.

Corresponding to each eigenvalue λ_i , an eigenvector u_i can be found such that

$$Cu_i = \lambda_i Au_i. \quad (7)$$

Likewise, a solution to the adjoint eigenvalue problem associated with the eigenvalue λ_j is expressed by

$$C^T v_j = \lambda_j A^T v_j. \quad (8)$$

Note that each column vector u_i or v_j is undetermined to the extent of an arbitrary multiplicative constant. Transpose the above equation to obtain

$$v_j^T C = \lambda_j v_j^T A. \quad (9)$$

Premultiply (7) by v_j^T and postmultiply (9) by u_i . It follows by subtraction that

$$(\lambda_i - \lambda_j) v_j^T A u_i = 0. \quad (10)$$

Provided $\lambda_i \neq \lambda_j$, the eigenvectors u_i and v_j are orthogonal, with A playing the role of a weighting matrix. Thus, the two sets of column vectors u_i and v_j are biorthogonal with respect to A if the corresponding eigenvalues are distinct. An extension to include repeated eigenvalues has been made by Ma & Caughey (1995).

Based on the above clarification, a biorthogonality relation between the eigenvectors u_i and v_j holds whether or not there are repeated eigenvalues. Normalization of these eigenvectors leads to

$$v_j^T A u_i = \delta_{ij}, \quad i, j = 1, 2, \dots, n. \quad (11)$$

Note that each eigenvector u_i and its adjoint eigenvector v_i are still determined within an arbitrary multiplicative constant. If the multiplier for u_i is a_i and that for v_i is b_i , the above equation determines only the product $a_i b_i$. In other words, the choice of either a_i or b_i separately is still arbitrary. The above relation implies, in addition, that

$$v_j^T C u_i = \lambda_i \delta_{ij}, \quad i, j = 1, 2, \dots, n. \quad (12)$$

Define the following square matrices of order n by

$$U = [u_1, u_2, \dots, u_n], \quad (13)$$

$$V = [v_1, v_2, \dots, v_n]^T, \quad (14)$$

$$\Lambda = \text{diag}[\lambda_1, \lambda_2, \dots, \lambda_n]. \quad (15)$$

The biorthogonality relations (11) and (12) can now be expressed in a compact form:

$$V A U = I, \quad (16)$$

$$V C U = \Lambda. \quad (17)$$

Let $q = Up$. Equation (3) may be simplified to

$$\ddot{p} + \Lambda p = V f(t), \quad (18)$$

which represents a completely decoupled system. Needless to emphasize, the solution of a decoupled system is immediate. The following statement has been established.

Theorem 1. *A linearized controlled structure that is not degenerate or defective and in which $B = 0$ can always be decoupled by equivalence transformation.*

The decoupling equivalence transformation is defined by two adjoint eigenvalue problems (5) and (6). It has been proved by Ma & Caughey (1995) that any other equivalence transformation that decouples system (3) must be derivable from these eigenvalue problems. As explained earlier, the decoupling transformation is uniquely determined within arbitrary multiplicative constants in the eigenvectors u_i and v_j if the associated eigenvalues are distinct. The complex eigenvectors u_i and v_j may be termed modes and adjoint modes respectively. In the case of repeated eigenvalues, the decoupling transformation is not unique.

For a symmetric and definite system, (5) takes the form

$$Ku = \lambda Mu, \quad (19)$$

leading to classical normal modes and natural frequencies (Meirovitch 1967). Due to symmetry of M and K , (5) and (6) are identical. The modes and adjoint modes are equal and are real. Solution of only the eigenvalue problem (5) is sufficient for determining the modes. Thus, *the decoupling equivalence transformation reduces to classical modal transformation if the coefficient matrices possess symmetry and definiteness.* The method of equivalence transformation represents a direct extension of classical modal analysis, and *the lack of symmetry in a system only approximately doubles the computational effort.*

The method of equivalence transformations offers physical insight. This can be briefly demonstrated by clarification of the meaning of natural frequencies of a linearized controlled structure. According to theorem 1, it is legitimate to write the equation of an undamped nongyroscopic structure in the form (18). For free vibration, in which $f(t) = 0$, the coordinate p admits a harmonic solution if and only if $\lambda_i > 0$ ($i = 1, 2, \dots, n$). Let $\lambda_i = \omega_i^2$, where each ω_i is real and positive. A component p_i of the vector p then has the solution

$$p_i = c_i \cos(\omega_i t - \phi_i), \quad i = 1, 2, \dots, n. \quad (20)$$

The real constants c_i and ϕ_i can be identified as amplitude and phase angle. Bearing in mind that $q = Up$, one obtains

$$q = \sum_{i=1}^n c_i u_i \cos(\omega_i t - \phi_i). \quad (21)$$

Validity of the following statement has therefore been demonstrated.

Theorem 2. *The components of a linearized controlled structure in which $B = 0$ can perform harmonic vibration with identical frequency if the associated eigenvalue problem (5) possesses positive eigenvalues.*

The natural frequencies of free vibration are simply the square roots of the eigenvalues. It remains to determine if there is any feature peculiar to the free vibration of a controlled structure. In a symmetric and definite system, the eigenvalues are real. Thus (21) implies that in harmonic motion with a specified

all components also vibrate *identical phase angle* ϕ_i . That need not be true for a controlled structure, whose eigenvectors u_i are generally complex. As is evident from (21), these complex eigenvectors induce phase differences among components of the response vector. Therefore, at a specified frequency ω_i , *the components of an undamped nongyroscopic structure usually vibrate with different phase angles*. Amplitudes of vibration of the components are proportional to the magnitudes of elements in u_i . For this reason, each complex eigenvector u_i still determines a mode shape, in analogy to classical modal vibration. The general response in free vibration is then the superposition of n harmonic motions of this kind.

3. General linearized structures

In classical modal analysis of a viscously damped system, the modal matrix diagonalizes the mass matrix M and stiffness matrix K but, in general, will not diagonalize the damping matrix D . Caughey & O'Kelly (1965) showed that D can be diagonalized by the modal matrix if and only if $M^{-1}D$ and $M^{-1}K$ commute in multiplication. In other words,

$$DM^{-1}K = KM^{-1}D \quad (22)$$

is a necessary and sufficient condition for the modal transformation to completely decouple a damped symmetric and definite system. Condition (22) is not usually satisfied. A common procedure in this case is to ignore the off-diagonal elements in the transformed damping matrix, especially when these elements are small. This procedure is termed the decoupling approximation in damping, which allows modal transformation to decouple an entire system. In addition, an iterative scheme can be used to improve the accuracy of approximate solution if the off-diagonal elements in the transformed damping matrix are not small. A discussion of this aspect was given by Udwadia & Esfandiari (1990) as well as Hwang & Ma (1993). Practically speaking, there is no objection to using the decoupling approximation in damping. But, as reviewed by Park *et al* (1994), regorous analysis of errors committed by such an approximation has not been reported in the open literature.

A similar situation arises in the analysis of linearized controlled structures. Referring to (1), an equivalence transformation diagonalizes A and C . As before, let this equivalence transformation be defined by the two nonsingular matrices U and V . Recall $q = Up$. Equation (1) may be expressed in the form

$$\ddot{p} + VBU\dot{p} + \Lambda p = Vf(t). \quad (23)$$

The transformed coefficient matrix of velocity VBU is in general not diagonal. That means the entire controlled structure is not decoupled by equivalence transformation. Clearly, an extension to the decoupling approximation in damping may be proposed: the off-diagonal elements in VBU can be ignored if they are small. Intuitively, the errors of approximation should be small if the off-diagonal elements in VBU are small. In addition, an iterative scheme, similar to the one for symmetric and definite systems, may be applied to improve the accuracy of approximate solution if the off-diagonal elements in VBU are not small. These approximate techniques have immense practical implications. However, as in classical modal analysis, these are also points of speculation. To continue to dwell upon them would merely be distracting.

It is possible to further refine the method of equivalence transformation. The coefficient matrices A and C in a controlled structure need not have the same divine rights as the symmetric matrices M and K . Sometimes it is more convenient to apply an equivalence transformation to diagonalize A and B instead. Afterwards, the entire structure may be decoupled through approximating the transformed coefficient matrix of displacement by a diagonal matrix. This digression will not be pursued. Henceforth, it will be assumed that an equivalence transformation will be chosen primarily to diagonalize A and C , in a fashion expounded earlier. An upshot at this stage in the following statement.

Theorem 3. *The linearized controlled structure (1) can be decoupled by an equivalence transformation if and only if the matrices $A^{-1}B$ and $A^{-1}C$ commute in multiplication.*

In other words, this extension of criterion (22) asserts that

$$BA^{-1}C = CA^{-1}B. \quad (24)$$

is a necessary and sufficient condition for an equivalence transformation to completely decouple linearized controlled structures. To prove this, it will be easier if condition (24) is first recast in a more transparent form. From (16), observe that

$$A^{-1} = UV. \quad (25)$$

Condition (24) is therefore equivalent to

$$B U V C = C U V B. \quad (26)$$

Premultiply the above equation by V and postmultiply by U . This gives

$$V B U V C U = V C U V B U. \quad (27)$$

Let $S = VBU$. It follows, on substitution of (17) into the above equation, that

$$S\Lambda = \Lambda S. \quad (28)$$

Conditions (24) and (28) are equivalent, satisfaction of one implies satisfaction of the other.

If the equivalence transformation defined by U and V decouples system (1), the matrix VBU must be diagonal. Since diagonal matrices commute in multiplication, condition (28) is satisfied. Condition (24) is therefore also satisfied.

On the other hand, assume condition (24) is valid. Satisfaction of condition (28) implies, on expansion, that

$$\lambda_j s_{ij} = \lambda_i s_{ij}, \quad i, j = 1, 2, \dots, n, \quad (29)$$

where s_{ij} is the ij th element of S . If all eigenvalues λ_i are distinct, the above equation implies that $s_{ij} = 0$ when $i \neq j$. That means S is diagonal, and the equivalence transformation which diagonalizes A and C decouples the entire system. The case of repeated eigenvalues can be treated similarly and the observation that S is diagonal remains valid (Ma & Caughey 1995). This completes the demonstration that condition (24) is both necessary and sufficient for system (1) to be decoupled by an equivalence transformation.

4. Discussion and example

The exposition of linear nonconservative vibrations by Inman (1983) provides an inspiring account for this investigation. This article also draws upon a remarkable study by Fawzy & Bishop (1976). There, under more restrictive assumptions, the authors attempted to derive orthogonality relations involving all three matrices A , B and C . As a result, their orthogonality relations contained the eigenvalues and became rather impractical. In view of theorem 3, an equivalence transformation cannot be constructed to diagonalize A , B and C in every case.

There are three practical implications of the method developed herein. First, this constructive method represents a direct extension of classical modal analysis and only approximately doubles the computational effort required of modal transformation. While the method is exact if $B = 0$, it is necessary to use some type of decoupling approximation for a general linearized structure. Extensive simulations have indicated that the method is substantially more efficient than the state-space approach. Reduction in computational effort, particularly in the case of large-scale systems, is indeed very attractive. Second, this method appears to possess *ample physical insight*, more of which has yet to be uncovered. For instance, in clarification of theorem 2, it has been pointed out that the complex eigenvectors u_i determine the mode shapes. Third, the method of equivalence transformations can be used to streamline computational algorithms based upon the method of weighted residuals. Many numerical techniques in this family of algorithms generate the same type of equations as (1). As an example, the collocation method leads to equations resembling that of a controlled structure with $B = 0$. These numerical techniques can be greatly streamlined by utilizing equivalence transformations.

As shown by Ma & Caughey (1995), any equivalence transformation that decouples system (3) must be derivable from the adjoint eigenvalue problems (5) and (6). It follows that a general theory of decoupling by equivalence transformations has been presented. Equivalence transformations are already the most general nonsingular linear transformations. It can therefore be stated that *no nonsingular linear transformation will ever diagonalize A , B and C simultaneously every time*. Further research to find universal decoupling transformations will not be necessary. Equation (23) is the simplest representation of a linearized controlled structure in Lagrangian coordinate.

Example. A linearized controlled structure, whose equation of motion has the form (1), is defined by

$$A = \begin{bmatrix} 7 & 1 & 2 \\ -1 & 7 & 0 \\ 1 & -1 & 6 \end{bmatrix}, \quad (30)$$

$$B = \begin{bmatrix} 2.2577 & -0.7016 & -0.0567 \\ 0.7305 & 4.4257 & 0.9294 \\ 1.4657 & 0.8812 & 3.9978 \end{bmatrix}, \quad (31)$$

$$C = \begin{bmatrix} 15.7158 & 9.0316 & 10.7895 \\ -35.0000 & -17.0000 & -24.5000 \\ 27.7368 & 11.4737 & 19.8421 \end{bmatrix}. \quad (32)$$

Solution of two adjoint eigenvalue problems (5) and (6) yields, after normalization,

$$U = \begin{bmatrix} -0.2136 & -0.5502 & -0.7315 \\ 1.0000 & -0.2893 & 0.0614 \\ -0.9580 & 1.0000 & 1.0000 \end{bmatrix}, \quad (33)$$

$$V = \begin{bmatrix} -0.3869 & -0.1728 & -0.1887 \\ -1.2311 & -0.9129 & -0.5196 \\ 0.8396 & 0.7751 & 0.5124 \end{bmatrix}. \quad (34)$$

With this equivalence transformation, the system can be reduced to the form (23), where

$$\Lambda = \text{diag}[1.9333, 0.2198, 0.0495]. \quad (35)$$

The natural frequencies are simply the square roots of the positive eigenvalues and are 0.22, 0.47 and 1.39 radians per second. All modes u_i , which are columns of U , are real in this case. Hence, if the coefficient matrix B were absent, all components of the system could perform harmonic vibration with identical phase angle at each natural frequency. The system still does not possess classical normal modes because the eigenvectors u_i are not orthogonal to each other with respect to A . The adjoint modes v_j constitute the rows of V . In addition to complementing biorthogonality relations, the role of the adjoint modes is to modify the generalized excitation $f(t)$.

An examination of the transformed coefficient matrix of velocity reveals that

$$VBU = \text{diag}[0.4685, 0.5109, 0.5733], \quad (36)$$

and therefore the system has been completely decoupled. As a result, this system can be regarded as composing of three independent single-degree-of-freedom systems. According to theorem 3, condition (24) must be satisfied. This can be verified by a simple calculation. In most applications, explicit verification of condition (24) at the start of computation is not advisable. An equivalence transformation should simply be applied to diagonalize the coefficient matrices A and C . Afterwards, one can examine the transformed coefficient matrix of velocity VBU to determine if the use of decoupling approximation would require a corrective scheme. Although the coefficient matrices A , B and C in this system can be diagonalized by equivalence transformation, they cannot be diagonalized by similarity transformation. Among other things, A itself is not diagonalizable by similarity transformation because there is only one eigenvector $[1, 1, -1]^T$ associated with the repeated eigenvalue 6. In addition, the coefficient matrices A , B and C cannot be simultaneously reduced to symmetric forms because A itself is not similar to a real symmetric matrix (Inman 1983). From this discussion, the power and generality of equivalence transformations are clear.

5. Conclusions

A time-honoured procedure for the approximate solution of nonlinear mechanical systems is linearization, or in some cases piecewise linearization. Development of an efficient method for analyzing and interpreting the equations of motion of

linearized controlled structures is timely due to increasing use of control devices in structures in recent years. The method expounded in this article represents a direct extension of classical modal analysis. This constructive method utilizes equivalence transformations in Lagrangian coordinates, and does not require conversion of the equations of motion to first-order forms. It is assumed, without practical loss of generality, that a linearized structure is not degenerate or defective. That means the coefficient of acceleration A is nonsingular, and the eigenvalue problem (5) possesses a full complement of independent eigenvectors. The major results, summarized in the following, are applicable for any generalized excitation $f(t)$.

- (1) A controlled structure in which $B = 0$ can always be decoupled by equivalence transformation. Compared with classical modal transformation, the lack of symmetry in a structure only approximately doubles the computational effort.
- (2) In free vibration, all components of an undamped nongyroscopic structure can perform harmonic vibration with identical frequency if the associated eigenvalue problem (5) possesses positive eigenvalues. The natural frequencies are simply the square roots of these positive eigenvalues, and the mode shapes can be determined from the corresponding complex eigenvectors. Unlike classical modal vibration, the system components generally vibrate with different phase angles.
- (3) The linearized controlled structure (1) can be decoupled by an equivalence transformation if and only if the matrices $A^{-1}B$ and $A^{-1}C$ commute in multiplication. Similar to classical modal analysis of a viscously damped system, it is often necessary to draw upon some type of decoupling approximation for fast solution.

Compared with the state-space approach, the method expounded herein offers substantial reduction in computational effort and ample physical insight. The method of equivalence transformations is applicable to nonsymmetric systems of any order, just as classical modal analysis is applicable to symmetric systems of arbitrary order. The tremendous power of equivalence transformation reflects its role as mathematically the most general nonsingular linear transformation. In addition, many numerical techniques involve equations resembling those of linearized controlled structures. These numerical algorithms will economize on both core memory and computing time if the method of equivalence transformations is incorporated. Among other things, it is hoped that the present paper would point to directions along which further research efforts can be profitably made. It appears feasible, for example, to examine stability and other qualitative features of a controlled structure with equivalence transformations. Analysis of errors committed by the application of decoupling approximation to a controlled structure is also worthwhile in a subsequent course of investigation.

I would like to thank Professor R N Iyengar for highly valuable comments. Mr. W C Lee has assisted with the preparation of numerical example. This research has been supported in part by the Alexander von Humboldt Foundation and by the National Science Foundation under Grant No. MSS-8657619. Opinions, findings, and conclusions expressed in this paper are those of the author and do not necessarily reflect the views of the sponsors.

References

- Caughey T K, Ma F 1993 Complex modes and solvability of nonclassical linear system. *ASME J. Appl. Mech.* 60: 26–28
- Caughey T K, O'Kelly M E J 1965 Classical normal modes in damped linear dynamic systems. *ASME J. Appl. Mech.* 32: 583–588
- Fawzy I, Bishop R E D 1976 On the dynamics of linear nonconservative systems. *Proc. R. Soc. London A* 352: 25–40
- Huseyin K, Leipholz H H E 1973 Divergence instability of multiple-parameter circulatory systems. *Q. Appl. Math.* 31: 185–197
- Hwang J H, Ma F 1993 On the approximate solution of nonclassically damped linear systems. *ASME J. Appl. Mech.* 60: 695–701
- Inman D J 1983 Dynamics of asymmetric non-conservative systems. *ASME J. Appl. Mech.* 50: 199–203
- Ma F, Caughey T K 1995 Analysis of linear non-conservative vibrations. *ASME J. Appl. Mech.* (in press)
- Meirovitch L 1967 *Analytical methods in vibrations* (New York: MacMillan) p. 78
- Müller P C, Schiehlen W O 1985 *Linear vibrations* (Dordrecht: Martinus Nijhoff) p. 37
- Park I W, Kim J S, Ma F 1994 Characteristics of modal coupling in nonclassically damped systems under harmonic excitation. *ASME J. Appl. Mech.* 61: 77–83
- Schmitz P D 1973 Normal mode solution to the equations of motion of a flexible airplane. *J. Aircraft* 10: 318–320
- Soom A, Kim C 1983 Roughness-induced dynamic loading at dry and boundary-lubricated sliding contacts, *ASME J. Lubrication Technol.* 105: 514–517
- Soong T T 1990 *Active structural control: Theory and practice* (Essex: Longman) p. 8
- Udwadia F E, Esfandiari R S 1990 Nonclassically damped dynamic systems: An iterative approach. *ASME J. Appl. Mech.* 57: 423–433
- Zurmühl R, Falk S 1984 *Matrizen und ihre Anwendungen* 5th edn (Berlin: Springer-Verlag) vol. 1, p. 180

On refined nonlinear theories of laminated composite structures with piezoelectric laminae

J N REDDY and J A MITCHELL

Department of Mechanical Engineering, Texas A & M University, College Station, TX 78843-3123, USA

Abstract. In this paper geometrically nonlinear theories of laminated composite plates with piezoelectric laminae are developed. The formulations are based on thermopiezoelectricity, and include the coupling between mechanical deformations, temperature changes, and electric displacements. Two different theories are presented: one based on an equivalent-single-layer third-order theory and the other based on the layerwise theory, both of which were developed by the senior author for composite laminates without piezoelectric laminae. In the present study, they are extended to include piezoelectric laminae. In both theories, the electric field is expanded layerwise through the laminate thickness. The dynamic version of the principle of virtual displacements (or Hamilton's principle) is used to derive the equations of motion and associated boundary conditions of the two theories. These theories may be used to accurately determine the response of laminated plate structures with piezoelectric laminae and subjected to thermomechanical loadings.

Keywords. Refined nonlinear theory; laminated composite structures; piezoelectric laminae; Hamilton's principle; thermomechanical loading.

1. Introduction

The study of embedded or surface mounted piezoelectric materials (e.g., conventional ferroelectric polycrystals in the form of ceramics, natural crystals, and polyvinylidene (PVDF)) in the active control of structures has received considerable attention in recent years. One reason for this is the possibility of creating certain types of structures and systems that can be adapted to or corrected for changing operating conditions using piezoelectric materials. The advantage of incorporating these special types of materials into a structure is that the sensing and actuating mechanism becomes part of the structure. These type of mechanisms are referred to as strain sensing and actuating (SSA). This advantage is especially apparent for structures which are deployed in space. Generally, space-borne structures are very flexible because they are not designed for operations in which the force of gravity is present. Most actuator systems other than the strain induced type add considerable weight and

possibly space to the structure and thereby change its mechanical properties significantly.

A laminated structure with piezoelectric laminae receives actuation through an applied electric field, and the piezoelectric laminae send electric signals that are used to measure the motion or deformation of the laminate. In these problems, the electric field that is applied to actuate a structure provides an additional body force, which couples the stress analysis problem to the electrostatic problem. This coupling is similar to a temperature field inducing a body force that couples the mechanical problem to the thermal problem.

The first nonlinear formulation of an electrically polarized elastic continuum is due to Toupin (1956). Following this work, many investigated the behaviour of continua in the presence of electric and/or magnetic fields (Erigen 1963; Tiersten 1964, 1971, 1981; Nelson 1978). Recently, Tiersten (1993) studied electroded plates undergoing large electric fields. In these works, thin, single-layer plates were considered with small strains and quadratic electric fields. A quadratic approximation of the mechanical displacements and a cubic approximation of the electric potential through the plate thickness were used to develop the plate theory.

In order to utilize the strain sensing and actuating properties of piezoelectric materials, the interaction between the structure and the SSA material must be well understood. Mechanical models for studying the interaction of piezoelectric patches that are surface mounted to beams have been developed by Crawley & de Luis (1987) and Chandra & Chopra (1993). The SSA lamina can offer both a discrete effect similar to patches as well as a distributed effect. Lee (1990) developed a theory for laminates piezoelectric plates using the classical laminate theory. In this theory, the linear piezoelectric constitutive equations were the only source of coupling between the electric field and the mechanical displacement field. Pai *et al* (1993) presented a geometrically nonlinear plate theory for the analysis of composite plates with distributed piezoelectric lamina. By using a layerwise type displacement similar to that proposed by Reddy (1987), they have enforced continuity of both displacements and interlaminar stresses. However, their model does not include the charge equations of electrostatics. In contrast, Tiersten (1969, 1993) modelled single-layer piezoelectric plates using the charge equations, but they did not study laminated plates. Tzou & Zhong (1993) developed governing equations for piezoelectric shells using the first-order shear deformation theory, and they included the charge equations of electrostatics. From these equations, classical and first-order shear deformation plate theories were derived for single-layer piezoelectric laminae.

In the present study, two different formulations are developed to study the extensional and flexural motions of plates laminated with orthotropic layers and piezoelectric laminae. In the first model an equivalent single-layer third-order theory (Reddy 1984, 1995) is used, and in the second one the layerwise theory (Reddy 1987) is used to approximate the displacement field. In both models, a layerwise expansion is used for the electric field. In addition, the formulations include geometric nonlinearity through the von Kármán strains. Variational statements, which are useful in the development of finite element models, and the governing equations of the two models for piezoelectroelasticity are developed from basic principles. Recently, the authors have used the model based on the third-order theory but with linear strains to study the bending and vibration of composite laminates with piezoelectric laminae (Mitchell & Reddy 1994).

2. Equations of thermoelectroelasticity

2.1 Thermodynamic principles

There are two principles of thermodynamics: the first law of thermodynamics and the second law of thermodynamics. The first law of thermodynamics, also known as the principle of conservation of energy, states that the time rate of change of the total energy is equal to the sum of the rate of work done by applied forces and the change of heat content per unit time. The second law of thermodynamics places restrictions on the interconvertibility of heat and work done. For irreversible heat transfer, the second law states that the entropy production is positive.

The principle of conservation of energy leads to the well-known heat conduction equation (see Reddy & Gartling 1994)

$$\rho c_v \frac{\partial T}{\partial t} = -\nabla \cdot \mathbf{q} + \rho r + \sigma : \nabla \mathbf{v}, \quad (1)$$

where T is the temperature, \mathbf{v} is the velocity vector, \mathbf{q} is the heat flux vector, r is the internal heat generation per unit mass, c_v is the specific heat at constant volume or constant strain and σ is the stress tensor. Equation (1) is used to determine the temperature distribution in the body. The viscous dissipation $\sigma : \nabla \mathbf{v}$ couples the thermal problem to the stress problem. Even when the viscous dissipation is neglected, the thermal problem is coupled to the stress problem through stress-strain relations, as explained in the next section.

The thermal problem for the solid requires the temperature or the heat flux to be specified on all parts of the boundary enclosing the heat transfer region:

$$T = \hat{T}(s, t) \text{ on } \Gamma_T, \quad (2)$$

$$\hat{\mathbf{n}} \cdot \mathbf{q} + h_c(T - T_c) = \hat{q}_n(s, t) \text{ on } \Gamma_q, \quad (3)$$

where Γ is the total boundary enclosing the heat transfer region, $\Gamma = \Gamma_T \cup \Gamma_q$, h_c is the convective heat transfer coefficient, T_c is a reference (or sink) temperature for convective transfer, \hat{q}_n is the specified boundary flux, and $\hat{\mathbf{n}}$ is the unit normal to the boundary.

2.2 Thermoelastic constitutive relations

The thermoelastic problem is governed by the strain-displacement equations, equations of motion, thermodynamic equations (1)–(3), and constitutive equations. The constitutive equation of the thermal problem is given by the well-known Fourier's heat conduction law (Carslaw & Jaeger 1959, Nowinski 1978, Reddy & Gartling 1994)

$$\mathbf{q} = -\mathbf{k} \cdot \nabla T, \quad q_i = -k_{ij}(\partial T / \partial x_j), \quad (4)$$

where \mathbf{k} denotes the *thermal conductivity tensor* of order two.

The constitutive equations of thermoelasticity are derived by assuming the existence of the *free-energy function*, $\Psi = \Psi(\epsilon_{ij}, T)$, of the form

$$\Psi(\epsilon_{ij}, T) = \frac{1}{2} C_{ijkl} \epsilon_{ij} \epsilon_{kl} - \beta_{ij} \epsilon_{ij} \theta + \frac{1}{2} m \theta, \quad (5)$$

such that (see Carslaw & Jaeger 1959; Nowinski 1978)

$$\sigma_{ij} = \partial \Psi / \partial \epsilon_{ij} = C_{ijkl} \epsilon_{kl} - \beta_{ij} \theta, \quad (6)$$

where $\theta = T - T_0$, T_0 is the reference temperature, and m and β_{ij} are material coefficients. Equation (6) is known as the *Duhamel-Neumann law* for an anisotropic body. Inverting relations (6), we obtain

$$\varepsilon_{ij} = S_{ijkl}\sigma_{kl} + \alpha_{ij}\theta, \quad (7)$$

where S_{ijkl} are the elastic compliances, and α_{ij} are the thermal coefficients of expansion related to β_{ij} by $\beta_{ij} = C_{ijkl}\alpha_{kl}$.

2.3 Constitutive relations of hygrothermal elasticity

Temperature and moisture concentration in fibre-reinforced composites cause reductions of both strength and stiffness (Jost 1952; Shen & Springer 1976; Browning *et al* 1977). Therefore, it is important to determine the temperature and moisture concentration in composite laminates under given initial and boundary conditions. As described in the previous section, the heat conduction problem described by (1)–(4) can be used to determine the temperature field.

The moisture concentration problem is mathematically similar to the heat transfer problem. The moisture concentration, c , in a solid is described by Fick's second law:

$$\frac{\partial c}{\partial t} = -\nabla \cdot \mathbf{q}_f + \Phi_f, \quad (8a)$$

$$\mathbf{q}_f = -\mathbf{D} \cdot \nabla c, \quad (8b)$$

where \mathbf{D} denotes the *mass diffusivity tensor* of order two, \mathbf{q}_f is the flux vector, and Φ_f is the moisture source in the domain. The negative sign in (8b) indicates that moisture seeps from higher concentration to lower concentration. The boundary conditions involve specifying the moisture concentration or the flux:

$$c = \hat{c}(s, t) \text{ on } \Gamma_1, \quad (9a)$$

$$\hat{\mathbf{n}} \cdot \mathbf{q}_f = \hat{q}_f(s, t) \text{ on } \Gamma_2, \quad (9b)$$

where $\Gamma = \Gamma_1 \cup \Gamma_2$ and quantities with a hat are specified functions on the respective boundaries.

The moisture-induced strains $\{\varepsilon\}^M$ are given by

$$\{\varepsilon\}^M = \{\alpha\}^M c, \quad (10)$$

where $\{\alpha\}^M$ is the vector of *coefficients of hygroscopic expansion*. Thus the hygroscopic strains have the same form as the thermal strains [see (7)]. The total strains are given by

$$\{\varepsilon\} = [\mathbf{S}]\{\sigma\} + \{\alpha\}^T(T - T_0) + \{\alpha\}^M(c - c_0), \quad (11)$$

where T_0 and c_0 are reference values from which the strains and stresses are measured. In view of the similarity between the thermal and moisture strains, we will use only thermal strains to show their contribution to governing equations.

2.4 Electroelasticity

Electroelasticity deals with the phenomena caused by interactions between electric and mechanical fields. The *piezoelectric effect* is a linear phenomenon of electroelasticity,

and it is concerned with the effect of the electric field and polarization on the deformation (Nye 1957; Penfield & Hermann 1967; Tierstein 1969; Reddy & Gartling 1994). The effect is described by the *polarization vector* \mathbf{P} , which represents the electric moment per unit volume or polarization charge per unit area. The relation between the stress tensor and polarization vector is known as the direct effect, and it is given by

$$\mathbf{P} = \mathbf{d} : \boldsymbol{\sigma} \text{ or } P_i = d_{ijk} \sigma_{jk} \quad (12)$$

where \mathbf{d} is the third-order tensor of piezoelectric moduli, $\boldsymbol{\sigma}$ is the stress tensor, and d_{ijk} and σ_{jk} denote their rectangular Cartesian components. The converse effect relates the electric field vector \mathbf{E} to the linear strain tensor $\boldsymbol{\varepsilon}$ by

$$\boldsymbol{\varepsilon} = \mathbf{E} \cdot \mathbf{d} \text{ or } \varepsilon_{ij} = d_{kij} E_k. \quad (13)$$

Note that d_{kij} is symmetric with respect to indices i and j because of the symmetry of the strain components ε_{ij} .

The coupling between the mechanical, thermal, and electrical fields can be established using thermodynamics principles and Maxwell's relations. Analogous to the strain energy density function U_0 for elasticity and the free-energy density function Ψ_0 for thermoelasticity, we assume the existence of a density function Φ_0

$$\begin{aligned} \Phi_0(\varepsilon_{ij}, E_i, T) &= U_0 - \mathbf{E} \cdot \mathbf{D} - \eta T \\ &= \frac{1}{2} C_{ijkl} \varepsilon_{ij} \varepsilon_{kl} - e_{ijk} \varepsilon_{ij} E_k - \beta_{ij} \varepsilon_{ij} \theta \\ &\quad - \frac{1}{2} \varepsilon_{kl} E_k E_l - (\rho c_v / 2 T_0) \theta^2, \end{aligned} \quad (14)$$

called the electric *Gibb's function* or *enthalpy function*, such that

$$\sigma_{ij} = \frac{\partial \Phi_0}{\partial \varepsilon_{ij}}, \quad D_i = -\frac{\partial \Phi_0}{\partial E_i}, \quad \eta = -\frac{\partial \Phi_0}{\partial T} = -\frac{\partial \Phi_0}{\partial \theta}, \quad (15)$$

where D_i are the components of the electric displacement vector, and η is the entropy (which is governed by the second law of thermodynamics). Use of (14) in (15) gives the linear constitutive equations of a piezoelectric medium:

$$\sigma_{ij} = C_{ijkl} \varepsilon_{kl} - e_{kij} E_k - B_{ij} \theta, \quad (16a)$$

$$D_k = \epsilon_{kij} \varepsilon_{ij} + \epsilon_{kl} E_l, \quad (16b)$$

$$\eta = \beta_{ij} \varepsilon_{ij} + \frac{\rho c_v}{T_0} \theta, \quad (16c)$$

where C_{ijkl} are the elastic moduli, e_{ijk} are the piezoelectric moduli, ε_{ij} are the dielectric constants, β_{ij} are the temperature expansion coefficients, c_v is the specific heat per unit mass, and T_0 is the reference temperature. In single subscript notation, (16) can be expressed as

$$\sigma_i = C_{ij} \varepsilon_j - e_{ji} E_j - \beta_i \theta, \quad (17a)$$

$$D_k = e_{kl} \varepsilon_l + \epsilon_{kl} E_l, \quad (17b)$$

$$\eta = \beta_i \varepsilon_i + \frac{\rho c_v}{T_0} \theta. \quad (17c)$$

Equations (17) provide linear constitutive relations for the problem at hand. For a general anisotropic material, there are 21 independent elastic constants, 18 piezoelectric constants, 6 dielectric constants, and 6 thermal expansion coefficients.

In the following derivations, we account for thermal (and hence, moisture) and piezoelectric effects only with the understanding that the material properties are independent of temperature and electricity, and that the temperature T is a known function of position (hence, its variation is zero: $\delta T = 0$). Thus temperature enters the formulation as a known function through constitutive equations (17). However, since we are primarily interested in developing the coupled equations of piezoelectricity, the electric field \mathbf{E} will be treated as a dependent variable (i.e., variable subject to variation). It can be shown that for electrostatics, the electric field \mathbf{E} is derivable from a scalar potential function ψ

$$\mathbf{E} = -\nabla\psi. \quad (18)$$

2.5 Approximation of electric field potential

In the interest of representing the electric potential more accurately through the thickness of the laminate, it is approximated using the layerwise expansion (see Nowinski 1978; Reddy 1987; Robbins & Reddy 1993)

$$\psi(x, y, z, t) = \sum_{j=1}^M \psi_j(x, y, t) \Phi^j(z), \quad (19)$$

where $\psi_j(x, y, t)$ denote the nodal values of ψ , M is the number of nodes through thickness, and Φ^j are the *global* Lagrange interpolation functions for the discretization of ψ through thickness (see Reddy 1993; Reddy & Gartling 1994). This is equivalent to modelling through-the-thickness variation of $\psi(x, y, z, t)$ with one-dimensional finite elements (see figure 1). Non-piezoelectric lamina can be modelled by simply setting the piezoelectric constants to zero and retaining the dielectric permittivity constants if necessary. In this way it is possible to model arbitrary applied potential loading conditions as well as more than one material type, including piezoelectric material.

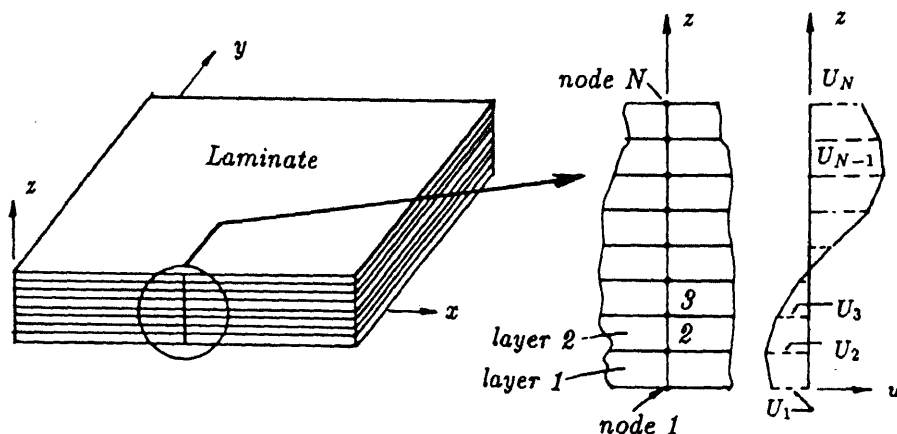


Figure 1. Layerwise approximation of a field variable, u , in a laminated plate.

3. The third-order theory

3.1 Preliminary comments

The equivalent single-layer (ESL) laminate theories are those in which a heterogeneous laminated plate is treated as a statically equivalent, single layer having a (possibly) complex constitutive behavior, reducing the 3-D continuum problem to a 2-D problem. The ESL theories are developed by assuming the form of the displacement field as a linear combination of unknown functions and the thickness coordinate (Mitchell & Reddy 1994). Then the governing equations are determined using the principle of virtual displacements (or its dynamic version, when time dependency is to be included). For plate structures, laminated or not, the integration over the domain of the plate is represented, because of the explicit nature of the assumed displacement field in the thickness coordinate, as the (tensor) product of integration over the plane of the plate and integration over the thickness of the plate (volume integral = integral over the plane \times integral over the thickness). Since all functions of the theory are explicit functions of the thickness coordinate, the integration over plate thickness is carried out explicitly, reducing the problem to a two-dimensional one. Consequently, the Euler–Lagrange equations will consist of differential relations involving the dependent variables (or generalized displacements) and thickness-averaged stress resultants. The resultants can be written in terms of the generalized displacements with the help of the assumed constitutive equations and kinematic relations. More complete development of this procedure is presented in the coming sections.

The classical and first-order theories of composite laminates are the most commonly used ones. The classical laminate theory does not account for the transverse shear deformation, while the first-order theory accounts for transverse shear strains as constant through the thickness and hence requires shear correction factors. Second and higher-order ESL laminated plate theories use higher-order polynomials in the expansion of the displacement components through the thickness of the laminate. The *third-order theory of Reddy* accounts for quadratic variation of transverse stresses through the thickness, and thus does not require shear correction factors.

3.2 Displacements and strains

Consider a plate of total thickness h composed of N orthotropic layers, some of which may be piezoelectric, with the principal material coordinates (x_1^k, x_2^k, x_3^k) of the k -th

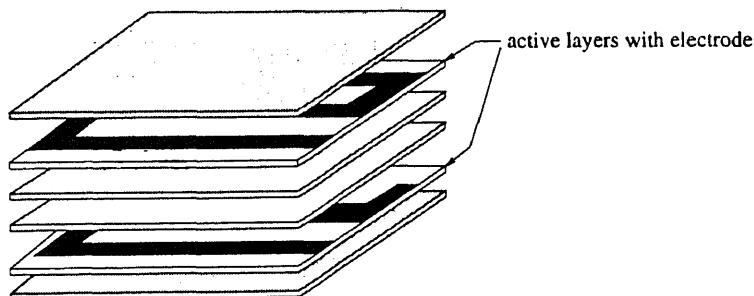


Figure 2. Schematic of a laminated plate with piezoelectric laminae.

lamina oriented at an angle θ_k to the laminate coordinate, x (see figure 2). The xy -plane of the plate coincides with the undeformed midplane Ω of the laminate. The z -axis is taken positive upward from the midplane. The k -th layer is located between the points $z = z_k$ and $z = z_{k+1}$ in the thickness direction. The total domain $\bar{\Omega}$ of the laminate is the tensor product of $\Omega \times (-h/2, h/2)$. Different parts of the boundary $\bar{\Gamma} \equiv \Gamma \times (-h/2, h/2)$ of $\bar{\Omega}$ are subjected to different generalized forces or generalized displacements. Here Γ denotes the boundary of Ω , the midplane of the laminate. A discussion of the boundary conditions is given later.

The total displacement components (u, v, w) along the coordinates (x, y, z) are approximated in the third-order laminate theory of Reddy (1984, 1995) as,

$$\begin{aligned} u &= u_0 + z(\varphi_x - c_0(\partial w_0/\partial x) - c_1 z^3 \varphi_x), \\ v &= v_0 + z(\varphi_y - c_0(\partial w_0/\partial y) - c_1 z^3 \varphi_y), \\ w &= w_0, \end{aligned} \quad (20)$$

where u_0, v_0, w_0, φ_x , and φ_y are unknown functions of position (x, y) and time t , and parameters c_0 and c_1 are introduced to identify the classical laminate theory ($c_0 = 1$ and $\varphi_x = \varphi_y = 0$) or the first-order laminate theory ($c_0 = c_1 = 0$) as special cases of the present theory. Note that (u_0, v_0, w_0) denote the displacements of a material point at $(x, y, 0)$ along the three coordinates, and $(\varphi_x - (\partial w_0/\partial x))$ and $(\varphi_y - (\partial w_0/\partial y))$ denote rotations of transverse normals at $z = 0$ about the y and x axes, respectively.

The von Kármán strains (see Reddy 1995) associated with the displacement field (20) are ($\varepsilon_{zz} = 0$),

$$\begin{Bmatrix} \varepsilon_{xx} \\ \varepsilon_{yy} \\ \gamma_{xy} \end{Bmatrix} = \begin{Bmatrix} \varepsilon_{xx}^{(0)} \\ \varepsilon_{yy}^{(0)} \\ \gamma_{xy}^{(0)} \end{Bmatrix} + z \begin{Bmatrix} \varepsilon_{xx}^{(1)} \\ \varepsilon_{yy}^{(1)} \\ \gamma_{xy}^{(1)} \end{Bmatrix} + z^3 \begin{Bmatrix} \varepsilon_{xx}^{(3)} \\ \varepsilon_{yy}^{(3)} \\ \gamma_{xy}^{(3)} \end{Bmatrix} \quad (21a)$$

$$\begin{Bmatrix} \gamma_{yz} \\ \gamma_{xz} \end{Bmatrix} = \begin{Bmatrix} \gamma_{yz}^{(0)} \\ \gamma_{xz}^{(0)} \end{Bmatrix} + z^2 \begin{Bmatrix} \gamma_{yz}^{(2)} \\ \gamma_{xz}^{(2)} \end{Bmatrix}, \quad (21b)$$

where

$$\begin{aligned} \varepsilon_{xx}^{(0)} &= \frac{\partial u_0}{\partial x} + \frac{1}{2} \left(\frac{\partial w_0}{\partial x} \right)^2, & \varepsilon_{xx}^{(1)} &= \frac{\partial \varphi_x}{\partial x} - c_0 \frac{\partial^2 w_0}{\partial x^2}, & \varepsilon_{xx}^{(3)} &= -c_1 \frac{\partial \varphi_x}{\partial x}, \\ \varepsilon_{yy}^{(0)} &= \frac{\partial v_0}{\partial y} + \frac{1}{2} \left(\frac{\partial w_0}{\partial y} \right)^2, & \varepsilon_{yy}^{(1)} &= \frac{\partial \varphi_y}{\partial y} - c_0 \frac{\partial^2 w_0}{\partial y^2}, & \varepsilon_{yy}^{(3)} &= -c_1 \frac{\partial \varphi_y}{\partial y}, \\ \gamma_{xy}^{(0)} &= \frac{\partial u_0}{\partial y} + \frac{\partial v_0}{\partial x} + \frac{\partial w_0}{\partial x} \frac{\partial w_0}{\partial y}, & \gamma_{xy}^{(1)} &= \frac{\partial \varphi_x}{\partial y} + \frac{\partial \varphi_y}{\partial x} - 2c_0 \frac{\partial^2 w_0}{\partial x \partial y}, \\ \gamma_{xy}^{(3)} &= -c_1 \left(\frac{\partial \varphi_x}{\partial y} + \frac{\partial \varphi_y}{\partial x} \right), \\ \gamma_{yz}^{(0)} &= \varphi_y + \bar{c}_0 \frac{\partial w_0}{\partial y}, & \gamma_{yz}^{(2)} &= -c_2 \varphi_y, & \gamma_{xz}^{(0)} &= \varphi_x + \bar{c}_0 \frac{\partial w_0}{\partial x}, & \gamma_{xz}^{(2)} &= -c_2 \varphi_x, \end{aligned} \quad (22)$$

and

$$c_1 = \frac{4}{3h^2}, \quad c_2 = \frac{4}{h^2}, \quad \bar{c}_0 = 1 - c_0.$$

It is easy to verify that the transverse shear strains ε_4 and ε_5 are zero at the upper and lower surfaces of the plate, and that they vary quadratically through the thickness. Although this particular approximation was developed for laminated plates without piezoelectric lamina, it also serves well when piezoelectric lamina are present since contributions to the shear stress on the major surfaces due to piezoelectric lamina are derived from the gradient of the potential function. Note that only the tangential component of the electric field is required to be continuous across boundaries having material discontinuities. A plate having piezoelectric laminae on its outer surfaces covered with a thin electrode will not have any component of inplane electric field on these surfaces because the electric field is zero inside the conductor. Further, since transverse shear stresses due to piezoelectric effects result from components of the inplane electric field (this depends upon the particular form of the constitutive relations), it follows that shear stresses on the free surfaces are only due to mechanical effects.

3.3 Equations of motion

Hamilton's principle (or the dynamic version of the principle of virtual displacements) is used to derive the equations of motion for a laminated plate with piezoelectric laminae. Hamilton's principle requires that

$$0 = \int_0^T (\delta\Phi + \delta V - \delta K) dt, \quad (23)$$

where $\delta\Phi$ is the virtual Gibb's energy (the volume integral of $\delta\Phi_0$), δV is the virtual work done by applied forces and possibly charge, and δK is the virtual kinetic energy. For the problem at hand, these are given by

$$\begin{aligned} \delta\Phi &= \int_{\Omega} \left\{ \int_{-(h/2)}^{(h/2)} (\sigma_{ij} \delta\varepsilon_{ij} - D_i \delta E_i) dz \right\} dx dy \\ &= \int_{\Omega_0} \left[N_{xx} \delta\varepsilon_{xx}^{(0)} + M_{xx} \delta\varepsilon_{xx}^{(1)} + K_{xx} \delta\varepsilon_{xx}^{(3)} \right. \\ &\quad + N_{yy} \delta\varepsilon_{yy}^{(0)} + M_{yy} \delta\varepsilon_{yy}^{(1)} + K_{yy} \delta\varepsilon_{yy}^{(3)} \\ &\quad + N_{xy} \delta\gamma_{xy}^{(0)} + M_{xy} \delta\gamma_{xy}^{(1)} + K_{xy} \delta\gamma_{xy}^{(3)} \\ &\quad + Q_x \delta\gamma_{xz}^{(0)} + S_x \delta\gamma_{xz}^{(2)} + Q_y \delta\gamma_{yz}^{(0)} + S_y \delta\gamma_{yz}^{(2)} \\ &\quad \left. - \sum_{I=1}^M \left(P_x^I \frac{\partial \delta\psi_I}{\partial x} + P_y^I \frac{\partial \delta\psi_I}{\partial y} + P_z^I \delta\psi_I \right) \right] dx dy, \quad (24) \end{aligned}$$

$$\begin{aligned} \delta V &= - \int_{\Omega_0} \left[q_b(x, y) \delta w_0 \left(x, y, -\frac{h}{2} \right) + q_t(x, y) \delta w_0 \left(x, y, \frac{h}{2} \right) \right. \\ &\quad \left. + p_b(x, y) \delta\psi \left(x, y, -\frac{h}{2} \right) + p_t(x, y) \delta\psi \left(x, y, \frac{h}{2} \right) \right] dx dy \\ &\quad - \int_{\Gamma} \int_{-(h/2)}^{(h/2)} \left\{ \hat{\sigma}_{mn} \left[\delta u_n + z \left(\delta\varphi_n - c_0 \frac{\partial \delta w_0}{\partial n} \right) - c_1 z^3 \delta\varphi_n \right] \right. \end{aligned}$$

$$\begin{aligned}
& + \hat{\sigma}_{ns} \left[\delta u_s + z \left(\delta \varphi_s - c_0 \frac{\partial \delta w_0}{\partial s} \right) - c_1 z^3 \delta \varphi_s \right] + \hat{\sigma}_{nz} \delta w_0 \Big] dz d\Gamma \\
= & - \int_{\Omega_0} \left[q \delta w_0 + \sum_{I=1}^M p^I \delta \psi_I \right] dx dy \\
& - \int_{\Gamma} \left\{ \hat{N}_{nn} \delta u_n + \hat{M}_{nn} \left(\delta \varphi_n - c_0 \frac{\partial \delta w_0}{\partial n} \right) + \hat{N}_{ns} \delta u_s \right. \\
& + \hat{M}_{ns} \left(\delta \varphi_s - c_0 \frac{\partial \delta w_0}{\partial s} \right) - c_1 (\hat{K}_{nn} \delta \varphi_n + \hat{K}_{ns} \delta \varphi_s) \\
& \left. + \hat{Q}_n \delta w_0 + \sum_{I=1}^M \hat{P}_n^I \delta \psi_I \right\} d\Gamma, \tag{25}
\end{aligned}$$

$$\begin{aligned}
\delta K = & \int_{\Omega_0} \left[\left(I_0 \dot{u}_0 + \bar{I}_1 \dot{\phi}_x - c_0 I_1 \frac{\partial \dot{w}_0}{\partial x} \right) \delta \dot{u}_0 + \left(I_0 \dot{u}_0 + \bar{I}_2 \dot{\phi}_x - c_0 I_2 \frac{\partial \dot{w}_0}{\partial x} \right) \delta \dot{\phi}_x \right. \\
& - \left(I_1 \dot{u}_0 + \bar{I}_2 \dot{\phi}_x - c_0 I_2 \frac{\partial \dot{w}_0}{\partial x} \right) \frac{\partial \delta \dot{w}_0}{\partial x} - c_1 \left(I_3 \dot{u}_0 + \bar{I}_4 \dot{\phi}_x - c_0 I_4 \frac{\partial \dot{w}_0}{\partial x} \right) \delta \dot{\phi}_x \\
& + \left(I_0 \dot{v}_0 + \bar{I}_1 \dot{\phi}_y - c_0 I_1 \frac{\partial \dot{w}_0}{\partial y} \right) \delta \dot{v}_0 + \left(I_1 \dot{v}_0 + \bar{I}_2 \dot{\phi}_y - c_0 I_2 \frac{\partial \dot{w}_0}{\partial y} \right) \delta \dot{\phi}_y \\
& - \left(I_1 \dot{v}_0 + \bar{I}_2 \dot{\phi}_y - c_0 I_2 \frac{\partial \dot{w}_0}{\partial y} \right) \frac{\partial \delta \dot{w}_0}{\partial y} - c_1 \left(I_3 \dot{v}_0 + \bar{I}_4 \dot{\phi}_y - c_0 I_4 \frac{\partial \dot{w}_0}{\partial y} \right) \delta \dot{\phi}_y \\
& \left. + I_0 \dot{w}_0 \delta \dot{w}_0 \right] dx dy, \tag{26}
\end{aligned}$$

where $q = q_b + q_t$, q_b is the distributed force at the bottom ($z = -h/2$) of the laminate, q_t is the distributed force at the top ($z = h/2$) of the laminate, $(\hat{\sigma}_{nn}, \hat{\sigma}_{ns}, \hat{\sigma}_{nz})$ are the specified stress components along the normal, tangential, and transverse directions respectively, at a point on the boundary $\bar{\Gamma}$; $(\delta u_n, \delta u_s)$ are the virtual displacements along the normal and tangential directions, respectively; ρ is the density of the plate material; and superposed dot on a variable indicates time derivative, $\dot{u}_0 = \partial u_0 / \partial t$. The subscripts n and s refer to normal and tangential directions to the midplane Ω , respectively.

Note that in (25)–(28), integration over the laminate thickness is carried out and thickness-averaged resultants are introduced as follows:

$$\begin{Bmatrix} N_{\alpha\beta} \\ M_{\alpha\beta} \\ K_{\alpha\beta} \end{Bmatrix} = \int_{-(h/2)}^{(h/2)} \sigma_{\alpha\beta} \begin{Bmatrix} 1 \\ z \\ z^3 \end{Bmatrix} dz, \quad \begin{Bmatrix} Q_\alpha \\ S_\alpha \end{Bmatrix} = \int_{-(h/2)}^{(h/2)} \sigma_{\alpha z} \begin{Bmatrix} 1 \\ z^2 \end{Bmatrix} dz, \tag{27}$$

$$\begin{Bmatrix} P_x^I \\ P_y^I \end{Bmatrix} = \int_{-(h/2)}^{(h/2)} \begin{Bmatrix} D_x \\ D_y \end{Bmatrix} \Phi^I dz, \quad P_z^I = \int_{-(h/2)}^{(h/2)} D_z \frac{d\Phi^I}{dz} dz, \tag{28}$$

$$I_i = \int_{-(h/2)}^{(h/2)} \rho_0(z)^i dz, \quad \bar{I}_i = I_i - c_1 I_{i+2}, \quad \hat{I}_i = \bar{I}_i - c_1 \bar{I}_{i+2}. \tag{29}$$

Note that in (29) i takes the values of 0, 1, 2, ..., 6, and in (27)–(29), α and β take the symbols x and y . The same definitions hold for the stress resultants with a hat. Note

should be made of the fact that the stress resultants defined above are the total resultants that contain the mechanical, thermal as well as the piezoelectric parts. We shall separate these parts later.

Substituting for $\delta\Phi$, δV , and δK from (24)–(26) into (23), noting that the virtual strains can be written in terms of the generalized displacements ($u_0, v_0, w_0, \varphi_x, \varphi_y, \psi_I$) using (22), integrating by parts to relieve the virtual generalized displacements in Ω of any differentiation, and using the fundamental lemma of calculus of variations (Reddy 1984), we obtain the following Euler–Lagrange equations:

$$\delta u_0: \frac{\partial N_{xx}}{\partial x} + \frac{\partial N_{xy}}{\partial y} = I_0 \frac{\partial^2 u_0}{\partial t^2} + \bar{I}_1 \frac{\partial^2 \varphi_x}{\partial t^2} - c_0 I_1 \frac{\partial^3 w_0}{\partial x \partial t^2}, \quad (30)$$

$$\delta v_0: \frac{\partial N_{xy}}{\partial x} + \frac{\partial N_{yy}}{\partial y} = I_0 \frac{\partial^2 v_0}{\partial t^2} + \bar{I}_1 \frac{\partial^2 \varphi_y}{\partial t^2} - c_0 I_1 \frac{\partial^3 w_0}{\partial y \partial t^2}, \quad (31)$$

$$\begin{aligned} \delta w_0: \bar{c}_0 \left(\frac{\partial Q_x}{\partial x} + \frac{\partial Q_y}{\partial y} \right) + c_0 \left[\frac{\partial}{\partial x} \left(\frac{\partial M_{xx}}{\partial x} + \frac{\partial M_{xy}}{\partial y} \right) + \frac{\partial}{\partial y} \left(\frac{\partial M_{xy}}{\partial x} + \frac{\partial M_{yy}}{\partial y} \right) \right] \\ + \mathcal{N}(w_0) + q = I_0 \frac{\partial^2 w_0}{\partial t^2} - c_0^2 I_2 \frac{\partial^2}{\partial t^2} \left(\frac{\partial^2 w_0}{\partial x^2} + \frac{\partial^2 w_0}{\partial y^2} \right) \\ + c_0 I_1 \frac{\partial^2}{\partial t^2} \left(\frac{\partial u_0}{\partial x} + \frac{\partial v_0}{\partial y} \right) + c_0 \bar{I}_2 \frac{\partial^2}{\partial t^2} \left(\frac{\partial \varphi_x}{\partial x} + \frac{\partial \varphi_y}{\partial y} \right), \end{aligned} \quad (32)$$

$$\delta \varphi_x: \frac{\partial \bar{M}_{xx}}{\partial x} + \frac{\partial \bar{M}_{xy}}{\partial y} - \bar{Q}_x = \bar{I}_1 \frac{\partial^2 u_0}{\partial t^2} + \hat{I}_2 \frac{\partial^2 \varphi_x}{\partial t^2} - c_0 \hat{I}_2 \frac{\partial^3 w_0}{\partial x \partial t^2}, \quad (33)$$

$$\delta \varphi_y: \frac{\partial \bar{M}_{xy}}{\partial x} + \frac{\partial \bar{M}_{yy}}{\partial y} - \bar{Q}_y = \bar{I}_1 \frac{\partial^2 v_0}{\partial t^2} + \hat{I}_2 \frac{\partial^2 \varphi_y}{\partial t^2} - c_0 \hat{I}_2 \frac{\partial^3 w_0}{\partial y \partial t^2}, \quad (34)$$

$$\delta \psi_I: \frac{\partial P_x^I}{\partial x} + \frac{\partial P_y^I}{\partial y} - P_z^I = p^I, \quad (35)$$

where

$$\mathcal{N}(w_0) = \frac{\partial}{\partial x} \left(N_{xx} \frac{\partial w_0}{\partial x} + N_{xy} \frac{\partial w_0}{\partial y} \right) + \frac{\partial}{\partial y} \left(N_{xy} \frac{\partial w_0}{\partial x} + N_{yy} \frac{\partial w_0}{\partial y} \right), \quad (36)$$

$$\bar{Q}_\alpha = Q_\alpha - c_2 S_\alpha, \quad \bar{M}_{\alpha\beta} = M_{\alpha\beta} - c_1 K_{\alpha\beta}, \quad (37)$$

where α and β take on the letters x and y . It must be recognized that the charge p^I can only be applied at a conductor dielectric interface. Therefore, unless node I corresponds to such an interface, $p^I = 0$, in most cases, ψ_I (nodal value of the electric potential, ψ) will be specified at such interfaces, and the corresponding equation will not be there. In these cases, the surface charge density is calculated *a posteriori*.

The natural boundary conditions of the theory are:

$$(\delta u_n, \delta u_s): N_{nn} - \hat{N}_{nn} = 0, \quad N_{ns} - \hat{N}_{ns} = 0,$$

$$\left(\delta w_0, \frac{\partial \delta w_0}{\partial n} \right): \bar{Q}_n - \left(\hat{Q}_n + c_0 \frac{\partial \hat{M}_{ns}}{\partial s} \right) = 0, \quad c_0 M_{nn} - \hat{M}_{nn} = 0,$$

$$(\delta \varphi_n, \delta \varphi_s): \bar{M}_{nn} - (\hat{M}_{nn} - c_1 \hat{K}_{nn}) = 0, \quad \bar{M}_{ns} - (\hat{M}_{ns} - c_1 \hat{K}_{ns}) = 0,$$

$$\delta \psi_I: P_n^I - \hat{P}_n^I = 0,$$

where

$$\begin{aligned}\bar{Q}_n \equiv & \bar{c}_0(Q_x n_x + Q_y n_y) + c_0 \frac{\partial M_{ns}}{\partial s} + \mathcal{P}(w_0) \\ & + \left[c_0 \left(\frac{\partial M_{xx}}{\partial x} + \frac{\partial M_{xy}}{\partial y} + I_2 \frac{\partial \bar{w}_0}{\partial x} \right) - I_1 \ddot{u}_0 - \bar{I}_2 \ddot{\phi}_x \right] n_x \\ & + \left[c_0 \left(\frac{\partial M_{xy}}{\partial x} + \frac{\partial M_{yy}}{\partial y} + I_2 \frac{\partial \bar{w}_0}{\partial y} \right) - I_1 \ddot{v}_0 - \bar{I}_2 \ddot{\phi}_y \right] n_y\end{aligned}\quad (39a)$$

$$\mathcal{P}(w_0) = \left(N_{xx} \frac{\partial w_0}{\partial x} + N_{xy} \frac{\partial w_0}{\partial y} \right) n_x + \left(N_{xy} \frac{\partial w_0}{\partial x} + N_{yy} \frac{\partial w_0}{\partial y} \right) n_y, \quad (39b)$$

$$\begin{Bmatrix} \bar{M}_{nn} \\ \bar{M}_{ns} \end{Bmatrix} = \begin{bmatrix} n_x^2 & n_y^2 & 2n_x n_y \\ -n_x n_y & n_x n_y & n_x^2 - n_y^2 \end{bmatrix} \begin{Bmatrix} \bar{M}_{xx} \\ \bar{M}_{yy} \\ \bar{M}_{xy} \end{Bmatrix}, \quad (40a)$$

$$\begin{Bmatrix} K_{nn} \\ K_{ns} \end{Bmatrix} = \begin{bmatrix} n_x^2 & n_y^2 & 2n_x n_y \\ -n_x n_y & n_x n_y & n_x^2 - n_y^2 \end{bmatrix} \begin{Bmatrix} K_{xx} \\ K_{yy} \\ K_{xy} \end{Bmatrix}, \quad (40b)$$

$$P_n^I \equiv P_x^I n_x + P_y^I n_y. \quad (41)$$

Thus the primary variables (i.e., generalized displacements) and secondary variables (i.e., generalized forces) of the theory are:

$$\text{primary variables: } u_n, u_s, w_0, \partial w_0 / \partial n, \varphi_n, \varphi_s, \psi_I, \quad (42a)$$

$$\text{second variables: } N_{nn}, N_{ns}, \bar{Q}_n, M_{nn}, \bar{M}_{nn}, \bar{M}_{ns}, P_n^I. \quad (42b)$$

Note that the boundary term involving the tangential derivative of w_0 was integrated by parts to obtain the boundary term

$$- \oint_{\Gamma} M_{ns} \frac{\partial \delta w_0}{\partial s} d\Gamma = \oint_{\Gamma} \frac{\partial M_{ns}}{\partial s} \delta w_0 d\Gamma - [M_{ns} \delta w_0]_{\Gamma}.$$

The term in the square bracket is zero since the end points of a closed curve coincide. This term is then added to Q_n (because it is a coefficient of δw_0). This boundary condition, $Q_n + (\partial M_{ns} / \partial s)$, is known as the *Kirchhoff free-edge condition* (see Reddy 1984, 1995).

The initial conditions of the theory involve specifying the values of the displacements and their first derivatives with respect to time at $t = 0$:

$$\begin{aligned}u_n &= u_n^0, & u_s &= u_s^0, & w_0 &= w_0^0, & \varphi_n &= \varphi_n^0, & \varphi_s &= \varphi_s^0, \\ \dot{u}_n &= \dot{u}_n^0, & \dot{u}_s &= \dot{u}_s^0, & \dot{w}_0 &= \dot{w}_0^0, & \dot{\varphi}_n &= \dot{\varphi}_n^0, & \dot{\varphi}_s &= \dot{\varphi}_s^0,\end{aligned}\quad (43)$$

for all points in Ω .

3.4 Special cases

The equations of motion of the third-order theory ($c_0 = 1$ and $\bar{c}_0 = 0$) contain, as special cases, the equations of motion of the classical and first-order laminate theories. These are outlined below.

The classical laminate theory

By setting $\varphi_x = 0$, $\varphi_y = 0$, $c_0 = 1$, $c_1 = 0$, and $c_2 = 0$ in (30)–(44), we obtain the equations of motion and the boundary conditions of the classical laminate theory. The equations of motion are:

$$\delta u_0: \frac{\partial N_{xx}}{\partial x} + \frac{\partial N_{xy}}{\partial y} = I_0 \frac{\partial^2 u_0}{\partial t^2} - I_1 \frac{\partial^3 w_0}{\partial x \partial t^2}, \quad (44)$$

$$\delta v_0: \frac{\partial N_{xy}}{\partial x} + \frac{\partial N_{yy}}{\partial y} = I_0 \frac{\partial^2 v_0}{\partial t^2} - I_1 \frac{\partial^3 w_0}{\partial y \partial t^2}, \quad (45)$$

$$\begin{aligned} \delta w_0: & \left(\frac{\partial^2 M_{xx}}{\partial x^2} + 2 \frac{\partial^2 M_{xy}}{\partial x \partial y} + \frac{\partial^2 M_{yy}}{\partial y^2} \right) + \mathcal{N}(w_0) + q \\ & = I_0 \frac{\partial^2 w_0}{\partial t^2} - I_2 \frac{\partial^2}{\partial t^2} \left(\frac{\partial^2 w_0}{\partial x^2} + \frac{\partial^2 w_0}{\partial y^2} \right) + I_1 \frac{\partial^2}{\partial t^2} \left(\frac{\partial u_0}{\partial x} + \frac{\partial v_0}{\partial y} \right), \end{aligned} \quad (46)$$

$$\delta \psi_I: \frac{\partial P_x^I}{\partial x} + \frac{\partial P_y^I}{\partial y} - P_z^I = p^I. \quad (47)$$

The first-order laminate theory

By setting $c_0 = 0$, $c_1 = 0$, and $c_2 = 0$ (hence, $\bar{c}_0 = 1$, $\bar{I}_i = \hat{I}_i = I_i$) in (30)–(37), we obtain the equations of motion of the first-order laminate theory:

$$\delta u_0: \frac{\partial N_{xx}}{\partial x} + \frac{\partial N_{xy}}{\partial y} = I_0 \frac{\partial^2 u_0}{\partial t^2} + I_1 \frac{\partial^2 \varphi_x}{\partial t^2}, \quad (48)$$

$$\delta v_0: \frac{\partial N_{xy}}{\partial x} + \frac{\partial N_{yy}}{\partial y} = I_0 \frac{\partial^2 v_0}{\partial t^2} + I_1 \frac{\partial^2 \varphi_y}{\partial t^2}, \quad (49)$$

$$\delta w_0: \frac{\partial Q_x}{\partial x} + \frac{\partial Q_y}{\partial y} + \mathcal{N}(w_0) + q = I_0 \frac{\partial^2 w_0}{\partial t^2}, \quad (50)$$

$$\delta \varphi_x: \frac{\partial M_{xx}}{\partial x} + \frac{\partial M_{xy}}{\partial y} - Q_x = I_1 \frac{\partial^2 u_0}{\partial t^2} + I_2 \frac{\partial^2 \varphi_x}{\partial t^2}, \quad (51)$$

$$\delta \varphi_y: \frac{\partial M_{xy}}{\partial x} + \frac{\partial M_{yy}}{\partial y} - Q_y = I_1 \frac{\partial^2 v_0}{\partial t^2} + I_2 \frac{\partial^2 \varphi_y}{\partial t^2}, \quad (52)$$

$$\delta \psi_I: \frac{\partial P_x^I}{\partial x} + \frac{\partial P_y^I}{\partial y} - P_z^I = p^I, \quad (53)$$

wherein φ_x and φ_y take the meaning of total rotations [they denote only shear rotations in (30)–(36)].

3.5 Constitutive relations

The theory presented here is valid for laminates with arbitrary lamination scheme. Since the laminate is made of several orthotropic layers, with their material axes oriented arbitrarily with respect to the laminate coordinates, the constitutive equations

of each layer must be transformed to the laminate coordinates. The linear constitutive relations for the k th orthotropic lamina are

$$\begin{Bmatrix} \sigma_1 \\ \sigma_2 \\ \sigma_6 \end{Bmatrix}^{(k)} = \begin{bmatrix} Q_{11} & Q_{12} & 0 \\ Q_{12} & Q_{22} & 0 \\ 0 & 0 & Q_{66} \end{bmatrix}^{(k)} \begin{Bmatrix} \varepsilon_1 - \alpha_1 \Delta T \\ \varepsilon_2 - \alpha_2 \Delta T \\ \varepsilon_6 \end{Bmatrix} - \begin{bmatrix} 0 & 0 & e_{31} \\ 0 & 0 & e_{32} \\ 0 & 0 & 0 \end{bmatrix}^{(k)} \begin{Bmatrix} E_1 \\ E_2 \\ E_3 \end{Bmatrix}^{(k)}, \quad (54a)$$

$$\begin{Bmatrix} \sigma_4 \\ \sigma_5 \end{Bmatrix}^{(k)} = \begin{bmatrix} Q_{44} & 0 \\ 0 & Q_{55} \end{bmatrix}^{(k)} \begin{Bmatrix} \varepsilon_4 \\ \varepsilon_5 \end{Bmatrix} - \begin{bmatrix} 0 & e_{24} & 0 \\ e_{15} & 0 & 0 \end{bmatrix}^{(k)} \begin{Bmatrix} E_1 \\ E_2 \\ E_3 \end{Bmatrix}^{(k)}, \quad (54b)$$

$$\begin{Bmatrix} D_1 \\ D_2 \\ D_3 \end{Bmatrix} = \begin{bmatrix} 0 & 0 & 0 & e_{15} & 0 \\ 0 & 0 & e_{24} & 0 & 0 \\ e_{31} & e_{32} & 0 & 0 & 0 \end{bmatrix}^{(k)} \begin{Bmatrix} \varepsilon_1 \\ \varepsilon_2 \\ \varepsilon_4 \\ \varepsilon_5 \\ \varepsilon_6 \end{Bmatrix} + \begin{bmatrix} \epsilon_{11} & 0 & 0 \\ 0 & \epsilon_{22} & 0 \\ 0 & 0 & \epsilon_{33} \end{bmatrix}^{(k)} \begin{Bmatrix} E_1 \\ E_2 \\ E_3 \end{Bmatrix}^{(k)}, \quad (54c)$$

where $Q_{ij}^{(k)}$, $e_{ij}^{(k)}$, and $\epsilon_{ij}^{(k)}$ are the plane stress-reduced stiffnesses, piezoelectric moduli, and dielectric moduli, respectively, for the k th lamina in its material coordinate system, $(\sigma_i, \varepsilon_i, E_i, D_i)$ are the stress, strain, electric field, and electric displacement components, respectively, referred to the material coordinate system (x_1, x_2, x_3) , α_1 and α_2 are the coefficients of thermal expansion along the x_1 and x_2 directions, respectively, and ΔT is the temperature increment from a reference state, $\Delta T = T - T_0$.

The constitutive equations (54), when transformed to the laminate coordinates (x, y, z) , take the form

$$\begin{Bmatrix} \sigma_{xx} \\ \sigma_{yy} \\ \sigma_{xy} \end{Bmatrix}^{(k)} = \begin{bmatrix} \bar{Q}_{11} & \bar{Q}_{12} & \bar{Q}_{16} \\ \bar{Q}_{12} & \bar{Q}_{22} & \bar{Q}_{26} \\ \bar{Q}_{16} & \bar{Q}_{26} & \bar{Q}_{66} \end{bmatrix}^{(k)} \begin{Bmatrix} \varepsilon_{xx} \\ \varepsilon_{yy} \\ \gamma_{xy} \end{Bmatrix} - \begin{Bmatrix} \alpha_{xx} \\ \alpha_{yy} \\ 2\alpha_{xy} \end{Bmatrix} \Delta T + \begin{bmatrix} 0 & 0 & \bar{e}_{31} \\ 0 & 0 & \bar{e}_{32} \\ 0 & 0 & \bar{e}_{36} \end{bmatrix}^{(k)} \begin{Bmatrix} \partial\psi/\partial x \\ \partial\psi/\partial y \\ \partial\psi/\partial z \end{Bmatrix}^{(k)}, \quad (55a)$$

$$\begin{Bmatrix} \sigma_{yz} \\ \sigma_{xz} \end{Bmatrix}^{(k)} = \begin{bmatrix} \bar{Q}_{44} & \bar{Q}_{45} \\ \bar{Q}_{45} & \bar{Q}_{55} \end{bmatrix}^{(k)} \begin{Bmatrix} \gamma_{yz} \\ \gamma_{xz} \end{Bmatrix} + \begin{bmatrix} \bar{e}_{14} & \bar{e}_{24} & 0 \\ \bar{e}_{15} & \bar{e}_{25} & 0 \end{bmatrix}^{(k)} \begin{Bmatrix} \partial\psi/\partial x \\ \partial\psi/\partial y \\ \partial\psi/\partial z \end{Bmatrix}^{(k)}, \quad (55b)$$

$$\begin{Bmatrix} D_x \\ D_y \\ D_z \end{Bmatrix} = \begin{bmatrix} 0 & 0 & \bar{e}_{14} & \bar{e}_{15} & 0 \\ 0 & 0 & \bar{e}_{24} & \bar{e}_{25} & 0 \\ \bar{e}_{31} & \bar{e}_{32} & 0 & 0 & \bar{e}_{36} \end{bmatrix}^{(k)} \begin{Bmatrix} \varepsilon_{xx} \\ \varepsilon_{yy} \\ \gamma_{yz} \\ \gamma_{xz} \\ \gamma_{xy} \end{Bmatrix} - \begin{bmatrix} \epsilon_{xx} & \epsilon_{xy} & 0 \\ \epsilon_{xy} & \epsilon_{yy} & 0 \\ 0 & 0 & \epsilon_{zz} \end{bmatrix}^{(k)} \begin{Bmatrix} \partial\psi/\partial x \\ \partial\psi/\partial y \\ \partial\psi/\partial z \end{Bmatrix}^{(k)}, \quad (55c)$$

where $\bar{Q}_{ij}^{(k)}$ are the plane stress-reduced elastic stiffnesses, referred to the laminate coordinates

$$\begin{aligned}
 \bar{Q}_{11} &= Q_{11} \cos^4 \theta + 2(Q_{12} + 2Q_{66}) \sin^2 \theta \cos^2 \theta + Q_{22} \sin^4 \theta, \\
 \bar{Q}_{12} &= Q_{11} \cos^2 \theta \sin^2 \theta + 2Q_{12}(\cos^4 \theta + \sin^4 \theta) + (Q_{22} - 4Q_{66}) \sin^2 \theta \cos^2 \theta, \\
 \bar{Q}_{22} &= Q_{11} \sin^4 \theta + 2(Q_{12} + 2Q_{66}) \sin^2 \theta \cos^2 \theta + Q_{22} \cos^4 \theta, \\
 \bar{Q}_{16} &= (Q_{11} - Q_{12} - 2Q_{66}) \sin \theta \cos^3 \theta + (Q_{12} - Q_{22} + 2Q_{66}) \sin^3 \theta \cos \theta, \\
 \bar{Q}_{26} &= (Q_{11} - Q_{12} - 2Q_{66}) \sin^3 \theta \cos \theta + (Q_{12} - Q_{22} + 2Q_{66}) \sin \theta \cos^3 \theta, \\
 \bar{Q}_{66} &= (Q_{11} + Q_{22} - 2Q_{12}) \sin^2 \theta \cos^2 \theta + Q_{66}(\sin^2 \theta - \cos^2 \theta)^2, \\
 \bar{Q}_{44} &= Q_{44} \cos^2 \theta + Q_{55} \sin^2 \theta, \\
 \bar{Q}_{45} &= (Q_{55} - Q_{44}) \cos \theta \sin \theta, \\
 \bar{Q}_{55} &= Q_{44} \sin^2 \theta + Q_{55} \cos^2 \theta,
 \end{aligned} \tag{56a}$$

α_x, α_y and α_{xy} are the transformed thermal coefficients of expansion,

$$\begin{aligned}
 \alpha_x &= \alpha_1 \cos^2 \theta + \alpha_2 \sin^2 \theta, \\
 \alpha_y &= \alpha_1 \sin^2 \theta + \alpha_2 \cos^2 \theta, \\
 2\alpha_{xy} &= 2(\alpha_1 - \alpha_2) \sin \theta \cos \theta,
 \end{aligned} \tag{56b}$$

\bar{e}_{ij} are the transformed piezoelectric moduli, and $\epsilon_{xx}, \epsilon_{yy}$ and ϵ_{xy} are transformed dielectric coefficients

$$\begin{aligned}
 \bar{e}_{31} &= e_{31} \cos^2 \theta + e_{32} \sin^2 \theta, \quad \bar{e}_{32} = e_{31} \sin^2 \theta + e_{32} \cos^2 \theta, \quad \bar{e}_{33} = e_{33}, \\
 \bar{e}_{36} &= (e_{31} - e_{32}) \sin \theta \cos \theta, \quad \bar{e}_{14} = (e_{15} - e_{24}) \sin \theta \cos \theta, \\
 \bar{e}_{24} &= e_{24} \cos^2 \theta + e_{15} \sin^2 \theta, \quad \bar{e}_{15} = e_{15} \cos^2 \theta + e_{24} \sin^2 \theta, \\
 \bar{e}_{25} &= (e_{15} - e_{24}) \sin \theta \cos \theta, \quad \epsilon_{xx} = \epsilon_{11} \cos^2 \theta + \epsilon_{22} \sin^2 \theta, \\
 \epsilon_{yy} &= \epsilon_{11} \sin^2 \theta + \epsilon_{22} \cos^2 \theta, \quad \epsilon_{xy} = (\epsilon_{11} - \epsilon_{22}) \sin \theta \cos \theta.
 \end{aligned} \tag{56c}$$

3.6 Laminate constitutive relations

The stress resultants in (27) and (28) can be expressed in terms of the strains using the lamina constitutive equations. We have

$$\begin{aligned}
 \begin{Bmatrix} N_{xx} \\ N_{yy} \\ N_{xy} \end{Bmatrix} &= \int_{-h/2}^{h/2} \begin{Bmatrix} \sigma_{xx} \\ \sigma_{yy} \\ \sigma_{xy} \end{Bmatrix} dz \\
 &= \begin{bmatrix} A_{11} & A_{12} & A_{16} \\ A_{12} & A_{22} & A_{26} \\ A_{16} & A_{26} & A_{66} \end{bmatrix} \begin{Bmatrix} \epsilon_{xx}^{(0)} \\ \epsilon_{yy}^{(0)} \\ \gamma_{xy}^{(0)} \end{Bmatrix} + \begin{bmatrix} B_{11} & B_{12} & B_{16} \\ B_{12} & B_{22} & B_{26} \\ B_{16} & B_{26} & B_{66} \end{bmatrix} \begin{Bmatrix} \epsilon_{xx}^{(1)} \\ \epsilon_{yy}^{(1)} \\ \gamma_{xy}^{(1)} \end{Bmatrix} \\
 &\quad + \begin{bmatrix} E_{11} & E_{12} & E_{16} \\ E_{12} & E_{22} & E_{26} \\ E_{16} & E_{26} & E_{66} \end{bmatrix} \begin{Bmatrix} \epsilon_{xx}^{(3)} \\ \epsilon_{yy}^{(3)} \\ \gamma_{xy}^{(3)} \end{Bmatrix} + \sum_{I=1}^M \begin{Bmatrix} B_{31}^I \\ B_{32}^I \\ B_{36}^I \end{Bmatrix} \psi_I - \begin{Bmatrix} N_{xx}^T \\ N_{yy}^T \\ N_{xy}^T \end{Bmatrix}, \tag{57}
 \end{aligned}$$

$$\begin{aligned}
 \begin{Bmatrix} M_{xx} \\ M_{yy} \\ M_{xy} \end{Bmatrix} &= \int_{-h/2}^{h/2} \begin{Bmatrix} \sigma_{xx} \\ \sigma_{yy} \\ \sigma_{xy} \end{Bmatrix} z \, dz \\
 &= \begin{bmatrix} B_{11} & B_{12} & B_{16} \\ B_{12} & B_{22} & B_{26} \\ B_{16} & B_{26} & B_{66} \end{bmatrix} \begin{Bmatrix} \varepsilon_{xx}^{(0)} \\ \varepsilon_{yy}^{(0)} \\ \gamma_{xy}^{(0)} \end{Bmatrix} + \begin{bmatrix} D_{11} & D_{12} & D_{16} \\ D_{12} & D_{22} & D_{26} \\ D_{16} & D_{26} & D_{66} \end{bmatrix} \begin{Bmatrix} \varepsilon_{xx}^{(1)} \\ \varepsilon_{yy}^{(1)} \\ \gamma_{xy}^{(1)} \end{Bmatrix} \\
 &\quad + \begin{bmatrix} F_{11} & F_{12} & F_{16} \\ F_{12} & F_{22} & F_{26} \\ F_{16} & F_{26} & F_{66} \end{bmatrix} \begin{Bmatrix} \varepsilon_{xx}^{(3)} \\ \varepsilon_{yy}^{(3)} \\ \gamma_{xy}^{(3)} \end{Bmatrix} + \sum_{I=1}^M \begin{Bmatrix} \bar{B}_{31}^I \\ \bar{B}_{32}^I \\ \bar{B}_{36}^I \end{Bmatrix} \psi_I - \begin{Bmatrix} M_{xx}^T \\ M_{yy}^T \\ M_{xy}^T \end{Bmatrix}, \quad (58)
 \end{aligned}$$

$$\begin{aligned}
 \begin{Bmatrix} K_{xx} \\ K_{yy} \\ K_{xy} \end{Bmatrix} &= \int_{-h/2}^{h/2} \begin{Bmatrix} \sigma_{xx} \\ \sigma_{yy} \\ \sigma_{xy} \end{Bmatrix} z^3 \, dz \\
 &= \begin{bmatrix} E_{11} & E_{12} & E_{16} \\ E_{12} & E_{22} & E_{26} \\ E_{16} & E_{26} & E_{66} \end{bmatrix} \begin{Bmatrix} \varepsilon_{xx}^{(0)} \\ \varepsilon_{yy}^{(0)} \\ \gamma_{xy}^{(0)} \end{Bmatrix} + \begin{bmatrix} F_{11} & F_{12} & F_{16} \\ F_{12} & F_{22} & F_{26} \\ F_{16} & F_{26} & F_{66} \end{bmatrix} \begin{Bmatrix} \varepsilon_{xx}^{(1)} \\ \varepsilon_{yy}^{(1)} \\ \gamma_{xy}^{(1)} \end{Bmatrix} \\
 &\quad + \begin{bmatrix} H_{11} & H_{12} & H_{16} \\ H_{12} & H_{22} & H_{26} \\ H_{16} & H_{26} & H_{66} \end{bmatrix} \begin{Bmatrix} \varepsilon_{xx}^{(3)} \\ \varepsilon_{yy}^{(3)} \\ \gamma_{xy}^{(3)} \end{Bmatrix} + \sum_{I=1}^M \begin{Bmatrix} \tilde{B}_{31}^I \\ \tilde{B}_{32}^I \\ \tilde{B}_{36}^I \end{Bmatrix} \psi_I - \begin{Bmatrix} K_{xx}^T \\ K_{yy}^T \\ K_{xy}^T \end{Bmatrix}, \quad (59)
 \end{aligned}$$

$$\begin{aligned}
 \begin{Bmatrix} Q_{yz} \\ Q_{xz} \end{Bmatrix} &= \int_{-h/2}^{h/2} \begin{Bmatrix} \sigma_{yz} \\ \sigma_{xz} \end{Bmatrix} dz \\
 &= \begin{bmatrix} A_{44} & A_{45} \\ A_{45} & A_{55} \end{bmatrix}^{(k)} \begin{Bmatrix} \gamma_{yz}^{(0)} \\ \gamma_{xz}^{(0)} \end{Bmatrix} + \begin{bmatrix} D_{44} & D_{45} \\ D_{45} & D_{55} \end{bmatrix}^{(k)} \begin{Bmatrix} \gamma_{yz}^{(2)} \\ \gamma_{xz}^{(2)} \end{Bmatrix} \\
 &\quad + \sum_{I=1}^M \begin{bmatrix} A_{14}^I & A_{24}^I \\ A_{15}^I & A_{25}^I \end{bmatrix} \begin{Bmatrix} \partial \psi_I / \partial x \\ \partial \psi_I / \partial y \end{Bmatrix}, \quad (60)
 \end{aligned}$$

$$\begin{aligned}
 \begin{Bmatrix} S_{yz} \\ S_{xz} \end{Bmatrix} &= \int_{-h/2}^{h/2} \begin{Bmatrix} \sigma_{yz} \\ \sigma_{xz} \end{Bmatrix} z^2 \, dz \\
 &= \begin{bmatrix} D_{44} & D_{45} \\ D_{45} & D_{55} \end{bmatrix}^{(k)} \begin{Bmatrix} \gamma_{yz}^{(0)} \\ \gamma_{xz}^{(0)} \end{Bmatrix} + \begin{bmatrix} F_{44} & F_{45} \\ F_{45} & F_{55} \end{bmatrix}^{(k)} \begin{Bmatrix} \gamma_{yz}^{(2)} \\ \gamma_{xz}^{(2)} \end{Bmatrix} \\
 &\quad + \sum_{I=1}^M \begin{bmatrix} \hat{A}_{14}^I & \hat{A}_{24}^I \\ \hat{A}_{15}^I & \hat{A}_{25}^I \end{bmatrix} \begin{Bmatrix} \partial \psi_I / \partial x \\ \partial \psi_I / \partial y \end{Bmatrix}, \quad (61a)
 \end{aligned}$$

$$\begin{aligned}
 \begin{Bmatrix} P_x^I \\ P_y^I \end{Bmatrix} &= \int_{-h/2}^{h/2} \begin{Bmatrix} D_x \\ D_y \end{Bmatrix} \Phi^I \, dz \\
 &= \left(\begin{bmatrix} A_{14}^I & A_{15}^I \\ A_{24}^I & A_{25}^I \end{bmatrix} \begin{Bmatrix} \gamma_{yz}^{(0)} \\ \gamma_{xz}^{(0)} \end{Bmatrix} + \begin{bmatrix} \hat{A}_{14}^I & \hat{A}_{15}^I \\ \hat{A}_{24}^I & \hat{A}_{25}^I \end{bmatrix} \begin{Bmatrix} \gamma_{yz}^{(2)} \\ \gamma_{xz}^{(2)} \end{Bmatrix} \right) \\
 &\quad - \sum_{J=1}^M \begin{bmatrix} E_{xx}^{IJ} & E_{xy}^{IJ} \\ E_{xy}^{IJ} & E_{yy}^{IJ} \end{bmatrix} \begin{Bmatrix} \partial \psi_J / \partial x \\ \partial \psi_J / \partial y \end{Bmatrix}, \quad (61b)
 \end{aligned}$$

$$\begin{aligned}
P_z^I &= \int_{-h/2}^{h/2} D_z \frac{d\Phi^I}{dz} dz \\
&= \{B_{31}^I \quad B_{32}^I \quad B_{36}^I\} \begin{Bmatrix} \varepsilon_{xx}^{(0)} \\ \varepsilon_{yy}^{(0)} \\ \gamma_{xy}^{(0)} \end{Bmatrix} + \{\bar{B}_{31}^I \quad \bar{B}_{32}^I \quad \bar{B}_{36}^I\} \begin{Bmatrix} \varepsilon_{xx}^{(1)} \\ \varepsilon_{yy}^{(1)} \\ \gamma_{xy}^{(1)} \end{Bmatrix} \\
&\quad + \{\tilde{B}_{31}^I \quad \tilde{B}_{32}^I \quad \tilde{B}_{36}^I\} \begin{Bmatrix} \varepsilon_{xx}^{(3)} \\ \varepsilon_{yy}^{(3)} \\ \gamma_{xy}^{(3)} \end{Bmatrix} - \sum_{J=1}^M \bar{E}_{zz}^{IJ} \psi_J,
\end{aligned} \tag{61c}$$

where $\{N^T\}$, $\{M^T\}$, and $\{K^T\}$ thermal force resultants

$$\{N^T\} = \sum_{k=1}^N \int_{z_k}^{z_{k+1}} [\bar{Q}]^{(k)} \{\alpha\}^{(k)} \Delta T dz, \tag{62a}$$

$$\{M^T\} = \sum_{k=1}^N \int_{z_k}^{z_{k+1}} [\bar{Q}]^{(k)} \{\alpha\}^{(k)} \Delta T z dz, \tag{62b}$$

$$\{K^T\} = \sum_{k=1}^N \int_{z_k}^{z_{k+1}} [\bar{Q}]^{(k)} \{\alpha\}^{(k)} \Delta T z^3 dz, \tag{62c}$$

and various laminate stiffnesses are defined as follows

$$(A_{ij}, B_{ij}, D_{ij}, E_{ij}, F_{ij}, H_{ij}) = \int_{-h/2}^{h/2} \bar{Q}_{ij}(1, z, z^2, z^3, z^4, z^6) dz, \tag{63}$$

$$(A_{ij}^I, \hat{A}_{ij}^I) = \int_{-h/2}^{h/2} \bar{e}_{ij} \Phi^I(1, z^2) dz, \tag{64}$$

$$(B_{ij}^I, \bar{B}_{ij}^I, \tilde{B}_{ij}^I) = \int_{-h/2}^{h/2} \bar{e}_{ij} \frac{d\Phi^I}{dz}(1, z, z^3) dz, \tag{65}$$

$$E_{xx}^{IJ}, E_{yy}^{IJ}, E_{xy}^{IJ} = \int_{-h/2}^{h/2} (\epsilon_{xx}, \epsilon_{yy}, \epsilon_{xy}) \Phi^I \Phi^J dz, \tag{66}$$

$$\bar{E}_{zz}^{IJ} = \int_{-h/2}^{h/2} \varepsilon_{zz} \frac{d\Phi^I}{dz} \frac{d\Phi^J}{dz} dz. \tag{67}$$

This completes the development of the third-order theory with piezoelectric laminae.

4. Layerwise theory

4.1 Displacements and strains

In contrast to the equivalent-single-layer theories, the layerwise theories are developed by assuming that the displacement field is C^∞ -continuous through the thickness of each layer of the laminate (see Reddy 1987, 1995; Robbins & Reddy 1993). This amounts to using ESL displacement fields in each (physical or numerical) layer of the laminate. Thus the displacement components are continuous through the laminate thickness but the transverse derivatives of the displacements may be discontinuous at various points through the thickness, thereby allowing for the possibility of continuous

transverse stresses at interfaces separating dissimilar material layers. A layerwise displacement field provides a kinematically correct representation of the moderate to severe cross-sectional warping associated with the deformation of moderately thick to very thick laminates.

In the layerwise theory of Reddy (1995), the total displacement field is represented as

$$\begin{aligned} u(x, y, z, t) &= \sum_{I=1}^N U_I(x, y, t) \Phi^I(z), \\ v(x, y, z, t) &= \sum_{I=1}^N V_I(x, y, t) \Phi^I(z), \\ w(x, y, z, t) &= \sum_{I=1}^M W_I(x, y, t) \Psi^I(z), \end{aligned} \quad (68a)$$

where (U_I, V_I, W_I) denote the values of (u, v, w) at the I th interface through the thickness, N is the number of nodes through the thickness, and Φ^I and the *global* interpolation functions for the discretization of the inplane displacements through thickness (see figure 1); M is the number of nodes and Ψ^I are the *global* interpolation functions for discretization of the transverse displacement w through thickness. Note that independent approximations for the inplane and transverse displacements are assumed ($\Psi^I \neq \Phi^I$). Consequently, inextensibility of transverse normals (i.e., $w = w(x, y)$) can be imposed, if desired, by simply setting $M = 1$ and $\Psi^1 = 1$ for all z .

The electric potential is also represented using a layerwise approximation

$$\psi(x, y, z, t) = \sum_{I=1}^N \psi_I(x, y, t) \Phi^I(z), \quad (68b)$$

where $\psi_I(x, y, t)$ denote the nodal values of ψ , N is the number of nodes through thickness, and Φ^I are the *global* Lagrange interpolation functions for the discretization of ψ through thickness.

For linear variation through each numerical layer, the functions Φ^I are given by

$$\begin{aligned} \Phi^1(z) &= \psi_1^{(1)}(z), \quad z_1 \leq z \leq z_2, \\ \Phi^I(z) &= \begin{cases} \psi_2^{(I-1)}(z), & z_{I-1} \leq z \leq z_I \\ \psi_1^{(I)}(z), & z_I \leq z \leq z_{I+1} \end{cases} \quad (I = 2, 3, \dots, n), \\ \Phi^N(z) &= \psi_2^{(n)}(z), \quad z_{N-1} \leq z \leq z_N, \end{aligned} \quad (69a)$$

$$\psi_1^{(k)} = 1 - \bar{z}/h_k, \quad \psi_2^{(k)} = \bar{z}/h_k, \quad 0 \leq \bar{z} \leq h_k, \quad (69b)$$

where $N = n + 1$, n is the number of numerical subdivisions through the thickness, h_k is the thickness of the k th layer, $\bar{z} = z - z_t^k$, and z_t^k denotes the z -coordinate of top of the k th numerical layer. Any desired degree of displacement variation through the thickness is easily obtained by either adding more linear finite element sub-divisions through the thickness or using higher-order elements through the thickness. The layerwise concept is very general in that the number of subdivisions through the thickness can be greater than, equal to, or less than the number of material layers through the thickness. Note that the sublaminate concept can be used (i.e. the number of thickness subdivisions is less than the number of material layers). The layerwise

displacement field (68a) contains, as special cases, the displacement fields of the ESL theories described in § 3.

The von Kármán nonlinear strains associated with the displacement field (48a) are:

$$\begin{aligned}
 \varepsilon_{xx} &= \sum_{I=1}^N \frac{\partial U_I}{\partial x} \Phi^I + \frac{1}{2} \left(\sum_{I=1}^M \frac{\partial W_I}{\partial x} \Psi^I \right) \left(\sum_{J=1}^M \frac{\partial W_J}{\partial x} \Psi^J \right), \\
 \varepsilon_{yy} &= \sum_{I=1}^N \frac{\partial V_I}{\partial y} \Phi^I + \frac{1}{2} \left(\sum_{I=1}^M \frac{\partial W_I}{\partial y} \Psi^I \right) \left(\sum_{J=1}^M \frac{\partial W_J}{\partial y} \Psi^J \right), \\
 \varepsilon_{zz} &= \sum_{I=1}^M W_I \frac{d\Psi^I}{dz}, \\
 \gamma_{yz} &= \sum_{I=1}^N V_I \frac{d\Phi^I}{dz} + \sum_{I=1}^M \frac{\partial W_I}{\partial y} \Psi^I, \\
 \gamma_{xz} &= \sum_{I=1}^N U_I \frac{d\Phi^I}{dz} + \sum_{I=1}^M \frac{\partial W_I}{\partial x} \Psi^I, \\
 \gamma_{xy} &= \sum_{I=1}^N \left(\frac{\partial U_I}{\partial y} + \frac{\partial V_I}{\partial x} \right) \Phi^I + \left(\sum_{I=1}^M \frac{\partial W_I}{\partial x} \Psi^I \right) \left(\sum_{J=1}^M \frac{\partial W_J}{\partial y} \Psi^J \right). \quad (70)
 \end{aligned}$$

Note that the transverse normal strain is nonzero, and that the strains are discontinuous at the layer interfaces because of the layerwise definition of the functions Φ^I and Ψ^J .

4.2 Equations of motion

The governing equations of motion for the present layerwise theory can be derived using Hamilton's principle. The virtual Gibb's energy $\delta\Phi$, virtual work done by applied forces δV , and the virtual kinetic energy δK are given by

$$\begin{aligned}
 \delta\Phi &= \int_{\Omega_0} \left\{ \int_{-h/2}^{h/2} [\sigma_{xx} \delta\varepsilon_{xx} + \sigma_{yy} \delta\varepsilon_{yy} + \sigma_{zz} \delta\varepsilon_{zz} \right. \\
 &\quad \left. + \sigma_{xy} \delta\gamma_{xy} + \sigma_{xz} \delta\gamma_{xz} + \sigma_{yz} \delta\gamma_{yz} \right. \\
 &\quad \left. - (D_x \delta E_x + D_y \delta E_y + D_z \delta E_z)] dz \right\} dx dy \\
 &= \int_{\Omega_0} \left\{ \sum_{I=1}^N \left[N_{xx}^I \frac{\partial \delta U_I}{\partial x} + N_{yy}^I \frac{\partial \delta V_I}{\partial y} + N_{xy}^I \left(\frac{\partial \delta U_I}{\partial y} + \frac{\partial \delta V_I}{\partial x} \right) \right. \right. \\
 &\quad \left. + Q_x^I \delta U_I + Q_y^I \delta V_I \right] + \sum_{I=1}^M \left[\tilde{Q}_x^I \frac{\partial \delta W_I}{\partial x} + \tilde{Q}_y^I \frac{\partial \delta W_I}{\partial y} + \tilde{Q}_z^I \delta W_I \right. \\
 &\quad \left. + \sum_{J=1}^M \left\{ \left(\tilde{N}_{xx}^{IJ} \frac{\partial W_I}{\partial x} + \tilde{N}_{xy}^{IJ} \frac{\partial W_I}{\partial y} \right) \frac{\partial \delta W_J}{\partial x} \right. \right. \\
 &\quad \left. \left. + \left(\tilde{N}_{xy}^{IJ} \frac{\partial W_I}{\partial x} + \tilde{N}_{yy}^{IJ} \frac{\partial W_I}{\partial y} \right) \frac{\partial \delta W_J}{\partial y} \right\} \right] \\
 &\quad \left. - \sum_{I=1}^M \left(P_x^I \frac{\partial \delta \psi_I}{\partial x} + P_y^I \frac{\partial \delta \psi_I}{\partial y} + P_z^I \delta \psi_I \right) \right\} dx dy, \quad (71)
 \end{aligned}$$

$$\begin{aligned}
\delta V = & - \int_{\Omega_0} \left[q_b(x, y) \delta w \left(x, y, -\frac{h}{2} \right) + q_t(x, y) \delta w \left(x, y, \frac{h}{2} \right) \right. \\
& \left. + p_b(x, y) \delta \psi \left(x, y, -\frac{h}{2} \right) + p_t(x, y) \delta \psi \left(x, y, \frac{h}{2} \right) \right] dx dy \\
& - \int_{\Gamma} \int_{-h/2}^{h/2} [\hat{\sigma}_{nn} \delta u_n + \hat{\sigma}_{ns} \delta u_s + \hat{\sigma}_{nz} \delta w] dz d\Gamma \\
= & - \int_{\Omega_0} [q_b \delta W_1 + q_t \delta W_M + p^I \delta \psi_I] dx dy \\
& - \int_{\Gamma} \left[\sum_{I=1}^N (\hat{N}_{nn}^I \delta U_I^n + \hat{N}_{ns}^I \delta U_I^s) + \sum_{I=1}^M \hat{Q}_n^I \delta W_I \right] d\Gamma, \quad (72)
\end{aligned}$$

$$\begin{aligned}
\delta K = & \int_{\Omega_0} \int_{-h/2}^{h/2} \rho_0 (\dot{u} \delta \dot{u} + \dot{v} \delta \dot{v} + \dot{w} \delta \dot{w}) dz dx dy \\
= & \int_{\Omega_0} \left[\sum_{I,J=1}^N I^{IJ} (\dot{U}_I \delta \dot{U}_J + \dot{V}_I \delta \dot{V}_J) + \sum_{I,J=1}^M \tilde{I}^{IJ} \dot{W}_I \delta \dot{W}_J \right] dx dy, \quad (73)
\end{aligned}$$

where

$$\mathcal{N}^I = \sum_{J=1}^M \left[\frac{\partial}{\partial x} \left(\tilde{N}_{xx}^{IJ} \frac{\partial W_J}{\partial x} + \tilde{N}_{xy}^{IJ} \frac{\partial W_J}{\partial y} \right) + \frac{\partial}{\partial y} \left(\tilde{N}_{xy}^{IJ} \frac{\partial W_J}{\partial x} + \tilde{N}_{yy}^{IJ} \frac{\partial W_J}{\partial y} \right) \right], \quad (74)$$

$$\begin{Bmatrix} N_{xx}^I \\ N_{yy}^I \\ N_{xy}^I \end{Bmatrix} = \int_{-h/2}^{h/2} \begin{Bmatrix} \sigma_{xx} \\ \sigma_{yy} \\ \sigma_{xy} \end{Bmatrix} \Phi^I dz, \quad \begin{Bmatrix} \tilde{N}_{xx}^{IJ} \\ \tilde{N}_{yy}^{IJ} \\ \tilde{N}_{xy}^{IJ} \end{Bmatrix} = \int_{-h/2}^{h/2} \begin{Bmatrix} \sigma_{xx} \\ \sigma_{yy} \\ \sigma_{xy} \end{Bmatrix} \Psi^I \Psi^J dz, \quad (75)$$

$$\begin{Bmatrix} Q_x^I \\ Q_y^I \end{Bmatrix} = \int_{-h/2}^{h/2} \begin{Bmatrix} \sigma_{xz} \\ \sigma_{yz} \end{Bmatrix} \frac{d\Phi^I}{dz} dz, \quad \begin{Bmatrix} \tilde{Q}_x^I \\ \tilde{Q}_y^I \end{Bmatrix} = \int_{-h/2}^{h/2} \begin{Bmatrix} \sigma_{xz} \\ \sigma_{yz} \end{Bmatrix} \Psi^I dz, \quad (76a)$$

$$\tilde{Q}_z^I = \int_{-h/2}^{h/2} \sigma_{zz} \frac{d\Psi^I}{dz} dz, \quad (76b)$$

$$I^{IJ} = \int_{-h/2}^{h/2} \rho_0 \Phi^I \Phi^J dz, \quad \tilde{I}^{IJ} = \int_{-h/2}^{h/2} \rho_0 \Psi^I \Psi^J dz. \quad (77)$$

The Euler-Lagrange equations of the layerwise theory are

$$\delta U_I: \quad \frac{\partial N_{xx}^I}{\partial x} + \frac{\partial N_{xy}^I}{\partial y} - Q_x^I = \sum_{J=1}^N I^{IJ} \frac{\partial^2 U_J}{\partial t^2}, \quad (78)$$

$$\delta V_I: \quad \frac{\partial N_{xy}^I}{\partial x} + \frac{\partial N_{yy}^I}{\partial y} - Q_y^I = \sum_{J=1}^N I^{IJ} \frac{\partial^2 V_J}{\partial t^2}, \quad (79)$$

$$\delta W_I: \quad \frac{\partial \tilde{Q}_x^I}{\partial x} + \frac{\partial \tilde{Q}_y^I}{\partial y} - \tilde{Q}_z^I + \mathcal{N}^I + q_b \delta_{I1} + q_t \delta_{IM} = \sum_{J=1}^M \tilde{I}^{IJ} \frac{\partial^2 W_J}{\partial t^2}, \quad (80)$$

$$\delta \psi_I: \quad \frac{\partial P_x^I}{\partial x} + \frac{\partial P_y^I}{\partial y} - P_z^I = p^I. \quad (81)$$

The natural (force) boundary conditions of the theory are:

$$N_{nn}^I - \hat{N}_{nn}^I = 0, \quad N_{ns}^I - \hat{N}_{ns}^I = 0, \quad (\tilde{Q}_n^I + \tilde{\mathcal{P}}^I) - \hat{Q}_n^I = 0, \quad (82a)$$

$$P_n^I - \hat{P}_n^I = 0, \quad (82b)$$

where (N_{nn}^I, N_{ns}^I) have meaning similar to (N_{nn}, N_{ns}) introduced in §3:

$$\tilde{Q}_n^I = \tilde{Q}_x^I n_x + \tilde{Q}_y^I n_y, \quad U_I^n = U_I n_x + V_I n_y, \quad U_I^s = -U_I n_x + V_I n_y, \quad (83a)$$

$$\tilde{\mathcal{P}}^I = \sum_{J=1}^M \left[\left(\tilde{N}_{xx}^{IJ} \frac{\partial W_J}{\partial x} + \tilde{N}_{xy}^{IJ} \frac{\partial W_J}{\partial y} \right) n_x + \left(\tilde{N}_{xy}^{IJ} \frac{\partial W_J}{\partial x} + \tilde{N}_{yy}^{IJ} \frac{\partial W_J}{\partial y} \right) n_y \right]. \quad (83b)$$

Thus, the primary variables (displacements) and secondary variables (forces) of the layerwise theory are:

$$\text{Primary variables: } U_I^n, U_I^s, W_I, \psi_I, \quad (84a)$$

$$\text{Secondary variables: } N_{nn}^I, N_{ns}^I, \tilde{Q}_n^I + \tilde{\mathcal{P}}^I, P_n^I. \quad (84b)$$

4.3 Laminate constitutive equations

The stresses in the k th layer may be computed from the 3-D stress-strain equations. For the k th (orthotropic) lamina we have

$$\begin{pmatrix} \sigma_{xx} \\ \sigma_{yy} \\ \sigma_{zz} \\ \sigma_{yz} \\ \sigma_{xz} \\ \sigma_{xy} \end{pmatrix}^{(k)} = \begin{bmatrix} \bar{C}_{11} & \bar{C}_{12} & \bar{C}_{13} & 0 & 0 & \bar{C}_{16} \\ \bar{C}_{12} & \bar{C}_{22} & \bar{C}_{23} & 0 & 0 & \bar{C}_{26} \\ \bar{C}_{13} & \bar{C}_{23} & \bar{C}_{33} & 0 & 0 & \bar{C}_{36} \\ 0 & 0 & 0 & \bar{C}_{44} & \bar{C}_{45} & 0 \\ 0 & 0 & 0 & \bar{C}_{45} & \bar{C}_{55} & 0 \\ \bar{C}_{16} & \bar{C}_{26} & \bar{C}_{36} & 0 & 0 & \bar{C}_{66} \end{bmatrix} \begin{pmatrix} \varepsilon_{xx} - \alpha_{xx} \Delta T \\ \varepsilon_{yy} - \alpha_{yy} \Delta T \\ \varepsilon_{zz} - \alpha_{zz} \Delta T \\ \gamma_{yz} \\ \gamma_{xz} \\ \gamma_{xy} - 2\alpha_{xy} \Delta T \end{pmatrix}^{(k)} + \begin{bmatrix} 0 & 0 & \bar{e}_{31} \\ 0 & 0 & \bar{e}_{32} \\ 0 & 0 & \bar{e}_{33} \\ \bar{e}_{14} & \bar{e}_{24} & 0 \\ \bar{e}_{15} & \bar{e}_{25} & 0 \\ 0 & 0 & \bar{e}_{36} \end{bmatrix}^{(k)} \begin{pmatrix} \partial \psi / \partial x \\ \partial \psi / \partial y \\ \partial \psi / \partial z \end{pmatrix}, \quad (85)$$

$$\begin{pmatrix} D_x \\ D_y \\ D_z \end{pmatrix} = \begin{bmatrix} 0 & 0 & 0 & \bar{e}_{14} & \bar{e}_{15} & 0 \\ 0 & 0 & 0 & \bar{e}_{24} & \bar{e}_{25} & 0 \\ \bar{e}_{31} & \bar{e}_{32} & \bar{e}_{33} & 0 & 0 & \bar{e}_{36} \end{bmatrix}^{(k)} \begin{pmatrix} \varepsilon_{xx} \\ \varepsilon_{yy} \\ \varepsilon_{zz} \\ \varepsilon_{yz} \\ \gamma_{xz} \\ \gamma_{xy} \end{pmatrix}$$

$$- \begin{bmatrix} \epsilon_{xx} & \epsilon_{xy} & 0 \\ \epsilon_{xy} & \epsilon_{yy} & 0 \\ 0 & 0 & \epsilon_{zz} \end{bmatrix}^{(k)} \begin{pmatrix} \partial \psi / \partial x \\ \partial \psi / \partial y \\ \partial \psi / \partial z \end{pmatrix}^{(k)}. \quad (86)$$

where the $\bar{C}_{ij}^{(k)}$, $\bar{e}_{ij}^{(k)}$, and $\varepsilon_{ij}^{(k)}$ are the transformed material coefficients in the (x, y, z) system. If inextensibility of transverse normals is assumed, one may use the plane stress-reduced stiffness in place of the 3-D stiffnesses. Note that the strains at a layer interface depend on the layer, i.e., $\{\varepsilon\}_P^k \neq \{\varepsilon\}_P^{k+1}$ at a point P on the interface of layers k and $k+1$.

The laminate constitutive equations for the layerwise theory can be derived using the lamina constitutive equations (56) and (57) and the definitions for the stress resultants in (75) and (76). In the layerwise theory distinction must be made between the number of physical layers (N_e) and the number of numerical layers (n) in the laminate. The integrals in the definition of the resultants must be evaluated only over the thickness interval over which the global interpolation functions, Φ^I and Ψ^I , are defined.

The relations between the stress resultants and the strains can be expressed as

$$\begin{aligned} \begin{Bmatrix} N_{xx}^I \\ N_{yy}^I \\ N_{xy}^I \end{Bmatrix} &= \sum_{k=1}^{N_e} \int_{z_b^k}^{z_t^k} \begin{Bmatrix} \sigma_{xx} \\ \sigma_{yy} \\ \sigma_{xy} \end{Bmatrix}^{(k)} \Phi^I dz \\ &= \sum_{J=1}^N \begin{bmatrix} A_{11}^{IJ} & A_{12}^{IJ} & A_{16}^{IJ} \\ A_{12}^{IJ} & A_{22}^{IJ} & A_{26}^{IJ} \\ A_{16}^{IJ} & A_{26}^{IJ} & A_{66}^{IJ} \end{bmatrix} \begin{Bmatrix} \frac{\partial U_J}{\partial x} \\ \frac{\partial V_J}{\partial y} \\ \frac{\partial U_J}{\partial y} + \frac{\partial V_J}{\partial x} \end{Bmatrix} + \sum_{J=1}^M \begin{Bmatrix} B_{13}^{IJ} \\ B_{23}^{IJ} \\ B_{36}^{IJ} \end{Bmatrix} W_J \\ &\quad + \sum_{J,K=1}^M \begin{bmatrix} A_{11}^{IJK} & A_{12}^{IJK} & A_{16}^{IJK} \\ A_{12}^{IJK} & A_{22}^{IJK} & A_{26}^{IJK} \\ A_{16}^{IJK} & A_{26}^{IJK} & A_{66}^{IJK} \end{bmatrix} \begin{Bmatrix} \frac{1}{2} \frac{\partial W_J}{\partial x} \frac{\partial W_K}{\partial x} \\ \frac{1}{2} \frac{\partial W_J}{\partial y} \frac{\partial W_K}{\partial y} \\ \frac{\partial W_J}{\partial x} \frac{\partial W_K}{\partial y} \end{Bmatrix} \\ &\quad + \sum_{J=1}^N \begin{Bmatrix} F_{31}^{IJ} \\ F_{32}^{IJ} \\ F_{36}^{IJ} \end{Bmatrix} \psi_J - \begin{Bmatrix} N_{xx}^{I(T)} \\ N_{yy}^{I(T)} \\ N_{xy}^{I(T)} \end{Bmatrix}, \end{aligned} \quad (87)$$

$$\begin{aligned} \begin{Bmatrix} \tilde{N}_{xx}^{IJ} \\ \tilde{N}_{yy}^{IJ} \\ \tilde{N}_{xy}^{IJ} \end{Bmatrix} &= \sum_{k=1}^{N_e} \int_{z_b^k}^{z_t^k} \begin{Bmatrix} \sigma_{xx} \\ \sigma_{yy} \\ \sigma_{xy} \end{Bmatrix}^{(k)} \Psi^I \Psi^J dz \\ &= \sum_{K=1}^N \begin{bmatrix} A_{11}^{KIJ} & A_{12}^{KIJ} & A_{16}^{KIJ} \\ A_{12}^{KIJ} & A_{22}^{KIJ} & A_{26}^{KIJ} \\ A_{16}^{KIJ} & A_{26}^{KIJ} & A_{66}^{KIJ} \end{bmatrix} \begin{Bmatrix} \frac{\partial U_K}{\partial x} \\ \frac{\partial V_K}{\partial y} \\ \frac{\partial U_K}{\partial y} + \frac{\partial V_K}{\partial x} \end{Bmatrix} + \sum_{K=1}^M \begin{Bmatrix} B_{13}^{KIJ} \\ B_{23}^{KIJ} \\ B_{36}^{KIJ} \end{Bmatrix} W_K \end{aligned}$$

$$\begin{aligned}
& + \sum_{K,P=1}^M \begin{bmatrix} A_{11}^{IJKP} & A_{12}^{IJKP} & A_{16}^{IJKP} \\ A_{12}^{IJKP} & A_{22}^{IJKP} & A_{26}^{IJKP} \\ A_{16}^{IJKP} & A_{26}^{IJKP} & A_{66}^{IJKP} \end{bmatrix} \left\{ \frac{1}{2} \frac{\partial W_K}{\partial x} \frac{\partial W_P}{\partial x} \right. \\
& \left. \frac{1}{2} \frac{\partial W_K}{\partial y} \frac{\partial W_P}{\partial y} \right. \\
& \left. \frac{\partial W_K}{\partial x} \frac{\partial W_P}{\partial y} \right\} \\
& + \sum_{K=1}^N \begin{bmatrix} F_{31}^{IJK} \\ F_{32}^{IJK} \\ F_{36}^{IJK} \end{bmatrix} \psi_K - \begin{bmatrix} \tilde{N}_{xx}^{IJ(T)} \\ \tilde{N}_{yy}^{IJ(T)} \\ \tilde{N}_{xy}^{IJ(T)} \end{bmatrix}, \quad (88)
\end{aligned}$$

$$\begin{aligned}
\begin{Bmatrix} Q_x^I \\ Q_y^I \end{Bmatrix} &= \sum_{k=1}^{N_e} \int_{z_b^k}^{z_t^k} \begin{Bmatrix} \sigma_{xz} \\ \sigma_{yz} \end{Bmatrix}^{(k)} \frac{d\Phi^I}{dz} dz \\
&= \sum_{J=1}^N \begin{bmatrix} D_{55}^{IJ} & D_{45}^{IJ} \\ D_{45}^{IJ} & D_{44}^{IJ} \end{bmatrix} \begin{Bmatrix} U_J \\ V_J \end{Bmatrix} + \sum_{J=1}^M \begin{bmatrix} \tilde{B}_{55}^{JI} & \tilde{B}_{45}^{JI} \\ \tilde{B}_{45}^{JI} & \tilde{B}_{44}^{JI} \end{bmatrix} \begin{Bmatrix} \partial W_J / \partial x \\ \partial W_J / \partial y \end{Bmatrix} \\
&+ \sum_{J=1}^N \begin{bmatrix} F_{15}^{JI} & F_{25}^{JI} \\ F_{14}^{JI} & F_{24}^{JI} \end{bmatrix} \begin{Bmatrix} \partial \psi_J / \partial x \\ \partial \psi_J / \partial y \end{Bmatrix}, \quad (89)
\end{aligned}$$

$$\begin{aligned}
\begin{Bmatrix} \tilde{Q}_x^I \\ \tilde{Q}_y^I \end{Bmatrix} &= \sum_{k=1}^{N_e} \int_{z_b^k}^{z_t^k} \begin{Bmatrix} \sigma_{xz} \\ \sigma_{yz} \end{Bmatrix}^{(k)} \Psi^I dz \\
&= \sum_{J=1}^N \begin{bmatrix} \tilde{B}_{55}^{IJ} & \tilde{B}_{45}^{IJ} \\ \tilde{B}_{45}^{IJ} & \tilde{B}_{44}^{IJ} \end{bmatrix} \begin{Bmatrix} U_J \\ V_J \end{Bmatrix} + \sum_{J=1}^M \begin{bmatrix} \tilde{A}_{55}^{IJ} & \tilde{A}_{45}^{IJ} \\ \tilde{A}_{45}^{IJ} & \tilde{A}_{44}^{IJ} \end{bmatrix} \begin{Bmatrix} \partial W_J / \partial x \\ \partial W_J / \partial y \end{Bmatrix} \\
&+ \sum_{J=1}^N \begin{bmatrix} E_{15}^{JI} & E_{25}^{JI} \\ E_{14}^{JI} & E_{24}^{JI} \end{bmatrix} \begin{Bmatrix} \partial \psi_J / \partial x \\ \partial \psi_J / \partial y \end{Bmatrix}, \quad (90)
\end{aligned}$$

$$\begin{aligned}
\begin{Bmatrix} P_x^I \\ P_y^I \end{Bmatrix} &= \int_{-h/2}^{h/2} \begin{Bmatrix} D_x \\ D_y \end{Bmatrix} \Phi^I dz \\
&= \sum_{J=1}^N \begin{bmatrix} F_{15}^{IJ} & F_{14}^{IJ} \\ F_{25}^{IJ} & F_{24}^{IJ} \end{bmatrix} \begin{Bmatrix} U_J \\ V_J \end{Bmatrix} + \sum_{J=1}^M \begin{bmatrix} E_{15}^{IJ} & E_{14}^{IJ} \\ E_{25}^{IJ} & E_{24}^{IJ} \end{bmatrix} \begin{Bmatrix} \partial W_J / \partial x \\ \partial W_J / \partial y \end{Bmatrix} \\
&- \sum_{J=1}^N \begin{bmatrix} \tilde{E}_{xx}^{IJ} & \tilde{E}_{xy}^{IJ} \\ \tilde{E}_{xy}^{IJ} & \tilde{E}_{yy}^{IJ} \end{bmatrix} \begin{Bmatrix} \partial \psi_J / \partial x \\ \partial \psi_J / \partial y \end{Bmatrix}, \quad (91)
\end{aligned}$$

$$\begin{aligned}
P_z^I &= \int_{-h/2}^{h/2} D_z \frac{d\Phi^I}{dz} dz \\
&= \sum_{J=1}^N \{ F_{31}^{JI} \ F_{32}^{JI} \ F_{36}^{JI} \} \begin{Bmatrix} \frac{\partial U_J}{\partial x} \\ \frac{\partial V_J}{\partial y} \\ \frac{\partial U_J}{\partial y} + \frac{\partial V_J}{\partial x} \end{Bmatrix} + \sum_{J=1}^M \bar{F}_{33}^{IJ} W_J
\end{aligned}$$

$$- \sum_{J=1}^N \tilde{E}_{zz}^{IJ} \psi_J + \sum_{J,K=1}^M \{F_{31}^{KJI} F_{32}^{KJI} F_{36}^{KJI}\} \left\{ \begin{array}{l} \frac{1}{2} \frac{\partial W_K}{\partial x} \frac{\partial W_J}{\partial x} \\ \frac{1}{2} \frac{\partial W_K}{\partial y} \frac{\partial W_J}{\partial y} \\ \frac{\partial W_K}{\partial x} \frac{\partial W_J}{\partial y} \end{array} \right\}, \quad (92)$$

$$\begin{aligned} \tilde{Q}_z^I &= \sum_{k=1}^{N_e} \int_{z_b^k}^{z_t^k} \sigma_{zz}^{(k)} \frac{d\Psi^I}{dz} dz \\ &= \sum_{J=1}^N \left[B_{13}^{JI} \frac{\partial U_J}{\partial x} + B_{23}^{JI} \frac{\partial V_J}{\partial y} + B_{36}^{JI} \left(\frac{\partial U_K}{\partial y} + \frac{\partial V_K}{\partial x} \right) \right] \\ &\quad + \frac{1}{2} \sum_{J,K=1}^M \left(B_{13}^{IJK} \frac{\partial W_J}{\partial x} \frac{\partial W_K}{\partial x} + B_{23}^{IJK} \frac{\partial W_J}{\partial y} \frac{\partial W_K}{\partial y} + 2B_{36}^{IJK} \frac{\partial W_J}{\partial x} \frac{\partial W_K}{\partial y} \right) \\ &\quad + \sum_{J=1}^M \tilde{D}_{33}^{JI} W_J - \sum_{J=1}^N G_{33}^{JI} \psi_J - \tilde{Q}_z^{I(T)}, \end{aligned} \quad (93)$$

and the thermal stress resultants are defined as

$$\left\{ \begin{array}{l} N_{xx}^{I(T)} \\ N_{yy}^{I(T)} \\ N_{xy}^{I(T)} \end{array} \right\} = \sum_{k=1}^{N_e} \int_{z_b^k}^{z_t^k} \left[\begin{array}{cccc} \bar{C}_{11} & \bar{C}_{12} & \bar{C}_{13} & \bar{C}_{16} \\ \bar{C}_{12} & \bar{C}_{22} & \bar{C}_{23} & \bar{C}_{26} \\ \bar{C}_{16} & \bar{C}_{26} & \bar{C}_{36} & \bar{C}_{66} \end{array} \right]^{(k)} \left\{ \begin{array}{l} \alpha_{xx} \\ \alpha_{yy} \\ \alpha_{zz} \\ 2\alpha_{xy} \end{array} \right\}^{(k)} \Delta T \Phi^I dz, \quad (94)$$

$$\left\{ \begin{array}{l} \tilde{N}_{xx}^{IJ(T)} \\ \tilde{N}_{yy}^{IJ(T)} \\ \tilde{N}_{xy}^{IJ(T)} \end{array} \right\} = \sum_{k=1}^{N_e} \int_{z_b^k}^{z_t^k} \left[\begin{array}{cccc} \bar{C}_{11} & \bar{C}_{12} & \bar{C}_{13} & \bar{C}_{16} \\ \bar{C}_{12} & \bar{C}_{22} & \bar{C}_{23} & \bar{C}_{26} \\ \bar{C}_{16} & \bar{C}_{26} & \bar{C}_{36} & \bar{C}_{66} \end{array} \right]^{(k)} \left\{ \begin{array}{l} \alpha_{xx} \\ \alpha_{yy} \\ \alpha_{zz} \\ 2\alpha_{xy} \end{array} \right\}^{(k)} \Delta T \Psi^I \Psi^J dz, \quad (95)$$

$$\tilde{Q}_z^{I(T)} = \sum_{k=1}^{N_e} \int_{z_b^k}^{z_t^k} (\bar{C}_{13} \alpha_{xx} + \bar{C}_{23} \alpha_{yy} + \bar{C}_{33} \alpha_{zz} + 2\bar{C}_{36} \alpha_{xy})^{(k)} \Delta T \frac{d\Psi^I}{dz} dz. \quad (96)$$

In the above equations, N_e denotes the number of physical layers in the laminate, z_b^k and z_t^k are coordinates of the bottom and top of the k th layer, and the laminate stiffnesses are defined as follows:

$$A_{ij}^{IJ} = \sum_{k=1}^{N_e} \int_{z_b^k}^{z_t^k} \bar{C}_{ij}^{(k)} \Phi^I \Phi^J dz, \quad (97a)$$

$$\tilde{A}_{ij}^{IJ} = \sum_{k=1}^{N_e} \int_{z_b^k}^{z_t^k} \bar{C}_{ij}^{(k)} \Psi^I \Psi^J dz, \quad (97b)$$

$$A_{ij}^{IJK} = \sum_{k=1}^{N_e} \int_{z_b^k}^{z_t^k} \bar{C}_{ij}^{(k)} \Phi^I \Psi^J \Psi^K dz, \quad (98)$$

$$A_{ij}^{IJKP} = \sum_{k=1}^{N_e} \int_{z_b^k}^{z_t^k} \bar{C}_{ij}^{(k)} \Psi^I \Psi^J \Psi^K \Psi^P dz, \quad (99)$$

$$B_{ij}^{IJ} = \sum_{k=1}^{N_e} \int_{z_b^k}^{z_i^k} \bar{C}_{ij}^{(k)} \Phi^I \frac{d\Psi^J}{dz} dz, \quad (100a)$$

$$\tilde{B}_{ij}^{IJ} = \sum_{k=1}^{N_e} \int_{z_b^k}^{z_i^k} \bar{C}_{ij}^{(k)} \Psi^I \frac{d\Phi^J}{dz} dz, \quad (100b)$$

$$B_{ij}^{IJK} = \sum_{k=1}^{N_e} \int_{z_b^k}^{z_i^k} \bar{C}_{ij}^{(k)} \frac{d\Psi^I}{dz} \Psi^J \Psi^K dz, \quad (101)$$

$$D_{ij}^{IJ} = \sum_{k=1}^{N_e} \int_{z_b^k}^{z_i^k} \bar{C}_{ij}^{(k)} \frac{d\Phi^I}{dz} \frac{d\Phi^J}{dz} dz, \quad (102a)$$

$$\tilde{D}_{ij}^{IJ} = \sum_{k=1}^{N_e} \int_{z_b^k}^{z_i^k} \bar{C}_{ij}^{(k)} \frac{d\Psi^I}{dz} \frac{d\Psi^J}{dz} dz, \quad (102b)$$

$$E_{ij}^{IJ} = \sum_{k=1}^{N_e} \int_{z_b^k}^{z_i^k} \bar{e}_{ij}^{(k)} \Phi^I \Psi^J dz, \quad (103)$$

$$F_{ij}^{IJ} = \sum_{k=1}^{N_e} \int_{z_b^k}^{z_i^k} \bar{e}_{ij}^{(k)} \Phi^I \frac{d\Phi^J}{dz} dz, \quad (104a)$$

$$\bar{F}_{ij}^{IJ} = \sum_{k=1}^{N_e} \int_{z_b^k}^{z_i^k} \bar{e}_{ij}^{(k)} \frac{d\Phi^I}{dz} \Psi^J dz, \quad (104b)$$

$$F_{ij}^{IJK} = \sum_{k=1}^{N_e} \int_{z_b^k}^{z_i^k} \bar{e}_{ij}^{(k)} \Psi^I \Psi^J \frac{d\Phi^K}{dz} dz, \quad (105)$$

$$(\tilde{E}_{xx}^{IJ}, \tilde{E}_{yy}^{IJ}, \tilde{E}_{xy}^{IJ}) = \sum_{k=1}^{N_e} \int_{z_b^k}^{z_i^k} (\epsilon_{xx}, \epsilon_{yy}, \epsilon_{xy})^{(k)} \Phi^I \Phi^J dz, \quad (106a)$$

$$\tilde{E}_{zz}^{IJ} = \sum_{k=1}^{N_e} \int_{z_b^k}^{z_i^k} \epsilon_{zz}^{(k)} \frac{d\Phi^I}{dz} \frac{d\Phi^J}{dz} dz, \quad (106b)$$

$$G_{33}^{IJ} = \sum_{k=1}^{N_e} \int_{z_b^k}^{z_i^k} \bar{e}_{33}^{(k)} \frac{d\Phi^I}{dz} \frac{d\Psi^J}{dz} dz. \quad (107)$$

Note that the sum over the number of layers in the definition of the laminate stiffnesses is limited to the numerical layers over which the functions Φ^I and Ψ^I are defined. The functions Φ^I and Ψ^I are defined at the most over two adjacent numerical layers. When the von Kármán nonlinearity is not included, all laminate stiffnesses with three and four superscripts will not enter the governing equations.

5. Closure

In this paper two theories are presented for extensional and flexural motion of laminated plates with piezoelectric laminae. The first one is based on a third-order

expansion of the displacement field and the second one is based on a layerwise expansion of the displacement field through the laminate thickness. The first one contains, as special cases, the classical and first-order laminate theories. In both theories, the scalar electric potential is approximated through the laminate thickness to allow independent and higher-order prescription of the electric field. Linear constitutive equations of thermoelectro-elasticity and the von Kármán nonlinear strains in the laminate are used in the development. The theories developed herein can be used to study the response of composite laminates with either surface mounted or embedded piezoelectric laminae.

The model based on the third-order laminate theory is computationally simple because it contains only five dependent variables. It is adequate for predicting global response characteristics or preliminary design of laminated structures. However, the theory does not predict interlaminar stresses accurately in thick composite structures. The model based on the layerwise theory is essentially a three-dimensional model, hence computationally more expensive. However, the model can be used to determine the local stress fields accurately. In practice, a combination of the two models – ESL model in (global) regions of 2-D stress state and layerwise model in (local) regions of 3-D stress state will prove most appropriate. Such hierarchical (or variable kinematic) models with the global-local strategies (Reddy & Robbins 1994) provide the most robust computational methodology for the analysis of practical structures.

The theories presented here can be extended to the case where the plates are subjected to large electric fields (Tiersten 1993). This allows modelling of a larger class of phenomenon – electrostriction and higher-order permeability effects. For quadratic nonlinear constitutive behavior of the electric field, the enthalpy function is assumed to be a quadratic function of strains and a cubic function of the electric field,

$$\begin{aligned}\Phi_0(\varepsilon_{ij}, E_i, T) = & \frac{1}{2} C_{ijkl} \varepsilon_{ij} \varepsilon_{kl} - e_{ijk} \varepsilon_{ij} E_k - \frac{1}{2} b_{ijkl} \varepsilon_{ij} E_k E_l - \beta_{ij} \varepsilon_{ij} \theta \\ & - \frac{1}{2} \varepsilon_{ij} E_i E_j - \frac{1}{6} \lambda_{ijk} E_i E_j E_k - \frac{1}{2} q_{ij} E_i E_j \theta - \frac{\rho c_v}{2T_0} \theta^2, \quad (108)\end{aligned}$$

so that

$$\sigma_{ij} = C_{ijkl} \varepsilon_{kl} - e_{ijk} E_k - \frac{1}{2} b_{ijkl} E_k E_l - \beta_{ij} \theta, \quad (109)$$

$$D_k = e_{ijk} \varepsilon_{ij} + \varepsilon_{jk} E_k + \frac{1}{2} \lambda_{ijk} E_i E_j + q_{jk} E_k \theta, \quad (100)$$

$$\eta = \beta_{ij} \varepsilon_{ij} + \frac{1}{2} q_{ij} E_i E_j + \frac{\rho c}{T_0} \theta, \quad (111)$$

where b_{ijkl} denote the effective electrostrictive constants, λ_{ijk} are the electric susceptibility constants, and q_{ij} are the pyroelectric coefficients.

References

- Browning C E, Husman G E, Whitney J M 1977 Moisture effects in epoxy matrix composites. *Composite materials: Testing and design, Fourth conference* ASTM STP 617, pp. 481–496
 Carslaw H S, Jaeger J C 1959 *Conduction of heat in solids* 2nd edn (London: Oxford University Press)

- Chandra R, Chopra I 1993 Structural modelling of composite beams with induced-strain actuators. *AIAA J.* 31: 1692–1701
- Crawley E, de Luis J 1987 Use of piezoelectric actuators as elements of intelligent structures. *AIAA J.* 25: 1373–1385
- Eringen A C 1963 On the foundations of electrostatics. *Int. J. Eng. Sci.* 1: 127–153
- Jost W 1952 *Diffusion in solids, liquids, and gases* (New York: Academic Press)
- Lee C K 1990 Theory of laminated piezoelectric plates for the design of distributed sensors/actuators. Part I: Governing equations and reciprocal relationships. *J. Acoust. Soc. Am.* 97: 1144–1158
- Mitchell J A, Reddy J N 1994 A refined hybrid plate theory for composite laminates with piezoelectric laminae. Department of Mechanical Engineering, Texas A & M University, College Station, Texas
Also *Int. J. Solids Struct.* 32: 2345–2367 (1995)
- Nelson D F 1978 Theory of nonlinear electrostatics of dielectric, piezoelectric crystals. *J. Acoust. Soc. Am.* 63: 1738–1748
- Nowinski J L 1978 *Theory of thermoelasticity with applications* (Alphen aan den Rijn, The Netherlands: Sijthoff & Noordhoff)
- Nye J F 1957 *Physical properties of crystals* (Cambridge: Oxford University Press)
- Pai P F, Nayfeh A H, Oh K, Mook D T 1993 A refined nonlinear model of composite plates with integrated piezoelectric actuators and sensors. *Int. J. Solid Struct.* 30 (12): 1603–1630
- Penfield P Jr, Hermann A H 1967 *Electrodynamics of moving media*. Research Monograph No. 40, Cambridge, Massachusetts
- Reddy J N 1984a *Energy and variational methods in applied mechanics* (New York: John Wiley & Sons)
- Reddy J N 1984b A simple higher-order theory for laminated composite plates. *J. Appl. Mech.* 51: 745–752
- Reddy J N 1987 A generalization of two-dimensional theories of laminated composite plates. *Commun. Appl. Numer. Meth.* 3: 173–180
- Reddy J N 1993 *An introduction to the finite element method* 2nd edn (New York: McGraw-Hill)
- Reddy J N 1995 *Theory and analysis of laminated composite plates and shells* (New York: John Wiley & Sons) (to be published)
- Reddy J N, Gartling D K 1994 *The finite element method in heat transfer and fluid dynamics* (Boca Raton, FL: CRC Press)
- Reddy J N, Robbins D H Jr 1994 Theories and computational models for composite laminates. *Appl. Mech. Rev.* 47 (6): 147–169
- Robbins D H Jr, Reddy J N 1993 Modelling of thick composites using a layerwise laminate theory. *Int. J. Numer. Meth. Eng.* 36: 655–677
- Shen C H, Springer G S 1976 Moisture absorption and desorption of composite materials. *J. Compos. Mater.* 10: 2–20
- Tiersten H F 1964 Coupled magnetomechanical equations for magnetically saturated insulators. *J. Math. Phys.* 5: 1298–1318
- Tiersten H F 1969 *Linear piezoelectric plate vibrations* (New York: Plenum)
- Tiersten H F 1971 On the nonlinear equations of thermoelectroelasticity. *Int. J. Eng. Sci.* 9: 587–604
- Tiersten H F 1981 Electroelastic interactions and the piezoelectric equations. *J. Acoust. Soc. Am.* 70: 1567–1576
- Tiersten H F 1993a Electroelastic equations for electroded thin plates subjected to large driving voltages. *J. Appl. Phys.* 74: 3389–3393
- Tiersten H F 1993b Equations for the extension and flexure of relatively thin electroelastic plates undergoing large electric fields. *Mechanics of electromagnetic materials and structures* (eds) J S Lee, G A Maugin, Y Shindo (New York: The American Society of mechanical Engineers) AMD-vol. 161, 21–34
- Toupin R A 1956 The elastic dielectric. *J. Rational Mech. Anal.* 5: 849–916
- Tzou N S, Zhong J P 1993 Electromechanics and vibrations of piezoelectric shell distributed systems. *J. Dyn. Syst., Meas. Control* 115: 506–517

Estimation of the order of an auto-regressive model

N SUDARSHAN RAO* and P S MOHARIR**

*Department of Electronics & Communication Engineering, Osmania University, Hyderabad 500 007, India.

**National Geophysical Research Institute, Uppal Road, Hyderabad 500 007, India.

MS received 21 April 1994; revised 24 October 1994

Abstract. There are no definitive solutions available for the order estimation of the auto-regressive process. First, the performance of the three criteria, namely FPE, AIC and MDL is illustrated. Next, it is indicated that there are possibilities of their performance being improved. The algorithm *tri* proposed here utilizes three minimum values of any of the conventional loss functions in the FPE, AIC and MDL methods. It also uses three statistics derived from these three minimum values. The estimated order is a rounded weighted average of these six statistics. The algorithm is found to do better in a qualified sense of yielding peakier distribution of the estimated orders when tested for 1000 synthetic models of orders 3, 5 and 7 each. The conclusion drawn is that there are open possibilities of improving upon the conventional order estimators for auto-regressive processes. This means that till axiologically sounder estimators are available one should be ready to use heuristic estimators proposed here.

Keywords. Algorithm *tri*; auto-regressive process; order estimation; plural criteria; order statistics.

1. Introduction

Consider a time series $x(n)$, $n = 0, 1, \dots, N - 1$ of finite length N . If

$$x(n) = \sum_{i=1}^r \alpha_{r,i} x(n-i) + u(n), \quad (1)$$

where $u(n)$ is an uncorrelated innovations process, then $x(n)$ is said to be an auto-regressive time-series (ARTS) of order r (Box & Jenkins 1976). Coefficients $\alpha_{r,i}$, $i = 1, 2, \dots, r$ are called auto-regressive or linear prediction coefficients (LPCs). As the true order r would be unknown and would have to be estimated, and as it determines the number of LPCs to be estimated, it is useful to make r an explicit part of

the notation for LPCs as done above. It also permits the possibility of referring to r LPCs under different assumed orders r , pending the estimation of r . The innovations process $u(n)$ is assumed to be zero-mean, white and Gaussian.

There are many methods to estimate the order r of ARTS. Three famous ones are final prediction error (FPE) (Akaike 1969, 1970), asymptotic information criterion (AIC) (Akaike 1973, 1974) and minimum description length (MDL) (Rissanen 1983). At times the 'A' in AIC is taken to be Akaike's rather than asymptotic to give the acronym an eponymic advantage. The basic structure of the three methods is similar. They use a loss function which is minimized. The three loss functions are:

$$\Lambda_{\text{FPE}}(N, r) = \hat{\sigma}^2(N + r + 1)/(N - r - 1). \quad (2)$$

$$\Lambda_{\text{AIC}}(N, r) = \ln \hat{\sigma}^2 + 2r/N, \quad (3)$$

$$\Lambda_{\text{MDL}}(N, r) = N \ln \hat{\sigma}^2 + r \ln N. \quad (4)$$

Each loss function depends on $\hat{\sigma}^2$ which is the estimated variance of the linear prediction error. This is expected to monotonically decrease as the assumed or fitted order r is increased. Then there is a modifier dependent on r , the assumed order and N , the length of the timeseries available. The purpose of the modifier is to arrange for a minimum in the loss function, possibly at the correct order. The modifier could be multiplicative as in the case of FPE or additive as in the case of AIC and MDL and a monotone transformation could be used on the variance of the prediction error before a modifier is applied as in the latter two cases.

Most users assume that the problem of estimating the order of the auto-regressive process is solved satisfactorily and use one of the standard methods available for the purpose. One of the aims of this paper is to suggest that the problem above is still an open one. Thus, initially the performance of the FPE, AIC and MDL methods is assessed *ab initio*. This has not been done adequately in the literature. For example, one study (Shibata 1976) reports the frequency distribution of the estimated order by the AIC method on the basis of 500 realizations when the correct order is unity. For $N = 50$ and $\alpha_{1,1} = \pm 0.8$ the order is estimated as unity about 74% times. When $\alpha_{1,1}$ is weaker the percentage of correct order estimation is even lower. Another more recent study (Broersen & Wensink 1993) used 10,000 realizations of ARTS of order two and $N = 25$ to obtain the frequency distribution of the estimated order by 10 different methods. The percentage of correct order estimation ranged between 35.6 and 74.4. There are many applications wherein the ARTS model of higher orders would be necessary (Makhoul 1975; Kay & Marple 1981). Therefore, true orders 3, 5 and 7 are used here to generate 1000 realizations each of ARTS and for $n = 50$, the frequency distribution of the estimated orders has been studied. The inference drawn is that the three conventional methods do not perform very satisfactorily, making their axiological elegance only of restricted practical utility.

The problem posed here is whether the performance of the conventional order estimators can be improved. It is a real problem, particularly in the context that it is not even widely known that the performance of the conventional order estimators is as bad as is brought out here, for values of r between 3 and 7.

The approach here is heuristic and is substantiated by extensive numerical simulation as better axiology was not available for more than two decades. To keep the computational efforts within manageable limits, the effects of sample size N have not been studied. N is chosen to be 50 which is larger of the values used in the two earlier

studies (Shibata 1976; Broersen & Wensink 1993) referred to above. The number of realizations of ARTS used to base the inference on is between the values used in the earlier two studies. The number of methods investigated here also lies in between. Taking these three considerations together, it may be said that the computational determinants of effort here form roughly the geometrical mean of the two earlier studies, given that three as against just one, and that too larger values of the correct order have been studied. Further, the computational effort put in is of the same order as for the latter of the two studies.

Motivation for the present work came through watching the loss functions of the three methods of ARTS order estimation. Unlike the formal expectation from equations (2)–(4), the loss functions do not show a sharp single minimum. Their shapes are at times very irregular and depend on the parameters (LPCs) of the ARTS realization. Therefore, it was believed that more information could be extracted from the loss functions to improve upon the conventional order estimators. The work reported establishes such a hope without claiming that the results here cannot be improved upon in a variety of ways.

2. Assessment of the conventional estimators

Thousand ARTS models of orders 3, 5 and 7 each have been generated. The basic idea was to make them representative of all the possibilities that could arise. This obviously needs proper definition. ARTS models are amenable to at least three different characterizations. They are in terms of their auto-correlation coefficients, linear prediction coefficients and reflection coefficients. The three characterizations are interconvertible. But it does not mean that they are equivalent for all purposes. For example, it has been shown that when ARTS models are to be ordered on the basis of their proximity to a prescribed model, the results may be different when the three characterizations above are used (Moharir 1993). This obviously means that the characterization to be relied upon must be chosen *a priori*. The characterization chosen here is in terms of the reflection coefficients. The reflection coefficient (RC)

$$k_j = \alpha_{j,j} \quad (5)$$

is the last LPC when an ARTS model of order j is imposed on the time series. There are some good reasons why the RCs have been chosen for a proper characterization of the ARTS models. When the Levinson–Durbin algorithm (LDA) (Kay & Marple 1981; Moharir 1985; Alexander 1986) is used for estimating the LPCs, reflection coefficients turn out to be important intermediate results (Makhoul 1975). But even more pertinently, the prediction on the basis of the ARTS model can be arranged entirely in terms of the RCs (Makhoul 1975; Kay & Marple 1981) with some advantages. Further, the Schur–Cohn stability condition (Proakis 1989) for the ARTS is that

$$|k_j| < 1. \quad (6)$$

Thus, the appropriate RC space is a hypercube. The stability conditions are more involved in terms of the other two characterizations of ARTS. Filling a hypercubical region uniformly with uncorrelated random numbers is possible and easy but it has been suggested (Hoel 1966) that for regions with other boundaries it may not even be possible in principle. Therefore, the definition of a set of models representative of all

Table 1. The assessment of the performance of the three methods, FPE, AIC and MDL, for the estimation of the order of the ARTS models.

The numbers of models which gave the estimated order are tabulated against the latter. Thousand synthetic models of true ARTS orders 3, 5 and 7 each were synthesized. See text for the non-numerical entries in the column 'estimated order'. Entries against them summarize the properties of the distribution of the estimated orders.

Estimated order	Correct order = 3			Correct order = 5			Correct order = 7		
	FPE	AIC	MDL	FPE	AIC	MDL	FPE	AIC	MDL
0	38	38	66	12	12	31	4	4	21
1	73	73	94	28	28	49	13	12	44
2	186	184	224	45	43	74	31	31	54
3	607	609	582	132	132	157	61	61	93
4	67	67	29	169	168	203	71	71	101
5	24	23	5	465	465	415	108	106	133
6	3	4		80	82	37	197	195	192
7	3	2		58	59	31	340	340	273
8				8	8	2	107	110	76
9				1	1	1	56	58	11
10				1	1		19	9	2
11				1	1			1	
12	—	—	—	—	—	—	—	—	2
<i>C</i>	607	609	582	465	465	415	340	340	273
<i>L</i>	297	295	384	386	383	514	485	480	638
<i>H</i>	97	96	34	149	152	71	183	180	89
N_s	860	860	835	714	715	655	644	645	541
N_o	793	793	806	634	633	618	537	535	465

possibilities was taken to mean a set in which RCs are chosen to spread uniformly and randomly over every axis of the hypercube.

For each of the 3000 ARTS models chosen, LDA was used to evaluate the RCs. A time-series sample of length $N = 50$ was used for this purpose. Then predictions were performed under various assumed orders and were compared against the extension of 50 values of the same ARTS to calculate $\hat{\sigma}^2$ of (2)–(4). The FPE, AIC and MDL estimates of ARTS order were obtained by minimizing the respective loss functions. The results are shown in table 1.

In the column for the estimated order in table 1, there are five non-numerical entries at the end. *C* refers to the correct order. Order 3 is correctly estimated less than 61% times by the FPE and AIC methods and about 58% times by the MDL method. For orders 5 and 7 the percentage of correct order estimation is even lower for all the methods. The difference between the performance of the MDL method and the other two also is seen to grow as the correct order increases. For the correct order of 7, the percentage of correct order estimation is about 34% for FPE and AIC methods and just about 27% for the MDL method. *L* stands for the 'orders lower than the correct one' and *H* for the 'orders higher than the correct one'. As the correct order increases, for all the three methods the percentage of underestimation or overestimation of the order increases, underestimation being more probable than the overestimation. The MDL method underestimates more and overestimates less than the other two. N_s stands for the 'symmetric neighbourhood of the correct order' comprising the

correct order and immediately adjacent orders, one on each side. When the order is incorrectly estimated, an underestimate may be preferred to an overestimate by the same amount because erroneous as both the estimates are, the former subsequently requires less effort or cost to predict. Further, simpler models have more philosophical appeal for those who adopt Occam's razor (Anderson 1963; Bernal 1969; Constable 1987; Moharir 1991). In this spirit N_o stands for the 'Occamic neighbourhood of the correct order' and includes the correct order and the next lower order. On the criteria of the estimated order being in the neighbourhood of the correct order, the three methods do much better than on the criterion of the correct order estimation. Major part of the improvement comes by going to the Occamic neighbourhood from the correct order, the further improvement obtained by enlarging the neighbourhood symmetrically being relatively smaller. The first improvement is larger for the MDL method than for the other two and the second one is relatively small. For the correct order of 3, the MDL method even does marginally better than the other two on the criterion of N_o . For all the methods studied, the distributions of the estimated order is asymmetrical with respect to the correct order.

Information summarized in table 1 and some preliminary numerical experiments suggested that the conventional order estimators may possibly be improved upon. One possible way of obtaining the improvement and the attendant difficulties are discussed in the next section.

3. Algorithm *tri*

The loss functions used by the FPE, AIC and MDL methods are motivated by the usefulness of deriving a measure which takes the least value for the correct order. But the above results indicate that it does not happen frequently enough. Further, it is believed to be a common experience with those who observe the loss functions plotted rather than the algorithm reporting the estimated order on their basis that these loss functions are not necessarily uni-minimal. Therefore, it is surmised that there is more information in the loss functions about the order of ARTS than is contained in their lowest minima. The question then was whether it could be extracted. The results presented below should be regarded rather as one such possibility than the final answer.

Table 2. One possibility in which three opinions about the ARTS order can be consensually corrected. The actual correction strategy used is a modification of this.

Ranking of the three opinions	Possible corrected values of the three opinions		
$r_1 < r_2 < r_3$	r_1	$r_2 - 1$	$r_3 - 2$
$r_1 < r_3 < r_2$	r_1	$r_3 - 1$	$r_2 - 2$
$r_2 < r_1 < r_3$	$r_2 + 1$	r_1	$r_3 - 1$
$r_2 < r_3 < r_1$	$r_2 + 2$	$r_3 + 1$	r_1
$r_3 < r_1 < r_2$	$r_3 + 1$	r_1	$r_2 - 1$
$r_3 < r_2 < r_1$	$r_3 + 2$	$r_2 + 1$	r_1

From the loss function graphs three order values were chosen which gave the three lowest values of the loss function. Let these orders viewed as three opinions be called r_1 , r_2 and r_3 . Then r_1 would be the conventional order estimate. These opinions can be ordered in six different ways as shown on the left of table 2. If the opinions are to be corrected, as they refer to the same correct order, one possible way of correcting, giving maximum credence to the first opinion, is shown on the right of table 2. The corrections applied are the least possible, given that the three opinions are different. This can be expressed in a single formula as follows:

$$P_j = r_j - [R(r_j) - R(r_1)], \quad j = 1, 2, 3, \quad (7)$$

where $R(\cdot)$ is the rank when the three opinions are ranked in the ascending order and P_j is the corrected value of the opinion r_j . Next, it is possible to modify (7) by making the correction depend on the spread of the three opinions. That is, if r_{\max} and r_{\min} are the maximum and minimum values of the order among the three opinions one could choose

$$P_j = r_j - \beta_j(r_{\max} - r_{\min})[R(r_j) - R(r_1)], \quad (8)$$

where β_j is called the degree of correction of r_j . Further if P_j turns out to be negative, it could rather be set to zero. The values of β_2 and β_3 were chosen as 0.2. Corrections applied amount to editing the opinions about the quantity to be estimated for achieving robustness and are in the spirit of Winsorization, trimming and jack kniving (Barnett & Lewis 1978; Diaconis & Efron 1983; Moharir 1988).

In addition to the three corrected opinions, three statistics are derived from the three opinions. They are:

$$P_4 = r_{\text{mid}}, \quad (9)$$

$$P_5 = r_{\max} - r_{\min}, \quad (10)$$

$$P_6 = (r_1 r_2 r_3)^{1/3}, \quad (11)$$

where r_{mid} is the middle value among r_1 , r_2 and r_3 . The averages of these three statistics are presumed to represent the central tendency, spread and third cumulant of the ARTS order distribution. Therefore, use of these three statistics is in the nature of stochastic feedback up to the third order moments or cumulants. The rounded value of the weighted average of P_j 's, $j = 1, 2, \dots, 6$ is taken to be the estimate r_{est} of the ARTS order. That is,

$$r_{\text{est}} = \frac{\sum_{j=1}^6 w_j P_j}{\sum_{j=1}^6 w_j}, \quad (12)$$

where for convenience the weight factors w_j are taken to be nonnegative multiples of 0.25. It can be readily seen that care has been taken to ensure that the quantities averaged are dimensionally compatible. In fact, the particular measures of central tendency, spread and skewness have been specifically chosen to satisfy this requirement.

It was found that the weight factors cannot be chosen uniquely to achieve that, for a given true order, the order estimates most frequently match the correct order. It was also found that a choice of weight factors which achieves this for a particular true ARTS order is not necessarily likely to achieve it simultaneously for other true orders. Therefore, the numerical experiment was performed as follows. For the true order three, a large number of combinations of weight factors which gave largest or near-largest overall

Table 3. Summary of the performance of *tri*-modification for ARTS order estimation, operating on the three conventional methods, viz. FPE, AIC and MDL. For the nonnumerical code for estimated order, see text.

Weight factors (a): [0.25, 0.75, 0.25, 4.25, 2, 1]
 (b): [0.25, 0.5, 0.5, 4.25, 2, 1]
 (c): [0, 0.75, 0.5, 4, 2, 1]
 (d): [0.5, 0.5, 0.5, 4, 2, 1]

Symbols for methods: *tri*-modified FPE = TFPE, etc.

Estimated order code	TFPE	TAIC	TMDL	TFPE	TAIC	TMDL
<u>(1) Correct order = 3</u>						
	<u>Weight factors a</u>			<u>Weight factors b</u>		
<i>C</i>	750	749	750	722	721	730
<i>L</i>	161	161	233	161	161	233
<i>H</i>	89	90	17	117	118	37
<i>N_s</i>	945	944	917	945	945	917
<i>N_o</i>	868	867	902	840	839	882
	<u>Weight factors c</u>			<u>Weight factors d</u>		
<i>C</i>	750	749	750	722	721	730
<i>L</i>	161	161	233	161	161	233
<i>H</i>	89	90	17	117	118	37
<i>N_s</i>	945	944	917	945	944	919
<i>N_o</i>	868	867	902	840	839	884
<u>(2) Correct order = 5</u>						
	<u>Weight factors a</u>			<u>Weight factors b</u>		
<i>C</i>	403	402	327	408	407	333
<i>L</i>	502	499	615	497	494	643
<i>H</i>	95	99	23	95	99	24
<i>N_s</i>	767	768	695	780	782	707
<i>N_o</i>	703	702	679	718	716	690
	<u>Weight factors c</u>			<u>Weight factors d</u>		
<i>C</i>	408	407	323	406	405	332
<i>L</i>	497	494	654	499	496	644
<i>H</i>	95	99	23	95	99	24
<i>N_s</i>	765	768	694	777	779	703
<i>N_o</i>	703	702	678	715	713	686
<u>(3) Correct order = 7</u>						
	<u>Weight factors a</u>			<u>Weight factors b</u>		
<i>C</i>	358	366	211	368	372	212
<i>L</i>	592	589	780	592	579	779
<i>H</i>	50	55	9	40	49	9
<i>N_s</i>	654	654	489	654	656	488
<i>N_o</i>	612	612	480	622	618	479
	<u>Weight factors c</u>			<u>Weight factors d</u>		
<i>C</i>	369	373	219	368	374	214
<i>L</i>	592	579	780	592	579	779
<i>H</i>	39	48	9	40	47	7
<i>N_s</i>	652	654	488	652	654	488
<i>N_o</i>	621	617	479	620	620	481

percentage of correct order estimation on the basis of the FPE, AIC and MDL loss functions of (2)–(4) were found. This was done on the basis of only one-fifth of the 1000 ARTS models of order 3 to save computational effort. Some hopeful combinations among them were tested for simultaneous good performance for true order 7 and were selected on that basis. Again the test was restricted to only one-seventh of the 1000 ARTS models generated. The results for the true order 5 were then taken as they came.

The numerical comparison is offered in table 3. The comparison is made for four different choices of weight factors. In one of them, one of the weights is zero. That means only five determinants of order are used. More particularly, the one that is not used is the conventional order estimate, but it does not seem to matter much! This is a very direct suggestion that the loss functions of equations (2)–(4) have more information than or parallel modes of information to the one utilised by the conventional order estimation methods.

What is provided in table 3 is basically the summary in terms of the non-numerical symbols regarding estimated order, introduced in the context of table 1. Comparing the relevant part of table 3 with that of table 1, it can be seen that for the correct ARTS order of 3, *tri* algorithm with all the four weight factors yields results better than the conventional algorithm on the criterion C though weight factors (b) and (d) do not do as well as (a) and (c). For the correct ARTS order 5, no weight factor yields *tri* results superior to the conventional methods on the criterion C . For the correct ARTS order 7, all the weight factors yield *tri* results better than the FPE and AIC methods. For correct order 7, the *tri* modification does better on the criterion N_o but not on N_s for the MDL method. This too is understandable because, of the three conventional methods, MDL has the strongest tendency to underestimate the order. On the criteria N_s or N_o for the correct ARTS orders 5, all the weight factors yield *tri* results better than those of the conventional methods. Thus, taking C as the first criterion and N_s and/or N_o as a supplementary criterion of considerable importance, it is possible to uniformly improve the performance of the conventional order estimators at least for the range of correct ARTS order considered. This uniformly better performance may not be the best at individual values of the correct order but that is just as well because, if the correct order is known, there is no order estimation problem; therefore order estimation algorithms should work over a range of true orders expected.

It should be pointed out that the results reported here are not the best possible because they are not based on proper optimization but only on incomplete search. Also the search for improvement has not been individualized for either the conventional criteria of FPE, AIC and MDL or for criteria C , N_s or N_o . Therefore, the results only hint at the possible inadmissibility of the conventional methods, a method being defined as inadmissible (Judge & Bock 1978) if it can be uniformly improved upon without any claims about the optimality of what is proposed. The *tri* algorithm also separates the order estimation problem from that of the estimation of ARTS coefficients. Once the former is solved, the latter also can be reapproached using unconventional techniques (Judge & Bock 1978; Vinod & Ullah 1981). Results along these lines will be reported separately.

4. Conclusion

Conventional methods of ARTS order estimation, viz. FPE, AIC and MDL were

assessed on the basis of 1000 synthetic models for true orders 3, 5 and 7 each. A heuristic order estimation procedure is suggested which may do uniformly better than these though as a compromise by not doing the best possible at individual orders. The procedure suggested uses three opinions from a conventional criteria and three statistics based on them to derive the order estimate. The objectives of showing that

- (a) the problem of ARTS order estimation is still an open problem and that there exist better possibilities than the conventional methods,
 - (b) the distribution of the estimated order can be improved upon, and
 - (c) heuristics may do better than the available axiological insights,
- are regarded as served.

The authors are grateful to Dr H K Gupta of the National Geophysical Research Institute for encouragement.

References

- Akaike H 1969 Power spectrum estimation through autoregressive model fitting. *Ann. Inst. Stat. Math.* 21: 407-409
- Akaike H 1970 Statistical predictor identification. *Ann. Inst. Stat. Math.* 22: 203-217
- Akaike H 1973 Maximum likelihood identification of Gaussian autoregressive moving average models. *Biometrika* 60: 255-265
- Akaike H 1974 A new look at statistical model identification. *IEEE. Trans. Autom. Control* 19: 716-723
- Alexander S T 1986 *Adaptive signal processing, theory and applications* (New York: Springer Verlag) pp. 34-45, 99-110
- Anderson C A 1963 Simplicity in structural geology. In *The fabric of geology* (ed.) C C Albritton, Jr (Stanford: Freeman, Cooper) pp. 175-183
- Barnett V, Lewis T 1978 *Outliers in statistical data* (Chichester: John Wiley) pp. 25-48
- Bernal J D 1969 *Science in history, The emergence of science* (Harmondsworth: Pelican) 1: 301
- Box G E, Jenkins G M 1976 *Time series analysis: forecasting and control* (San Francisco: Holder Day) p. 575
- Broersen M T, Wensink H E 1993 On finite sample theory for autoregressive model order selection. *IEEE Trans. Signal Process.* 41: 194-204
- Constable S C, Parker R L, Constable C G 1987 Occam's inversion, a practical algorithm for generating smooth models for electromagnetic sounding data. *Geophysics* 52: 289
- Diaconis P, Efron B 1983 Computer intensive methods in statistics. *Sci. Am.* 248: 116
- Hoel P G 1966 *Introduction to mathematical statistics* (New York: John Wiley) p. 44
- Judge G G, Bock M E 1978 *The statistical implications of pretest and Stein-rule estimators in econometrics* (Amsterdam: North Holland) p. 340
- Kay S M, Marple Jr S L 1981 Spectrum analysis - a modern perspective. *Proc. IEEE* 69: 1380-1419
- Makhoul J 1975 Linear prediction: A tutorial review. *Proc. IEEE* 63: 561-580
- Moharir P S 1985 Predictive deconvolution. Parts 1 & 2. *J. Inst. Electron. Telecommun. Eng.* 31: 111-121, 157-168
- Moharir P S 1988 Central tendency and dispersion: a broader look *Proc. 6th Indian Geol. IGC, Roorkee*, pp. 217-219
- Moharir P S 1991 Non-optimality and positive Occam's gradient. *Inst. Eng. India J.* 71: 116-121
- Moharir P S 1993 Induced Condorcet paradox. In *Signal processing and communications* (eds) T V Sreenivas, K V S Hari (New Delhi: Tata McGraw-Hill) 129-134

- Proakis J G, Manolakis D G 1989 *Introduction to digital signal processing* (London: Maxwell Macmillan) 203–205
- Rissanen J 1983 A universal prior for the integers and estimation by minimum description length. *Ann. Stat.* 11: 417: 431
- Shibata R 1976 Selection of order of an autoregressive model by Akaike's information criterion. *Biometrika* 73: 117–126
- Vinod H D, Ullah 1981 *Recent advances in regression methods* (New York: Marcel Dekker)

Surface characterization and parameter estimation for industrial vision system

S JAGDISH, PRABIR KUMAR BISWAS, JAYANTA MUKHERJEE
and B N CHATTERJI*

Department of Electronics and Electrical Communication Engineering,
Indian Institute of Technology, Kharagpur 721 302, India

MS received 15 July 1994; revised 18 May 1995

Abstract. In this paper we have presented some geometric techniques to characterize and parametrize surfaces of industrial parts in range images. The surfaces are characterized to one of plane, sphere, cylinder and cone, because they form the majority of object surfaces in man-made industrial parts. The problem has been studied for two different situations. In the first case, *a priori* knowledge about the surface shape is assumed. In such a situation the problem of surface characterization reduces to that of surface parameter estimation. The standard deviations of the estimated parameters give a measure of uncertainty of characterizing a surface patch to one of the four surface types. In the second case, no *a priori* information regarding the shape of a surface is available. This includes partially visible surfaces also. To deal with such a situation, a fuzzy classifier is designed using the uncertainty values. The fuzzy classifier classifies the unknown surface patch (including partially visible surfaces) to one of the four surface types. Experimental results with synthetic range images are presented to highlight the distinctive features of our technique.

Keywords. Range image; geometric surface fitting; parameter estimation; fuzzy classification; occlusion.

1. Introduction

The major aim of any computer vision system is to recover useful information about the three dimensional world from huge image arrays of sensed values. In the past these image arrays were digital intensity images. At each point in an intensity image the brightness value encodes information about surface geometry, surface reflectance characteristics, surface texture, scene illumination, the distance from the camera to an object surface, the characteristics of the intervening medium and the camera characteristics. However, such images do not contain explicit information about depth¹

In recent years digital range images (also known as $2\frac{1}{2}$ -D images) have become available owing to the development of various active and passive

techniques. Range data are produced in the form of an array of numbers, where the numbers quantify the distance from the sensor focal plane to the object surface within the field of view along rays emanating from points on a regularly spaced grid. Thus the range images provide direct geometrical information about the shape of visible surfaces. Therefore, the process of recognising objects by their shape is less difficult in range images than in intensity images. Such images find wide application in industrial automation such as assembly automation, automated inspection of industrial parts etc.

Surface characterization and parameter estimation are two of the major problems of computer vision utilising range images in industrial environment. The estimated surface parameters can be used efficiently by the matching process for object recognition and pose determination even in presence of many undefined or occluded surface regions. A number of approaches for surface characterization and parameter extraction have been reported in the literature. The optimization and eigenvalue analysis (Faugeras 1984) approach employs global analysis of 3-D or $2\frac{1}{2}$ -D (range) data. This approach is more general in the sense that it is applicable to all sorts of quadrics and planar surfaces. Characterization by quadric invariants (e.g. sign of curvatures) (Besl & Jain 1984, 1988; Brady *et al* 1985) employs computation of differential properties of the surface at each surface point. This technique requires spatial ordering of surface points. Surfaces are characterized according to the signs of mean and Gaussian curvatures.

Though eigenvalues or quadric invariants are good discriminators in a mathematical sense, they are often very sensitive to noise and quantization errors (Han *et al* 1987). Moreover in man-made industrial parts, the majority of object surfaces belong to planar, spherical, cylindrical and conical surfaces (Bolle & Cooper 1984). Hence, for such applications it is not necessary to work with general quadric surfaces but rather to deal with a narrow domain of surface types, such as plane, sphere, cylinder and cone. Hough transform (Muller & Mohr 1984) or modified Hough transform (Lin & Wee 1985) techniques have been used in such cases for surface characterization purposes.

Parametric estimation technique by Han *et al* (1987) calculates the geometric properties of a sufficient set of shapes, namely plane, sphere and cylinder, based upon an analysis of the surface normals. This approach uses a mixture of histogramming and parameter-fitting techniques to estimate surface parameters.

We have presented in this paper some new geometric techniques which use transformation invariant properties of surface normals and surface tangents to obtain the description of an unknown surface in terms of plane, sphere, cylinder or cone. This work presumes surfaces in range images are already segmented. Range image segmentation is not addressed here. A number of techniques for range image segmentation have been discussed by Biswas *et al* (1990). Unlike Han *et al* (1987) who use histogram analysis of surface normals to extract surface regions of a particular type, our technique uses mean and standard deviation of parameters characterizing different surfaces. The standard deviation of a parameter represents the measure of uncertainty of fitting a particular type of surface with respect to that parameter. The problem has been attempted for two different situations. In the first case, it has been assumed that *a priori* knowledge about the shape of the surface is available. In such situations, a surface of proper type is fitted to the set of points representing the surface patch and the parameters of the fitted surface are extracted. This strategy of selective surface fitting reduces the amount of computation. In the second case, when no *a priori* information regarding the shape of the unknown surface is available, the characterization of the surface is obtained in the

form of a fuzzy membership vector. A fuzzy classifier is designed using the uncertainty measures which classifies an unknown surface to one of the surface types.

Geometric surface fitting and parameter estimation is discussed in §2. Section 3 describes the fuzzy classifier to classify an unknown surface. Occluded surface characterization is discussed in §4.

2. Surface characterization through geometric method

The geometric method described in this section is guided by *a priori* information regarding the shape of a surface patch to fit an appropriate surface and extract the parameters of the fitted surface. The parameters extracted for each of planar, spherical, cylindrical and conical surfaces are the surface normal and the perpendicular distance from the origin for a plane, the centre coordinates and the radius for a sphere, the axis and the radius for a cylinder and the apex, the apex angle and the axis for a cone. The geometric method of surface fitting for these surfaces is facilitated from the existence of certain unique and transformation invariant properties of their surface normals and surface tangents as listed below:

Plane: All surface normals are parallel (to the normal to the plane).

Sphere: All surface normals are concurrent (at the centre of the sphere).

Cylinder: All surface normals are perpendicular to the axis of the cylinder.

Cone: All tangential planes to the surface intersect at a point (at the apex of the cone).

In the following discussion the input is taken to be a set of M points in three dimensional space. The i th point is referred to as $X_i \equiv (x_i, y_i, z_i)$ or equivalently by \mathbf{X}_i , the vector joining the origin $(0, 0, 0)$ to (x_i, y_i, z_i) . The set of corresponding normals is taken to be $\{\mathbf{N}_i | i = 1, 2, \dots, M\}$. The normal \mathbf{N}_i at point \mathbf{X}_i is computed by fitting a plane to the 5×5 neighbourhood of X_i using least square error method (Taylor *et al* 1989).

2.1 Characterization of a plane

A plane is characterized by the direction of the normal to the plane and the perpendicular distance of the plane from the origin (refer figure 1). The estimate of the normal to the plane approximating the set of input points is given by

$$\mathbf{N}_{av} = \frac{\sum_{i=1}^M \mathbf{N}_i}{\left| \sum_{i=1}^M \mathbf{N}_i \right|}, \quad (1)$$

where \mathbf{N}_i is the unit normal vector at point X_i and ' Σ ' in (1) represents vector addition. The uncertainty in the estimation of the surface normal is given by the standard deviation σ_N of \mathbf{N}_{av} where

$$\sigma_N^2 = \frac{1}{M} \sum_{i=1}^M |\mathbf{N}_i - \mathbf{N}_{av}|^2, \quad (2)$$

where $|\cdot|$ represents the magnitude of a vector. The lesser the value of σ_N , the more reliable is the normal estimate. The perpendicular distance d of the plane from the

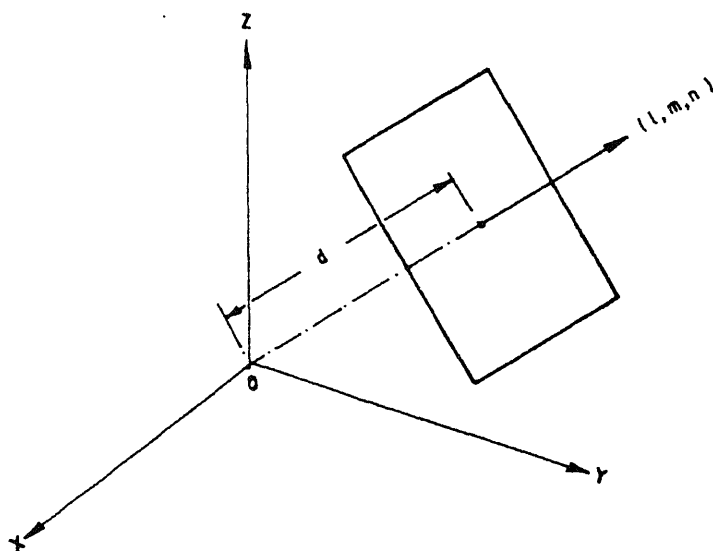


Figure 1. Direction of normal to a plane and the perpendicular distance of the plane from the origin.

origin and the standard deviation σ_d of d are given by

$$d = \frac{1}{M} \sum_{i=1}^M (\mathbf{N}_{av} \cdot \mathbf{X}_i), \quad (3)$$

$$\sigma_d^2 = \frac{1}{M} \sum_{i=1}^M (\mathbf{N}_{av} \cdot \mathbf{X}_i - d)^2. \quad (4)$$

The values of σ_N and σ_d together reflect the uncertainty of fitting a plane to the set of points.

2.2 Characterization of a sphere

Ideally, all the surface normals pass through the centre of a sphere. But in practice, owing to the presence of noise in the range data and to computational round-off errors, such a unique point cannot be determined. Rather, the majority of surface normals pass through a small neighbourhood of the centre of the sphere. So, for every pair of nonparallel normals \mathbf{N}_i and \mathbf{N}_j (refer figure 2), the position of the line perpendicular to both of them is determined (Shanti Narayan 1985). The length of the line segment intercepted between the two normal vectors also gives the shortest distance between them. The points of intersection p_i and p_j of this common perpendicular with the two normals are taken as two estimates of the centre of the sphere. The mean position of the centre \mathbf{X}_c and the standard deviation σ_x are computed from these estimates.

Once the position of the centre is found, the radius R can be estimated as

$$R = \frac{1}{M} \sum_{i=1}^M |\mathbf{X}_i - \mathbf{X}_c|. \quad (5)$$

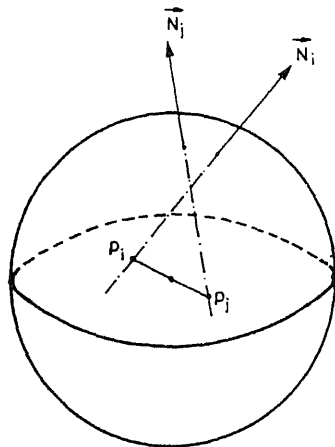


Figure 2. Estimation of the centre of a sphere.

The standard deviations of the centre σ_x and the radius σ_R together give a measure of uncertainty in fitting the sphere to the set of points.

2.3 Characterization of a cylinder

The parameters of interest in this case are the orientation and position of the axis and the radius of the cylinder. Every normal on the surface of a cylinder is perpendicular to the direction of the axis. Thus the cross-product of any two nonparallel surface normals gives an estimate of the orientation of the cylinder axis. The cross-products are calculated for all possible pairs of nonparallel surface normals. The average orientation of all these cross-products determines the candidate axis direction. Thus, $\forall i, j$ where N_i and N_j are nonparallel, the k th estimate of axis orientation is given by the vector τ_k where

$$\tau_k = (N_i \times N_j) / |N_i \times N_j|, \quad (6)$$

From these estimates the average orientation τ_{av} and the standard deviation σ_τ are computed. The position of the axis is determined by finding a point on the axis which is done in the following manner.

At each point X_i , the plane on which X_i , N_i and τ_{av} lie is determined. The intersection of two such nonparallel planes (Shanti Narayan 1985) gives an estimate of the axis position (refer figure 3). From these estimates average estimate X_{av} and standard deviation σ_x are computed.

A point to be noted is that to get an estimate of the same point on the axis in all cases, the estimates are considered for the point at which the cylinder axis intersects the $x = 0$ plane if axis is not parallel to that plane, else the $y = 0$ plane if axis is not parallel to that plane, else the $z = 0$ plane.

Once the orientation and the position of the axis are fixed, at each point X_i , the radius R_i of the cylinder (refer figure 4) can be estimated as follows.

$$R_i = |X_i - X_{av}| \sin \theta = |(X_i - X_{av}) \times \tau_{av}|, \quad (7)$$

From different estimates of R_i we compute R_{av} and σ_R .

The standard deviations of the axis orientation σ_τ , axis position σ_x and the radius σ_R together give a measure of the uncertainty of fit.

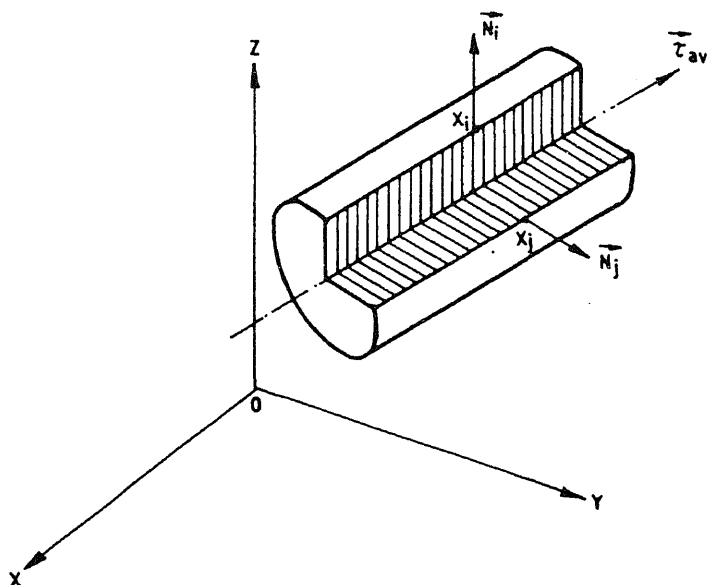


Figure 3. Estimation of the axis position of a cylinder.

2.4 Characterization of a cone

A cone is described by the position of its apex, orientation of its axis and the apex angle. Ideally the point of intersection of all tangential planes specifies the apex point.

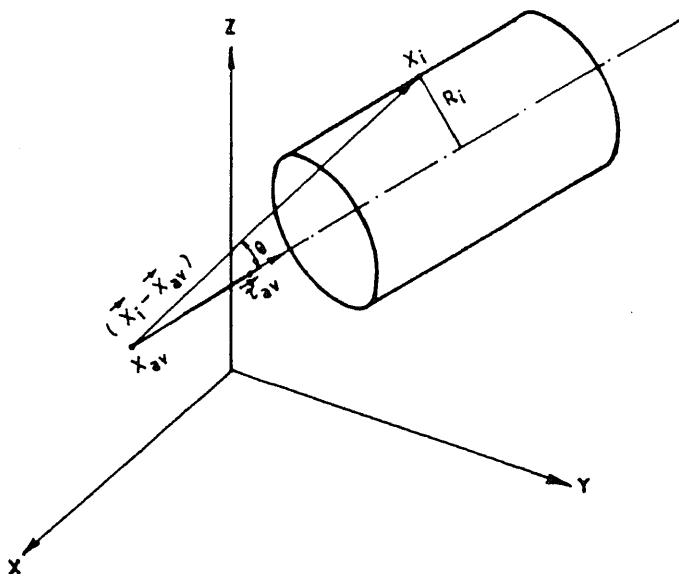


Figure 4. Estimation of the radius of a cylinder.

However in practice, such a unique point cannot be determined due to the same reasons as stated earlier. Hence, the apex is estimated in the following manner. For all points X_i with normals N_i , the equation of the plane, tangent to the surface at X_i is obtained. Taking the intersection of three such pairwise nonparallel planes (Shanti Narayan 1985) an estimate V_k of the apex is obtained. Average of all such estimates gives the mean apex position V_{av} . The uncertainty in the estimation of the position of apex is given by the standard deviation σ_v of apex.

Once the position of the apex (V_{av}) is fixed, the axis of the conical surface is estimated in the following manner. $\forall i, 1 \leq i \leq M$, the normal h_i to the plane containing the points V_{av} , X_i and N_i (normal to the surface at X_i) is determined as follows (refer figure 5).

$$h_i = (X_i - V_{av}) \times N_i. \quad (8)$$

The orientation of the axis of the cone is given by the cross product of two such nonparallel vectors h_i and h_j , where $1 \leq i, j \leq M$ and $i \neq j$. Thus $\forall i, j$, where h_i and h_j are not parallel, the k th estimate of the axis orientation is given by the vector τ_k where

$$\tau_k = (h_i \times h_j) / |h_i \times h_j|, \quad (9)$$

From these estimates the expected orientation τ_{av} and the standard deviation σ_τ are computed.

Once the apex V_{av} and the axis orientation are available, for each point X_i an estimate of the semi apex angle γ_i is obtained

$$\sin \gamma_i = |(X_i - V_{av}) \times \tau_{av}| / |(X_i - V_{av})|, \quad (10)$$

From different estimates of γ we can compute average semi apex angle γ_{av} and standard deviation σ_γ . The standard deviations of the apex, the axis and the semi apex angle together give a measure of uncertainty in fitting the conical surface to the set of points.

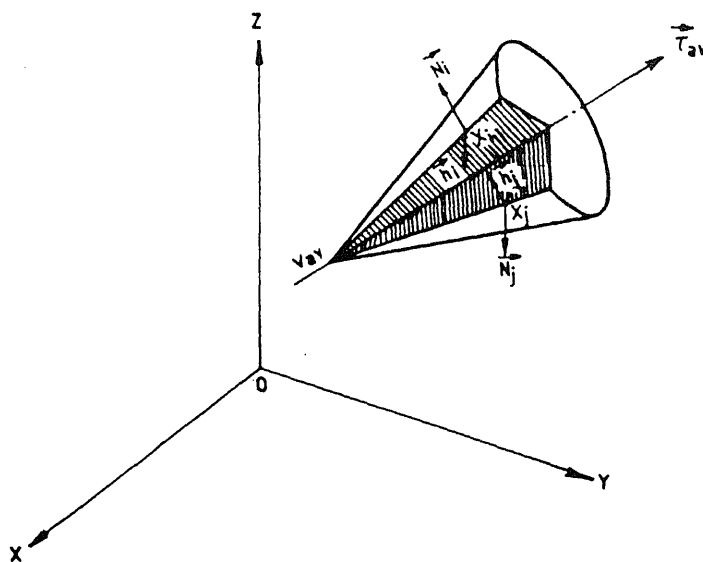


Figure 5. Estimation of the axis of a cone.

Table 1. Geometric surface fitting.**a) Plane samples.**

N normal to the plane; l, m, n direction cosines of the normal; d perpendicular distance from the origin; % error (N) = $\frac{1}{3}$ (% error(l) + % error(m) + % error(n)).

Sample	Original parameters				Estimated parameters				%Error in estimation		Standard deviation of estimates	
	l	m	n	d	l	m	n	d	N	d	N	d
PL-1	0.24	0.24	0.94	25.0	0.24	0.24	0.94	24.45	0.00	2.20	0.03	0.27
PL-2	0.45	0.45	0.77	25.0	0.45	0.45	0.77	24.66	0.00	1.36	0.02	0.22
PL-3	0.61	0.61	0.50	25.0	0.61	0.61	0.50	24.72	0.00	1.12	0.00	0.14
PL-4	0.23	0.59	0.78	16.67	0.23	0.59	0.78	16.40	0.00	1.62	0.01	0.21
PL-5	0.00	0.00	1.00	25.00	0.00	0.00	1.00	25.00	0.00	0.00	0.00	0.00

b) Sphere samples

Centre centre of the sphere; x_c, y_c, z_c coordinates of the centre; R radius of the sphere; %error(centre) = $\frac{1}{3}$ (% error(x_c) + %error(y_c) + % error(z_c)).

Sample	Original parameters				Estimated parameters				%Error in estimation		Standard deviation of estimates	
	x_c	y_c	z_c	R	x_c	y_c	z_c	R	Centre	R	Centre	R
SP-1	25.00	25.00	25.00	25.0	25.02	25.02	25.19	24.45	0.31	2.2	3.11	0.28
SP-2	25.00	25.00	25.00	30.00	24.96	24.96	26.24	30.97	1.76	3.23	7.21	0.35
SP-3	25.00	25.00	25.00	9.0	25.00	25.00	24.99	9.1	0.01	1.11	1.76	0.17
SP-4	25.00	25.00	25.00	22.0	25.04	25.04	24.22	21.82	1.14	0.82	3.02	0.24
SP-5	25.00	25.00	25.00	41.00	24.92	24.92	25.50	41.03	0.88	0.07	2.95	0.25

c) Cylinder samples.

R radius of the cylinder; l, m, n direction cosines of the axis of the cylinder; x, y, z a point on the axis; % error (axis) = $\frac{1}{3}$ (% error(l) + % error(m) + % error(n)); % error(point) = $\frac{1}{3}$ (% error(x) + % error(y) + % error(z)).

Sample	Original parameters							Estimated parameters							%Error in estimation			Standard deviation of estimates		
	<i>l</i>	<i>m</i>	<i>n</i>	<i>x</i>	<i>y</i>	<i>z</i>	<i>R</i>	<i>l</i>	<i>m</i>	<i>n</i>	<i>x</i>	<i>y</i>	<i>z</i>	<i>R</i>	Axis	Point	<i>R</i>	Axis	Point	<i>R</i>
CL-1	0.71	0.71	0	0	6	13	15	0.71	0.71	0	0	6.49	17.67	14.63	0	14.69	2.45	0.00	10.57	0.72
CL-2	0.66	0.66	0.34	0	6	10.94	30	0.69	0.64	0.33	0	6.94	10.63	29.02	2.5	9.3	3.3	0.30	45.98	0.39
CL-3	0.54	0.54	0.64	0	6	8.25	9	0.57	0.52	0.63	0	7.68	9.66	9.30	3.6	22.5	3.3	0.33	62.01	0.39
CL-4	0.35	0.35	0.87	0	6	3.20	22	0.37	0.34	0.86	0	6.54	2.81	21.47	3.2	10.6	2.4	0.25	48.59	0.42
CL-5	0.12	0.12	0.98	0	6	-19.08	41	0.13	0.12	0.98	0	5.42	-26.40	40.12	2.8	24.0	2.1	0.18	96.45	0.19

d) Cone samples.

θ semi apex angle of cone; l, m, n direction cosines of the axis of the cone; x_v, y_v, z_v apex of the cone; % error(axis) = $\frac{1}{3}$ (% error(l) + % error(m) + % error(n)); % error(apex) = $\frac{1}{3}$ (% error(x_v) + % error(y_v) + % error(z_v)).

Sample	Original parameters							Estimated parameters							%Error in estimation		Standard deviation of estimates			
	l	m	n	x _v	y _v	z _v	θ	l	m	n	x _v	y _e	z _v	θ	%Error in estimation		Standard deviation of estimates			
															Axis	Apex	θ	Axis	Apex	θ
CN-1	0	1	0	4	10	13	30°	-0.09	0.97	0.20	5.74	9.94	13.74	28.71°	11.5	16.60	4.28	0.42	66.67	3.56
CN-2	0	0.34	0.94	4	10	13	20°	0.00	0.35	0.94	4.08	10.34	13.43	20.3°	1.5	2.90	1.5	0.12	20.41	0.36
CN-3	0	0.94	0.34	4	10	13	30°	-0.04	0.93	0.35	3.96	9.02	13.28	22.39°	2.0	3.8	11.9	0.31	24.37	0.95
CN-4	0	0.77	0.64	4	10	13	30°	0.01	0.71	0.7	4.06	13.31	13.16	34°	8.6	11.9	13.3	0.36	20.46	1.74
CN-5	0	0	1	4	10	13	40°	0.09	0.06	0.95	6.4	11.43	10.11	46.45°	3.5	32.18	16.1	0.24	43.88	5.33

2.5 Experimental results

Experimental results on synthetic range images of size 50×50 are presented. To reduce the amount of computation, surface normals are computed at some sample points, distributed uniformly over the surface patch. At each sample point, surface normal is estimated by fitting a plane to a 5×5 neighbourhood of the point, using least square error method. A set of five images from each of the classes plane, sphere, cylinder and cone are considered. For each sample the corresponding surface is fitted geometrically. The results obtained are tabulated in table 1.

It is observed from table 1 that the percentage of errors in the estimated parameter values are quite low for plane and sphere fitting ($< 3.5\%$). For the cylinder samples the percentage errors in the estimations of axis orientation are low ($< 3.6\%$) and also in the estimations of radius ($< 3.3\%$). Estimation of a point on the axis has given a large error in most cases (10.6–24%). This is due to the fact that even a slight error in estimating the axis orientation can significantly change the estimated point position. In the case of cone samples, the error in estimation of axis orientation is quite low (1.5–11.5%). Angle estimation also has low percentage error (1.5–16.1%). The error in estimation of apex position has shown wide variation (2.9% to 32.2%). From the results on synthetic range images it can be said that errors in an orientation estimation (e.g., axis, normal) or a distance estimation (e.g., radius) have been less as compared to estimation of a point position (e.g., apex, centre).

3. Fuzzy characterization of surfaces

In the previous section on geometric surface fitting it has been shown how an appropriate surface may be fitted when the input image is of planar, spherical, cylindrical or conical types. The implicit assumption has been that *a priori* information regarding the surface nature is available. But even in the absence of *a priori* information the geometric surface fitting proves to be useful. In such cases all four surfaces are fitted to the set of points and in each case the uncertainties, as given by the standard deviations of the parameters, are noted. These measures of uncertainty in parameter estimation are used to classify the surface as a planar or spherical or cylindrical or conical surface. The details of the method involved are discussed in this section.

The simplest strategy to design the classifier is to assign the input image to that class whose parameters have been estimated with the least amount of uncertainty. However, the solution is not so straightforward because parameters for different types of surfaces are obtained with different methods of estimation. Also the numbers of parameters for different types of surfaces are different. This has led to the development of a fuzzy classifier, where two thresholds are set for the standard deviation of each parameter of a particular surface. The lower threshold denotes the maximum uncertainty expected when the surface patch in the input image is of the same type as the surface fitted. The upper threshold denotes the least amount of uncertainty expected when the input is from any class other than that of the surface fitted. The input is assigned a membership to the class by comparing the standard deviation values obtained for a parameter of the fitted surface with the corresponding thresholds. Fuzziness in the classification is introduced by grading the membership if a standard deviation value falls between the two thresholds. Finally, the membership values obtained with each parameter of a fitted surface type are

combined to get an overall membership. This procedure is repeated for each of the four surface types namely, planar, spherical, cylindrical and conical surfaces. The result is a membership vector giving the membership of the input surface with respect to the four different classes. The vector itself can be taken as the characterization of the surface. Alternatively, the sample is classified into the class with the maximum membership value (the dominant class) and characterized by the corresponding parameters. Designing the classifier involves finding the thresholds, the details of which are discussed below.

3.1 Classifier design

A set of images, henceforth referred to as training images or samples, are taken from each of the four classes. All four surfaces are fitted geometrically to each of the samples. In each case the parameters and their standard deviations are noted. The fact that for any particular type of fitted surface, samples from the same class should yield lower standard deviation values as compared to samples from other classes, is used to obtain the lower thresholds. If θ is a parameter of a class denoted by class(θ), then the lower threshold for θ is defined as

$$lo_{\theta} = \text{mean}(\sigma_{\theta_i}) + \text{standard deviation}(\sigma_{\theta_i}), \quad (11)$$

where

$$\begin{aligned} i &= 1 \dots M \text{ is the set of sample images from class}(\theta), \\ \theta_i &= \text{value of parameter } \theta \text{ for the } i\text{th sample,} \\ \sigma_{\theta_i} &= \text{standard deviation in estimating } \theta_i. \end{aligned}$$

The upper threshold for parameter θ can be set by considering the standard deviations obtained with sample images from all classes other than class(θ). Thus the upper threshold is defined as

$$hi_{\theta} = \min(\sigma_{\theta_k}), \quad (12)$$

for all k , where $k = 1 \dots N$ is the set of samples not belonging to class(θ) and $\sigma_{\theta_k} > lo_{\theta}$.

The value of lo_{θ} has been selected considering the distribution of standard deviation values of the samples from the same class as that of the surface fitted. The value of hi_{θ} has been selected in order to reduce the misclassification of samples from other classes into the class of the surface fitted.

The membership function for class(θ) with respect to the parameter θ can be defined as μ_{θ} where

$$\begin{aligned} \mu_{\theta} &= 1, & \text{if } \sigma_{\theta} \leq lo_{\theta}, \\ \mu_{\theta} &= (hi_{\theta} - \sigma_{\theta}) / (hi_{\theta} - lo_{\theta}), & \text{if } lo_{\theta} \leq \sigma_{\theta} \leq hi_{\theta}, \\ \mu_{\theta} &= 0, & \text{if } hi_{\theta} \leq \sigma_{\theta}. \end{aligned} \quad (13)$$

The membership function μ_{θ} is graphically shown in figure 6.

Overall membership of a sample in a class can now be defined in terms of the membership with respect to individual parameters of the class. For a class ω if $\theta^d, d = 1 \dots D_{\omega}$ are the parameters which characterize the class, the overall class membership μ_{ω} for a sample is given by

$$\mu_{\omega} = (1/D_{\omega}) \sum_{d=1}^{D_{\omega}} \mu_{\theta^d},$$

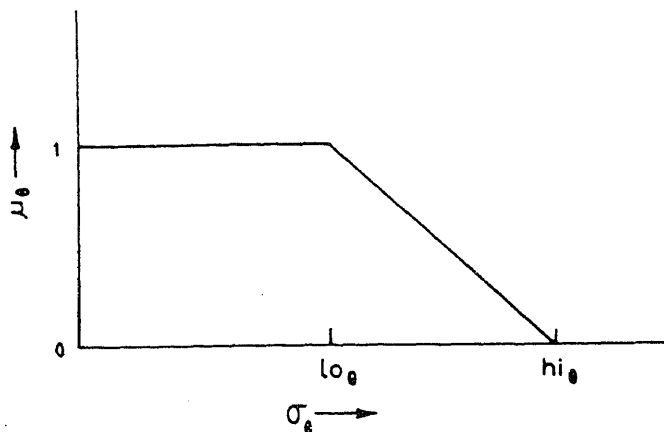


Figure 6. Fuzzy membership function (μ_θ).

where the class ω represents one of {plane, sphere, cylinder, cone} and μ_{θ^d} is the membership obtained for parameter θ^d as per (13).

3.2 Experimental results and discussions

To design the classifier five training samples from each of the four classes are taken. The standard deviations of different parameters obtained when all the four surfaces are fitted to each training sample are listed in table 2. The lower and upper thresholds for each parameter are tabulated in table 3.

Once the classifier is designed, classification results for other images from the four classes (henceforth referred to as test samples) are presented. For each test sample all the four surfaces were fitted and the standard deviations of the various parameters were noted. From the standard deviations, the membership values with respect to the different classes were derived using the corresponding membership functions ((30) and (31)). The results are tabulated in table 4. The table also shows the dominant class displayed by each of these test samples. It may be seen that only one sample out of 20 has been misclassified. Another point of interest is the nature of the membership vectors for test samples from various classes. Some planar test samples have shown conical behaviour as well (although not dominant). When a cone is to be fitted to a surface, each apex estimate is formed from three tangential planes where the line of intersection of two planes is not parallel to the third. Ideally, for a planar surface, all surface normals are parallel. Hence, fitting a cone fails at the stage of finding the apex itself, since no suitable combinations of three pairwise nonparallel tangential planes can be found. This conical behaviour is seen only in cases where the effects of quantization noise in the input image are so severe that it has been possible to find combinations of three normals to find apex estimates. In all these cases the semi apex angle is close to 90° and axis of the cone is normal to the plane. Thus conical behaviour exhibited by the planar samples is acceptable since any plane can be considered as a cone with semi apex angle of 90° . Sphere samples also have exhibited conical behaviour. Sphere samples actually represent the visible portion of a sphere which may be a hemisphere or a part of it. In all

Table 2. Standard deviations of the parameters obtained when all the four surface types are fitted to the training samples.**a) Planar training samples**

Unable to fit surface; plane: σ_N s.d. of the normal direction, σ_d s.d. of perpendicular distance from origin; sphere: σ_X s.d. of the centre, σ_R s.d. of the radius; cylinder: σ_t s.d. of axis orientation, σ_x s.d. of a point on the axis, σ_R s.d. of the radius; cone: σ_v s.d. of the apex, σ_t s.d. of the axis orientation, σ_θ s.d. of the semi apex angle.

Sample	Type of surface fitted									
	Plane		Sphere		Cylinder			Cone		
	σ_N	σ_d	σ_X	σ_R	σ_t	σ_x	σ_R	σ_v	σ_t	σ_θ
PL-1	0.00	0.00	—	—	—	—	—	—	—	—
PL-2	0.02	0.27	406.42	6.98	0.54	1248.51	8.32	—	—	—
PL-3	0.01	0.22	—	—	0.40	642.61	3.74	—	—	—
PL-4	0.00	0.14	—	—	0.44	826.92	4.62	—	—	—
PL-5	0.01	0.22	—	—	0.81	653.74	3.89	81.42	0.98	0.92

b) Spherical training samples.

Unable to fit surface; plane: σ_N s.d. of the normal direction, σ_d s.d. of perpendicular distance from origin; sphere: σ_X s.d. of the centre, σ_R s.d. of the radius; cylinder: σ_t s.d. of axis orientation, σ_x s.d. of a point on the axis, σ_R s.d. of the radius; cone: σ_v s.d. of the apex, σ_t s.d. of the axis orientation, σ_θ s.d. of the semi apex angle.

Sample	Type of surface fitted									
	Plane		Sphere		Cylinder			Cone		
	σ_N	σ_d	σ_X	σ_R	σ_t	σ_x	σ_R	σ_v	σ_t	σ_θ
SP-1	0.74	3.78	3.11	0.28	0.84	494.2	2.27	64.87	0.72	0.41
SP-2	0.67	5.77	7.21	0.35	0.81	227.1	3.38	126.77	0.78	0.73
SP-3	0.78	2.89	1.76	0.17	0.85	197.8	1.90	98.39	0.76	0.68
SP-4	0.73	4.77	3.02	0.20	0.83	522.2	3.08	95.25	0.74	0.4
SP-5	0.49	3.42	2.95	0.25	0.79	301.0	2.40	86.12	0.97	0.44

c) Cylinder training samples.

Unable to fit surface; plane: σ_N s.d. of the normal direction, σ_d s.d. of perpendicular distance from origin; sphere: σ_X s.d. of the centre, σ_R s.d. of the radius; cylinder: σ_t s.d. of axis orientation, σ_x s.d. of a point on the axis, σ_R s.d. of the radius; cone: σ_v s.d. of the apex, σ_t s.d. of the axis orientation, σ_θ s.d. of the semi apex angle.

Sample	Type of surface fitted									
	Plane		Sphere		Cylinder			Cone		
	σ_N	σ_d	σ_X	σ_R	σ_t	σ_x	σ_R	σ_v	σ_t	σ_θ
CL-1	0.57	3.27	19.20	5.14	0.00	10.57	0.72	—	—	—
CL-2	0.44	3.97	39.51	3.56	0.30	45.98	0.30	295.45	0.46	0.98
CL-3	0.59	2.16	56.66	9.02	0.33	62.00	0.58	129.59	0.80	0.37
CL-4	0.57	5.01	55.09	12.37	0.25	48.59	0.41	463.24	0.77	0.30
CL-5	0.36	3.57	85.91	39.63	0.18	96.45	0.19	629.80	0.82	0.38

Table 2. (Continued)

d) Conical training samples.

Unable to fit surface; plane: σ_N s.d. of the normal direction, σ_d s.d. of perpendicular distance from origin; sphere: σ_X s.d. of the centre, σ_R s.d. of the radius; cylinder: σ_τ s.d. of axis orientation, σ_X s.d. of a point on the axis, σ_R s.d. of the radius; cone: σ_V s.d. of the apex, σ_τ s.d. of the axis orientation, σ_θ s.d. of the semi apex angle.

Sample	Type of surface fitted									
	Plane		Sphere		Cylinder			Cone		
	σ_N	σ_d	σ_X	σ_R	σ_τ	σ_X	σ_R	σ_V	σ_τ	σ_θ
CN-1	0.30	9.5	66.42	3.15	0.64	158.34	1.24	66.67	0.42	0.06
CN-2	0.74	3.1	45.31	94.11	0.44	164.12	21.73	20.41	0.12	0.01
CN-3	0.43	2.15	32.8	18.84	0.73	330.0	4.21	24.37	0.31	0.02
CN-4	0.50	3.29	35.30	2.86	0.63	784.8	7.93	20.46	0.36	0.03
CN-5	0.48	3.64	47.79	4.57	0.74	105.29	2.47	43.88	0.24	0.09

these cases, the axis of the fitted cone is perpendicular to the plane of the image, i.e., along the z-axis. The standard deviations of the apex and the axis are low enough to fall below the corresponding lower threshold. These two parameters thus contribute a membership value of 1 each. The third parameter, the apex angle, has given a high standard deviation above the higher threshold. Thus contribution of this parameter to overall membership function is 0. Thus an overall membership of 0.67 has resulted for these samples when a cone is fitted. The 0.33 membership with respect to cylindrical classes shown by sphere samples can be explained similarly. The point estimate has given a low standard deviation below the lower threshold in all the cases while the other two parameters have crossed the higher threshold. Cylinder samples have shown no other behaviour significantly apart from cylindrical behaviour. Two cone samples have shown some amount of planar behaviour out of which one cone sample has been misclassified as planar because in that case value of the semiapex angle was very high.

Table 3. Lower and upper thresholds of different parameters for different surface classes

PL = planar surface; SP = spherical surface; CL = cylindrical surface; CN = conical surface.

Surface type	Parameters	Lower threshold	Upper threshold
PL	Normal N	0.015	0.30
	Distance d	0.28	2.15
SP	Centre X_c	5.48	19.2
	Radius R	0.31	2.86
	Axis τ	0.33	0.40
CL	Point X	80.42	105.29
	Radius R	0.63	1.24
	Apex V	53.15	64.87
CN	Axis τ	0.39	0.46
	Angle θ	0.07	0.30

Table 4. Fuzzy classification of plane, sphere, cylinder and cone samples.

Sample	Membership vector				Dominant class	Correctly classified (Y/N)
	PL	SP	CL	CN		
PL-6	0.93	0.06	0.00	0.67	PL	Y
PL-7	1.00	0.00	0.00	0.67	PL	Y
PL-8	0.98	0.38	0.00	0.88	PL	Y
PL-9	0.94	0.00	0.00	0.67	PL	Y
PL-10	1.00	0.00	0.00	0.00	PL	Y
SP-6	0.00	1.00	0.33	0.67	SP	Y
SP-7	0.00	1.00	0.33	0.67	SP	Y
SP-8	0.00	1.00	0.33	0.67	SP	Y
SP-9	0.00	1.00	0.33	0.67	SP	Y
SP-10	0.10	1.00	0.33	0.67	SP	Y
CL-6	0.00	0.00	1.00	0.00	CL	Y
CL-7	0.00	0.00	1.00	0.00	CL	Y
CL-8	0.07	0.00	1.00	0.30	CL	Y
CL-9	0.00	0.00	1.00	0.00	CL	Y
CL-10	0.00	0.00	0.54	0.22	CL	Y
CN-6	0.00	0.00	0.03	0.33	CN	Y
CN-7	0.00	0.00	0.00	0.52	CN	Y
CN-8	0.00	0.09	0.00	0.41	CN	Y
CN-9	0.53	0.00	0.00	1.00	CN	Y
CN-10	0.59	0.00	0.00	0.22	PL	N

Abbreviations as in table 3

Classification results for general quadratic surfaces not belonging to any of the four classes, plane, sphere, cylinder and cone, are also presented. The aim is to see if a general pattern of membership vectors is derivable for a set of samples from the same quadratic class. This may be useful in characterising that quadratic class. The results of this experimentation are given in table 5. The classification based on the dominant class behaviour is also indicated in the table. It is interesting to note that samples from the same quadratic class show the same dominant class behaviour. For example cylindrical behaviour is predominantly shown by samples from elliptical and hyperbolic cylinder classes, while ellipsoids are predominantly spherical, hyperboloids are predominantly conical.

4. Occluded surface characterization

In a range image with more than one object, usually some objects may be partially occluded by the others. This makes the problem of understanding range images more difficult since certain regions in the image representing surfaces of objects may be missing or partially occluded. Since due to occlusion the object surfaces are partially visible, local surface properties should be used to characterize them. The geometric method for surface characterization, discussed in §2, obtains descriptions through surface normal analysis. Since the normal to a surface is the local property of the surface at the point with respect to the point

Table 5. Fuzzy classification of general quadric surface samples.

Surface type	Sample	Membership vector				Dominant class
		PL	SP	CL	CN	
Elliptic cylinder	1	0.00	0.19	0.67	0.00	CL
	2	0.40	0.00	1.00	0.33	CL
	3	0.00	0.19	0.67	0.00	CL
	4	0.43	0.15	1.00	0.00	CL
	5	0.00	0.00	0.33	0.00	CL
Hyperbolic cylinder	1	0.00	0.00	0.33	0.00	CL
	2	0.07	0.28	1.00	0.00	CL
	3	0.00	0.00	0.67	0.00	CL
	4	0.00	0.09	0.78	0.00	CL
	5	0.00	0.00	0.33	0.00	CL
Ellipsoid	1	0.00	0.40	0.33	0.33	SP
	2	0.00	0.53	0.33	0.25	SP
	3	0.11	0.93	0.33	0.33	SP
	4	0.16	0.93	0.33	0.36	SP
	5	0.22	0.99	0.46	0.67	SP
Elliptic cone	1	0.00	0.00	0.00	1.00	CN
	2	0.27	0.55	0.00	1.00	CN
	3	0.00	0.00	0.11	1.00	CN
	4	0.00	0.00	0.00	0.67	CN
	5	0.00	0.00	0.00	0.33	CN
Hyperboloid	1	0.00	0.00	0.00	0.33	CN
	2	0.00	0.00	0.00	0.33	CN
	3	0.00	0.00	0.00	0.33	CN
	4	0.00	0.00	0.31	0.33	CN
	5	0.00	0.00	0.00	0.33	CN
Hyperbolic paraboloid	1	0.00	0.00	0.00	0.33	CN
	2	0.00	0.00	0.00	0.27	CN
	3	0.00	0.00	0.00	0.33	CN
	4	0.00	0.00	0.00	0.33	CN
	5	0.00	0.00	0.00	0.33	CN

Abbreviations as in table 3

the geometric method also forms a reliable tool for characterizing partially visible surfaces.

The shape of a surface (i.e., planar, spherical, cylindrical or conical) is uniquely determined by the global parameters of the surface. For example, a spherical surface is uniquely characterized by its centre and radius. The geometric method estimates the global surface parameters from the locally calculated surface normals. Since the estimation of global parameters at different regions of a surface should be very close to each other, it is also possible to determine if two or more partially visible surface patches are parts of the same surface. This is achieved in the following manner.

Let a surface class ω , $\omega \in \{\text{plane, sphere, cylindrical, cone}\}$, be characterized by a set of parameters $\{\theta^d | 1 \leq d \leq D_\omega\}$, where D_ω is constant whose value is different for different surface classes. This set of parameters defines a D_ω -dimensional space, henceforth referred to as parameter space, such that the mean values of the parameters θ_i^d describing a surface S_i of class ω represent a point p_i in the parameter space. Because

of the uncertainty in the measurement of θ_i^d , different estimates of θ_i^d may occur anywhere in the region $(\theta_i^d - hi_{\theta_i^d}^d)$ to $(\theta_i^d + hi_{\theta_i^d}^d)$ where $hi_{\theta_i^d}^d$ is the upper threshold used in the fuzzy classifier and is given in (29). Thus different estimates of the point p_i may occur anywhere within a hyper rectangular parallelepiped bounded within the region $[\theta_i^d - hi_{\theta_i^d}^d, \theta_i^d + hi_{\theta_i^d}^d]$ for $1 \leq d \leq D_\omega$. This region is referred to as region of occurrence of S_i . Let this region for surface S_i be denoted by R_i . Now two partially visible surface patches S_i and S_j , both of same surface type ω , are assumed to be possible parts of the same surface if $R_i \cap R_j \neq \phi$. If this condition is satisfied then surfaces are fitted over the region $S_i \cup S_j$. If the fitted surface also shows a dominant class ω then S_i and S_j are identified as parts of the same surface and the parameters of the fitted surface are extracted. If the fitted surface shows a dominant class other than ω then S_i and S_j are identified as different surfaces.

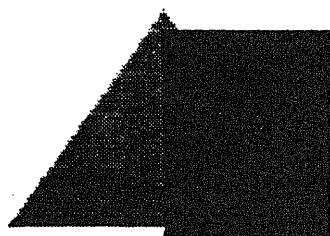
4.1 Experimental results

Experimental results on six synthetic range images, each containing occluded surfaces, are presented. All the synthetic images are of size 128×128 and are shown in figures 7a–7f. These images are referred to as image-1, image-2, image-3, image-4, image-5 and image-6 respectively. Boundaries of the surface patches in these images are shown in figures 8a–f respectively, where each surface region is marked with an integer. Each of these images contain one or more occluded surface patches. The fuzzy classification results are shown in table 6. The table shows the original class and the original parameters of the surfaces, the dominant class of the fitted surfaces and the estimated parameters when surfaces of respective dominant classes are fitted.

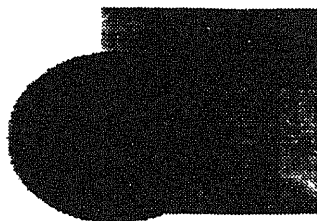
From table 6 it is seen that the occluded surfaces, i.e., the cone in image-1 (figure 7a), the cylinder in image-2 (figure 7b) and the sphere in image-3 (figure 7c), are correctly classified and the estimated parameters of the fitted surfaces closely approximate the original parameters. Image-4 (figure 7d) contains two partially visible hemispherical surfaces (surface patches 2 and 4 in figure 8d), one with radius 55 and the other with radius 30. Both of them have the same centre (63, 63, 150). Both these hemispherical surfaces are correctly classified and parametrized individually. But since the region of occurrence of one hemisphere does not intersect that of the other, they are not considered as part of a single surface. Whereas in image-5 (figure 7e), though the regions of occurrence of two partially occluded hemispheres (surface 2 with radius 50 and surface 4 with radius 55 in figure 8e) intersect, the combined surface shows conical behaviour though individually they are dominantly spherical. Hence they also cannot comprise a single surface. Two partially visible conical surface patches (2 and 4 in figure 8f) in image-6 (figure 7f) together construct a single conical surface whose estimated parameters closely approximate the estimated parameters of the individual surfaces and also those of the original surface. The cylindrical surfaces in all these three images are correctly classified and parametrized.

5. Conclusion

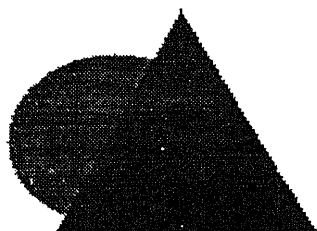
In this paper various geometric methods for surface fitting and surface characterization have been considered. Geometric surface fitting techniques give best results when the input is from the restricted domain of plane, sphere, cylinder and cone. The problem



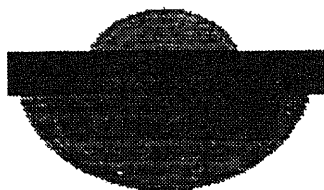
(a)



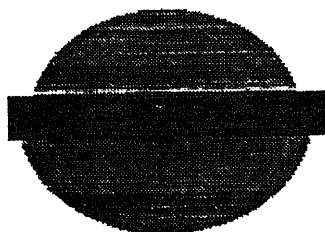
(b)



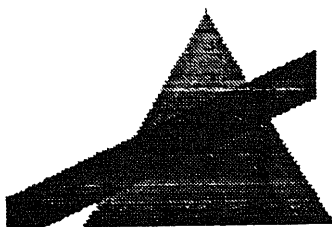
(c)



(d)



(e)

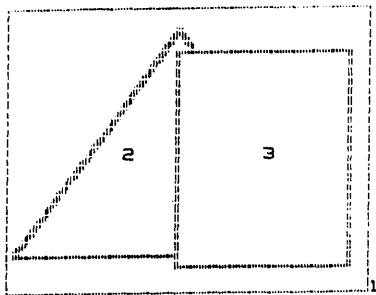


(f)

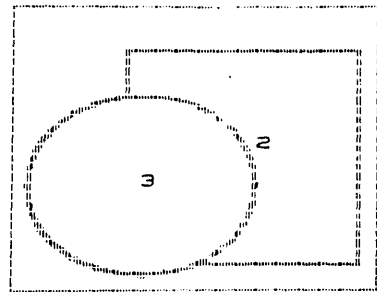
Figure 7. Synthetic range images containing occluded surfaces: (a) Image-1, (b) image-2, (c) image-3, (d) image-4, (e) image-5, and (f) image-6.

has been attempted for two different situations. In the first case, it has been assumed that *a priori* knowledge about the shape of the surface is available. In such situations, a surface of the proper type is fitted to the set of points representing the surface patch and the parameters of the fitted surface are extracted. This strategy of selective surface fitting reduces the amount of computation.

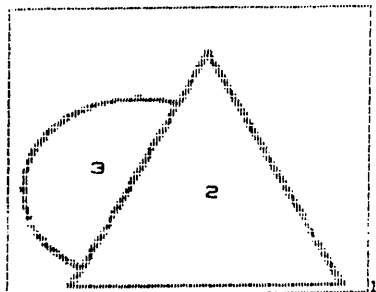
In the second case, when no *a priori* information regarding the shape of the unknown surface is available, the characterization of the surface is obtained in the form of a fuzzy membership vector. The unknown surface is taken as belonging to the class with maximum membership value. In this case the burden of fitting all four classes of surfaces cannot be avoided. The design of the fuzzy classifier plays a crucial role in determining the performance of the system. The performance of the classification scheme depends upon how correctly it can classify unknown surfaces. Thus the choice



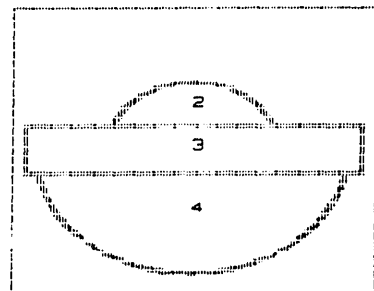
(a)



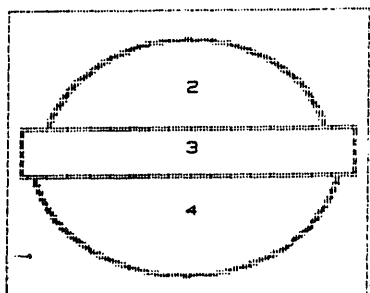
(b)



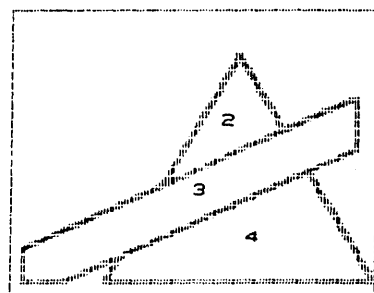
(c)



(d)



(e)



(f)

Figure 8. Boundaries of surface patches in synthetic range images: (a) Image-1, (b) image-2, (c) image-3, (d) image-4, (e) image-5, and (f) image-6.

of training samples to design the classifier is also very important. Experiments on partially visible surfaces indicate that the geometric method with the fuzzy classification scheme forms a reliable tool for

Table 6. Fuzzy classification of synthetic range images containing occluded surface patches.

Image no.	Surface no. and type	Original parameters	Membership vector				Dominant Class	Estimated parameters
			PL	SP	CL	CN		
1	2 CN	Apex 60, 10, 120 Axis $l = 0, m = 1, n = 0$ Semi apex angle 30°	0.32	0	0	0.67	CN	Apex 46.8, 49.6, 107.1 Axis $l = 0.3, m = 0.8, n = 0.4$ Semi apex angle 35.2°
	3 CL	Axis $l = 0, m = 1, n = 0$ Axis point 90, 0, 60 Radius 30	0	0	1	0	CL	Axis $l = 0, m = 1, n = 0$ Axis point 90.7, 0, 58.9 Radius 29.4
2	2 CL	Axis $l = 0, m = 1, n = 0$ Axis point 80, 0, 150 Radius 40	0	0	1	0.33	CL	Axis $l = 0, m = 1, n = 0$ Axis point 79, 0, 146 Radius 37.9
	3 SP	Centre 45, 80, 110 Radius 40	0.3	0.9	0.3	0	SP	Centre 45.25, 80.26, 107.27 Radius 38.43
3	2 CN	Apex 70, 20, 100 Axis $l = 0, m = 1, n = 0$ Semi apex angle 25°	0	0	0	0.52	CN	Apex 64.8, 38.9, 95.4 Axis $l = 0, m = 0.9, n = 0.1$ Semi apex angle 38.6°
	3 SP	Centre 45, 80, 150 Radius 40	0	1	0.33	0.67	SP	Centre 45.2, 80, 149.7 Radius 40.26
4	2 SP	Centre 63, 63, 150 Radius 30	0	1	0.3	0.7	SP	Centre 62.8, 63.7, 149.4 Radius 30.4
	3 CL	Axis $l = 1, m = 0, n = 0$ Axis point 0, 63, 90 Radius 10	0	0	1	0	CL	Axis $l = 1, m = 0, n = 0$ Axis point 0, 62.5, 91.6 Radius 10.5
	4 SP	Centre 63, 63, 150 Radius 55	0	1	0.3	0.3	SP	Centre 63.2, 62.9, 149.5 Radius 55

2 SP	Centre 63, 63, 150 Radius 50	0	1	0.3	0.3	0.3	SP	Centre 63.2, 62.8, 150 Radius 50
4 SP	Centre 63, 63, 150 Radius 55	0	1	0.3	0.3	0.3	SP	Centre 63.2, 62.9, 149.5 Radius 55
4 SP	Apex 80, 20, 150 Axis $l = 0, m = 1, n = 0$	0	0.5	0.3	0.7	0.7	CN	Apex 78, 27.7, 146.6 Axis $l = 0.1, m = 0.9, n = 0.2$
2 CN	Semi apex angle 30° Apex 80, 20, 150 Axis $l = 0, m = 1, n = 0$	0	0	0	0.33	0.33	CN	Semi apex angle 34.6° Apex 81.9, 39.2, 141.9 Axis $l = 0, m = 0.9, n = 0.1$
4 CN	Semi apex angle 30° Apex 80, 20, 150 Axis $l = 0, m = 1, n = 0$	0	0.2	0.3	0.7	0.7	CN	Semi apex angle 37.4° Apex 80.75, 34.7, 143.6 Axis $l = 0, m = 0.9, n = 0.1$
4 CN	Semi apex angle 30° Axis $l = -0.8, m = -0.5, n = 0$	0	0	0	0.62	0.62	CN	Semi apex angle 35.8° Axis $l = -0.8, m = -0.4, n = 0$
3 CL	Axis point 0, 120, 100 Radius 10	0	0	1	0.3	0.3	CL	Axis point 0, 118.2, 100.1 Radius 10.5

The authors are grateful to one of the reviewers for his/her valuable comments on an earlier version of this paper.

References

- Besl P J, Jain R C 1984 Surface characterization for three dimensional object recognition. RSD-TR-20-84, Electrical Eng. and Computer Science Dept. University of Michigan, Ann Arbor, Michigan
- Besl P J, Jain R C 1988 Segmentation through variable order surface fitting. *IEEE Trans. Pattern Anal. Mach. Intell.* 10: 167–192
- Biswas P K, Mukherjee J, Chatterji B N 1990 Segmentation of range images. *Proc. Workshop on Signal Processing, Communications and Networking*, Indian Inst. Sci., Bangalore, 123–130
- Bolle R M, Cooper D B 1984 Bayesian recognition of local 3-D shape by approximating image intensity functions with quadric polynomials. *IEEE Trans. Pattern Anal. Mach. Intell.* 6: 418–429
- Brady M, Ponce J, Yuille A, Asada H 1985 Describing surfaces. *Comput. Vision Graph. Image Process.* 32: 1–28
- Faugeras O D 1984 New steps toward a flexible 3-D vision system for robotics. *Int. Conf. on Pattern Recognition* 2: 796–805
- Han J H, Volz R A, Mudge T H 1987 Range image segmentation and surface parameter extraction for 3-D object recognition of industrial parts. *Proc. IEEE Int. Conf. on Robotics and Automation* 1: 380–386
- Lin X, Wee W G 1985 Shape detection using range data. *IEEE Int. Conf. on Robotics and Automation* pp. 34–39
- Muller Y, Mohr R 1984 Planes and quadrics detection using Hough transform. *7th Int. Conf. on Pattern Recognition* pp 1101–1103
- Shanti Narayan 1985 *Analytical solid geometry* (New Delhi: S Chand)
- Taylor R W, Savini M, Reeves A P 1989 Fast segmentation of range imagery into planar regions. *Comput. Vision Graph. Image Process.* 45: 42–60

High-temperature effects in hypersonic flows

DINESH K PRABHU

Computational and Theoretical Fluid Dynamics Division, National Aerospace Laboratories, Bangalore 560 017, India

MS received 31 August 1994; revised 21 January 1995

Abstract. The hypersonic ($M = 25$) flow past a 10° right circular cone at 0° angle of attack has been computed using an implicit, noniterative, finite-difference scheme for the Parabolized Navier–Stokes (PNS) equations. Three different gas models have been considered in the study – (1) ideal gas ($\gamma = \text{constant}$), (2) equilibrium air, and (3) five species (N_2 , O_2 , NO , N , O) chemical nonequilibrium air. For the nonequilibrium air case, three different models have been considered – (a) one in which the constituent species have no internal structure (i.e., species are ideal gases), (b) one in which the constituent species have internal structure (i.e., species are thermally perfect gases), and (c) one in which the species have internal structure and their thermodynamic properties have been obtained from quantum mechanical and spectroscopic calculations.

Keywords. Hypersonic flows; chemical equilibrium/nonequilibrium flows; planar/axisymmetric flows; finite-difference formulation.

1. Introduction

Research in the area of hypersonic aerothermodynamics in India has received a great impetus from the success of the Agni re-entry vehicle (especially from the point of designing its heat shield). In addition to the Agni programme, there are also plans for a one-stage-to-orbit Hyperplane whose design will require the integration of the aerothermodynamic and propulsive (supersonic combustion of H_2 and air) aspects of flight. The development, design and testing of such vehicles and perhaps future space vehicles will require ground-based experimental facilities capable of simulating the extreme conditions normally encountered at hypersonic speeds. Ground-based test facilities are expensive from an operational point of view and the ones currently available in India are inadequate. This handicap can be overcome to a large extent through the use of high-speed digital computers that are widely available today.

It is conventional to classify any flow whose Mach number exceeds 5 as hypersonic flow. However, this is merely a rule of thumb and is insufficient (Anderson 1989). Hypersonic flow is markedly different from the usual supersonic flow. For instance, the

elevated temperatures (due to high enthalpies) in the hypersonic viscous shock layer result in the occurrence of several complex physical phenomena such as vibrational relaxation, chemical reactions, ionisation, radiation, etc. which are not present in conventional supersonic flows. These phenomena are generally termed as "real-gas effects" ("high-temperature effects" is a more appropriate term) and are usually rate processes (mostly due to atomic, molecular, electronic or photonic collisions) which could be either fast or slow compared to the characteristic flow time. On the one hand, if the rate processes are infinitely fast, especially in the denser reaches of the atmosphere, then one has a local thermodynamic equilibrium situation. For this case, the local thermodynamic state is defined uniquely by any two-state variables such as the internal energy and density (two commonly used dependent variables in CFD). The usual Navier-Stokes equations expressing the conservation of mass, linear momentum, and energy with suitable modifications to the equation of state are enough to model the flow. On the other hand, if the rate processes occur at finite rates, especially in the rarer reaches of the atmosphere, then one has a nonequilibrium situation. For this case, apart from the usual Navier-Stokes equations, one must consider the equations governing the rate processes (Anderson 1989; Park 1990). For instance, if chemical reactions occur at finite rates, then one has to take into consideration the conservation of mass of each of the species that makes up the gas mixture. This implies that the governing equation set is expanded (considerably if one has a large number of species). In addition to these phenomena, one must also take into account the internal structures of the species that compose the flow stream. As a first approximation, one can assume the atomic species to be point masses and the molecular species to be rigid rotors. For a more rigorous analysis, however, one must account for the realistic structure of the atomic and molecular species.

Once the flow has been modelled mathematically, the equations governing the flow must be solved subject to some boundary conditions. The usual approach is to solve the equations numerically since they are intractable to analytical solution. There are several approaches that are possible (Anderson *et al* 1982), (1) solve the time-dependent form of the equations iteratively till a steady-state solution (usually the one of interest) is reached, (2) solve the time-independent form of the equations by means of space marching along the dominant flow direction, or (3) a combination of the two. The first approach is usually resource intensive for the three-dimensional case, both in terms of computer memory and time. The second approach reduces the dimensionality of the problem by one, i.e., some initial solution surface is marched in the dominant flow direction (time-like axis). This approach is subject to some restrictions (for example, the inviscid flow must be everywhere supersonic), but in the cases where such an approach is viable, it provides solutions of accuracy comparable to that obtained from the first approach and is also substantially less resource intensive. Some examples of the space-marching method are the Viscous Shock Layer (VSL) method, and the Parabolised Navier-Stokes (PNS) method (Rubin & Tannehill 1992) etc.

The PNS equations are obtained from the time-dependent Navier-Stokes equations by dropping the time terms and the viscous terms in the streamwise direction. The equations so obtained are actually hyperbolic-elliptic due to the presence of the subsonic layer near the wall. This layer permits pressure disturbances to travel upstream (upstream influence) resulting in exponentially growing solutions (departure solutions). Consequently, the equations are not well posed for a space-marching method. There are several ways of overcoming this difficulty; the ones due to Vigneron

et al (1978) or Schiff & Steger (1979) are commonly used. In the Schiff and Steger method, the pressure at the sonic point within the boundary layer is imposed in the direction normal to the body throughout the subsonic zone. In the technique due to Vigneron *et al* (1978), only a fraction of the streamwise pressure gradient is retained in the subsonic boundary layer. This fraction, which is a function of the local streamwise Mach number, is obtained from an eigenvalue analysis of the governing equations. The eigenvalue analysis also reveals that the PNS equations cannot be used in flows where the inviscid Mach number is less than 1, e.g., the nose of a blunt body which has a large embedded subsonic zone in the shock layer. In conjunction with time-dependent Navier–Stokes equations, PNS methods have been successfully used by many researchers for a variety of problems ranging from three-dimensional ideal supersonic flow to three-dimensional reacting hypersonic flow (Rakich *et al* 1984; Prabhu & Tannehill 1986; Prabhu 1987, 1993; Prabhu *et al* 1988, 1993).

After the choice of time or space-marching method has been made, one has a choice of several numerical algorithms – (i) explicit methods, (ii) implicit methods, or (iii) hybrid explicit-implicit methods (Anderson *et al* 1982). Explicit methods are usually slow since they are limited by the “effective time scale” of the problem in addition to the CFL limit. Implicit methods, however, do not normally have CFL limitations and can resolve multiple scales within the problem but require a lot more computer resources and time. The choice of method is actually dictated by the problem. For instance, unsteady nonequilibrium flows require the use of explicit methods to capture both the flow time scale and the reaction time scale (Cambier *et al* 1992). For a steady equilibrating flow, where the reaction time scale is much less than the flow time scale, an implicit method is more appropriate (Cambier & Prabhu 1992).

Other considerations in choosing the numerical scheme are the choice of finite-difference or finite-volume method and the representation of the numerical flux. Until recently, the finite-difference method was used with a symmetric representation of fluxes, i.e., central differences. With advances in numerical analysis, the choice has since shifted to finite-volume methods with biased representation of numerical fluxes, i.e., upwind differencing.

In the present work, a finite-difference method with central-differencing of fluxes is chosen to solve the PNS equations for steady, reacting/nonreacting, laminar, hypersonic flow past a simple geometry such as a right circular cone. The primary objectives of the study are:

- To bring out the salient features of hypersonic viscous shock layers through the study of high-temperature effects such as chemical reactions.
- To study the influence of the grid on the computed solution.
- To study the influence of various gas models (ideal, equilibrium, and nonequilibrium air) on the computed solution.
- To provide a comprehensive set of “benchmark” results for code validation.

With these objectives in mind, a two-dimensional planar/axisymmetric PNS code has been developed. The code is based on an implicit, finite-difference method with central differencing of inviscid/viscous fluxes. Three types of gas models have been included in the code – (1) ideal gas ($\gamma = 1.4$), (2) equilibrium air whose thermodynamic and transport properties are based on piecewise continuous curve fits developed by Srinivasan *et al* (1987a, b), and (3) nonequilibrium air consisting of five species – N_2 , O_2 , NO, N, and O. For the last case, three further sub-cases are considered – (a) the

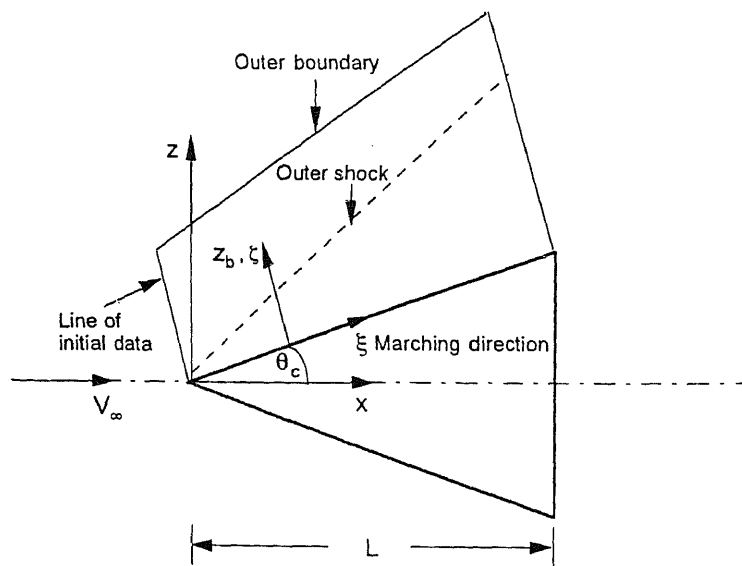


Figure 1. Coordinate system used in the present study. ξ, ζ are generalised coordinates (not necessarily orthogonal). L is the characteristic length. The outer boundary is placed far enough from the body to be able to capture the outer shock.

constituent species have no internal structure, (b) the constituent species have internal structure and their thermodynamic properties are obtained from Blottner *et al* (1971), and (c) the constituent gases possess internal structure and their thermodynamic properties are obtained from accurate spectroscopic constants and potentials (Liu & Vinokur 1989).

2. Governing equations and boundary conditions

2.1 Ideal/Equilibrium gas

The equations governing the steady, two-dimensional planar/axisymmetric, laminar flow of an ideal/equilibrium gas can be written for a general curvilinear coordinate system (ξ, ζ) shown in figure 1 as:

$$\frac{\partial}{\partial \xi}(\mathbf{E}^i) + \frac{\partial}{\partial \zeta}(\mathbf{G}^i - \mathbf{G}^v) = j(\mathbf{S}^i - \mathbf{S}^v), \quad (1)$$

where $j=0$ for planar flow, and $j=1$ for axisymmetric flow. The superscripts i and v represent the inviscid and viscous quantities, respectively. The coordinate ξ is identified as the primary or streamwise coordinate and ζ as the normal coordinate.

The inviscid flux vectors, \mathbf{E}^i and \mathbf{G}^i , are given by

$$\mathbf{E}^i = \frac{1}{J} \begin{Bmatrix} \rho \hat{U} \\ \rho u \hat{U} + \xi_x p \\ \rho w \hat{U} + \xi_z p \\ (\rho e_t + p) \hat{U} \end{Bmatrix}, \quad \mathbf{G}^i = \frac{1}{J} \begin{Bmatrix} \rho \hat{W} \\ \rho u \hat{W} + \zeta_x p \\ \rho w \hat{W} + \zeta_z p \\ (\rho e_t + p) \hat{W} \end{Bmatrix}, \quad (2)$$

where ρ (kg/m³) is the mass density of the gas, p (Pa) is the static pressure, u, w (m/s) are the Cartesian components of velocity, and e_t (J/kg) is the specific total energy given by:

$$e_t = e + \frac{1}{2}(u^2 + w^2), \quad (3)$$

where e (J/kg) is the specific internal energy of the gas.

The viscous flux vector, \mathbf{G}^v , is given by

$$\mathbf{G}^v = \frac{1}{J} \begin{pmatrix} 0 \\ \mu(l_1 u_\zeta + l_3 w_\zeta) \\ \mu(l_3 u_\zeta + l_2 w_\zeta) \\ \mu[(l_1 u + l_3 w)u_\zeta + (l_3 u + l_2 w)w_\zeta] + \kappa l_4 T_\zeta \end{pmatrix}, \quad (4)$$

where μ (Pa·s) is the coefficient of viscosity and κ (W/m·K) is the coefficient of thermal conductivity. The subscript ζ indicates partial differentiation w.r.t. the coordinate ζ . The coefficients l_1, \dots, l_4 are given by

$$l_1 = \frac{4}{3}\zeta_x^2 + \zeta_z^2, \quad l_2 = \zeta_x^2 + \frac{4}{3}\zeta_z^2, \quad l_3 = \frac{1}{3}\zeta_x \zeta_z, \quad l_4 = \zeta_x^2 + \zeta_z^2, \quad (5)$$

$\xi_x, \xi_z, \zeta_x, \zeta_z$ are the metrics and J is Jacobian of the coordinate transformation $[(x, y) \rightarrow (\xi, \zeta)]$. \hat{U} and \hat{W} are the contravariant components of velocity and are given by

$$\hat{U} = \xi_x u + \xi_z w, \quad \hat{W} = \zeta_x u + \zeta_z w. \quad (6)$$

Note that the viscous flux contains terms in the ζ direction only, i.e., the streamwise (ξ) terms are assumed to be much smaller than those in the normal (ζ) direction. The equations are thus said to be "parabolized". The governing equations, however, are still hyperbolic-elliptic and hence improperly posed for space-marching solutions. The conditions for well-posedness are elaborated on in a later section.

The vectors \mathbf{S}^i and \mathbf{S}^v are source terms for the axisymmetric formulation and are not given here.

For the case of the ideal/equilibrium gas, the vector of conservation variables \mathbf{Q} is chosen as

$$\mathbf{Q} = \{\rho, \rho u, \rho w, \rho e_t\}^T. \quad (7)$$

2.2 Nonequilibrium gas

The chemically reacting gas is actually a mixture of gases that react with one another. The rates of these reactions are finite as compared to the equilibrium gas where the reaction rates are infinitely large. Therefore, in addition to the conservation of mass of the gas mixture as a whole, one has to satisfy the law of conservation of mass for each constituent species.

The equations governing the steady, two-dimensional planar/axisymmetric, laminar flow of a chemically reacting gas consisting of n constituents can be written for a general curvilinear coordinate system (ξ, ζ) shown in figure 1 as:

$$\frac{\partial}{\partial \xi}(\mathbf{E}^i) + \frac{\partial}{\partial \zeta}(\mathbf{G}^i - \mathbf{G}^v) = j(\mathbf{S}^i - \mathbf{S}^v) + \mathbf{W}^c, \quad (8)$$

where the superscript c represents the chemical source terms. The other symbols retain the same meanings as before. The inviscid flux vectors, \mathbf{E}^i and \mathbf{G}^i , are given by

$$\mathbf{E}^i = \frac{1}{J} \begin{pmatrix} \rho \hat{U} \\ \rho u \hat{U} + \xi_x p \\ \rho w \hat{U} + \xi_z p \\ \rho H \hat{U} \\ \rho c_1 \hat{U} \\ \rho c_2 \hat{U} \\ \vdots \\ \rho c_{n-1} \hat{U} \end{pmatrix}, \quad \mathbf{G}^i = \frac{1}{J} \begin{pmatrix} \rho \hat{W} \\ \rho u \hat{W} + \xi_x p \\ \rho w \hat{W} + \xi_z p \\ \rho H \hat{W} \\ \rho c_1 \hat{W} \\ \rho c_2 \hat{W} \\ \vdots \\ \rho c_{n-1} \hat{W} \end{pmatrix}, \quad (9)$$

where c_1, c_2, \dots, c_{n-1} are the mass fractions of the species and H (J/kg) is the specific total enthalpy of the mixture. This is given by

$$H = h + \frac{1}{2}(u^2 + w^2), \quad (10)$$

where h (J/kg) is the specific static enthalpy of the mixture.

Note that only $n-1$ equations are considered for the conservation of species mass. The n th equation has been replaced by the global mass conservation equation and the mass fraction of the n th species is obtained from the algebraic relation

$$c_n = 1 - \sum_{s=1}^{n-1} c_s. \quad (11)$$

Compare the flux vectors given by (2) with those given in (9) – for the nonequilibrium case the flux vectors have $n+3$ components while for the ideal/equilibrium gas case the vectors have 4 components. Therefore, the equation set for a nonequilibrium case can be very large depending on the value of n .

The viscous flux vector, \mathbf{G}^v , is given by

$$\mathbf{G}^v = \frac{\mu}{J} \begin{pmatrix} 0 \\ (l_1 u_\zeta + l_3 w_\zeta) \\ (l_3 u_\zeta + l_2 w_\zeta) \\ [(l_1 u + l_3 w)u_\zeta + (l_3 u + l_2 w)w_\zeta] + \\ l_4 \left(\frac{\kappa}{\mu} T_\zeta + \sum_s h_s \frac{\mathcal{D}}{v} c_{s\zeta} \right) \\ \frac{\mathcal{D}}{v} l_4 c_{1\zeta} \\ \vdots \\ \frac{\mathcal{D}}{v} l_4 c_{n-1\zeta} \end{pmatrix}, \quad (12)$$

where μ (Pa·s) is the coefficient of viscosity, $v = \mu/\rho$ is the kinematic viscosity,

κ (W/m \cdot K) is the coefficient of thermal conductivity, and \mathcal{D} (m²/s) is the coefficient of binary diffusion. The coefficients l_1, \dots, l_4 are given by (5).

The chemical source vector, \mathbf{W}^c is

$$\mathbf{W}^c = \{0, 0, 0, 0, \dot{w}_1, \dot{w}_2, \dots, \dot{w}_{n-1}\}^T, \quad (13)$$

where \dot{w}_s (kg/m³·s) represents the mass production rate of species s .

The vectors \mathbf{S}^i and \mathbf{S}^v are source terms for the axisymmetric formulation. They are not given here and can be found elsewhere (Prabhu *et al* 1988).

For the case of the nonequilibrium gas, the vector of conservation variables \mathbf{Q} is chosen as

$$\mathbf{Q} = \{\rho, \rho u, \rho w, \rho H, \rho c_1, \rho c_2, \dots, \rho c_{n-1}\}^T. \quad (14)$$

2.3 Boundary conditions

The domain of interest is bounded by two boundaries – (a) the far field boundary and (b) the inner or wall boundary.

At the outer boundary freestream conditions are applied. This means that any discontinuities that arise in the flowfield are “captured” as part of the solution. This is possible due to the strong conservation-law form of the equations.

Since the flow is viscous, “no-slip” boundary conditions are applied at the wall, i.e.,

$$u = w = 0. \quad (15)$$

The wall is assumed to be isothermal with a constant wall temperature, i.e.,

$$T_w = \text{constant}. \quad (16)$$

Further, the pressure gradient in the normal direction (ζ) is assumed to be zero at the wall. Strictly speaking, one has to solve the normal momentum equation at the wall. In practice, however, this approximation from boundary-layer arguments works well. This boundary condition is expressed mathematically as:

$$\frac{\partial p}{\partial \zeta} = 0. \quad (17)$$

In addition to these boundary conditions, conditions have to be imposed on the species mass densities (or equivalently mass fractions) for the chemical nonequilibrium case. We will assume the wall to be noncatalytic, i.e., the species density gradients normal to the wall are zero. This is expressed as:

$$\left. \frac{\partial c_s}{\partial \zeta} \right|_w = 0. \quad (18)$$

3. Gas models

In order to close the system of governing equations, relations between the thermodynamic quantities and expressions for the transport properties of the gas or gas mixture are required. The relations and expressions depend on the type of gas considered and are discussed in what follows.

3.1 Thermodynamic and transport properties: Ideal gas

The ideal gas obeys the following equations of state (thermal and caloric):

$$p = \rho RT, \quad (19)$$

$$p = (\gamma - 1)\rho e, \quad (20)$$

where p (Pa) is the static pressure, ρ (kg/m³) is the mass density, R (J/kg·K) is the specific gas constant, T (K) is the static temperature, e (J/kg) the specific internal energy and γ (= a constant) is the ratio of specific heats. The speed of sound a (m/s) is defined as

$$a = (\gamma p / \rho)^{1/2}. \quad (21)$$

The coefficient of viscosity (Pa·s) is obtained from Sutherland's formula

$$\mu = \mu_{\text{ref}} T^{3/2} / (T + C), \quad (22)$$

where μ_{ref} is a reference viscosity and C (= 110·4 K) is Sutherland's constant. The coefficient of thermal conductivity (W/m·K) is obtained from the definition of the Prandtl number

$$\text{Pr} = \mu C_p / \kappa = \text{constant} \Rightarrow \kappa = \mu C_p / \text{Pr}, \quad (23)$$

where the specific heat C_p (J/kg·K) at constant pressure is given by

$$C_p = \gamma R / (\gamma - 1) = \text{constant}. \quad (24)$$

3.2 Thermodynamic and transport properties: Equilibrium gas

The equilibrium gas is actually a mixture of gases in which we have local thermodynamic equilibrium. For this case, given any two state variables (for instance ρ and e) we can determine the chemical composition of the gas using Gibbs free-energy minimisation (Gordon & McBride 1976), or equilibrium constants method (Bailey 1967). Such iterative methods are quite time consuming because the gas composition has to be determined at every grid point at every spatial step. Fortunately, for the special case of air, gas compositions over a wide range of densities and temperatures have already been computed and curve fits for the thermodynamic and transport properties have been obtained (Srinivasan *et al* 1987a, b). These piecewise continuous curve fits are of adequate accuracy and are briefly described in what follows.

Recall that the primary variables used in the ideal/equilibrium gas formulation are ρ and e . For this choice of state variables the curve fits for the thermodynamic properties p , T and a are in functional form (Srinivasan *et al* 1987a)

$$p = p(\rho, e); \quad a = a(\rho, e); \quad T = T(\rho, e). \quad (25)$$

We also require the following curve fits for the implementation of boundary conditions (this is explained in a subsequent section):

$$h = h(p, \rho); \quad T = T(p, \rho). \quad (26)$$

In addition to these curve fits, we need a link between the fluid dynamics and the equilibrium chemistry. This link is provided by two parameters $\bar{\gamma}$ and $\bar{\beta}$ which are

defined as

$$\bar{\gamma} = h/e, \quad (27)$$

$$\bar{\beta} = p/\rho RT. \quad (28)$$

The first parameter is analogous to the usual isentropic exponent γ which is the ratio of specific heats. For the case of ideal gas $\bar{\gamma}$ and γ are identical. The second parameter is the compressibility of the gas and measures the departure of the gas from its ideal behaviour. For the case of an ideal gas $\bar{\beta}$ is identically 1.

The first correlation given in (25) is actually obtained from a curve fit of $\bar{\gamma}$,

$$\bar{\gamma} = \bar{\gamma}(\rho, e), \quad (29)$$

in conjunction with

$$p = (\bar{\gamma} - 1)\rho e. \quad (30)$$

Using (30) with the definition of compressibility the temperature can be rewritten as

$$T = [(\bar{\gamma} - 1)/\bar{\beta}](e/R). \quad (31)$$

Through the use of (30) and (31), the formulation for the case of equilibrium air is the same as that for ideal gas with γ being replaced by $\bar{\gamma}$.

As in the case of the thermodynamic properties, the transport properties are also available in the form of piecewise continuous curve fits (Srinivasan *et al* 1987b) with ρ and e as the primary variables. The curve fits in functional form are:

$$\mu = \mu(\rho, e); \quad \kappa = \kappa(\rho, e) \quad (32)$$

3.3 Thermodynamic and transport properties: Chemical nonequilibrium gas

In the present context, chemical nonequilibrium gas refers specifically to air consisting of five species – N_2 , O_2 , NO , N and O . These species react with one another and the reactions are assumed to be far from equilibrium, i.e., occur at a finite rate.

We have to consider the properties of the individual species as well as those of the gas mixture. The properties of the individual species depend on the kind of structure the species possess. For instance, we can assume the atomic species to be point masses or take into account their actual quantum structure. These assumptions lead to different values and behaviour of the thermodynamic properties.

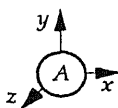
The component gases obey the thermal equation of state,

$$p_s = \rho_s \mathcal{R} T / (\mathcal{M}_s), \quad (33)$$

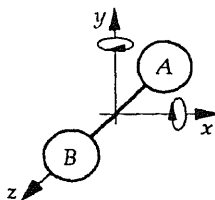
where p_s (Pa) is the partial pressure of species s , \mathcal{R} is the universal gas constant (8314.34 J/kmol·K), \mathcal{M}_s (kg/kmol) is the molecular mass of species s . The caloric equation of state depends on the nature of the constituent species. Three models are considered in the present study. These models differ in the kind of structure possessed by the constituent species of the gas mixture. In the first gas model, the species are assumed to have no internal structure – each atomic species is assumed to be a point mass with three translational degrees of freedom and each diatomic species is assumed to be a rigid rotor with three translational and two rotational degrees of freedom. In other words, the species that constitute the gas mixture are ideal gases. In the other two models, each species has an internal structure – each atomic species has quantised

IDEAL

(a)

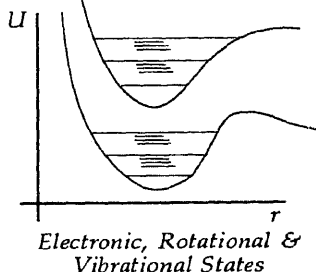
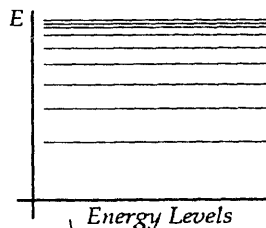
3 Trans. d.o.f. ($f=3$)

(b)

3 Trans. and 2 Rot. d.o.f. ($f=5$)

$$C_p = \frac{f+2}{2} \frac{R}{M} = \text{constant}$$

REAL



$$C_p = C_p(T)$$

Figure 2. Schematic representation of atoms and molecules in the ideal and real senses. Atoms are idealised as point masses (a) while diatomic molecules are idealised as rigid rotors (b). In reality the internal structure is quantised – atoms have discrete energy levels and molecules have electronic, vibrational, and rotational states. The specific heats of the species are constants for the ideal case and functions of temperature for the real case.

energy levels and the diatomic species has quantised electronic states which further contain vibrational and rotational levels. These models are schematically represented in figure 2.

3.3a Mixture of ideal gases: In this model, the atoms are assumed to be point masses with 3 translational degrees of freedom and the diatomic molecules are assumed to be rigid rotors with 3 translation and 2 rotational degrees of freedom (vibrational degrees of freedom being neglected). The specific heat and enthalpy of each individual species are given by

$$C_{p,s} = [(f+2)/2](R/M_s) = \text{constant}, \quad (34)$$

$$h_s = C_{p,s} T + h_s^0, \quad (35)$$

where h_s^0 (J/kg) is heat of formation of species s and f the number of degrees of freedom.

3.3b Mixture of perfect gases – Blottner model: In this model, the internal structure of the atoms and molecules are taken into account. Consequently, the specific heats and enthalpies are no longer constant and are dependent on the temperature. This is

expressed as

$$C_{p,s} = A_{1,s}(T), \quad (36)$$

$$h_s = T A_{2,s}(T) + h_s^0, \quad (37)$$

where $A_{1,s}$ and $A_{2,s}$ are tabulated functions of temperature (Blottner *et al* 1971). In the present study, cubic spline interpolation is used to determine the intermediate values of $A_{1,s}$ and $A_{2,s}$.

3.3c Mixture of perfect gases – Liu–Vinokur model: As in the previous model, the internal structure of the atoms and molecules are taken into account. However, more exact methods utilizing the latest available spectroscopic constants are used in determining the thermodynamic properties (Liu & Vinokur 1989). The properties are then curve fit using cubic splines and the spline coefficients tabulated as functions of temperature. This is expressed as

$$C_{p,s} = C_{1,s} + C_{2,s}(z + T) + C_{3,s}(z^2 + 2zT) + C_{4,s}(z^3 + 3z^2 T), \quad (38)$$

$$h_s = T(C_{1,s} + C_{2,s}z + C_{3,s}z^2 + C_{4,s}z^3) + h_s^0, \quad (39)$$

where $C_{1,s}$, $C_{2,s}$, $C_{3,s}$ and $C_{4,s}$ are tabulated values of the spline coefficients over a temperature range 250–25,000 K (in steps of 250 K). The parameter z is defined as

$$z = T - \text{int}(T/\Delta T)\Delta T. \quad (40)$$

In the above equation $\text{int}(\cdot)$ indicates the integer part of the argument.

For each of the gas models considered for the nonequilibrium case, the static pressure of the mixture is obtained from Dalton's law of partial pressures, i.e.,

$$p = \rho \mathcal{R} T \sum_s (c_s / \mathcal{M}_s) = \rho \mathcal{R} T / \mathcal{M}. \quad (41)$$

The specific heat and enthalpy of the mixture are computed as weighted sums (the weights being the mass fractions of the species) of the species properties, i.e.,

$$C_{p_f} = \sum_s c_s C_{p,s}, \quad (42)$$

$$h = \sum_s c_s h_s. \quad (43)$$

The frozen speed of sound a_f for the nonequilibrium case is given by

$$a_f = [\mathcal{R} C_{p_f} T / (\mathcal{M} C_{p_f} - \mathcal{R})]^{1/2}. \quad (44)$$

The viscosity (Pa·s) of each individual species is obtained from curve fits due to Blottner *et al* (1971). These curve fits are of the form

$$\mu_s = 0.1 \exp[(A_s \ln T + B_s) \ln T + C_s], \quad (45)$$

where A_s , B_s and C_s are constants. The thermal conductivity (W/m·K) of species s is computed using a semi-empirical formula due to Eucken (1913)

$$\kappa_s = \frac{\mu_s \mathcal{R}}{\mathcal{M}_s} \left(C_{p,s} \frac{\mathcal{M}_s}{\mathcal{R}} + \frac{5}{4} \right). \quad (46)$$

The transport properties of the gas mixture are then obtained through the use of mixing rules. The mixing rule due to Wilke (1950) is considered adequate for non-ionizing

mixtures and is written for the coefficient of viscosity as

$$\mu = \sum_s \left(\mu_s / \left[1 + \sum_{r \neq s} \frac{X_r}{X_s} \frac{\mathcal{M}_s}{\mathcal{M}_r} \left(\frac{5}{3} \frac{1}{A_{sr}^*} + \frac{\mathcal{M}_r}{\mathcal{M}_s} \right) \right] \right) \Phi_{sr}, \quad (47)$$

where

$$\Phi_{sr} = \left[\frac{\mathcal{M}_s}{8(\mathcal{M}_s + \mathcal{M}_r)} \right]^{1/2} \left[F_{sr} + \left\{ \frac{\mu_s}{\mu_r} \left(\frac{\mathcal{M}_r}{\mathcal{M}_s} \right)^{1/2} \right\}^{1/2} B_{sr} \right]^2. \quad (48)$$

The values of the constants A_{sr}^* , B_{sr} and F_{sr} are

$$A_{sr}^* = \frac{5}{3}, \quad F_{sr} = 1.0, \quad B_{sr} = 1.0. \quad (49)$$

The same mixing rule is used for the coefficient of thermal conductivity with μ_s being replaced by κ_s in (47).

In the present study, the mass diffusion is assumed to be binary. The justification for this is provided by the fact that air consisting of 5 species can be treated as a binary gas with the "heavy" particles N_2 , O_2 and NO (nearly the same molecular weight) and "light" particles N and O (nearly the same atomic weight). The binary diffusion coefficient is obtained from the definition of the Lewis number which is assumed to be a constant.

$$Le = \rho C_p \mathcal{D} / \kappa \Rightarrow \mathcal{D} = \kappa Le / \rho C_p. \quad (50)$$

3.4 Reaction model: Chemical nonequilibrium gas

Consider a multicomponent system of n species undergoing m simultaneous elementary reactions. These reactions can be represented symbolically as

$$\sum_{s=1}^n v'_{l,s} A_s \rightleftharpoons \sum_{s=1}^n v''_{l,s} A_s \quad l = 1, 2, \dots, m, \quad (51)$$

where $v'_{l,s}$, $v''_{l,s}$ are stoichiometric coefficients and A_s is chemical symbol of species s . Using the law of mass action, the rate of production of species s is

$$\dot{w}_s = \mathcal{M}_s \sum_{l=1}^m (v''_{l,s} - v'_{l,s}) \left\{ k_{f,l}(T) \prod_{r=1}^n [\rho \gamma_r]^{v'_{l,r}} - k_{b,l}(T) \prod_{r=1}^n [\rho \gamma_r]^{v''_{l,r}} \right\}, \quad (52)$$

where γ_r is the mole-mass ratio of species r and $k_{f,l}$ and $k_{b,l}$ are, respectively, the forward and backward reaction rates of reaction l . These reaction rates are expressed in modified Arrhenius form (Blottner *et al* 1971) as:

$$k_{f,l} = A_{f,l} T^{n_{f,l}} \exp(-E_{f,l}/kT); \quad k_{b,l} = A_{b,l} T^{n_{b,l}} \exp(-E_{b,l}/kT), \quad (53)$$

where $A_{f,l}$, $A_{b,l}$, $n_{f,l}$, $n_{b,l}$, $E_{f,l}$ and $E_{b,l}$ are constants for a particular reaction l and k is the Boltzmann constant.

In the present work, the following reactions between the various species have been considered:

- (1) $O_2 + M_1 \rightleftharpoons 2O + M_1$
- (2) $N_2 + M_2 \rightleftharpoons 2N + M_2$
- (3) $NO + M_3 \rightleftharpoons N + O + M_3$
- (4) $NO + O \rightleftharpoons O_2 + N$
- (5) $N_2 + O \rightleftharpoons NO + N$

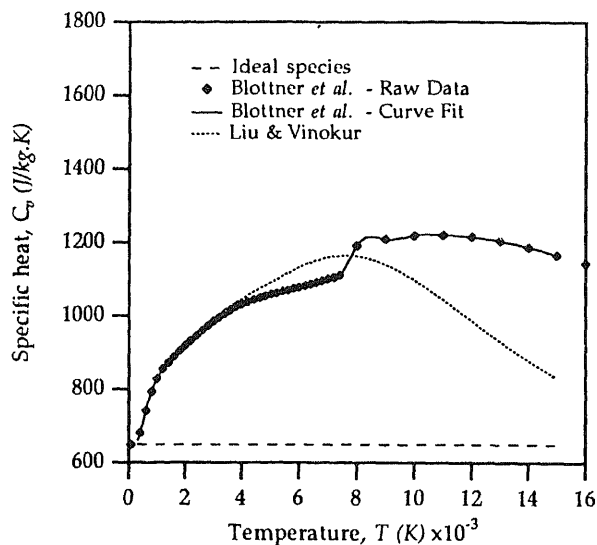


Figure 3. Temperature variation of the specific heat (C_v) of molecular oxygen (O_2).

In reactions 1–3 (also called three-body reactions), M_1 , M_2 and M_3 represent the catalytic third body which undergoes no change during the reaction and could be any one of the species, N_2 , O_2 , NO , N , or O . Reactions 4 and 5 are called “shuffle” or exchange reactions. Therefore, there are 17 reactions in the above set.

3.5 Discussion

The inclusion of the internal structure of the species changes their thermodynamic properties. In figures 3–5, the specific heats (at constant volume) of O_2 , NO , and O are

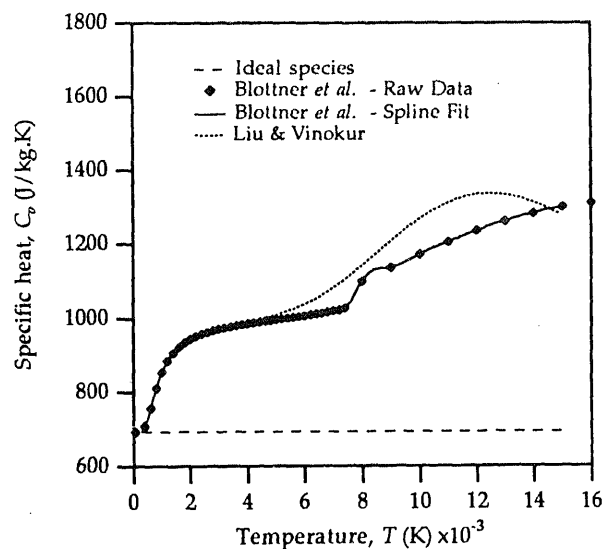


Figure 4. Temperature variation of the specific heat (C_v) of nitric oxide (NO).

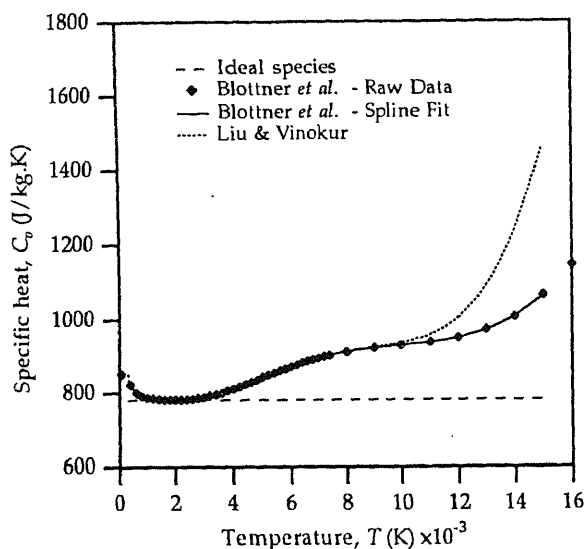


Figure 5. Temperature variation of the specific heat (C_v) of atomic oxygen (O).

plotted as functions of temperature. It is clearly seen that the species with no internal structure have a constant specific heat while those with internal structure have heat capacities that increase with increasing temperature (the heat capacity decreases in the diatomic species when their dissociation limits are reached). In the case of atomic oxygen, the agreement between the C_v values of Blottner *et al* (1971) and those of Liu & Vinokur (1989) is very good for temperatures less than about 8000 K. Beyond this temperature, the differences are large. For the diatomic species, however, large differences occur between the models from around 3000 K. The Liu–Vinokur model is to be considered as more accurate because it uses the latest available data for spectroscopic constants and intermolecular potentials in conjunction with accurate numerical methods.

4. Analysis

4.1 Parabolization

As mentioned earlier, the word “parabolized” in the PNS equations is a misnomer. The governing equations are actually hyperbolic-elliptic in the ξ direction. The ellipticity is introduced into the system due to the presence of the subsonic zone in the boundary-layer at the wall. This subsonic zone permits the pressure signals to travel upstream (upstream influence). Hence, a single-sweep space-marching method, wherein the spatial evolution (in ξ) of a line of initial data is computed, is not properly posed and leads to exponentially growing solutions called departure solutions. There are several ways of getting rid of this ellipticity (Vigneron *et al* 1978; Schiff & Steger 1979). Following Vigneron *et al* (1978), an analysis was carried out for the various gas models considered in the present study. The details of the analyses are not given here but only the salient points are mentioned.

An eigenvalue (linear) analysis (Vigneron *et al* 1978; Prabhu & Tannehill 1986; Prabhu *et al* 1988) of the governing equations reveals that the governing equations are

hyperbolic-parabolic, i.e., well-posed for space marching in ξ if and only if – (1) there is no flow separation in the axial (ξ) direction, (2) the local Mach number is greater than unity in the inviscid part of the flowfield, and (3) only a fraction ω ($0 \leq \omega \leq 1$) of the streamwise pressure gradient is retained in the subsonic part of the flowfield. The magnitude of ω depends on the local streamwise Mach number and is given by the expression

$$\omega = \min \{1, \sigma \bar{\gamma} M_\xi^2 [1 + (\bar{\gamma} - 1) M_\xi^2]^{-1}\}, \quad (54)$$

where σ ($0 \leq \sigma \leq 1$, typically a value of 0.85 or less is used) is a factor of safety to account for nonlinear effects neglected in the analysis. The parameter $\bar{\gamma}$ in the above equation is given by

$$\bar{\gamma} = \begin{cases} \gamma & \text{(ideal gas)} \\ h/e & \text{(equilibrium air)} \\ \mathcal{M}C_{p_i}/(\mathcal{M}C_{p_i} - \mathcal{R}) & \text{(nonequilibrium air)} \end{cases} \quad (55)$$

and the local streamwise Mach number is given by

$$M_\xi = \hat{U}/(a|\nabla\xi|), \quad (56)$$

where the speed of sound a is given by (21) for an ideal gas, by the second correlation of (25) for equilibrium air, or by (44) for chemical nonequilibrium air.

Note that when $\omega = 0$ the streamwise pressure gradient is completely omitted and when $\omega = 1$ the streamwise pressure gradient is completely retained. In the inviscid part of the flowfield, since the Mach number must be greater than unity, the streamwise pressure gradient is completely retained. In the subsonic viscous region close to the wall only a fraction of $\partial p/\partial\xi$ is retained.

4.2 Treatment of the streamwise pressure gradient

From the preceding paragraphs, it is clear that for a single sweep space-marching solution to be viable, the streamwise pressure gradient has to be treated specially. The streamwise inviscid flux \mathbf{E}^i is now split into two parts \mathbf{E}^{i*} and \mathbf{P}^i as shown below

$$\mathbf{E}^i = \mathbf{E}^{i*} + \mathbf{P}^i, \quad (57)$$

where \mathbf{E}^{i*} and \mathbf{P}^i are

$$\mathbf{E}^{i*} = (1/J) \{ \rho \hat{U}, \rho u \hat{U} + \xi_x \omega p, \rho w \hat{U} + \xi_z \omega p, (\rho e_t + p) \hat{U} \}^T, \quad (58)$$

$$\mathbf{P}^i = (1/J) \{ 0, \xi_x(1 - \omega)p, \xi_z(1 - \omega)p, 0 \}^T, \quad (59)$$

for the ideal/equilibrium case, and

$$\mathbf{E}^{i*} = \frac{1}{J} \begin{pmatrix} \rho \hat{U} \\ \rho u \hat{U} + \xi_x \omega p \\ \rho w \hat{U} + \xi_z \omega p \\ \rho H \hat{U} \\ \rho c_1 \hat{U} \\ \rho c_2 \hat{U} \\ \vdots \\ \rho c_{n-1} \hat{U} \end{pmatrix}, \quad \mathbf{P}^i = \frac{1}{J} \begin{pmatrix} 0 \\ \xi_x(1 - \omega)p \\ \xi_z(1 - \omega)p \\ 0 \\ 0 \\ 0 \\ \vdots \\ 0 \end{pmatrix} \quad (60)$$

for the nonequilibrium case.

The governing equations (1) or (8) can now be written as

$$\frac{\partial}{\partial \xi}(\mathbf{E}^{i*}) + \frac{\partial}{\partial \xi}(\mathbf{G}^i - \mathbf{G}^v) = j(\mathbf{S}^i - \mathbf{S}^v) + [\mathbf{W}^c] - \frac{\partial}{\partial \xi}(\mathbf{P}^i). \quad (61)$$

Normally, the last term of (61) is not included in the computations and the systems of equations that is actually solved is

$$\frac{\partial}{\partial \xi}(\mathbf{E}^{i*}) + \frac{\partial}{\partial \xi}(\mathbf{G}^i - \mathbf{G}^v) = j(\mathbf{S}^i - \mathbf{S}^v) + [\mathbf{W}^c]. \quad (62)$$

5. Numerical method

The PNS equations, (62), cannot be solved analytically and must be solved numerically. In the present study, a finite-difference approach has been taken for the numerical solution of the governing equations. The method of discretisation of the solution domain, the numerical algorithm, and the numerical implementation of boundary conditions are discussed in this section.

5.1 Discretisation and grid generation

As mentioned earlier, the computational domain consists of two boundaries – (1) an outer freestream boundary and, (2) an inner wall boundary. The outer boundary is chosen in such a way that the bow shock lies completely within this domain. The domain is then discretised algebraically for implementation of a finite-difference procedure. In this procedure, at any given ξ station, a point on the body surface and a point on the outer boundary are connected by a straight line and grid points distributed on this line using the following stretching function

$$s(\zeta) = 1 - \beta \left[\frac{(\beta + 1)^{1-\zeta} - (\beta - 1)^{1-\zeta}}{(\beta + 1)^{1-\zeta} + (\beta - 1)^{1-\zeta}} \right], \quad (63)$$

$$\zeta = (k - 1)/(NK - 1), \quad k = 1, 2, \dots, NK, \quad (64)$$

where $\beta (\beta > 1)$ is the stretching function and NK the total number of points on the grid line. Note that $s(0) = 0$ and $s(1) = 1$ and the points are clustered close to the wall for values of β close to 1. Such clustering is necessary for good resolution of the subsonic viscous layer.

The coordinates of the grid points on the grid line are obtained from

$$x(\xi, \zeta) = x_w(\xi) + n_1(\xi)s(\zeta)\delta(\xi), \quad (65)$$

$$y(\xi, \zeta) = y_w(\xi) + n_2(\xi)s(\zeta)\delta(\xi), \quad (66)$$

where n_1 and n_2 are direction cosines of the unit vector along the grid line and δ is the linear distance of the outer boundary from the body surface.

5.2 Algorithm

An implicit, noniterative finite-difference scheme is used to solve the PNS equations, (62). This algorithm is an adaptation of one developed by Tannehill *et al* (1982).

Associating the index i with the streamwise direction ξ and the index k with the normal direction ζ , this algorithm in delta form is

$$\begin{aligned} \{ \mathbf{A}_{i,k}^* + \Delta\zeta \frac{\partial}{\partial\zeta} (\mathbf{B}_{i,k} - \mathbf{M}_{i,k}) - \mathbf{D}_2 \} \Delta\mathbf{Q}_{i,k} = \\ - \Delta\zeta \left\{ \frac{\partial}{\partial\zeta} (\mathbf{G}_{i,k}^i - \mathbf{G}_{i,k}^v) + \mathbf{S}_{i,k}^i - \mathbf{S}_{i,k}^v - [\mathbf{W}_{i,k}^c] \right\} + \mathbf{D}_4 \mathbf{E}^i, \end{aligned} \quad (67)$$

where the change in the vector of dependent variables is

$$\Delta\mathbf{Q}_{i,k} = \mathbf{Q}_{i+1,k} - \mathbf{Q}_{i,k}, \quad (68)$$

and the Jacobian matrices of the various fluxes are,

$$\mathbf{A}^* = \frac{\partial \mathbf{E}^i}{\partial \mathbf{Q}}, \quad \mathbf{B} = \frac{\partial \mathbf{G}^i}{\partial \mathbf{Q}}, \quad \mathbf{M} = \frac{\partial \mathbf{F}^v}{\partial \mathbf{Q}}. \quad (69)$$

The derivative $\partial/\partial\zeta$ is replaced by the conventional 3-point central-difference operator. \mathbf{D}_2 and \mathbf{D}_4 are second-order implicit and fourth-order explicit smoothing operators, respectively. These are required to stabilize the central-difference algorithm. In the linearization of the viscous flux, the transport properties are assumed to be locally constant. Note that all the source terms have been lagged in the present formulation.

The left hand side of the algorithm, (67), corresponds to a block-tridiagonal system of equations. The blocks are square matrices of order 4 and order $(n+3)$ for the ideal/equilibrium gas case and the nonequilibrium case, respectively. Specifically, for the five-species nonequilibrium air model considered in the present calculations, these blocks are square matrices of order 8.

The code developed in the present study is a unified code for all the three gas models. Therefore, the block tridiagonal solver developed here is meant for systems of any block order m ($m > 1$). The penalty paid in using a general solver instead of using one for order 4 and one for order 8 is not substantially large.

5.3 Decoding the \mathbf{Q} vector

At the end of the solution step given by (68), we have just the vector $\mathbf{Q}_{i+1,k}$. From this vector we have to extract all the thermodynamic and transport coefficients and apply the boundary conditions. The decoding procedure and implementation of the boundary conditions for each of the gas models are considered in what follows.

5.3a Ideal air: Decoding the \mathbf{Q} vector for an ideal gas is rather simple. One can easily obtain the variables ρ , u , w , and e_t from \mathbf{Q} . Knowing the variables u , w , and e_t , the variable e is obtained from (3). The variables T , p , a , μ and κ follow from (19)–(23), respectively.

5.3b Equilibrium air: Decoding the \mathbf{Q} vector for this case is a little more involved. As before, we can easily obtain the variables ρ , u , w and e_t from \mathbf{Q} . Again, using (3) and the values of u , w and e_t , we can compute the value of e . Knowing e and ρ , we can use the correlations given in (25) to determine the values of p , a and T . Using (27) and (28), we

compute the parameters $\bar{\gamma}$ and $\bar{\beta}$. The transport properties are easily determined from (32).

5.3c Nonequilibrium air: Decoding the \mathbf{Q} vector for this case is again quite involved. We can easily obtain the variables ρ , u , w , H , and c_1, c_2, \dots, c_{n-1} from \mathbf{Q} . The mass fraction c_n is computed from (11). Using (10) and the values of u , w , and H we can compute the value of h . Knowing h and the mass fractions c_1, c_2, \dots, c_n , we compute the temperature T of the mixture iteratively using the Newton-Raphson method.

$$T^{p+1} = T^p - \frac{\sum_{s=1}^n c_s h_s(T^p) - h}{\sum_{s=1}^n c_s C_{p,s}(T^p)}, \quad (70)$$

where p is an iteration index. The Newton-Raphson method usually requires no more than 3 to 5 iterations for convergence. Once the temperature has been computed, the other thermodynamic and transport properties (for both the species and the mixture) are computed using expressions listed in the section on gas models.

5.4 Numerical boundary conditions

The implementation of boundary conditions (discussed in the section on governing equations) is considered here. In the implicit portion of the algorithm (left hand side of 67) boundary conditions are applied to only first-order accuracy. This is done to preserve the block tridiagonal structure of the matrix. After the integration step, the boundary conditions are updated explicitly. This is discussed for each of the gas models in what follows.

5.4a Ideal gas: At the wall, the pressure is assumed to be the same as the pressure one grid point above it (17). Using this value of pressure and the given wall temperature T_w , the value of the mass density of the wall can be computed. No-slip conditions are implemented by setting the values of u and w to zero.

At the freestream boundary, \mathbf{Q} at the grid point is updated using the values at the grid point just in the interior of the domain, i.e., a zero-gradient condition is imposed on \mathbf{Q} .

5.4b Equilibrium air: At the wall, the pressure is assumed to be the same as the pressure one grid point above it (17). Now the temperature of the wall is specified as T_w . Using the second correlation of (26), i.e.,

$$T_w = T_w(p_w, \rho_w) \quad (71)$$

the wall density ρ_w is determined iteratively using a secant method (Prabhu & Tannehill 1986). Using the first correlation of (26), the enthalpy at the wall is determined for given values of p and ρ . The internal energy at the wall is then updated using the definition of the enthalpy

$$e_w = h_w - (p_w/\rho_w). \quad (72)$$

This is done in order to ensure consistency in the use of curve fits. No-slip conditions are implemented by setting the values of u and w to zero.

At the freestream boundary, a zero-gradient condition is imposed on \mathbf{Q} .

5.4c *Nonequilibrium air*: At the wall, the pressure is assumed to be the same as the pressure one grid point above it (17). Now the temperature of the wall is specified as T_w . The mass fractions of the species are computed using zeroth-order extrapolation from the interior. Using these values of mass fractions, temperature, and pressure, the density of the gas mixture is computed from the equation of state (41). No-slip conditions are implemented by setting the values of u and w to zero.

At the freestream boundary, a zero-gradient condition is imposed on Q .

6. Results

6.1 Test conditions

The laminar hypersonic flow past a sharp right circular cone has been computed in the present study. The details of the test conditions are given in table 1. The ambient conditions correspond to an altitude of 61 km approximately. The Mach and Reynolds numbers for these conditions are 25 and 0.13×10^6 per m, respectively.

6.2 Preliminaries

The calculations were started at $x = 1 \times 10^{-3}$ m from the tip of the cone. This was done to avoid the singularity at $x = 0$ where $z = 0$. The line of initial data was initialised using freestream values and this line was marched downstream to a location of $x = 1.276$ m with the marching step-size varying linearly from $\Delta x = 5 \times 10^{-4}$ m to $\Delta x = 1.2 \times 10^{-3}$ m over 1500 steps. The spacing at the wall was also varied linearly from $\Delta z_b = 5 \times 10^{-5}$ m to $\Delta z_b = 10^{-4}$ m. The outer boundary height, however, was kept fixed at $\delta(x) = 0.5$ m. The number of grid points was chosen after detailed grid sensitivity studies were carried out. A sampling of the results obtained from the various studies in this work is presented in what follows (some more results and details can be found in Prabhu 1993).

In the presentation of the results, the following nondimensional quantities – surface pressure coefficient C_p , skin-friction coefficient C_f , and Stanton number St have been defined as

$$C_p = \frac{p_w - p_\infty}{\frac{1}{2} \rho_\infty U_\infty^2}, \quad C_f = \frac{\tau_w}{\frac{1}{2} \rho_\infty U_\infty^2}, \quad St = \frac{-\dot{q}_2}{\rho_\infty U_\infty (H_\infty - H_w)}, \quad (73)$$

where p_w is wall pressure (Pa), τ_w is surface shear stress (N/m^2), \dot{q}_w (W/m^2) and H_w (J/kg) are respectively, the total heating and the total enthalpy at the wall. The total heating at

Table 1. Test conditions.

Cone half angle (θ_c)	10°
Freestream velocity (U_∞)	8100 m/s
Freestream pressure (p_∞)	20.35 Pa
Freestream temperature (T_∞)	252.6 K
Wall temperature (T_w)	1200 K
Freestream N_2 mass fraction (c_{N_2})	0.79
Freestream O_2 mass fraction (c_{O_2})	0.21
Noncatalytic wall	

the wall is conductive heating in the case of an ideal gas, and the sum of conductive and diffusive heating in the case of equilibrium and nonequilibrium air.

6.3 Grid study

The sensitivity of the computed solution to varying grid sizes was studied first to establish the consistency of the numerical scheme. Six different grid sizes – $NK = 67, 75, 101, 125, 151$, and 167 were tried for the ideal gas ($\gamma = 1.4$) and the nonequilibrium air models. Some of the results for the nonequilibrium case are presented here and the grid sensitivity of the solution for the ideal gas case can be found in Prabhu (1993).

The axial variation of the surface pressure coefficient C_{p_w} for the various grid sizes is shown in figure 6. The impact of the grid resolution is clearly seen in the picture. As the grid is refined the solution changes. Though the changes are very pronounced for the coarser grids, for the two finest grids ($NK = 151$ and 167) the differences between the solutions are negligibly small. This indicates the independence (from the grid) of the solution. The Newtonian value of the surface pressure coefficient is also shown in the figure. The deviation between the PNS results and the Newtonian results is due to the viscous-inviscid interaction which is rather strong at the tip of the cone for the chosen Mach number and Reynolds number in the present study.

Figure 7 shows the pressure profiles at the base of the cone (at $x = 1.276$ m) for various grid sizes. The grid size has a significant impact on the pressure. The shock gets progressively sharper and the post-shock pressure rises with grid fineness. For the finest two grids, however, the differences in the profiles are negligibly small.

The pressure profiles also show oscillations which are characteristic of central-difference schemes. The amplitudes of these oscillations grow with the grid fineness. Recall that central differencing has been used for the inviscid fluxes. This means that the flux differencing is not biased in the direction of signal propagation and hence, the numerical damping that is necessary for algorithm stability will smear any discontinuities

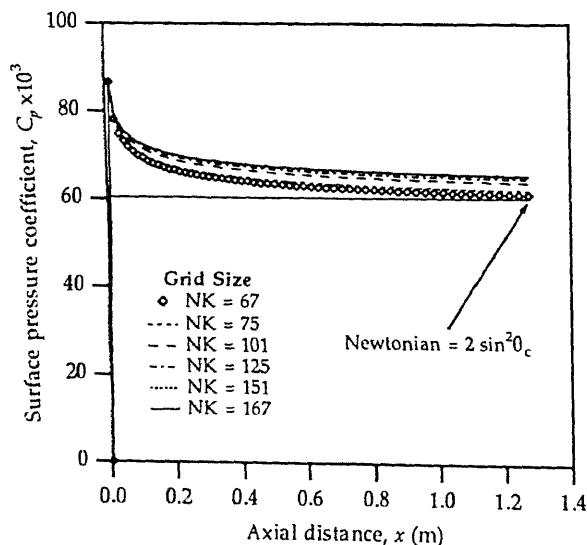


Figure 6. Axial variation of the computed surface pressure coefficient for various grid sizes for the nonequilibrium gas model of Blottner *et al* (1971). The Newtonian pressure coefficient distribution is also shown.

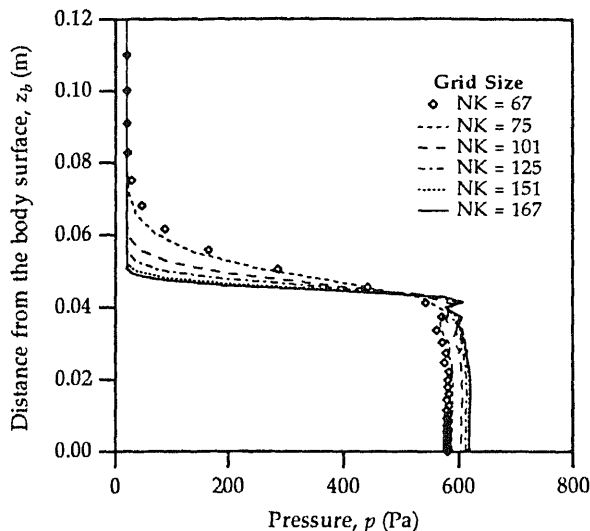


Figure 7. Effect of grid size on the static pressure. Profiles of p at $x = 1.276$ m for various grid sizes. The oscillations are due to the use of central differences for the inviscid fluxes.

that are captured as part of the solution. In the coarse mesh the captured outer shock smears over quite a few grid points which are spaced rather widely apart. In the fine mesh the shock still spreads over nearly the same number of grid points which are, however, quite closely spaced resulting in a sharper definition of the captured shock. It must be mentioned here that the numerical smoothing coefficient was kept constant (and at a low value) across all grid sizes. This causes a problem in the finer grids where high-frequency errors need to be damped out with a larger amount of artificial viscosity. This explains the increased amplitude of the oscillations for the finest grids.

Figure 8 shows the temperature profiles at the base of the cone (at $x = 1.276$ m) for various grid sizes. The agreement is good at all points except at the points in the shock

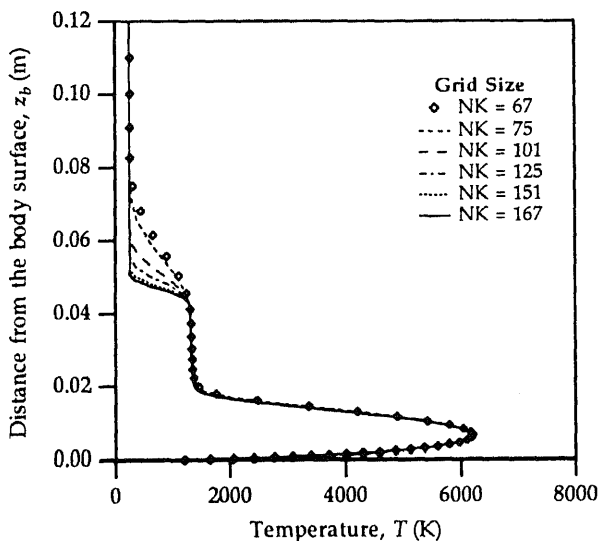


Figure 8. Effect of grid size on the static temperature. Profiles of T at $x = 1.276$ m for various grid sizes.

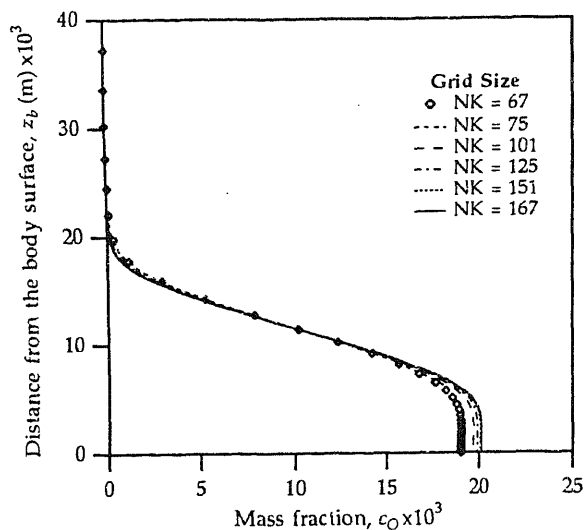


Figure 9. Effect of grid size on the mass fraction of O (atomic oxygen). Profiles of c_O at $x = 1.276$ m for various grid sizes.

region. The grid fineness has little or no impact on the peak temperature in the boundary layer and the temperature profiles do not exhibit the oscillations seen in the pressure.

The mass fraction profiles of two representative species – atomic oxygen (O) and molecular nitric oxide (NO) are shown in figures 9 and 10, respectively. Again, the grid refinement has a significant influence on the chemistry. The changes in the mass fractions, however, decrease at the finest grid levels. Large changes in the chemistry in the coarser grids can pose problems in radiation calculations which are very sensitive to changes in the species concentrations.

On the basis of the grid sensitivity study for both the ideal gas and nonequilibrium air gas models, a grid size of $NK = 151$ points was chosen for all subsequent calculations.

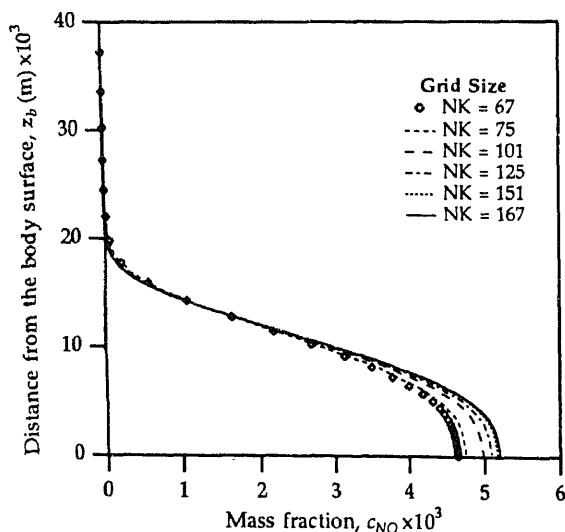


Figure 10. Effect of grid size on the mass fraction of NO (nitric oxide). Profiles of c_{NO} at $x = 1.276$ m for various grid sizes.

This was done in order to avail the gain in accuracy (with finer grids) while keeping the computing times down to a reasonable level.

6.4 Species structure study

After having studied the grid dependence of the computed solution for the nonequilibrium air case, the impact of the thermodynamic properties of the constituent species was studied for three models of the internal structure – (1) ideal species model, (2) model due to Blottner *et al* (1971), and (3) model due to Liu & Vinokur (1989).

The pressure profiles at $x = 1.276$ m for the three species structure models are shown in figure 11. While the results of the Blottner and Liu–Vinokur models are indistinguishable, they are very different from those of the ideal species model, especially in the shock region. At the body, however, all three models predict nearly the same surface pressure. This is understandable because the pressure being a “mechanical” variable is less dependent on the internal structure of the species. The shock standoff distance, on the other hand, depends on the thermodynamic properties of the species. In the region behind the shock where there are very high temperatures, the internal degrees of freedom of the species are excited.

The temperature profiles at $x = 1.276$ m for the three species structure models are shown in figure 12. Again, the results of the Blottner and Liu–Vinokur models are indistinguishable. However, these results are very different from those of the ideal species model. The post-shock and peak boundary layer temperatures are higher for the ideal species model. This is purely due to the internal structure of the species. The internal structure enables the species to absorb the collisional energy thereby lowering the temperatures.

Since the ideal species lack internal structure, the collisional energy can only lead to increased dissociation. This is clearly seen in figures 13 and 14 which depict the mass fraction profiles of atomic oxygen (O) and nitric oxide (NO), respectively. While the

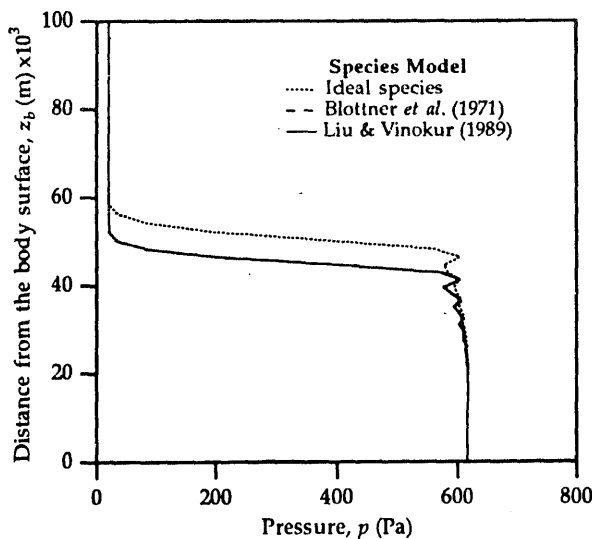


Figure 11. Effect of species model on pressure profiles.

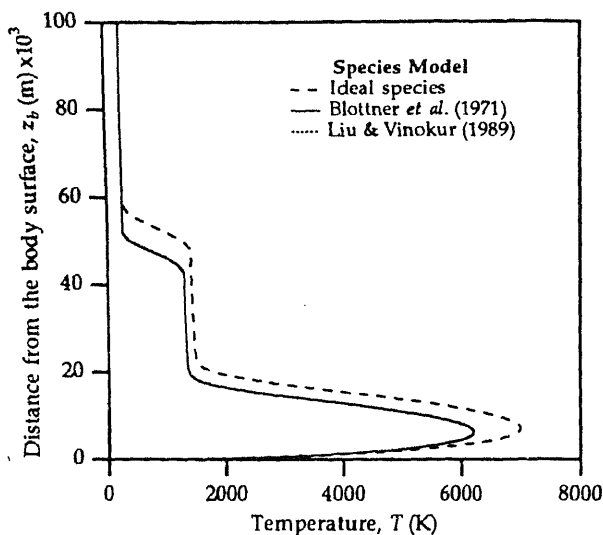


Figure 12. Effect of the internal structure of atoms and molecules on the temperature. Temperature profiles at $x = 1.276$ m are shown here for the nonequilibrium model.

difference between the results of the Blottner and Liu–Vinokur models are negligibly small, the ideal species model leads to larger amount of dissociation.

6.5 Gas model study

The principal aim of this portion of the work is to study the ideal, equilibrium, nonequilibrium (Liu–Vinokur) air models in the context of external hypersonic flows and determine their influence on the thermodynamic environment. Again a fine grid ($NK = 151$) was chosen and identical marching step sizes and grid spacings were used for all the computations.

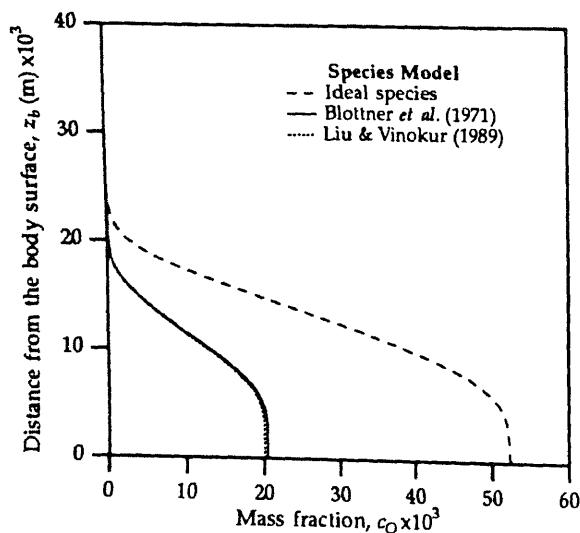


Figure 13. Effect of the internal structure of atoms and molecules on the chemistry. Mass fraction profiles of atomic oxygen (O) at $x = 1.276$ m are shown here for the nonequilibrium model.

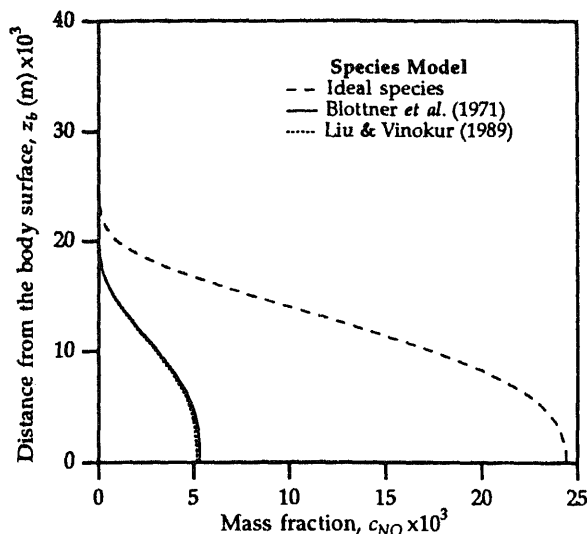


Figure 14. Effect of the internal structure of atoms and molecules on the chemistry. Mass fraction profiles of nitric oxide (NO) at $x = 1.276$ m are shown here for the nonequilibrium model.

The pressure and temperature profiles at $x = 1.276$ m are shown in figures 15 and 16, respectively. There are differences in the shock standoff distances for the three gas models with the shock standoff distance being the largest for ideal gas and the smallest for equilibrium air. The elevated temperatures behind the shock serve to excite the internal degrees of freedom of the gases that constitute the mixture. The effect of this is to alter the value of $\bar{\gamma}$ behind the shock, thus altering the standoff distance. The peak temperature within the boundary layer are significantly different between the three models. The effect of chemical reactions (finite or infinite rates) is to drain the kinetic energy contained in the fluid and use it in the chemical reactions and/or excitation of

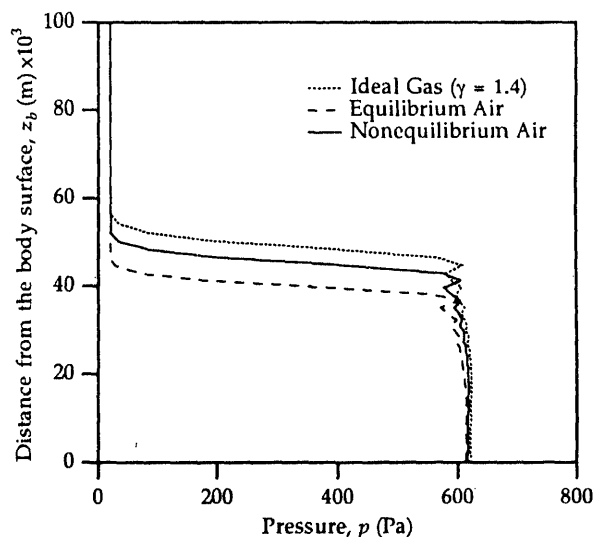


Figure 15. Pressure profiles at $x = 1.276$ m for ideal, equilibrium and nonequilibrium air models. Oscillations in the pressure are typical of central-difference schemes.

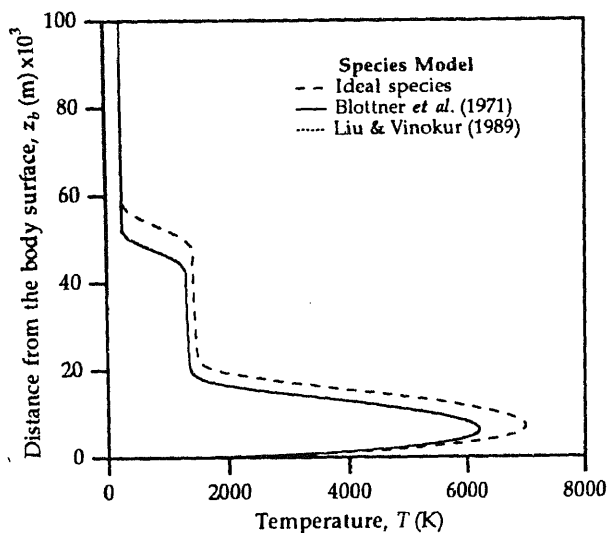


Figure 12. Effect of the internal structure of atoms and molecules on the temperature. Temperature profiles at $x = 1.276$ m are shown here for the nonequilibrium model.

difference between the results of the Blottner and Liu-Vinokur models are negligibly small, the ideal species model leads to larger amount of dissociation.

6.5 Gas model study

The principal aim of this portion of the work is to study the ideal, equilibrium, nonequilibrium (Liu-Vinokur) air models in the context of external hypersonic flows and determine their influence on the thermodynamic environment. Again a fine grid ($NK = 151$) was chosen and identical marching step sizes and grid spacings were used for all the computations.

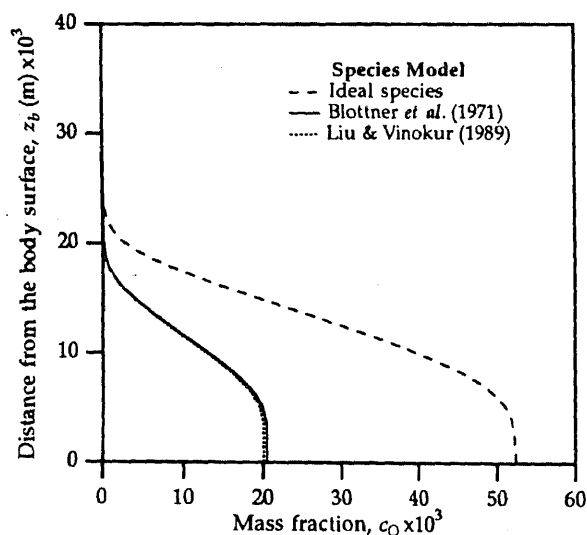


Figure 13. Effect of the internal structure of atoms and molecules on the chemistry. Mass fraction profiles of atomic oxygen (O) at $x = 1.276$ m are shown here for the nonequilibrium model.

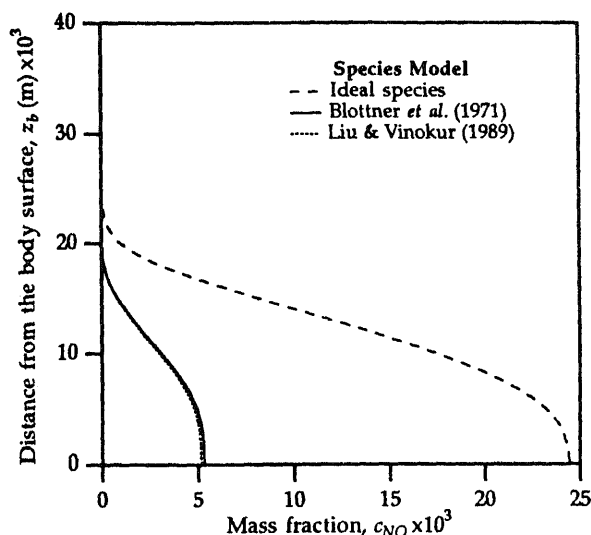


Figure 14. Effect of the internal structure of atoms and molecules on the chemistry. Mass fraction profiles of nitric oxide (NO) at $x = 1.276$ m are shown here for the nonequilibrium model.

The pressure and temperature profiles at $x = 1.276$ m are shown in figures 15 and 16, respectively. There are differences in the shock standoff distances for the three gas models with the shock standoff distance being the largest for ideal gas and the smallest for equilibrium air. The elevated temperatures behind the shock serve to excite the internal degrees of freedom of the gases that constitute the mixture. The effect of this is to alter the value of $\bar{\gamma}$ behind the shock, thus altering the standoff distance. The peak temperature within the boundary layer are significantly different between the three models. The effect of chemical reactions (finite or infinite rates) is to drain the kinetic energy contained in the fluid and use it in the chemical reactions and/or excitation of

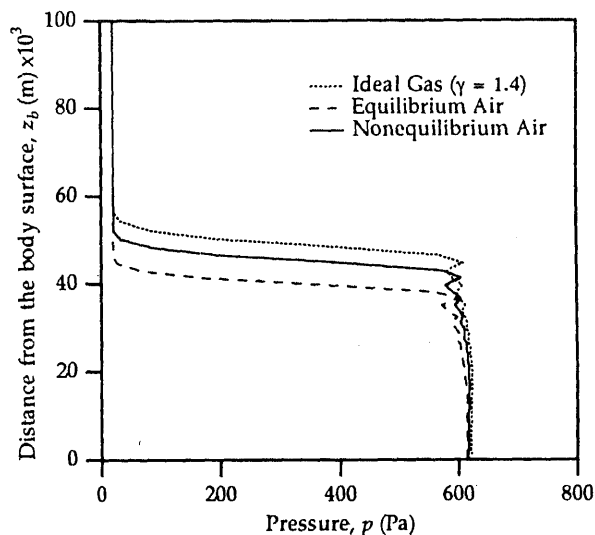


Figure 15. Pressure profiles at $x = 1.276$ m for ideal, equilibrium and nonequilibrium air models. Oscillations in the pressure are typical of central-difference schemes.

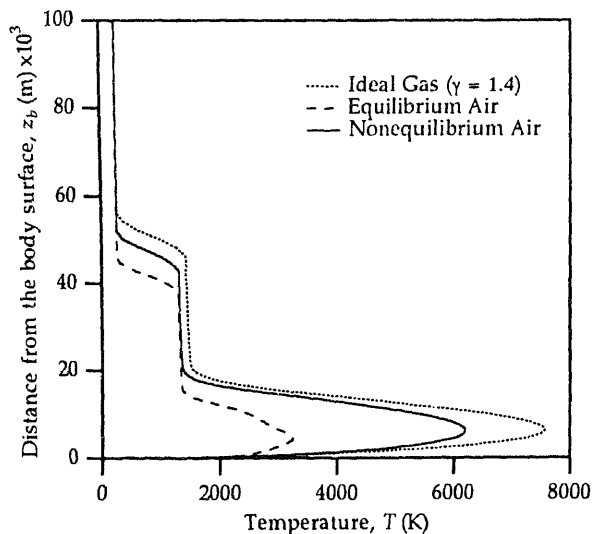


Figure 16. Temperature profiles at $x = 1.276$ m for ideal, equilibrium and nonequilibrium air models.

internal states of the constituent species. This shows up as an overall reduction in the peak temperature in the boundary layer.

The departure of the gas from ideal behaviour can be studied using the two parameters $\bar{\gamma}$ and $\bar{\beta}$ defined previously. The profiles of $\bar{\gamma}$ and $\bar{\beta}$ at $x = 1.276$ m are depicted in figures 17 and 18, respectively. Note that $\bar{\gamma}$ changes from its usual value of 1.4 immediately before the shock to about 1.3 for the nonequilibrium case and about 1.18 m in the equilibrium case. This is to be expected because the internal energy and enthalpy of the species are dependent on the local temperature which varies depending

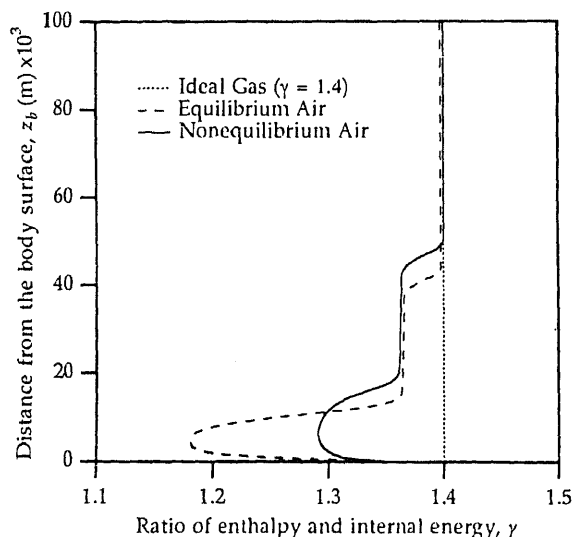


Figure 17. Profiles of the ratio of enthalpy and internal energy at $x = 1.276$ m for ideal, equilibrium and nonequilibrium air models.

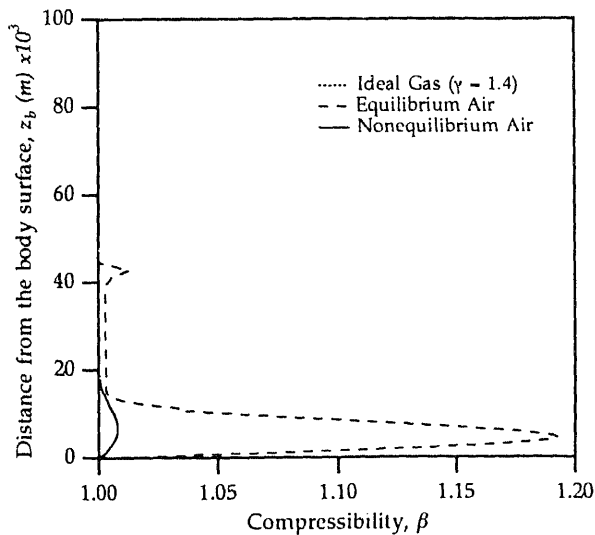


Figure 18. Profiles of the gas compressibility (β) at $x = 1.276$ m for ideal, equilibrium and nonequilibrium air models.

on the gas model. The parameter $\bar{\beta}$ which is a ratio of the local molecular weight to the average molecular weight varies from 1 to about 1.2. This parameter becomes important only in the reaction zone where the mass concentrations vary. Hence, there is no difference at the shock but there is substantial variation in the boundary layer. For the equilibrium air case, $\bar{\beta}$, varies at the shock. This difference can perhaps be attributed to the piecewise continuity of the curve fits for equilibrium air. This effect has to be studied in greater detail.

The axial variation of the surface pressure coefficient (C_p) is shown in figure 19. The ideal and nonequilibrium surface pressures are very nearly the same but differ from that for equilibrium air. This is quite surprising since the surface pressure is expected to be

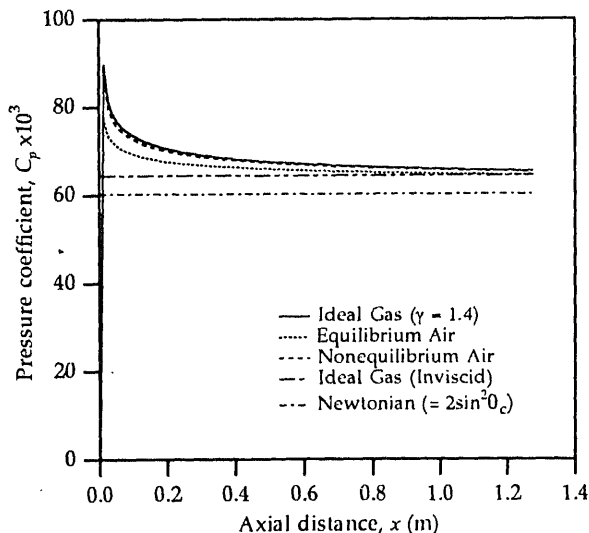


Figure 19. Effect of ideal, equilibrium and nonequilibrium air models on the computed surface pressure coefficient. The inviscid ideal gas value of C_p is extrapolated from the tables of Sims (1964).

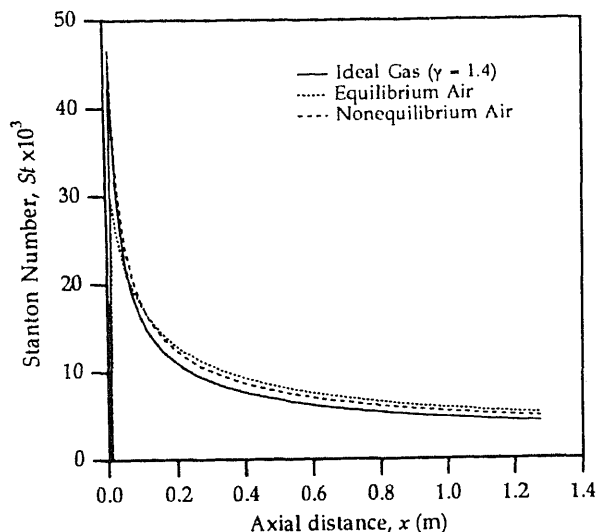


Figure 20. Effect of ideal, equilibrium and nonequilibrium air models on the computed Stanton number.

nearly the same irrespective of the gas model. The Newtonian value of the pressure coefficient is also shown along with the inviscid ideal gas value obtained from the tables of Sims (1964). Actually, the cone tables of Sims provide C_p values for freestream Mach numbers ranging from 1.5 to 20.0 and for cone angles ranging from 2.5° to 30° . The value corresponding to $M_\infty = 25$ for a cone angle of 10° was extrapolated from the tabulated values. The computed surface pressure coefficient for the ideal gas model asymptotes to the inviscid ideal gas value of Sims in the weak interaction zone.

The axial variation of the Stanton number (St) is shown in figure 20. The Stanton number is higher for the equilibrium case than the nonequilibrium case which, in turn, is higher than that for the ideal gas case.

The displacement thickness $\delta^*(m)$ of a wall boundary layer is defined as:

$$\delta^* = \int_0^{z_b} (1 - (\rho u_t)/\rho_e u_{te}) dz_b, \quad (74)$$

where z_b (m) is measured along a line normal to the cone surface, u_t (m/s) is the velocity tangential to the cone surface, and the subscript e denotes edge values. In the present PNS code the grid lines are always normal to the body surface. Consequently, locating the boundary-layer edge is quite simple. The edge of the boundary layer is located (at every step) by using the specific total enthalpy H of the gas. For an isothermal wall, the specific total enthalpy is dissipated in the viscous region close to the wall. The point z_b , at which the dissipation ceases, or equivalently where the total enthalpy reaches 98% of its freestream value, is chosen as the boundary-layer edge. See for instance the profiles of H at $x = 1.276$ m shown in figure 21. Using the value of z_b and (74), the displacement thickness is computed.

The axial variation of the displacement thickness of the boundary layer is shown in figure 22. There are two important features to be noted here. The first is that the axial variation of δ^* is shown only from about $x = 0.2$ m. This is because there was difficulty in locating the boundary-layer edge near the tip of the cone. For a high Mach number and low Reynolds number flow, the viscous-inviscid interaction near the tip region is

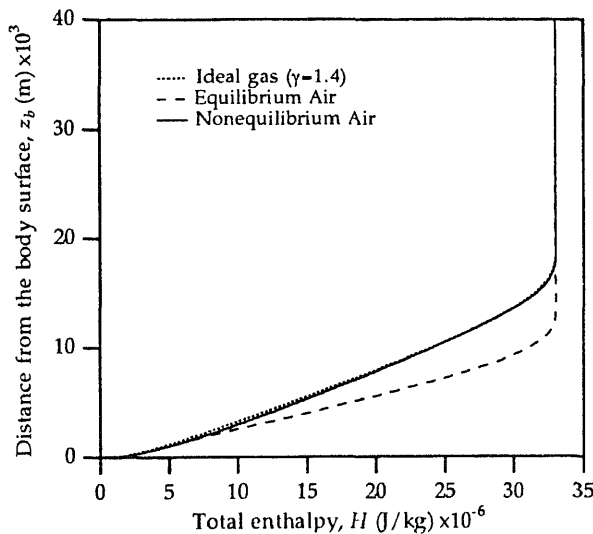


Figure 21. Profiles of total enthalpy at $x = 1.276$ m. The total enthalpy is dissipated in the viscous layer close to the wall when the wall is isothermal. This profile helps in locating the boundary-layer edge which is then used in the computation of displacement thickness.

very strong. In fact there is a merger of the shock and viscous boundary layer making it difficult to define the boundary-layer edge. While the boundary layer in the equilibrium gas is considerably thinner, the boundary layers in the ideal and nonequilibrium gases are nearly of the same thickness. The value of viscosity for the nonequilibrium and ideal gas cases is not very different from each other except in the high-temperature region near the wall. Further, the rate at which the total enthalpy dissipates in the boundary layer is the same for both the ideal and nonequilibrium cases.

An important feature of hypersonic external flows is that the viscous shock layers are extremely thin. This was verified in the present computations through the shock standoff distance. The approximate shock standoff distance at every x station was

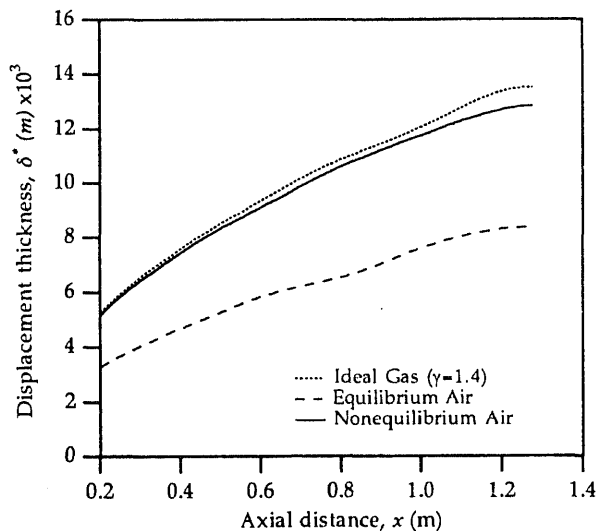


Figure 22. Axial variation of the computed displacement thickness for the ideal, equilibrium and nonequilibrium gas models. The computed data before $x = 1.276$ m are not reliable due to strong viscous-inviscid interaction which poses difficulties in locating the boundary-layer edge.

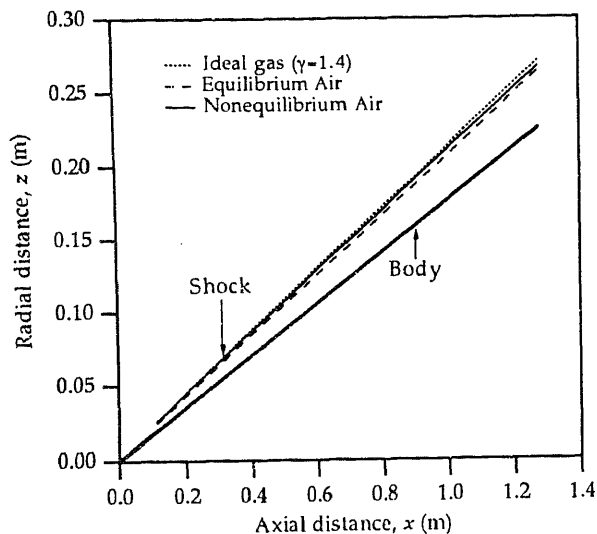


Figure 23. Comparison of shock shapes for ideal, equilibrium and nonequilibrium air models. The shock is "captured" as part of the solution. The shock is located by the peak in the pressure profile. Due to strong viscous-inviscid interaction it is not possible to locate the shock very accurately before $x = 0.1$ m.

determined by locating the peak point in the pressure profile at that station. Since the shock was not "fit" as an infinitesimally thin discontinuity but was captured, the pressure peak location was assumed to be a good measure. The shock standoff distance as a function of x for the ideal, equilibrium, and chemical nonequilibrium air models is shown in figure 23. Again the axial variation is shown only from $x = 0.1$ m because distinguishing between the shock and boundary layer before this location is quite difficult. It is clearly seen that the shock angle (measured from the body) is quite small. Further, the shock standoff distance for equilibrium air is the smallest while that for ideal gas is the largest. This is because of $\bar{\gamma}$ varying between 1.4 for the ideal gas and 1.18 for equilibrium air.

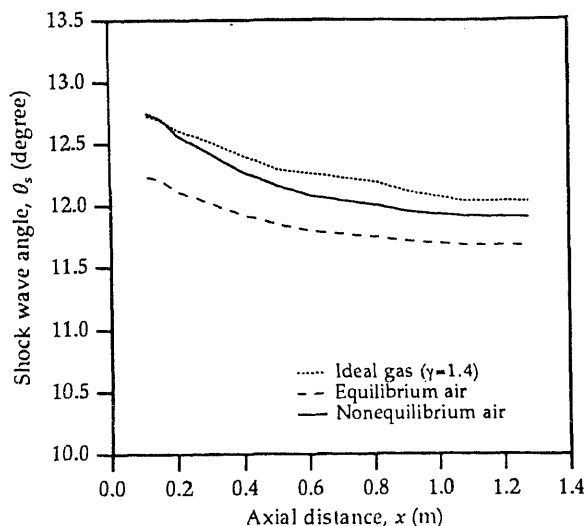


Figure 24. Approximate shock wave angles for ideal, equilibrium, and nonequilibrium air models. The displacement effect of the boundary layer causes the shock top curve initially (in the strong interaction zone) before it straightens out further downstream.

To determine whether or not the outer shock was conical, the local inclination of the shock was computed. The axial variations of the local shock angle for the ideal, equilibrium and chemical nonequilibrium air models are shown in figure 24. The shock inclination varies as a function of x while asymptoting to a constant value due to the displacement effect of the boundary layer. The fairly thick boundary-layer at the leading edge pushes up against the shock thus altering the conical nature. As the inviscid-viscous interaction decreases downstream, the shock becomes nearly conical.

All these results presented here were obtained on an HCL Magnum Multi-RISC computer in the CTFD Division of NAL. The ideal gas calculations took 166 s of CPU time, the equilibrium air calculations took 204 s of CPU time, and the nonequilibrium gas calculations with the Liu-Vinokur model for species thermodynamic properties took about 580 s of CPU time.

7. Concluding remarks

The laminar hypersonic flow of air around a 10° cone has been successfully computed using a finite-difference algorithm. Three gas models have been considered – (1) ideal gas ($\gamma = 1.4$), (2) equilibrium air with curve-fits for thermodynamic and transport properties, and (3) nonequilibrium air with finite-rate chemistry. Based on the results of the calculations the following observations can be made.

- The numerical algorithm chosen for the present study is consistent, in the sense that the solution converges with diminishing grid spacing. This has been verified for both the ideal and nonequilibrium air cases.
- The choice of an unbiased differencing scheme such as central difference leads to poor definition of the captured shock. Artificial dissipation which is introduced in an *ad hoc* manner in such schemes is essential to stabilise the solution and get rid of the high-frequency errors. Low levels of artificial dissipation lead to “ringing” at the shock. Further, this artificial dissipation has to be increased with increasing grid size. The arbitrariness associated with artificial smoothing can be removed through the use of robust upwind methods – methods which bias the differencing in the direction of acoustic signal propagation (Lawrence 1991).
- The results of the calculations can change significantly depending on the choice of the gas model. The idealisation that the species lack an internal structure is not very good. However, for the test case chosen in the present study, the results obtained using the Blottner model (Blottner *et al* 1971) for nonequilibrium calculations are not significantly different from those obtained using a more accurate model developed by Liu & Vinokur (1989). This is because the temperatures in the flowfield do not exceed 8000 K and below this temperature the thermodynamic properties of the species are nearly the same. However, the thermodynamic model of Liu and Vinokur is recommended for its accuracy above temperatures of 8000 K.
- Some key features of hypersonic shock layers have been shown in the present study – thinness of the viscous shock layer, the displacement effect on the outer shock due to the boundary layer, the strong viscous-inviscid interaction near the nose of the cone, the effects of high temperatures in the shock layer etc. have been demonstrated.

Apart from the accuracy of the species thermodynamic properties, there are also issues associated with the accuracy of the species transport properties and reaction

rates. The reaction rates and transport coefficients due to Blottner *et al* (1971) are fairly old and need to be updated. The sensitivity of the solutions to the accuracy of these parameters must be studied.

There is a paucity (at least in the public domain) of experimental results for hypersonic speeds and this makes the task of validation of a hypersonic code with high-temperature effects very difficult. To some extent, the aerothermodynamic environment encountered at hypersonic speeds can be created through a large shock tunnel (either combustion or free piston driven). This, however, does not currently exist in India.

In the present code, the block-tridiagonal solver is written for a general block of order n and this solver does not use any pivoting (either partial or full) in the LU decomposition of the block and is thus quite fast. However, this solver is slower than the one that is "hardwired" for a particular block size. This disadvantage of the general solver has to be carefully weighed against the advantage of reusability that such a solver has to offer.

I thank the AR & DB for support of this work under NAL Project No. CF-1-124. I also wish to thank Dr SS Desai for his encouragement. A portion of this work was presented at a Fluid Dynamics Colloquium at the Jawaharlal Nehru Centre of Advanced Scientific Research, Indian Institute of Science, Bangalore on September 22, 1993 for which I am grateful to Prof R Narasimha. Finally, I would like to thank the reviewers for their comments and suggestions.

List of symbols

a	speed of sound (m/s);
C_p	pressure coefficient; specific heat at constant pressure (J/kg.K);
C_v	specific heat at constant volume (J/kg.K);
\mathcal{D}	binary diffusion coefficient (m^2/s);
e	specific internal energy (J/kg);
e_t	specific total energy (J/kg);
\mathbf{E}	ξ -component of the flux tensor;
\mathbf{G}	ζ -component of the flux tensor;
H	specific total enthalpy (J/kg);
h	specific static enthalpy (J/kg);
Le	Lewis number;
M	Mach number;
Pr	Prandtl number;
p	static pressure (Pa);
\mathbf{Q}	algebraic vector of conservative variables;
\mathbf{q}	heat flux vector (W/m^2);
\mathcal{R}	universal gas constant (8314.34 J/kmol.K);
R	specific gas constant (J/kg.K);
Re	Reynolds number;
\mathbf{S}	inviscid/viscous source vector (axisymmetric);

St	Stanton number;
T	static temperature (K);
u	fluid velocity (mass-averaged) (m/s);
W	chemical source vector;
\dot{w}	mass rate of production (kg/m ³ .s);
β	grid stretching parameter;
$\bar{\beta}$	compressibility;
γ	ratio of specific heats (isentropic exponent);
$\bar{\gamma}$	ratio of specific enthalpy and internal energy;
θ	angle (degree);
κ	coefficient of thermal conductivity (W/m.K);
μ	coefficient of viscosity (Pa.s);
ρ	mass density (kg/m ³);
ξ, ζ	computational coordinates;
$\Delta\xi, \Delta\zeta$	grid spacing in computational space;
σ	safety factor;
ω	streamwise pressure gradient factor.

Subscripts

e	equilibrium quantity;
f	frozen quantity;
i, k	spatial indices;
r, s	species;
w	wall;
ξ, ζ	components in the ξ, ζ directions; derivatives w.r.t. ξ, ζ coordinates;
∞	freestream.

Superscripts

c	chemical quantity;
i	inviscid quantity;
v	viscous quantity.

References

- Anderson J D 1989 *Hypersonic and high-temperature gas dynamics* (New York: McGraw-Hill)
- Anderson D A, Tannehill J C, Pletcher R H 1982 *Computational fluid dynamics* (New York: McGraw-Hill)
- Bailey H E 1967 Programs for computing equilibrium thermodynamic properties of gases. NASA TN D-3921
- Blottner F G, Johnson M, Ellis M 1971 Chemically reacting viscous flow program for multi-component gas mixtures. Report no. SC-RR-70-754, Sandia Laboratories, Albuquerque, New Mexico
- Cambier J-L, Prabhu D K 1992 Numerical simulations of nonequilibrium shock layers with highly efficient implicit schemes. AIAA paper no. 92-2973
- Cambier J-L, Tokarcik S, Prabhu D K 1992 Numerical simulations of unsteady flow in a hypersonic shock tunnel facility. AIAA paper no. 92-4029
- Eucken A 1913 On the heat conductivity, the specific heat, and the internal friction of gases. *Phys. Zeit.* 14: 324-332
- Gordon S, McBride B J 1976 Computer program for calculations of complex chemical equilibrium compositions, rocket performance, incident and reflected shock, and Chapman-Jouguet detonations. NASA SP-273

- Lawrence S L 1991 Parabolized Navier–Stokes methods for hypersonic flows. *VKI Lecture Series in Computational Fluid Dynamics 1991–01* (Belgium: Von Karman Institute for Fluid Dynamics)
- Liu Y, Vinokur M 1989 Equilibrium gas flow computations: I. Accurate and efficient calculation of equilibrium properties. AIAA paper no. 89–1736
- Park C 1990 *Nonequilibrium hypersonic aerothermodynamics* (New York: John Wiley)
- Prabhu D K 1987 *A new parabolized Navier–Stokes code for chemically reacting flow fields* Ph D Dissertation, Iowa State University, Ames, IA
- Prabhu D K 1993 High-temperature effects in hypersonic flows. NAL PD CF-9319, National Aerospace Laboratories, Bangalore
- Prabhu D K, Tannehill J C 1986 Numerical solution of Space Shuttle Orbiter flowfield including real-gas effects. *J. Spacecr. Rockets* 23: 264–272
- Prabhu D K, Tannehill J C, Marvin J G 1988 A new PNS code for chemical nonequilibrium flows. *AIAA J.* 26: 808–815
- Prabhu D K, Subramanian N R, Saxena S K 1993 Hypersonic viscous flow computations using parabolized Navier–Stokes equations. NAL PDCF-9303, National Aerospace Laboratories, Bangalore
- Rakich J V, Venkatapathy E, Tannehill J C, Prabhu D 1984 Numerical solution of Space Shuttle Orbiter flowfield. *J. Spacecr. Rockets* 21: 9–15
- Rubin S G, Tannehill J C 1992 Parabolized/reduced Navier–Stokes computational techniques. *Annu. Rev. Fluid Mech.* 24: 117–144
- Schiff L B, Steger J L 1979 Numerical simulations of steady supersonic viscous flows. AIAA paper no. 79–0130
- Sims J L 1964 Tables for supersonic flow around right circular cones at zero angle of attack. NASA SP-3004
- Srinivasan S, Tannehill J C, Weilmuenster K J 1987a Simplified curve fits for the thermodynamic properties of equilibrium air. NASA RP-1181
- Srinivasan S, Tannehill J C, Weilmuenster K J 1987b Simplified curve fits for the transport properties of equilibrium air. NASA CR-178411
- Tannehill J C, Venkatapathy E, Rakich J V 1982 Numerical solution of supersonic viscous flow over blunt delta wings. *AIAA J.* 20: 203–210
- Vigneron Y C, Rakich J V, Tannehill J C 1978 Calculation of supersonic flow over delta wings with sharp subsonic leading edges. AIAA paper no. 78–1137
- Wilke C R 1950 A viscosity equation for gas mixtures. *J. Chem. Phys.* 18: 517–519

Trends in radar absorbing materials technology

K J VINOY and R M JHA*

Computational Electromagnetics Lab, Aerospace Electronics & Systems
Division, National Aerospace Laboratories, Bangalore 560 017, India

MS received 28 October 1994

Abstract. The research in the area of Radar Absorbing Materials (RAMs) has been actively pursued for at least four decades. Although resonant RAMs were originally designed by transmission line approach, and the broad band RAMs were obtained by multilayering, the quest for ultrawide band performance has led to novel approaches such as chirality and even exploring biochemical products. It is observed that radome materials are frequently used as RAMs. The understanding of the underlying principles of electromagnetic analysis and design, fabrication and the trends in RAMs reviewed in this paper could lead to indigenisation, and even pioneering next generation of RAM technology.

Keywords. Radar absorbing materials (RAM); Radar cross section (RCS) reduction.

1. Introduction

The introduction of microwave radar, during the Second World War revolutionised the contemporary air defense scenario. The use of microwaves, enabled radars to detect even distant aircraft targets, independent of weather and diurnal variations. This provided the initial motivation for designing aircraft which would be “invisible” to radar. Since the late 1970s, research efforts in this direction have intensified considerably.

Radar signal strength, reflected from a target, determines its detectability. This depends on the shape and size of the target and it is identified as its Radar Cross Section (RCS). Hence, the detectability of a target can be decreased by reducing its RCS. The RCS reduction is in fact important in many military and civilian applications. For the military, the RCS reduction of targets such as aircraft and missiles in hostile terrain is an important consideration. Similarly, making aircraft hangars near an air traffic control radar less reflective is a civilian application.

*For correspondence

Several techniques have been suggested for RCS reduction. They are:

- (i) Shaping,
- (ii) active loading,
- (iii) discrete (passive) loading, and
- (iv) distributed loading.

Shaping involves modifying the external features of the scatterer to reduce the reflections, usually in the backscatter direction. Although shaping appears to be an excellent method for RCS reduction, it has several limitations as well. Normally reduction is achieved only in a limited angular region and at the expense of increased RCS in other regions. Furthermore, shaping is effective only at higher frequencies; in fact, at lower frequencies, it is almost ineffective. Finally, shaping must be integrated in the system design stage, right from the beginning; it cannot be implemented as an afterthought (Knott *et al* 1985).

Methods (ii) and (iii), employ active/passive elements at selected points on the target (where the reflections are maximum), to reduce the overall RCS by means of phase cancellation. But these are narrow bandwidth methods, still mostly of academic interest.

The distributed loading technique (iv) is considered to be the most useful and universal one. It consists of covering the scatterer with suitable materials called the radar absorbing materials (RAMs). The RCS reduction in this case is achieved by both, absorption and redirection of electromagnetic energy. Ideally, RAM should be an ultrawide band paint, effective at all polarisations, and angles of incidence. For application to flying objects, it should also have high tensile and compressive strengths, resistance to impact, tolerance to fuels and hydraulic fluids, and most importantly, low density (Bhattacharyya & Sengupta 1991).

In order to increase their utility, suitable methods must be found to design broad band absorbers with narrow band RAMs as constituent components. Better still would be to search for alternative materials which have (ultra) wide band absorption characteristics. The answers to these are not readily available, owing to this being a classified area.

Although, almost all the literature on RAM is indeed classified, it is worth mentioning that historically, the origins of RAM have involved rather elementary principles in electromagnetic theory. Hence, considerable amount of relevant literature is also available in the open domain beginning from the late thirties. A closer scrutiny of this literature could give clues even to the RAMs that have been classified. Such a study could also give a feel of the historical perspective and the trends in RAM.

The historical perspective to the evolution of RAMs, including their basic performance characteristics is presented in §2 of this paper. Fundamental electromagnetic principles for the *analysis of RAMs*, both on the flat and curved surfaces are outlined in §3. This is followed by the *design and fabrication* of RAM where both the resonant and broad band RAMs (including chirals) have been discussed. Since the characterisation of RAMs is extremely important from the design and development perspective, relevant *measurement techniques* have been introduced in §5. Although RAMs were primarily intended for RCS reduction of aerospace vehicles, they have found *applications* in several other areas as well; they have been comprehensively listed in §6. Finally, a review of the *trends in RAM* is presented in §7.

2. The evolution of RAMs

Although the commercial production of RAMs started during the 1950s, the research on it was well underway even during the 1930s. The first absorber material to be patented was the one developed in the Netherlands in 1936 (*Naamlooze Vennootschap Machinerieën* 1936). This was a quarterwave resonant material in the 2 GHz region, in which carbon black was used to achieve dissipation, and TiO₂ to achieve a high dielectric constant.

As pointed out earlier, with the advent of radars during the World War II, the quest for absorbers intensified. Germany and the United States began to work on projects to develop such materials. It is interesting to know the contrast between the ultimate motives of the two countries; Germany was primarily looking for absorbers for radar camouflage, while in the US, the research was directed primarily toward absorbers that would improve the radar performance (Emerson 1973).

Two types of materials (MacFarlane 1945; Schade 1945) were successfully developed in Germany for use in submarines. The first, called *Wesch material* consisted of a semiflexible rubber sheet loaded with carbonyl iron powder, and was resonant around 3 GHz. The second material, *Jaumann absorber* was developed by a multilayer approach. This provided reflection coefficients, typically lower than -20 dB over a wide band (2-15 GHz) near normal incidence.

In the US, two types of absorbers, generally called HARP (Halpern-anti-radar-paint) were developed during the same time (Halpren & Johnson), which offered a reflection reduction of 15-20 dB at resonance. The airborne version, MX-410, was actually akin to a paint which utilised artificial dielectric materials of high relative permittivity. The second type was a rugged shipboard version consisting of a high concentration of iron particles in a neoprene binder. As with the MX-410, this too could operate in the X-band with a typical thickness of 0.07 inch. A salient feature of this version was the broadening of absorption around the resonant frequency (Montgomery *et al* 1948).

A well-known absorber developed around the same time as HARP, was the *Salisbury screen* (Salisbury 1952). A resistive sheet placed at quarter wavelength from the scatterer, was spaced by a low dielectric material. Salisbury screens operate by resonant technique, and were widely used in earlier anechoic chamber designs.

Yet another resonant absorber in wide use, was the *Dallenbach layer* (Ruck *et al* 1970). It consisted of a homogeneous lossy layer on a metal plate. The thickness of the lossy layer was selected so as to match its input impedance with the intrinsic impedance of the free space.

As discussed above, the absorbers developed in earlier stages were mostly narrow band in nature. This necessitated research towards obtaining broad band RAMs. Probably the very first approach to be tried was a multilayer structure (c.f. Jaumann absorbers discussed above). Most of the practical broad band RAMs were constructed using this technique. For example, the broadening of bandwidth of Salisbury screens was achieved by introducing additional layers of resistive sheets and spacers (Emerson 1973).

In some applications *bulk absorbers* were also used in place of sheets/layers. The conductivity of the bulk material reduces upon infusion of carbon in a matrix of spongy urethane foam. Based on this approach, the US Naval Research Laboratory developed a broad band absorber in the early 1950s. The conductivity was reduced here, by

dipping or spraying carbon onto a mat of loosely spun animal hair. These bulk absorbers could be readily used for controlling reflections for both, the indoor (anechoic) as well as the outdoor antenna measurement ranges.

During the late 1950s the focus shifted to problems of anechoic chamber implementation, such as (i) development of RAMs with reflection coefficients of -40 to -60 dB, (ii) lowering the operational frequency limit, and (iii) improved measurement techniques for RAM/anechoic chamber.

Attempts were also made to modify the resonant absorbers. For example, *circuit analog RAM* (CA-RAM) were obtained as Salisbury screen derivatives. CA-RAMs were obtained by depositing lossy material in geometric patterns on a thin lossless film (Severin 1956; Ruck *et al* 1970). The thickness of the deposit controlled the effective resistance of the layer, while the geometry of the pattern controlled its effective inductance and capacitance. Thus, the layer could be tailored into any value of impedance and its characteristic analysed in terms of lumped elements. The advantage of the CA-RAMs was that better performance could be obtained with comparatively less thickness.

In the 1960's, the possibility of using magnetic materials as RAM was explored intensively. Thin *magnetic RAMs* (e.g. the ferrites) with low reflection coefficients were fabricated which could operate at lower resonant frequencies than had earlier been feasible with the dielectric materials (Bowman 1968). Although thinner compared to the dielectrics, these materials are much heavier and prone to disintegration at higher frequencies.

It came to light in the 1980s by serendipity, that some biotech products have ultrawide band absorption characteristics. Subsequent experiments confirmed that substantial RCS reduction was indeed possible by dissolving these compounds in aircraft structural materials. Following this spectacular revelation, the Department of Defense, US, immediately classified the compound. There are, however, conjectures that this *ultrawide band RAM* is a retinyl compound belonging to the class of Schiff-base salts. This is a powdery black substance which is much lighter (1/10) than the ferrites; it is also said to have been used in making RAM paints for stealth aircraft (Adam 1988).

More recently, a new class of homogeneous materials, making use of the chiral property have also found applications as RAMs (Jaggard & Enghetta 1989). Such chiral RAMs depend upon their optical activity and circular dichroism, and the backscatter RCS is independent of polarisation. As compared to the dielectric and magnetic RAMs discussed above, the chiral RAMs have vastly superior RCS reduction characteristics (Jaggard *et al* 1990, 1991).

3. Approaches to the analysis of RAM

The radar absorbing materials are characterised by their electromagnetic (EM) properties such as the permittivity ϵ , and the permeability μ . These are usually normalised with respect to the corresponding free space quantities (ϵ_0, μ_0).

$$\epsilon_r = \epsilon/\epsilon_0, \quad (1)$$

$$\mu_r = \mu/\mu_0. \quad (2)$$

The relative permittivity ϵ_r and the relative permeability μ_r are in general complex

quantities, denoted by

$$\varepsilon_r = \varepsilon'_r + j\varepsilon''_r, \quad (3)$$

$$\mu_r = \mu'_r + j\mu''_r, \quad (4)$$

where ε'_r and μ'_r are the real components and ε''_r and μ''_r are the imaginary components of the dielectric constant and the relative permeability of the medium respectively. The imaginary components account for the losses in the medium. ε''_r depends on the conductivity of the medium, and μ''_r on the intensity of magnetisation. Equations (3) and (4) are usually written for convenience as

$$\varepsilon_r = \varepsilon'_r(1 + j\tan\delta_e), \quad (5)$$

$$\mu_r = \mu'_r(1 + j\tan\delta_m), \quad (6)$$

where

$$\tan\delta_e = \varepsilon''_r/\varepsilon'_r, \quad (7)$$

$$\tan\delta_m = \mu''_r/\mu'_r. \quad (8)$$

In (7) and (8), $\tan\delta_e$ and $\tan\delta_m$ are known as the electric and magnetic loss tangents and are used to express the losses in the medium. Materials having large values for their dielectric loss tangents are generally called dielectric materials, while those with large $\tan\delta_m$, the magnetic materials.

Both the dielectric and the magnetic materials could be used in the fabrication of RAMs. Although the loss mechanism in these differs, both absorb the EM energy and convert it into heat. Since the distances from the transmitting radars are usually large, this absorption of energy may not heat up the material much. But absorption is not the only mechanism by which RAMs operate. The reflections at the *RAM free space interface* could be controlled by properly designing the coatings.

Two important parameters that dictate the propagation of waves through a medium are its refractive index n , and the characteristic impedance Z . In terms of the fundamental EM parameters, these are defined as

$$n = (\mu_r \varepsilon_r)^{1/2}, \quad (9)$$

$$Z = [\mu/\varepsilon]^{1/2} = Z_0 [\mu_r/\varepsilon_r]^{1/2}, \quad (10)$$

where Z_0 is the intrinsic impedance of the free space. This is a constant ($= 377\Omega$) and is independent of frequency. It is clear from (9) and (10) that both n and Z are complex quantities.

3.1 Analysis of RAMs on flat surfaces

The method most commonly used for the analysis of a flat surface coated with a RAM is the transmission line approach. In this approach, the RAM is expressed as a lossy matching network between the free space and the scatterer which is represented in terms of a complex impedance.

Reflections occur when the EM wave travels from one medium to another. This reflection is represented by a term called the reflection coefficient r . In the case of a wave entering into a large flat surface from free space,

$$r = (Z_1 - Z_0)/(Z_1 + Z_0), \quad (11)$$

where Z_1 is the input impedance at the boundary surface.

Thus the condition for zero reflection is:

$$Z_1 = Z_0. \quad (12)$$

Equation (12) requires that the surface input impedance be independent of frequency, and real. The input impedance for a wave entering at normal incidence at the interface with free space is given by

$$Z_1 = Z \tanh \gamma d, \quad (13)$$

where Z is the characteristic impedance of the RAM defined in (10), d is the thickness of the RAM,

$$\gamma = (j\omega\mu(\sigma + j\omega\epsilon))^{1/2}, \quad (14)$$

$$\omega = 2\pi f, \quad (15)$$

γ being the complex propagation constant of the medium, σ the electrical conductivity of the medium, and f the operational frequency.

The reflection coefficient of a coated body is affected by the interference of the waves reflected at the surface of the RAM and at the metal-RAM interface. Their phases depend on ϵ , μ and d while their relative amplitudes depend on the losses in the material (c.f. (13) & (14)).

The input impedances for the parallel and perpendicular polarisations are different for oblique incidence. At an angle of incidence θ with respect to the normal, $Z_{1\text{para}}$, the input impedance for the parallel polarisation is given by:

$$Z_{1\text{para}} = Z \cos \theta \tanh(\gamma d \cos \theta), \quad (16)$$

and $Z_{1\text{perp}}$ for the perpendicular polarisation is defined as

$$Z_{1\text{perp}} = [Z \tanh(\gamma d \cos \theta)] / \cos \theta. \quad (17)$$

The corresponding reflection coefficients are

$$r_{\text{para}} = (Z_{1\text{para}} - Z_0 \cos \theta) / (Z_{1\text{para}} + Z_0 \cos \theta), \quad (18)$$

$$r_{\text{perp}} = (Z_{1\text{perp}} \cos \theta - Z_0) / (Z_{1\text{perp}} \cos \theta + Z_0), \quad (19)$$

where r_{para} is the reflection coefficient for parallel polarisation and r_{perp} is the reflection coefficient for perpendicular polarisation.

Thus knowing ϵ_r , μ_r and σ of the material, the input impedance can be determined by substituting (1)–(4), (10) and (13)–(15) in (11). Similarly by using (16)–(19) the reflection coefficient corresponding to an angle of incidence θ can also be determined (Ono & Suzuki 1967).

Multilayer absorbers having broad band absorption characteristics can also be used for the RAM applications. Their analyses are similar to those of the single layer RAMs. The input impedance of the entire substrate, upon inclusion of an additional layer, depends on the properties of all the previous layers. A numerical program for computing the characteristics of multilayered RAM using a minimisation method is presented by Maffioli (1970). Ono & Suzuki (1967) computed the reflection coefficient and the attenuation for both the perpendicular and parallel polarisations for multilayered RAM structures using the transmission line approach. The measurements on actual samples (Ono *et al* 1967) showed their method to be viable.

3.2 Analysis of curved surfaces coated with RAM

The foregoing discussion is valid for the RAMs on flat surfaces in general. Analysis and design of coatings on curved surfaces, in contrast, is extremely complex.

3.2a Theorems on absorbers: Two theorems introduced by Weston (1963) facilitate the analysis of RAM on curved surfaces.

Theorem 1. *If a plane EM wave is incident upon a body consisting of material such that $\mu_r = \epsilon_r$, then the far zone backscattered field is zero, provided that the direction of incident propagation is parallel to an axis of the body about which a rotation of 90° leaves the shape of the body together with its material medium invariant.*

Theorem 2. *If a plane wave is incident upon a body consisting of a material such that the total tangential EM field components satisfy the impedance boundary condition*

$$\mathbf{E} - (\mathbf{n} \cdot \mathbf{E})\mathbf{n} = Z[\mu_0 \epsilon_0]^{1/2} \mathbf{n} \times \mathbf{H}, \quad (20)$$

on the surface, and the surface of the body is invariant under a 90° rotation about some axis, then the far-field backscattered field is zero if the direction of incidence is along this axis. In the above expression \mathbf{n} is the unit outward normal of the surface and $Z = 1$ is the free space.

The above theorems are extended to predict the specular backscatter from any smooth arbitrarily convex bodies.

3.2b Effect of curvature: Bodies with curved surfaces in the high frequency domain (i.e. when they are electrically large) have two components for their backscatter, viz. the specular, and the diffracted field contributions. The specular contribution from an absorber covered body is $|r|^2 \sigma$. Here r is the flat plate reflection coefficient, and σ is the specular reflection. The calculation for the diffracted field contribution is rather involved as it is affected by the shape of the scatterer, its conductivity and the direction of the ray with respect to the axis of the body. A detailed analysis is given by Weston (1963) and Bowman & Weston (1966).

For extending these theorems to bodies in the resonance region (i.e. when their largest dimension is comparable to the wavelength), additional conditions must be satisfied by these curved surfaces. These ensure that, the creeping wave contribution is also reduced considerably for a general smooth convex scatterer. The boundary condition defined by the second theorem is a very good approximation under the assumptions (Leontovich 1957):

- (i) The refractive index of the material is very large and has a large imaginary part.
- (ii) The EM fields outside the boundary vary slowly in the near field, exterior to the scatterer.
- (iii) The radii of curvature of the surface are large compared to the interior wavelength (i.e. corresponding to the wavelength of EM wave propagating inside the scattering medium).
- (iv) Variations of ϵ and μ in the body over the distance of the interior wavelength are small. This condition is relaxable for thin coatings on metallic surfaces.

To summarise, an absorber with a large and complex refractive index significantly reduces the backscattered RCS in the resonance region of arbitrary convex bodies for the resonant frequencies where the main contribution to scattering is from the specular reflections and the creeping waves.

3.3 Approaches to analysis of RAMs on a general surface

In the EM scattering and diffraction problems, the method of moments (MOM) presents one of the most versatile approaches. MOM is well known to predict accurate solution for the class of problems it treats. The applicability of MOM and other grid based approaches to the RAM analysis have therefore been explored by various workers. Rogers (1986) applied MOM to the RCS prediction of arbitrarily shaped conducting bodies coated with RAMs. MOM was also modified to effectively analyse the shapes used in the construction of anechoic chambers. Yang *et al* (1992) have developed a periodic moment method (PMM) for the analysis of two dimensional lossy dielectric scatterers. CRAY-YMP was used to calculate the reflection and transmission coefficients of periodically distributed wedges illuminated by a plane wave.

The grid-like segmentation of the MOM is also employed in the spatial network method by Kashiwa *et al* (1990). The scattering body, an aircraft, is divided into a number of cells of size $\lambda/30$. In this time domain method, the equivalent circuit of the coated scatterer is constructed in terms of bulk impedances to compute the field patterns.

Yet another time domain analysis conforming to the Bergeron's method in three dimensional space and time is used to analyse resonant RAMs (Aoto *et al* 1987). The variation of field distribution for the changes in magnetic loss is given. Absorption waveform in the time domain are expressed as a function of the

FDTD) approach is used in conjunction with an optimisation routine for forward scattering (Strickel & Taflové 1990). The scattering of electromagnetic waves from three dimensional targets are also provided by Holland & Cho (1986) reported that the scattering from cylindrical targets and cylinders even though only coarse

numerical methods, including the FDTD is used to analyse scatterers. However, with the trend towards higher frequencies (in GHz range) most of the realistic scatterers (or such *electrically large* scatterers, which are analysed using Physical Optics (PO) (Macleod 1989) for large objects coated with RAMs

an expression for RCS analyses of thin shells. They considered both the specular and creeping waves. They concluded that the latter gave rise to the backscattering, while its effects are negligible for the forward scattering. An attempt was made using semiempirical methods for cylindrical scatterers (Swarnakumar *et al* 1989) treated as the phasor sum of the field

scattered by the air-dielectric interface and that by the equivalent conducting body which differs from the actual body because of the lens action of the shell.

Alexopoulos (1969) applied GO to obtain the reflected electric field for large spheres ($ka = 50$ to 1000) coated with inhomogeneous dielectrics. A series solution was also obtained for the backscattering GO computations for bodies of revolution coated with homogeneous RAMs (Arsaev 1982). The effect of the curvature of the scatterer and the conditions for the RCS reduction were also examined.

Although the GO is extremely simple to apply, it is well known to give rise to singularities and also predict discontinuous fields. This was overcome by the introduction of a class of high-frequency asymptotic theories which essentially introduced corrections to the GO in the form of diffraction coefficients. The Geometrical Theory of Diffraction (GTD) is one such example which has been extremely popular and also extensively modified to suit the various modelling requirements. Consequently, the asymptotic theories have found their way into the analysis of RAMs as well.

The RCS reduction of structures such as a cavity absorber has been pioneered by Lee *et al* (1985) for coatings on circular waveguides. They presented a high frequency asymptotic method to analyse EM scattering from circular waveguides coated with lossy materials. It was observed that a coating less than 1% of the radius can give 13 dB reduction in the RCS of circular waveguide terminated with a perfect electric conductor. It was also found that large reductions in RCS are possible at small angles of incidence.

The asymptotic high frequency techniques could also be employed for the estimation of monostatic RCS of finite planar metallic structure coated with a lossy dielectric. The RCS is expressed in terms of the diffraction coefficient involving the Maliuzhinets's function (Bhattacharyya & Tandon 1984). Bhattacharyya (1990) used the uniform asymptotic theory of diffraction (UAT) which is a modification of the GTD, to analyse the performance of flat plates.

More recently, Shi *et al* (1993) have analysed conducting bodies covered partially with absorbent materials. A salient contribution of this work is in establishing an equivalence between the RAMs to be used in the scale model and the prototype.

4. Design and fabrication of RAMs

The design of RAMs involves identifying suitable materials, and specifying their dimensions and compositions. Similarly, the steps involved in the fabrication of these materials are crucial to their performance.

There are basically two concepts that are used in the design of absorbers for the RCS reduction (Musal & Hahn 1989) as given below.

Matched characteristic impedance concept: The characteristic impedance of the material is made nearly equal to the intrinsic impedance of free space. This essentially means that the values of its relative permittivity and relative permeability must be equal.

$$Z = Z_0, \quad (21)$$

hence from (10),

$$\epsilon_r = \mu_r. \quad (22)$$

Equation (22) is the condition for zero reflection at the front surface of the material. The material must be made sufficiently thick so that the EM wave is attenuated considerably as it propagates into the material. The internal reflections produced when backed by a metallic surface attenuate in the round-trip path.

Matched wave impedance concept: The wave impedance at the front surface of a metal-backed absorber layer (the impedance when looking into it) is made equal to the intrinsic impedance of the free space. This results in the complete absorption of the EM energy falling on the surface.

Thus for an absorber of finite thickness backed by a conducting plate, (13) gives the wave impedance. Combining (12) and (13), the thickness is determined as,

$$Z_0 = Z \tanh \gamma d. \quad (23)$$

Thus the formulae (1)–(19) can be used appropriately for computing the thickness of the RAM required for a specified performance. Knott (1979) has derived the formulae for the minimum thickness condition, for a specified reflectance of a single layer absorber, of given characteristic impedance and refractive index.

The matched wave impedance concept is frequently used in the design of the *resonant absorbers*. Although such resonant RAMs require comparatively thin layers of absorber, they satisfy the conditions for RCS reduction only at one or more discrete frequencies. On the other hand, the *nonresonant absorbers* have RCS reduction over a broader band of frequency. Hence these constitute the two basic types of RAMs.

4.1 Resonant RAM

The thickness of the resonant i.e. narrow band RAMs are related to the material properties and the operating wavelength.

4.1a Salisbury screen: The resonant absorbers discussed in §2, strive to efface the reactive part of their surface impedance by suitably incorporating the unique properties of quarter wavelength. The simplest method is to make use of a resistance card, whose surface resistance is equal to the free space impedance. When sheet is placed at a quarter of a wavelength from the metal plate, the input impedance in the plane of the sheet and the impedance of free space are in perfect match. Such absorbers are called Salisbury screens (figure 1). A detailed analysis of the Salisbury screen is available in Ruck *et al* (1970).

The equivalent circuit for the Salisbury screen is shown in figure 2. The conditions to be satisfied by the resistive sheet are:

$$\epsilon_r'' \gg \epsilon_r', \quad (24)$$

$$Z_0 = 1/\sigma d, \quad (25)$$

i.e.,

$$d = 1/Z_0 \sigma, \quad (26)$$

where d is the thickness of the resistive sheet. The choice of the material for the sheet is constrained by (24) while its thickness is determined from (26).

A proprietary material, Uskon cloth manufactured by the US Rubber Company was used as the resistive sheet in the Salisbury screens. Materials of relative permittivity

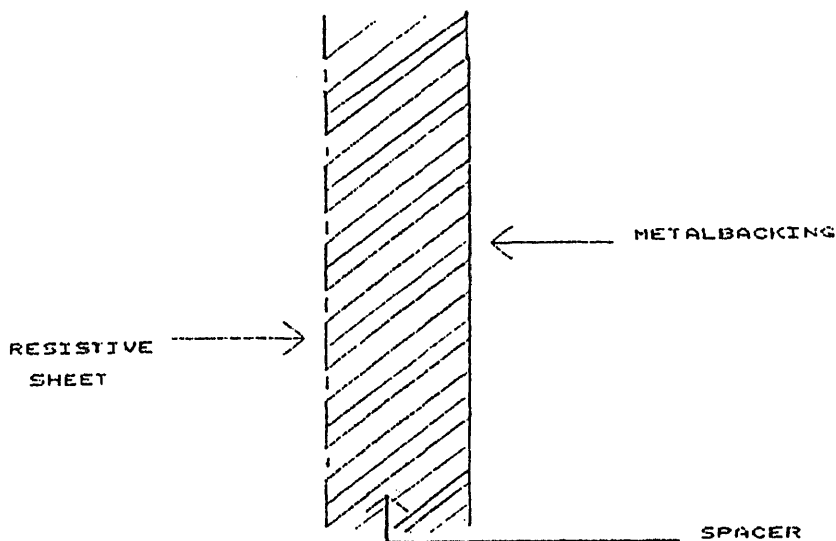


Figure 1. The Salisbury screen.

approximately equal to unity, were used as spacers. The operational bandwidth is reduced if the spacer material has a higher permittivity, as the wavelength inside it, is a function of this value. Plywood or some jelly type material having $\epsilon_r < 1.05$ can be used as spacer. In one such case, the calculated frequency sensitivity for VSWR was found to be below 1.10 (that is, the reflection coefficient of 0.05) over a bandwidth of $\pm 5\%$ (Emerson 1973).

The operational frequency range for the Salisbury screen can be broadened by using a number of such layers. Fante & McCormack (1988) describe the analysis for Salisbury screens using multiple resistive sheets. The cases in which the screen is electric or magnetic or their multiple combinations are discussed. It is also shown that a relatively large reduction in specular reflection is possible over considerably wide bandwidths by using relatively few Salisbury screens. Furthermore, these reductions can be achieved

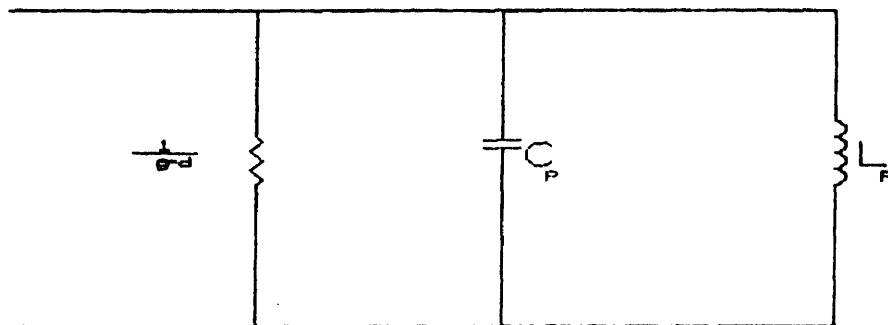


Figure 2. The equivalent circuit of the Salisbury screen.

even if the incident wave is not normal to the surface, or the surface is curved, or the fabrication is not accurate.

A multilayer Salisbury screen uses several layers of Salisbury screens, suitably spaced to resonate at discrete frequencies, which results in broad band RAMs. The bandwidth of such a structure depends on the number of sheets used. Their construction is similar to the Jaumann absorber. The resistance of these sheets decreases near-exponentially towards the back plate.

4.1b Magnetic absorbers: The electric Salisbury screens place the lossy material where the electric field is maximum. It is also possible to place a magnetic screen where the magnetic field is maximum, that is, right on the metal surface.

The necessary conditions to be satisfied are:

$$\mu'' \gg \mu', \quad (27)$$

$$\omega u'' d, \quad (28)$$

$$\mu'' \gg \mu', \quad (29)$$

μ and d , satisfies (13) along with (27)–(29) at the frequency of interest for fabrication. When the thickness is very small compared to λ , the conditions (from (13)) to be satisfied by these materials are (21):

$$(30)$$

$$(31)$$

$$(32)$$

of the order of $\lambda/10$. Thus the magnetic parts as they require less thickness

the presence of carbonyl iron or ferrites in these materials which try to orient themselves fast, the dipoles lag the impressed magnetic energy in the material. The dissipating element. Each ferrite has thicknesses which are related to an optimum value (Naito & Suetake 1971). The thickness such a way that the first matching occurs. The first matching thickness is 1 mm. This peculiar characteristic of ferrites (Naito 1970). Three mechanisms for the relaxation magnetisation, the resonance motion. The first among

due to their magnetic properties tend to shift the Curie point (typically 500–1000°F). At high temperatures, they are constrained by

The permeability of the ferrites depends on their composition. The peaks of the permeability curves of such materials can be shifted over frequency by replacement of Fe^{+3} ions in the lattice by divalent and tetravalent metal ions such as Co^{+2} and Ti^{+4} (Amin & James 1981). Cobalt-substituted barium hexaferrite has significant variation of permeability in the microwave region. The ferromagnetic resonant frequency of this hexagonal ferrite varies between 2 and 46.5 GHz depending on the amount of cobalt substituted.

The ferrites are typically sintered in the form of small rigid tiles. The density of these tiles depends upon the composition and the method of processing (i.e. different temperatures and pressures applied during manufacture). The surface resistance can be varied during manufacture by suitable selection of molecular structure and loading concentration. The material is hot-pressed onto the metallic surface at several thousands of psi pressure. Bonding of the materials is also a crucial process. It is thus possible to obtain magnetic RAMs with different characteristics by slightly varying the fabrication procedure (Hahn 1991). The effects on the magnetic permeability of different $\text{Ni}_{0.1}\text{Zn}_{0.5}\text{Fe}_2\text{O}_4$ samples are studied in a number of such cases. It is observed that the real and imaginary parts of permeability increase with the tile density.

The commonly used binding media are natural rubber or synthetic elastomers such as isoprene, neoprene, nitrile, silicone, urethane, and fluoroelastomer. Although the EM absorption properties of the binding media normally remain constant, there are instances where they behave anomalously. It is reported (Veinger *et al* 1990) that at low filler contents, low molecular weight rubbers such as dimethyl-phenyl-siloxane rubber, dimethyl-diphenyl-siloxane rubber, and dimethyl-siloxane rubber showed strong absorption near 10 GHz.

High frequency absorption of a random assembly of noninteracting single domain ferromagnetic particles with positive uniaxial magnetic anisotropy can be calculated numerically for values of the signal frequency below the natural resonant frequency of such materials (Hempel & Roos 1981). If the lower frequencies are used, an additional absorption is found to be present at the negative field at which the resonance frequency crosses the signal frequency. A set of measurements has also been specifically reported by Hempel & Roos (1981) for the polycrystalline barium ferrites.

Just as their dielectric counterparts, the magnetic RAMs too can be used in multilayered forms. Basically, this is done to enable the employment of materials that have favourable permeability curves at different frequencies.

4.1c Dallenbach (homogeneous) layer: Yet another dielectric RAM, the *homogeneous absorber* typically consists of a binding medium (e.g., polyurethane foam) in which carbon powder and TiO are dispersed. The amount of carbon determines the dissipation factor, while the TiO content accounts for the high permittivity thereby resulting in a thinner layer.

The design for the absorber is generalised by Fernandez & Valenzuela (1985). They considered the case for a single layered absorber backed by a perfectly conducting flat surface for normal incidence. Substituting (5), (6) and (10) in (13) one obtains

$$\mu_r/\epsilon_r = \{(\cosh 2\beta ds + \cos 2\beta d)\cos \delta_m\}/\{(\cosh 2\beta ds - \cos 2\beta d)\cos \delta_e\}, \quad (33)$$

$$\sin 2\beta d = p \sinh 2\beta ds, \quad (34)$$

where

$$s = \tan [(\delta_m + \delta_e)/2], \quad (35)$$

$$p = \tan[(\delta_m - \delta_e)/2], \quad (36)$$

$$\beta = \{2\pi(\mu_r \epsilon_r)^{1/2} \sin[(\delta_m + \delta_e)/2]\} / \{\lambda(\cos \delta_e \cos \delta_m)^{1/2}\}. \quad (37)$$

The design curves for different conditions are obtained from (33) and (34). These lead to the solution for d as:

$$d = \pi/[2\beta(1 + ps)], \quad p < 0.25, \quad (38)$$

$$d = (1/2\beta)[6(1 - ps)/(1 + ps)]^{1/2}, \quad p \geq 0.25. \quad (39)$$

The quarter-wavelength solution is obtained by substituting $p = 0$ in (38).

The lowest order solution for the materials having both electric and magnetic losses, is given in terms of plots by Fernandez & Valenzuela (1985). They have also concluded that the materials having moderate losses will have a larger bandwidth for absorption.

An alternate solution along with optimal design curves for the EM and physical parameters such as the surface impedance, and magnetic and dielectric loss tangents, and the thickness in wavelength is given (Musal & Hahn 1989) for the normal incidence. Design curves are plotted for different d/λ and $\tan \delta_e$.

A further generalisation by Musal & Smith (1990) resulted in an integrated single design curve which is plotted as contours of constant $d/\lambda \operatorname{Re}(\epsilon)$ and contours of constant $\operatorname{Im}(\epsilon)/\operatorname{Re}(\epsilon)$ on a plane of $(d/\lambda \operatorname{Im}(\mu), d/\lambda \operatorname{Re}(\mu))$.

Yet another example for the *homogeneous absorbers* is the Halpern Anti-Radar Paint (HARP). Disk-shaped aluminium flakes dispersed in a rubber matrix serve as the dissipating elements in HARP. High concentration and a high degree of alignment of these disks resulted in a large permittivity (Knott *et al* 1985).

A new kind of single layer absorber postulated by Gauss (1982) could be made from filaments of radar absorbing chaff mixed in a solid binder. Metallic strands of 50 micrometers length could be dispersed in the medium having a dielectric constant of about unity at spacings of about one-third their length. Theoretically, RCS reduction of about 30 dB is achievable over 10–100 GHz if the filaments are distributed uniformly.

Multiple layers of the homogeneous absorbers, each with a different composition could also be used to obtain broad band absorbers. In practice, this results in an inhomogeneous absorber to be discussed later in § 4.2c.

4.1d Circuit analog RAM: If the continuous resistive sheets of the Salisbury screens are replaced by a conductive layer deposited in appropriate geometrical patterns, circuit analog RAMs (CA-RAM) are obtained. These shapes, usually in the form of loop antennas, dipoles, crosses or triangles may have susceptance as well as conductance, which improves the flexibility of the design of such RAMs.

The design of these patterns is similar to that of a frequency selective surface (FSS). But CA-RAM is different from the FSS since the latter does not require resistance variation. Both involves the design of frequency sensitive reactive elements.

Control over admittance of the conductive sheet in CA-RAM is obtained by depositing the conducting materials in suitable geometrical shapes. The shapes employed have the property of resonating at a discrete frequency, thus dissipating the energy falling on it. Typical shapes include strips, wires, intersecting wires, dipoles, crossed dipoles, Jerusalem cross structure etc. These sheets with the lossy elements are separated from the conducting surfaces by lossless dielectric spacers.

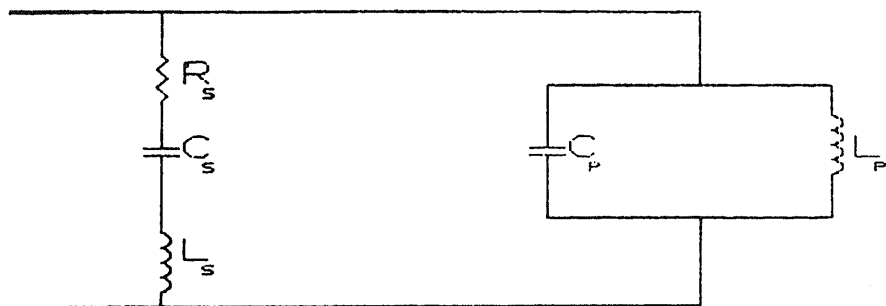


Figure 3. The equivalent circuit of the CA-RAM.

The equivalent circuit of the CA-RAM is shown in figure 3. By adjusting the shape of the elements, and/or by adjusting the number of elements per unit area, the resonance, and the zero reflection may be obtained at any frequency. The optimum values for both of these are selected. It is clear that a better uniform loading is obtained when the elements are in the molecular level; i.e., by using magnetic dipoles in molecules.

For a periodically loaded surface, the input impedance at oblique incidence, for the parallel and perpendicular polarisations (i.e., E parallel and perpendicular to the plane of incidence respectively) are:

$$Z_{1\text{para}} = X \cos \theta \quad (\text{parallel polarisation}) \quad (40)$$

$$Z_{1\text{perp}} = X / \cos \theta \quad (\text{perpendicular polarisation}), \quad (41)$$

where X is the element impedance and θ the angle of incidence. The reflection coefficients are obtained by substituting these expressions in (18) and (19) (Ruck *et al* 1970). Consequently, at normal incidence ($\theta = 0^\circ$), the impedances and hence the reflection coefficients for the two polarisations are identical.

The absorber is effective only if the magnetic vector of the incident wave has a component in the direction of the magnetic dipoles. Hence two separate grids with arrays of elements in parallel, with an angle of orientation of 90° between the grids, each for a polarisation, may be used to make a RAM independent of polarisation.

4.2 Broad band absorbers

Unlike the resonant absorbers discussed above, the broad band absorbers have a wider band of frequency over which considerable RCS reduction is possible. This band of frequency is usually limited only by the changes in the material properties.

4.2a $\mu = \epsilon$ absorbers: Thick layers of materials satisfying the condition $\mu_r = \epsilon_r$ are used in the first type of nonresonant absorbers called the $\mu = \epsilon$ absorber. In these RAMs most of the incident energy is absorbed by the material itself, before reaching the metal plate at the back. Thus for a material with both dielectric and magnetic losses (Severin 1956),

$$Z = [\mu_0 / \epsilon_0]^{1/2} [\mu(1 - \tan \delta_m) / \epsilon(1 - \tan \delta_e)]^{1/2}. \quad (42)$$

For the matching condition with free space, the characteristic impedance of the

material should be:

$$Z = Z_0 = 377 \Omega. \quad (43)$$

An efficient $\mu = \epsilon$ absorber should have large and equal values for dielectric and magnetic loss angles, and relative permittivity and permeability. Ideally, these EM parameters should also be independent of frequency.

The electric and magnetic field strengths are attenuated in the bulk of the material exponentially. Thus the minimum thickness for a specified attenuation is determined from (Hurmuth 1983)

$$[E_r/E_i] = e^{-2\beta d}, \quad (44)$$

or,

$$d = (1/2\beta) \ln[E_r/E_i], \quad (45)$$

where E_r and E_i are the reflected and incident fields respectively.

Although absorbers with μ_r equal to ϵ_r are ideal, this is one of the most difficult conditions to meet in fabrication. The EM properties of the materials depend on the composition and are in general frequency sensitive. Some ferrites have been made with this constraint for a limited frequency range (Bhattacharyya & Sengupta 1991).

4.2b Low density absorbers: The low density absorbers are made with the materials with relative permittivity nearly equal to that of free space. If the relative permeability is also 1, the material will absorb all the energy falling on it. Most of the materials satisfying these conditions are materials of low density. Thick layers of these materials are used to dissipate the energy, thus reducing the reflections when backed by a metal plate. *For analysis and design purpose, this may be considered as a special case of the $\mu = \epsilon$ absorber.*

One such material manufactured, Spongex was 2 inches thick, and had a reflection coefficient of about -20 dB over a frequency range of 2.4-10.0 GHz. It was possible to further lower the (low) frequency limit by increasing the material thickness (Emerson 1973).

4.2c Inhomogeneous layer absorber: The absorbers should present a minimum discontinuity at the free space-absorber interface and the losses should increase, as one moves into it, to absorb the incident EM energy completely. This is obtained either by tapering of homogeneous layers of absorber material, or by arranging different layers parallel to the metal surface such that the loss tangent increases toward the base plate. The latter results in an *inhomogeneous absorber*. In another method of construction, layers of lossless dielectric and sheets of poorly conducting material, the surface resistivity of which decreases towards the base metal plate by a constant factor from one sheet to the next, are placed alternately. Theoretical predictions for one such case shows that reflection is below 0.1 for nearly 3 octaves (Bowman 1968). However, these values are not achievable in practice, since it is difficult to fabricate a number of layers having different parameters accurately.

In a bulk absorber with a multilayered structure, the EM properties of different layers are made to vary for obtaining maximum absorption of the incident energy. The thickness of the bulk material is not important. The refractive indices of the layers are such that the value increases as one goes into the material. A simple fabrication technique, where the foam is dipped in an aqueous solution of graphite, the aquadag, of different concentrations, is described by Jones & Wooding (1964). The injection of carbon is made uniform by alternately compressing and expanding the foam inside the

solution. Yet another multilayer absorber was fabricated by making use of pyrolysed polyacrylonitrile fibre blankets for different layers (Ono *et al* 1967).

It is possible to synthesise an inhomogeneous absorber with a number of layers with different composition of carbon using the convergence circle method (Ono *et al* 1979). The propagation constant is related by an empirical relation to the graphite density in the media. The thickness of the material as well as the required concentration of the graphite content in a polystyrene foam for a given angle of incidence and figure of merit have been computed. (The figure of merit is defined (Shimizu & Suetake 1969) as the ratio of the RAM thickness to the wavelength of the lowest frequency at the maximum angle of incidence.) These *wide incidence angle response absorbers* are reported to have very good reflection properties (-20 dB) at normal as well as at oblique incidences up to $\pm 70^\circ$.

Analytical determination of the functional form of the variation of $\mu(z)$ and $\varepsilon(z)$ necessary to produce a specified maximum reflection coefficient over a range of frequencies and incidence angles for a particular thickness of the material is an intractable problem. In practice, some model variations are assumed for $\mu(z)$ and $\varepsilon(z)$ to analyse the material (Ruck *et al* 1970; Perini & Cohen 1991).

Naito & Suetake (1965) used a relay impedance method to design a multilayered absorber which was primarily meant for anechoic chambers. With the input impedance at the metallic wall being zero and the intrinsic impedance of free space 377 ohms, the absorber layer is essentially a transformer between these. When multiple layers are used, obviously, this transition is achieved in steps. Naito & Suetake (1965) have computed the frequency response of absorbers with different number of layers and plotted this for comparison. These formulae were later modified (Shimizu & Suetake 1967) for the optimum thickness using lossy dielectric materials. They have reported a figure of merit of 0.42 as compared to the earlier designs, for which it was nearly 2.

4.2d Geometric transition absorbers: The difficulty in making multiple layers with different values of surface resistivity can be bypassed by using a single layer of uniform material in geometrical shapes in which the absorption coefficient increases towards the metal surface. Wedge, pyramidal, and conical shapes are typically used for this purpose. Such shaped absorber panels are widely used in the wall construction of anechoic chambers. However, these are not used in airborne applications due to obvious aerodynamic considerations. The geometric transition method can also be combined with the inhomogeneous layer method to further increase the bandwidth of the absorber. Combining these two techniques, results in a better angular performance. Typically, for an inhomogeneous pyramidal absorber, the reflection coefficient is below 0.1 for incidence angles up to 50 – 60° (Ruck *et al* 1970).

This section is concluded by emphasising that the broad band absorbers cannot be used by themselves, for aircraft and missile applications due to their inherent bulkiness. However, when mixed with structural materials, composites are obtained having broad band RCS reduction characteristics.

4.3 Chiral materials

The materials discussed so far are in general composites, and are sometimes even anisotropic in nature. The design and the manufacture of these materials are often

Table 1. Comparison of characteristics of simple isotropic and chiral media (Jaggard & Engheta 1989).

Characteristics	Simple medium	Chiral medium
Constitutive relations	$D = \epsilon E$ $H = (1/\mu)B$	$D = \epsilon E + j\zeta B$ $H = j\zeta E + (1/\mu)B$
Wave equation	$\nabla \times \nabla \times E - \beta^2 E = 0$	$\nabla \times \nabla \times E - \beta^2 E - 2\omega\mu\zeta \nabla \times E = 0$
Wave numbers	$\beta = \omega[(\mu\epsilon)]^{1/2}$	$\beta_{\pm} = \pm \omega\mu\zeta + [\beta^2 + (\omega\mu\zeta)^2]$
Wave intrinsic impedance	$Z = [(\mu/\epsilon)]^{1/2}$	$Z_c = Z/(1 + Z^2\zeta^2)$
Eigen modes	Linear polarisation allowed	Only right and left circular polarisation allowed

difficult. Their EM properties are frequency-dependent and hence they are usually narrow band. In contrast, a new class of materials based upon EM chirality (handedness) when used as RAMs (Jaggard & Engheta 1989), offer an increased bandwidth along with improved reflection coefficient characteristics.

Chirality combines optical activity (rotation of the plane of polarisation) and circular dichroism (change in polarisation ellipticity) in the medium which is expressed by two unequal wave numbers corresponding to the two circularly polarised eigen modes with opposite handedness. These materials are isotropic as well as reciprocal. The fundamentals of chirality are available in literature (Post 1962; Kong 1975). The constitutive relationships and characteristics of such media are compared with simple isotropic media in table 1.

In table 1, ζ is the chirality admittance which expresses the handedness of the medium, and affects the wave transmitted through the medium. In fact, ζ is a measure of the cross coupling of electric and magnetic fields in the medium. The twist in the major axis of the polarisation ellipse depends on the sign of ζ .

The chirals consist of an isotropic host medium which is embedded with randomly oriented identical microstructures, such as the microhelices. The geometric dimensions and density of these chiral microstructures determine the EM parameters ϵ , μ and ζ .

The absorption in chiral materials is determined by the chiral skin depth while their reflection properties are governed by ϵ , μ and ζ . The backscattering in these materials is independent of polarisation. Hence the introduction of these chiral materials for Salisbury screens and Dallenbach layers, results in increased absorption over wider frequency band with the added advantage of thinner layers (Jaggard *et al* 1990). For the electric Salisbury screen, the surface impedance may be expressed as

$$Z_1 = jZ_c \cot \beta_c d, \quad (46)$$

while for the magnetic screen, it is given as

$$Z_1 = -jZ_c \tan \beta_c d. \quad (47)$$

Substituting these in (23), the thicknesses of the chiral layer for a required maximum reflection coefficient can be determined. Thicknesses of the order of $\lambda/5$ give rise to 20 dB more absorption as compared to nonchiral materials (Jaggard *et al* 1990).

An EM pulse propagation analysis in the chiral media has shown that the chiral coatings can be used for broad band RCS reduction even in high power pulsed radar environment (Engheta & Zablocky 1990).

More recently, thin layers of biisotropic (nonreciprocal) chiral materials that can act as polarisation transformers with ultrawide range of frequency have been proposed by Tretyakov & Oksanen (1991).

4.4 The construction of RAMs in practice

Antenna mount structures, especially those employed in measurement ranges or chambers are fabricated by using nonreflective materials. Blore (1964) describes the fabrication and testing of four different polyfoam structures made for this purpose. The scattering mechanism for polyfoam includes the effect of cell size, material homogeneity, water content, surface finish and matching methods. The low echo area, mechanical rigidity and relative ease for manufacture and usage make these materials the best suited for antenna support.

Bradshaw (1989) has studied the effect of construction methods on the RCS reduction in structural materials such as syntactic foam, light weight honeycomb, single skin fibre reinforced composites (FRC) as well as the sandwich composites. The application of these materials having microwave absorption properties for the aircraft RCS reduction is quite apparent.

Broad band response becomes essential for RAMs used in radar targets in a wide band radar environment. The reflectivity curves of Eccosorb (NZ-series) materials suitable for such applications have been evaluated by Hurmuth (1983). Their performance is analysed for a relative bandwidth of about unity. Compared to the performance at a relative bandwidth of 0.01, these absorbers are still less helpful in hiding targets from wide band radars (He *et al* 1992).

Some of the Eccosorb materials have good absorption properties even above 35 GHz. In particular, the CR-series Eccosorb materials have been characterised by Hemmati *et al* (1985). It is concluded that the measurements are in perfect match with the curves formed by extending the specifications for these materials at lower frequencies. The reflection and absorption coefficients increase with the density of iron in the material. It is also found that the absorption coefficient decreases by a factor of two, when the samples are cooled to cryogenic temperatures.

Ferrites or carbon may be interspersed in rubber to make absorbers for covering the edges of paraboloidal reflectors (Yokoi & Fukumaro 1971). The antenna performance is improved by as much as 10 dB at 70°–180°. The addition of carbon increases the permittivity of acetylene black rubber, with the change in the imaginary part being more predominant; theoretical computations for the same have been compared with the experimental results by Kumar (1987).

Aspects of modelling with spinel ferrites, magneto and dielectric composite materials for forming RAM are overviewed by Deleuze (1992). Ferrofluid composites containing mono layers of aluminium particles dispersed in a decalin carrier are considered by Davies *et al* (1986) for frequencies above 100 GHz. Chains of aluminium particles with oxide coatings are developed. It is observed that if the plane of polarisation is parallel to the chain axis, there is a minimum effect on the variation of frequency.

Ferrite sludge obtained by precipitation treatment of industrial waste water has been reported to possess microwave absorbing properties (McCauley *et al* 1980). The powder so obtained is sintered into a mechanically coherent ferrite ceramic material. Composites of ferrites and resins 9.5 mm thick are reported to operate as microwave absorbers. These composites are found to be operational in the S-band (68% composite)

as well as in the X-band (75% composite), and are suggested as an inexpensive choice for RCS reduction.

A broad band absorber with 50% relative bandwidth is obtained with a two-layer ferrite-resin mixture incorporating short metal fibres. Materials of 4-6 mm thickness with fibres of 1-4 mm length and 60 micrometer diameter are found to be useful in the X-band (8-13 GHz). Good performance for wide angles of upto 45° is also obtained for these materials (Hatakeyama & Inui 1984).

The constitutive relations for the maximum absorption of EM energy falling on a medium has been presented by de Hoop (1981). Metal coated carbon fibres were also used as conducting elements in RAM (Yi & Gan 1991). The use of such fibres results in improved attenuation and a wider bandwidth. The absorption properties are independent of the thickness of the material, but are related to fibre dimension and concentration.

Broad band microwave absorption cannot be achieved by homogeneous materials. However, it was noticed experimentally that some compounds made with small conducting grains dispersed in a dielectric host can be used as broad band RAMs (Guillot & Bobillot 1991). Various mixture laws for such designs are developed by Guillot (1992) for the computation of dielectric permittivity. Mixtures, for which the quasistatic approximation is not matched inside the conducting medium, are considered. This results in artificial lossy diamagnetic behaviour for which a model is derived.

The application of chiral materials on spherical targets offers significant improvement in the reflection coefficient (15-25 dB) as compared to the conventional materials for the radii of curvature of the order of half a wavelength or larger (Jaggard *et al* 1991).

Polymers containing silicon are observed to possess superior electrical and mechanical properties and can be used for RCS reduction of aircraft. A fabrication process, in which electropolymerised film comprising such polymers or copolymers is deposited on the surface of an anode, is described by Nagasubramanian *et al* (1990). Conductive polymers like polypyrrolle, polyaniline and polyacrylthiophenes have also been reported in literature as materials in the fabrication of RAMs (Olmedo 1992).

5. Absorber measurement techniques

The measurements on RAMs are conducted either to survey or verify product performance and material properties. In this context, usually three forms of material are measured:

- (i) Finished absorber panels or products,
- (ii) Thin sheets used as components in the design and fabrication process,
- (iii) Samples of uniform bulk materials.

A number of methods are explained in various books and papers on microwave measurements (Ginzton 1957; Montgomery 1957; Ono *et al* 1983; Knott *et al* 1985; Curran 1993). Some of the important methods are listed below.

- | | |
|--------------------------------|-------------------------|
| ■ Parallel plate | ■ Resonant cavity |
| ■ Coaxial probe | ■ Admittance tunnel |
| ■ Transmission line techniques | ■ Free space techniques |
| ■ Waveguide system | |

5.1 Parallel plate method

The parallel plate method requires that the material being tested is homogeneous, and nonmagnetic. The sample taken should be thin (less than 10 mm), flat and perfectly smooth. An LCR meter or an impedance analyser measures the impedance across a pair of parallel plates separated by the sample. The errors in this low frequency (less than 100 MHz) method are mainly due to fringing fields at the edges. Guarded electrodes can be used to eliminate the edge capacitance.

The features of this method are as below.

- Broad band
- Accurate and sensitive
- Simple and convenient
- Inexpensive

The RAMs, though usually operative in the microwave region, can nevertheless be accurately characterised in the audio frequency region. Lynnworth (1964) observed that the insertion loss in the microwave region is correlated to the capacitance of the material at the audio frequencies. Avcoat and polyurethane foams have been tested by the parallel plate method successfully (Lynnworth 1964). Acrylic panels in which molybdenum wires of 1 mil diameter are embedded at varying spacings are used as the standard for establishing the correlation.

5.2 Coaxial probe technique

The coaxial probe technique is useful for isotropic, homogeneous and nonmagnetic materials. Samples of 'infinite' thickness with one flat surface, and without any air gap may be tested with this method. This method is best suited for liquids and inviscid fluids. The minimum thickness for solid samples is about $20/\epsilon_r^{1/2}$ mm (Curran 1993).

The advantages of the method are:

- Broad band
- Simple and convenient

5.3 Waveguide system

Reflectivity measurements of finished products at lower frequencies (typically 100–400 MHz), can be performed by placing a test sample at the aperture of a waveguide. Since the measuring probe is not movable, adjustments are made at the attached shorting stub. Although only single frequency measurement is possible at a time, stepped frequency measurements is also possible with additional equipment. Swept frequency interferometer has been used with an aperture matched exponential horn for the rapid real time assessment of inhomogeneities in planar microwave absorber panels (Baker & van der Neut 1988). The residual reflection in such a system is as low as –37 dB.

A circular waveguide can be used more effectively than coaxial cables for measuring the plane wave reflection properties of layered dielectrics (Rudduck & Yu 1974). This method is applicable to media containing high refractive index absorbing materials. The measurement set up can be very easily calibrated and the method is obviously nondestructive.

5.4 Transmission line techniques

The transmission line techniques require that the voltage reflection coefficient of a homogeneous material sample be measured. This is done by multiple measurements with different terminations using slotted section. The samples must be carefully machined so as to accurately fit inside waveguide or coaxial line without any air gaps and their faces should be flat, smooth and perpendicular to the line of axis. The thickness of the samples must be in the range $\lambda/18$ to $\lambda/2$. Periodic dropouts, when the sample thickness approaches $\lambda/2$, is a major failure of the method. This method is suitable for anisotropic and magnetic materials.

In the case of coaxial cable environment, the diameter of the standard cable may not be big enough for a test sample to be placed inside. This problem is avoided by using a larger section of cable of about one inch diameter connected to the standard cables using suitable taper sections. Unambiguous determination of the electrical thickness of the sample necessitates multiple frequency measurements. The sample is backed by metal sheet (a short), or an open circuited termination. The changes in the standing wave pattern inside the line upon inserting the sample lead to the characterisation of the material.

The attractive features of the method include its being (i) broad band, and (ii) simple and convenient.

The transmission line technique using coaxial cables is accurate up to 10%, whereas, the waveguide method is precise up to 5% if the samples are machined properly (to a precision of 0.03 mm).

Although the transmission line techniques are useful to a great extent in characterising the RAM, they have some limitations as well. Better results are guaranteed by the SCOC and thin sample methods if some precautions are taken (Falkenbach 1965). The sample thickness should be of the order of $\lambda/50$ for the thin sample method, while it should be $\lambda/5$ for the SCOC method. It is preferred that the material sample have dc resistance of about 1 k Ω /mm thickness.

Some of the algorithms used in computation of results from transmission line measurements are listed in table 2.

Table 2. A comparison of computational algorithms employed in transmission line methods (Curran 1993).

Algorithm	Measures	Computes	Ideal for
Nicolson-Ross	$S_{11}, S_{12}, S_{21}, S_{22}$	ϵ_r, μ_r	Magnetic, short & lossy samples; fastest computation speed
Precision (NIST)	$S_{11}, S_{12}, S_{21}, S_{22}$	ϵ_r	Long low-loss samples; highest accuracy if no discontinuities present
Fast	$S_{11}, S_{12}, S_{21}, S_{22}$	ϵ_r	Faster and better method for lossy materials than the previous one
Short-backed	S_{11}	ϵ_r	Liquids and powders
Arbitrary-backed	S_{11}	ϵ_r	Thin films, and high temperature applications

With swept signal sources or using time domain reflectometry technique, fast measurements are possible over a wide range of frequencies. The time domain reflectometry technique involves sending a narrow pulse waveform which is scanned by a computer controlled broad band sampling oscilloscope. This is transformed into the frequency domain by the fast Fourier transform (FFT). Selection of timing windows is crucial for the accuracy of the measurements. Improved stability of the pulse generators as well as the sharpness of the pulses result in more accurate performance.

5.5 Cavity technique

A part of the cavity resonator is filled with the sample without affecting the field distribution inside. This technique, essentially a single frequency one, involves complex analysis. But it is suitable for anisotropic materials as well. This is the most accurate technique, especially for low loss homogeneous materials and liquids. Tunable cavities are used in practice when multiple frequency measurements are required.

5.6 Admittance tunnel method

The admittance tunnel is a long absorber-lined box illuminated by a small antenna at one end and fitted with a test aperture at the other. A hybrid Tee is used to isolate the transmitted and received signals. A continuous wave (CW) signal source is used for transmission. Since the transmitting and receiving antennas are the same, the residual reflections could be minimised. The box shape is useful in obtaining a near planar incident wave with little disturbance from the outside environment. This method, developed by Rockwell International Corporation, is ideal for thin sheets.

5.7 Free space techniques

The free space techniques are in general high frequency, non-contacting and non-destructive methods, typically applicable to large, flat, parallel faced homogeneous samples. Notwithstanding the title, the measurements are not always performed in free space-like environment, but are not done inside the confines of a waveguide or a cavity. It is difficult to measure the loss of thin and low loss samples with these methods. In general, the errors in free space techniques are due to: (i) finite sample size, (ii) non-plane wave illumination (iii) mechanical instability or misalignment between sample and antenna, and imperfect quality of anechoic environment.

Typically, the accuracy of measuring ϵ_r is 1–5% while the value of $\tan(\delta)$ is precise to ± 0.005 . Some of the important methods under this category are listed below.

- NRL arch method
- RCS range method
- Tunnel method
- S-parameter method
- Interferometer method (open resonator)
- Direct spatial standing wave measurements
- Double horn-reflector system

5.7a NRL arch method: This near-field method, developed by Naval Research Laboratory (NRL), operates by illuminating the absorber panel by a small horn antenna. A second horn antenna, which is also mounted on the same arch-like

framework, receives the reflected energy. This being a near-field method results in lower reflectivity values. Only the amplitude characterisation of the reflected signals is possible here. Using swept oscillators, the measurement over a range of frequencies can be taken (Lehto *et al* 1991).

5.7b RCS range method: The RCS range method is a far-field technique in which the material sample is mounted on a flat plate which is in turn installed upon a target support column in a vertical position. The panels are evaluated in a more realistic environment akin to the one in which they may actually be used. In order to accommodate swept frequency signal sources, dedicated costly instrumentation may be required. The size of the plate is selected to be greater than 3λ , typically, 5λ . Due to limitation in determining the null width, the maximum length of the edges of the sample should be less than 15λ .

5.7c Interferometer method: The nature of reflections from a sample measured outside the confines of a closed system can also lead to characterisation of EM properties of the material. This set-up is similar to that of transmission line technique (§5.4) but for the sample holder and sliding short, which are replaced by a tuner and a horn. The sample is mounted on a metal support plate, a few feet in front of the horn. The tuner is used to remove the residual reflections. At higher frequencies, this method is similar to the Fabri Perot Optical Interferometer technique, used in characterising optical materials. An open cavity is used at microwave frequencies.

The open cavity method has been used successfully to obtain the complex magnetic permeability of materials loaded with conducting powders (Guillot & Bobillot 1991). The material characteristics are obtained by measuring the resonant frequency and the quality factor of the cavity when a slab of the sample is placed inside. This method is, however, not suitable for taking measurements at high temperatures.

5.7d Free space tunnel method: The sample in the form of a sheet is placed between transmitting and receiving antennas. The spacing on either side of the sample should be greater than $2d^2/\lambda$, where d is the largest dimension of the antenna or the sheet. The power transmitted through the sample is measured to determine its EM properties.

5.7e Free space S-parameter method: This is an accurate measurement method in which the S parameters are measured both in amplitude and phase using sophisticated equipment such as a vector network analyser. Although the material characterisation is better, the capital expenses are high.

5.7f Direct spatial standing wave measurement technique: The direct spatial standing wave measurement technique is used for precise characterisation of absorber panels, especially of pyramidal shape. An infinitesimal dipole antenna is moved about the panel and the field strength is measured at each position.

This method is suitable for measurements at oblique angles of incidence. Absorbers can be quickly characterised over a wide range of frequencies and incident angles with this method. The scattering parameters like VSWR and scatter angle have been measured for pyramidal absorbers using this method (Ono *et al* 1983). The error in the

measurement is found to be $\pm 20\%$ for VSWR and $\pm 3^\circ$ for scattering angle at 4 GHz, when measurements are taken 1.5 m away from the sample.

5.7g Double horn-reflector system: A new method of characterising rectangular panels of homogeneous RAMs have been suggested by Kent (1982). In this wide band technique, the permittivity and permeability of the materials are obtained from the measured values for S_{11} and S_{21} . The accuracy of this frequency domain method is stated to be 5–10%.

Of the methods discussed above, the NRL arch method is the most famous and the most frequently used. Although this method is universal, it has some disadvantages as well. The disadvantages of this method are listed and some novel free space methods are suggested by Brumely (1987). These are

- (i) inverse synthetic aperture radar imaging for samples with large area;
- (ii) wide band coherent radar measurements and;
- (iii) modification to the conventional time gathered RCS measurements, which are made as a function of the aspect angle of the sample wall of the targets.

Yet another nondestructive technique for characterising absorber-lined chambers is to use short dipoles as the measuring probes (Mishra *et al* 1982). These dipoles are reported to have a discrimination of the order of -25 dB. The microwave goniometer could also be used for characterising absorber panels (Jones & Wooding 1964).

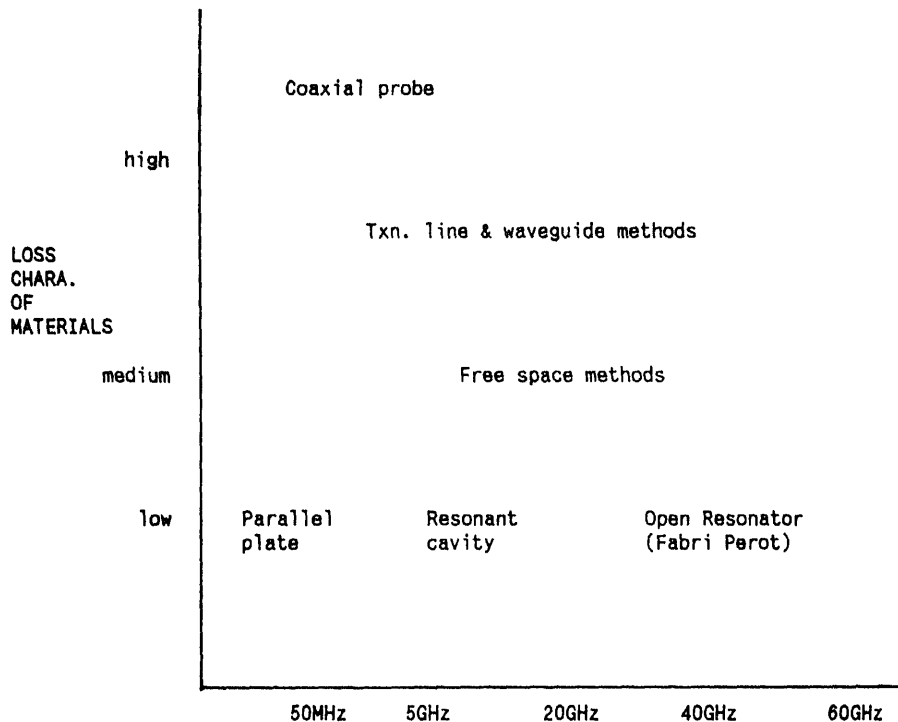


Figure 4. The suitability of the measurement methods for given frequency range and the nature of the material.

Other novel methods also reported are *microwave diversity imaging* (Li *et al* 1989) and *microwave scanning method* (Wims & Palmer 1991) which are essentially non-destructive in nature.

The frequency ranges of application of some of the measurement methods discussed above are given in figure 4 (Curran 1993). The optimum method for an application is chosen after taking the various limitations and advantages of these methods into consideration. Methods usually selected for different applications are listed below.

Product evaluation	Free space techniques
	Interferometer
	Waveguide
EM properties of bulk materials	Waveguide
	Parallel plate
	Transmission line techniques
Sheet materials	Admittance tunnel
	Free space techniques

6. Applications of RAM

Although initially intended for camouflaging aircraft, and for enhancing radar performance, RAMs have found their way into numerous other areas. Some of the important applications of the RAMs are given below.

6.1 RCS reduction of aerospace vehicles

RAMs are primarily used to achieve broad band RCS reduction for aircraft (Walkington & Huster 1979; Sweetman 1982, 1987; McCluggage 1987; Schmitman & Warwick 1990; Cobucci 1991; Brown 1992; Martin 1992) and missiles (Hanson & Kiehle 1982). Ferrite-based paints are one such class of materials developed earlier that were found to be useful, not only over wide band but also at the lower frequencies. Lighter RAMs were fabricated subsequently, but most of them are still on the classified list.

6.2 Improvement of radar performance

Absorber sheets are used to shield such reflecting objects in the vicinity of the radar that may otherwise cause spurious effects on radar signals at the base of the radome, parts of the antenna mechanism etc. In shipboard applications, the mast and the bulkhead are also covered with absorbers. Similarly, treating the buildings near an air traffic control radar with RAM, improves radar performance (Emerson 1973).

6.3 Reduction of antenna RCS

In some military applications it becomes necessary to keep the RCS of antennas as low as possible. Covering the aperture with an absorber coating can lead to considerable RCS reduction. In a typical case with a circular waveguide termination (Lee *et al* 1985), this RCS reduction can be as much as 13 dB.

6.4 Antenna sidelobe reduction

The sidelobe level of antennas can be significantly reduced by placing the antenna within a tube made of absorber panels. Similarly obstructions from feed supports in reflector antennas are eliminated by covering them with absorber panels (Emerson 1973). The effect of edge diffraction in very large reflector antennas can be significantly reduced by covering the edges of the reflector with absorber sheets (Yokoi & Fukumaro 1971).

6.5 Anechoic chambers

Anechoic chambers are required in taking diverse EM measurements such as the aircraft RCS patterns, the antenna radiation patterns, the radome boresight error and various other simulation studies. An anechoic chamber for this purpose has to be isolated from the outside environment so that ideally no signal crosses the wall in either direction. The walls, floor and ceiling of such chambers are made absorptive to create a free-space-like environment.

The suitability and design of various RAMs for this application are widely reported in open literature (Severin 1956; Cherepanov 1974; Mitsmakher 1980; Brumely 1987; Joseph 1988). The design of broad band absorbers for electromagnetic susceptibility (EMS) measurements chambers was suggested by Mishra *et al* (1982).

Most of the chambers use absorbers cut in the pyramidal, conical or even an aggregate sine-wave shape for improved performance. Such chambers in the test region have maximum reflection levels 70 dB below the direct path signal, and shielding isolation as low as -140 dB (Emerson 1973). State of the art anechoic chambers have a frequency range of about 100 MHz-100 GHz.

6.6 Improvement of outdoor range performance

The effect of scattering from isolated objects in an outdoor range can be offset by covering them with RAMs. This results in a free-space-like environment so that the tests are more reliable. Polyfoam structures are found to be very effective in such applications (Blore 1964).

6.7 EMI applications

With the increasing use of higher frequencies in electronic circuits, it has become necessary to provide shielding from the electromagnetic interference (EMI) from/to nearby systems. Absorber-lined enclosures may be used when an ideal free space condition has to be met without disturbing the surroundings for electronic circuits. Customised absorbers are used in high power applications (Emerson 1973).

6.8 As part of the microwave components

A number of waveguide and coaxial microwave components make use of some absorbing material inside. For example, resistive vanes made of such materials are employed in

making microwave attenuators (Nagornov *et al* 1978) and phase shifters (Tretyakov & Oksanen 1991; Marty *et al* 1992). Absorber materials are also used for harmonic suppression in transmitters, and for gain stabilisation in amplifiers (Bostick 1985).

6.9 *Mode suppresser in circular waveguides*

When the inside surface of a circular waveguide is coated with RAM, the lower order modes are suppressed significantly. The amount of suppression depends on how lossy the material is. Such a mode of suppression can also result in the RCS reduction of circular structures. Coating the inside surface of a cavity with RAM reduces its RCS significantly (Lee *et al* 1985, 1986; Chou *et al* 1987; Chou 1988).

6.10 *In parallel plate waveguides*

When the inner surface of a parallel plate waveguide is covered with a RAM, it can propagate $TM(e)_{10}$ and $TM(e)_{10}$ modes over unlimited bandwidth. Such parallel plate waveguides are much more useful than a corrugated horn as a feed antenna. A detailed analysis of such structures is described by Cheng & Ostertag (1986). It is shown that the performance is insensitive to the RAM characteristics.

6.11 *Protective shields in microwave oven*

A household application of RAM comes in the form of protective shields in microwave ovens. Ferrite paints are coated over the oven casings to reduce any possible leakage of the radiation to the atmosphere. A commercially available paint from the Japanese company TDK was effectively used for this purpose (Ashley & Gilmore 1988).

6.12 *Removal of ghost images in TV pictures*

A paint from NEC could reduce the reflections significantly in the frequency range 3.5–20 GHz (Ashley & Gilmore 1988). This sandwich ferrite RAM was successfully used for removing ghosts in TV pictures due to clutter effects from nearby buildings. Interestingly, in the early stages of the US Department of Defense stealth programme, this Japanese paint was in high demand.

6.13 *Electronic countermeasure applications*

Innovative applications of RAMs have also been proposed in Electronic Countermeasures (ECM). A recent patent suggests coating the inner surface of countermeasure cartridge with plastisol (Tsuji 1992). The heat generated while expending the countermeasure payload softens the plastisol coating so that the entire container acts as a radar absorber rather than a reflector.

6.14 *RCS enhancement of the missile decoys*

Quite ironically, absorber materials can themselves be used to increase the RCS as well. In order to improve the detectability and hence the effectiveness of a missile decoy, its

rear side is coated with absorbers (Harrington 1987). This reduces the creeping waves, thus resulting in increased RCS in the head-on, i.e. the backscattering direction.

7. Trends in RAM

As mentioned in §§ 1 and 2 of this paper, contrary to the popular belief, RCS reduction is not one of the latest "emerging" technologies. The active research endeavor in this area is at least three, possibly four, decades old. The Soviets by 1965 had already noticed and were alarmed by the massive and increasing US funding to explore RCS reduction as an effective means of combat. The US interest and the intensification of the programme could be judged by the sharp funding increase by the US Air Force from 35.5 million (in 1962) to 119 million (in 1963) to 155 million dollars (in 1964) (Shneyderman 1985). Hence, the genesis for active research in RCS reduction can be traced back to the late Fifties rather than, as is popularly believed, to the early Seventies.

When the stealth programme was officially unveiled in the early Eighties, the cost of Raytheon B-2 was placed at 650 millions per piece (as compared to 15 million for the Lockheed F-16). As was later to be extensively commented upon by the experts in the aerospace industry, B-2 is highly inoptimal from aerodynamic considerations; its novelty lies in its stealth characteristics. Of these, shaping as a means for RCS reduction was known, and depended solely on enormous computer time for the stealth design. It is apparent from the external features of B-2, that it used smooth blended convex profiles as a means of shaping. It can therefore be presumed that much of this money for RCS reduction (B-2 is a 20 billion-dollar programme) went for the novel research on RAM technology.

A parallel exists in the Lockheed *Have Blue* and its successor F-117A models. From the shaping point of view, both the *Have Blue* and F-117A had a rather incongruous profile consisting of large external flat plates. The second means of achieving RCS reduction was to incorporate RAM in the aircraft structure itself. The cost of Lockheed F-117A is once again prohibitively large.

Although US agencies have closely monitored the development of RAM technology in foreign countries, for example Russia and China, it has not been possible to put a cost tag to these efforts. In case of China, it is opined that much of the effort is being funded indirectly through the science and technology budget. It is conjectured that rather large RAM research programmes exist with the other four super powers, sometimes without even logical conclusion. For example, the French have displayed an extensive research interest in RAMs without apparently having a corresponding military aircraft programme.

It has indisputably emerged, from the figures connected with stealth programme, that the price of RAM technology has tended to be prohibitively high. Much of this research must have been directed towards analysis, design and development, fabrication and measurement aspects of RAM. We propose to look into the trends in RAM technology with this perspective.

7.1 Bandwidth

The EM absorbers made a rather modest beginning. It started with the quarter-wavelength transmission line concept of impedance matching. A constraint in applying

dielectric RAMs is their bulkiness. This could be offset by applying thin coatings of ferrites and other magnetic RAMs. However, both the dielectric and magnetic RAMs were frequency-dependent, and therefore *narrow band absorbers*.

The narrow band RAMs can be used in multiple layers to obtain broad band absorbers. However, either due to the bulkiness (dielectric RAMs) or higher density (magnetic RAMs), the weight penalty is still considerably high.

A new class of RAM based on the principle of EM chirality is reported to be much lighter than the ferrites and requires thinner coatings ($\lambda/5$ to $\lambda/6$) than the conventional RAMs. Of late, a newer class of RAM based on Schiff-base compounds has been reported which is said to be as much as ten times lighter than the magnetic RAMs for the same absorptive performance. Furthermore, these retinyl derivatives (bacteriorhodopsin) are reported to have ultrawide band absorption characteristics.

7.2 Analysis

The analysis of RAM for future prediction has followed the developments in computational electromagnetics. In the high frequency domain, the methods initially used in the 1960s were geometrical optics (GO) and its extensions. The modification of GO to the GTD-type theories permitted RAM analysis of increasing complexity; these are discernible in the shooting and bouncing ray (SBR) method of Lee (1985) to analyse the RAM-coated engine cavity. The approach taken in the low-frequency domain has been that of the method of moments (MOM).

However, both GTD-type theories, and the MOM and its derivatives suffer from severe shortcomings. The GTD requires the scatterer to be convex, and the symmetrical cavities have stretched the SBR method to its limit. As of today, asymptotic ray-theoretic methods cannot handle either a scatterer having concave and convex surfaces in the neighbourhood, or a surface of arbitrary concavity. The MOM can solve such problems with remarkable ease but the size of the scatterers must be electrically small. Unfortunately, the size (electrical) of the scatterer encountered in reality makes the application of MOM computationally intractable.

The time domain methods, (based on finite difference), which are similar to the MOM, have of late caused much interest. The finite difference time domain (FDTD) method was proposed in 1966 (Yee 1966). But it is only with the advent of parallel computers that its potential seems to have been unlocked. FDTD can yet solve only low-frequency scatterers, although at a speed usually one order of magnitude better than the MOM. Kashiwa *et al* (1990) have successfully presented a three-dimensional time domain analysis of an electrically small aircraft structure coated with thin resonant absorbers. It is expected that, if the technological breakthroughs in parallel computers continue at the current pace, FDTD algorithms should be able to solve electrically large problems in another ten years time. In this context, it must be mentioned that the fastest supercomputers to date, require 10 days on stand-alone basis to analyse aircraft coated with RAM.

7.3 Design

Since most of the military and particularly the electronic warfare applications require wide bandwidths, it is essential that RAMs have broad band or even ultrawide band

characteristics. The present practice is to obtain broad band RAMs by multilayering of resonant RAMs. In actual practice however determining the thickness of individual layers and the concentration gradients are highly computation intensive. Bastiere (1989) has applied fuzzy set theory to evolve a multi-criteria optimisation method for designing RAMs consisting of as many as 5 different layers.

7.4 Measurements

As mentioned in § 5, well-known methods exist for characterising RAMs right from the audio frequencies up to 60 GHz with varying degrees of accuracy. In contrast, Hemmati *et al* (1985) made transmittance and reflectance measurements on Eccosorb in the frequency range 35 GHz–3 THz at both ambient and cryogenic temperatures. The development of measurement techniques in the quasi-optical range has acquired additional significance, since the extensive use of this section of EM spectrum for next-generation military applications is imminent. Such developments tie well with the *NASA Terahertz Technology Programme* which is being funded on a priority basis.

7.5 Fabrication

Although applying RAMs to military aircraft structures is decidedly advantageous, it is somewhat offset by the weight penalty it imposes on the cruise performance of the aircraft. It is now feasible to use radar absorbing structures (RAS) in the construction of the aircraft. Since the RAS consists of embedding RAMs within the parts of the aircraft structure, there is almost no weight penalty. The concept of RAS is also consistent with the present day trend of increasing use of composites in the fabrication of fighter aircraft. In the state-of-the-art Lockheed F-18 aircraft (which interestingly has inherent stealth characteristics) the composites used are 9.9% by volume. In contrast, for the YF-23 ATF, a future aircraft programme, this percentage is to go up by as much as 45–50% (Cobucci 1991).

RAS have been obtained by embedding magnetic RAMs in polymeric matrix (Stonier 1991). Similarly the use of bismaleide resins have also been reported in these composites. In the vicinity of engines, which is a major contributor to the overall RCS of the aircraft, polyamides have been used (Stonier 1991). Finally, novel fabrication techniques for RAS have succeeded in sustaining the RCS reduction characteristics at temperatures as high as 350°F which is well in excess of the maximum temperature encountered by the state-of-the-art supersonic fighter aircraft.

As a further corollary of the RAS concept, the possibility of constructing inherently stealth radomes is also being considered (Kumar *et al* 1994; Vinoy & Jha 1994). Polyethylene fibres in composites result in RAS of high strength which can be used for EM window (radome) applications (Cain & Corda 1991).

It is interesting to note that several radome material derivatives e.g., spinel ferrites (Deleuze 1992) have been successfully used as RAMs. This is hardly surprising since the electromagnetic analysis and design of radome and RAM involve similar physical parameters such as dielectric and magnetic loss tangents (Kumar 1994; Vinoy & Jha 1994).

Since the exterior of the aerospace vehicles are subject to environmental hazards, the current trend is to develop RAMs which are inherently resistant to the environmental

elements. Silicone rubber, which is a well-known anti-rain erosion material, has been tested as RAM (Army Material Development and Readiness Command 1982). Similarly RAMs have been developed with antiablation and nuclear-damage resistance properties. Inorganic ceramics Al_2O_3 and ZrO_2 have been tested in this context. Once again, it may be worthwhile to recall that both these inorganic ceramics are extensively used in constructing hypersonic radomes for missiles (Kumar 1994; Kumar *et al* 1994).

8. Summary

The research in Radar Absorbing Materials (RAMs) as a viable means for RCS reduction has been actively pursued for at least four decades. The RAMs fabricated initially were based upon transmission line approach and were narrow band absorbers. The applicability of these resonant absorbers was enhanced by multilayering to obtain broad band absorbers.

Analyses have however shown that the ultrawide band radars can be effectively used as electronic countermeasures against broad band absorbers. This has motivated the current search for ultrawide band RAMs. Compared to the transmission line approach and multilayer concept, the initial successes reported in the area of ultrawide band RAMs have come from the completely novel approach of chirality and by exploring even biochemical products for this purpose.

In order to overcome the penalty of weight imposed by multilayered dielectric or ferrite RAMs coated on the aircraft structures, there is a decided shift towards using Radar Absorbing Structures (RAS) where the RAMs are embedded in the polymeric composite matrix. The concept of RAS is compatible with the trend of using increasing volumes of composites in the fabrication of the latest and of future generation fighter aircraft.

A comparison with our concurrent study in radomes has shown that several RAMs are actually radome materials. This observation is significant since the RAMs in general are classified, whereas extensive information on the radome materials is available in the open literature.

Besides the obvious military applications, RAMs have many prevailing and potential applications in the industrial and even domestic sectors. RAM has thus emerged as a typical dual-use technology, where commercially viable research and development can be pursued independent of the defense sector.

An awareness of the underlying principles of RAM analysis, design and fabrication methods, and the actual materials used as RAMs, could enable material scientists to indigenise and even pioneer the next generation of RAMs.

References

- Adam J A 1988 How to design an invisible aircraft. *IEEE Spectrum* (4): 26–31
- Alexopoulos N G 1969 Radar cross section of perfectly conducting spheres coated with a certain class of radially inhomogeneous dielectrics. *IEEE Trans. Antennas Propag.* AP-17: 667–669
- Amin M B, James J R 1981 Techniques for the utilization of hexagonal ferrites in radar absorbers, Part I. *Radio Electron. Eng.* 51: 209–218
- Aoto T, Yoshida N, Fukai I 1987 Transient analysis of the electromagnetic field for a wave absorber in three-dimensional space. *IEEE Trans. Electromagn. Compat.* EMC-29: 18–23

- Army Material Development and Readiness Command 1982 Radiation-resistant radar materials: Analytical and experimental study identifies materials potentially resistant to nuclear radiation damage. NTIS Tech Note, PB82970294XSP.
- Arsaev I E 1982 Plane wave scattering by bodies of revolution. *Radiotech. Electron.* 27: 2101–2109
- Ashley S, Gilmore C P 1988 Stealth. *Pop. Sci.* (7): 46–51
- Baker D E, van der Neut C A 1988 Reflection measurements of microwave absorbers. *Microwave J.* 31: 95–98
- Bastiere A 1989 Decision-making aid for multi-layer radar absorbent coverings. Tech. Rep. ESA-TT-1173, European Space Agency, Paris
- Bhattacharyya A K 1990 Radar cross section reduction of a flat plate by RAM coating. *Microwave Opt. Technol. Lett.* 3: 324–327
- Bhattacharyya A K, Sengupta D L 1991 *Radar cross section analysis and control* (Norwood MA: Artech House)
- Bhattacharyya A K, Tandon S K 1984 Radar cross section of a finite planar structure coated with a lossy dielectric. *IEEE Trans. Antennas Propag.* AP-32: 1003–1007
- Blore W E 1964 The radar cross section of polyfoam towers. *IEEE Trans. Antennas Propag.* AP-12: 237–238
- Bostick G 1985 Damping spurious microwave responses with absorbing materials. *EMC Technol.* 14(2): 21–27
- Bowman J J 1968 Effects of absorbers. In *Methods of radar cross-section analysis* (eds) J R Crispin Jr, K M Siegel (New York: Academic Press)
- Bowman J J, Weston V H 1966 The effect of curvature on the reflection coefficient of layered absorbers. *IEEE Trans. Antennas Propag.* AP-14: 760–767
- Bradshaw P S 1989 Signature management and structural materials. In *Materials and processing—Move to the 90's, Proc. of SAMPE* (Amsterdam: Elsevier Science) pp 187–196
- Brown A 1992 Fundamentals of stealth design. *Lockheed Horizons* 31(8): 6–12
- Brumley S 1987 Better RCS data with anechoic absorber characterization. *Micro. RF* 26: 143–148
- Cain R N, Corda A J 1991 Active radar stealth device. Patent 5 036 323, Dept. of the Navy, Washington DC
- Cheng Y B, Ostertag E L 1986 An absorber-wall parallel-plate waveguide. *IEEE Trans. Microwave Theory Tech.* MTT-34: 761–766
- Cherepanov A K 1974 Reflection of electromagnetic waves from an absorptive spiky surface. *Radio Eng. Electron. Phys.* 19: 120–123
- Chou R, Ling H, Lee S W 1987 Reduction of the radar cross section of arbitrarily shaped cavity structures. Tech. Rep. NASACR180307, Illinois Univ., Urbana-Champaign
- Chou R-C 1988 Modal attenuation in multilayered coated waveguides. *IEEE Trans. Microwave Theory Tech* MTT-36: 1167–1176
- Cobucci F 1991 Building air superiority. *Aerosp. Mater. Compos.* 3: 16–19
- Curran J 1993 HP radar/EW testing solutions. *HP RF and Microwave Test Symp.* Bangalore
- Davies P, Popplewell J, Llewellyn J P 1986 Microwave absorption in ferrofluid composites. *IEEE Trans. Magn.* MAG-22: 1131–1133
- de Hoop A T 1981 Theorem on maximum absorption of electromagnetic radiation by a scattering object of bounded extent. *Radio Sci.* 16: 971–974
- Deleuze C 1992 Radar absorbing materials. *Chocs* 6: 15–29
- Emerson W H 1973 Electromagnetic wave absorbers, anechoic chambers through the years. *IEEE Trans. Antennas Propag.* AP-21: 484–490
- Engheta N, Zablocky P G 1990 A step towards determining transient response of chiral materials - Kramers-Kronig relations for chiral parameters. *Electron. Lett.* 26: 2132–2134
- Falkenbach G J 1965 Limitations in determining absorbing material parameters. *Proc. IEEE* 53: 1097–1098
- Fante R L, McCormack M T 1988 Reflection properties of the Salisbury screen. *IEEE Trans. Antennas Propag.* AP-36: 1443–1454
- Fernandez A, Valenzuela A 1985 General solution for single-layer electromagnetic wave absorber. *Electron. Lett.* 21: 20–21
- Gauss A 1982 A new method of EM absorbing coating. Tech. Rep., AD A117472, Ballistic Research Lab., Aberdeen Proving Ground, MD

- Ginzton E L 1957 *Microwave measurements* (New York: McGraw Hill)
- Guillot T 1992 *Contribution to the modelling of the electromagnetic properties of random dielectric-conductor mixtures*. Ph D thesis (Rep. ETN-93-93046), Office National d'Etudes et de Recherches Aerospatiales, Paris
- Guillot T, Bobillot G 1991 Microwave measurement of the electrical conductivity of an elementary grain of a conducting powder. ONERA Tech. Rep. TP 1991-40 Paris
- Hahn H T 1991 The variation of permeability with ferrite file density. *J. Appl. Phys.* B69: 6195-6197
- Halpren O, Johnson M J Jr Radar summary report of Harp project. OSRD Div 14, vol. 1 (part π), ch. 9-12
- Hanson R L, Kiehle M H 1982 Performance considerations in the design of subsonic missile. *AIAA Aerosp. Sci. 20th Meeting* (Paper No. 82-0371)
- Harrington J J 1987 Missile decoy radar cross section enhancer. Patent NTIS ADD0135608XSP, Department of the Air Force, Washington DC
- Hatakeyama K, Inui T 1984 Electromagnetic wave absorber using ferrite absorbing material dispersed with short metal fibers. *IEEE Trans. Magn.* MAG-20: 1261-1263
- He J, Lu Z, Su Y 1992 Experimental investigation on the ultra-wideband radar characteristics of coating RAMs targets. *IEE Proc. Int. Conf. London*: pp. 493-496
- Hemmati H, Mathur J C, Eichhorn W L 1985 Submillimeter and millimeter wave characterization of absorbing materials. *Appl. Opt.* 24: 4489-4492
- Hempel K A, Roos W 1981 Microwave absorption along minor hysteresis loops of single domain particles with uniaxial magnetic anisotropy. *IEEE Trans. Magn.* MAG-17: 2642-2644
- Holland R, Cho K S 1986 Radar cross-section of damped cylinders and dielectric strips. Tech. Rep. APITR129 (Applied Physics Inc. Albuquerque NM)
- Hurmuth H F 1983 On the effect of absorbing materials on electromagnetic waves with large relative bandwidth. *IEEE Trans. Electromagn. Compat.* EMC-25: 32-39
- Jaggard D L, Engheta N 1989 Chiroshield as an invisible medium. *Electron. Lett.* 25: 173-174
- Jaggard D L, Engheta N, Liu J 1990 Chiroshield - a Salisbury/Dallenbach shield alternative. *Electron. Lett.* 26: 1332-1334
- Jaggard D L, Liu J C, Sun X 1991 Spherical chiroshield. *Electron. Lett.* 27: 77-79
- Jones A K, Wooding E R 1964 A multilayer microwave absorber. *IEEE Trans. Antennas Propag.* AP-12: 508-509
- Joseph P J 1988 *UTD (Uniform geometrical theory of diffraction) scattering analysis of pyramidal absorber for design of compact range chambers*. Master's thesis (AFITCINR88193), Air Force Inst. of Technol., Wright-Patterson AFB OH
- Kashiwa T, Yoshida N, Fukai I 1990 Simulation of the reduction characteristics of scattering from an aircraft coated with a thin-type absorber by the spatial network method. *Electron. Lett.* 26: 289-290
- Kent B 1982 An automated dual horn-reflector microwave absorber measurement system. Tech. Rep. AFWALTR811284 (Air Force Wright Aeronautical Labs Wright-Patterson AFB, OH.) Vol I
- Knott E F 1979 The thickness criterion for single layer radar absorbers. *IEEE Trans. Antennas Propag.* AP-27: 698-701
- Knott E F, Shaeffer J F, Tuley M T 1985 *Radar cross section* (Norwood MA: Artech House)
- Kong J A 1975 *Theory of electromagnetic waves* (New York: Wiley Interscience)
- Kumar A 1987 Acetylene black-A single-layer microwave absorbers. *Electron. Lett.* 23: 184-185
- Kumar P M 1994 EM design aspects of airborne radomes. Project Report, National Aerospace Laboratories, Bangalore
- Kumar P M, Vinoy K J, Jha R M 1994 An indexed database of radome (1960-1993). NAL Project Document PD AL 9405, National Aerospace Laboratories, Bangalore
- Lee C S, Lee S W, Chuang S L 1986 Normal modes in an overmoded circular waveguide coated with lossy materials. *IEEE Trans. Microwave Theory Tech.* MTT-34: 773-785
- Lee S W, Lo Y T, Chuang S L, Lee C S 1985 Numerical methods for analyzing electromagnetic scattering. Semian. Rep., NAS126176141, Illinois Univ., Urbana-Champaign
- Lehto A, Tourinen J, Raisanen A 1991 Reflectivity of absorbers in 100-200 GHz range. *Electron. Lett.* 27: 1699-1700
- Leontovich M A 1957 Appendix of diffraction, refraction and reflection of radio waves. Rep. AD 117276 (US Govt. Printing Press, Washington DC)

- Li H J, Farhat N H, Shen Y 1989 Radar cross section reduction by absorber covering. *J. Electromagn. Waves Appl.* 3: 219-235
- Lynnworth L C 1964 Audio frequency characterization of RAM. *Proc. IEEE* 52: 98-99
- MacFarlane G G 1945 Radar camouflage research and development by the Germans. Tech. Rep. T1905 M/99 TRE
- Macleod J B 1989 *Modeling of camouflage netting for radar cross section analysis*. Master's thesis (AFITGEENG89J2), School of Engineering Air Force Inst. of Technol., Wright-Patterson AFB OH
- Maffioli F 1970 Constrained variable metric optimization of layered electromagnetic absorbers. *Alta Freq. (Eng. Edn.)* 39: 154-164
- Martin P W 1992 Development of F-117 stealth fighter. *Lockheed Horizons* 31: 18-23
- Marty V, Combes P-F, Borderies P 1992 Radar cross section of a rectangular waveguide array with complex load and covered with dielectric. *La Rech. Aerosp.* 4: 15-25
- McCauley J W, Halpin Jr. B M, Hynes T, Eitelman S D 1980 Radar absorptive ferrite/resin composites from industrial effluent. *Ceramic Eng. Sci. Proc.* 1: 356-369
- McCluggage W A 1987 *Study of radar cross section (RCS) characteristics and their application in future weapon systems*. Master's thesis (ETN8892081), RAF College, Cranwell
- Mishra S R, Pavlasek J J F, Yazar M N 1982 Design criteria for costeffective broad band absorber-lined chambers for EMS measurements. *IEEE Trans. Electromagn. Compat. EMC-24*: 12-19
- Mitsmakher M Iu 1980 Quality of modern anechoic chambers and radio wave absorbing materials. *Antenny* 28: 147-164
- Montgomery C G 1957 *Techniques of microwave measurements* (New York: McGraw-Hill)
- Montgomery C G, Dicke R H, Purcell E 1948 *Principles of microwave circuits. Radiation Lab Series 8* (Boston, MA: Boston Technol.)
- Moreland J, Peters L Jr 1966 The specular radar cross section of absorber coated bodies. *IEEE Trans. Antennas Propag.* AP-14: 799-800
- Musal H M, Hahn H T 1989 Thin layer electromagnetic absorber design. *IEEE Trans. Magn.* MAG-25: 3851-3853
- Musal H M, Smith D C 1990 Universal design chart for specular absorbers. *IEEE Trans. Magn.* MAG-26: 1462-1464
- Naamlooze Vennootschap Machinerieën 1936 *French Patent* 802 728
- Nagasubramanian G, Distefano S, Liang R H 1990 Silicon containing electroconductive polymers, structures made therefrom. Patent Application Rep. PAT-APPL-7-479 485, (NASA, Pasadena CA)
- Nagornov A I, Postnikov A I, Vasil'ev V P, Gordeev V A 1978 Study of the absorption properties of resistive films aligned perpendicular to the waveguide axis. *Radiofizika* 21: 151-153
- Naito Y 1970 Generalised Snock's limits in ferrite. *Jpn. J. Phys.*
- Naito Y, Suetake K 1965 Construction of multilayer absorbing wall for microwaves. *Electron. Commun. Jpn.* 48(12): 112-121
- Naito Y, Suetake K 1971 Application of ferrite to Electromagnetic wave absorber and its characteristics. *IEEE Trans. Microwave Theory Tech.* MTT-19: 65-72
- Olmedo L 1992 Absorbing materials based on conductive polymers *Chocs* 6: 53-65
- Ono M, Suzuki M 1967 Reflection and attenuation characteristics of multilayer absorber at oblique incidence. *Electron. Commun. Jpn.* 50(9): 84-92
- Ono M, Okokawa S, Suzuki M 1967 Fundamental characteristics of the microwave absorber. *Yamagata Univ. Bull. (Eng.)* 9: 569-579
- Ono M, Ikuta A, Katagiri Y 1979 Synthesis of an electromagnetic wave absorber with good reflection characteristics at both normal and oblique incidence. *Electron. Commun. Jpn.* 62: 59-62
- Ono M, Yokoto T, Shibuya T 1983 A practical method of measuring the scattering characteristics of the pyramidal absorbers. *Electron. Commun. Jpn.* 66: 63-71
- Perini J, Cohen L S 1991 Design of radar absorbing materials for wide range of angles of incidence. *IEEE Int. Symp. on Electromagn. Compat.* (New York: IEEE) pp 418-424
- Post E J 1962 Formal structure of electromagnetics (Amsterdam: North Holland)
- Rogers S W 1986 *Radar cross section prediction for coated perfect conductors with arbitrary geometries*. Master's thesis (Rep. AFITCINR86105T), Air Force Inst. of Technol., Wright-Patterson AFB, OH

- Ruck G T, Barrick D E, Stuart W D, Krichbaum C K 1970 *Radar cross-section handbook* (New York: Plenum) vol. 2
- Rudduck R C, Yu C L 1974 Circular waveguide method of measuring reflection properties of absorber panels. *IEEE Trans. Antennas Propag.* AP-22: 251-256
- Salisbury W W 1952 Absorbent body for electromagnetic waves. *US Patent* 2599944
- Schade H A 1945 Schornsteinfeger US tech. mission to Europe. Tech. Rep. 90 45 AD-47746
- Schmitman C, Warwick G 1990 Building the B-2. *Flight Int.* 139: 24-27
- Severin A 1956 Nonreflecting absorbers for microwave radiation. *IEEE Trans. Antennas Propag.* AP-4: 385-392
- Shi Z, Ding C, Jia Y 1993 Effects of absorbent materials on the RCS of a partially coated scatterer. *Microwave Opt. Technol. Lett.* 6: 109-111
- Shimizu Y, Suetake K 1969 Minimum thickness design of broadband absorbing wall. *Electron. Commun. Jpn.* 52-B(4): 90-97
- Shneyderman Y A 1985 Radio-absorbing materials. Tech. Rep. NTIS Rep. ADA1574961XSP (Foreign Technol. Div.), Wright-Patterson AFB, OH
- Stonier R A 1991 Stealth aircraft and technology from World War II to the Gulf. *SAMPE J.* 27(4): 9-17
- Strickel M A, Taflove A 1990 Time domain synthesis of broad band absorptive coatings for two dimensional conducting targets. *IEEE Trans. Antennas Propag.* AP-38: 1084-1091
- Swarnar W G, Peters L Jr 1963 Radar cross sections of dielectric or plasma coated conducting spheres and circular cylinders. *IEEE Trans. Antennas Propag.* AP-11: 558-569
- Sweetman B 1982 The bomber that radar cannot see. *New Sci.* 93: 565-568
- Sweetman B 1987 Stealth in service. *Interavia* 42: 39-40
- Tret'yakov S A, Oksanen M I 1991 Biisotropic layer as a polarization transformer. Tech. Rep., ISBN-951-22-0770-2, Electromagnetics Lab. Helsinki Univ. of Technology, Espoo, Finland
- Tsuji K 1992 Low observability aperture design for expendable countermeasures devices. Patent Rep., Patent-5 083 128, Dept. of the Navy, Washington, DC
- Veinger A I, Zabrodskii A G, Krasikov L A, Khorosheva N E 1990 Anomalous microwave absorption in magnetically filled low-molecular-weight rubbers. *Am. Inst. Phys.* 855-856
- Vinoy K J, Jha R M 1994 Radar absorbing materials (RAM): a cross indexed bibliography (1956-1993). NAL Project Document PD AL 9404, National Aerospace Laboratories, Bangalore
- Walkington J W, Huster L W 1979 Achieving effective radar cross section flight profiles on the B-1 aircraft. In *Soc. Fli. Test Eng., Proc. 10th Annu. Symp.* (Lancaster, CA: Soc. Flight Test Eng.)
- Weston V H 1963 Theory of absorbers in scattering. *IEEE Trans. Antennas Propag.* AP-11: 578-584
- Wims P R, Palmer D D 1991 Nondestructive microwave scanning measurements for material property evaluation. Review of progress in quantitative nondestructive evaluation. *Proc. 17th Annu. Rev.* (New York: Plenum P.) A10: 551-558
- Yang C F, Burnside W D, Rudduck R C 1992 A periodic moment method solution for TM scattering from lossy dielectric bodies with application to wedge absorber. *IEEE Trans. Antennas Propag.* AP-40: 652-660
- Yee K S 1966 Numerical solution of initial boundary value problems involving Maxwell's equations in isotropic media. *IEEE Trans. Antennas Propag.* AP-14: 302-307
- Yi P, Gan Y 1991 Investigation on microwave absorber with additive of metal coated carbon fiber. *Acta Aeronaut. Astronaut. Sin.* B12: 655-657
- Yokoi H, Fukumaro H 1971 Low-sidelobe paraboloidal antenna with microwave absorbers. *Electron. Commun. Jpn.* 54: 34-39

Growth and development of *Thiobacillus ferrooxidans* for engineering applications

SANGHAMITRA MUKHOPADHYAY and K A NATARAJAN

Department of Metallurgy, Indian Institute of Science, Bangalore 560 012, India

MS received 31 May 1994

Abstract. A bioprocessing approach for the extraction of base, nuclear and precious metals from refractory and lean grade ores has been reviewed in this paper. Characteristic morphological features of *Thiobacillus ferrooxidans*, the organism which has been extensively used for biooxidation of sulphide ores have been discussed. Mechanisms of chemoautotrophy and mineral oxidation have been illustrated. The current engineering applications of this microorganism have also been brought out. Various methods for accelerating the growth of *Thiobacillus ferrooxidans* for faster biooxidation and genetic manipulation for development of desired strains have been outlined.

Keywords. *Thiobacillus ferrooxidans*; chemoautotrophy; iron oxidation; sulphur oxidation; bioleaching; genetic manipulation.

1. Introduction

Thiobacillus ferrooxidans, the most widely implicated bacterium in the bioleaching of sulphide minerals was isolated for the first time from the acid drainage of coal mines in 1947 (Colmer & Hinkle 1947). Since then tremendous research activity followed in order to characterize these organisms and investigate their potential in the oxidation of various sulphide minerals (Duncan *et al* 1964; Brierley 1978; Dugan & Apel 1978; Harrison 1982; Norris & Kelly 1982; Groudev 1985; Huber *et al* 1986; McCready 1988).

Its commercial application in the leaching of copper from waste grade ore dumps was demonstrated by the Kennecott Copper Corporation, USA in 1963. During the last three decades, the commercial utility of this microorganism has been proved in the extraction of copper and uranium from waste and lean grade ores as well as tailings. Over 30% of the world's copper is currently estimated to be produced through bioleaching operations. For about a decade, the industrial application of bioprocessing has been further extended to enhance gold recovery from refractory ores and concentrates containing encapsulated gold particles in a sulphide matrix such as pyrite and arsenopyrite (Lawrence 1990).

Commercially, the following techniques have been adopted to bring about biooxidation of the desired mineral.

- Dump/heap leaching,
- solution mining or *in situ* leaching,
- vat leaching and use of bioreactors.

Although it has been proved technically feasible to bioleach almost any sulphide mineral to recover zinc, nickel, cobalt, molybdenum and a variety of other metals, its widespread commercialisation has been currently restricted due to unfavourable process kinetics. Unlike a number of heterotrophs, *Thiobacillus ferrooxidans*, a chemoautotrophic acidophile grows very slowly exhibiting large generation periods ranging between 16 and 20 h. The slowness of their growth coupled with difficulties associated with generation of higher amounts of biomass, limit the universal industrial acceptance of this biotechnology. Current research efforts, therefore, have been directed towards finding ways and means to accelerate the growth of *T. ferrooxidans* with a view to enhancing bioleaching rates.

In this paper different methods developed to augment biomass generation of *T. ferrooxidans* are analysed. The microbiology of the bacterium is brought out with respect to biochemical mechanisms. Engineering aspects of biomass growth and bioleaching technology are illustrated.

2. *Thiobacillus ferrooxidans*

Since *Thiobacillus ferrooxidans* is the most widely implicated organism in bioleaching operations, its microbiology is discussed in detail here. It is a motile organism having a single polar flagellum. It is non-spore forming, gram-negative, rod-shaped (0.5–1.5 μm), aerobic, acidophilic (pH 2–3.5), and essentially mesophilic (optimum temperature 30°C, but also tolerates moderately thermophilic conditions). It divides by binary fission and occurs either singly or in pairs. It derives its carbon from atmospheric CO_2 and obtains its energy for metabolism through the oxidation of ferrous and reduced-valence inorganic sulphur compounds. An electron micrograph of *T. ferrooxidans* with its characteristic morphological features is shown in figure 1. The medium used for growing the organisms under laboratory conditions is illustrated in table 1.

The surface structures of cells of *T. ferrooxidans* differ depending on whether they are grown in liquid or on solid substrates. When grown in a medium containing sulphur, the cells develop peritrichous, rod-shaped, filamentous appendages called pili. The diameter of the pili can vary from 0.7 to 3.0 microns. On the other hand, when grown in 9 K medium, the bacterium does not develop such characteristics. Hence, it can be inferred that pili facilitate cellular contact with the mineral surface for oxidising elemental sulphur to sulphuric acid (Gromova *et al* 1978).

3. Mechanisms of chemoautotrophy

3.1 Sulphur oxidation

The details of the complex mechanisms involved in sulphur oxidation are beyond the scope of this article and hence are considered only in brief here. Oxidation of S^{2-} , S^0 ,

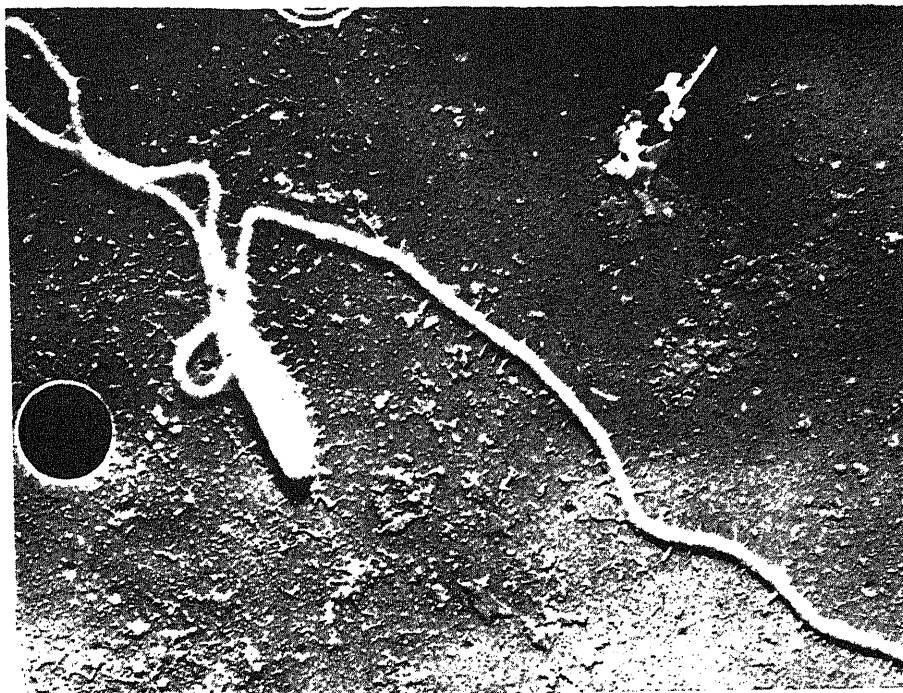
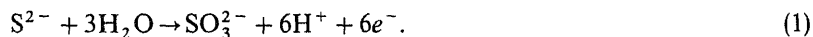


Figure 1. Electron micrograph of *T. ferrooxidans* (20 000 ×).

$S_2O_3^{2-}$ and SO_3^{2-} by the bacteria are considered. A schematic representation of sulphur oxidation by *T. ferrooxidans* is depicted in figure 2.

Sulphide is oxidised directly to sulphite:



The enzyme involved is sulphite reductase. Sulphide can also be oxidised to elemental sulphur (S^0) with the help of enzyme, sulphide oxidase (Parker & Prisk 1953; Kasprzak & Steenkamp 1983).

Table 1. Silverman and Lundgren* medium (9 K medium).

Nitrogen source	$(NH_4)_2SO_4 - 3 \text{ g/l}$
Growth factors	$KCl - 0.1 \text{ g/l}$
	$K_2HPO_4 - 0.5 \text{ g/l}$
	$MgSO_4 \cdot 7H_2O - 0.5 \text{ g/l}$
	$Ca(NO_3)_2 - 0.01 \text{ g/l}$
Energy source	$FeSO_4 \cdot 7H_2O - 44.8 \text{ g/l}$
Distilled water	1 l
pH	2 - 2.3

*Silverman & Lundgren (1959)

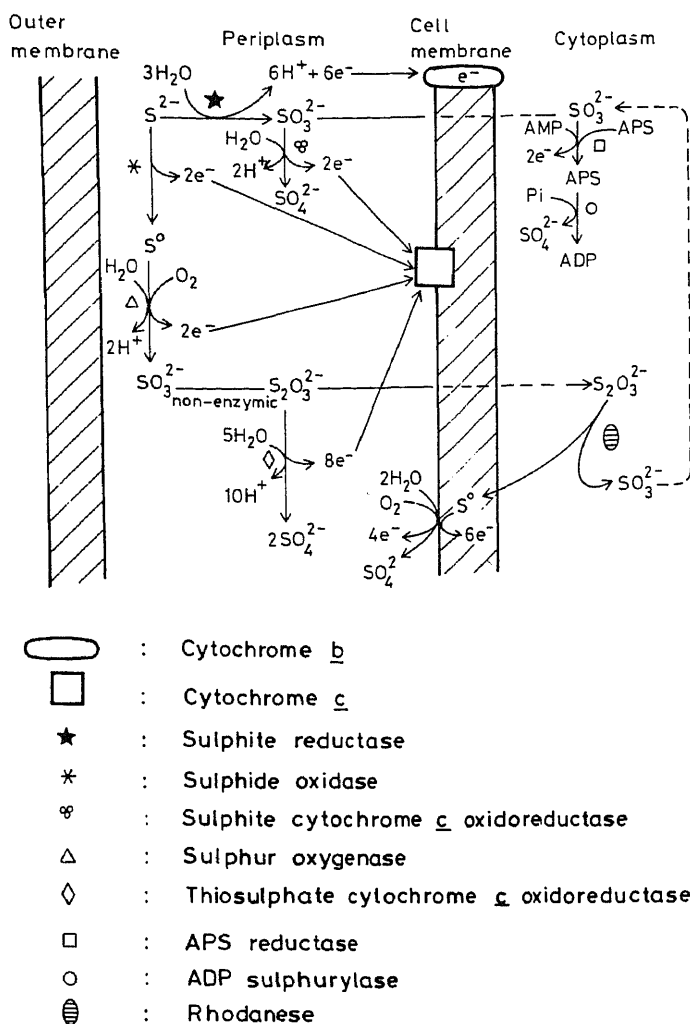


Figure 2. A schematic representation of sulphur oxidation by *T. ferrooxidans*.

Sulphur:



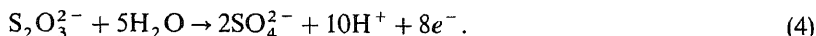
Elemental or colloidal sulphur is insoluble. It is necessary that the cells establish direct physical contact with elemental sulphur before oxidation can occur. Therefore, sulphur is oxidised at the cell surface, dissolved in the cell membrane, or taken up as elemental sulphur by the cells. The enzyme involved has been shown to be an oxygenase (Karavaiko & Pivovarov 1973).

Thiosulphate: All the species of thiobacilli studied oxidise thiosulphate to sulphate. Two mechanisms of oxidation are observed depending on the species of thiobacilli; the

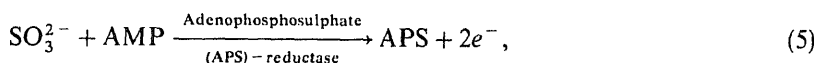
first involves the initial splitting of the S-S bond by enzyme rhodanase with the formation of sulphite and elemental sulphur.



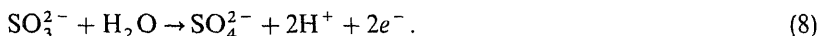
Sulphur is also found to be associated with the membrane and subsequently converted to sulphate. This mechanism involves thiosulphate: cytochrome *c* oxidoreductase (Peck 1960; Charles & Suzuki 1966; Schedel & Truper 1979).



Sulphite: Two mechanisms operate in the oxidation of sulphite depending on the species of thiobacilli. The AMP (adenosine-5-monophosphate)-dependent sulphite oxidation is cytoplasmic.



In the second mechanism, the enzyme is extracytoplasmic, namely, sulphite oxidase (sulphite cytochrome *c* reductase). The reaction catalysed by this enzyme is (Peck 1960; Bowen *et al* 1966; Yamanaka *et al* 1981; Toghrol & Southerland 1983; Lu & Kelly 1984).



3.2 Ferrous oxidation

A schematic representation of ferrous iron oxidation by *T. ferrooxidans* is given in figure 3 (Pringsheim 1949; Lundgren *et al* 1974; Black *et al* 1989). The oxidation of ferrous iron does not involve production of protons produced in the enzyme-catalysed reaction:



The ferric iron formed undergoes abiotic hydrolytic reactions which result in the release of protons on the extracytoplasmic side. The most significant reaction at pH 2.0 is:



The cell membrane associated electron transporters involved in the iron oxidation include iron oxidase, cytochrome *c* and a terminal oxidase cytochrome *a*. The soluble electron transport component include cytochrome *c* and a blue copper protein rusticyanin. An iron cytochrome *c* reductase or iron oxidation st

been reported by several authors (Blaylock & Nason 1963; Yates *et al* 1967; Sugio *et al* 1981). It is indicated by several observ

oxidation takes place outside the cell membrane, that is, in th

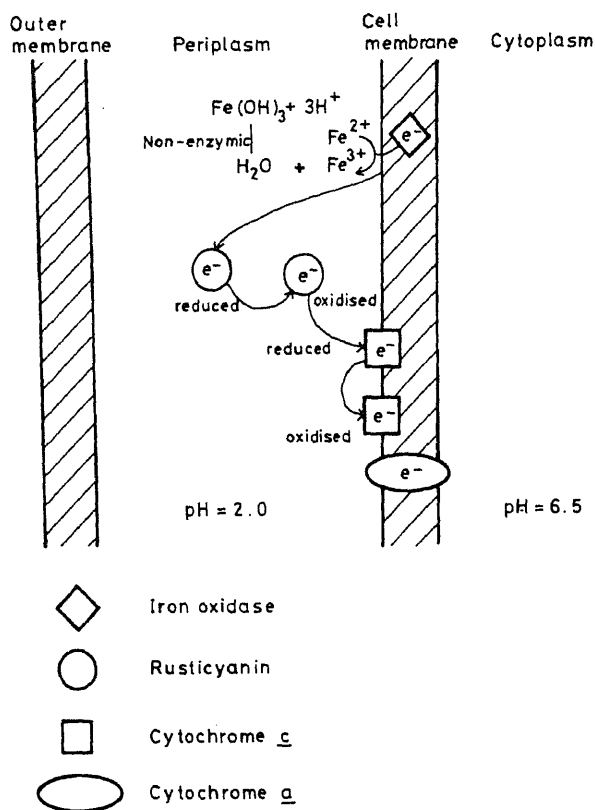


Figure 3. A schematic representation of ferrous oxidation by *T. ferrooxidans*.

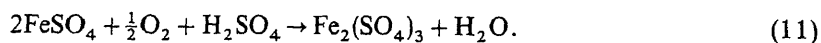
inferred from the fact that iron would be rapidly autooxidised at cytosolic pH values (pH 6.5) and that ferric iron formed at this pH would be insoluble.

4. Mechanisms of mineral oxidation

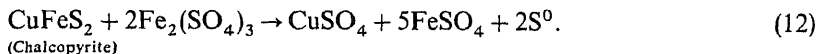
Mechanisms involved in biooxidation of minerals are very complex. When the organisms interact with mineral substrates in an acid medium, a number of reactions occur. The microbe-mineral interactions influence the rate of mineral dissolution by various chemical, biochemical and electrochemical factors. The main leaching mechanisms involved are indirect, direct and electrochemical oxidation.

4.1 Indirect leaching

In this process, the bacteria do not attach to the mineral surfaces. Indirect leaching involves biological regeneration of ferric sulphate.



Ferric sulphate produced, is a strong oxidant and is capable of dissolving a wide variety of sulphide minerals. For example,



The elemental sulphur formed in the reaction can be converted to sulphuric acid by *T. ferrooxidans*.



The sulphuric acid generated, not only maintains the pH at levels favourable to the bacteria but also leaches a variety of copper oxide minerals like azurite $[\text{Cu}_3(\text{OH})_2(\text{CO}_3)_2]$, chrysolla $(\text{CuSiO}_3 \cdot 2\text{H}_2\text{O})$ and tenorite (CuO) very effectively.

4.2 Direct leaching

T. ferrooxidans also leaches mineral sulphides by attachment to mineral surfaces. This process can be described by the following reaction,



where *M* is a bivalent metal. Incubation of *T. ferrooxidans* with the mineral substrates results in oxygen consumption and metal solubilization.

Since iron sulphides are invariably present in the natural leaching environments, probably both direct and indirect leaching mechanisms occur simultaneously. Bacterial attachment was found to be governed by particle size of the mineral, period of incubation and by stationary or agitation conditions used during incubation (Natarajan 1992). Some of the researchers attribute enhanced mineral dissolution to the direct mechanism, while others suggest that bacterial assistance in the enhancement of mineral dissolution is due to constant supply of ferric ions. The attachment of *T. ferrooxidans* to a number of sulphide minerals has been studied quantitatively by estimating its protein and nitrogen concentrations.

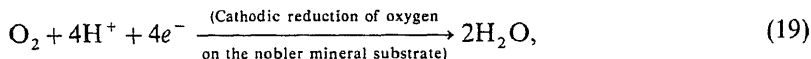
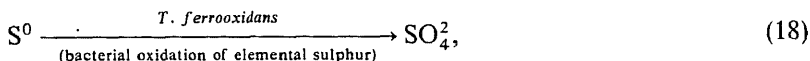
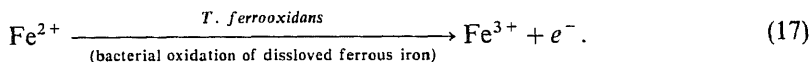
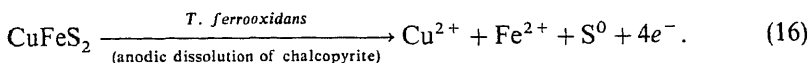
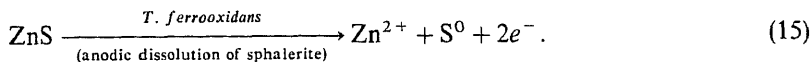
Attachment of *T. ferrooxidans* on to pyrite mineral was observed to be influenced by reducing particle size and increasing incubation periods. It has been also observed that increased bacterial attachment to pyrite mineral surfaces promoted iron dissolution (Murthy & Natarajan 1992).

4.3 Electrochemical leaching

Principles of electrochemistry are applicable to mineral dissolution in leaching processes (Natarajan 1990). Many natural minerals behave as electrodes in the presence of a leaching medium. Thus in leaching systems containing more than one mineral, galvanic interactions essentially come into play. When two sulphide minerals establish contact in a leaching medium, a galvanic cell will be formed; the more active mineral in the couple will undergo corrosion while the nobler (less active) one will be cathodically protected. Considering the example of a chalcopyrite-pyrite couple, chalcopyrite has the lower electrical rest potential and becomes the anode while pyrite behaves as a cathode. As a result, the chalcopyrite phase undergoes rapid dissolution while the pyrite phase remains essentially unaffected. *T. ferrooxidans* further catalyses the above

electrochemical reactions by continuously oxidising the film of elemental sulphur formed on mineral surfaces which would otherwise form a physical hindrance to diffusion of copper and iron salts away from the reacting phase. Prediction of the electrochemical behaviour of sulphide minerals in multiple combinations is more difficult.

Typical reactions illustrating galvanic interaction mechanisms are given below:



Thus, the galvanic dissolution of an active mineral (chalcopyrite, sphalerite etc.) when contacted with a nobler mineral like pyrite, in the presence of *T. ferrooxidans*, is increased several fold (Natarajan 1988, 1992; Jyothi *et al* 1989)

5. Current engineering applications

Microbial leaching is rapidly becoming an important process tool for the treatment of especially low and lean grade ore reserves. The role of microorganisms in the leaching of a number of minerals has long been established. The microorganisms, in most of the cases occur indigenously to the various mining operations. From a metallurgical point of view, as the grade of the ore becomes lower and lower, the technology for metal extraction becomes more and more difficult and expensive. The mineral industries are seeking development of modified extraction processes and lowering of costs. Dump/heap leaching, *in situ* solution mining and bioreactor leaching with the help of *T. ferrooxidans* have been attractive innovations in this direction.

5.1 Copper

On a commercial scale, dump/heap leaching operations at the mine site for lean and waste mined copper ores are being employed in many parts of the world. Biological copper leaching is practised in many countries such as USA, Russia, Chile, Peru, Australia, Spain, Canada and Mexico.

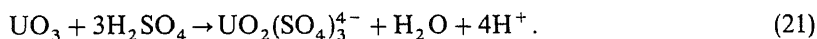
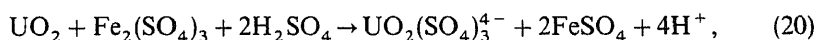
Engineering layouts for leaching operations all over the world are remarkably uniform. Essentially, copper ore mined from open pits is segregated. Higher grade material is concentrated to produce a feed for smelting, while the lower-grade ore is subjected to leaching. The ore is piled on until a dump/heap of suitable dimension accumulates, the top of the dump is levelled and then the leach solution is flooded or

sprayed onto the dump. Bacterial colonization occurs mainly in the top layers. The temperature generally rises to 80°C–90°C in the central regions of the dump due to exothermic reactions. In this case indirect leaching by ferric sulphate prevails. Leach solutions enriched with copper exit at the base of the dump and are conveyed to a central recovery facility. The barren solution is then recycled to the leach dumps.

In situ leaching is yet another popular technique in this direction. It facilitates extraction of deeper low value mineral reserves without the need for mining and expensive operations. It involves breaking the ore body with powerful explosives to make the deposit penetrable to solution. Leach solution and air are then injected under pressure. The resulting copper-enriched solutions are then recovered below the ore body. Copper is recovered by conventional methods. *In situ* mining eliminates environmental pollution problems associated with large scale mining (Ehrlich 1963; Duncan *et al* 1964; Brierley & Lockwood 1977).

5.2 Uranium

Uranium leaching using bacteria has been implemented since the 1960s in Canada. The process involves intermittent spraying or flooding of worked-out stopes and tunnels of underground mines with water or dilute sulphuric acid solution at regular intervals. The activity of *T. ferrooxidans* is limited to oxidation of pyrite and ferrous ions because it does not directly interact with uranium minerals. Uranium leaching proceeds according to the following reactions:



Uranium bearing solution drains to the lower portions of the mine and accumulates in sumps. The solution is then pumped to the surface for uranium recovery (Harrison *et al* 1966; Tuovinen & Kelly 1974; Ferroni *et al* 1986; McCready 1988).

5.3 Coal desulphurization

Although bioprocessing has not been applied to coal on an industrial scale, a number of possible applications have been examined in the laboratory and on pilot scales.

A preliminary economic analysis has shown that microbial desulphurization compares favourably with alternative chemical coal-cleaning methods. The parameters governing rates of pyrite dissolution in coal are particle size, pulp density, solution pH and temperature, inoculum size and characteristics of the leaching bacteria. In some instances, leaching rates are enhanced by supplemental nutrients and carbon dioxide. Fine coal slurries could be subjected to oxidation by *T. ferrooxidans* at a pH of 2.0–2.5 and temperatures in the range of 25°C–35°C.

The use of *T. ferrooxidans* in coal desulphurization involves surface modification of the pyrite. It has been observed that pyrite is more easily separated from coal during froth flotation following an initial exposure to these bacteria, because pyrite is rendered more hydrophilic by selective attachment of the bacteria; flotability increases with increase of hydrophobic character. Coal cleaning by this method would avoid the long

retention period required for microbial dissolution of pyrite (Dugan & Apel 1978; Kargi 1982; Monticella & Finnerty 1985; Huber *et al* 1986).

5.4 Gold

The most important application of biotechnology to gold recovery is the treatment of refractory ores and concentrates to increase gold dissolution during cyanide leaching (Natarajan 1993). In many such ores, finely divided gold is encapsulated in pyrite or arsenopyrite minerals and thus cannot be dissolved by the cyanide solutions unless the ore is very finely ground. An alternative to grinding is to use bacteria to selectively dissolve enough of the sulphides to expose the gold, and then to leach with cyanide by the normal process. The use of bacteria keeps the cost of sulphide mineral dissolution at a reasonable level, and since it is only necessary to dissolve a fraction of the pyrite to expose the gold, the leaching time can be kept to a few days.

Large scale application of bioleaching of refractory gold ores and concentrates before cyanidation has been demonstrated at the Fairview mine in South Africa in 1986. This industrial plant treats 18 t/day of high grade gold concentrates. The San Bento plant in Brazil was commissioned in 1990 to treat 300 t/day of low grade concentrate. A large number of commercial biotreatment plants have since been commissioned for processing of refractory gold concentrates in Australia and Ghana (Livesey-Goldblatt *et al* 1977, 1983; Griffin & Luinstra 1989; Hackl *et al* 1989; Morin & Ollivier 1989; Lawrence 1990; Torma Oolman 1992).

6. Methods for accelerating growth of *T. ferrooxidans* for faster biooxidation

T. ferrooxidans is a very slow-growing organism. Its generation time varies between 16 and 20 h. Therefore obtaining a large biomass for industrial purposes using the classical methods is very time-consuming and complicated. Under normal growth conditions in 9 K medium, it takes upto 30–40 h to obtain a cell mass of about 10^8 cells/ml. Hence there is a quest for developing methods which would produce large amounts of biomass in a shorter time, with a view to enhance leaching rates. Some methods developed for the enhancement of the biomass of *T. ferrooxidans* are illustrated below.

6.1 Bacterial film oxidation (BACFOX process)

This method is proposed to raise the number of bacteria in the medium during heap and underground leaching. The method comprises the following procedures.

Cells of *T. ferrooxidans* are placed in the form of a film on a corrugated surface of bioactive material. The corrugated material coated with the film of bacteria is submerged in ferrous sulphate solution saturated with air. Oxidation of Fe^{2+} takes place. Bacteria bind with the precipitated jarosite; the film containing bacteria and jarosite may be grown on various materials like glass, plastic etc. Livesey-Goldblatt *et al* (1977) reported that the best results are obtained in the media where bacterial film was fixed on corrugated plastic. Maximum specific rate of ferrous to ferric oxidation was observed to be 7.5 g/h/m² of bacterial film. A schematic representation of the BACFOX process is depicted in figure 4.

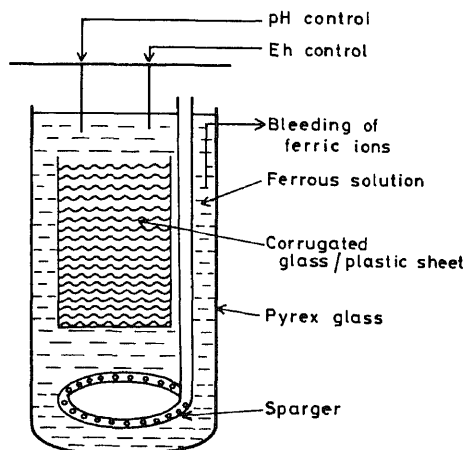


Figure 4. Bacterial film oxidation (BACFOX).

6.2 Biomass production by using electrical energy

Another way to increase the cell concentration in the culture and at the same time to overcome all the above mentioned drawbacks of the classical methods is offered by the method proposed by Kinsel & Umbreit (1964). Several researchers have proposed similar methods (Kovrov *et al* 1978; Denisov *et al* 1980; Yunker & Radovich 1985; Natarajan 1992b). The main feature of this method is combining two processes, namely, the microbiological oxidation of Fe^{2+} and electrochemical reduction of Fe^{3+} to Fe^{2+} . The method comprises electrochemical reduction of bacterially generated ferric ions

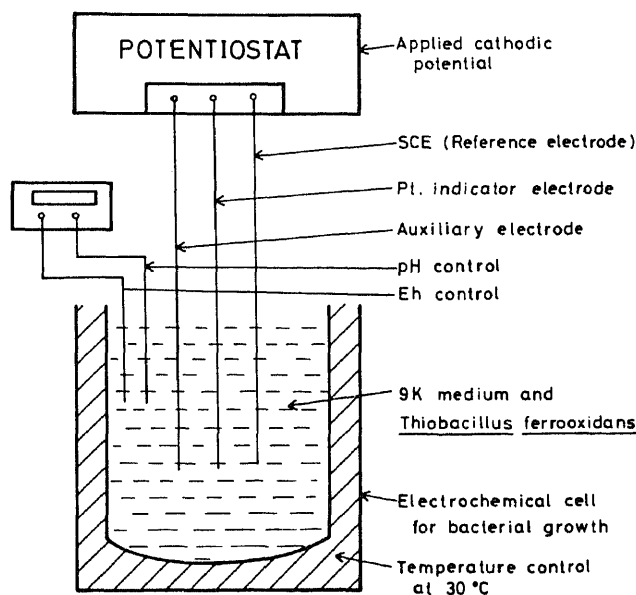


Figure 5. A schematic representation of biomass production using applied DC potentials.

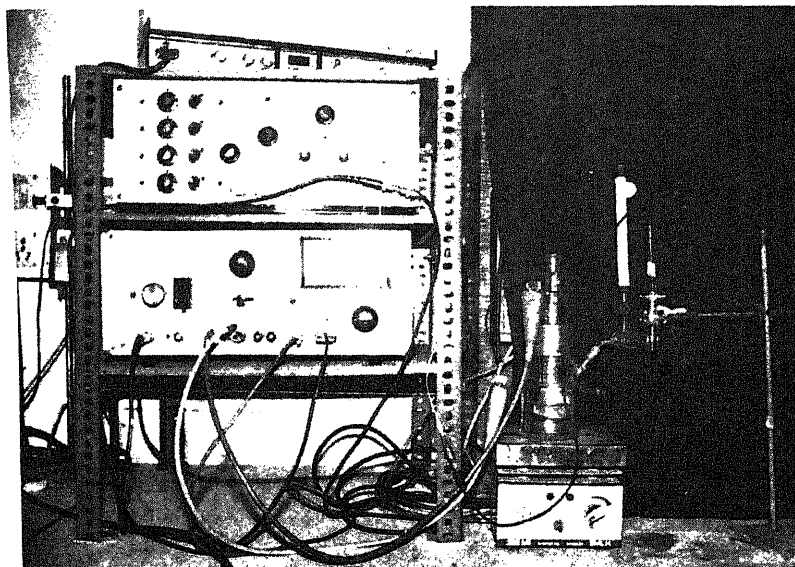


Figure 6. Experimental set-up of electrochemical cell.

directly in the culture. Figure 5 shows a scheme of reactions taking place in an electrochemical cell that provides the energy source for *T. ferrooxidans*. The energy for cell growth comes from the electrochemical cell's electrodes, while the energy providing substrate (ferrous ion), serves merely as a carrier of energy from the cathode to the bacterial cell. The Fe^{2+} is not supplied from outside but is formed in the culture on the anode surface. Figure 6 shows a typical laboratory experimental set-up of electrochemical instrumentation.

The electrochemical reduction of ferric ion is coupled with continuous cultivation of *T. ferrooxidans*. The concept involves the correlation of two mutually opposing reactions, namely: the bacterial oxidation of Fe^{2+} and the electrochemical reduction of Fe^{3+} . Most useful for practical application is the method of maintaining a constant cathode potential. The optimal bacterial biomass concentration during continuous cultivation ranges from 5 to 10 g/l (dry weight).

Application of negative DC potentials in the range of -500 mV to -1000 mV to a bacterial culture containing ferric ion, effectively converts ferric ion to the ferrous state, promoting bacterial activity and growth. Under a negative applied potential of -500 mV the cell number of *T. ferrooxidans* increased from 2.5×10^7 cells/ml to about 1.3×10^8 cells/ml within a period of about 60 h (Natarajan 1992b). Subsequent impression of -500 mV to a fully grown culture containing 1.3×10^8 cells/ml promoted significant growth of the bacteria (Natarajan 1992). It has been reported that the generation time of *T. ferrooxidans* can be reduced from 16 h to 10 h with a ten-fold increase in biomass when an applied potential of -500 mV is maintained (figure 7). Electrobioreaching also enables faster and selective dissolution of the desired mineral phase from complex sulphides, unlike the case with only bioleaching, as depicted in figure 8. Zinc dissolution from binary mixtures containing either pyrite or chalcopyrite in addition to sphalerite was observed to be the highest at an applied potential of -500 mV in the presence of *T. ferrooxidans* (Natarajan 1992b).

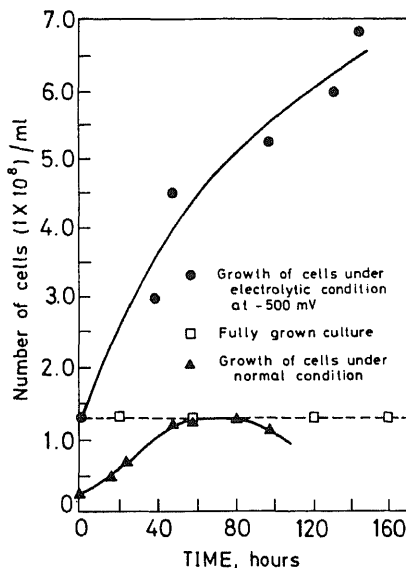


Figure 7. Variation in number of cells per ml with time in the growth of *T. ferrooxidans*.

6.3 Oxidation in packet-bed reactors

Bacterial biomass can also be enhanced by using *T. ferrooxidans* in a fixed-film bioreactor containing glass beads, activated carbon particles or ion-exchange resin (Grishin & Tuovinen 1988). Both batch and continuous flow modes of operation have been studied for the biological oxidation of ferrous sulphate to ferric sulphate. Various packed-bed reactors have been designed to improve the rate of iron oxidation. Three

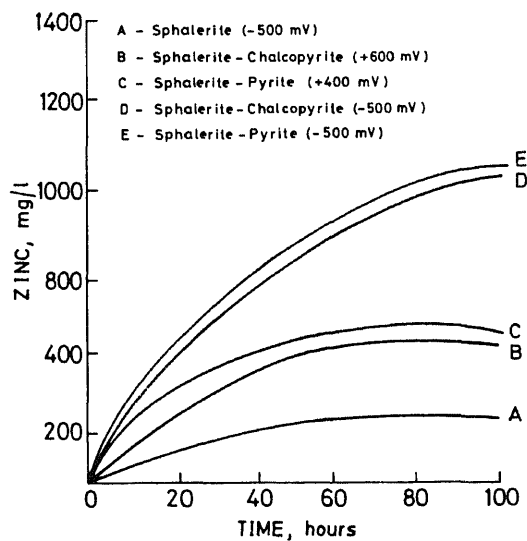


Figure 8. Zinc dissolution from binary mixtures containing pyrite or chalcopyrite with sphalerite under applied potential.

parameters were taken into consideration; namely, providing a larger surface area for attachment of *T. ferrooxidans* to the support matrices, to reduce loss of biomass and the use of a low pH (between 1.3 to 1.5) to provide more extensive adsorption of the bacteria and also to eliminate ferric precipitation.

The activated-carbon packed-bed reactor had the highest level of biomass, amounting to 32 mg of protein per ml of interstitial liquid or 128 micro g/cm² of matrix surface. The ability of the glass beads to retain biomass was about 50 times less.

6.4 Growth in solid medium

Growing *T. ferrooxidans* on a solid medium so far has been a very time-consuming and tedious process; the solidifying agent, agar-agar, neither forms a stable gel when sterilised at low pH values nor properly solidifies due to hydrolysis. To overcome these problems, a new medium has been designed by Khalid *et al* 1993. They have used bacterial polysaccharide, 'Gellan Gum' or 'Gelrite' as solidifying agent for acidophilic thiobacilli. This medium has been devised for estimating the growth of *T. ferrooxidans* on the solid substrate. The plating efficiency was determined to be $92.1 \pm 5.8\%$. Dark brown, circular, well-differentiated colonies developed within 72–96 h. The cell count was approximately 7×10^6 cells/ml for ATCC 13661 strain of *T. ferrooxidans*. Dry biomass of 650 mg/l can be obtained by this method which corresponds to 320 mg total protein/l. A linear relationship has been found which gave a value where 0.5 g dry mass/l was equivalent to 2.8×10^6 cells/ml of the ATCC 13661. This medium can be employed to purify cultures of *T. ferrooxidans* strains which have frequently been reported to have been associated with other acidophiles. The high plating efficiency also indicates that this method can be used for selection of mutants resistant to toxic metals and also for genetic investigation of *T. ferrooxidans*.

6.5 Genetic manipulation for development of special strains

The necessity to develop special strains of *T. ferrooxidans* which possess both high metal and temperature tolerance as well as better leaching capability becomes very evident because accumulation of toxic metal ions such as arsenic, copper and zinc hinders bacterial activity. Development of metal-tolerant, preadapted bacterial strains is thus necessary to obtain efficient bacterial activity during leaching. Adapted strains are found to be more efficient in gold liberation compared to the unadapted wild strains. One of the principal objectives of genetic manipulation is to develop techniques to introduce the desired characteristics into the leaching bacteria. Attempts have already been made to detect the plasmid DNA in *T. ferrooxidans*. Methods of plasmid isolation and identification from *T. ferrooxidans* have been worked out. The possibility of cloning them into *Escherichia coli* has also been evaluated. However, the development of genetically engineered *T. ferrooxidans* is still far-fetched (Groudeva *et al* 1980; Cox & Boxer 1986; Rawlings *et al* 1986; Yates & Holmes 1987; Holmes *et al* 1988; Yates *et al* 1988; Holmes & Yates 1990).

Much progress has been made in understanding the pathways of ferrous and sulphur oxidation, energy coupling, and carbon assimilation. However, physiological descriptions do not at present appear to be leading toward a coherent taxonomic analysis of the thiobacilli.

The ribosomal ribonucleic acid (rRNA) of *T. ferrooxidans* is independent of growth conditions and metabolic status. So they are useful for comparing even physiologically disparate species. 5S rRNA is sufficiently conserved in all species. Hence sequence homologies are evident even between organisms that have immeasurably low overall deoxyribonucleic acid (DNA) homology. Mixed or contaminated cultures are readily evident by detection of more than one type of 5S rRNA. The rRNA sequence, therefore, provides incisive criteria for the classification of new strains. It is understood that phylogenetic framework will offer a more directed approach toward the comparative biochemistry of these organisms. Since there is presently a great deal of interest in 'engineering' these economically important bacteria, knowledge of their natural evolutionary relationships should be of use in constructing fruitful *recombinants*.

Thus, DNA and rRNA analyses are being used to classify strains into different genomic groups within the species. This will provide useful selection of genotypes and phenotypes best suited for particular application. Twenty-three strains of *T. ferrooxidans* were examined by Harrison (1982), which were genomically diverse.

A strategy for obtaining recombinants by genetic engineering is presented here.

- (i) The chromosomal and plasmid DNA from *T. ferrooxidans* are isolated by standard procedures.
- (ii) Both the chromosomal and plasmid DNA are subjected to restriction digestion with the help of restriction enzymes to cut the DNA into fragments.
- (iii) With advanced molecular biology techniques the gene of interest is selected and isolated. (Explanation of the procedures is beyond the scope of this review.)
- (iv) Once the gene of interest is isolated, it is incorporated into an *Escherichia coli* plasmid. This plasmid is a small circular DNA.
- (v) The circular plasmid DNA is cut with a restriction enzyme to form a linear strand.
- (vi) The gene of interest is then added to the linear strand of DNA. The gene then gets attached to the linear plasmid to form a recombinant molecule comprising part of the plasmid DNA, hence the term *recombinant DNA*.
- (vii) The recombinant DNA molecule is then sealed to reform a circle with an enzyme called ligase.
- (viii) The recombinant plasmid is then put back into *E. coli*. This process is called *transformation*.
- (ix) The *E. coli* cell is then allowed to divide many times in the culture media, producing a large number of colonies, each identical to the starting bacterium. Since the recombinant plasmid is also present in all the progeny bacteria, the inserted gene of interest is said to have been *cloned*.
- (x) After cloning, the recombinant plasmids are then isolated from the host *E. coli*, giving amplified copies of a single gene of interest. The characteristics of this gene are then expressed.

A schematic representation of this method is depicted in figure 9.

7. Summary

Biological processing of minerals and metals is a rapidly growing, diverse field whose importance will become considerable in the near future. The use of genetic engineering

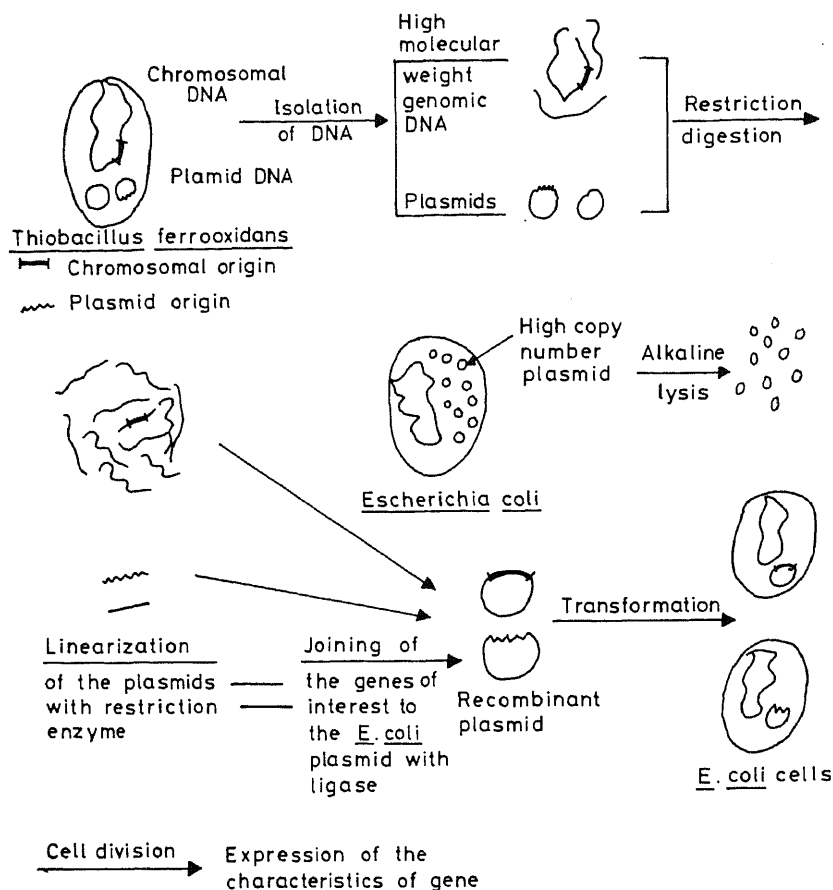


Figure 9. A strategy for obtaining recombinants by genetic engineering.

techniques will allow organisms to be precisely tailored to their applications and thus improve their effectiveness.

Further development of bioleaching technology is aimed at extending the range of metals and ores that may be processed. New organisms, especially thermophilic bacteria, may accelerate the rates of metal extraction. There is a need for more fundamental research to determine the factors which limit the rate of microbial ore leaching, the characteristics of the ore bioleaching environment, the interactions of microorganisms and their effect on ore leaching.

References

- Black R C, Shute E A, White K J 1989 Enzymology of respiratory iron oxidation. *Biohydrometallurgy*: 391–401
- Blaylock B A, Nason A 1963 Electron transport systems of the chemoautotroph *Ferroplasma ferrooxidans*: Cytochrome *c* containing iron oxidase. *J. Biol. Chem.* 238: 3453–3462
- Bowen T J, Happold F C, Taylor B F 1966 Studies on adenosine-5-phosphosulphate reductase from *Thiobacillus denitrificans*. *Biochem. Biophys. Acta* 118: 566–576

- Brierley C L 1978 Bacterial leaching. *CRC Crit. Rev. Microbiol.* 6: 207-262
- Brierley J A, Lockwood S J 1977 The occurrence of thermophilic iron oxidizing bacteria on a copper leaching system. *FEMS Microbiol. Lett.* 2a: 163-165
- Charles A M, Suzuki I 1966 Mechanism of thiosulfate oxidation by *Thiobacillus novellus*. *Biochem. Biophys. Acta* 1281: 510-521
- Colmer A R, Hinkle M E 1947 The role of microorganisms in acid mine drainage. *Science* 106: 253-256
- Cox J C, Boxer D M 1986 The role of rusticyanin, a blue-copper protein, in the electron transport chain of *Thiobacillus ferrooxidans* grown on iron or thiosulfate. *Biotechnol. Appl. Biochem.* 8: 269-275
- Denisov G V, Kovrov B G, Trubachev I N, Gribovskaya I V, Stepen A A, Novoselova O I 1980 Composition of a growth medium for continuous cultivation of *Thiobacillus ferrooxidans*. *Mikrobiologiya* 49: 3: 473-478
- Din G A, Suzuki I, Lees H 1967 Ferrous iron oxidation by *Ferrobacillus ferrooxidans*, purification and properties of Fe^{++} cytochrome and reductance. *Can. J. Biochem.* 45: 1523-1546
- Dugan P R, Apel W A 1978 Microbiological desulfurization of coal (eds) L E Murr, A E Torma, J A Brierley. *Metallurgical applications of bacterial leaching and related microbiological phenomena* (New York: Academic Press) pp 223-50
- Duncan D W, Trussell P C, Waldin C C 1964 Leaching of chalcopyrite with *Thiobacillus ferrooxidans*, Effect of surfactants and shaking. *Appl. Microbiol* 12: 122-126
- Ehrlich H L 1963 Microorganisms in acid drainage from a copper mine. *J. Bacteriol* 86: 350-352
- Ferroni G D, Leduc L G, Todd M 1986 Isolation and temperature characterization of psychrotrophic strains of *Thiobacillus ferrooxidans* from the environment of a uranium mine. *J. Gen. Appl. Microbiol.* 32: 169-175
- Griffin E A, Luinstra L 1989 Bioreactor scale-up: Practical considerations for biologically assisted gold recovery. *Biohydrometallurgy*. pp. 221-230
- Grishin S I, Tuovinen O H 1988 Fast kinetics of Fe^{++} oxidation in packed-bed reactors. *Appl. Env. Microbiol.* 54: 3092-3100
- Gromova L A, Pereverzev N A, Karavaiko G I 1978 Pili of *Thiobacillus ferrooxidans*. *Mikrobiologiya*. 47: 293-295
- Groudeva V I, Groudev S N, Markar K I 1980 Nitrosoguanidine metagenesis of *Thiobacillus ferrooxidans* in relation to the levels of its oxidizing activity. *Bulg. Acad. Sci.* 83: 1401-1404
- Groudev S N 1985 Differences between strains of *Thiobacillus ferrooxidans* with respect to their ability to oxidize sulphide minerals. In *Biogeotechnology of metals* (eds) G I Karavaiko, S N Groudev UNEP, Centre of International Projects (Moscow: GKNT) pp 83-96
- Hackl R P, Wright F R, Gormely L S 1989 Bioleaching of refractory gold ores - out of the lab and into the plant. *Biohydrometallurgy* pp 533-549
- Harrison A P Jr 1982 Genomic and physiological diversity amongst strains of *Thiobacillus ferrooxidans* and genomic comparison with *Thiobacillus thiooxidans*. *Archiv. Microbiol.* 131: 68-76
- Harrison V F, Gow W A, Hughson M R 1966 Factors influencing the application of bacterial leaching to a Canadian uranium ore. *J. Met.* 18: 1189-94
- Holmes D S, Yates J R, Schrader J 1988 Mobile repeated DNA sequences in *Thiobacillus ferrooxidans* and their significance for biomining. In *Biohydrometallurgy, science and technology letters*. (eds) P R Norris, D P Kelly (Kew: Sci. Technol. Lett.) pp 153-160
- Holmes D S, Yates J R 1990 Basic principles of genetic manipulation of *Thiobacillus ferrooxidans* for biohydrometallurgical applications In *Microbial mineral recovery* (eds) H L Ehrlich, C L Brierley (New York: McGraw-Hill) chap. 2, pp 29-54
- Huber G, Huber H, Stetter K O 1986 Isolation and characterization of new metal mobilizing bacteria. In *Workshop on Biotechnology for the Mining, Metal-Refining and Fossil Fuel Processing Industries* (eds) H L Ehrlich, H S Holmes (New York: Wiley) pp 239-251
- Jyothi N, Sudha K N, Natarajan K A 1989 Electrochemical aspects of selective bioleaching of sphalerite and chalcopyrite from mixed sulphides. *Int. J. Miner. Process.* 27: 189-203
- Karavaiko G I, Pivovarova T A 1973 Mechanism of oxidation of reduced sulphur compounds by *Thiobacilli*. *Microbiology*. 42: 389-393

- Kargi F 1982 Enhancement of microbial removal of pyritic sulfur from coal using concentrated cell suspension of *T. ferrooxidans* and an external carbon dioxide supply. *Biotechnol. Bioeng.* 24: 749–752
- Kasprzak A A, Steenkamp D J 1983 Localization of the major dehydrogenases in two methylotrophs by radio-chemical labeling. *J. Bacteriol.* 156: 348–353
- Khalid A M, Bhatti T M, Umar M 1993 An improved solid medium for isolation, enumeration and genetic investigations of autotrophic iron and sulphur oxidizing bacteria. *Appl. Microbiol. Biotechnol.* 39: 259–263
- Kinsel N A, Umbreit W W 1964 Method for electrolysis of culture medium to increase growth of the sulfur oxidising iron bacterium *Ferrobacillus sulfooxidans*. *J. Bacteriol.* 87: 1243–1244
- Kovrov B G, Denisov G V, Sekacheva L G 1978 Effect of concentration of ferrous iron on its rate of oxidation by *Thiobacillus ferrooxidans*. *Mikrobiologiya* 47: 400–402
- Lawrence R W 1990 *Biorecovery of gold ores, microbial mineral recovery* (eds) H L Ehrlich, C Brierley (New York: McGraw Hill) pp 127–148
- Livesey-Goldblatt E, Tunley T H, Nagy I F 1977 *Int. Conference on Bacterial leaching*. (ed.) W Schwartz (Weinheim, New York: Verlag Chemie) 175
- Livesey-Goldblatt E, Norman P, Livesey-Goldblatt D R 1983 Gold recovery from arsenopyrite/pyrite ore by bacterial leaching and cyanidation. *Recent progress in Biohydrometallurgy* (eds) G Rossi, A E Torma (Iglesias, Italy: Assoc. Mineraria, Sarda) pp 627–641
- Lundgren D G, Vestal J R, Tabita F R 1974 The iron oxidising bacteria. In *Microbial iron metabolism* (ed.) J B Neiland (New York: Academic Press) pp 457–473
- Lu W P, Kelly D P 1984 Properties and role of sulphite: cytochrome and oxidoreductase purified from *Thiobacillus versutus* (A2). *J. Gen. Microbiol.* 130: 1683–1682
- McCready R G L 1988 Progress in the bacterial leaching of metals in Canada. In *Biohydrometallurgy, Proc. Int. Symp. Warwick, Science and Technology Letters*, Kew (eds) P R Norris, D P Kelley pp 177–195
- Monticella D J, Finnerty W R 1985 Microbial desulfurization of fossil fuels. *Annu. Rev. Microbiol.* 37: 371–89
- Morin D, Ollivier P 1989 Pilot practise of continuous bioleaching of a gold refractory sulfide concentrate with a high AS content. *Biohydrometallurgy* pp 563–577
- Murthy K S N, Natarajan K A 1992 The role of surface attachment of *Thiobacillus ferrooxidans* on the biooxidation of pyrite. *Miner. Metall. Process.* 9: 20–24
- Natarajan K A 1988 Electrochemical aspects of bioleaching of multisulfide minerals. *Mimer. Metall. Process.* 5: 61–65
- Natarajan K A 1990 Electrochemical aspects of bioleaching of base metal sulfides. In *Microbial mineral recovery* (eds) H L Ehrlich, C L Brierley (New York: McGraw Hill) chap. 4, pp 79–106
- Natarajan K A 1992a Bioprocessing of enhanced gold recovery *Miner. Process Extractive Metall. Rev.* 8: 143–153
- Natarajan K A 1992b Bioleaching of sulphides under applied potentials. *Hydrometallurgy* 29: 161–172
- Natarajan K A 1992c Electrobioleaching of base metal sulfides. *Metall. Trans.* B23: 5–11
- Natarajan K A 1992d Effect of applied potentials on the activity and growth of *Thiobacillus ferrooxidans*. *Biotech. Bioeng.* 39: 907–913
- Natarajan K A 1993 Biotechnology in gold processing. *Bull. Mater. Sci.* 16: 501–508
- Norris P R, Kelly D P 1982 The use of mixed microbial cultures in metal recovery. In *Microbial Interactions and communities* (eds) A T Bull and J H Slater (London: Academic Press) 443–474
- Parker C D, Prisk J 1953 The oxidation of inorganic compounds of sulphur by various sulphur bacteria *J. Gen. Microbiol.* 8: 344–364
- Peck H D 1960 Adenosine 5'-phosphosulfate as an intermediate in the oxidation of thiosulfate by *Thiobacillus thioparus* *Proc. Natl. Acad. Sci. USA* 46: 1053–1057
- Pringsheim E G 1949 Iron bacteria. *Biol. Rev.* 24: 200–250
- Rawlings D E, Sewcharan R, Woods D R 1986 In *Fundamentals and applied biohydrometallurgy* (eds) R W Lawrence, R M R Branion, H G Ebnur (Amsterdam: Elsevier) pp 419–427
- Schedel M, Truper H G 1979 Purification of *Thiobacillus denitrificans* siroheme sulfite reductase and investigation of some molecular and catalytic properties. *Biochim. Biophys. Acta* 56: 454–467
- Silverman M P, Lundgren D G 1959 Studies on the chemoautotrophic iron bacterium

- F. ferrooxidans*. *J. Bacteriol.* 642-647
- Sugio T, Tano T, Imai K 1981 Isolation and some properties of two kinds of cytochrome *c* oxidase from iron grown *Thiobacillus ferrooxidans*. *Agric. Biol. Chem.* 45: 1791-1797
- Toghrol F, Southerland W M 1983 Purification of *Thiobacillus morellus*, sulfite oxidase. *J. Biol. Chem.* 258: 6762-6786
- Torma A E, Oolman T 1992 Bioliberation of gold. *Int. Mater. Rev.* 37: 187-193
- Tuovinen O H, Kelly D P 1974 Studies on the growth of *Thiobacillus ferrooxidans* IV. Influence of monovalent metal cations on ferrous iron oxidation and uranium toxicity in growing cultures. *Archiv. Microbiol.* 98: 167-74
- Yamanaka T, Yoshiska T, Kimura K 1981 Purification of sulphite: cytochrome C reductase of *Thiobacillus novellus* and the reconstitution of its sulphite oxidase system with the purified constituents. *Plant Cell Physiol.* 22: 613-622
- Yates J R, Holmes D S 1987 Two families of repeated DNA sequences in *Thiobacillus ferrooxidans*. *J. Bacteriol.* 169: 1861-1870
- Yates J R, Cunningham R R, Holmes D S 1988 A new insertion sequence in *Thiobacillus ferrooxidans*. *Proc. Natl. Acad. Sci., USA*, 85: 7284-7287
- Yates M G, Nason A 1966 Electron transport systems of the chemoautotroph *Ferrobacillus ferrooxidans* II purification and properties of a heat-labile iron cytochrome *c* reductase. *J. Biol. Chem.*, 244: 4872-4880
- Yunker S B, Radovich J M 1985 Enhancement of growth and ferrous iron oxidation rates of *Thiobacillus ferrooxidans* by electrochemical reduction of ferric iron. *Biotech. Bioeng.*, 27: 1867-1875



Three-dimensional vortex flow field around a circular cylinder in a quasi-equilibrium scour hole

SUBHASISH DEY

Department of Applied Mechanics, Regional Engineering College,
Durgapur 713 209, India

MS received 3 November 1994; revised 7 July 1995

Abstract. The three-dimensional flow field around a circular cylinder in a quasi-equilibrium scour hole under a clear water regime has been investigated experimentally. The distribution patterns of tangential, radial and vertical components of velocity upstream and longitudinal component of velocity downstream of a cylinder have been presented in this paper. The flow simulation results show the existence of a helical motion of fluid around the cylinder.

Keywords. Three-dimensional flow; hydrodynamics; vortex flow; scouring; flow around cylinder; velocity profiles.

1. Introduction

A cylinder, embedded vertically in a loose bed, causes obstruction to form a three-dimensional separation of boundary layer flow and is conducive to the development of a localized scour. As a result of the interaction between the two-dimensional approaching boundary layer flow and the adverse pressure gradient set by the cylinder, the problem becomes complex. Detailed study of the general flow pattern for such a case has been reported by Hjorth (1975), Melville (1975), and Dargahi (1987). The components of the flow field are the downflow, horseshoe vortex, wake vortex and bow wave, as shown schematically in figure 1. The approaching flow gradually becomes zero along the vertical line in the front face of the cylinder. Since the profile of the approaching velocity along the vertical decreases downward, starting with a maximum at the free surface and becoming zero at the bed, the stagnation pressure gradient is negative downward. Thus, the flow is driven down in the close front of the cylinder. The horseshoe vortex, developed due to the separation of flow at the edge of the scour hole upstream, rolls to form a large helical flow which migrates along the sides of the cylinder downstream (Raudkivi 1986). A bow wave is formed at the upstream free surface adjacent to the cylinder, rotating in the opposite direction of the horseshoe vortex. The stagnation pressure also accelerates the flow past the cylinder, resulting in flow separation at the sides of the cylinder and creating the wake with the cast off vortices at the interfaces to the main flow. Enhanced

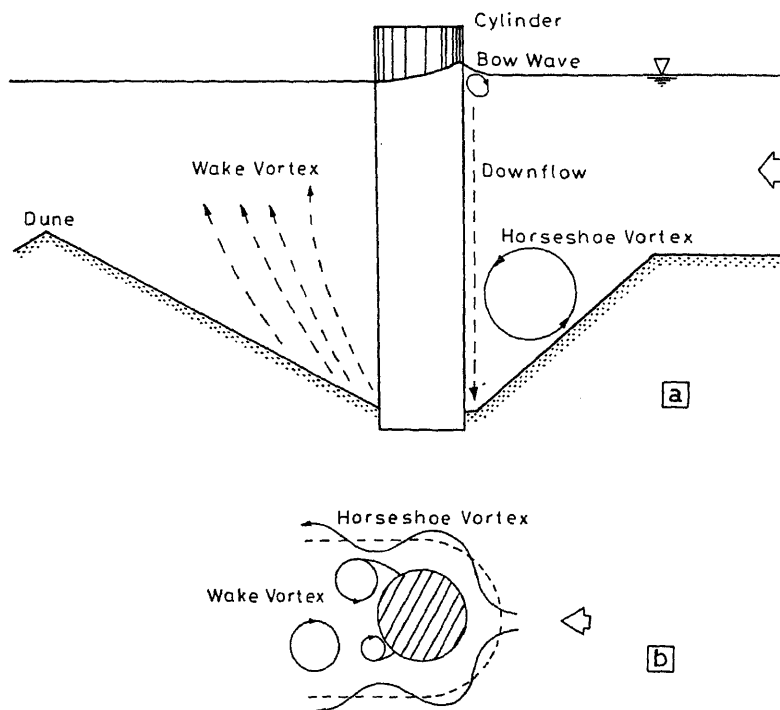


Figure 1. Definition sketch.

velocities in front of and to the sides of a cylinder scour the loose bed and carve out U-shaped scour hole with open ends of the U directing downstream.

Depending on the supply of sediment by the approaching flow, localized scour occurs in two ways. Clear water scour refers to the situation where no sediment is supplied by the approaching flow into the scour zone. Live bed scour, in contrast, occurs where there is a general transport of sediment by the approaching flow to the zones subjected to scour. Summary pertaining to the work on local scouring has been comprehensively reviewed by Breusers *et al* (1977) and Dargahi (1982). Although the characteristic features of the general flow structure around a circular cylinder in the scour zone have been documented, the nature of the distribution patterns of the velocity components seems to have received little attention so far.

The aim of the present experimental investigation is to determine the behavioural patterns of the distribution of velocity components of the three-dimensional vortex flow field around a circular cylinder in a quasi-equilibrium scour hole under a clear water regime. The experimental data are utilized to obtain the flow simulation results.

2. Experimentation

2.1 Experimental set-up and programme

The experiments were conducted in a 1.3 m long, 0.81 m wide and 0.25 m deep test section located 6 m away from the inlet of a 10 m long flume. A false floor was

constructed along the length of the flume 0.25 m above the bottom, and uniformly graded fine sand of mean diameter (d_{50}) 0.58 mm used for local scouring was glued along its surface. Geometric standard deviation (σ_g) of the particle size distribution given by $(d_{84}/d_{16})^{1/2}$ was 1.31 which was less than 1.4 for a uniformly graded sand (Dargahi 1987). A perspex circular cylinder of diameter (b) 0.076 m was placed at the middle of the test section. Experiments were run under clear water scour at an approaching flow depth (h) of 0.05 m and a mean approaching velocity (U) of 0.261 m/s. Although a ratio h/b up to 3 was found to be desirable for severe scouring, in this study h/b was set to 0.66 to have the controlled flow in the flume. The flow field, to be measured, would however remain similar for higher values of h/b . The semi-logarithmic plot of the velocity at 2 m upstream from the cylinder centre, found to be free flow, was used to determine the shear velocity of approaching flow (u_*). The magnitude of u_* found to be 0.0169 m/s was less than the critical bed shear velocity u_{*c} for the initiation of particle motion i.e. 0.017 m/s. The experiments were started, setting the inflow rate by the inlet valve and maintaining the required flow depth by the downstream control. Run time for a period of 12 h was taken to ensure that the quasi-equilibrium state (discussed in the succeeding section) was reached. After 12 h, the inflow rate was slowly reduced to zero and the water was carefully drained out from the scour hole.

2.2 Bed stabilization

A synthetic resin mixed with water (1:3 by volume) was sprayed on the scour bed when it was reasonably dry. The sand was sufficiently impregnated with the resin when it was left to set for 12 h. The resin was polymerized by spraying a coat of dilute formic acid. After 48 h, the bed profile became rock-hard, facilitating measurements.

2.3 Measuring techniques

The three components of velocity vectors were measured using a five-hole pitot sphere (Shukry 1950) which had a spherical sensing head of 8 mm diameter and five holes lay on two meridians perpendicular to each other. The appropriate calibration curves enabled the pitch angle and the velocity magnitude to be determined. The direction in the horizontal plane of velocity vector was determined by a protractor attached to the probe, equalizing pressures at the two pressure points opposed in plan. In the regions of negligible vertical velocity (at 75° upstream and in the downstream), a three-tube yaw probe (Rajaratnam & Muralidhar 1967) was used to measure the horizontal velocity vectors. This probe was made of three brush tubes of 3 mm OD and 1.8 mm ID, rigidly fixed together. The centre tube had a flat nose, while the side tubes were chamfered at an angle 45°. The downflow in the front face of the cylinder was measured using a specially made pitot tube because pitot sphere was unsuitable there. As there was no flow across the downflow i.e. the pressure gradient normal to the flow direction is zero, this probe was found to be useful. It had a vertical static tube with radial holes at the end and a stagnation tube facing the downflow, with 2 mm OD and 1 mm ID each. All the probes were connected to the precision manometers (inverted type) which had air at the top. The manometer reading up to 0.1 mm accuracy was measured by a Vernier attachment. The minimum velocity vector was registered to be 0.04 m/s. The flow

direction and magnitude within the scour hole changed extensively making the measurement difficult. A light aluminium fin, known as direction finder, was attached to the end of a steel rod of 1 mm diameter. The fin could rotate freely about its axis to show the flow direction approximately when it was dipped in the flow. It was estimated, however, that the mean velocity directions were within $\pm 10^\circ$. The most difficult part in the flow measurement was to ascertain the reversed flow which was successfully carried out by the fin. To get the exact flow direction, the pitot sphere/yaw probe was placed at the appropriate position to face the flow and was rotated along a horizontal plane until it registered the same pressure in the side holes. Also, the points of detachment of the horseshoe vortex on both sides of the cylinder determined by the fin were at $\pm 75^\circ$. The flow field in the wake region was ill-defined and was beyond the realm of the study.

2.4 Measurement errors and corrections

The errors for pitot tube (Nwachukwu 1979) which may possibly occur in the measurements are: (i) the error in presence of a pitot tube near to the bed which results in higher impact of pressure record than the actual one due to shifting of streamlines; and (ii) the error due to the turbulent fluctuation. The error in the measured velocity near bed, based on 1/7th power law of velocity distribution, was found to be 7% (Tingsanchali & Maheswaran 1990). Since no attempt has been made to quantify this type of instrumental error for a five-hole pitot sphere and three-tube yaw probe, it was assumed that these were subjected to the same error magnitude as that of the pitot tube. The error in the mean velocity due to turbulence was estimated from the relationship given by Goldstein (1983). Based on the turbulent intensity for equilibrium scour measured by Melville & Raudkivi (1977), the local velocity was found to be overestimated by 2% (Dey 1991). So no correction was applied to suppress it. All the measurements were repeated with good accuracy until the two separate measurements at a point were registered to be equal. The errors of the measurements carried out in the reversed flow regions were usually higher than in other regions of the flow, which were taken with some reservation.

The approaching flow crossed the upper portion of the pitot sphere and the reversed flow near bed was affected. However, the correction factor, determined using a micro-pitot tube, was used for the data of velocity measurements. The velocities measured by a micro-pitot tube along the sloping bed, providing a free passage of approaching flow, were compared with those measured by the pitot sphere. The correction factors estimated at 0° , 15° and 30° were 1.18, 1.11 and 1.05 respectively.

3. Quasi-equilibrium scour

The process of digging by the downflow at the cylinder base and the erosion of slant bed continued until a quasi-equilibrium state (Dey *et al* 1992b) was reached. This happens when the particles can no longer be dislodged by the impact of the downflow. In this state, the slant bed eroded continually in the form of a few rolling particles which were subsequently carried out by the arms of the horseshoe vortex, without any noticeable change in scour depth. Full equilibrium was reached, when the rolling motion was ceased, after an impractically long experimental time. The average angle of the upstream sloping bed, in the quasi-equilibrium state, was about 15% greater than the

3-D vortex flow field around a circular cylinder

angle of repose (ϕ) of the bed sand in still water. The greater angle, maintained by the shear force of the reversed flow along the slope of the hole, may be termed "dynamic angle of repose" (Dey 1991; Dey *et al* 1992b). This was also evident in Melville & Raudkivi (1977) and Jain & Fischer (1979). In the present study the dynamic angle of repose was found to be 37° , with an upstream conical scour hole of depth 0.096 m below the original bed for the sand having ϕ of 32° .

4. Simplified geometry of scour hole

In the upstream, the azimuthal section of the quasi-equilibrium scour hole (figure 2) is divided into zone 1 i.e. vertically above the sloping bed and zone 2 i.e. vertically above

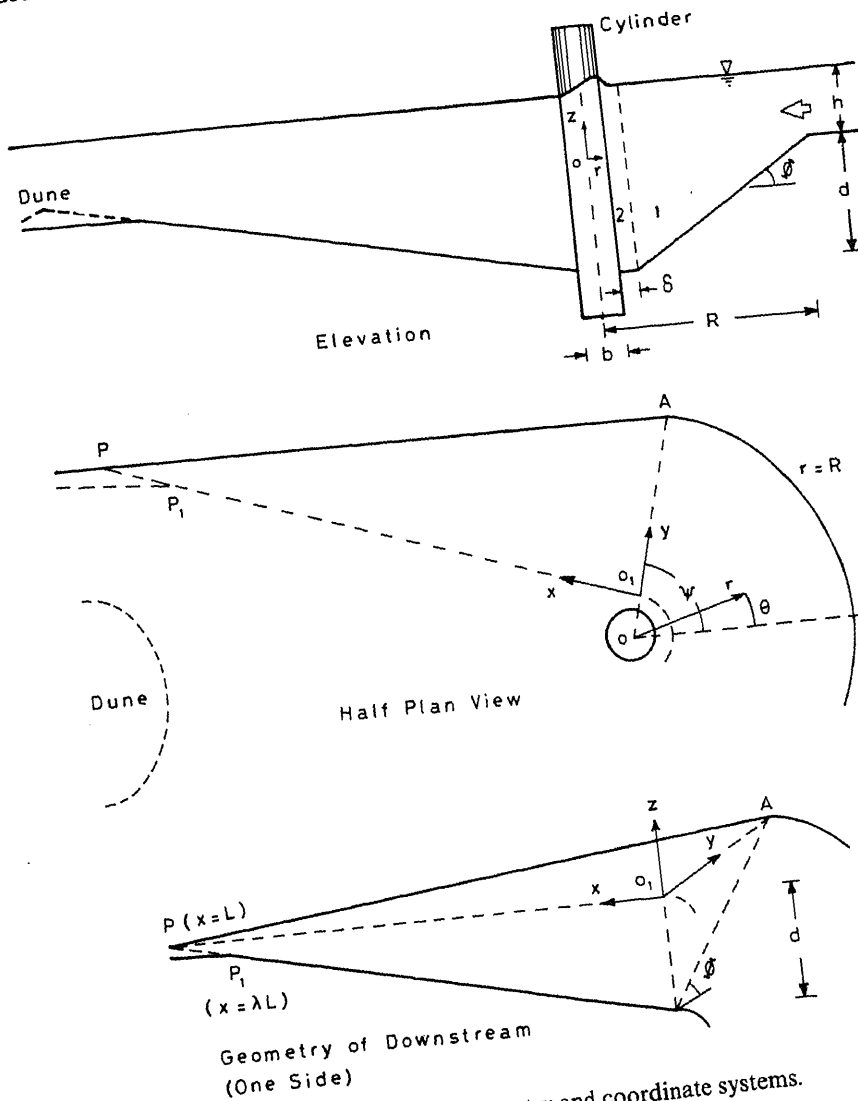


Figure 2. Scour geometry and coordinate systems.

the flat base adjacent to the cylinder. The edge of the hole was found to be a circular arc up to the point of detachment of the horseshoe vortex from the cylinder at $\theta = \pm \psi (\approx \pm 75^\circ)$. The width of zone 2 can be expressed as $\delta = \varepsilon(R - 0.5b)$, where ε = a geometric factor, and was found to be 0.1 (Dey 1991); R = radius of the scour hole i.e. $[d/(1 - \varepsilon)] \cot \Phi + 0.5b$; d = depth of scour; and Φ = dynamic angle of repose. In cylindrical polar coordinates, the quasi-steady velocities in (θ, r, z) are represented by (u_r, v_r, w_r) .

In the downstream, the measurement was confined to zone 1, because in zone 2 the flow separation took place to form the wake. L , the linear distance from O_1 to P (figure 2), can be approximated by $(R - 0.5b)(1 - \varepsilon) \tan \psi$. The bed was further washed out at $x \geq \lambda L$ to attain another flatter slope due to an increase in longitudinal velocity with the distance. The factor λ was found to be 0.8–0.9. The quasi-steady velocities in (x, y, z) are denoted by (u_d, v_d, w_d) .

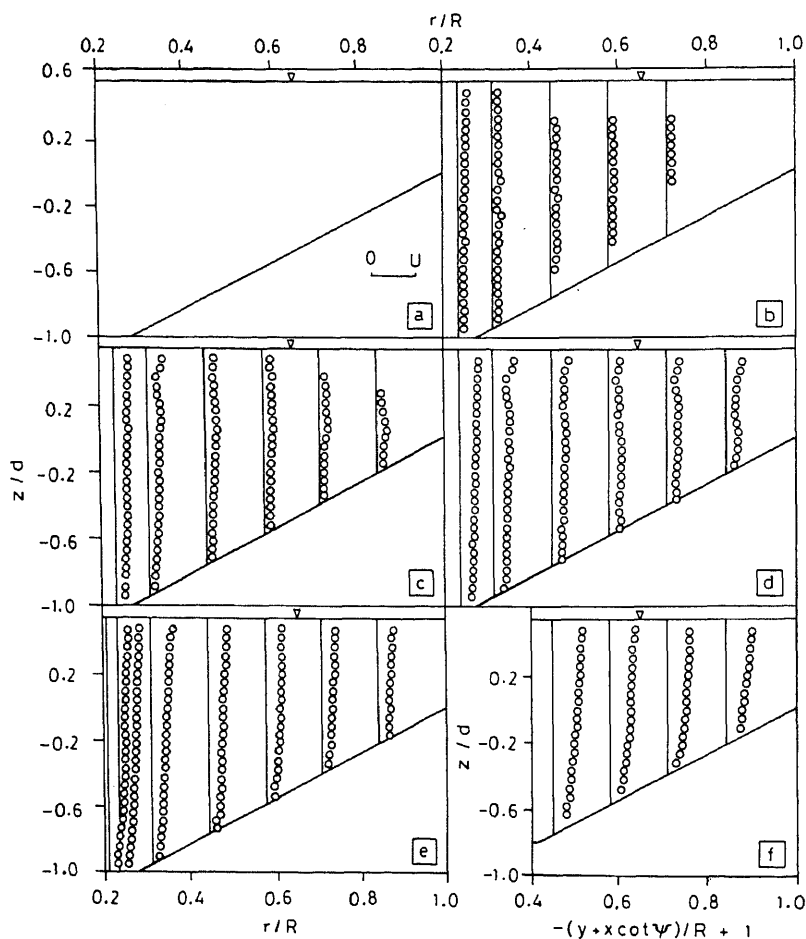


Figure 3. Vertical distributions of u_r in the azimuthal planes at (a) 15° , (b) 30° , (c) 45° , (d) 60° and (e) 75° upstream; and u_d in the transverse plane at (f) $0.2L$ downstream.

5. Results

The velocity measurements were undertaken in the azimuthal planes at 0° , 15° , 30° , 45° , 60° and 75° upstream, and in the transverse plane at $0.2L$ downstream. At the upstream edge of the scour hole, the vertical profile of the approaching velocity, reduced considerably due to a larger exposure of flow area ahead, was similar to the profile of the free approaching velocity. The mean velocity at the edge of the hole estimated, comparing the velocity profile at $r = R$ with the profile of the free approaching velocity at $2m$ upstream of the cylinder centre, was $0.8U$.

The vertical distributions of normalized tangential component u_θ/U and longitudinal component u_d/U are shown in figure 3. Here, u_θ and u_d show the characteristic features of the passage of the main flow, as a skewed velocity profile, around the cylinder. The tangential component u_θ was too small for experimental detection at 15° ; and also full detection of u_θ was not possible at 30° . The distribution of u_θ is similar to the turbulent flow over a flat surface and can, therefore, be represented by a power law with no-slip at the bed. In zone 2, the passage of downflow by the side of the cylinder enhances u_θ substantially. The radial distribution of u_θ is not shown here. However, from a close examination of the vertical distribution of u_θ it is revealed that there is a considerable skewness in the distribution pattern. This is believed to be due to the pronounced effect of the horseshoe vortex, which is a helical motion like flow, around the cylinder. While fitting the velocity profiles (as a function of normal distance from the bed) by a power law with an exponent $1/n$, it was found that the ranges of n were $3 \leq n \leq 6$ for meandering channels (Odgaard 1989) and $7 \leq n \leq 10$ for straight channels. In the present case, n is found to be approximately 3.8. Hence, the value of n decreases with increase in circulatory motion of vortex flow. Consequently, the skewness of the velocity distribution is more in both radial and vertical directions with the strong circulation in the azimuthal planes. The magnitude of u_θ is found to be increased with increase in θ , starting with zero at 0° and becoming a maximum at 75° . In fact, the horseshoe vortex, which originates at 0° , is drifted by the tangential component u_θ by the side of the cylinder. In the downstream, the longitudinal component u_d is similar, in nature, to its preceding upstream part u_θ with increased magnitude.

The vertical distributions of normalized radial component v_r/U are shown in figure 4. The flow separation at the edge of the scour hole produces a reversal nature of v_r in the hole. Thus, the radial component v_r changes sign, in the scour hole, on either side of the locus of $v_r = 0$. This may be compared with the radial velocity in meandering channels (Odgaard 1989). The locus may be assumed to be a median of the triangular section in zone 1. The vertical distribution of v_r varies linearly in the hole, starting with zero at the mid-depth of the hole and becoming a maximum (positive) locally at the bed due to the reversed flow along the slope and a maximum (negative) at $z = 0$, with same magnitude. The variation of v_r along z -axis is exponential above the hole, due to the effect of the approaching flow, starting from the profile at $z = 0$ and becoming an overall maximum at the free surface. Although the radial distribution of v_r is not shown, a close examination of the vertical distribution reveals a parabolic variation of v_r along r -axis, starting with zero at the cylinder boundary and becoming a maximum (positive) at the bed following a negative v_r on other side of the locus of $v_r = 0$ in the hole and a maximum (negative) at $r = R$ above the hole. The decreasing nature of v_r with increase in θ is evident.

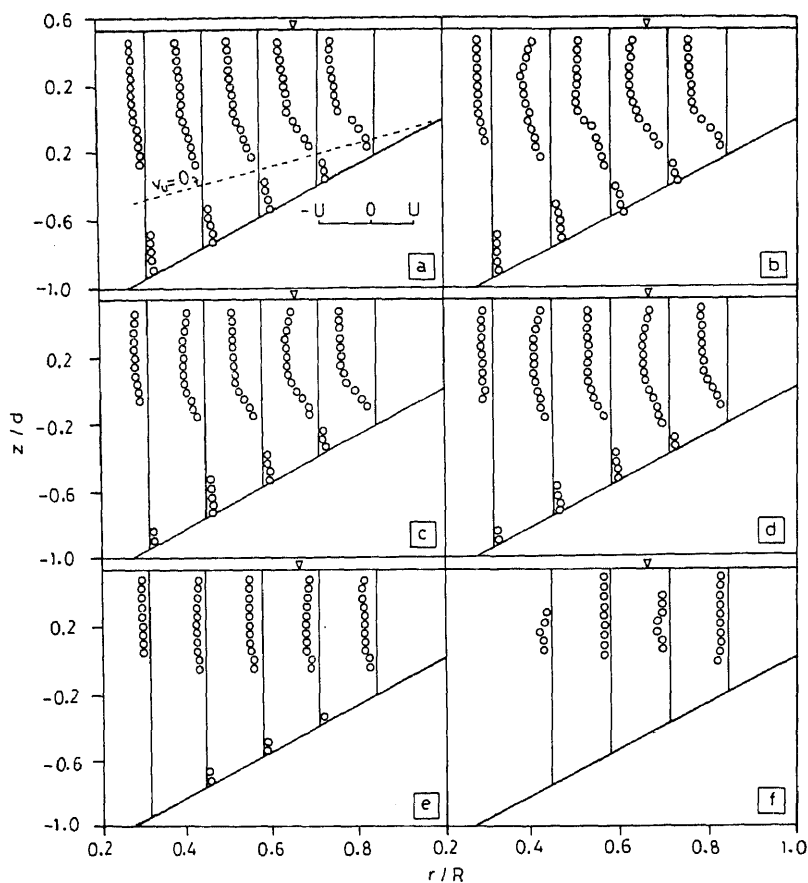


Figure 4. Vertical distributions of v_u in the azimuthal planes at (a) 0, (b) 15, (c) 30, (d) 45, (e) 60 and (f) 75 upstream.

The radial distributions of normalized vertical component w_u/U are shown in figure 5. At the edge of the scour hole, the flow separation is also evident from the reversal nature of w_u in the hole. The variation of w_u is parabolic in the hole, starting with a positive value due to the reversed flow along the sloping bed and becoming a maximum (negative) at the cylinder boundary along r -axis and also increasing towards negative value along z -axis (revealed from the radial distribution), with opposite signs and a higher magnitude due to the downflow in zone 2. Locus of $w_u = 0$ is a curved line meeting at the extreme ends of the sloping bed of the hole. w_u changes sign on either side of the locus. At 75° , w_u was very feeble for detection. However, there lies a large helical motion of flow within the scour hole.

In the downstream region, due to the attenuating nature of swirl flow, v_d and w_d were too small to be detected experimentally. The swirl flow loses its identity after travelling a distance of 5 to 6 cylinder diameters. However, the longitudinal velocity component is dominating.

Based on the three-dimensional flow simulation developed by Dey *et al* (1992a), the flow field around the cylinder in the quasi-equilibrium scour hole was visualized by the

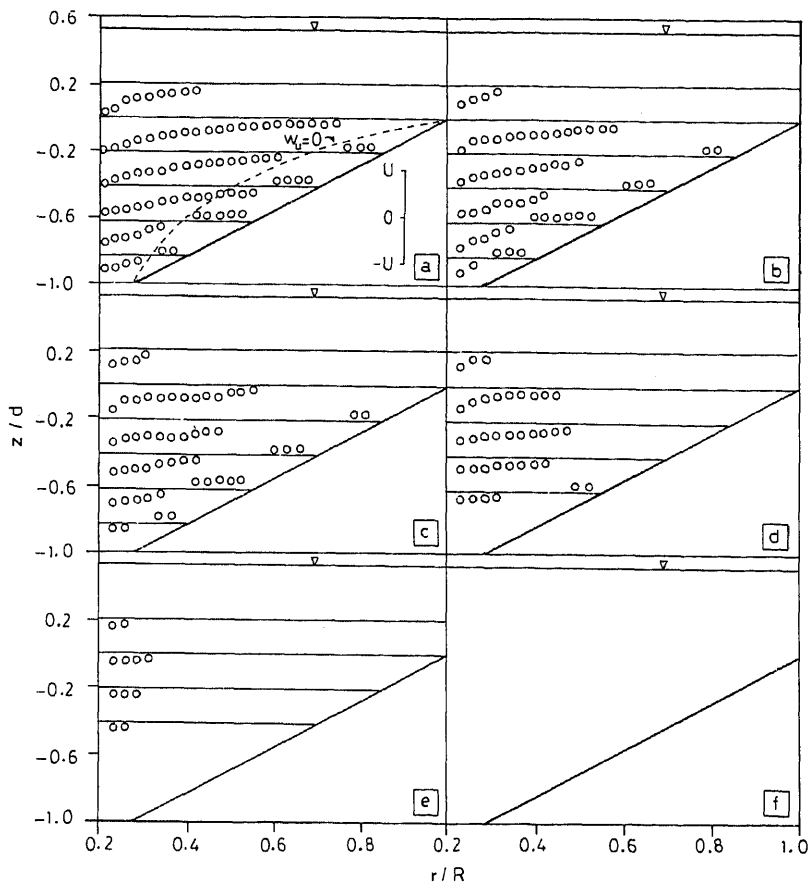


Figure 5. Radial distributions of w_u in the azimuthal planes at (a) 0° , (b) 15° , (c) 30° , (d) 45° , (e) 60° and (f) 75° upstream.

EGA colour monitor using the measured data. Figure 6 exhibits the velocity vectors in the azimuthal planes. The characteristics of circulatory flow in the scour hole together with the strong downflow along the upstream face of the cylinder are depicted. The circulation is strong along the upstream face and decreases with increase in θ . In $z > 0$, the flow is horizontal for $1 > r/R \geq 0.8$, and then the lower half of the flow gradually curves down and becomes almost vertical adjacent to the cylinder. In contrast, the upper half of the flow is slightly directed upward due to the obstruction caused by the cylinder. However, the flow velocity at the base of zone 2 is about $0.2 U$ in the present case. It was measured by Melville (1975) $0.3 U$. The result is quite reasonable, because the velocity beneath the horseshoe vortex on flat bed, estimated from the formula given by Qadar (1981), $v_u = 0.092b^{-0.5}U^{0.83}$, is $0.4 U$ which reduces considerably in the quasi-equilibrium state due to the expansion of vortex size. The magnitude of total (three-dimensional) velocities around the cylinder in the azimuthal planes are exhibited in figure 7. In absence of u_u at 0° , the total velocity is solely circulatory as already shown in figure 6. At 75° , u_u dominates and the circulatory flow becomes weak. In other azimuthal planes, the evolution of the circulatory flow to the exponential distribution of velocity is displayed. The horizontal velocity vectors in the horizontal planes are

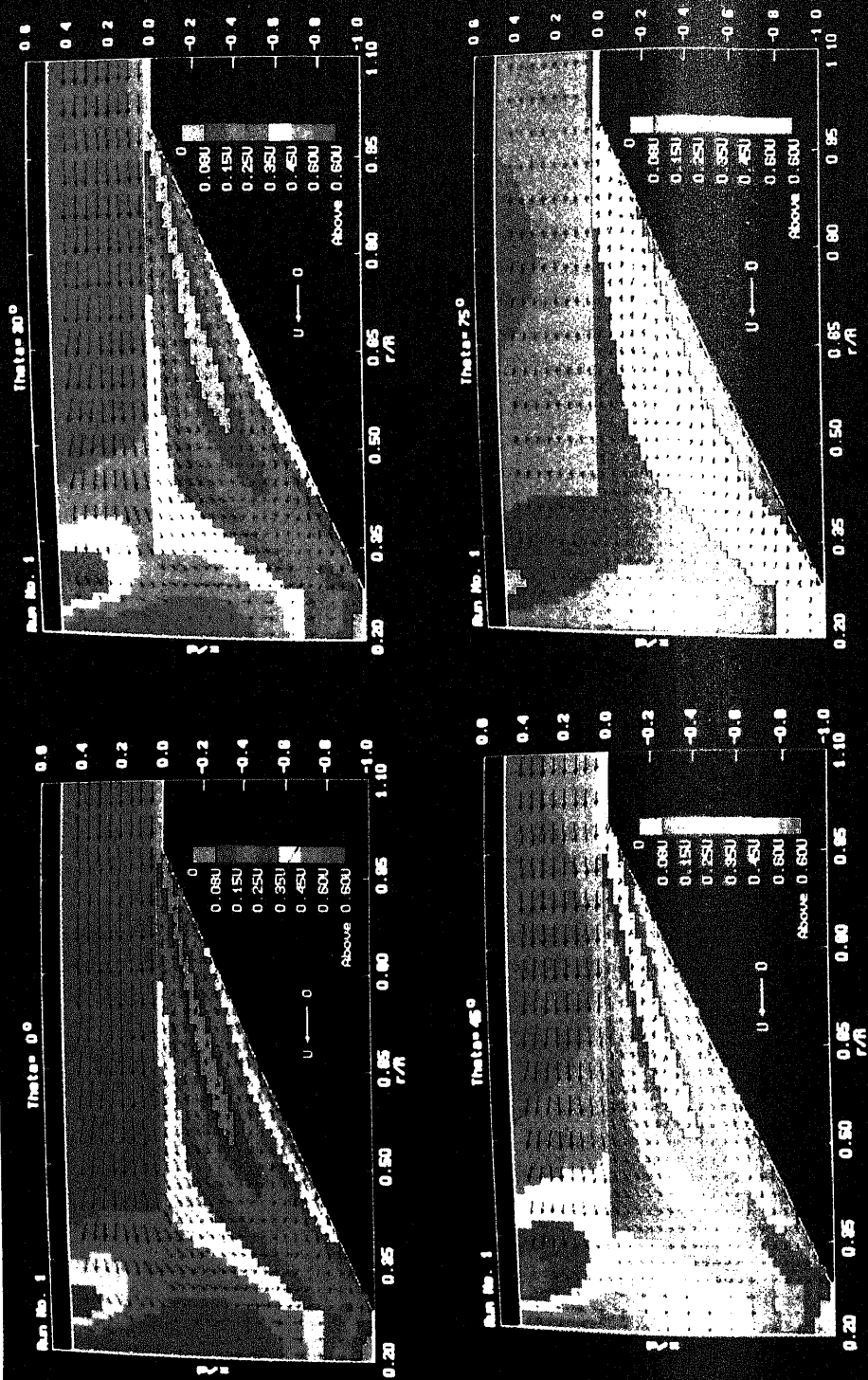


Figure 6. Velocity vectors in the azimuthal planes.

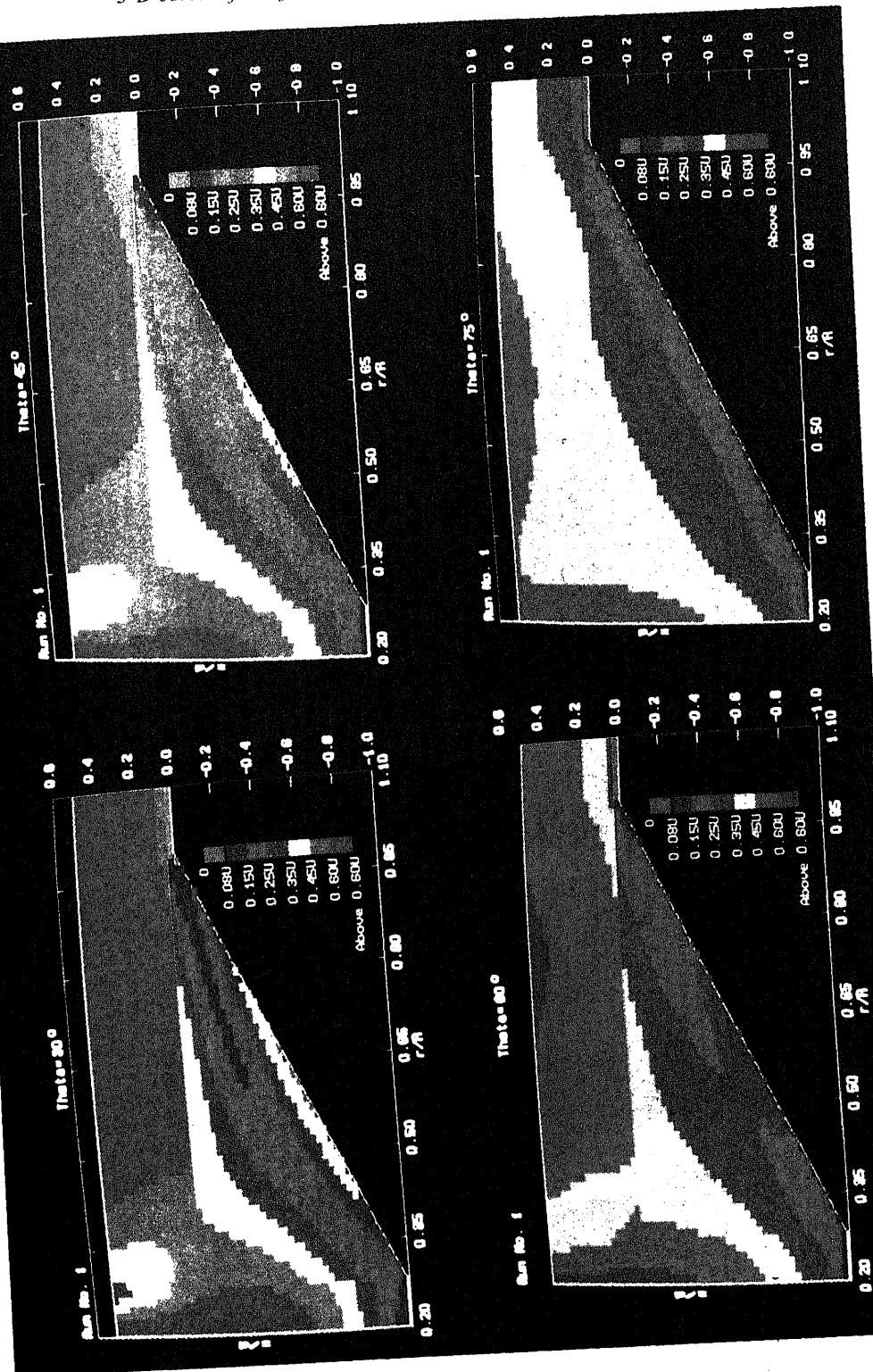


Figure 7. Magnitude of total (three-dimensional) velocities in the azimuthal planes.

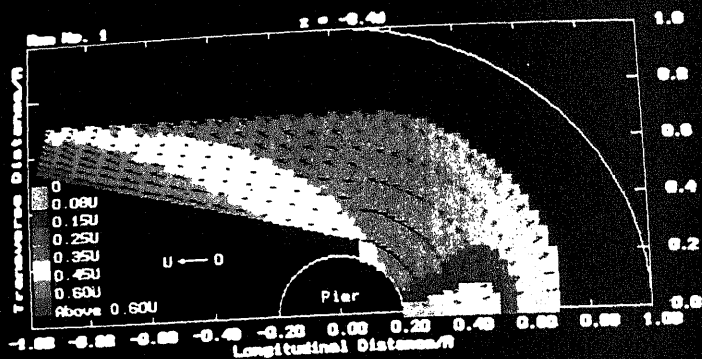
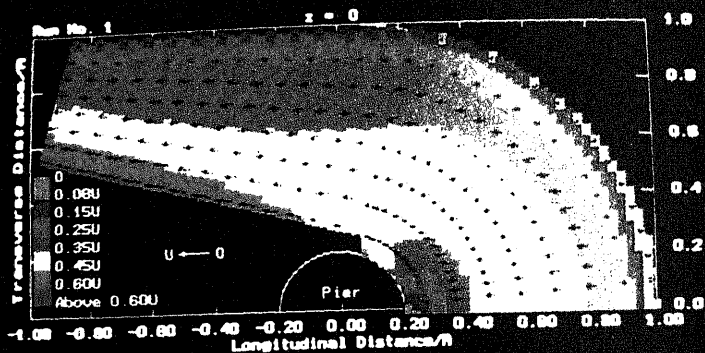
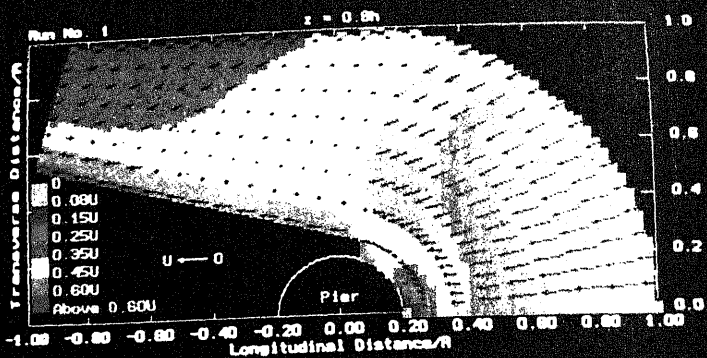


Figure 8. Velocity vectors in the horizontal planes (half plan views).

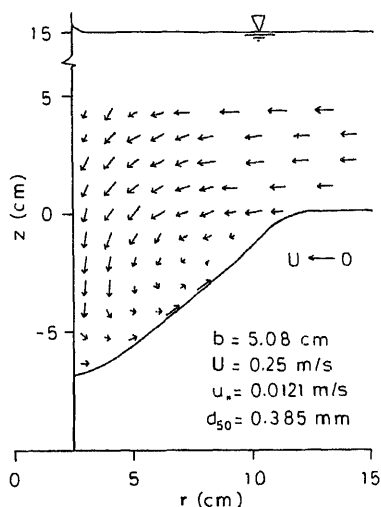


Figure 9. Velocity vectors at 0° (after Melville & Raudkivi 1977) used for comparison purposes.

depicted in figure 8. The horizontal velocity vector at $z = 0.8h$ shows the inward motion of the flow. At $z = 0$, the flow resembles the irrotational flow past a circular cylinder. The helical motion of flow, in the scour hole, is evident from the flow field at $z = -0.4d$. Figure 9, used for the comparison of a part of the present data, shows the observations of Melville & Raudkivi (1977) at 0° under equilibrium scour. Their observations agree with the flow characteristics at 0° presented in figure 6, which establishes the validation of the present measuring technique.

The physics of the flow is analyzed with the help of the above results. The main characteristic features of the flow around a cylinder are a relatively large secondary vortex flow and skewed velocity distributions. The approaching flow separates at the upstream edge of the scour hole, known to be a line of separation, to form a vortex flow in the hole which acts as a zone of separation. The limiting streamlines along the original bed upstream (due to the approaching flow) and the sloping bed (due to the reversed flow) merge at the edge of the scour hole forming separated streamlines. Thus, a surface of separation is produced in the form of an envelope. In this process, the approaching flow curves down into the hole and rolls to form a vortex flow which migrates downstream by the sides of the cylinder.

6. Concluding remarks

The experimental results of the distribution patterns of velocity components for a three-dimensional vortex flow around a circular cylinder in a quasi-equilibrium scour hole under a clear water regime have been presented. In the upstream, the tangential component u_θ follows a power law, starting with zero at the bed and becoming a maximum at the free surface and at the cylinder boundary, with a higher magnitude in zone 2. The radial component v_r varies linearly in the hole along z -axis, starting with zero at the mid-depth of the scour hole and becoming a maximum locally at the bed and at $z = 0$, with opposite signs and same magnitude. v_θ varies exponentially above the hole along z -axis, starting from the profile at $z = 0$ and becoming an overall maximum

at the free surface. Along r -axis, the distribution of v_u is parabolic, starting with zero at the cylinder boundary and becoming a maximum at the bed in the hole and at $r = R$ above the hole. The variation of vertical component w_u is parabolic in the hole, starting with a positive value at the bed and becoming a maximum at the cylinder boundary along r -axis and at $z = 0$ along z -axis, with opposite signs and a higher magnitude in zone 2. In the downstream, the attenuating nature of swirl flow becomes very feeble and the longitudinal component u_d becomes gradually stronger than its preceding part u_u upstream. The flow simulation results show a helical motion of fluid around the cylinder.

This investigation is a part of the doctoral dissertation work by the author in the Department of Civil Engineering, Indian Institute of Technology, Kharagpur under the joint supervision of S K Bose and G L N Sastry. The helpful suggestions from S C Jain, Institute of Hydraulic Research, University of Iowa, are gratefully acknowledged. The author also appreciates the assistance provided by B Dey during the investigation.

List of symbols

b	cylinder diameter;
d	quasi-equilibrium depth of scour;
d_{16}, d_{50}, d_{84}	16, 50, 84% finer particle diameters;
h	approaching flow depth;
L	longitudinal extension of scour hole downstream;
n	exponent;
R	radius of scour hole;
U	mean approaching velocity;
u_u, v_u, w_u	velocities in cylindrical polar coordinates upstream;
u_d, v_d, w_d	velocities in Cartesian coordinates downstream;
u_*	shear velocity;
u_{*c}	critical shear velocity;
x, y, z	Cartesian coordinates;
ε, λ	factors;
δ	width of zone 2;
ϕ	angle of repose;
Φ	dynamic angle of repose;
θ, r, z	cylindrical polar coordinates;
ψ	angle of detachment of horseshoe vortex;
σ_g	geometric standard deviation.

References

- Breusers H N C, Nicollet G, Shen H W 1977 Local scour around cylindrical piers. *J. Hydraul. Res.* 15: 211–252
- Dargahi B 1982 Local scouring around bridge piers – A review of practice and theory. *Bulletin* No. 114, Hydraulics Lab, Royal Inst. Technol., Stockholm

- Dargahi B 1987 Flow field and local scouring around a cylinder. Bulletin No. 137, Hydraulics Lab, Royal Inst. Technol., Stockholm
- Dey S 1991 *Clear water scour around circular bridge piers: A model*. Ph D thesis, Indian Inst. Technol., Kharagpur
- Dey S, Bose S K, Sastry G L N 1992a Clear water scour at circular piers, part I: Flow model. *Proc. 8th Cong. IAHR Asian and Pacific Div. IIIC*: 69–80
- Dey S, Bose S K, Sastry G L N 1992b Clear water scour at circular piers, part II: Design formula. *Proc. 8th Cong. IAHR Asian and Pacific Div. IIIC*: 81–92
- Goldstein R J 1983 *Fluid mechanics measurements* (New York: Hemisphere)
- Hjorth P 1975 Studies on the nature of local scour. Bulletin. Series A No. 46, Dept. of Water Resources Eng., Univ. of Lund
- Jain S C, Fischer E E 1979 Scour around circular piers at high Froude numbers. Report No. FHWA-RD-79-104, US Dept. of Transportation, Federal Highway Administration, Washington, DC
- Melville B W 1975 Local scour at bridge sites. Report No. 117, Univ. of Auckland
- Melville B W, Raudkivi A J 1977 Flow characteristics in local scour at bridge piers. *J. Hydraul. Res.* 15: 373–380
- Nwachukwu B A 1979 *Flow and erosion near groyne like structures*. Ph D thesis, University of Alberta
- Odgaard A J 1989 River-meander model I: Development. *J. Hydraul. Eng., Am. Soc. Civ. Eng.* 115: 1433–1450
- Qadar A 1981 The vortex scour mechanism at bridge piers. *Proc. Inst. Civ. Eng.* 71: 739–757
- Rajaratnam N, Muralidhar D 1967 Yaw and pitch probes. Hydraul. Instrum. Series, Dept. Civ. Eng., University of Alberta
- Raudkivi A J 1986 Functional trends of scour at bridge piers. *J. Hydraul. Eng. Am. Soc. Civ. Eng.* 112: 1–13
- Shukry A 1950 Flow around bends in open flumes. *Trans. Am. Soc. Civ. Eng.* 115: 715–779
- Tingsanchali T, Maheswaran S 1990 2-D depth-averaged flow computation near groyne. *J. Hydraul. Eng., Am. Soc. Civ. Eng.* 116: 71–86

Studies in multigrid acceleration of some equations of interest in fluid dynamics¹

J P SINGH

Flosolver Unit, CTFD Division, National Aerospace Laboratories,
Bangalore 560 017, India

MS received 28 April 1995; revised 12 September 1995

Abstract. The paper describes the multigrid acceleration technique to compute numerical solutions of three equations of common fluid mechanical interest; Laplace equation, transonic full potential equation and Reynolds averaged Navier–Stokes equations. Starting with the simple and illustrative multigrid studies on the Laplace equation, the paper discusses its application to the cases of full potential equation and the Navier–Stokes equations. The paper also discusses some elements of multigrid strategies like V- and W-cycles, their relative efficiencies, the effect of number of grid levels on the convergence rate and the large CPU time saving obtained from the multigrid acceleration. A few computed cases of transonic flows past airfoils using the full potential equations and the Navier–Stokes equations are presented. A comparison of these results with the experimental data shows good agreement of pressure distribution and skin friction. With the greatly accelerated multigrid convergence, the full potential code typically takes about 10 seconds and the Navier–Stokes code for turbulent flows takes about 5 to 15 min of CPU time on the Convex 3820 computer on a mesh which resolves the flow quantities to good levels of accuracy. This low CPU time demand, made possible due to multigrid acceleration, on one hand, and the robustness and accuracy on the other, offers these codes as designer's tools for evaluating the characteristics of the airfoils.

Keywords. Multigrid; full-potential solution; Navier–Stokes solution; Laplace equation.

¹ Various parts of this paper have been presented at the following conferences; (i) 5th Asian Cong. on Fluid Mech., Taejon, Korea, 1992, (ii) Int. Conf. on Methods of Aerophysical Research, Novosibirsk, 1992, (iii) Fluid Dyn. Symp. in honour of Prof. R Narasimha on his 60th birthday, 1993

1. Introduction

Starting with the pioneering work of Federenko (1964), the theory and application of multigrid has come of age. The large time saving due to the multigrid acceleration has offered great relief to the workers in many areas of science and technology, especially in the developing countries where multi-megaflop computing machines are not yet common. Even today at many of these institutions, a typical 2-D turbulent Navier–Stokes solution on a grid size of, say, 385×65 , requires 2 to 3 days of turn-around time. The multigrid technique has also provided an opportunity or potential to several codes to be used as designer's tool. The combined effect of the high speed computing machines and the multigrid accelerated codes has led to such realistic design computations that a well converged 3-D Navier–Stokes flow computation past a wing-body-nacelle configuration can be obtained in as little as 4 min of CPU time (Jameson 1993) on some of the high speed computers. Historically, the first publication on multigrid method put to practice was brought out by Brandt (1972) followed by another publication (Brandt 1977) five years later with convincing results which set the pace for rapid progress in multigrid methods and applications (Wesseling 1990). From the same historical angle, it may be mentioned that Hackbusch (1976) (as mentioned in Wesseling 1990) also independently discovered the multigrid method. Today, the multigrid method has crossed its domain of application to elliptic systems for which basically its theory was developed. One can find large scale application of multigrid in solving the time dependent Navier–Stokes equations and several other hyperbolic problems. During the last few years, multigrid has also made inroads in the areas of hydrodynamic stability, integral and integro-differential equations, many-body interactions, semiconductor device simulation, general relativity, theory of material defects and atomic physics, real time optimal control, protein folding, combinatorial optimisation, linear programming etc. (Brandt 1988).

In CFD, one seeks converged solution to viscous flow problems on a grid which is fine enough to resolve all the length scales involved. In most of the cases, the actual number of node points thus obtained is quite large leading to a large number of algebraic equations to be solved resulting from the discretization. Also, most of the relaxation schemes are efficient at smoothing out the high frequency errors as seen on the scale of the grid. The solution on a single fine grid is too expensive for two reasons, (i) due to the large number of algebraic equations resulting from the discretization process, (ii) due to the relaxation schemes taking very long time to smooth out the low frequency errors. Quoting a concept from Brandt (1977), the multigrid method uses a sequence of grids “taking advantage of the relation between different discretizations of the same problem. This method can be viewed in two complementary ways: one is to view the coarse grids as the correction grids, accelerating convergence of a relaxation scheme on the finest grid by efficiently liquidating smooth error components. Another point of view is to regard finer grids as the correction grids by correcting their forcing terms”. The first view of Brandt (1977), which is an early and monumental work on the multigrid methods, refers to the definition of high frequency components with respect to each grid which are smoothed fastest by most relaxation schemes. The second view offers the possibility to “manipulate accurate solutions on coarser grids, with only infrequent ‘visits’ to pieces of finer levels”.

The next section gives a brief description of the basic elements of multigrid technique, followed in the present work, to get accelerated convergence of (a) solution of Laplace

equation on Cartesian grids, (b) solution of transonic potential flow equations, and (c) solution of Navier–Stokes equations for 2-D transonic flow.

2. A brief description of multigrid method

Let $G^h, G^{2h}, \dots, G^{Mh}$ be a hierarchy of grids with h indicating the finest level. Let the equation to be solved be given as

$$L\Phi = f. \quad (1)$$

The discretized form of (1) on grid level h is written as;

$$L^h\Phi^h = f^h. \quad (2)$$

If ϕ is an approximate solution of Φ and ψ is the correction term, then

$$L^h(\phi^h + \psi^h) = f^h, \quad (3)$$

or

$$L^h(\phi^h + \psi^h) - L^h\phi^h = f^h - L^h\phi^h = \mathcal{R}^h. \quad (4)$$

\mathcal{R}^h is known as residual on grid G^h . A certain number of relaxation sweeps are made to obtain ϕ^h . Ideally, when the convergence slows down, the relaxation on the present level is stopped and the solution and the residual is injected down to the next coarser level $2h$ where one can write (4) for this grid as follows;

$$L^{2h}(\mathcal{J}_h^{2h}(\phi^h + \psi^h)) - L^{2h}\mathcal{J}_h^{2h}\phi^h = \tilde{\mathcal{J}}_h^{2h}\mathcal{R}^h, \quad (5)$$

where \mathcal{J}_h^{2h} and $\tilde{\mathcal{J}}_h^{2h}$ are injection operators which need not be the same. Equation (5) is rewritten as;

$$\begin{aligned} L^{2h}\hat{\phi}^{2h} &= \tilde{\mathcal{J}}_h^{2h}\mathcal{R}^h + L^{2h}\mathcal{J}_h^{2h}\phi^h \\ &= \tilde{\mathcal{J}}_h^{2h}(f^h) + (L^{2h}\mathcal{J}_h^{2h}\phi^h - \mathcal{J}_h^{2h}(L^h\phi^h)), \\ &= \tilde{\mathcal{J}}_h^{2h}(f^h) + f^{2h}, \end{aligned} \quad (6)$$

where

$$\hat{\phi}^{2h} = \mathcal{J}_h^{2h}(\phi^h + \psi^h). \quad (7)$$

f^{2h} is the truncation error of the coarse grid relative to the fine grid. It is seen that without the addition of the term f^{2h} in (6), the discretized coarse grid equation has the same form as (2) for fine grid. In fact, when the solution has converged, the coarse grid solution will be same as the injected fine grid solution and f^{2h} will vanish. In that sense, the term f^{2h} , also known as forcing function, is identified as the “fine to coarse grid defect correction”. This term can also be seen to represent the interplay between the discretization and the solution process.

This procedure is carried on till the coarsest grid is reached. The corrected coarse grid solution thus obtained needs to be transferred to the fine grid to obtain the updated fine grid solution. This step is written as;

$$\phi_{\text{new}}^h = \phi_{\text{old}}^h + \tilde{\mathcal{J}}_h^{2h}(\phi^{2h} - \mathcal{J}_h^{2h}\phi^h), \quad (8)$$

where $\tilde{\mathcal{J}}$ is a suitable interpolation operator. Note that if the coarse grid solution was simply prolonged to the fine grid without adding correction term as above, it would be devoid of all the high frequency components of the solution and also it would

contain interpolation error. In this sense, the process has taken the best advantage of the high frequency smoothing property of the chosen relaxation scheme on each level and a lot of CPU time is saved by working on coarser grid levels.

3. Application to Laplace equation

The Laplace and Poisson equations (differing only by the absence or the presence of the nonhomogeneous term) are of fundamental importance to fluid dynamics. The Laplace equation occurs as the main governing equation for the incompressible, inviscid and irrotational fluid flow, and the Poisson equation occurs as a component equation in case of incompressible Navier–Stokes flows. Also, the simplicity of this equation makes it a very illustrative platform.

Since the Laplace equation is linear, the operator L in (3) can be linearly distributed over ϕ and ψ and one can proceed to solve directly for correction ψ using what is called the “Correction Scheme”. But in this work, a more general method called Full Approximation Storage (FAS) scheme, as applicable to the nonlinear equations, is used.

Here the interest is to solve the Laplace equation using multigrid acceleration. In this section, the work of Singh (1989) for multigrid strategy will be followed. The Laplace equation is written as;

$$\nabla^2 \phi = 0. \quad (9)$$

The boundary conditions are taken to be as follows; at (i) $y = 0$, $\phi = 0$, (ii) $y = \pi$, $\phi = 0$, (iii) $x = 0$, $\phi = \sin(y)$, and (iv) $x = 1$, $\phi = e.\sin(y)$. The problem is discretized over a domain given by $0 \leq x \leq 1$ and $0 \leq y \leq \pi$ using the Cartesian grid.

The problem being purely elliptic, the equation is discretized by writing the second derivatives using the central difference scheme. The resulting difference equations are solved by successive line relaxation technique. A V-cycle FAS multigrid strategy with independently selected number of sweeps at various grid levels will be used. The results are presented for grid levels up to six.

Figure 1 shows several convergence histories of the solution procedure as a function of number of grid levels used. In each case the solution is sought on the finest grid level of size 65×129 . The figure shows the effect of number of grid levels on the multigrid convergence. The gain in terms of speed of convergence rapidly increases as the number of grid levels is increased from 1 to 4. The gain slows down when 5 grid levels are used. Beyond this, one can see that there is just about no gain in the rate of convergence at all as the number of grid levels is increased from 5 to 6. The results of this study are summarised in table 1 below.

Table 1 shows the level of error obtained using one-level computation and multilevel computations using 2 to 6 grid levels after 100 work units. L_2 (norm) stands for the absolute value of the L_2 -norm of the residual. The drastic gain in the solution convergence is clear. One can see that after 100 work units, the 5-grid level solution has converged to an accuracy of about 14 orders lower than the corresponding convergence on a single level. Of course, it is a different matter that, in practical applications, one never needs to drive convergence to more than, say, 3 to 4 orders of magnitude which is obtained here in far too fewer work units. The basic nature of this observation is true in general for all systems, i.e., the law of diminishing return applies as the number

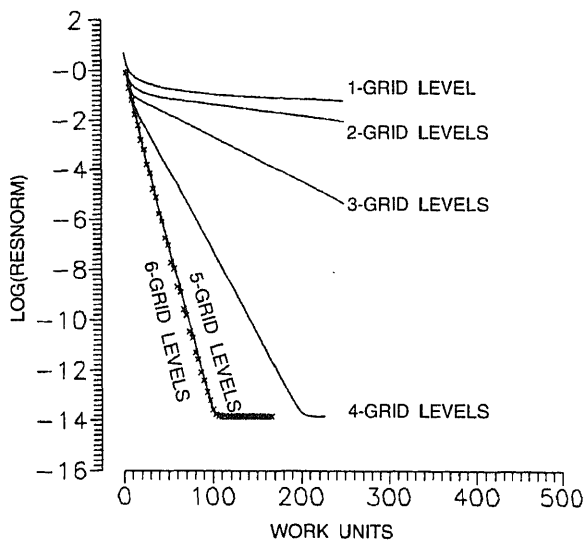


Figure 1. Multigrid convergence and effect of number of grid levels.

of coarser meshes beyond optimum number is increased. Often four to five grid levels are optimum. Of course, as far as the level to which the solution converges after certain number of work units is concerned, it depends on the system being solved (nonlinearity, constraints, presence of discontinuities etc. tend to degrade the multigrid performance). The next two examples of full potential equation and Navier–Stokes solution will elucidate this point.

3.1 *Effect of boundary condition “defect” on multigrid convergence*

In the above, the Laplace equation has been solved with the exact boundary condition. This does not involve any approximation of the boundary values. However, when a problem is solved which involves approximation (and hence error) in the boundary values, that we call “boundary condition defect” here, the performance of the same multigrid accelerated iterative procedure is impaired significantly. To study this, we consider a computationally similar problem (Singh 1992) that involves extrapolation to compute boundary condition and hence, introduces error or “boundary condition defect”. To see this, we present the results of the following demonstration computations, Study-1: The solution of Laplace equation with rectangular boundary and exact boundary conditions for comparison of convergence history, Study-2: the problem in study-1 is recomputed using the difference form of the Neumann boundary condition $\partial\phi/\partial y = \exp(x)\cos(y)$ as the boundary condition on the bottom edge. The truncation

Table 1. Efficiency of multigrid scheme with respect to the number of grid levels used.

	1-level	2-level	3-level	4-level	5-level	6-level
Abs. value of L_2 (norm) after 100 work units	8.28	4.7×10^{-2}	2.5×10^{-3}	6.3×10^{-8}	2.8×10^{-14}	2.8×10^{-14}

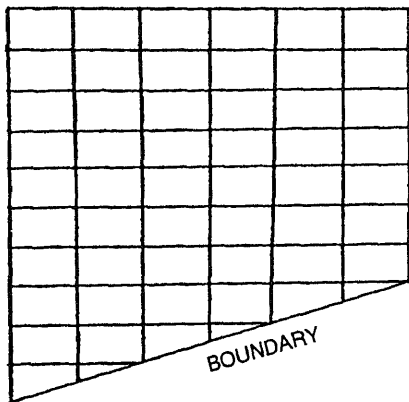


Figure 2. Computational domain for Studies 3 and -4.

error of the difference scheme introduces some error, Study-3: The problem in Study-1 is solved with the following modification; the bottom edge is cut slant as shown in figure 2. The boundary condition implementation at this edge requires values of ϕ at the dummy points for which the exact values are provided. The boundary conditions on the left, right and top edges remain the same, Study-4: all features identical to Study-3 except that the values at the bottom boundary point were obtained using Taylor series expansion as described below. This adds further to the errors.

The value of ϕ at the slant bottom boundary is written as follows by opening a Taylor series around $(i, j - 1)$;

$$(\phi)_{y_b} = (\phi)_{y_{i,j-1}} + (y_b - y_{i,j-1})(\phi)_{yy_{i,j-1}}, \quad (10)$$

where

$$(\phi)_{yy_{i,j-1}} = (-3(\phi)_{i,j-1} + 4(\phi)_{i,j} - (\phi)_{i,j+1})/2\Delta y \quad (11)$$

and

$$(\phi)_{yy_{i,j-1}} = ((\phi)_{i,j-1} - 2(\phi)_{i,j} + (\phi)_{i,j+1})/\Delta y^2. \quad (12)$$

The subscript 'b' indicates values on the slant boundary. The values of $(\phi)_{y_b}$ are provided exactly to compute $(\phi)_{i,j-1}$. The higher level of truncation error introduced artificially is obvious. Figure 3 shows the comparison of the convergence histories of the above studies. The study illustrates the level of stagnation residues in various studies. The residue level ($\approx 10^{-7}$ in 32-bit arithmetics, $\approx 10^{-15}$ in 64-bit arithmetics) is the lowest in Study-1 where no "defect" is involved in the boundary condition implementation. Study-2 has relatively higher level of stagnation residue ($\approx 10^{-6}$ in 32-bit arithmetics) where there is a relatively smaller amount of boundary condition "defect". Even though we have considered a slant bottom edge in Study-3, which requires use of the dummy point, the stagnation residue level is the same as that in Study-1 because the value there is provided exactly. Study-4, which has the highest level of "defect", leads to the highest level of stagnation residue ($\approx 10^{-4}$ in 64-bit arithmetics).

The effect of the boundary condition "defect" can also be seen by explicitly adding a perturbation term to the exact boundary condition in Study-1. Let the perturbation term to the boundary condition be chosen as $A \sin(n\pi x)$ where $n = 1, 2, 3, \dots$ with $0 \leq x \leq 1$. The term is explicitly added to the boundary condition on the bottom edge in Study-1. One can infer from figure 4 that as the amplitude A increases, the magnitude of the boundary condition "defect" increases, which leads to convergence process stagnating

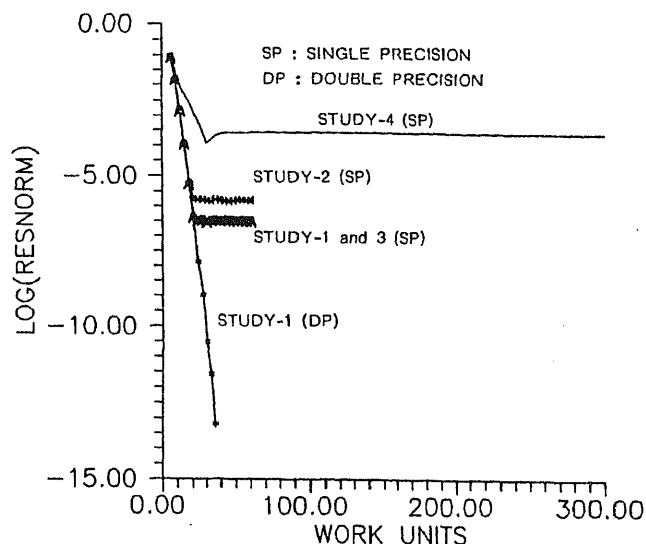


Figure 3. Comparison of convergence rates for studies 1 to 4.

at higher levels. The above study illustrates the sensitivity of the convergence history in the multigrid process as it is affected by the boundary condition "defect".

4. Application to full potential transonic flow computation

Even today, most of the CFD codes that are used in the preliminary aircraft aerodynamic design are based on simpler methods like panel method and full potential

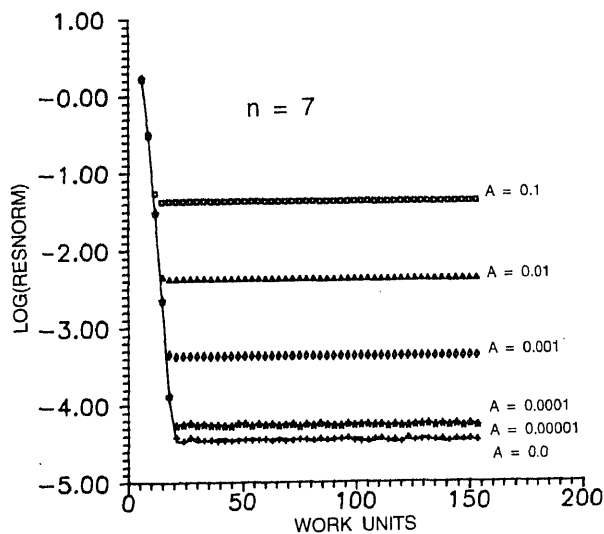


Figure 4. Effect of boundary condition "defect" on multigrid convergence.

equations. Thus, it is useful to have these codes accelerated using techniques like multigrid. In this section, the implementation of multigrid acceleration in a full potential transonic flow solver due to Garabedian & Korn (1971) is described. Historically, the first successful application of the multigrid acceleration to potential function based formulation for the transonic flow was due to South & Brandt (1977). In their work, they presented the accelerated solution of small perturbation equation for non-lifting flow past airfoil. Singh (1989) used the multigrid acceleration to get solutions for flow past airfoils using the code of Garabedian & Korn (1971) modified and adapted by him at NAL. An acceleration of about 5 to 7 times (in terms of work units) was obtained using the multigrid strategy described. The basic method of Garabedian & Korn (1971) is described below.

The 2-D full potential flow equation in Cartesian coordinates is;

$$(c^2 - u^2)\phi_{xx} - 2uv\phi_{xy} + (c^2 - v^2)\phi_{yy} = 0, \quad (13)$$

where ϕ is the velocity potential, u, v the velocity components in x and y directions, and c the local speed of sound given by the Bernoulli's law

$$(u^2 + v^2)/2 + c^2/(\gamma - 1) = (1/2) + M^2/(\gamma - 1). \quad (14)$$

Using Sell's conformal mapping, the entire infinite flow field is mapped on to the inner circle of unit radius such that the perimeter of the circle corresponds to the airfoil contour and the centre corresponds to infinity. In this plane, using (r, θ) coordinates, the full potential equation, (13), is written as;

$$\begin{aligned} (c^2 - r^2 f^{-2} \phi_\theta^2) \phi_{\theta\theta} - 2r^4 f^{-2} \phi_\theta \phi_r \phi_{\theta r} + r^2 (c^2 - r^4 f^{-2} \phi_r^2) \phi_{rr} \\ + r (c^2 - r^2 f^{-2} \phi_\theta^2 - 2r^4 f^{-2} \phi_r^2) \phi_r + f^{-3} (r^2 \phi_\theta^2 + r^4 \phi_r^2) \\ (f_\theta \phi_\theta + r^2 f_r \phi_r) = 0, \end{aligned} \quad (15)$$

where $f = r^2 |F'(re^{i\theta})|$ and F is the mapping function defined as $x + iy = F(re^{i\theta})$. The boundary conditions for the problems are (a) the flow tangency condition on the surface, i.e.,

$$\partial\phi/\partial n = 0, \quad (16)$$

and (b) outer boundary condition written as;

$$\Phi = (\Gamma/2\pi) \tan^{-1}((1 - M_\infty^2)^{1/2} \tan(\theta + \alpha)), \quad (17)$$

where Φ is the full potential, α is the angle of attack, θ is the coordinate in the (r, θ) plane and M_∞ is the free stream Mach number. Equation (15) is discretized using the mixed finite difference scheme due to Murman & Cole (1971).

4.1 Multigrid acceleration of full potential equation

The nonlinearity of the full potential transonic flow equation with shock sitting on the airfoil surface poses special problems in the multigrid process by making the solution very sensitive. It turns out that the high frequency errors introduced during the coarse grid correction interpolation, especially in the vicinity of the shock, keep offsetting the smoothness obtained on the finer levels. This impairs the rate of convergence.

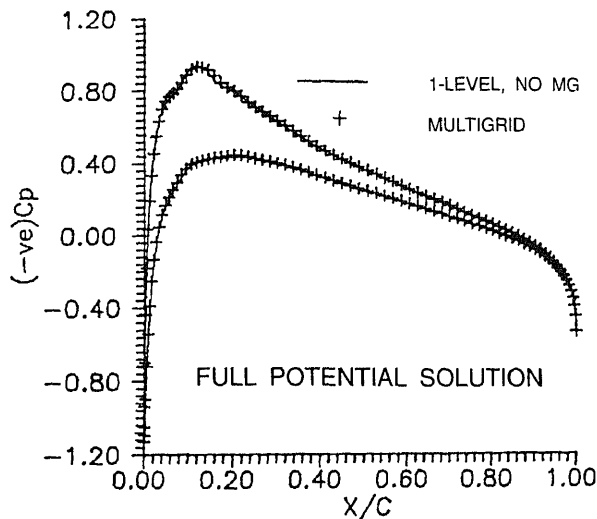


Figure 5. Comparison of pressure distribution with and without multigrid, NACA 0012, $M = 0.7$, $\alpha = 1^\circ$.

The multigrid strategy selected here also is the FAS scheme starting at the finest of the 3-level grid hierarchy with V-cycle. The finest grid is 160×32 . The next two coarser grids are obtained by omitting the alternate points in both r and θ directions. The coarse grid correction is interpolated using simple algebraic averaging of the values at the two coarse grid nodes. The relaxation sweep strategy adopted for the results presented here consists of a constant number of sweeps at all levels in both restriction as well as in the prolongation phases (though a choice exists to select any number of sweeps at any level). The boundary conditions are updated at all the grid levels. The computations are terminated when the L_2 -norm of the residuals becomes less than 10^{-4} .

Using this simple strategy, two typical results are presented for flow computations made for (i) NACA 0012 airfoil at $M_\infty = 0.7$ and $\alpha = 1^\circ$ and (ii) Garabedian-Korn

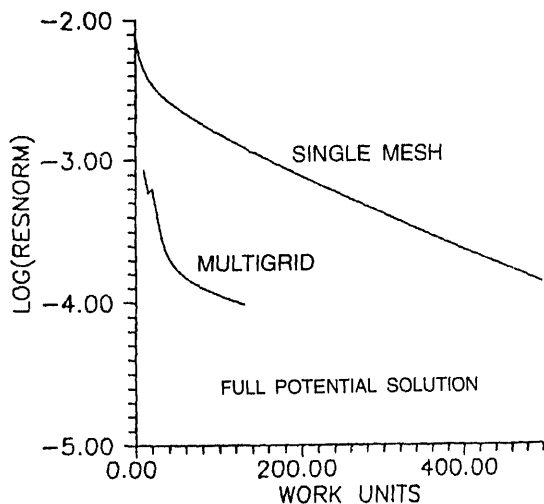


Figure 6. Comparison of convergence with and without multigrid, NACA 0012, $M = 0.7$, $\alpha = 1^\circ$.

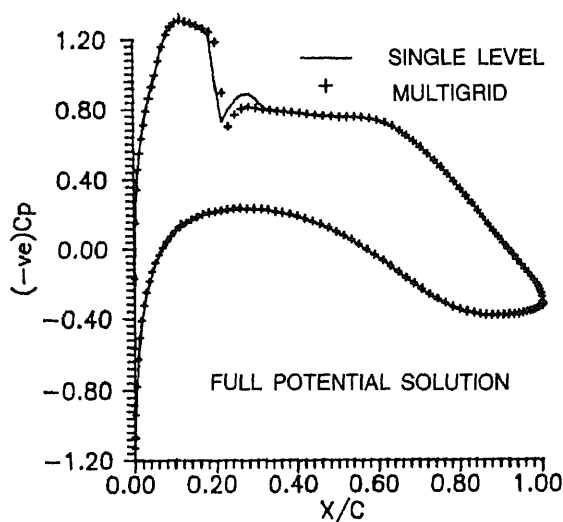


Figure 7. Comparison of pressure distribution with and without multigrid, G-K airfoil, $M = 0.702$, $\alpha = 1.1^\circ$.

airfoil, $M_\infty = 0.702$ and $\alpha = 1.1$. Figure 5 shows the pressure distribution for case (i) which is supercritical though without a shock. The agreement between the single grid computation and multigrid solution is just about total. Figure 6 shows the convergence history for this case. The single grid computation took 562 work units to converge to the specified tolerance level while the multigrid solution took only 125 work units leading to an acceleration of about 4.5 times in terms of work units. Figure 7 shows the comparison of pressure distribution for case (ii). This is a supercritical case with shock.

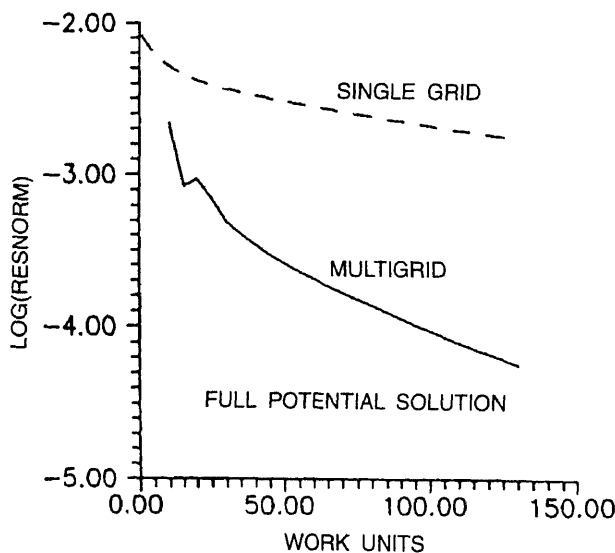


Figure 8. Comparison of convergence with and without multigrid, G-K airfoil, $M = 0.702$, $\alpha = 1.1^\circ$.

Like the earlier case, the agreement between the single grid computation and multigrid solution is good except for a small difference in the vicinity of the shock. The reason for this is explained earlier which is associated with the interpolation of coarse grid correction. Figure 8 shows the convergence history for this case. The single grid solution took 696 work units to converge to the specified tolerance level, whereas the multigrid solution took only 100 work units giving nearly 7 times faster convergence speed. The gain in convergence speed for more difficult cases like the ones with strong shock and high angle of attack is higher. This is because the instability of shock which greatly impairs the single grid convergence is effectively handled by the smoothing capability of the basic scheme at multiple levels with the added advantage of the coarse grid correction of the multigrid process. (The simple grid sequencing technique also derives the advantage of multiple levels though without the advantage of any interaction between the solution process and the discretization seen in the form of coarse grid correction.) In fact, this speed-up can be further improved by adopting strategies like implementing convergence rate based switching criterion from fine to crude grid in the injection phase, working on additional coarser levels, using W-cycles and full multigrid, trying out a better smoothing of corrections in the prolongation phase etc. Next, in the following section, implementation of multigrid acceleration to obtain solution of a more complex system, i.e., compressible Reynolds averaged Navier–Stokes equations, is described.

5. Multigrid acceleration of Navier–Stokes solver

The full Navier–Stokes equations are believed to provide complete physics of the various fluid flow phenomena. Thanks to the developments in the area of efficient algorithms and acceleration techniques, particularly the multigrid technique, on one hand, and the faster computing machines, on the other, that it has become possible to compute Navier–Stokes flows around practical configurations in reasonable turn-around time. Still when it comes to simulating turbulence, the situation is not very encouraging at least as far as the computing resources are concerned. In spite of these difficulties, the solutions of Navier–Stokes equations are of great interest where one solves what is called Reynolds averaged Navier–Stokes equations which involve introduction of an empirical model to simulate turbulence. The details on these aspects are now available in the text books and only a brief description is presented here for ready reference. Some important aspects of discretization of these equations, the solution process and the implementation of multigrid will be described in the next sections. This will be followed by discussions of a few cases of multigrid solution of the transonic flow computations. The performance of the multigrid convergence of the present Navier–Stokes code, based on the described strategy, has been tested over a range of Mach numbers between 0.1 to about 4.0 (Singh *et al* 1993).

Most of the progress in the multigrid solution of the Navier–Stokes equations has taken place during the last ten years or so. Several algorithms and methods have been devised to handle specific flow situations. A good number of these Navier–Stokes solvers use the finite volume discretization and Runge–Kutta time stepping scheme with addition of an explicit artificial viscosity to stabilise the solution. The solver in the present work is based on this method. (for details see Jameson *et al* (1981), Jameson (1985), Martinelli (1987), Kloppmann *et al* (1993), Singh *et al* (1993) and additional references therein).

5.1 The Navier–Stokes equations

The time-dependent Navier–Stokes equations for two-dimensional flow are written as (Singh *et al* 1993a);

$$\frac{\partial}{\partial t} \iiint \mathbf{W} d(\text{vol}) + \iint \mathbf{H} \cdot \hat{\mathbf{n}} dS = 0, \quad (18)$$

where vector \mathbf{W} is the cell averaged mass, momentum and total energy and is written as;

$$\mathbf{W} = (\rho, \rho u, \rho w, \rho E)^T, \quad (19)$$

and $\hat{\mathbf{n}}$ is the unit vector normal to the cell boundaries. u and w are the Cartesian velocities. The energy equation is written as;

$$E = e + (u^2 + w^2)/2, \quad (20)$$

where e is the mass averaged internal energy given as;

$$e = p/(\rho(\gamma - 1)), \quad (21)$$

and p is the pressure. The flux tensor \mathbf{H} is given as;

$$\mathbf{H} = \begin{bmatrix} \rho u & \rho w \\ \rho u^2 - \sigma_x & \rho w u - \tau_{zx} \\ \rho u w - \tau_{xz} & \rho w^2 - \sigma_z \\ (\rho E - \sigma_x)u - \tau_{xz}w + q_x & (\rho E - \sigma_z)w - \tau_{zx}u + q_z \end{bmatrix}, \quad (22)$$

with

$$\sigma_x = -p + \frac{2}{3}\mu(2u_x - w_z)$$

$$\sigma_z = -p + \frac{2}{3}\mu(2w_z - u_x)$$

$$\tau_{xz} = \tau_{zx} = \mu(u_z + w_x)$$

q_x and q_z are the components of the heat flux vector.

$$q_x = -kT_x, \quad q_z = -kT_z.$$

μ is the molecular viscosity and is computed using the Sutherland law. k is the thermal conductivity. For turbulent flows, the Baldwin–Lomax (1978) model for eddy viscosity has been used.

5.2 Spatial discretization

The time dependent Navier–Stokes equations (18) are discretized based on the method of lines in which the spatial derivatives are discretized using the cell centred finite volume scheme. Applying these conservation equations to one of these cells, we can write

$$\frac{d\mathbf{W}_{i,k}}{dt} + (\mathbf{Q}_c + \mathbf{Q}_v - \mathbf{D})_{i,k} = 0. \quad (23)$$

In the above, \mathbf{Q}_c and \mathbf{Q}_v are the convective and viscous flux vectors. This discretization amounts to central differencing and requires explicit addition of artificial viscosity to provide (a) a high order background dissipation to avoid the odd-even decoupling and

(b) a second component active in the vicinity of the shock to prevent shock-induced oscillations. This term is indicated by \mathbf{D} in (23) and is described in the sub-section 5.3.

5.3 Artificial dissipation

In the present work, the Jameson–Schmidt–Turkel (Jameson *et al* 1981) scheme for the numerical dissipation has been used which contains a blend of second and fourth differences of the flow variables. The second difference term damps oscillations in the vicinity of the shock sensed by a pressure based sensor. The fourth difference term helps to avoid the odd-even decoupling and provides the background dissipation in the smooth regions of the flow. This scheme is described below. The Jameson–Schmidt–Turkel numerical dissipation scheme (Jameson *et al* 1981; Martinelli 1987) is given as;

$$\mathbf{D}_{i,k} = d_{i+1/2,k} - d_{i-1/2,k} + d_{i,k+1/2} - d_{i,k-1/2}, \quad (24)$$

where

$$d_{i+1/2,k} = \lambda_{i+1/2,k} [\varepsilon_{i+1/2,k}^{(2)} \delta_x d_{i,k} - \varepsilon_{i+1/2,k}^{(4)} \delta_x^3 d_{i-1,k}]. \quad (25)$$

δ_x is the forward difference operator. The coefficients $\varepsilon^{(2)}$ and $\varepsilon^{(4)}$ are written as;

$$\varepsilon_{i+1/2,k}^{(2)} = k^{(2)} \max(v_{i+1}, v_i), \quad (26)$$

$$\varepsilon_{i+1/2,k}^{(4)} = \max(0, k^{(4)} \varepsilon_{i+1/2,k}^{(2)}). \quad (27)$$

The pressure sensor v is given as;

$$v = |p_{i+1,k} - 2p_{i,k} + p_{i-1,k}| / (|p_{i+1,k}| + |2p_{i,k}| + |p_{i-1,k}|). \quad (28)$$

The Navier–Stokes grids are highly stretched. The grid spacing near the wall in the direction normal to it is typically of the order of $10^{-5}c$ (c being the airfoil chord) to resolve the boundary layer leading to streamwise aspect ratio of the cells very much larger than unity in the vicinity of the airfoil. This leads to a large value for artificial dissipation leading, in turn, to a large drag. In the far field, the situation is reversed as a result of which the cell aspect ratio defined as before is less than and often much less than unity. This disparity leads to very different high frequency modes in the two directions, and cause difficulty for both the convergence and accuracy of the steady-state flow computation as well as adversely affecting the multigrid procedure. To surmount this difficulty, the variable scaling factor (Martinelli 1987; Swanson & Turkel 1987) Λ has been used instead of λ in (25). For this, λ is written as

$$\lambda_{i+1/2,k} = 0.5 [(\Lambda_x)_{i,k} + (\Lambda_x)_{i+1,k}], \quad (29)$$

where

$$\Lambda_x = \phi_x \lambda_x, \quad \phi_x = 1 + (\lambda_z/\lambda_x)^\sigma,$$

λ_x and λ_z are the scaled spectral radii of the Jacobian matrices of the convective fluxes, σ is a constant. With this, it has been possible to handle highly stretched grids with significantly improved damping properties.

5.4 Runge–Kutta time stepping

The semi-discrete equation (23) may be written as;

$$(d\mathbf{W}_{i,k}/dt) + \mathcal{R}(\mathbf{W}_{i,k}) = 0. \quad (30)$$

\mathcal{R} is the discretized flux term and is known as residual. A hybrid 5-stage Runge–Kutta scheme has been used to advance the solution of (30) in time. Following Jameson (1985), this is written as

$$\begin{aligned}\mathbf{W}^{(0)} &= \mathbf{W}^{(n)}, \\ \mathbf{W}^{(m)} &= \mathbf{W}^{(0)} - \alpha_m \Delta t [Q_c(\mathbf{W}^{(m-1)}) + Q_v(\mathbf{W}^{(0)}) - D^{(m-1)}], \\ \mathbf{W}^{(n+1)} &= \mathbf{W}^{(5)},\end{aligned}\quad (31)$$

m is the Runge–Kutta stage number (1 to 5 for 5-stage), n the time index, $\mathbf{W}^{(0)}$ the starting solution or the solution at previous time step. The convective fluxes are computed at every stage. For time economy, the viscous fluxes, considered in full, are computed only at the first stage and the numerical fluxes are computed at alternate stages employing a combination of present and previous values as follows

$$\begin{aligned}D^{(0)} &= D^{(1)} = D(\mathbf{W}^{(0)}), \\ D^{(2)} &= D^{(3)} = \beta D(\mathbf{W}^{(2)}) + (1 - \beta) D^{(0)}, \\ D^{(4)} &= \gamma D(\mathbf{W}^{(4)}) + (1 - \gamma) D^{(2)}.\end{aligned}\quad (32)$$

The weighting factors used above are $\beta = 0.56$ and $\gamma = 0.44$. The coefficients α_m are taken as $\alpha_1 = 1/4$, $\alpha_2 = 1/6$, $\alpha_3 = 3/8$, $\alpha_4 = 1/2$, $\alpha_5 = 1$. It has been shown by Martinelli (1987) that this scheme has a large parabolic stability limit. Since only the steady state solution is of interest here, a local time stepping scheme is used to accelerate the solution process wherein the time steps for each cell are taken to be the maximum permitted by the local CFL criterion.

5.5 Implicit residual smoothing

A second technique that is used to accelerate the solution procedure is that of implicit residual smoothing which enlarges the stability range of the basic time stepping scheme enabling larger time steps to be taken. Also, the implicit residual smoothing is known to significantly enhance the smoothing characteristics of the time marching scheme for use with multigrids (Wigton & Swanson 1990). In two dimensions, the residual smoothing operation is defined as follows;

$$(1 - \varepsilon_x \delta_{xx})(1 - \varepsilon_z \delta_{zz}) \mathcal{R}^* = \mathcal{R} \quad (33)$$

where \mathcal{R}^* is the smoothed residual. The smoothing parameters ε 's are different for each cell because of different aspect ratios. The coefficients ε developed by Martinelli (1987) are quite effective for highly stretched meshes and have been used in the present scheme. These locally varying coefficients are given as;

$$\varepsilon_x = \max \left\{ 0, \frac{1}{4} \left[\left(\frac{\text{CFL}}{\text{CFL}_0} \frac{\lambda_x}{\lambda_x + \lambda_z} \phi_x \right)^2 - 1 \right] \right\}. \quad (34)$$

CFL_0 is the natural Courant–Friedrich–Lewis (CFL) number of the basic scheme. The expressions for ε_z can be written in a similar way. While this variable coefficient implicit procedure requires additional CPU time to compute ε 's for each cell, this is more than compensated for by the fact that it allows CFL numbers two to three times larger than the original scheme. The highest CFL number tried in the present computations is about 7.5.

5.6 Boundary conditions

The airfoil surface is treated as an adiabatic wall on which no-slip boundary condition is applied and zero normal pressure gradient is assumed. The formulation being cell centred, the variables are not specified on the surface. This requires considering a dummy cell adjacent to the boundary. To apply the wall boundary condition, simple extrapolation of pressure to the dummy cell is done and the density is found by symmetry. The velocity components are set antisymmetric.

The farfield boundary condition is based on the use of Riemann invariants for one-dimensional flow normal to the boundary. The boundary conditions for normal velocity component and speed of sound are constructed by adding and subtracting the invariants (for details see Kroll & Jain 1987). For subsonic free streams, the tangential velocity components and entropy are extrapolated from the interior at an outflow boundary and are equated to freestream values at the inflow boundary. With this, the flow variables in farfield are computed.

5.7 Multigrid strategy

The basic features of the multigrid scheme used here are along the lines developed by Jameson (1985). The specific features of the present method can be seen in Singh *et al* (1993) and Kloppmann *et al* (1993). The Runge–Kutta time marching procedure quickly smoothes out the high frequency errors (short waves) on the fine meshes where further smoothing operations would become progressively slower. Note here that in the context of multigrid, the schemes like Gauss–Seidel, predictor–corrector, Runge–Kutta and so on are seen as smoothers rather than solvers. This is because one intends to get a good coarse grid approximation from the fine grid solution by having the fine grid starting approximation smoothed, i.e., high frequency errors diminished. The solution with the remaining error components are passed on to the next coarser mesh until that coarsest mesh is reached where the low frequency errors (long waves) of the finer meshes are seen as high frequency errors. The basic Runge–Kutta smoother is again used to remove these long wave (with respect to the finest mesh level on which the solution is sought) errors.

The scheme may use any number of levels of mesh refinement which is read as input in the code. In all the results presented here, the Full Approximation Storage scheme is used in which one starts with an initial solution on the finest mesh. In the present computations, three or four mesh levels have been used with V or W-cycles. The scheme for the residual transfer and correction interpolation are important steps for a good multigrid performance. The scheme should be such that the coarse grid correction improves the finer grid solution in smooth regions as well as correcting the discontinuity location. Towards this requirement, the flow variables are transferred from fine to coarse grid as follows (in the following, the subscript will indicate the grid level identifier).

$$\mathbf{W}_{2h}^{(0)} = \sum V_h \mathbf{W}_h / V_{2h}, \quad (35)$$

where V is the cell volume and h and $2h$ refer to the finer and coarser meshes levels, respectively. The summation is performed over the four fine cells constituting one coarse cell. This volume weighted averaging preserves mass, momentum and energy

conservation. The residuals are transferred as simple sums of the residuals in the four constituent fine cells. The eddy viscosity is computed only on the finest mesh and is carried on to the coarser mesh by simple averaging. To update the solution on the coarse mesh, the residual is modified by adding the forcing function defined as;

$$f_{2h} = - \sum R_h(\mathbf{W}_h) + R_{2h}(\mathbf{W}_{2h}^{(0)}). \quad (36)$$

The summation is performed as before. With this, the multistage scheme on the coarser mesh is written as;

$$\begin{aligned} \mathbf{W}_{2h}^{(0)} &= \mathbf{W}_{2h}^{(n)}, \\ \mathbf{W}_{2h}^{(1)} &= \mathbf{W}_{2h}^{(0)} - \alpha_1 \Delta t (R_{2h}^{(0)} - f_{2h}), \\ &\dots\dots\dots \\ \mathbf{W}_{2h}^{(m)} &= \mathbf{W}_{2h}^{(0)} - \alpha_m \Delta t (R_{2h}^{(m-1)} - f_{2h}), \\ &\dots\dots\dots \\ \mathbf{W}_{2h}^{(n+1)} &= \mathbf{W}_{2h}^{(m)}, \end{aligned} \quad (37)$$

where n is time level and m is the number of stages. Note that in the first stage above, the entire corrected residual reduces to $\sum R_h(\mathbf{W})_h$ implying that the evolution on the coarse mesh is influenced by the residuals on the finer mesh. This procedure is followed until the coarsest mesh is reached. Only a single fine grid boundary condition update offers computation time economy without sacrificing the accuracy of the solution. The corrections computed on the coarse mesh are prolonged to the finer mesh by simple linear interpolation. This step introduces high frequency errors causing degradation of the convergence which is more pronounced if the grids are highly stretched. To improve the situation, the corrections are smoothed before update. An effective way to take into account the effect of high grid stretching is to use the implicit residual smoothing. The coarse grid correction is transferred to the finer mesh by

$$\mathbf{W}_h = \mathbf{W}_{h(\text{old})} + \tilde{\mathcal{I}}_h^h (\mathbf{W}_{2h} - \mathcal{I}_h^{2h} \mathbf{W}_{h(\text{old})}), \quad (38)$$

where \mathcal{I} and $\tilde{\mathcal{I}}$ are suitable interpolation operators.

5.8 Results from Navier–Stokes computations

The multigrid accelerated Navier–Stokes code developed and based on the above strategy has been extensively used to compute several flow conditions on a variety of airfoils. Table 2 lists the four typical cases of airfoils and the corresponding flow conditions for which the computed results will be presented.

For the cases presented, a 257×41 size C-grid with a total of 64 points in the wake or 321×65 size C-grid with a total of 128 points in the wake has been used. The farthest grid points are placed at about 12 to 18 chords away from the airfoil and the grid line just above the airfoil is about 10^{-5} chords away to enable a good resolution of the boundary layer. The computations have been performed on the Convex 3820 computer at the CSIR Centre for Mathematical Modelling and Computer Simulation, Bangalore. Depending on the mesh size and the flow conditions, the solutions, converged to the level of acceptable tolerance, take just about 5 to 15 min of CPU time. The corresponding single grid solution takes about 2–3 hours of CPU time for similar

Table 2. Cases selected for Navier–Stokes computations.

Case	Airfoil	Grid	M_∞	$\alpha(\text{deg})$	$Re(10^6)$	Xtr
1.	CAST-7	257 × 41	0.70 0.70 0.70	2.00 2.64 3.60	4.0 6.0 6.0	7% 8% 8%
2.	RAE 2822	321 × 65	0.73	2.79	6.5	3%
3.	NACA 66, 2-215	257 × 41	0.601	2.0	1.5	64% up 73% low
4.	NACA 0012	257 × 41	0.6 0.6	8.437 9.0	9.0 9.0	5% 5%

xtr – transition location as % of chord

and, in most cases, higher levels of residuals. This feature of the code, along with its robustness and accurate prediction capabilities, offers itself as a designer's tool for evaluating the characteristics of the airfoils.

5.8a CAST-7 airfoil: This is 11.8% thick supercritical airfoil with moderate rear loading, designed by the Dornier Company. This airfoil has been extensively studied by this author during the early phase of the work with this code without multigrid (Singh 1990). Table 3 shows the details of the studies made on this airfoil and presented in this report.

The single level computation and 3-level grid sequencing computations at serial numbers 1 and 2 are included from the point of view of illustrating the effect of factors other than multigrid as will be explained. The single grid computation (no. 1) refers to

Table 3. Comparison of performance of Navier–Stokes code with and without multigrid (Cast-7 airfoil).

Computational strategy	c_l	c_d	Work units	Convergence level	CFL	Remarks
1. Single grid	0.8197	0.01905	6500	$\approx 1.97 \times 10^{-1}$	0.6	4-stg RK, No IRS std JST
2. 3-Level grid sequencing	0.8175	0.01899	3437	—	0.6	4-stg RK, No IRS std JST
3. Single grid	0.8117	0.01898	3000	$\approx 10^{-5}$	1.6	5-stg hybrid RK, VC-JST, VC-IRS
4. 3-Level MG V-cycle	0.8174	0.01926	147	2.06×10^{-4} for stabilised Cl	1.6	5-stg hybrid RK, VC-JST, VC-IRS
5. 3-Level MG V-cycle	0.8172	0.01921	496	9.51×10^{-8} for convergence tolerance of 10^{-7}	1.6	5-stg hybrid RK, VC-JST, VC-IRS

4- and 5-stg RK – 4- and 5-stage standard Runge–Kutta scheme

IRS – implicit residual smoothing

VC – variable coefficient (eigenvalue weighted)

JST – Jameson–Schmidt–Tukel artificial dissipation

CFL – normalised CFL number defined as CFL/CFL_0 (see (34))

the original status of the code when the work on the development of the accelerated Navier–Stokes code was started under the NAL–DLR (Göttingen) collaboration. Computation no. 2 refers to the first stage of the acceleration work using grid sequencing (Singh 1990). Both these computations use a standard 4-stage Runge–Kutta scheme with the Jameson–Schmidt–Turkel dissipation (Jameson *et al* 1981). Also, to stabilise the solution properly, a normalised CFL number of 0.6 has been used which gives slow convergence rates in these two cases. The single grid version at serial number 3 and the multigrid version have additional features like eigenvalue scaled dissipation coefficients, hybrid 5-stage Runge–Kutta time integration and variable coefficient implicit residual smoothing whose effects are described in §§ 5.3 to 5.5. These elements offer the multigrid version of the code not just the weighted dissipation but higher CFL too. The normalised CFL used in the presented multigrid example is 1.6. These points should be borne in mind while making comparisons based on the data in table 3.

Figure 9 shows the comparison of the pressure distributions obtained using single grid (dashed line), 3-level grid sequencing results (shown by *) and 3-level multigrid V-cycle results (full line). This study presents the validation test to check the faithful reproduction of earlier verified and well-studied single mesh and 3-level grid sequencing computations (Singh 1990) by the present multigrid computations. Under these flow conditions, the airfoil develops a shock of moderate strength on the upper surface at around 35–37% of chord. The agreement of C_p -distributions obtained from the three computations is almost total. Figure 10 shows a similar comparison of the skin friction (normalised with respect to free stream quantities) obtained from the single grid version (dashed line), the grid sequencing version (no. 2 with *) and the multigrid version (no. 4, full line). As in the case of C_p , the agreement of skin friction obtained from these versions is also nearly total. The skin friction is a more sensitive quantity

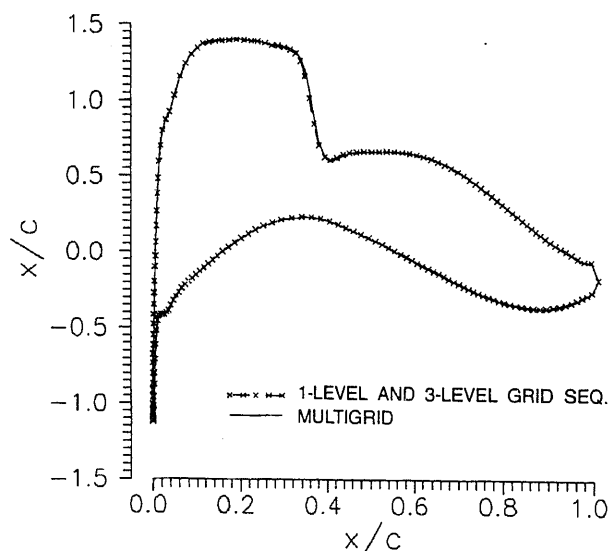


Figure 9. Comparison of pressure distribution with and without multigrid, N–S solution, Cast-7, $M = 0.7$, $\alpha = 2^\circ$.

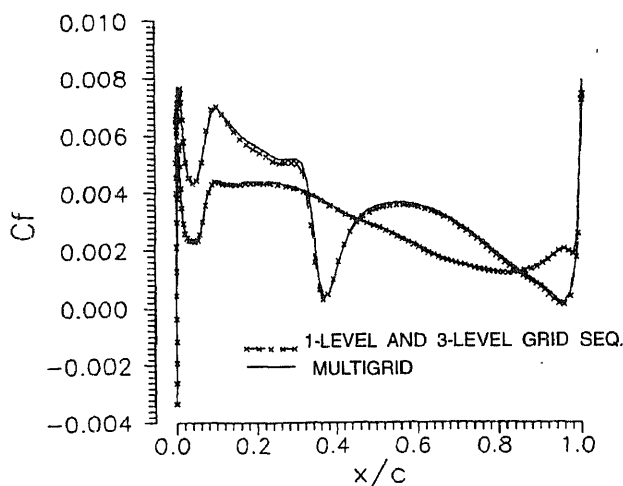


Figure 10. Comparison of skin-friction, N-S MG solution, Cast-7 airfoil, $M = 0.7$, $\alpha = 2^\circ$.

than C_p and these agreements confirm the general reliability of the codes as well as that of the multigrid implementation. Figure 11 shows the comparison of convergence rates of the single grid computation (case 3) and multigrid computations. This figure shows that to achieve a drop of five orders in the normalised maximum residual, the multigrid requires approximately 280 work units, whereas the single grid computation requires approximately 2800 work units. Figure 12 shows the comparison of evolution of the lift. It is seen that while the single grid computation takes about 1200–1300 work units to reach stabilised lift level (but with higher residue level), the multigrid computation shows a rapid and smooth evolution stabilising in about 200 work units with one order smaller residue level. This rapid stabilisation of lift coefficient, which is sustained without any oscillation, indicates a reliable, robust and stable computation.

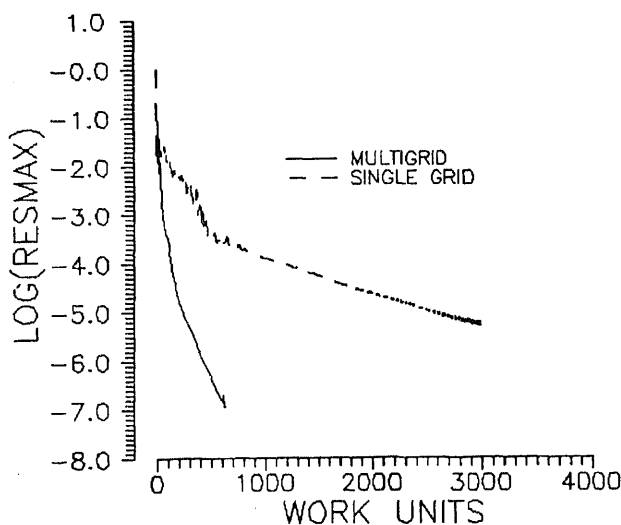


Figure 11. Comparison of convergence history, N-S solution, Cast-7, $M = 0.7$, $\alpha = 2^\circ$.

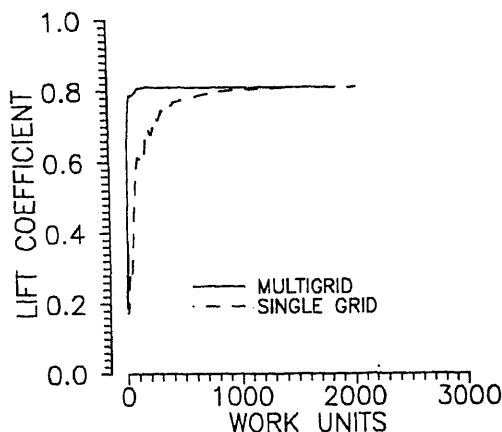


Figure 12. Comparison of lift evolution, N-S MG solution, Cast-7, $M = 0.7$, $\alpha = 2^\circ$.

Before proceeding further to discuss a few computations and their comparisons with experimental data, it would be of interest to discuss here the effects of V and W multigrid cycles and the number of smoothings at each level on the performance of multigrid technique. Figure 13 shows the effect of V and W-cycles on the convergence history of flow past RAE 2822 airfoil. The two computations have all other inputs identical. A marginal gain in convergence rate is seen with W-cycle (Kloppmann *et al* 1993). Figure 14 shows the effect of number of smoothings performed at each grid level and also the effect of V and W-multigrid cycle strategies for flow past NACA 0012 airfoil. The numbers in the legend indicate the strategy used. For example, "case 1:3-lvl V-cycle 8/4/2 & 0/0/0" indicates that the computation in case 1 uses 3 level V-cycle with 8 smoothings at the coarsest level, 4 at the medium level and 2 at the finest level in the injection phase and no smoothing during the prolongation phase. This experiment showed that most computations, especially the ones using W-cycle, failed to converge if no smoothing was performed during the prolongation phase. The figure also indicates faster drop of residual with larger number of smoothings performed on the coarser

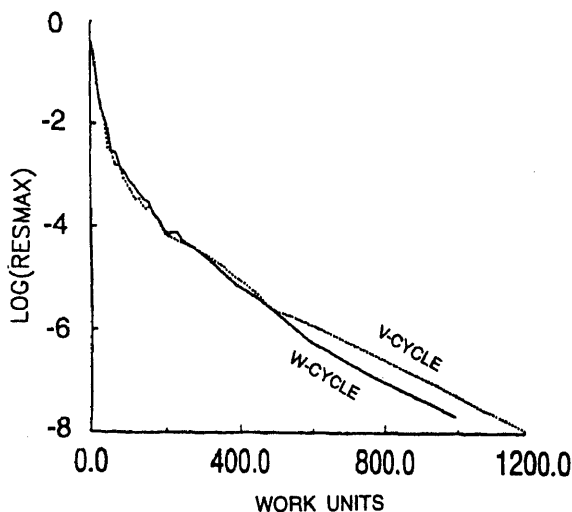


Figure 13. Effect of V- and W-cycles on the multigrid convergence.

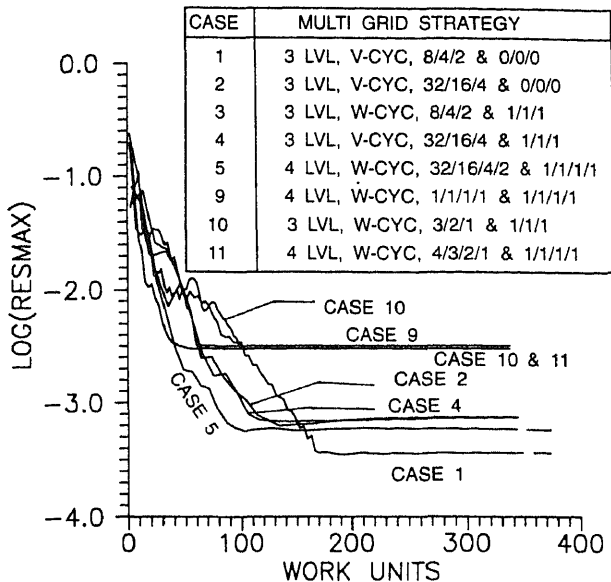


Figure 14. Effect of number of smoothings on the multigrid convergence.

levels. The fastest convergence is obtained with the combination used in case 5 whereas the residual is driven to the lowest level in case 1.

Next, the results of some computations for transonic flow past airfoils will be presented and compared with the experimental data to demonstrate the robustness and accuracy of the code and the efficiency obtained due to multigrid technique.

Figure 15 and 16 show the comparisons of the predicted pressure distributions with experimental data (Stanewski *et al* 1979) for flow past Cast-7 airfoil at $M = 0.7$ at angles of attack of (i) 2.64° and (ii) 3.6° . The Reynolds number for both cases is about 6×10^6 with transition forced at 8% chord. The agreement for the case (i) is good everywhere including the shock location and its intensity. The agreement for the case (ii) is also good but the computed shock intensity is somewhat stronger. The grid for this case is a 257×41 C-grid with 64 points in the wake and 193 points on the airfoil. The lateral separation of the grid is such that there are nearly 25 grid lines inside the boundary layer and the grid lines in the outer flow are sparsely located. This indicates that if the flow inside the boundary layer is well resolved, the outer mesh density plays a secondary role. This fact is well borne out not just by the good pressure prediction but also by the well predicted drag. Table 4 summarises the quantitative comparison for these two cases.

5.8b RAE 2822 airfoil: For this study, the standard transonic test case number 9 from the AGARD set of data (Stanewski *et al* 1979) is selected. This computation has been carried out on a fairly fine mesh of size 321×65 . The experimental incidence for this case is 3.19° . The present computations have been made at a corrected angle of attack of 2.79° as suggested by the experimenters (Stanewski *et al* 1979) to accommodate the effect of wind tunnel wall interference. Figure 17 shows the comparison of computed pressure distribution with the AGARD data (Stanewski *et al* 1979). The agreement is seen to be good almost everywhere including at the peak plateau and

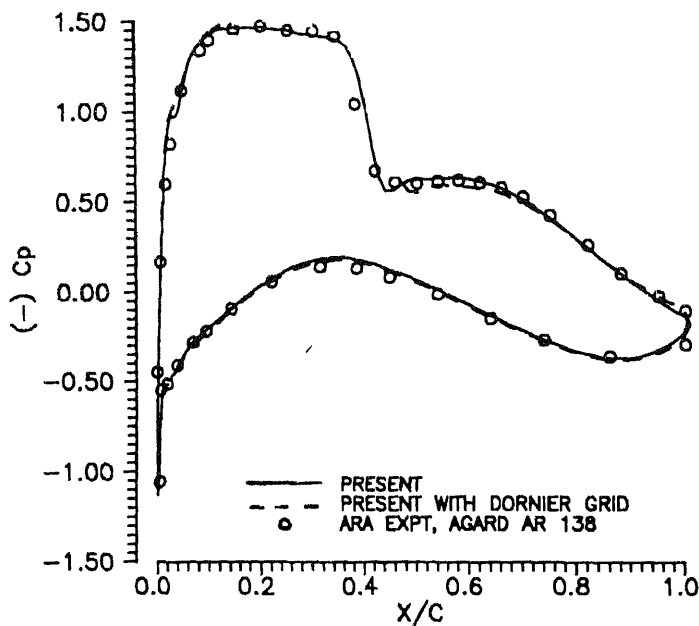


Figure 15. Comparison of C_p -distribution, Cast-7, $M = 0.7$, $\alpha = 2.64^\circ$, $Re = 6 \times 10^6$.

shock location. It may be pointed out that very often in the literature, a significant difference is seen in the peak plateau region. The experimental values of lift and drag coefficients ($c_l = 0.803$ and $c_d = 0.0168$ respectively) agree well with the predicted values ($c_l = 0.799$ and $c_d = 0.019$ respectively). As seen in figure 18, the comparison of skin

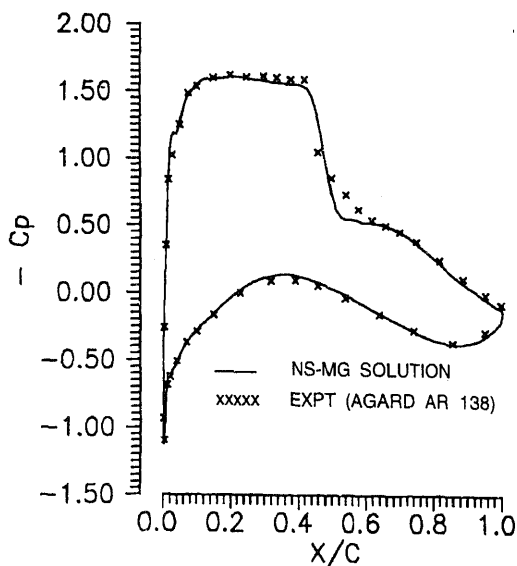


Figure 16. Comparison of C_p -distribution, Cast-7, $M = 0.7$, $\alpha = 3.6^\circ$, $Re = 6 \times 10^6$.

Table 4. Quantitative comparison with experimental data Cast-7 Airfoil.

Case	M_∞	α (deg)	Re 10^6	Xtr	c_l (present)	c_l^*	c_d (present)	c_d^*
(i)	0.70	2.64	6.0	8%	0.8809	0.867	0.02548	0.01879
(ii)	0.70	3.60	6.0	8%	1.0289	1.027	0.0393	0.03286

*Reference – Stanewski (1993b)

friction (normalised with respect to the quantities at the boundary layer edge to be in conformity with the experimental data) is also in good agreement with the experimental data.

5.8c NACA66,2-215 low drag airfoil: This is one of the low drag airfoils (what is now known as NLF airfoils) designed at the erstwhile NACA during the 40's. Its characteristics are studied and reported (Graham *et al* 1945). The airfoil was designed to perform at high subsonic Mach numbers. The transition points on the upper and lower surfaces, as given in table 2, were fixed at locations approximately predicted using the Granville criterion as the related information was not available. Figure 19 shows the comparison of the computed pressure distribution with experimental data (Graham *et al* 1945). The agreement is seen to be good. Figure 20 shows the corresponding convergence history. The residual drops to about 3×10^{-5} in about 400 work units.

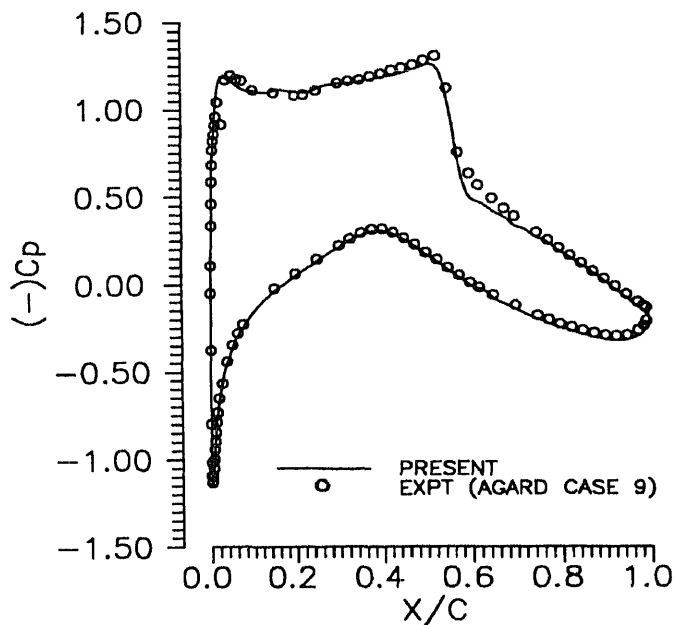


Figure 17. Comparison of C_p -distribution. N-S MG solution, RAE 2822, $M = 0.73$, $\alpha = 2.79^\circ$, $Re = 6.5 \times 10^6$.

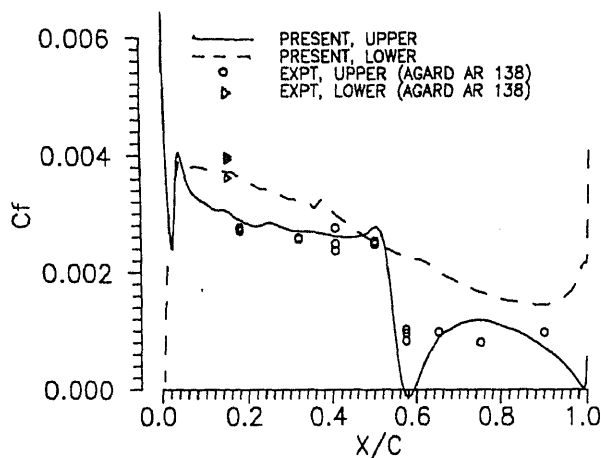


Figure 18. Comparison of skin-friction. N-S MG solution, RAE 2822 airfoil, $M = 0.73$, $\alpha = 2.79^\circ$, $Re = 6.5 \times 10^6$.

5.8d NACA 0012 airfoil: This airfoil was chosen to demonstrate the application of the multigrid Navier–Stokes code to compute flows at high angles of attack with large trailing edge separation. The Baldwin–Lomax model for turbulence is not adequate when the flow is largely separated. With the present experience, the Granville correction to this model appears to give results in much better agreement under separated flow conditions (Singh *et al* 1993). However, under the nonequilibrium conditions of shock induced separation, this model does not seem to be as effective as under the conditions of the trailing edge flow separation at low speeds. Figure 21 shows the comparison of C_p distribution at $M_\infty = 0.6$, $\alpha(\text{corrected}) = 8.437^\circ$, $Re = 9 \times 10^6$ and transition fixed at 5% chord. This case corresponds to the stall condition with

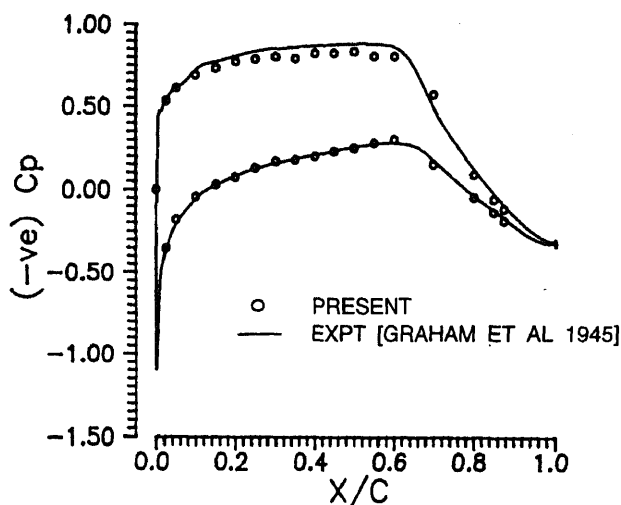


Figure 19. Comparison of pressure distribution, NACA 66, 2-215 airfoil, $M = 0.601$, $\alpha = 2^\circ$, $Re = 1.5 \times 10^6$.

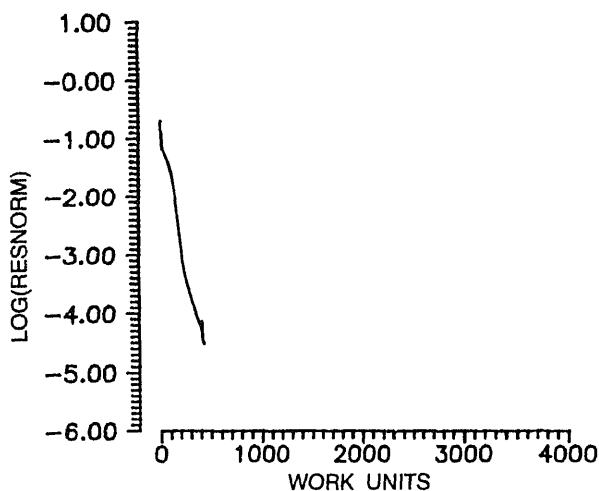


Figure 20. Convergence history, NACA 66, 2-215 airfoil, $M = 0.6$, $\alpha = 2^\circ$, $Re = 1.5 \times 10^6$.

$\alpha_{\text{expt}} = 9.86^\circ$. The results are compared with the experimental data of Harris (1981). The predicted pressure distribution with the Granville correction is seen to be in better agreement with the experimental data than that predicted using the original Baldwin-Lomax model. Figure 22 shows the computed skin friction (quantities normalised with respect to free stream values). A separation bubble between about 16% to 23% of chord is seen with a brief reattachment followed by separation on the entire upper surface. Figure 23 shows streamline pattern around this airfoil under the same conditions but at slightly higher (corrected) angle of attack of 9° . The separation bubble, which was very small for the case with $\alpha = 8.437^\circ$ to offer good graphic representation is slightly enlarged in the present case and can be seen clearly in figure 24. The flow reattaches briefly after the bubble and separates again over the

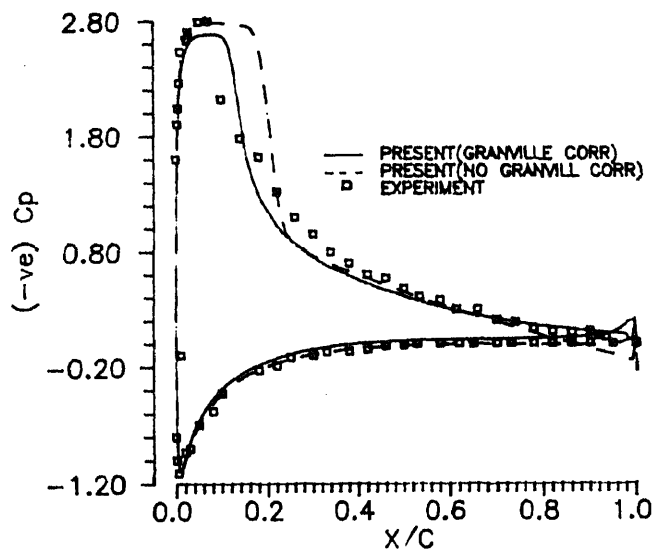


Figure 21. Comparison of pressure distribution, NACA 0012 airfoil, $M = 0.6$, $\alpha(\text{corr}) = 8.437^\circ$, $Re = 19 \times 10^6$, $x_{tr} = 5\%$, stall condition.

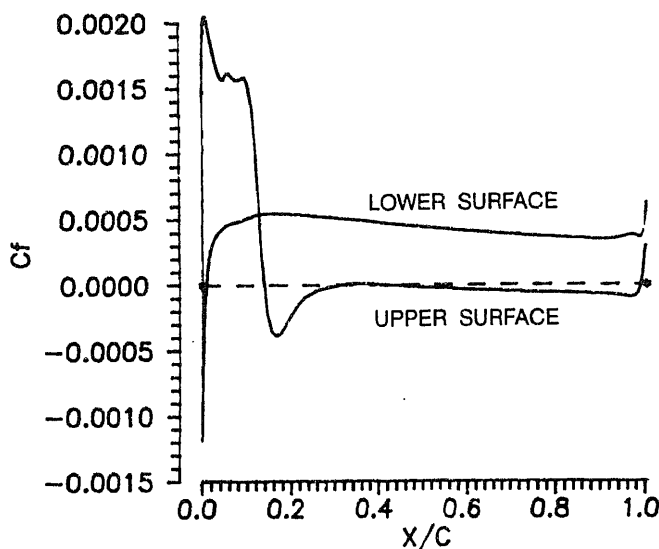


Figure 22. Computed skin friction NACA 0012 airfoil, $M = 0.6$, $\alpha(\text{corr}) = 8.437^\circ$, $Re = 9 \times 10^6$.

entire upper surface. The skin friction inset in figure 24 clearly shows the location of the bubble and the separated flow on the upper surface. The flow evolution for this computation is wavy with lift coefficient oscillating over a couple of hundreds of work units with the amplitude of oscillation of lift continuously reducing and finally settling down. This indicates that the flow has still not become unsteady and the results are fairly acceptable for design estimates as indicated by the stabilised lift. The normalised residual could not be driven below about 10^{-2} .

6. Conclusions

The multigrid technique is, perhaps, the best known acceleration technique for iterative solution procedures. It offers the possibility of a realistic turn-around time for many computations which otherwise take hours and days on most of the commonly used

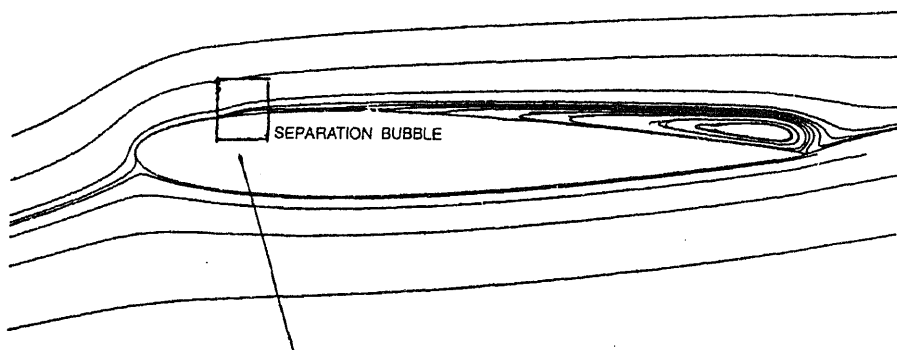


Figure 23. Streamline pattern, N-S MG solution, NACA 0012 airfoil, $M = 0.6$, $\alpha(\text{corr}) = 9^\circ$ (Granville correction to B-L model, stall condition).

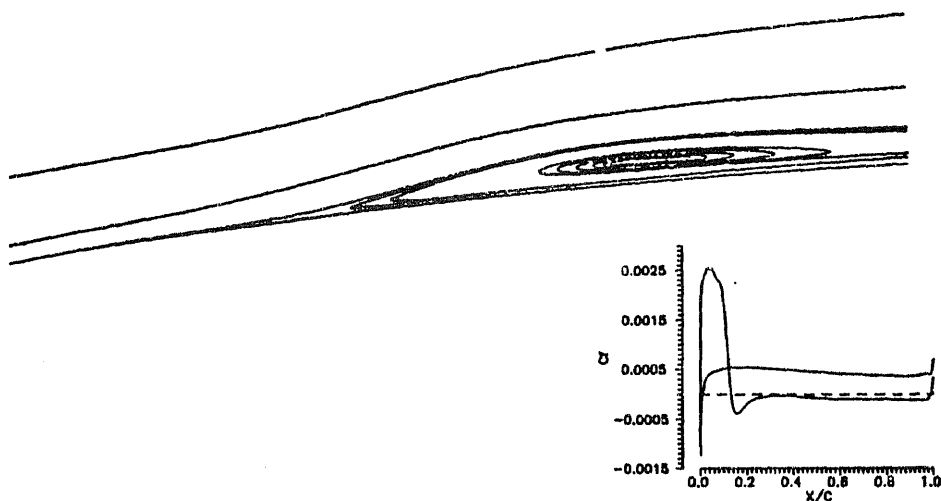


Figure 24. Magnified view of the separation bubble of figure 23. The inset shows the skin friction. The reversed flow inside the bubble and the fully separated flow downstream is clear from the negative skin friction.

computing machines. Its application to three common fluid dynamical problems is demonstrated and the quantitative gains are seen to be in the range of 3 to 10 times in terms of work units. The accelerated codes, which have been demonstrated to be fairly robust and accurate, offer themselves as designer's tools for evaluating the characteristics of the airfoils, especially when used on high speed computing machines.

References

- Baldwin B S, Lomax H 1978 Thin layer approximation and algebraic model for separated turbulent flows. AIAA Paper 78-257
- Brandt A 1972 Multi-level adaptive technique (MLAT) for fast numerical solution to boundary value problems. *Proc. of Third ICNMFD. Lecture Notes in Phys. 18* (Berlin: Springer Verlag) vol. 1, pp 82-89
- Brandt A 1977 Multi-level adaptive solutions to boundary-value problems. *Math. Comput.* 31: 333-390
- Brandt A 1989 The Weizmann Institute Research in multilevel computation: 1988 Report. *Proc. of 4th Copper Mountain Conf. on Multigrid Methods*
- Federenko R P 1964 On the speed of convergence of an iterative process. *USSR Comput. Math. Math. Phys.* 4: 227-235
- Garabedian P, Korn D 1971 Analysis of transonic airfoils. *Commun. Pure Appl. Math.* 24: 841-851
- Graham D J, Nitzberg G E, Olson R N 1945 A systematic investigation of pressure distribution at high speeds over five representative NACA low drag and conventional airfoil sections. NACA TR-832
- Hackbusch W 1976 Ein iteratives Verfahren zur schnellen Auflösung elliptischer Randwertprobleme. Report 76-12, Universität Köln
- Harris C D 1981 Two-dimensional aerodynamic characteristics of the NACA 0012 airfoil in the Langley 8-foot transonic pressure tunnel. NASA TM 81927

- Jameson A, Schmidt W, Turkel E 1981 Numerical simulation of the Euler equations by finite volume methods using Runge–Kutta time stepping-schemes. *AIAA Paper* 81–1259
- Jameson A 1985 Multigrid algorithm for compressible calculations. *MAE Report* 1743, Princeton University
- Jameson A 1993 Numerical wind tunnel – vision or reality. *AIAA 24th Fluid Dynamics Conference*, Orlando, FL, *AIAA Paper* 93–3021
- Kloppmann Ch, Schwaborn D, Singh J P 1993 Multigrid solutions of the 2-D Navier–Stokes equations for transonic internal and external flows. *4th European Conference on Multigrid*, Amsterdam
- Kroll N, Jain R K 1987 Solution of two-dimensional Euler equations – Experience with a finite volume code. *DFVLR-FB* 87-41, DLR, Braunschweig
- Martinelli L 1987 *Calculation of viscous flows with a multigrid method*. PhD dissertation, Mechanical & Aerospace Engineering Department, Princeton University, Princeton, NJ
- Murman E M, Cole J D 1971 Calculation of plane steady transonic flow. *AIAA J.* 9: 114–121
- Singh J P 1989 Solution of Laplace equation using full approximation storage multigrid technique. *NAL PD CF* 8927, NAL, Bangalore
- Singh J P 1992 Multigrid accelerated relaxation solution of transonic full potential flow equation. *NAL PD CF* 8942. Also *Proc. Int. Conf. on Methods of Aerophysical Research*, Novosibirsk
- Singh J P 1990 Accelerated Navier–Stokes solution. Part I: Grid sequencing. *IB* 221–90 A 20, DLR, Göttingen
- Singh J P 1992 An illustrative study of the impact of boundary condition defect on driving the multigrid procedure. *5th Asian Congress on Fluid Mechanics* (Taejon, Korea: Department of Aerospace Engineering, KAIST)
- Singh J P, Schwaborn D, Kloppmann Ch 1993a Development of a general purpose multigrid accelerated Navier–Stokes solver. *NAL SP*-9315, NAL, Bangalore
- Singh J P, Schwaborn D, Kloppmann Ch 1993b Multigrid Navier–Stokes solution of flow past airfoil around stall. *5th Int. Symp. on CFD* (Sendai, Japan: Jpn. Soc. Comput. Fluid Dynamics)
- South J C, Brandt A 1977 Application of a multi-level grid method to transonic flow computations. In *Transonic flow problems in turbomachinery* (eds) T C Adamson, M F Platzer (Washington: Hemisphere)
- Stanewski E, Puffert W, Mueller R, Bateman T E B 1979 Supercritical airfoil Cast-7 – surface pressure, wake and boundary layer measurements. In *Experimental data base for computer program assessment*, AGARD AR 138
- Swanson R C, Turkel E 1987 Artificial dissipation and central difference schemes for the Euler and Navier–Stokes equations. *AIAA Paper* 87–1107
- Wesseling P 1990 Multigrid methods in computational fluid dynamics. *Z. Angew. Math. Mech.* 70: T337–T347
- Wigton L B, Swanson R C 1990 Variable coefficient implicit residual smoothing. *Proceedings of the 12 ICNMF D. Lecture Notes in Phys.* 371 (Berlin: Springer-Verlag)

Numerical simulation of a 2-D jet-crossflow interaction related to film cooling applications: Effects of blowing rate, injection angle and free-stream turbulence

S SARKAR and T K BOSE

Department of Aerospace Engineering, Indian Institute of Technology, Madras 600 036, India

MS received on 3 October 1994

Abstract. The aerodynamics of a coolant jet in a hot crossflow in an environment representative of the gas turbine practice, is numerically investigated for film cooling applications. The time-dependent, mass-averaged Navier–Stokes equations coupled with the compressible form of a two-equation low-Reynolds number (k - ϵ) model are solved based on an explicit finite volume formulation. The computed flow-field and surface temperature distributions along with the turbulence quantities are presented to illustrate the variation of flow-physics and heat transfer phenomena which occur in a jet-crossflow interaction with changing blowing rates, slot angles, and inlet free-stream turbulence levels.

Keywords. Numerical simulation; slot-film cooling; turbulent flow.

1. Introduction

Components of a modern aircraft gas turbine are exposed to extremely high temperature. Control of both temperature level and gradient is needed for reliable operation and prolonged useful life of these components. Film cooling, one of the most popular methods, is widely used for this purpose. A cold secondary fluid is locally injected into the hot crossflow through a slot or a series of holes at one or more discrete locations along the surface to be protected. The secondary fluid is expected to create an insulating film which would reduce the convective heat transfer rate from the hot gas stream to the exposed surface. The flow-field near the injected coolant jet is very complex with high gradients of velocity, temperature, turbulence intensity and a local flow reversal (figure 1).

Studies on film cooling are widespread in the literature. Unfortunately, most of these investigations are only devoted to the analysis of surface heat transfer phenomena. Aerodynamic aspects related to the jet-mainstream interactions and the coolant layer formation are not yet completely understood. Numerical analysis, which provides detailed information of flow-field and heat transfer phenomena, can improve the

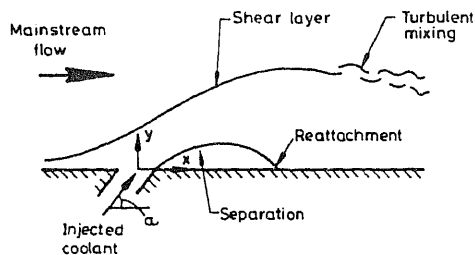


Figure 1. A general description of flow-field.

understanding of film cooling process when used in conjunction with experimental studies.

The highly complex flow-field created by the secondary fluid injection, depends on a wide variety of parameters such as the injection angle (α), the blowing ratio (m), the density ratio (DR), the free stream turbulence intensity and the state of incoming boundary layer. An excellent review by Goldstein (1971) describes some of these factors and earlier experimental investigations on film cooling.

There are several experimental studies that measure the adiabatic wall temperature to define the film cooling effectiveness (η) for different slot and hole injection configurations and also for different density and blowing ratios (Papell 1960; Petersen *et al* 1977; Foster & Lampard 1980; Sinha *et al* 1990). The flow-field generated by injection from a row of holes is more complicated than that of slot injection because of three-dimensionality. Aerodynamic investigations related to the film cooling rarely appear in the open literature. Among the very few, Andreopoulos & Rodi (1984) and Pietrzyk *et al* (1989) made a detailed turbulence study and aerodynamic description of a jet in a crossflow.

The free-stream turbulence is a strong influencing parameter for the turbine blade cooling application. Experimental investigations (Brown & Minty 1975; Ko & Liu 1980) indicated a loss of cooling effectiveness with an increase of free-stream turbulence for both slot and hole injection due to greater mixing of the injected secondary air with the mainstream. Kadotani & Goldstein (1979) reported the effects of free-stream turbulence, both in intensity and scale, on a turbulent jet. They concluded that the free-stream intensity and scale affected a number of parameters such as the boundary layer thickness, the height of the jet penetration and the mixing between the mainstream and the injected flow. Jumper *et al* (1991) pointed that a strong interaction with the cooling film would be expected as the free-stream turbulence levels are raised to a level comparable to that in the film. They concluded that the high turbulence levels of 14–17% could result in significant reduction in the film cooling effectiveness compared to the data bases with low turbulence level. Thus, the use of the data base with low free-stream turbulence would not be appropriate in assessing heat transfer phenomena for turbomachinery applications.

In the present study, the low-Reynolds number compressible form of a two-equation model, coupled with Favre-averaged mean flow equations (Favre 1965), is implemented into a purely explicit scheme which is applicable for a wide range of Mach numbers. There are limited attempts which incorporate the higher order turbulence models into an explicit solution, as it might have been thought that the stiffness associated with the

explicit treatment is mainly due to the large source terms in the transport equations of turbulence models. But, the analysis of Kunz & Lakshminarayana (1991) illustrates that the slower convergence rates that occur when explicit schemes are used to compute turbulent flows, are primarily due to the hyperbolic and parabolic stability constraints associated with the high grid clustering, and not due to the stiffness associated with large source terms in the transport equations of the turbulence models. Numerical results of flow and thermal fields along with turbulence quantities are presented to illustrate the effects of free-stream turbulence in a jet-crossflow interaction for film cooling applications in an environment representative of gas turbine practice. The variation of aerodynamics, shifting positions of flow reversal and change in film cooling effectiveness due to the change in blowing rate and injection angles are also discussed. The analysis is limited to a two-dimensional simulation.

2. Governing equations and turbulence models

In the present analysis, the density-weighted time-averaging (Favre 1965) is used. The density-weighted averaging leads to a simpler form of the governing equations with terms that are more amenable to physical interpretation. This is used for velocity components, temperature, turbulent kinetic energy and dissipation rate, whereas, the conventional time averaging is used for pressure, density, stress tensor and heat flux vector (Cebeci & Smith 1974). The effects of fine scale turbulence are simulated by incorporating a two-equation model of turbulent kinetic energy k , and turbulent dissipation ϵ and by specifying a turbulent Prandtl number $Pr = 0.9$. The low-Reynolds number terms of Lam-Bremhorst (1981) is used here in order to improve near wall modelling.

The two-dimensional, time-dependent, mass-averaged compressible Navier-Stokes equations along with two additional equations for k and ϵ can be expressed for each discrete quadrilateral cell in the integral form as,

$$\frac{\partial}{\partial t} \int_{\Omega} \mathbf{U} d\Omega + \int_s \bar{\mathbf{Q}} \cdot d\bar{\mathbf{S}} = \int_{\Omega} \mathbf{H} d\Omega, \quad (1)$$

where

$$\mathbf{U} = \begin{bmatrix} \rho \\ \rho u \\ \rho v \\ \rho e \\ \rho k \\ \rho \epsilon \end{bmatrix}; \quad \bar{\mathbf{Q}}, \text{ the flux vector} = (\mathbf{F}, \mathbf{G})$$

$$\mathbf{F} = \begin{bmatrix} \rho u \\ \rho u^2 + p - \tau_{xx} \\ \rho uv - \tau_{xy} \\ (\rho e + p - \tau_{xx})u - \tau_{xy}v + q_x \\ \rho uk - (\mu + \mu_t/\sigma_k)\partial k/\partial x \\ \rho u\epsilon - (\mu + \mu_t/\sigma_\epsilon)\partial \epsilon/\partial x \end{bmatrix}, \quad (2)$$

$$\mathbf{G} = \begin{bmatrix} \rho v \\ \rho uv - \tau_{yx} \\ \rho v^2 + p - \tau_{yy} \\ (\rho e + p - \tau_{yy})v - \tau_{yx}u + q_y \\ \rho vk - (\mu + \mu_t/\sigma_k)\partial k/\partial y \\ \rho v\varepsilon - (\mu + \mu_t/\sigma_\varepsilon)\partial \varepsilon/\partial y \end{bmatrix},$$

$$\mathbf{H} = \begin{bmatrix} 0 \\ 0 \\ 0 \\ 0 \\ P_k - \rho\varepsilon \\ c_{\varepsilon 1}f_{\varepsilon 1}P_k\varepsilon/k - c_{\varepsilon 2}f_{\varepsilon 2}\frac{\rho\varepsilon^2}{k} \end{bmatrix}.$$

The total stress tensor and the heat flux vector are given in Cartesian coordinates as:

$$\tau_{ij} = \mu \left[\left(\frac{\partial u_i}{\partial x_j} + \frac{\partial u_j}{\partial x_i} \right) - \frac{2}{3} \delta_{ij} \frac{\partial u_k}{\partial x_k} \right] + \tau_{t_{ij}}, \quad (3)$$

and

$$q_i = -\frac{\mu c_p}{Pr} \frac{\partial T}{\partial x_i} + q_{ti}. \quad (4)$$

In the present study, the laminar viscosity coefficient μ is assumed to be a function of temperature only, and is evaluated following Sutherland's law. The perfect gas equation of state $p = \rho R T$, is also considered to be applicable where,

$$T = \frac{1}{c_v} \left[e - \frac{V^2}{2} \right].$$

In preceding expressions, $\tau_{t_{ij}}$ and q_{ti} represent the turbulent stress tensor and heat flux vector, which are to be evaluated for the closure of (1). Incorporating an eddy viscosity formulation, the turbulence stress tensor and heat flux vector are given by:

$$\tau_{t_{ij}} = \mu_t \left[\left(\frac{\partial u_i}{\partial x_j} + \frac{\partial u_j}{\partial x_i} \right) - \frac{2}{3} \delta_{ij} \frac{\partial u_k}{\partial x_k} \right] - \frac{2}{3} \delta_{ij} \rho k, \quad (5)$$

and

$$q_{ti} = -\left(\frac{\mu_t c_p}{Pr_t} \right) \frac{\partial T}{\partial x_i}, \quad (6)$$

where, the eddy viscosity

$$\mu_t = c_\mu f_\mu (\rho k^2/\varepsilon). \quad (7)$$

The production term P_k is expressed in Cartesian coordinates as:

$$P_k = \tau_{tx} \frac{\partial u}{\partial x} + \tau_{ty} \left(\frac{\partial u}{\partial y} + \frac{\partial v}{\partial x} \right) + \tau_{tz} \frac{\partial v}{\partial y}, \quad (8)$$

Here, c_μ , $c_{\varepsilon 1}$, $c_{\varepsilon 2}$, σ_k and σ_ε are the model constants. f_μ , $f_{\varepsilon 1}$, $f_{\varepsilon 2}$ are the damping functions used to simulate the low-Reynolds number effects. For the Lam-Bremhorst

(k - ϵ) model, considered in the present analysis, they are as follows:

$$\begin{aligned} f_\mu &= [1 - \exp(-0.0165 \text{Re}_y)]^2 (1 + 20.5/\text{Re}_T) \\ f_{\epsilon 1} &= 1 + (0.05/f_\mu)^3 \\ f_{\epsilon 2} &= 1 - \exp(\text{Re}_T^2) \\ c_\mu &= 0.09; c_{\epsilon 1} = 1.44; c_{\epsilon 2} = 1.92; \sigma_k = 1.0 \text{ and } \sigma_\epsilon = 1.3. \end{aligned} \quad (9)$$

On solid wall, $k = 0$ and $\epsilon = (\mu/\rho)(\partial^2 k/\partial y^2)$.

It should be noted that, although the k - ϵ equations have been cast in compressible form, the modelling assumptions invoked here are essentially those for incompressible flow. The terms containing density fluctuation and pressure diffusion are neglected.

3. Numerical procedure

The unsteady equations (1) are marched in time using the explicit, second order accurate time-split, cell centred finite volume scheme based on MacCormack & Paulay (1972) until the steady state is achieved. The advantage of a time-split system is that the computation proceeds with larger time increments as the stability criteria are less stringent.

In order to maintain stability in the presence of steep gradient of flow variables and to suppress any odd-even decoupling in the numerical solution, artificial dissipation terms are added to the finite volume formulation. Artificial dissipation used here is similar to that derived by Jameson *et al* (1981), which is a blend of second and fourth order differences with coefficients that depend on local pressure gradients. Thus, the artificial dissipation is introduced in the present formulation by defining an effective numerical flux across the cell face as,

$$\mathbf{F}_{i+1/2,j}^{(AV)} = \mathbf{F}_{i+1/2,j} - \mathbf{D}_{i+1/2,j} \quad (10)$$

where, $\mathbf{F}_{i+1/2,j}$ is the physical flux and $\mathbf{D}_{i+1/2,j}$ is the dissipation term, given by

$$\begin{aligned} \mathbf{D}_{i+1/2,j} &= \sigma_{i+1/2,j} [\epsilon_{i+1/2,j}^{(2)} (\mathbf{U}_{i+1,j} - \mathbf{U}_{i,j}) \\ &\quad - \epsilon_{i+1/2,j}^{(4)} (\mathbf{U}_{i+2,j} - 3 \cdot \mathbf{U}_{i+1,j} + 3 \cdot \mathbf{U}_{i,j} - \mathbf{U}_{i-1,j})]. \end{aligned}$$

The scaling factor

$$\sigma_{i+1/2,j} = \max(\Omega_{i+1,j}/\Delta t, \Omega_{i,j}/\Delta t).$$

The coefficients $\epsilon^{(2)}$ and $\epsilon^{(4)}$ use the pressure as a sensor for shocks and stagnation points, and they are defined as

$$\begin{aligned} \epsilon_{i+1/2,j}^{(2)} &= k^{(2)} \min[\max(v_{i+1,j}, v_{i,j}), 0.5] \cdot \min(M_{i+1/2,j}/M_\infty, 1), \\ \epsilon_{i+1/2,j}^{(4)} &= \max[0, (k^{(4)} \min(M_{i+1/2,j}/M_\infty, 1) - \epsilon_{i+1/2,j}^{(2)})], \end{aligned}$$

$$v_{i,j} = \frac{|p_{i+1,j} - 2p_{i,j} + p_{i-1,j}|}{|p_{i+1,j}| + 2|p_{i,j}| + |p_{i-1,j}|},$$

where $k^{(2)}$ and $k^{(4)}$ are constants set at $1/4$ & $1/256$ respectively. To reduce the effect of artificial dissipation within the viscous region of flow, a function of local Mach number normalised with respect to the free-stream Mach number, the maximum value of which is limited to unity, is used here. Similar dissipation terms are defined in the j -direction.

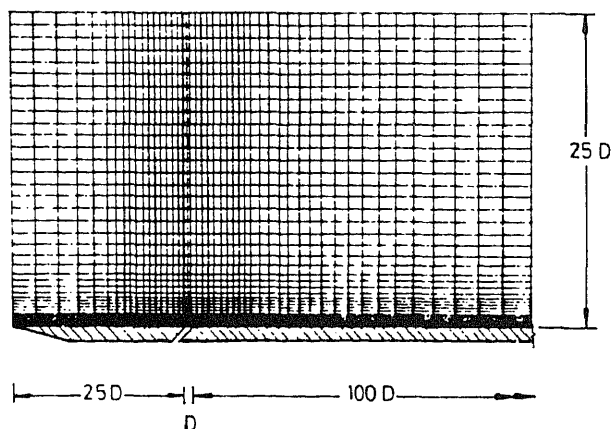


Figure 2. Computational grid.

4. Grid generation

The geometry consists of a flat plate with a slot of width $D = 6.35$ mm, represented in figure 2. An algebraically generated non-uniform Cartesian computational mesh, consisting of 60×50 grid points in x and y directions respectively, is used. For computational purposes, the geometry is divided into the following three regions: (i) the region near the slot where most of the interaction takes place; (ii) the region between the inlet and the beginning of the interaction zone; and (iii) the rest of the computational domain. The grid in the x -direction is generated judiciously by placing a number of fine uniform grid points in the interaction region, within the slot and stretching the grid towards the inlet and the exit. A fine exponentially stretched mesh spacing is employed in the region near the wall for resolving viscous layer and a coarse uniform mesh spacing is used in the outer region. The first mesh point above the plate surface is chosen such that the average y^+ is of the order of unity.

5. Boundary conditions

At the inlet, the total pressure, total temperature and the flow angle are specified; the static pressure is extrapolated from interior and hence the other variables at the inlet are updated for each time integration. The exit plane is positioned considerably far downstream of the injection ($100D$) so that a zero gradient condition is applied for all variables at this plane. On solid surfaces, no-slip conditions are imposed along with vanishing normal temperature gradient to simulate the adiabatic wall condition. The upper boundary of the computational domain is chosen sufficiently far from the plate and a 'slip-wall' type boundary condition seems to be appropriate. Thus, a slip condition is imposed by setting v -component of velocity and normal gradients of all other dependent variables to zero. The two-equation model needs specification of k and ϵ values at inlet. The constant values of k and ϵ are imposed at the inflow boundary based on the specified free-stream turbulence intensity and length scale as,

$$k_\alpha = 1.5 Tu_\alpha^2 V_\alpha^2,$$

$$\epsilon_\alpha = c_\mu^{3/4} k^{3/2} / l_\alpha.$$

The free-stream turbulence intensity is considered as 2–12%.

The experimental study of Pietrzyk *et al* (1989) indicates that a uniform mean velocity profile at the jet exit may be a better approximation of the actual film cooling conditions. Therefore, across the slot exit the following uniform conditions are applied.

$$\rho u = m_s \cos \alpha,$$

$$\rho v = m_s \sin \alpha,$$

$$T = T_s,$$

$$p = p_s,$$

$$k = 1.5 Tu_s^2 V_s^2,$$

$$\varepsilon = c_\mu^{3/4} k_s^{3/2} / 0.5 D, \quad (14)$$

where Tu_s is considered as 8% here.

6. Results and discussions

6.1 Model validation

Comparisons of the computed flow-field with experiment are presented in this section. All computations have been made on a PC-AT 486 based machine which has a CPU speed of 1 MFLOPS. The solutions are assumed to be converged when the logarithmic value of residuals have dropped by at least four orders of magnitude. Steady state has been achieved in 25,000 to 30,000 time steps.

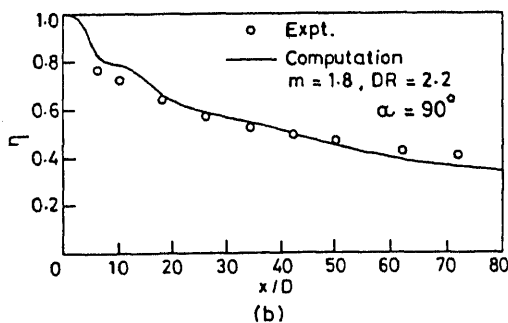
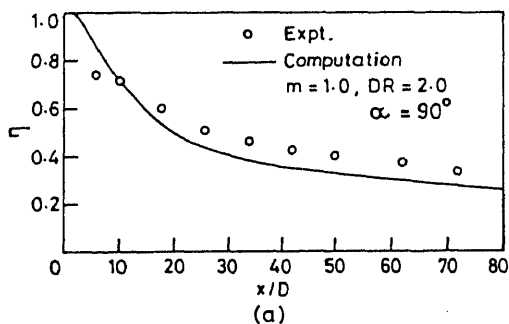


Figure 3. Streamwise variation of adiabatic film cooling effectiveness for two different blowing and density ratios. Experimental values from Papell (1960).

A majority of experiments, appearing in the open literature on film cooling for the gas turbine practice and consequent computational studies made to simulate those experiments, have considered low free-stream velocity. An exception is the work of Papell (1960) where the free-stream conditions were more representative of the gas turbine environment with $M_x = 0.5$ or above, $T_x = 790\text{ K}$ and $DR \approx 2.0$. For this reason, the data set provided in Papell (1960) is chosen for validation.

Figures 3a and b compare the predicted and measured film cooling effectiveness downstream of a normally injected coolant jet for different blowing ratios, $m = 1.0$ and 1.8 with $DR \approx 2.0$. Although the overall streamwise trend is correct, the film cooling effectiveness is under-predicted to some extent at $m = 1.0$ (figure 3a). At a relatively higher blowing ratio of $m = 1.8$ (figure 3b), predicted distribution of film cooling

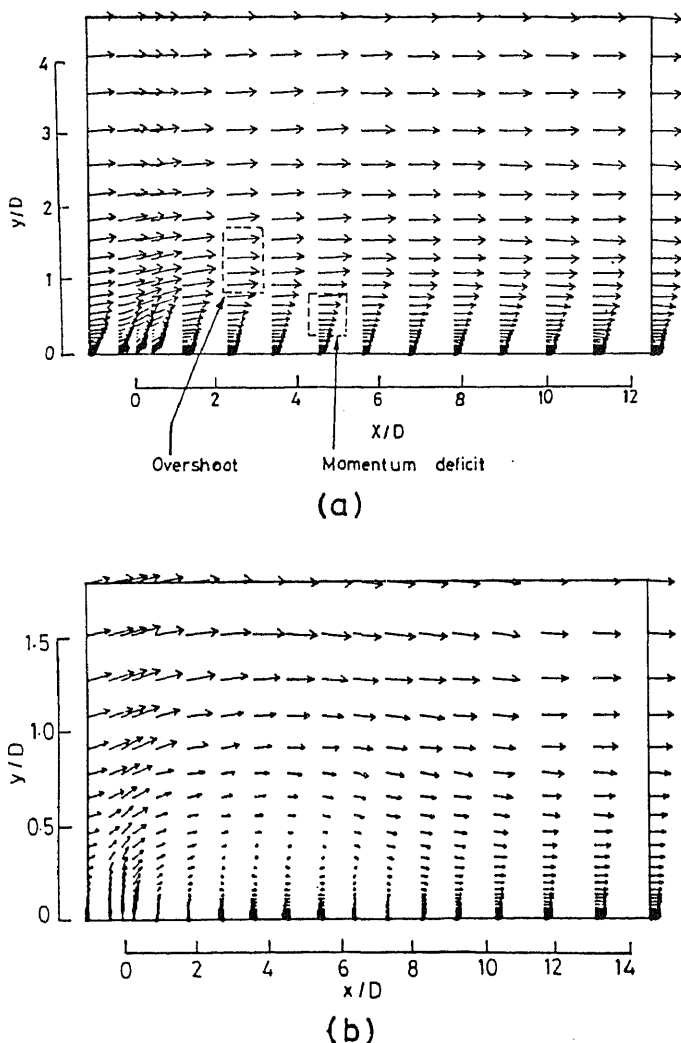


Figure 4. Computed velocity field (a) $m = 1.0$, $\alpha = 45^\circ$; (b) $m = 1.0$, $\alpha = 90^\circ$.

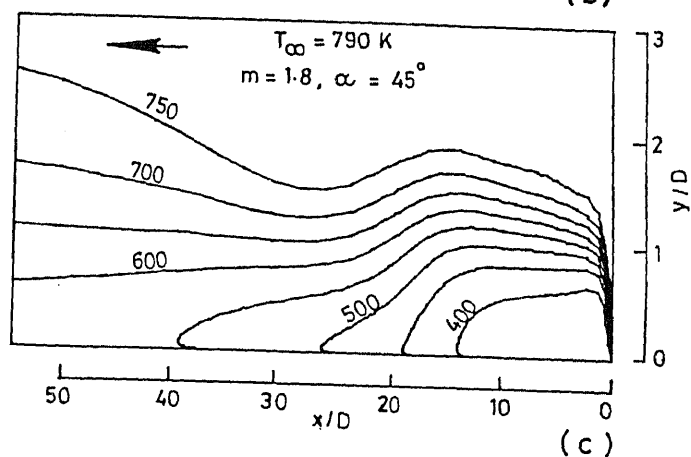
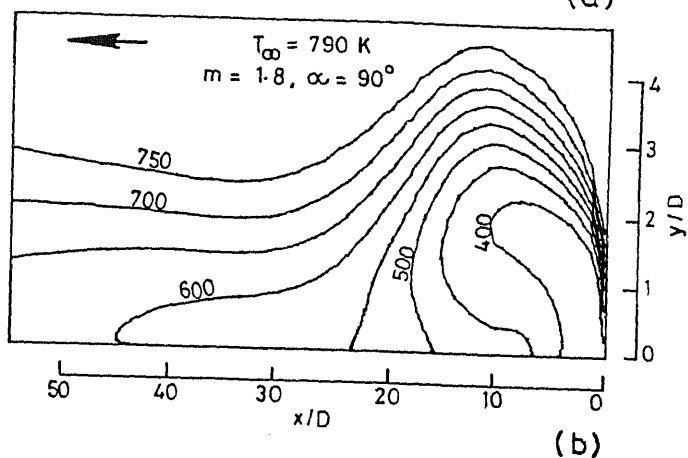
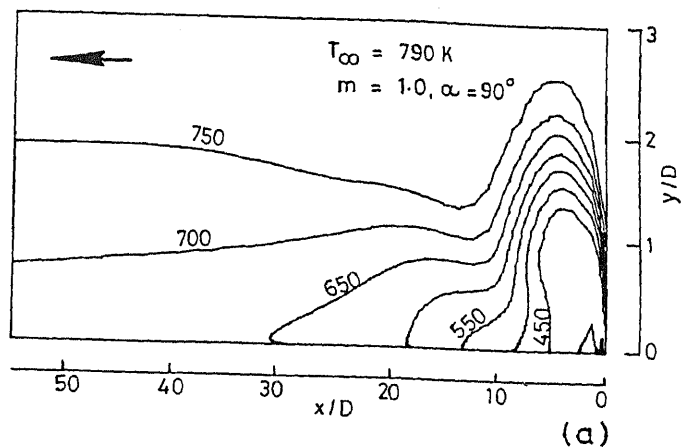


Figure 5. Computed temperature contours indicating effect of blowing rate and injection angle on the coolant jet trajectory due to different blowing ratios and injection angles.

effectiveness matches very well with experiment. The under-prediction of film cooling effectiveness for a relatively lower blowing rate may possibly be attributed to the over-predicted mixing by the turbulent model used in the present study. Another uncertainty is that the upstream boundary layer thickness and its character is not clearly specified in Papell (1960). Hence, for the present study, the length upstream of the slot is fixed as $x/D = 25$, considering the fact that the influence of upstream boundary layer is not very strong for slot injection (Seban 1960), though this may slightly affect the prediction. The free-stream turbulence considered here is 2% which gives the turbulent velocity profile near the leading edge. However, the overall magnitude and trend of effectiveness are reasonably well predicted by the present flow-solver. On this basis, the variation of flow-field and heat transfer phenomena with changing blowing rate, injection angle and free-stream turbulence are numerically investigated.

6.2 Numerical results

6.2a Effects of injection angles and blowing rates: The computed velocity field downstream of an injected jet at an angle of 45° for $m = 1.0$ and $DR = 2$ is shown in figure 4a. These velocity profiles are very similar to those measured by Pietrzyk *et al* (1989) and they clearly demonstrate a near-field wake region and a far-field relaxation region. In the wake region, the velocity profile exhibits two distinguishable zones, (i) the momentum deficit zone indicating the development of a shear layer between the outer edge of the injected jet and the crossflow, and (ii) right above the momentum deficit

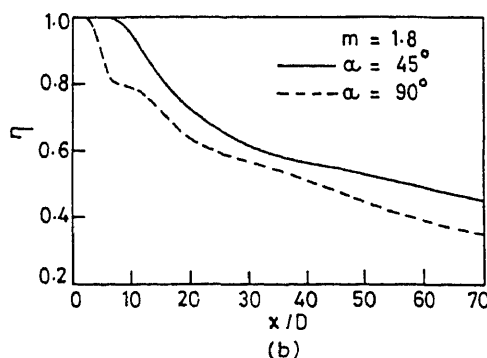
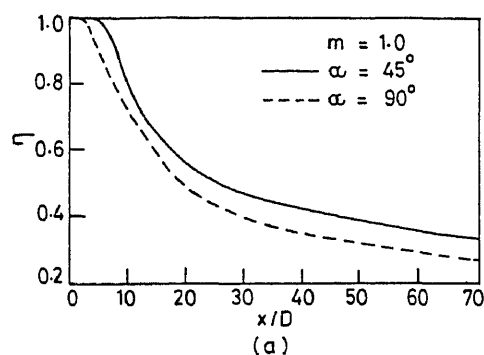


Figure 6. Computed stream-wise variation of adiabatic film cooling effectiveness demonstrating effects of blowing rate m and injection angle.

zone, a region with a slight velocity overshoot caused by the crossflow accelerating over the coolant jet. There is no flow separation downstream of the slot exit. For the same blowing rate, as α is increased to 90° , the aerodynamics of the jet in crossflow has remarkably changed (figure 4b). The jet penetrates more into the mainstream, bends over, reattaches to the surface forming a separation bubble and subsequently flows downstream approaching the boundary layer type flows. Injected coolant undergoes turbulent mixing with the mainstream while crossing over the bubble and at the same time, a small fraction of the injected coolant mass drifts into the recirculating bubble, inducing cooling action near the slot. This leads to high effectiveness very near the slot exit with downstream flow separation also for 2-D slot injection. But in 3-D hole injection, the region beneath the jet is ventilated by the mainstream and a low effectiveness occurs.

One important aspect for film cooling processes is the jet trajectory which depends mainly on the injection angle and the momentum ratio. A high trajectory implies deeper penetration of jet into the crossflow, development of a reversal zone, pronounced flow mixing and hence less effectiveness. On the other hand, a low trajectory results in an attached coolant layer, less mixing and high effectiveness. In the present study, temperature field is used to determine the trajectory of the coolant jet.

Figures 5a and b illustrate the temperature contours for jet-crossflow interaction with $DR \approx 2$ and $m = 1.0$ and 1.8 respectively, for $\alpha = 90^\circ$. As seen from the above figures, with the increase of blowing ratio, the coolant tends to retain its wall-jet character with strong penetration into the crossflow and thereby makes a high trajectory. To show the influence of injection angles on the trajectory, the temperature contours due to $\alpha = 45^\circ$ for $m = 1.8$ are presented in figure 5c. This clearly demonstrates that for the low angle of injection, the coolant hugs the surface to be protected, retaining its identity for a larger length. Thus, under this condition, high cooling effectiveness is expected even far-field. As the angle of injection increases, the coolant penetrates more into the crossflow resulting in more jet dilution which would cause a rapid decay of film-cooling effectiveness.

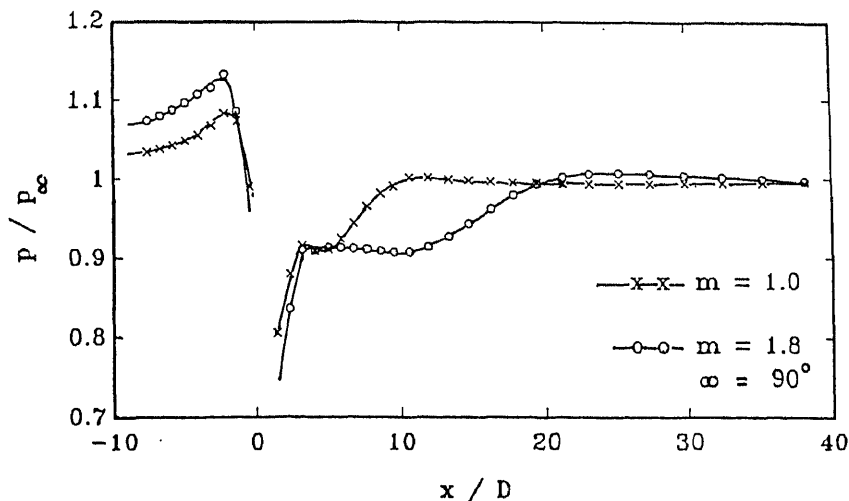


Figure 7. Computed streamwise variation of pressure ratio for different blowing rates.

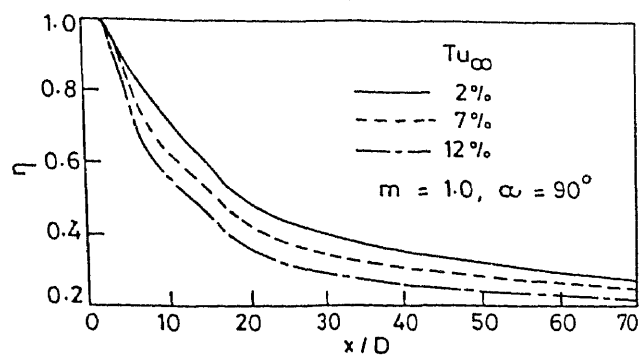
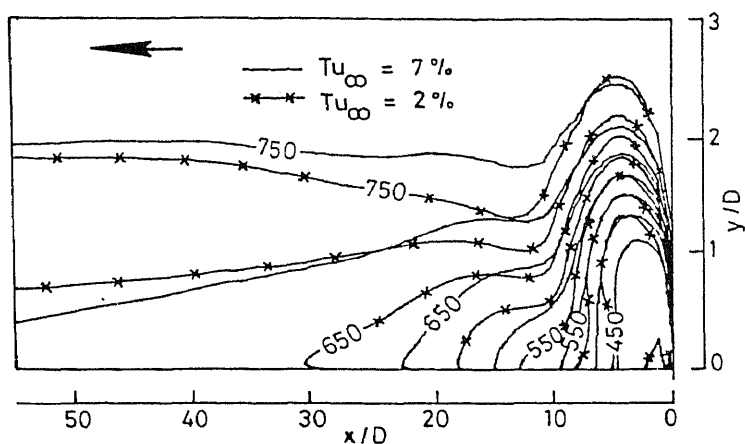
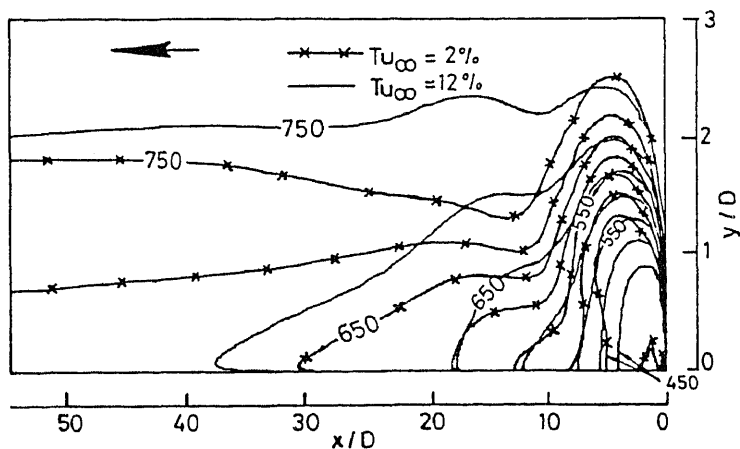


Figure 8. Streamwise variation of adiabatic film cooling effectiveness for different free-stream turbulence levels.



(a)



(b)

Figure 9. Computed temperature contours demonstrating effect of free-stream turbulence intensity Tu ($m = 1.0$, $\alpha = 90^\circ$).

Figures 6a and b indicate cooling effectiveness for different angles of injection and blowing ratios. They clearly demonstrate that the film cooling effectiveness increases in proportion to the injected mass flow rate both in the near and far field region for a low injection angle ($\alpha = 45^\circ$) but only in the far field region for a high injection angle ($\alpha = 90^\circ$). Increased α leads to a higher jet trajectory and also forms a separation bubble. The size of the separation bubble and turbulence mixing change with blowing ratios, strongly influencing near field effectiveness. Figure 5 also reveals that a shallow injection always improves cooling effectiveness because of attached coolant layer and low mixing.

The static pressure distribution along the surface is depicted in figure 7 for different blowing ratios. As seen, for $m = 1$, the ratio of p/p_x increases to a maximum of 1.08 at the upstream of jet, drops suddenly to a minimum of 0.8 at the slot trailing edge and subsequently recovers downstream. The upstream pressure rise increases with the increase of blowing ratios, indicating that the static pressure developed at the upstream corner of the slot is approximately equal to the injection total pressure. The flow separation downstream of the slot is pronounced with the enhancement of the blowing ratio, which is reflected by the clearly seen pressure plateau in figure 7, especially for $m = 1.8$.

6.2b Effects of free-stream turbulence: Figure 8 shows the distribution of η as the inlet free-stream turbulence (Tu_x) changes for $m = 1.0$ and $\alpha = 90^\circ$. It clearly demonstrates that as Tu_x increases, η decreases due to the pronounced mixing of the injected coolant jet and the crossflow. Effectiveness decreases almost by 25% as Tu_x is increased from 2% to 12%. Temperature fields, as shown in figures 9a and b, also illustrate the change in mixing characteristics and jet trajectory as Tu_x changes. The near-field mixing is more for high Tu_x resulting in a thick downstream thermal layer.

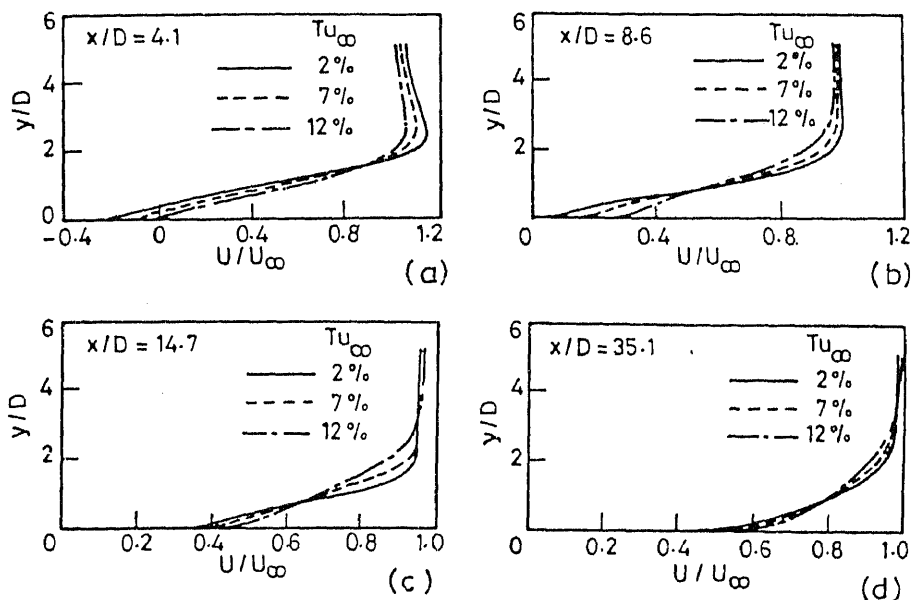


Figure 10. Effect of free-stream turbulence on mean velocity profiles ($m = 1.0$, $\alpha = 90^\circ$) at different values of x/D .

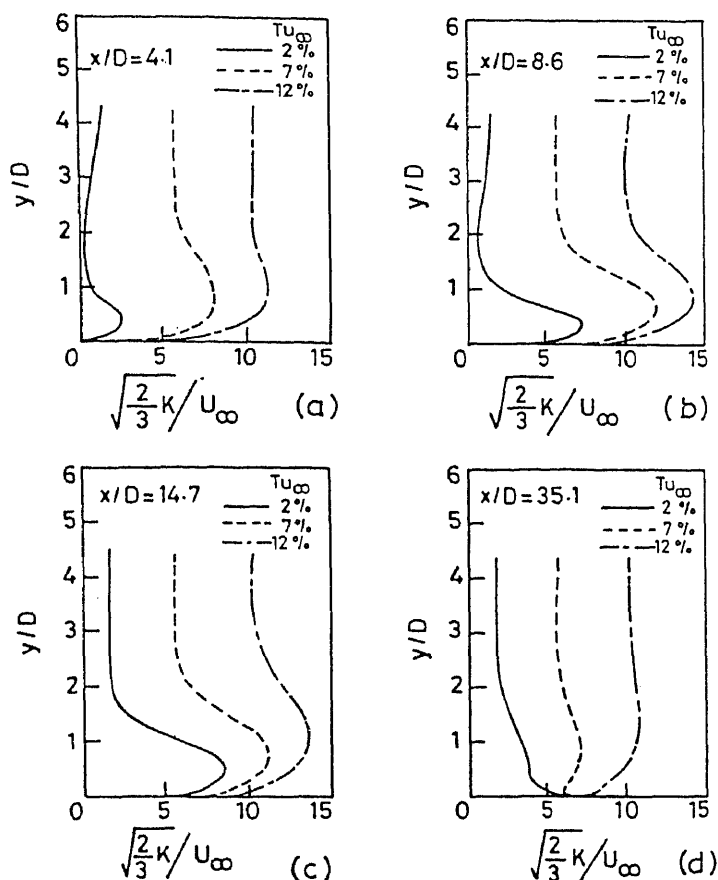
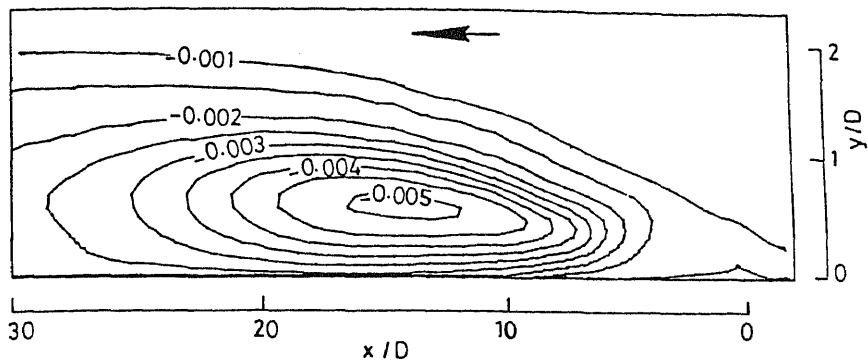


Figure 11. Effect of free-stream turbulence on turbulent kinetic energy profiles ($m = 1.0$, $\alpha = 90^\circ$) at different x/D values.

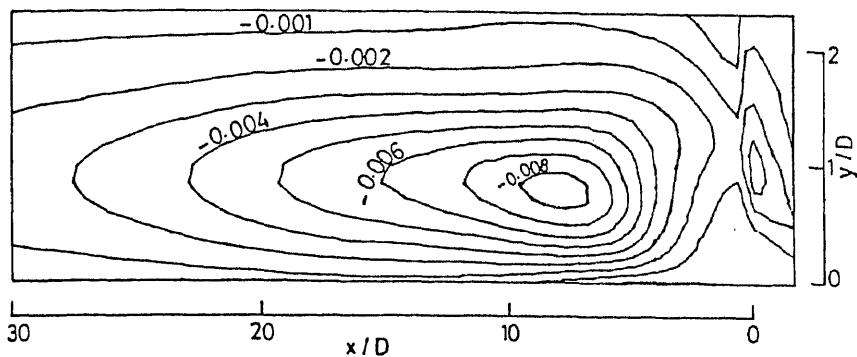
The mean velocity profiles and the distribution of local turbulence levels ($2/3^{1/2} k/V_\alpha$) are presented in figures 10 and 11 respectively for different spanwise locations for the same blowing rate and injection angle, $m = 1.0$; $\alpha = 90^\circ$. Figure 10a shows a separation region and velocity overshoot for $Tu_\alpha = 2\%$ indicating the local crossflow acceleration over the coolant jet and a corresponding drop of turbulence kinetic energy at $y/D \simeq 2$ as in figure 11a. With the enhancement of inlet turbulence intensity both the separation region and velocity overshoot decreases due to the enhanced mixing. At all other stations near the wall the gradient of velocity profiles decreases with increase of Tu_α . Highest turbulence occurs in the interaction zones ($x/D < 20$) due to shear layer that develops between the coolant jet and the crossflow and is seen to increase with increase of Tu_α . The trends of distributions of mean velocity profiles and local turbulence levels are similar to those observed by Seban (1960).

The computed normalised turbulent shear stress ($\overline{u'v'}/V_\alpha^2$) for $m = 1.0$ and $\alpha = 90^\circ$ are presented in figure 12 for different free-stream turbulence level. As seen, the magnitude of maximum value of the shear stress increases and its location is also shifted towards the slot as Tu_α increases because of increased mixing.

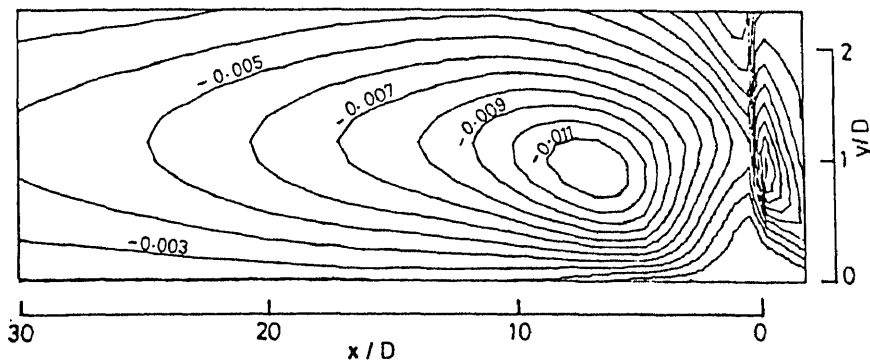
$$m = 1.0, \alpha = 90^\circ$$



(a)



(b)



(c)

Figure 12. Predicted normalised turbulent shear stress contours for different free-stream turbulence levels $Tu_\infty = 2\%$ (a), $= 7\%$ (b), $= 12\%$ (c).

6.2c Turbulence quantities: The computed results presented in this sub-section aim to highlight the complex turbulent field created by the jet-crossflow interactions for changing blowing ratios and injection angles.

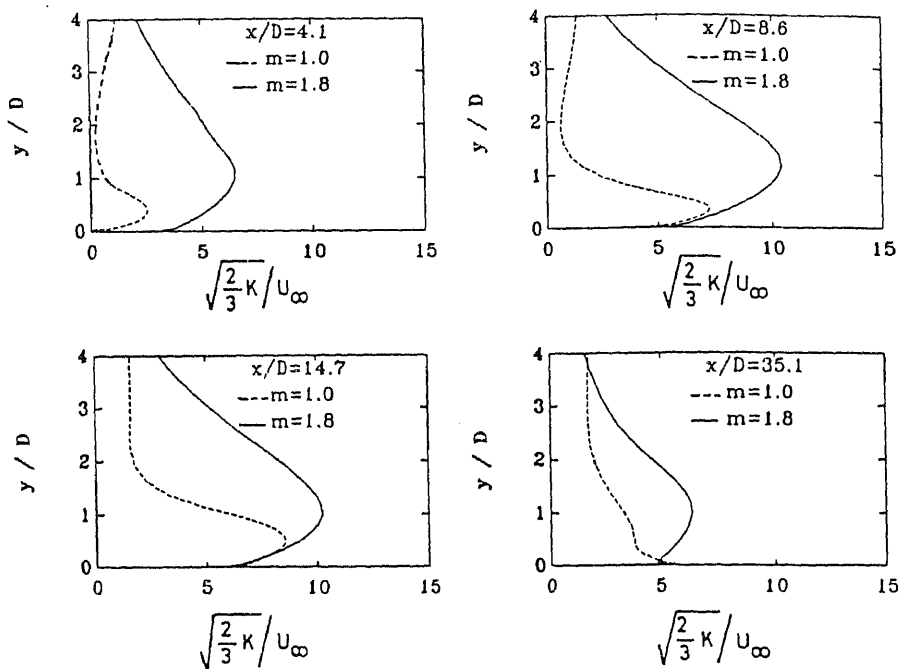


Figure 13. Predicted turbulent kinetic energy profiles at different spanwise locations and varying blowing ratios for an injection angle, $\alpha = 90^\circ$.

Figure 13 shows local turbulent kinetic energy distributions at different spanwise locations downstream of the slot exit for an angle of injection, $\alpha = 90^\circ$ with varying blowing ratios, $m = 1.0$ and $m = 1.8$. The same is represented in figure 14 for a shallow injection, $\alpha = 45^\circ$. The corresponding velocity profiles at the same axial locations are presented in figures 15 and 16 respectively. They clearly explain that a shallow injection produces less generation and a gradual diffusion of turbulent kinetic energy because of an attached coolant layer and a slower mixing rate. Thus, injection at low angles would result in a high film cooling effectiveness. Figure 14 also demonstrates that except very near the injection, the predicted maximum level of turbulent kinetic energy has not increased, but rather has dropped at the axial location of $x/D = 14.7$, as the blowing ratio is increased to 1.8. The corresponding velocity profiles (figure 16) reveal that for shallow injections, the momentum deficit between the injected jet and the crossflow, which is the main source of turbulence generation for these kind of problems, has dropped with an increase of blowing ratio. But, for a high injection angle ($\alpha = 90^\circ$), the maximum level of turbulence is increased and the peak in turbulent kinetic energy profiles (figure 13) is shifted outwards with blowing ratios because of more jet penetration and flow mixing. Here also, the peak in turbulent kinetic energy profiles can be directly linked with the maximum momentum deficit in velocity profiles (figure 16) which demonstrate a drastic change in the relaxation behaviour of velocity and length of flow separation as blowing ratio increases. As seen in figure 14, the flow has not relaxed to turbulent boundary layer type flow even far downstream, $x/D = 35$, for $m = 1.8$ with $\alpha = 90^\circ$.

As expected, because of less penetration and slow mixing of the coolant jet at a low injection angle, the maximum level of normalised shear stress has dropped to -0.0025

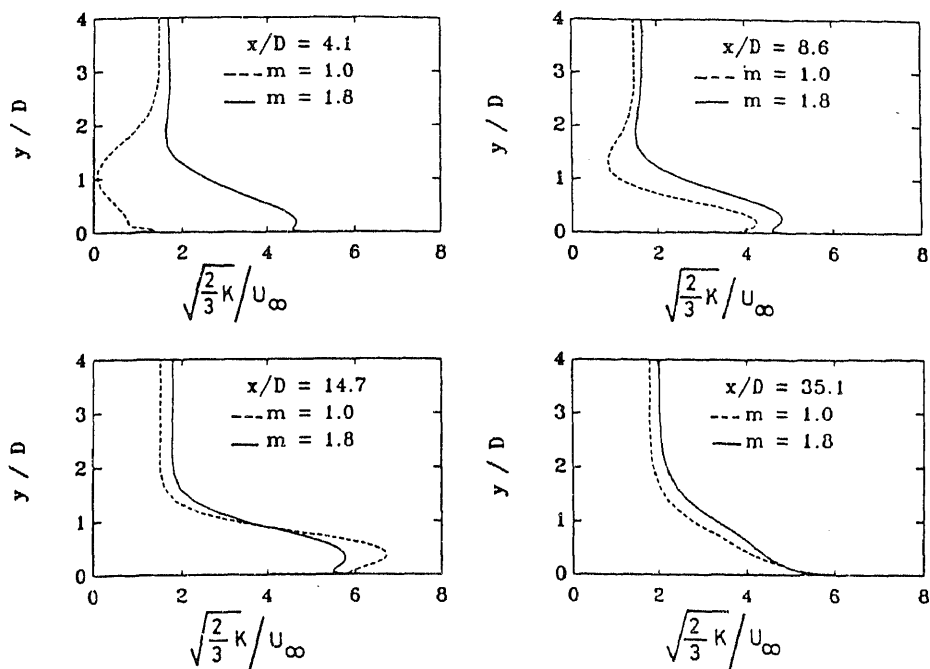


Figure 14. Predicted turbulent kinetic energy profiles at different spanwise locations for a shallow injection angle, $\alpha = 45^\circ$.

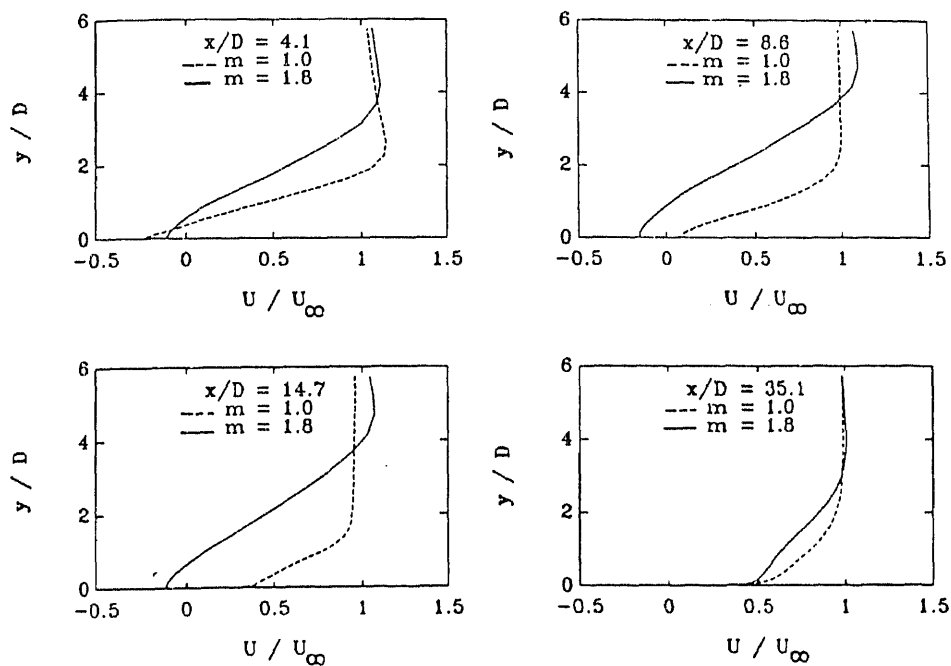


Figure 15. Predicted velocity profiles at different spanwise locations and varying blowing ratios for an injection angle, $\alpha = 90^\circ$.

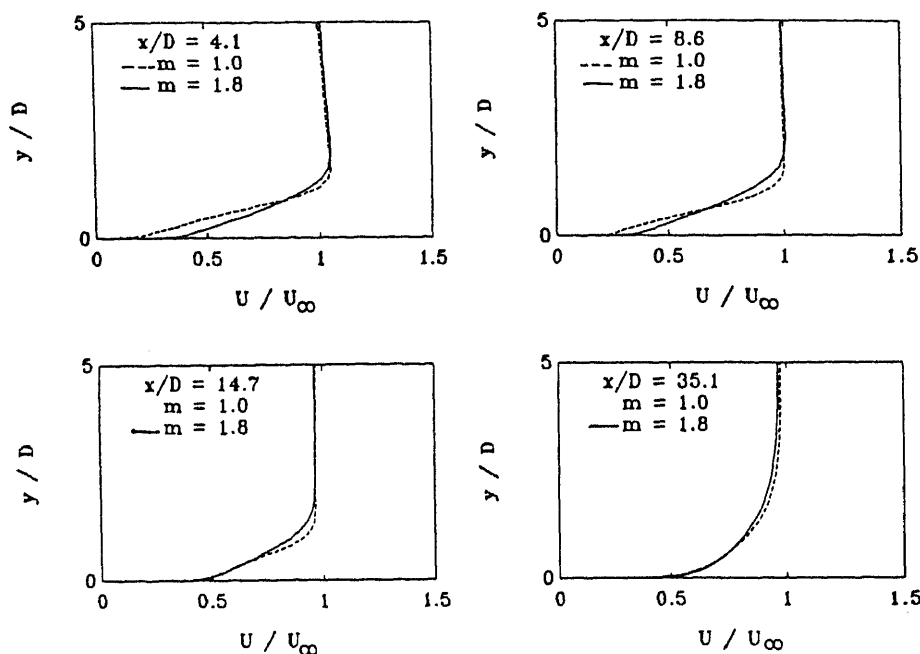


Figure 16. Predicted velocity profiles at different spanwise locations and varying blowing ratios for a shallow injection angle, $\alpha = 45^\circ$.

from -0.005 for $m = 1.0$. For a high blowing rate ($m = 1.8$), the maximum value of computed shear stress decreases further to -0.002 (figure 17) because of greater uniformity in velocity profiles as already explained.

7. Conclusions

A Navier-Stokes procedure coupled with compressible low-Reynolds number form of the $k-\epsilon$ turbulence model in an explicit finite volume treatment is used to simulate

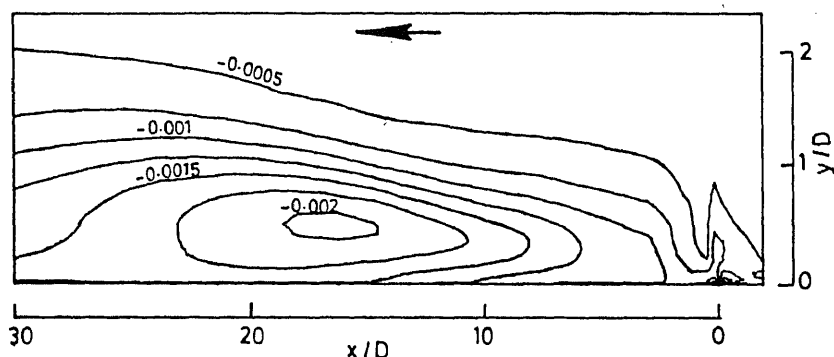


Figure 17. Computed normalised turbulent shear stress for $m = 1.8$, and $\alpha = 45^\circ$.

jet-crossflow interactions with changing free-stream turbulence levels, blowing ratios and injection angles for film cooling applications. The present analysis is limited to a two-dimensional simulation where free-stream conditions are similar to the gas turbine practice.

The following important points emerge from the present investigation.

- (i) The injection angle and blowing ratio strongly influence the aerodynamics of a coolant jet in a crossflow and thus downstream adiabatic film cooling effectiveness. For large injection angles, the coolant penetrates more into the crossflow resulting in greater turbulence generation, followed by enhanced mixing and a rapid turbulent diffusion which leads to a faster decay of film cooling effectiveness in the near field region. A flow reversal also occurs just downstream of the slot exit. For shallow injection angles, the coolant hugs the surface with low turbulence generation and slow mixing rate, retaining its identity for a larger length. This results in high cooling effectiveness even in the far field region. For an increase in blowing rate, the overall downstream film cooling effectiveness improves due to the thickened thermal layer and more available cold fluid.
- (ii) The free-stream turbulence affects the temperature distributions downstream of a coolant jet significantly by changing the mixing characteristics, local turbulence levels, mean velocity profiles and the jet trajectory. Film cooling effectiveness drops by almost 25% as inlet free-stream turbulence increases from 2 to 12%.
- (iii) Shallow injection changes the computed turbulent field indicating less generation and a gradual diffusion of turbulent kinetic energy. At a relatively low injection angle, an increase of blowing rate reduces the momentum deficit and in turn the maximum turbulence level which confirms that the shear layer between the crossflow and the coolant jet is the main source of turbulence generation for this kind of problem.

List of symbols

D	coolant injection slot width;
DR	density ratio = ρ_s/ρ_x ;
e	total energy per unit mass;
F, G	flux vectors;
l	turbulence length scale;
M	Mach number;
m	blowing ratio = $(\rho V)_s/(\rho V)_x$;
m_s	coolant mass flow rate;
Pr, Pr_t	Prandtl numbers;
p	pressure;
q_i	Cartesian components of heat flux vector;
R	gas constant;
Re	Reynolds number;
\bar{S}	surface normal to a side of the cell;
T	temperature;
T_{aw}	adiabatic wall temperature;
T_r	mainstream recovery temperature;
T_{rs}	recovery temperature of coolant;
Δt	time step;

Tu	turbulence intensity
\mathbf{U}	solution vector;
u_τ	friction speed $= (\tau_w/\rho)^{1/2}$;
u, v	Cartesian velocity components;
V	magnitude of velocity vector;
x, y	Cartesian coordinates (defined in figure 1);
y^+	law-of-the-wall coordinate $= y [(\rho/\mu)(\delta u/\delta y)]_w^{1/2}$;
α	injection angle of the coolant jet;
δ_{ij}	Kronecker delta;
η	adiabatic film effectiveness $= (T_{aw} - T_r)/(T_{rs} - T_r)$;
μ, μ_t	molecular and turbulent viscosities;
ρ	density;
τ_{ij}	Cartesian components of stress tensor;
Ω	cell volume.

Superscripts

,	fluctuating quantity in density-weighted time averaging;
\sim	density-weighted time-averaged quantity.

Subscripts

i, j	logical cell indices in space;
s	coolant slot exit conditions;
t	turbulent;
w	wall condition;
α	mainstream conditions at the inlet plane.

References

- Andreopoulos J, Rodi W 1984 Experimental investigation of jets in a crossflow. *J. Fluid Mech.* 138: 93–127
- Brown A, Minty A G 1975 The effects of mainstream turbulence intensity and pressure gradient on film cooling effectiveness for cold air injection slits of various ratios. ASME Paper No. 75-WA/HT-17
- Cebeci T, Smith A M O 1974 *Analysis of turbulent boundary layers* (New York, San Francisco, London: Academic Press)
- Favre A 1965 Equations des Gaz Turbulents Compressible: I, Formes Generales, *J. Mec.* 4: 361–390
- Foster N W, Lampard D 1980 The flow and film cooling effectiveness following injection through a row of holes. *ASME, J. Eng. Power* 102: 584–588
- Goldstein R J 1971 Film cooling. *Advances in heat transfer* (New York and London: Academic Press) vol. 7, pp. 321–379
- Jameson A, Schmidt W, Turkel E 1981 Numerical solutions of the Euler equations by finite volume methods using Runge–Kutta time-stepping schemes. AIAA Paper 81–1259
- Jumper G W, Elrod W C, Rivir R B 1991 Film cooling effectiveness in high-turbulence flow. *ASME, J. Turbomach.* 113: 479–483
- Ko S, Liu D 1980 Experimental investigations of effectiveness, heat transfer coefficient and turbulence of film cooling. *AIAA J.* 18: 907–913

- Kadotani K, Goldstein R J 1979 On the nature of jets entering a turbulent flow, Part A - Jet-mainstream interaction. *J. Eng. Power* 101: 459-465
- Kunz R, Lakshminarayana B 1991 Stability of explicit 3-D Navier-Stokes/ k - ϵ procedures in complex internal flow calculations. *AIAA Paper* 91-0018, pp. 1-14
- Lam C K G, Bremhorst K 1981 A modified form of the k - ϵ model for predicting wall turbulence. *ASME J. Fluids Eng.* 103: 456-460
- MacCormack R W, Paullay A J 1972 Computational efficiency achieved by time splitting of finite difference operators. *AIAA Paper* 72-154
- Papell S S 1960 Effect on gaseous film cooling injection through angled slots and normal holes. *NASA TN-D-299*
- Petersen D R, Eckert E R G, Goldstein R J 1977 Film cooling with large density differences between the mainstream and secondary fluid measured by heat-mass transfer analogy. *ASME, J. Heat Transfer* 99: 620-627
- Pietrzyk J R, Bogard D G, Crawford M E 1989 Hydrodynamics measurements of jet in crossflow for gas turbine film cooling applications. *ASME, J. Turbomach.* 111: 139-145
- Seban R A 1960 Effects of initial boundary-layer thickness on a tangential injection system. *ASME J. Heat Transfer* 82: 392-393
- Sinha A K, Bogard D G, Crawford M E 1990 Film cooling effectiveness of a single row of holes with variable density ratio. *ASME Paper No.* 90-GT-43

1

Development of picosecond time resolution optical and X-ray streak cameras

V N RAI, M SHUKLA, H C PANT and D D BHAWALKAR

Centre for Advanced Technology, Indore 452013, India

MS received 23 September 1994; revised 9 January 1995

Abstract. We describe the development of an optical and an X-ray streak camera with picosecond time resolution. The entire peripheral electronics and testing systems have been developed indigenously. Both the streak cameras provide ~ 15 mm/1 ns streak rate with a sweep voltage of ~ 1 kV amplitude and rise time of 1 ns. The time and spatial resolution of the optical streak camera have been found to be ~ 17 ps and $100\text{ }\mu\text{m}$ respectively. The sweep pulse generator developed for this purpose provides a step pulse of rise time ≤ 1 ns and amplitude ~ 2 kV. The laser diode used for testing the optical streak camera provides multiple pulsation when the pump current is increased beyond a critical threshold.

Keywords. Optical and X-ray streak cameras; picosecond time resolution; multiple pulsation.

1. Introduction

A streak camera is one of the most versatile instruments (Schelev *et al* 1972; Bradley *et al* 1980; Campillo & Shapiro 1983; Kinoshita *et al* 1983; Stradling *et al* 1983; Tsuchiya 1983; Dashevsky *et al* 1988) used today for high speed photometry in the field of physics, chemistry, biology and nonlinear optics. Conventional optical detectors such as biplanar photodiode and PIN silicon photodiode used with the fastest available oscilloscope provide a time resolution of 10^{-10} s. Various other techniques generally used for investigating very fast events are the autocorrelation method, second harmonic generation, two-photon fluorescence and four-photon parametric mixing. However, certain amount of errors (inaccuracies) are always associated with these measurements. Amongst all the available methods, streak photography is considered to be the best for recording ultrafast optical phenomenon with an excellent time resolution (< 1 ps). It can provide a temporal profile of any optical event directly even in a single-shot operation. In addition to the time duration, rise time as well as shape of the optical pulse also can be recorded along with intensity modulation (fine structure) if present, during the optical event. However, measurements will be limited by the time resolution of the streak camera. Streak cameras with nanosecond time resolution were

built long ago, but temporal resolutions of the order of picoseconds or sub-picoseconds has been achieved only a few years ago. A new streak camera with femtosecond time resolution has also been reported (Kinoshita *et al* 1987). Highly sensitive streak cameras with picosecond time resolution are now commercially available which are capable of recording any phenomenon in the spectral range extending from near infrared to ultraviolet and soft X-ray (100 eV–10 keV) regions with the help of suitable photocathode attachment (Schelev *et al* 1972; Bradley *et al* 1980; Campillo & Shapiro 1983; Kinoshita *et al* 1983; Stradling *et al* 1983; Tsuchiya 1983; Dashevsky *et al* 1988). In fact, the streak camera can functionally be referred to as a > 300 GHz band width optical oscilloscope. However, the streak camera possesses many more special features and scores over an ordinary oscilloscope, for example, it can provide three-dimensional information such as spatially time-resolved as well as time-resolved spectroscopic intensity profiles (Campillo & Shapiro 1983; Tsuchiya 1983). Either a photographic system or a digital image memory is used to store and analyse three-dimensional streak images. The latter provides almost real-time measurements of the events.

The present paper reports on the development of a picosecond resolution optical (Rai *et al* 1994b) and X-ray streak cameras (Rai *et al* 1994c) intended for studying fast processes in IR, visible, UV and soft X-ray wavelength regions. The design of the instrument, its peripheral electronics, radiation sources for testing the cameras as well as test results are presented. Section 2 describes both types of streak tubes used in these experiments. Section 3 reports the development of related electronics to drive the streak camera. Section 4 provides information about various kinds of optical sources used for testing the streak cameras. Test results and discussions are presented in § 5, whereas conclusions are given in § 6.

2. Streak tubes

2.1 Optical streak tube

We have used the optical streak and image intensifier tubes manufactured by General Physics Institute, Moscow for building our optical streak camera (figure 1). It has an S1 type photo cathode (Ag–O–Cs) deposited on a flat glass plate of 5 mm diameter and is sensitive in the spectral range 450–1150 nm with peak response at 800 nm. An accelerating grid placed at distance of 1 mm from the photocathode has 60% transmission. The grid is used for gating as well as for reducing the time resolution limit of the tube to ≤ 1 ps. The tube has a focussing electrode which focusses the photo electrons on to the phosphor screen and also decides the spatial resolution of the tube. The photo cathode, accelerating grid and focussing electrodes require biasing voltages of -15 , -13 and -12 to -13 kV respectively. It has an anode which acts as an aperture in the tube and remains at the ground potential. There are two pairs of deflector plates out of which one pair is used to sweep the photo electrons on the screen whereas the other pair is used to fly back the photo electrons to the initial position without streaking back on the screen to the position from where sweeping started. The phosphor screen of the camera is made of aluminized P11 material which has peak response at 460 nm (blue region) and is coupled to the output face of an optical fibre plate. The tube is of the sealed-off type with a glass window on the photocathode side. An image intensifier tube

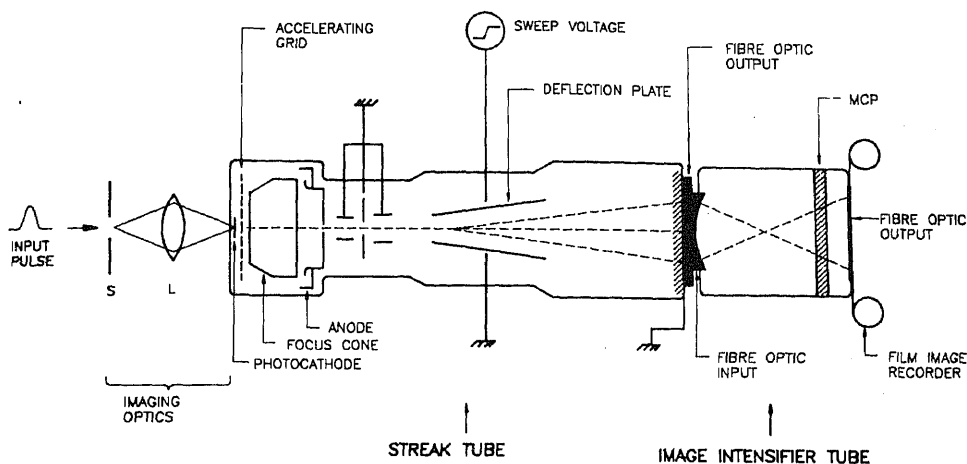


Figure 1. Schematic diagram of streak camera.

is coupled to the streak tube as shown in figure 1. The image intensifier tube consists of a photocathode, a phosphor screen and a multichannel plate (MCP) to multiply the photoelectrons. This system is used to enhance the intensity of the image obtained at the phosphor screen of the streak tube. It has a maximum gain of $\sim 10^4$ divided into 5 steps. Finally, the image on the screen of the intensifier is recorded by using a contact photograph or a charge coupled device (CCD) camera.

2.2 X-ray streak tube

The input end of the X-ray streak tube (also obtained from the Institute of General Physics, Moscow) is attached to a metallic flange, which has a clearance for the photocathode at the centre and a number of small holes around it to evacuate the tube. Generally, an X-ray streak tube has a demountable photocathode and is evacuated directly during experiments. The rest of the parts of the tube are similar to that of optical streak tube. The X-ray sensitive photocathode consists of a 300 \AA thick gold film deposited on a 1000 \AA thick parylene or nitrocellulose film which is fixed on the cathode disc having a $100 \mu\text{m} \times 9 \text{ mm}$ slit. This photocathode is sensitive to soft X-rays ranging from 100 eV to 10 keV as well as to UV radiation. The slit image produced by the incident soft X-rays is focussed on to the phosphor screen by the electron lens made by the combination of accelerating mesh, the focussing electrode and the anode. The photoelectrons are streaked on the 40 mm diameter screen by means of the vertical deflection electrodes. The intensity of the image is then enhanced by the image intensifier tube and the output image is recorded using a camera.

3. Electronics

The peripheral electronics of the streak camera contain various kinds of fast and high- as well as low-voltage pulser circuits. The main high voltage pulse requirements for the operation of streak camera are (i) a high voltage ($\sim 1 \text{ kV}$) linear ramp of dual polarity

for full deflection of the image across a 25 mm image intensifier screen, (ii) a short rectangular pulse of variable time duration (100 ns – 2 μ s) and amplitude (max 2 kV) to gate the accelerating grid as well as to increase the time resolution of the camera, (iii) a trigger pulse generator, which triggers the sweep circuit. This generator is externally triggered by a fast photo diode signal, (iv) high voltage DC power supplies to bias various electrodes of streak and intensifier tubes such as photocathode, accelerating grid and focus electrode as well as to drive the sweep and gate pulse circuits.

3.1 Sweep pulse circuit

A picosecond time resolution is obtained in a streak camera by streaking the photo-electrons with a streak velocity $\sim 10^{10}$ cm/s. This indicates the requirement of a sweep voltage having a rise time ≤ 1 ns. Rise time obtained using an RLC integrated circuit is slower than this requirement. In order to prevent image distortion and improve camera dynamics as well as spatial resolution, two symmetrical well-balanced sweep pulses are required which in fact makes the sweep pulse faster in comparison to the single sweep of same rise time. The nonlinearity in the sweep pulse and, as a result, the sweep speed are improved by increasing the amplitude of the sweep pulse beyond the required value (overpulsing). Many circuits have been reported for generating a sweep pulse for the streak camera. These utilize various kinds of fast switching elements such as krytron (Bradley *et al* 1972), power-beam microwave triode (Alcock *et al* 1970), laser triggered spark gap (Alcock *et al* 1970; Schelev *et al* 1972) as well as avalanche transistors (Cunin *et al* 1980; Baker 1991). The transistorized circuits available to date provide rise times of 1.5 to 2 ns depending on whether avalanche transistors are used in a series stack mode or in a Marx bank configuration. Two pulser circuits (Rai *et al* 1994a; Rai & Shukla 1994) were developed in our laboratory. One of the pulser circuits was developed (Rai & Shukla 1994) by using a stack of 15 avalanche transistors, 2N 5551, connected in series as a single switching element which is shown in figure 2. A transmission line of 75(50) Ω impedance and ~ 1.5 m in length was charged to 4.5 kV and discharged through a 75(50) Ω load. We obtained a square step pulse of ~ 2 kV across a 75(50) Ω resistor instead of ~ 2.25 kV as a result of a small voltage drop across the

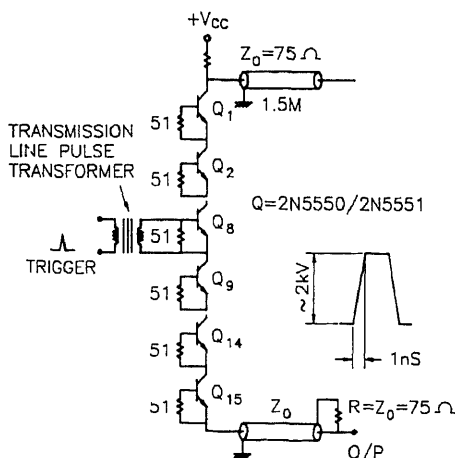


Figure 2. Diagram of sweep pulse generator circuit.

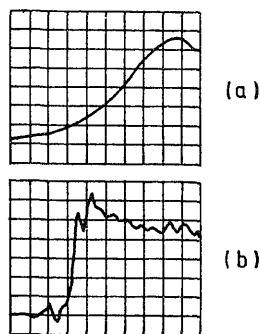


Figure 3. Oscillograms of sweep pulses recorded on a Tektronix model 7104 oscilloscope (1 GHz) having vertical plug in model 7A29. (a) Horizontal – 200 ps/div., vertical – 400 V/div.; (b) horizontal – 2 ns/div., vertical – 400 V/div.

transistors due to its finite resistance during the breakdown. This circuit provides a square pulse of rise time 800 ps (10–90%) as shown in figure 3 when recorded on a Tektronix oscilloscope (model 7104) having a vertical plug in model 7A 29 which had a combined bandwidth of 1 GHz. To achieve rise times better than 1 ns, with a series combination of transistors; reduction in excess leads and proper soldering are needed to reduce the extra inductance in the circuit. A carefully designed printed circuit board was prepared for this purpose. This circuit was triggered through a wide band pulse transformer which consists of a small toroidal ferrite core with five turns of 50 Ω coaxial cable, where the cable shield acts as a primary and the central conductor as a secondary. Triggering of any transistor in the stack switches the circuit, but better stability was obtained when a middle transistor of the stack was triggered. Triggering pulse was sharpened using a 20 PF capacitor and 50 Ω resistance at the output of the transmission line pulse transformer in a differentiation mode. Small pulse width of the trigger pulse effectively protects the base emitter junction of the transistor being triggered and as a result enhances the life time of the circuit. Many earlier reported circuits (Cunin *et al* 1980; Baker 1991) use a ballast resistance between emitter and collector of each transistor to avoid self-triggering in the circuits. We, however did not observe any self-triggering in our circuits even without the ballast resistances. Nevertheless, a properly designed ballast circuit may decrease the high jitter (< 500 ps) observed in this case to < 100 ps and may keep the string from self-triggering over a wide temperature range.

A simple technique was used for generating two symmetrically opposite polarity pulses from a single pulse of either polarity. This arrangement is shown in figure 4 which had two similar length (2 m) 75(50) Ω impedance cables connected in parallel at the output of the pulser circuit and terminated with 75(50) Ω resistances. Towards the

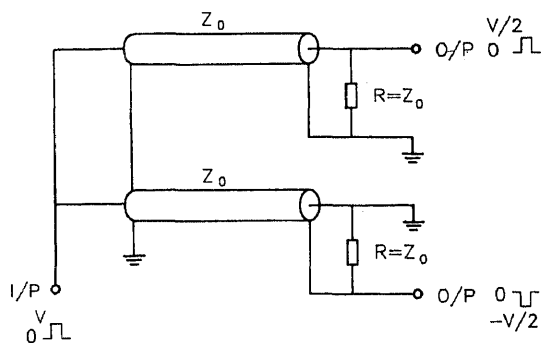


Figure 4. Arrangement to obtain positive and negative polarity pulses from a pulse of either polarity.

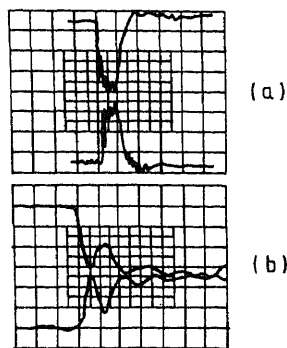


Figure 5. Oscillograms of two opposite polarity pulses recorded on a Tektronix model 7348 oscilloscope (400 MHz) having vertical plug in model 7A19. (a) 10 ns/small div., vertical – 160 V/small div.; (b) 1 ns/small div., vertical – 160 V/small div.

termination end, the first cable was grounded at the shield and the output was taken from the central pin which provided a similar polarity pulse, like an input pulse but around one half in amplitude. The second cable has its central pin grounded at the termination end and the output was taken from the shield of the cable (figure 4) which provided an opposite polarity pulse in comparison to the input pulse and similar in amplitude as was obtained from the first cable. Care must be taken to isolate the shield of the latter cable with the normal ground at the termination end, otherwise the rising edge of the pulse becomes distorted. Figure 5 shows the two symmetrically opposite polarity pulses of rise time better than 1 ns. In the case of application of these pulses in the streak camera only the rise time, amplitude and a small delay are important parameters of the pulser circuit. These opposite polarity pulses were used to operate the streak camera. However, it was noticed that the rise time of the pulse was modified to ~ 2.5 ns due to capacitive loading from the deflection plate. The superimposed fluctuations observed on the pulses in figures 3 and 5 appear to be due to the unwanted signals travelling on the outside of the outer conductor. These fluctuations can be removed or minimised by placing the circuit in a properly shielded box or by wrapping the coaxial cable on a large ferrite core. The signal on the outside of the outer conductor will travel at a slower velocity due to the high μ value of the ferrite. For the slow streak velocity, an RLC integrator was used at the output of the circuit.

3.2 Gate pulse circuit

It has been reported earlier (Schelev *et al* 1972) that the resolution of the streak camera strongly depends on the electric field between photocathode and grid. Normally 1–2 kV is sufficient but for better time resolution a higher voltage is required on the grid beyond the normal value, which is provided in the form of a pulse to avoid undesirable effects (Schelev *et al* 1972). Sometimes a gating is needed to avoid the background noise also. For this purpose, a gate pulse of positive polarity is required, having amplitude 1–2 kV and time duration ~ 100 ns, much higher than the sweep voltage time (~ 1 –20 ns) but synchronized with it. A pulse of this time duration (100 ns) can be obtained by using the earlier circuit (figure 2) with at least ~ 10 m length of a coaxial cable of 50 Ω impedance. To simplify this circuit the coaxial cable was replaced by a discrete element transmission line. The impedance of this transmission line was increased to 1000 Ω to decrease the current flowing in the circuit to avoid the failure of transistors as was observed in the case of a 50 Ω impedance line providing ≥ 100 ns time duration pulses.

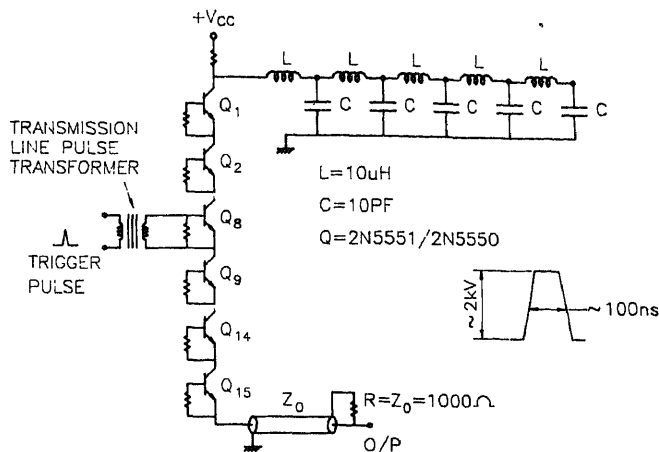


Figure 6. Diagram of gate pulse circuit.

The gate pulse circuit is shown in figure 6 which provides a square pulse of ~ 100 ns duration with 1.5 kV amplitude. This line also acts as a low pass filter for all the frequencies between zero and $(2\pi(LC)^{1/2})^{-1}$ whereas the impedance of the line is given by

$$R_L = (L/C)^{1/2}. \quad (1)$$

The quantity $(LC)^{1/2}$ represents the delay time per section of the line (low pass filter). Therefore, an n -section filter will produce a pulse of duration τ given by,

$$\tau = 2n(LC)^{1/2}. \quad (2)$$

The values of $L = 10 \mu\text{H}$ and $C = 10 \text{ pF}$ was calculated for a discrete component $n = 5$ section transmission line considering $R_L = 1000 \Omega$ and $\tau = 100 \text{ ns}$ using (1) and (2). The output of the gate pulse was connected to the accelerating grid through a capacitor to isolate the high voltage present on the grid with gate circuit.

3.3 Trigger pulse circuit

A fast ($\leq 1.5 \text{ ns}$ rise time) trigger pulse generator was developed to trigger the sweep as well as the intensifier circuit. The block diagram of the circuit is shown in figure 7. This pulse generator employs transistors (2N5551) in avalanche mode as switching elements. A capacitor of 40 pF was charged up to 300 volts and discharged through a resistive divider to provide pulses of ~ 50 volts amplitude and $< 3 \text{ ns}$ duration across a 50Ω load. It could be operated in manual, external or internal modes. The frequency of operation in the internal mode was from 10 Hz to 100 kHz. Manual operation in this generator was achieved by using 4001 CMOS ICs in mono stable mode where IC₁ acts as a buffer and IC₂ acts as dual monoshot IC. Internal mode operation of the generator was achieved using 4047 CMOS IC in a stable mode as shown in figure 7, where the frequency of operation from 10 Hz to 100 kHz was achieved by proper selection of R and C. The transistor T2 (2N5551) had a 50Ω resistance at its base for triggering

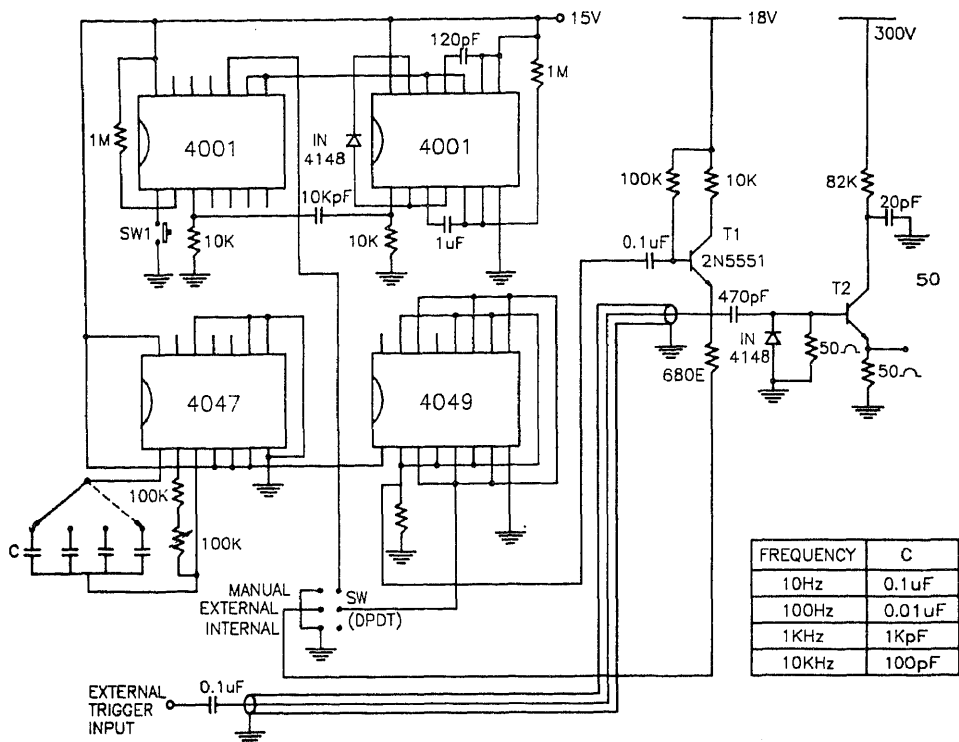


Figure 7. Trigger pulse generator circuit.

purposes. Since CMOS ICs can drive only high impedance loads, another transistor T1 (2N5551) was used in the saturation mode to amplify the current level. The external triggering of the generator was achieved by direct application of an external trigger at the base of the transistor T2. The mode of operation, that is internal, manual or external is obtained with the help of a DPDT switch. The fast electrical pulse obtained from this circuit is shown in figure 8.

3.4 Biasing power supply

Several DC high voltage power supplies are needed to drive the picosecond streak camera. The photocathode, accelerating grid and focussing electrode of the X-ray streak camera require biasing voltages of -12 , -10 and -11 kV respectively, with

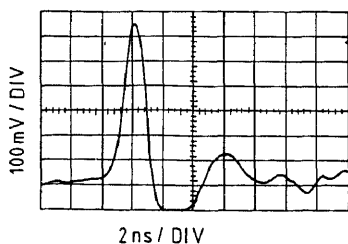


Figure 8. Oscillogram of the fast trigger pulse recorded on Lecroy model 9360 oscilloscope (5 GHz).

respect to the anode and the phosphor screen. A 4.5 kV power supply drives the sweep voltage and the gate circuit whereas a variable ± 500 V supply controls the position of the streak on the screen. Similar power supplies were used to test the optical streak camera also instead of the -15 , -15 , -13 kV biasing voltages required for photocathode, accelerating mesh and focussing electrode respectively.

4. Setup for streak camera testing

4.1 Laser diode: A source for optical streak camera

A single heterojunction GaAs laser diode LD-62 emitting at 904 nm was used as an optical source for testing the optical streak camera. These optical pulses were generated with the help of a driving circuit (Rai *et al* 1995a) having series stack of two 2N5551 transistors operating in avalanche mode (figure 9). A capacitor of 40 pF charged to ~ 600 volts was discharged through the laser diode. The peak current in the laser diode was decided by charge stored in the capacitor ($Q = CV$). The value of C and V can be changed according to the requirement of current in the diode. The rise time and pulse duration of the electrical pulse were recorded as ~ 1 ns and ~ 2.5 ns respectively. The current pulse duration depends on the value of C and the resistance in the discharging path. However, an attempt to reduce the rise time and the time duration of the current pulse by increasing the breakdown current was not successful. The laser diode driver circuit was triggered by the trigger pulse generator described in § 3.3. Trigger pulse was applied through a fast transmission line pulse transformer to isolate the driver circuit with other components. The laser diode (LD-62) obtained from Laser Diode Incorporated, USA has a lasing threshold current ~ 6 A, maximum peak forward current ~ 20 A and total peak radiant flux 5–6 W with peak emission wavelength at 904 nm. There is no critical requirement of power (radiant flux) emitted from the laser diode to test the streak camera. Even a diode laser operating below the threshold current of lasing (spontaneous emission mode) can be used to test the camera due to its better sensitivity. This diode was mounted on an aluminium block which acted as a heat sink. The circuit diagram of the laser driver is shown in figure 9. The laser diode was operated in three modes, (i) manual mode (ii) external trigger mode and (iii) internal trigger mode. Optical pulses were available with repetition rates varying from 10 Hz to 10 kHz when operated in internal mode and in single pulse when operated in external or manual mode. The laser diode could provide the smallest light pulse of 120 ps time duration.

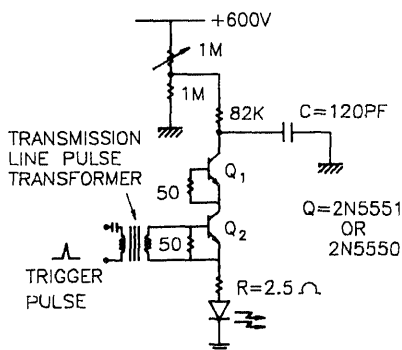


Figure 9. Driving circuit for the laser diode.

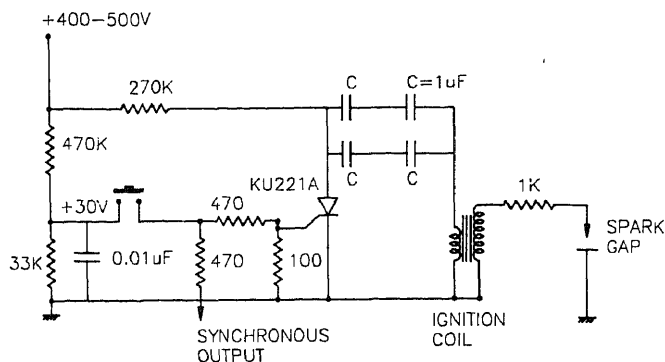


Figure 10. Circuit diagram of the spark gap driver.

4.2 Source for testing X-ray streak camera

Two types of sources were used to test the X-ray streak camera, (i) UV radiations from a spark gap kept in a vacuum chamber and (ii) soft X-rays emitted from the laser produced plasmas.

4.2a Spark gap driver: Figure 10 shows the circuit diagram of the spark gap driver. In this circuit $1\ \mu\text{F}$ capacitor charged up to $\sim 400\ \text{V}$ was discharged through the ignition coil by triggering the SCR. It provided a high voltage pulse at the output of the ignition coil which was connected to one of the electrodes (pin-like sharp) of the spark-gap (kept in 10^{-5} torr vacuum and separated by a fraction of a millimetre), whereas the other electrode was grounded (a plate). About $5\ \text{kV}$ pulse applied on the spark gap produced a spark of duration $\sim 1\text{--}3\ \mu\text{s}$. It has been reported (Dashevsky *et al* 1988) that the radiation spectrum of such a source has a maximum in the UV range and has sufficient power to produce a bright image of the slit on the screen of the streak camera. This source was operated manually. This driver was used to test the operation of streak camera for nanosecond time resolution. Low energy reproducibility in different shots is the main disadvantage of the spark gap driver. Pulsed UV emissions from the spark gap were studied using a slow sweep voltage ($\sim 5\text{--}20\ \mu\text{s}$) applied on the deflection plates of streak camera which are generated with the help of transistors. Experimental results indicate the presence of a substructure of $\sim 100\ \text{ns}$ duration within the flash duration ($\sim \mu\text{s}$).

4.2b X-rays from laser produced plasma: The short time duration X-rays generated from the laser produced plasma are used as a source to test the picosecond X-ray streak camera. The experimental system (figure 11) consists of a target chamber of $20\ \text{cm}$ diameter and $20\ \text{cm}$ height with 6 ports in radial directions out of which 4 ports are at 90° and two ports are at 45° in comparison to the port which is used for passing the laser beam. The streak camera was attached to the chamber at a port 90° to the laser axis. A copper target was kept at the centre of the chamber evacuated upto 10^{-5} torr. A 35-picosecond mode locked Nd:YAG laser delivering $75\ \text{mJ}$ energy was focussed onto the copper target to produce the plasma and as a result a subnanosecond duration soft X-ray pulse was emitted. A portion of the laser pulse energy was used as a reference

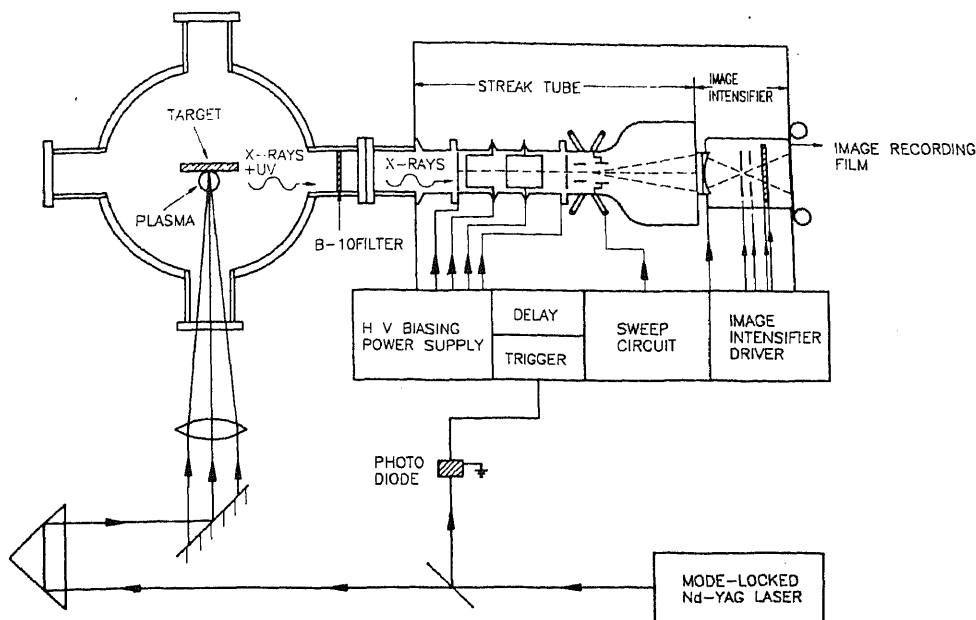


Figure 11. Experimental set-up for testing X-ray streak camera.

for triggering the sweep and gate circuits. The main laser beam generating the plasma and X-rays was delayed by ~ 25 ns to synchronise the arrival of photoelectrons and the start of the sweep voltage on the deflection plates. Two parallel plates, one at -12 kV and other at ground voltage were kept in front of the photocathode in such a way as to deflect and collect the ions and electrons generated in the chamber avoiding any direct impact of charged particles on the photocathode. A B-10 polycarbonate foil was used to cover only half of the vertically located slit such that the open part of the photocathode was sensitive to UV and soft X-rays whereas the covered part was sensitive to soft X-rays only. A 5-ns rise time sweep streaked the image in the horizontal direction.

4.3 Recording system

The streaked image from the screen of streak camera was recorded on a polaroid film by the contact photography method as well as by using the CCD camera. The images recorded using the CCD camera were analysed on a personal computer using the software PROMISE (Profile Measurement of Image Size and Edge location) to obtain the temporal intensity profile of the image (Vora *et al* 1994).

5. Results and discussion

5.1 Study of multiple pulsation in diode laser using optical streak camera

The experimental setup for testing the optical streak camera is shown in figure 12. The optical pulse from a laser diode was focussed on the photocathode of optical streak

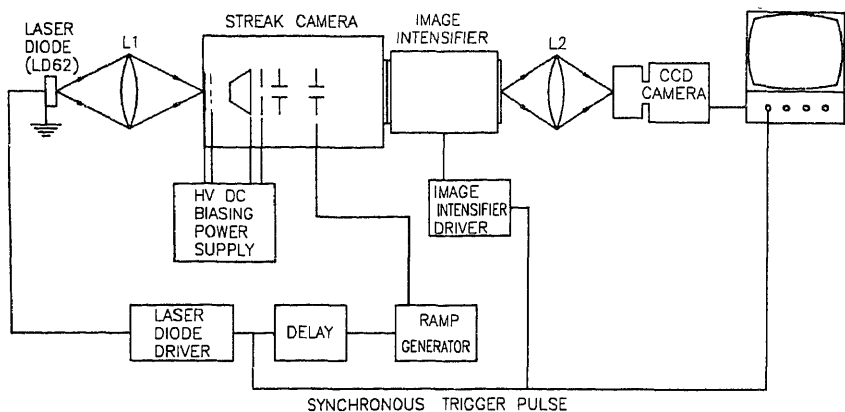


Figure 12. Experimental set-up for testing optical streak camera.

camera using an $f/1$ lens of $f = 5$ cm. The photoelectrons were streaked on the screen using a 1-ns sweep circuit and the image was recorded on the polaroid film. A second shot was taken by delaying the arrival of the light pulse by 1 ns. The images of the first and the second light pulse were separated by ~ 15 mm in space which corresponds to 1 ns. This provided us with a fastest experimental streak rate of ~ 15 mm/1 ns (streak velocity 1.5×10^9 cm/s) which is less than the expected value of ~ 40 mm/1 ns. This is due to the capacitive loading of the deflection plates which slows down the sweep rise time to ~ 2.5 ns and ultimately provides less streak velocity. By shifting the single optical pulse on screen using a known delay in steps we found the linearity in the sweep within 10%. The measurements indicate that the smallest duration light pulse from the laser diode lasts for ~ 120 ps when the charging capacitor is ≤ 40 pF. The pulse duration increases to ~ 180 ps for a capacitor value of 120 pF (figure 13). This indicates that the optical pulse duration is dependent on the RC time constant of the circuit and intensity is dependent on the product of capacitance and the charging voltage. Figure 14 shows the variation of light intensity emitted from diode laser with the pumping current which was recorded using the photodiode. Here the diode laser was operated by discharging two capacitors $C = 270$ pF and 120 pF one by one. This indicates that the emitted intensity increases slowly up to the threshold ($I_0/I_{Th} \sim 1$) and then increases very quickly. The intensity variation was similar whether the diode laser was operated

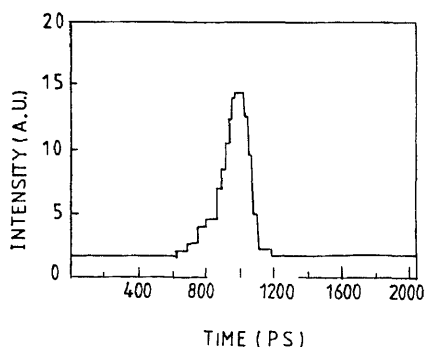


Figure 13. Single optical pulse emitted from laser diode and recorded using optical streak camera.

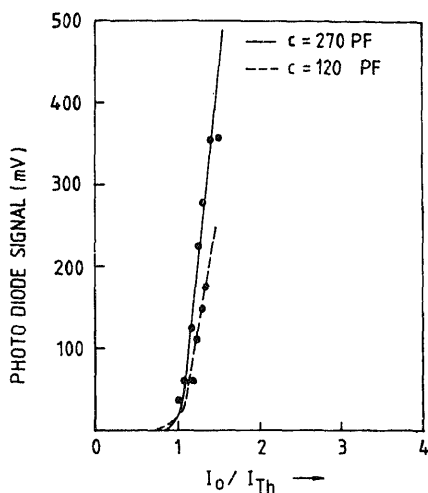


Figure 14. Variation of optical intensity emitted from laser diode with pumping current pulse (injection current/threshold lasing current).

by discharging $C = 270$ pF or by $C = 120$ pF except for a higher lasing threshold in the latter case. It was noticed that a single optical pulse was obtained just above the threshold current for lasing. By increasing the current above the threshold, i.e. the charging voltage on the capacitor, the number as well as the duration of the light pulse emitted from the diode laser increases (Rai *et al* 1995b) (figure 15A). A further increase in the laser diode current decreases the time separation between the emitted light pulses which ultimately merge with one another to form a long duration pulse similar to a current pulse. This type of behaviour has been observed earlier in various cw and pulsed semiconductor diode lasers (figure 15B, from Elliot *et al* 1983), and is known as self-sustained pulsation (Chik *et al* 1980; Elliot *et al* 1983; Lau *et al* 1983; Yariv 1985; MacFarlane & Tatum 1992; Rai *et al* 1995a). These pulses occur at certain frequencies which coincide with the relaxation oscillation frequencies of the diode lasers (Rai *et al* 1995b). Figure 16 shows the variation of experimentally observed relaxation oscillation

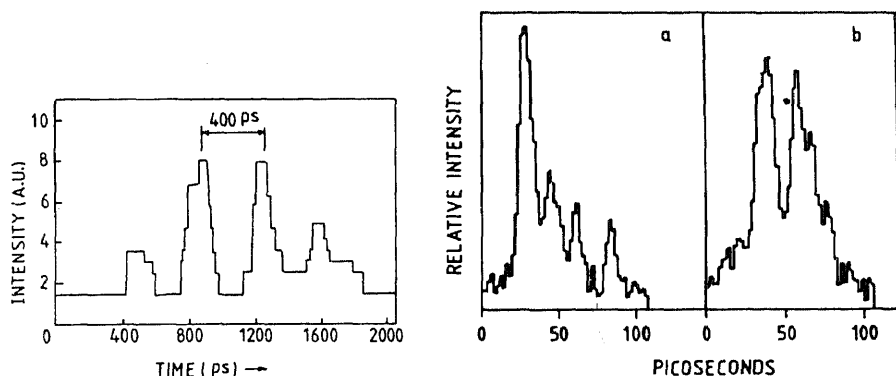


Figure 15. (A) Multiple pulsation observed in laser diode emission at $I_0/I_{Th} \sim 1.32$ which is recorded using optical streak camera. (B) Multiple pulsation observed with GaAlAs diode laser. (a) and (b) are two typical examples of individual pulses (Elliot *et al* 1983).

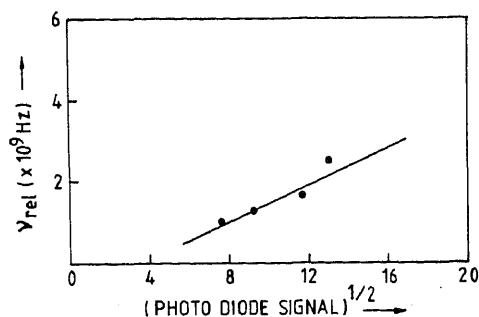


Figure 16. Variation of measured relaxation oscillation frequency with the root of intensity emitted from diode laser.

frequencies (ν_{rel}) with the square roots of the emitted light intensities, proportional to the photodiode signals. A linear variation of data points indicates better agreement with the relation given by Lau *et al* (1983) for relaxation oscillation frequency as

$$\nu_{rel} = (1/2\pi)(AP_0/\tau_p)^{1/2}$$

where P_0 is the steady state photon density in the active region, τ_p is photon life time and A is optical gain coefficient. This could be because (Yariv 1985) optical pulse generation combining the relaxation oscillation phenomenon of laser diode with the large current capability of avalanche transistors can lead to optical pulses of ~ 100 ps width. According to Baker (1991) if the current impulses of the avalanche transistors return to zero before the occurrence of the second oscillation of the laser diode, only one optical impulse will be generated, whereas a current step applied on laser diode generates a train of pulses. This type of phenomena (Chik *et al* 1980; Elliot *et al* 1983; MacFarlane & Tatum 1992) seems to be due to the presence of defects in the laser cavity. These defects act as saturable absorbers for laser light and, as a result, produce small time duration optical pulses. Detailed emission characteristics of these diode lasers are published elsewhere (Rai *et al* 1995b).

This phenomenon of multiple pulsation observed in the laser diode, has been used to test the streak camera (Rai *et al* 1995a). Figure 15 shows the intensity profile in time of a laser diode emission at $I_0/I_{Th} \sim 1.32$ where I_0 and I_{Th} are the pump and threshold currents of the diode laser. It shows the time period of repetition of pulses as ~ 400 ps. Figure 17 shows a similar period of repetition (~ 400 ps) when optical pulses were

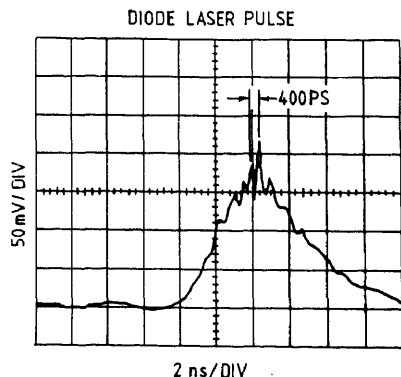


Figure 17. Multiple pulsation similar to figure 14 but recorded using L&T Gould model 7074 oscilloscope (100 MHz).

recorded using a fast photodiode and an oscilloscope (L and T Gould model 7074) in equivalent time sampling mode. This indicates the successful operation of the streak camera. The equi-distant optical pulses provided similar information about the linearity of the sweep (within 10%) as well as similar streak velocity ($\sim 1.5 \times 10^9$ cm/s) as was observed by shifting the single optical pulse as discussed before. Comparison of figures 15 and 17 indicates that the streak camera record has two equal intensity peaks between two small pulses, while the CRO trace has a single central pulse of large intensity. The above discrepancy is due to the amplitude jitter in the diode laser emission because figures 15 and 17 were recorded during two different shots. In each and every shot the amplitudes of the optical pulses changed, while the nature and time period between the pulses remain the same. However, a time jitter of ~ 500 ps has been recorded from one shot to another.

5.2 Temporal resolution of optical streak camera

The temporal resolution of streak camera is mainly dependent on three factors (Tsuchiya 1983); (i) the transit time spread which is caused by the initial velocity distribution of the photoelectrons emitted from the photocathode at the same time. This occurs in the low velocity domain between the photocathode and the mesh electrode and is given by

$$t_1 = 2.34 \times 10^{-6} [(\Delta\epsilon)^{1/2}/E], \quad (3)$$

where $\Delta\epsilon$ is FWHM in energy distribution of the emitted photoelectrons which is ~ 0.4 eV when a photon of 904 nm falls on the S1 photocathode. E is the accelerating electric field near the photocathode which is $\sim 10^6$ V/m in our case, and can provide a time spread $\Delta t_1 \sim 1.5$ ps. However, a small time spread will exist between the mesh and the phosphor screen, which is very small in comparison to this time.

(ii) The technical or streak limited time resolution is given by

$$\Delta t_2 = 1/\delta v, \quad (4)$$

where $v \sim 1.5 \times 10^{10}$ mm/s is the measured streak velocity and $\delta \sim 10$ lp/mm is the measured spatial resolution of the streak camera. This provides $\Delta t_2 \sim 6.6$ ps.

(iii) The time spread Δt_3 which occurs due to the effect of the deflection electric field on the photoelectron beam. It depends on the beam diameter, length of the deflecting plate, the deflection electric field and on the axial (directional) velocity of the electrons. This time spread is typically ~ 1 ps. The actual time resolution of streak camera Δt will be given by

$$\Delta t = (\Delta t_1^2 + \Delta t_2^2 + \Delta t_3^2)^{1/2} \quad (5)$$

which comes out to be ~ 7 ps. This is the estimated time resolution of the streak camera obtained using (5).

The time resolution of this streak camera was measured using a Michelson interferometric system with a mode-locked Nd:YAG laser (M/s Continuum, USA). The main beam was split into two beams and was directed towards a pin hole which was focussed on the photocathode of the streak camera. By moving one of the two mirrors of the interferometer one pulse was delayed with respect to the other according to the requirement. This experiment provided the time duration of the laser and time

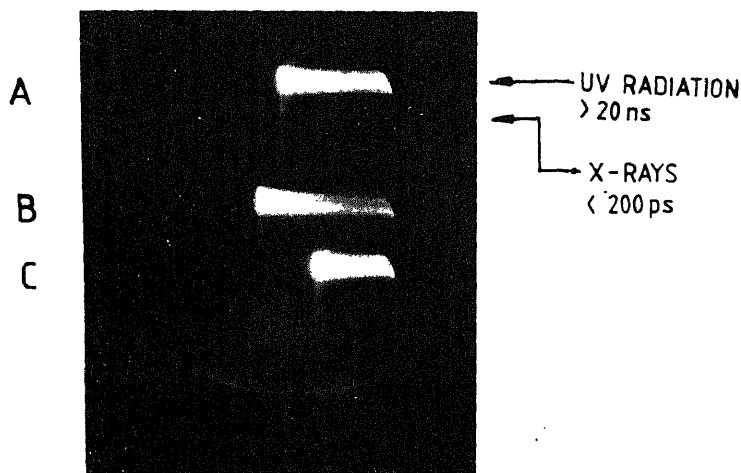


Figure 18. Contact photograph of streak image of X-rays and UV emission from laser produced plasma. A, B and C are images of different shots.

resolution of streak camera as a ~ 39 ps and ~ 40 ps respectively. However, time resolution was also calculated using the following relation

$$\tau_M = (\tau_R^2 + \Delta t^2)^{1/2}, \quad (6)$$

where $\tau_M \approx 39$ ps and $\tau_R \approx 35$ ps are the measured and reported (M/s Continuum, USA) time durations of the Nd:YAG laser pulse respectively. Equation (6) provides a time resolution $\Delta t \approx 17$ ps which is more than the expected value of ~ 7 ps and less than the measured value of ~ 40 ps. This indicates that the measured value of time resolution is being limited by the large time duration of the test pulse (35 ps). Even 10–20% error is possible in the measurement of time duration from the recorded images. These factors can lead to increased value of measured time resolution. This indicates the necessity of a smaller time duration optical pulse as well as a good optical image recording system for the measurement of time resolution of the streak camera. However, optimization of the camera parameters, such as biasing voltages, wiring arrangement in streak camera at deflection plates and improvement in optical imaging system at the input and output of the camera will essentially provide an even better time resolution and accurate time information about the events.

5.3 Study using X-ray streak camera

Figure 18 shows the photograph of UV and X-ray radiations emitted from the laser produced plasma using a 35 picosecond mode locked laser irradiated copper target. The time duration of UV radiation was found more than 20 ns whereas, X-ray emission last for < 200 ps. The streak rates were found as ~ 8 mm/ns and 15 mm/ns when a sweep voltage of 5 ns and 1 ns rise time were used respectively. These parameters are similar to that of an optical streak camera because of the similarity in the streak and intensifier tubes along with its driving electronics systems.

In spite of all similarity in both the cameras, the photocathodes used are different. The transit time spread (Δt_1) of photoelectrons emitted from gold photocathode

(energy spread, $\varepsilon = 5$ eV) in the case of X-ray streak camera, is calculated to be ~ 5 ps. This factor leads to a higher value of time resolution than the optical streak camera. The expected time resolution for this streak camera is ~ 15 ps. However, we could not find the experimental value of time resolution for X-ray streak camera due to experimental limitations.

6. Conclusions

In summary, we have developed an optical and an X-ray streak camera which is operating successfully with a fastest streak speed of $\sim 1.5 \times 10^9$ cm/s and temporal resolution of ~ 17 ps (optical streak camera). Since the sweep circuit developed for this purpose provides a positive and negative polarity ~ 1 kV amplitude pulse with a rise time < 1 ns, therefore, an improvement in wiring arrangement for applying sweep voltage to deflection plates and an optimization of the biasing voltages along with better input and output imaging and recording systems will improve the streak speed and time resolution of the streak camera. However, to measure the time resolution accurately it is necessary to have an optical pulse of few ps time duration. A combination of trigger pulse generator and laser diode driver circuit used with single heterojunction GaAs laser diode provided a simple and stable picosecond optical pulse generator which generated a single as well as multiple pulses depending on the amplitude of input current flowing in it. It was used successfully to test the optical streak camera.

The helpful discussions with V Chevokin from General Physics Institute, Moscow, S Majumder of Delli Delti, UK, B S Narayan, K S Bindra, A G Bhujle are gratefully acknowledged. We are thankful to R Arya for providing some of the high voltage power supplies, R K Khardekar for providing CCD camera and H S Vora for providing the software 'PROMISE' to analyse the streak camera images.

References

- Alcock A J, Richardson M C, Schelev M Ya 1970 The application of laser triggered spark gaps to electro-optical imageconverter camera. *Proc. IX Int. Congress on High Speed Photography* (New York: SMPTE) pp 192–197
- Bradley D J, Leddy B, Sibbet W, Sleat W E 1972 Picosecond electron-optical chronography. *Appl. Phys. Lett.* 20: 219–221
- Bradley D J, Jones K W, Sibbet W 1980 Picosecond and femtosecond streak cameras: present and future designs. *Philos. Trans. R. Soc. London A* 298: 281–285
- Baker R J 1991 High voltage pulse generation using current mode second breakdown in a bipolar junction transistor. *Rev. Sci. Instrum.* 62: 1031–1036
- Cunin B, Miehe J A, Sipp B, Schelev M Ya, Serduchenko J N, Thebault J 1980 Sweep devices for picosecond image converter streak cameras. *Rev. Sci. Instrum.* 51: 103–110
- Chik K D, Dymont J C, Richardson B A 1980 Self sustained pulsations in semiconductor lasers: experimental results and theoretical confirmation. *J. Appl. Phys.* 51: 4029–4037
- Campillo A J, Shapiro S L 1983 Picosecond streak camera fluorometry – A review. *IEEE J. Quant. Electron.* QE19: 585–602
- Dashevsky B E, Podvyaznikov V A, Prokhorov A M, Prokhindev A V, Chevokin V K 1988 An X-ray streak tube with demountable photocathodes. *Adv. Electron. Electron Phys.* 74: 233–238

- Elliot R A, Huang De Xin, Defreez R K, Hunt J M, Rickman R G 1983 Picosecond optical pulse generation by impulse train current modulation of a semiconductor. *Appl. Phys. Lett.* 42: 1012–1014
- Kinoshita K, Inuzuka E, Takiguchi Y, Okada H, Suzuki K, Hayashi I, Tsuchiya Y, Oba K, Medicki H, Straddling G 1983 Demountable photocathode X-ray streak camera. *Proc. SPIE* 427: 36–44
- Kinoshita K, Ito M, Suzuki Y 1987 Femtosecond streak tube *Rev. Sci. Instrum.* 58: 932–938
- Lau K Y, Bar-Chaim N, Ury I, Harder Ch, Yariv A 1983 Direct amplitude modulation of short cavity GaAs lasers upto X-band frequencies. *Appl. Phys. Lett.* 43: 1–3
- MacFarlane D L, Tatum J A 1992 Short pulse generation in a visible diode laser by resonant excitation of a sustained oscillation. *IEEE J. Quant. Electron.* QE-28 1320–1324, and references therein
- Rai V N, Shukla M, Khardekar R K 1994a A transistorized Marx bank circuit providing sub-nanosecond high voltage pulses. *Meas. Sci. Tech.* 5: 447–449
- Rai V N, Shukla M, Pant H C, Bhawalkar D D 1994b Development of a picosecond optical streak camera and observation of self sustained oscillation in GaAs laser diode emission. Proceedings National Laser Symposium. CAT Indore, 29 Jan-1 Feb, pp 254–255, and research report No. CAT/95-11
- Rai V N, Shukla M, Pant H C, Bhawalkar D D 1994c A picosecond X-ray streak camera for X-ray diagnostics of laser produced plasma. *Plasma science and technology* (ed.) I M L Das (New Delhi: Allied Publication) pp 447–450
- Rai V N, Shukla M 1994 A high voltage pulser circuit with subnanosecond rise time *Rev. Sci. Instrum.* 65: 2134–2136
- Rai V N, Shukla M, Khardekar R K, Pant H C 1995a A picosecond optical pulse generator to calibrate the optical streak camera. *Rev. Sci. Instrum.* 66: 3125–3130
- Rai V N, Shukla M, Pant H C 1995b Generation of picosecond optical pulses from single heterostructure GaAs diode laser and study of their emission characteristics. *Pramana, J. Phys.* (to be published)
- Schelev M Ya, Richardson M C, Alcock A J 1972 Operation of a grid – shuttered image converter tube in the picosecond region. *Rev. Sci. Instrum.* 43: 1819–1829
- Stradling G L, Attwood D T, Kauffman R L 1983 A soft X-ray streak camera. *IEEE J. Quant Electron.* QE-19: 604–615
- Tsuchiya Y 1983 Picosecond streak camera and its applications. *Picosecond* (A technical bulletin of Hamamatsu) 14: 2–18
- Vora H S, Nakhe S V, Sarangpani K K, Saxena P, Bhatnagar R, Shirke N D 1994 Profile monitor for laser beam parameter measurements. *Proceedings of National Laser Symposium* (Centre for Adv. Technol., Indore) pp 260–261
- Yariv A 1985 *Optical electronics* (New York: Holt, Rinehart and Winston) pp 188–193

Steady flow simulation in irrigation canals

RAJEEV MISRA

Department of Civil Engineering, Indian Institute of Technology, Bombay
400 012, India

MS received 14 February 1994; revised 9 May 1995

Abstract. A mathematical model is developed for the analysis of spatially varied steady flow in irrigation canals. The model accounts for canal seepage and effect of control structures at the upstream and downstream ends of the canal. Two computational methods developed to solve the spatially varied steady flow equations for the irrigation canals are presented here. The governing differential equations are solved iteratively using fourth order explicit Runge–Kutta method. The model results are verified with experimentally observed water surface profiles available in literature. The effects of bed seepage, canal condition and backwater curves on the discharge carrying capacity and variation of flow depth are studied through model application on a canal reach. It is found, that in most of the situations the backwater curves spread sufficiently upstream and significantly affect the performance of the control structure at the upstream end. In many situations, it may not even be possible to operate the canal at design discharges.

Keywords. Steady flow; open channels; irrigation canals.

1. Introduction

By and large, canals are designed based on uniform flow criterion coupled with regime concepts. However, there is an ambiguity about the applicability of the uniform flow concept to spatially varied flows. In practice, seepage losses are estimated based on experience and are lumped at canal ends. However, the water is continuously lost as seepage along the canal reach. Even under idealized conditions of no seepage, a uniform flow at all locations in a canal reach is not feasible due to the presence of measuring/regulation control structures. The actual depth and discharge in the canals are significantly different from the design discharges. In developing countries like India, almost all the canal systems are manually controlled type. The supplies are made under steady state. The steady flow simulation in irrigation canals can play a very important role in irrigation scheduling of the existing canal systems and in design and planning of proposed canal irrigation projects.

The analysis of spatially varied steady flow in irrigation canals involves the solution continuity and momentum equation for open channels. In the limiting case of no lateral flow, these equations reduce to dynamic equation of gradually varied steady flow. Many methods, such as graphical methods, direct integration methods and step methods (Chow 1959; French 1986) are used to numerically integrate the dynamic equation of gradually varied flow. Standard step method is widely used to compute varied flow profiles. This procedure involves the iterative solution of nonlinear algebraic equations at every computational node (Paine 1992). The use of same numerical techniques to analyse gradually varied or spatially varied flow problems in an irrigation canal is not simple.

Hager (1983, 1991) and Schropp & Fontijn (1989) presented a general theory of spatially varied flows with increasing and decreasing discharges. They discussed in detail the nature of steady spatially varied flow profiles, requirement of boundary conditions, properties of saddle and nodal (singular) points. Many investigators (Chow 1959; Hager 1983) analysed the problem of side channel spillway (increasing discharge) wherein the rate of lateral inflow is independent of the flow in the channel being modelled. Whereas in case of a side weir or in a channel with bottom racks (decreasing discharges) usually channel friction and bed slope are not considered (Subramanya 1986; Uyumaz & Smith 1991). However, the seepage from canals is characterized by canal size and shape, hydraulic conductivity of the soil, location of water table, weed growth and flow depth in the canal (Leliavsky 1965; Wachyan & Rushton 1987). The order of magnitude of bed slope, friction and seepage terms in governing equations are comparable (Misra 1993).

1.1 Statement of the problem

The analysis problem often encountered in irrigation canals is to compute water surface profile and evaluate discharge carrying capacity of a canal reach for given canal geometry, roughness, seepage coefficients and control structure settings at both the canal ends (figure 1a). The problem is implicit in the sense that the discharge or depth at either of the boundaries is not known. The discharge from the upstream control structure may depend on the flow depth at the upstream end (submerged gate) and is not known *a priori*. On the other hand, the depth at the tail end depends upon the discharge which can not be fixed without estimating seepage losses and discharge from the upstream gate. Moreover, the rate of seepage at a location in a canal, depends upon the flow depth and is not a constant.

French (1986) suggested an iterative procedure to compute discharge released into a channel from a reservoir, for a given channel geometry for specified upstream or downstream depth. However, he did not include the effect of seepage, downstream control and submergence of upstream control as stated above.

This paper presents a mathematical model for the analysis of spatially varied steady flow in irrigation canals. Two iterative computational procedures to analyse spatially varied steady flow in canals are presented. In both the methods iterations are performed to satisfy the boundary conditions. The continuity and momentum equations of spatially varied steady flow are solved using fourth order explicit Runge-Kutta method. The model results are compared with the experimental observations of Schropp & Fontijn (1989). The effect of canal seepage, canal condition, and backwater

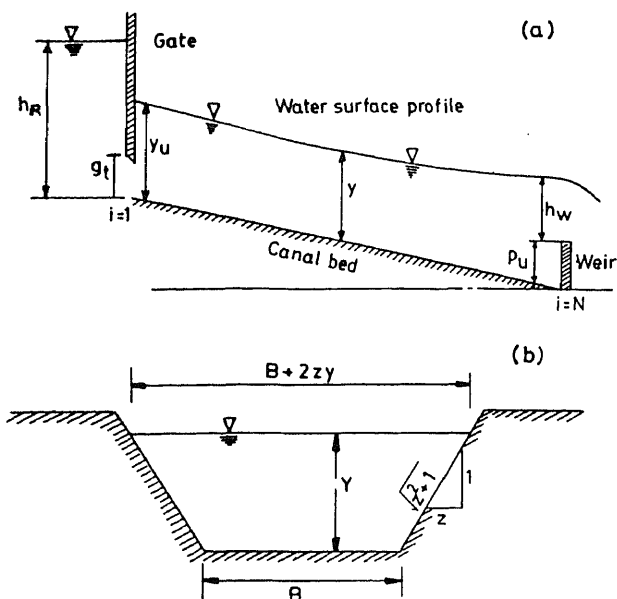


Figure 1. Definition sketch of a canal reach (a) elevation and (b) cross-section.

curves on varied flow profiles and canal capacity are studied through model application for different sets of parameters on a canal reach.

2. Governing equations

The governing equations of spatially varied steady flow in a canal are written as (Chow 1959),

$$dQ/dx = q_s \quad (1)$$

$$\frac{dy}{dx} = \left[S_o - S_f - \frac{2\beta Q q_s}{gA^2} \right] / \left[1 - \beta \frac{Q^2 T}{gA^3} \right], \quad (2)$$

where x = distance along the canal; Q = discharge; y = depth of flow; g = acceleration due to gravity; T = top width; A = area of cross-section; S_o = bed slope; β = momentum correction coefficient, which is taken as 1; S_f = friction slope given by Manning's equation written as,

$$S_f = n^2 Q^2 / A^2 R^{4/3} \quad (3)$$

where n = Manning's coefficient and R = hydraulic radius.

In (1) and (2), q_s = rate of seepage per unit length and is given by

$$q_s = -P_s(\alpha y^\beta + \gamma), \quad (4)$$

where α , β and γ = constants; P_s = perimeter of seepage face. For $\alpha = K_d/d$, $\beta = 1$,

$\gamma = K_d$, (4) reduces to Darcy's law, written as,

$$q_s = -K_d P_s [(y + d)/d] \quad (5)$$

where K_d = permeability; d = thickness of the porous bed. However, in field situation it is difficult to estimate the thickness d . In canal engineering, it is customary to express canal losses in units of length/time (Wachyan & Rushton 1987) thereby inferring that the canal losses are the function of the wetted perimeter of the canal. By substituting $\alpha = K$; $\beta = 0$; $\gamma = 0$ in (4), we get

$$q_s = -KP_s, \quad (6)$$

where K = seepage coefficient expressed in cumecs/million m^2 . Depending upon the soil texture and type of lining, suitable values of K can be chosen (Leliavsky 1965; Wachyan & Rushton 1987).

By and large, the irrigation canals are trapezoidal in shape and for this shape the governing equations (1) and (2) can be written as,

$$dQ/dx = \mathcal{G}(x, y) = K(B + 2y(z^2 + 1)^{1/2}), \quad (7)$$

$$\frac{dy}{dx} = \mathcal{F}(x, y, Q) =$$

$$\left\{ S_o - \left[\frac{n^2 Q^2 (B + 2y(z^2 + 1)^{1/2})^{4/3}}{\{(B + zy)y\}^{10/3}} \right] - \left[\frac{2\beta K Q (B + 2y(z^2 + 1)^{1/2})}{g \{(B + zy)y\}^2} \right] \right\} \\ \div \left\{ 1 - \left[\beta \frac{Q^2 (B + 2zy)}{g \{(B + zy)y\}^3} \right] \right\}, \quad (8)$$

where B = bed width of the canal; z = side slope (figure 1b). For all the results presented in § 6 of this paper, (7) and (8) are used.

2.1 Boundary conditions

To solve (1) and (2) for two unknowns $Q(x)$ and $y(x)$, two boundary conditions are required. The specified depth and discharge or rating curve can be used as boundary condition. The discharge equations from the control structures such as weirs, gates, siphons, falls etc. can also be used as boundary condition. Under subcritical flow conditions, which by and large prevail in irrigation canals, at least one boundary condition is to be specified at the downstream end and flow profile computations are carried out opposite to the direction of flow. However, both depth and discharge can also be specified at the downstream end, though it is not common. In case of an irrigation canal, the discharge is regulated by the control structure situated at the upstream end, whereas supply level (flow depth) is maintained using the downstream control.

For the results presented in this paper, a submerged gate at the upstream end and a rectangular weir at the downstream end are used as boundary conditions (figure 1). The submerged gate discharge equation is written as (Bos 1976),

$$Q = (2g)^{1/2} C_d C_v b_c g_t (h_R - y_u)^{1/2} \quad (9)$$

and the discharge equation for the weir is written as,

$$Q = \frac{2}{3} \left(\frac{2g}{3} \right)^{1/2} C_d C_v b_c h_w^{3/2}, \quad (10)$$

where Q = discharge from the structure; C_d = coefficient of discharge and for a weir it depends upon many factors such as, shape, (h_u/l) , (h_u/p) etc.; b_c = width of the control section; g_t = gate opening; h_u = head upstream of the control structure; h_d = head downstream of the control structure; C_v = approach velocity coefficient and is obtained from,

$$C_v^{2/3} - \left[1 + \frac{4}{27} C_v^2 \left(C_d \frac{A_o}{A_u} \right)^2 \right] = 0 \quad (11)$$

where, A_u = area of flow upstream of the control structure; A_o = area of flow at control structure and for a gate $A_o = b_c g_t$ and for a weir $A_o = b_c h_u$.

3. Computational procedure

The initial guess values of unknowns viz., y and Q are to be specified to start the iterative procedure. For the guessed/corrected discharges, the depth at the downstream end is computed using the downstream boundary condition by Newton's method. For this depth, spatially varied flow computations are performed in the canal. Knowing the depth at the upstream end of the canal, the discharge in the canal is corrected. The discharge at the downstream end is now updated, and the procedure of computing the depth at the downstream end and varied flow profile computations, is repeated until the depth and discharge convergence is met.

Based on the above procedure, two different computational methods are developed. These methods mainly differ in the procedure used to solve varied flow equations. The concept of standard step method can also be extended to solve spatially varied flow equations. But this method requires an iterative procedure to compute depth and discharge at every computational node and may not be computationally economical. Hence, in the present analysis fourth order explicit Runge-Kutta method is used for both the methods as discussed below.

3.1 Method 1

In this method, spatially varied flow equations (1) and (2), are solved as a coupled system of differential equations from the tail end to the upstream end using four point explicit Runge-Kutta method on a variable grid. The computational procedure is as given below.

- (I) For the known/guessed discharge, obtain depth at downstream end using downstream boundary condition such as (10). Newton's method is used.
- (II) Solve (1) and (2) or (7) and (8) for the entire canal reach using the depth and discharge at downstream end as starting values. The fourth order explicit Runge-Kutta method is used. The depth and discharge computations are performed from downstream end to upstream end of the canal.
- (III) Correct the discharge at the upstream end for the upstream depth obtained from step II, using upstream boundary condition such as (9).

- (IV) Check for convergence in discharge at upstream end. If convergence is not reached, correct the discharge at the downstream end and go to step I. The new discharge (corrected) at the downstream end is obtained as,

$$Q_d = Q'_d + \alpha \Delta Q_u \quad (12)$$

where α = relaxation coefficient; Q_d = new discharge at the downstream end, and Q'_d = previous iteration value of the discharge. ΔQ_u = discharge correction made at the upstream end.

The solution procedure using Runge–Kutta method for solving coupled system of differential equations (1) and (2) is as follows:

Depth is computed from,

$$y_i = y_{i+1} + \frac{1}{6} [a_1 + 2a_2 + 2a_3 + a_4]; \quad i = (N-1) \cdots 1 \quad (13)$$

and discharge is computed from,

$$Q_i = Q_{i+1} + \frac{1}{6} [b_1 + 2b_2 + 2b_3 + b_4]; \quad i = (N-1) \cdots 1 \quad (14)$$

where

$$\begin{aligned} a_1 &= \Delta x \mathcal{F}(x_{i+1}, y_{i+1}, Q_{i+1}), \\ b_1 &= \Delta x \mathcal{G}(x_{i+1}, y_{i+1}), \\ a_2 &= \Delta x \mathcal{F}(x_{i+1} + (\Delta x/2), y_{i+1} + (a_1/2), Q_{i+1} + (b_1/2)), \\ b_2 &= \Delta x \mathcal{G}(x_{i+1} + (\Delta x/2), y_{i+1} + (a_1/2)), \\ a_3 &= \Delta x \mathcal{F}(x_{i+1} + (\Delta x/2), y_{i+1} + (a_2/2), Q_{i+1} + (b_2/2)), \\ b_3 &= \Delta x \mathcal{G}(x_{i+1} + (\Delta x/2), y_{i+1} + (a_2/2)), \\ a_4 &= \Delta x \mathcal{F}(x_{i+1} + \Delta x, y_{i+1} + a_3, Q_{i+1} + b_3), \\ b_4 &= \Delta x \mathcal{G}(x_{i+1} + \Delta x, y_{i+1} + a_3), \end{aligned} \quad (15)$$

where N = number of computational nodes and Δx = space step and is taken as $(x_i - x_{i+1})$. Here i indicates the node numbering from upstream end to downstream end. In (15) $\mathcal{F}(x, y, Q)$ and $\mathcal{G}(x, y)$ are given by (7) and (8) respectively.

3.2 Method 2

In this method, (1) and (2) or (7) and (8) are solved separately. Runge–Kutta method is modified as discussed below. This method consists of two steps: (i) solving for discharges in the forward sweep and (ii) solving for depth in the backward sweep. In the forward sweep, for the discharge obtained from the upstream boundary condition and for the guessed/known depth in the canal, the discharge computations are made from upstream end to downstream end of the canal using the continuity equation (7). For the computed discharge at the downstream end, the depth is obtained from the boundary condition using Newton's method. For this depth and known discharge in the canal, the momentum equation, (8) is solved for the depth in the canal from downstream end to upstream end. This procedure is repeated until the depth and discharge convergence

is met at boundaries. The discharge computations (forward sweep) using Runge-Kutta method on a variable grid are as follows:

$$Q_{i+1} = Q_i + (1/6)[b_1 + 2b_2 + 2b_3 + b_4]; \quad i = 1 \dots (N-1) \quad (16)$$

where

$$\begin{aligned} b_1 &= \Delta x \mathcal{G}(x_i, y_i), \\ b_2 &= \Delta x \mathcal{G}(x_i + (\Delta x/2), y_i + (\bar{a}_1/2)), \\ b_3 &= \Delta x \mathcal{G}(x_i + (\Delta x/2), y_i + (\bar{a}_2/2)), \\ b_4 &= \Delta x \mathcal{G}(x_i + \Delta x, y_i + \bar{a}_3), \end{aligned} \quad (17)$$

where, $\Delta x = x_{i+1} - x_i$; N = number of computational nodes; and $\mathcal{G}(x, y)$ is given by (7). In (17), \bar{a} are obtained using a values in the backward sweep for depth computations using (19). The depth computations in the backward sweep using Runge-Kutta procedure are as follows:

$$y_i = y_{i+1} + (1/6)[a_1 + 2a_2 + 2a_3 + a_4]; \quad i = (N-1) \dots 1 \quad (18)$$

where

$$\begin{aligned} a_1 &= \Delta x \mathcal{F}(x_{i+1}, y_{i+1}, Q_{i+1}), \\ a_2 &= \Delta x \mathcal{F}(x_{i+1} + (\Delta x/2), y_{i+1} + (a_1/2), Q_{i+1} + (\bar{b}_1/2)), \\ a_3 &= \Delta x \mathcal{F}(x_{i+1} + (\Delta x/2), y_{i+1} + (a_2/2), Q_{i+1} + (\bar{b}_2/2)), \\ a_4 &= \Delta x \mathcal{F}(x_{i+1} + \Delta x, y_{i+1} + a_3, Q_{i+1} + \bar{b}_3), \end{aligned} \quad (19)$$

where $\Delta x = x_i - x_{i+1}$ and $\mathcal{F}(x, y, Q)$ is given by (8). In (19), b are obtained using b values in the forward sweep for discharge computations using (17).

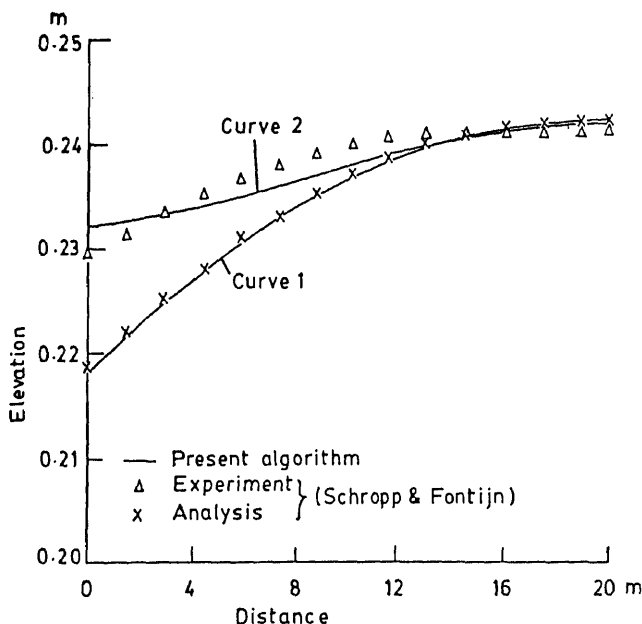


Figure 2. Comparison of water surface profile I.

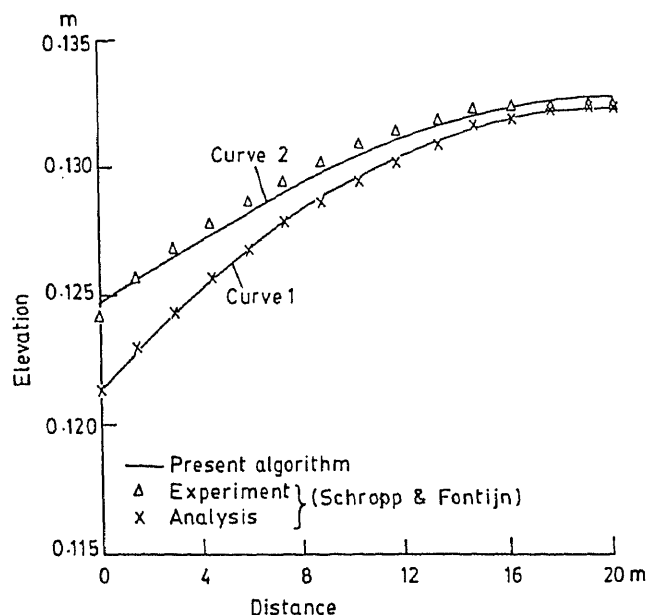


Figure 3. Comparison of water surface profile II.

4. Model verification

The model results are verified for many steady flow problems (no seepage) presented by Chow (1959) and French (1986). The results of varied flow analysis with seepage are verified with experimentally observed water surface profiles obtained by Schropp & Fontijn (1989) on a laboratory channel. The seepage rate q_s is obtained from (5). Both the numerical methods presented above gave identical results. Figure 2 presents the comparison for profile I (higher discharge) whereas figure 3 presents the comparison for profile II (lower discharge) of Schropp & Fontijn (1989). In figure 2 and 3, curve 1 presents the comparison of water surface profile obtained using proposed numerical methods with the ones computed by Schropp & Fontijn (1989) using same roughness and seepage coefficients. The two results agree very well with each other. A better fit to the experimental data could be obtained (curve 2 in figures 2 and 3) by tuning the roughness coefficient as given in table 1. From the table it is found that Manning's n value is significantly different for the two discharges. This may be

Table 1. Data for model verification.

Parameters	Computed		Experimental	
	Profile I	Profile II	Profile I	Profile II
Manning's n	0.010	0.010	0.0265	0.0156
$K_d (10^{-3} \text{ m/s})$	1.690	0.980	1.690	0.980
$d(\text{m})$	0.100	0.100	0.100	0.100
$Q_s (10^{-3} \text{ m}^3/\text{s})$	0.091	0.035	0.091	0.035
Width(m)	0.80	0.80	0.80	0.80

associated with the significant differences in seepage rates for the two discharges (Rao *et al* 1994).

5. Comparison of methods

The relative merits and demerits of the two methods are studied through their application to a number of steady flow situations on different canals. These merits and demerits are discussed in terms of their generality to simulate complex steady flow in a canal, their simplicity in implementation, storage requirement and computational efficiency. The requirement of initial guess for the two methods, to start the iterative procedure, is also discussed.

The method 2 requires the initial guess values of Q and y at all computational nodes, whereas method 1 requires only the initial guess of discharge at the downstream end to start the computations. The uniform flow depth and discharges are used as the initial guess of unknowns in the present study. Apart from the initial guess, method 2 requires the initial values of $\bar{a}_1, \bar{a}_2, \bar{a}_3$ and \bar{a}_4 to start the iterative procedure. The starting values of these Runge-Kutta coefficients are computed using initial guess values of Q and y for all the computational nodes. It should be noted here that method 2 requires extra storage for Runge-Kutta coefficients such as a and b , which is not required for method 1. The method 2 is found to be computationally more efficient. Both the methods produced identical results for all the problems studied. Based on the experience method 2 is recommended.

6. Application

To demonstrate the applicability of the numerical methods and to study the effect of different parameters on water surface profiles in irrigation canals, the results obtained for a canal reach are presented. The canal is bounded by a submerged gate at the upstream end and a weir at the downstream end. Following data are used in the computations.

Canal geometry: Bed width = 2.0 m; side slope = 1:1.5; bed slope = 1:2500; length = 2000.0 m; shape = trapezoidal;

Upstream gate: Width = 2.0 m; gate opening = 1.4 m; coefficient of discharge = 0.6; sill height = 0.0; upstream head = 2.0 m;

Downstream weir: width = 1.75 m; weir height (p) = 0.6 m; weir length (l) = 2.0 m; coefficient of discharge is given as (a fit to the experimental data of Ramakrishnan 1979),

$$\begin{aligned} h_u/l &\leq 0.4, C_d = 0.867, \\ 0.4 < h_u/l < 1.6, C_d &= 0.191(h/l) + 0.792, \\ h_u/l &> 1.6, C_d = 1.09. \end{aligned} \quad (20)$$

6.1 Effect of seepage

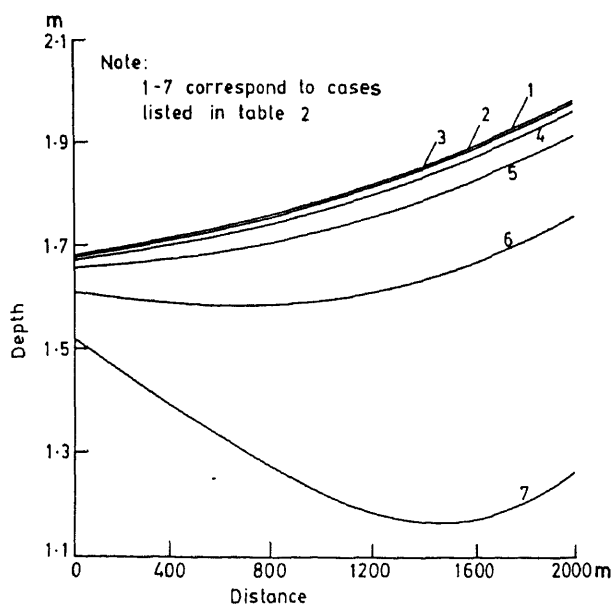
To study the effect of seepage on varied flow, the results obtained for different seepage coefficients are presented. Equation (6) is used to estimate the rate of seepage from the

Table 2. Discharge distribution for different seepage coefficients.

Case	Seepage (10^{-6} m/s)	Discharge (m^3/s)	
		Upstream end	Downstream end
1	0.0000	4.424	4.424
2	0.3048	4.426	4.421
3	2.4384	4.438	4.396
4	9.7536	4.477	4.313
5	30.4800	4.583	4.077
6	100.0000	4.883	3.311
7	304.8000	5.415	1.383

canal. Table 2 presents the values of seepage parameter K and the corresponding discharges at the upstream and downstream ends of the canal. Case 1 presents the limiting case of spatially varied flow analysis, wherein the governing equations (1) and (2) or (7) and (8) reduce to gradually varied flow equations (Chow 1959). It should be noted here that no computational procedure is suggested for the analysis of gradually varied flow in irrigation canals as discussed in § 1.1. Cases 2–5 present the field range of K values for irrigation canals (Leliavsky 1965). Cases 6 and 7 simulate the flow situations due to excessive seepage. Figure 4 presents the variation in the flow depth along the canal reach.

It is observed that for a very low seepage (case 2 in table 2) the flow profile in the canal is very close to the gradually varied flow profile (case 1 in table 2) in the canal (figure 4) as may be expected. For the practical range of seepage coefficients (2–5 in table 2) the change in flow depth at the upstream end is not very significant as can be seen from

**Figure 4.** Effect of seepage on flow depth.

curves 2-5 in figure 4. The change in depth between 2 and 5 is 1.38%, whereas the seepage coefficient is increased 100 times. Due to the smaller change in depth with seepage coefficient, the change in discharge at the gate is not significant. The difference in discharges between cases 2 and 5 is 3.42% (table 2). However at the downstream end, the flow depth depends on the tail end discharge and the characteristic of the weir. Due to increased seepage losses from cases 2-5, the discharge at the downstream end is reduced (table 2). Due to this reduced discharge the flow depth also gets reduced. The changes in depth at tail end between cases 2 and 5 are more significant (3.13%) as compared to upstream end. It should be noted here that for cases 1-5 (table 2) the effects of canal slope are dominant over the cumulative effects of canal friction and seepage, i.e. all along the canal reach,

$$S_o > (S_f - (2\beta KQP_s/gA^2)), \quad (21)$$

and hence, the water surface profile exhibits the characteristics similar to the backwater profile discussed in Chow (1959).

In situations of excessive seepage (cases 6 and 7), the depth and discharge changes at upstream canal ends are significant as seen in table 2 and figure 4. For these cases, the nature of water surface profile gets changed within the canal reach. The variation in flow depth along the canal exhibits the characteristics of both, backwater and drawdown profiles. For the distances ($0 < x < L_c$) upto which,

$$S_o < (S_f - (2\beta KQP_s/gA^2)), \quad (22)$$

the water surface profile exhibits the characteristics similar to the drawdown profile, and for the distances ($L_c < x < L$), for which

$$S_o > (S_f - (2\beta KQP_s/gA^2)), \quad (23)$$

the water surface exhibits the characteristics similar to the backwater profile. At $x = L_c$ the water surface is parallel to the bed. However, finding such a location by analytical means is not possible. For case 6 such a situation occurs at $x = 650$ m whereas for case 7 such a situation occurs at $x = 1550$ m. In case 6, the backwater effects due to the weir are felt upto 1350 m from the downstream end whereas in case 7 the backwater effects are felt only upto 450 m from the downstream end. The drawdown in the upstream canal reach ($0 \text{ m} < x < 650 \text{ m}$ for case 6 and $0 \text{ m} < x < 1550 \text{ m}$ for case 7) is mainly due to excessive seepage from the canal. It should be noted here that the nature of these drawdown profiles due to seepage is not the same as drawdown profiles discussed in Chow (1959); French (1986) for gradually varied flow (no seepage).

6.2 Effect of canal condition

With the passage of time and due to inadequate maintenance, the condition of canals deteriorates. The canals become irregular in shape due to silting, erosion and weed growth changing the roughness characteristics and seepage losses. All these effects in general considerably reduce the discharge carrying capacity of the canals. In the present study, it is assumed that the mean canal shape is maintained. The effect of backwater profiles, changed roughness and seepage loss on discharge carrying capacity of the canals are studied through simulations made for different sets of parameters given in table 3. The data regarding canal geometry, upstream gate and downstream

Table 3. Roughness and seepage coefficients for different canal conditions.

Case	Manning's n	Seepage coefficient $K(10^{-6}\text{m/s})$	Canal condition
1	0.012	0.3048	Very good (improved)
2	0.020	2.4384	Good (improved)
3	0.030	9.7536	Reference (design)
4	0.040	9.7536	Poor (deteriorated)
5	0.050	30.4800	Bad (deteriorated)

weir are same as given earlier. Table 4 presents the discharges at both the ends of the canal for different sets of parameters listed in table 3. For comparison purposes, the last column in the table presents the discharge assuming uniform flow in the canal as used in design. This discharge is obtained by solving the gate equation and uniform flow equation simultaneously. Figure 5 presents the variation in depth along the canal, whereas figure 6 presents the water surface profiles, for all the cases listed in table 3.

As the canal condition deteriorates, the roughness and seepage losses are increased. The increased roughness increases the flow depth in the canal which in turn reduces the discharge from the upstream gate. On the other hand the increase in seepage loss should decrease the flow depth which will lead to higher discharge from the upstream gate. However, for the range of parameters studied (cases 1–5 in table 3), it is observed that the effects of increased canal roughness on flow profiles are more dominant as compared to increase in canal seepage. In general, the increased roughness and seepage losses affect the performance of the upstream control significantly. The discharge from upstream gate is reduced by 35.8% as the canal condition deteriorates from case 1 to case 5, whereas the associated increase in upstream depth is 20% (table 4 and figure 5).

The flow depth at the tail end depends upon the discharge and the characteristics of the downstream control (weir). The cumulative effect of reduced upstream discharge and increased seepage losses significantly reduce the discharge at the canal end. For the range of parameters studied (table 3) the discharge at the tail end of the canal is reduced by 44.8%, whereas the reduction in depth is 22.0% (table 4 and figure 5).

Table 4. Discharges for different canal conditions.

Canal condition (case)	Discharge (m^3/s)		
	Actual		Design (Uniform flow)
	Upstream end	Downstream end	
1	5.565	5.560	6.728
2	5.069	5.028	5.631
3	4.477	4.313	4.668
4	3.929	3.765	3.954
5	3.575	3.071	3.397

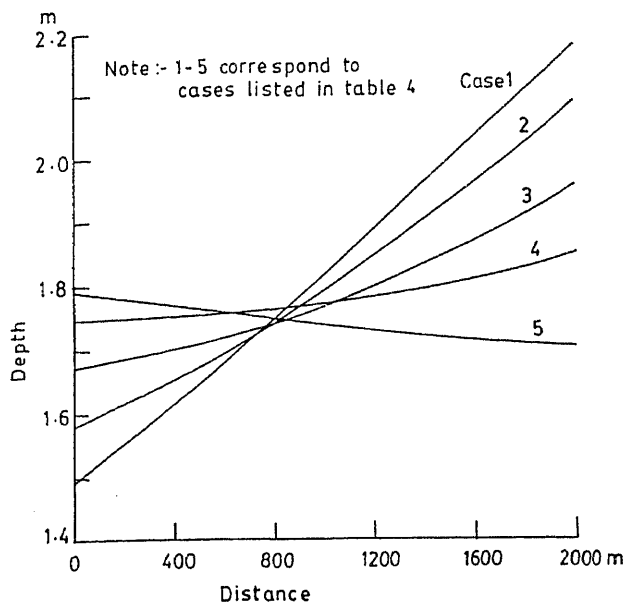


Figure 5. Effect of canal condition on flow depth.

6.3 Backwater effect

By and large, canals are designed based on uniform flow criterion and control structures are also designed based on the uniform flow depth. But uniform flow at all locations in a canal is not feasible due to efflux created by the control at the downstream

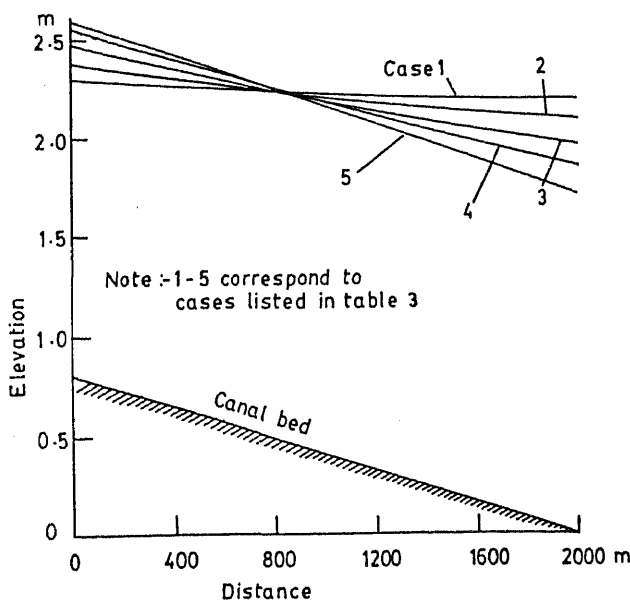


Figure 6. Effect of canal condition on water surface profiles.

end. Furthermore, in the presence of seepage, the concept of uniform flow is itself ambiguous. In several situations, the backwater effects due to downstream control may extend sufficiently upstream so as to effect the performance of the control structure at the upstream end. The present comparisons show that for cases 1–4 (table 3) the actual depth is more than the uniform flow depth confirming the effects of backwater. Hence, the design discharges for these cases are considerably higher than the actual discharge in the canal. In some situations, it may not be feasible to operate the canal at design discharges as flow may overtop the embankment. Also, there may not be adequate flexibility available in the gate opening to compensate for these effects. In case 5 of table 3, it is found that uniform flow depth is more than the actual flow depth. This is due to the drawdown caused by higher seepage. For this case the actual discharge is higher than the design discharge as seen in table 4.

In general, the cumulative effects of seepage, canal condition and backwater, reduce the discharge carrying capacity of the canal significantly. A comparison of the discharges obtained from uniform flow concept for very good canal condition (case 1, column 4 in table 4) with the actual discharge for very bad canal condition (case 5, column 2 in table 4) shows a reduction of 46.86% in the canal carrying capacity.

7. Conclusion

A mathematical model is developed for the simulation of steady flow in a canal reach. The model accounts for canal seepage and control structures at upstream and downstream ends of the canal. Two iterative methods are also presented to compute spatially varied steady flow profiles in a canal reach. Method 2 is found to be computationally more efficient. The results are compared with both observed and computed water surface profiles available in the literature. The effects of seepage coefficient, canal condition and backwater on spatially varied flow in the canal are studied. In general, it is observed that for the range of field parameters, the effect of roughness on varied flow profiles and the performance of upstream control are more significant than seepage. However, excessive seepage may considerably change the nature of the water surface profile. It is observed that in general, the cumulative effects of seepage, canal condition and backwater significantly reduce the discharge carrying capacity of the canal. In some situations, it may not be possible to achieve design discharge in the canal.

References

- Bos M G 1976 *Discharge measurement structures* (New Delhi: Oxford and IBH)
- Chow V T 1959 *Open channel hydraulics* (New York: McGraw-Hill)
- French R H 1986 *Open channel hydraulics* (New York: McGraw-Hill)
- Hager W H 1983 Open channel hydraulics of flows with increasing discharge. *J. Hydraul. Res.* 21: 177–193
- Hager W H 1991 Flow profiles for steady spatially varied flow. *J. Hydraul. Res.* 29: 284–287
- Leliavsky S 1965 *Design text books in civil engineering* (New Delhi: Oxford and IBH) vol. 2
- Misra R 1993 *Analysis, parameter estimation and operational control of canal systems*. Ph D thesis, Indian Institute of Science, Bangalore
- Paine J N 1992 Open channel flow algorithm in Newton–Raphson form. *J. Irrig. Drain. Div., Am. Soc. Civ. Eng.* 118: 306–319

- Ramakrishnan 1979 *Flow characteristics of rectangular and trapezoidal finite crest width weirs and triangular profile weirs*. Ph D thesis, Indian Institute of Science, Bangalore
- Rao A R, Vedula S, Thayumanavan S, Namboodiripad D 1994 Seepage effects on sand bed channels. *J. Irrig. Drain. Eng., Am. Soc. Civ. Eng.* 120: 60
- Schropp M, Fontijn H L 1989 Flow profiles for steady spatially varied flow—An explorative analysis. *J. Hydraul. Res.* 27: 135–147
- Subramanya K 1986 *Flow in open channels*. Revised edn, (New Delhi: Tata McGraw Hill)
- Uyumaz A, Smith R H 1991 Design procedure for flow over side weirs. *J. Irrig. Drain. Div., Am. Soc. Civ. Eng.* 117: 79
- Wachyan E, Rushton K R 1987 Water losses from irrigation canals. *J. Hydrol.* 92: 275–288



ERRATA

Analytical formulation of small signal stability analysis of power systems with nonlinear loads

R K RANJAN, M A PAI and P W SAUER

Sādhana, vol. 18, Part 5, 1993, pp. 869–889

1. Page 876: Equation (16) – add the following terms to the left hand side of equation

$$- I_{qio} V_{io} \sin(\delta_{io} - \theta_{io}) \Delta \delta_i + I_{qio} V_{io} \sin(\delta_{io} - \theta_{io}) \Delta \theta_i$$

2. Page 877: Third line from top – remove $k \neq i$ in the second term. It should read

$$- \sum_{k=1}^n V_{ko} Y_{ik} \cos(\theta_{io} - \theta_{ko} - \alpha_{ik})$$

3. Page 877: Sixth line from top – remove $k \neq i$ from second term and add $V_{io} Y_{ii} \sin \alpha_{ii}$.

Subject Index

- Airframe structural integrity
 Studies on fatigue crack growth for airframe structural integrity applications 247
- Algorithm *tri*
 Estimation of the order of an auto-regressive model 749
- Arch structures
 Some aspects of chaotic and stochastic dynamics for structural systems 583
- Auto-regressive process
 Estimation of the order of an auto-regressive model 749
- Averaging
 Higher order averaging method of coefficients in Fokker-Planck equation 373
- Bifurcation diagram
 Computation of the Kolmogorov entropy for MDOF systems 655
- Bifurcations
 Chaos in mechanical systems - A review 529
- Bifurcations
 Dynamical behaviour of a friction oscillator with simultaneous self and external excitation 627
- Bioleaching
 Growth and development of *Thiobacillus ferro-oxidans* for engineering applications 851
- Chaos
 Chaos in mechanical systems - A review
 Dynamical behaviour of a friction oscillator with simultaneous self and external excitation 627
 Non periodic flutter of a buckled composite panel 671
- Chaotic motion
 Computation of the Kolmogorov entropy for MDOF systems 655
- Chemical equilibrium/nonequilibrium flows
 High-temperature effects in hypersonic flows 781
- Chemoautotrophy
 Growth and development of *Thiobacillus ferro-oxidans* for engineering applications 851
- Classical modal analysis
 Analysis of the equations of motion of linearized controlled structures 709
- Cleavage mechanisms
 Stress corrosion cracking and component failure: Causes and prevention 165
- Cold-cracking
 Weldability and weld joint failures 213
- Complex response characteristics
 Random excitation of nonlinear elastic structures with internal resonances 403
- Continuum damage mechanics
 Mathematical modelling of creep/environment interactions 185
- Convex model
 Homology design of vibration mode shape under uncertain boundary conditions 441
- Corrosion/erosion rates
 Creep life extension of high temperature components under wall thinning conditions 331
- Cr-Mo/Cr-Mo-V steels
 Creep life extension of high temperature components under wall thinning conditions 331
- Crack tip opening displacement
 Application of fracture mechanics for weld integrity assessment 233
- Creep crack growth
 Creep crack growth in power plant materials 53
- Creep modelling
 Mathematical modelling of creep/environment interactions 185
- Creep resistant steels
 Remaining life assessment of high temperature components using threshold stress concept 87
- Creep strain damage
 Remaining life assessment of high temperature components using threshold stress concept 87
- Creep-fatigue crack growth
 Creep crack growth in power plant materials 53
- Creep-fatigue interaction
 High temperature low cycle fatigue 123
- Crystal rotation
 Mechanisms and modelling of creep in superalloys 287
- Crystallographic anisotropy
 Mechanisms and modelling of creep in superalloys 287
- Damage
 Mathematical modelling of creep/environment interactions 185
- Decohesion theory
 The effect of hydrogen induced cracking on the integrity of steel components 199

- Defects
 - Non-destructive testing and evaluation for structural integrity 5
- Degradation
 - Mathematical modelling of creep/environment interactions 185
- Diffusion
 - Mathematical modelling of creep/environment interactions 185
- Dissolution mechanisms
 - Stress corrosion cracking and component failure: Causes and prevention 165
- Drift force
 - Stochastic response of guyed tower under second-order wave force 513
- Duffing oscillator
 - Analysis of nonlinear structural dynamics by the concept of stability measure 615
- Dynamic response
 - Nonlinear dynamics of offshore structures under sea wave and earthquake forces 501
- Dynamic strain ageing
 - High temperature low cycle fatigue 123
- Embrittlement
 - The effect of hydrogen induced cracking on the integrity of steel components 199
- Environmental effects
 - High temperature low cycle fatigue 123
- Equivalence transformation
 - Analysis of the equations of motion of linearized controlled structures 709
- FP equation
 - Higher order averaging method of coefficients in Fokker-Planck equation 373
- Fatigue crack growth
 - Studies on fatigue crack growth for airframe structural integrity applications 247
- Finite element sensitivity analysis
 - Homology design of vibration mode shape under uncertain boundary conditions 441
- Finite-difference formulation
 - High-temperature effects in hypersonic flows 781
- First passage probability
 - Nonlinear dynamics of offshore structures under sea wave and earthquake forces 501
- Flow around cylinder
 - Three-dimensional vortex flow field around a circular cylinder in a quasi-equilibrium scour hole 871
- Fokker-Planck equation
 - Nonlinear deterministic and random response of shallow shells 427
- Fossil power plants
 - Life-assessment technology for fossil power plants 301
- Fractographic techniques
 - Studies on fatigue crack growth for airframe structural integrity applications 247
- Fracture mechanics
 - Application of fracture mechanics for weld integrity assessment 233
- Fracture toughness
 - Application of fracture mechanics for weld integrity assessment 233
- Friction oscillator
 - Dynamical behaviour of a friction oscillator with simultaneous self and external excitation 627
- Full-potential solution
 - Studies in multigrid acceleration of some equations of interest in fluid dynamics 887
- Fuzzy classification
 - Surface characterization and parameter estimation for industrial vision system 759
- Gas bubble formation
 - Mathematical modelling of creep/environment interactions 185
- Genetic manipulation
 - Growth and development of *Thiobacillus ferro-oxidans* for engineering applications 851
- Geometric surface fitting
 - Surface characterization and parameter estimation for industrial vision system 759
- Global stochastic bifurcations
 - Some aspects of chaotic and stochastic dynamics for structural systems 583
- Grain boundary precipitation
 - Stress corrosion cracking and component failure: Causes and prevention 165
- Grain boundary segregation
 - Stress corrosion cracking and component failure: Causes and prevention 165
- Hamilton's principle
 - On refined nonlinear theories of laminated composite structures with piezoelectric laminae 721
- Harmonic balance
 - Coupled in-line and transverse flow-induced structural vibration: Higher order harmonic solutions 691
- High temperature crack growth
 - Creep crack growth in power plant materials 53
- High temperature fatigue
 - Multiaxial fatigue - An overview 103
- Homology design
 - Homology design of vibration mode shape under uncertain boundary conditions 441
- Hot cracking
 - Weldability and weld joint failures 213
- Hydrodynamics
 - Three-dimensional vortex flow field around a circular cylinder in a quasi-equilibrium scour hole 871

- Hydrogen absorption
 - The effect of hydrogen induced cracking on the integrity of steel components 199
- Hydrogen-induced cracking
 - The effect of hydrogen induced cracking on the integrity of steel components 199
- Hypersonic flows
 - High-temperature effects in hypersonic flows 781
- Hysteretic structure
 - Stochastic control of hysteretic structural systems 475
- Implicit Euler Mil'shtein and balanced methods
 - Effects of distributed delays on the stability of structures under seismic excitation and multiplicative noise 451
- In-phase out-of-phase fatigue
 - Multiaxial fatigue – An overview 103
- Integrity assessment
 - Application of fracture mechanics for weld integrity assessment 233
- Internal resonances
 - Random excitation of nonlinear elastic structures with internal resonances 403
- Iron oxidation
 - Growth and development of *Thiobacillus ferrooxidans* for engineering applications 851
- Irrigation canals
 - Steady flow simulation in irrigation canals 955
- Isotropic/anisotropic model
 - Mechanisms and modelling of creep in superalloys 287
- J-integral
 - Application of fracture mechanics for weld integrity assessment 233
- Kolmogorov entropy
 - Computation of the Kolmogorov entropy for MDOF systems 655
- Lagrangian coordinates
 - Analysis of the equations of motion of linearized controlled structures 709
- Laminated composite plates
 - Nonperiodic flutter of a buckled composite panel 671
- Laminated composite structures
 - On refined nonlinear theories of laminated composite structures with piezoelectric laminae 721
- Laplace equation
 - Studies in multigrid acceleration of some equations of interest in fluid dynamics 887
- Life assessment
 - Non-destructive testing and evaluation for structural integrity 5
 - Life assessment
 - Multiaxial fatigue – An overview 103
 - Life extension strategies
 - Life-assessment technology for fossil power plants 301
 - Life of power plants
 - Creep crack growth in power plant materials 53
 - Life prediction techniques
 - High temperature low cycle fatigue 123
 - Life-assessment technology
 - Life-assessment technology for fossil power plants 301
- Line profile analysis
 - Residual stresses of types II and III and their estimation 39
- Linearized control structures
 - Analysis of the equations of motion of linearized controlled structures 709
- Low cycle fatigue
 - High temperature low cycle fatigue 123
 - Mechanisms and modelling of creep in superalloys 287
- Lyapunov exponent
 - Some aspects of chaotic and stochastic dynamics for structural systems 583
- Melnikov analysis
 - Some aspects of chaotic and stochastic dynamics for structural systems 583
- Microstrain
 - Residual stresses of types II and III and their estimation 39
- Microstresses
 - Residual stresses of types II and III and their estimation 39
- Microstructures
 - Non-destructive testing and evaluation for structural integrity 5
- Moore-Penrose generalized inverse
 - Homology design of vibration mode shape under uncertain boundary conditions 441
- Multiaxial fatigue
 - Multiaxial fatigue – An overview 103
- Multibody systems
 - Analysis of nonlinear structural dynamics by the concept of stability measure 615
- Multigrid
 - Studies in multigrid acceleration of some equations of interest in fluid dynamics 887
- Multiple pulsation
 - Development of picosecond time resolution optical and X-ray streak cameras 937
- Navier-Stokes solution
 - Studies in multigrid acceleration of some equations of interest in fluid dynamics 887

- Nickel base superalloy
 - Mechanisms and modelling of creep in superalloys 287
- Non-destructive evaluation
 - Non-destructive testing and evaluation for structural integrity 5
- Non-periodic motion
 - Nonperiodic flutter of a buckled composite panel 671
- Non-smooth systems
 - Dynamical behaviour of a friction oscillator with simultaneous self and external excitation 627
- Nonlinear dynamics
 - Some aspects of chaotic and stochastic dynamics for structural systems 583
- Nonlinear elastic structures
 - Random excitation of nonlinear elastic structures with internal resonances 403
- Nonlinear hydrodynamic damping
 - Nonlinear dynamics of offshore structures under sea wave and earthquake forces 501
- Nonlinear systems
 - Methods of nonlinear random vibration analysis 345
 - Chaos in mechanical systems – A review 529
- Nonlinear vehicle model
 - Active control of non-stationary response of a two-degree of freedom vehicle model with nonlinear suspension 489
- Nonlinear vibration
 - Methods of nonlinear random vibration analysis 345
 - Transient and stationary response statistics of van der Pol oscillators subjected to broad band random excitation 389
 - Nonlinear deterministic and random response of shallow shells 427
 - Stochastic response of guyed tower under second-order wave force 513
- Nonstationary response
 - Active control of non-stationary response of a two-degree of freedom vehicle model with nonlinear suspension 489
- Numerical methods
 - Effects of distributed delays on the stability of structures under seismic excitation and multiplicative noise 451
- Numerical simulation
 - Numerical simulation of a 2-D jet-crossflow interaction related to film cooling applications: Effects of blowing rate, injection angle and free-stream turbulence 915
- Occlusion
 - Surface characterization and parameter estimation for industrial vision system 759
- Offshore guyed tower
 - Stochastic response of guyed tower under second-order wave force 513
- Offshore structure
 - Nonlinear dynamics of offshore structures under sea wave and earthquake forces 501
- Offshore structures
 - Coupled in-line and transverse flow-induced structural vibration: Higher order harmonic solutions 691
- Open channels
 - Steady flow simulation in irrigation canals 955
- Optical and X-ray streak cameras
 - Development of picosecond time resolution optical and X-ray streak cameras 937
- Optimal control
 - Active control of non-stationary response of a two-degree of freedom vehicle model with nonlinear suspension 489
- Order estimation
 - Estimation of the order of an auto-regressive model 749
- Order statistics
 - Estimation of the order of an auto-regressive model 749
- Panel flutter
 - Nonperiodic flutter of a buckled composite panel 671
- Parameter estimation
 - Surface characterization and parameter estimation for industrial vision system 759
- Picosecond time resolution
 - Development of picosecond time resolution optical and X-ray streak cameras 937
- Piezoelectric laminae
 - On refined nonlinear theories of laminated composite structures with piezoelectric laminae 721
- Planar/axisymmetric flows
 - High-temperature effects in hypersonic flows 781
- Plural criteria
 - Estimation of the order of an auto-regressive model 749
- Power plant applications
 - Creep crack growth in power plant materials 53
- Preventive measures
 - Stress corrosion cracking and component failure: Causes and prevention 165
- Primary resonance
 - Nonlinear deterministic and random response of shallow shells 427
- Profile fitting
 - Residual stresses of types II and III and their estimation 39
- Radar absorbing materials (RAM)
 - Trends in radar absorbing materials technology 815

- Radar cross section (RCS) reduction
 - Trends in radar absorbing materials technology 815
- Rainflow technique
 - Studies on fatigue crack growth for airframe structural integrity applications 247
- Random excitation
 - Methods of nonlinear random vibration analysis 345
 - Random excitation of nonlinear elastic structures with internal resonances 403
- Random oscillations
 - Effects of distributed delays on the stability of structures under seismic excitation and multiplicative noise 451
- Random response
 - Transient and stationary response statistics of van der Pol oscillators subjected to broad band random excitation 389
- Random vibration
 - Higher order averaging method of coefficients in Fokker-Planck equation 373
- Range image
 - Surface characterization and parameter estimation for industrial vision system 759
- Reaction-front kinetics
 - Mathematical modelling of creep/environment interactions 185
- Reference stress
 - Creep life extension of high temperature components under wall thinning conditions 331
- Refined nonlinear theory
 - On refined nonlinear theories of laminated composite structures with piezoelectric laminae 721
- Remaining life
 - Remaining life assessment of high temperature components using threshold stress concept 87
- Repassivation
 - Stress corrosion cracking and component failure: Causes and prevention 165
- Residual stresses
 - Residual stresses of types II and III and their estimation 39
- Rupture life
 - Creep life extension of high temperature components under wall thinning conditions 331
- Rupture strength
 - Creep life extension of high temperature components under wall thinning conditions 331
- SCC tests
 - Stress corrosion cracking and component failure: Causes and prevention 165
- Scouring
 - Three-dimensional vortex flow field around a circular cylinder in a quasi-equilibrium scour hole 871
- Second-order wave force
 - Stochastic response of guyed tower under second-order wave force 513
- Seismic excitation
 - Effects of distributed delays on the stability of structures under seismic excitation and multiplicative noise 451
- Self-excitation
 - Dynamical behaviour of a friction oscillator with simultaneous self and external excitation 627
- Service exposure
 - Creep life extension of high temperature components under wall thinning conditions 331
- Shallow shells
 - Nonlinear deterministic and random response of shallow shells 427
- Shape change
 - Mechanisms and modelling of creep in superalloys 287
- Shear deformation
 - Nonperiodic flutter of a buckled composite panel 671
- Single crystal turbine blade
 - Mechanisms and modelling of creep in superalloys 287
- Slot-film cooling
 - Numerical simulation of a 2-D jet-crossflow interaction related to film cooling applications: Effects of blowing rate, injection angle and free-stream turbulence 915
- Snap-buckling
 - Nonlinear deterministic and random response of shallow shells 427
- Snap-through
 - Nonlinear deterministic and random response of shallow shells 427
- Stability assessment
 - Analysis of nonlinear structural dynamics by the concept of stability measure 615
- Steady flow
 - Steady flow simulation in irrigation canals 955
- Stick-slip vibrations
 - Dynamical behaviour of a friction oscillator with simultaneous self and external excitation 627
- Stochastic characteristics
 - Stochastic response of guyed tower under second-order wave force 513
- Stochastic differential equations
 - Effects of distributed delays on the stability of structures under seismic excitation and multiplicative noise 451
- Stochastic estimate
 - Stochastic control of hysteretic structural systems 475
- Stochastic excitation
 - Transient and stationary response statistics of van der Pol oscillators subjected to broad band random excitation 389

- Stochastic linearization
 - Stochastic control of hysteretic structural systems 475
 - Active control of non-stationary response of a two-degree of freedom vehicle model with non-linear suspension 489
- Stochastic optimal control
 - Stochastic control of hysteretic structural systems 475
- Stochastic stability
 - Effects of distributed delays on the stability of structures under seismic excitation and multiplicative noise 451
- Strange attractors
 - Chaos in mechanical systems - A review 529
- Stress corrosion cracking
 - Stress corrosion cracking and component failure: Causes and prevention 165
- Stress intensity factor
 - Application of fracture mechanics for weld integrity assessment 233
- Stress rupture tests
 - Creep life extension of high temperature components under wall thinning conditions 331
- Stress-strain parameters
 - Multiaxial fatigue - An overview 103
- Stresses
 - Non-destructive testing and evaluation for structural integrity 5
- Structural integrity
 - Non-destructive testing and evaluation for structural integrity 5
- Sulphur oxidation
 - Growth and development of *Thiobacillus ferrooxidans* for engineering applications 851
- Thermochemical loading
 - On refined nonlinear theories of laminated composite structures with piezoelectric laminae 721
- Thiobacillus ferrooxidans*
 - Growth and development of *Thiobacillus ferrooxidans* for engineering applications 851
- Three-dimensional flow
 - Three-dimensional vortex flow field around a circular cylinder in a quasi-equilibrium scour hole 871
- Threshold stress
 - Remaining life assessment of high temperature components using threshold stress concept 87
- Time-temperature parameter
 - Creep life extension of high temperature components under wall thinning conditions 331
- Truss structure
 - Computation of the Kolmogorov entropy for MDOF systems 655
- Turbulent flow
 - Numerical simulation of a 2-D jet-crossflow interaction related to film cooling applications: Effects of blowing rate, injection angle and free-stream turbulence 915
- Uncertain boundary conditions
 - Homology design of vibration mode shape under uncertain boundary conditions 441
- Van der Pol oscillator
 - Transient and stationary response statistics of van der Pol oscillators subjected to broad band random excitation 389
- Velocity profiles
 - Three-dimensional vortex flow field around a circular cylinder in a quasi-equilibrium scour hole 871
- Vibration analysis
 - Methods of nonlinear random vibration analysis 345
- Vibration mode shape
 - Homology design of vibration mode shape under uncertain boundary conditions 441
- Vibrations
 - Coupled in-line and transverse flow-induced structural vibration: Higher order harmonic solutions 691
- Vortex dynamics
 - Coupled in-line and transverse flow-induced structural vibration: Higher order harmonic solutions 691
- Vortex flow
 - Three-dimensional vortex flow field around a circular cylinder in a quasi-equilibrium scour hole 871
- Weak and strong time delay
 - Effects of distributed delays on the stability of structures under seismic excitation and multiplicative noise 451
- Weld failures
 - Weldability and weld joint failures 213
- Weld repair
 - Weldability and weld joint failures 213
- Weldability
 - Weldability and weld joint failures 213
- Welding
 - Application of fracture mechanics for weld integrity assessment 233
- White noise
 - Higher order averaging method of coefficients in Fokker-Planck equation 373

Author Index

- Anh N D
Higher order averaging method of coefficients in
Fokker-Planck equation 373
- Baldev Raj
Non-destructive testing and evaluation for struc-
tural integrity 5
- Bhawalkar D D
see Rai V N 937
- Bisht R S
see Datta T K 513
- Biswas P K
see Jagdish S 759
- Bontempi F
Computation of the Kolmogorov entropy for
MDOF systems 655
- Bose T K
see Sarkar S 915
- Casciati F
see Bontempi F 655
- Chandiramani N K
Non-periodic flutter of a buckled composite panel
671
- Chandrasekharaiah M N
Weldability and weld joint failures 213
- Chatterjee U K
Stress corrosion cracking and component failure:
Causes and prevention 165
- Chatterji B N
see Jagdish S 759
- Chattopadhyay L
see Ghosh R N 331
- Chattoraj I
The effect of hydrogen induced cracking on the
integrity of steel components 199
- Chaudhuri S
see Ghosh R N 331
- Datta T K
Stochastic response of guyed tower under second-
order wave force 513
- Dey S
Three-dimensional vortex flow field around a cir-
cular cylinder in a quasi-equilibrium scour hole 871
- Doyle M M
see Sri Namachchivaya N 583
- Dyson B F
Mathematical modelling of creep/environment
interactions 185
- Ghanem R
Coupled in-line and transverse flow-induced
structural vibration: Higher order harmonic sol-
utions 691
- Ghosh R N
see McLean M 287
- Grover P S
Creep crack growth in power plant materials 53
- Hegstad B K
see Naess A 389
- Heuer R
Nonlinear deterministic and random response of
shallow shells 427
- Hinrichs N
see Popp K 627
- Hu B
see Schiehlen W 615
- Ibrahim R A
Random excitation of nonlinear elastic structures
with internal resonances 403
- Irschik H
see Heuer R 427
- Iyengar R N
Foreword 341
- Jagdish S
Surface characterisation and parameter estimation
for industrial vision system 759
- Jain A K
see Datta T K 513
- Jayakumar T
see Baldev Raj 5
- Jha R M
see Vinoy K J 815
- Karmeshu
Effects of distributed delays on the stability of
structures under seismic excitation and multi-
plicative noise 451
- Kawano K
see Venkataramana K 501

- Lee B H
 see Ibrahim R A 403
- Librescu L
 see Chandiramani N K 671
- Ma F
 Analysis of the equations of motion of linearized controlled structures 709
- Malhotra N
 see Sri Namachchivaya N 583
- Mannan S L
 see Rodriguez P 123
- Manohar C S
 Methods of nonlinear random vibration analysis 345
- McLean M
 Mechanisms and modelling of creep in superalloys 287
- Misra R
 Steady flow simulation in irrigation canals 955
- Mitchell J A
 see Reddy J N 721
- Moharir P S
 see Rao N S 749
- Mukherjee J
 see Jagdish S 759
- Mukhopadhyay S
 Growth and development of *Thiobacillus ferro-oxidans* for engineering applications 851
- Naess A
 Transient and stationary response statistics of van der Pol oscillators subjected to broad band random excitation 389
- Nair P K
 Residual stresses of types II and III and their estimation 39
- Nakagiri S
 Homology design of vibration mode shape under uncertain boundary conditions 441
- Narayanan S
 see Raju G V 489
 see Sekar P 529
- Natarajan K A
 see Mukhopadhyay S 851
- Oestreich M
 see Popp K 627
- Osgerby S
 see Dyson B F 185
- Pan L M
 see McLean M 287
- Pant H C
 see Rai V N PE 631
- Plaut R H
 see Chandiramani N K 671
- Popp K
 Dynamical behaviour of a friction oscillator with simultaneous self and external excitation 627
- Prabhu D K
 High-temperature effects in hypersonic flows 781
- Radhakrishnan V M
 Multiaxial fatigue - An overview 103
- Rai V N
 Development of picosecond time resolution optical and X-ray streak cameras 937
- Raju G V
 Active control of non-stationary response of a two-degree of freedom vehicle model with nonlinear suspension 489
- Ranganath V R
 Application of fracture mechanics for weld integrity assessment 233
- Rao B P C
 see Baldev Raj 5
- Rao N S
 Estimation of the order of an auto-regressive model 749
- Rao P R
 Foreword 1
- Reddy J N
 On refined nonlinear theories of laminated composite structures with piezoelectric laminae 721
- Rodriguez P
 High temperature low cycle fatigue 123
- Roy N
 see Ghosh R N 331
- Sarkar S
 Numerical simulation of a 2-D jet-crossflow interaction related to film cooling applications: Effects of blowing rate, injection angle and free-stream turbulence 915
- Saxena A
 see Grover P S 53
- Schiehlen W
 Analysis of nonlinear structural dynamics by the concept of stability measure 615
- Schurz H
 see Karmeshu 451
- Sekar P
 Chaos in mechanical systems - A review 529
- Shukla M
 see Rai V N 937
- Singh J P
 Studies in multigrid acceleration of some equations of interest in fluid dynamics 887
- Singh R
 Remaining life assessment of high temperature components using threshold stress concept 87
- Spanos P
 see Ghanem R 691

otic and stochastic dynamics
18 583

crack growth for airframe
applications 247

f hysteretic structural systems
475

Venka. Ramana K

Nonlinear dynamics of offshore structures under
sea wave and earthquake forces 501

Vinoy K J

Trends in radar absorbing materials technology
815

Viswanathan R

Life-assessment technology for fossil power plants
301